



12th INTERNATIONAL CONFERENCE
ON HIGH-POWER PARTICLE BEAMS

BEAMS'98

HAIFA, ISRAEL, JUNE 7-12, 1998

PROCEEDINGS - VOLUME I



**EDITED BY:
MEIR MARKOVITS
AND
JOSEPH SHILOH**



REPORT DOCUMENTATION PAGE

Form Approved OMB No. 0704-0188

Public reporting burden for this collection of information is estimated to average 1 hour per response, including the time for reviewing instructions, searching existing data sources, gathering and maintaining the data needed, and completing and reviewing the collection of information. Send comments regarding this burden estimate or any other aspect of this collection of information, including suggestions for reducing this burden to Washington Headquarters Services, Directorate for Information Operations and Reports, 1215 Jefferson Davis Highway, Suite 1204, Arlington, VA 22202-4302, and to the Office of Management and Budget, Paperwork Reduction Project (0704-0188), Washington, DC 20503.

1. AGENCY USE ONLY (Leave blank)		2. REPORT DATE 1998	3. REPORT TYPE AND DATES COVERED 7-12 June 1998 Final Report
4. TITLE AND SUBTITLE International Conference on High-Power Particle Beams (12 th) (BEAMS'98). Held in Haifa, Israel on June 7-12, 1998. Proceedings, Volume 1.			5. FUNDING NUMBERS
6. AUTHOR(S) Meir Markovits and Joseph Shiloh, Editors			
7. PERFORMING ORGANIZATION NAME(S) AND ADDRESS(ES)			8. PERFORMING ORGANIZATION REPORT NUMBER ISBN 0-7803-4287-9
9. SPONSORING/MONITORING AGENCY NAME(S) AND ADDRESS(ES) Office of Naval Research, European Office PSC 802 Box 39 FPO AE 09499-0039			10. SPONSORING/MONITORING AGENCY REPORT NUMBER
11. SUPPLEMENTARY NOTES See also Volume 2. This work relates to Department of the Navy Grant issued by the Office of Naval Research International Field Office. The United States has a royalty free license throughout the world in all copyrightable material contained herein.			
12a. DISTRIBUTION/AVAILABILITY STATEMENT Approved for Public Release; Distribution Unlimited. U.S. Government Rights License. All other rights reserved by the copyright holder.			12b. DISTRIBUTION CODE A
12. ABSTRACT (Maximum 200 words) This is volume 1 of 2 of the Proceedings of the 12 th International Conference on High-Power Particle Beams (BEAMS'98) held in Haifa, Israel on June 7-12, 1998. The conference covered all topics relevant to the physics and technology of intense beams of charge particles and included sessions devoted to pulsed power and accelerator technology, ion beams and diodes, ICF, electron beams generation and propagation, radiation sources, HPM, beam-matter sources, z-pinchs and explosive generations. Special emphasis was given to newly emerging fields and industrial application.			
13. SUBJECT TERMS ONR, Foreign reports, Conferences, High-power particle beams			15. NUMBER OF PAGES
			16. PRICE CODE
17. SECURITY CLASSIFICATION OF REPORT UNCLASSIFIED	18. SECURITY CLASSIFICATION OF THIS PAGE UNCLASSIFIED	19. SECURITY CLASSIFICATION OF ABSTRACT UNCLASSIFIED	20. LIMITATION OF ABSTRACT UL

NSN 7540-01-280-5500

Standard Form 298 (Rev. 2-89)
Prescribed by ANSI Std. Z39-18
298-102

20011203 230



BEAMS'98

*The Organizing Committee thanks the
following organizations
for their support of BEAMS'98:*

SPONSORS

Naval Research Laboratory, **USA**
Office of Naval Research, **USA**
European Office of Naval Research, **USA**
Sandia National Laboratories, **USA**
Los Alamos National Laboratory, **USA**
Primex Physics International, **USA**
Maxwell Technologies, **USA**
Nichicon Corporation, **Japan**
Nissin Electric Corporation, **Japan**
Nissin High Voltage Corporation, **Japan**
ESC Medical Systems, **Israel**
Ministry of Defense, **Israel**
Rafael, **Israel**
Haifa Municipality

TECHNICAL CO-SPONSORS



IEEE

IEEE Electron Devices Society, **USA**
American Physical Society, **USA**

HOSTED BY



BEAMS'98 - PROCEEDINGS OF THE 12th INTERNATIONAL CONFERENCE
ON HIGH POWER PARTICLE BEAMS

IEEE Catalog Number:
ISBN:

98EX103
0-7803-4287-9 Microfiche Edition



BEAMS'98

PROCEEDINGS OF THE
12th INTERNATIONAL CONFERENCE
ON HIGH-POWER PARTICLE BEAMS



Edited By:
Meir Markovits
and Joseph Shiloh
Rafael, Haifa

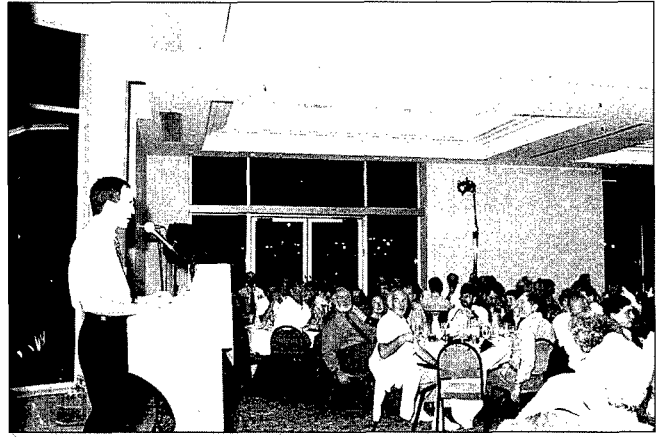
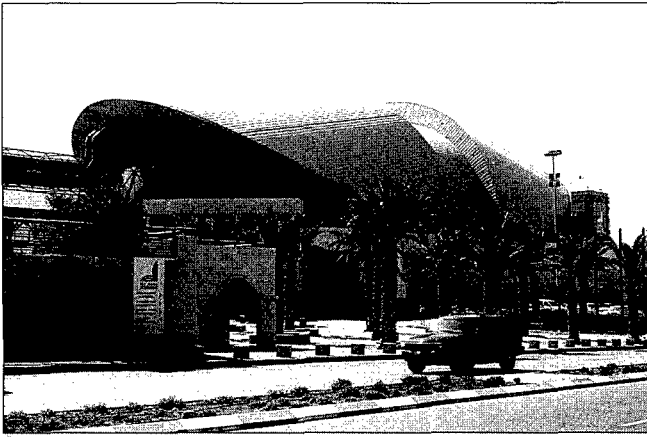
AQ F02-02-0277

U.S. Government Rights License

This work relates to Department of the Navy Grant or Contract issued by Office of Naval Research (ONR) International Field Office-Europe. The United States Government has a royalty-free license throughout the world in all copyrightable material contained herein.

TABLE OF CONTENTS

VOLUME I	Page No.
COMMITTEES	VII
LETTER FROM THE CHAIRMEN	IX
BEAMS PRIZES AWARD	X
LIST OF PROCEEDINGS	XI
ORALS	1
PULSED POWER AND ACCELERATOR TECHNOLOGY	3
ELECTRON BEAM GENERATION AND PROPAGATION	19
DIAGNOSTICS AND EXPERIMENTAL METHODS	39
RADIATION SOURCES, HPM	53
X-RAY SOURCES, Z PINCHES AND EXPLOSIVE GENERATORS	69
BEAM-MATTER INTERACTION AND INDUSTRIAL APPLICATIONS	103
ELECTRON BEAM GENERATION AND PROPAGATION	125
RADIATION SOURCES, HPM	143
PULSED POWER AND ACCELERATOR TECHNOLOGY	163
MODELS AND SIMULATIONS	183
ION BEAMS AND DIODES, ICF	193
X-RAY SOURCES, Z PINCHES AND EXPLOSIVE GENERATORS	227
POSTERS	249
PULSED POWER AND ACCELERATOR TECHNOLOGY	251
ELECTRON BEAM GENERATION AND PROPAGATION	355
DIAGNOSTICS AND EXPERIMENTAL METHODS	445
MODELS AND SIMULATIONS	511
AUTHOR INDEX	XXXI
 VOLUME II	
LIST OF PROCEEDINGS	VII
POSTERS continued	
X-RAY SOURCES, Z PINCHES AND EXPLOSIVE GENERATORS	565
RADIATION SOURCES, HPM	681
ION BEAMS AND DIODES, ICF	905
BEAM-MATTER INTERACTION AND INDUSTRIAL APPLICATIONS	959
BEAMS STATISTICS	1060
LIST OF PARTICIPANTS	XXVII
AUTHOR INDEX	XLV





COMMITTEES

CONFERENCE CHAIRMAN

Joseph Shiloh Rafael, *Israel*

CO-CHAIRMAN

Meir Markovits Rafael, *Israel*

ORGANIZING COMMITTEES

INTERNATIONAL ADVISORY COMMITTEE

A. Blaugrund	The Weizmann Institute of Science, <i>Israel</i>
H. Bluhm	Forschungszentrum Karlsruhe, <i>Germany</i>
T. Coffey	Naval Research Laboratory, <i>USA</i>
D. Cook	Sandia National Laboratories, <i>USA</i>
G. Cooperstein	Naval Research Laboratory, <i>USA</i>
H. Doucet	C.E.A. Ecole Polytechnique, <i>France</i>
V. Fortov	Academy of Sciences, <i>Russia</i>
K. Jungwirth	Academy of Sciences, <i>Czech Republic</i>
G. Kessler	Forschungszentrum Karlsruhe, <i>Germany</i>
V. Koidan	Budker Institute of Nuclear Physics, <i>Russia</i>
A. Kolb	Maxwell Technologies Inc., <i>USA</i>
G. Mesyats	Academy of Sciences, <i>Russia</i>
D. Rej	Los Alamos National Laboratory, <i>USA</i>
J. Shiloh	Rafael, <i>Israel</i>
V. Smirnov	Triniti Troitsk, <i>Russia</i>
C. Stallings	Primex Physics International, <i>USA</i>
R. Sudan	Cornell University, <i>USA</i>
R. White	Maxwell Technologies Inc., <i>USA</i>
K. Yatsui	Nagaoka University of Technology, <i>Japan</i>
G. Yonas	Sandia National Laboratories, <i>USA</i>

TECHNICAL / PROGRAM COMMITTEE

J. Benford	Microwave Sciences, <i>USA</i>
A. Fisher	Naval Research Laboratory, <i>USA</i>
V. Granatstein	University of Maryland, <i>USA</i>
D. Hinshelwood	Naval Research Laboratory, <i>USA</i>
H. Kirbie	Lawrence Livermore Laboratory, <i>USA</i>
F. Mako	FM Technologies, <i>USA</i>
Y. Maron	The Weizmann Institute of Science, <i>Israel</i>
T.A. Mehlhorn	Sandia National Laboratories, <i>USA</i>
N.R. Pereira	Berkeley Research Associates, <i>USA</i>
J. Ma Pierre	Defense Special Weapons Agency, <i>USA</i>
J.P. Quintenz	Sandia National Laboratories, <i>USA</i>
C. Roberson	Office of Naval Research, <i>USA</i>
L. Rudakov	Kurchatov Institute, <i>Russia</i>
L. Shachter	Technion - I.T.T., <i>Israel</i>
P. Sincerny	Primex Physics International, <i>USA</i>

LOCAL STEERING COMMITTEE

S. Eckhouse	ESC Medical Systems, <i>Israel</i>
B. Etlicher	Ecole Polytechnique, <i>France</i>
J. Felsteiner	Technion - I.T.T., <i>Israel</i>
A. Gover	Tel Aviv University, <i>Israel</i>
Y. Krasik	Technion - I.T.T., <i>Israel</i>
B. Mandelbaum	Rafael, <i>Israel</i>
M. Markovits	Rafael, <i>Israel</i>
W. Peter	FM Technologies, <i>USA</i>
D. Shvarts	NNRC, <i>Israel</i>
A. Sternlieb	Ministry of Defense, <i>Israel</i>
J. Ullschmied	Academy of Sciences, <i>Czech Republic</i>
A. Zigler	The Hebrew University of Jerusalem, <i>Israel</i>
Z. Zinamon	The Weizmann Institute of Science, <i>Israel</i>



BEANZ'98





LETTER FROM THE CHAIRMEN

The 12th International Conference on High-Power Particle Beams (BEAMS'98) took place in Haifa, Israel, during June 7-12, 1998. The Conference sessions were held at the new Haifa International Exhibition & Convention Center in the traditional BEAMS format, with oral (invited and contributed) presentations - without parallel sessions, and daily poster presentations. The Conference covered all topics relevant to the physics and technology of intense beams of charged particles and included sessions devoted to pulsed power and accelerator technology, ion beams and diodes, ICF, electron beams generation and propagation, radiation sources, HPM, beam-matter interaction and industrial applications, diagnostics and experimental methods, models and simulations, x-ray sources, z-pinchs and explosive generators. Special emphasis was given to newly emerging fields and industrial applications. Approximately 400 papers were presented (347 posters and 56 oral presentations), by 273 participants from 19 countries, (BEAMS'98 statistics are presented in Vol. 2 of these proceedings). Unfortunately, only 240 papers were submitted for inclusion in the Proceedings, in spite of numerous extensions of the deadline and several appeals to the authors.

At the opening ceremony, participants were welcomed by the Conference Chairmen as well as by Prof. Jacob Ziv, President of the Israel National Academy of Science and the Humanities. Social events included a get together reception on Sunday evening, on Tuesday evening a guided tour of the ancient city of Ceasaria on the Mediterranean sea followed by an unforgettable Roman feast, the setting being identical to that of feasts attended by the Roman Emperor 2000 years ago. An impressive farewell banquet was enjoyed by all on the last evening with a performance by a talented violinist and an opera singer. During the Banquet a lecture was given by Prof. Yakir Aharonov from Tel Aviv University on "What can we learn from modern physics about ourselves".

A new tradition (if one does not count the included lunches) was launched at BEAMS'98 with Gerold Yonas and Amnon Fisher receiving awards at an official BEAMS Prize ceremony. In addition to the rewarding scientific meeting and social events, the participants enjoyed pleasant sunny weather in Haifa and other parts of Israel, during the 50th anniversary of the State of Israel. Some participants also attended the Conference on High-Power Electromagnetics (EUROEM'98), held in Tel Aviv in the week following BEAMS'98.

We wish to thank all participants and those who contributed to the success of this Conference. In particular, we acknowledge the assistance of the following:

Session chairpersons R.Arad, A.E.Blaugrund, H.Bluhm, A.Deutsch, A.N.Didenko, V.E.Fortov, H.T.Hawkins, K.Jungwirth, Ya.E.Krasik, B.R.Kusse, B.Levush, G.A.Mesyats, I.Navon, N.R.Pereira, J.P.Quintenz, D.J.Rej, C.H.Stallings, R.White, K.Yatsui and G.Yonas;


Concluding panel discussion moderator D.Cook and panel members H.Bluhm, G.Cooperstein, A.Gover, Y.Maron, G.A.Mesyats, J.P.Quintenz, and D.J.Rej.

We are indebted to staff members of KENES Organizers of Congress and Tour Operators Ltd. Special thanks are due to Benny Mandelbaum and Yakov Krasik and last but not least to our wives Hanna and Zvia.

See you all at BEAMS'2000 in Nagaoka.

Joseph Shiloh

Joseph Shiloh
Conference Chairman


Meir Markovitz

Meir Markovits
Conference Co-Chairman

1998 BEAMS PRIZES AWARD

A new tradition was launched at BEAMS'98 in Haifa, the award of the BEAMS Prizes. The Prizes were awarded at the farewell banquet by Roger White, Chairman of the BEAMS'98 Prize Committee, Joseph Shiloh, Chairman of BEAMS'98 Conference, and Meir Markovits, Co-Chairman of BEAMS'98 Conference.

The 1998 BEAMS Prizes were awarded to:

Amnon Fisher for

Major scientific and technological contributions to the field of High-Power Particle Beams and Z-Pinch,

And to:

Gerald Yonas for

Starting the BEAMS Conferences in 1975 and making original contributions as well as helping to create the field of Beams and sustaining it over the years.

Following the citations by the prize committee chairman, the prize winners had a few words in response:

Amnon's response: ...Listening to the citation I am like a bride coming from the beauty parlor, hardly recognizable. Let me say a few words about the two most important aspects of the way I work: First, I thrive on cooperation. I may be good but not that good. I need the interaction with other people, their ideas, questions and criticism. In all the places I have worked in my life, RAFAEL, Cornell University, UC Irvine and NRL, I have had very good times and some hard times. I owe my success to the people in those places with whom I interacted with and they deserve as much credit as I am getting here tonight. Second, I learned to fail. I can probably count all my good ideas on one hand. Many hands are needed to count all the ideas that went to nowhere. Failing is difficult, sometimes a week, a month, or a year is lost and it is a painful experience. However doing science is like training for a marathon. One cannot learn to run in an armchair. The blisters, the muscle pain, the shortness of breath are all needed before one can cross the finish line. I had many failures, however the few successes were worth all the agony and pain.

Gerry's response: ...I am honored and delighted to be recognized for the BEAMS award by my colleagues primarily of their acceptance of my jokes and the tolerance for my longevity. I want to express my gratitude to all of you with whom I have worked over the years for all the opportunities to learn together and share the excitement of discovery that comes with working in this field. One important individual has been a friend, a mentor, and a teacher, and that person is Charlie Martin. I want to wish him good health and continued participation with all of us as we go forward. Lastly and most important, I want to acknowledge the support and encouragement I have had from my wife and family who have always been there for me.





BEAMS'98

12th INTERNATIONAL CONFERENCE
ON HIGH-POWER PARTICLE BEAMS



LIST OF PROCEEDINGS

Vol. I

VOLUME 1

ORALS

PULSED POWER AND ACCELERATOR TECHNOLOGY

- COMPARISON OF POS-LOAD DYNAMICS USING DIFFERENT PLASMA SOURCES ON HAWK
B.V. Weber, D.C. Black, B. Moosman, S.J. Stephanakis, D.D. Hinshelwood, R.J. Commisso,
S.B. Swanekamp, J.W. Schumer, P.F. Ottinger, Naval Research Laboratory, Washington DC,
J.J. Moschella, C. Vidoli, HY-Tech Research Corp., Radford VA, USA 5
- PULSED POWER FUSION PROGRAM UPDATE
J.P. Quintenz, R.G. Adams, G.O. Allshouse, J.E. Bailey, D.D. Bloomquist, G.A. Chandler, R.S. Coats,
D.L. Cook, M.E. Cuneo, C. Deeney, M.S. Derzon, M.P. Desjarlais, M.R. Douglas, D.L. Fehl, A.B. Filuk,
T.A. Haill, D.L. Hanson, D.J. Johnson, M.L. Kiefer, J.S. Lash, R.J. Leeper, B.M. Marder, M.K. Matzen,
D.H. McDaniel, E.J. McGuire, T.A. Melhorn, L.P. Mix, A.R. Mots, T.J. Nash, C.L. Olson, R.E. Olson,
T.D. Pointon, J.L. Porter, C.L. Ruiz, T.W.L. Sanford, J.F. Seamen, D.B. Seidel, S.A. Slutz,
R.B. Spielman, W.A. Stygar, M.A. Sweeney, R.A. Vesey, D.F. Wenger, Sandia National Laboratories,
Albuquerque NM, USA 9
- URT-0,5 REPETITIVE PULSED ELECTRON ACCELERATOR
Yu.A. Kotov, S.Yu. Sokovnin, Russian Academy of Sciences, Ekaterinburg, Russia 15

ELECTRON BEAM GENERATION AND PROPAGATION

- CRITICAL ELECTRON-HOLE PROCESSES IN DIELECTRIC INDUCED BY SYNCHRONOUS ACTION
OF HIGH ELECTRIC FIELD AND HIGH-CURRENT-DENSITY ELECTRON BEAM
D.I. Vaisburd, Tomsk Polytech University, Tomsk, Russia 21
- ROD PINCH ELECTRON BEAM DIODES AS X-RAY RADIOGRAPHY SOURCES
G. Cooperstein, R.J. Commisso, D.D. Hinshelwood, P.F. Ottinger, S.J. Stephanakis, Naval Research
Laboratory, Washington DC, D.V. Rose, S.B. Swanekamp, F.C. Young, Jaycor, Vienna VA, USA 31
- DENSE PLASMA HEATING BY 200 KJ-ELECTRON BEAM AT THE GOL-3-II FACILITY
A.V. Arzhannikov, V.T. Astrelin, A.V. Burdakov, V.G. Ivanenko, V.S. Koidan, V.V. Koryukhov,
K.I. Mekler, P.I. Melnikov, V.S. Nikolaev, S.V. Polosatkin, V.V. Postupaev, A.F. Rovenskikh, S.L. Sinitsky,
Budker Institute of Nuclear Physics, Novosibirsk, Russia 35

DIAGNOSTICS AND EXPERIMENTAL METHODS

- ION LOSSES IN EXPANDED LASER-PRODUCED PLASMA
J. Krasa, L. Laska, K. Rohlena, M. Pfeifer, J. Skala, B. Kralikova, P. Straka, M. Makarova, Institute of
Physics, Prague, Czech Republic, E. Woryna, J. Wolowski, Institute of Plasma Physics and Laser
Microfusion, Warsaw, Poland 41
- STOPPING POWER OF PROTON BEAMS FOR DENSE PLASMA DIAGNOSTIC
V.E. Fortov, V. Gryaznov, M. Kulish, V.B. Mintsev, A. Filimonov, ICP RAS, Moscow, Russia,
B.Y. Sharkov, A. Golubev, A. Fertman, V. Turtikov, A. Vishnevskiy, A. Kozodaev, ITEP, Moscow,
D.H.H. Hoffmann, U. Funk, S. Stoewe, M. Geissel, GSI, Darmstadt, Germany, D. Gardes, M. Chabot,
INP, Orsay, France 45
- MULTIFUNCTION X-RAY SPECTROGRAPH
S. Attelan-Langlet, B. Etlicher, Ecole Polytechnique, Palaiseau, France, M.V. Fedulov, V.O. Michensky,
G.S. Volkov, V.I. Zaitsev, TRINITI, Troitsk, Russia 49

RADIATION SOURCES, HPM

GENERATION OF POWERFUL ULTRASHORT MICROWAVE PULSES BASED ON SUPERRADIANCE OF SUBNANOSECOND HIGH-CURRENT ELECTRON BUNCHES

N.S. Ginzburg, I.V. Zotova, Yu.V. Novozhilova, A.S. Sergeev, Russian Academy of Science, Nizhny Novgorod, Russia, A.D.R. Phelps, A.W. Cross, S.M. Wiggins, University of Strathclyde, Glasgow, UK, V.G. Shpak, M.I. Yalandin, S.A. Shuailov, M.R. Ulmaskulov, Russian Academy of Science, Ekaterinburg, Russia

55

ELECTRON BEAM PRODUCTION FOR MICROWAVE GENERATION USING A FERROELECTRIC CATHODE

J.D. Ivers, D. Flechtner, J. Nation, G. Liu, L. Schachter, Cornell University, Ithaca NY, USA

61

RESEARCH OF MICROWAVE GENERATION EFFICIENCY FOR TRIODE WITH VIRTUAL CATHODE (VIRCATOR TRIODE)

A.N. Didenko, Russian Academy of Sciences, Moscow, A.G. Zherlitsyn, G.V. Melnikov, Tomsk Polytechnic University, Tomsk, Russia

65

X-RAY SOURCES, Z-PINCHES AND EXPLOSIVE GENERATORS

PERSPECTIVE OF KILOTERAWATT SOFT X-RAY SOURCE BASED ON THE SLOW INDUCTIVE STORE WITH ENERGY OF 1 GIGAJOUL

V.A. Glukhikh, V.G. Kuchinsky, O.P. Pechersky, Efremov Research Institute, St Petersburg, E.P. Velikhov, Russian Scientific Center, Moscow, E.A. Azizov, E.V. Grabovskii, V.A. Jagnov, S.L. Nedoseev, G.M. Oleinik, V.D. Pismenny, V.P. Smirnov, V.I. Zaitsev, S.V. Zakharov, Troitsk Institute for Innovation and Fusion Research, TRINITI, Troitsk, P.V. Sasorov, Institute for Theoretical and experimental Physics, Moscow, Russia

71

PLASMA SPECTROSCOPY OF PULSED POWER DRIVEN Z-PINCH TITANIUM PLASMAS

J. Davis, R.W. Clark, J.L. Guiliani Jr., J.W. Thornhill, Naval Research Laboratory, Washington DC, R. Schneider, Defense Special Weapons Agency, Alexandria VA, C. Deeney, Sandia National Laboratory, Albuquerque, NM, USA

77

EXPLOSIVE COMPLEX FOR GENERATION OF PULSED FLUXES OF SOFT X-RAY RADIATION

V.D. Selemir, V.A. Demidov, A.V. Ivanovsky, V.F. Yermolovich, V.G. Kornilov, V.I. Chelpanov, S.A. Kazakov, Yu.V. Vlasov, A.P. Orlov, VNIIEF, Sarov, Russia

83

THE APPLICATION OF HIGH INTENSIVE Z-PINCH RADIATION AND HEAVY ION BEAMS FOR RESEARCH ON HIGH ENERGY DENSITY PHYSICS

V.E. Fortov, K. Dyabilin, M. Lebedev, High Energy Density Research Center RAS, Moscow, E.V. Grabovskii, V.P. Smirnov, TRINITI, Troitsk, B.Y. Sharkov, A. Golubev, ITEPh, Moscow, Russia, D.H.H. Hoffmann, Technische Universitat, Darmstadt, K. Eidmann, Max-Planck-Institute fur Quantenoptic, Germany

89

LONG-IMPLOSION PLASMA RADIATION SOURCE DEVELOPMENT

J. Levine, P.L. Coleman, B. Failor, D. Kortbawi, D. LePell, H. Murphy, J. Riordan, I. Roth, L. Schlitt, P. Sincerny, Y. Song, C. Stallings, E. Waisman, B. Whitton, Maxwell Physics, San Leandro CA, C. Coverdale, C. Deeney, D. Jobe, J. McGurn, K. Struve, Sandia National Laboratories, Albuquerque NM, J. Apruzese, F. Cochran, R.J. Comisso, J. Davis, A. Fisher, B. Moosman, D. Mosher, S. Stephanakis, J. Thornhill, B.V. Weber, Naval Research Laboratory, Washington DC, R. Schneider, Defense Special Weapons Agency, Alexandria VA, P. Spence, Pulse Sciences, Inc, San Leandro CA, E.J. Yadlowsky, HY-Tech Research Corp, Radford VA, M. Krishnan, Alameda Applies Sciences Corp, San Leandro CA, USA

95

BEAM-MATTER INTERACTION AND INDUSTRIAL APPLICATIONS

METALLIC MATERIALS PROCESSING WITH INTENSE PULSED ELECTRON BEAMS V.P. Rotshtein, State Pedagogical University, Tomsk, Russia	105
APPLICATIONS OF INTENSE PULSED LIGHT ION BEAMS TO MATERIALS SCIENCE K. Yatsui, W. Jiang, N. Harada, T. Sonegawa, Nagaoka University of Technology, Nagaoka, Japan	111
APPLICATIONS OF DIELECTRIC BARRIER DISCHARGES Z. Falkenstein, Los Alamos National Laboratory, Los Alamos NM, USA	117
THIN FILM DEPOSITION BY PULSED ION BEAM EVAPORATION W. Jiang, K. Ohtomo, M. Igarashi, K. Yatsui, Nagaoka University of Technology, Nagaoka, Japan	121

ELECTRON BEAM GENERATION AND PROPAGATION

OPTICAL GUIDING AND STABILITY OF INTENSE SHORT LASER PULSES IN PLASMA CHANNELS P. Sprangle, B. Hafizi, Naval Research Laboratory, Washington DC, USA	127
LONG PULSE ELECTRON BEAMS PRODUCED FROM CARBON FIBER CATHODES A. Fisher, Naval Research Laboratory, Washington DC, E. Garate, University of California, Irvine CA, USA	133
RELATIVISTIC ELECTRON BEAMS FROM CATHODES AT 1GV/m GRADIENT T. Srinivasan-Rao, J. Smedley, J. Schill, Brookhaven National Laboratory, Upton NY, USA	137

RADIATION SOURCES, HPM

THE DUTCH FREE-ELECTRON MASER : 730 kW, 200 GHz W.H. Urbanus, W.A. Bongers, C.A.J. Van Der Geer, P. Manintveld, J. Plomp, J. Pluygers, A.J. Poelman, A.V. Saviolov, P.H.M. Smeets, F.S. Schuller, A.G.A. Verhoeven, FOM Instituut voor Plasmafysica 'Rijnhuizen', Nieuwegein, The Netherlands, V.L. Bratman, G.G. Denisov, Institute for Applied Physics, Nizhny Novgorod, Russia, M. Caplan, Lawrence Livermore National Laboratories, Livermore CA, USA, A.A. Varfolomeev, Russian Research Center "Kurchatov Institute" Moscow, Russia	145
HIGH-POWER MICROWAVES AT 25 YEARS - THE CURRENT STATE OF DEVELOPMENT J.A. Swegle, Lawrence Livermore National Laboratory, Livermore CA, J.N. Benford, Microwave Sciences, Lafayette CA, USA	149
X-BRAND KLYSTRON DEVELOPMENT AT KEK K. Takata, Y.H. Chin, H. Mizuno, S. Fukuda, S. Tokumoto, S. Michizono, S. Matsumoto, H. Tsutsui, KEK, Ibaraki-ken, Japan, S.A. Kazakov, BINP, Moscow, Russia	153
DEVELOPMENT OF HIGH POWER GYRO-AMPLIFIERS AT Ka-BAND AND W-BAND FOR RADAR APPLICATIONS B. Levush, M. Blank, J.P. Calame, M. Garven, J.J. Choi, B.G. Danly, K. Nguyen, D.E. Pershing, Naval Research Laboratory, Washington DC, USA	157

PULSED POWER AND ACCELERATOR TECHNOLOGY

INTENSE BEAMS: THE PAST, PRESENT, AND FUTURE G. Yonas, M.A. Sweeney, Sandia National Lab, Albuquerque NM, USA	165
X-1: THE CHALLENGE OF HIGH FUSION YIELD D.L. Cook, J.J. Ramirez, P.S. Raglin, G.E. Rochau, M.K. Matzen, R.J. Leeper, J.L. Porter, R.E. Olson, D.H. McDaniel, R.B. Spielman, C. Deeney, J.P. Quintenz, Sandia National Laboratories, Albuquerque NM, R.R. Peterson, University of Wisconsin, Madison WI, USA	171
DEVELOPMENT OF HIGH ENERGY INDUCTION ACCELERATOR, "ETIGO-III" A. Tokuchi, N. Nimomiya, Nichicon Corporation, Shiga, K. Yatsui, G. Imada, Q. Zhu, W. Jiang, K. Masugata, Nagaoka University of Technology, Nagaoka, Japan	175
ENERGETIC ELECTRONION FLOW AND MICROWAVE RADIATION DURING POS OPERATION Ya.E. Krasik, A. Dunaevsky, J. Felsteiner, Technion, Haifa, Israel, J.R. Goyer, Maxwell Technologies, San Diego CA, USA	179

MODELS AND SIMULATIONS

TOOLS FOR MHD SIMULATION OF HOT DENSE PLASMA S. Semushin, B. Etlicher, Ecole Polytechnique, Palaiseau, France	185
THE LAUNCHED ELECTRONS: SIMPLE THEORETICAL MODELING AND NUMERICAL SIMULATIONS A.V. Gordeev, RRC Kurchatov Institute, Moscow, Russia, A.S. Chuvatin, H. Ghalila, Ecole Polytechnique, Palaiseau, France	189

ION BEAMS AND DIODES, ICF

COLLIDING BEAM FUSION REACTORS N. Rostoker, M. Binderbauer, University of California, Irvine CA, H.J. Monkhorst, University of Florida, Gainesville FL, USA	195
TIME DEPENDENT FIELD AND PARTICLE DENSITY MEASUREMENTS IN THE ACCELERATION GAP OF A HIGH POWER ION DIODE V. Licht, H. Bluhm, P. Hoppe, S.J. Yoo, Forschungszentrum Karlsruhe, Karlsruhe, Germany	203
THE PROSPECT FOR FUSION ENERGY WITH LIGHT IONS T.A. Mehlhorn, R.G. Adams, J.E. Bailey, M.E. Cuneo, M.P. Desjarlais, A.B. Filuk, D.L. Hanson, D.J. Johnson, C.L. Olson, T.D. Pointon, S.A. Slutz, R.A. Vesey, D.F. Wenger, Sandia National Laboratories, Albuquerque NM, D.R. Welch, Mission Research Corporation, Albuquerque NM, USA	208
HIGH-CURRENT PULSED SOURCES OF BROAD GASEOUS AND METALLIC ION SOURCES FOR SURFACE TREATMENT APPLICATIONS N.V. Gavrilov, S.P. Nikulin, Institute of Electrophysics RAS, Yakaterinburg, Tomsk, E.M. Oks, P.M. Schanin, High Current Electronics Institute RAS, Tomsk, Russia	212
THE KALIF-HELIA ACCELERATOR: DESCRIPTION, PROGRAM AND STATUS P. Hoppe, W. Bauer, H. Bluhm, G. Kessler, K. Leber, W. Ratajczak, D. Rusch, J. Singer, Forschungszentrum Karlsruhe, Karlsruhe, Germany, V. Carboni, J. Fockler, K. Prestwich, I.D. Smith, P. Spence, Pulse Sciences Inc., San Leandro CA, USA, K. Nielsen, Physics International, San Leandro CA, USA	218
CHARACTERISTICS OF FLASHOVER ION SOURCES IN MAGNETICALLY INSULATED ION DIODE K. Masugata, E. Chishiro, K. Yatsui, Nagaoka University of Technology, Niigata, Japan	222

X-RAY SOURCES, Z PINCHES AND EXPLOSIVE GENERATORS

WIRE ARRAY Z-PINCH INSIGHTS FOR HIGH X-RAY POWER GENERATION T.W.L. Sanford, R.C. Mock, B.M. Marder, M.P. Desjarlais, T.J. Nash, R.B. Spielman, Sandia National Laboratories, Albuquerque NM, D.L. Peterson, Los Alamos National Laboratory, Los Alamos NM, K.G. Whitney, J. Apruzese, P.E. Pulsifer, D. Mosher, Naval Research Laboratory, Washington DC, USA	229
STABLE IMPLOSION OF DOUBLE GAS PUFF WITH LONG TIME IMPLOSION R.B. Baksht, A.V. Fedunin, A.Y. Labetsky, V.I. Oreshkin, A.G. Russkikh, A.V. Shishlov, High Current Electronics Institute, Tomsk, Russia, A. Van Drie, University of California, Irvine CA, USA	235
ELECTRON BEAM MEASUREMENTS IN A PULSED CAPILLARY DISCHARGE M. Favre, H. Chuaqui, E. Wyndham, Pontificia Universidad Catolica de Chile, Santiago, Chile, P. Choi, C. Dumitrescu-Zoita, J. Larour, J. Rous, Ecole Polytechnique, Palaiseau, France	240
IMPLODING PLASMA INVESTIGATIONS IN THE FRAME OF THE "LINER-CONVERTER" SCHEME Yu.L. Bakshaev, A.V. Bartov, P.I. Blinov, A.S. Chernenko, S.A. Dan'ko, uY.G. Kalinin, A.S. Kingsep, V.D. Korolev, V.I. Kosarev, A.I. Lobanov, V.I. Mizhiritskii, L.I. Rudakov, A.Yu. Shashkov, RRC Kurchatov Institute, Moscow, Russia	244

POSTERS

PULSED POWER AND ACCELERATOR TECHNOLOGY

SPECTROSCOPIC INVESTIGATIONS OF THE MAGNETIC FIELD EVOLUTION AND PLASMA FLOW IN A MICROSECOND POS R. Arad, K. Tsigutkin, Yu.V. Ralchenko, A. Fruchtmann, N. Chakrabarti, Y. Maron, Weizmann Institute of Science, Rehovot, Israel	253
PULSED X-RAY SOURCES FOR RESEARCH AND INDUSTRIAL APPLICATIONS A. Radu, D. Martin, V. Zoita, M. Toma, E. Iliescu, C. Oproiu, S. Marghitu, M. Radoiu, V. Bestea, National Institute for Laser, Plasma and Radiation Physics, Bucharest, Romania	257
TO THE THEORY OF A PLASMA FILLED ION DIODE L.I. Rudakov, RRC Kurchatov Institute, Moscow, Russia, A.S. Chuvatin, Ecole Polytechnique, Palaiseau, France	261
POLARITY-DEPENDENT PLASMA DYNAMICS IN A TRI-PLATE POS R.J. Commisso, R.A. Riley, J.M. Grossmann, B.V. Weber, D.D. Hinshelwood, T.G. Jones, P.F. Ottinger, Naval Research Laboratory, Washington DC, USA, S.B. Swanekamp, JAYCOR Inc, McClean VA, USA, J.J. Watrous, NumerEx, Albuquerque NM, USA	265
HELICAL CASCADE FCG POWERED BY PIEZOGENERATOR V.A. Demidov, V.D. Sadunov, S.A. Kazakov, L.N. Plyashkevich, T.V. Trischenko, S.N. Golosov, A.V. Blinov, I.K. Fetisov, M.V. Korotchenko, Ye.V. Shapovalov, VNIIEF, Sarov, Russia	269
RECENT OPENING SWITCH RESULTS ON DECADE MODULE 1 J.R. Goyer, J.R. Thompson, D. Kortbawi, R.J. Crumley, Maxwell Technologies, Inc., San Diego CA, S.W. Gensler, Alameda Applied Sciences Corp, San Leandro CA, USA	273
BIDIRECTIONAL PULSE GENERATOR SYSTEM FOR LINEAR INDUCTION ACCELERATOR J. Ohmura, M. Ozawa, E. Hotta, Department of Energy Sciences, Tokyo Institute of Technology, Yokohama, A. Okino, Department of Electrical and Electronic Engineering, Tokyo Institute of Technology, Tokyo, Japan, J.H. Park, K.C. Ko, Hanyang University, Seoul, South Korea	277
INVESTIGATION OF PLASMA INHOMOGENEITIES IN A PLASMA OPENING SWITCH BY LASER METHODS G.I. Dolgachev, Yu.G. Kalinin, A.S. Kingsep, M.S. Nitishinsky, A.Yu. Shashkov, "Kurchatov Institute", Moscow, Russia	281
CONTROLLED DISCHARGE ON DIELECTRIC SURFACE A.I. Kormilitsyn, V.S. Diyankov, V.B. Bratchikov, Russian Federal Nuclear Center, Snezhinsk, Russia	285
400 KA INDUCTIVE VOLTAGE ADDER-INDUCTIVE ENERGY STORAGE PULSED POWER GENERATOR ASO-X I.V. Lisitsyn, S. Kohno, Y. Teramoto, S. Katsuki, H. Akiyama, Kumamoto University, Kumamoto, Japan	289
RADIOACTIVE RESISTANCE OF SOLID DIELECTRICS B. Loncar, D. Novakovic, P. Osmokrovic, University of Belgrade, Belgrade, Yugoslavia	293
A STUDY OF PARAMETERS USEFUL FOR DESCRIBING PLASMA-OPENING SWITCHES C.W. Mendel Jr., Cove Consulting, Albuquerque NM, D.B. Seidel, S.E. Rosenthal, Sandia National Laboratories, Albuquerque NM, USA	297
ECTON PROCESSES IN PULSED HIGH-CURRENT ELECTRON BEAMS G.A. Mesyats, Russian Academy of Sciences, Ekaterinburg, Russia	301
COMPACT PULSE <<COLD CATHODE>> FLASH X-RAY TUBE POWER SUPPLY UNIT WITH SOLID-STATE OPENING SWITCH A. Dunaevsky, K. Golubinsky, A. Lomako, O.N. Morgun, Laboratoriya Medicinskoy Rentgenovskoy Techniki Ltd., Kharkov, Ukraine	302
POS EXPERIMENTS ON HAWK USING AN INVERSE PINCH GAS PLASMA SOURCE J.J. Moschella, R.C. Hazelton, C. Vidoli, E.J. Yadlowsky, HY-Tech Research Corporation, Radford VA, Washington DC, B.V. Weber, D.C. Black, D.D. Hinshelwood, B. Moosman, S.J. Stephanakis, Naval Research Laboratory, Washington DC, USA	306

PLASMA EVOLUTION OF A POS: COMPARISON OF THEORY AND EXPERIMENT ON ACE 4 AND HAWK D.E. Parks, P. Steen, P.L. Coleman, J.R. Goyer, J.R. Thompson, Maxwell Technologies, Inc., San Diego CA, USA	310
NEW SCHEME OF TWO BEAM ACCELERATOR DRIVER BASED ON LINEAR INDUCTION ACCELERATOR A.V. Elzhov, A.A. Kaminsky, A.K. Kaminsky, V.I. Kazacha, E.A. Peresltein, S.N. Sedykh, A.P. Sergeev, Joint Institute for Nuclear Research, Dubna, Russia	314
EXPLOSIVE MAGNETIC SOURCE OF HIGH VOLTAGE PULSES V.D. Selemir, V.A. Demidov, S.A. Kazakov, Yu.V. Vlasov, I.V. Konovalov, V.G. Kornilov, N.V. Stepanov, E.V. Shapovalov, K.V. Shibalko, VNIIEF, Sarov, Russia	318
HALL MHD SIMULATION OF PLASMA BEHAVIOUR IN AN OPENING SWITCH S. Semushin, A.S. Chuvatin, Laboratoire de Physique des Milieux Ionises, Palaiseau, France	322
THE USE OF THE FERROMAGNETIC SWITCH WITH ORTHOGONAL CONTROL FIELD FOR DIVERTING OF CURRENT IN AN INDUCTANCE-CAPACITANCE STORAGE G.A. Shneerson, Yu.N. Botcharov, I.P. Efimov, S.I. Krivosheev, St. Petersburg State Technical University, St. Petersburg, Russia	326
FORMING OF HIGH-SPEED RADIAL PLASMA FLOW DUE TO ITS HEATING BY INDUCED AZIMUTHAL CURRENT IN ELECTRICAL EXPLOSION OF WIRES IN EXTRA-HIGH MAGNETIC FIELD Yu.E. Adamyan, V.M. Vasilevsky, S.N. Kolgatin, G.A. Shneerson, St. Petersburg State Technical University, St. Petersburg, Russia	330
WAVE-FORM OPTIMIZATION FOR A 60 MA Z-PINCH DRIVER K. Struve, Mission Research Corp., Albuquerque NM, D.H. McDaniel, Sandia National Laboratories, Albuquerque NM, USA	334
PLASMA OPENING SWITCH-LOAD COUPLING ON ACE 4 J.R. Thompson, P.L. Coleman, R.J. Crumley, P.J. Goodrich, J.R. Goyer, J.E. Rauch, Maxwell Technologies Inc., San Diego CA, J.J. Moschella, E.J. Yadlowsky, HY-Tech Research Corporation, Radford VA, USA	338
GAS PRE-IONIZATION SYSTEM FOR DECADE MODULE 2 PRS EXPERIMENTS B.V. Weber, S.J. Stephanakis, B. Moosman, D.D. Hinshelwood, R.J. Commisso, A. Fisher, Naval Research Laboratory, Washington DC, R.C. Fisher, JAYCOR, McLean VA, USA, J.C. Riordan, P.D. LePell, J. Levine, Y. Song, Maxwell Physics International Company, San Leandro CA, USA	342
THE TIME-DEPENDENT ELECTRON DENSITY AND MAGNETIC FIELD DISTRIBUTIONS IN A 70-ns PLASMA OPENING SWITCH A. Weingarten, C. Grabowski, A. Fruchtman, Weizmann Institute of Science, Rehovot, Israel, Y. Maron	346
ELECTRODYNAMICS OF A MICROSECOND PLASMA OPENING SWITCH O. Zabaidullin, M.S. Nitishinsky, Institute of Nuclear Fusion, Russian Research Centre, Moscow, Russia	350

ELECTRON BEAM GENERATION AND PROPAGATION

GENERATION OF AN ANNULAR REB OF MICROSECOND PULSE DURATION AND STABILIZED TRANSVERSE DIMENSIONS IN A DIODE WITH A FIELD-EMISSION CATHODE O.T. Loza, P.S. Strelkov, Russian Academy of Sciences, Moscow, Russia	357
MEASUREMENT OF STRONG LANGMUIR TURBULENCE FIELDS USING AN ELECTRON BEAM PROBE R. Ando, S. Taniguchi, K. Kamada, M. Masuzaki, Kanazawa University, Kanazawa, Japan, I.N. Onishchenko, National Scientific Center, Kharkov, Ukraine	361
PULSE SHORTENING BY SCATTERING FROM TURBULENT ELECTRIC FIELDS IN BACKWARD WAVE OSCILLATORS G. Benford, University of California, Irvine CA, USA	365
IGNITION OF A BEAM-PLASMA DISCHARGE BY ELECTRONS EMITTED FROM A FERROELECTRIC V.A. Borissenok, D.R. Goncharova, A.E. Dubinov, A.N. Klevtsov, V.A. Kruchinin, S.A. Sadovoy, V.D. Selemir, RFNC-VNIIEF, Sarov, Russia	369

TRANSPORTATION OF OVER-LIMITING BEAM IN THE WAVEGUIDE WITH PLASMA DAMS A.L. Babkin, V.I. Chelpanov, A.E. Dubinov, S.M. Galkin, D.L. Gladilin, A.A. Khizhnyakov, V.G. Kornilov, V.D. Selemir, A. Sudovtsov, V.S. Zhdanov, Russian Federal Nuclear Center, Sarov, Russia	372
GENERATION OF HIGH-CURRENT ELECTRON BEAMS BY THE USE OF PLASMA CATHODES Ya.E. Krasik, A. Dunaevsky, J. Felsteiner, Technion, Haifa, Israel	376
HIGH BRIGHTNESS ELECTRON BEAM INJECTOR FOR THE DARHT FACILITY E. Henestroza, S. Eylon, D. Anderson, W. Fawly, H. Rutkowski, S. Yu, Lawrence Berkeley National Laboratory, USA	380
PULSE COMPRESSION OF AN INTENSE RELATIVISTIC ELECTRON BEAM USING MULTI-STAGE AUTOACCELERATION D. Hasegawa, K. Kamada, K. Shimizu, M. Miyamoto, R. Ando, M. Masuzaki, Kanazawa University, Kanazawa, Japan	384
MODELING AND PARTICLE SIMULATIONS OF MAGNETICALLY INSULATED TRANSMISSION LINES WITH CROSS SECTIONAL CHANGES K. Hiraoka, M. Nakajima, K. Horioka, Tokyo Institute of Technology, Midori-ku Yokohama, Japan, M. Shiho, Japan Atomic Energy Research Institute, Tokai-mura, Ibaraki, Japan	388
ACCELERATING WAKE-FIELD ENHANCEMENT OF EXCITED BY LONG RELATIVISTIC ELECTRON BUNCH OWING TO SELF-MODULATION V.I. Karas, V.A. Balakirev, Ya.B. Fainberg, G.V. Sotnikov, I.V. Karas, National Scientific Center, Kharkov, Ukraine, V.D. Levchenko, Yu.S. Sigov, Russian Academy of Sciences, Moscow, Russia	392
HIGH-BRIGHTNESS ELECTRON LINAC FOR BEAM-PLASMA INTERACTION STUDIES M.I. Ayzatsky, A.N. Dovbnya, V.A. Kushnir, V.V. Mitrochenko, D.L. Stepin, Kharkov Institute of Physics & Technology, Kharkov, Ukraine	396
STUDYING THE ELECTRON BEAM CHARACTERISTICS OF MAGNETRON INJECTION GUNS WITH A METAL SECONDARY EMISSION CATHODE M.I. Ayzatsky, A.N. Dovbnya, P.I. Gladkikh, V.V. Zakutin, V.A. Kushnir, V.V. Mitrochenko, N.G. Reshetn'yak, V.P. Romas'ko, V.F. Pokas, Yu.D. Tur, Kharkov Institute of Physics & Technology, Kharkov, Ukraine	400
INFLUENCE OF ELECTRONS REFLECTED FROM TARGET ON OPERATION OF DIODE AND TRIODE ELECTRON SOURCES G. Mueller, Forschungszentrum Karlsruhe, Karlsruhe, Germany, V. Engelko, V. Kuznetsov, G. Vijazmenova, Efremov Institute of Electrophysical Apparatus, St. Petersburg, Russia	404
GENERATION OF UNIFORM PLASMA EMITTERS IN DISCHARGES WITH A MAGNETIC FIELD S.P. Nikulin, S.V. Kuleshov, Institute of Electrophysics, Ekaterinburg, Russia	408
HOLLOW CATHODE ELECTRON GUN FOR BEAM GENERATION IN FOREVACUUM GAS PRESSURE V. Burdovitsin, State University of Control Systems and Radioelectronics, Tomsk, E. Oks, High Current Electronics Institute Russian Academy of Sciences, Tomsk, A. Serov, Russian Research Center "Kurchatov Institute", Moscow, Russia	412
ELECTRODYNAMICS OF THE PLASMA-FILLED INVERTED CHAIN OF COUPLED CAVITIES A. Korostelev, I.N. Onishchenko, G. Sotnikov, NSC Kharkov Institute of Physics & Technology, Kharkov, Ukraine, Russia	416
HIGH-CURRENT DIODE FOR OPEN AIR OPERATION Yu.E. Kolyada, Priazovsky Technical University, Mariupol, N.I. Onishchenko, NSC Kharkov Institute of Physics & Technology, Kharkov, Ukraine	420
TIME DEPENDENCE OF HIGH-CURRENT VACUUM DIODE IMPEDANCE RESULTING FROM CATHODE PLASMA EXPANSION S.Ya. Belomytsev, S.D. Korovin, I.V. Pegel, Russian Academy of Sciences, Tomsk, Russia	424
OPTIMISATION OF THE CROSSED-FIELD SECONDARY EMISSION ELECTRON SOURCE Y.M. Saveliev, W. Sibbett, University of St. Andrews, St. Andrews, Fife Scotland, D.M. Parkes, DERA, Great Malvern, UK	428

THE SPECTRUM BROADENING OF EXCITED OSCILLATIONS IN COAXIAL SLOWING STRUCTURE WHEN FILLING BY PLASMA E.A. Kornilov, P.I. Markov, G.V. Sotnikov, Institute of Plasma Electronics & New Methods of Accelerations NSC KIPT, Kharkov, Ukraine	432
SPECTROSCOPIC DETERMINATION OF TURBULENT LANGMUIR FIELDS IN A REB-HEATED PLASMA J. Ullschmied, K. Kolacek, M. Ripa, Czech Academy of Sciences, Prague, Czech Republic	436
OPERATION OF LIA-10 LINEAR INDUCTION ACCELERATOR IN THE MODE OF ENERGY TRANSPORT ALONG VACUUM COAXIAL LINE A.M. Chlenov, V.F. Zinchenko, E.V. Tulisov, V.D. Shijan, Research Institute of Scientific Instruments, Lytkarino, Moscow Region, Russia	440

DIAGNOSTICS AND EXPERIMENTAL METHODS

SPECTRA OF LASER SCATTERING ON POWERFUL REB A.V. Arzhannikov, V.S. Burmasov, S.A. Kuznetsov, S.S. Popov, S.L. Sinitsky, M.A. Shcheglov, Budker Institute of Nuclear Physics SB RAS, Novosibirsk, Russia	447
X-RAY SPECTROSCOPY APPLICATION FOR MAGNETIC FIELD AND ELECTRON BEAM MEASUREMENTS IN LASER PRODUCED PLASMA E.O. Baronova, G. Sholin, RRC Kurchatov Institute, Moscow, Russia	451
RETRIEVAL OF REFRACTIVE INDEX DISTRIBUTION IN AN ANODE LAYER FROM FOURIER IMAGE OF PROBE LASER BEAM V.S. Cherkassky, B.A. Knyazev, Novosibirsk State University, Novosibirsk, Russia	455
X-RAY SPECTROSCOPY AT "S-300" FACILITY S.A. Dan'ko, RRC Kurchatov Institute, Moscow, Russia	459
A DIAGNOSTIC OF GYROTRON CATHODES QUALITY BASED ON THEIR CURRENT-VOLTAGE CHARACTERISTICS M.Y. Glyavin, A.N. Kuftin, A.S. Postnikova, N.P. Venediktov, M.V. Yulpatova, V.E. Zapevalov, I.E. Zasyapkina, Institute of Applied Physics Russian Academy of Sciences, Nizhny Novgorod Region, Russia	463
A RE-EVALUATION OF CURRENT MEASUREMENTS DOWNSTREAM OF THE PLASMA OPENING SWITCH ON DECADE MODULE 1 J.R. Goyer, J.R. Thompson, D. Kortbawi, Maxwell Technologies, Inc., San Diego CA, USA	467
ATOMIC BEAM SOURCE FOR ION DIODE DIAGNOSTICS B.A. Knyazev, Novosibirsk State University, Novosibirsk, Russia, W. An, H. Bluhm, L. Buth, Forschungszentrum Karlsruhe, Karlsruhe, Germany	471
"TRIPLY-ACTIVE" DIAGNOSTIC METHOD FOR ION BEAM DIODES B.A. Knyazev, Novosibirsk State University, Novosibirsk, Russia, J.B. Greenly, D.A. Hammer, LPS Cornell University, Ithaca NY, USA	475
DIAGNOSTIC PROBES COMPLEX AND IMPLOSIVE LINERS DYNAMICAL PARAMETERS RECORDING METHODS A.M. Buyko, B.E. Grinevich, V.K. Chernyshev, A.I. Kuzyaev, V.N. Mokhov, A.A. Petrukhin, V.B. Yakubov, All Russia Scientific and Research Institute of Experimental Physics, Sarov, Russia	479
MULTICHANNEL LASER INTERFEROMETER - REFRACTOMETER WITH HIGH SPATIAL AND TEMPORAL RESOLUTIONS I.V. Lisitsyn, S. Kohno, S. Katsuki, H. Akiyama, Kumamoto University, Kumamoto, Japan	483
CALIBRATION OF THE GALILEO MICRO CHANNEL PLATE WITH THE Xe(7+) - Xe(43+) IONS IN THE ENERGY RANGE FROM 2keV/q UP TO 154keV/q W. Mroz, A. Prokopiuk, Institute of Optoelectronics, MUT, Warsaw, Poland, D. Fray, A.P. Stockli, B. Walch, Kansas State University, Manhattan KS, USA	487
TIME RESOLVED XUV LINE EMISSION MEASUREMENT V. Piffel, Institute of Plasma Physics AS CR, Prague, A. Krejci, World Trend, Prague, Czech Republic, A.V. Golubev, Marinfo, St Petersburg, Russia	491
"CONTROL" DIAGNOSTIC X-RAY APPARATUS WITH A DIGITAL IMAGE VISUALIZATION SYSTEM A.L. Filatov, S.R. Korjenevski, S.V. Scherbinin, Institute of Electrophysics, Ekaterinburg, Russia	495

DIAGNOSTICS OF PULSED PLASMA-ION BEAMS FROM DIFFERENT COAXIAL INJECTORS F. Skladnik-Sadowska, J. Baranowski, M. Sadowski, J. Stanislawski, J. Zebrowski, The Andrezej Soltan Institute for Nuclear Studies, Warsaw, Poland	499
DIAGNOSTIC METHODS OF MEASURING MEGAVOLT VOLTAGES AND MEGAAMPER CURRENTS A.S. Boriskin, M.I. Dolotenko, A.S. Kravchenko, V.G. Kornilov, I.M. Markevtsev, A.N. Moiseyenko, V.D. Selemir, O.M. Tatsenko, V.I. Chelpanov, VNIIEF, Sarov, Russia	503
SPECTROSCOPY OF COMPOSITE Z-PINCH ON ANGARA-5 -1 INSTALLATION A.S. Chuvatin, B. Etlicher, Ecole Polytechnique, Palaiseau, P. Zehnter, CEA, Bruyeres-le-Chatel, France, S.A. Dan'ko, M.V. Fedulov, V.O. Michensky, G.S. Volkov, V.I. Zaitsev, TRINITI, Troitsk, Russia	507

MODELS AND SIMULATIONS

STATIONARY PARTICLE-IN-CELL SIMULATIONS ON ELECTRON AND ION DIODES W. Bauer, E. Stein, Forschungszentrum Karlsruhe, Karlsruhe, B. Schrempp, T. Westermann, Fachhochschule, Karlsruhe, Germany	513
BEAM DYNAMICS IN THE 1.4 MeV TANDEM ACCELERATOR FOR TAU FEL A. Abramovich, S. Efimov, A. Gover, I. Merhasin, Tel-Aviv University, Ramat Aviv, Y. Pinhasi, The College of Judea and Samaria, Israel	517
RAYLEIGH -- TAYLOR INSTABILITY OF IMPLoding PLASMA SHELL BY LOW DENSITY PLASMA A.V. Gordeev, Russian Research Centre, Moscow, Russia	521
NON-LINEAR ELECTROMAGNETIC WAVE IN PLASMA-FILLED TRANSMISSION LINE A.V. Gordeev, S.V. Levchenko, Russian Research Centre Kurchatov Institute, Moscow, Russia	525
SIMULATION STUDY OF A 32GHz GYROTRON USING AN ELECTROMAGNETIC PIC CODE J.J. Barroso, R.A. Correa, LAP, INPE, Sao Jose dos Campos, Brazil, K.G. Kostov, I.P. Spassovsky, Sofia University, Sofia, Bulgaria	529
2D SIMULATION OF FUEL IN TARGET INDIRECT-DRIVEN BY PROTON BEAM K. Niu, Teikyo Heisei University, Chiba, Japan	533
GEOMETRIC METHODS TO TREAT ENERGY TRANSPORT PHENOMENA C. Passow, Karlsruhe, Germany	537
KADI2D - A PARTICLE-IN-CELL CODE BASED ON FINITE-VOLUME METHODS C.D. Munz, Institute fur Aerodynamik und Gasdynamik der Universitat Stuttgart, Stuttgart, Germany, P. Omnes, R. Schneider, E. Stein, Forschungszentrum Karlsruhe, Karlsruhe, Germany, E. Sonnendruker, Universite Henri Poincare Nancy I, Vandoeuvre les Nancy Cedex, France, U. Voss, Polytechnique, Palaiseau Cedex, France, T. Westermann, Fachbereich Naturwissenschaften der FH Karlsruhe, Karlsruhe, Germany	541
SIMPLE MODEL OF MAGNETIC SELF-INSULATION FOR SIMULATION OF NON-UNIFORM TRANSMISSION LINES A.V. Gordeev, Russian Research Center, Moscow, Russia, S. Semushin, A.S. Chuvatin, Ecole Polytechnique, Palaiseau, France	545
COMPARISON OF ELECTROSTATIC AND TIME DEPENDENT SIMULATION CODES FOR MODELING A PULSED POWER GUN T. Srinivasan-Rao, J. Smedley, Brookhaven National Laboratory, Upton NY, K. Batchelor, J.P. Farrell, G. Dudnikova, Brookhaven Technology Group, Stony Brook NY, USA	549
SIMULATIONS ON HALO FORMATION IN HIGH INTENSITY ION BEAMS V. Variale, T. Clauser, V. Stagno, Dipartimento di Fisica and INFN sez. di Bari, Bari, Legnaro, Italy, A. Bazzani, Dipartimento di Fisica and INFN sez. di Bologna, Italy, A. Pisent, INFN Laboratori Nazionali Legnaro, Legnaro, Italy	553
DIODE SIMULATIONS WITH KADI2D C.D. Munz, Institut fur Aerodynamik und Gasdynamik der Universitat Stuttgart, Stuttgart, R. Schneider, E. Stein, Forschungszentrum Karlsruhe, Karlsruhe, T. Westermann, Fachbereich Naturwissenschaften der FH Karlsruhe, Karlsruhe, Germany	557
A POSSIBLE MECHANISM OF RUNAWAY ELECTRONS GENERATION IN PULSED PLASMAS O. Zabaidullin, Institute of Nuclear Fusion, Russian Research Center, Moscow, Russia, J. Dubau, Observatoire de Paris, Meudon, France	561

VOLUME II

POSTERS continued

X-RAY SOURCES, Z PINCHES AND EXPLOSIVE GENERATORS

- 2D DYNAMICS OF DOUBLE LINER IMPOLED BY HIGH CURRENT PULSE
R. Benattar, Ecole Polytechnique, Palaiseau Cedex, France, S.V. Zakharov, Laboratoire de Physique des Milieux Ionises, Trinité, A.F. Nikiforov, V.G. Novikov, KIAM, V.A. Gasilov, A.Yu. Krukovski, IMM, Russia 567
- CAUCHIOS SPECTROGRAPH APPLICATION FOR INVESTIGATION OF BREMSSTRAHLUNG AND LINE SPECTRA, EMITTED BY PLASMA FOCUS DISCHARGE
E.O. Baronova, V.A. Rantsev-Kartinov, M.M. Stepanenko, RRC Kurchatov Institute, Moscow, Russia 572
- INVESTIGATION OF NeX AND NeX LINE EMISSION FROM A GAS-PUFF Z-PINCH PLASMA USING ROSS FILTER SYSTEMS
I.N. Bogatu, L. Grogorian, E. Klodzh, E. Kroupp, Y. Maron, Yu.V. Ralchenko, Weizmann Institute of Science, Rehovot, Israel 577
- GENERATION OF POWERFUL BREMSSTRAHLUNG IN A HEAVY GAS TARGETS
V.V. Chorny, O.I. Frolov, V.M. Dubina, V.T. Kolisnyk, G.V. Tsepilov, V.S. Solovjov, Kharkov State University, Kharkov, Ukraine 581
- MHD-NOZZLE DEVICE AS A THERMONUCLEAR TARGET IN MAGO/MTF FUSION CONCEPT
A.N. Demin, V.K. Chernyshev, V.P. Korchagin, V.N. Mokhov, V.A. Ivanov, S.V. Pak, V.B. Yakubov, S.F. Garanin, V.I. Mamyshev, S.D. Kuznetsov, A.N. Subbotin, O.M. Burencov, Yu.N. Dolin, V.I. Dudin, I.V. Morozov, A.A. Volkov, S.V. Trusilo, P.L. Usenko, A.N. Skobelev, V.I. Shpagin, All Russia Scientific Institute of Experimental Physics, Nizhny Novgorod Region, Russia 585
- DISK EXPLOSIVE MAGNETIC GENERATOR WITH LOW RISE TIME IN THE LOAD
V.A. Demidov, A.N. Demin, S.A. Kazakov, Yu.V. Vlasov, V.A. Yarenko, All Russia Scientific Institute of Experimental Physics, Sarov, Russia 588
- MICROSECOND PLASMA OPENING SWITCH AS A BREMSSTRAHLUNG GENERATOR
N.U. Barinov, G.I. Dolgachev, D.D. Maslennikov, M.S. Nitishinsky, A.G. Ushakov, L.P. Zakatov, Kurchatov Institute, Moscow, Russia 591
- ION BEAM MEASUREMENTS IN A SMALL PLASMA FOCUS OPERATING IN HYDROGEN/GAS MIXTURES
P. Silva, M. Favre, H. Chuaqui, E. Wyndham, Pontificia Universidad Católica de Chile, Santiago, Chile, P. Choi, C. Dumitrescu-Zoita, Ecole Polytechnique, Palaiseau, France 595
- PECULIARITIES OF WIRE RESISTANCE BEHAVIOR ON INITIAL STAGE OF EXPLOSION
V.V. Branitskii, E.V. Grabovskii, I.N. Frolov, G.M. Oleinik, A.A. Samokhin, V.P. Smirnov, G.S. Volkov, M.V. Zurin, Troitsk Institute for Innovation and Thermonuclear Investigation, Troitsk, Russia, P.V. Sasorov, Institute for Theoretical and Experimental Physics, Moscow, Russia, R.B. Spielman, Sandia National Laboratories, Albuquerque NM, USA 599
- ON AZIMUTHAL MAGNETIC FLUX PENETRATION DURING DOUBLE LINER IMPLOSION
A.V. Branitskii, E.V. Grabovskii, I.N. Frolov, G.M. Oleinik, V.P. Smirnov, S.V. Zakharov, M.V. Zurin, Troitsk Institute for Innovation and Thermonuclear Investigation, Troitsk, A.Yu. Krukovski, Institute for Mathematical Modeling, Moscow, Russia 603
- FOAM LINER PREIONISATION BY EXTERNAL CURRENT SHELL ON "PF-1000" AND "ANGARA-5-1"
L. Karpinski, M. Scholtz, W. Stepniewski, Institute of Plasma Physics and Laser Microfusion, Warsaw, A. Szydłowski, Soltan Institute for Nuclear Studies, Swierk, Poland, A.V. Branitskii, M.V. Fedulov, I.N. Frolov, E.V. Grabovskii, S.F. Medovshikov, S.L. Nedoseev, G.M. Oleinik, G.V. Rjabtsev, V.P. Smirnov, M.V. Zurin, Troitsk Institute for Innovation and Fusion Research, TRINITI, Troitsk, Russia 607
- NUMERICAL AND EXPERIMENTAL STUDY OF BEHAVIOR OF GAS-PUFF Z-PINCH PLASMA PRODUCED BY INDUCTIVE PULSED POWER GENERATOR
K. Imasaka, Y. Kawauchi, K. Kawazoe, J. Suehiro, M. Hara, Kyushu University, Fukuoka, Japan 611

ELECTRON BEAMS AND X-RAY POLARIZATION EFFECTS IN PLASMA-FOCUS DISCHARGES L. Jakubowski, M. Sadowski, The Andrzej Soltan Institute for Nuclear Studies, Swierk, Poland, E.O. Baronova, V.V. Vikhrev, RRC Kurchatov Institute, Moscow, Russia	615
COMPARISON OF COMPUTED AND MEASURED PARAMETERS OF A DRIVER FOR FAST CAPILLARY DISCHARGE K. Kolacek, V. Bohacek, J. Schmidt, P. Sunka, J. Ullschmied, M. Ripa, Academy of Sciences of the Czech Republic, Prague, Czech Republic	619
DENSE Z-PINCH NECK DEVELOPMENT DYNAMICS INVESTIGATION ON S-300 GENERATOR Yu.L. Bakshaev, P.I. Blinov, A.S. Chernenko, S.A. Dan'ko, E.M. Gordeev, V.D. Korolev, E.A. Smirnova, V.I. Mizhirsksii, V.I. Tumanov, Russian Research Center "Kurchatov Institute", Moscow, S.F. Medovshikov, S.L. Nedoseev, Troitsk Institute of Innovative and Fusion Research, Troitsk, Russia	623
MONOCHROMATIC VUV-RADIATION OF Z-PINCH CARBON ROD P. Kubes, J. Kravarik, FEE Czech Technical University, Prague, Czech Republic, L. Karpinski, Institute of Plasma Physics and Laser Microfusion, Warsaw, Poland, L. Aschke, H.-J. Kunze, Institut fur Experimentalphysik V, Bochum, Germany, Z. Andreic, Ruder Boskovic Institute, Zagreb, Croatia	627
OPERATIONAL MODE OF <<COLD CATHODE>> FLASH X-RAY TUBES WHICH PROVIDES SUB-MILLIMETER FOCAL SPOT SIZE AND ELECTRON BEAM ENERGY ADJUSTING A. Dunaevsky, K. Golubinsky, A. Lomako, O.N. Morgun, Laboratoriya Medicinskoy Rentgenovskoy Techniki Ltd., Kharkov, Ukraine	631
THE EXPERIMENTAL STUDY OF PLASMA PARAMETERS IN MAGO CHAMBER V.K. Chernyshev, A.N. Demin, Yu.N. Dolin, V.I. Dudin, V.P. Korchagin, I.V. Morozov, A.N. Subbotin, G.I. Volkov, P.L. Usenko, All Russian Research Institute of Experimental Physics, Sarov, Russia	634
NEUTRAL ATOMS INFLUENCE ON THE DYNAMICS OF Z-PINCH CAPILLARY DISCHARGE X-RAY LASER R. Nemirovsky, A. Ben-Kish, M. Shuker, A. Ron, Technion-IIT, Haifa, Israel	638
PULSED HIGH-VOLTAGE SOURCE BASED ON HELICAL MCG FOR POWER SUPPLY OF HIGH-CURRENT REB ACCELERATORS E.V. Chernikh, V.E. Fortov, K.V. Gorbachev, E.V. Nesterov, S.A. Roschupkin, V.A. Stroganov, I.O. Zolotikh, High Energy Density Research Centre, RAS, Moscow, Russia	642
THE STUDY OF VARIABLE MASS LINER ACCELERATION IN ORDER TO CREATE THE SOURCE OF SOFT X-RAYS A.M. Bujko, V.K. Chernyshev, S.F. Garanin, Y.N. Gorbachev, V.A. Demidov, G.G. Ivanova, V.N. Kostyukov, S.D. Kuznetsov, A.I. Kuzyaev, A.B. Mezhevov, V.N. Mokhov, A.A. Petrukhin, V.N. Sofronov, A.I. Startsev, V.B. Yakubov, All Russia Scientific Institute of Experimental Physics, Sarov, Russia, B.G. Anderson, C.A. Ekdahl, J.L. Kammerdiener, I.R. Lindemuth, R.E. Reinovsky, P.J. Rodriguez, L.R. Veaser, S.M. Younger, W.D. Zerwekh, D.A. Poling, R.C. Kirkpatrick, Los Alamos National Laboratory, NM, T.J. Englert, G.F. Kiuttu, Phillips Laboratory, Albuquerque NM, USA	646
SIMULATION OF MULTI-WIRE LINER DYNAMICS DURING Z-PINCH IMPLOSION S. Semushin, B. Etlicher, Ecole Polytechnique, Palaiseau, France	654
DEVELOPMENT OF ACCELERATOR FOR HIGH-POWER MICROWAVE APPLICATIONS BASED ON THE FORMING LINE SUPPLIED WITH CURRENT V.E. Fortov, V.A. Kamensky, V.M. Mihailov, E.V. Nesterov, V.Y. Petrov, S.D. Plaksina, S.A. Roschupkin, V.P. Shumilin, V.A. Stroganov, High Energy Density Research Centre, RAS, Moscow, Russia	658
TWO MECHANISMS OF HIGH ENERGY IONS GENERATION IN THE Z-PINCH V.V. Vikhrev, E.O. Baronova, RRC Kurchatov Institute, Moscow, Russia	662
ELECTRON BEAM GENERATION IN STRONG LOCAL ELECTRIC FIELDS OF Z-PINCH DISCHARGES V.V. Vikhrev, E.O. Baronova, RRC Kurchatov Institute, Moscow, Russia	666
MHD INSTABILITIES OF IMPLoded LINERS S.V. Zakharov, LPMI, Trinita, V.S. Zakharov, Moscow State University, Moscow, Russia	670
STUDIES OF MULTIWIRED ARRAY PLASMA FORMATION USING X-RAY BACKLIGHTING T.A. Shelkovenko, S.A. Pikuz, A.R. Mingaleev, D.A. Hammer, B.R. Kusse, Cornell University, Ithaca NY, USA	676

DESIGN OF A 7 MW, 95 GHz, THREE-CAVITY GYROKLYSTRON M.R. Arjona, W. Lawson, University of Maryland, College Park MD, USA	683
PROGRESS IN INVESTIGATIONS ON MICROWAVE FEL DRIVEN BY MICROSECOND SHEET BEAM N.V. Agarin, A.V. Arzhannikov, V.B. Bobylev, V.G. Ivanenko, S.A. Kuznetsov, V.S. Nikolaev, M.A. Shcheglov, S.L. Sinitsky, V.D. Stepanov, Budker Institute of Nuclear Physics, Novosibirsk, N.S. Ginzburg, N.Yu. Peskov, Institute of Applied Physics, N.Novgorod, Russia	687
GENERAL SCALING OF PULSE SHORTENING IN EXPLOSIVE-EMISSION-DRIVEN MICROWAVE SOURCES J.N. Benford, Microwave Sciences, Lafayette CA, D. Price, PRIMEX Physics International, San Leandro CA, USA	691
LOWERED PLASMA VELOCITY WITH CESIUM IODIDE/CARBON FIBER CATHODES AT HIGH ELECTRIC FIELDS J.N. Benford, Microwave Sciences Inc., Lafayette CA, D. Price, W. DeHope, PRIMEX Physics International, San Leandro CA, USA	695
EFFECT OF PLASMA NONLINEARITY ON RADIATION SPECTRUM IN PLASMA-FILLED TRAVELING-WAVE TUBES Yu.P. Bliokh, Ya.B. Fainberg, M.G. Lyubarsky, V.O. Podobinsky, National Science Center "KHPHTI", Kharkov, Ukraine, G.S. Nusinovich, Y. Carmel, V.L. Granatstein, S. Kobayashi, University of Maryland, College Park Maryland, USA	699
INSTATIONARITY OF E-BEAM PUMP PROCESSES IN SHORT-PULSE-DURATION GAS LASERS OF VUV-RANGE V.A. Burtsev, Efremov Scientific Research Institute of Electrophysical Apparatus, St. Petersburg, Russia	703
INFLUENCE OF AN OVERMODED SLOW-WAVE STRUCTURE MATCHING ON A CERENKOV GENERATOR EXCITATION I.A. Chernyavsky, M.P. Deichuly, V.I. Koshelev, High Current Electronics Institute RAS, Tomsk, Russia	707
ON THE LIMITING ADMISSIBLE POWER LEVEL OF PULSED MICROWAVE GENERATORS BASED ON HIGH-CURRENT ELECTRON ACCELERATORS A.N. Didenko, Russian Academy of Sciences, Moscow, Russia	711
AN AXIALLY TWICE ACCELERATION LOW IMPEDANCE HPM SOURCE W. Ding, Institute of Applied Physics and Computational Mathematics, Beijing, China	714
MICROWAVE GENERATOR WITH VIRTUAL CATHODE, WORKING IN STOCHASTIC RESONANCE REGIME (STOCHASTRON) A.E. Dubinov, K. Mikheyev, V.D. Selemir, A. Sudovtsov, VNIIEF, Sarov, Russia	720
HIGH-FREQUENCY ELECTRON BEAM MODULATION IN A DIODE WITH AN ACTIVE PLASMA CATHODE Ya.E. Krasik, A. Dunaevsky, J. Felsteiner, Technion, Haifa, Israel	724
VERSATILE e - BEAM PREBUNCHER FOR FEMs AND OTHER HIGH POWER BEAM DEVICES A.L. Eichenbaum, H. Kleinman, M. Arbel, A. Gover, Tel Aviv University, Tel Aviv, Israel	728
A HIGH-POWER RELATIVISTIC MAGNETRON OF NEW CONCEPTION: SIMULATION AND EXPERIMENT V.A. Bogachenkov, V.A. Papadichev, P.N. Lebedev Institute of RAS, Moscow, V.M. Fedorov, V.P. Tarakanov, High Energy Density Research Centre of RAS, Moscow, V.A. Silin, General Physics Institute of RAS, Moscow, Russia	732
EXPERIMENTAL INVESTIGATION OF ELECTRON ENERGY SPECTRUM IN GYROTRONS M.Y. Glyavin, A. Goldenberg, A.N. Kuftin, A.S. Postnikova, N.P. Venediktov, V.E. Zapevalov, Institute of Applied Physics Russian Academy of Sciences, Nizhny Novgorod Region, Russia	736
A REVIEW OF RECENT PROGRESS IN RELTRON TUBE DESIGN R.B. Miller, K.W. Habiger, Titan Advanced Innovative Technologies, Albuquerque NM, USA	740

ELECTRON BEAM FORMATION FOR RELATIVISTIC CRMS V.L. Bratman, Yu.D. Grom, Yu.K. Kalynov, V.N. Manuilov, M.M. Ofitserov, S.V. Samsonov, Russian Academy of Science, Nizhny Novgorod, Russia	744
OBTAINMENT OF ELECTROMAGNETIC RADIATION AT INTERACTION OF ELECTRON BEAM WITH RING PLASMA WAVEGUIDE V.A. Balakirev, V.I. Karas, E.A. Kornilov, Ya.B. Fainberg, O.N. Shulika, I.N. Onishchenko, V.O. Podobinsky, National Scientific Center, Kharkov, Ukraine	748
TRANSFORMATION OF EXCITED BY ELECTRON BEAM PLASMA WAVES INTO ELECTROMAGNETIC RADIATION (EMR) OWING TO PARAMETRIC PROCESSES ON LAYER PLASMA WAVEGUIDE V.A. Balakirev, V.I. Karas, E.A. Kornilov, Ya.B. Fainberg, National Scientific Center, Kharkov, Ukraine	752
DIELECTRIC WAKE-FIELD GENERATOR V. Kiselev, A. Linnik, V. Mirny, N. Zemliansky, R.N. Kochergov, I.N. Onishchenko, G. Sotnikov, Ya.B. Fainberg, NSC Kharkov Institute of Physics & Technology, Kharkov, Ukraine	756
PLASMA NONLINEARITY INFLUENCE ON HF OSCILLATION EXCITATION BY THE ELECTRON BEAM IN HYBRID PLASMA WAVEGUIDES V.S. Antipov, A.N. Antonov, V.A. Balakirev, Yu.P. Bliokh, A.M. Egorov, Ya.B. Fainberg, V.I. Karas, O.F. Kovpik, E.A. Kornilov, M.G. Lubarsky, K.V. Matyash, V.O. Podobinsky, G.V. Sotnikov, V.G. Svichensky, NSC Kharkov Institute of Physics and Technology, Kharkov, Ukraine	760
RELATIVISTIC MILLIMETER-WAVELENGTH RANGE CERENKOV GENERATORS V.I. Koshelev, V.A. Popov, High Current Electronics Institute RAS, Tomsk, Russia	764
MWCG WITH BIPEIODIC OUTPUT SECTION M.P. Deichuly, V.I. Koshelev, High Current Electronics Institute RAS, Tomsk, Russia	768
HIGH-POWER MICROWAVE GENERATION BY AN AXIAL TRANSIT-TIME OSCILLATOR J.J. Barroso, R.A. Correa, LAP, INPE, Sao Jose dos Campos, Brazil, K.G. Kostov, I.P. Spassovsky, Sofia University, Sofia, Bulgaria	772
NUMERICAL SIMULATION AND EXPERIMENTAL STUDY OF THE HELICAL ELECTRON BEAMS OF 170 GHZ/1MW GYROTRONS A.N. Kuftin, V.K. Lygin, A.S. Postnikova, V.E. Zapevalov, Russian Academy of Sciences, Nizhny Novgorod, Russia	776
EXPERIMENTAL STUDY OF TRAPPED ELECTRONS INFLUENCE ON THE HELICAL ELECTRON BEAM PARAMETERS FOR MILLIMETER WAVE RANGE GYROTRONS A.N. Kuftin, V.E. Zapevalov, Russian Academy of Sciences, Nizhny Novgorod, Russia	780
INVESTIGATION OF SMALL-DIMENSIONAL MAGNETRON SECONDARY EMISSION GUNS WITH EXTERNAL TRIGGERING M.I. Ayzatsky, A.N. Dovbnya, P.I. Gladkikh, V.V. Zakutin, V.A. Kushnir, V.V. Mitrochenko, V.F. Pokas, N.G. Reshetn'yak, V.P. Romas'ko, Yu.D. Tur, Kharkov Institute of Physics & Technology, Kharkov, Ukraine	784
OPERATING CHARACTERISTICS OF EFFICIENT, HIGH POWER COAXIAL GYROKLYSTRON AMPLIFIERS W. Lawson, M. Castle, J. Cheng, V.L. Granatstein, B. Hogan, M. Reiser, X. Xu, University of Maryland, College Park MD, USA	788
NUMERICAL SIMULATION STUDIES OF COAXIAL VIRCATOR H. Shao, G. Liu, Z. Song, Y. Fan, X. Song, Northwest Institute of Nuclear Technology, Xi'an, China	792
NUMERICAL STUDY OF FOILLESS DIODE Z. Sung, G. Liu, Y. Fan, H. Shao, Northwest Institute of Nuclear Technology, Xi'an, China	796
EFFECT OF EMISSION INHOMOGENEITIES ON LOW-FREQUENCY OSCILLATIONS IN GYROTRON-TYPE ELECTRON BEAMS V.N. Ilyin, V.E. Mjasnikov, L.G. Popov, GYCOM Ltd., Moscow, O.I. Louksha, G.G. Sominski, St. Petersburg Technical University, St. Petersburg, Russia	800
NON-STATIONARY SIMULATION OF THE GYROTRON HELICAL ELECTRON BEAMS A.N. Kuftin, V.K. Lygin, V.N. Manuilov, Russian Academy of Sciences, Nizhny Novgorod, Russia	804

CONTROL REGIMES POSSIBILITY IN SYSTEM WITH VIRTUAL CATHODE AND INTERNAL FIELD FEEDBACK Yu.P. Bliokh, I.I. Magda, National Science Center "KHPHTI", Kharkov, Ukraine	808
GENERATION OF DENSITY MODULATED ELECTRON BEAM IN AN OPEN RESONATOR B. Maly, J. Nation, L. Schachter, Technion-IIT, Haifa, Israel	812
LINEAR ANALYSIS OF INSTABILITIES IN A PLASMA-FILLED DIELECTRIC-LINED CIRCULAR WAVEGUIDE IMMERSSED IN A FINITE AXIAL MAGNETIC FIELD M. Masuzaki, H. Tsukuda, N. Toyosugi, K. Kamada, R. Ando, Kanazawa University, Kanazawa, T. Watanabe, National Institute for Fusion Science, Tokyo, Japan, C.Y. Lee, Pukyong National University, Pusan, South Korea	816
OBSERVATION OF SELF MODULATION REGIMES OF GENERATION IN POWERFUL BWO N.S. Ginzburg, N.I. Zaitsev, I.S. Kulagin, Yu.V. Novozhilova, M.I. Petelin, A.S. Sargeev, A.K. Tkachenko, Institute of Applied Physics RAS, N.Novgorod, Russia	820
INVESTIGATION OF PLASMA-BEAM AMPLIFIERS WITH REFERENCE TO THE USE IN COMMUNICATION SYSTEMS V.I. Perevodchikov, Y. Kuznetsov, L. Mitin, A. Shapiro, M. Zavialov, All Russian Electrotechnical Institute, Moscow, Russia	824
EFFICIENT SCHEMES OF MILLIMETER WAVE FEM-OSCILLATOR AND AMPLIFIER N.S. Ginzburg, G.G. Denisov, N.Yu. Peskov, A.S. Sargeev, Institute of Applied Physics RAS, Nizhny Novgorod, Russia, A.A. Kaminsky, A.K. Kaminsky, S.N. Sedykh, A.P. Sargeev, Joint Institute for Nuclear Research, Dubna, Russia	829
FREE ELECTRON LASERS WITH SHEET ELECTRON BEAMS AND TWO- DIMENSIONAL PLANAR BRAGG RESONATORS N.S. Ginzburg, N.Yu. Peskov, A.S. Sargeev, I.V. Konoplev, Institute of Applied Physics RAS, Nizhny Novgorod, A.V. Arzhannikov, S.L. Sinitsky, Institute of Nuclear Physics RAS, Novosibirsk, Russia	833
ON THE POSSIBILITY OF CONCRETE DESTRUCTION UNDER HIGH-POWER MICROWAVES GENERATED BY E-BEAM A.V. Arzhannikov, P.V. Kalinin, V.S. Koidan, K.I. Mekler, Budker Institute of Nuclear Physics, Novosibirsk, V.A. Bychenkov, G.V. Kovalenko, Yu.N. Lazarev, P.V. Petrov, A.V. Petrovtsev, Russian Federal Nuclear Center, Snezhinsk, Russia, G. Kessler, Forschungszentrum Karlsruhe, Karlsruhe, J. Eibl, University Karlsruhe, Karlsruhe, Germany	837
HIGH-POWER MICROWAVE GENERATION BY A PLASMA-LOADED BACKWARD-WAVE OSCILLATOR B.-L. Qian, C.-L. Li, Y.-G. Liu, H.-H. Zhong, J.-D. Zhang, Q.-M. Tan, J.-L. Liu, C.-H. Liu, D.-Q. Chen, X.-S. Li, C.-B. Liu, National University of Defense Technology, Hunan, China	841
RELATIVISTIC BWO WITH ELECTRON BEAM PRE-MODULATION A.V. Gunin, S.D. Korovin, I.K. Kurkan, I.V. Pegel, V.V. Rostov, E.M. Totmeninov, Institute of High Current Electronics, Tomsk, Russia	849
GRATING TRANSITION RADIATION - A NEW SOURCE OF MONOCHROMATIC LIGHT USING RELATIVISTIC ELECTRONS O. Haeberle, P. Henri, P. Rullhusen, Institute for Reference Materials and Measurements, Geel, N. Maene, Vlaamse Instelling voor Technologisch Onderzoek, Mol, W. Mondelaers, Universiteit Gent, Gent, Belgium	853
A GYRO-TWT WITH A WEAK SENSITIVITY TO ELECTRON VELOCITY SPREAD V.L. Bratman, G.G. Denisov, S.V. Samsonov, Institute of Applied Physics, RAS, Nizhny Novgorod, Russia, A.W. Cross, W. He, A.D.R. Phelps, K. Ronald, C. Whyte, University of Strathclyde, Glasgow, Scotland, UK	857
NEW CATHODES FOR A RELATIVISTIC MAGNETRON Y.M. Saveliev, W. Sibbett, University of St. Andrews, St. Andrews, Fife, Scotland, S.N. Spark, B.A. Kerr, M.I. Harbour, S.C. Douglas, DERA, Great Malvern, Worcs, UK	861
CYCLOTRON AUTORESONANCE MASER IN THE REGIME OF TRAPPING AND ADIABATIC DECELERATION OF ELECTRONS V.L. Bratman, Yu.K. Kalynov, S.V. Samsonov, A.V. Savilov, Russian Academy of Sciences, Nizhny Novgorod, Russia, A.W. Cross, A.D.R. Phelps, University of Strathclyde, Glasgow, Scotland, UK	865

RECENT RESULTS FROM A LONG PULSE, RELATIVISTIC VACUUM AND PLASMA-FILLED BACKWARD WAVE OSCILLATOR EXPERIMENT E. Schamiloglu, F. Hegeler, C. Grabowski, D. Borovina, University of New Mexico, Albuquerque NM, USA	869
COAXIAL CONFIGURATION FOR A HIGH-POWER RELATIVISTIC TRAVELING WAVE TUBE OPERATING IN THE LOWEST NON-AXISYMMETRIC WAVEGUIDE MODE A.S. Shlapakovski, Institute of Nuclear Physics of Tomsk Polytechnical University, Tomsk, Russia	873
EXCITATION OF BROADBAND OSCILLATIONS BY ELECTRON BEAM IN COAXIAL DISK LOADED TRANSMISSION LINE E.A. Kornilov, P.I. Markov, G.V. Sotnikov, Institute Plasma Electronics & New Methods Accelerations NSC KIPT, Kharkov, Ukraine, I.N. Onishchenko, Ukraine	877
RELATIVISTIC CHERENKOV PLASMA MASER OF MICROSECOND PULSE DURATION O.T. Loza, P.S. Strelkov, I.E. Ivanov, Russian Academy of Sciences, Moscow, Russia	881
ELECTRON BEAM MODULATION AND LEAKAGE CURRENTS DURING SELF-SUSTAINING SECONDARY EMISSION IN MAGNETRON GUNS A.V. Agafonov, P.N. Lebedev Institute of RAS, Moscow, Russia, V.M. Fedorov, V.P. Tarakanov, High Energy Density Research Center, Moscow, Russia	885
EFFECT OF BEAM MODULATION ON A BROADBAND MM RADIATION FROM A STRONG BEAM- TURBULENT PLASMA H. Yoshida, M. Masuzaki, S. Ooyama, R. Ando, K. Kamada, Kanazawa University, Kanazawa, Japan	889
THERMIONIC ELECTRON GUNS FOR HIGH-POWER TRANSIT-TYPE SOURCES OF MICROWAVE RADIATION N.I. Zaitsev, E.V. Ilyakov, I.S. Kulagin, G.S. Korablyov, V.K. Lygin, Russian Academy of Sciences, Nizhny Novgorod, Russia	893
PROBLEMS OF CATHODE DESIGN AND BREAKDOWN AVOIDANCE RELEVANT TO HIGH-POWER BROADBAND GAS-PLASMA-FILLED MICROWAVE SOURCES M. Zavialov, V.I. Perevodchikov, A. Shapiro, All Russian Electrotechnical Institute, Moscow, Russia	897
GENERATION OF SUBNANOSECOND MICROWAVE PULSES BY INTENSE ELECTRON BUNCHES IN A PERIODIC BACKWARD WAVE STRUCTURE IN THE SUPERRADIATIVE REGIME N.S. Ginzburg, Yu.V. Novozhilova, I.V. Zotova, A.S. Sergeev, N.Yu. Peskov, Institute of Applied Physics RAS, N. Novgorod, Russia, A.D.R. Phelps, A.W. Cross, S.M. Wiggins, W. He, K. Ronald, University of Strathclyde, Glasgow, Scotland, UK, V.G. Shpak, M.I. Yalandin, S.A. Shunailov, M.R. Ulmaskulov, Institute of Electrophysics RAS, Ekaterinburg, V.P. Tarakanov, High Energy Density Research Center of RAS, Moscow, Russia	901

ION BEAMS AND DIODES, ICF

INVESTIGATION OF LARGE-AREA MULTIARC PULSED ION SOURCE PLASMA PARAMETERS V. Engelko, B. Ljublin, Efremov Institute of Electrophysical Apparatus, St. Petersburg, Russia, H. Giese, S. Schalk, Forschungszentrum Karlsruhe, Karlsruhe, Germany	907
THE EFFECT OF THE PLASMA POTENTIAL ON CHARACTERISTICS OF BEAMS FORMED BY ELECTROSTATIC ION OPTICS N.V. Gavrilov, D.R. Emlin, V.V. Bersenev, Institute of Electrophysics RAS, Ekaterinburg, Russia	911
MAGNETICALLY INSULATED ION DIODE IN PLASMA OPTICAL MODE A. Goncharov, I. Litovko, I. Protsenko, Institute of Physics NASU, Kiev, Ukraine	915
EFFECTS OF AXIAL CURRENT IN AN EXTRACTION GEOMETRY APPLIED-B ION DIODE J.B. Greenly, D. Sinars, B.R. Kusse, Cornell University, Ithaca NY, USA	919
IMPROVEMENT OF BEAM DIVERGENCE BY EMISSION PROFILES WITH BETTER HOMOGENEITY P. Hoppe, H. Bluhm, L. Buth, D. Rusch, O. Stoltz, W. Vath, Forschungszentrum Karlsruhe, Karlsruhe, Germany, M.P. Desjarlais, Sandia National Laboratories, Albuquerque NM, USA	923

DEVELOPMENT OF LONG PULSE ION INDUCTION LINAC K. Horioka, M. Nakajima, D. Hashimoto, M. Watanabe, Dept of Energy Sciences, Tokyo Institute of Technology, Yokohama, M. Yoshida, J. Hasegawa, M. Ogawa, Research Laboratory for Nuclear Reactors, Tokyo Institute of Technology, Tokyo, K. Takayama, J. Kishiro, National Laboratory for High Energy Physics (KEK), Tsukuba, S. Maebara, M. Shiho, Japan Atomic Energy Research Institute (JAERI), Tsukuba, S. Kawasaki, Dept of Physics, Saitama University, Urawa, Japan	927
CHARGE COMPENSATION AND ACCELERATION OF A THICK-WALLED HIGH-CURRENT ION BEAM IN INDUCTION LINAC N.G. Belova, Russian Academy of Sciences, Moscow, V.I. Karas, O.N. Shulika, National Scientific Center, Kharkov, Russia	931
DETAILED MODELING OF KALIF BEAM-TARGET EXPERIMENTS H. Marten, K. Baumung, H.-J. Bluhm, P. Hoppe, G. Meisel, Forschungszentrum Karlsruhe, Karlsruhe, Germany, J.J. MacFarlane, P. Wang, PRISM Computational Sciences, Madison WI, USA	935
ION EMISSION FROM PLASMA IN THE PRESENCE OF CHARGE TRANSFER S.P. Nikulin, Institute of Electrophysics, Ekaterinburg, Russia	939
BEAM-PLASMA INTERACTION EXPERIMENTS BETWEEN LOW-ENERGY HEAVY IONS AND LASER PLASMA M. Ogawa, U. Neuner, K. Nishigori, A. Sakumi, H. Kobayashi, M. Takizawa, K. Horioka, Y. Oguri, Tokyo Institute of Technology, Tokyo, Japan	943
EXPERIMENTAL RESEARCH ON ION EJECTION FROM PREVIOUSLY CREATED EXPLOSION-EMITTED PLASMA IN MAGNETIC INSULATED DIODES M.S. Opekounov, G.E. Remnev, I.I. Grushin, Tomsk Polytechnic University, Tomsk, Russia	947
INTENSE ION BEAM GENERATION IN AN ANOMALOUS GLOW DISCHARGE WITH NON-METALLIC LIQUID ANODE I.M. Roife, Yu.A. Vasilevskaya, E.G. Yankin, D.V. Efremov Institute of Electrophysical Apparatus, St. Petersburg, Russia	951
HIGH CURRENT ION SOURCE BASED ON A HOLLOW-CATHODE GLOW DISCHARGE WITH E-BEAM INJECTION E.M. Oks, High Current Electronics Institute RAS & State University of Control System and Radioelectronics, Tomsk, Russia, A.V. Vizir, G.Yu. Yushkov, High Current Electronics Institute RAS, Tomsk, Russia	955

BEAM-MATTER INTERACTION AND INDUSTRIAL APPLICATIONS

INVESTIGATION OF THE EFFECT OF HIGH-ENERGY ELECTRON BEAM IRRADIATION ON THE PROCESS OF FORMATION OF INTERMETALLIC PHASES IN Mo-Ni SYSTEM G.G. Bondarenko, V.A. Belov, A.N. Tikhonov, E.M. Slyusarenko, M.M. Yanunkin, Moscow State Institute of Electronics and Mathematics, Moscow, Russia	961
STIMULATED CONDENSATION OF NONSATURATED VAPORS: A NEW EFFECT IN THE NONEQUILIBRIUM PLASMA AND ITS APPLICATION FOR AIR CLEANING S.P. Bugaev, A.V. Kozyrev, B.A. Kuvshinov, N.S. Sochugov, High Current Electronics Institute, Tomsk, Russia	965
AN APPLICATION OF BARRIER DISCHARGE FOR METHANE OXIDATIVE CONVERSION WITH STIMULATED CONDENSATION OF INCOMPLETE OXIDATION PRODUCTS S.P. Bugaev, A.V. Kozyrev, B.A. Kuvshinov, N.S. Sochugov, High Current Electronics Institute, Tomsk, Russia	969
DEPOSITION OF A-C:H FILMS ON LARGE-AREA PLANE DIELECTRIC SUBSTRATES BY MEANS OF PULSED SURFACE DISCHARGE AT ATMOSPHERIC PRESSURE S.P. Bugaev, K.V. Oskomov, N.S. Sochugov, High Current Electronics Institute, Tomsk, Russia	973
MEDICAL EQUIPMENT STERILIZATION USING SUPERHIGH DOSE RATE X-RAY IRRADIATION N.U. Barinov, G.I. Dolgachev, D.D. Maslennikov, M.S. Nitishinsky, A.G. Ushakov, L.P. Zakatov, O.A. Zinoviev, Kurchatov Institute, Moscow, Russia	977
AIR INJECTED HIGH POWER REPETITIVE ELECTRON BEAM FOR RADIATION TREATMENT G.I. Dolgachev, M.S. Nitishinsky, A.G. Ushakov, Kurchatov Institute, Moscow, Russia	981

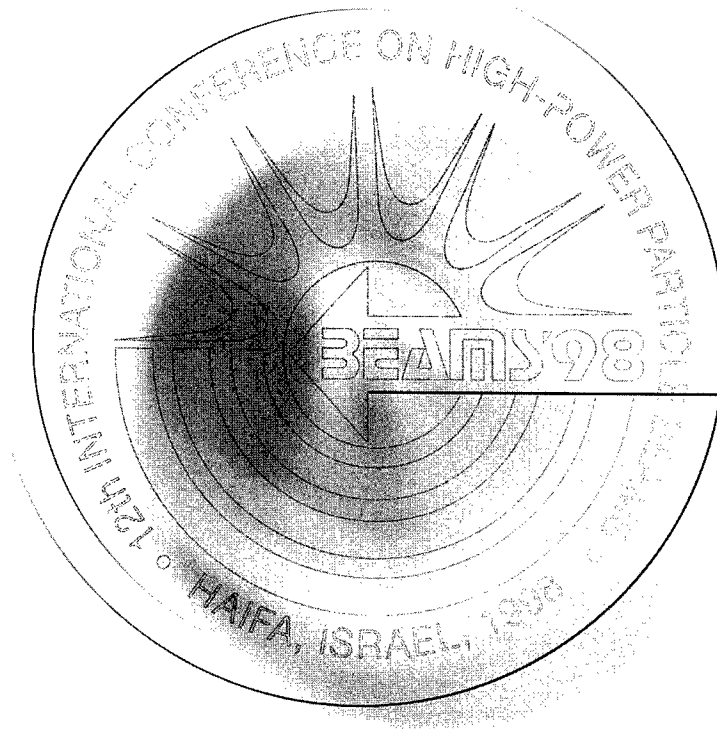
CHARACTERIZATION AND PERFORMANCE OF A HIGH-CURRENT-DENSITY ION IMPLANTER WITH MAGNETIZED HOLLOW-CATHODE PLASMA SOURCE Z. Falkenstein, D.J. Rej, Los Alamos National Laboratory, Los Alamos NM, USA, N.V. Gavrilov, Institute of Electrophysics, Ekaterinburg, Russia	985
FAST SILICON DIODES OBTAINED BY ELECTRON BEAMS E. Iliescu, V. Banu, A. Niculescu, Electron Accelerators Laboratory, Bucharest-Magurele, Romania	989
SIMULATION OF THERMOELASTIC EFFECTS IN THE ION TREATMENT OF METALS I. Amikhanov, V. Fedyanin, Kh. Kholmurodov, I. Puzynin, V. Samoilov, Laboratory of Computing Techniques and Automation, Joint Institute for Nuclear Research, Dubna, Russia	993
MODIFICATION OF POLYURETHANE ENDOPROSTETICS SURFACE BY PULSE ION BEAM V. Begishev, I. Osorgina, Natural - Scientific Institute, Perm State University, Perm, N.V. Gavrilov, G.A. Mesyats, Institute of Electrophysics, Russian Academy of Science, Ekaterinburg, Y. Klyachkin, A. Kondyurin, Institute of Technical Chemistry, Russian Academy of Science, Perm, I. Kondyurina, Perm, Russia	997
USING HIGH-CURRENT NANOSECOND ELECTRON BEAMS TO STERILIZE BONE MEAL Yu.A. Kotov, S.Yu. Sokovnin, Russian Academy of Sciences, Ekaterinburg, P.V. Kolotov, Open Joint Stock Company "Ekaterinburg Meat Factory", Ekaterinburg, Russia	1001
ION IRRADIATION OF CARBON FIBRES N.V. Gavrilov, D.E. Emlin, A.E. Ligachev, G.A. Mesyats, Institute of Electrophysics RAS, Ekaterinburg, E.A. Ligacheva, L.V. Galyaeva, Moscow Aviation and Technology Institute, Moscow, Russia	1004
OXIDE SCALE GROWTH ON MCrAlY COATINGS AFTER PULSED ELECTRON BEAM TREATMENT G. Mueller, G. Schumacher, D. Strauss, F. Zimmermann, Forschungszentrum Karlsruhe, Karlsruhe, Germany, V. Engelko, Efremov Institute of Electrophysical Apparatus, St Petersburg, Russia	1008
REMOVAL OF NO _x BY PULSED INTENSE ELECTRON BEAM IRRADIATION Y. Nakagawa, H. Kawauchi, Osaka City University, Osaka, Japan	1012
PULSED ELECTRON BEAMS FOR REMOVAL OF CS ₂ FROM AIR Yu.N. Novoselov, G.V. Denisov, A.I. Suslov, Russian Academy of Sciences, Ekaterinburg, Russia	1016
THE REMOVAL OF VOLATILE ORGANIC COMPOUNDS FROM AIR BY PULSED ELECTRON BEAMS I.E. Filatov, Yu.N. Novoselov, Russian Academy of Sciences, Ekaterinburg, Russia	1020
NANOMETER-SIZED YSZ POWDERS PRODUCTION BY MEANS OF TARGET EVAPORATION USING HIGH-EFFICIENT PULSED-REPETITIVE CO ² -LASER V.V. Osipov, Yu.A. Kotov, M.G. Ivanov, O.M. Samatov, S.Yu. Sokovnin, P.B. Smirnov, Russian Academy of Sciences, Ekaterinburg, Russia	1023
PRODUCTION OF LOW-ENERGY HIGH-CURRENT ELECTRON BEAMS IN A REFLECTED-DISCHARGE PLASMA-ANODE GUN G.E. Ozur, D.I. Proskurovsky, V.M. Gaponenko, High Current Electronics Institute RAS, Tomsk, Russia	1027
POWER SUPPLY OF A STREAMER CORONA USING FITCH PULSE GENERATOR SWITCHED BY THYRATRONS V.D. Bochkov, V.M. Djagilev, V.G. Ushich, Ryazan, Moscow, Russia, G. Harris, S.P. Kryutchkov, A.P. Shvedchikov, Pulsatron Tec. Ltd, Los Angeles CA, USA, A.Z. Ponizovskiy, L.Z. Ponizovskiy, V.Y. Starobinsky, SEDB "Horizont", Moscow, Russia	1031
APPLICATION OF THE PULSED ELECTRON-BEAM TREATMENT OF ELECTRODE SURFACES FOR INCREASING THE ELECTRIC STRENGTH OF VACUUM GAPS A.V. Batrakov, S.D. Korovin, G.E. Ozur, S.A. Popov, D.I. Proskurovsky, V.P. Rotshtein, Institute of High Current Electronics, Tomsk, Russia, D.H. McDaniel, Sandia National Laboratories, Albuquerque NM, USA	1035
TECHNOLOGICAL APPLICATIONS OF INDUSTRIAL ELECTRON ACCELERATORS OF ELV SERIES A.F. Vaisman, M.G. Golkovski, A.I. Korchagin, N.K. Kuksanov, A.V. Lavruhin, S.E. Petrov, R.A. Salimov, S.N. Fadeev, Budker Institute of Nuclear Physics, Novosibirsk, Russia	1039
USING X-RAY RADIATION TO ERASE INFORMATION FROM A CMOS PROGRAMABLE READ-ONLY MEMORY Yu.A. Kotov, S.Yu. Sokovnin, V.A. Skotnikov, Russian Academy of Sciences, Ekaterinburg, Russia	1045

FOIL ACCELERATION OF HIGH DENSITY ABLATION PLASMA BY INTENSE PULSED LIGHT ION BEAM	
N. Harada, Y. Shinkai, W. Jiang, K. Yatsui, Nagaoka University of Technology, Nagaoka, Japan	1048
NANOSIZE POWDER PRODUCTION BY PULSED WIRE DISCHARGE	
W. Jiang, K. Yatsui, Nagaoka University of Technology, Nagaoka, Japan	1052
SYNTHESIS ON AlN NANOSIZE POWDERS BY PULSED LASER ABLATION	
W. Jiang, M. Hirai, K. Yatsui, Nagaoka University of Technology, Nagaoka, Japan	1056



BEAMS'98

12th INTERNATIONAL CONFERENCE
ON HIGH-POWER PARTICLE BEAMS



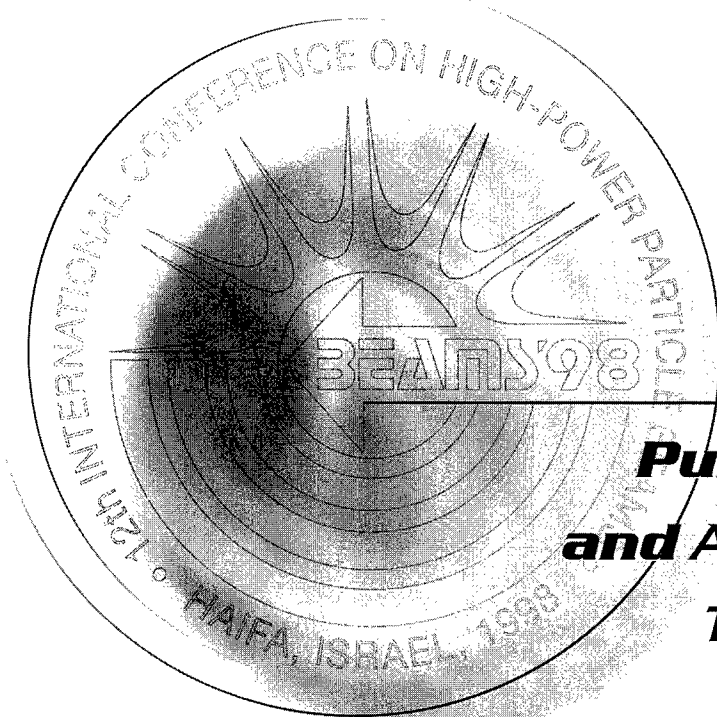
ORALS

Vol. I



BEAMS'98

12th INTERNATIONAL CONFERENCE
ON HIGH-POWER PARTICLE BEAMS



ORALS

***Pulsed Power
and Accelerator
Technology***

Vol. I

COMPARISON OF POS-LOAD DYNAMICS USING DIFFERENT PLASMA SOURCES ON HAWK[†]

B. V. Weber, D. C. Black,* B. Moosman,* S. J. Stephanakis, D. D. Hinshelwood,
R. J. Commisso, S. B. Swanekamp,** J. W. Schumer,* P. F. Ottinger
Plasma Physics Division, Naval Research Laboratory
Washington, DC, 20375 USA

J. J. Moschella and C. Vidoli
HY-Tech Research Corp. Radford, VA 24141 USA

Abstract: Hydrogen Plasma Opening Switch (POS) experiments on Hawk show potential for increasing bremsstrahlung radiation on DECADE. Interferometry indicates that the density of POS plasma is greatly reduced over a large fraction of the interelectrode region (> 1 cm out of 2.2 cm) at the time of opening. This low-density region is much larger for the hydrogen POS than for flashover-source POSs used previously on Hawk (and DECADE), and may result in a significantly larger effective vacuum gap, improving the efficiency of energy coupling to loads. Species separation may be responsible for the difference in plasma dynamics between single- and multi-species POSs.

INTRODUCTION

The POS is a critical component of the multi-module DECADE generator.¹ At present, maximum bremsstrahlung is produced on DECADE Module 1 (DM1) when the POS conduction time is 265 ns and the conduction current is 1.4 MA.² In principle, it is possible to double the load current (from the present 0.8 MA average value to 1.6 MA) by improving POS operation.³ Attempts to increase the POS conduction time to about 300 ns thus far resulted in reduced voltage and radiation.⁴

POS experiments on the Hawk generator at NRL are a cost-effective way to explore alternative POS techniques for DECADE, even though the Hawk current, I , is about 1/3, and the rise time, t , is about 3 times the DM1 values. Both generators operate in the "MHD-dominated" conduction regime,⁵ where $I^2 t^2 \propto n r^2 l^2 M_i / Z$. Here, M_i / Z is the ion mass to charge ratio, n is the electron density, r is the radius where opening occurs and l is the plasma length. The same POS on DM1 and Hawk will conduct to the same It product before opening begins. POS experiments in this MHD regime indicate similar effective magnetically-insulated gap sizes when the POS is open, according to $D = 1.6 \times (2\pi m_e c / e \mu_0) \sqrt{\gamma^2 - 1} (r / I_G) = 2 - 4 \text{ mm}$.⁶ Increasing this effective gap size for greater It values is required to improve the DM1 x-ray output.

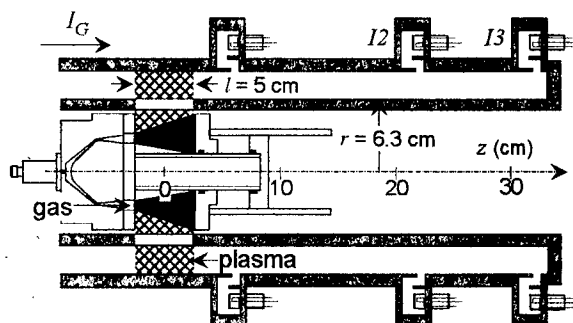


Figure 1. Hawk Inverse-Pinch/POS configuration.

[†] Work supported by the US Defense Special Weapons Agency

* NRC/NRL Research Associate

** JAYCOR, McLean, VA

HAWK POS EXPERIMENTS WITH DIFFERENT PLASMA SOURCES

Recent Hawk POS experiments using an "Inverse Pinch" (IP) gas-plasma source⁷ show potential for increased radiation on DECADE. These experiments were inspired by results⁸ from the Institute of Nuclear Physics, Tomsk, which demonstrated significantly increased POS voltage using a hydrogen plasma, compared with experiments using plasmas created from heavier gases or more traditional flashover (flashboard or cable gun) sources. Increased voltage was not obtained at higher currents using similar gas-plasma sources on Hawk⁹ or GIT-4 in Tomsk¹⁰.

The Hawk IP POS experiment is depicted in Fig. 1. The IP is described in Ref. 7. Voltage and current are measured upstream of the POS, and currents are measured at several locations between the POS and load. An eight-channel laser interferometer measures axially-integrated electron densities spanning the radial gap between the inner and outer conductors. Cable gun plasma was injected through the outer conductor for a direct comparison with the IP POS shots.

POS shots using hydrogen indicate faster, more efficient current transfer to the load than for heavier gases or cable guns, exemplified by the I_3 current waveforms in Fig. 2. These three shots have almost identical conduction times of 0.95-1.0 μs , but used different POS plasmas. (The Hawk generator current, I_G , starts at $t = 0$.) The maximum voltage at the plasma injection location ($z = 0$) is systematically greater ($\sim 2\times$) for hydrogen shots compared with cable guns or heavier gases.⁷

Using hydrogen, axially-integrated interferometry indicates that much of the radial interelectrode region (1.5 cm out of 2.2 cm) becomes cleared of plasma (within measurement uncertainty) at the time current is transferred to the load, as shown in Fig. 3 for the hydrogen POS shot in Fig. 2. Seven of the eight signals decrease rapidly, becoming approximately zero at the time current is measured in the load ($t = 0.95 \mu\text{s}$). Several of the interferometer signals (3, 4, 5) near the center of the electrode gap remain small for an additional 0.5 μs before high density plasmas from both electrodes move into the lines-of-sight.

This low-density region is much larger for the hydrogen IP POS than for flashover-source POSs used previously on Hawk, and may result in a significantly larger effective vacuum gap size, the critical parameter that determines the efficiency of energy coupling from a POS to a load.⁶ Radial density distributions are compared in Fig. 4 for three POS sources: cable guns, flashboards and hydrogen IP. The flashover source measurements were made previously¹¹ using a smaller center conductor radius of 5 cm. For the flashover-source POSs, the initial density is redistributed during the conduction phase resulting in a small radial region where the density is low enough to imagine the possibility for gap formation, consistent with the ~ 3 mm gap size inferred from shots with high impedance loads. The

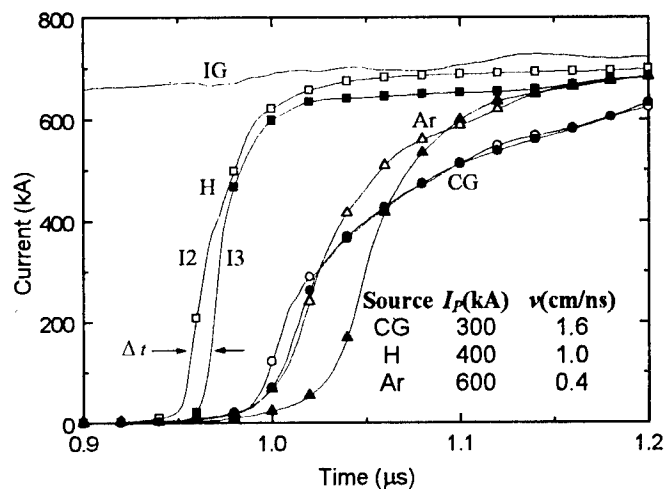


Figure 2. Load currents (I_2 and I_3) for different POS plasma sources with similar conduction times in the same configuration ($r = 6.3$ cm). Open symbols indicate currents at the I_2 location and solid symbols indicate currents 10 cm downstream at the I_3 location. Squares correspond to the hydrogen IP, circles to the cable-gun and triangles to the argon IP. The time interval between symbols is 20 ns.

hydrogen IP POS data indicate a much larger region where the density is small.

DIFFERENCES BETWEEN SINGLE- AND MULTI-SPECIES POS

Species separation can occur in a multi-species POS. This may explain the differences between the IP/POS and the flashover-source POS. This idea was first proposed by researchers at the Weizmann Institute who determined that a proton plasma moves ahead of the heavier species (carbon ions, etc) in their POS experiments and conducts most of the current, based on spectroscopic measurements.¹² Analytic treatments¹³ and PIC simulations¹⁴ support this picture. The heavy plasma remaining behind the light, current-carrying plasma can limit the gap size. Hawk data for the multi-species flashover sources (Fig. 4) and more detailed measurements¹⁵ in a planar cable-gun POS on Hawk show this remaining plasma

extending across most of the interelectrode gap after opening. With a single-species plasma, no species separation can occur and the $\mathbf{J} \times \mathbf{B}$ force can more effectively sweep the high density plasma radially toward the electrodes and axially toward the load, producing conditions more conducive for opening a larger magnetically insulated gap.

The currents measured near the load (Fig. 2) provide clues about the plasma reaching the load region. The initial rise of the I_2 and I_3 signals show a time difference, Δt . Later, the I_2 and I_3 signals meet at a current less than the generator current. The two signals then

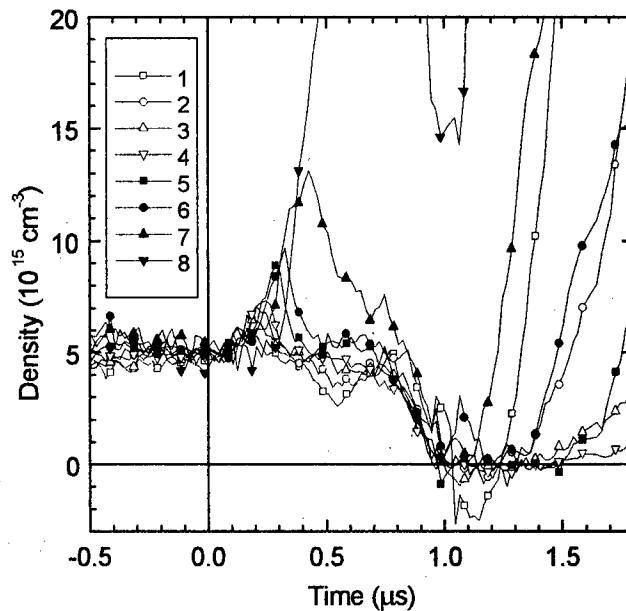


Figure 3. Line-averaged electron densities vs. time for hydrogen POS showing drastic reduction in density at time of opening (0.95 μs). The eight beams each sample a 2.5 mm radial region, covering 20 of the 22 mm radial electrode gap. Signal #1 is closest to the center conductor and #8 is closest to the outer conductor.

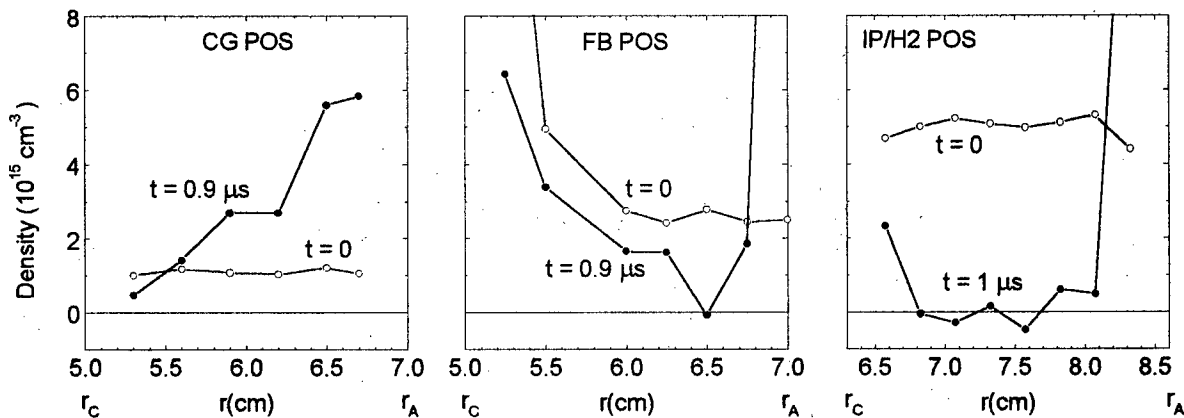


Figure 4. Comparison of average densities at $t = 0$ (initiation of Hawk current) and at opening for cable gun and flashboard POSs ($r = 5$ cm) (from Ref. 11) and for the hydrogen IP POS ($r = 6.3$ cm). The horizontal axes indicate the radial location of the cathode (r_C) and anode (r_A). Open symbols correspond to the initial density distribution, solid symbols correspond to the density distribution when the POS is open.

increase together and approach the generator current. This behavior is the same as would be produced by a propagating current channel with current $I_p < I_G$, moving past the probe locations with velocity v , shown schematically in Fig. 5. After the current channel passes the probes, the load current continues to increase because the remaining generator current is flowing through the "opened POS," producing voltage that drives current through the inductive load. The velocity of the current channel can be estimated from the axial distance between the I_2 and I_3 probes (10 cm) divided by Δt . The current in the channel is approximately the value where the I_2 and I_3 signals meet. The I_p and v values are shown in Fig. 2.

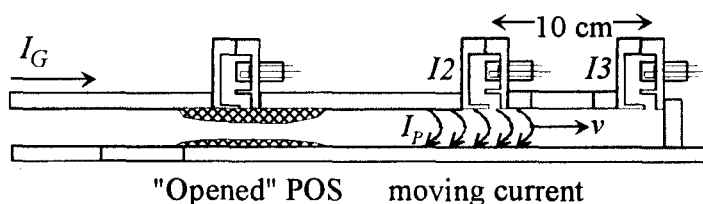


Figure 5. Schematic of opened POS and downstream current-carrying plasma consistent with load current measurements.

The force on the current channel (while the load current is zero) is proportional to I_p^2 . Of the three examples in Fig. 2, the force on the cable-gun POS is smallest and the velocity is greatest, therefore the current-channel mass is smallest. The argon POS has the greatest force and smallest velocity, therefore the greatest mass. The mass for the hydrogen POS is between the other two. This qualitative comparison is consistent with the species separation picture. Only a small fraction of the multi-species flashover-source plasma (presumably protons) is accelerated ahead of the heavier species, while for the IP plasmas, species separation will not occur and a larger fraction of the injected plasma will move downstream. The parameters of this translating plasma may determine the optimum location of diode or PRS loads for efficient energy coupling.

SUMMARY AND CONCLUSIONS

The hydrogen IP POS is an exciting alternative for DECADE. The Hawk IP experiments indicate a larger radial region cleared of the initial injected plasma, compared with flashover-source POSs. This makes it possible for larger gaps to form, consistent with the factor-of-two improvements demonstrated in 1991 in Tomsk. Current measurements indicate more downstream plasma with the IP sources compared with flashover sources, possibly related to species separation in multi-species POSs. This downstream plasma density may be circumvented by simply moving the load a sufficient distance from the POS to allow the downstream plasma to dissipate. Experiments to test this POS with e-beam diode loads are planned in the near future on Hawk and subsequently on DM1.

¹ P. Sincerny, et al., *Proc. 11th International Pulsed Power Conf.*, (Baltimore, 1997), p. 698.

² J. R. Goyer, et al., *IEEE Trans. Plasma Sci.* **25**, 176 (1997).

³ B. V. Weber, et al., *Proc. 11th International Pulsed Power Conf.*, (Baltimore, 1997), p. 153.

⁴ J. R. Thompson, et al., *Proc. 11th International Pulsed Power Conf.*, (Baltimore, 1997), p. 269.

⁵ B. V. Weber, et al., *Phys. Plasmas* **2**, 3893 (1995).

⁶ R. J. Commisso, et al., *Phys. Fluids B* **4**, 2368 (1992).

⁷ J. J. Moschella, et al., these proceedings.

⁸ P. S. Ananjin, et al., *IEEE Trans. Plasma Sci.* **20**, 537 (1992).

⁹ P. J. Goodrich, et al., *Proc. 10th International Conf. High Power Particle Beams* (San Diego, 1994), p. 299.

¹⁰ A. A. Sinebryukhov, private communication.

¹¹ B. V. Weber, et al., *IEEE Trans. Plasma Sci.* **25**, 189 (1997).

¹² A. Weingarten, et al., these proceedings.

¹³ L. Rudakov, *Proc. 10th International Conf. High Power Particle Beams* (San Diego, 1994), p. 284.

¹⁴ S. B. Swanekamp, et al., *IEEE Conference Record - Abstracts* (1998 IEEE ICOPS, Raleigh) p. 147.

¹⁵ R. J. Commisso, et al., these proceedings.

PULSED POWER FUSION PROGRAM UPDATE*

J. P. Quintenz, R. G. Adams, G. O. Allshouse, J. E. Bailey, D. D. Bloomquist, G. A. Chandler, R. S. Coats, D. L. Cook, M. E. Cuneo, C. Deeney, M. S. Derzon, M. P. Desjarlais, M. R. Douglas, D. L. Fehl, A. B. Filuk, T. A. Haill, D. L. Hanson, D. J. Johnson, M. L. Kiefer, J. S. Lash, R. J. Leeper, B. M. Marder, M. K. Matzen, D. H. McDaniel, E. J. McGuire, T. A. Mehlhorn, L. P. Mix, A. R. Moats, T. J. Nash, C. L. Olson, R. E. Olson, T. D. Pointon, J. L. Porter, C. L. Ruiz, T. W. L. Sanford, J. F. Seamen, D. B. Seidel, S. A. Slutz, R. B. Spielman, W. A. Stygar, M. A. Sweeney, R. A. Vesey, D. F. Wenger

*Sandia National Laboratories
Albuquerque, NM 87185-1191*

Abstract

The U. S. Department of Energy has supported a substantial research program in Inertial Confinement Fusion (ICF) since the early 1970s. Over the ensuing 25 years, pulsed power approaches to inertial fusion have remained of interest primarily because of the high energy, efficiency, and relatively low cost of the technology when compared to the mainline ICF approach involving large glass lasers. These compelling advantages, however, have been tempered with the difficulty in concentrating the energy in space and time to create the high energy and power density required to achieve temperatures useful in indirect drive ICF. Since the Beams '96 meeting, the situation has changed dramatically, and extremely high x-ray power (290 TW) and energy (1.8 MJ) have been produced in fast z-pinch implosions on the Z accelerator. These sources have been utilized to heat hohlraums to > 150 eV and have opened the door to important ICF capsule experiments. Although light ion beams offer a long term potential for fusion energy, we are suspending our ion beam research this year to maximize progress with z pinches.

Introduction

For more than two decades, scientists in laboratories around the world have used pulsed power drivers with very short (10s of nanoseconds) pulse lengths for Inertial Confinement Fusion (ICF) experiments. In the United States, this research has been sponsored by Defense Programs within the Department of Energy. During this period, the fundamental pulsed power components and accelerator architectures have evolved to a remarkable extent and, today, electrical pulses of 60 TW are routinely obtained on the Z accelerator at Sandia National Laboratories. Many of the technological advances were driven by the demanding requirements placed upon accelerators by the needs of the fusion program. These requirements are driven by the goal of achieving up to 1 GJ of fusion yield from an ICF capsule for energy and defense applications. While the fusion yield goal has remained remarkably the same for the better part of two decades, the required driver energy, capsule symmetry, and capsule drive pulse shape

* This work was supported by the United States Department of Energy under Contract DE-AC04-94AL85000.

have evolved considerably as the community learned more about the coupling of driver energy into the capsule ablator and the capsule response to this energy deposition.

As the capsule drive requirements were changing, the driver options for pulsed power were evolving. Early driver technologies included intense electron beams and z pinches. In the late 70s after the development of intense electron beam diodes, a shift from electrons to ions was dictated by the favorable deposition characteristics of the ions. Z-pinch experiments continued and z pinches were applied to other applications, but funding from the ICF program was suspended in favor of ions. While advances in understanding the physics of intense light ion beams were substantial, the record ion beam intensities that have been achieved (5 TW/cm² - protons, 2 TW/cm² - lithium) remain far below the requirements of ICF (100 TW/cm²).

By 1994 on the Saturn accelerator (formerly PBFA I), z-pinch x-ray power and energy output had been increased to the level (~20 TW and ~400 kJ) that important ICF experiments could begin. The success of these experiments and the recent breakthroughs in z-pinch performance on the Z accelerator (290 TW and 1.8 MJ of x rays, >150 eV in a hohlraum) have led to another major shift in emphasis in pulsed power fusion. Beginning in 1999, the entire pulsed power fusion effort at Sandia will be directed toward developing z-pinch x-ray sources for ICF. This paper will describe the present status of the pulsed power fusion program at Sandia and the plans to develop further this promising path to fusion.

The long-term goal of ICF research is high yield. High yield in this context means thermonuclear yield of 200-1000 MJ. In 1993, glass laser technology was chosen to demonstrate ignition in the laboratory. The National Ignition Facility will be capable of delivering 1.8 MJ of 3 ω (350 nm) light to a target. The 1.8 MJ of laser energy will result in 100 - 150 kJ of x-ray energy absorbed in the capsule. The predicted yield with this absorbed energy is 2 - 20 MJ. Ignition demonstration on the NIF would be a major step toward obtaining high yield in the laboratory. However, a high-yield target is expected to require 1-2 MJ of x rays absorbed in the capsule ablator and radiation symmetry on the capsule surface of better than 2%. To achieve this radiation symmetry, a large case-to-capsule radius ratio is needed. Consequently, a driver must supply approximately 10 MJ of x-ray energy, prohibitively expensive using laser technology. In addition, the x-ray power pulse incident on the capsule must have an appropriate time variation to adiabatically compress the DT fuel. Furthermore, an energy application of ICF will require a repetitive pulse capability of 4 Hz. Pulsed-power-driven ICF offers an attractive alternative to lasers with affordable, high-energy, high-efficiency drivers and the potential for repetitive pulse operation.

Progress in Z-pinch Development

The recent remarkable progress in x-ray generation using z pinches has prompted a major shift in Sandia's ICF program. Z pinches are now seen as the fastest route to demonstration of high yield in the laboratory. Pulsed power accelerators have been used for many years to drive magnetic implosions (z pinches). The loads in these implosions have varied from cylindrical arrays of wires arranged at constant radius, to annular gas puffs and low-density foams. In the application as an x-ray source, the kinetic energy in the imploding system is converted into x rays when the imploding plasma stagnates on axis or on a central cylindrical cylinder. Z pinches have historically been efficient at coupling electrical energy into kinetic energy in the implosion system, but the x-ray power available has been limited to less than 20 TW. Beginning in the summer of 1995, however, breakthroughs in load fabrication (which allowed

several hundred 5 $\mu\text{g}/\text{cm}$ Al or W wires to be mounted to form a 2 - 4 cm diameter cylindrical array) and improved understanding of load behavior have resulted in dramatic improvements in the x-ray power available from these sources. By early 1996, the x-ray power available from a tungsten load exceeded 75 TW, by far the most power ever generated in a laboratory device. The energy in x rays remained nearly constant at 400 - 500 kJ as the power increased. These results were obtained on the Saturn accelerator. Such high power and energy x-ray sources have major applications in the ICF program.

While the breakthrough experiments were being conducted on Saturn, a major modification to the Particle-Beam Fusion Accelerator (PBFA II) was underway. The intent of the modification was to allow z-pinch experiments at higher currents than possible on Saturn to validate the scaling of x-ray power and energy with accelerator current. The modified accelerator configuration was first called PBFA-Z and later shortened to Z. Ambitious goals set for Z included delivering 18 MA to the pinch, producing 1.5 MJ and 150 TW of x-ray energy and power and, using this x-ray source, heating a vacuum hohlraum to > 100 eV and a dynamic hohlraum to > 120 eV. The first radiation producing experiment on Z was conducted in October 1996 and within the first month of operation, the current, energy and power milestones were met.

The x-ray power available from a z-pinch implosion is limited by the Rayleigh-Taylor (R-T) instability. Mitigating the effects of this instability can greatly increase the total radiated power. Progress in this area has been significant, with a major advance occurring when nested wire arrays are employed. Analysis and computer simulations suggested that if one wire array were imploded onto another wire array at smaller radius, growth of the R-T instability would be reduced. Experiments that optimized the mass ratio between the inner and outer wire arrays resulted in a 40% increase in radiated power. Today, the x-ray output of Z has climbed to 290 TW and 1.8 MJ. The energy and power scaling with current has been confirmed ($E, P \propto I^2$). Figure 1 shows the agreement in radiated energy scaling with z-pinch current over two decades. The x-ray power increase as a function of year in Fig. 2 illustrates the very rapid progress of the past two years.

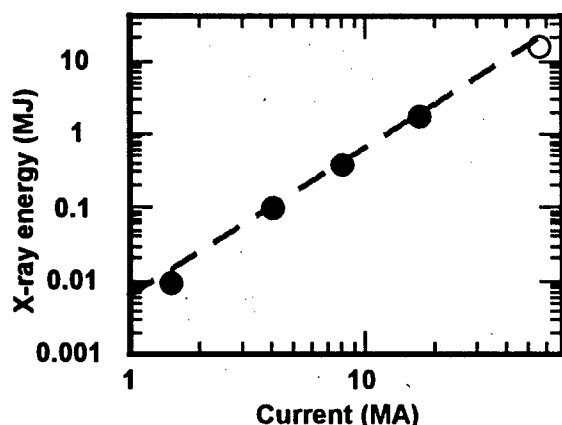


Figure 1. X-ray energy vs. z-pinch current

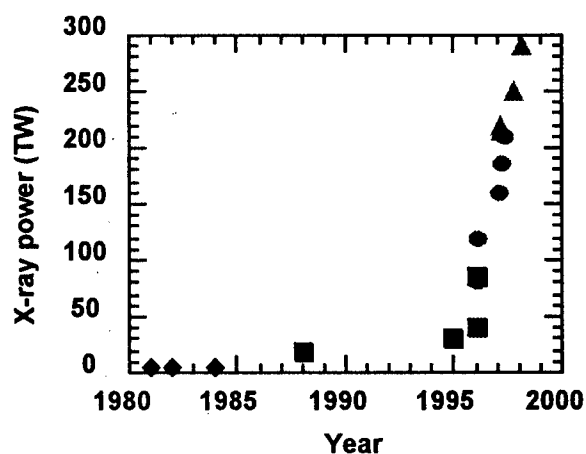


Figure 2. X-ray power vs. year

Hohlraum heating and target concepts

The high x-ray power output has enabled experiments to optimize the temperature in hohlraums. Progress in this area has also been rapid. To both increase the x-ray intensity and

improve the spatial uniformity, we have enclosed the wire-array x-ray sources within large (up to 5-cm diameter, 2-cm long) cylindrical hohlraums. This configuration is denoted a "z-pinch driven" or "vacuum" hohlraum. If we assume that 80% of the x ray energy incident on the high-Z inner walls of this hohlraum is re-radiated back into the hohlraum volume, a simple power balance predicts that the x-ray intensity inside the container will be a factor of five larger than the power generated by the z-pinch source itself. Measurements indicate the hohlraum temperature reaches 150 eV when a 20-mm-diameter, 300-wire tungsten array implodes within a 10-mm-long, 23-mm-diameter hohlraum. The re-radiation of the z-pinch x rays from the hohlraum wall effectively produces a Planckian source. If the imploding array itself contains (re-radiates) radiation into the cylindrical region within the array, a dynamic hohlraum can be formed. Experiments in this configuration have shown that a dynamic hohlraum does indeed form and that significant gains in radiation temperature are achieved. In experiments on Z, a nested wire array was imploded onto a plastic annular target (2.5 mm radius, 3 mg). The peak temperature obtained while the hohlraum remained useful for driving a capsule experiment (that is, the mean free path of the x rays was large compared to the radius of the imploding cylinder) was > 155 eV.

Three generic z-pinch driven capsule configurations are being considered for high yield (Fig. 3) ranging from the vacuum to the dynamic. The concepts explore variations in the level of conservatism in the z-pinch source characteristics versus drive temperature and efficiency of driving the capsule.

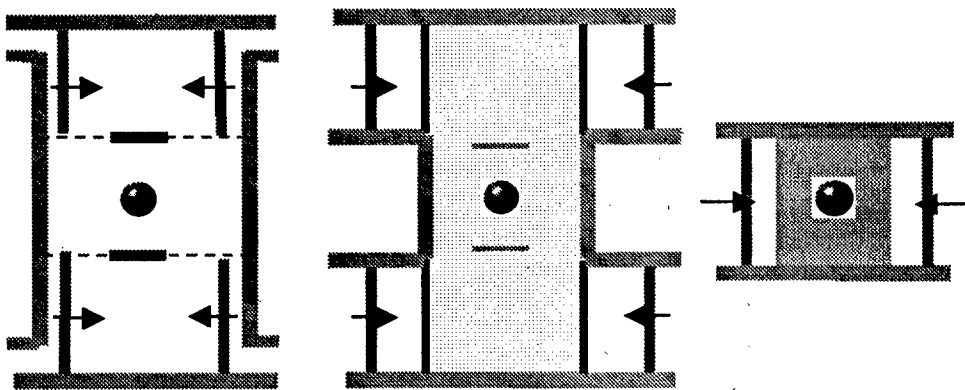


Figure 3. Three hohlraum/capsule concepts for high yield.

The high hohlraum temperatures (>150 eV) enable the first capsule experiments which are scheduled to begin this year. These experiments will employ dynamic hohlraums driven by nested wire arrays. Currently the dynamic hohlraum provides our highest radiation temperatures in an open volume while simultaneously producing a reasonably symmetric radiation drive. At the time of this writing, a 240- on 120-wire nested tungsten array of 3 mg total mass striking a 2.5-mg deuterated plastic cylinder of 5-mm diameter yields a first strike temperature of 80 eV which linearly ramps to 180 eV over roughly 7 ns. While the high-temperature of the dynamic hohlraum is preferred over configurations where the capsule hohlraum is external to the z-pinch x-ray source, target designs are constrained by the time between first-strike of the imploding z pinch on a central cylinder and the stagnation of the entire target on the cylindrical axis of symmetry.

Capsule design and modeling for the first dynamic hohlraum capsule experiments are being carried out with the LASNEX radiation hydrodynamics code. High-resolution capsule performance simulations are accomplished with 1-D calculations using experimentally obtained

drive histories. Integrated 2-D simulations incorporating the tungsten wire impact on the dynamic hohlraum are used to address capsule drive symmetry. The current capsule design is a 1.6-mm inner-diameter sphere with a 30-micron thick polystyrene shell fabricated by General Atomics. To enhance the fill gas lifetime, a permeation barrier of approximately 4 microns of PVA and 0.6 microns of aluminum is coated on the shell. The capsules will be filled with 16-18 atm of deuterium gas with an optional 0.1 atm of a diagnostic dopant gas such as argon. Clean 1-D simulations predict a neutron yield of 3×10^{10} for an undoped polystyrene shell while the yield increases to 1×10^{11} with a 2.5% atomic fraction germanium doping.

Experimental diagnostics for this series can be divided into source diagnostics and capsule diagnostics. Characterization of the dynamic hohlraum environment will be determined through filtered XRDs both on- and off-axis, and filtered, time-resolved x-ray framing cameras. Capsule performance will be assessed through neutron time-of-flight, neutron activation and a filtered, time-resolved x-ray framing camera for imaging the imploding capsule emission. Careful characterization of the experiment is a necessity, as comparison of the capsule performance with simulation will provide the starting foundation for our high-yield dynamic hohlraum targets for the proposed X-1 facility.

X-1 is a proposed facility that would deliver 60 MA to a z-pinch load. The scaling curves suggest that X-1 would be capable of producing 16 MJ and > 1000 TW of x-ray energy and power and of heating hohlraums to > 250 eV. Simulations indicate that these conditions would allow capsule/hohlraum configurations to yield in excess of 200 MJ fusion output. X-1, if approved, could be built and high yield experiments begun by 2010.

Status of Light Ion Beam Development

Light ion beams have the potential of capitalizing on the efficiency of pulsed power in applications for inertial fusion energy (IFE) by offering standoff and repetitive pulse operation. Progress in developing light ion beams for ICF has been substantial but many obstacles remain. The key physics principles of an indirectly driven ion beam target demonstrated in radial diode experiments have included ion beam deposition, radiation conversion, tamping of the radiation case by an optically thin foam, and radiation smoothing. Using light ion beams for IFE will require extraction ion diodes with much higher beam brightness than has been demonstrated. The remaining ion beam issues fall into two main areas: beam intensity and standoff. The ion beam intensity is determined by the total ion beam power and the ion beam divergence. Simulations of ion diodes suggest that an electromagnetic contribution to the ion beam divergence can be reduced by controlling the electron sheath through high magnetic fields or by physical limiters that keep electrons away from the anode. Electron control is also important because cross-field diffusion allows electrons to reach the anode and reduces power efficiency. The electron loss also heats the anode leading to thermal and stimulated desorption of monolayer surface contaminants that become ionized and generate a parasitic (e.g. non-lithium ions) loss current of ions. RF discharge cleaning of the electrode surfaces can help suppress this parasitic current; the efficiency of lithium production has increased substantially on the SABRE accelerator using these techniques. An active ion source where an independent energy source is used to prepare an anode plasma is required to allow both control of the electron distribution and reduce the source divergence to an acceptable level. Light lab experiments have determined the minimum laser fluence on the anode to produce a uniform plasma ion source. An experimental series that integrates all of these concepts at once (high

magnetic field, active laser-produced ion source, electron limiter, and improved anode conditioning) is in progress on SABRE.

Standoff is required for high yield applications to protect the ion diode from the target blast. The baseline transport mode in previous studies was an achromatic lens system that required an ion beam divergence of 6-8 mrad. Self-pinch ion beam transport is an attractive mode for both light and heavy ion fusion energy applications and could relax the ion beam divergence requirements on the ion diode. Self-pinch transport experiments are being conducted at the Naval Research Laboratories. Success in establishing scaling laws and controlling solutions for these key issues on the SABRE, COBRA, and GAMBLE accelerators could lead to future higher-power ion diode experiments and eventually to a repetitive high yield facility for energy production.

Conclusions

Pulsed power provides an economical source of x-ray energy and power for ICF research. Experiments on pulsed power accelerators have demonstrated that x rays can be generated with high efficiency using fast z pinches. Experiments are planned to continue to optimize these sources for application to ICF. The first capsule experiments on Z using a z-pinch x-ray source are planned for later this summer. These and similar capsule experiments will provide validation of computer models of capsule designs. Z pinches represent the best means to generate high-energy, high-power x-ray environments for exploring pulsed power driven ignition and high-yield relevant capsule physics. In the far term if the remaining ion beam brightness and transport issues can be resolved, light-ion driven ICF could offer repetitive high yield for energy production. Sandia's pulsed power ICF program is focused upon exploiting the advantages of pulsed power in fusion research.

Acknowledgments

The authors would like to recognize the extraordinary contributions to this research made by George Allshouse and Alex Filuk, both recently deceased. They have had a profound impact on our understanding of pulsed power fusion. The pulsed power ICF program is an international effort. Important contributions to the field are being made by scientists and engineers from around the world. This presentation has emphasized activities at Sandia National Laboratories; however, the authors would like to acknowledge our many colleagues who have contributed to the recent progress. Many of these advances are presented elsewhere at this conference.

URT-0,5 REPETITIVE PULSED ELECTRON ACCELERATOR

Yu.A. Kotov, S.Yu. Sokovnin

*Institute of Electrophysics, Russian Academy of Sciences
34 Komsomolskaya St., Ekaterinburg, Russia, 620049*

Abstract

URT-0,5 repetitive pulsed electron accelerator with a semiconductor opening switch and a vacuum diode with a metal-dielectric cathode were created for commercial application. The electric circuit of this unit is based on a SOS-technology and utilizes a thyatron-magnetic compression of the energy.

The accelerator produce electron beam with an electron energy of 500 keV, a current of 200 A, an FWHM pulse duration of 50 ns, a pulse repetition rate up to 200 pps, and a diameter of cross-sectional area 10 cm.

As a X-rays generator it had produced 30,4 Gy per minute at 5cm from the anode on the axis.

Introduction

The cheapness, ease of service, reliability, and longevity of accelerators are the decisive factors determining their commercial application. Among the large number of available types of electron accelerators, accelerators based on semiconductor opening switch (SOS-technology) [1] meet these requirements to the highest degree. The use of magnetic compression of energy in combination with SOS allowed the development of a number of compact accelerators and oscillators [2] with a long service life. A SOS serves as final power amplifier and converts a microsecond pumping pulse to a nanosecond output pulse.

Usually preliminary magnetic compression of the energy using with semiconductor switch - thyristor [3]. But there is a not simply way, because of there are usually three-four linked magnetic circuits which put into operation too difficulty. We prefer another way to use magnetic compression of the energy with a thyatron [4]. A thyatron is high voltage unit and it is possible to use only one steep of magnetic compression.

Electric circuit diagram and design of the accelerator

Electric circuit diagram of the accelerator is shown in Fig. 1. The device consists of a high-voltage energy storage (HVES), a control panel and a high-voltage oil tank, which houses a thyatron V1, high-voltage capacitors C1 and C2, a high-voltage pulse transformer-compressor PT1, SOS and load - vacuum diode V2. The dimensions of the oil tank, which weights approximately 250 kg, are: diameter 0,5 m and height ~ 1 m.

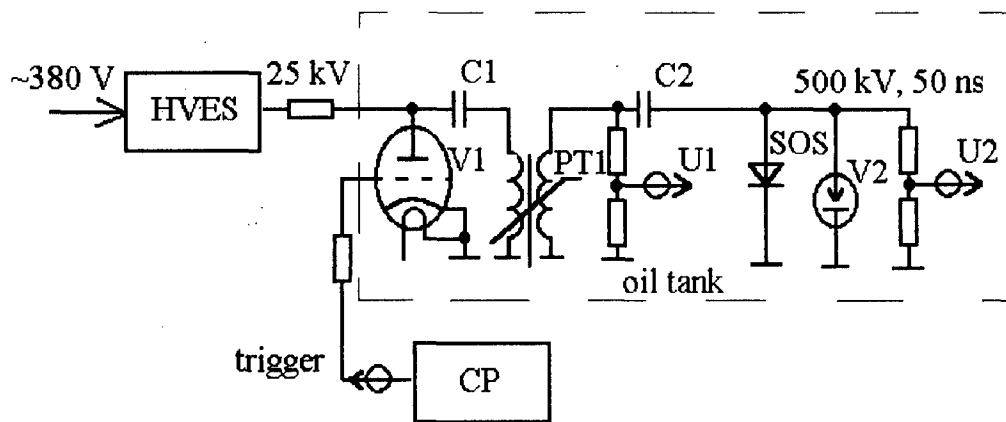


Fig. 1. Electric circuit diagram

The vacuum diode of the accelerator works with a pressure of 10^{-4} Torr. The vacuum insulator, with a height of 18 cm, has a shielded acrylic dielectric surface [5]. A metal-dielectric cathode is used [6]. A 100-mm diameter window covered with an Al foil $35 \mu\text{m}$ thickness serves as the beam exit.

The voltages at the capacitor C1 (U1) and vacuum diode (U2) were measured with the use of resistive dividers (Fig. 1.) based on the carbon resistors with a digital oscilloscope.

The accelerator is supplied by a three-phase 50-Hz mains with voltage 380V by using a high-voltage converter in HVES.

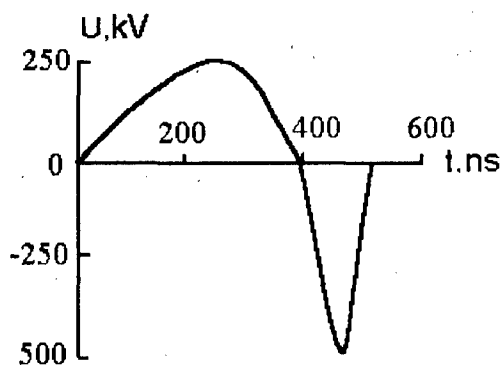


Fig. 2. Oscillogram of the voltage pulse of the capacitor C2

The accelerator operates in the following way. The capacitor C1 is charged to the voltage $\sim 25 \text{ kV}$ from HVES. The charge current of this capacitor reverses magnetization of the core of the pulse transformer-compressor PT1 (permalloy 50 NP with thickness 0.02 mm). When the thyatron V1 is turned on, the energy is transferring from C1 through PT1 to capacitor C2 in time $\sim 350 \text{ ns}$ to voltage level $\sim 250 \text{ kV}$ (Fig. 2). The same time it is the process of forward pumping of the SOS. The SOS consists of two parallel branches, each comprising 4 se-

ries-connected opening switches (CДЛ-1600-04 diode). The amplitude of the forward pumping current is $\sim 0.5 \text{ kA}$. Upon saturation of the core of PT1, the capacitor C2 is discharging. The reverse current is pumping of the SOS ($\sim 1.5 \text{ kA}$), as soon as the SOS cuts off the current, an output pulse is generated at the load. A breakdown occurs at triple

points (metal-insulator-vacuum) of the cathode, and the generated plasma emits electrons. The electrons are accelerated, by the applied pulse and escape to the atmosphere through the foil.

Test results

The accelerator was tested in electron beam and X-ray mode (Table 1 and Fig. 3). Given pulse repetition rate is limited only by the thermal load on the core of the pulse transformer-compressor. As a X-rays generator the accelerator had produced 30,4 Gy per minute at 5cm from the anode on the axis. The target consists of Ta and Al with thickness 0.1 and ~2 mm correspondingly. The X-rays pulse (P) was measured using a pin-detector (Fig. 3.).

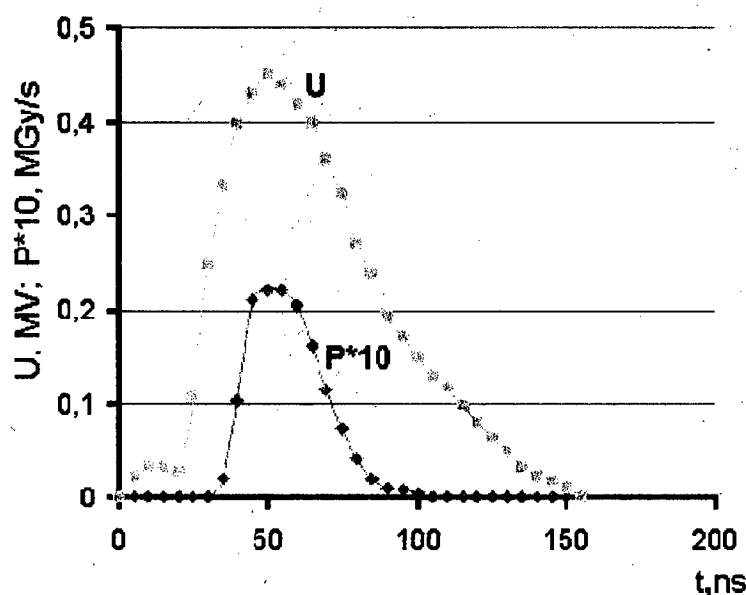


Fig. 3. Oscillogram of the voltage (U) and X-rays (P) pulses.

The absorbed dose of the electron beam at the accelerator exit was measured with the use of plastic dosimeter films [7]. Detectors were placed at the surface of the exit foil. In one measurement, a detector allowing the obtaining of the full beam print was used. In each measurement, 1500 pulses with a frequency of 50 Hz were applied.

The electron current density behind the foil was calculated from the

measured absorbed dose D_0 (calculated to the single pulse, of course), using the formula obtained from the relation for calculating the dose due to electrons [4]. It was $J=3.1 \text{ A/cm}^2$ that corresponded the total pulse current 250 A (in the atmosphere). The effective

electron energy E , was measured with the filter technique [4]. The adsorbed dose was measured before D_0 and behind D_1 the filter (35 μm Al foil). Then the effective electron energy E can be found from the relation for attenuation of fast electrons in a filter material. The results of calculations

Table 1. Parameters of the accelerator

Electron energy, MeV	~ 0.5
Pulse current in the vacuum diode, A	~ 350
Average output beam power, kW	~1.25
Pulse duration, ns	50
Pulse repetition rate, pps	200
Beam area, sq. Cm	~ 80
Consumed power, kW	~4

and voltage values U_2 measured at the vacuum diode are listed in the Table 2 as well.

The accelerator service life is determined by the operational life of the components used. The basic components can withstand $> 10^{10}$ pulses. The limitation is due to the thyatron, with a certified service life of 500 h [3]. But this limitation is not essential, because the thyatron operates in a mode of substantial power underloading, and the accelerator design allows prompt replacement of the thyatron.

Table 2. The results of calculations.

N	D_0 , κGy	D_1 , κGy	D_0 / D_1	E , keV	U_2 , κV	J , A/cm^2	Note
1	30,1	20,06	1,5	486	500	3,1	
2	20,06	13,84	1,45	516	500	2,06	Both detectors are additionally covered with a 35 μm Al foil

Conclusion

It is possible to use this accelerator in such application of a high-current electron beam and bremsstrahlung as: conducting chemical reactions, sterilization, water cleaning, luminescence and other commercial applications.

The accelerator is so reliable, because we use industrially robust or well-tested components. Nevertheless, all components are not so expensive and so it is possible to rebuild or replaced them in short time.

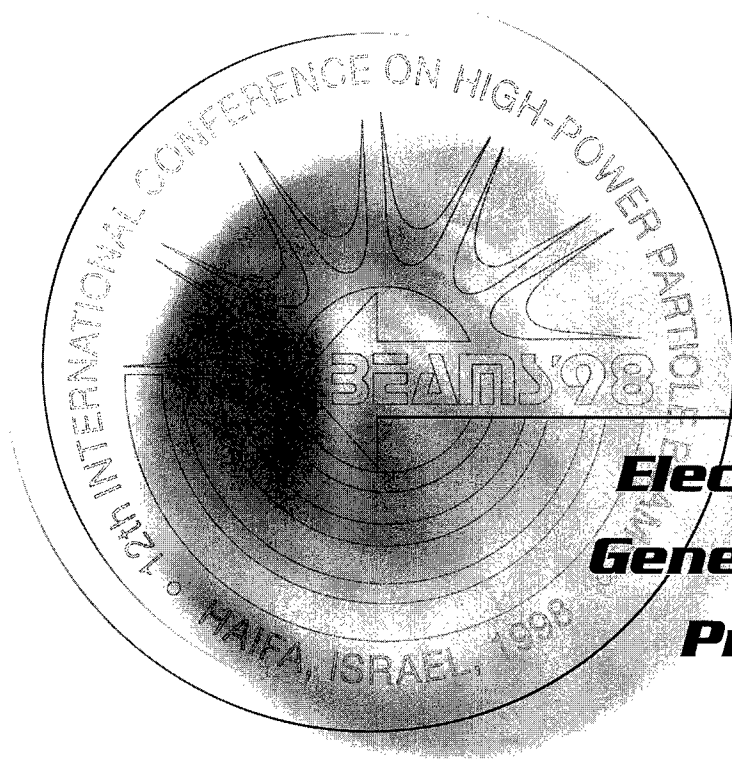
Reference

- [1]. Kotov, Yu.A., Mesyats, G.A., Rukin, S.N., and Filatov, A.L., *Dokt. Russ. Akad. Sci.*, 1993, vol. 330, p. 315.
- [2]. Kotov, Yu.A., Mesyats, G.A., Rukin, S.N., *et al.*, *Digest of Technical Papers 9th IEEE Pulsed Power Conf.*, Albuquerque, 1993, vol. I, p. 134.
- [3]. Katsnel'son, B.V., Kalugin, A.M., and Larionov, A.S., *Elektrovakuumnye elektronnye i gazorazryadnye pribory: Spravochnik* (Vacuum-Tube Electronic and Gas-Discharge Devices. Handbook), Moscow: Radio i Svyaz', 1985. (in Russian)
- [4]. Kotov Yu.A., Sokovnin S.Yu., *Prib. Tekh. Eksp.*, 1997, no. 4, p. 84.
- [5]. Kotov, Yu.A., Filatov, A.L., Rodionov, N.E., *et al.*, *Prib. Tekh. Eksp.*, 1986, no. 2, p. 138.
- [6]. Mesyats, G.A., *Generirovanie moshchnykh nanosekundnykh impul'sov* (Generation of High-Power Nanosecond Pulses), Moscow: Sov. Radio, 1974. (in Russian)
- [7]. Generalova, V.V., and Gurskii, M.N., *Dovmetriya v radiatsionnoi tekhnologii* (Dosimetry in Radiation Engineering), Moscow: Izd. Standartov, 1981. (in Russian)



BEAMS'98

12th INTERNATIONAL CONFERENCE
ON HIGH-POWER PARTICLE BEAMS



ORALS

***Electron Beam
Generation and
Propagation***

Vol. I

Proceedings

CRITICAL ELECTRON-HOLE PROCESSES IN DIELECTRIC INDUCED BY SYNCHRONOUS ACTION OF HIGH ELECTRIC FIELD AND HIGH-CURRENT-DENSITY ELECTRON BEAM

D. I. Vaisburd

Tomsk Polytech University, 30 Lenin Avenue, Tomsk 634034 Russia

Abstract

Injection of high-current-density (HCD) electron beam of nanosecond pulse duration into a dielectric creates strong electric field, from one side, and high density of electrons and holes trapped at the shallow levels in the band-gap, from the other side. Two types of high intensity electron emission from dielectric into vacuum are studied experimentally and considered theoretically. The first one is field electron emission from dielectric (FEED), which arises owing to intense detrapping electrons from shallow levels in high electric field. The second one is critical electron emission from dielectric (CEED), which arises when FEED current density exceeds critical value and induced point explosions of the microtips on the dielectric surface and ejections atom-ion plasmas from this points into vacuum. Full theoretical and computer simulation of FEED and CEED needs to take into account a lot of ultrafast excitation/relaxation processes in dielectric under HCD electron beam irradiation.

1. Introduction.

Wide-band-gap dielectrics (WBGD) have found a lot of applications to scientific and industrial instruments and technologies, first of all owing to the transparency in the visible region and low intrinsic electrical and thermal conductivity. Among the main fields of their use there are laser technique, optics, optoelectronics, thermal and electrical insulation. Damage of a dielectric is usually yielded from critical (catastrophic) processes like optical and electrical breakdown, brittle fracture, plastic flow, etc. But research, understanding and theoretical description of them are far from being completed because the earliest decisive stages of these processes such as high electronic excitation and ultrafast many-channel relaxation have very short lifetimes: from 10^{-17} to 10^{-8} s. Direct experimental investigation of high electronic excitation and ultrafast relaxation in WBGD becomes possible through application first, of high-current-density (HCD) electron accelerators and second of pulsed power lasers high order harmonics generation. Our Lab for nonlinear physics at Tomsk Polytech University has been starting the first research of WBGD under pulsed power electron irradiation many years ago in 1969 using HCD electron accelerators of GIN-type (1-20 ns, $0.1-10000 \text{ A/cm}^2$, 0.2-0.45 MeV) and has observed and studied some transient effects in dielectrics: 1. Intraband radioluminescence, 2. High-energy intraband electrical conductivity, 3. HCD critical electron emission and its transition to vacuum discharge and bulk breakdown, 4. Cold brittle destruction, when fast heating the dielectric by electron beam does not exceed 10° , 5. Acoustic longitudinal and flexural waves generation, 6. Dislocation avalanches generation and plastic bending filamentary crystals (whiskers). The (1) and (2) reflect some early stages of electronic relaxation in a dielectric after pulsed power excitation. The observed components of luminescence (1) and electrical conductivity (2) are proportional to dose rate, have picosecond lifetimes and weakly depend on impurities and intrinsic defects. The luminescence quantum yield does not depend on temperature up to melting point (and even above it). The conductivity has quasi-metallic (falling) temperature dependence. Detailed comparison of numerical experimental data with theoretical evaluations shows that so-called 'non-ionising' electrons and holes (n-i e-h) with kinetic energies of the order of 0.1-10 eV bring in the decisive contribution to fast electronic processes in a dielectric at high dose rates. The n-i electrons of conduction band and holes of valence band are free of impact and Auger ionising the medium. They do not create e-h pairs, excitons, plasmons and other intrinsic electronic excitations and transfer the energy excess to the lattice by generation short wave phonons first of all and long-wave acoustic and optical ones too. The rate of the energy relaxation $B(E) = -dE/dt$ and lifetime τ are of the order 10 eV/ps and 1 ps

respectively. The drift of n-i e-h in electric field gives the observed high-energy intraband conductivity. Direct radiative transitions of the same n-i e-h between subbands of the sole band give the observed 'intraband luminescence'. When electric field inside the dielectric reaches such a critical value that the average power obtained by electron from field exceeds the rate of its energy loss then the electron will perform the transition from passive n-i states to active ionising ones and induce avalanche of ionisation which is the first stage of electrical breakdown process. It is difficult to achieve pulse duration of HCD electron beam shorter than hundred ps and investigate the earliest femtosecond stages of electronic relaxation. Farther progress has been achieved by application of high intensity lasers high order harmonics generation. Now the current state of the art allows us to divide the time scale of entire excitation/relaxation process into the main temporal stages having the following characteristic times:

1. Primary electronic excitation resulting from multistep e-e impact and e-h-e Auger collisions (in the case of HCD electron beam action) and the same processes after multiphoton absorption of high intensity laser harmonics and generation of highly excited e-h during 10^{-17} – 10^{-15} s,
2. Formation of 'instant' spectra of n-i e-h before the start of electron-phonon (e-ph) scattering, not longer than 10^{-15} – 10^{-14} s,
3. Electron-phonon relaxation of high energy n-i e-h and temporal evolution of their energy-momentum distribution from instant to quasistationary ones under 'long' (more than 10^{-11} s) action of laser or HCD electron beam,
4. Thermalisation and trapping e-h through self-trapping, coupling into excitons and capture by intrinsic and impurity defects during 10^{-13} – 10^{-10} s,
5. Detrapping e-h from shallow levels induced by combined action of thermal fluctuations, high optical or microwave or static electric fields and impact or Auger ionisation of traps by high energy n-i e-h during 10^{-11} - 10^{-7} s,
6. Spectral and space redistribution of e-h owing to heating in high electric fields, impact and Auger ionisation of traps, transport within dielectric owing to induced transient conductivity and electron emission from dielectric into vacuum during 10^{-11} - 10^{-7} s. Enumerated temporal stages of excitation/relaxation process form the prelude to such critical phenomena as optical or electrical breakdown and explosive electron emission.

2. Review of experimental data on critical electron emission from dielectric induced by injection of HCD electron beam.

Several types of critical electron emission from dielectric into vacuum induced by electron beam injection have been observed and studied during the last sixty years. The most known ones are discovered by Malter (1936) and Dow, Nablo and Watson (1967-68) [1,2]. But application of low-current-density (LCD) electron beams has not allowed them to measure intrinsic temporal properties of the emission because long time is needed to accumulate trapped charge of critical density in a sample under LCD injection. Started the experimental research of electron emission of dielectrics in 1975 we have been applying HCD electron accelerators of GIN-type for injection and subnanosecond temporal resolution in the measurements. It has allowed us to observe the intrinsic properties of critical electron emission of dielectrics (CEED) [3, 4, 5].

1. CEED arises sharp when the density of negative charge injected by primary electron beam and trapped in the sample reaches $(1-8) \cdot 10^{-7}$ C/cm² and creates electric field of critical value in the range $(0.2-1.2) \cdot 10^6$ V/cm for different dielectrics: LiF, NaF, NaCl, KCl, quartz, fused silica, polyethylene, teflon, polyvinyl, PMMA. Critical field strength is of the same order for both CEED and nonuniform electrical breakdown of dielectrics.
2. CEED induced by HCD electron beam arises in the form of gigantic single pulse, which duration is several nanoseconds and somewhat longer than injection one.
3. CEED pulse delays from injection one for 1-20 ns. The time delay decreases along with increase of primary beam current density.
4. CEED coefficient may be estimated as ratio of emission pulse area to that of injection one. It varies from 0.7 to 1.0, i.e. the overage emission current density is of the order of injection one: 10-1000 A/cm². This fact is of high importance for understanding the CEED mechanism. The detailed research of transient electrical conductivity of dielectrics induced by HCD electron beams action shows that

major part of that has picosecond lifetime, i.e. disappears simultaneously with irradiation pulse. When the emission pulse has delayed several nanoseconds from the end of injection one then the conduction current arisen through the impact ionisation of medium by primary electron beam is so small that cannot supply the intense emission observed. These data are direct experimental evidence for intensive generation of conduction electrons in dielectric's subsurface owing to traps ionisation in high electric field, i.e. detrapping.

5. CEED performs phase transition to vacuum discharge between the dielectric surface and metallic collector if the electron current to emission centers is maintained at the necessary level. Vacuum discharge when arriving always follows the emission. No emission, no discharge. Bulk breakdown when arriving always follows the vacuum discharge. No vacuum discharge, no bulk breakdown. The time sequence of the events is such: primary beam injection - critical electron emission - vacuum discharge - bulk breakdown.

6. Photopictures of dielectric surface and vacuum gap through the CEED demonstrate directly its space nonuniformity. Evaluations taking into account the emission current cross nonuniformity give the peak value of CEED current density from the local emission centers on the dielectric surface : $10^5 - 10^6 \text{ A/cm}^2$.

7. Energy distribution of emitted electrons is governed by electric field on the dielectric surface. The stopping potential up to -6 kV applied to metallic collector does not essentially influence on the emission current.

8. Detailed description of experimental data with figures and tables is given in [5].

3. Primary electronic excitation of dielectric by HCD electron beam and forming instant spectra of non-ionising conduction electrons and valence holes

The instant spectra of n-i e-h are the energy distributions of them in conduction and valence bands respectively prior to beginning of e-ph relaxation. Initial data for computing the instant spectra are: energy distribution of primary electron beam $f_0(E)$, which is given in Fig.1 for HCD electron accelerator GIN; energy spectrum of density of filled states including discrete sequence of deep quasiautomic levels $g(I_i)$ and continuous spectrum within the valence band $g(I)$, which are given in Fig.2 for NaCl; top energy for n-i electron E_A and hole E_H (above such energies e-h regain the ability to ionise the dielectric medium); differential cross-section for impact ionisation $\sigma(E, I, \varepsilon)$ where ε is the energy of secondary electron. The instant spectrum is calculated in a recurrent process. The first step gives the spectrum of secondary electrons

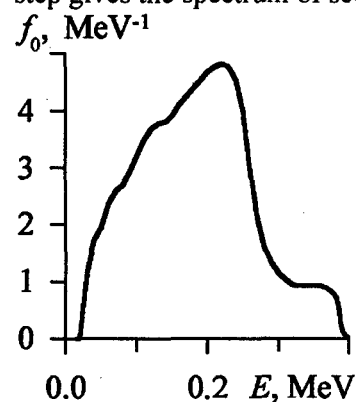


Fig.1: Energy spectrum of primary high-current-density (HCD) electron beam generated by HCD desk-top accelerator GIN designed and produced in Tomsk Politech University and Institute for High Current Electronics Russia Academy of Science.

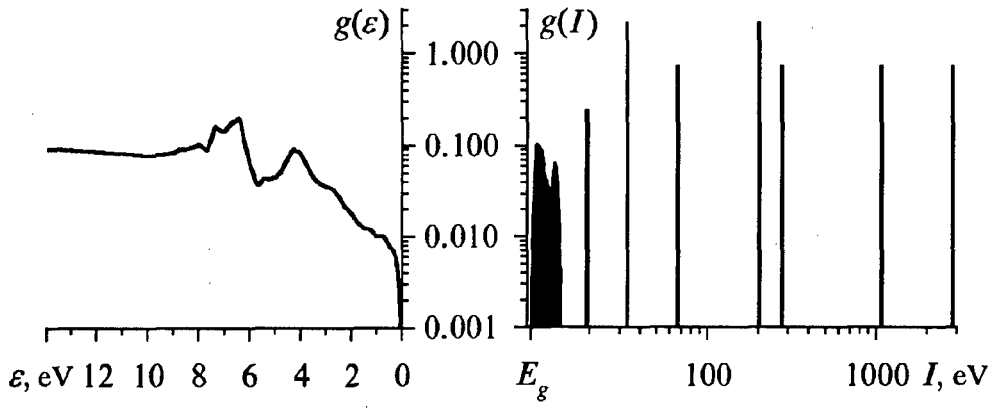


Fig.2: Energy spectra of densities of filled states including discrete sequence of deep quasiautomic levels $g(I_i)$ and continuous one within the valence band $g(I)$ and free states in the conduction band $g(\varepsilon)$ in NaCl crystal.

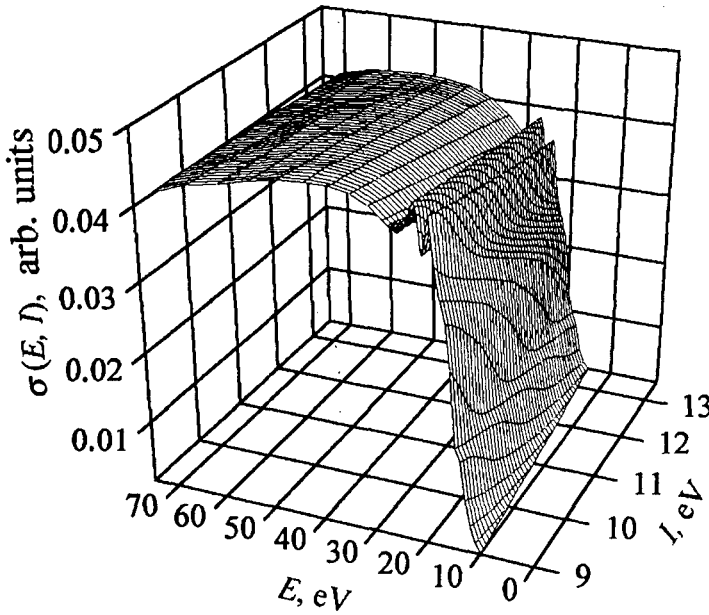


Fig.3: Differential cross-section for ionisation of filled level with ionisation potential I and generation of secondary electron of energy ε and hole of energy $(-I)$ by primary electron of kinetic energy E in NaCl crystal.

$$f_1(\varepsilon) = \left[\sum_i g(I_i) + \int g(I) dI \right] \int_{\varepsilon+I}^{E_s} \sigma(E, I, \varepsilon) f_0(E) dE, \quad (1) \text{ where } E_s \text{ is}$$

supreme energy of primary beam electrons, the expression in square brackets is operator which implies summation over discrete and integration over continuous spectra of filled states. The n-i e-h part must be subtracted from the spectrum of secondary electrons and the remained part of $f_1(\varepsilon)$ is substituted in place of $f_0(\varepsilon)$ for the second step of calculation which gives $f_2(\varepsilon)$ and so on. The differential cross-section for impact or Auger ionisation is corrected through taking into account the real spectrum of density of final states in the conduction band (Fig.3).

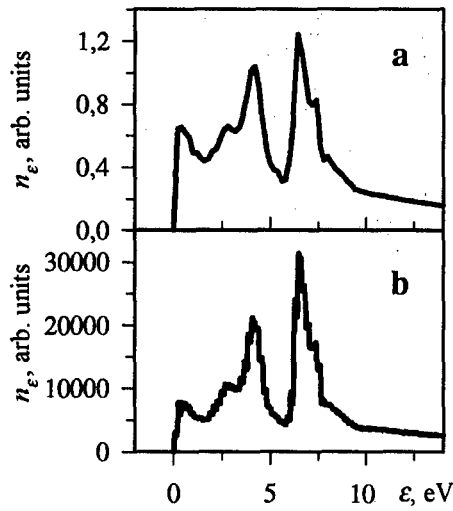


Fig.4: Instant spectrum of non-ionising electrons in conduction band of NaCl crystal being irradiated by HCD electron beam: a - theoretical calculations, b - Monte-Carlo simulation.

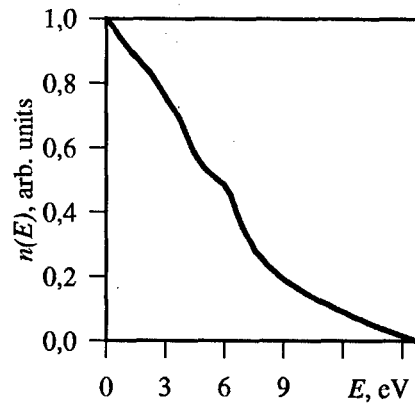


Fig.5: Quasistationary energy distribution of non-ionising electrons in conduction band of NaCl crystal under the irradiation by HCD electron beam.

The instant spectrum of n-i conduction electrons generated by HCD electron beam in NaCl has been computed both in the recurrent process described and via Monte-Carlo simulation. The results practically coincide (Fig.4).

4. Temporal evolution of n-i e-h energy distribution from instant to quasistationary ones

The first approximation of n-i e-h energy distributions temporal evolution can be received by solving the Boltzmann's kinetic equation. Such consideration neglects some essentially quantum effects: tunnelling among subbands and conservation of phase coherence over many collisions with phonons, etc. Nevertheless, detailed analysis has shown the Boltzmann's kinetic equation to be valid for computing temporal evolution of e-h energy distribution inside wide conduction and valence bands in a dielectric. Input data necessary for calculation are: density of states spectra for the material, n-i e-h instant spectra which are the initial distribution functions, and the spectrum of energy relaxation rate $B(E)$. The temporal evolution of n-i electrons energy distribution $f(\epsilon, t)$ within wide conduction band looks very simple in 'energy-age' space. In this case Boltzmann's equation reduces to continuity one

$$\partial f / \partial t - \partial (f B) / \partial \epsilon = 0. \quad (2)$$

The n-i e-h lifetimes are of the order of 10^{-13} - 10^{-12} s. If the duration of primary excitation is much more than lifetime then the temporal evolution of n-i e-h energy distribution yields the quasistationary spectra. The exact solution of eq.(2) reads

$$n_{\epsilon}(\epsilon, t) = \left[G(t) / B(\epsilon) \right] \left[\int_{\epsilon}^{E_A} f(\epsilon') d\epsilon' / \int_0^{E_A} f(\epsilon') d\epsilon' \right], \quad (3)$$

where $G(t)$ is the rate of n-i e-h generation, $n_{\epsilon}(\epsilon, t)$ is the spectral density of n-i e-h on the level ϵ , $f(\epsilon)$ is the instant spectrum. The result is simple, enough exact and valid as well for the cases of two-photon and multiphoton excitation by laser beam of pulse duration more than 10^{-11} s. The quasistationary energy distribution of n-i conduction electrons in NaCl crystals excited by HCD electron beam of 10^{-10} - 10^{-8} s pulse duration is given in Fig.5. The transient intraband conductivity and intraband luminescence of n-i e-h are computed with using their quasistationary energy distribution. The results of calculations are in good agreement with experimental data on luminescence (Fig.6) and conductivity.

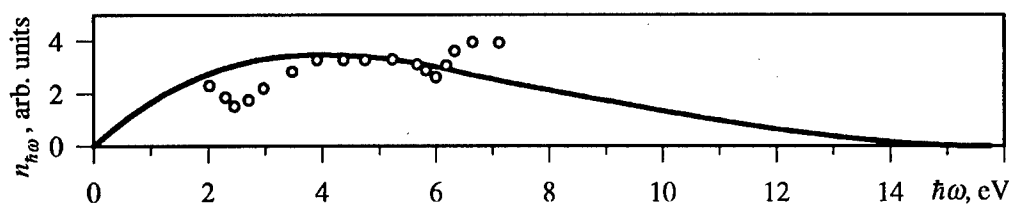


Fig.6: Intraband luminescence spectrum of non-ionising conduction electrons in NaCl under irradiation by HCD electron beam

5. Spectral and space redistribution of e-h in high and superhigh electric fields

The last stages of ultrafast n-i e-h relaxation – thermalisation and trapping - have been investigated by using laser methods of subpicosecond time resolution. The most advanced research is done by G. Petite with collaborators at CEA (Saclay, France) [6]. They have developed an optical interferometric technique (transient frequencial interferometry) allowing direct measurement of conduction electrons density and lifetime in a dielectric with 50 fs time resolution. The fast trapping electrons in the band-gap is associated with the formation of self-trapped excitons (STE). The shortest lifetimes 150 fs of n-i electrons in conduction band are observed in SiO₂ and in this material the STE formation kinetics does not depend on the pump laser intensity, while the trapping rate increases in NaCl with the growth of excitation density. This result is interpreted as a direct evidence of exciton self-trapping in SiO₂ and electron trapping by a hole after its self-trapping in NaCl [6]. The fundamental correlation between lattice elasticity and self-trapping excitons and holes is observed: the more C/ξ the more self-trapping probability will be (C is deformation potential and ξ is elastic constant). If self-trapping is absent then e-h are trapped from the bands by intrinsic and impurity defects only and their lifetimes rise up to 10^{-10} s as in MgO and Al₂O₃.

Detrapping e-h from shallow levels can be induced by combined action of high optical or microwave or static electric fields, thermal fluctuations and impact or Auger ionisation of traps by high energy n-i e-h. The typical duration of these processes is in the range 10^{-11} - 10^{-7} s. Thermally overcoming the Shottky barrier between local level and band edge in high electric field is named Poole-Frenkel effect [7]. Tunnelling from local level to band in high electric field is described like Fowler-Nordheim theory for field electron emission. Impact and Auger ionisation of traps by high energy and hot n-i carriers is described according to Keldysh's theory [8].

All detrapping processes in high and superhigh electric fields are accompanied by sharp rise of induced electrical conductivity in a dielectric. Having the purpose of experimental research and separation of different detrapping processes in superhigh electric field author has proposed to synchronise in one setup three modules: two HCD electron accelerators of GIN type (0.45 MeV, 0.1-10000 A/cm², 1-20 ns), generator of high voltage and apparatus for registration. Such setup named "Synchrogin" is applied to study the conductivity of a dielectric in superhigh electric field escaping the breakdown. The idea of experiment is following. Induced e-h conductivity of a dielectric rises up to very high value 10^{-3} - 10^{-1} (Ohm·cm)⁻¹ under the irradiation by HCD electron beam. If pulse of high voltage is placed within the irradiation one then the breakdown will not occur even in superhigh electric field exceeding the breakdown threshold. "Synchrogin" allows us to measure the Volt-Ampere characteristic of thin dielectric up to field strength $2 \cdot 10^6$ V/cm (Fig.7). Below 10^5 V/cm the transient conductivity does not depend on field strength and equals σ_0 , i.e. the Ohm's law is valid. Above $2 \cdot 10^5$ V/cm it rapidly increases along with the field strength. This dependence is described by empirical formula

$$\sigma = \sigma_0 \exp(bF^a) \quad (4)$$

where F is field strength in V/cm, $a = 2.5 \div 2.7$, $b = 10^{-15}$ for NaCl crystal.

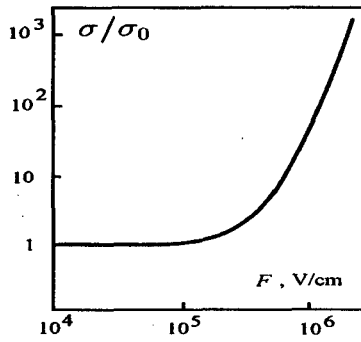


Fig.7: Transient electrical conductivity vs field strength F in NaCl crystals under the synchronous action of pulsed HCD electron beam and superhigh electric field

6. High-power field electron emission from dielectric into vacuum induced by injection of HCD electron beam

Theoretical description of the critical electron emission from dielectric (CEED) needs to take into account all ultrafast and fast processes considered and mentioned above. Two theoretical models are developed. The first is field electron emission from dielectric (FEED) induced by HCD electron beam injection pulse. It takes into account the following processes: 1. Charge and energy deposition of incident electron beam in dielectric, 2. Time-space distribution of electric field created by injected and trapped charge of primary beam and additional stopping the beam by this field, 3. Enhancement of the electric field on the nonuniformities of the surface relief, 4. Generation of n-i e-h and excitons owing to impact and Auger ionisation of the medium and instant space distribution of their densities, 5. Recombination of e-h and excitons, 6. Self-trapping the holes, 7. Trapping the electrons by self-trapped holes, self-trapped excitons, biographical traps (intrinsic and impurity defects) and color centers created by irradiation, 8. Detrapping the electrons from shallow levels owing to Poole-Frenkel effect and tunnelling to the conduction band, 9. Heating/thermalisation of electron gas in high electric field due to impact ionisation of traps and e-e collisions of free carriers, 10. Electron transport in dielectric via induced conductivity, 11. Electron emission from dielectric surface into vacuum according to generalised Fowler-Nordheim theory. The FEED model is two-dimensional. A little part of dielectric surface which contains one microtip enhancing the local electric field is considered. And this microtip is the main source of the emission. The FEED model is realised in the nonlinear system of 19 equations initial and boundary conditions:

$$\begin{aligned} \frac{\partial n_e(r, z, t)}{\partial t} = & G - an_e n_b - bn_e n_{eb} - cn_e (N - n_{eN}) + \gamma(F) n_{eb} + \frac{1}{e} \operatorname{div} \vec{J} + \\ & + \frac{n_{eeb}}{\tau_{eeb}} + \kappa_{eb} \nu_d n_e n_{eb} + \kappa_{eeb} \nu_d n_e n_{eeb}, \end{aligned} \quad (5)$$

$$\frac{\partial n_{eN}(r, z, t)}{\partial t} = cn_e (N - n_{eN}), \quad (6)$$

$$\frac{\partial n_b(r, z, t)}{\partial t} = G - an_e n_b + \kappa_{eb} \nu_d n_e n_{eb}, \quad (7)$$

$$\frac{\partial n_{eb}(r, z, t)}{\partial t} = an_e n_b - bn_e n_{eb} + \gamma(F) n_{eb} - \frac{n_{eb}}{\tau_{eb}} - \kappa_{eb} \nu_d n_e n_{eb} + \kappa_{eeb} \nu_d n_e n_{eeb}, \quad (8)$$

$$\frac{\partial n_{eeb}(r, z, t)}{\partial t} = b n_e n_{eb} - \gamma(F) n_{eeb} - \frac{n_{eeb}}{\tau_{eeb}} - K_{eeb} v_d n_e n_{eeb}, \quad (9)$$

$$\text{div}[\varepsilon(r, z) \text{grad} U] = \frac{\rho_v}{\varepsilon_0}, \quad (10)$$

$$\rho = e(n_b - n_e - n_{eN} - n_{eeb}), \quad (11)$$

$$\vec{J} = \vec{J}_e + \vec{J}_b + \vec{J}_c, \quad (12)$$

$$\vec{J}_c(r, z, t) = \mu_e n_e \vec{F}, \quad (13)$$

$$\gamma(F) = \nu \exp \left[- \frac{\left(I_{tr} - 2 \sqrt{e^3 F / 4 \pi \varepsilon \varepsilon_0} \right)}{2 k_B T} \right], \quad (14)$$

$$G = \frac{J_b(r, z, t) \langle dE_e / dz \rangle}{(1.5 E_g e)}, \quad (15)$$

$$J_c = \frac{e n_e(z_c(r), t)}{2(k_B T)^{3/2} \sqrt{3m}} \int_{F=0}^{1/2 k_B T} \left[\int_0^{E_z^{\max}} D(E_z) dE_z \right] dE, \quad (16)$$

$$D(E_z) = \exp \left[- \frac{8 \pi \sqrt{2m}}{3 e F b} (\psi - E_z)^{1/2} \times \theta \left(\frac{\Delta \psi}{\psi - E_z} \right) \right], \quad (17)$$

$$\Delta \psi = \sqrt{\frac{e^3 F}{4 \pi \varepsilon_0} \cdot \frac{\varepsilon - 1}{\varepsilon + 1}}. \quad (18)$$

$$J_b(r, z, t) = J_b^{\max} f_1(t) f_2(z - z_c(r)), \quad (19)$$

The following boundary and initial conditions are used:

$$U(r, -d_1, t) = U_1, \quad U(r, d_2, t) = U_2, \quad (20)$$

$$\frac{\partial J}{\partial z} = \begin{cases} \left. \frac{\partial J}{\partial z} \right|_{z=z_s(r)} + \frac{J_e(r, z_s, t) - J_e(r, t)}{\delta}, & \text{if } z_s(r) < z < z_s(r) + \delta, \\ \frac{\partial J}{\partial z} + \frac{\partial J}{\partial z}, & \text{if } z_s(r) + \delta < z < d_2, \end{cases} \quad (21)$$

$$n_e(r, z, 0) = n_h(r, z, 0) = n_{eN}(r, z, 0) = n_{eh}(r, z, 0) = n_{eeh}(r, z, 0) = 0, \quad (22)$$

$$\varepsilon(r, z) = \begin{cases} 1, & \text{if } z < z_s(r), \\ \varepsilon, & \text{if } z > z_s(r), \end{cases} \quad (23)$$

where N is initial density of biographical defects; n_e , n_h , n_{eh} , n_{eeh} , and n_{eN} are densities (concentrations) of free electrons (e), holes (h), excitons and color centers containing one electron and one hole (eh), centers containing two electrons and one hole (eeh), and electrons trapped in the biographical defects (eN) respectively; v_d is drift velocity of electron in electric field; F and U are electric field strength and potential respectively; G is the rate of e-h generation per unit volume by primary beam; $\chi(F)$ is the probability rate of detrapping electrons through Poole-Frenkel effects and tunnelling from the shallow level in band-gap to conduction band; κ_{eh} and κ_{eeh} are the rates of impact and Auger ionisations of eh - and eeh -centers respectively calculated via Keldysh's theory [8]; a , b and c are the rates of trapping electrons by self-trapped holes, eh -centers and biographical defects respectively; τ_{eh} and τ_{eeh} are lifetimes of excitons, eh - and eeh -centers according to inner recombination processes; ε_0 and ε are absolute and relative permittivities respectively, T is the absolute temperature; ρ_s is the space charge density, J_b , J_c , and J_e are primary beam, conduction and emission current densities respectively; J_b relaxation in dielectric is computed via Ito-Tabata algorithm [9], μ_e is the conduction electron mobility; I_r is ionisation potential of the trap; ν is frequent factor; dE_e/dz is energy deposited to the medium by primary electron per unit path at the depth z computed via Ito-Tabata algorithm [9]; E_g is the band-gap; $z_s(r)$ is the form of dielectric surface containing a microtip; $D(E_z)$ is the probability of tunnelling; θ is Nordheim function [10]; ψ is the height of barrier for conduction electron emission from dielectric and $\Delta\psi$ is its reduction due to Shottky effect; d_1 and d_2 are the vacuum gap and dielectric thickness respectively; U_1 and U_2 are the external potentials applied to the collector and rear electrode respectively.

The algorithm for numerical solving the system has been developed, Mac Cormac method for eq.(5) and differencing method for others being used.

One of the main results of computations is shown in Fig. 8. The pulse of primary beam current density J_b is of supercritical value. Intense electron emission J_e starts with time delay of 2 ns and continues for several nanoseconds after the end of injection pulse J_b owing to detrapping electrons from various shallow levels. The FEED is highly nonuniform. Its current density averaged upon the surface $\langle J_e \rangle$ is about 20% of the injection one, i.e. of the order of 10^1 - 10^3 A/cm². But peak value of emission current density $J_{e \max}$ taking place on the top of the microtip is of the order of 10^5 - 10^6 A/cm². It means that the density of energy deposition is of the order of 10^4 - 10^5 J/cm³ there. It is enough to induce explosive boiling of the substance and ejection atom-ion plasmas from the microtip into the vacuum gap. And FEED performs the phase transition to CEED. The model of the latter takes into account the existence of critical current densities J_c^{cr} and J_e^{cr} .

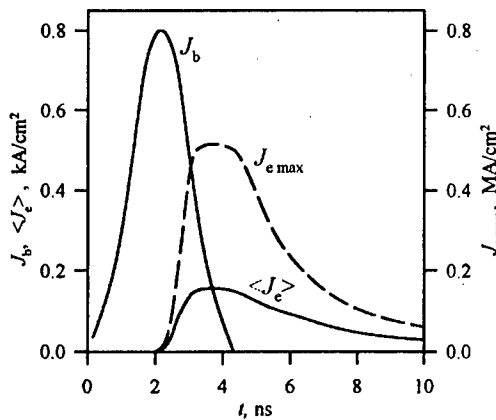


Fig. 8: Results of computer simulation: current density pulses of primary beam (J_b), field emission averaged upon surface ($\langle J_e \rangle$) and that from the top of the microtip ($J_{e \max}$).

7. Summary and conclusion

Application of HCD electron beams with nanosecond pulse duration for charge injection into dielectrics has allowed to determine the intrinsic time-dependent properties of the critical electron emission from dielectric into vacuum. Theoretical model of electron emission from dielectric induced by injection of HCD electron beam is proposed. The model is two-dimensional and takes into account the non-uniformity of the emission current. A little part of dielectric surface which contains one microtip enhancing the electric field is considered. The model is realised in the system of nonlinear equations. Algorithm for numerical solving this system is developed. The computations give that peak value of emission current density on the top of the microtip is of the order of 10^5 – 10^6 A/cm². It is enough to induce microexplosions of the microtip and ejection of plasmas from the microtip into the vacuum gap and perform a nonequilibrium phase transition of FEED to CEED and vacuum discharge and bulk breakdown.

8. References

- [1] L. Malter, Phys. Rev. **49**, 879 (1936); Ibid. **50**, 48 (1936).
- [2] J. Dow and S. V. Nablo, IEEE Trans. Nucl. Sci. **NS-14**, 231 (1967), A. Watson and J. Dow, J. Appl. Phys. **39**, 5935 (1968).
- [3] I. N. Balichev, D. I. Vaisburd, and G. I. Hering, "Powerful emission from dielectric induced by high density electron beam", Russian Physics Journal No. 3, 157 (1975).
- [4] I. N. Balichev, D. I. Vaisburd, and G. I. Hering, "Powerful critical emission from dielectric induced by high density electron beam of nanosecond pulse duration", Pisma JTP (Lett. Russian J. Appl. Phys.) **2**, No. 7, 327, (1976).
- [5] S. Tverdokhlebov and D. Vaisburd, "Critical high-power electron emission from dielectric induced by high-density electron beam injection", Proc. 2nd Int. Conf. on Space Charge in Solid Dielectrics, SFV, Antibes-Juan-les-Pins, France, 118-125 (1995).
- [6] P. Martin, S. Guizard, Ph. Daguzan, and G. Petite, "Subpicosecond study of carrier trapping dynamics in wide-band-gap crystals", Phys. Rev. B **55**, No. 9, 5799 (1997).
- [7] Y. I. Frenkel "Theory of electrical breakdown in dielectrics and semiconductors", JETP (J. Appl. and Theor. Phys.), **8**, No. 12, 1292 (1938).
- [8] L. V. Keldysh "Theory of impact ionisation in semiconductors", JETP (J. Appl. and Theor. Phys.) **48**, No. 6, 1692 (1965).
- [9] T. Tabata and R. Ito, "An algorithm for the energy deposition by fast electrons", Nucl. Sci. and Eng., **52**, 226 (1974).
- [10] R. Fisher and H. Neumann, "Autoelectronic emission of semiconductors", Fortshritte der Physik, No. 14, 603 (1966).

ROD-PINCH ELECTRON BEAM DIODES AS X-RAY RADIOGRAPHY SOURCES*

G. Cooperstein, R.J. Commisso, D.D. Hinshelwood, P.F. Ottinger, D.V. Rose⁺,
S.J. Stephanakis, S.B. Swanekamp⁺, and F.C. Young⁺
Plasma Physics Division, Naval Research Laboratory
Washington, DC 20375-5346

Abstract: This paper reports on recent NRL Gamble II experiments with rod-pinch diodes which duplicate and extend previous results. These diodes utilize a thin annular cathode surrounding a small diameter anode rod extending through and beyond the plane of the cathode. Up to seven rods were simultaneously pulsed with each rod displaying well behaved electrical characteristics (0.8 - 1.5 MV at impedances of 15 to 30 ohms). Time and spatially resolved x-ray Pin diode detectors demonstrated efficient current (>50%) propagation along each rod. The 50 rads Si that was measured 30 cm from each carbon rod (0.16 cm radius) with Ta cone tips at 1.5 MV corresponds to 10 - 1000 times the dose of other point radiography sources. While previous rod-pinch experiments were performed with solid rods, a new high-velocity, high-efficiency propagation mode was demonstrated using a hollow cylinder with a 6- μ m Al wall and a carbon end plug. It is speculated that the propagation was via electron reflexing through the thin anode rod without the need for anode ion production. Also, when no end plug was used, the electron beam appeared to reflex along the entire length of the rod until it lost its energy.

INTRODUCTION

Pulsed-power-based radiography systems are designed to produce the maximum x-ray yield from the smallest source area. Present systems employ positive-polarity, high-impedance electron-beam diodes comprising of thin annular cathodes surrounding tapered anodes. Since the endpoint voltage is determined by the specific application and the anode-cathode gap size is limited by plasma closure, the current in these non-self-pinched diodes can only be increased by increasing the cathode area. This has the undesirable effect of both increasing the spot size and reducing the ability to pack multiple sources close together. Rod-pinch diodes, which were first reported on in 1978,[1] can potentially mitigate these problems by extending the anode well beyond the cathode plane thereby uncoupling the geometry-dependent diode impedance from the final x-ray output spot size. A rod-pinch diode utilizes a thin annular cathode surrounding a small diameter anode rod extending through and beyond the plane of the cathode. The initial electron flow is radial and the current is space-charge limited. After the current increases beyond the critical current ($I_{crit} \sim 8500 (\gamma^2 - 1)^{1/2} / \ln(r_K/r_A)$ where r_K and r_A are the cathode and anode radii and γ is the relativistic factor) the electron flow becomes magnetically limited. The intense ($\sim 10^5 - 10^6$ A/cm²) electron beam then propagates efficiently along the rod beyond the cathode plane as an anode plasma is produced at the beam front in a manner similar to the collapsing hollow electron beam in a planar self-pinch diode.[2] When the electron beam reaches the end of the rod it forms a tight pinch at the tip and a very intense x-ray pulse with a spot size on the order of a mm is produced. The early rod-pinch experiments were performed on the NRL SOL generator at 400 kV and 20 kA

and the NRL Gamble I generator at 800 kV and 40 kA. They demonstrated efficient electron beam propagation on solid rods with lengths up to 20 cm, propagation velocities of up to 0.5 cm/ns, and up to two rods were successfully driven from a single source. This paper reports on recent NRL Gamble II experiments with up to seven rods driven from a single power source at 1.3 MV and 45 kA per rod with a 50 ns FWHM radiation pulse.

GAMBLE II EXPERIMENTAL RESULTS AND CONCLUSIONS

Up to seven magnetically isolated rod-pinch diodes (six in an 18 cm diam. hexagonal array with one in the center) were driven in parallel by the NRL Gamble II generator operated in positive polarity. A common vacuum chamber with a plexiglass end plate was placed around the seven individual rod-pinch diodes. This experimental arrangement allowed the high current Gamble II generator to efficiently drive multiple rod-pinch diodes in parallel and allowed independent measurements to be carried out on each rod-pinch diode for efficient data collection. A schematic cross section of a typical rod-pinch diode is shown in Fig. 1. The current in each diode was measured with a B-dot loop and the common voltage was determined by inductively correcting the voltage measured at the vacuum insulator. X-ray

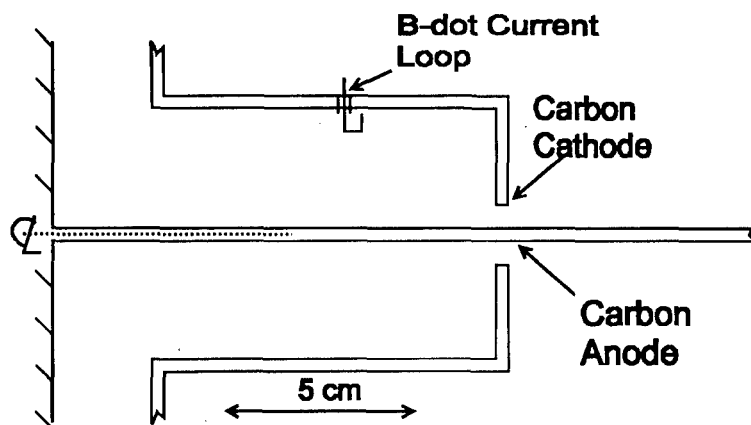


Figure 1. Experimental schematic of single rod-pinch diode.

diagnostics included a time integrated x-ray pinhole camera, and time resolved collimated x-ray Pin diodes which were used to estimate the distribution of electron current along the anode rods. For the particular subset of experiments reported on here, each carbon cathode was 0.32 cm thick with $r_k=8$ mm and each solid carbon anode rod was between 5 and 13 cm long with $r_A=1.6$ mm. An end-on x-ray pinhole photo of seven 5-cm long carbon anodes is shown in Fig. 2. The equal x-ray intensities suggests that equal electron energy is deposited on each of the rods. X-ray pinhole data viewing the side of a 13 cm long rod anode (Fig. 3) shows a tight pinch at the tip of the rod and suggests that most of the radiation is produced from the last 1-cm of each anode. In addition, a conical taper at the end of each anode produces a tight electron beam pinch at the tip of the taper (Fig. 4). Here a 2 cm long Ta cone was placed at the end of a 9 cm long carbon anode. Intense x-rays can only be seen from the last 1 cm, and it is possible that anode plasma expansion increased the effective source size at the tip. The 50 rads-Si that was measured 30 cm from each Ta cone tip represents 10 - 1000 times the dose measured from other high-impedance point radiography sources.



Figure 2. X-ray pinhole camera, 2 mm diam., centered on diode axis at 117 cm from rod tips for Gamble II shot 6917.



13 cm

Figure 3. X-ray pinhole camera, 20 mil diam., at 50° from the diode axis looking along rod anode for Gamble II shot 6927.



1 cm

Figure 4. X-ray pinhole camera, 10 mil diam., at 70° from the diode axis looking at the Ta cone tip for Gamble II shot 6925.

More quantitative data, illustrated in Fig. 5, taken with time and spatially resolved x-ray Pin diode detectors demonstrates efficient electron beam propagation to the end of the solid carbon anodes. The experimental schematic at the top of Fig. 5 shows a 13-cm long carbon

anode which was viewed from the side with three x-ray Pin diodes, each of which have been collimated to only view a 1-cm length along the anode. A time integrated x-ray pinhole photo, similar to Fig. 3, is shown below the schematic. The individual x-ray signals generated from each of the three Pin diodes, as the electron beam propagates along the anode, is shown at the bottom of Fig. 5. At about 70 ns (voltage starts

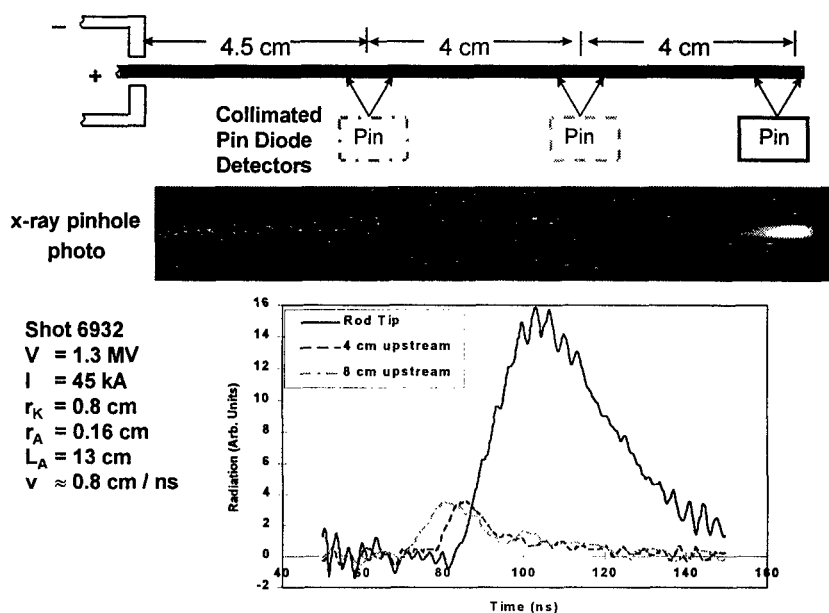


Figure 5. X-ray Pin diode signals for solid carbon anode.

at 30 ns), the x-ray signal from the Pin diode located 8 cm from the tip of the rod starts to rise. About 5 ns later, the x-ray signal from the Pin diode at 4 cm from the rod tip starts to rise and about 5 ns later the x-ray signal from the last Pin diode viewing the tip of the rod starts to rise. The beam front propagation velocity is approximately 0.8 cm/ns. What is interesting is that, as this last signal continues to rise, the signals from the first two Pin diodes decrease. It is estimated that greater than 50% of the peak radiation is coming from the rod tip if the amplitude from the other detectors is integrated over the whole 13 cm length of the anode and compared to the peak radiation. It appears that the self-magnetic field from the return current from the rod's tip magnetically inhibits the electrons flowing closer to the cathode from hitting the anode.

In addition, a new high-velocity, high-efficiency propagation mode was demonstrated using a thin hollow cylinder. The experimental schematic and the placement of the three x-ray Pin diodes is the same as illustrated at the top of Fig. 5 except that the solid carbon anode was replaced with an freestanding, hollow cylinder with a 6- μm Al wall thickness and a 1-cm long solid carbon end plug. The data from the three x-ray Pin diodes are illustrated in Fig. 6

where, in contrast to the solid carbon anode data in Fig. 5, all three signals start almost simultaneously and the signal from the solid carbon tip has a wider duration. Although the end Pin diode has the same amplitude as in Fig. 5., the signal from the other two Pin diodes have a lower amplitude even though aluminum is twice as efficient as carbon in producing x-rays. This suggests a higher propagation efficiency to the anode's tip than achieved with the solid carbon anode. The propagation appears to be via electron reflexing through the thin anode rod without the need for anode ion production. Preliminary NRL rod-pinch simulations show that propagation and pinch formation at the rod tip require anode ions if reflexing through the rod is not allowed. A similar reflexing mode with the corresponding high propagation velocity much greater than 1 cm/ns was previously observed with hollow, planar self-pinch cathodes and less-than electron range thick anodes.[2]

When no end plug was used, the electron beam appeared to reflex along the entire length of the rod until it lost its energy. This is illustrated in Fig. 7 where signals from the same three x-ray Pin diodes positioned as in Figs. 5 and 6 are shown. Here all the signals appear to start approximately at the same time and have approximately the same amplitude. It appears that, without the solid plug absorbing electrons at the tip of the anode, there is insufficient return current along the anode to magnetically inhibit electrons from striking it. This mode of operation may have an application as a very efficient reflexing electron bremsstrahlung converter.

Finally, we speculate that even lower impedance electron beam propagation and/or reflexing could be achieved at small anode diameters by combining the hollow anodes with a plasma fill between the cathode and anode. This plasma fill could result in a small effective anode-cathode gap spacing leading to a much lower impedance than could ordinarily be achieved with small anode diameters. Clearly many physics issues remain to be investigated and numerical simulations are in progress.

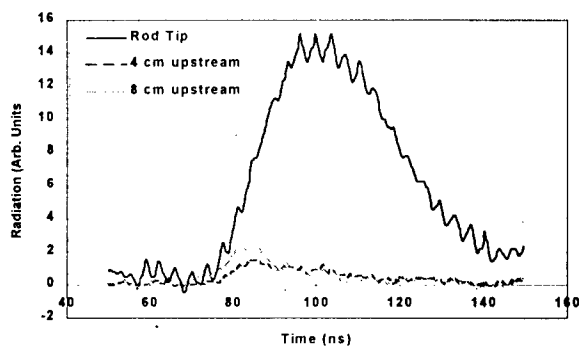


Figure 6. X-ray Pin diode signals for hollow 6 μm Al anode with carbon end plug for Gamble II shot 6940.

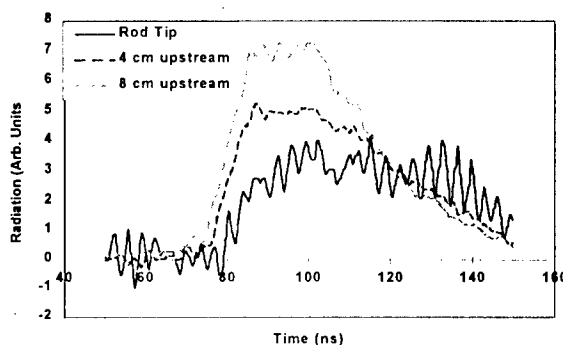


Figure 7. X-ray Pin diode signals for hollow 6 μm Al anode with no end plug for Gamble II shot 6941.

* Work supported by ONR

+ JAYCOR, Vienna VA

[1] R.A. Mahaffey, J. Golden, Shyke A. Goldstein, and G. Cooperstein, *Appl. Phys. Lett.* 33, 795 (1978).

[2] "Processes Governing Pinch Formation in Diodes," A.E. Blaugrund, G. Cooperstein and S.A. Goldstein, *Proc. of the International Topical Conf. on Electron Beam Res. and Tech.*, edited by Gerald Yonas (SAND 76-5122, Sandia Labs, Albuquerque, NM, 1975) p. 233, A.E. Blaugrund, G. Cooperstein, *P.R.L.* 34 461 (1975), and A.E. Blaugrund, G. Cooperstein, and S.A. Goldstein, *Phys. Fluids*, 20, 1185 (1977).

DENSE PLASMA HEATING BY 200 KJ - ELECTRON BEAM AT THE GOL-3-II FACILITY

A.V. Arzhannikov, V.T. Astrelin, A.V. Burdakov, V.G. Ivanenko, V.S. Koidan,
V.V. Konyukhov, K.I. Mekler, P.I. Melnikov, V.S. Nikolaev, S.V. Polosatkin,
V.V. Postupaev, A.F. Rovenskikh, S.L. Sinitsky.

Budker Institute of Nuclear Physics, 630090, Novosibirsk, Russia.

1. INTRODUCTION

Collective interaction of microsecond electron beam with a plasma and its fast heating is being investigated at the GOL-3-II facility. This activity is mainly directed for production of hot dense (10^{15} - 10^{17} cm⁻³) plasma in long open trap in order to study then the multimirror and «wall» confinement of such a plasma [1,2]. The plasma that is already obtained and can in principle be obtained in this facility is of interest for the broad spectrum of applications, like controlled fusion, pulsed neutron source, X-ray flash lamps, UV laser etc. Collective beam-plasma interaction is also studied in other groups [3,4,5].

In this paper recent results performed at the GOL-3-II facility are presented.

2. GOL-3-II FACILITY

The detail description of this facility is given in [2]. Layout of the device is given in Fig.1. The U-2 generator of the electron beam is used for experiments. In described experiments the energy content of the injected beam was around 200 kJ (1 MeV, 30 kA, 8 μ s). The longitudinal magnetic field is up to 4,5 T in the uniform part of the solenoid and 9 T in its end

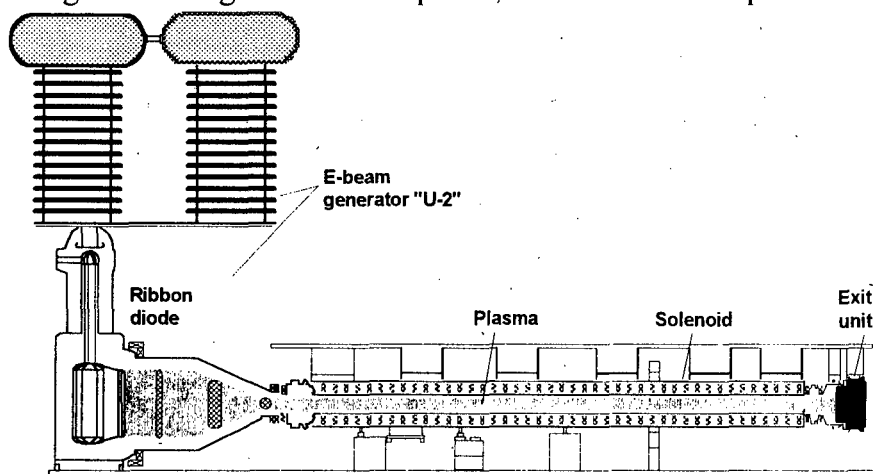


Fig.1. Layout of GOL-3-II device.

mirrors. Magnetic field configuration can be varied at the facility. The plasma has a diameter 6 cm and 12 m length. Plasma density can be varied in 10^{14} - 10^{17} cm⁻³ range and can be as of fixed density distribution along the device length and varied one.

The device is equipped by a set of various diagnostics.

3. RESULTS

The results of the first experiments at GOL-3-II facility are given in [1,2]. In new experiments, the conditions for the most efficient relaxation of the beam in plasma and for obtaining its maximum heating are found.

At the beam injection into a plasma the two-stream instability is developed resulting in the beam energy loss and heating plasma electrons. The change in the distribution of beam electrons over energies as a result of their collective deceleration was measured with the use of magnetic analyzer (see [6]) installed on the beam output from a plasma. For plasma density $(1 \div 2) \cdot 10^{15} \text{ cm}^{-3}$ the beam electron energy distribution is shown in Fig. 2.

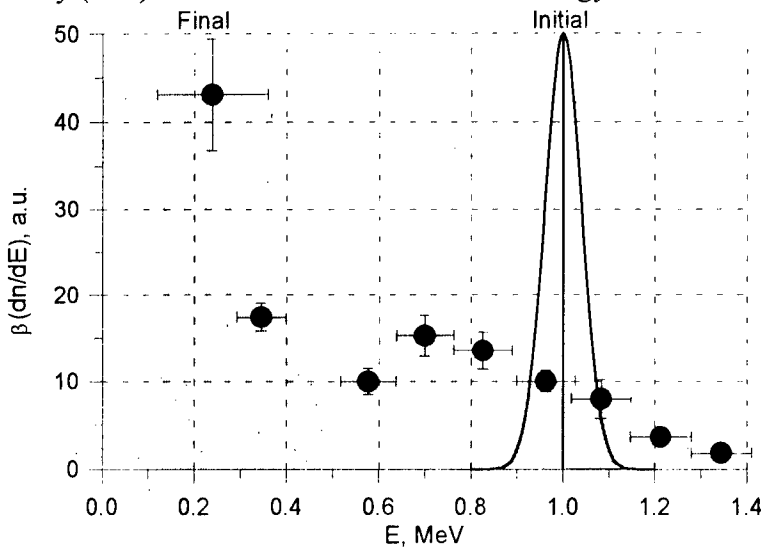


Fig. 2. Beam energy spectrum after interaction with the plasma measured in $4 \mu\text{s}$ after start, initial beam energy is 1.00 MeV

The characteristic feature of beam relaxation under conditions of the GOL-3-II device is output beam spectrum which is quite unique for the beam-plasma systems. In contrast to the earlier obtained spectra (see [6]) substantially stronger spreading of beam spectrum is observed. One can see in Fig. 2 that after beam-plasma collective interaction there is no beam on the system output but there is a flux of electrons with a spectrum which decreases to high energies. The total energy losses calculated by the observed spectrum of a beam passed a 12 m long plasma column achieves 40%. Note also that in the electron energy spectrum detected by magnetic analyzer, a large group of particles is near to the lower boundary of energies. These particles can be both the beam electrons lost over 70% of their energies or a small group of plasma electrons accelerated by turbulent fields up to energies of a few hundred keV.

The features of plasma heating are mainly revealed by the laser diagnostics. For finding the energy distribution of plasma electrons the system of Thomson scattering of the second harmonic of the neodymium laser light was used. The light pulse of 15 J and 10 ns was focused onto the axis of plasma column at a distance of 4 m from the beam input into the plasma. Finding the electron distribution function over velocities corresponding to energies ranging from 0.5 to 5 keV was made by the analysis of spectrum of radiation scattered at an angle 8° simultaneously in three fixed directions: along the beam transportation, in opposite direction, and perpendicular to the beam axis. In addition, the low energy fraction (in range up to 500 eV) of electron distribution function was detected by 90° scattering system. In the cases where the detected spectra do not correspond to the Maxwellian distribution of electrons over velocities, terms "transverse" T_\perp and "longitudinal" T_\parallel temperatures mean the double value of the average energy of electron motion in the selected direction that for the Maxwellian distribution correspond to the standard definition of temperature.

In the experiments the evolution of electron distribution function was studied at different plasma density and a fixed beam energy content of $170 \pm 10 \text{ kJ}$ (Fig. 3). At a plasma density of $1 \cdot 10^{15} \text{ cm}^{-3}$ measured transverse temperature T_\perp was $(0.9 \pm 0.2) \text{ keV}$. At the same time, the longitudinal temperature of plasma electrons following the beam propagation was found to be $(2.9 \pm 0.6) \text{ keV}$ and for electrons moving in the opposite direction it was $(1.7 \pm 0.4) \text{ keV}$. Thus, temperature of electrons co-directed with the beam turns to be 4 times higher than that transversal one. With the increase in plasma density the longitudinal temperature drops fast but the transverse temperature changes insignificantly. As a result, at a density $2.5 \cdot 10^{15} \text{ cm}^{-3}$ they both become equal approximately of 0.5 keV and the electron distribution function becomes

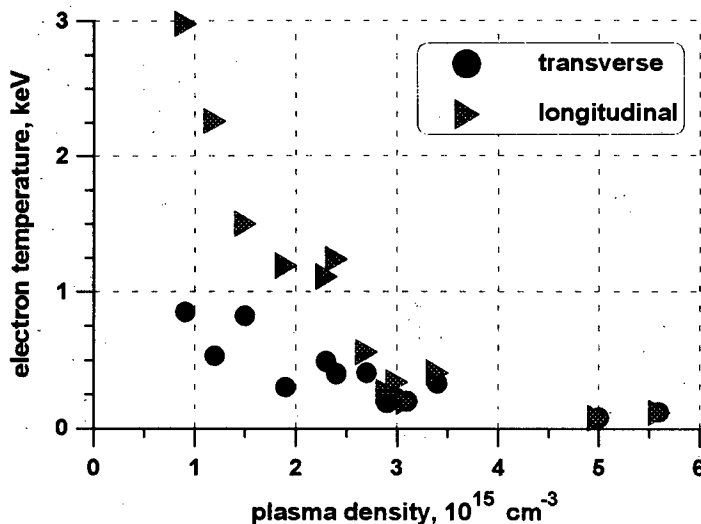


Fig.3. Plasma temperature vs. density, measured by $0.53 \mu\text{m}$ Thomson scattering

Maxwellian. With further increase in density up to $6 \cdot 10^{15} \text{ cm}^{-3}$ the electron distribution function remains to be Maxwellian and electron temperature decreases inversely to the density ($T \propto 1/n$).

Presence of the density threshold in the dependence of electron distribution function on plasma density is natural in frame of considerations of the influence of the binary Coulomb collisions. The plasma pressure nT_{\perp} remains to be about the same at the variation of plasma density within range $(1 \div 5) \cdot 10^{15} \text{ cm}^{-3}$. Under these conditions, electron temperature has an

inversely proportional dependence on density ($T \propto 1/n$). Then, the classic mean free path of electrons determined in terms of a density and temperature as $\lambda \propto T^2/n$ becomes strongly dependent on plasma density $\lambda \propto 1/n^3$. If one takes into account that at lower density mean longitudinal energy grows even faster, the free path length depends in this region even stronger on density. As shown by estimates at $n \approx 2.5 \cdot 10^{15} \text{ cm}^{-3}$ the free path length of the plasma electrons becomes comparable with the longitudinal size of the magnetic trap and at $n \approx 1.5 \cdot 10^{15} \text{ cm}^{-3}$ it is already much larger than the device length. In this case, the electron distribution function is formed only by turbulent fields occurred as a result of beam-plasma interaction and it is non-Maxwellian. It is interesting to note that under these conditions when considering transfer processes in the plasma it cannot be considered as a free collisionless plasma because of strong collisions of its electrons with turbulent fields. In fact, the experiments evidence that electron heat transfer and plasma conductivity along the magnetic field turn to be much lower than the classical ones [6].

Under experimental conditions described above (uniform plasma density along the device) quite strong heating of plasma electrons was observed. Ion temperature achieves only $20 \div 30 \text{ eV}$.

For substantial increase in the ion temperature and probably for obtaining plasma with $\beta > 1$ a method of a two-stage heating of a dense plasma is being developed on the device [7]. In this case, in the background "rare" plasma which is heated directly by an electron beam due to collective interactions, a dense gas bunch (one or several) is formed by gas-puffing. As a result, hot electrons of the "rare" plasma transfer their energy to electrons and ions of the dense bunch by binary collisions. Feasibility of this method is already proved at the first stage of the GOL-3 facility [7].

New experiments in this direction are also started on the GOL-3-II device. To do so, in the beginning of the device the deuterium cloud of a few meters in length and density of $\sim 10^{16} \text{ cm}^{-3}$ is formed. On the rest of the device the plasma density is of $\sim 10^{15} \text{ cm}^{-3}$. In this case, the dense plasma has the electron temperature of $300 \div 500 \text{ eV}$ and the ion temperature increases up to $100 \div 200 \text{ eV}$ (see Fig.4).

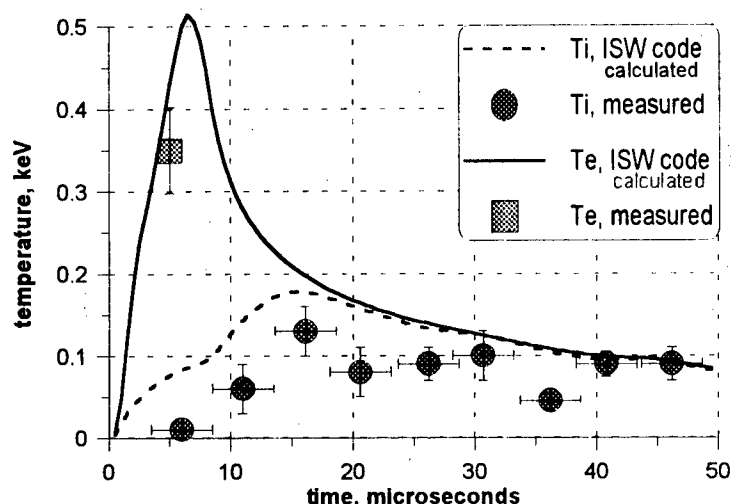


Fig.4. Dynamics of electron and ion temperature near $z = 4$ m ($n = 4.8 \cdot 10^{15} \text{ cm}^{-3}$).

In order to improve the parameters of a dense plasma it is planned not only to optimize the conditions of its heating but also to improve confinement of the bunch. To this aim, it is planned to mount at the device the short (~ 1 m) section with lower magnetic field ("magnetic pit") where a dense plasma will be confined similarly as in a "gasdynamic" trap [8]. As shown by calculations, under the conditions of the GOL-3-II device it is possible to obtain bunch of hot dense plasma (~ 1 keV) with $\beta \geq 1$. This will enable one to start the experiments on the multimirror and

"wall" confinement of plasma.

4. CONCLUSION

- 1) High level (up to 30÷40%) of collisionless energy losses of 200 kJ-relativistic electron beam in the plasma of 10^{15} cm^{-3} density is achieved.
- 2) Effective heating of a plasma with this density up to $T_e \approx 2.0$ keV due to collective beam-plasma interaction is obtained.
- 3) Plasma with density $\approx 5 \cdot 10^{15} \text{ cm}^{-3}$ is heated up to 0.5 keV electron temperature and up to 0.1÷0.2 keV ion temperature by two-stage scheme.
- 4) There are good prospects for production at GOL-3-II facility of hot dense plasma with parameters available for experiments on multimirror and «wall» confinement and other applications.

This work was carried out under financial support of Ministry of Science of Russia and Russian Foundation of Basic Research, project 96-02-19436.

REFERENCES

- [1] M.A. Agafonov et al., Proc. 11th Int. Conf. on High Power Particle Beams, Prague, 1996, Vol.1, p.182.
- [2] A.V. Arzhannikov et al., Plasma Phys. and Contr. Fusion, 1996, Vol.38, p.A93.
- [3] V.S. Burmasov et al., Fizika Plasmy, 1997, Vol.23, p.142 - in Russian.
- [4] J. Ullschmied et al., Proc. 11th Int. Conf. on High Power Particle Beams, Prague, 1996, Vol.1, p.343.
- [5] H. Koguchi et al., Proc. 11th Int. Conf. on High Power Particle Beams, Prague, 1996, Vol.1, p.331.
- [6] A.V. Burdakov et al., JETP, 1996, Vol.82, p.1120.
- [7] V.T. Astrelin et al., JETP, 1998, Vol.113, p.897.
- [8] A.V. Arzhannikov et al., IAEA TCM "Innovative Approaches to Fusion Energy", Pleasanton, CA, 1997, p.27.



BEAMS'98

12th INTERNATIONAL CONFERENCE
ON HIGH-POWER PARTICLE BEAMS



ORALS

*Diagnostics and
Experimental
Methods*

Vol. I

ION LOSSES IN EXPANDED LASER-PRODUCED PLASMA

J. Krása, L. Láská, K. Rohlena, M. Pfeifer, J. Skála, B. Králiková, P. Straka, M. Makarova

Institute of Physics, Acad. Sci. CR, Na Slovance 2, Prague 8, 180 40, Czech Republic

E. Woryna, J. Wołowski

Institute of Plasma Physics and Laser Microfusion, 23 Hery St., Warsaw, 01-908, Poland

ABSTRACT

Losses of charge carried by Ag ions emitted from a laser-produced plasma are measured up to a distance of 187 cm from the target. The plasma was generated by a high power iodine laser delivering the power density up to $\sim 10^{15}$ W/cm² on the target surface. Two ion collectors of different construction located coaxially were applied, which made the ion current measurement in the same direction and at two distances from the target simultaneously possible. The variation of the charge, ΔQ , of ions escaping the plasma at $\sim 10^\circ$ to the target normal with the distance, L , from the target was found to be of the form $\Delta Q \sim L^{-2}$.

INTRODUCTION

The laser-driven ion sources (LIS) represent a new efficient technique, providing sufficient ion yield at high charge states for a very wide choice of elements. As a driver various pulse lasers are applied. For example, a commercial CO₂ laser was used for production of Ta and Pb ions with the charge state up to 24+ and 34+, respectively [1,2]. Much higher maximum charge states were measured when the iodine laser PERUN was used: Ta⁵⁵⁺, Pb⁵¹⁺, Pt⁵⁰⁺, W⁴⁹⁺, Au⁴⁹⁺, etc. [3]. The ions from an expanding laser-produced plasma can be extracted and processed for an application [1,2,4] and/or, if their kinetic energy is high enough, they can be used, e.g., for implantation without extraction [5].

The decisive key parameters of an ion source are the number of emitted ions and their kinetic energy. For their estimation the distribution of charge states and velocities is measured employing an ion mass analyzer. The distance, L , from the point of laser beam impact to the point at which these measurements are done, must be considered as another parameter due to the space dependence of the distributions mentioned above. For receiving comparable data from different experiments, the measured data are usually recalculated applying, for example, the law $\Delta Q \sim L^{-2}$ for the charge and the law $j \sim L^{-3}$ for the ion current [2,4]. These laws do not take into account any losses of ions and of their charge outside the laser-plasma interaction space, that is during the plasma expansion into a vacuum system. It is supposed that the recombination processes in the expanding laser plasma slow down quickly with the distance, and a "freezing" of charge states appears, because the electron density, N_e , decreases with the distance as L^{-3} and the electron temperature, T_e , as L^{-2} [4]. The decrease in T_e with increasing L was, for example, measured for a Be plasma [6]. It was evaluated from the vacuum UV radiation of the Be plasma that the decrease in T_e ends at a distance of 10 cm and for larger distances, T_e is independent of L . A decrease in the number of ions emitted from a carbon plasma was observed up to a distance of 145 cm, while at longer distances it remained approximately constant with the increasing L [7]. Even if experimental results are not fully

consistent, the idea of the “freezing” of charge states can be expressed by a critical distance, L_{cr} , from which the recombination of ions can be neglected. Roudskoy defined L_{cr} as a distance from the irradiated target where the initial sharp rise of the recombination losses $\sim L^3$ is changed to the slow descend $\sim L^{-15/13}$ [8]. This simple Roudskoy’s model renders a scaling law

$$L_{cr} \approx T_e^{13/12} v^{14/6} \tau_l^{13/6} / n_{cr}^{8/18} d^{8/6},$$

where v is the ion velocity, τ_l the laser pulse duration, n_{cr} the critical plasma density, and d the focal spot diameter. All considerable charge-state changes should happen in the region limited by L_{cr} because for the larger distances where $T_e \sim L^{-15/13}$ the “freezing” of ion charge states takes place. For a Pb plasma produced by a CO₂ laser (a pulse width higher than 1 ns, a power of 0.2 GW, and a focal spot diameter of 1 or 0.3 mm), Roudskoy calculated that L_{cr} can reach a few meters. One can deduce from this large range of L_{cr} that any comparison of different ion laser sources could be misleading without knowledge of ion charge losses during the expansion of plasma into a vacuum system.

An ideal tool for determination of ion charge losses is a time-of-flight ion-current analysis because a short burst of ions is produced by a short duration laser pulse compared with the flight time of ions. The simultaneous use of ion collectors located at different distances from the laser-beam focus-spot makes it possible to compare not only the decrease in the ion current with the distance but also the decrease in the total charge carried by all collected ions, integrating the time resolved ion collector signals.

EXPERIMENT ON ION CHARGE LOSSES

The losses of highly charged ions in the expanding plasma were measured far from a flat Ag target that was irradiated by a focused high-power laser pulse. The iodine laser system PERUN at the Institute of Physics in Prague operating at the second harmonics ($\lambda = 657$ nm) at 350 ps laser pulse duration was used [9]. The laser pulse energy ranged from 13 J to 29 J and was focused into a spot with a diameter of about 0.1 mm. It made it possible to deliver a power density from 4×10^{14} W/cm² to 1×10^{15} W/cm² on the target.

The above mentioned procedure based on a time-of-flight method was applied using the advantage due to the pulsed nature of the laser-produced plasma. For measurement of ion currents during the plasma expansion, two ion collectors of different construction were used. One of these collectors, IC1, was a ring detector with the inner diameter $\varnothing_{in} = 3.8$ cm and with the outer one $\varnothing_{out} = 5$ cm, and the other, IC2, was a circular detector with a diameter of 1.5 cm. The ring detector was located at the fixed distance $L_{IC1} = 83$ cm from the plasma. The distance, L_{IC2} , of the circular detector ranged from 94 to 187 cm. The scheme of the experiment is shown in Fig. 1. The laser pulse strikes the target at $\sim 30^\circ$ to the surface normal. The ion collectors detect the ions escaping from the plasma at $\sim 10^\circ$ to the target normal. The target was an Ag slab of 1 mm thickness.

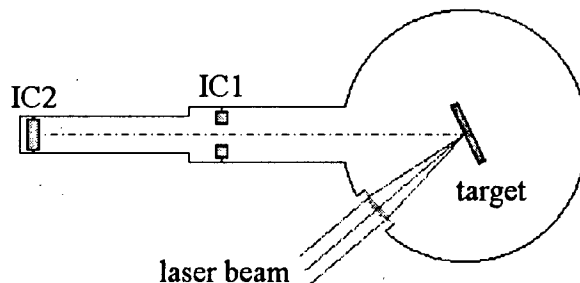


Fig.1 Schematic diagram of the experiment

All the ion collector signals recorded by a Tektronix TDS 723 oscilloscope were recalculated in line with the scaling laws mentioned above. For the determination of ion losses

during the plasma expansion, the amplitude of all the collector signals was multiplied by a ratio $L^2/\Delta S$, since the charge, ΔQ , collected by a detector with an area ΔS is proportional to the solid angle element $\Delta\Omega = \Delta S/L^2$. We suppose that the time-of-flight of ions is not affected by the time period of the ion emission in our measurement due to the fact that the plasma generated by the iodine laser emits ions during a finite time of only about 10 ns; this value was estimated from the temporal width of ion pulses measured with a cylindrical electrostatic ion energy analyzer at a long distance of ~ 2 m for a selected ratio of ion kinetic energy and charge state, E_i/z .

Fig. 2 shows an example of ion currents measured with the IC1 and with IC2 that were located at a distance of 83 cm and of 169 cm from the target, respectively. The highest ion peak of both the curves is a response to the impact of fast ions. The corresponding velocity calculated at this peak maximum is $\sim 4 \times 10^7$ cm/s. The second broad maximum corresponds to slower thermal ions. It is evident that the ion current decayed roughly to a half over a twofold distance. Integrating under the curves of Fig. 2 for a time period, $< t_1, t_2 >$, one can estimate

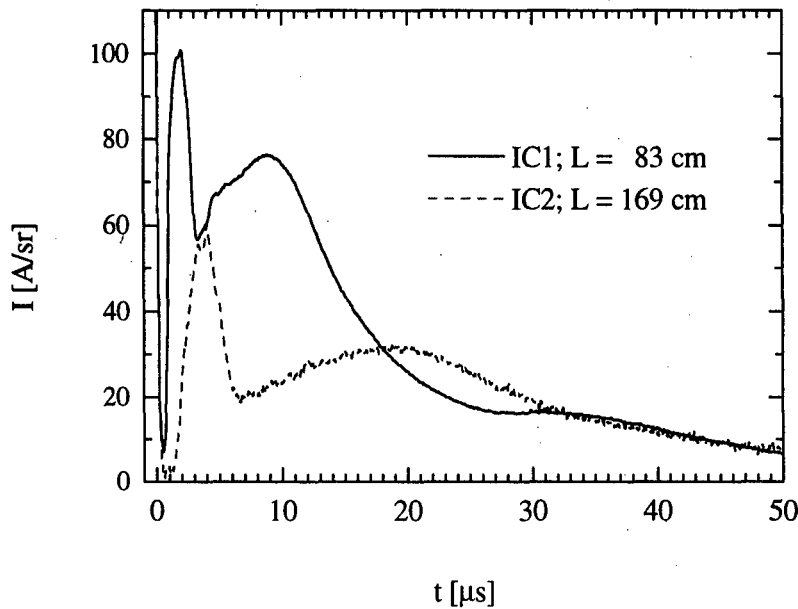


Fig. 2 Ion current measured by ion collectors IC1 and IC2 located at different distances from the target.

the decrease of the charge carried by ions on the path from IC1 to IC2. Because the ion collectors are located at different distances from the target, the limits of integration, t_i , must fulfill the relation $t_{iIC2} = (L_{IC2}/L_{IC1}) t_{iIC1}$. Fig. 3 shows a correlation between the charge, Q_{IC2} , collected with the removable IC2 and the charge, Q_{IC1} , measured with IC1 for different positions of IC2. It is evident that the distance L_{IC2} does not affect this correlation if the measured ion charge is related to the solid angle. It indicates that we don't need to consider the recombination of ions during the plasma expansion.

Fig. 2 shows two groups of ions that expand with different mean velocities. This effect was ascribed to the formation of a two temperature plasma [10,11]. The fast ion group consists of ions with the charge state that is several times higher than the charge state of the slow ions [11, 12]. Both the short time-of-flight and the high potential energy of the fast ions are a reason why their recombination during the plasma expansion was measured separately

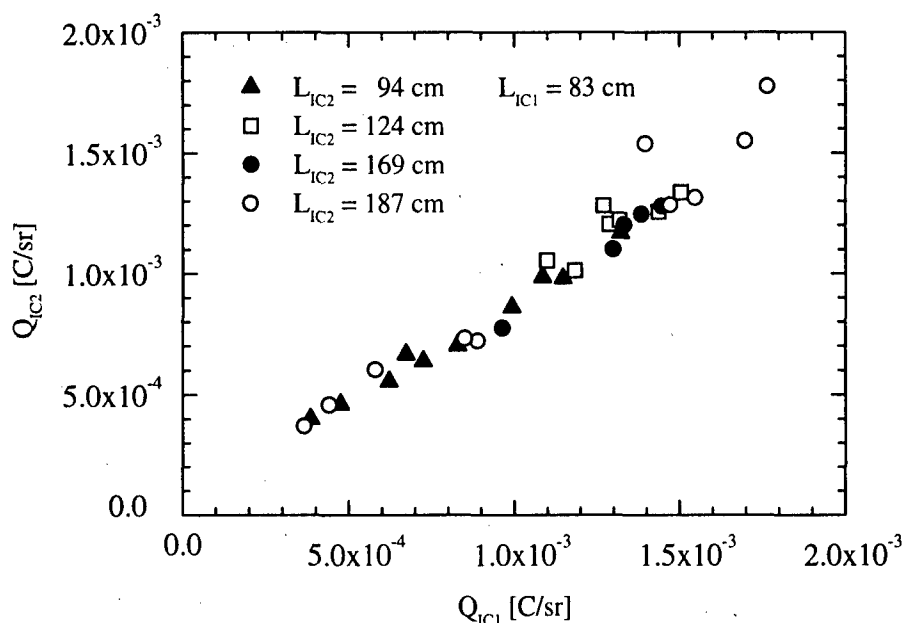


Fig. 3 Ion charge, Q_{IC2} , measured with IC2 versus ion charge, Q_{IC1} , measured with IC1 for different L_{IC2} .

from the slower ions, but the measurement does not confirm this effect. We can conclude that the decrease in the charge of Ag ions was found to have the form $\Delta Q \sim L^{-2}$ and that only the dilution of ions must be considered due to expansion of the plasma into the vacuum.

ACKNOWLEDGMENT

This work was supported by a grant A1010819 (1998) of the Grant Agency of the ASCR.

REFERENCES

- [1] H. Haseroth et al.: in Proc. of the XVIII Int. Linear Accelerator Conference, (ed. C. Hill and M. Vretenar), Geneva, Switzerland, 1996, p. 570.
- [2] V. Yu. Baranov et al.: *Laser and Particle Beams* **14** (1996) 347.
- [3] J. Krása et al.: in Advances in Laser Interaction with Matter and Inertial Fusion (ed. G. Velarde, J. M. Martínez-Val, E. Minguez, J. M. Perlado), World Scientific, Singapore, 1997, p.103.
- [4] V. A. Monchinsky, I. V. Kalagin, A. I. Govorov: *Laser and Particle Beams* **14** (1996) 439.
- [5] F. P. Boody et al.: in: Laser Interaction and Related Plasma Phenomena, 13th International Conference, Monterey, CA 1997, ed. G.H. Miley and E.M. Campbell, AIP Conference Proceedings 406, AIP Woodbury, New York, pp. 539-546.
- [6] E. Woryna et al.: *Laser and Particle Beams* **14** (1996) 293.
- [7] V. V. Afrosimov et al.: *Pis'ma Z. Techn. Fiz. (JTP Lett.)* **10** (1984) 1017.
- [8] G. J. Tallents: *Plasma Phys.* **22** (1980) 709.
- [9] I. V. Roudskoy: *Laser and Particle Beams* **14** (1996) 369.
- [10] M. Chvojka et al.: *Czech. J. Phys.* **42** (1992) 899.
- [11] L. M. Wickens, J. L. Allen and P. T. Rumsby: *Phys. Rev. Lett.* **41** (1978) 243.
- [12] H. Haseroth, H. Hora: *Laser and Particle Beams* **14** (1996) 393.

STOPPING POWER OF PROTON BEAMS FOR DENSE PLASMA DIAGNOSTIC

V. Fortov, V. Gryaznov, M. Kulish, V. Mintsev, A. Filimonov

Institute for Chemical Physics Research,

Chernogolovka, Moscow reg., 142432, Russia

B. Sharkov, A. Golubev, A. Fertman, V. Turtikov, A. Vishnevskiy, A. Kozodaev

Institute for Theoretical and Experimental Physics,

B. Chermushkinskaya 25, 117259, Moscow, Russia.

D. H. H. Hoffmann, U. Funk, S. Stoewe, M. Geißel

Gesellschaft für Schwerionenforschung, D-64220, Darmstadt, Germany

D. Gardes, M. Chabot

Institute National de Physique Nucleaire, 91406, Orsay, France

ABSTRACT

A new method to generate plasma targets with electron densities $n_e \geq 10^{20} \text{ cm}^{-3}$ behind strong shock waves to study the energy loss of protons and heavy ions is discussed. The problems of matching of large scale accelerator facility and explosive technique are considered. It is suggested to use a small ($< 150 \text{ g TNT}$) vacuum pumped explosive metallic chambers with fast valves in such experiments. Details on the construction and performance of small-sized explosively driven generators of strong shock waves are presented. The experimental setup including the proton accelerator ISTRA-36 and the explosive chamber, which have been installed in ITEP, is presented. The measured values of proton beam energy losses were 100-400 keV in dependence on plasma parameters. Comparison of the first experimental data with the theoretical models is discussed.

INTRODUCTION

To investigate the heating of matter by particle beams detailed knowledge of the energy loss in dense plasma at high pressures and temperatures are crucial. Experiments carried out at GSI with discharge plasmas having electron densities up to $n_e \sim 10^{19} \text{ cm}^{-3}$ show a considerable contribution of free electrons to the stopping [1]. With increasing plasma density the influence of the effects of the Coulomb coupling are expected to be of great importance. Shock wave techniques make it possible to produce plasmas with electron densities of up to $n_e \sim 10^{22} \text{ cm}^{-3}$ [2]. For this goal explosively driven plasma generators have been developed [3]. In such devices plasma is created behind the plane front of an intense shock wave generated by the detonation of chemical high explosive. Standard shock wave plasma generators contain more than 500 g of high explosive, to produce shock compressed strongly coupled plasma with temperatures of 1-10 eV, pressures of 1-200 kbar and Coulomb coupling parameters of 1-5 [2]. Explosively driven plasma targets look very attractive for beam-plasma interaction experiments because of the absence of strong electromagnetic fields like in discharges, which significantly effect the beam transport.

EXPLOSIVELY DRIVEN PLASMA GENERATOR

To use standard explosive devices in beam areas of accelerator facilities it is necessary to build large-scaled explosive chambers and to solve the problems of matching high vacuum beam lines with the explosive apparatus. As the first step we suggest to use small charge ($< 150 \text{ g TNT}$) explosive generators in a vacuum pumped explosive metallic chamber with fast valves

in such experiments. To optimize the explosive plasma generators numerical simulations of plasma shock compression and a special series of shock wave experiments were carried out [4]. They show the possibility to construct small-sized linear and cumulative explosively driven generators with shock front velocities of about 6-20 km/s having a high explosive charge not exceeding 30-150 g. Using these devices we will investigate experimentally (i) the effect of strong interparticle interactions in plasma on the energy loss of fast ions and (ii) the stopping power of plasma at high ionization degrees.

The performance of one type of such explosively driven generators is shown on Fig. 1. Through transparent tubes 1' and 1'' the registration of velocities of shock waves and contact surfaces was conducted. Steel flying plate was accelerated by products of detonation (60g TNT) to values of 6.5 km/s. In the first parts of shock tube 2' velocity of shock wave in Xe was of constant value $D_0=6.9$ km/s. At passing of conic part the speed of shock wave grew and

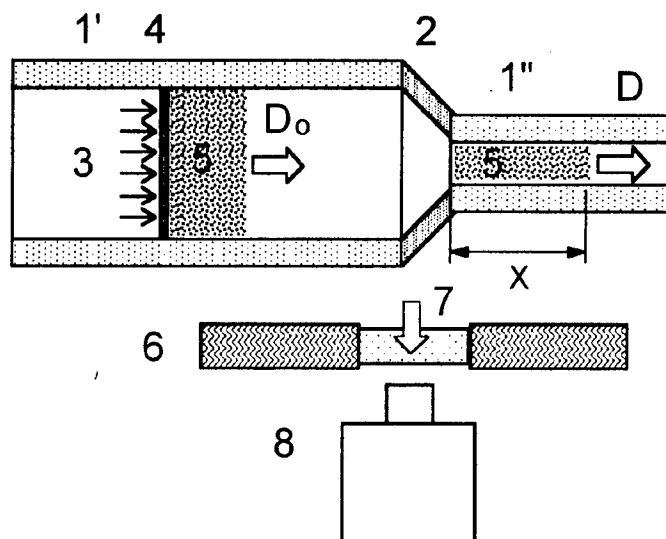


Figure 1. Experimental assembly. 1', 1''- glass tubes; 2-conical section; 3- products of detonation; 4- flying plate; 5- shock compressed plasmas; 6- protection wall; 7- optical window; 8- streak camera.

was increased the thickness of layer of plasma. The thickness of plasma slug was of >10 mm which provide fixed parameters for a time of $1 \mu\text{s}$ for the performance of the experiment with ion beam. The measured velocity of shock wave in section 1'' with diameter of 6 mm is shown

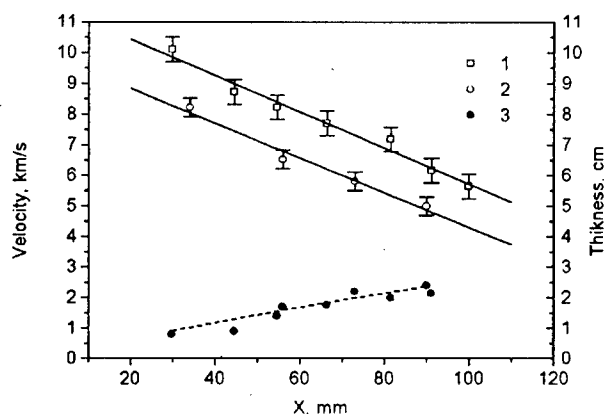


Figure 2. Velocity of shock wave and thickness of plasma slug in the direction of motion versus distance X from the cone. 1- initial density of $5.39\text{E-}04$ g/cc; 2- $1.62\text{E-}03$ g/cc; 3- thickness of plasma slug.

on Fig. 2. The velocity is damped out which is connected with small diameter of tube. Shock wave velocity and brightness temperature were measured in every experiment. Plasma parameters are estimated in frames of Debye approximation in grand canonical ensemble are placed in Table 1.

Table 1.

Initial density of xenon 5.39E-04 g/cc				
X, mm	T, K	P, bar	e, 1/cc	XeII, 1/cc
20	46700	530	6.0E+19	2.6E+18
40	40500	420	5.3E+19	5.9E+18
60	34000	320	4.5E+19	1.3E+19
80	28700	234	3.5E+19	2.0E+19
Initial density of xenon 1.62E-03 g/cc				
X, mm	T, K	P, bar	e, 1/cc	XeII, 1/cc
20	41200	1140	1.4E+20	2.9E+19
40	34800	870	1.2E+20	4.9E+19
60	29200	635	9.0E+19	6.4E+19
80	23300	430	6.5E+19	6.2E+19

EXPERIMENTAL SETUP

Experimental equipment for the investigations of stopping power of proton beam in explosively driven plasma behind powerful shock waves is presented on Fig. 3. A 3 MeV 60 us duration proton beam pulses delivered by 148.5 MHz ISTRA-36 RFQ linac at ITEP and compact metallic vacuum pumped chamber for explosions up to 150 g TNT were the main unit of this set-up. Differential pumping and fast valves proved to be sufficient for the protection of high vacuum beam line from the high pressure detonation products.

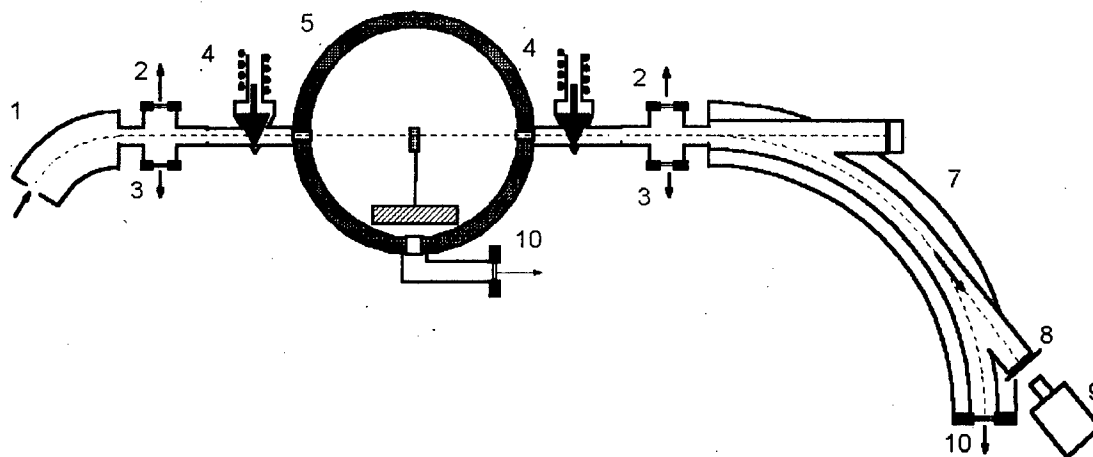


FIGURE 3. Experimental set-up.

1 - Banding magnet R=500, 2 - Differential pumping, 3 - Vacuum checking, 4 - Fast valves, 5 - Explosive chamber, 6 - Explosive generator, 7 - Analysing magnet R=707, 8 - MCP plate, 9 - PCO camera, 10 - Pumping

The position of the proton beam on a scintillator after the analysing magnet was recorded by a fast shutter camera (PCO-camera). Typical picture of the experiment is shown on Fig.4. The time gates of the PCO-camera was about 50 us in this shot. The undisturbed position of the proton beam passing through cold xenon at the initial pressure 10 kPa is seen to the right. The time about 1 us is necessary for plasma slug ($D \sim 8$ km/s) to cross the beam line. The image of the proton beam interacting with the explosively driven plasma is to the left on the Fig.4. The intensity of the beam image is low because of the small time of the process and additional scattering of the beam. The estimated value of the energy losses in this experiment is $\Delta E_{\text{exp}} = 150$ keV.



FIGURE 2. Image of 3-MeV proton beam in the beam-explosively driven plasma interaction experiment. ($P_0 = 10$ kPa).

The plasma temperature and shock velocity were measured in the experiment. Pressure $P \sim 50$ Mpa, temperature $T \sim 4$ eV, density $\rho \sim 6 \cdot 10^{-3}$, electron concentration $n_e \sim 6 \cdot 10^{19}$ 1/cc and nonideality parameter $\Gamma \sim 0.35$ were realised. Calculated value of the energy losses in frame of the model [4] ($\Delta E_c = 200$ keV) is in a reasonable agreement with the measured one.

So the first shots with the weakly nonideal xenon plasma showed a reliable operation of the experimental set-up.

This work was supported in part by INTAS Grant N94-1638.

REFERENCES

1. J.Jacoby et al. *Phys.Rev. Lett .E.* **53** (3), 2701 (1996).
2. V.Fortov, I.Yakubov. *Physics of Nonideal Plasma* (Hemisphere, 1990).
3. V.B.Mintsev, V.E.Fortov. *Explosively driven shock tubes*. High Temperatures **20** (1982) 584.
4. W. Ebeling, A.Foerster, V. Fortov, V.Gryaznov, A. Polishchuk, *Thermophysical Properties of Hot Dense Plasmas* (Teubner, Stuttgart-Leipzig 1991).

MULTIFUNCTION X-RAY SPECTROGRAPH

S.Attelan-Langlet¹, B.Etlicher¹, M.V.Fedulov²,
V.O.Michensky², G.S.Volkov², V.I.Zaitsev²

¹*LPMI, Ecole Polytechnique, 91128, Palaiseau, France*

²*Troitsk Institute for Innovation and Fusion Research
TRINITI, Troitsk, 142092, Moscow reg., Russia*

ABSTRACT

The x-ray spectrograph on base of MICA crystal ($2d=19.9\text{\AA}$) for spectrum analysis is described. The device construction (Θ - 2Θ scheme) is suit to use several types of radiation detectors: film, charge coupling device (CCD) and microchannel plate (MCP). X-ray film is used for spectrum measurements in working range of device ($3\text{\AA}\div 18\text{\AA}$). The part of the device working range is measured by means CCD. The CCD length is 3cm. It correspond to $\Delta\lambda=4\text{\AA}$ range of x-ray spectrum. Analog CCD signal is transformed to digital form and goes to computer of IBM PC type. The computer software have codes for plasma parameters determination (Te, ne) according to measuring dates. Preliminary the CCD characteristics in to x-ray region had been researched. Some of this results are given. In the same time there are two time resolved detectors for plasma dynamic measurements. The construction of this detectors is based on the micro channel plates. The x-ray range of MCP detector is $\Delta\lambda=0,1\text{\AA}$. Some results of this device application at the pulsed power facilities ANGARA-5 and GAEL are given.

INTRODUCTION

The full information about hot plasma radiation must contain the time- and space-distribution of X-ray spectrum. There are the different schemes of X-ray spectroscopy researches of plasma [1,2]. The main parts of traditional spectroscopy scheme are dispersion element (crystal, grating) and X-ray sensor. The inclusion into spectroscopy scheme the elements of X-ray optic gives possibility to measure plasma characteristic with spatial resolution [3]. The time resolution is conditioned the sensor type. Usually the film is using as X-ray sensor. In this case the integral in time plasma parameters can be measuring only. Besides the procedure of film processing increases the time of the experimental researches. Application of charge coupled devices (CCD) as X-ray sensor [4] gives possibility to connect sensor with computer and to have measuring results just after experiment. Now CCD can operate with frequency $\leq 100\text{ MHz}$. It allows to measures spectrum pictures through $10\div 100\text{ }\mu\text{s}$. Because typical times of high-power processes are more less in this case the CCD registration can provide time-integrated pictures also [5]. Spectrum dynamic can be measure by inclusion into spectrograph scheme the sensors with high time resolution. In this paper the X-ray spectrograph is described where in the same time with CCD sensor the fast X-ray detectors are used. Detectors are designed on the micro channel plates (MCP) base. Detectors construction provides the placing of detectors on different spectrum areas and changing sensitivity of ones.

INSTRUMENT DESIGN

Figure 1 shows a geometry of the X-ray spectrograph. The typical Θ - 2Θ scheme is used. The analyzer is based on a convex mica crystal (interplanar spacing $2d=19.9\text{\AA}$). In order to protect the crystal from damage by the plasma discharge products and optical radiation, we

used a 18- μm thick beryllium foil at the entrance of the spectrograph chamber. A high reflectivity of mica in the first and second orders [6] gives additional possibilities to device, namely, extends the effective spectral range of the X-ray spectrograph. The full spectral range of device (3A÷18A) is realized by film registration. A cassette with X-ray film is arranged coaxially with respect to the crystal axis. Usually film registration is made on the initial stage experiment to obtain survey spectra pictures. In most cases the detection is performed using the linear CCD (LCCD) and MCP as sensors. The LCCD is placed in the first order of reflectivity. In the same time MCP detectors measure intensity X-ray lines in the second order. The LCCD and MCP detectors are mounted on a table holder that could be rotated with high precision around the crystal axis. The length of the LCCD active area is sufficient to observe a spectral band with a width of about 4A, which is selected within the working range of spectrograph. The LCCD control and analog-to-digital conversion are performed by means special electronic unit. Digital LCCD signal (RS-232 interface) is transferred to IBM PC-compatible computer, which allows to process data immediately after the experiment. The size of each MCP detector covers the 0.1 A spectral range of device. Signals of MCP detectors come to digital oscilloscope.

REGISTRATION SYSTEM

The adjusting registration is performed by means usually X-ray film. The LCCD based on an commercial chip, in which the protective glass is replaced by a two layer filter formed with a 2- μm lavsan film coated with a thin (0.1 μm) aluminum layer. The LCCD structure consists of the 2700 working cells with dimensions $11 \times 11 \mu\text{m}^2$. To determine this CCD characteristics into X-ray range the special researches was performed. In detail the method of one was described in [4]. The CCD characteristics (sensitivity and space resolution) were determined in the

quantum energy range from 0.2 to 25 keV. It was shown that energy range 0.8-4 keV intrinsic signal broadening caused by the charge diffusion in the LCCD does not exceed the one cell size. According to dispersion of device (8mm/A) a full width at half maximum (FWHM) of spectral line is about 11 LCCD cells wide. Therefore,

the LCCD registration system does not decrease the spectral resolution of the instrument, which is $E/\Delta E \approx 10^3$ for this spectrograph. The LCCD operation can be synchronized with the working cycle of the experimental setup. Because the control unit was mounted on the spectrograph chamber and, hence, occurred in the immediate vicinity of a source of strong electromagnetic field, special measures were taken in order to increase the noise stability of the device (double shielding of the unit and connecting cables, separate grounding of the circuit). The analog signal from LCCD was converted to the 10-bit digital code and passed to computer.

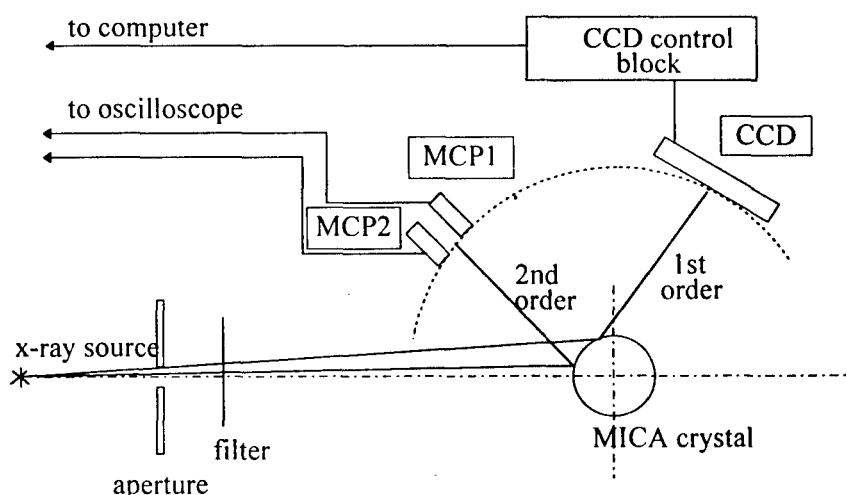


Fig.1. Scheme of X-ray spectrograph

By design of the time resolution mode of spectrograph the main task was the selection of the fast sensors with high sensitivity to provide registration of signals from LCCD and time-resolved detectors in the same time. Besides it was necessary to have changeable sensitivity of detectors to provide measurements by different times of processes. The analysis and experimental researches have showed that MCP have such characteristics. The time resolution of one is $\sim 10^{-9}$ sec. The MCP sensitivity depends on voltage on the plates and can changes in wide range. We used two-plates MCP that had the rectangular sensitive area (1×10 mm). It was possible to change the MCP positions in according to X-ray lines picture.

We have developed a special program package for control of the spectrograph operation and process of the experimental date. Now this soft is realized on IBM PC-type computer.

DEVICE APPLICATION

We used this device in Z-pinch experiments on two installations with markedly differing energy parameters: ANGARA-5-1 (Russia, TRINITI, Z-pinch current $I_{\max}=5$ MA) and GAEL (France, ECOLE POLYTECHNIQUE, $I_{\max}=300$ kA). The duration of X-ray radiation was in range $30 \div 80$ ns. In spite of great installations difference the application of this X-ray spectrograph was successful in the both cases.

In the ANGARA-5-1 installation, the load is represented by a hollow gas (argon) jet created by an electromagnetic valve with a supersonic nozzle. As a result of the current passing through the gas shell, the jet collapse on a cylindrical formy-solid load on the jet axis. The formy-solid load was made of agar-agar with KCl additives. The experiments showed intense emission of H- and He-like lines of the matter load. Fig.2 shows lines of argon, potassium, chlorine in second order. In the same time it is possible to see the Al lines (matter of cathode) in the first order. Calculation using the relative total radiant energy yields of the resonance lines of He- and H-like chlorine and

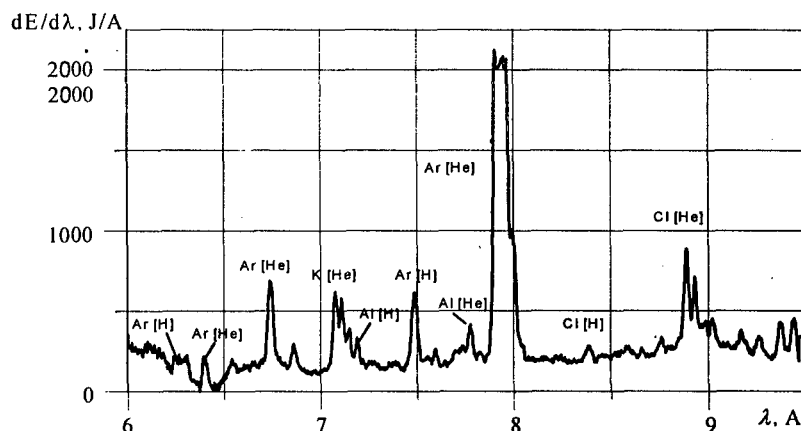


Fig.2. Line emission spectrum: Ar, K and Cl-second order, Al-first order reflection of crystal, ANGARA-5 facility.

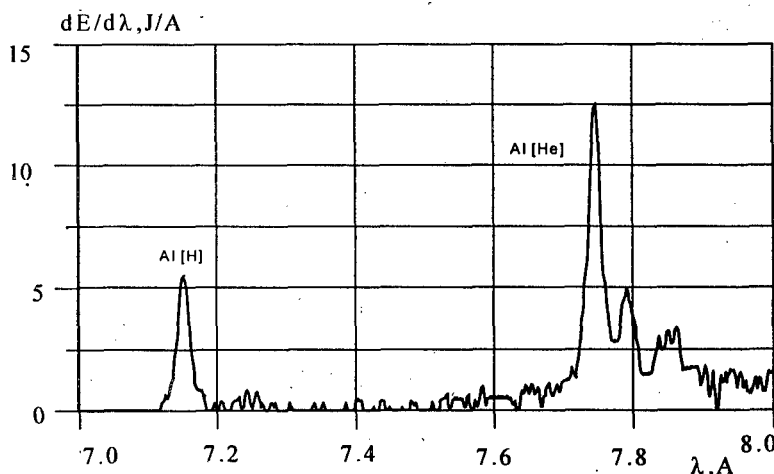


Fig.3. Al-spectrum, first order reflection, GAEL facility.

potassium ions gives T_e values with a scatter (from one experiment to another) within 0.8-1.2keV. The calculation was performed taking into account of intensities of the resonance and intercombination lines of He-like chlorine ions. This ratio depends primary on the electron density, which allows the n_e (electron density) value to be estimated. It was found that $n_e \approx 10^{21} \text{ cm}^{-3}$, which implies that the electron density perfectly agrees with initial density of a homogenized foam, assuming an ionization state corresponding to $T_e \approx 1 \text{ keV}$. In the GAEL installation, the load is produced by a plasma generated by the electric explosion of an aluminum foil and formed by a ring-shaped nozzle. An aluminum wire with diameter of 10-50 μm was placed at the plasma jet axis.

The linear density of the plasma was approximately equal to that of the wire. The example X-rayspectrum (the first reflection order) is shown in fig.3. In the second reflection order of crystal two MCP detectors were placed. The time duration (FWHM) of X-ray radiation (fig.4) from Al Z-pinch is approximately 20ns. The processing of experimental data gives the following plasma parameters: $T_e \approx 350\text{-}400 \text{ eV}$, $n_e \approx (24) \times 10^{21} \text{ cm}^{-3}$.

It is necessary to note that such parameters have approximately 6-10% only.

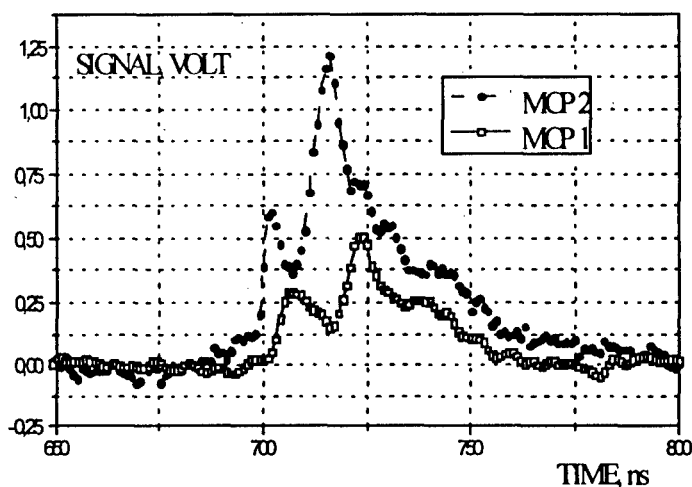


Fig.4. Signals from MCP detectors, second order reflection, GAEL facility

CONCLUSION

It is shown that time-resolved MCP detectors can be successful use in the X-ray crystal spectrograph together with space-resolved LCCD detector. The inclusion of the time-resolved detectors into spectrograph scheme extends possibility of device and allows to determine the dynamic of plasma parameters. The measuring setup performs the digital experimental data and includes computer technique that decreases of data process.

REFERENCES

- [1] A.B.Filik, J.E.Bailey, R.G.Adams et al., Proc. BEAMS'96, Prague, v.I, pp.48-51, 1996
- [2] O.Renner, E.Krouky, A.Krejci et al., Proc. BEAMS'96, Prague, v.II, pp.733-736, 1996
- [3] A.Ya.Faenov, Yu.A.Agafonov, S.A.Pikuz et al., Physica Scripta, 50, 333, 1994
- [4] Michenski V.O., Volkov G.S., Zaitsev V.I. Zazhivikhin V.V., Proc. BEAMS'96, Prague, v.II, pp.1080-1083, 1996
- [5] S.Attelan-Langlet, B.Etlicher, V.O. Michenski, et al., Proc. BEAMS'96, Prague, v.II, pp.1064-1067, 1996
- [6] Henke B.L., Yaanimagi P.A., Rev. Sci.Instr., N8, p.119, 1985



BEAMS'98

12th INTERNATIONAL CONFERENCE
ON HIGH-POWER PARTICLE BEAMS



ORALS

***Radiation
Sources, HPM***

Vol. I

Proceedings

GENERATION OF POWERFUL ULTRASHORT MICROWAVE PULSES BASED ON SUPERRADIANCE OF SUBNANOSECOND HIGH-CURRENT ELECTRON BUNCHES

N.S.Ginzburg, I.V.Zotova, Yu.V.Novozhilova, A.S.Sergeev
Institute of Applied Physics, RAS, 603600, Nizhny Novgorod, Russia

A.D.R.Phelps, A.W.Cross, S.M.Wiggins
University of Strathclyde, Glasgow, G4 0NG, UK

V.G.Shpak, M.I.Yalandin, S.A.Shunailov, M.R.Ulmaskulov
Institute of Electrophysics, RAS, 620049 Ekaterinburg, Russia

The first experimental results of the observation of superradiance from a single subnanosecond high current electron bunch are presented. Superradiance was associated with different varieties of stimulated emission (Cherenkov, bremsstrahlung, cyclotron, etc). The Ka band microwave pulses with unique short duration 300ps and peak power up to 60 MW have been obtained. The repetition rate mode up to 25 pps realized.

INTRODUCTION.

In recent years much attention has been given to theoretical considerations of superradiance (SR) from space-localized nonequilibrium ensembles of electrons [1-5]. This phenomena includes features of present in both stimulated (selfbunching and coherence) as well as spontaneous processes (absence of threshold). It is reasonable to consider SR in a specific situation when the electron pulse duration substantially exceeds the operating wavelength (otherwise effective traditional spontaneous emission) while at the same time is less or comparable with the interaction length (in contrast with traditional mechanisms of stimulated emission of quasi-continuous electron beams which are used extensively in microwave electronics - FEL, TWT, BWO, CRM, etc). Coherent emission from the entire electron pulse can only occur when a selfbunching mechanism typical for stimulated emission develops. Another natural condition of coherent emission is the mutual influence of different fractions of the electron beam pulse. In the absence of external feedback such influences can be caused by slippage of the wave with respect to the electrons due to a difference between the electron drift velocity and electromagnetic wave group velocity.

SUPERRADIANCE AND MECHANISMS OF STIMULATED EMISSIONS.

Superradiance can be related with different mechanisms of stimulated emission: bremsstrahlung, cyclotron, Cherenkov, etc. In [6] results of observation of bremsstrahlung SR from serious of picosecond electron bunch in the low gain regime have been reported. In this experiment a superradiance-like regime was obtained in the FELIX FEL operating in the infrared. In this paper we present results of the experimental observation of different types of SR from

isolated electron bunch in the high gain regime in K_a frequency band. The SR pulses have been observed from a bunch of electrons moving along helical as well as rectilinear trajectories. The first type of trajectory was realized when electrons started to rotate in a uniform magnetic field after passing through a kicker (cyclotron emission) or oscillated in a combined undulator and guiding magnetic field (undulator emission). The corresponding resonance condition can be presented in the form

$$\omega - kV_{\parallel} = \Omega \quad (1)$$

where Ω is gyrofrequency ω_H for cyclotron SR and $\Omega = 2\pi V_{\parallel}/\lambda_u$ is the bounce frequency for undulator SR, and λ_u is undulator period.

In the case of a bunch of electrons moving along rectilinear trajectories in a guiding magnetic field Cherenkov type SR has been studied for two types of slow-wave structures. The first was a periodically corrugated metallic waveguide where a bunch radiates under synchronism with the slow spatial harmonic of the backward wave

$$\omega = (-k + k_c)V_{\parallel} \quad (2)$$

where $k_c = 2\pi/\lambda_c$, λ_c is the corrugation period. The second used a dielectric loaded waveguide where forward wave radiation occurred under synchronism

$$\omega = kV_{\parallel} \quad (3)$$

EXPERIMENTS ON OBSERVATION OF SR IN SINGLE SHORT REGIME.

A RADAN 303 accelerator equipped with a subnanosecond pulse sharpener (slicer) was used to inject typically 0.3-0.8 ns, 0.2-2 kA, 250 keV single electron pulses [7]. These electron pulses were generated from a magnetically insulated coaxial diode, which utilized a cold explosive emission cathode. The fast rising electron beam current and accelerating voltage pulses were measured using a Faraday cage strip line current probe and an in line capacitive voltage probe respectively, with both signals recorded using a 7 GHz Tektronix 7250 digitizing oscilloscope. In the first experiments high current electron pulses were transported through the interaction space over a total length of up to 30 cm in a longitudinal guiding magnetic field of pulse solenoid. The magnetic field varied between 1-2 T. For measurement of the radiation a hot carrier germanium detector which had a transient characteristic of 200 ps was used

We started our experiments with cyclotron SR [8]. According to theoretical considerations for observation of cyclotron SR the most favorite regime it is regime of group synchronism when electron bunch velocity coincide with e/m wave group velocity (Fig.1). The advantages of such regime became obvious in the reference system moving with electrons. In this system electrons rotating in uniform magnetic field will radiate at quasi cut-off frequency, like in gyrotrons. As a results sensitivity to the spread of electrons parameters will much less then in other regimes. The process of cyclotrons SR includes azimuthal selfbunching and consequent coherent emission. As a result SR pulse duration defines by times of electrons bunching

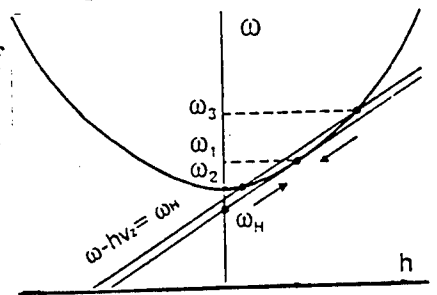


Fig.1 Dispersion curves for cyclotron superradiance experiment

and debunching. It is important to note that bunch radiates isotropically in $\pm z$ direction in comoving reference frame. At the time in lab frame both components should propagate in positive direction. On dispersion diagram one component associated with high frequency intersection while another one with low frequency intersection. As a result signal on the detector should consist of two pulses (Fig.2a). Carrier frequency of first pulse should exceed frequency of

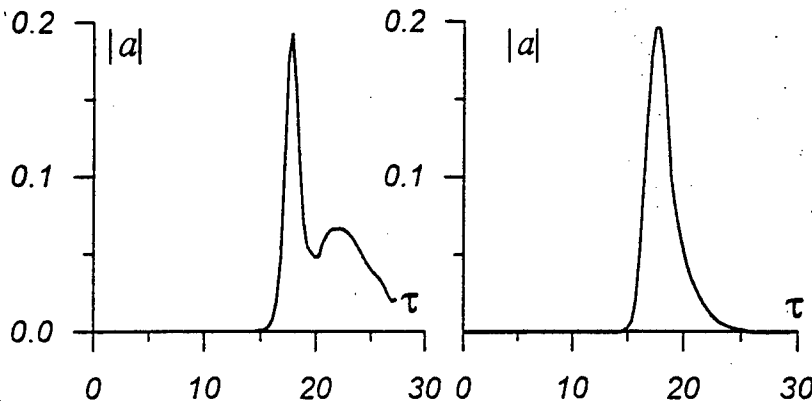


Fig.2 Simulation of transformation of cyclotron SR pulse waveform with decreasing of guide magnetic field

second pulse. At the same time when magnetic field decreases both frequencies tends to one grazing frequency and double pulse should be converted into monopulse (Fig.2b). This conclusion was confirmed experimentally. SR pulses were observed in a rather narrow range of detuning of the uniform magnetic fields corresponding to grazing conditions with TE_{21} and TE_{01} modes. For excitation of TE_{21} mode transformation of waveform with changing of axial magnetic field is presented in Fig.3. According to theoretical prediction with increasing of magnetic field monopulse converts into double pulse. The peak power of cyclotron SR was several hundreds kilowatt, minimal pulse duration about 400 ps. Relative spectrum width was about 20%. For spectral measurements we used a system of cutoff waveguides.

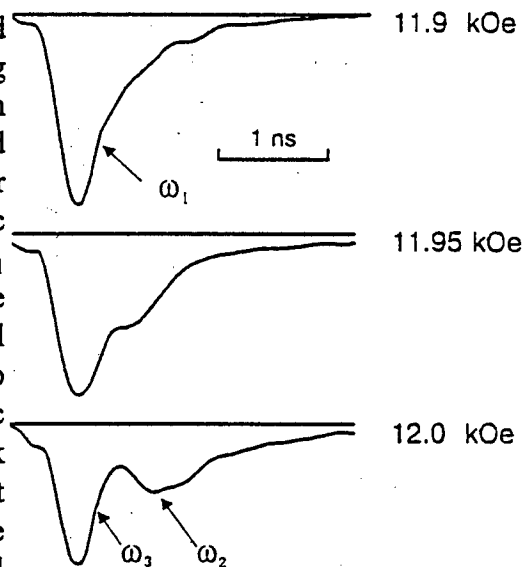


Fig.3 Transformation of cyclotron SR pulse waveform with changing of axial magnetic field for constant electron pitch angle

Approximately the same level of peak power has been obtained in experiments on observation of SR from electron bunch moving in wiggler field. Actually in this experiment electrons moved in a combined longitudinal uniform and

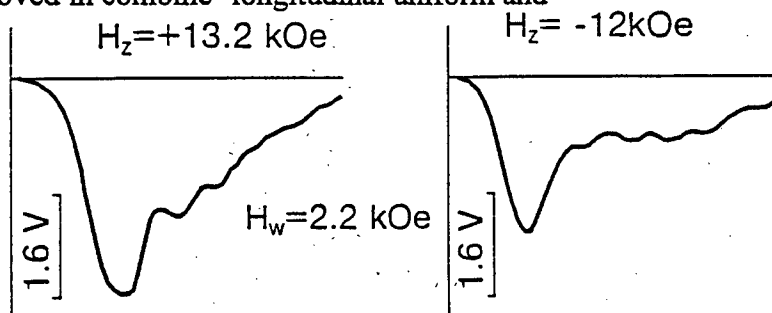


Fig.4 FEL superradiance pulses obtained for the direct and reverse guiding magnetic field

transverse periodical magnetic field. Generation of SR pulses was observed for both (direct and reversed) orientations of guide magnetic field. Fig.4 [9].

Results of the first experimental observation of Cherenkov SR of electron bunch moving in dielectric loaded waveguide is presented in Fig.5 [9]. Note that for electron bunches with a size of several wavelengths it was traditionally assumed that radiation could be related only with density fluctuations inside the electron bunch (incoherent component) or with coherent emission from the sharp edges of the bunch. Only recently it was recognized that much more intense coherent emission can occur from the entire volume of such bunches due to selfbunching arising from the mutual influence of different fractions of the electron bunch, i.e. with superradiative mechanism of emission. The exponential like dependence of peak power on interaction distance (Fig.6) demonstrates that the generation of such pulses was really related is self-bunching and therefor can be considered as SR. For the total interaction length of 30 cm peak power of Cherenkov SR amounted several megawatt but radiation was presented the superposition of TM_{01} and hybrid HE_{11} modes of dielectric loaded waveguide with rather broad spectrum.

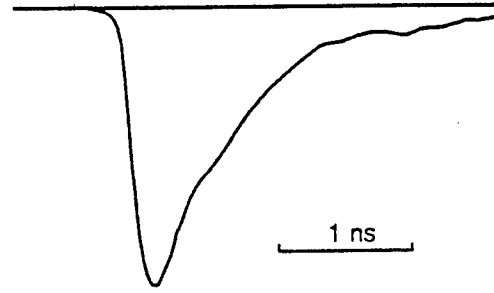


Fig.5 Cherenkov SR pulse

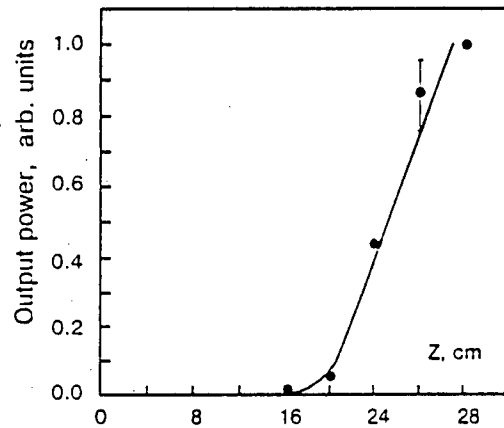


Fig.6 Cherenkov SR power as a function of interaction length

Excitation of pure TM_{01} mode was observed in the case of emission in the periodical corrugated waveguide under resonance condition (2), when electrons interact with backward propagation wave (BWO mechanism) [9]. The radiation in this case was characterized by high level of stability and reproducibility. Fig.7 demonstrates the oscilloscope traces from 10 SR pulses. These results were obtained for the slow

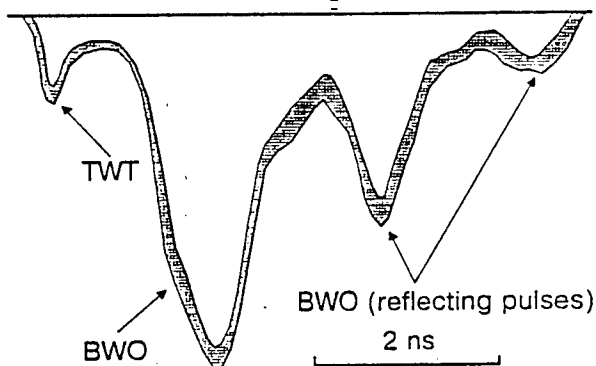


Fig.7 Reproducibility of BWO SR pulses

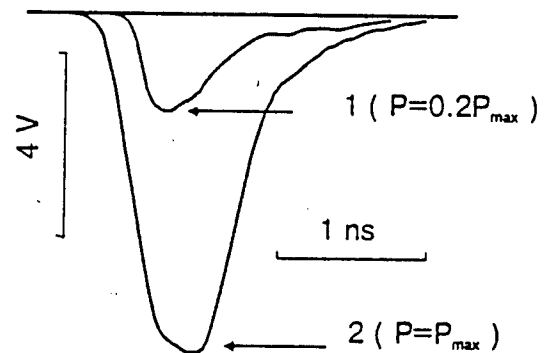


Fig.8 SR pulse in dielectric loaded waveguide (1) and in hybrid system (2)

wave system of the length about 10 cm and guide magnetic field about 1.7 T. The first small peak corresponded to the high frequency radiation propagating in the same direction as the electron beam (TWT mechanism), while the second larger peak corresponded to the designed counter-propagating emission mechanism. Subsequent bursts are related with reflection of radiation from the edges of the slow-wave system. Using this reflection it is possible to estimate the wave group velocity as $0.3 c$ that corresponds to theoretical calculations. Peak power achieved in the first BWO experiment was smaller then in the case of Cherenkov emission.

To combine high stability of BWO system with high peak power achieved in Cherenkov system we constructed hybrid system in which short BWO section was used as modulator of electron bunch which subsequently radiate in dielectric loaded waveguide [10]. As follows from Fig. 8 BWO section increase in several times peak power. Maximal power in this experiment amount 2-3 MW. The modulator also improved pulse stability and direction diagrams.

EXPERIMENTS ON OBSERVATION OF BWO SR IN REPETITION RATE MODE

In the first experiments rather low guide magnetic fields up to 2T were used. For the BWO system this value of magnetic field was less than the cyclotron resonance value. At the same time it is known from previous studies of long (5-30 nanoseconds) pulse relativistic BWO [11-13] that as the magnetic field is varied BWOs have two operating ranges separated by the cyclotron absorption region. Cyclotron absorption arises when cyclotron resonance conditions are fulfilled for the fundamental harmonic the wave propagating in the periodic structure. Based on this experience it was reasonable to assume that for the short pulse injection regime for high guide magnetic fields the peak power of SR spikes should be several times higher as compare with those attained in the previous experiments. The increased power should be related first of all with the improved quality of the electron bunch injected by the explosive-emission cathode. Note also that the containment of the electron bunch in the strong magnetic field gives the possibility of decreasing the gap between the electrons and the slow-wave structure and as a consequence there results a substantial increase of the electrons/e.m. wave coupling and the related gain. A superconducting magnet was used in a new series of experiments to generate a longitudinal magnetic field with strengths of up to 10 T. Using a permanent solenoid instead of the pulsed one used in the previous experiments permits us to operate in the burst-repetitive mode.

Detail descriptions of this experiment are presented in [14]. The maximal peak power measured by detector achieved 60 MW. Note that increasing power was achieved also by optimization of bunch parameters: injected current was increased up to 1.8 kA and electron pulse duration up to 0.8nc. A rather high level of radiation power was indicated also by the illumination of a neon bulb panel when the radiation signal irradiated the panel at a distance of 30 cm from the output horn Fig.9. The radiation pattern accurately corresponded to the excitation of the designed TM_{01} mode. One more important evidence of the high peak power was

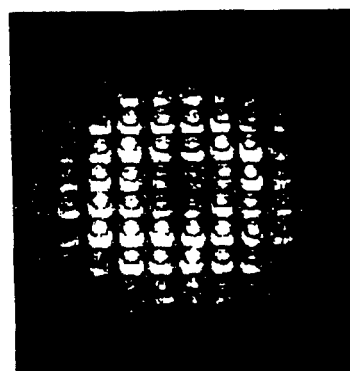


Fig.9 Luminescence of the matrix gas-discharge panel irradiated by the BWO SR pulse

obtained from the observation of RF breakdown of ambient air for subnanosecond pulses in the focus of parabolic reflector as well as inside receiving concentrating conical horn. Comparison with the results of previous observations of breakdown from long nanosecond microwave pulses [15] demonstrates that the absolute power really correspond 60 MW. The realized repetition rate 25 pps mode of operation give reason to consider that in fact novel source of powerful subnanosecond Ka band pulses has been realized.

CONCLUSION.

Summarizing the experimental results presented we believe that the radiation observed was related with a novel mechanism of stimulated coherent emission of short electron bunches, namely superradiance. We should emphasize here that coherent emission occurs from an isolated subnanosecond electron bunch. Of course, the results discussed here give only a rather general physical picture of superradiance, which needs further investigation, which would specifically concentrate on more accurate measurements and comparison with theoretical simulations. However even at the this stage it must be emphasized that the radiation especially in the case of BWO-like regimes was characterized by a high level of stability and reproducibility from pulse to pulse. The efficiency of energy transformation amounted to 6% for the backward wave mechanism. The unique characteristic of microwave pulses such as duration (0.3 ns) in combination with 60 MW power levels and repetition rate mode 25 pps is encouraging for future applications in areas such as novel diagnostics and the studying of nonlinear phenomena in plasmas and solids. Another advantage of the RADAN subnanosecond accelerator and consequently any associated experiments is that the whole system is in the form of a table-top system.

This work was supported by the Russian Fund of Fundamental Research, grant 98-02-17308 and by the United Kingdom DRA and EPSRC.

- [1] R. H. Bonifacio, B. W. J. McNeil and P. Pierini, Phys. Rev. A 40, 4467 (1989).
- [2] V.V.Zhelyeznyakov, V.V.Kocharovskiy and V.V.Kocharovskiy, Usp.Fiz.Nauk, 159, 194 (1989)
- [3] N.S.Ginzburg, Sov. Tech. Phys. Lett. 14, 197 (1988)
- [4] G.R.M.Robb, N.S.Ginzburg, A.D.R.Phelps, and A.S.Sergeev, Phys.Rev.Lett., 77, 1492 (1996)
- [5] N.Piovella, P.Chaix, G.Svets and D.Jaroszynski, Phys. Rev. E53, 5470 (1995)
- [6] D.A.Jaroszynski, P.Chaix, N.Piovella et al., Phys. Rev. Lett., 78, 1699 (1997)
- [7] M.I.Yalandin, V.G.Shpak, S.A.Shunailov, M.R.Ulmaskulov Proc. XVIIth International Symposium on Discharges and Electrical Insulation in Vacuum.- Berkeley, CA, USA.- 1996.- Vol.2.- P.635-639.
- [8] N.S.Ginzburg et al, Phys. Rev. Lett, 78, 2365 (1997)
- [9] N.S.Ginzburg, I.V.Zotova, I.V.Konoplev, A.S.Sergeev, V.G.Shpak, M.I.Yalandin S.A.Shunailov, M.R.Ulmaskulov, Nucl. Instr. and Meth. in Phys. Res. A 375 553 (1996)
- [10] M.I.Yalandin et al, Pis'ma v ZhTF, 23, 14 (1997)
- [11] E.A.Abubakirov, N.S.Ginzburg, N. F.Kovalev and M.I.Fuchs, Radiotekhnika i Elektronika 34, 1058, 1989
- [12] C.D.Korovin et al. Pis'ma v ZhTF, 11, 1972 (1985).
- [13] M.I.Yalandin, G.T.Smirnov, V.G.Shpak, S.A.Shunailov, Proc. 9th IEEE International Pulsed Power Conference.- Albuquerque, NM, USA, 1993.- P.388-391.
- [14] N.S.Ginzburg, N.Yu.Novozhilova, I.V.Zotova et al, Proc. of this Conf.
- [15] M.I.Yalandin, G.T.Smirnov, V.G.Shpak, S.A.Shunailov, Proc. 9th IEEE International Pulsed Power

ELECTRON BEAM PRODUCTION FOR MICROWAVE GENERATION USING A FERROELECTRIC CATHODE

J. D. Ivers, D. Flechtner, J.A. Nation, G. Liu*, and L. Schachter**

Laboratory of Plasma Studies and School of Electrical Engineering,
Cornell University, Ithaca, NY 14853, USA.

ABSTRACT

Data is presented on the production of electron beams from a ferroelectric cathode at voltages of order 0.5 MV and current densities of order 100 A/cm². In comparison with data at lower voltages the beam current scales as the three halves power of the voltage. An interpretation of this scaling, based on the coupling of electrostatic energy from the ferroelectric to the gun is presented.

INTRODUCTION

Ferroelectric Cathodes have been extensively studied over the last several years^{1,2,3} in an attempt to develop a means of emitting a high current density electron beam from a robust room temperature cathode, which is insensitive to its environment and, is not susceptible to poisoning if ultra high vacuum is not maintained. Most of the research has focussed on two types of cathode, namely:

- a. PLZT compositions e.g. 4/95/5 in which emission occurs when an applied electric field causes the material to switch from the anti-ferroelectric state to the ferroelectric state. Switching occurs when an applied electric field of order 10-20 kV/cm is applied across the anti-ferroelectric. Recent work has suggested that higher fields, of order 65 kV/cm are required to initiate the electron emission and,
- b. Ferroelectric compositions of PZT and PLZtin which the electron emission is triggered by the 'switching' of the ferroelectric around a minor hysteresis loop. Fields of order 10 kV/cm, typically applied across a 1 mm thick sample, result in the electron emission.

In this paper we summarize data obtained with a PZT cathode in an electron gun configuration to generate an electron beam at energies in the range 200-550 keV, with a beam current of up to 350 Amperes in pulses having a duration in excess of 200 ns. The application of the source is to high power microwave generation using a TWT amplifier in X and Ka bands. These results extend emission characteristics previously reported by more than one order of magnitude in voltage and by a factor of 3 in the current density. The data also presents the first reported results applicable to electron gun design.

In the following sections we describe the experimental arrangement used for this work, the results obtained, and their interpretation.

* Permanent Address: Northwest Institute of Nuclear Technology, China.

** Permanent Address: Electrical Engineering Department, Technion, Haifa, Israel.

Experimental Configuration.

The electron gun used in this work employs a pulse transformer system capable of generating a 500 kV, 200A, 250 ns electron beam and uses a ferroelectric cathode as the electron source. It is designed for use in high power microwave generation experiments. The system operates at a repetition rate of about 0.1 Hz which is limited by the available power supplies. Vacuum levels are presently in the vicinity of $5 \cdot 10^{-6}$ Torr, but will be modified shortly for high vacuum use. The modulator has been described previously at the Particle Accelerator Conference⁴ and will not be described here. The output of the transformer is connected to a diode/electron gun located in the fringing field of a 5 cm diameter solenoid. The peak axial magnetic field used in this work is about 3 kG.

The ferroelectric emitter is located in the cathode surface and has a diameter of 1.9 cm. The emitter is a 1 mm thick PZT sample, commercially available LTZ2 from Transducer products. It is pre-poled, and mounted with the Polarization vector pointing into the vacuum region. The beam was confined, but not focussed by the applied magnetic field.

The ferroelectric emitter is prepoled and has a surface polarization charge density of about $6 \mu\text{C}/\text{cm}^2$. Normally emission is produced by the application of a negative voltage pulse to the rear surface of the ferroelectric (the front surface grid, which has a number of 200 μ width silver strips spaced from each other by 200 μ , and is grounded). In this case, however, a positive trigger pulse is applied to the rear surface of the ferroelectric. This results in electron emission from the metallic grids which drives Fowler Nordheim field emission in the vicinity of the metallic grid, ferroelectric, vacuum, triple point. The duration of the field emission is determined by the applied pulse duration ($\sim 100\text{ns}$) and by the hysteresis properties of the ferroelectric so that the total emission may exceed $1\mu\text{s}$.

Experimental Observations

The pulser is typically run at 0.1 Hz for about 100 shots prior to taking data. During the initial break-in of the cathode there is spiking in the emission with $\sim 10\text{-}20\text{ns}$ current bursts, probably associated with out-gassing of the ferroelectric. Following use, the incidence of spiking seems to decrease and the emission pulses are similar to the data presented in figure 1. The data shows the voltage across the transformer secondary $\sim 300\text{kV}$, the ferroelectric trigger pulse $\sim 1\text{kV}$, the beam current $\sim 80\text{A}$, collected by a graphite Faraday cup located well into the magnetic field coil region, and finally the current through the transformer primary. A second set of diode voltage current characteristics are shown at the rated voltage 500 kV, and current of 200A and were obtained with a cathode to drift tube spacing of 6.6 cm. A copper sulfate resistor was mounted in parallel with the anode-cathode gap to improve the impedance match between the beam output and the primary. The impedance of the parallel resistor was varied with the operating conditions and was typically in the range 500-1000 Ω . The best beam performance was obtained with the ferroelectric trigger pulse occurring at the start of the voltage maximum on the secondary. The trigger pulse shown in fig 1 should be delayed by approximately 110 ns to show the correct timing. While the output voltage rises in about 200 ns the current rise time, which is instrument limited is more like 20 ns. With varying cathode-anode spacing the surface electric field at the cathode varied up to 100

kV/cm, however electron emission from the ferroelectric did not occur until after the ferroelectric trigger pulse was applied.

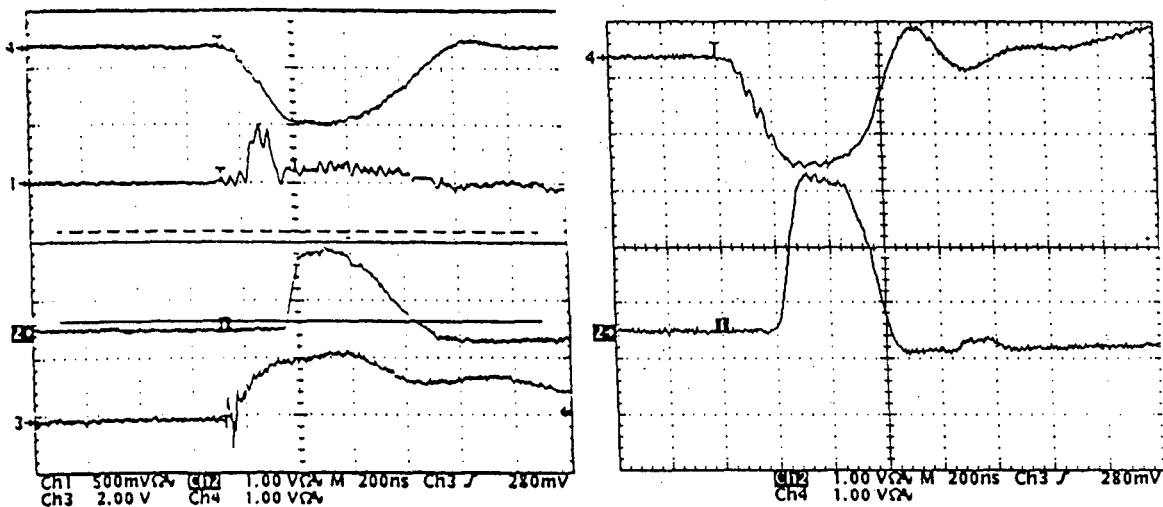


Fig. 1. Data showing a 300kV (top trace), 80A (3rd trace) and 500kV, 200A beam emission pulses respectively from a ferroelectric illustrating the switching of the beam current by the ferroelectric trigger pulse (2nd trace). The current rise time is less than that for the secondary voltage.

In figure 2 we show plots of the gun current versus the three halves power of the gun voltage for gap spacings of 6.6 and 4.6 cm respectively. The dashed line on each curve represents the results found from the EGUN code for space charge limited emission with the actual geometry and magnetic field arrangement used in the experiments. These data are based on representative results obtained over several thousand events with most of the data obtained with a 6.6 cm anode cathode spacing. The exposed cathode area of the ferroelectric disk was 2.8 cm². The data indicates that emission current densities of up to 125 A/cm² were obtained while still yielding reasonably shaped beam current pulses.

Discussion of Results

The emission data reported in this article considerably expands the range of the emission characteristics for PZT and provides the data needed for an electron gun design. Unlike our earlier data at voltages of < 50 kV the emission appeared to scale with the three halves power of the gun voltage and to be within a factor of about 2 of that expected in space charge limited flow as predicted by the EGUN code. The large spacing between the cathode and the collector surfaces make it very unlikely that plasma closure plays any significant role in the emission process but does not preclude explosive field emission on the cathode surface. The electrostatic field, due to the trigger pulse applied to the ferroelectric, at the vacuum/grid/dielectric boundary is in the sense to extract electrons from the metallic grid and will cause emission from the grid.

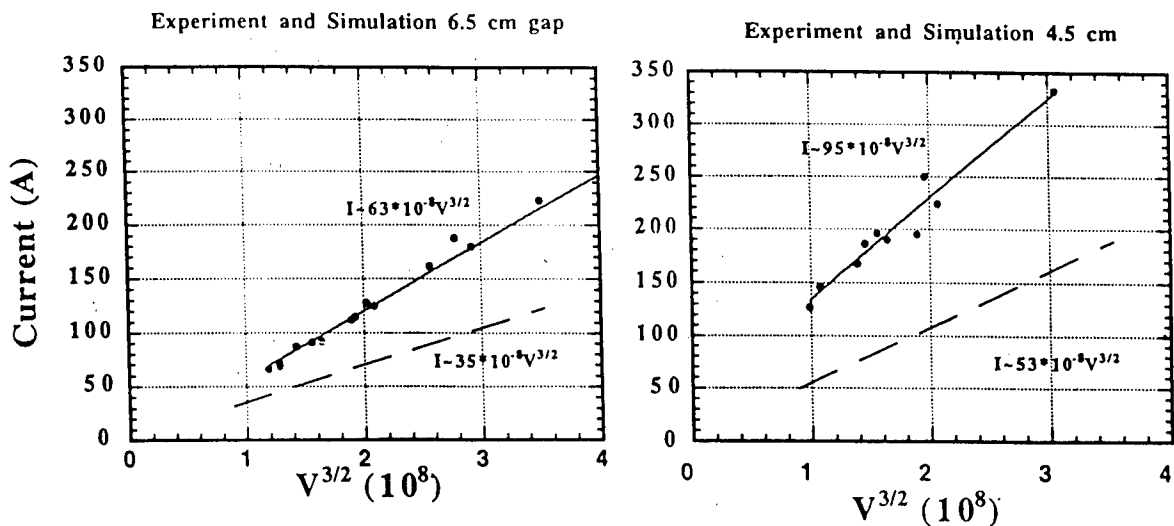


Fig 2. V-I Characteristics of the electron gun for a cathode to drift tube (anode) spacing of 6.6 cm. (left) and for a spacing of 4.5 cm. (right).

Schachter⁵ has calculated the emission from a wedge on the surface of a high dielectric constant slab. He showed that the emission is several orders of magnitude greater than that found from the same wedge in the absence of the dielectric. The calculation depends solely on Fowler Nordheim emission. More recent work has examined the emission from an array of ferroelectric/metallic strips in a geometry similar to that in the experiment described above. This work shows that the emission level results from the coupling of energy stored in the ferroelectric material into the diode gap. The energy coupled to the gap exceeds that stored in the gap (due to the anode potential) at low (<50 kV) gun voltages by a factor of order 1000. As high gun voltages ~500 kV the factor drops to order unity and the emission reverts to that predicted by the Child Langmuir law.

References

1. C. B. Fleddermann and J.A. Nation, "Ferroelectric Sources and their application to Pulse Power: A review," IEEE Transactions on Plasma Science 25, 2, 212-220, (1997).
2. H. Riege, "Electron emission from ferroelectrics: A review" Nucl. Insts. and Methods Phys. Res. A. 340, 80-89, (1994)
3. S.E. Sampayan, G. J. Caporaso, C. L. Holmes, D. Prosnitz, D.O. Trimble and G. A. Westenscōw, "Emission from ferroelectric cathodes", Nucl. Inst. and Methods Phys. Res. A. 340, 90-95, (1994)
4. J.D. Ivers, D. Fletcher, Cz. Golkowski, J.A. Nation, and L. Schachter. Proc. of the Particle Accelerator. Conf, Vancouver, May 1997. To be published.
5. L. Schachter, "Analytic expression for triple-point emission from an ideal edge" Appl. Phys. Letts. 72, 4, 421-23, (1998)
6. L. Schachter, D. Fletcher, J.D. Ivers and J. A. Nation. Submitted for publication to J. Appl. Physics.

RESEARCH OF MICROWAVE GENERATION EFFICIENCY FOR TRIODE WITH VIRTUAL CATHODE (VIRCATOR TRIODE)

A.N.Didenko, A.G.Zherlitsyn*, G.V.Melnikov*

Corresponding Member of RAS, Leninsky Ave. 32a, Moscow 117334, Russia;

** Nuclear Physics Institute, Tomsk Polytechnic University,
Lenin Street 2a, Tomsk 634050, Russia*

INTRODUCTION

In research of microwave generation of different vircator types, the most actual questions is increase of the beam energy transformation to microwave radiation energy. The recent experiments show that, as a rule, vircator efficiency is some percents. The experiments with vircator triode carried out in S-band show that it is possible to generate gigawatt level power with efficiency up to 12% [1], whereas for low level power the efficiency can reach up to 30% [2]. This report presents results of the microwave radiation generation of the vircator triode.

OPTIMIZATION OF THE VIRCATOR TRIODE PARAMETERS

Unlike other types of vircators, the processes of the beam formation and the beam energy transformation to the microwave energy takes place in the same volume in the triode with virtual cathode (fig.1). This volume serves as the vircator electrodynamic structure (resonator). It influences to the generation process and efficiency, because the feedback between the resonator beam and the microwave field, excited in the triode, is the most effective in this case. In the work [3] a vircator, named "virtod", is described, where a special additional feedback was organized for increasing the generation efficiency up to 17%. The

vircator triode does not need such additional feedback. Moreover, this system forms optimal feedback self-consistent with the microwave radiation excitation by the beam automatically. The influence of the feedback in the vircator triode to the generation efficiency is experimentally studied. A cylindrical vacuum chamber with 60 cm diameter, 60 cm length and absorbing inside coating (reflection coefficient in the S-band less than 3%) was used as a triode resonator. Microwave radiation was extracted through a window with 60 cm diameter. The experiments were carried at the electron energy of 0.5MeV, current up to 10.4 kA and pulse duration of 160 ns. The feedback in the chamber was varied by means of special screens, made of metal foil ribbons and placed on the absorbing surface (fig.2).

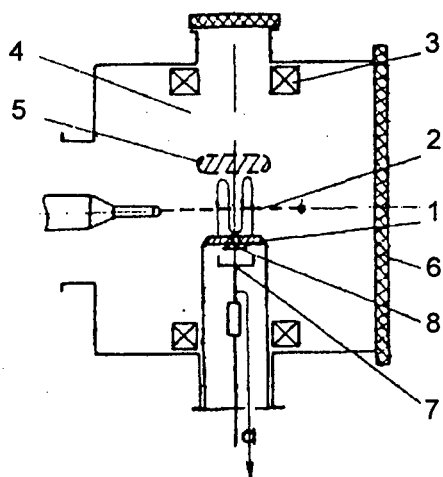


Fig. 1. Vircator triode. 1 - cathode, 2 - anode, 3 - inductance coil, 4 - vacuum chamber, 5 - virtual cathode region, 6 - microwave output window, 7 - Faraday cup, 8 - aluminum foil.

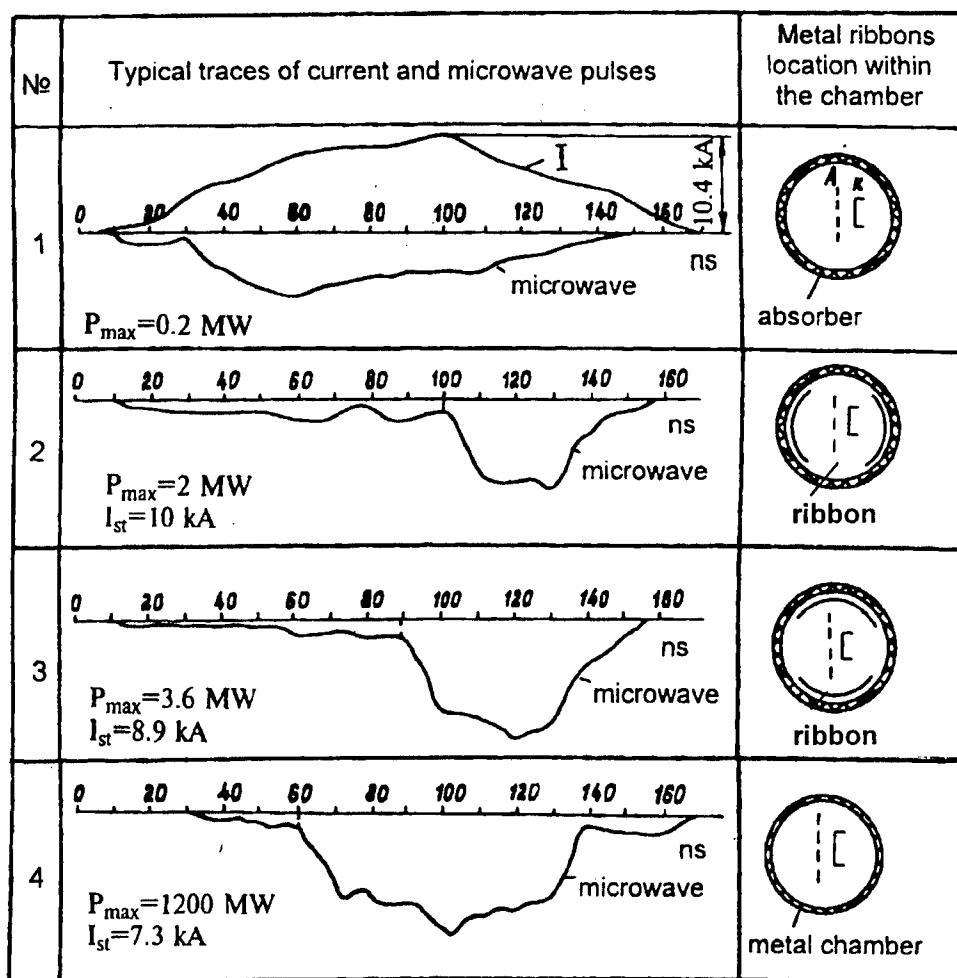


Fig.2. Influence of vacuum chamber to the radiation generation process.

Without feedback, when all radiation is absorbed (fig.2 (1)), radiation starts with current of oscillated electrons; it is changing according to the current changing. Observed radiation can be considered as radiation of oscillated electrons in space. Location of ribbons according to fig.2 (2-4) leads to changing of generation process. Possibility of repeated interaction of microwave radiation with oscillated beam leads to considerable growth of radiation power for some values of current (start current I_{st}). Maximal radiation power was observed for metal chamber (fig.2 (4)) with the same geometrical shape and sizes, as for chamber with absorbing material. In this chamber, radiation intensity reached 1.2 GW, start current reduced to $I_{st}=7.3 \text{ kA}$. Thus, the research show that using of metal chamber serving as a vacuum volume where the beam is formed, and a resonant system provides automatically conditions of optimal feedback and high efficient generation.

The theoretical investigations on the generation efficiency in the vircator triode are executed assuming that the factor determining the electron beam grouping is non-isochromatic oscillations of electrons in self-consistent potential well. Considering the influence of external oscillated circuit and finite lifetime for electrons in interaction region, it is shown that the vircator triode can generate stationary with electron efficiency of $\sim 10\%$. Experimental efficiency more than 10% shows, that side by side with phase grouping, other mechanisms are working. One of such mechanisms is a phase selection of electrons on the triode electrodes.

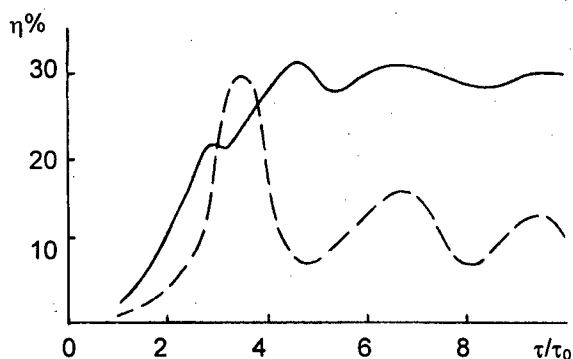


Fig.3. Dependence of microwave triode electron efficiency on time τ/τ_0 . Solid curve - with consideration of phase selection, dashed line - without consideration, t_0 - time of electron transit from cathode to vircator triode.

In the fig.3, the results of electron efficiency calculations are presented for anode transparency $T = 0.8$. For comparison, the dashed curve is plotted that was obtained at the same parameters without taking the phase selection process into account. The carried out experiments confirm that a phase selection mechanism takes place in the vircator triode. The experiment were carried out according to the scheme presented in the fig.1. To find "wrong-phase" electrons at microwave oscillation generation in triode system, a hole was drilled in the center of cathode 1, and Faraday cup was placed behind it.

The hole was covered by aluminum foil 8 with 10 μm thickness to avoid the process of hitting of triode ions, accelerated by cathode-anode gap, to the cylinder. In presence of phase selection, "wrong-phase" electrons, having additional energy of high frequency field and moving against cathode potential, are hitting to the Faraday cup through the hole in the cathode. High frequency (HF) modulation of flow of "wrong-phase" electrons was registered; the frequency of this modulation was measured. It was found, that modulation takes place on frequency, generated in triode of microwave oscillations. Energy of these electrons was evaluated by foils with different thickness as much as 100 keV. It corresponds to the calculated value of "wrong-phase" electrons. Thus, the experiments show, that phase selection mechanism takes place in the vircator triode. Both mechanisms of grouping are existing simultaneously, i.e. both phase grouping and phase selection do not stop influence to electron flow at the generation process.

The same region for formation of electron flow and transformation of the beam energy to radiation energy allows providing optimal conditions for feedback in the triode and effective electron grouping; it leads to microwave radiation generation with high efficiency. However, it is necessary to determine the most optimal parameters (or requirements to these parameters) for elements of the vircator triode. The vircator triode includes such parameters as a pulsed voltage source, a vacuum chamber, serving as the triode resonance system, an explosion emission (cold) cathode and a grid anode.

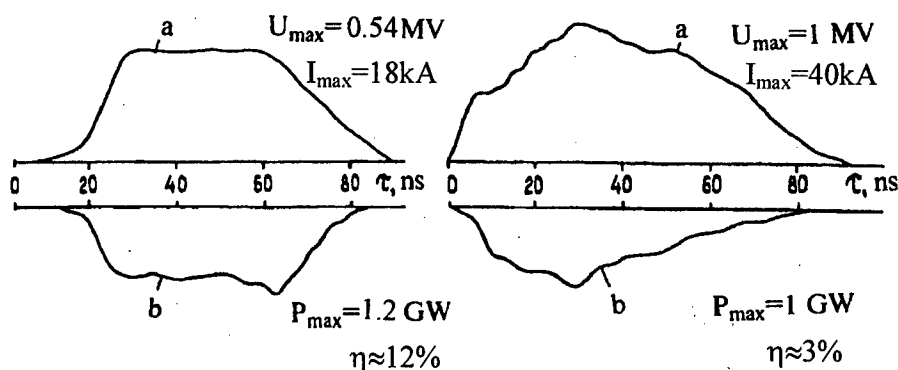


Fig. 4. Traces of voltage (a) and microwave radiation (b) pulses for the same system supplied from accelerators "VERA" (left) and "TONUS" (right).

Generation efficiency and stability depend on shape of voltage pulse, applied to cathode-anode gap, and triode current. For example, influence of voltage pulse shape to the generation process is seen from comparison of pulse oscilloscope traces, presented in fig.4. For both cases, vircator triode parameters were the same. Analysis of vircator triode experiments shows, that certain requirements for formation of voltage and current pulses in triode should be met for effective and stable microwave generation in S-band. These requirements are the following:

- The voltage pulse should have the extended "flat top" (like in any other microwave oscillator). It leads to more stable and effective generation.
- Current should reached starting value when voltage arises or is at "flat top" but does not fall. This provides "stationary" generation regime.
- Voltage pulse duration should exceed a number of tenth nanoseconds.

Like for other microwave devices, the radiation power level, efficiency and stability of operation for the vircator triode depends on conditions of electron beam formation. Usually, the electron flows are formed by external magnetic fields. Research on influence of external magnetic field to the generation process shows that magnetic field does not strongly influent to the radiation parameters for the nanosecond pulse regime. For the microsecond regime, the magnetic field increases the velocity of plasma transportation from the cathode to the anode. Hence, the generation efficiency is decreased. In practice, for the nanosecond regime, the vircator triode can generate without external magnetic field, whereas for the microsecond regime the magnetic field should not be applied. Experiments show that formation of homogeneous (in cross-section) electron flow is one of the most important conditions of efficient and stable operation of the generator. Thus, one of the main conditions is electron beam uniformity along its cross-section. Ability to provide stable homogeneous emission of electrons from the surface is one of the main requirements to the cathode. It is achieved by the proper design of the cathode as well as by the choice of cathode material. Studies on cathode optimization were performed, and special cathodes for a vircator triode were developed. Type of a vircator triode cathode depends on the voltage pulse duration which may be conventionally divided into two intervals: nanosecond ($\tau_p < 100$ ns) and microsecond ($\tau_p > 100$ ns). The anode of a vircator triode should provide small energetic losses and angular divergence of passing electrons, be of rather high transparency and heat conductivity. Grid anodes are simple and much more reliable than foil anodes. It is very significant to employ the grids with a certain optimum value of transparency, i.e. ratio of holes area to the total area of the grid. Actual optimum transparency values depend on anode-cathode distance, cathode type and geometry and voltage pulse parameters.

CONCLUSION

The obtained results on research of the vircator triode microwave radiation generation show that a microwave radiation source with high efficiency can be developed on the basis of the vircator triode. This source can generate nanosecond and microsecond pulses in S-band.

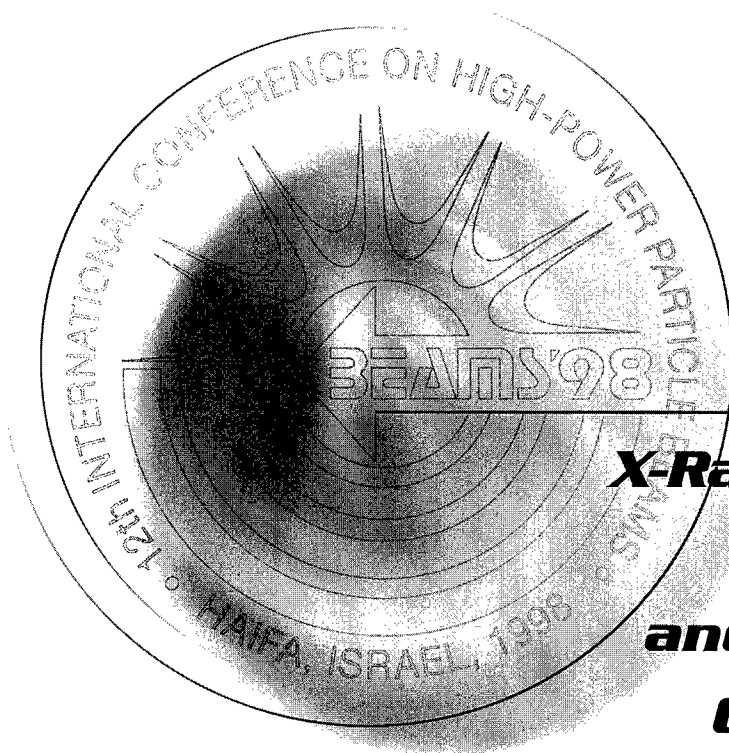
REFERENCES

- [1] A.N.Didenko, Ya.E.Krasik, S.F.Perelygin, G.P.Fomenko. Letters to JTPh, 1979, v.5, #6, p.321;
- [2] A.G.Zherlitsyn, S.I.Kuznetsov, G.V.Melnikov, G.P.Fomenko, V.I.Tsvetkov, Letters to JTPh, 1985, v.11, #17, po.1083;
- [3] N.P.Gazetsky, I.I.Magda, S.I.Neister, Yu.V.Prokopenko. V.I.Chumakov. Plasma Physics, 1993, v.19, #4, p.530.



BEAMS'98

12th INTERNATIONAL CONFERENCE
ON HIGH-POWER PARTICLE BEAMS



ORALS

***X-Ray Sources,
Z Pinches
and Explosive
Generators***

Vol. I

Proceedings

PERSPECTIVE OF KILOTERAWATT SOFT X-RAY SOURCE BASED ON THE SLOW INDUCTIVE STORE WITH ENERGY OF 1 GIGAJOUL.

Glukhikh V.A., Kuchinsky V.G., Pechersky O.P.,
Efremov Research Institute, 189631, St. Petersburg, RUSSIA

Velikhov E.P.
Russian Scientific Center "Kurchatov Institute", Moscow, RUSSIA

Azizov E.A., Grabovsky E.V., Jagnov V.A., Nedoseev S.L., Oleinik G.M., Pismenny V.D.,
Smirnov V.P., Zajtsev V.I., Zakharov S.V.,
Troitsk Institute for Innovations and Thermonuclear Investigations, TRINITI, 142092, Troitsk, Moscow region, RUSSIA

Sasorov P.V.
Institute for Theoretical and Experimental Physics, Moscow, 117259, RUSSIA

The fast liner implosion program is under development at TRINITI on "Angara-5-1" facility -8-module pulsed power facility with maximum power 9 TW, pulse rise time 90 ns, and peak load current 4 MA. The main program objective is directed on high intensity soft X-ray source creation for ICF and basic research. Double liner concept has been suggested as a promising way to provide a dynamic hohlraum for pellet irradiation.

As a more achievable way to get pulsed power generator with multy tens megaamper current a joint team of scientists from TRINITI, Efremov Institute, Arzamas-16, Chelyabinsk-70, IVTAN, Tomsk and Ekaterinburg laboratories have developed the concept of Super Angara facility, tentatively named as Baikal. The design is based on using of existing infrastructure of tokamak T-14 in TRINITI.

DOUBLE LINER SCHEME TO CONFINE RADIATION INSIDE A CAVITY FOR ICF

Since 1988, its principal research is developing power sharpening techniques for soft x-ray radiation generated by conversion of kinetic energy of an imploding cylindrical shell (liner), and to the application of intense soft x-ray pulse for target studies.

We are discussing here cylindrical shells, even though the most effective way for energy concentration could be a magnetic implosion scheme in three dimensions, a spherical shell with conical electrodes. This scheme's problems include production of light mass distributed on shaped shells and their enhanced instability during 3-D compression under azimuthal (2-D) magnetic field pressure.

The Double Liner (DL) concept (dynamic hohlraum) was proposed in [1]. It permits to convert liner kinetic energy to radiation with a pulse that is significantly shorter than the generator pulse. Theoretical and experimental studies of the Double Liner with ANGARA-5 were carried out and first results were reported in [2,3].

DOUBLE LINER COLLISION EXPERIMENT.

The Double Liner used on Angara-5 is a cascade system with two coaxial liners doped by materials with high atomic number $Z \gg 1$ [1]. After acceleration by magnetic pressure the external liner collides with the internal one. Thermal X-ray radiation generated by a high-velocity shock wave ($V = 4.5 \cdot 10^7$ cm/s) penetrates into the internal liner cavity and irradiates a hohlraum-like target. The external liner gives energy confinement and at the same time

hinders radiation escape to the outside, thereby increasing the radiation intensity in the hot cavity. The inner liner serves both to stagnate the imploding outer plasma, to convert plasma kinetic energy into radiation, and hydrodynamically to isolate the target from the imploding plasma before its ignition.

In experiments on ANGARA-5, the outer liner hollow gas puff with Mach number 6 was produced by a supersonic ring nozzle with diameter of 32 mm and ring gap of 2 mm. Xenon or neon were used as working gases. A jet specific mass was 0.1-0.2 mg/cm, its height between cathode and anode grid - 1 cm. The internal liner with 4 mm diameter, was prepared from a foam with average density of 10 mg/cm³, doped by Mo.

Optical and X-ray cameras show a typical liner velocity of $4-6 \cdot 10^7$ cm/s at the moment of collision. At this time the radiation intensity from the outer surface increases up to 1.5 TW/cm² with rise time of 3 ns. During the next 5 ns the outer surface temperature drops rapidly, suggestive of radiative (non-hydrodynamic) cooling of plasma. The radiation yield during the liners' collision is about 7-10 kJ. The cavity internal surface radiation intensity reaches 3 TW/cm² with a rise time of 3-5 ns. The radiation intensity in the internal cavity remains on the same level or drops slightly while it decreases outside.

This intensity difference between inside and outside demonstrates the radiation screening effect by the outer liner. The radiation's spectral characteristics at collision differ from a Plankian at the measured intensity level. Comparisons of simulations with experimental results permit to explain this difference by the liner collision's local character due to initial axial and azimuthal non-uniformity in the gas puff and instabilities. In fact, the radiation intensity rise time measured locally is 2 ns. Laser shadow and streak camera pictures show the zipper effect and the theoretically expected instabilities.

After collision the liners implode further together due to inertia and magnetic field pressure. A Z-pinch forms from the stagnated plasma and a second high power radiation pulse occurs with rise time 5-10 ns, total radiation yield about 50 kJ, and power 3 TW.

ON AZIMUTHAL MAGNETIC FLUX PENETRATION DURING DOUBLE LINER IMPLOSION.

There is an important question about an azimuthal magnetic flux penetration through the external liner during the DL implosion. Anomalous resistance of external liner plasma and MHD instabilities like Rayleigh-Taylor or Hall effect could be reasons of this process. Phenomena of the azimuthal magnetic flux penetration through the low density external liner is considered in [6], formation of the plasma prepinch - in [7].

Magnetic flux can change the dynamic of the strike. The strike will be more elastic and the radiation power will be reduced.

On the installation Angara-5-1 the investigations of a magnetic flux penetration through the outer shell were performed. Penetration of magnetic flux should excite the current through the internal liner. In these experiments cylindrical shunt was established on the axis of the charging gap instead of the internal liner to measure this current. The shunt diameter was the same as inner liner one - 4-5 mm. This shunt allows to check the penetration of the magnetic flux to the axis as the appearance of the current at the shunt.

The external liner was produced by hollow xenon jet with high Mach number (~6) and diameter of 32 mm, generated by pulse annular nozzle. The specific mass of the external xenon shell was 200 μg/cm.

The results are presented on the figure. Outer shell shadowgraphy and soft X-ray frames show the existence of Rayleigh-Taylor instability with wave length about 3 mm up to 30 ns before strike. Nevertheless the current through the shunt from the beginning up to the strike is absent with the accuracy of 1% of the main load current amplitude. The current absence

through the shunt before strike with the existence of the instability in this time is the evidence that magnetic flux does not penetrate through inner surface of the outer shell. It could mean that instabilities take place mainly on the outer surface of the outer shell and anomalous magnetic flux diffusion through the inner surface of the outer shell is absent.

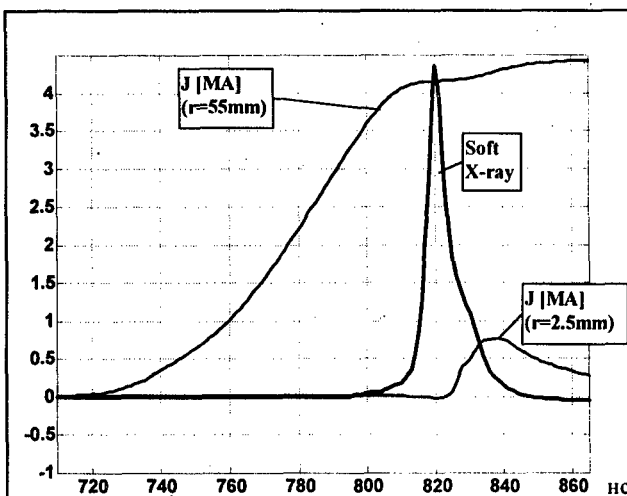


Fig. 1. Results of experiment of outer shell implosion on the shunt. J [MA] - Currents on radius 55 mm and on radius 2.5 mm, Soft X-ray - Relative intensity of soft X-ray radiation.

It should be noted that a replacement of the internal liner by a dense metal shunt changes conditions of experiment. Nevertheless valuations show that a resistance of the shunt and plasma of the internal liner are comparable. An absence of a current on the shunt before strike means as appear the absence of a current through the inner liner before strike.

It should be noted that one could explain the results obtained as the absence of magnetic flux penetration through outer shell before the moment of soft X-ray appearance and magnetic flux penetration in the moment of soft X-ray appearance. Anomalous resistance of external liner plasma in this moment could be the reason

of both the soft X-ray production and the current switching to central region. This point of view on behavior of low density external liner is described in [8]. However the whole complex of experimental data which were obtained in previous DL investigations is the evidence of normal high density outer shell acceleration up to strike.

The main result is the absence of a current in the shunt before strike. It is possible to assert that an anomalous resistance of plasma of the external liner is absent up to the strike moment with the internal one. A penetration of a magnetic flux with cross plasma jets or due to sliding of a liner on electrodes is absent too.

The experimental confirmation of the theoretical predictions on the DL scheme is obtained: up to the moment of strike the current does not penetrate into the internal area and flows just through the outer plasma shell.

PECULIARITIES OF WIRE RESISTANCE BEHAVIOR ON INITIAL STAGE OF EXPLOSION.

During last time the large achievements in soft X-ray production were obtained by Sandia with multywire array implosion. The efficiency of the generator energy conversion to radiation strongly depends upon the quality of plasma shell. Thus the investigation of initial stage of wire explosion and the way of plasma shell creation are very important. To study the different process of plasma creation at initial stage of wire explosion the precision voltage on wire array axis and current measurements have been carried out.

The experiments were done for different wire arrays from tungsten and molybdenum, wire diameter: $4\mu\text{m}$, $6\mu\text{m}$, $10\mu\text{m}$, $20\mu\text{m}$. An effort was mounted to provide a good contact of wires with the electrodes and a homogeneous current distribution through wires. Single Angara-5-1 module was used in this experiment. The microsecond prepulse suppression was done by the using of additional prepulse switch. This switch provides the voltage level on wires during prepulse smaller then 10V. The heating of $4\mu\text{m}$ tungsten wire during prepulse was less then 10°C .

The voltage on wire array axis was measured by the voltage probe placed at a center of wire array. Temporal resolution of voltage probe is about 3 ns. Current through the wire array was recorded by means of coaxial resistive shunt probe with time resolution of 5 ns inserted in cathode electrode.

The values of voltage amplitude for different arrays were about 5-15 kV with pulse duration of 10 ns. Both the voltage amplitudes and voltage profile widths were significantly smaller than those in the case of the array absence. Small voltage means small wire resistance value.

So, main result obtained for tungsten and molybdenum wires is that the voltage on axis drops during first 10 ns. The voltage value measured on axis at the current beginning is too small for metal wire array resistance increasing upon temperature. The plasma appearance on the wire surface during first 10 ns could explain the measured voltage dropping. Thus, the wire array resistance is resistance of plasma produced on the wire surfaces.

The energy deposition in wire up to moment of plasma production is too small for complete wire substance melting by Ohms heating of metal wires. So, the wire at initial stage of current action can be presented as heterogeneous system: solid or liquid wire with plasma on the wire surface.

For better understanding of results of the experiments we performed some simulations of tungsten wire electric explosion. We compared simulations of naked tungsten wire explosion with explosion of tungsten wire dressed with thin envelope formed by light substance (that is impurity) covering of tungsten wire surface before current pulse. The impurity thickness corresponds to a few atomic layers of carbon.

We conclude that the wire doesn't explode as naked one. The most probable reason of strong decreasing of the voltage amplitude and of the delivered energy, is that the wire is covered with very thin impurity layer. It is evaporated in course of discharge quite before the moment of tungsten evaporation. After breakdown of the corona the current leaves the wire so its Ohm heating is stopped after this moment. The typical temperature of tungsten after the breakdown is of order of 0.23 eV. It corresponds to evaluated temperature of tungsten using measured values of voltage and current. After the plasma corona breakdown, the wire heats mainly due to heat flux from the corona to the wire surface.

The reason of plasma appearing at wire surface could be a thin layer of light impurities at the wire surface. After voltage applying the wire temperature will increase; the temperature increasing would produce the vaporization of light impurities from the wire surface and the appearance of a gas (and then a plasma corona) near the wire. In the region of nearest vicinity of wires the plasma productive layer is originated due to Joule current heating of plasma corona and thermal flux transfer to wire surface.

FOAM LINER PREIONIZATION WITH PLASMA FOCUS CURRENT SHELL.

We consider the Plasma Focus current shell as a possible preionizer for the multiterawatt driver. The high current plasma shell, being accelerated during some microseconds in a plasma focus accelerator, could deliver its kinetic, thermal and magnetic energy to a liner positioned in the shell focus region in rather short period, ~ 100 ns, providing appropriate initial conditions for fast implosion. We use a microheterogeneous solid foam as the plasma producing substance, because our foam liner technology allows us to produce liners with different sizes, shaping and radiative dopants. Homogeneity of plasma liner produced was the main problem of interest.

To produce a plasma liner the PF-1000 current shell imploded onto an agar foam liner, positioned on the top of inner electrode of the plasma focus' coaxial accelerator. The foam liners have diameter 20 mm and length 15 mm with 20 $\mu\text{g}/\text{mm}$ or diameter 5.4 mm and length

To produce a plasma liner the PF-1000 current shell imploded onto an agar foam liner, positioned on the top of inner electrode of the plasma focus' coaxial accelerator. The foam liners have diameter 20 mm and length 15 mm with 20 $\mu\text{g}/\text{mm}$ or diameter 5.4 mm and length 15-20 mm with 25-28 $\mu\text{g}/\text{mm}$. The operating parameters of the PF-1000 were capacitance $C = 1$ mF, charging voltage $V_{\text{max}} = 25$ kV, hydrogen pressure ~ 5 Torr, current $I_{\text{max}} \sim 1$ MA, current rise time 4-5 μs . The details of the experiment are published in our joint report. The initial results of our joint experiment are encouraging:

1. The low mass plasma focus current shell interacting with a higher mass foam liner has produced rather homogeneous foam plasma liner. We could not see filaments in the liner plasma, and the foam liner did not expand dramatically during the process.
2. The foam plasma produced has temperature $T \geq \sim 20$ eV and, consequently, liner electric conductivity is sufficient to start an effective implosion driven by a 3-5 MA current with $dI/dt \geq 5 \cdot 10^{13}$ A/s.
3. Combining a plasma focus with a multiterawatt driver and their synchronized operation are possible in principle. We can't couple PF-1000 and "Angara-5-1" to test preionization effects of ≥ 1 MA current, available on PF-1000. We believe this current level will be good for drivers that are more powerful than "Angara-5-1." Consequently, testing of this preionization method is planned on "Angara-5-1" at the 100 kA level for foam cylinder with mass 200 μg and diameter 20 mm..

GENERATORS "BAIKAL" FOR KILOTERAWATT SOFT X-RAY SOURCE.

TRINITI has initiated a project to build a new multiterawatt machine to produce 5 - 10 MJ pulses of soft x-rays, the "BAIKAL" generator. The generator is to have electric pulse power 500 - 1000 TW. TRINITI has a unique complex of 3 pulsed electric generators with inductive store and commutators, originally built to power the magnets of the T-14 tokamak. The complex is situated in special buildings in the vicinity of "Angara-5-1." It is proposed as the primary energy source for "Baikal". New systems as intermediate power amplifiers, reactor chamber and control system are to be created. Preliminary evaluations show that the machine's total price is 4-5 times lower when using the available inductive energy source compared to using a capacitor bank with the same stored energy. A multiterawatt installation project is initiated now in TRINITI. The main goal is creation of "Baikal" generator for 10-20 MJ pulse of soft X-ray radiation production. Parameters of proposed X-ray generator are:

X-ray pulse energy - 5 - 10 MJ with pulse duration - 10 ns;

Method of X-ray generation - plasma shell current implosion;

Load current amplitude - 50 MA;

Load current pulse duration through the imploding load - 100 ns.

The layout of "BAIKAL" is presented on fig. 2. A mechanical energy of 3 GJ is stored in three generators TKD-200. The generators supply the primary windings of 32-sectional inductive store TIN-900 with a current of 150 kA for 6 seconds, delivering 900 MJ. Then the TIN-900 is disconnected from the generators and crowbarred by a mechanical switch. The store secondary winding has 32 sections as well, with each section generating a current of ~ 1.7 MA. The energy stored at the secondary winding is 600MJ. Using a symmetric scheme of triple current doubling the energy transfers into transforming inductive store IN-2, having 16 groups of commutation, and its primary winding is crowbarred as well. The energy transfer into IN-2 secondary winding, coupled with vacuum inductive store IN-3, occurs during ~ 100 ms. Then, 48 synchronized explosive opening switches provide fast current transfer (2-3 ms) into the last stage of current sharpening. The energy stored at the IN3 is equal to 120 MJ.

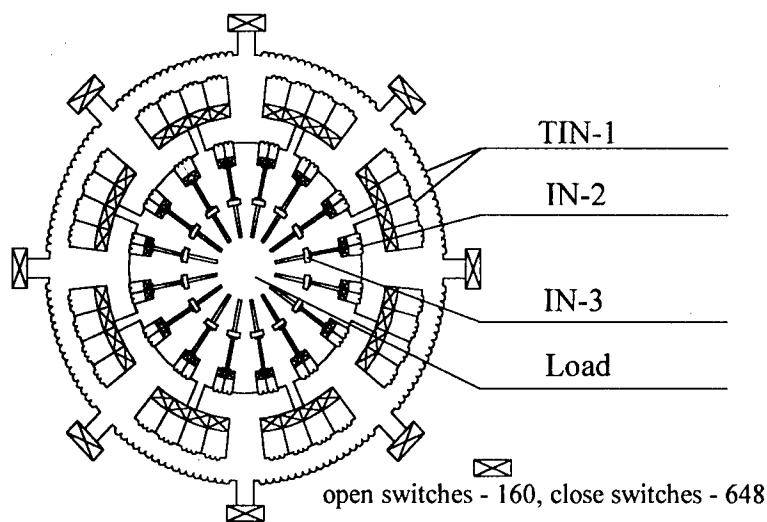


Fig.2 Bajkal layout.

Two kinds of the last stage are being analyzed now. The former one is a current sharpening system, based on plasma opening switches to produce 50 MA, 100 ns current pulse in the load. The plasma open switches with time pulse duration $\sim 1-2 \mu\text{s}$ has tested up to current $\sim 5-8$ MA at GIT 16. The physics of POS at the current ~ 50 MA is absent now. So, the second kind is being analyzed, with water

insulating pulse forming lines.

SUMMARY

As a result of investigations on ANGARA-5, the general features of implosion and strike of liners are studied. The effect of energy confinement by the outer liner is observed. High radiation power sharpening inside the cylindrical cavity with pulse rise time duration of 3-5 ns and kinetic energy conversion efficiency of 30-50% was obtained in the Double Liner scheme. These values are comparable with code calculations provided that the initial gas puff density distribution and liner instabilities are taken into account. The development of technologies for foam liner production allows the use of liners with appropriate parameters. Experiments carried out on ANGARA-5 and calculations permit us to consider the Double Liner as a high intensity soft X-ray source for ICF target ignition.

The "Baikal" generator is a new project at TRINITI. The generator is to have electric pulse power 500 - 1000 TW and a soft x-ray output of 5 to 10 MJ.

REFERENCES

1. Zakharov S.V., Smirnov V. P. et. al., Collision of Current Driven Cylindrical Liners. Kurchatov Institute of Atomic Energy. Moscow. Preprint 4587/6, 1988.
2. Smirnov V. P., Grabovskii E.V., Zaitsev V. I., Zakharov S.V. et. al., Progress in Investigations on a Dense Plasma Compression on ANGARA-5-1. Proc. of BEAMS'90. World Scientific, 1991. V.1, p.61 (I.07) Investigations on a Dense Plasma Compression on ANGARA-5-1. Proc. of BEAMS'90. World Scientific, 1991. V.1, p.61 (I.07).
3. Zakharov S.V., Smirnov V. P., Tsarfin V. Ya. ANGARA-5 High Intensity Soft X Ray Source with Imploding Liner Cascade for Inertial Confinement Fusion. Proc. of 14th Int. Conf. on Pl.Phys. and Cont. Nuc. Fus. Res. Wurzburg, 1992. IAEA. Vienna, 1993. V.3, p.481 (IAEA-CN-56/G-3-9).
4. X Ray Source with Imploding Liner Cascade for Inertial Confinement Fusion. Proc. of 14th Int. Conf. on Pl.Phys. and Cont. Nuc. Fus. Res. Wurzburg, 1992. IAEA. Vienna, 1993. V.3, p.481 (IAEA-CN-56/G-3-9).
5. Gasilov V.S., Zakharov S.V., Panin V.M., Influence of Azimuthal Instabilities on the Acceleration Dynamics of Radiating Liners. Preprint IAE 5464/6, 1992.
- [6] A.V.Branitsky, S.A.Dan'ko, A.V.Gerusev et all. Plasma Physics Rep. v.22, N4, p. 307, 1996.
- [7] I.K.Aivazov, V.D.Vikharev, L.B.Nikandrov et all. Letters in JETPh, 1987, v.45, N.1, p.23.

PLASMA SPECTROSCOPY OF PULSED POWER DRIVEN Z-PINCH TITANIUM PLASMAS

J. Davis^a, R.W. Clark^a, J.L. Giuliani^a, Jr., J.W. Thornhill^a, R. Schneider^b and C. Deeney^c

a. Plasma Physics Division, Naval Research Laboratory, Washington, D.C. 20375

b. Defense Special Weapons Agency, Alexandria, Va 22310

c. Sandia National Laboratory, MS-1194, PO Box 5800, Albuquerque, N.M. 87185

Abstract

In this paper we investigate the radiative behavior of a titanium wire load driven on the Z facility. A radiation hydrodynamic model self-consistently driven by a circuit describes the evolution of the plasma and its self-generated environment. Numerical simulations are carried out to compare the Total and K-shell soft x-ray emission as a function of the ionization dynamic model. The ionization dynamic models are represented by 1) a time-dependent non-equilibrium (GSO) model, 2) a Collisional Radiative Equilibrium (CRE) model and 3) a Local Thermodynamic Equilibrium (LTE) model. For all three scenarios the radiation is treated 1) in the free streaming optically thin approximation where the plasma is treated as a volume emitter and 2) in the optically thick regime where the opacity for the lines and continuum is self-consistently calculated online and transported through the plasma. Each simulation is carried out independently to determine the sensitivity of the implosion dynamics to the ionization and radiation model, i.e., how the ionization dynamic model affects the radiative yield and emission spectra. Results are presented for the Total and K-shell radiation yields and emission spectra as a function of photon energy from 10 eV to 10 keV.

Introduction

Z-pinch physics is enjoying a modern day renaissance due in part to the successful demonstration of the Z-facility's radiative performance. The experimental results have thus far been spectacular, culminating with the production of about 290 TW of radiated power from a double nested wire array initially investigated and theoretically studied by NRL.¹ Total radiation yields of the order of 2 megajoules have been reported from a number of tungsten, titanium and stainless steel wire array implosions.² Z-pinch loads that are imploded to generate large amounts of soft x-rays oftentimes exhibit structure during implosion indicative of growing plasma instabilities. One of the goals of the program is to minimize the formation of plasma structure and produce more nearly 1-D cylindrically symmetric implosions. Better stability means a tighter Z-pinch at the stagnation phase, better energy coupling from the machine to the load, more uniform radiating plasma, and therefore, higher radiative output, and, in particular, greater K-shell yield. This indicates the importance of designing experiments that are more 1-D-like. Modeling two- and three-dimensional effects in Z-pinch plasmas should be viewed as a tool for designing loads that minimize instabilities and produces uniformly radiating plasma.

The theoretical description and numerical simulation of pulsed power driven Z-pinch plasma loads is based on a variety of models that vary from very simple, as in the case of the simple slug model, or to very complex 1-2- and 3-D scenarios. The accuracy and reliability of a model is assessed by how well it provides a basis for an improved understanding of the observations as well as the capability to accurately predict the behavior of planned

experiments. In some instances, simple slug models, coupled to a two level atom model, have been employed to crudely estimate the implosion time and the magnitude of the emitted K-shell x-ray pulse. At the other extreme there are 1-2- and 3-D RMHD (Radiation Magnetohydrodynamic) scenarios that incorporate a portfolio of subroutines for the equation of state, non-LTE ionization physics, transport properties, etc. These models attempt to describe the dynamic evolution of the plasma including growth of plasma instabilities and how they affect the integrity of the implosion and the emitted x-ray pulse.

Models can be validated by comparing theoretically generated databases with experimentally observed results for as many plasma parameters as possible. The parameters most commonly selected include the magnitude of the radiative yield, the x-ray pulse length and shape, x-ray pinhole photos of the assembling plasma, and emission spectra. The temperature and density are inferred from unfolding the experimental results in conjunction with an ionization dynamic model. In order to explore the sensitivity of the emission spectrum to variations in the model we have performed a series of numerical simulations of a titanium wire array driven by the Z accelerator. The simulations were performed using a 1-D radiation MHD model to quantify how the emission features and radiation signatures are influenced as the atomic and opacity models are modified. The use of a full 1-D model is sufficient to illustrate the sensitivity of the emission history to the choice of atomic and opacity models. For example, in the case of the multiple wire Al array loads (having 40 or more individual wires) investigated on the Saturn accelerator, the implosion appeared to be less influenced by azimuthal asymmetries and, to first order, adequately represented by a 1-D implosion model.³ Also, comparing and contrasting the synthetically generated spectrum with the experimentally observed spectrum has the potential to validate the reliability of the simulation and identify the model's strengths and weaknesses. The numerical simulations presented here to characterize the dynamics of a radially imploding Z-pinch plasma are based on a one-dimensional two temperature multi-zone non-LTE-radiation-magnetohydrodynamic model, DZAPP, with a transmission line circuit model representing the driving generator. A thorough discussion of the model is presented in reference 4.

The titanium model contains all the ground states and a manifold of excited states distributed throughout the various ionization stages. Only the strongest lines, i.e., lines with the largest oscillator strengths, were included in the simulation. Finally, except where noted, the majority of numerical simulations were carried out using an atomic model that contained over 300 spectral lines distributed throughout the K, L, and M shells. This assumption represents a reasonable compromise between the atomic model and computational constraints, particularly when the medium is opaque and radiation needs to be transported through the plasma. The ionization dynamics and radiation transport are a strongly coupled interactive system and must be solved together as demonstrated in ref. 5. The radiation transport of the bound-bound and bound-free transitions is carried out using the probability of escape formalism described by Apruzese.⁶ Multifrequency transport is used for the free-free radiation.

Results

The current profile that results from driving the circuit with a changing load inductance is shown on Fig. 1. The peak short circuit current is about 20 mega-amperes. The load in this case is represented by a multiwire array of titanium wires with a total mass of 3240 μ gms, a length of 2 cm and an initial array radius of 2 cm.

A snapshot view of the evolution of selected hydrodynamic parameters from the DZAPP model is shown on Fig. 2 as a function of radius $[(r) \text{ in cm}]$ and time $[\text{in } \mu\text{sec}]$ with a time dependent collisional-radiative ionization dynamic model (referred to as GSO). The electron

and ion temperatures are represented as E-Temp and I-Temp, respectively, and are measured in eV. The density is in gm/cm^3 and the radiative cooling in kW/cm^3 . The "log-scale" adjacent and to the right of each insert on the Figure quantifies the degree of shading. The bounce occurs around 140 ns where the ion temperature is about 300 keV and the electron temperature rises to about 20 keV in a highly localized region.

The ionization dynamic models used here to produce emission spectra are represented by GSO, CRE and LTE for optically thick and thin simulations. All the simulations are self-contained in the sense that for each ionization model a complete simulation was performed rather than the post processing of a single hydrodynamic simulation. This produced slight differences in the implosion times and minimum radius. All the simulations were integrated in time until the plasma reached a final radius about 2.5 times the minimum implosion radius which included the first bounce and subsequent re-expansion out to the terminated radius. The total time integrated spectra produced from the GSO model will serve as our benchmark simulation and is shown on Fig. 3. Some selected spectral lines are identified along with the transition energy (keV) and radiated energy (kJ). The helium- and hydrogen-like resonance lines account for about 15 % of the radiated K-shell energy. The calculated Total and K-shell radiated energy emitted is presented in Table 1.

RADIATIVE YIELDS

Ionization Model	Rad Transfer	Total Yield (kJ)	K-Shell Yield (kJ)
GSO	THICK	988	131.5
CRE	THICK	989	128.2
LTE	THICK	599	163.7
GSO	THIN	701	47.8
CRE	THIN	678	50.2
LTE	THIN	456	239.9

TABLE 1

The THIN simulations are presented for comparison since the optically thin approximation is often employed erroneously as a means of cooling the plasma by radiative losses. Also, the THIN simulations undergo radiative collapse which drives the current down at stagnation and limits the late time energy coupling to the pinch. As the plasma evolves the opacity (which is a function of plasma conditions, pathlength, and oscillator strength) can potentially influence the population of excited states and consequently the emitted radiation. A comparison of the magnitude of the Total and K-shell thick radiative yield shows that the CRE simulation is in excellent agreement with the GSO calculation. Table 1 also illustrates that the LTE assumption, even with opacity, predicts a Total yield reduced by about 40% and a K-shell yield higher by about 20% than the GSO model. As the density increases during peak compression the GSO and CRE L-shell excited state populations should exhibit trends toward LTE. However, the temperature remains too high and the density too low for the entire plasma to go into LTE. The experimental observations for the 110 multiple wire Ti load (shot Z88) produced a total yield of about 1 MJ and a K-shell yield of about 125 kJ. The GSO and CRE predictions of total and K-shell yield are in reasonably good agreement with the observations. Just prior to the bounce the plasma showed signs of developing perturbations reminiscent of the spike and bubble structure which is the trademark of the Rayleigh-Taylor

instability. We can speculate that as the structure evolves it seeds “bright spots” and it is these bright spots that are the origin of energetic photons lying beyond the K-shell. The radiation originating from the plasma structures will be the topic of a forthcoming paper.

The total emission spectra are shown on Figs. 3-8 for the cases represented in Table 1. Fig. 3 represents the GSO thick result and is considered the benchmark simulation for these comparisons. The Figures provide an overview of the line spectra superimposed on the continuum indicating the relative height and magnitude of each component and how each are altered as the model varies. The global view of the line and continuum features reveals differences both in the magnitude and shape of lines and continuum, especially between the THIN and THICK simulations. Rather than point out the specific differences, it is left as an exercise for the reader to conclude the obvious: that there are easily identifiable spectral features that can be used to validate and benchmark one's model.

The question always arises whether the plasma exhibits trends toward LTE during its evolution. One way of observing this trend is to follow the departure coefficients for selected states. The departure coefficient is generally defined as the ratio of the population of a state to the population it would have if the state were in LTE. The behavior of the departure coefficients will be discussed at length in a forthcoming publication. We comment here that for most of its history the plasma is definitely not in LTE. However, in the region of peak radiated power, which occurs at $x \cong 0.1$ cm and $t \cong 140$ ns, the $n \geq 2$ levels of hydrogenlike titanium are in LTE in a highly localized region. All the other levels shown are generally far removed from LTE. This has major consequences both for the evolving dynamics as well as the emission spectra for models assuming radiation diffusion with a blackbody source function or Rosseland weighted opacities in conjunction with the Eddington approximation. Usually, any agreement between numerical simulations based on these models and experiment is purely fortuitous unless, of course, the plasma is a blackbody radiator in LTE.

The intent of this investigation was to: 1) generate and characterize the emission spectra from an imploding multiwire Ti array plasma driven by the 20 MA Z accelerator, 2) compare and contrast synthetically generated spectra for three different but standard models of the ionization dynamics, and 3) use the synthetic spectra as a tool for validating the accuracy and reliability of the numerical simulation model. These issues have been addressed and we have concluded that the synthetically generated spectra can be used to benchmark and validate various aspects of numerical simulations. The key to benchmarking and validating models depends on obtaining reliable and reproducible measurements.

Acknowledgements

The authors would like to thank Dr. John Rogerson for assisting in generating the numerical results and Drs. Apruzese, Terry and Whitney for many helpful discussions and for making available the results of their analysis of multiple wire experiments. This work was supported in part by DSWA and DOE.

References

- [1]. J. Davis, N. Gondarenko, and A. Velikovich, *Appl Phys Lett* **70**, 170 (1997).
- [2]. C. Deeney, T. Nash, et. al., *Phys Rev E* **56**, 5945 (1998),
C. Deeney, T. Nash, et. al., *Phys Plasmas* **5**, 1 (1998),
R. Spielman, C. Deeney, et. al. *Phys Plasmas* **4**, 1519 (1997).
- [3]. T. Sanford, G.O. Allshouse, et. al., *Phys Rev Lett* **77**, 5063 (1996),
K. Whitney, J. Thornhill, et. al., *Phys Rev E* **56**, 1 (1997),
T. Sanford, T. Nash, et. al., *Rev Sci Instrum* **68**, 852 (1997).
- [4]. J. Davis, J. Giuliani, Jr., M. Mul Brandon, *Phys Plasmas* **2**, 1766 (1995).
- [5]. D. Duston, R. Clark, J. Davis, J. Apruzese, *Phys Rev A* **27**, 1441 (1983).
- [6]. J. Apruzese, *J Quant Spect & Rad Transfer*, **25**, 419 (1981).

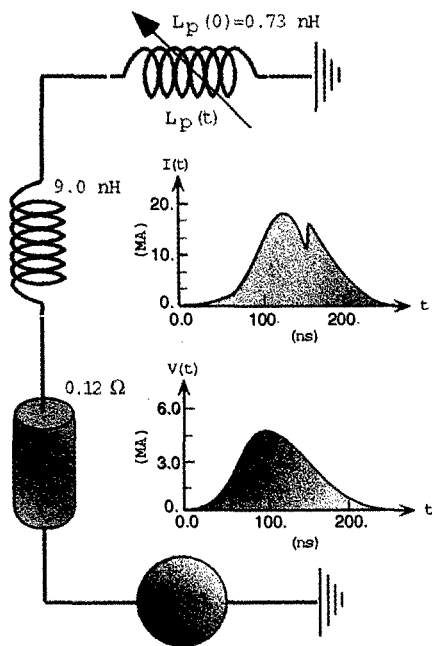


Figure 1. Equivalent electrical circuit.

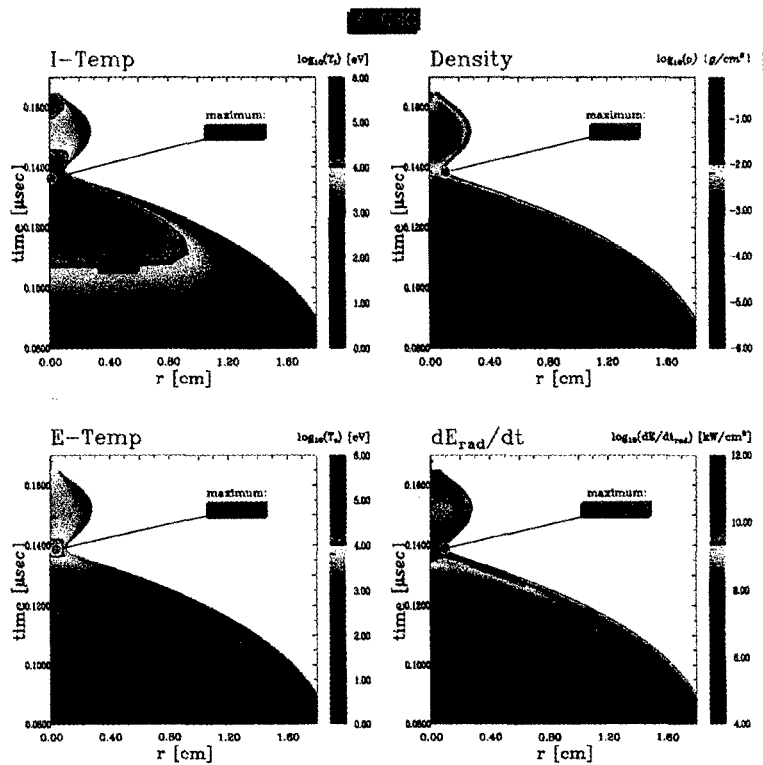


Figure 2. Time dependent Collisional Radiative (GSO) model results for the ion and electron temperatures, mass density, and radiative cooling as functions of radius (cm) and time (μsec).

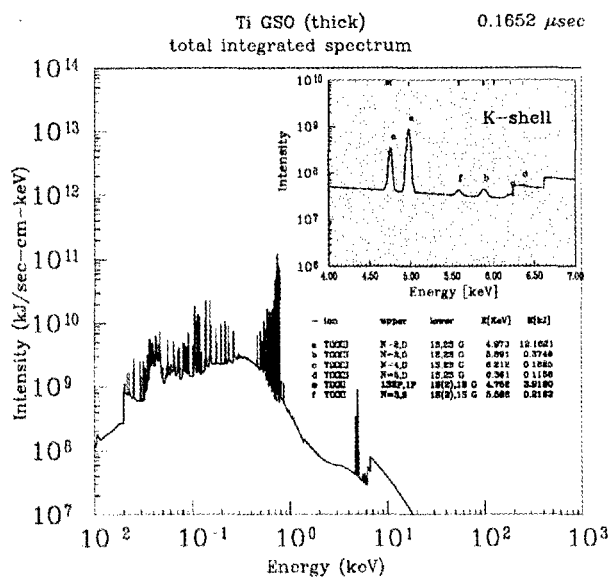


Figure 3. Emission spectra for the time dependent GSO model.

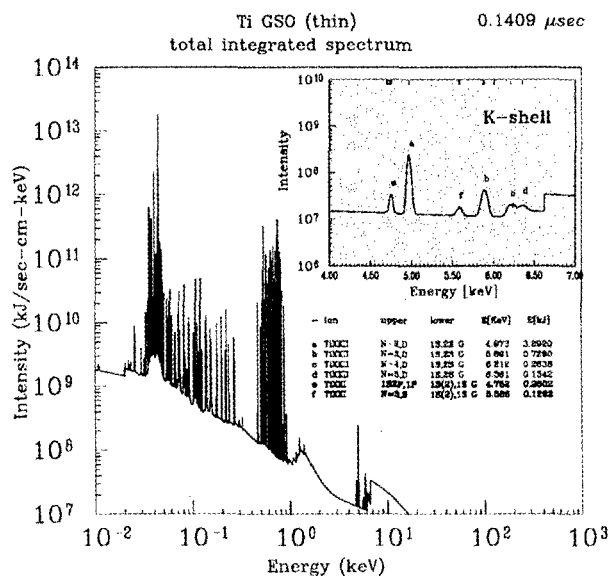


Figure 4. Emission spectra for the optically thin GSO model.

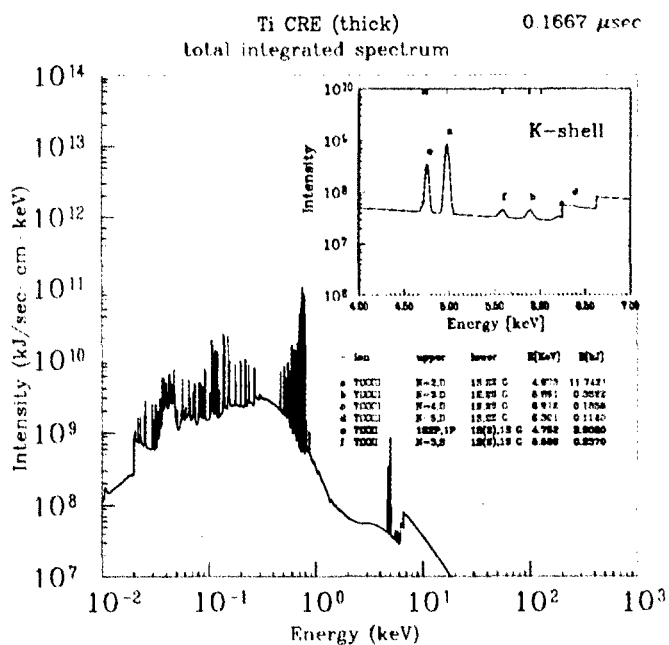


Figure 5. Emission spectra for the CRE model.

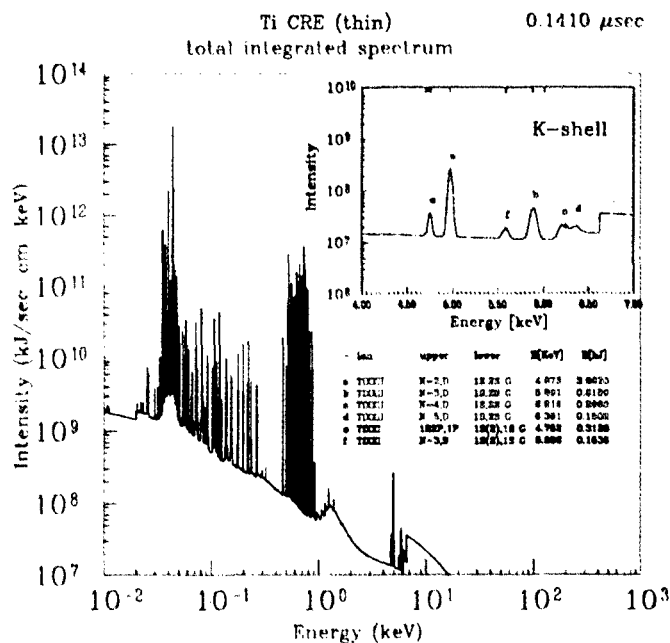


Figure 6. Emission spectra for the optically thin CRE model.

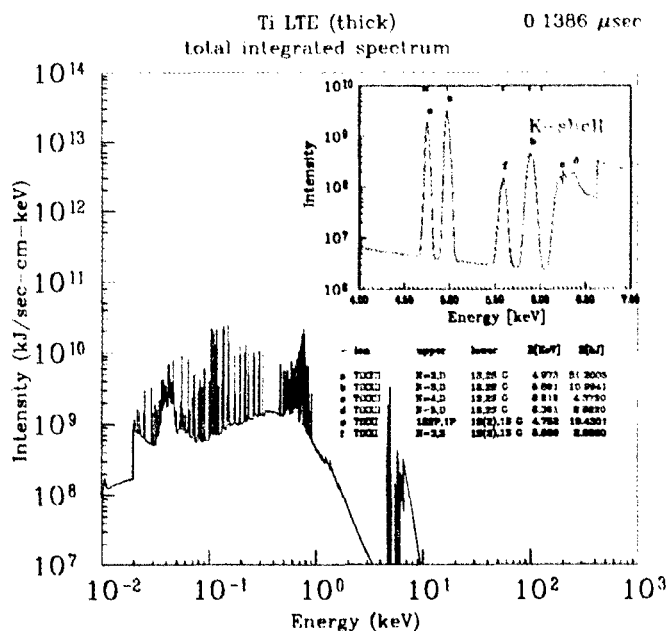


Figure 7. Emission spectra for the LTE model.

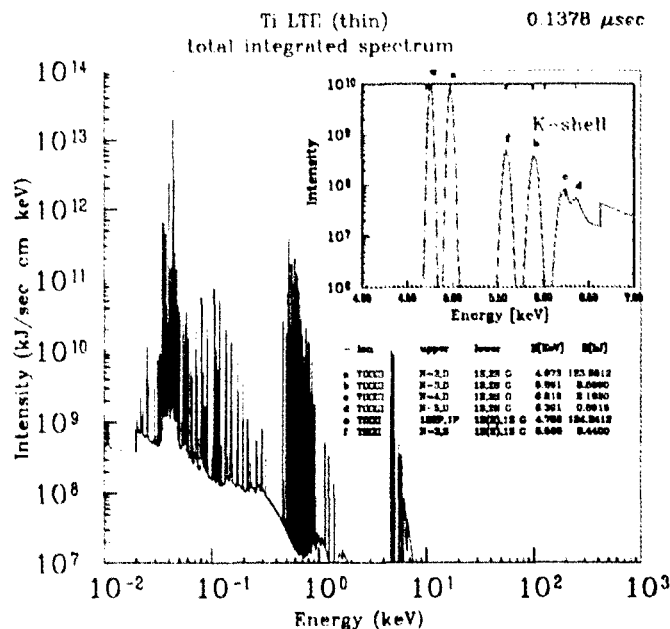


Figure 8. Emission spectra for the optically thin LTE model.

EXPLOSIVE COMPLEX FOR GENERATION OF PULSED FLUXES OF SOFT X-RAY RADIATION

V.D.Selemir, V.A.Demidov, A.V.Ivanovsky, V.F.Yermolovich, V.G.Kornilov,
V.I.Chelpanov, S.A.Kazakov, Yu.V.Vlasov, and A.P.Orlov

VNIIEF, Sarov, 607190, Russia

INTRODUCTION

High-energy density physics uses the devices, allowing to input high energy into the substance for a short time period. Maximum power and energy density are obtained in laser devices. However the progress, achieved during the last few years in the development of electrophysical devices with inductive energy storage and generation of soft x-ray radiation (SXR) in the devices of z-pinch type [1] opens the perspective of creation of more compact and cheap energy systems for investigations in the field of high-energy density physics and simulation of thermonuclear compression processes.

This paper describes the concept and realization principles of the project of explosive electrophysical complex EMIR for generation of pulsed fluxes of soft x-ray radiation. Complex EMIR is based on the developed in VNIIEF technologies of high-power flux compression generators (FCG) and transforming systems on the basis of lines with distributed parameters and current opening switches. Vacuum lines with magnetic insulation or water coaxial lines are considered for energy pulses transmitting to the load. Transformation of the magnetic energy to the kinetic one, thermalization and SXR radiation are performed in z-pinch with double liner system.

CONCEPTION AND METHODS OF COMPLEX REALIZATION

Complex EMIR is based on the module principle. Block scheme is presented in Fig.1.

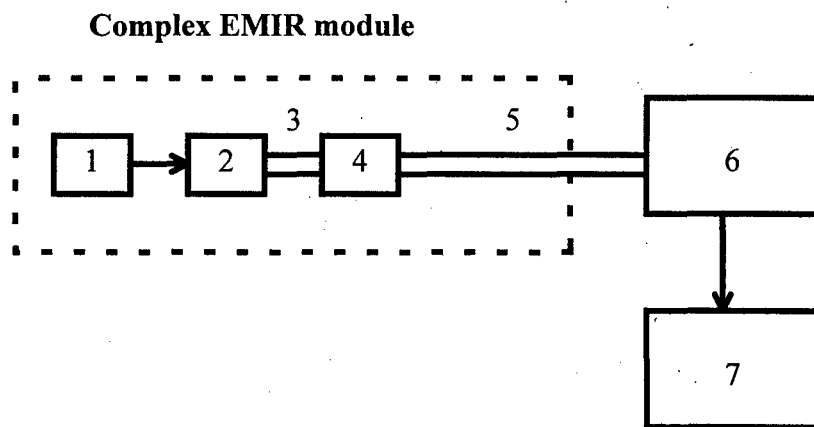


Fig.1. Block scheme of the complex EMIR.

1 – helical FCG, 2 – disk FCG, 3 – cable line, 4 – transforming device,
5 – transmission line, 6 – summator, 7 – load.

Disk FCG. Multi-element disk FCG (DFCG) is a power base of the complex. It is powered with preamplifier 1. Current pulse from the DFCG with the cable line 3 is transmitted to the device 4 for voltage increasing and fore front reduction. Transformed pulse is transmitted with the line 5 to the summator 6, combining all complex EMIR modules for energy pulse formation on the load 7.

Fig.2 shows the draft of the disk FCG with cable energy output. This generator (DFCG-240) contains 20 serially connected elements with HE-charges of 240 mm diameter. Its calculation was made with the software [2], which was tested according to the earlier performed experiments. According to the calculations, at initial powering of ~ 7 MA DFCG-240 provides in the load of 20 nH the current of ~ 40 MA with the characteristic rise time less than $4 \mu\text{s}$ [3].

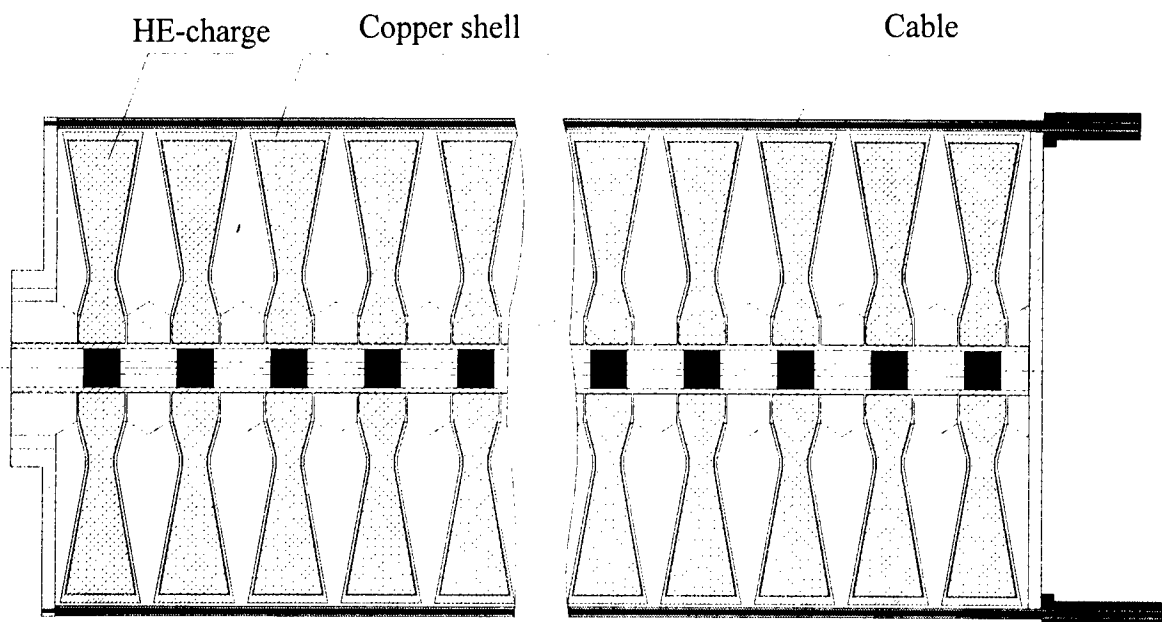


Fig.2. Disk FCG.

Transforming system. Transforming system of the complex EMIR is based on the linear inductive accelerator (LIA) scheme with inductors on the short-circuit lines with distributed parameters [4,5]. The scheme of LIA on the basis of the short-circuit line is presented in Fig.3. The key element of this scheme is an opening switch. Its operating time should be less than the run time of the electromagnetic wave along the short-circuit line and the final resistance R_k should be greater than the line wave resistance ρ_0 . Plasma-erosion opening switches meet this requirements. Their analysis was made based on experimental results, obtained earlier in VNIIEF [6] and other laboratories.

Homogeneous radial lines with the external diameter $D = 300$ cm and internal one $d = 100$ cm are used in the complex EMIR transformer (Fig.4). The base transformer module will consist of 5 inductors with full inductance of ≤ 20 nH. DFCG-240 provides the initial current $I_0 = 8$ MA in the short-circuit inductor line. The value of the output voltage of one

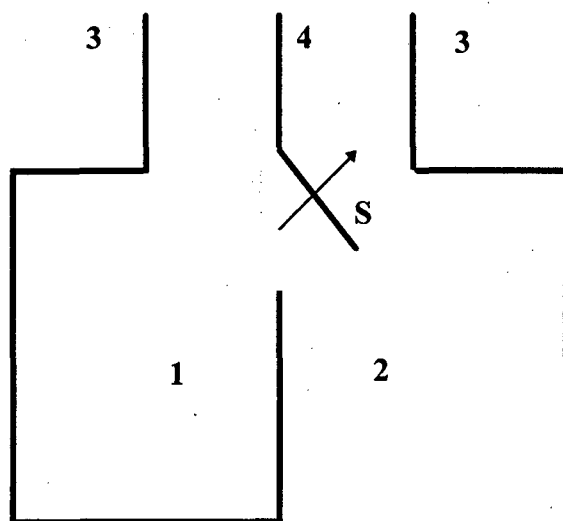


Fig.3. Inductor LIA on the basis of short-circuit radial line.

1 - short-circuit radial line, 2 - transmission radial line, 3,4 – energy supply from external source, S – opening switch.

inductor at $R_k \cong 2 \Omega$, $\rho_0 \cong 0.67 \Omega$ and transmission line resistance $\rho_1 \cong 1 \Omega$ is ~ 2 MV, and voltage pulse, formed by 5 inductors on the load $Z_0 = 5\rho_1 \cong 5 \Omega$ will reach ~ 10 MV. Pulse duration in the transformer with water isolator of 3 m diameter will be ~ 120 ns.

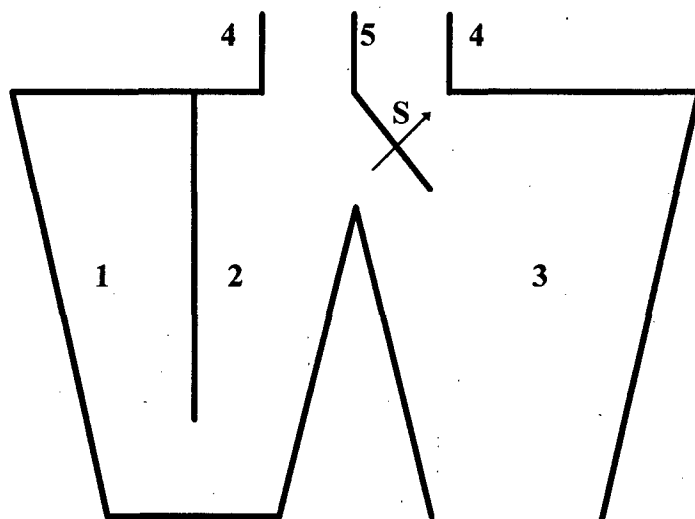


Fig.4. Scheme of base module EMIR inductor.

1,2 – short-circuit line, 3 – transmission line, 4,5 –energy supply from DFCG, S – opening switch.

Transmission line. Vacuum or water transmission lines are proposed to use for energy transmission from the transformer to the summator and the load.

To connect vacuum transmission line to the inductors on the short-circuit lines with water dielectric it is necessary to create insulators, separating vacuum volume and deionized water. Electric field intensity on the insulator surface will be ~ 10 MV/m. The confinement of such fields nowadays is a rather complicated technical problem.

At the application of water transmission line the crucial problem is the creation of output insulator construction with surface electric strength of 10-20 MV/m. However, small pulse duration (~ 120 ns) and magnetic self-insulation gives the hope on realization of such construction.

Summator. Energy pulses, formed by base modules, are transported to the radial (biconical) line with the load in the center. Depending on the experimental conditions, the number of the base modules could be changed. According to this, the wave resistance of the summator line is also changed. It should be equal to Z_0/n , where Z_0 – transmission line wave resistance, n – module number.

In particular, at the considered parameters of the base modules the realization of the wave resistance of the radial summator line of $\sim 0.1 \Omega$ requires the parallel operation of 48 modules.

ESTIMATION OF SXR CHARACTERISTICS

Principal scheme of the device, forming SXR, is presented in Fig.5. Energy supply system, consisting of direct 1 and reverse 2 current conductors, provides powering of the external liner 3. External liner kinetic energy, acquired at the interaction with the magnetic field, is transmitted to the internal liner 4 in the result of a blow. Appearing in the result of the internal liner collapse SXR goes through the window 5 to the spherical cavity 6 with the thermonuclear target.

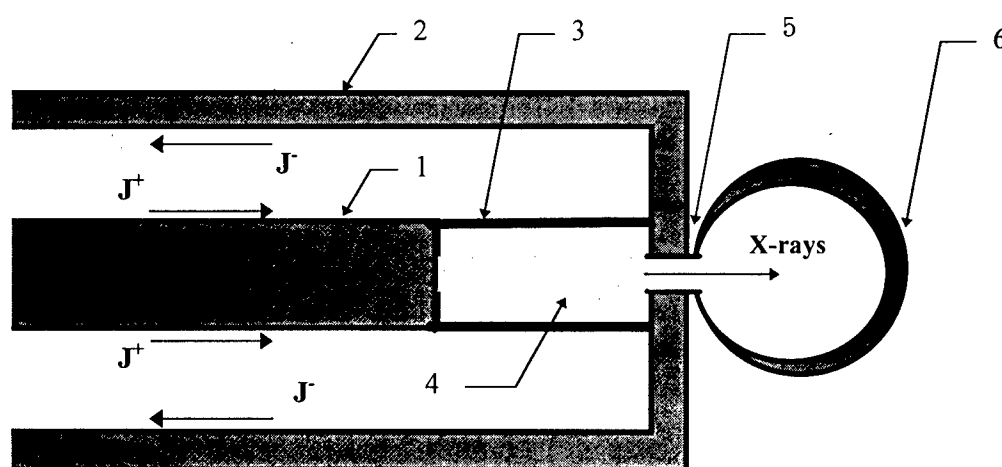


Fig.5. Scheme of the plasma element, forming SXR.

- 1 - supplying current conductor, 2 - reverse current conductor, 3 - external liner,
- 4 - internal liner, 5 - radiation output window, 6 - spherical cavity.

External liner is made of heavy metal (e.g. tungsten), and internal one is made of light material to provide great radiation runs along the axis. Linear masses m of the liners as equal. The scheme is approved on the Angara-5 device [7] at electromagnetic energy of ~ 1 MJ.

Liner parameters at the moment of thermalization start were determined from semi-empiric model [8]. In the considered conditions it was obtained

$$m r_0^2 \approx 0.1 \cdot \frac{\mu_0}{4\pi} \frac{U_0^2 t_0^2}{R_0^2} \approx 0.1 (\text{g} \cdot \text{cm}); \quad \frac{r_0}{g_0 t_0} \approx 0.23; \quad \Delta r \approx 0.05 r_0, \quad (1)$$

where r_0 – initial radius of the external liner, g_0 , Δr – liner velocity and width at the moment of thermalization beginning. Numerical estimations correspond to the voltage pulse of $U_0 = 10$ MV, wave resistance $R_0 = 0.1 \Omega$, pulse duration $t_0 = 100$ ns.

Hydrodynamical equations were solved to determine SXR parameters

$$\begin{aligned} \frac{d\rho}{dt} &= -\rho \operatorname{div}(\vec{u}), \\ \frac{d\vec{u}}{dt} &= -\frac{1}{\rho} \operatorname{grad}(P), \\ \frac{dE}{dt} &= -\frac{P}{\rho} \operatorname{div}(\vec{u}) + \iint \chi_{\omega a} (I_{p\omega} - I_{\omega}) d\omega d\Omega \end{aligned} \quad (2)$$

in combination with the equation of radiation transfer

$$\frac{\partial I_{\omega}}{\partial t} + \vec{c} \vec{s} \nabla I_{\omega} + \chi_{\omega} I_{\omega} = \chi_{\omega a} I_{p\omega} + \frac{\chi_{\omega s}}{4\pi} \int I_{\omega} d\Omega, \quad (3)$$

in 2D-geometry. In the equations (2), (3): ρ , \vec{u} , P , E – density, velocity, pressure and specific internal energy; I_{ω} – radiation intensity with the frequency ω ; $I_{p\omega}$ – equilibrium radiation intensity with the frequency ω ; \vec{s} – single vector in the direction of photon movement; $\chi_{\omega} = \chi_{\omega a} + \chi_{\omega s}$ – spectral coefficients of absorption and dispersion.

Equations of state $P=P(\rho, T)$, $E=E(\rho, T)$ were used in the approximation of Tomas-Fermi [9]. Brake absorption, photoionization, absorption in the lines [10] are considered in $\chi_{\omega}(\rho, T, \omega)$.

Numerical investigations showed, that the maximum intensity of the coming into the cavity SXR are reached at $g_0 \cong 7 \cdot 10^7$ cm/s, position of the internal boundary of the liner $r_{in} \cong 0.2 \cdot r_0$, liner system length (at $m \cong 0.035$ g/cm, $r_0 \cong 1.7$ cm) $l \geq 1.5$ cm. Time dependence on SXR intensity and radiation temperature in the cavity of $V = 1$ cm³ volume are presented in the Figs. 6, 7.

Calculation energy balance: supplied electromagnetic energy $W_k = 85$ MJ; liner kinetic energy $E_k \cong 17$ MJ; energy of the radiation, coming into the cavity $E_v \cong 1.7$ MJ ($E_v \cong 0.02 \cdot W_k$).

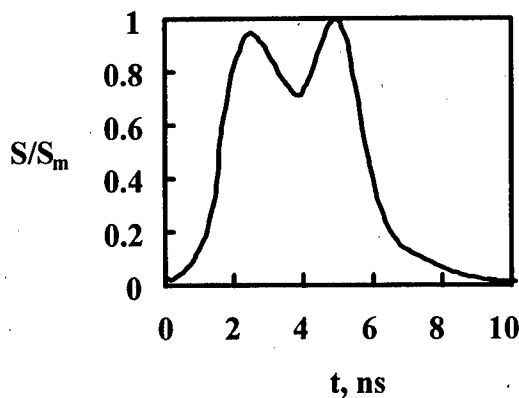


Fig.6. Time dependence on radiation intensity ($S_m \approx 0.5$ MJ/ns).

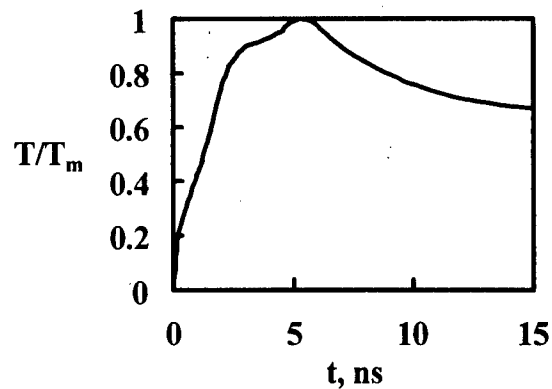


Fig.7. Time dependence on radiation temperature in the cavity ($T_m \approx 0.3$ keV).

REFERENCES

1. R.B.Spielman et al. PBFA-Z: A 20 MA Z-Pinch Driver for Plasma Radiation Source, in: Proceedings of the 11th International Conference on High Power Particle Beams. BEAMS'96, v.1, p.150-153.
2. A.M.Buyko, V.M.Danov, V.I.Mamyshev, V.B.Yakubov. Method of Numerical Simulation of Disk Magnetocumulative Generators with Electrodischarge Current Sharpener and Liner Load. VANT, ser. MMFP, 1995, iss. 4, p.12-18.
3. V.D.Selemer, V.A.Demidov, S.A.Kazakov et al. High-Power Energy Sources Based on Serial and Parallel EMG, in: Proceedings of the 11th IEEE International Pulsed Power Conference, Baltimore, Maryland, June 29 - July 2, 1997.
4. Ya.S.Itshoki. Pulsed Devices. Moscow: Soviet Radio, 1959.
5. V.S.Bossamykin, V.S.Gordeev, A.I.Pavlovskii. New Schemes for High-Voltage Pulsed Generators Based on Stepped Transmission Lines, in: Proceedings of the 9th International Conference on High-Power Particle Beams, Washington, May 25-29, 1992, v.1, p.511-516.
6. A.L.Babkin, V.I.Chelpanov, V.G.Kornilov et al. Electron Accelerator Powered by Inductive Storage Based on Induction Plasma Injectors, in: Proceedings of the 9th IEEE International Pulsed Power Conference, Albuquerque, 1993, p.908-909.
7. K.S.Dyabilin, M.E.Lebedev, V.E.Fortov, V.P.Smirnov et al. Investigation of Thermalphysic Substance Properties at Effect of High-Power Pulse of Soft X-ray Radiation of Z-pinch Plasma. TVT, 1996, v.34, No.3, p.479.
8. J.Katzenstein. Optimum Coupling of Imploding Loads to Pulse Generators, J.Appl.Phys. 1981, v.52(2), p.676.
9. G.M.Yeliseev, G.E.Klinishov. Equations of State of Solid Bodies and its Spline Approximation. Preprint IPM AS USSR, 1982, No.173.
10. N.N.Degtyarenko, G.M.Yeliseev. About Fractal and Spline-Spectrum of Cross-Sections of Photons Absorption in Plasma, in: Fractals in Applied Physics, Ed. A.Ye.Dubinov, Arzamas-16: VNIIEF, 1995.

THE APPLICATION OF HIGH INTENSIVE Z-PINCH RADIATION AND HEAVY ION BEAMS FOR RESEARCH ON HIGH ENERGY DENSITY PHYSICS

V.Fortov, K.Dyabilin, M.Lebedev

(High Energy Density Research Center, Izhorskaya 13/19, Moscow, Russia)

E.Grabovskij, V.Smirnov

(Troitsk Institute for Innovative and Thermonuclear Research, 142092 Troitsk, Russia)

B.Sharkov, A.Golubev

(Institute for Theoretical and Experimental Physics, 117259, Moscow, Russia)

D.H.H. Hoffmann,

(Technische Universität, Darmstadt, Germany)

K.Eidmann

(Max-Planck-Institut für Quantenoptik, D-85748 Garching, Germany)

INTRODUCTION

The progress of the development of the powerful pulsed power generators and the last achievements in the technique of the focused heavy ions opens new possibilities for the studies in the high energy density physics: extremal states of the matter, equation of states, heat and mass transport and so on. In the last years on the PBFA-Z the hot dense plasma with temperatures more than hundred electronvolts and radiation fluxes of some hundreds terrawatts was obtained. This means that the physical processes which will take place in the National Ignition Facility experiment could be well studied on the Z-pinch installations [1].

ANGARA-5-1 Z-pinch facility produces plasma with temperatures up to 80 eV and the radiation flux up to 5 TW/cm^2 . The definite attention is paid on the studies of the interaction of the powerful radiation with different substances. The experiments with the targets with normal density allow to study formation and propagation of the shock waves, to accelerate thin foils and in accompany with the numerical modelling to investigate the thermodynamical and hydrodynamical properties of the matters. The experiments with the ultralow density targets allow to study heat waves and give information about the transport phenomena and optical characteristics of the foams.

Inherent for heavy ions is the volume energy deposition by focusing of intense ion beam on the targets. Upgrade programs of accelerator facilities at ITEP-Moscow and GSI-Darmstadt are aiming at production of hot, strongly compressed matter with extremely high energy density levels (more than 1MJ/g) capable to generate an uniform well-characterised intense shock waves in solids and plasmas required for thermodynamic measurements in 10-100 Mbar pressure region.

ANGARA-5-1 Z-PINCH

Angara-5-1 is eight modules high power generator with current up to 5.5 MA and current raise time equal to 90 ns. The load compressed by current magnetic field is used to produce nanosecond raise time pulse of soft X-ray emission to irradiate the samples. The sample is placed near load at distance about several millimeters. The double liner scheme was used as the generator load [2]. The double liner loads consist on Xe supersonic jet with Mach number 5-6 (outer liner) and Agar-Agar dopped Mo cylinder-inner liner. Mass of both liners was 150-300 mkg. Height was equal to 1 cm.

EXPERIMENTS OF THE SHOCK WAVE EXCITATION ON ANGARA-5-1

An important question in investigations of this kind is the degree of spatial homogeneity of the irradiated region [3]. Under our conditions, the theoretical calculations predict an inhomogeneity of order 3% on the 4 mm (liner diameter), which is due to the geometry of experiment. Direct estimations of the inhomogeneity one can get from the time of the shock wave coming on the free surface of the targets (shock wave front inhomogeneity). The radiation inhomogeneity can be estimated as

$$\zeta = \Delta q/q = \Delta t/t * \{ 2 / \partial \ln P / \partial \ln q \}$$

where $\Delta t/t$ is the time difference and the factor $\{ 2 / \partial \ln P / \partial \ln q \}$ takes into account the dependence of the pressure in matter P induced by the radiation flux q . These estimations from streak camera records (see fig.1) give the value about 3-4% , what is close to geometrical inhomogeneity [4].

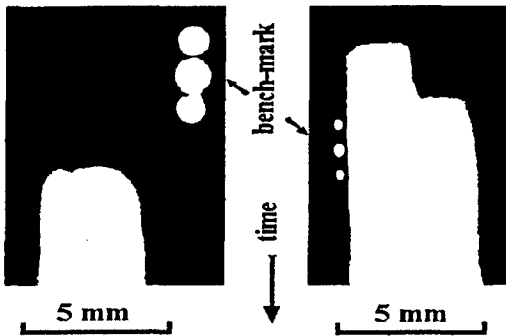


Fig.1. Streak camera records (positive) of shock break out from sample obtained in ANGARA-5-1 experiments : left-plane target:lead-180mkm; right-stepped target: tin-16mkm, lead-180mkm. Between bench-marks - 13 ns

The results of the shock wave experiments and theory are shown in Fig. 2. The averaged (over the target volume) shock wave velocity for Al plus Pb stepped target is (7.3 ± 0.6) km/s for 80mkm Pb thickness, and (4.6 ± 0.3) km/s for 200mkm. In accordance with the Huguenot lead adiabat this means that the shock compression pressures are 3 Mbar and 0.9 Mbar correspondingly [5]. In stepped tin plus lead target shock compression of lead (thickness 180mkm) about 1.2 Mbar was measured.

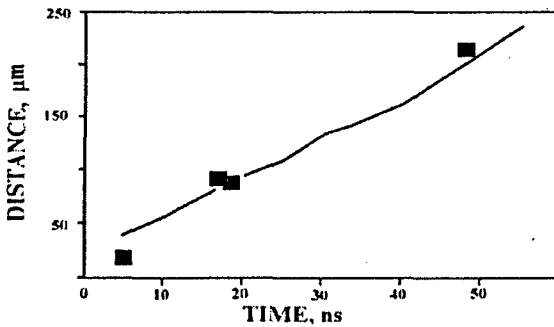


Fig.2 Position of shock front for stepped target (aluminium 16 mkm, lead up to 200mkm). The power level is 1.2 TW/cm^2 .

Solid line - numerical calculations [6].

THIN FOILS ACCELERATION ON THE ANGARA-5-1

The radiation of the plasma with the temperature about 100 eV can be effectively used for the acceleration of the thin plates (flyers) and for the following study of the equation of states (EOS) of the matters under the intensive pulse actions. Under these conditions, the parameters of the extreme stations are higher than at the direct samples irradiation. The installations with the Z-pinch plasmas as sources of the soft x-ray radiation allow to irradiate samples with the high space uniformity and, consequently, to use the flyers with the more big sizes. Because of the pulse duration in these experiments is

substantially more than in laser ones it is possible to increase the thickness of the flyers and to avoid their substance preheating and to do the measurements more reliable.

For the good acceleration it is necessary that all the SXR energy to be absorbed. For the most reliable registration of the shock wave parameters the detection time is to be tens of nanoseconds. And, consequently, the thickness of the flyer is to be tens of micrometers. The distance from the flyer to target is to be chosen such as the flyer to be without mechanical loads (to be decompressed), from the other hand the flyer should be stable.

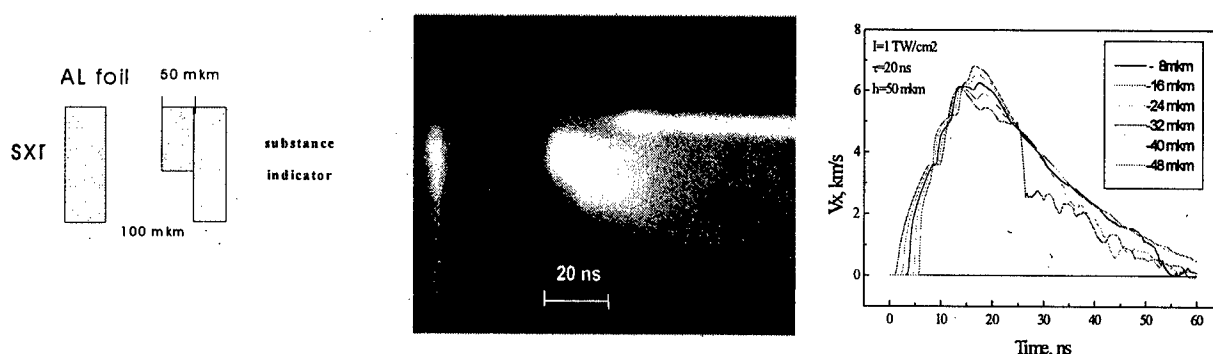


Fig.3 Shot #2953. Soft x-ray power on target 0.5 TW/cm^2 . Simulations show axial mass velocity evolution for several points on the Al target depth

Fig.3 presents the experimental scheme of the flyer acceleration used in shot #2953 : the 52 mkm aluminium flyer accelerated by x-ray radiation knocked on stepped indicator target (mylar, step size 50mkm). The SFER streak camera record and results of numerical modelling are shown. The estimated flyer velocity was 4-5 km/s what is roughly close to value predicted in calculations.

SUPERSONIC HEAT WAVE IN LOW DENSITY FOAMS GENERATED BY SOFT X-RADIATION FROM A Z-PINCH PLASMA ON ANGARA-5-1

The study of the propagation of the heat waves generated in the low density condensed matters by the intensive soft x-ray flux is of importance for many fields such as inertial confinement fusion, x-ray lasers, and astrophysics.

On the ANGARA-5-1 the experiments with foam targets in the density range $5\text{--}50 \text{ mg/cm}^3$ and a thickness up to some millimeters were carried out. The radiation with intensity about 1 TW/cm^2 was incident on the planar target, which was positioned under the liner. The targets were made of agar-agar ($\sim \text{C}_{12}\text{H}_{18}\text{O}_9$)_n or aerogel (SiO_2).

Shot	target	Density, mg/cm^3	intensity, 10^{12} W/cm^2	Thickness, mm	Breakout time, ns	Calculated breakout time, ns
2967	agar	10	1.0	1	11	11
				2	31	27
2970	agar	20	0.85	1	26	22
				2	43	42
2981	agar	20	0.6	1	11	
	aerogel	50		2	61	
2982	agar	5	0.25	1	15	10
				2	27	33
2983	aerogel	50	0.55	7.5	163	
2989	aerogel	50	1.0	15	365	
2992	aerogel	50	1.1	2.6	32	
2996	aerogel	50	0.17	3.6	91	
2999	agar	20	0.3	1.7	39	26
				2.7	55	43

Table presents experimental and calculated results, the simulations were carried out by using code MULTI radiative hydrocode [7]. Fig.4 presents thermal wave front position versus time for the experiment #2967.

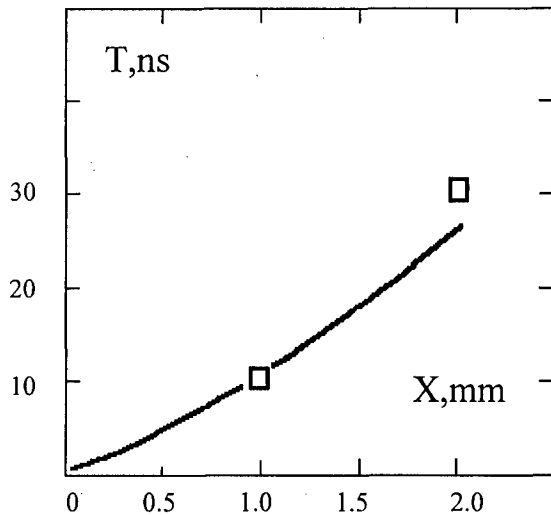


Fig.4 Thermal wave front position for experiment #2967 : agar-agar, density 10mg/cm^3 , x-ray intensity 1TW/cm^2 , stepped target 1mm and 2mm. Squares - experiment. Solid curve - code MULTI. The radiative opacities and emissivities were calculated in local thermal equilibrium by using the SNOP atomic physics code [8,9].

The agreement between theory and experiment is within a factor 1.5. The deviations are attributed to uncertainties in the measured x-ray intensity (about 30%) and also due to several approximations in calculations concerning the spectral and temporal dependence of the drive pulse. Nevertheless, the results demonstrate that the experimental technique is well suited to study radiation hydrodynamics and opacities of hot dense plasma.

HEAVY ION BEAMS RESEARCH

Basic research in the field of plasma physics with heavy ion beams is motivated as follows:

- heavy ion beams are excellent tools for the generation of dense plasmas - plasmas with solid state density - because they deposit their energy in matter along their path in a well understood manner and by direct and rather homogeneous heating of an extended volume. Thus, they open new opportunities for the study of dense plasmas and allow experiments with improved or complementary techniques.
- for inertial confinement fusion (ICF) the heavy ion accelerator is obviously the superior choice for a reactor driver because of its high efficiency and excellent repetition rate. Consequently, it is the interaction of heavy ion beams with dense plasmas and the hydrodynamic and radioactive properties of beam heated target matter that need to be investigated. This includes the development of new diagnostic techniques and the design of appropriate heavy ion targets.

There are two accelerator facilities in process of upgrading to higher intensities: ITEP-TWAC facility at ITEP-Moscow and UNILAC-SIS-18 at GSI-Darmstadt, which could contribute to a great number of problems as the most advanced accelerator facilities with high-power heavy ion beams.

With heavy ion beams, research in this field has been carried out in recent years using the available low intensities at the GSI accelerator facilities with heavy ion beams ranging from a few keV/u up to several hundred MeV/u, mainly with externally heated plasma targets. After completion of the injector upgrade now under construction and a new powerful rf-buncher, target temperatures of up to 10 eV will be obtained at GSI in the very near future. With this upgrade the intensity for beams of very heavy ions will be increased by about a factor of 100 which will open the investigation of hydrodynamic phenomena of dense plasmas.

The expected output parameters of ITEP-TWAC facility are: the energy on target is 100 kJ in 100 ns, or ~ 1 TW of the beam power. The specific deposition power is ~ 10 TW/g, in a spot radius of 500 microns. The temperature reached in a solid Au target is calculated to be up to 40 eV.

The investigation of the interaction process of ion beams with dense plasma is one of the key issues of physics of inertial confinement fusion driven by heavy ion beams. Experiments carried out in Russia (at ITEP-Moscow), in Germany (at GSI-Darmstadt) and in France (at IPN-Orsay) with the discharge plasma up to the electron densities $\sim 10^{19} \text{ cm}^{-3}$ show on a considerable contribution of free electrons to the process of beam-plasma interaction. With the increasing of plasma density influence of the effect of Coulomb coupling are expected to be of great importance. Shock wave technique makes it possible to produce plasma with electron densities up to 10^{22} cm^{-3} . For this goal small-size linear and cumulative explosive driven plasma generators which yields velocities of shock front about 6-20 km/s whereas amount of high explosive does not exceed 30-150g have been developed (fig.5).

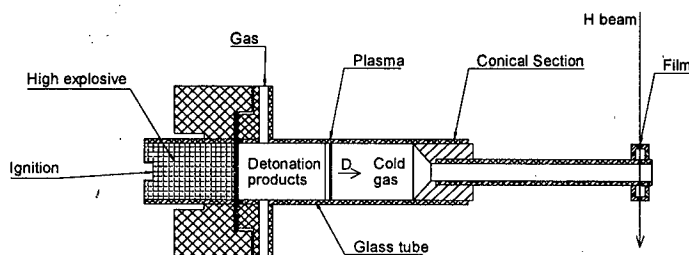


Fig 5. Cumulation explosively driven shock tube.

Detonation products in this device push metal impactor that shapes flat front in investigated gas. Glass tube remains immobile during the time of about $1 \mu\text{s}$ in passage of plasma through the channel. Plasma slug of cylindrical form with diameter from 0.5 to 2cm and thickness of 1cm is created. This plasma object exists about several microseconds that is enough to carry out measurements with ion beams. To protect all the accelerator equipment from the explosion products, plasma generator is placed into special compact vacuum pumped (up to 10^{-2} torr) steel chamber with the diameter of 80cm, which allows to apply charges up to 150g of TNT. This chamber is special designed for the ion beam experiments and provides complete matching with beam line and other experimental diagnostic devices. Differential pumping was provided to be sufficient for insulation of the deep vacuum beam line from low vacuum explosive chamber. To protect beam line from the moving detonation products fast valves were used. They were closed before the moment when explosive products impact the chamber walls.

The proton energy losses were analyzed by using a dipole magnet with a deflection angle of 48° over a radius of 707 mm. The image of the proton beam in the perpendicular to the beam axis was registered by using a microchannel analyzer consisting of a microchannel plate (MCP) and a phosphor screen mounted on a fiber optic disk. The spot image of the proton beam on the screen of the microchannel analyzer was tracked by a charge-coupled-device (CCD) camera (fig.6). Plasma temperature and shock velocity in every explosive experiment was measured. First shots with weakly nonideal xenon plasma (with low initial gas pressure) show good agreement with theoretical predication.

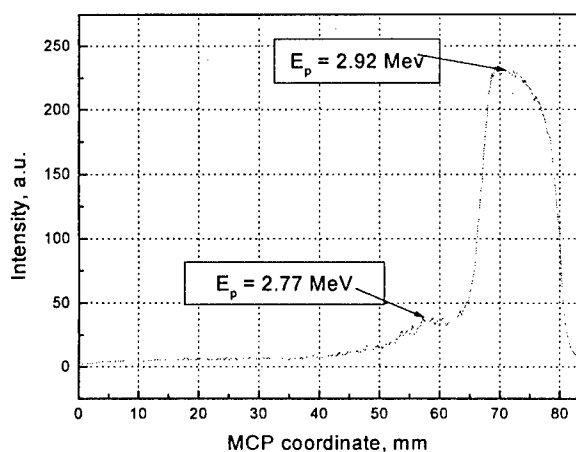


Fig 6. Energy distribution and image of 3-MeV proton beam in the beam - explosively plasma interaction experiment ($P_0 = 0.1$ bar)

CONCLUSION.

The results of the investigations showed that a Z-pinch plasma is a promising source for the high energy density physics studies. The greater duration of the radiation pulse together with high space homogeneity of the irradiation flux compared with conversion of laser radiation into x-rays makes it possible to increase the target thickness and, thus, significantly reduce the effect of sample preheating, which distorts the hydrodynamical picture of the process.

The set of parameters of the ITEP-TWAC facility opens opportunity for :

- experiments addressing some fundamental issues in the physics of dense plasmas like EOS, thermodynamics of strongly compressed matter, plasma phase transitions etc. and
- experiments related to the physics of HIF targets, especially cylindrical targets with magnetized fuel.

REFERENCES

- [1].J.D. Lindl, "Development of the Indirect Drive Approach to ICF and the Target Physics Basis for Ignition and Gain", Phys. Plasmas 2 (11),3933-4024 (1995)
- [2].V.Gasilov, S.Zakharov, V.Smirnov. JETP Lett. **53**,85 (1991)
- [3].P.J.Turchi and W.L.Baker, J.Appl.Phys. **44**,4936(1973)
- [4].V.Fortov, K.Dyabilin, M.Lebedev et al. Laser and Particle Beams (1996),v.14,n0.4,pp.789-792.
- [5].A.Bushman, I.Lomonosov, V.Fortov, The Equation of State of Metals at High Energy Densities. Institute of Chemical Physics, Chernogolovka, Russia, (1992).
- [6].E.Grabovskij, V.Smirnov, S.Zakharov, O.Vorob'ev, K.Dyabilin, M.Lebedev, V.Fortov, A.Frolov. JETP **82**(3),1996, pp.445-450.
- [7].M.Lebedev, K.Dyabilin, K.Eidmann, V.Fortov, E.Grabovskij, V.Smirnov. Physics Letters A,v.240 (1998), pp.73-76.
- [8].Ramis et al Comput. Phys. Commun. (1988) 49, 475
- [9].K. Eidmann.. Laser and particle beams (1994), vol.12, no. 2, pp. 223-244

LONG-IMPLOSION PLASMA RADIATION SOURCE DEVELOPMENT*

J. Levine, P. Coleman, B. Failor, D. Kortbawi, D. LePell, H. Murphy, J. Riordan,
I. Roth, L. Schlitt, P. Sincerny, Y. Song, C. Stallings, E. Waisman, B. Whitton
Maxwell Physics International, San Leandro, CA 94577, USA

C. Coverdale, C. Deeney, D. Jobe, J. McGurn, K. Struve
Sandia National Laboratories, Albuquerque, NM 87185, USA

J. Apruzese, F. Cochran, R. Commisso, J. Davis, A. Fisher,
B. Moosman, D. Mosher, S. Stephanakis, J. Thornhill, B. Weber
Naval Research Laboratory, Washington, DC 20375, USA

R. Schneider
Defense Special Weapons Agency, Alexandria, VA 22310, USA

P. Spence
Pulse Sciences, Inc., San Leandro, CA 94577, USA

E. Yadlowsky
HY-Tech Research Corp., Radford, VA 24141, USA

M. Krishnan
Alameda Applied Sciences Corp., San Leandro, CA 94577, USA

INTRODUCTION

Efficient production of soft x-rays (1 to 5 keV) has been achieved in many laboratories using z-pinch plasma radiation sources (PRS). Typically, the pulsed power generators that drive the PRS loads produce multi-mega-ampere currents with an implosion (conduction) time less than 100 ns. Empirical and theoretical scaling laws indicate that the x-ray yield increases rapidly with current (scaling as I^4 at lower current and I^2 at higher current) [1].

Increasing the current to ever higher levels, with a constant implosion time, would require generators with ever higher voltages and powers, with substantially increased cost, complexity and risk.

We are pursuing an alternative approach: to increase the conduction time of the PRS load before implosion. Maintaining the same x-ray yield requires that the long-implosion-time PRS achieve a temperature and density comparable to that achieved with the 100 ns-implosion-time PRS. Maintaining the temperature requires that the initial radius increase proportionately with implosion time ($r_0 \propto t_{imp}$) to give the same value of η^* (the ratio of JxB work per ion to the internal energy E_{min} when ionized to the K-shell [2]). This leaves the mass unchanged [$m \propto (It_{imp}/r_0)^2$]. Since the final plasma radius must be maintained constant to maintain the

* Work Supported by the Defense Special Weapons Agency

plasma density, the compression ratio must scale with the implosion time ($r_0/r_f \propto t_{imp}$). This increases the number of linear e-foldings for the MHD-Rayleigh-Taylor (MRT) instability to disrupt the implosion ($\gamma_{lin} t_{imp} \propto \sqrt{n_0/\lambda}$). Furthermore, the lower initial density ($n_0 \propto r_0^{-2}$) may produce non-uniform initiation that seeds the MRT instability.

To overcome these potential risks, we will be investigating the application of advanced PRS loads. In this paper we will discuss our experiments with a “solid fill” gas puff, which should experience “snowplow stabilization” of the MRT instability [3] (as compared to the annular shells typically employed). In the future, we plan to field a gas puff producing nested annular shells [4].

The immediate application for this work is at the DECADE Quad facility, currently under construction with initial operation expected in late 1999. In its initial configuration, DQ will be four independent modules employing inductive energy storage and opening switch pulse compression, producing bremsstrahlung radiation. There is a proposal to modify it with a convolute so that the four modules drive a common PRS load with a current risetime of 300 ns and a peak current of approximately 10 MA. X-ray yields of >100 kJ may be possible for an argon load that successfully uses the full DQ capability.

LONG IMPLOSION TIME EXPERIMENTS

Figure 1 shows the gas puff nozzle we employed for this research. It has a 7 cm ID with a central stub that tapers to 1 cm diameter. (The stub protects the puff valve and reduces the required nozzle length.) The anode is a wire mesh, 4 cm from the nozzle, with 12 current return posts on a 15 cm diameter. Twelve notches in the nozzle allow wires to be strung across it, creating an equipotential and a current path for the imploding load.

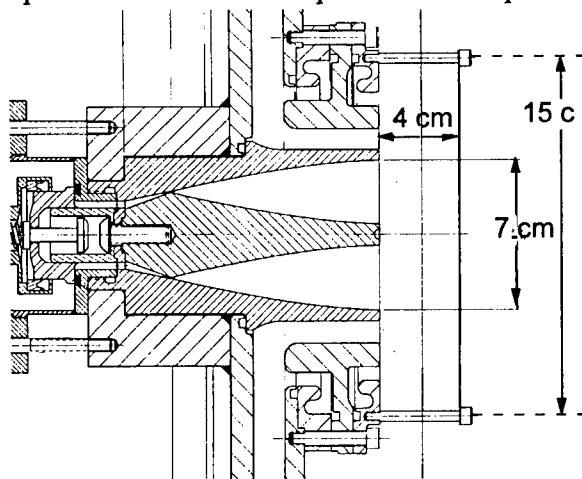


Figure 1. 7 cm solid fill gas puff nozzle.

Measurements of the gas column created by this nozzle are shown in Figure 2. The density minimum on axis, caused by the center stub, has a minimal effect on the mass loading and is predicted to have minimal effect on the implosion dynamics.

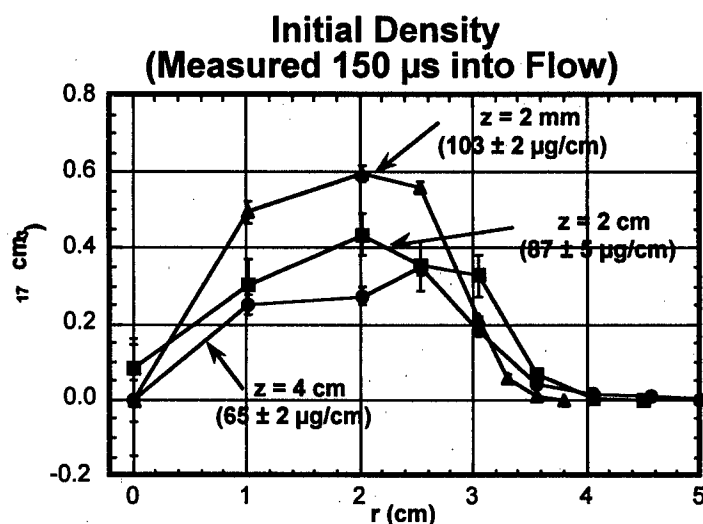


Figure 2. Gas density at three axial locations measured 150 μ s after the onset of gas flow (the time the discharge is typically fired).

To ionize the argon before the discharge, flash cards were sometimes used. On DM2, the flash cards were configured in a ring for uniform UV illumination of the argon [5]; on Saturn, flash cards were placed on two points outside the current return cage, 90° apart.

We report on the results of experiments carried out at the DECADE Module 2 (DM2) facility at Maxwell Physics International and the Saturn facility at Sandia National Laboratories. At DM2, additional experiments with argon in a 10 cm diameter nozzle and with neon in the 7 cm nozzle were performed.

DM2 Results

We have produced 300 ns implosions, at a peak of 2.3 MA, on DM2, as shown in Figure 3, using a 7 cm diameter argon gas puff, yielding 1.7 kJ from the argon K-shell. Figure 4 presents the K-shell x-ray yields from a series of similar shots, with varying mass loads, with and without the nozzle wires described above and with and without preionization. Recognizing the spread in the results, but looking at the envelope of the data points, we see that neither the nozzle wires nor preionization is absolutely necessary for obtaining peak performance, but that each of them is useful, in a statistical sense, for making a good shot more probable.

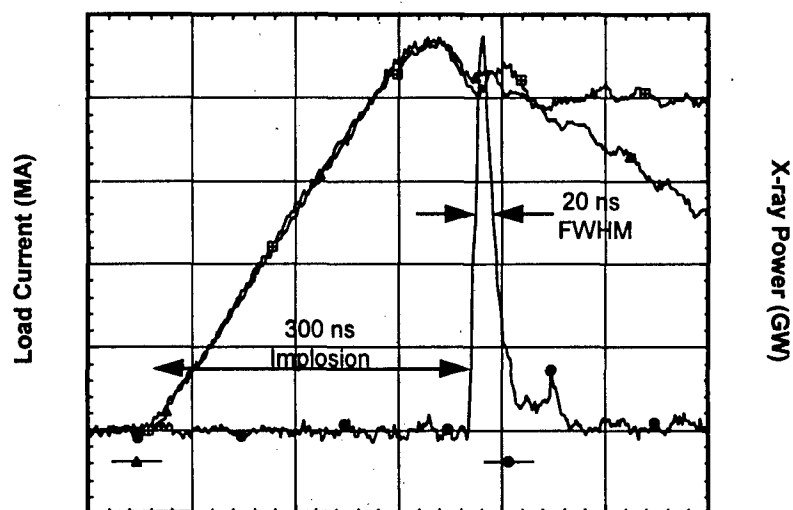


Figure 3. Current and X-ray signal for a 300 ns implosion on DM2.

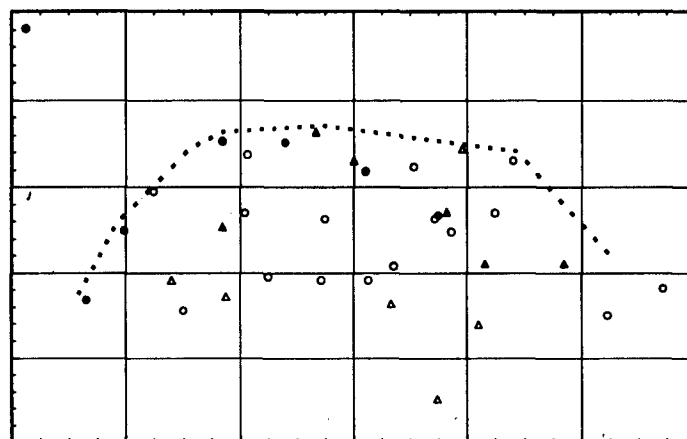


Figure 4. Yield vs. implosion time for a series of DM2 experiments. The dashed curve indicates the envelope of best results.

As discussed above, the anticipated limitation to achieving a good pinch was the Rayleigh-Taylor instability. To determine the uniformity of the final pinch, we used a time-resolved pin-hole camera, sensitive to x-ray energy >3 keV. A series of four images, each separated by 10 ns, is shown in Figure 5. Clearly, as seen in the first frame, the pinch assembles well with no macroscopic disruptions, but breaks up in a non-uniform way, suggesting sausage or kink MHD instabilities.

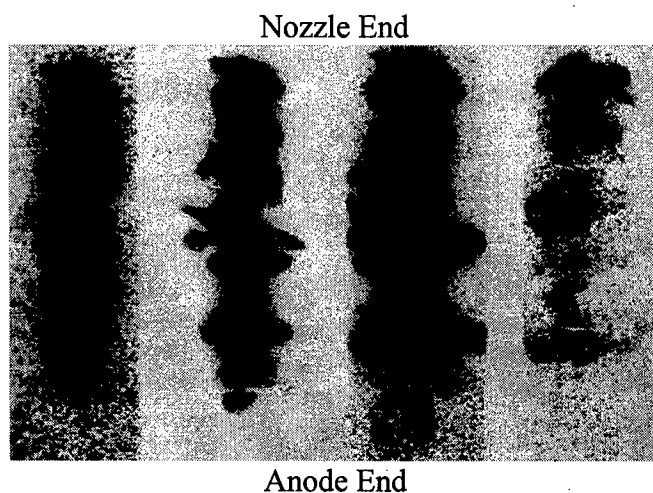


Figure 5. Four K-shell images (10 ns interframe time) of DM2 pinch.

The initiation phase of the pinch was also monitored with time-resolved cameras in both the visible and the XUV (≈ 200 eV). As seen in Figure 6, axial filaments, consistent with the twelve-fold symmetry of the wire meshes at the anode and the nozzle, are often observed. They are more prominent on those shots with nozzle wires. The azimuthal asymmetry they provide may mitigate the $m=0$ Rayleigh-Taylor instability [6].

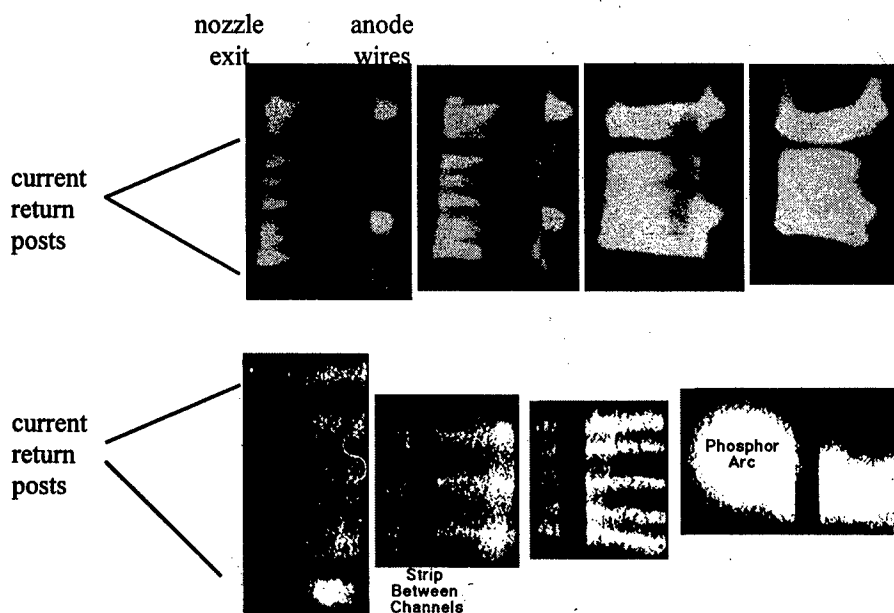


Figure 6. Four optical (21 ns interframe time) and XUV (40 ns interframe time) images of the initial phase of the pinch on DM2.

Spectroscopic analysis of the discharges, using a 2% CF_2Cl_2 dopant in the argon to provide optically thin Cl lines, indicate an electron temperature and density of 0.84 keV and $4.0 \times 10^{20} \text{ cm}^{-3}$, respectively, and an ion energy of 6.9 keV. The value of η^* was 1.1, which is marginal for good x-ray production.

In an attempt to achieve higher η^* , and higher electron temperature, we replaced the 7 cm nozzle with a 10 cm nozzle of similar design. The load mass was reduced to provide the same 300 ns implosion time. While this did result in a higher electron temperature and ion energy (0.95 keV and 16.6 keV, respectively), the pinch was unstable and axially non-uniform. The peak yield was 1.2 kJ. We believe that the Rayleigh-Taylor instability was exacerbated by

inhomogeneous initiation in the lower initial gas density and by the additional e-foldings possible with the larger initial diameter.

To achieve higher η^* with the 7 cm nozzle, we performed a few experiments using a neon gas puff, which has a much lower E_{\min} than argon. The x-ray yield was 13 kJ.

Saturn Results

For these tests, Saturn was configured for long-pulse operation by shorting out the water switches. We took a series of argon shots with the 7 cm nozzle at peak currents of 5.0 to 6.5 MA and implosion times of 160 - 200 ns, producing up to 18 kJ of K-shell radiation. The resultant yields are summarized in Figure 7.

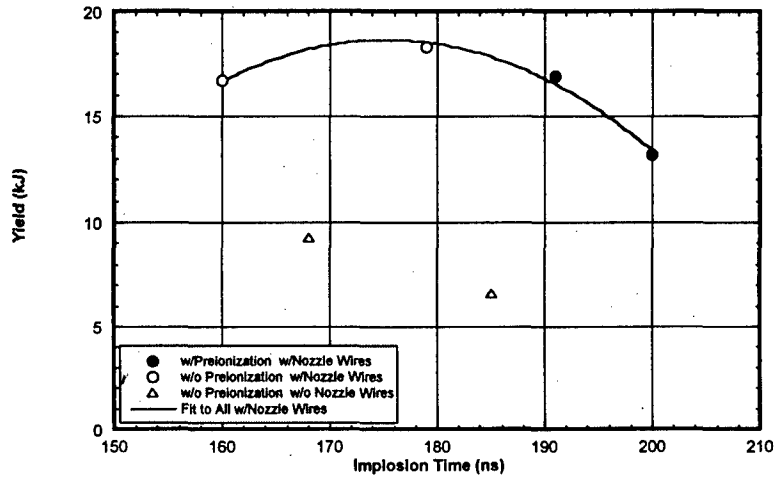


Figure 7. Yield vs. implosion time for the 7 cm argon gas puff shots on Saturn.

The importance of the nozzle wires is evident: they produced approximately a doubling of the K-shell yield. The use of preionization had no effect on the yield. (As discussed above, the preionization was extremely non-uniform.)

As on DM2, the K-shell images, as shown in Figure 8, demonstrate that the pinch assembled stably, without macroscopic disruptions due to Rayleigh-Taylor instabilities.

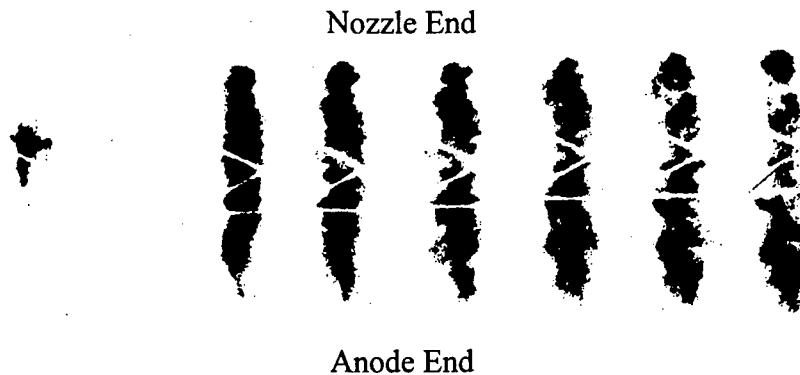


Figure 8. Eight K-shell images (3 ns interframe time) of Saturn pinch. (The second frame is blank due to a dead strip in the camera.)

Using the optically thin Cl lines from the dopant, the measured electron temperature and density were 1.16 keV and $8.8 \times 10^{20} \text{ cm}^{-3}$, respectively, and the ion energy was 12.1 keV. η^* was 1.5.

SUMMARY

We have created large diameter, long implosion time, PRS loads that produce a stable pinch and a narrow x-ray pulse. Operation scaled successfully with current from 2 MA on DM2 to 6 MA on Saturn. The K-shell yields are comparable to those produced by short-pulse operation at a similar current. This approach, therefore, allows substantial savings to be realized in the pulsed-power driver cost, complexity and risk.

REFERENCES

- [1] J. W. Thornhill, K. G. Whitney, C. Deeney, and P. D. LePell, *Phys. Plasmas*, **1**, 321 (1994).
- [2] K. G. Whitney, J. W. Thornhill, J. P. Apruzese, and J. Davis, *J. Appl. Phys.*, **67**, 1725 (1990).
- [3] M.R. Douglas, C. Deeney, and N. F. Roderick, *Phys. Rev. Lett.*
- [4] P. Sincerny, S. Wong, V. Buck, C. Gilman, and T. Sheridan, *Proc. of the Vth Pulsed Power Conf.*, p. 701, IEEE 85C 2121-2 (1985).
- [5] Gas Pre-ionization System for Decade Module 2 PRS Experiments, B. V. Weber, S. J. Stephanakis, B. Moosman, D. D. Hinselwood, R. J. Comisso, A. Fisher, R. C. Fisher, J. C. Riordan, and P. D. LePell, this conference.
- [6] M. S. Derzon, T. J. Nash, and D. D. Ryutov, *Bull. of Am. Phys. Soc.*, **42**, 2069 (1997).



BEAMS'98

12th INTERNATIONAL CONFERENCE
ON HIGH-POWER PARTICLE BEAMS



ORALS

***Beam-Matter
Interaction and
Industrial
Applications***

Vol. I

METALLIC MATERIALS PROCESSING WITH INTENSE PULSED ELECTRON BEAMS

V.P. Rotshtein

*Tomsk State Pedagogical University
75, Komsomol'sky Ave., Tomsk, 634041, Russia*

Abstract. *The paper reviews the results of studies of the mechanisms for modification of the structure and properties of metals and alloys with intense pulsed electron beams over wide ranges of beam parameters ($10\text{--}10^3$ keV, $0.02\text{--}300\text{ }\mu\text{s}$, $1\text{--}2000\text{ J/cm}^2$). For pure metals (Fe and Cu) and Fe-C alloys used as examples, it has been demonstrated that increasing the amount and input rate of the energy delivered to a target allows various conditions for the formation of the beam-affected zone to be realized: from fast melt quenching to shock-wave loading. This makes it possible to produce various nonequilibrium structure-phase states, including nanocrystalline and shock-wave induced structures. It has been shown that low-energy, high-current electron beams are most convenient for the study of microstructural processes at pulsed melting. The sources of this type of beams are most suitable for the surface treatment of articles made of constructional and tool alloys aimed at improving their performance.*

1. INTRODUCTION

In the last few decades, new techniques for surface modification of metallic materials have been developed, which are based on using intense pulsed laser [1], electron [2–4], ion [5,6], and plasma [7] beams. These beams induce superfast heating, melting, and evaporation, superfast solidification as well as stress waves or shock waves. These effects offer the possibility, on the one hand, to investigate nonequilibrium structure-phase transformations and, on the other hand, to solve applied problems related to surface treatment of materials.

Intense pulsed electron beams (PEBs) have a number of important advantages over other types of beam, the main of which is that it is possible to readily vary the penetration depth of electrons by varying their energy. We pioneered the study of the action of PEBs on metals in the mid-70's [8]. In 80's, a series of investigations have been performed by Follstaedt [9] and Demidov [2]. These studies were performed with limited number of materials over comparatively narrow ranges of beam parameters. Therefore, some important features of the formation of the beam-affected zone remained unknown.

The paper reviews the results of studies of the features and mechanisms of PEB modification of the structure and properties for a broad spectrum of metallic materials. Owing to the use of a series of PEB sources created at the Institute of High Current Electronics (Tomsk), the experiments could be carried out for wide ranges of parameters, namely, the electron energy $E = 10\text{--}10^3$ keV, the pulse duration $\tau = 0.02\text{--}300\text{ }\mu\text{s}$, the energy density $E_s = 1\text{--}2000\text{ J/cm}^2$, and the power density $\dot{W}_s = 10^5\text{--}10^{11}\text{ W/cm}^2$. This allowed a target variation of the conditions and mechanisms for the formation of the beam-affected zone: from fast melt quenching to shock-wave loading. The potentialities of using PEBs for surface treatment are discussed as well.

2. CONDITIONS FOR THE FORMATION OF THE BEAM-AFFECTED ZONE

As a result of the absorption of the beam energy in the surface layer of the target, a beam-affected zone is formed which can be subdivided by convention into a heat-affected zone (HAZ) and a zone affected by the stress wave generated on pulsed heating. We determined the temperature field characteristics and the parameters of the stress wave at moderate power densities ($10^6\text{--}10^9\text{ W/cm}^2$) by solving numerically a set of uncoupled one-dimensional equations of thermoelasticity [10, 11]. For modes with evaporation, the amplitude of the stress wave (shock wave) was estimated from the specific absorbed energy and using the data available in the literature [12]. The experiments and the calculations have shown that for Fe within the PEB parameter range under investigation the melt thickness is $10^{-5}\text{--}10^{-2}\text{ cm}$, the HAZ thickness is $10^{-3}\text{--}10^{-2}\text{ cm}$, the maximum values of the melt quenching rate and of the crystal-

lization front velocity achievable at the surface are 10^{10} C/s and about 5 m/s, respectively, and the maximum amplitude of the shock wave is about 50 GPa.

3. SURFACE MODIFICATION OF PURE METALS

Let us consider the effect of irradiation on the microstructure of pure metals with increasing the energy density and the rate of energy delivery to a target.

On irradiation of a pure Fe with a low-energy, high-current electron beam (LEHCEB) in a premelting mode (~ 20 keV, $0.8 \mu\text{s}$, 2 J/cm^2) an extended ($\sim 100 \mu\text{m}$) depth-graded dislocation and grain structure is formed [13]. This is due to the nonuniformity of plastic deformation resulting from the existence of a gradient of the compressive quasi-static stresses ($\sigma \leq 400 \text{ MPa}$) acting on irradiation and due to the following recrystallization processes caused by the heat propagation into the material bulk. After completion of the pulse, residual tensile stresses are formed in the surface layer, whose intensity is about an order of magnitude lower than that of the stresses acting during irradiation [14].

As the melting threshold of iron ($\sim 2.5 \text{ J/cm}^2$) is achieved, layers of increased microhardness having a thickness of $\sim 1\text{--}2 \mu\text{m}$, are formed as a result of fast melt quenching ($\sim 10^{10}$ C/s). It has been established that the vacancy-type defect density in the near-surface layer increases. As the melt thickness increases and the crystallization process correspondingly slows down, the defectness level becomes lower, which can be related to the epitaxial crystallization occurring on the polycrystalline substrate [15].

In an experiment on the action of an LEHCEB with $\tau \sim 50 \text{ ns}$ on recrystallized copper it has been established [8] that plastic deformation of the surface layer occurs as well on irradiation in premelting modes ($\sim 0.5 \text{ J/cm}^2$, $\sim 10^7 \text{ W/cm}^2$); however, twinning is observed along with conventional slipping. The presence of twins is direct evidence of fast loading. The amplitude of the bipolar stress wave at which twinning takes place is $\sim 200 \text{ MPa}$. This is about two orders of magnitude lower than that realized on high-speed impact [16]. The more pronounced tendency to twinning on pulsed heating may be related to the sign-varying character of the loading. As the melting threshold is achieved, despite the high quenching rate, the dislocation density decreases substantially. This correlated with the above data obtained for iron.

With $W_s \geq 10^8 \text{ W/cm}^2$ ($\sim 250 \text{ keV}$, $\sim 10^{-7} \text{ s}$), the bipolar wave amplitude increases to $\sim 2 \text{ GPa}$ and the role of the wave in the formation of the microstructure becomes more pronounced [17]. Using Fe and Cu targets as examples, it has been established that on irradiation in these modes a depth-graded structure is formed that has two characteristic maxima of vacancy density: one at the surface and other at the depth $\sim 30 \mu\text{m}$ [18]. From calculations it follows that the first maximum is formed as a result of melt quenching. The second maximum is located beyond the HAZ at that depth where the compressive pulse amplitude reaches the dynamic yield limit in the process of formation of a stress wave [19].

4. PRODUCTION OF HARDENED LAYERS IN CARBON STEELS

The character and degree of hardening of carbon steels depends on the original state of the material and on the PEB parameters. For Steel 45 (0.45% C) as an example, irradiated with a low-energy PEB in surface melting modes, it has been established that with $\tau \geq 10^{-5} \text{ s}$ and $W_s = 10^5\text{--}10^7 \text{ W/cm}^2$ a thermal (quenching) mechanism of the surface hardening is realized. The maximum hardening is attained for previously quenched steels [12, 20].

As the pulse duration is decreased to $\sim 1 \mu\text{s}$ (LEHCEB action), the character of hardening changes abruptly. In this case, an extended ($\sim 200 \mu\text{m}$) hardened zone is formed with two microhardness maxima (Fig. 1,a), and on repeated irradiation the microhardness reaches abnormally high values ($H_\mu \sim 1600 \text{ kg/mm}^2$). No hardening occurs at the surface [21].

As the number of pulses is increased, the γ -phase is accumulated in the HAZ ($\sim 15 \mu\text{m}$), which is related to the increase in carbon concentration. Layer-by-layer transmission electron microscopy (TEM) has shown that a depth-graded structure is formed in the HAZ, such that a thin ($\sim 0.2 \mu\text{m}$) near-surface layer quenched from melt contains a nanocrystalline structure consisting of grains of α - and γ -phases and not involving martensite crystals (Fig. 1,b). This correlates with the observation that the melt quenching rate and the crystallization front velocity reach their maxima ($\sim 10^{10} \text{ C/s}$ and $\sim 5 \text{ m/s}$, respectively) at the surface [21].

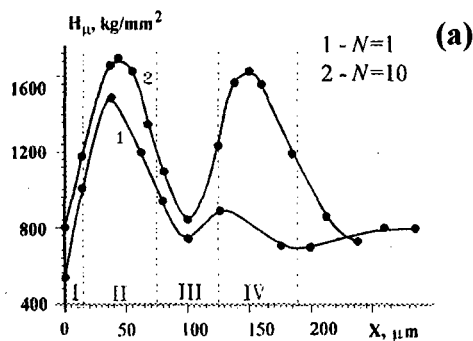


Fig 1. Microhardness profiles (a) and a TEM dark-field image (reflex of $[110] \alpha\text{-Fe}$) and a diffraction pattern of the near-surface layer (b) for prequenched steel 45 irradiated by an LEHCEB (2.5 J/cm^2 , $0.7 \mu\text{s}$).

It has been established that on quenching from liquid state, martensitic transformation is realized only if the thickness of the molten layer is over a critical value equal to $\sim 5 \times 10^{-4} \text{ cm}$. This is related to the existence of a minimum critical size of the original phase grain ($\sim 10^{-4} \text{ cm}$) necessary for nucleation of martensite crystals [20].

In the maximum microhardness regions lying beyond the HAZ, fragmentation and twinning of the original martensite crystals, an increase in long-range stresses, and segregation of dispersed particles of cementite are observed. The greatest contribution to the increase in microhardness is associated with grain-boundary hardening (fragmentation of martensite) and dispersion hardening (segregation of cementite) [21]. The experiments have shown that the formation of hardened layers is due to the action on martensite of cyclic bipolar low-amplitude waves [12, 22]. We believe that the dominant role here is played by the carbon present in the original martensite structure. As distinct from the original ferritic-pearlitic structure, martensite contains carbon in a weakly bound state (mainly, at vacancies and dislocations). Therefore, even at low amplitudes of the stress wave, the carbon in martensite is prone to diffusion, accumulation at certain sites, and formation of dispersed cementite.

With increasing E and W_s the contribution of stress waves to the formation of hardened layers becomes more substantial. This is most pronounced for thin (0.6 mm) targets prepared from prequenched Steel U10A (1% C) irradiated with an HCEB (350 keV, 40 ns, $\sim 10^9 \text{ W/cm}^2$). In this case, along with the near-surface hardened layer (due to quenching from high temperatures), two layers located at the face and rear surfaces are formed (Fig. 2). Comparison of the microhardness profile with that predicted by numerical simulation has shown that the formation of the subsurface microhardness maxima is due to a local increase in the amplitude of the stress wave (to 2.5 GPa) on its reflection from free surfaces (Fig. 3). According to TEM data, the martensite in the regions of microhardness maxima undergoes the same structure-phase transformations as on irradiation with an LEHCEB. In bulky specimens, only the surface (quenched) hardened layer is formed, since the stress wave has time to damp substantially until it arrives at the rear surface [11].

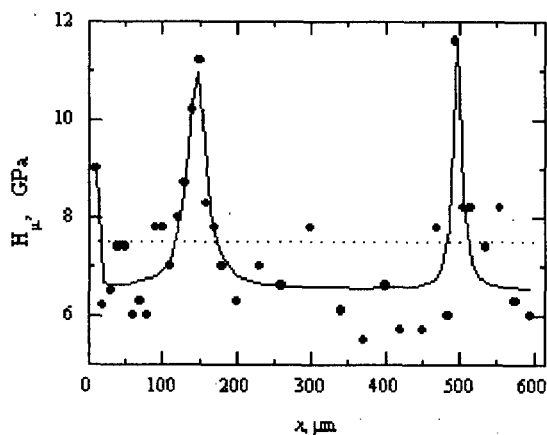


Fig 2. Microhardness profile for a thin specimen of prequenched steel U10A (1% C) irradiated with HCEB ($\sim 350 \text{ keV}$, $\sim 10^9 \text{ W/cm}^2$, $\sim 40 \text{ ns}$). $N=10$.

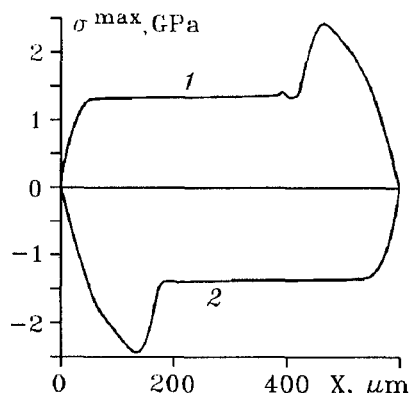


Fig 3. Depth distributions of the maximum values of positive (1) and negative (2) stresses achieved in the target for the case presented in Fig 2.

Further increasing energy input (~ 1 MeV, ~ 50 ns, 5×10^{10} W/cm²) leads to the formation of a shock wave (~ 50 GPa) and to rear spalling. In a bulky specimen of previously quenched Steel 45 irradiated in a prespalling mode, a quasi-periodically hardened structure is formed throughout the specimen thickness [23]. As in the above experiment, the abnormally high microhardness in the hardened layers is related to the fragmentation of original martensite crystals and to the formation of dispersed particles of cementite. This is evidence of a unified deformation-wave mechanism of hardened of the original martensite structure irrespective of the parameters of the stress wave (shock wave).

On the rear side of the same specimens, nonequilibrium structures, namely, graphite-ferritic, ferritic, and other are formed that are regularly disposed in depth [23]. This may be related to a redistribution of carbon and to a pulsed heating of the rear surface on reflection of the shock wave. For gray cast iron specimens loaded under the same conditions, a new phase corresponding to diamond is formed on the rear side [12]. This correlates with abnormally high microhardness (~ 2500 kg/mm²) and with the data reported elsewhere [24].

Thus, it has been shown that varying the beam parameters, one can vary the contributions of the quenching and strain-stress-wave mechanisms of hardening in the carbon steels and to produce controllable depth-graded structures showing high strength properties.

5. MODIFICATION OF METALLIC ALLOYS WITH LEHCEBS

In practical terms, the sources of LEHCEBs of duration $\sim 10^{-6}$ s are most convenient for surface treatment [3, 22]. The results of investigations for carbon steels have been discussed in Sec. 4. Testing has shown that the hardening of these steels is accompanied by an about twofold decrease in wear rate. Let us dwell on results obtained for other materials.

Stainless steels. It has been shown [25] that repeated pulsed melting of austenitic steel (similar to Steel 304) results in smoothing and cleaning of the surface and allows a substantial enhancement of the corrosion resistance. More detailed investigations with specimens of Steel 440A and Steel 304 have demonstrated that the near-surface layer (~ 0.2 μ m) is enriched with chromium due to its liquid-phase diffusion from deep-lying molten layers to the carbonized surface. Depending on E_s and, hence, on the crystallization conditions, partial or complete dissolving of the originally present particles of second phases take place. As a result of rapid resolidification, a nondisoriented nanosized (up to ~ 100 nm) or submicron structure is formed at the surface of Steel 440A (Fig. 4) and Steel 304, respectively. This structure is stable due to the presence of dispersed second-phase segregates at intraphase boundaries. These structure-phase transformations, as expected, enhance the corrosion resistance [22].

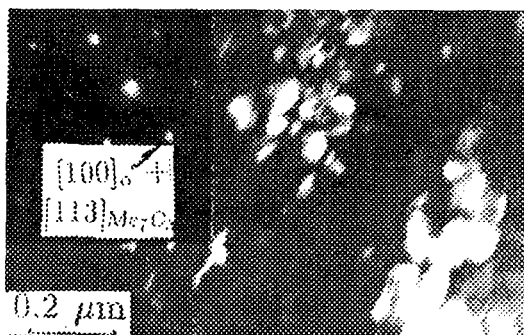


Fig. 4. TEM dark-field image in the reflex of $[110] \alpha\text{-Fe} + [113] \text{M}_7\text{C}_3$ and a diffraction pattern of the microstructure of the near-surface layer of stainless steel 440A irradiated with an LEHCEB (27 J/cm^2 , $2.5 \mu\text{s}$, $N=1$)

Aluminum alloys. After pulsed melting (melt region ~ 7 μ m), in the surface layer of thickness 0.4 μ m, complete (Al2024 alloy) or partial (Al6061 alloy) dissolving of coarse (≥ 1 μ m) particles takes place and the second-phase segregates become smaller. When the irradiation of Al2024 alloy is more intense (melt region ~ 25 μ m), an ordered structure is formed in the surface layer of thickness ~ 1 μ m as a result of dissolving of coarse particles followed by decay of an oversaturated solid solution. This structure consists of nondisoriented submicron grains of the matrix phase and nanosized CuAl_2 segregates coherently bound with the matrix. Moreover, microcracks are observed, which may be related to the shrinkage of the molten layer on solidification. For Al6061 alloy under similar conditions, complete dissolving of all second-phase particles and segregates take place. On the surface itself, an Al_2O_3 film homogeneous in thickness (~ 30 nm) is formed. This enhances substantially the corrosion resistance. Irradiation also results in surface hardening of both alloys [26].

Titanium alloys. Experiments were performed with specimens of types BT8M (Ti-5.8 Al-3.7 Mo) and BT18Y (Ti-6.3 Al-4.5 Zr) alloys. Investigations [27] have shown that pulsed melting makes it possible to clean the surface of oxygen and carbon impurities, to increase the Al content in the near-surface layer to 20%, to attain a more uniform distribution of the components throughout this layer, and to reduce the surface roughness to 0.10 μm . However, this changes the phase composition to some extent, gives rise to low-intensity residual tensile stresses, and results in microcraters appearing on the surface. Optimum irradiation modes allow suppression of the crater formation, and subsequent annealing permits the original phase composition to be recovered. As a result, the fatigue limit increases by more than 20% and the fatigue life by more than tenfold (Fig. 5). As revealed by fractography, this is due to the fact that the fracture mechanism changes from surface to subsurface.

Hard alloys. Used for the study were cutting inserts made of hard alloys of types BK8 (WC-8 Co), T15K6 (WC-15 TiC-6 Co), and T5K10 (WC-5 TiC-10 Co). As the energy density is increased, the degree of liquid-phase dissolving of the carbide and binding phases increases gradually as a result of contact melting. This leads to extra saturation of the binder with W and C, its grains becoming smaller. As a result, the microhardness at the surface increases by $\sim 20\%$ over the original value. Further increasing energy density leads to degradation of the surface and to a reduction in microhardness. The latter is related to the formation of low-strength metastable carbides with an fcc lattice.

Testing has shown that after irradiation, the durability of the inserts has increased twofold or even threefold (Fig. 6). This may be due to the fact that the diffusion of the components of the material under treatment into the binding in the process of cutting is hindered substantially because of the grain becoming smaller and the formation of a Co-base solid solution. This prevents the cutting edge from brittlement. On the other hand, contact melting increases the linkage strength between the carbide and binding the phase due to liquid-phase diffusion [22].

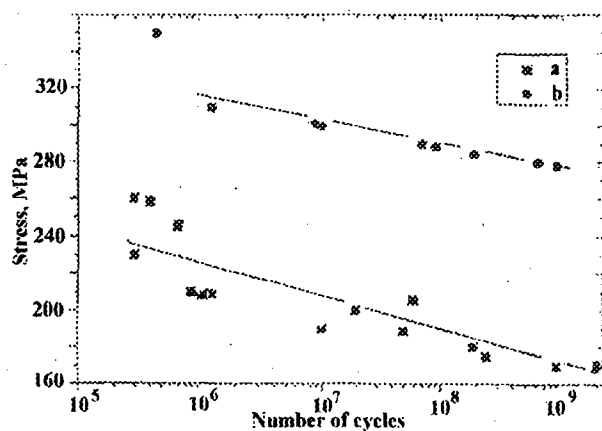


Fig 5. Fatigue curves for BT8M alloy specimens in the original state (a) and after irradiation (2.5 J/cm^2 , 40 shots) and annealing (b).

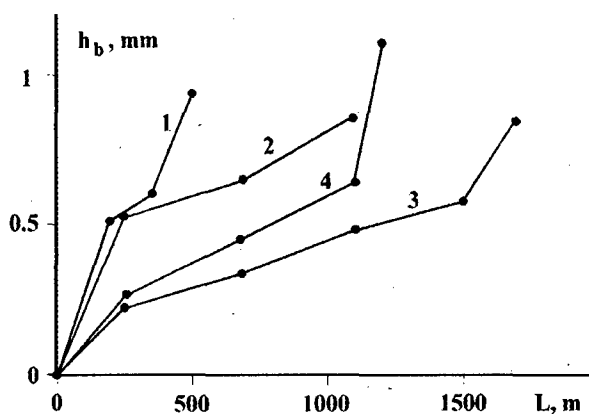


Fig 6. Wear test curves for inserts made of T5K10 hard alloy before (1) and after irradiation by an LEHCEB with different values of E_s (2-4).

6. OTHER PROMISING APPLICATIONS OF LEHCEBS

Smoothing of heat-resistant protective coatings. Heat-resistant protective coatings based on Ni (e.g., Ni-Cr-Al-Y) have originally a rather rough surface. Surface melting enhances their resistance to heat owing to an abrupt reduction in roughness [28].

Removal of heat-resistant protective coatings. LEHCEB irradiation can be used instead of the routine, laborious and ecologically harmful technology for removal of waste coatings. Experiments have shown that coatings like these can be removed efficiently ($\sim 1 \mu\text{m}$ per pulse) with $E_s \geq 20 \text{ J/cm}^2$. With that, the structure of the substrate changes only slightly [28].

Production of high-concentrated surface alloys. With $E_s \geq 10 \text{ J/cm}^2$, it is possible to produce surface alloys by pulsed deposition of coatings and remelting of the surface layer. Experimentation with Cu-Fe and other systems has shown that the concentration of the alloying component is much over its equilibrium concentration. The thickness of the so produced layers is an order of magnitude greater than that realized on ion implantation [22].

Enhancement of electric strength of vacuum insulation. Pulsed melting smoothes and cleans the electrode surfaces. When combined with subsequent conditioning of the gap with low-current pulsed discharges, this decreases substantially the prebreakdown currents and enhances the electric strength of the vacuum insulation [29].

7. SUMMARY

Using PEBs with parameters varied over wide ranges, which has made possible modeling of various conditions and mechanisms for the formation of the affected zone, it has been investigated how the changes in the structure-phase state and physical, chemical, and strength properties of metals and alloys caused by PEB irradiation are related to the characteristics of the temperature and stress fields responsible for these changes. It has been demonstrated that PEBs offer an efficient tool both for studying nonequilibrium structure-phase transformations and fast deformation in metals and alloys and for developing new efficient techniques for surface treatment of materials and articles. LEHCEB sources have been shown to be promising for solving a number of material science and applied problems.

The author would like to thank G.A. Mesyats for his interest and support of this work, D.I. Proskurovsky, V.I. Itin, S.V. Lykov, Yu.F. Ivanov, E.F. Dudarev, A.B. Markov, V.A. Shulov, A.D. Pogrenjak, and G.E. Ozur for numerous contributions to the research. The work was supported in part by the U. S. Department of Energy through Sandia National Laboratories.

REFERENCES

- [1] N.N. Rykalin, A.A. Uglov, I.V. Zuev, and A.N. Kokora. *Laser and Electron Beam Treatment of Materials*. Handbook. Moscow. Mashinostroenie, 1985, 496 p.
- [2] L.I. Rudakov, B.A. Demidov, V.C. Uglov. *Fiz. i Himiya Obrab. Mater.*, 1989, 5, p. 11.
- [3] D.I. Proskurovsky, V.P. Rotshtein, G.E. Ozur. *Surf. Coat. Technol.* 96, 1997, 1, p. 115.
- [4] G. Miller, G. Shumacher, D. Straus, et al. *BEAMS'96*, Prague, 1996, v.2, p. 809.
- [5] G.E. Remnev, I.F. Isakov, M.S. Opekunov, et al. *Surf. Coat. Technol.* 96, 1997, 1, p. 103.
- [6] R.W. Stinnett, R.G. Buchheit, F.A. Greulich, et al. *J. Mat. Res. Soc. Symp. Proc.* 1994, 316, p. 521.
- [7] B.A. Kalin, V.L. Yakushin, V.I. Vasiliev, et al. *Surf. Coat. Technol.* 96, 1997, 1, p. 110.
- [8] V.P. Rotshtein, L.S. Bushnev, D.I. Proskurovsky. *Izv. Vyssh. Uchebn. Zaved. Fiz.*, 1975, 3, p. 130.
- [9] D.M. Follstaedt. In book: *"Laser and Electron Beam Interaction with Solids"*, Ed. by B.R. Appleton and G.K. Celler, North-Holland, New York, 1982, p. 377.
- [10] A.B. Markov, V.P. Rotshtein. *Nucl. Instr. And. Meth.* B132 (1), 1997, p. 79.
- [11] A.B. Markov, V.P. Rotshtein. *Fiz. i Himiya Obrab. Mater.*, 1997, 6, p. 37.
- [12] V.P. Rotshtein. *D. Sc. Thesis*, Institute of High Current Electronics, Tomsk, 1995.
- [13] E.F. Dudarev, L.A. Kornienko, C.V. Lykov, et al. *Izv. Vyssh. Uchebn. Zaved. Fiz.*, 1993, 5, p. 42.
- [14] E.F. Dudarev, G.P. Pochivalova, D.I. Proskurovsky, et al. *Izv. Vyssh. Uchebn. Zaved. Fiz.*, 1996, 3, p. 126.
- [15] A. Zecca, R. Brusa, M. Duarte Naia, et al. *Phys. Lett. A*, v. 175, 6, 1993, p. 433.
- [16] M.A. Mogilevsky, L.S. Bushnev. *Fizika Goreniya i Vzryva*, 1990, 2, p. 95.
- [17] S.V. Lykov, V.I. Itin, G.A. Mesyats, et al. *Dokl. Akad. Nauk SSSR*, 1990, v. 310, 4, p. 858.
- [18] V.I. Itin, C.V. Lykov, G.A. Mesyats, et al. *Proc. Int. Conf. "Energy Pulse Modification of Materials"*, Dresden, 1989, (Physical Research, 1990, Akademie-Verlag, Berlin, p. 331.
- [19] V.I. Itin, C.V. Lykov, D.I. Proskurovsky, et al. *Proc. III Conf. on Modification of Properties of Construct. Materials by Charged Particles Beams.* Tomsk, Russia, 1994, v. 1, p. 166.
- [20] Yu. F. Ivanov, M.P. Kashchenko, A.B. Markov, V.P. Rotshtein, *Zh. Tekhn. Fiz.*, 1995, 65, 3, p. 98.
- [21] Yu. F. Ivanov, V.I. Itin, S. V. Lykov, et al. *Izvestiya RAN. Metall.*, 1993, 3, p. 130.
- [22] D.I. Proskurovsky, V.P. Rotshtein, G.E. Ozur, et al. *J. Vac. Sci. and Tech. (A)* 16 (4), July/August, 1998.
- [23] I.M. Goncharenko, A.M. Efremov, Yu. F. Ivanov, et al. *BEAMS'92*, Washington, DC, 1991, v. 3, p. 1948.
- [24] Yu. N. Taran, V.V. Sobolev, S.I. Gubenko, et al. *Doklady Akad. Nauk SSSR*, 1991, v. 319, 4, p. 1374.
- [25] I.M. Goncharenko, V.I. Itin, S.V. Isichenko, et al. *Zashchita Metallov*, 1993, v. 29, 6, p. 932.
- [26] D.S. Nazarov, A.B. Markov, G.E. Ozur, et al. *Proc. of 5 Intern. Conf. On Electron Beam Technologies, (EBT'97)*, Varna, Bulgaria, 1997, p. 215.
- [27] N.A. Nochovnaja, V.A. Shulov, V.P. Rotshtein, et al. *EBT'97*, p. 215.
- [28] Yu.D. Yagodka, K.M. Pastuhov, S.I. Kuznetsov, et al. *Himija Obrab. Mater.*, 1995, 5, p. 111.
- [29] A. V. Batrakov, A.B. Markov, G.E. Ozur, et al. *IEEE Trans. on Dielectric. and Electric Insul.*, Apr. 1995, 2, p. 237.

APPLICATIONS OF INTENSE PULSED LIGHT ION BEAMS TO MATERIALS SCIENCE

K. Yatsui, W. Jiang, N. Harada and T. Sonegawa

Laboratory of Beam Technology, Nagaoka University of Technology

Nagaoka, Niigata 940-2188, Japan

Abstract By an intense pulsed light ion beam (LIB) interaction with target, high density ablation plasma is produced (ion beam ablation plasma: IBAP) due to short range of LIB. Since the first preparation of thin films of ZnS by IBAP in 1988 (ion beam evaporation: IBE), we prepared various kinds of thin films. In addition to standard front side deposition by IBE (FS/IBE), where a substrate is located in front of the target, significant improvement has been achieved of the film quality by back side deposition (BS/IBE), where the substrate is placed just behind the holder. Characteristics of the films by BS/IBE will be shown. By rapid cooling of IBAP, we synthesized nanosize powders. Fullerene has also been successfully prepared. Furthermore, foil acceleration has been studied by the irradiation of LIB on a target. Quick overview will be given on the applications of IBAP in materials science.

1. INTRODUCTION

Inherent to short range of ion beams in targets, high-density ablation plasma can be obtained by the intense pulsed LIB interaction with solid targets. The method to prepare thin films by IBAP has been named IBE, which has the following features [1-9]. 1) Due to high-density plasma (typically 10^{19} cm^{-3}), the deposition rate is extremely high ($\sim \text{cm/s}$). 2) Since the pulse width of LIB is short compared to thermal conduction time, the phenomenon is considered as adiabatic. Inherent to very high density, we do not need to heat the substrate. Thus, it is basically low temperature process. 3) Since the preparation takes place within very short time scale, the contamination problems are not so serious due to poor chance to interact with impurities. Thus, good agreement of the composition ratio has been obtained between the target and the films prepared, resulting in excellent stoichiometry.

Since the first demonstration of preparing thin films of ZnS in 1988, we have successfully prepared various kinds of thin films, such as YBaCuO, ITO, c-BN, ZrO_2 , C, BaTiO₃, and apatite. Taking $(\text{Ba}_x\text{Sr}_{1-x})\text{TiO}_3$ as an example, several data will be shown in this review.

If the diameter of particles is less than $1 \mu\text{m}$, which is called ultrafine nanosize powders, the characteristics significantly differ from those of the bulk. Inherent to its huge specific surface area, noticeable reduction of the melting point has been reported as well as decrease in the sintering temperature. There were proposed two methods: chemical and pulsed laser deposition (PLD). However, there were problems on purity and byproducts with the former method, while a drawback on mass production with PLD. Here, several characteristics on the powder production by IBE will be introduced [7, 10, 11]. In addition, a new method will be introduced to produce powders by a pulsed wire discharge. It is very simple in principle and very cheap, which will be very attractive to produce a large amount of powders.

Recently, a lot of attention has been paid on fullerene, the shape of which is known to be similar as a soccer ball. It is physically stable, but chemically unstable. Using IBAP, we have successfully prepared a fullerene, which involves their higher orders as well.

Using IBAP, we have started the foil acceleration to obtain high density/pressure. Thick

foil of Al was irradiated by LIB, and the rest of the range was accelerated by the reaction [12].

2. PREPARATION OF THIN FILMS BY IBE [1~9]

Very efficient preparation of thin films has been achieved by FS/IBE. Though it has the extremely high instantaneous deposition rate, there has been often found droplets or splashing particles as similarly found by PLD. To avoid them, we have proposed BS/IBE, where the substrate is placed just behind the holder. As an example, characteristics of $(\text{Ba}_x\text{Sr}_{1-x})\text{TiO}_3$ films prepared by BS/IBE will be presented, being x (composition ratio) as a parameter.

Figure 1 shows the basic principle of FS/IBE and BS/IBE. A magnetically insulated diode (MID) focused geometrically was used. Typical beam parameters were beam energy ~ 1 MeV and energy density ~ 30 J/cm². Though the deposition rate of BS/IBE is one order of magnitude lower than that by FS/IBE, the film surface is very smooth with good morphology.

Figure 2 shows a typical SEM photograph of the cross section of SrTiO_3 film prepared by 30 shots with BS/IBE, where $x = 0$. From Fig. 2, the film thickness is seen to be ~ 800 nm, giving the deposition rate ~ 27 nm/shot. From the thickness distribution of the film, we have observed the uniformity to be $\sim \pm 8\%$. It is noticed that the film is prepared like a column.

Figure 3 shows an AFM data of SrTiO_3 film prepared by one shot (BS/IBE). From Fig. 3, we see there are few droplets on the surface. Furthermore, the roughness has been estimated to be R_a (average) ~ 2.5 nm, R_{ms} (mean square) ~ 3.2 nm, and R_{max} (maximum) ~ 30 nm.

Figure 4 shows a RBS (Rutherford backscatter spectroscopy) data (dots) of the film obtained by BS/IBE using $(\text{Ba}_{0.5}\text{Sr}_{0.5})\text{TiO}_3$ target, being compared with the theoretical estimate (solid line) for $\text{Ba}:\text{Sr}:\text{Ti}:\text{O} = 0.5:0.5:1:3$. As seen in Fig. 2, the composition ratio of the film is in very good agreement with that of the target, indicating an excellent stoichiometry.

3. SYNTHESIS OF ULTRAFINE NANOSIZE POWDERS BY IBE [7,10,11]

By rapid cooling of IBAP with the interaction with the gaseous molecules, it has been demonstrated to synthesize nanosize powders. Powders synthesized were collected by three membrane filters located at 330 mm downstream from the target, and characterized by XRD (X-ray diffraction), SEM (scanning electron microscope), TEM (transmission electron microscope), and TED (transmission electron diffraction). Furthermore, the specific surface area and average diameters have been determined by BET (Brunauer-Emmett-Teller) method based upon the measurement of the absorbed nitrogen before and after the powders.

Figure 5 shows a typical TEM photograph of $\gamma\text{-Al}_2\text{O}_3$, where the target and the ambient gas were aluminum and oxygen (~ 10 Torr), respectively. It is clear that there exist a lot of powders of spherical shape, and that the diameter is less than several tens of nm.

Using various combinations of the target and ambient gas, we have successfully synthesized many kinds of powders, which are summarized in Table I. From survey on the experimental parameters, it has been found that the size and its distribution strongly depend on ambient gas pressure as well as the parameters of IBAP and LIB.

4. SYNTHESIS OF FULLERENE BY IBE

By the LIB irradiation on carbon graphite, we have recently succeeded in the synthesis of fullerene (C_{60}). As well known, its shape is similar to a soccer ball. To obtain the ablation plasma more efficiently, the ablation plasma has been collected in the concave box. Figure 6 shows a mass spectrometer data of the soot collected. In addition to C_{60} , it is clearly found the presence of higher order of fullerene up to C_{96} . Optimization is being carried out on the formation of fullerene by surveying the experimental conditions.

5. PREPARATION OF THIN FILMS AND NANOSIZE POWDERS BY PULSED WIRE DISCHARGE [13]

Pulsed wire discharge has been successfully applied to synthesize ultrafine nanosize powders. By use of a capacitor bank, pulsed current flows through a metal wire located in an ambient gas. The current deposits the electrical energy in the wire due to finite resistance. The deposited energy melts, evaporates, and ionizes the wire, resulting in a plasma that expands into the ambient gas. The high temperature plasma is then cooled down by the interaction with the ambient gas, giving rise to high temperature vapor of the wire material that condenses uniformly in the gas. The discharge was carried out by peak current of ~ 10 kA, pulse width of ~ 20 μ s, and pulse energy of ~ 80 J.

Figure 7 shows the specific surface area and average diameter of TiN powders as a function of nitrogen pressure, where a wire of titanium was used. At lower pressure, the surface area increases rapidly, while the average diameter decreases.

Table II summarizes the results of the powders synthesized. As mentioned in the powders by IBAP, it has been made clear to control the size, the size distribution, and the average diameter, as well as the specific surface area by experimental parameters.

6. FOIL ACCELERATION BY IBAP [12]

Figure 8 shows the basic principle of the foil acceleration by IBAP. The target (aluminum) is irradiated by LIB. The material within the range will be ablated, the rest of which will be accelerated forward. The ion diode used was MID or self-magnetically insulated spherically plasma focus diode (SPFD). Typically, the energy density was ~ 100 J/cm² and ~ 4 kJ/cm² for MID and SPFD, respectively. From the velocity measurement, we have obtained the velocity of ~ 3 km/s and the pressure of ~ 5 GPa by using SPFD. It is noted here that a significant increase in the hardness has been observed of the target accelerated and collided onto the dumped wall.

7. CONCLUDING REMARKS

Recent progress has been overviewed on the applications of high density IBAP inherent to short range of LIB in targets, mainly associated with the applications to materials science in LBT, Nagaoka. Compared to normal FS/IBE, quality of thin films has been significantly improved by BS/IBE, giving very good morphology. By rapid cooling of the IBAP with ambient gas molecules, we have succeeded in efficient synthesis of nanosize powders. Furthermore, the production of higher order of fullerene has been demonstrated by IBAP. Pulsed wire discharge has been found to be very useful to produce nanosize powders as well. Foil acceleration has been demonstrated by IBAP. By the LIB interaction with thick foil of aluminum, we have obtained the velocity ~ 3 km/s and the pressure ~ 5 GPa. Significant increase in hardness has been observed of the accelerated foil. In addition to being initially developed as an energy driver for an inertial confinement fusion in late 1970, new and novel applications of LIB have been available nowadays, particularly in materials science.

REFERENCES

- [1] Y. Shimotori et al.: J. Appl. Phys. **63**, 968 (1988).
- [2] Y. Shimotori et al.: Jpn. J. Appl. Phys. **28**, 468 (1989).
- [3] K. Yatsui: Laser Part. Beams **7**, 733 (1989).
- [4] K. Yatsui et al.: Phys. Plasmas **1**, 1730 (1994).
- [5] T. Sonegawa et al.: Appl. Phys. Letters **69**, 2193 (1996).
- [6] T. Sonegawa et al.: Laser and Particle Beams **14**, 537 (1996).
- [7] K. Yatsui et al.: Jpn. J. Appl. Phys. **36**, 4928 (1997).
- [8] K. Yatsui et al.: Proc. 11th IEEE Int'l Pulsed Power Conf., Baltimore, **I**, 13 (1997).
- [9] K. Yatsui et al.: Mater. Chem. & Phys. **54**, 219 (1998).
- [10] K. Yatsui et al.: Appl. Phys. Letters **67**, 1214 (1995).
- [11] Y. Nakagawa et al.: J. Mater. Sci. **33**, 529 (1998).
- [12] W. Jiang et al.: Nucl. Instr. Methods A (in press) (1998).
- [13] W. Jiang et al.: submitted for publication in IEEE Trans. Plasma Sci. (1998).

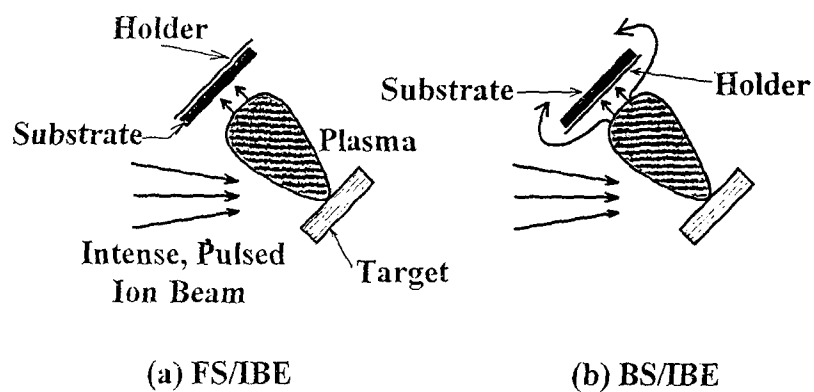


Fig. 1 Principle of IBE technique: (a) FS/IBE, (b) BS/IBE.

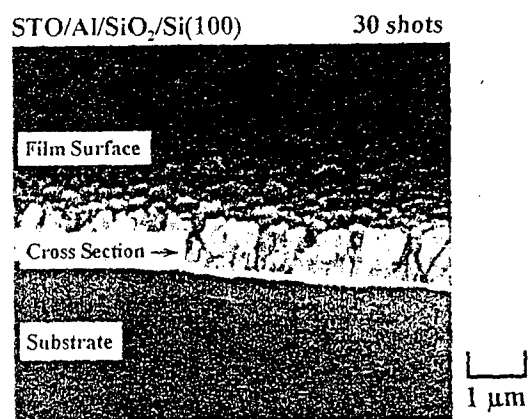


Fig. 2 SEM photograph of cross-section of SrTiO₃ film prepared by BS/IBE with 30 shots.

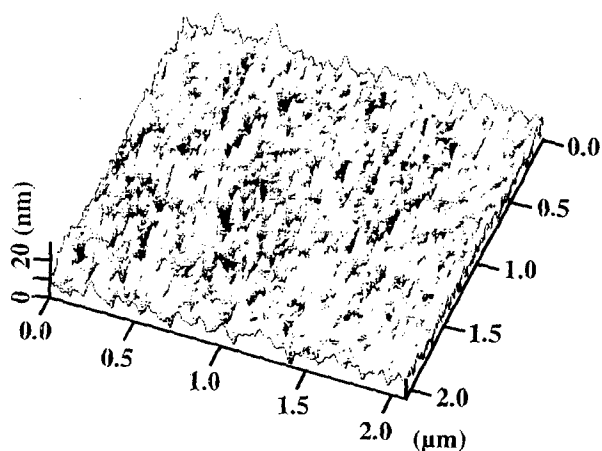


Fig. 3 AFM data of SrTiO₃ prepared by BS/IBE with 1 shot.

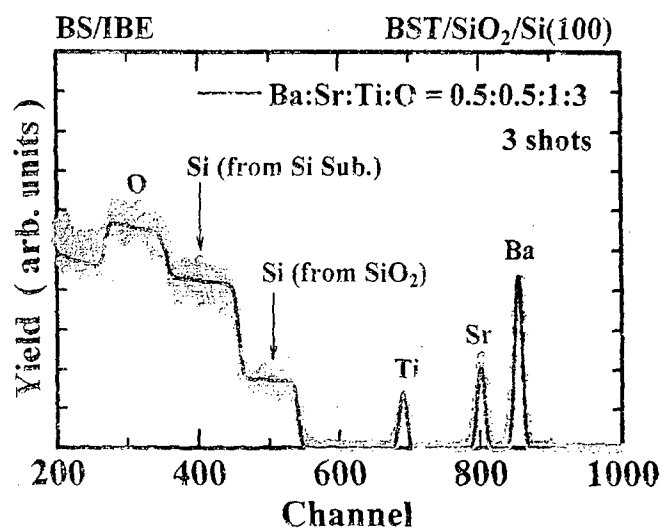


Fig. 4 RBS data of (Ba,Sr)TiO₃ film prepared by BS/IBE with 3 shots.

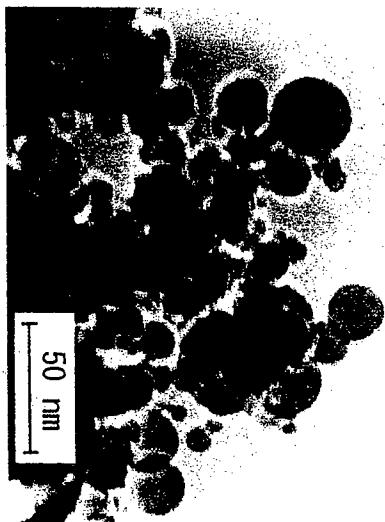


Fig. 5 TEM photograph of γ - Al_2O_3 (IBE).

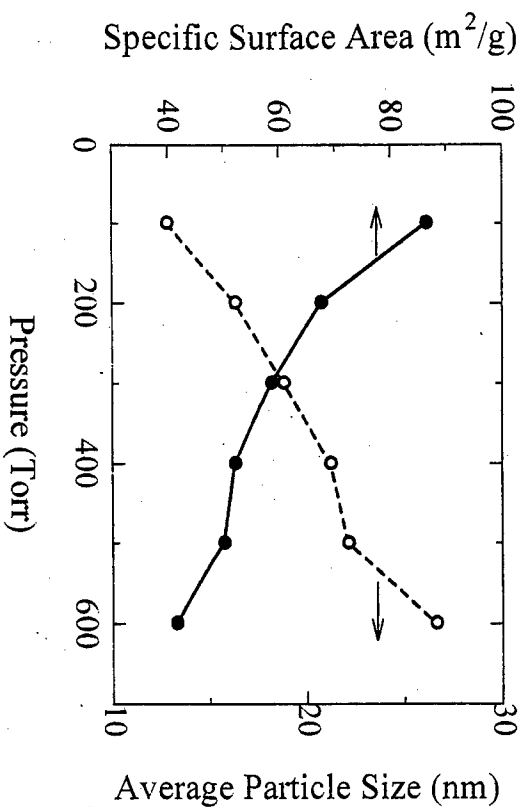


Fig. 7 Specific surface area and average diameter of TiN powders as a function of nitrogen pressure, where Ti wire was used.

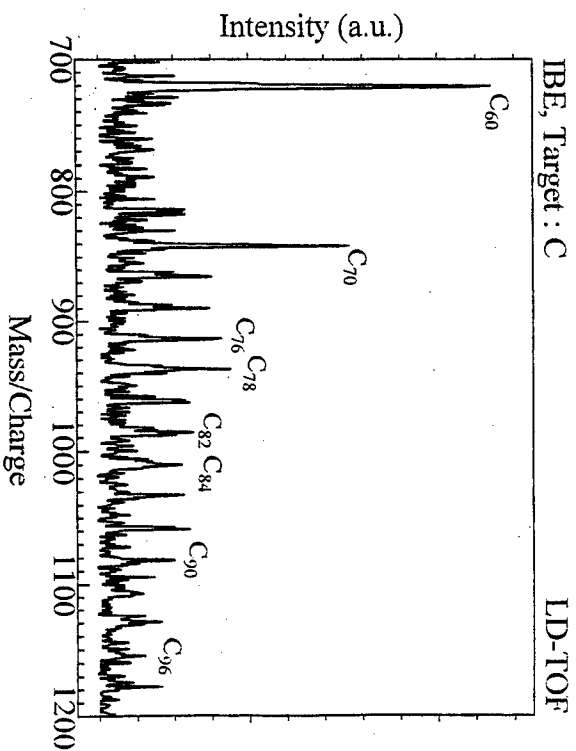


Fig. 6 Mass spectrometer data showing C_{60} and higher order fullerenes (IBE).

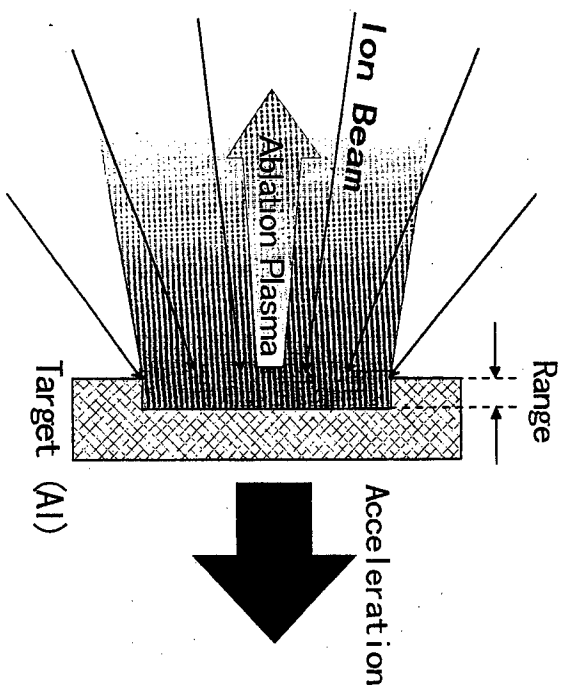


Fig. 8 Principle of foil acceleration by IBAP.

Table I Characteristics of powders synthesized by IBE, where a), b) and c) are diagnosed by SEM, TEM and both SEM/TEM, respectively. Species were identified by XRD.

Target Material	Ambient Gas	Pressure (Torr)	Target-Collector Distance (mm)	Particles Identified	Particle Size, Min~Max (nm)
Ti 99.5 %	Oxygen 99.5 %	1	100	TiO+TiO ₂	380 ~ 2,410 ^{a)}
			330	TiO+TiO ₂	4 ~ 40 ^{b)}
		10	100	TiO ₂	320 ~ 2,000 ^{a)}
			330	TiO ₂	4 ~ 45 ^{b)}
	Nitrogen 99.5 %	1	100	TiN+TiO	5 ~ 1,800 ^{c)}
			330	TiN	5 ~ 38 ^{b)}
		10	100	TiN	380 ~ 1,420 ^{a)}
			330	TiN	5 ~ 23 ^{b)}
TiN 99.5 %	Nitrogen 99.5 %	1	100	TiN	350 ~ 2,270 ^{a)}
			330	TiN	350 ~ 1,050 ^{a)}
		10	100	TiN	350 ~ 3,850 ^{a)}
			330	TiN	350 ~ 700 ^{a)}
Al 99.5 %	Oxygen 99.55 %	1	330	Al ₂ O ₃	5 ~ 50 ^{b)}
		10	330	Al ₂ O ₃	5 ~ 65 ^{b)}
	Nitrogen 99.5 %	5	330	Al	250 ~ 750 ^{a)}
		10	330	Al	5 ~ 30 ^{b)}
AlN 99.5 %	Nitrogen 99.5 %	1	330	AlN+Al	150 ~ 1,600 ^{a)}
		10	330	AlN+Al	5 ~ 35 ^{b)}

Table II Nanosize powders prepared by pulsed wire discharge.

Wire	Ambient Gas (400 Torr)	Nanosize Particles	Specific Surface Area (m ² /g)	Average Particle Size (nm)
Ti	O ₂	TiO ₂	40.1	35.3
Fe	O ₂	Fe ₂ O ₃	26.9	42.9
Cu	O ₂	CuO+Cu ₂ O	16.1	62.1
Zr	O ₂	ZrO ₂	30.4	35.6
Mo	O ₂	MoO ₂ +MoO ₃	26.0	49.1
Ti	N ₂	TiN	52.0	21.2
Fe	N ₂	Fe	15.7	48.7
Mo	N ₂	Mo	15.9	41.9
Pd	N ₂	Pd	30.0	16.4
Al	Ar	Al	28.9	77.0
Cu	Ar	Cu	10.8	62.2

APPLICATIONS OF DIELECTRIC BARRIER DISCHARGES

Zoran Falkenstein

Los Alamos National Laboratory, P.O. Box 1663, Los Alamos, NM 87545, USA

12th International Conference on High-Energy Particle Beams, Beams '98

Haifa, Israel, June 7-12, 1998

ABSTRACT

Dielectric barrier discharges (DBDs) in oxygen and air are well established for the production of large quantities of ozone and are more recently being applied to a wider range of plasmachemical processes. As an introduction of this type of gas discharge, the main plasmaphysical features of sinusoidal-driven DBDs (transient, non-thermal plasmas at atmospheric pressure) will be described, and plasmachemical reaction pathways for the generation of ozone will be briefly discussed.

The generation of atomic oxygen for ozone synthesis leads inevitably to the second application of DBDs, the non-thermal oxidation of volatile organic compounds (VOCs) in dry and humid air. Experimental results on the degradation of VOCs (isopropanol, trichloroethylene, carbon tetrachloride) as well as by-product formation will be presented for stand-alone DBD treatment, as well as for simultaneous (V)UV illumination of the discharge. Illumination of the discharge with (V)UV can change the plasmachemistry by enhanced formation of certain species of radicals – and thereby can change byproduct formation – but also can change the discharge physics, known as the Joshi effect.

Another application of DBDs is the generation of excited dimers and exiplexes for the production of incoherent (V)UV/visible light. As an example, experimental results on a XeBr* excimer UV light source will be presented, which LANL has developed to the stage of commercialization. Effects of the total and partial gas pressure of a Xe/Br₂ system, the gap spacing, and the applied driving frequency on the UV radiant efficiency will be presented.

The last and latest application of DBDs is the surface processing near atmospheric pressures. As an example, results of photoresist ashing on Si wafers in an oxygen plasma will be shown as function of gas pressure, gap spacing, and applied frequency. The surface of the etched photoresist is characterized by profilometry and scanning electron microscopy (SEM).

INTRODUCTION

Dielectric barrier discharges (DBDs), historically also called silent electrical discharges (SDPs) by Warburg (1904), have been first used by Werner Siemens (1857). They can be obtained when high voltage is applied to electrodes that are separated by a gas gap and at least one dielectric barrier (usually quartz, glass, or ceramics). Using typical gap spacings (0.5 mm to 1 cm), ambient gas pressures (100 mbar to 2 bar) and ac applied voltages (typically 500 V to 20 kV at 1 Hz to <1 MHz) will cause a multitude of transient filaments (lifetime in a range of ns to 100's of ns) with electron densities of about 10^{14} to 10^{15} cm⁻³ and mean electron energies of typically 1-10 eV. Through electron impact with gas molecules in the bulk gas, excited species, dissociation products, and ionized species will be formed in

the ignition and discharge phases which will initiate a complex set of plasmachemical reactions to produce new species. The key feature of DBDs is hereby, unlike other plasma sources, to produce non-thermal, medium ionized plasmas (degree of ionization 10^{-5} to 10^{-4}) even at atmospheric pressure.

EXPERIMENTAL SETUP

Typical arrangements used for DBDs in ozone generation, flue gas treatment, generation of (V)UV light, and surface processing, with the materials used, are shown in Figures 1 A-C.

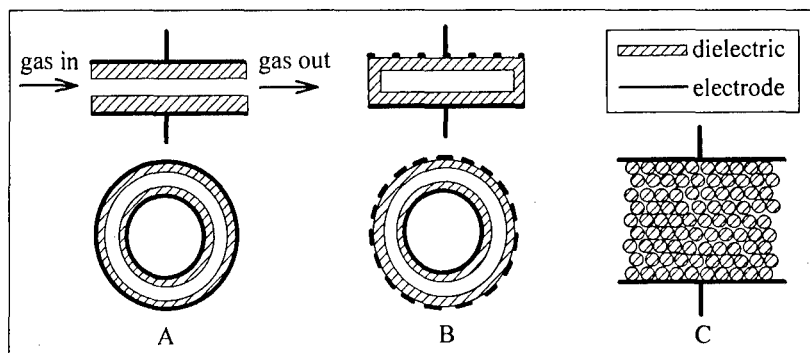
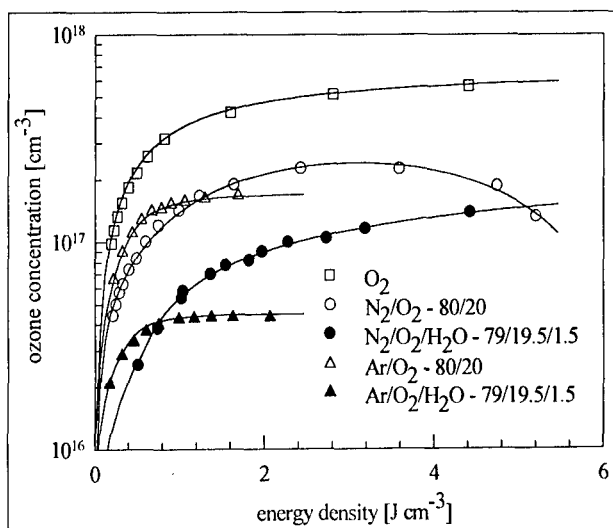


Figure 1 Schematic sketch of possible double dielectric barrier discharge cells (a and b) with a) solid electrodes and b) one transparent electrode. Especially for waste gas treatment, sometimes a packed-bed-reactor c) is used.

RESULTS AND DISCUSSION

Ozone formation



Ozone is the dominant agent used (next to chlorine) for purification and sterilization of drinking water. Almost all ozone generators that are used to produce large quantities of ozone (as in municipal water treatment plants and in chemical industry) use the dielectric barrier discharge in oxygen (or dry air) which is the most efficient method for ozone generation.

Figure 2 Ozone concentrations obtained in various gases in dependence of the supplied energy density.

In the application of DBDs to ozone generation (and to off-gas treatment) in air and air-like gas mixtures reactive, oxidizing species in the background gas are primarily formed by direct electron impact with molecular oxygen [$O(^1D) + O(^3P)$ by dissociation in the Schumann Runge band or -continuum, $O(^3P) + O(^3P)$ by dissociation in the Herzberg band, $O_2(^1\Delta)$ by excitation, and O_2^- by attachment]. Ozone will then mainly be formed by the reaction

$$O + O_2 + M \longrightarrow O_3 + M.$$

Flue gas treatment

At moderate and low VOC concentrations (ppb-ppm), effluents are typically treated by thermal (700 °C to 900 °C) or catalytic (350 °C to 450 °C) oxidation, which requires energy in form of flammable additives in order to provide the necessary temperatures (enthalpy). Here, DBDs can be used as efficient alternative as they provide a possibility of a 'cold combustion' as no additives or supplemental oxidants are needed. Similarly to DBDs for ozone generation, reactive, oxidizing species ($O(^3P)$, $O(^1D)$), and, by the reaction $O(^1D) + H_2O \rightarrow 2 OH$ also OH) in humid flue gases (which are air or air-like gas mixtures) are formed. When one of these radicals reacts

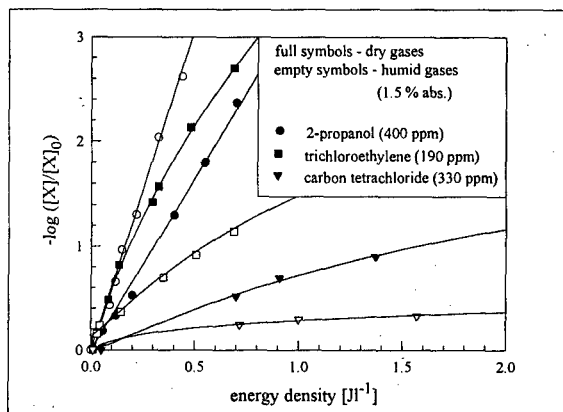


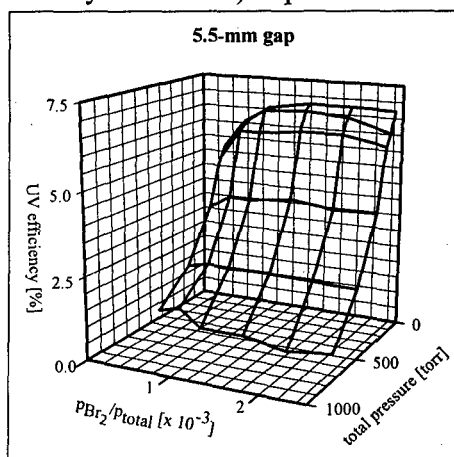
Figure 3 Removal efficiency of various VOCs in air-like flue gases ($N_2/O_2 = 80/20$) in dependence of the supplied energy density.

with a VOC molecule, a complex set of plasmachemical reactions is initiated, leading to its oxidation, fragmentation, and ideally mineralization. Figure 3 shows the destruction and removal efficiency of various VOCs in dry and humid air in logarithmic scaling as function of the energy density applied into the gas.

A possibility to increase the concentration of atomic oxygen and (by chemical quenching with water) hydroxyl radicals and to alter the chemical reaction pathway hereby, is to illuminate the discharged gas with (V)UV light which will cleave ozone to produce atomic and molecular oxygen. As (V)UV sources, a low-pressure mercury lamp (emitting mainly at 253.7 nm) and a self-made Xe_2^* excimer source (emitting at 172 ± 7 nm) have been employed. The results on degradation and by-product formation are reported elsewhere [1].

Generation of (V)UV

In the last few years silent discharge-driven UV sources have been developed and investigated using the silent discharge of selected gas mixtures, where a wide range of the (V)UV spectrum can be covered. Here, as an example a $XeBr^*$ excimer UV source (emitting mainly at 282 nm) is presented. As for all excimers in UV generation, non-thermal discharges



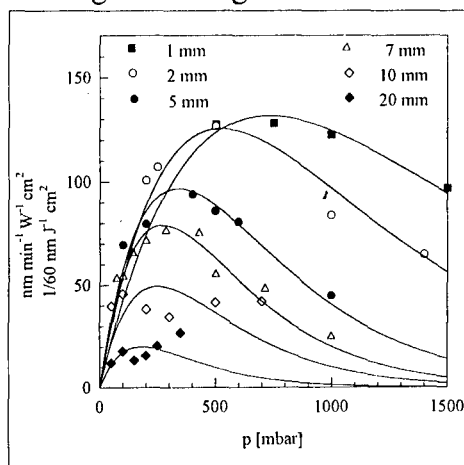
are crucial since, at elevated temperatures, energetically higher vibrational states of the excimer states become more populated and only resonance radiation is obtained. In Figure 4 the efficiency of a $XeBr^*$ excimer UV is given for a 5.5-mm gap spacing at 15 kHz driving frequency as function of gas pressures and ratio of Xe/Br_2 . Here, UV sources with transparent electrodes have been made as schematically shown in Figure 1b.

Figure 4 UV radiant efficiency of a $XeBr^*$ excimer system as function of the total and relative gas pressure of Xe/Br_2 , obtained at a driving frequency of 15 kHz.

By measuring the emitted UV radiant power and the electrical power that is coupled into each gas filling at a constant applied voltage of 13 kV_{peak}, the UV radiant efficiency is obtained. The optimal condition for the 5.5-mm gap is found at a Br₂/Xe ratio of 0.125 % at a total pressure of 125 mbar. Similar results were obtained for the other gap spacings. Results for the dependency of the UV radiant efficiency as function of the applied frequency (when using optimal gas fillings, i.e., a Br₂/Xe ratio of 0.125 % at a total pressure of 125 mbar are reported elsewhere [2].

Surface processing

To evaluate DBDs for surface processing, we have selected the well documented process of photoresist ashing using an oxygen discharge. Typical power-density specific etching rates achieved with conventional low-pressure, non-thermal plasmas in oxygen for the same type of photoresist are about 100 nm min⁻¹ W⁻¹ cm² at equal conditions, i.e. low temperatures no additions of CF₄, etc. and low ion energies (<20 eV) which are known to largely improve the etching rates. Figure 5 shows the power-density specific etching rate of a Novolak-type



photoresist on Si wafers as function of the gas pressure at six different gap spacings, obtained with a 2-kHz (sinusoidal) silent discharge in pure oxygen. The results show that the power-density specific etch rates are comparable with 'conventional' low-pressure discharges, however, SEM reveals that strong surface damaging may occur, especially at small gaps and high gas pressures [3]. This can be improved by increase of the applied frequency [4].

Figure 5 Power-density specific etching rate of a Novolak-type photoresist on Si as function of oxygen pressure at various gap spacings.

ACKNOWLEDGEMENTS

The author would like to express his gratitude to the many friends and co-workers involved in the different projects. I would like to thank Dr. L. Rosocha, Dr. J. Coogan, H. Garcia, M. Garcia and Dr. R. Korzekwa, H. Canavan, J. Roberts and M. Monagle, M. Kang, McIlWaine Archer, Dr. G. Anderson and Dr. D. Zerkle, Dr. D. Cremers, Dr. R. Sze, J. Smith, Dr. K. Walter, Dr. G. Salvyn and Dr. D. Rej from the Los Alamos National Laboratory, as well as B. Kleiner, Prof. Dr. H. Popp and Prof. Dr. M. Neiger from the Lighting Technology Institute, University of Karlsruhe, Germany. The author acknowledges the financial support provided by the U. S. DOE and Triton Thalassic Technologies Inc. (SB-CRADA LA95C10261-A001) and the Energy and Environment Research (EER) Corp. (SB-CRADA LA94-C10164). Additional DOE support from EM-50 is also acknowledged.

- [1] Z. Falkenstein, J. Adv. Oxid. Technol. **2**, 223 (1997).
- [2] Z. Falkenstein and J.J. Coogan, J. Phys. D: Appl. Phys. **30**, 2704 (1997).
- [3] Z. Falkenstein and J.J. Coogan, J. Appl. Phys. **82**, 6273 (1997).
- [4] Z. Falkenstein, J. Appl. Phys. **83**, 5095 (1998).

THIN FILM DEPOSITION BY PULSED ION BEAM EVAPORATION

W. Jiang, K. Ohtomo, M. Igarashi, and K. Yatsui

*Laboratory of Beam Technology, Nagaoka University of Technology
Nagaoka, Niigata 940-2188, Japan*

Abstract Thin films of (Ba,Sr)TiO₃ (BST) and SiC were obtained by using the technology of intense, pulsed ion beam evaporation (IBE). The IBE takes advantage of high-temperature, high-density nature of the ablation plasmas generated by intense, pulsed ion beam. As a result, the thin films obtained by IBE are characterized by many special properties that can not be obtained by other thin-film deposition technologies. In this paper, we report the analytical results obtained by X-ray diffraction (XRD) and scanning electron microscope (SEM). In addition, the BST samples were analyzed by using the Sawyer-Tower circuit for dielectric constant measurement and the SiC samples were analyzed by the scratch test measurement.

1. INTRODUCTION

The intense, pulsed ion beam evaporation (IBE) has been developed for thin-film deposition and nanosize powder synthesis [1-4]. In IBE, the intense, pulsed ion beam is irradiated on the surface of a solid target. Due to the very high energy density produced by the ion beam, the target material close to the surface is evaporated and ionized resulting in high-temperature, high-density plasma. The plasma expands toward the surrounding vacuum or low-pressure area, giving rise to a plume of evaporated target material. This expanding plasma is called the ablation plasma.

If the ablation plasma reaches a substrate, some of the plume material will deposit on the substrate surface resulting in a thin film. This is the basic principle of IBE. One of the advantages of IBE is the elimination of substrate heating [5].

We have found that the thin films can be obtained on both the front and the back surfaces of the substrate. In addition, the thin film obtained on the front surface, front side IBE (FS/IBE), has very high deposition rate ($\sim \mu\text{m}/\text{shot}$) while that obtained on the back surface, backside IBE (BS/IBE), has very good surface quality and physical property [5]. We have successfully obtained many kinds of thin films and nanosize powders by using IBE [1-7]. In this paper, we report the details of the thin film deposition of (Ba, Sr)TiO₃ (BST) and SiC and the results of thin film analysis.

The BST material has very high dielectric constant, making it a hopeful candidate as the capacitor material for the next-generation super-high density integrated circuit. The BST thin films have been obtained by sputtering, CVD and pulsed laser deposition. However, all these processes need very high substrate temperature. Taking the advantage of the elimination of substrate heating of IBE, we used the BS/IBE to BST thin film deposition.

Generally, the SiC thin films are produced by sputtering or chemical vapor deposition (CVD) techniques where the deposition rate is very low (typically $\sim 1 \mu\text{m}/\text{hour}$). Therefore, taking the advantage of very high deposition rate of FS/IBE, we have tried to apply it on SiC thin film deposition.

All samples were analyzed by X-ray diffraction (XRD), scanning electron microscope (SEM), atomic force microscope (AFM) and Rutherford backward scattering (RBS). In addition, the BST samples were analyzed by using the Sawyer-Tower circuit for dielectric constant measurement and the SiC samples were analyzed by the scratch test measurement,

respectively.

2. EXPERIMENTAL SETUP

Figure 1 shows the experimental setup. The ion beam is extracted from a magnetically insulated ion-beam diode which is driven by the pulsed power generator "ETIGO-II". The ion beam consists of 80% of proton and 20% of carbon and oxygen ions. The peak ion energy is ~ 1 MeV and the pulse width is ~ 50 ns. The energy density deposited by the ion beam on the target surface is variable in the range of $34 < E_b < 67 \text{ J/cm}^2$.

BS/IBE was used for BST thin film deposition. The target was sintered $(\text{Ba}_x\text{Sr}_{1-x})\text{TiO}_3$ ($x = 0, 0.25, 0.5, 0.75, 1.0$) ceramics. The substrate was a very thin aluminum layer coated on SiO_2 of 300 nm in thickness on Si (100) (Al/SiO₂/Si(100)). The distance between the target and the substrate was $d_{\text{TS}} = 40$ mm. The deposition was carried out under the pressure of $\sim 10^{-4}$ Torr with the substrate at room temperature. The samples were obtained by 30 ion-beam shots.

FS/IBE was used for SiC thin film deposition. The target was sintered SiC solid and the substrate was Si (100). The distance between the target and the substrate was $d_{\text{TS}} = 40, 45$, or 50 mm. The deposition was carried out under the pressure of $\sim 10^{-4}$ Torr with the substrate at room temperature. The samples were obtained with 1, 5, 10 of ion-beam shots.

3. EXPERIMENTAL RESULTS

3-1 BST thin films

Figure 2 shows the typical XRD results of BST thin films obtained with BS/IBE under the following condition: 30 shots, $x = 0, 0.5, 1$, $d_{\text{TS}} = 40$ mm, and $E_b \sim 67 \text{ J/cm}^2$. It is easily confirmed that the diffraction peaks of BST at different value

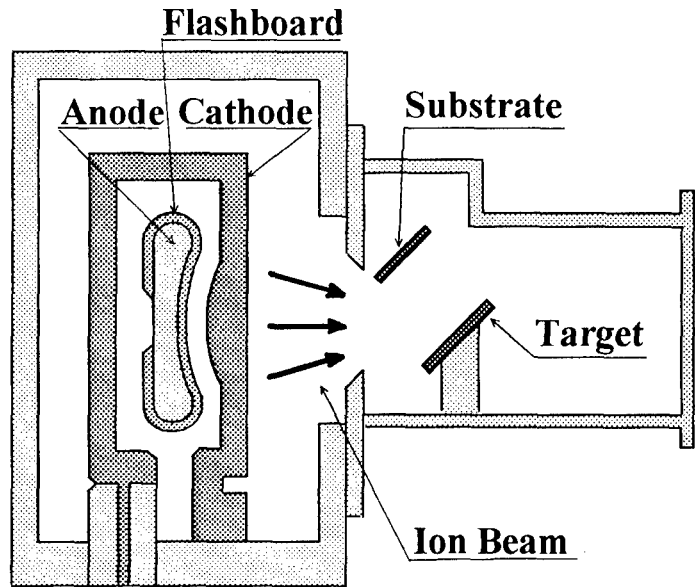


Fig. 1 Experimental setup of IBE.

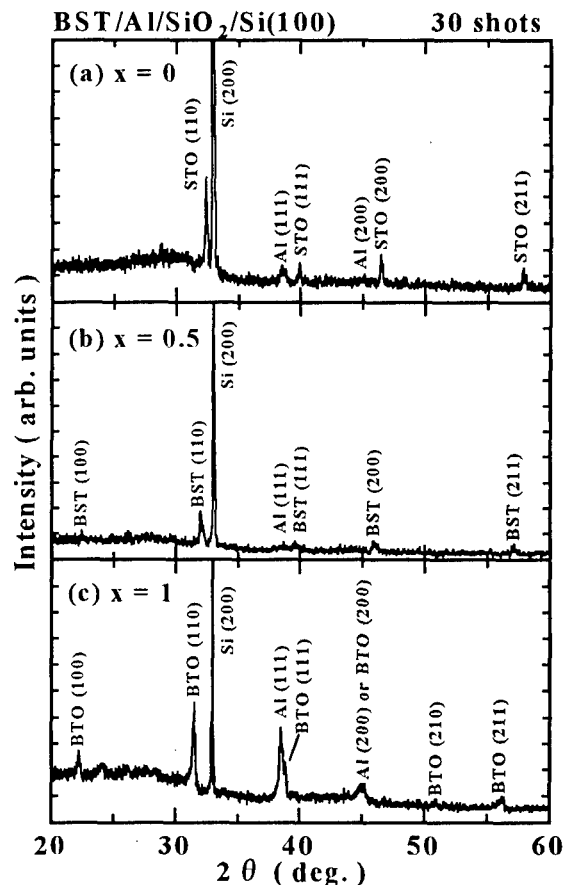


Fig. 2 XRD patterns of BST films deposited at composition of (a) $x = 0$, (b) $x = 0.5$ and (c) $x = 1$ (BS/IBE, 30 shots, Al/SiO₂/Si(100) substrate).

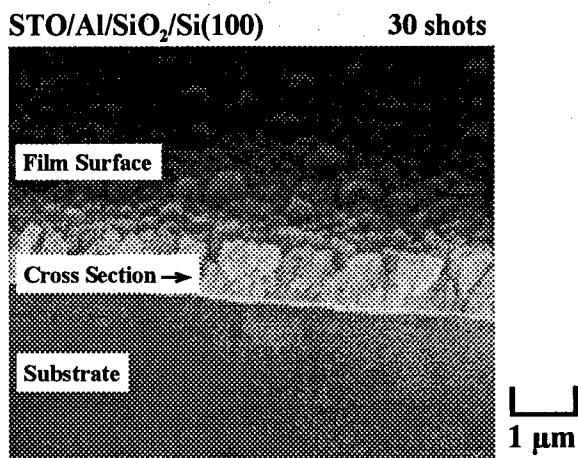


Fig. 3 SEM photograph of SrTiO_3 thin film.

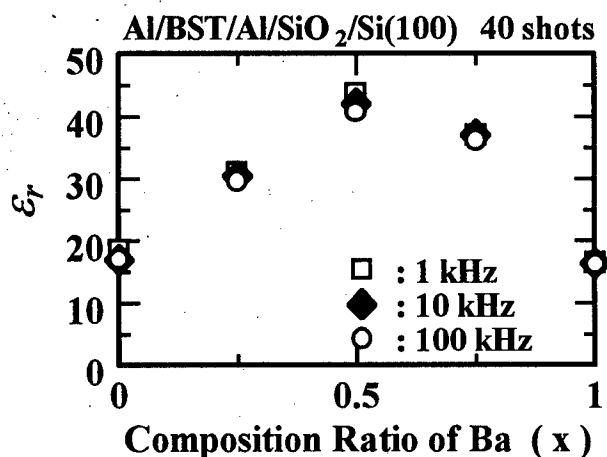


Fig. 4 Dependence of relative dielectric constant (ϵ_r) on x .

of x are clearly identified. The Si (200) and Al(111) peaks are caused by the substrate.

Figure 3 shows the typical photograph of BST thin films obtained by SEM. The sample was obtained with the following condition: 30 shots, $x = 1$, $d_{TS} = 40$ mm, and $E_b \sim 67$ J/cm². From Figure 3, film thickness was obtained as ~ 800 nm, giving the deposition rate of ~ 26 nm/shot. The surface mean roughness obtained by AFM measurement was ~ 4 nm. The RBS results of BST thin films have shown that thin film composition is the same as that of the target.

Figure 4 shows the relative dielectric constant measured by using the Sawyer-Tower circuit. The samples were obtained with the condition of $x = 0, 0.25, 0.5, 0.75$ and 1 , 10 shots, $d_{TS} = 40$ mm, and $E_b \sim 67$ J/cm². It is seen from Fig. 4 that, the relative dielectric constant depends on the value of x and has a peak at $x \sim 0.5$.

3-2 SiC thin films

Figure 5 shows the typical XRD patterns of SiC thin films obtained with $d_{TS} = 40$ mm, $E_b \sim 67$ J/cm² and ~ 34 J/cm². Both samples were obtained after 10 shots of the ion beam. In Fig. 5, Si (200) and Si(400) are diffraction peaks of the substrate while the peaks at $2\theta = 35.77^\circ$ and 60.08° were that of cubic SiC (111) and (220). Therefore, it is confirmed that polycrystalline SiC exists in the thin films.

Figure 6 shows the dependence of the film thickness on the distance between the target and the substrate. The samples were obtained by 10 shots with ion-beam energy density of ~ 34 J/cm².

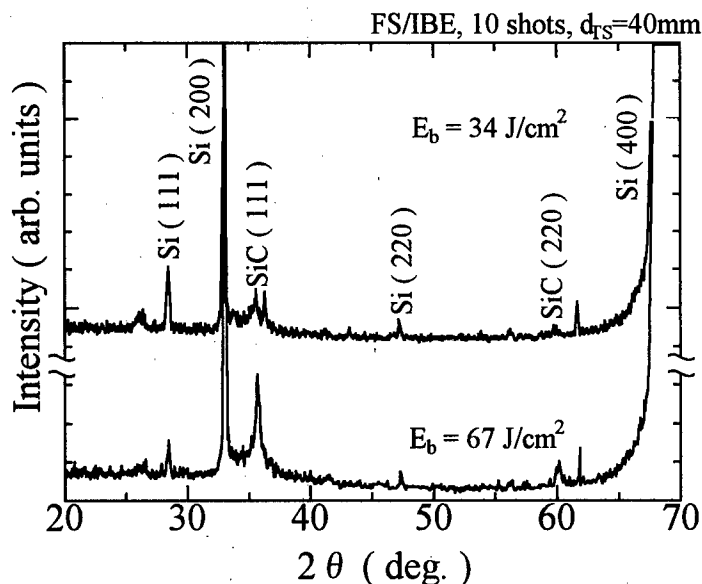


Fig. 5 XRD patterns of SiC thin films obtained with different ion-beam energy densities.

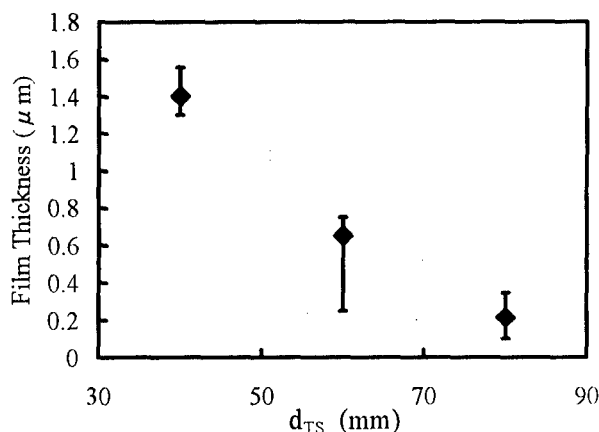


Fig. 6 Dependence of SiC film thickness on target-substrate distance.

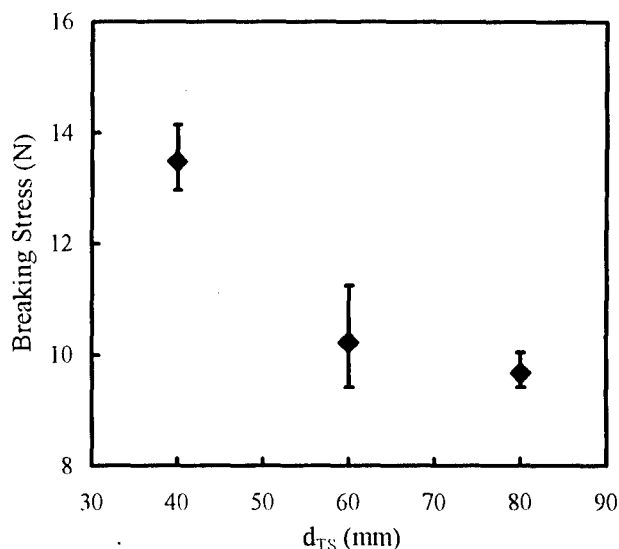


Fig. 7 Results of scratch test for SiC samples obtained with different d_{TS} .

Figure 7 shows results of scratch test of the SiC thin films. In Fig. 7, the critical stress represents the adhesion of the thin film on the substrate. The samples were obtained with $E_b \sim 67 \text{ J/cm}^2$ with 10 shots of ion beam. From Fig. 7, it is seen that the critical stress of the SiC thin film decreases as d_{TS} is increased.

4. CONCLUSIONS

Backside ion beam evaporation (BS/IBE) has been used for BST thin-film deposition giving the following conclusions.

- 1) Polycrystalline BST thin film was obtained on substrate at room temperature.
- 2) Deposition rate was $\sim 26 \text{ nm/shot}$.
- 3) Mean roughness of the film surface was $\sim 4 \text{ nm}$.
- 4) Relative dielectric constant depends on the value of x and its peak appears at $x \sim 0.5$.

Results of SiC thin films deposition by frontside ion beam evaporation (FS/IBE) have given the follows conclusions.

- 1) Deposition rate of $\sim 140 \text{ nm/shot}$ was obtained with ion beam energy density of $E_b \sim 34 \text{ J/cm}^2$.
- 2) Critical stress of the film increases as the target-substrate distance is decreased.

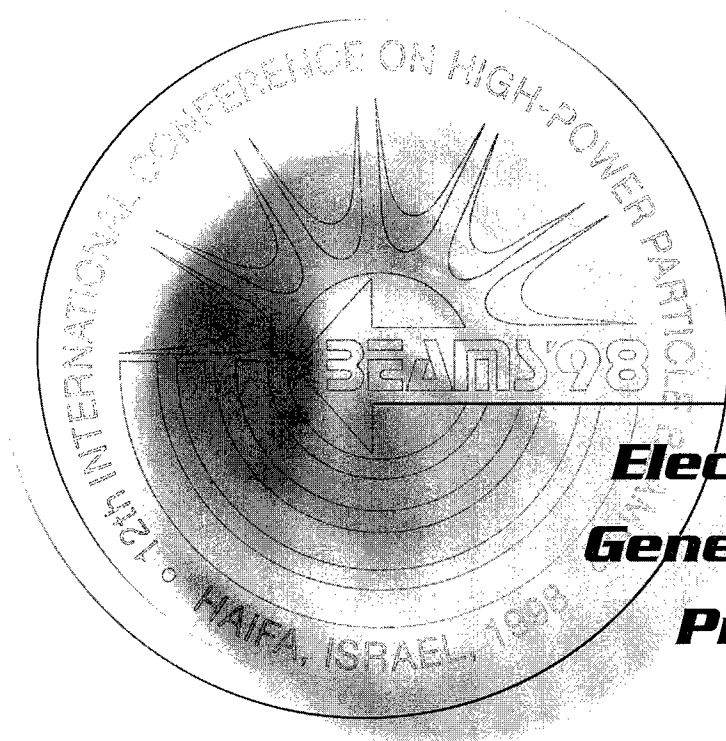
REFERENCES

- [1] Y. Shimotori, M. Yokoyama, S. Harada, K. Masugata and K. Yatsui: J. Appl. Phys. **63**, 968 (1988).
- [2] K. Yatsui, X. D. Kang, T. Sonogawa, T. Matsuoka, K. Masugata, Y. Shimotori, T. Satoh, S. Furuuchi, Y. Ohuchi, T. Takeshita and H. Yamamoto: Phys. Plasmas **1**, 1730 (1994).
- [3] X. D. Kang, K. Masugata and K. Yatsui: Jpn. J. Appl. Phys. **33**, 1155 (1994).
- [4] K. Yatsui, C. Grigoriu, H. Kubo, K. Masugata and Y. Shimotori: Appl. Phys. Lett. **67**, 1214 (1995).
- [5] T. Sonogawa, C. Grigoriu, K. Masugata, K. Yatsui, Y. Shimotori, S. Furuuchi and H. Yamamoto: Appl. Phys. Lett. **69**, 2193 (1996).
- [6] K. Yatsui, C. Grigoriu, K. Masugata, W. Jiang, T. Sonogawa: Jpn. J. Appl. Phys., **36**, 4928 (1997).
- [7] Y. Nakagawa, C. Grigoriu, K. Masugata, W. Jiang, and K. Yatsui: J. Mat. Sci., **33**, 529 (1998).



BEAMS'98

12th INTERNATIONAL CONFERENCE
ON HIGH-POWER PARTICLE BEAMS



ORALS

***Electron Beam
Generation and
Propagation***

Vol. I

Optical Guiding and Stability of Intense Short Laser Pulses in Plasma Channels

Phillip Sprangle¹ and Bahman Hafizi²

¹Plasma Physics Division, Naval Research Laboratory, Washington, DC 20375

²Icarus Research, Inc., P.O. Box 30780, Bethesda, MD 20824-0780

Laser pulse propagation can be strongly influenced by nonlinear effects (relativistic and/or atomic electrons), ionization processes and finite pulse length effects. In this paper these processes are included in the analysis of the propagation and stability of intense laser pulses in plasmas. An envelope equation, which includes ionization and nonlinear effects, is derived and the spot size is found to be unstable to an ionization-modulation instability. Short laser pulses propagating in plasma channels are found to undergo an envelope modulation that is always damped in the front and initially grows in the back of the pulse. An example of laser wakefield acceleration to electron energies greater than 2.5 GeV in a plasma channel is described.

Introduction

The propagation of high intensity optical pulses in plasma channels [1-6] and partially-stripped plasmas is relevant to a wide range of applications, such as ultrabroadband optical generators [7], optical harmonic generators [8,9], x-ray sources [10], laser-driven accelerators [11-20] and "fast ignitor" laser fusion [21].

This paper addresses three processes relevant to the propagation, guiding and stability of intense laser pulses in plasmas. These processes are ionization [6], finite pulse length effects [22] and the effect of bound electrons on the stability and guiding of laser pulses [23]. The various contributions to the refractive index are stated and used in an envelope equation describing the laser spot size. An envelope equation for a laser pulse propagating in a preformed plasma channel, including nonlinear effects, is derived. The critical power for optical guiding is obtained in terms of the channel depth and critical powers for relativistic and atomic guiding. When ionization effects are included an ionization-modulation instability develops. A perturbed envelope equation is obtained for

short laser pulses propagating in a preformed plasma channel. This equation shows that finite length effects result in significant modification of the nonlinear processes as well as a laser envelope modulation that is eventually damped due to frequency spread phase mixing. Finally an example of laser wakefield acceleration to energies greater than 2.5 GeV in a plasma channel is described.

Refractive Index

The general refractive index associated with an intense laser pulse in a partially-stripped plasma [23] is $\eta = \eta_0 + \Delta\eta$, where $\Delta\eta = \Delta\eta_p + \Delta\eta_r + \Delta\eta_a + \Delta\eta_c + \Delta\eta_\perp$. Here, $|\Delta\eta| \ll 1$, $\eta_0 \cong 1$ is the linear index associated with the bound (atomic) electrons, $\Delta\eta_p = -\omega_p^2 / 2\omega_0^2$ is the linear contribution from the free (plasma) electrons, $\Delta\eta_r = -\Delta\eta_p a_0^2 / 4$ is the relativistic contribution from plasma electrons, $\Delta\eta_a = \eta_2 I$ is the nonlinear contribution from the atomic electrons, i.e., the optical Kerr effect, $\Delta\eta_c = (\Delta n_c / n_p) r^2 / r_0^2$ is the contribution from a preformed plasma

channel and $\Delta\eta_{\perp} = -2c^2/(\omega_0 r_0)^2$ is the contribution from the finite spot size of the laser pulse. In the above, ω_0 is the laser frequency, r_0 is the initial laser spot size, $\omega_p = (4\pi q^2 n_p / m)^{1/2}$ is the plasma frequency, n_p is the ambient plasma density, a_0 the normalized (unitless) peak amplitude of the laser vector potential, η_2 is the nonlinear refractive index associated with the bound electrons, I is the time averaged laser intensity and Δn_c is the depth of the preformed plasma density channel. For a linearly polarized laser $a_0^2 = 7.32 \times 10^{-19} \lambda_0^2 [\mu\text{m}] I [\text{W}/\text{cm}^2]$, where $\lambda_0 = 2\pi c / \omega_0$ is the laser wavelength.

Envelope Equation

Using the source dependent expansion (SDE) method [6,24] an envelope equation describing the evolution of the laser spot size r_s can be derived. In the SDE method, the optical field is expanded in a complete set of source-dependent orthogonal Laguerre-Gaussian functions that implicitly depend on the propagation distance z through the spot size, wavefront curvature, amplitude, and phase. The envelope equation may be written in the form

$$\frac{\partial^2 R}{\partial Z^2} - R^{-3} - \frac{2R^{-1}Z_{R0}^2}{\eta_0^2 r_0^2} \int_0^\infty d\chi (\partial\eta^2 / \partial\chi) \chi \exp(-\chi) = 0, \quad (1)$$

where $R(z) = r_s / r_0$, $Z = z / Z_{R0}$, $Z_{R0} = \eta_0 \pi r_0^2 / \lambda$ is the Rayleigh length and $\chi = 2r^2 / r_s^2$.

Focusing of the laser beam requires that the refractive index be peaked on axis. The refractive indices associated with the relativistic plasma $\Delta\eta_r$, bound electrons $\Delta\eta_a$ and a preformed plasma channel Δn_c can individually cause focusing of the laser pulse. The envelope equation in this case become

$$\frac{\partial^2 R}{\partial Z^2} - \left(1 - \frac{\Delta n_c}{n_p} - \frac{P}{P_r} - \frac{P}{P_a} \right) R^{-3} = 0, \quad (2)$$

where $P = (\pi/2)\eta_0 I r_s^2$ is the laser power, P_r is the critical relativistic focusing power and P_a is the critical atomic focusing power.

Critical Power for Guiding

The critical powers are, respectively, $P_r = 2c(q/r_e)^2 (\omega_0 / \omega_p)^2$ [6,23,25-27], and $P_a = \lambda_0^2 / (2\pi\eta_0\eta_2)$ [6,28], where $r_e = q^2 / mc^2$ cm is the classical electron radius. The ratio $R_c = P_r / P_a$ can be much greater than unity and scales with laser frequency to the fourth power. In practical units,

$R_c = 1.22 \times 10^{40} \eta_0 \eta_2 [\text{cm}^2 / \text{W}] / (\lambda_0^4 [\mu\text{m}] n_p [\text{cm}^{-3}])$, where η_2 is proportional to the atomic gas density, n_a . Taking $\eta_2 \equiv 10^{-19} \text{ cm}^2 / \text{W}$ for typical neutral gases at standard temperature and pressure, $n_a = n_p = 2.7 \times 10^{19} \text{ cm}^{-3}$ and $\lambda_0 = 0.5 \mu\text{m}$, we find that $R_c \equiv 710$. For these parameters, the critical powers for relativistic and atomic focusing are $P_r = 2.8 \text{ TW}$ and $P_a = P_r / 710 = 3.9 \text{ GW}$, respectively. From Eq. (2), the critical power for guiding in a preformed plasma channel with relativistic and atomic electron effects is given by $P_{crit} = (1 - \Delta n_c / n_p) P_c$, where $P_c = P_r P_a / (P_r + P_a)$. The effect of a plasma channel is to reduce the power required for guiding.

Laser Envelope Equation in an Ionizing Gas

The contribution to the refractive index from ionizing plasma electrons is

$$\Delta\eta_p = -\omega_p^2(r, z, t) / 2\omega^2. \text{ Substituting } \eta = \eta_0 + \Delta\eta_p + \Delta\eta_r + \Delta\eta_a \text{ into Eq. (1) yields [6]}$$

$$\frac{\partial^2 R}{\partial Z^2} - \left(1 - \frac{P}{P_r} - \frac{P}{P_a} + R^2 (r_0 k_a)^2 f_g / 2 \right) R^{-3} = 0, \quad (3)$$

where $k_a^2 = 4\pi q^2 n_a / mc^2$ and

$$f_g = \int_0^\infty d\chi (n_p / n_a) (1 - \chi) \exp(-\chi)$$

represents a filling factor. The ionization term in Eq. (3) represents the defocusing effect of the ionizing plasma.

Ionization-Modulational Instability

The laser envelope described by Eq. (3) can undergo an ionization-modulation (IM) instability [6]. The IM instability arises from the variation of ionization along the beam. The perturbation on the envelope is $\sim \exp[(1 \pm i\sqrt{3})N_e]$, where N_e is the e-folding length,

$$N_e(\xi, Z) = \frac{3}{2} \left[\frac{n_p(\xi, 0) r_0^2 k_a^2 Z^2}{4n_a} \right]^{1/3}, \quad (4)$$

and $\xi = z - \eta_0 ct$. The IM instability disrupts the tail of the beam and the disruption point propagates towards the front [6].

Short Laser Pulse Effects

In this section we consider a short laser pulse propagating in a preformed partially stripped plasma channel consisting of free and bound electrons. We have derived elsewhere an envelope equation for the perturbed laser beam radius, correct to second order in λ/r_0 and λ/ℓ_0 , where r_0 and ℓ_0 are the spot size and pulse length and λ is the vacuum wavelength [22]. In the limit of low laser power ($\ll P_c$), the perturbed envelope equation is

$$\frac{\partial^2 \delta R}{\partial Z^2} + 4\delta R + 4\varepsilon \frac{\partial \delta R}{\partial Z} - 6 \frac{c}{\omega} \frac{\partial^2 \delta R}{\partial \xi \partial Z} = 0, \quad (5)$$

with solution

$$\delta R = R - 1 = \delta R_0 \exp(-2\varepsilon Z - Z^2 / Z_d^2) \cos(2Z),$$

where $\delta R_0 = \delta R(Z=0)$, $\partial \delta R / \partial Z = 0$ at $Z=0$, $Z_d = \omega \ell_0 / (2\sqrt{6}c)$ is the phase mixing length normalized to Z_R and $\varepsilon = (4/\pi\eta_0) \lambda \xi / \ell_0^2$. The last term in Eq. (5) results in overall damping due to phase mixing caused by the frequency spread associated with the pulse. The modulation amplitude, proportional to $\exp[-8\lambda \xi Z / (\pi\eta_0 \ell_0^2) - Z^2 / Z_d^2]$, is always damped at the front of the pulse ($\xi > 0$) while the back ($\xi < 0$) initially grows but is eventually damped due to frequency spread phase mixing. Overall damping of the modulation occurs for $Z > 4\pi|\xi|/(3\eta_0\lambda)$. In

Figs. 1-3 the parameters are $\lambda = 1\mu m$, $\omega_p/\omega \ll 1$, $\ell_0 = 20\mu m$ (67 fs), $P = 0.56 P_c$, with an initial mismatch in the spot size compared to the equilibrium spot size, i.e., $R_0 = R(0,0) = 1$ and $R(0) = 1.15$. Figure 1(a) shows the spot size $R(Z, \xi)$ as a function of $Z = z/Z_R$ and ξ/λ , with finite pulse length effects ($\varepsilon \neq 0$) included. For comparison Fig. 1(b) shows the same plot in the absence of finite length effects ($\varepsilon = 0$). The laser pulse modulation is clearly apparent in Fig. 1(a) where the spot-size at the front ($\xi > 0$) of the pulse is damped and in the back ($\xi < 0$) is unstable. Finite pulse effects not only result in a laser envelope modulation but also significantly enhance nonlinear focusing. This is shown in Fig. 2 where the spot size with finite pulse length effects (solid curve) approaches zero at $\xi/\lambda \approx -3$ for $Z=15$. The

spot size without finite length effects (dotted curve) shows less than a 10% decrease at $\xi \approx 0$ for $Z = 15$. Figures 3(a) and (b) show the laser pulse amplitude $b(Z, \xi)$ as a function of Z and ξ/λ with and without finite pulse length effects, respectively. As a result of the enhanced nonlinear focusing due to the finite pulse length, Fig. 3(a) shows a significant increase in the pulse amplitude at $Z = 15$ compared to Fig. 3(b).

Electron Acceleration to GeV Energies in a Plasma Channel

In the laser wakefield accelerator [11-20] the interaction length in uniform plasma is limited to a few Rayleigh ranges, depending on the degree of re guiding. If the wakefield can be generated in a long plasma channel, electron acceleration to energies in excess of 1 GeV can be achieved. Consider a $\lambda = 1 \mu\text{m}$, 170 fs ($\ell_0 = 50 \mu\text{m}$) laser pulse with spot size $r_0 = 30 \mu\text{m}$ and $a_0 = 1$ ($I = 2.75 \times 10^{18} \text{W/cm}^2$, circular polarization) that is matched to a plasma channel with on-axis density $n_{p0} = 2 \times 10^{17} \text{cm}^{-3}$ (plasma wavelength $\lambda_p = 75 \mu\text{m}$). The peak accelerating gradient associated with the wakefield is $\sim 24 \text{GV/m}$ and the peak transverse electric focusing field is $\sim 5 \text{GV/m}$. By contrast the one-dimensional, cold fluid relativistic wave breaking field is $E_{WB} = [2(\gamma_{ph} - 1)]^{1/2} E_0$, where $\gamma_{ph} = [1 - (v_{ph}/c)^2]^{-1/2}$, v_{ph} is the plasma wave phase velocity and $E_0 = c m \omega_{p0}/q \sim 96 \{n_{p0} [\text{cm}^{-3}]\}^{1/2} \text{V/m}$. Typically, $\gamma_{ph} \sim \lambda_p/\lambda_0$ and hence $E_{WB} \sim 522 \text{GV/m}$ for $n_{p0} = 2 \times 10^{17} \text{cm}^{-3}$ and $\lambda = 1 \mu\text{m}$. Electrons can be injected into the wakefield either from an external source or by a localized injection process. For electrons injected on axis behind the laser pulse with axial momentum $0.3mc$, simulations show that energies in excess of 2.5 GeV can be achieved in a distance $\sim 16 \text{cm}$ (~ 56 Rayleigh ranges). Beyond this distance phase slippage occurs. In this illustration a number of issues, such as the

injection process and instabilities, have been neglected. These will be addressed in a forthcoming paper.

Conclusions

The main laser plasma processes addressed in this paper are ionization and finite pulse length. An envelope equation, which includes ionization and nonlinear (relativistic and bound electron) effects, is found to be unstable due to an ionization-modulation instability. A perturbed envelope equation that includes finite pulse length effects, as well as nonlinearities is also discussed. Finite pulse length effects modify nonlinear focusing processes and result in a laser envelope modulation. Finally, an example of a laser wakefield accelerator in a plasma channel achieving more than a few GeV in a distance of less than 20 cm is given.

The authors acknowledge useful conversations with R.F. Hubbard, A. Ting, C.I. Moore, S. Suckewer, A. Zigler, D. Kaganovich and P. Serafim. This work was supported by the Office of Naval Research and the Department of Energy.

References

1. P. Sprangle and E. Esarey, Phys. Fluids B **4**, 2241 (1992).
2. H. Milchberg, C. Durfee, and J. Lynch, J. Opt. Soc. Am. B **12**, 731 (1995); S.P. Nikitin, T.M. Antonsen, T.R. Clark, Y. Li and H.M. Milchberg, Opt. Lett. **22**, 1787 (1997).
3. A. Zigler, Y. Ehrlich, C. Cohen, J. Krall, and P. Sprangle, J. Opt. Soc. Am. B **13**, 68 (1996); Y. Ehrlich, C. Cohen, D. Kaganovich, A. Zigler, R.F. Hubbard, P. Sprangle and E. Esarey, J. Opt. Soc. Am. B **12**, 2416 (1998).
4. K. Krushelnick, A. Ting, C.I. Moore, H.R. Burris, E. Esarey, P. Sprangle, and M. Baine, Phys. Rev. Lett. **78**, 4047 (1997).

5. A. Braun, G. Korn, X. Liu, D. Du, J. Squier, and G. Mourou, *Opt. Lett.* 20, 73 (1995).
6. P. Sprangle, E. Esarey, and J. Krall, *Phys. Rev. E* 54, 4211 (1996).
7. P.B. Corkum, C. Rolland, and T. Rao, *Phys. Rev. Lett.* 57, 2268 (1986).
8. A. L'Huillier, L.A. Lompre, G. Mainfray, and C. Manus, in *Atoms in Intense Laser Fields*, edited by M. Gavrilu (Academic, San Diego, 1992), p. 139.
9. J. Zhou, J. Peatross, M.M. Murnane, H.C. Kapteyn, and I.P. Christov, *Phys. Rev. Lett.* 76, 752 (1996).
10. S. Suckewer and C.H. Skinner, *Science* 247, 1553 (1990); D.C. Eder, P. Amendt, L. B. DaSilva, *et al.*, *Phys. Plasmas* 1, 1744 (1994); B.E. Lemoff, G.Y. Yin, C. L. Gordon III, C. P. J. Barty and S. E. Harris, *Phys. Rev. Lett.* 74, 1574 (1995); P. Eisenberger and S. Suckewer, *Science* 274, 201 (1996).
11. P. Sprangle, E. Esarey, A. Ting, and G. Joyce, *Appl. Phys. Lett.* 53, 2146 (1988).
12. P. Sprangle, E. Esarey, and A. Ting, *Phys. Rev. Lett.* 64, 2011 (1990); *Phys. Rev. A* 41, 4463 (1990).
13. E. Esarey, P. Sprangle, J. Krall, A. Ting, and G. Joyce, *Phys. Fluids B* 5, 2690 (1993).
14. N.E. Andreev, L.M. Gorbunov and A.A. Frolov, *Plasma Phys. Rep.* 24, 825 (1998).
15. A. Modena, Z. Najmudin, A.E. Dangor, *et al.*, *Nature* 377, 606 (1995).
16. C.E. Clayton, M.J. Everett, A. Lal, D. Gordon, K.A. Marsh, and C. Joshi, *Phys. Plasmas* 1, 1753 (1994).
17. D. Umstadter, S.-Y. Chen, A. Maksimchuk, G. Mourou, and R. Wagner, *Science* 273, 472 (1996).
18. A. Ting, *et al.*, *Phys. Plasmas* 4, 1889 (1997); C. I. Moore, *et al.*, *Phys. Rev. Lett.* 79, 3909 (1997).
19. C.D. Decker, W.B. Mori, K.-C. Tzeng, and T. Katsouleas, *Phys. Plasmas* 3, 2047 (1996).
20. B. Hafizi, E. Esarey and P. Sprangle, *Phys. Rev. E* 55, 3539 (1997).
21. M. Tabak, J. Hammer, M.E. Glinsky, *et al.*, *Phys. Plasma* 1, 1626 (1994).
22. P. Sprangle, B. Hafizi, and P. Serafim, *Phys. Rev. Lett.* 82 (1999); *Phys. Rev. E* 59 (1999); to be published.
23. P. Sprangle, E. Esarey, and B. Hafizi, *Phys. Rev. Lett.* 79, 1046 (1997); *Phys. Rev. E* 56, 5894 (1997).
24. P. Sprangle, A. Ting, and C.M. Tang, *Phys. Rev. Lett.* 59, 202 (1987); *Phys. Rev. A* 36, 2773 (1987).
25. A.G. Litvak, *Sov. Phys. JETP* 30, 344 (1969).
26. P. Sprangle, C.M. Tang, and E. Esarey, *IEEE Trans. Plasma Sci.* PS-15, 145 (1987).
27. G.Z. Sun, *et al.*, *Phys. Fluids* 30, 526 (1987); A.B. Borisov, *et al.*, *Phys. Rev. A* 45, 5830 (1992).
28. R.W. Boyd, *Nonlinear Optics* (Academic, San Diego, 1993).

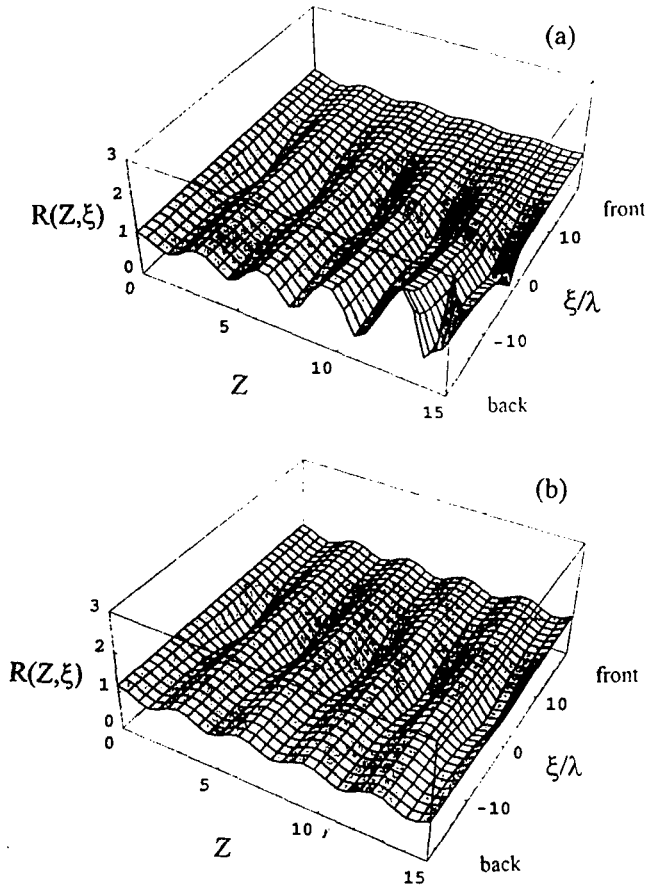


Fig. 1 Surface plots of spot size R as a function of ξ/λ and propagation distance $Z = z/Z_R$ with (a) finite pulse length effects ($\epsilon \neq 0$) and (b) finite pulse length effects neglected ($\epsilon = 0$). The parameters are $\lambda = 1\mu\text{m}$, $\ell_0 = 20\mu\text{m}$, $P = 0.56P_c$.

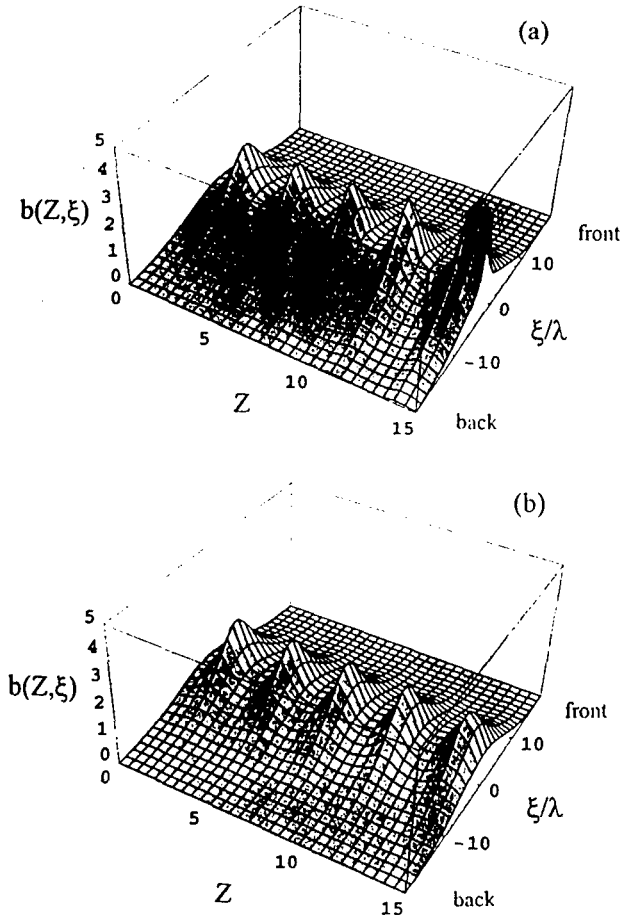


Fig. 3 Surface plots of laser pulse amplitude b as a function of ξ/λ and propagation distance $Z = z/Z_R$ with (a) finite pulse length effects ($\epsilon \neq 0$) and (b) finite pulse length effects neglected ($\epsilon = 0$). Parameters are the same as in Fig. 1.

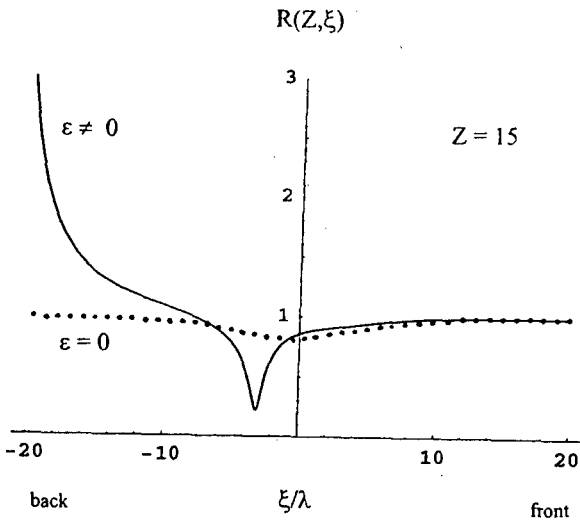


Fig. 2 Plot of spot size R as a function of ξ/λ after a propagation distance equal to 15 Rayleigh lengths ($Z = 15$). The solid (dotted) curve includes (neglects) finite pulse length effects. Parameters are the same as in Fig. 1.

LONG PULSE ELECTRON BEAMS PRODUCED FROM CARBON FIBER CATHODES

Amnon Fisher

Naval Research Laboratory
Beam Plasma Branch Code 6795
Washington, DC 20375-5000

Eusebio Garate

Department of Physics and Astronomy
University of California
Irvine, CA 92697

Abstract--Carbon fiber cathodes have been used to produce electron beams from 10's of nanoseconds to 10's of microseconds. Cathode areas can vary from a single fiber (~ 10 micron diameter) to many hundreds of square cm. The micron size diameter of the fiber is responsible for the high electric field produced at the tips which allows operation of these cathodes at average fields as low as 10 kV/cm. During operation the emitting tips heat up and some plasma forms and erosion takes place. However, carbon has the highest sublimation energy per unit volume among all the elements. It does not melt and its sublimation temperature is high (4000 K). Therefore, no rounding of the tips takes place (metals always melt and form a small sphere which turns off the emission). These properties allow producing cathodes with very million shot lifetimes at current densities of 10's to 1000's of A/cm². We will describe our work on carbon fiber cathodes which range in operation from 6 kV to 500 kV anode-cathode voltage and up to a few microseconds pulse duration.

Introduction--Carbon fiber cathodes have been studied as sources of long (compared to solid explosive emitters) pulsed, high current emission at the University of California, Irvine (UCI) since the late 1970's [1]. This research was motivated by studies of carbon fibers as field emitters, either singly or in clusters, to provide DC current emission without plasma formation [2,3]. In this early work carbon fibers were obtained either from yarn or cloth or felt material. In the yarn and cloth material the fibers are oriented and long and in the felt the fibers are short and randomly oriented. The felt material was found to be much inferior as a cathode source than either the yarn or cloth fibers. The early work also demonstrated a very important feature of carbon fiber cathodes, namely that current emission occurs at low average threshold fields of about 10 kV/cm. Current densities of as small as an A/cm² and up to the space charge limit could be generated. Pulse durations for this early work at Irvine varied between 1 to 2 microseconds at the higher current densities (1 kA/cm²) to about 100 microseconds for the lower current densities.

Thermionic cathodes are limited to about 10 A/cm² current density. For pulsed power applications, where 100's or even many kA/cm² of current density are required, thermionic cathodes are not suitable. Various solid 'field emission' cathodes, which are really plasma cathodes, have been developed over the years to meet the pulsed power demands. However, most of the cathodes used, because of gap closure, limit the pulsed duration to about 100 ns. In addition, these cathodes usually have high threshold fields in excess of 100 kV/cm. Velvet cathodes have lower field thresholds than solid cathodes and pulse lengths can be up to several hundred nanoseconds, however at high current densities, > 1 kA/cm², their lifetime is limited to about 1000 shots and therefore they are not suitable for rep rated systems. As stated earlier, carbon fiber cathodes have the lowest current initiation threshold, pulse lengths can be extended to many microseconds and the

lifetime of a 1 kA/cm^2 , 1 microsecond pulsed cathode is one million shots.

Cathode Geometries--Oriented carbon fibers, like cloth and yarn, are used mostly in carbon fiber reinforced components. These are continuous fibers and woven fabric that contain tens of thousands of fibers per bundle. Fibers range from a few microns to tens of microns in diameter and can have a wide a range of electrical and mechanical properties. The work we have done does not indicate any correlation between the electrical and mechanical properties of the fiber and the performance of the cathode. Carbon fiber cathodes are inexpensive and easy to construct. We have constructed linear cathodes (0.2 mm x 2 cm), planar cathodes (up to about 15 cm diameter), annular cathodes (up to 15 cm diameter and thicknesses less than 1 mm) and point like cathodes (~ 0.2 mm diameter) which generate a conical like beam when used in the absence of a magnetic field. Some details of construction for various cathodes can be found in [1, 4]. A point like cathode can be seen in Figure 1 and current traces for this cathode are shown in Figure 2.

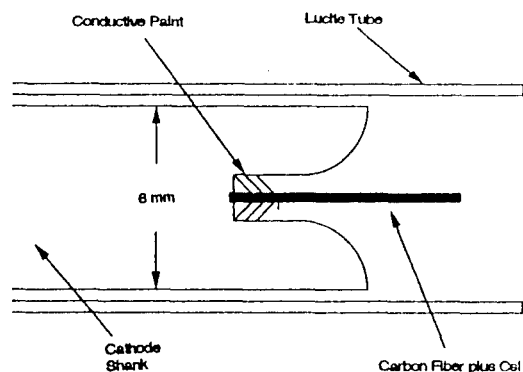


Figure1: Point like cathode.

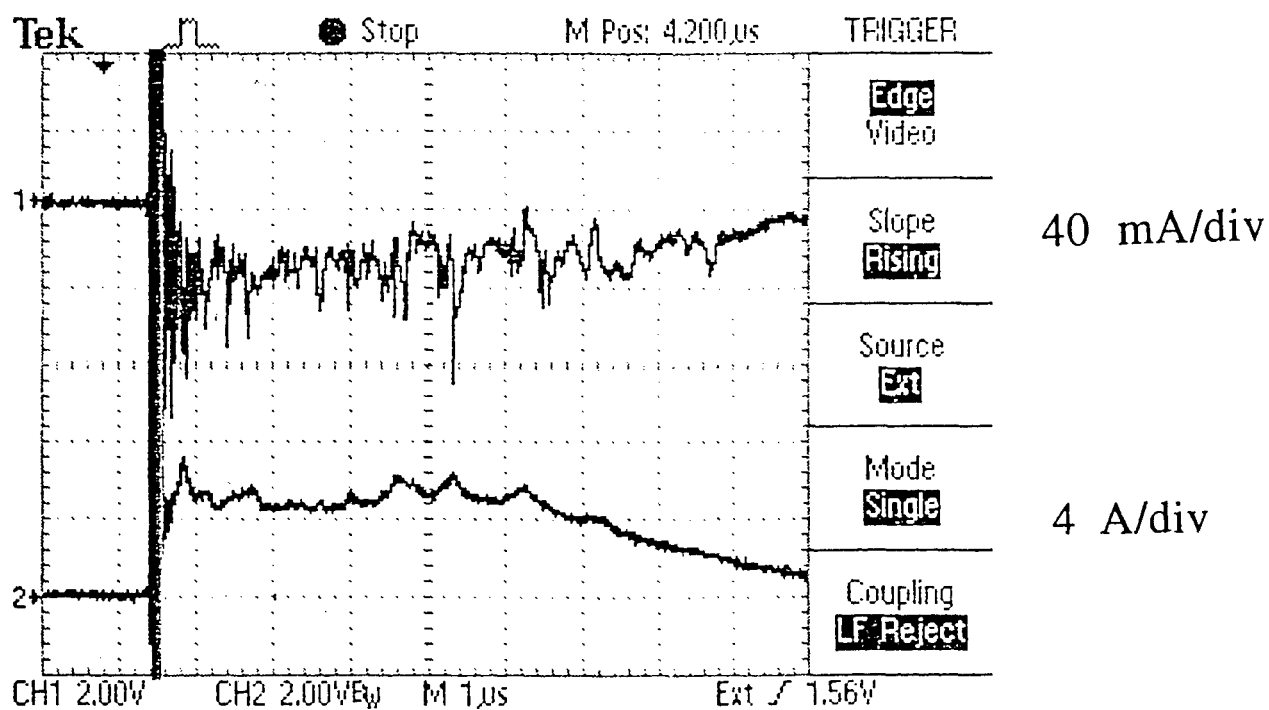


Figure 2: Capacitor discharge into the diode. The capacitor is charged to 10 kV. Upper trace is Faraday cup signal sampling about 1% of the beam current. Lower trace is the cathode current. The AK gap is 4 cm.

Figure 3 shows a V-I trace for a 10 cm diameter planar cathode energized by a 500 kV Marx generator with a crowbar circuit at the output. The AK gap is 6 cm and the current density is about 20 A/cm^2 . Figure 8 is a V-I trace for a 2 cm annular cathode of $\sim 1 \text{ mm}$ annulus immersed in a 1 Tesla magnetic guide field and energized by the Marx generator of Figure 3. The current density is greater than 1 kA/cm^2 .

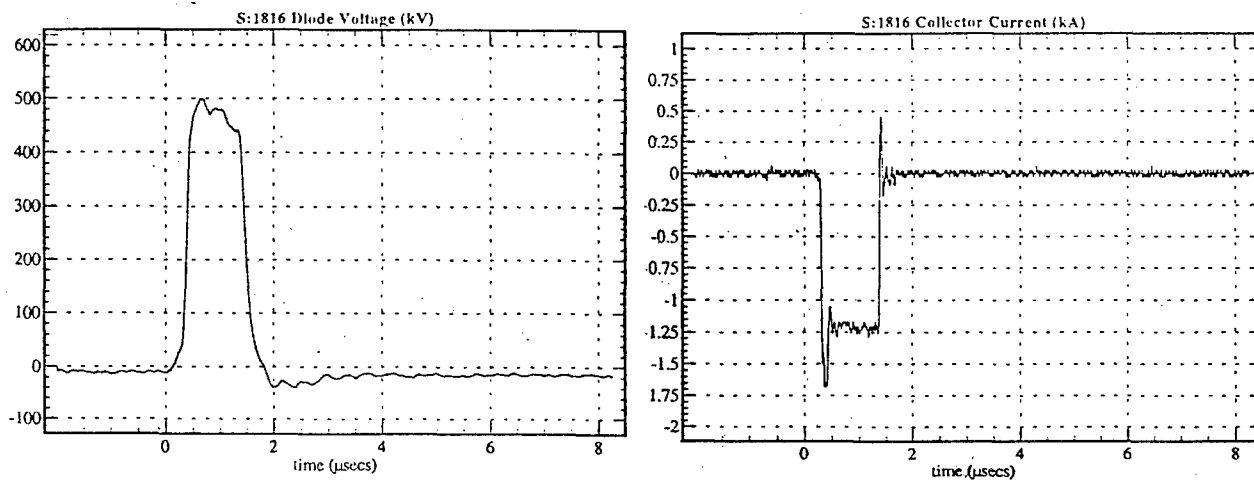


Figure 3: V-I traces for a 10 cm diameter planar cathode and 6 cm AK gap. No magnetic guide field.

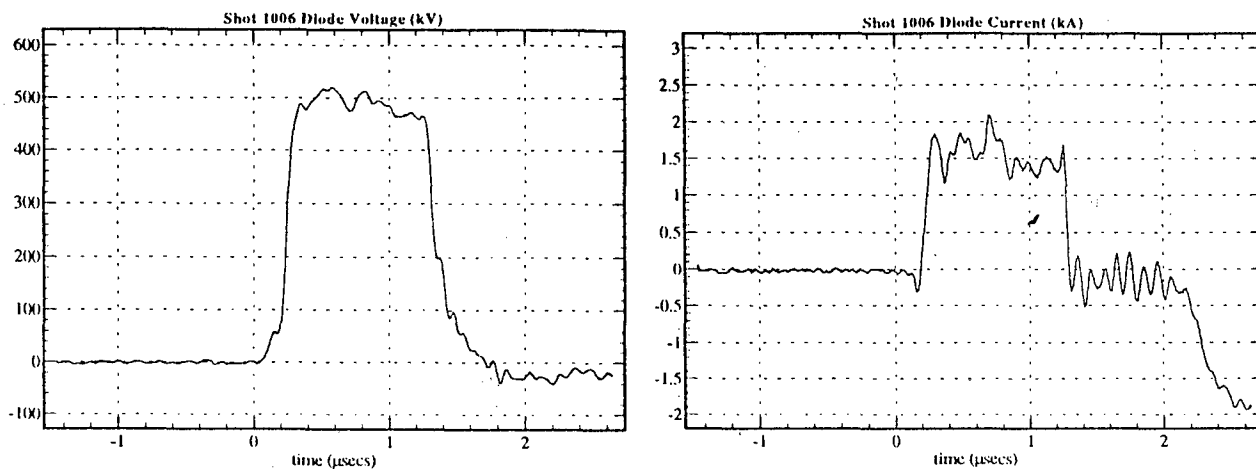


Figure 4: V-I traces for a 2 cm diameter, 1 mm thick annular cathode. The distance to the nearest ground electrode is 4.5 cm. 1 Tesla magnetic guide field.

We speculated that a low melting point, heavy ion compound which is a good photo and secondary emitter would improve the performance of the cathode with respect to gap closure and threshold voltage. CsI fits these properties and we have found that carbon fiber cathodes coated with CsI did reduce the gap closure rate, in some cases, by a factor of 3 [4,5]. CsI has also resulted in a lowered threshold field to a few kV/cm (for the point like cathodes). However, CsI is not as immune to erosion as bare carbon fiber cathodes. Also, the adhesion of the CsI to the carbon fibers is poor and mechanical shocks and vibration tend to shake some of the CsI from the carbon fibers.

Conclusions--Over the years we and other groups have constructed many different cathodes of various shapes and sizes. The cathodes have been used to generate x-rays and high power electromagnetic radiation from millimeter to tens of cm wavelengths. We have also used carbon fiber cathodes as pre-ionisers in gas jets, for plasma heating and surface modification of materials. We have not measured the beam quality for any of the cathodes we have constructed. However, based on our radiation production results and results of other groups, we think beams generated using carbon fiber cathodes have a beam quality at least as good or better as those generated using solid cathodes.

References

- 1) R. Prohaska and A. Fisher, Rev. Sci. Instrum. 53 (7), 1092, 1982.
- 2) F.S. Baker, A.R. Osborn and J. Williams, J. Phys. D vol. 7, 2105, 1972.
- 3) M. Faubel, W.M. Holber and J.P. Toennies, Rev. Sci. Instrum. Vol. 49, 449, 1978.
- 4) E. Garate, R.D. McWilliams, D.E. Voss, A.L. Lovesee, K.J. Hendricks, T.A. Spencer, M. Collins Clark and A. Fisher, Rev. Sci. Instrum. 66 (3), 2528, 1995.
- 5) H. Kosai and A. Fisher, Rev. Sci. Instrum, 61 (7), 1880, 1990.

Relativistic Electron Beams from Cathodes at 1 GV/m Gradient

T. Srinivasan-Rao, J. Smedley and J. Schill
Brookhaven National Laboratory, Upton, NY 11973

INTRODUCTION

In the past decade, there has been extensive research [1] in the development of low emittance, high brightness electron injectors for linear collider and free electron laser applications. RF injectors with a few nC charge in a few ps, with an emittance of $\sim 1-5 \pi$ mm mrad are operational in a number of facilities [2-4]. In these devices, a laser beam irradiates a photocathode embedded in an RF cavity. The photoelectrons released by the laser are immediately accelerated to relativistic velocities, thereby reducing the space charge effects. The frequency of the RF and the design of the cavity are chosen to minimize the RF and space charge effects on the electron bunch so that low emittance, high brightness electron beam could be generated. Minimization of RF effects on emittance growth require a low RF frequency while minimizing the space charge effects require high field and hence high RF frequency. The design is hence a compromise between these two conflicting requirements. Some of these limitations could be overcome by using a large pulsed electric field at the cathode rather than a RF field. The duration of the pulsed field should be chosen so that it is longer than the electron bunch length and the transit time in the accelerating region, but short enough to avoid breakdown problems.

An added advantage of these high fields on metal surface is the lowering of the work function due to Schottky effect. For a field of 1 GV/m, and a field enhancement factor of 3, the change in the work function can be calculated to be ~ 2 eV[5]. This opens up the possibility of using either the infrared or visible radiation to overcome the work function and to extract the electrons from low work-function metals such as yttrium or magnesium. The complexity and cost of the laser system associated with the photocathode is then significantly reduced.

Development of a high brightness electron source using this scheme requires a pulse generator, a laser pulse of sufficient energy to trigger and synchronize the electrical pulses, and a short laser pulse to irradiate the photocathode and generate electron pulses to be accelerated. In the following sections, the designs of these components are described. Critical issues to be addressed are the capability of metals to withstand the high fields without causing electrical breakdown, relative contributions of field emission current and the photocurrent, change in the work-function of the metal as well as its quantum efficiency to photoemission and synchronization of the high voltage pulse and the laser pulse driving the photocathode. The first two critical issues, and synchronization between the trigger laser and the electrical pulse have been investigated and results are presented in this paper. Detailed simulations of electron emission and transport in this diode using MAFIA and PBGUN are presented in a companion paper in this conference.

EXPERIMENTAL APPARATUS:

The breakdown studies conducted by Juttner et. al. [6] and Mesyats et. al. [7] indicate that metals could withstand field gradients of a few GV/m if the duration of the field is ~ few ns. According to these studies, for HV pulses with pulse duration less than 10 ns, both cathode initiated and anode initiated breakdowns become less probable. In addition, the breakdown voltage becomes relatively insensitive to the cathode and anode materials. Formation of microscopic craters due to explosive emission become less frequent and the erosion of the electrodes decreases significantly. Hence uniform field gradients of ~1 GV/m on macroscopic surfaces would necessitate a HV pulse with voltage amplitude ~ 1 MV, pulse duration of a few ns with subns rise and fall times.

A photograph of the pulse generator that would meet these criteria are shown in Figures 1a and 1b. Detailed description of the pulser can be found in Reference 8. This pulse generator is capable of delivering 1 MV with a duration of ~1 ns and rise and fall time of ~150 ps to a 80 Ohm load. The HV pulse is synchronized to an external clock by triggering one of the sharpening switches (a gas switch with SF₆ or its mixture with argon) with a laser.

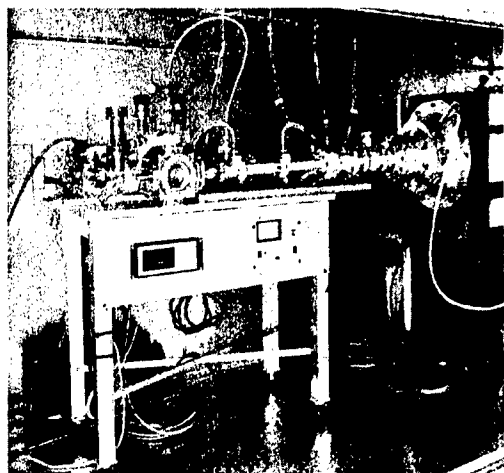


Fig.1b. Photograph of the HV pulse generator, electron gun, and cube containing the diagnostics. A 70 cm ruler is shown nearby for dimensions of the device

The SF₆ gap consists of a hemispherical electrode connected to the HV transformer and a flat electrode connected to the transmission line with an electrically isolated stainless steel wire in the middle of the gap to aid in laser triggering. Two CaF₂ windows centered on the wire permit the laser to irradiate the wire normal to the gap. The laser beam was focused between the stainless steel wire and the high voltage electrode of the SF₆ gap such that the beam nearly fills the gap between the two. In the current scheme, the laser beam triggering the gas switch is derived from a KrF laser. Jitter measurements with this laser arrangement are discussed in the following section

The electron gun generating the high brightness electron beam consists of a photocathode and a grounded anode held parallel to the cathode with the high voltage pulse applied to the cathode. A stainless steel cube enclosing the electrodes maintains a vacuum level of ~10⁻⁸ Torr in the vicinity of the electrodes and surrounding diagnostic equipment. Both the electrodes are removable and hence the performance of the diode for different electrode material and geometry can be investigated without changing the characteristics of the applied voltage significantly. Alternately, for a given electrode material and geometry, the performance of the diode can be studied for various shapes and amplitudes of the voltage pulse, by changing the SF₆ gas pressure, the amplitude of the low voltage and the length of the pulse forming line, without breaking the vacuum.

The diagnostics for the electron beam consist of an electrically isolated Faraday cup to measure the charge, a pepper pot, phosphor screen and relay optics system to measure the spot size of the electron beam and hence calculate the emittance. The pulser and the diode with its diagnostics are housed in an enclosure designed to filter the electromagnetic noise associated with such a system. A joule meter to measure the energy of the laser beam irradiating the

cathode and an imaging system to measure the spot size of the laser on the cathode provide the laser beam diagnostics.

MEASUREMENTS AND DISCUSSION:

JITTER MEASUREMENTS:

The amplitude of the HV pulse, 15 cm upstream of the cathode, can be measured using a capacitive probe built in the transmission line. This probe also has sufficient bandwidth to measure the rise and fall times of the pulse. The signal from this probe is fed directly to a digitizing oscilloscope with 7 GHz bandwidth. The probe has been precalibrated such that 1 V signal in the scope corresponds to 575 kV at the transmission line. A typical voltage trace from the oscilloscope is shown in Figure 2. Deconvoluting the response time of the scope and the attached delay line yields a rise and fall time of ~ 150 ps. The maximum voltage obtained is ~ 900 kV.

In order to measure the synchronization of the high voltage pulser, the SF_6 switch was irradiated with the KrF laser. A laser beam of 75 mJ energy, $2 \times 0.2 \text{ mm}^2$ spot size and ~ 20 ns pulse duration irradiated the gap between the high voltage electrode and the stainless steel wire in the gap. The synchronization of the HV pulse depends critically on the location and the arrival time of the laser beam at the gap, the gas mixture and gas pressure. Each of these parameters was varied keeping the other parameters constant. The optimum set of parameters, defined as the ones resulting in maximum voltage with minimum delay and jitter, was established. The maximum voltage amplitude measured at the last probe was 0.92 MV with

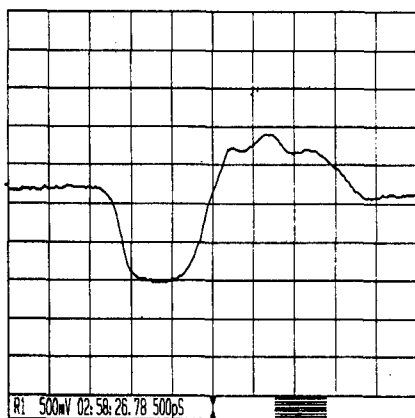


Fig. 2. Shape of the high voltage pulse. The maximum amplitude is 0.9 MV and deconvoluted rise and fall times are ~ 150 ps.

pure SF_6 at 6 atmospheres. As seen in Figure 3, the corresponding delay between the arrival of the laser at the gap and the breakdown of the gap was ~ 30 ns, with a jitter of 0.7 ns. A 5:2 mix of argon: SF_6 at this pressure reduces the voltage by 10% and jitter to 0.5 ns and the delay to 5 ns. Since these jitter values include the fluctuations in the laser energy and hence the trigger time of the oscilloscope, the real jitter between the laser and the HV pulse is expected to be much smaller than the measured 0.5 ns. Jitter values of ~ 150 ps have been reported [9] with similar arrangements.

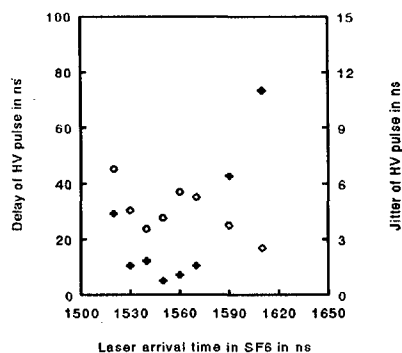


Fig. 3. Delay (o) and jitter (+) of the HV pulse with reference to the laser pulse for 90 psi of SF_6

DARK CURRENT MEASUREMENTS:

The dark current measurements were done with the pulser in the self-trigger mode, without the laser irradiating the SF₆ gap. This enabled us to apply the maximum field on the diode. Two different cathode materials, stainless steel and copper, were tested for their voltage hold off properties and dark current emission. Fields exceeding 1 GV/m could be applied to both the cathodes. As can be expected, the dark current depended critically on the background pressure between the electrodes. The dark current from stainless steel after conditioning, in a field gradient of 0.7 GV/m, was below the detection limit of our system even at background pressures of $\sim 10^{-3}$ Torr. Copper on the other hand yielded a dark current of 200 A under similar conditions. When the background pressure was reduced to 10^{-7} Torr, the dark current fell below the detection limit of our system, 0.5 mA. The interelectrode gap was then decreased to 0.5 mm so that field gradients exceeding 1 GV/m can be explored. A typical current trace with copper cathode and stainless steel anode at 1.7 GV/m gradient is shown in Figure 4. The fast rise time of the first peak indicates that this peak is caused by the fast rising voltage pulse. The subsequent pulses, however, have a slower rise time. In addition, the locations of these peaks do not match exactly with the modulation in the voltage waveform, although the number of peaks matches the number of modulations observed in the voltage waveform. The origin of the current peaks appearing after a delay of 5 ns is still under investigation. The possible sources could be secondary emission from either the cathode or the anode, and transport of the primary electrons modulated by the voltage waveform.

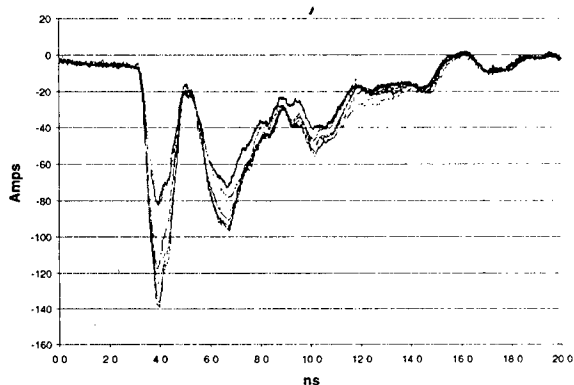


Fig. 4. Dark current trace for an applied field of 1.7 GV/m. 16 traces are overlapped on each other.

A Fowler-Nordheim plot for the current in the first peak alone was created. If the work function of copper is assumed to be 4.6 eV [10], the field enhancement calculated from these data is ~ 25 , implying that surface fields exceeding 40 GV/m can be sustained by copper cathodes without causing high voltage breakdown. This is in agreement with the pulsed high voltage breakdown measurements reported by Messyats [8]. Experiments are now in progress to characterize the field emission current further.

CONCLUSION:

In conclusion, a high voltage pulser capable of delivering up to 1 MV with a duration of ~ 1 ns and rise and fall times of ~ 0.15 ns has been constructed and tested. Copper and stainless steel cathodes have been tested to withstand 1 GV/m gradient. Under background pressures of 10^{-7} Torr, the dark current is below the detection limit of our system at 1 GV/m gradient and hence would not contribute significantly to the photocurrent. Copper cathode and stainless steel anode have been shown to withstand applied fields of 1.7 GV/m without experiencing high voltage breakdown. Dark current measurements and Fowler-Nordheim plot for fields exceeding 1 GV/m indicate that surface fields experienced by these electrodes could

be as high as 40 GV/m. Further characterization of this field emitted current is currently in progress.

The authors would like to thank Drs. V. Radeka, R. Palmer, W. Willis, and I. Ben-Zvi for their support. The authors would also like to thank X. J. Wang, P. Farrell and K. Batchelor for the fruitful discussions. This work was supported by DE-AC02-98CH10886.

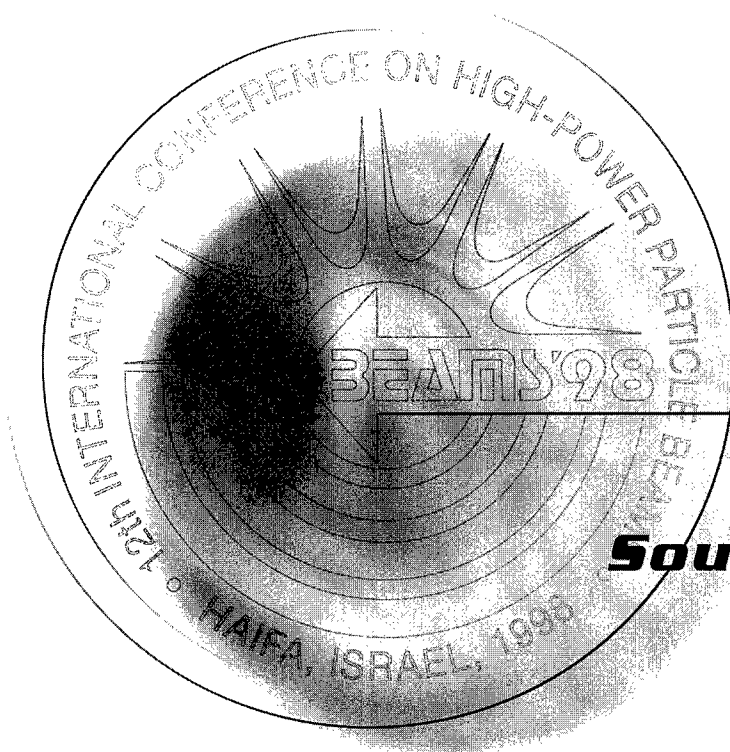
REFERENCES

1. C. Travier, Nucl. Instr. and Meth in Phys. Res. A 340, (1994), 26.
2. B. Carlsten, IEEE J. Quant. Electron. QE 27, (1991), 2580.
3. K. Batchelor et.al., Nucl. Instr. and Meth. in Phys. Res. A 318, (1992), 372.
4. R. Sheffield et.al. in Proc. 1992 Linear Acceleration Conf., Ottawa, Canada, Aug. 24-28, 1992.
5. T. Srinivasan-Rao, J. Fischer, and T. Tsang, J. Opt. Soc. Am. B8, (1991), 294.
6. B. Juttner, V. F. Puchkarev, and W. Rohrbeck, preprint ZIE 75-3 (Akad. Wiss., Berlin, GDR 975), B. Juttner, w. Rohrbeck, and H. Wolff, Proc. iii Int'l Symp. on Discharge and Electrical Insulation in Vacuum, Paris, France, 1968, p. 209.
7. G. A. Mesyats, and D. I. Proskurovsky, Pulsed Electrical Discharge in Vacuum, (Springer- Verlag, 1989), Chap 1-5
8. T. Srinivasan-Rao, j. Smedley, Advanced Accelerator Concepts workshop, AIP Conference Proceedings 398, Ed. S. Chattopadhyay, J. McCullough and P. Dahl, AIP Press, NY 1997, P. 7307.
9. A. H. Guenther, J. R. Bettis, R. E. Anderson and R. V. Wick, IEEE J. Quant. Electron. QE 6, (1970), 492.
10. CRC Handbook of Chemistry and Physics, Ed. R. C. Weast, CRC Press, Boca Raton, Florida, 1984, p E-76



BEAMS'98

12th INTERNATIONAL CONFERENCE
ON HIGH-POWER PARTICLE BEAMS



ORALS

***Radiation
Sources, HPM***

Vol. I

Proceedings

THE DUTCH FREE-ELECTRON MASER : 730 kW, 200 GHz

W.H. Urbanus, W.A. Bongers, V.L. Bratman¹⁾, M. Caplan²⁾, G.G. Denisov¹⁾,
C.A.J. van der Geer, P. Manintveld, J. Plomp, J. Pluygers, A.J. Poelman, A.V., Savilov,
P.H.M. Smeets, F.C. Schüller, A.A. Varfolomeev³⁾, A. G. A. Verhoeven

*FOM Instituut voor Plasmafysica Rijnhuizen, Association EURATOM-FOM,
Postbus 1207, 3430 BE Nieuwegein, The Netherlands*

ph: +31-30-6096999, fax: +31-30-6031204, email: urbanus@rijnh.nl

¹⁾ Institute for Applied Physics, Ulitsa Ulyanova 46, Nizhny Novgorod, 603600 Russia

²⁾ Lawrence Livermore National Laboratories, P.O. Box 808, Livermore, CA 94551, U.S.A

³⁾ Russian Research Centre "Kurchatov Institute", Moscow, 123182 Russia

ABSTRACT

At the FOM Institute for Plasma Physics "Rijnhuizen", The Netherlands, an electrostatic high power free-electron maser is operated at various frequencies. An output power of 730 kW at 206 GHz is generated by a 7.2 A, 1.77 MeV electron beam, and 360 kW at 167 GHz is generated by a 7.0 A, 1.61 MeV electron beam. The lower output power at the latter frequency is due to relatively high losses in the present mm-wave cavity. It is shown experimentally and by simulations that, depending on the electron beam energy, the FEM can operate in single-frequency regime. So far, the pulse length was limited to some 12 μ s. Nevertheless, many aspects of generation of mm-wave power have been explored, such as the dependency on electron beam current and energy and settings of the mm-wave cavity.

1. INTRODUCTION

The principal target of present free-electron maser (FEM) research is the realisation of a source of mm-wave radiation of high average power, high system efficiency, and broad tunability. The achievement of these targets may culminate in the use of FEMs as power sources for electron cyclotron applications on magnetically-confined plasmas in future fusion research devices, such as ITER. For such applications power sources of at least 1 MW in the frequency range from 140 to 200 GHz at a system efficiency of 50% are required. Fast tunability over a small range and a Gaussian output beam would be an advantage.

In a FEM radiation is generated by a relativistic electron beam oscillating in an undulator. A promising approach to realise long pulse operation is the use of electrostatic beam acceleration and deceleration. In this scheme the electron beam is accelerated to the interaction region, and afterwards it is decelerated and collected in a multistage depressed collector. In this scheme, the main beam power is supplied at the collector side, i.e., at low voltage, while the accelerator voltage generator has to supply only the beam loss current. Consequently, to reach long-pulse operation, the loss current has to be extremely low, in our case of the order of 0.2%.

2. LAYOUT OF THE FEM

A description of the Fusion-FEM experiment is given in ref. [1]. The system basically consists of an 80-kV triode electron gun, a dc accelerator and a mm-wave cavity with the undulator [2]. In a later stage the dc decelerator and the depressed collector will be added. In the experiments described here, the beam recovery system was not installed. Consequently, the beam current is fed from the capacitance of the HV terminal (1 nF), and thus the beam energy (terminal voltage) drops by $1 \text{ kV} / I_{\text{beam}} / \mu\text{s}$.

The mm-wave cavity consists of the undulator waveguide - a rectangular corrugated waveguide with a cross section of $15 \times 20 \text{ mm}^2$ - and two stepped waveguides at either side, see fig. 1 [3]. In the stepped waveguides the mm-wave beam emerging from the undulator

waveguide is split into two identical off-axis beams. At the position of full separation, mirrors are placed. The backward propagating beams merge into one beam. This way, a 100 % reflector is realized, at the upstream side of the undulator. At the downstream side a similar system is used, but here one of the mirrors can be shifted in longitudinal direction (direction of beam propagation). Upon propagating backwards, the beams have a phase difference, which results into one on-axis beam and two off-axis beams. The on-axis beam is the feedback power, the two off-axis beams are coupled out. By adjusting the position of the mirror, the feedback can be varied between 0 and 100 % [4].

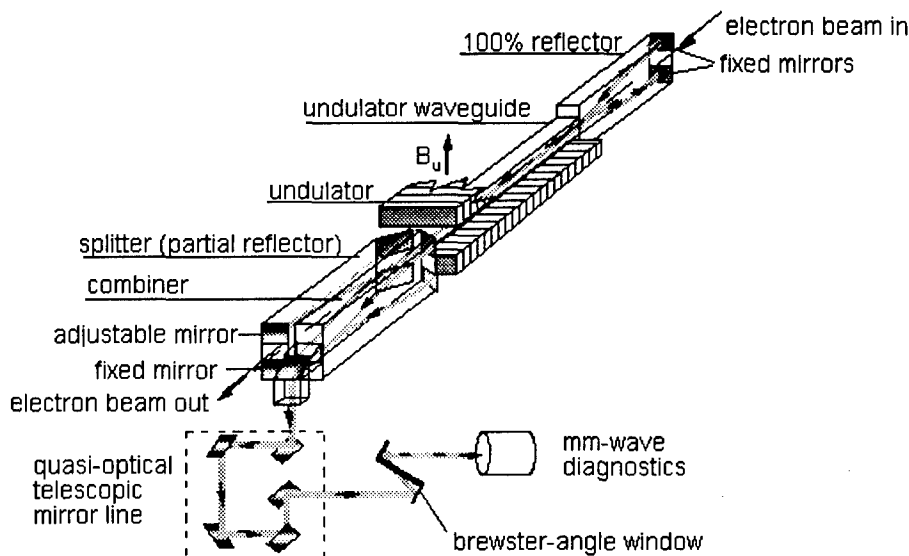


Fig. 1 Layout of the mm-wave cavity, for details see text. Behind the window is a second telescopic system (not shown) to transform the elliptical beam on the window into a circular beam. The diagnostics system consists of a fast semi-conductor detector coupled to a mixer, a calorimeter and an absorption sheet viewed by an IR-camera.

The two mm-wave beams coupled out merge back into one beam in a fourth waveguide. Via a quasi-optical mirror line, which covers a frequency band from 130 - 250 GHz, the beam passes through a Brewster-angle window. Once outside the vacuum, the output mm-wave beam is analysed by a fast semi conductor detector to investigate the temporal characteristics and to analyze the frequency spectrum via a heterodyne mixer, a calorimeter to measure the output power, and an absorption sheet with an infrared camera to view the spatial power distribution of the beam.

Frequency tuning of the stepped waveguides requires the upper and lower walls of the waveguides to be adjusted. The undulator waveguide is wide band and does not need any adjustment.

The electron beam enters and leaves the cavity through an opening between the mirrors and follows a straight path. This set-up was chosen to minimise electron beam losses.

3. MM-WAVE POWER

As mentioned before, no beam recovery is installed yet. Consequently, the beam energy drops and thus the gain curve shifts across the frequency band of the cavity. This changes the characteristics of the interaction and results in variation of the output power during the pulse.

A net output power of 730 kW was generated by a 1.77 MeV, 7.2 A electron beam, see fig. 2.a. For this beam energy single-frequency operation was reached, see fig. 2.b. For a slightly lower electron beam energy the mm-wave output power showed to be more chaotic, see fig. 2.c. As seen in fig. 2.d, several frequencies are generated, and the output power strongly fluctuates on a short time scale.

The FEM was operated at 161 GHz for an electron beam energy around 1.65 MeV and

by adjusting the stepped waveguides. Fig. 3.a and 3.b show the mm-wave output power for an 1.61 MeV, 7.1 A electron beam (single frequency), and for a 1.59 MeV, 7.0 A electron beam (multi frequency), respectively. Again, the same relation is seen between the setting of the cavity (frequency band) and the electron beam energy.

The spatial power distribution (profile) of the output beam as measured with an IR camera and an absorption sheet inserted in the beam is shown in fig. 4, for 206 GHz and 167 GHz beams. Gauss fits taken between the top of the signal and a level just above the noise level result in a Gaussian mode content exceeding 99.8 % for both cases.

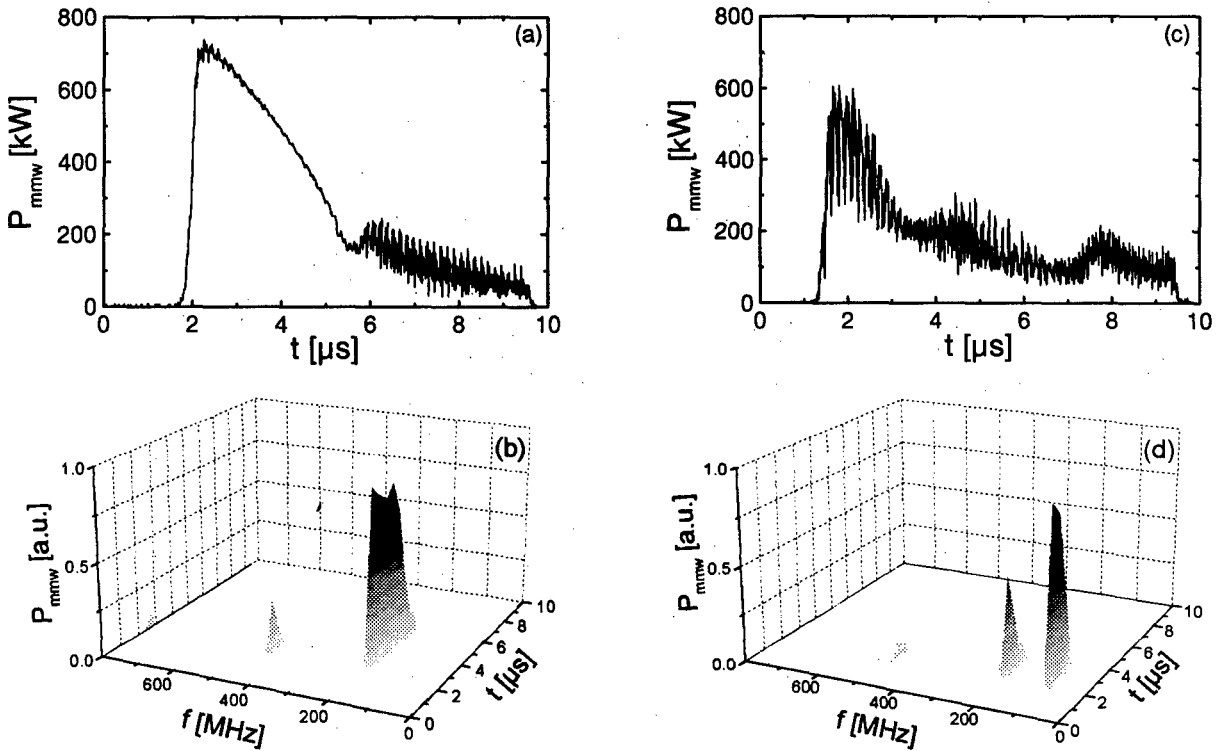


Fig. 2 Single-frequency mm-wave output power, P_{mmw} , for a 1.77 MeV, 7.2 A electron beam (a), and the corresponding frequency spectrum, shifted over 205.7 GHz (b). Multi-frequency mm-wave output power for a 1.76 MeV, 7.2 A electron beam (c), and the corresponding frequency spectrum, shifted over 205.7 GHz (d). The electron beam starts at $t = 0$.

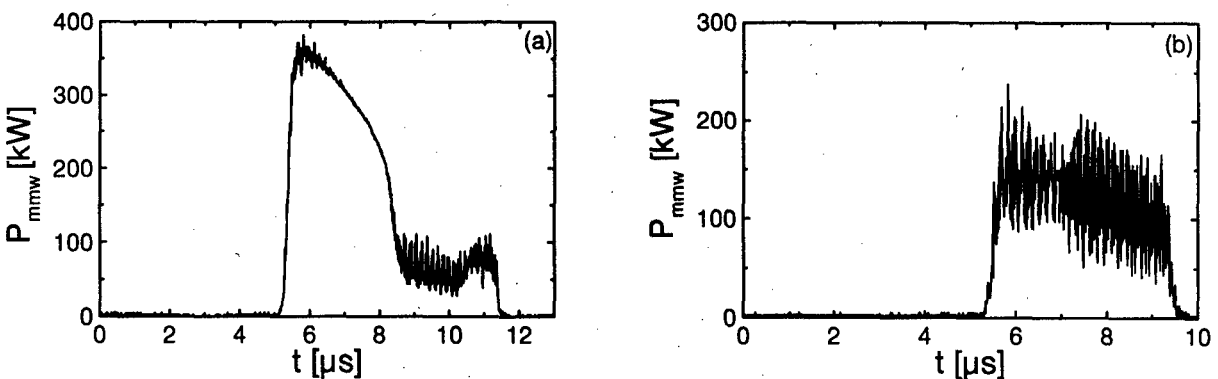


Fig. 3 mm-wave output power, P_{mmw} , for a 1.61 MeV, 7.1 A electron beam (single frequency) (a), and for a 1.59 MeV, 7.0 A electron beam (multi frequency) (b).

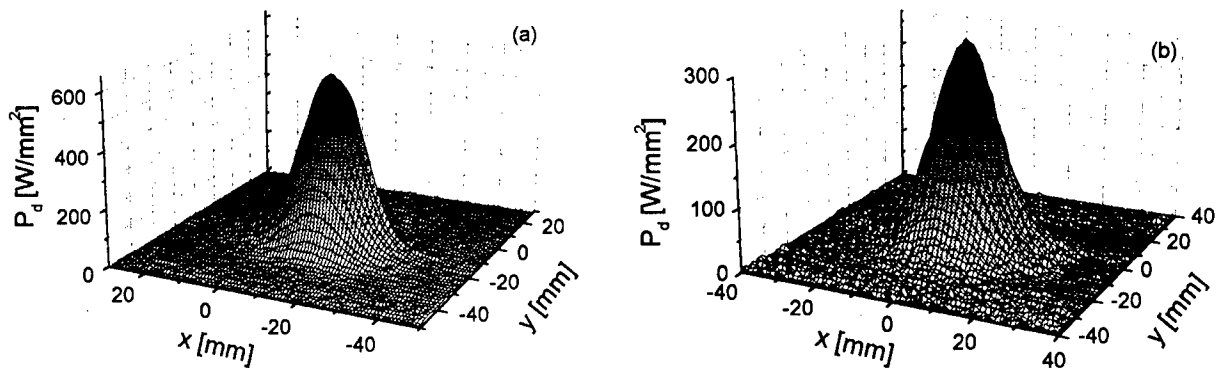


Fig. 4 Beam profiles for a 206 GHz beam. (a) and a 167 GHz beam (b), as measured with an heat-absorbing foil and an IR-camera. P_d is the power density.

4. DISCUSSION AND CONCLUSION

FEM can generate single-frequency output beams at all operating frequencies. This regime is reached when the gain curve overlaps with the higher frequencies of the cavity transmission curve, while FEM generates multi-frequency output when the gain curve overlaps with the lower frequencies. In the latter situation FEM operates almost in the linear regime, because (a) due to the voltage drop the gain curve runs out of the cavity curve in a short time and the interaction time is rather short, and (b) the reflection of the stepped waveguides is frequency-dependent, and decreases for frequencies away from the central frequency. Due to these two effects, the power does not grow strongly, i.e., FEM operates almost in the linear regime, and no mode competition and mode suppression takes place.

On the other hand, for high initial voltage the interaction time is much longer, and - more important - the gain curve passes through the central frequency region with a high reflection coefficient. The output power grows to a high level and reaches the non-linear regime. Mode competition takes place and the mode with strongest interaction grows on expanse of the side band and parasitic modes. This results in single-mode operation [5].

FEM generates 730 kW of mm-wave power, for a 7.2 A, 1.77 MeV electron beam. The start up time of the mm-wave beam agrees well with simulations. The electronic efficiency is 5.7 %, which is slightly higher than expected. These results were obtained for a setting with low cavity losses, in our case around 200 GHz. At all frequencies the Gaussian mode content of the output beams exceeds 99.8 %.

5. ACKNOWLEDGEMENT

This work was performed as part of the research programme of the association agreement of EURATOM and the 'Stichting voor Fundamenteel Onderzoek der Materie' (FOM) with financial support of the 'Nederlandse Organisatie voor Wetenschappelijk Onderzoek' (NWO) and EURATOM.

6. REFERENCES

- [1] W. H. Urbanus et al., Nucl. Instr. Meth. **A331** (1993) 235.
- [2] A. A. Varfolomeev et al., Nucl. Instr. Meth. **A341** (1994) 462.
- [3] G.G. Denisov, M. Yu. Shmelyov, in Proc. 21st Intl. Conf. on IR and MM-waves, eds. M. von Ortenberg and H.U. Müller, IR and MM-waves, Vol. 1 (1996) pp. BF3.
- [4] W.A. Bongers, et al., in Proc. 10th Workshop on ECE and ECRH, EC10, eds. A.J.H. Donné and A.G.A. Verhoeven, World Scientific, Singapore (1998), pp. 507-514.
- [5] A.V. Savilov, Optics Communications, **123** (1996) pp. 133-138.

High-Power Microwaves at 25 Years: The Current State of Development

John A. Swegle

Lawrence Livermore National Laboratory, Livermore, CA USA
and

James N. Benford

Microwave Sciences, Inc., Lafayette, CA USA

Abstract

The field of high-power microwaves (HPM) has matured considerably in the 25 years since the initial development of relativistic backward wave oscillators (BWOs) by researchers from the Institute of Applied Physics and the Lebedev Institute in Russia [1] and from Cornell University in the US [2,3]. In this paper, we review some of the signs of the maturity of the field, including changes such as an observed narrowing in the number of source types under development, an increase in commercial suppliers, and a growing internationalization of the research field. In addition, within the context of historical developments in the field, we discuss the development of high peak power systems and the apparent abandonment of the pursuit of ever-higher power in favor of the development of gigawatt-level systems with manageable weight and volume, repetitive operation, and tunability.

Introduction

This year is the 25th anniversary of the publication of the first paper providing experimental results for a true, high-power microwave source [1]. In the paper, researchers from the Institute of Applied Physics in Nizhny Novgorod and the Lebedev Institute in Moscow described a relativistic BWO producing 400 MW in 10-ns output pulses. A year later, workers at Cornell University, following up on Nation's discovery of low-efficiency microwave emission in electron beam experiments [2], produced a somewhat higher power in a similar device [3]. Since that time, power levels of a gigawatt or more have been generated with a wide variety of sources, some relativistic versions of conventional devices such as the magnetron, and others with operating features unique to the field of HPM, such as the vircator. These power levels have been generated at frequencies ranging from about 1 GHz to deep into the millimeter-wave range at 140 GHz. Power levels have approached, and in a few instances, surpassed 10 GW, and the scaling to even higher power levels has been considered in several cases.

On this 25th anniversary, signs of maturity can now be recognized in the field. They can be found in changes in the composition of the field, in terms of the participants, the sources under investigation and the applications driving their development, and in the geographic diversity of interest. Signs of maturity can be found also in the research agenda for the field. Two trends stand out in particular. First, we perceive a trend toward the production and use of versatile gigawatt- or near-gigawatt-level systems with manageable weights and volumes, repetitive operation, and frequency-tunable output. Second, we note the community-wide pursuit of longer pulses with microwave output tracking the power pulse of the electron beam driving the source. This latter work is summarized very succinctly in the proceedings of last summer's International Workshop on High Power Microwave Generation and Pulse Shortening, held in Edinburgh [4]. In this paper, we'll outline the changes we see in the field and review the trends we perceive in the development of versatile high-power systems.

Changes in the field of HPM

We see three notable signs that point to the growing maturity of the field of HPM: the narrowing of the types of sources under active development and the applications that drive that

development; an increase in the number of commercial suppliers of HPM systems; and a growing internationalization of the research field. With regard to the focus in source development, we note that three types of sources are becoming increasingly popular among users and researchers, in part because each has strong commercial support: relativistic magnetrons, high-power BWOs and TWTs, and reltrons and super-reltrons. Two other sources also continue to attract significant interest: the magnetically-insulated line oscillator (MILO), attractive because it offers power levels now reaching 1 GW in a low-impedance source without the complexity and bulk of an applied magnetic field; and the low-impedance relativistic klystron amplifier (RKA), another low-impedance source that has generated power levels around the 10-GW mark with pulse energies of about 1 kJ.

In addition to these sources, broadly attractive to researchers interested in high-peak power applications, we also see focused efforts driven by two well-defined applications:

- RF linacs for TeV electron colliders -- klystrons, based both on upgraded conventional tube technology and on relativistic source technology; magnicons; gyroklystrons; and TWTs.
- ECRH heating of fusion plasmas -- gyrotrons and, notably, the FEL under development by the FOM Institute in the Netherlands.

The application for RF linacs requires sources producing power in the 100-MW range at frequencies between about 10 and 30 GHz. On the other hand, the plasma heating application requires high average power in a continuous mode at frequencies in the range of 150 GHz and above. Strictly speaking, this latter is not an HPM regime, but the requirement for high-average power at these high frequencies stresses the state of the art.

In contrast to the aforementioned sources, we see a number of types falling by the wayside. Most notably, perhaps, is the virtual cathode oscillator, or vircator. This source offers high power levels in a relatively simple, low-impedance configuration that doesn't require an applied magnetic field. Unfortunately, vircators tend to up-chirp in frequency, due to gap closure in the electron beam diode, and they suffer from poor efficiency in many cases. The virtode, invented in Ukraine, offers some solutions, but to date it hasn't been widely pursued. Another factor contributing to the vircator's lack of popularity is the fact that magnetrons and reltrons offer attractive alternatives at the frequencies of interest. Relativistic gyrotrons and cyclotron autoresonance masers, which originally promised high peak power at higher frequencies, also seem to have fallen out of favor, although, as mentioned earlier, high average power gyrotrons still enjoy favor in their niche. The reasons for the lack of popularity here can perhaps be traced to reduced interest in high peak power sources at high frequencies, particularly at the expense of high operating voltages. Finally, the high-peak-power free electron laser (FEL) has fallen out of favor. While this source can be made to operate over a wide frequency range, the complexity of the required wiggler magnets, the high-voltage needed for high-frequency operation, and the guiding magnetic field additionally needed for high-power operation at lower frequencies perhaps result in a source of undesired complexity.

A sure sign of maturity in the field is the growing number of commercial suppliers for HPM systems. US firms find that the HPM hardware market in the 1990s mostly lies abroad due to diminished US-government purchases. We estimate total hardware revenue of about \$4M per year. Industrial research and development in the US, however, has steadily declined in the 1990s and is about zero now due to low profit margins. The smallness of this business makes larger defense firms reluctant to enter the field.

Current exporters of HPM equipment -- sources and pulsed power -- in the US are Titan Corp. (reltrons, systems) and Maxwell Physics International (relativistic magnetrons, vircators, complete turnkey systems). Integrated Technologies and Kiser Research distribute Russian equipment (BWOs, orotrons, RADANs, systems) around the world, as do the Russian institutes, notably the Institutes of Applied Physics, Electrophysics, and High-Current Electronics, themselves. Thomson Shorts has entered the European market, which is currently dominated by American firms.

Overall, the internationalization of HPM research can be traced to an interest in HPM as possibly a key emerging defense technology of the 21st century. The early programs in the USSR and US have evolved and influenced other countries to take an interest. The collapse of the USSR led to the dispersal of some Russian and Ukrainian HPM workers and the eagerness

of others to collaborate in international programs. At the current time, we would divide the various national efforts as follows:

- Major programs -- US and Russia;
- Medium-scale programs -- UK, France, China, and Ukraine; and
- Emerging programs -- Sweden, Germany, Israel, Taiwan, India, and Australia.

Depending on the scale of the effort in each country, work can be found at government laboratories, industrial firms, and in the universities.

Development of versatile HPM systems

The trend toward the development of versatile HPM systems is particularly interesting when viewed in historical context. We point to four significant programs in the development of HPM sources:

- Vircator experiments conducted on the AURORA accelerator at the Harry Diamond Laboratories (circa 1986-1991). AURORA was an enormous radiation effects simulator, and one arm of this four-arm accelerator, producing an approximately 7-MW, 160-kA beam, was used for HPM experiments. The cathode and drift-tube diameters in these experiments were 53 and 122 cm, and the A-K gap was varied up to 35 cm. At this large size, frequencies varied from about 0.7-1.0 GHz. Peak power levels of 1-4 GW were extracted from each of 18 ports, and a total pulse energy of about 1 kJ was generated. Unfortunately, the power was highly variable during a pulse, and the frequency was also highly variable from shot to shot.
- The Naval Research Laboratory RKA experiments (circa 1985-1996). This source operated at low-impedance and utilized near-virtual-cathode formation to very effectively bunch electrons in an amplifier configuration. Power levels of 6 GW could be generated reliably in 140-ns pulses at 1.3 GHz, giving pulse energies approaching 1 kJ. Single shots at levels up to 15 GW were seen at times. Further increases in power were expected to require a triaxial configuration, in which a high-current electron beam was propagated in a coaxial drift tube in order to raise the space-charge limiting current of the device, although this source never came to full realization.
- The Lawrence Livermore and Lawrence Berkeley National Laboratories high-peak-power FEL (circa 1982-1995). These experiments demonstrated gigawatt production at high-efficiency using wiggler tapering on the ETA-1 accelerator. Later experiments on the upgraded ETA-2 accelerator produced gigawatt-level output at 140 GHz, as well as high average power in 2-kHz bursts using magnetic switching technology. Ultimately, this experiment was terminated when it was deemed that the technology was overly complex, in contrast to high average power gyrotrons, for ECRH heating of fusion plasmas, the application for which it was ultimately funded.
- The multiwave Cerenkov generator (MWCG) and relativistic diffraction generator (RDG) experiments conducted on the GAMMA accelerator at the Institute of High-Current Electronics. The long-pulse accelerator, operating in flat pulses to one microsecond, was used to drive sources producing power levels approaching 10 GW in X-band, and gigawatt power levels at frequencies of 30-40 GHz. Pulse energies of the order of 1 kJ were generated, and a variety of pulse shortening mechanisms were examined. Ultimately, scaling experiments showed the way to operation at high ratios of the diameter of the source to the output wavelength. Unfortunately, this scaling also pointed to a requirement for extremely large capacitor banks to drive the field coils producing the guide field in the interaction region.

In common, each of these significant experiments was very large. In the case of the RKA and the MWCG/RDG systems, scaling experiments pointed the way to power levels potentially in the tens to hundreds of GW, but the sizes and complexity of these systems became daunting. In the case of the FEL, size and complexity once again became problematic, particularly in regard to alternatives for the ultimate application.

Today, we point to three systems enjoying widespread popularity among researchers and users because of their high output power, of the order of a gigawatt, their manageable size and weight, their tunability, and their demonstrated capability for repetitive operation. In addition, each is essentially available from a commercial supplier:

- Relativistic magnetrons, produced by Maxwell Physics International, generating power in the gigawatt range and pulse energies of about 100 J, at frequencies in the L- and S-bands;
- BWOs and TWTs, produced at the Institute of High-Current Electronics, producing power levels up to and beyond a gigawatt and energies of 100 J or more, depending on the size of the pulsed power unit, primarily in the X-band; and
- Reltrons and super-reltrons, built by Titan in Albuquerque, NM, with power levels approaching a gigawatt and energies of 200 J and more, primarily in the L- and S-bands, with scaling to higher frequencies at lower power.

The relativistic magnetrons, when powered by a compact linear induction accelerator (CLIA), also developed at Maxwell Physics International on the model of a system developed at the Institute of Nuclear Physics at the Tomsk Polytechnic Institute, have utilized magnetic switching technology to operate at kilohertz rates. Using an in-house developed technique, they have also been shown to have a tuning range at high power of about 30% in S-band. These systems are also widely used in pulse-lengthening research and in the development of coherently-phased arrays of HPM sources.

The BWOs, driven by IHCE SINUS pulsed power generators, can also operate at repetition rates of 100 Hz. These X-band machines have been the drivers for experiments in the development of high-efficiency BWOs that can be mechanically tuned over about a 5% bandwidth while operating at constant power using control systems developed at the University of New Mexico.

The reltrons and super-reltrons are, in themselves, quite compact, their size being determined almost solely by the pulsed power systems driving them. They've become workhorses in simulation and effects studies, and tunable output is available using a variety of different modulating cavities, as well as different extraction cavities operating at harmonics of the modulation frequency.

Summary

The field of HPM is maturing in its 25th year. Years of investigation have led to a sharpening of the research focus, created a commercial supplier base, and generated international interest in the technology. While earlier experiments have demonstrated very high power levels over a broad range of frequencies, users and the research community have fixed on several systems with very versatile features and relatively compact dimensions. Nevertheless, research continues on several other sources with attractive prospects. Looking into the future, the prospects for the near term appear to favor sources aimed at defense interests, with linear accelerators and ECRH plasma heating constituting additional technology drivers.

References

1. N. F. Kovalev, M. I. Petelin, M. D. Raizer, A. V. Smorgonskii, and L. E. Tsopp, *ZhETF Pis. Red.* **18**, 232 (1973) [*JETP Lett.* **18**, 138 (1973)].
2. J. A. Nation, *Appl. Phys. Lett.* **17**, 491 (1970).
3. Y. Carmel, J. Ivers, R. E. Kribel, and J. Nation, *Phys. Rev. Lett.* **33**, 1278 (1974).
4. International Workshop on High Power Microwave Generation and Pulse Shortening -- Papers, Edinburgh International Conference Center, June 10-12, 1997, printed by the University of New Mexico and the Phillips Laboratory, Albuquerque, NM.

X-BAND KLYSTRON DEVELOPMENT AT KEK

K. Takata, Y. H. Chin, H. Mizuno, S. Fukuda, S. Tokumoto,

S. Michizono, S. Matsumoto and H. Tsutsui

KEK, 1-1, Oho, Tsukuba, Ibaraki, 305-0801, Japan

S. Kazakov

BINP, 142284, Protvino, Moscow, Russia

Abstract

X-band klystrons (XB-72K) designed for the next linear collider (JLC) are described. Klystrons having traveling-wave output structures in order to reduce the electric fields and an rf output power of around 70 MW have been obtained. A new klystron-simulation code using "MAGIC" has been developed at KEK, and the simulation results agree well with the experimental data. The next klystron was designed using the code; an rf output of 120 MW is obtained in the simulation. The klystron is being manufactured and it will be tested this November.

1. Introduction

X-band (11.424GHz) high-power pulse klystrons will be used in the next linear-collider (JLC) project. Ten X-band klystrons (XB-72K (Fig.1) #1 to #9 and PPM #1) have been made at KEK for R&D. The RF discharges in the output cavity were repeatedly observed at the prototype #2 to #5 XB-72K tubes employing a single gap output structure [1]. These discharges limited the rf pulse duration to at most 100 ns at 90 MW (or 200 ns with 30 MW output power). The discharges were considered to be due to high electric fields on the surface and/or spread of the beam due to deceleration. In order to avoid discharging, a travelling-wave (TW) type multi-cell structure, having lower electric fields and a larger bore radius, was adopted. In this paper we describe the results of the klystron based on the TW-structure output.

A new simulation code using "MAGIC[2]" has been developed at KEK in order to simulate TW structures precisely. The performance of the klystrons can be analyzed using the code and a next klystron (XB-72K #10) was designed by the code. The design goal, which was changed during the elaboration process of the JLC parameters, is to produce a 120 MW-class klystron with a pulse length of 1.5 μ s.

2. X-band klystron with travelling wave (TW) structure

The prototype (#7 to #9) klystrons were same to prototype #5 except output. In these klystrons, nose cone removed pillbox cavities were adopted, except for the input cavity, in order to reduce electric fields on the surfaces of the cavities [1]. The output structures were designed by BINP with the one-dimensional code "DISKLY" developed at BINP.

The basic output structure of #7 to #9 klystrons is the $\pi/2$ -mode travelling wave; also many modifications have been made according to the energy conversion from beam to the structure.

The output structure of prototype #7 has a choke (4 cells + 1 choke) in order to suppress any leakage-fields from the final cell. Although the maximum surface fields decreased, higher order modes coupled with the choke and the collector caused an instability.

The output structure of #8 had no choke, and one more cell (5 cells) was used in order to increase the efficiency. Although the

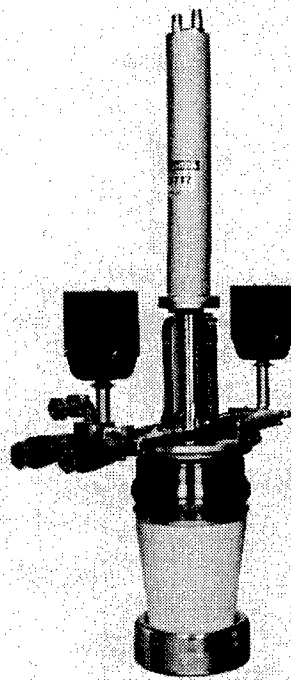
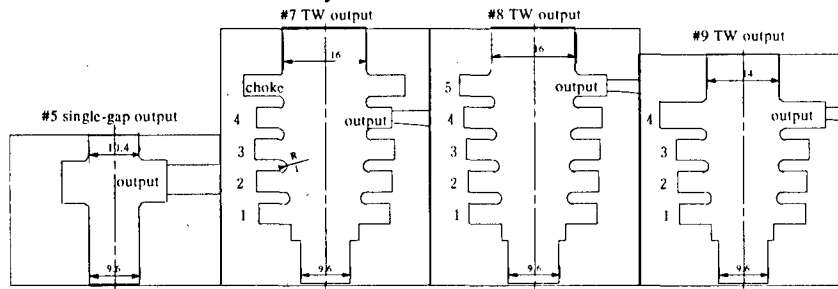


Fig.1 Photograph of the XB-72K klystron

Table 1 Rf structures of KEK X-band klystrons



	#5	#7	#8	#9	XBPPM#1	#10
Cavities except output	4	Same to #5	Same to #5	Same to #5	5	5
Output structure	Single-gap	TW (4+choke)	TW (5cells)	TW (4cells)	Same to #9	TW (4cells)
Total length (input to output cav.)	240 mm	260mm	260mm	260mm	400mm	330mm
Magnet	Electro-	Electro-	Electro-	Electro-	permanent	Electro-
Max. magnetic field	7kG	Same to #5	Same to #5	Same to #5	3.8kG	7kG
Design method	FCI	DISKLY	DISKLY	DISKLY	DISKLY	MAGIC
MicroPervance	1.2	1.2	1.2	1.2	(0.98)	(1.2)
Beam voltage	580kV	505kV	535kV	520kV	(550kV)	(550kV)
Rf output	90MW*	54.5MW**	55MW	72MW	(110MW)	(120MW)
Pulse width	100ns	100ns	500ns	100ns***		(1.5μs)
Efficiency	29%	25%	22%	31%	(50%)	(44%)

*serious discharge takes place. ** Rf output is unstable. ***Conditioning is in progress.
():design value.

efficiency was low, an rf output power of 55MW with a long pulse (400 ns) was achieved.

The output structure of the #9 klystron consists of 4 cells; it has a more optimal structure than did the previous ones. The bore diameter between the collector and the final output cell was reduced from 16 mm (#7) to 14 mm (#9) in order to avoid higher order modes. The efficiency increased to 31% and no rf instabilities were observed. The maximum output power is 72 MW and conditioning is now in progress with increasing the pulse width.

A PPM (periodic permanent magnet) klystron designed by BINP is now being delivered. The klystron consists of 18 periodic permanent magnet (PPM: the magnet material is NeFeB) elements with 5 rf cavities and a TW output. The design pervance was decreased to 0.98μ in order to avoid a large space-charge force and to increase the efficiency. It will be tested this month (June-1998).

The experimental results and the design parameters of these klystrons are summarized in Table 1 along with a figure of output structures. The output performance is shown in Fig.2.

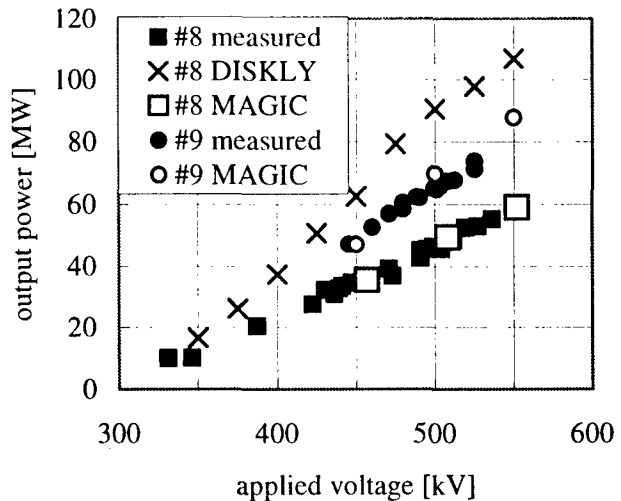


Fig.2 Output results of #8 and #9 klystrons together with simulation results.

3. Analysis of X-band klystrons by "MAGIC"

A klystron with a single output cavity, such as the S-band klystron used in KEKB, can be simulated by Arsenal-

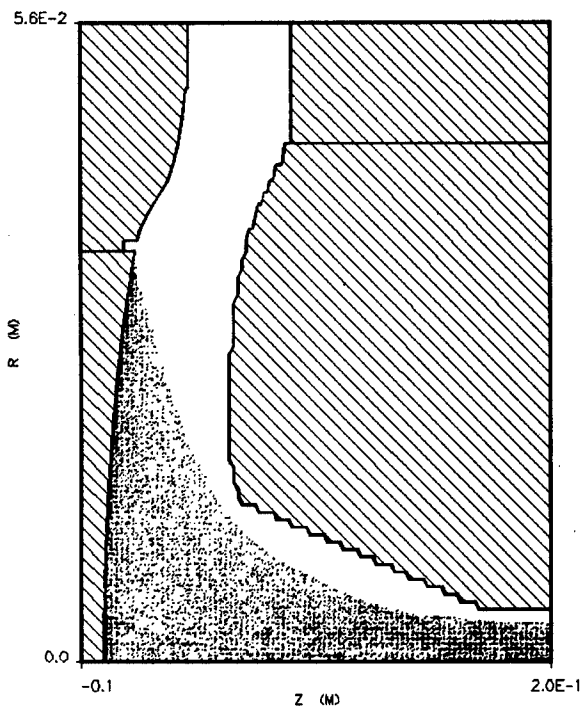


Fig.3 Particle trace of the electron gun region by the code using "MAGIC".

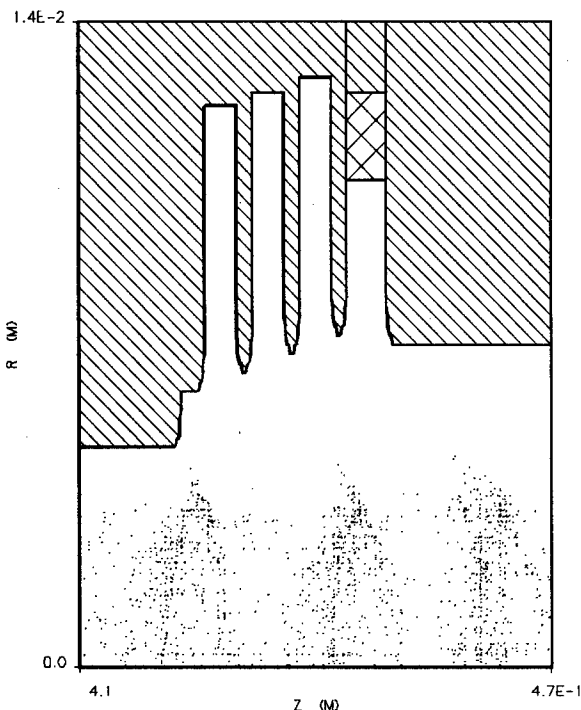


Fig.4 Particle trace of the TW structure of #9 klystron.

MSU, which was developed at MSU and can simulate from a gun to a collector, and FCI [3]. However, no available simulation-codes, except for the 1D code "DISKLY", were able to simulate a TW structure. "DISKLY" uses a port approximation and equivalent circuits in TW structures.

Fig.2 also shows the simulation results. The experimental output power of the #8 klystron was about half that obtained by "DISKLY". The difference is probably due to an insufficient port model and/or a limitation of the 1D code, which does not consider beam blowup.

In order to simulate a klystron precisely, we started to use a 2.5D particle-in-cell (PIC) program "MAGIC", which is used in plasma-physics problems. In "MAGIC", neither a port approximation nor an equivalent-circuit model is used, and only a geometry of the structure is necessary to be input. By using a general program ("MAGIC"), one can modify and develop a simulation system by oneself even if a new idea for klystrons occurs.

In the simulation, the klystron is divided into three parts (gun, buncher and output). In the gun region [4], the calculated perveance agreed well with the experimental one, and a similar profile of the current density to that of "EGUN" [5] was observed. Fig.3 shows the particle trace of the XB-72K klystron. The particle data (r, z, P_r, P_z, P_ϕ) are exported to the next buncher section.

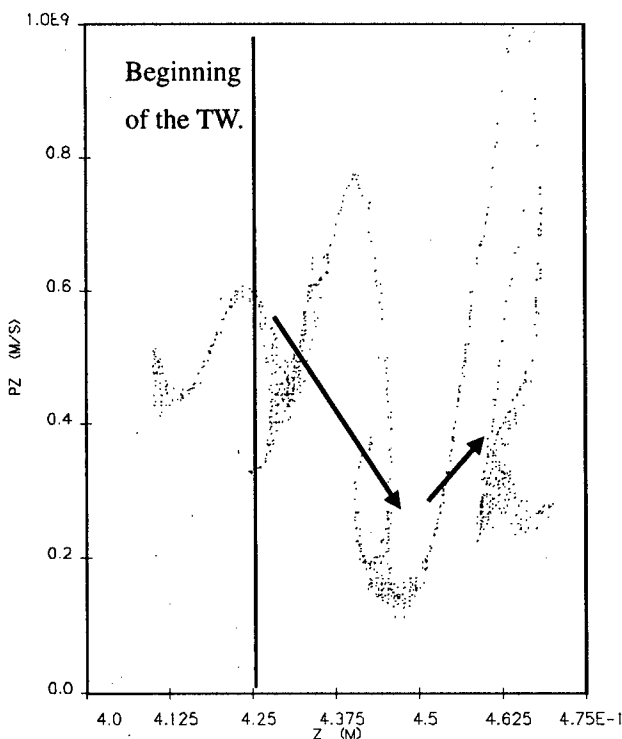


Fig.5 Electron momentum (γv) change at TW structure of #8. The electrons are decelerated at the beginning, but accelerated at the end.

In the buncher, particle traces and development of a harmonic current in the drift tube were observed [6]. Also, the particle data are exported to a next TW structure. After an approximation of the 3D output waveguide into 2D [7], the output power and the particle trace (Fig.4) can be calculated. The output power calculated by the code using "MAGIC" agrees well with the experimental results as shown in Fig.2.

The #8 and #9 klystrons were analyzed using "MAGIC". It was found that a rather poor efficiency of the #8 klystron results from a large deceleration at the beginning of output structure, which results in particle acceleration at the end; also, the energy-conversion efficiency (from beam to rf) becomes low (Fig.5). Although the output structure of the #9 klystron has been found not to be bad, the small gain of the harmonic current ($I_1/I_0=1.3$: as shown in Fig.6) causes a low output power. A longer drift length and/or a modification of the cavity configuration are desired for a larger harmonic component.

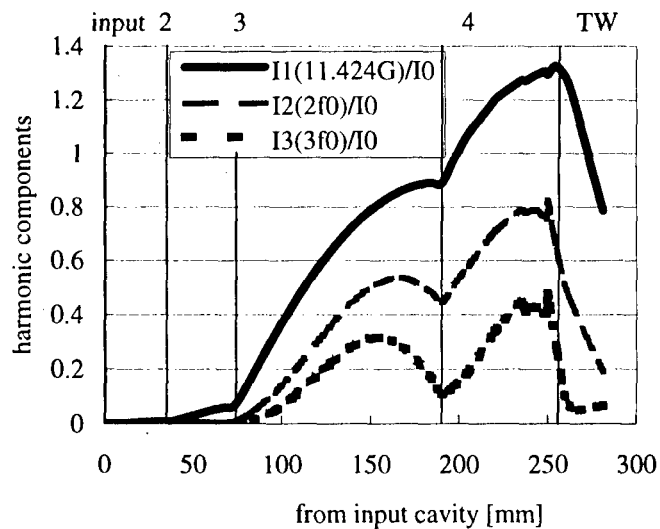


Fig.6 Development of harmonic currents simulated by using "MAGIC". (#9 klystron)

4. Prototype #10 klystron

The next XB72K #10 klystron was designed using "MAGIC". A longer drift length and an additional penultimate cavity were adopted in order to increase a harmonic component ($I_1/I_0=1.55$) and stagger tuning was applied for a wider band-width (60MHz @#9 klystron to 100MHz @#10). The basic output structure is $2/3\pi$ -mode in order to reduce the surface fields (the wave length of each cell is longer than in the $1/2\pi$ -mode). By modifying the output cells, a fairly constant gradient (the maximum surface field 20% less than #9 structure) was achieved. An output power of 120 MW was being obtained in the simulation. The design parameters are summarized in Table 1. XB72K #10 is now being manufactured and a high-power test is scheduled to start from this November.

5. Summary

X-band klystrons designed for the JLC projects are summarized. The test results of the #8 and #9 klystrons have been compared with the newly developed simulation code using "MAGIC". The simulated output power agrees well with the experimental results. The analysis by "MAGIC" revealed that the TW structure is not optimal for the #8 klystron. It has also been found that the insufficient configuration of the rf cavities and the short total length cause a low output power (#9). The next #10 klystron was designed using the code, and an output power of 120 MW was obtained in the simulation. The klystron will be tested from this November.

References

- [1] J.Odagiri et al., Proceedings of the 17th International Linac Conference, Tsukuba, Japan, 1994, p.469.
- [2] Mission Research Corporation, Virginia, USA.
- [3] S.Fukuda, Proceedings of the 3rd Workshop on Pulsed RF Sources for Linear Colliders (RF96), Hayama, Japan, 1996, p.123.
- [4] S.Michizono et al., to be presented at LINAC98, Chicago, USA, August 23-28.
- [5] W.B.Herrmannsfeldt, "Electron trajectory program," SLAC266, Stanford Linear Accelerator Center, Nov.1979.
- [6] S.Matsumoto et al., to be presented at LINAC98, Chicago, USA, August 23-28.
- [7] H.Tsutsui et al., to be presented at LINAC98, Chicago, USA, August 23-28.

Development of high power gyro-amplifiers at Ka-band and W-band for radar applications*

B. Levush, M. Blank, J.P. Calame, M. Garven⁺, J.J. Choi[#], B.G. Danly,
K. Nguyen[&] and D.E. Pershing^{\$}

*Code 6840 Naval Research Laboratory
Washington, D.C. 20375*

Abstract

Potential applications for millimeter wave radar include high resolution imaging, precision tracking and cloud physics studies. For most of the applications in the millimeter wave band the relatively high atmospheric absorption necessitates the use of high power sources. In addition, many of the applications call for extended instantaneous bandwidth. Recent investigations at Naval Research Laboratory have been focused on enhancement of the power-bandwidth product in millimeter wave gyro-amplifiers. Both gyroklystron and gyrotwystron type circuits have been investigated to achieve this goal. The two cavity gyroklystron circuit at Ka-band produced 210 kW output power at 37% efficiency with a 125 MHz FWHM bandwidth [1]. A three-cavity Ka-band gyroklystron achieved 225 kW peak output power with 286 MHz FWHM bandwidth [2]. At W-band four cavity gyroklystron circuit produced 60 kW peak output power at 25% efficiency with a 640 MHz FWHM bandwidth [3-4]. The gyrotwystron circuit achieved 50 kW peak output power at 17% efficiency with 925 MHz FWHM bandwidth [5]. This represent a record power-bandwidth product at W-band. The experimental results are in excellent agreement with theoretical predictions. Transition of the gyroamplifier technology into millimeter wave radar systems will offer significant improvements in radar detection, imaging and tracking.

Ka-BAND GYROKLYSTRON EXPERIMENTS

A schematic of the three-cavity, gyroklystron amplifier experiment is shown in Fig. 1. An electron beam of up to 12 A is produced from a thermionic, double anode magnetron injection gun by applying voltages of 65-75 kV. The magnetic field at the cathode can be varied with the gun coils to control the beam velocity ratio, α (v_{\perp}/v_z).

The beam is adiabatically compressed as it enters the region of high magnetic field (approx. 13 kG) generated by the 14 coil superconducting magnet. The three cavities of the gyrokystron circuit are positioned in the region of constant magnetic field. Each cavity operates in the TE_{011} cylindrical waveguide mode. Drive power is directed into a passive TE_{411} coaxial resonator which surrounds the TE_{011} input cavity. Power is coupled to the circular-electric mode inside the inner cavity by four axial slots placed every 90 degrees in azimuth. The measured cold resonant frequency of the input cavity is 34.89 GHz and the loaded Q_L is 188 (primarily diffractive due to the coupling slots). The intermediate (buncher) cavity employs an annular ring of lossy ceramic against the upstream endwall to provide the desired cold-test Q_L of 194 and a resonant frequency of 34.62 GHz. The downstream end of the output cavity employs an outward radial step and a nonlinear uptaper to achieve a cold-test Q_L of 175 and a resonant frequency of 34.83 GHz. The frequency upshift due to the presence of the electron beam is approximately 70 MHz. The drift tubes between cavities are loaded with lossy ceramic rings to suppress instabilities.

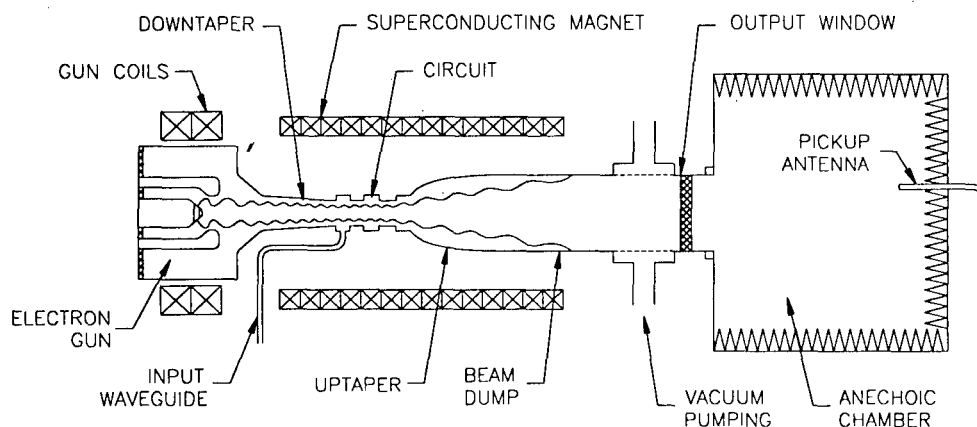


FIGURE 1. Schematic diagram of the Ka-Band gyrokystron experiment.

A 3.81 cm, half-wavelength thick BeO disk positioned immediately after the pumping manifold functions as the output window. The experiment employed two different diagnostic systems for measuring output power. The main diagnostic was an anechoic chamber joined to the output waveguide which had an absolute accuracy of 8% and a relative accuracy of 0.25%. A high-average power calorimeter with 5% absolute accuracy was also used to confirm the higher power measurements.

Systematic studies were performed over a wide range of operating voltages, currents, magnetic fields, and drive frequencies. A peak power of 225 kW at 34.90 GHz, with a -3 dB bandwidth of 0.82%, a saturated gain of 30.3 dB, and an efficiency of 32% was

obtained [2]. These values were measured with a beam voltage of 70.2 kV, a current of 10 A, a magnetic field of 13.1 kG and a pulse width of 2 μ s. The beam velocity ratio α was determined to be 1.27 ± 0.05 using a capacitive probe placed just upstream of the input cavity. The frequency response for this case is shown in Fig. 2.

Additional enhancements in bandwidth were achieved with magnetic field adjustments and changes in beam voltage and current, at the expense of output power. For example, raising the voltage to 73.10 kV and the nominal magnetic field to 13.40 kG produced a -3 dB bandwidth of 0.94% but with a lower peak output power of 200 kW (shown in Fig. 3). The beam current was 10 A, and the efficiency was 27.5% for this case. Detailed studies of how the bandwidth varies with operating parameters will be presented, along with comparisons to theory. In general, the measured bandwidth of the three-cavity device is 2.0-2.7 times as large as that obtained from the previous two-cavity gyrokystron experiment [1].

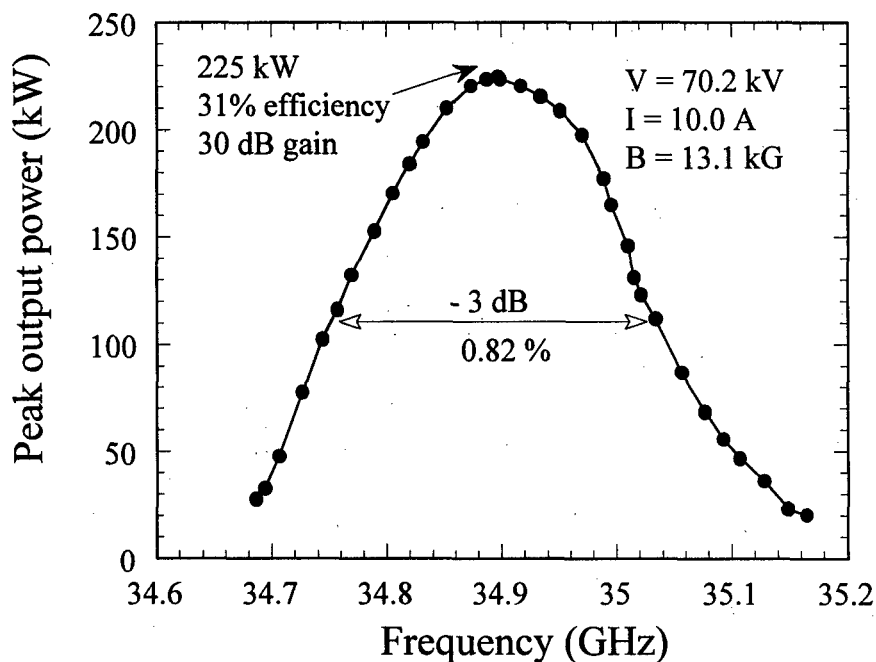


FIGURE 2. Experimental frequency response of 3 cavity Ka-band circuit at 13.10 kG.

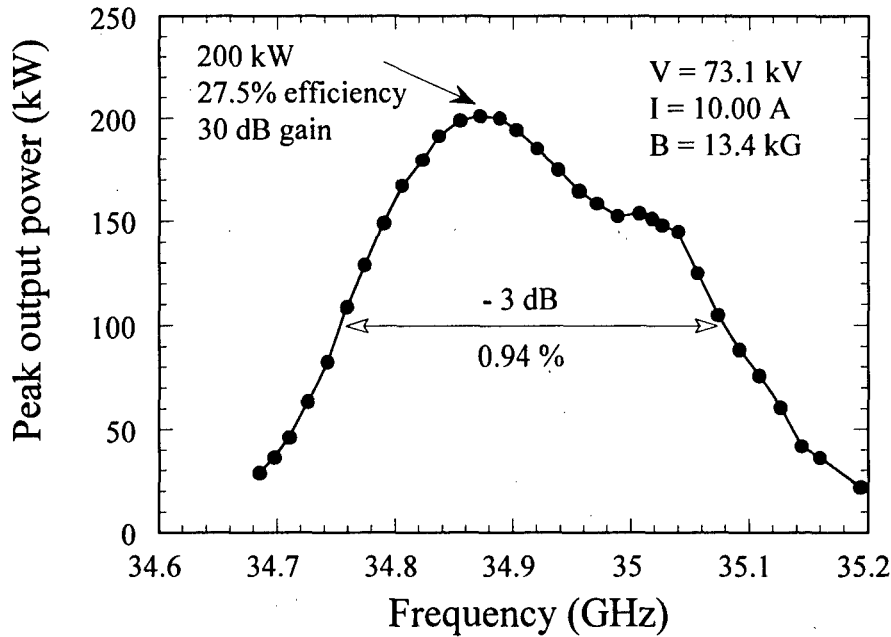


FIGURE 3. Experimental frequency response of 3 cavity Ka-band circuit at 13.40 KG.

W-BAND GYRO-AMPLIFIER EXPERIMENTS

Several TE_{011} mode W-band gyro-amplifiers operating near the fundamental cyclotron frequency have been built and tested. Each circuit consists of four or five interaction sections separated by drift sections cutoff to the operating mode. For each circuit, a coaxial drive cavity, similar to that described above for the Ka-band experiment, was used. The input cavity parameters were determined through theoretical modeling with HFSS, a finite element code that computes field distributions and S-parameters for passive 3D structures.

As in the case of the Ka-band buncher cavity, the desired Q values (100-200) of the intermediate cavities are achieved by ohmically loading the cavities with rings of lossy ceramic placed at one end of each cavity. In the output sections, where no ceramic loading is used, power is diffractively coupled through a 5 degree linear uptaper to the collector radius. For each circuit, the parameters of the intermediate cavities and the output cavities/sections were determined through cold test measurements. A 2 kW peak power, mechanically tunable Extended Interaction Oscillator was used to supply the drive power. The tests were typically performed with 2 μ sec pulses at 250 Hz for 0.05% duty. The measured results for five recently demonstrated W-band gyro-amplifier circuits are shown in Table 1.

TABLE 1. Measured performance of NRL W-band gyro-amplifiers.

Circuit	Peak Output Power (kW)	Efficiency (%)	Bandwidth (MHz)	Gain (dB)	Power x BW (kW-GHz)
WGKL1	67	28	460	29	30.8
WGKL2	60	25	640	27	38.4
WGTWY1	50	18	925	30	46.3

Results from the WGKL1 circuit [3], which was used to benchmark the design tools, and WGKL2 [4] have been previously reported.

In the four section WGTWY1 circuit, the output cavity was replaced by a traveling wave section to maximize the bandwidth of the device. Figure 4 shows the measured and theoretically predicted peak output power and efficiency versus drive frequency for a 57 kV, 5 A electron beam. As shown in Fig.4, the measured FWHM bandwidth was 925 MHz and the peak output power was 50 kW, corresponding to a power-bandwidth product of 46.25 kW-GHz [5]. This power-bandwidth product represents a significant increase over the power-bandwidth product of the gyrokystron amplifiers (see Table 1). The measured data and predictions of non-linear theory are in good agreement. The cavity and output section parameters are also indicated on the plot. The traveling wave output section has a measured Q of 70, which is 15% below the minimum diffractive Q.

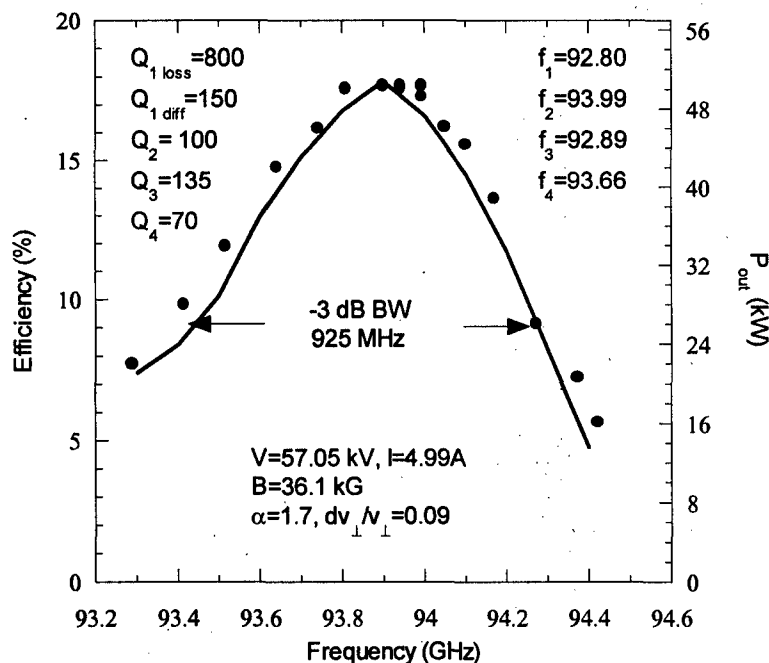


FIGURE 4. Measured (filled circles) and theoretical (solid line) peak output power and efficiency versus drive frequency for the WGTWY1 circuit.

SUMMARY

Several multi-cavity Ka-band and W-band gyro-amplifiers have been experimentally demonstrated at the Naval Research Laboratory. Each circuit was designed to optimize certain aspects of performance such as output power, bandwidth, or gain. A three-cavity, Ka-band gyro-klystron amplifier has demonstrated a peak output power of 225 kW at 34.90 GHz, with a -3 dB bandwidth of 0.82%, 30 dB saturated gain and 31% efficiency. A four-cavity gyro-klystron amplifier has achieved 60 kW peak output power at 25% efficiency with 640 MHz bandwidth. A four section W-band gyrotwyston demonstrated 50 kW peak output power at 925 MHz bandwidth. Both, K_a-band and W-band, experiments demonstrated a record power-bandwidth product. The success of the experiments was due in large part to a battery of improved large-signal, stability and cold test codes employed in the modeling and design stage [6].

This work supported by the Office of Naval Research. The computational work was supported in part by a grant of HPC time from the DoD HPC Center NAVO and the ARL HPC center.

- (+) Permanent Address: University of Maryland, College Park, MD.
- (#) Current Address: Kwangwoon University, Seoul, South Korea.
- (&) Permanent Address: K-N Research, Silver Spring, MD.
- (\$) Permanent Address: Mission Research Corp., Newington, VA.

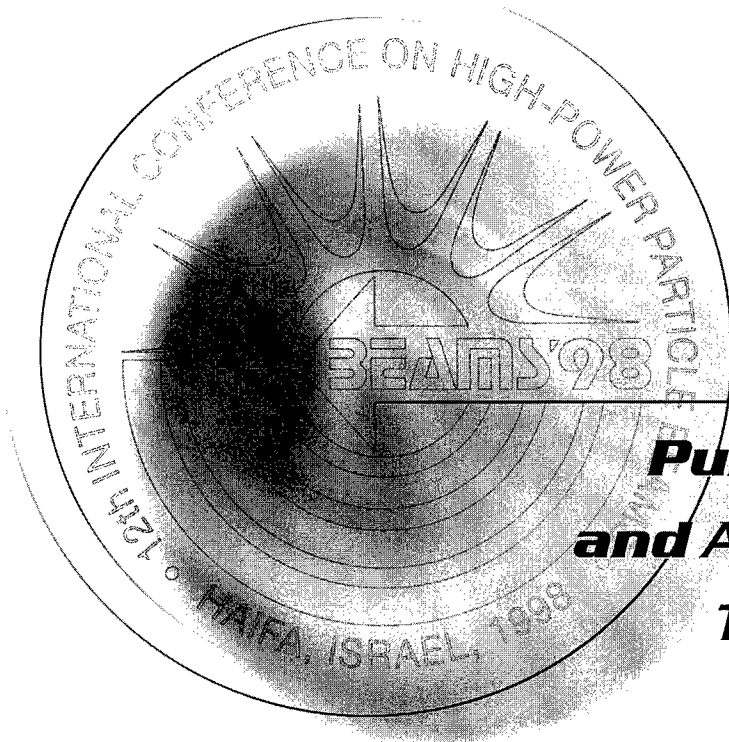
REFERENCES

1. J. J. Choi *et al.*, "Experimental investigation of a high power, two-cavity, 35 GHz gyro-klystron amplifier," *IEEE Trans. Plasma Sci.* **26**, 416-425 (1998).
2. J.P. Calame *et al.* "Experimental studies of bandwidth and power production in a three-cavity, 35GHz gyro-klystron amplifier", *Phys. of Plasmas*, **6**, 285-297 (1999)
3. M. Blank *et al.*, "Experimental demonstration of a W-band gyro-klystron amplifier," *Phys. Rev. Lett.* **79**, 4485-4488 (1997).
4. M. Blank *et al.*, "Experimental Investigation of W-band (93 GHz) gyro-klystron amplifiers," *IEEE Trans. Plasma. Sci.* **26**, 409-415 (1998).
5. M. Blank *et al.* "Experimental Demonstration of a W-band (94GHz) Gyrotwyston Amplifier", to be published, *IEEE Trans. Plasma Sc.*, 1999.
6. B. Levush *et al.* " Modeling and design of millimeter wave gyro-klystron", to be published, *Phys. of Plasmas*, 1999.



BEAMS'98

12th INTERNATIONAL CONFERENCE
ON HIGH-POWER PARTICLE BEAMS



ORALS

***Pulsed Power
and Accelerator
Technology***

Vol. I

Proceedings

INTENSE BEAMS: THE PAST, PRESENT, AND FUTURE*

G. Yonas, M. A. Sweeney

Sandia National Laboratories, Albuquerque, NM 87185-0151

INTRODUCTION

Nobody could have predicted the circuitous course of the last 30 years of progress in intense beams and pulsed power. There were many discoveries and twists and turns along the way, but the steady flow of understanding and technological advances has sustained the field. Pulsed power research began in the early 1960s with the development of the technology to test the reliability of nuclear weapons in a pulsed radiation environment. Because of the effort in the 1970s on an electron beam approach to inertial confinement fusion (ICF) at Sandia National Laboratories and at the Kurchatov Institute, simulation codes, diagnostics, and innovative pulsed power techniques such as self-magnetic insulation were developed. The electron approach ended in 1979, and the more promising ion approach continued. At the same time, z-pinchs, used since the early 1970s to evaluate the response of materials to keV x-rays, were considered as an alternative to drive ICF capsules. The use of z-pinchs for ICF was discontinued in 1984 because of budget cuts and the belief that ions offered a route to the standoff requirement for energy applications. Now, in 1998, because of budget limitations and the 1995 discovery that the soft x-ray power achievable in a z-pinch implosion can be greatly enhanced, the ion approach has been suspended, and a new facility, X-1, is proposed to achieve high yield in the laboratory with z-pinchs.

In this paper we review the research paths that led to these changes, describe the present status of z-pinchs, and predict what the future holds. Although nobody can predict the future, the past 30 years have taught us some lessons that can be applied to the next 30 years. The paper concludes with some of these "lessons learned."

THE PAST

Intense beam research is based on pulsed power capabilities developed to provide bremsstrahlung sources of short duration for testing the resistance of weapons components to nuclear radiation bursts at what is now called the Atomic Weapons Establishment in Aldermaston, England, under Charlie Martin.¹ There, a series of ideas led to the first pulsed power accelerator, SMOG, in 1964 and formed the basis of the prolific international pulsed power technology that exists today and includes research at Sandia, Cornell University, Naval Research Laboratory (NRL), Physics International (PI), Maxwell Technologies, Los Alamos National Laboratory, the Blackett Laboratory at Imperial College, Weizmann Institute, Forschungszentrum at Karlsruhe, Nagaoka University, the Institute of High Current Electronics, Kurchatov, Arzamas, and the Trinitite Institute.

In the United States, pulsed power technology has mainly been funded by the Department of Energy and the Defense Special Weapons Agency. Short-pulse energy storage devices at Sandia during this early period (SPASTIC, Hermes I and II, Nereus, Hydra) produced an electron beam at the cathode from the explosion of small whiskers as the diode current increased, or produced an x-ray source to provide high-dose-rate radiation for weapons effects testing and to assess the response of materials to rapid energy deposition.

**This work is supported by the U.S. Department of Energy contract DE-AC04-94-AL85000.*

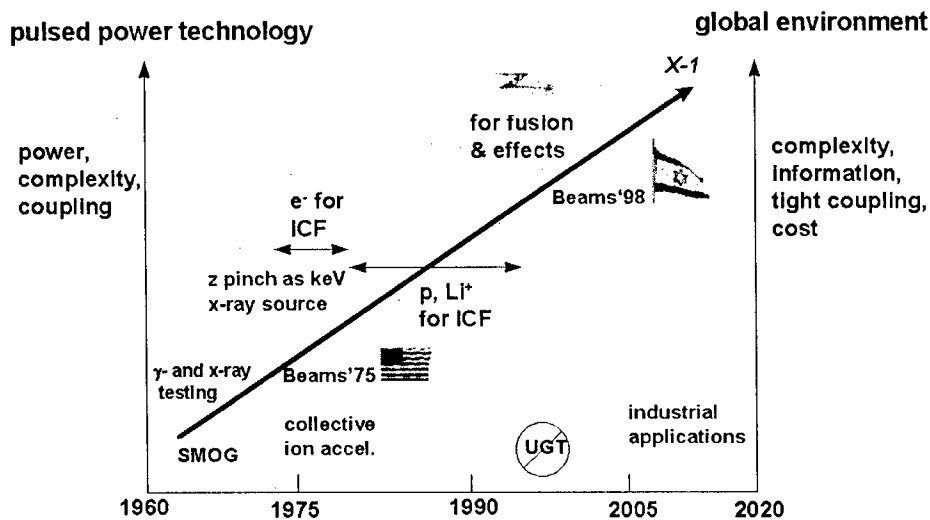


Figure 1. Timeline showing highlights in intense beams and pulsed power technology, beginning with operation of the first submicrosecond pulsed power device in 1964.

Energy in a pulsed power accelerator is taken slowly from local power grids stored in a bank of high-voltage capacitors, called a Marx, quickly discharged in a microsecond, and compressed in time in a coaxial pulse-forming line using a high-speed switch to get high power. Power is then compressed in space in the accelerator center to get high power density. Over the years, the problem of transporting the electromagnetic energy at increasingly higher power density has been addressed by improved design of pulse-forming components, selection of dielectrics of higher breakdown strength, use of self-magnetically-insulated transmission lines, and laser triggering to synchronize pulses in separate, azimuthally-arranged modules. Technological advances have occurred since completion of PBFA II, the largest pulsed power accelerator, in 1985. One of the most significant of these is the efficient, compact, and versatile linear voltage addition in the water sections of Hermes III and SABRE.

In a pulsed power accelerator, electrons or ions are produced by forming a plasma gap between two electrode surfaces and accelerating the particles across a small inter-electrode gap. Specific geometry and magnetic field configurations produce electron flow or, instead, suppress this flow using a “virtual cathode” that enhances the flow of ions and, with space charge and current neutralization, allows ions to propagate ballistically or in a current-carrying channel to a target.

In the early 1970s, it was recognized that the electrons could be concentrated to high enough intensities for ICF.² In 1976, 10^6 fusion neutrons were obtained on Angara at Kurchatov by heating a gold foil with reflexing electrons and using a multiple shell target containing deuterium. The following year, Sandia obtained fusion neutrons from the “ Φ target” on REHYD, by electrical breakdown along a CD_2 wire embedded in a capsule that both preheated the fuel and established a magnetic field to reduce energy losses during the implosion.³ Also, at NRL and Sandia, electron beams were propagated several meters to a target in a plasma channel containing a strong magnetic field. Soon, however, it was recognized that ions have better properties for igniting the fuel because of their shorter range in materials and the absence of bremsstrahlung that can degrade the fuel compression. In 1968 Graybill and Young at Ion Physics Corporation discovered, for low v_e/γ_e beams, that the collective effects of a large number of electrons could be used to accelerate a smaller number of ions to high energies; during the 1970s these studies were extended to high v_e/γ_e beams.⁴

Nevertheless, until the late 1970s, efficient ways to produce intense ion beams had not been devised. Then, rapid progress at Cornell, Sandia, and NRL changed the program emphasis from electrons to light ions, and facility development underway to produce electrons (PBFA I) was reoriented to produce ions. The more promising ion approach grew and continued as we learned more about diagnostics, theory, instabilities, and beam propagation.⁵

An issue for inertial confinement fusion with electrons and ions, and with pinches as well, is to be able to transport the charged particles or x-rays a considerable distance in order to protect the accelerator hardware from the intense radiation environment. In the 1970s and 1980s, experiments^{6,7} were done to focus and guide a high-current electron beam many meters. Using a foilless diode with a system of lenses and solenoids was found to produce a fairly-laminar (cold) beam of small diameter compared to the use of a foil diode with a gas transport system. At the same time as the emergence of the ion approach, z-pinches, which had been produced since the early 1970s as an energetic source of keV x-rays,⁸ were examined as a way to generate soft x-rays to drive a capsule. When the z-pinch approach died because of the standoff needed for energy applications, two parts continued—phonon-pumped x-ray laser research for the Strategic Defense Initiative and K-shell x-rays for radiation effects. Researchers at that time tried to maximize the x-ray energy from pinches, rather than maximizing x-ray power as we are doing now, by driving hollow gas puffs, thin metal foils, or a few wires on Proto II and Saturn at Sandia, on Double Eagle at PI, and on Blackjack 5 at Maxwell. Then, in the early 1990s, the impending cessation of underground testing created a need to test the predictions of simulation tools over a broad range of x-ray pulse widths and energies to guarantee the safety and reliability of nuclear weapons. A 1994 "PBFA Z" project⁹ to design a z-pinch version of PBFA II to fill in existing gaps in radiation effects testing then led to the discovery in 1995 on Saturn that many fragile wires, rather than just a few,¹⁰ strung on spool-sized hardware could greatly enhance the soft x-ray power output.¹¹

The major issues for ions were whether the electromagnetic energy could be converted efficiently to a single-species ion beam and whether that beam could be focused onto a hohlraum at a sufficient intensity to generate x-rays that would then compress a capsule. Unfortunately, the high ion current causes collective effects that defocus the beam unless electromagnetic instabilities are carefully controlled. Particle-in-cell simulations have demonstrated that high magnetic fields and metal limiters can be used to keep the instability in the less damaging, high-frequency diocotron mode for which the ion divergence does not grow.¹² A 15-mrad beam divergence was obtained in 1984 for protons on Proto I and, the following year, these experiments were successfully scaled to the higher current and larger diode on PBFA I. Sandia, Cornell, and Osaka experiments indicated that the beam divergence would decrease with an increase in ion mass and lithium had an optimal range, so PBFA II was designed for singly-charged lithium. With the decision in 1983 to convert the accelerator energy into lithium ions instead of protons, a voltage of 30 MV was needed, and this was to be obtained with a magnetically-controlled plasma opening switch; however, the voltage attained on PBFA II never got much above 10 MV. The lithium power density has not yet exceeded 2 TW/cm^2 , although scaling from the 1.5 TW/cm^2 and 5 TW/cm^2 achieved with protons on PBFA I and PBFA II, respectively, had predicted 100 TW/cm^2 on PBFA II with lithium, even without a decrease in divergence.⁵ Difficulties were also encountered with achieving a high-purity, uniform, preformed lithium ion beam via a variety of active sources (the Laser EVaporation Ion Source, or LEVIS, the Laser Ionization Based on Resonant Saturation, or LIBORS, source or the Electrohydrodynamic, or EHD, source) in spite of using high magnetic fields, discharge cleaning, and anode heating to remove contaminant ions resulting from thermal and stimulated desorption of the anode surface and subsurface layers.

THE PRESENT

In 1998, because of budget limitations and discovery of the more promising approach using wire arrays, the tables have turned, with the ion vs. z-pinch decision of 1984 reversed and the ion approach suspended. Since the first z-pinch radiation shot on Z (the renamed z-pinch modification of PBFA II) in October 1996, an x-ray power of 290 TW¹³ has been achieved on Shot 179 (Fig. 2), our understanding of the role of magnetohydrodynamic instabilities in the z-pinch implosion process has increased, x-ray yields for effects testing have increased an order of magnitude,¹⁴ to 150 kJ for titanium wire arrays at > 4.5 keV and, as shown in Table 1, four milestones have been exceeded (150 TW, 1.5 MJ, 100 eV in a static hohlraum, 150 eV in an imploding hohlraum). Diagnostics added to Z include an end-on x-ray pinhole camera to provide time- and energy-resolved images of the imploding plasma, a time-integrated, space-resolved crystal spectrometer, and a velocity interferometer to provide a measure of hohlraum temperature that is independent of the more traditional XRD- and spectrometer-based data. With the application of a concept, developed by the ICF community and tested on Livermore's Nova laser, of using a hohlraum to contain the soft x-rays,¹⁵ Z is now used for high energy density physics experiments that were previously limited to high-power lasers. And, with recent increases in hohlraum temperature to >150 eV, Z is becoming a route to the X-1 concept for high yield and for simulating the entire cold (<10 keV) and warm (>10 keV) x-ray environment. The latest turn of events is scaling of the design of the National Ignition Facility target concept to X-1 conditions.

Table 1: Achieved pulsed power milestones for Z performance

Milestones	Required Value	Achieved Value	Date Achieved
x-ray energy	1.5 MJ	2.0 MJ	Nov. 1996, 1.8 MJ Mar. 1997, 2 MJ
x-ray power	150 TW	290 TW	Nov. 1996, 200 TW Jan. 1998, 290 TW
hohlraum temperature for weapons physics applications	100 eV	150 eV	Apr. 1997, 100 eV Oct. 1997, 140 eV Apr. 1998, 150 eV
hohlraum temperature for capsule compression	150 eV	155 eV	Aug.-Sept. 1997, 140 eV Mar. 1998, 155 eV

THE FUTURE

This admittedly incomplete recounting of past history shows that optimism and perseverance, along with innovation and creativity, are necessary virtues for people in this field. In this spirit, we can predict that by continuing in the path of the past 30 years, and with expanded cooperation with universities, industry, and government laboratories around the world, in the not too distant future we can achieve the first high-yield fusion conditions in a laboratory on X-1 by 2010 and then go on to begin a fusion power plant exploration beginning in 2020 and, perhaps, to practical energy applications by the middle of the next century, if a method can be devised to allow standoff with z-pinchs or with some combination of ions and pinches. The design for X-1 should be flexible enough to fulfill three objectives: a high-yield fusion output of 200 to 1000 MJ to address the long-term mission of the National ICF program, a flexible, well-characterized source for weapons physics applications, and a cold (<10 keV) and warm (10 to 80 keV) x-ray environment for radiation effects testing.

Complex technical problems remain to be solved. One is whether a factor of three higher current (60 MA) can be crammed into the same size hohlraum as used on Z (5 cm^3). The reason this enormous concentration of power into small cavities works—magnetic insulation—was discovered almost 30 years ago at Kurchatov, PI, and Sandia. Recently, a gap of 1.5 mm between the wires and the hohlraum wall, compared to the conservative 5-mm gap we started with, has stayed open, allowing further increases in the energy coupled into x-rays and decreases in radiation losses. Other issues are whether the efficiency of conversion to x-rays stays at the 15% level seen on Z, whether instabilities remain under control, and whether we can achieve the symmetry and shape of the radiation pulse onto the capsule that computer simulations suggest are needed. Three distinct hohlraum concepts to get high yield are shown in Fig. 3.^{11,16} The z-pinch loads on X-1 will require more massive wires or a return to the use of foils, but with the preferential vertical current flow direction embedded in the foils, and, perhaps, the design of a more spherically symmetric z-pinch load.

At present, the expectations for future commercial applications are higher for deeper penetrating hard x-rays and particle beams than for soft x-rays. The pulsed beam applications would include destruction of organic wastes, large-scale food sterilization, and low cost surface treatment of materials. However, intense soft x-rays can be expected to provide practical tools for novel applications such as the ability to study features in the several hundred angstrom range in physical materials and biological samples and a lithographic technique to imprint submicron-scale electronic circuit patterns on silicon memory chips. And, with the techniques being developed on Z, biologists may be able to observe the structure and dynamic processes of living cells at high spatial resolution over nanosecond time periods.

LESSONS LEARNED

Nobody can predict or control the future, but optimism and perseverance are likely to carry the day when the research foundations are valid. What are some of the lessons that we have learned in the past 30 years that can be applied in the next 30?

- Mother Nature is a hard taskmaster, and difficult problems such as stockpile stewardship and fusion demand enormous patience, dedication, innovation, and skill.
- We learn by a gradual increase in knowledge that is gained by the efforts of many people at various stages in their careers and with various educational backgrounds who practice their craft in a large variety of research settings. The open sharing of information—locally, nationally, and internationally—is the best way to make progress.
- Empirical discoveries happen, and we must be alert to notice them and to understand what these serendipitous discoveries are telling us about the next step to take.
- Government funding of basic research plays an irreplaceable role in this process. Experience in industry and in the national laboratories has shown that private industry would not be able to pick up the slack if this government funding were not provided. Government funding, particularly in the early stages, allows researchers not just to stick with the “sure thing” but to engage in risky, but innovative, research that leads to practical applications.

Basic scientific research is underfunded everywhere and that fact should be, and is, driving more and more cooperation. The problem is how to make that happen while still having open competition that brings out the best in everyone. The answer is to both cooperate and to compete.

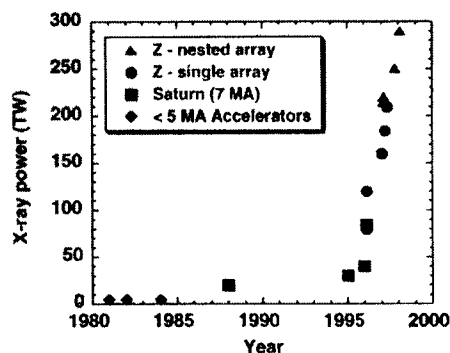


Figure 2. Progress in increasing the power radiated from wire-array z-pinch experiments. The 25 years of progress, with large advances in the last two years, is based on an evolution from single-wire experiments to complex-multiple-wire, nested array experiments possible with the present high-current accelerators and from comparatively simple analysis of radiation sources to modeling the interaction of the magnetic fields, the radiation, and the moving plasma with high-performance computers.

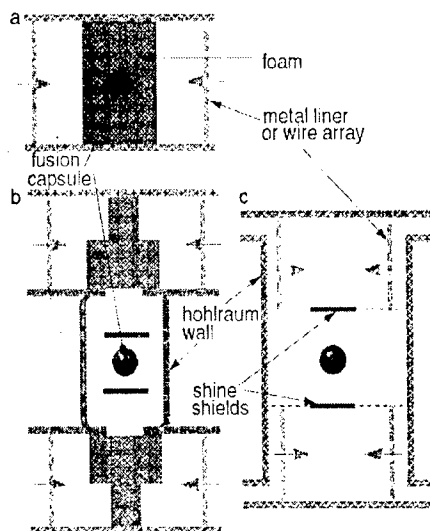


Figure 3. Three hohlraum concepts for high yield on the proposed X-1: a) an imploding liner (or dynamic) hohlraum, driven by a nested array of wires or a metal liner, with the capsule imbedded in foam; b) a central static-walled hohlraum with z-pinch x-ray sources at either end; and c) a central, vacuum hohlraum with imploding arrays or liners at each end that is isolated from the capsule by burn-through barriers and shine shields.

REFERENCES

- [1] J. C. Martin on *Pulsed Power*, ed. T. H. Martin, A. H. Guenther, M. Krisiansen (Plenum Press, NY, 1996).
- [2] G. Yonas, *Scientific American* **239**, pp. 50-61 (1978).
- [3] J. S. T. Chang, et al, *Proc. 2nd Int'l. Top. Conf. on High Power Electron and Ion Beam Research and Technology* (Cornell University, NY, 1978), vol. 1, p. 195.
- [4] C. L. Olson, "Collective Ion Acceleration with Linear Electron Beams," in *Springer Tracts in Modern Physics: Collective Ion Acceleration* (Springer-Verlag, NY, 1979), vol. 84, pp. 1-144.
- [5] T. A. Mehlhorn, *IEEE Transactions on Plasma Science* **25**, pp. 1336-1356 (1997).
- [6] P. A. Miller, *Phys. Rev. Lett.* **39**, 92 (1977).
- [7] R. B. Miller, et al, *J. Appl. Phys.* **51**, 3506 (1980); M. G. Mazarakis, R. B. Miller, J. W. Poukey, R. J. Adler, *J. Appl. Phys.* **62**, 4024 (1987).
- [8] N. R. Pereira, J. Davis, *J. Appl. Phys.* **64**, pp. R1-R27 (1988).
- [9] R. B. Spielman, et al, *Proc. 11th Int'l. Conf. on High Power Particle Beams*, ed. K. Jungwirth, J. Ullschmied (Institute of Plasma Physics, Prague, 1996), pp. 150-153.
- [10] C. Stallings, K. Nielsen, R. Schneider, *Appl. Phys. Lett.* **29**, pp. 404-406 (1976).
- [11] M. K. Matzen, *Physics of Plasmas* **4**, pp. 1519-1527 (1997).
- [12] J. P. Quintenz, et al, *Proceedings IEEE* **80**, 971 (1992). [13] R. B. Spielman, et al, *Physics of Plasmas* **5**, 2105 (1998).
- [14] C. Deeney, et al, "Scaling of above 4 keV X-ray Sources to 100 kJ Yields from the Z Accelerator," 39th Annual Meeting of the Division of Plasma Physics, Pittsburgh, PA, 17-21 November 1997; to be submitted to *Physics of Plasmas*.
- [15] J. D. Lindl, *Physics of Plasmas* **2**, pp. 3933-4024 (1995).
- [16] J. D. Lindl, private communication, 1998.

X-1: THE CHALLENGE OF HIGH FUSION YIELD*

D. L. Cook, J. J. Ramirez, P. S. Raglin, G. E. Rochau, M. K. Matzen, R. J. Leeper, J. L. Porter,
R. E. Olson, D. H. McDaniel, R. B. Spielman, C. Deeney, and J. P. Quintenz

*Sandia National Laboratories
Albuquerque, NM 87185-1190*

R. R. Peterson
*University of Wisconsin
Madison, WI 53706*

ABSTRACT

In the past three years, tremendous strides have been made in x-ray production using high-current z-pinches¹⁻⁵. Today, the x-ray energy and power output of the Z accelerator⁶ (formerly PBFA II) is the largest available in the laboratory. These z-pinch x-ray sources have great potential to drive high-yield inertial confinement fusion (ICF) reactions at affordable cost if several challenging technical problems can be overcome. Technical challenges in three key areas are discussed in this paper: the design of a target for high yield, the development of a suitable pulsed power driver, and the design of a target chamber capable of containing the high fusion yield.

INTRODUCTION

The Z accelerator at Sandia National Laboratories now produces a peak x-ray output energy of 1.8 MJ and a peak x-ray output power of 280 TW from a z-pinch driven at approximately 20 MA. Optimization of z-pinch behavior on the Z accelerator and three prior generations of accelerators (Saturn at 10 MA, Proto II at 5 MA, and SuperMite at 1.5 MA) has shown that the x-ray energy output from high-current z-pinches scales quadratically with z-pinch current. This scaling is in agreement with simple zero-dimensional analytic theory. For fixed output pulse width, the x-ray power also scales quadratically with current. When the z-pinch is used to drive a hohlraum, the hohlraum radiation (σT^4) is proportional to the z-pinch source radiation (I^2), and the hohlraum temperature is proportional to the square root of the z-pinch current. These basic relationships, demonstrated conclusively on the Z accelerator, indicate that a single accelerator with about three times the current of Z (or about 60 MA), or two accelerators, each having about twice the current of Z (or about 40 MA), should be sufficient to drive a fusion capsule to high fusion yield. The features of this accelerator, called X-1, are discussed in this paper. It is a remarkable result that the energy conversion efficiency, from electrical energy stored in the Marx generator to x-ray energy produced in a short pulse by a fast z-pinch, exceeds 15% on the Z accelerator. The implications of this result are that sufficient x-ray energy can be produced at modest cost in X-1 to drive an ICF capsule to high yield.

*Sandia is a multiprogram laboratory operated by Sandia Corporation, a Lockheed Martin Company, for the United States Department of Energy under Contract DE-AC04-94AL85000

REQUIREMENTS FOR HIGH YIELD

The capsule design criteria for high fusion yield come from multi-dimensional target calculations. With an x-ray energy greater than 10 MJ, x-ray power greater than 1000 TW, hohlraum temperature greater than 225 eV, radiation asymmetry smaller than 1-2%, and a temporal pressure profile at the capsule ablation surface appropriate for nearly isentropic compression of cryogenic fusion fuel, calculations give yields in the range of 200 - 1200 MJ. The X-1 facility, which is being explored at the pre-conceptual level now, will be designed to produce 16 MJ and 1000 TW of x-rays, and a hohlraum temperature of 300 eV. Three ways to provide radiation symmetry are being explored, as depicted in Figure 1. The first approach separates the x-ray source from the fusion capsule by placing a z-pinch x-ray source on each end of a cylindrical hohlraum containing the fusion capsule, much like the existing heavy-ion-driven ICF target designs. In this design (1a), each z-pinch produces radiation when it stagnates on the axis, and the radiation fills a stationary hohlraum containing the fusion capsule. In the second approach (1b), the z-pinches strike a central cylinder which is filled with a low-Z gas or foam. The combination of the strike upon the cylinder and the final stagnation of the combined z-pinch and cylinder mass provides a pulse-shaped x-ray input for the ICF hohlraum. In the third approach (1c) a single z-pinch drives a dynamic hohlraum which also contains the fusion capsule inside a density-tailored foam at the interior of the cylindrical, or quasi-spherical, z-pinch. In going from 1a to 1c, the hydrodynamic risk of non-reproducible z-pinch behavior or of a hydrodynamic interaction between the z-pinch(es) and the fusion capsule is increased, but progressively smaller volumes must be heated, and higher drive temperatures become possible. The required time-dependent pressure profile at the capsule ablation surface can be provided by a combination of time-dependent x-ray pulse shaping and pressure tailoring via material layers in the capsule ablator. In order to achieve high yield in an efficient manner (i.e., achieve high gain at the same time), the fusion fuel in the capsule must be initially cryogenic, and the fuel must be compressed to a density of more than 100 times liquid density on an adiabat whose pressure is not more than a factor of about 4 from the Fermi-degenerate value at the same final density.

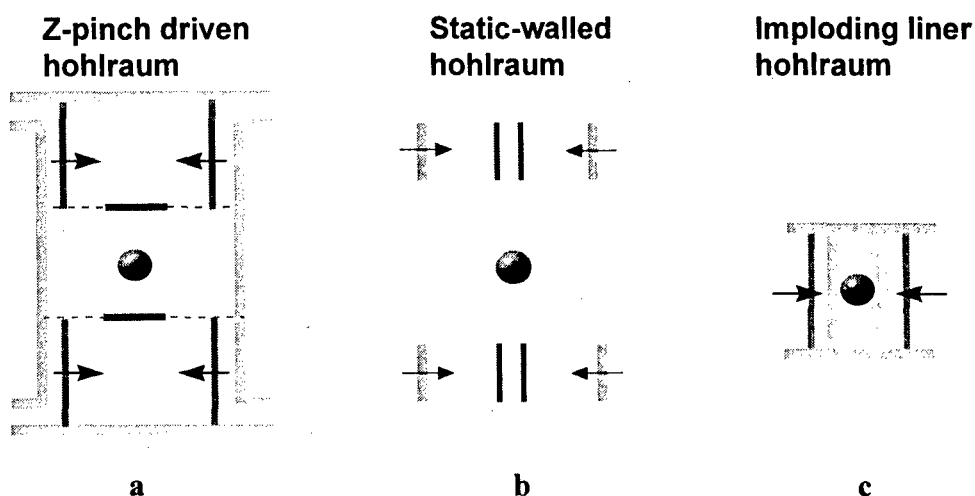


Figure 1. Three target configurations for high fusion yield.

PULSED POWER DRIVER

The pulsed power driver for X-1 consists of four basic sections: the energy storage section, the dielectric pulse forming section, the power transition section, and the vacuum power flow section. Several alternative design options are being evaluated in a pre-conceptual design study. A representative sketch for a driver topology similar to that of the Saturn and Z accelerators is shown in Figure 2. In the particular design shown, there are 144 Marx generators, 288 dielectric pulse forming lines, a single centrally located vacuum insulator stack, and a six-feed conically shaped vacuum power flow section.

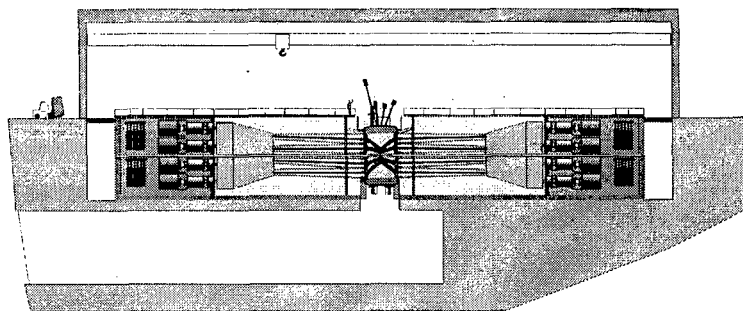


Figure 2. A representative sketch of the pulsed power driver for X-1

Efficient flow of electromagnetic power in vacuum is a major challenge in the X-1 design. Even with no ICF capsule being driven, the magnetic pressure produced by the flow of a 60 MA current to a 10 nH z-pinch will be in the Mbar range. Sustaining an open channel for this electrical power for 100-200 ns through anode-cathode gaps in the range of 2-5 mm in the presence of radiation from the imploding z-pinch is a key technical issue for X-1. Recent experiments on the Z accelerator with a 1.5 mm gap, a drive time of 110 ns, and a current per unit length ($I/2\pi r$) of about 2.4 MA/cm have been very successful, but these results have not yet been scaled to the level required for X-1 (5-8 MA/cm). In addition, other recently obtained data from experiments on the Saturn accelerator indicate that greater overall efficiencies than 15% can be achieved by using a longer z-pinch implosion time than 110 ns, but in order to scale these results to X-1, the requirements placed on the power flow channel to remain open will be even more demanding.

YIELD CONTAINMENT

Containment of the pressure pulse and activated debris produced by a high-yield ICF capsule is a particularly challenging task for X-1. At a yield of 200 MJ, with 40 MJ in x-rays, the hydrodynamic pressure pulse will be about four times that produced by the 16 MJ of x-rays from the z-pinch alone. The neutron output of 160 MJ will activate target region hardware, and an important task will be to minimize activation outside this region. A sketch of the target chamber area for X-1 is shown in Figure 3. The final design must include cryogenic target insertion, neutron and x-ray diagnostics, and isolation of activated debris using explosive closures.

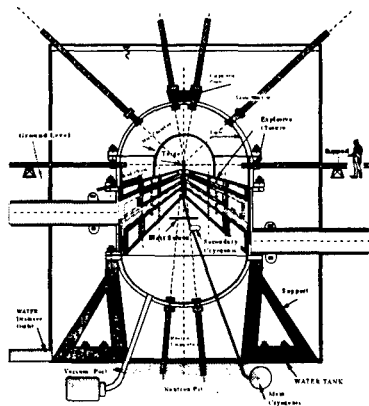


Figure 3. A sketch of the X-1 target chamber area

CONCLUSION

The successful experiments on the Saturn and Z accelerators in the past three years have provided new insights into the fundamental behavior of fast high-current z-pinchs. The large levels of x-ray energy and x-ray power produced by these z-pinchs, and the experimental evidence that their gross behavior follows simple scaling laws, suggests that they may be able to drive fusion capsules to high fusion yield. Preliminary scoping investigations have identified a number of important technical challenges associated with high fusion yield, and the potential solutions to these challenges are motivating further experiments on the Saturn and Z accelerators, and an increased number of target, accelerator, and yield containment design options for X-1.

ACKNOWLEDGEMENT

The spectacular technical progress made in fast z-pinchs within the past three years using the highest current accelerators, which are located at Sandia, has its origins within several nations and over several decades. Without the persistence of individual researchers involved in pulsed power and in z-pinchs over at least the last three decades, and without the free exchange of scientific results as they were developed, the rate of progress would have been substantially slower, and the now encouraging prospects for ultimate achievement of high fusion yield would be considerably poorer.

REFERENCES

1. T. W. L. Sanford, et al., Phys. Rev. Lett. **77**, 5063 (1996).
2. M. K. Matzen, Phys. Plasmas **4**, 1519 (1997).
3. T. W. L. Sanford, et al., Rev. Sci. Instrum. **68**, 852 (1997).
4. C. Deeney, et al., Rev. Sci. Instrum. **68**, 653 (1997).
5. M. R. Douglas, et al., Phys. Rev. Lett. **78**, 4577 (1997).
6. R. B. Spielman, et al., Proc. 11th Intl. Conf. on High Power Particle Beams, K. Jungwirth and J. Ullschmied, eds., Prague, Czech Republic, 1996, p. 150.

DEVELOPMENT OF HIGH ENERGY INDUCTION ACCELERATOR, "ETIGO-III"

A. Tokuchi and N. Ninomiya

Nichicon Corporation, 2-3-1 Yagura, Kusatsu, Shiga 525-0053, Japan

and

K. Yatsui, G. Imada, Q. Zhu, W. Jiang, and K. Masugata

Laboratory of Beam Technology, Nagaoka University of Technology, Nagaoka, Niigata 940-2188, Japan

Abstract

A new induction accelerator "ETIGO-III" has been developed to generate high current relativistic electron beam for applications in materials science, high-power microwave generation and intense X-ray generation.

Using the Marx generator of "ETIGO-I", we have produced the initial pulse of 670kV (60 ns pulse width). Through the four transmission lines, the pulse was fed to four induction cells. Three cores are installed inside each cell. The output voltage of 2 MV was obtained by the initial cell. Specifically, it is possible to obtain the final output parameters of 8 MeV, 5 kA, 60 ns. Various diagnostics have been carried out on the characteristics of the electron beam generated by "ETIGO-III". The beam currents at different cells were monitored by Rogowski coils. The cross-sectional view of the electron beam was observed by damage pattern on acrylic plate.

1. Introduction

A new induction accelerator "ETIGO-III" has been developed to generate high current relativistic electron beam for applications in materials science, high-

power microwave generation and intense X-ray generation [1].

Figure 1 shows the block diagram of "ETIGO-III". Using the established pulsed power generator "ETIGO-I" [2], the initial pulse (670kV, 132 kA, 60 ns)

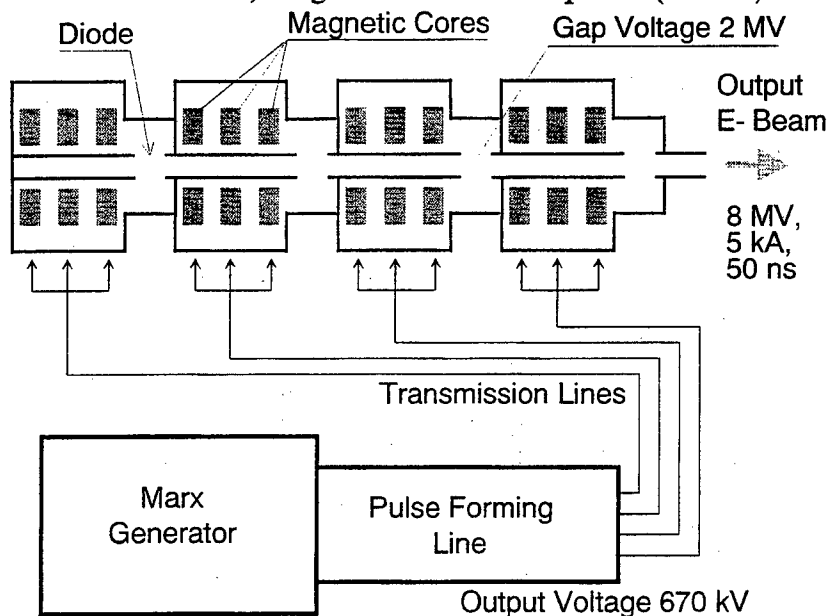


Fig. 1 Block diagram of the induction accelerator, "ETIGO-III".

Table 1 Specifications of the amorphous cores..

Cell No.	Material	D_{out} (mm)	D_{in} (mm)	W (mm)	S (m ²)	ΔB (T)	$V \cdot t$ (Vs)
A / B	2605SC (Allied)	ϕ 692	ϕ 292	50.8x3	0.03	1.76	0.053
C / D	AC10 (TDK)	ϕ 700	ϕ 300	96x1	0.019	1.77	0.034

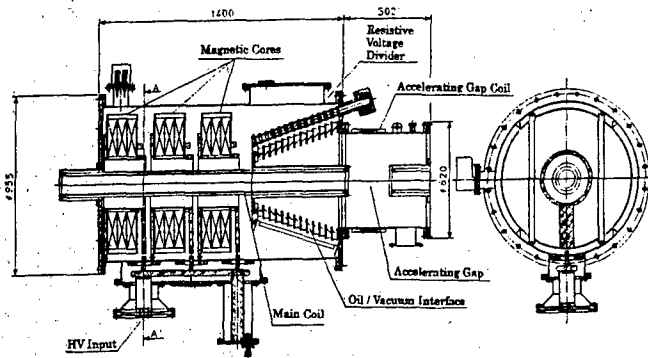


Fig. 2 Inner structure of the induction cell.

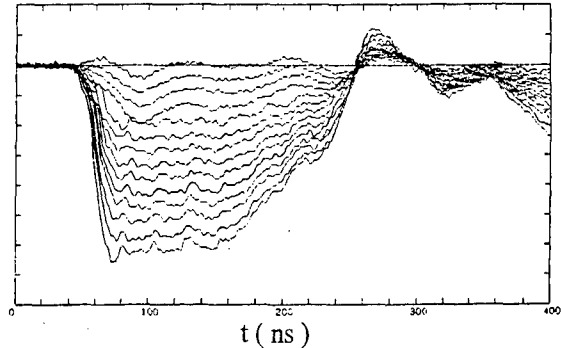


Fig. 3 Voltage waveforms on the grading rings.

is generated. Through the four transmission lines, the pulse is fed to four induction cells. Three cores are installed inside each cell, and the voltage is added as 3 times ($670 \text{ kV} \times 3 = 2 \text{ MV}$) per cell. Specifically, it is possible to obtain the final output parameters of 8 MeV, 5 kA, 60 ns by using four induction cells.

2. Induction Cells

Figure 2 shows the inner structure of the induction cell. Three cores are installed inside each cell, by which 2 MV is obtained by the initial voltage of 670 kV. Iron-based amorphous cores AC10 (made by TDK) and 2605SC (made by Allied) are used for two cells on the upstream side and the other two cells on the downstream side, respectively. Specifications of the amorphous cores are shown in Table 1. Inner diameter of the metallic bobbin to support the core is 259 mm and outer diameter of the beam pipe is 165 mm. If the voltage of 1340 kV ($= 670 \text{ kV} \times 2$) is applied between them, the radial electric field strength on the beam pipe is 360 kV/cm.

The initial pulse (670 kV, 33 kA, 60 ns) is fed to each cell through the transmission lines from "ETIGO-F". As this current is

separated into three cores, each core is driven by the current of 11 kA. The current of $\sim 4 \text{ kA}$ is flown to excite the core. The rest (7 kA) is flown toward the load.

The induction cell is filled with an insulation oil for high voltage insulation. The interface between oil and vacuum in the accelerating chamber is made by stacking structure of 13 acrylic rings (29 mm thick) and 14 aluminum rings (7 mm thick). When the voltage of 2 MV is applied on the interface, the axial electric field strength is 53 kV/cm. The interface structure has the conical shape to reduce stray capacitance, resulting in the fast rise time of the output pulse. The resistive voltage divider using copper sulfate solution is installed outside the interface to get the uniform voltage difference between each grade rings. The total resistance of the divider is 2 k Ω .

Figure 3 shows the measured voltage of each rings if the external pulsed voltage was applied on the interface. As seen in Fig. 3, good uniformity was obtained. A copper sulfate resistor to measure the output voltage of the induction cell is also installed outside the interface. Its resistance is also 2 k Ω . The current of 1 kA flows each resistor. Finally, the beam current of 5 kA can be obtained.

Inner diameter of the vacuum chamber

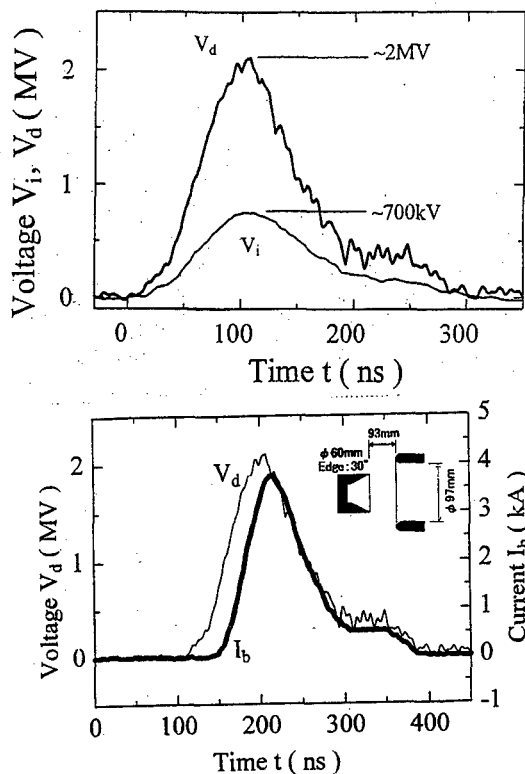


Fig. 5 Diode voltage and beam current.

is 500 mm and outer diameter of the beam pipe is 165 mm. When the voltage of 2 MV is applied on the acceleration gap the radial electric field strength on beam pipe is transport the electron beam. When pulse current with the duration of ~ 60 ms flow in

3. Transmission Lines

The output of "ETIGO-I" and four induction cells are connected with four transmission lines. The transmission lines, filled with the insulation oil, have cylindrical shape, inner diameter of the outer conductor is 159 mm and outer diameter of the inner conductor is 89 mm, giving the characteristic impedance of 23Ω . That is well matched with the output impedance of "ETIGO-I" ($5 \Omega \times 4 = 20 \Omega$) and the input impedance of the induction cell (20Ω). The radial electric field strength is 260 kV/cm when the voltage of 670 kV is transmitted. The connection of the transmission lines and the induction cells is bellows joint for easy maintenance.

The branch point to four transmission lines is located at the center between the first

Fig. 4 Input voltage and output voltage.

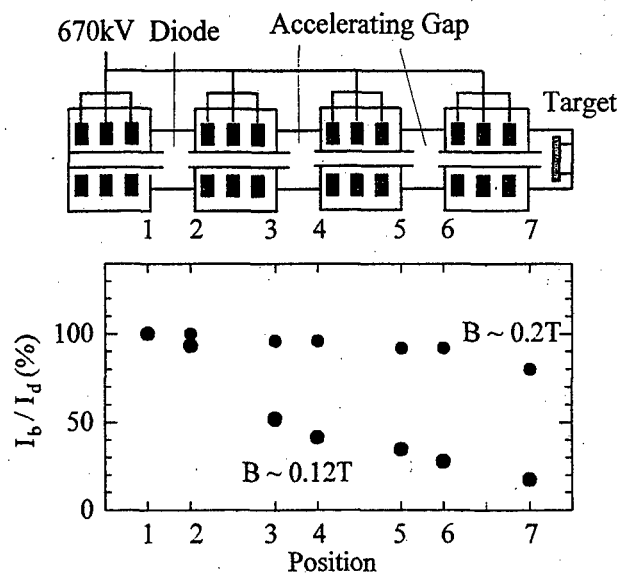


Fig. 6 Beam transport efficiency with the magnetic field density as a parameter.

220 kV/cm.

Coils are installed outside the beam pipe in the induction cell and outside the vacuum chamber to guide and the coils from the external capacitor bank, the magnetic field of 0.3 T can be generated.

induction cell and the second. This location makes time difference less than 10 ns between the timing that the beam crosses the acceleration gaps and the timing that the acceleration voltage is applied on the gaps. It should be mentioned that there are no problems on the jitter of the each driving pulse. Thus, the stable operation has been available by the procedure that the four induction cells are driven by a single pulse generator.

4. Beam Test

Figure 4 shows the waveforms of the input voltage into the induction cell and the output voltage. The input voltage was measured by a static probe, while the output voltage by a copper sulfate resistive voltage divider. The input voltage was ~ 700 kV, and

the output voltage ~ 2 MV. We have found a factor of 3 increase by the voltage adder. The pulse width of the output voltage was ~ 100 ns (FWHM).

Figure 5 shows the waveforms of the diode voltage and the electron beam current on the first acceleration stage. Cylindrical cold cathode (outer diameter 60 mm) was used in the test. The beam current was measured by a Rogowski coil. The beam current of ~ 4 kA was obtained at the initial accelerating voltage of 2 MV.

We measured characteristics of the beam transport through the four induction cells. The results of the transport efficiency are shown in Fig. 6 with the magnetic flux density as a parameter. The current on the position #1 shows the diode current of the first acceleration stage. When the magnetic field is 0.12 T, the transport efficiency to the

final stage is ~ 20 %, Very good transport efficiency of ~ 80 % has been achieved by increasing up to 0.2 T.

The cross-sectional view of the electron beam was also observed by damage patterns on acrylic plate located in each acceleration stage. The damage patterns of each stage are shown in Fig. 7. The beam had cylindrical shape with outer diameter of ~ 60 mm, that is consistent to the shape of the cathode electrode. Figure 8 shows the maximum depth of the electron-beam trajectory in the acrylic plates. These results show that the beam energy increases with increasing the number of the acceleration stage.

Finally, we have found that there are no problems concerned with high voltage insulation during the full power test in the induction accelerator, "ETIGO-III".

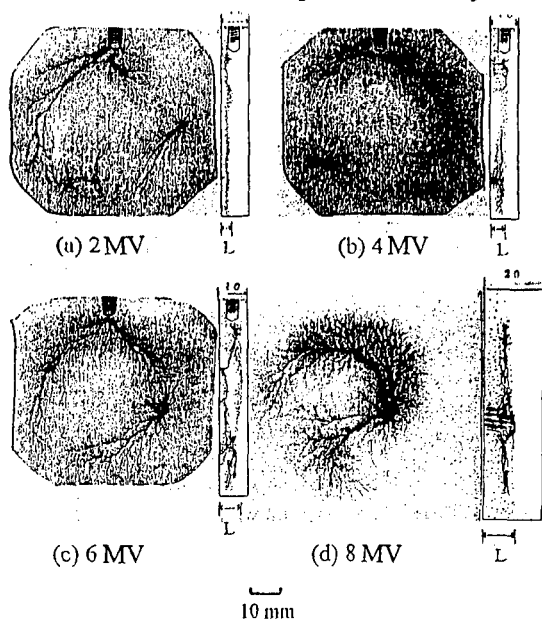


Fig. 7 Electron-beam damage patterns.

5. Conclusions

New high-energy induction accelerator "ETIGO-III" using iron based amorphous cores has been constructed. By using four induction cells which involves three cores, the accelerating voltage of 8 MV was obtained when the input voltage was 670 kV. The initial electron beam with the current of 4.9 kA was generated in the first

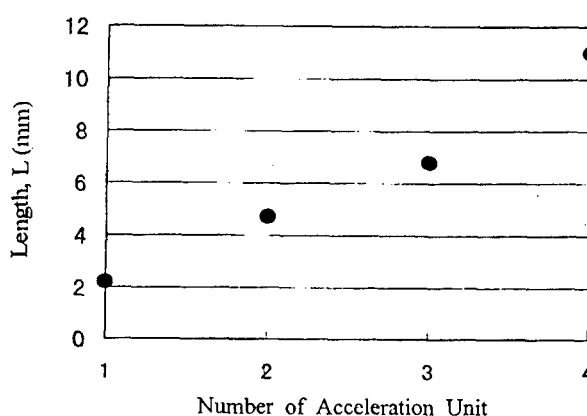


Fig.8 Maximum depth of electron-beam trajectory in acrylic plate.

acceleration stage. The transport efficiency through the four induction cells was 80 % at magnetic field strength of 0.2 T. It was found that the beam energy increases with increasing the number of the acceleration stage.

References

- [1] K. Yatsui: Proc. 11th IEEE Int'l Pulsed Power Conf., **I**, 13 (1997).
- [2] K. Yatsui et al.: Laser and Particle Beams **3**, 119 (1985).

ENERGETIC ELECTRON/ION FLOW AND MICROWAVE RADIATION DURING POS OPERATION

Ya. E. Krasik, A. Dunaevsky, J. Felsteiner, and J. R. Goyer*

Department of Physics, Technion, 32000 Haifa, Israel

*Maxwell Technologies, Systems Division, San Diego, CA 92123

Results of experimental investigations of high-energy electron/ion beam generation and transportation in the region downstream of a submicrosecond plasma opening switch ($I_{pos} \leq 35 \text{ kA}$, $\tau_{1/4} \approx 300 \text{ ns}$) are presented. Experiments were carried out with different loads: short-circuit, high-impedance, and planar electron diode. It is shown that the electron/ion beam appearance in the region downstream of the POS load occurs almost simultaneously with the beginning of the inductive voltage, independently of the type of load. Generation of high-power microwave radiation ($f_{mw} \leq 10 \text{ GHz}$, $P_{mw} \leq 200 \text{ MW}$) was observed for all types of loads.

The POS configuration, shown in Fig. 1, consists of a coaxial anode and cathode with radii of 5 cm and 1 cm, respectively. The POS upstream

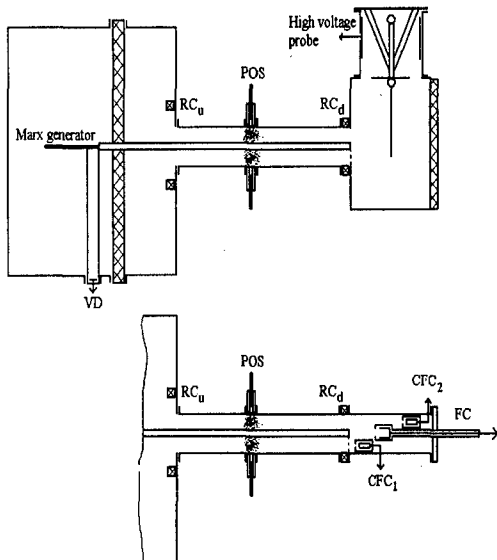


Fig. 1. Experimental setup.

inductance, L_u , is 450 nH. Three types of POS loads were used: short-circuit coaxial lines, planar electron diode, and high-impedance loads. The POS was driven by Marx generator delivering a negative current pulse, $I_u \approx 30 \text{ kA}$ and $\tau_{1/4} \approx 300 \text{ ns}$. Plasma was produced by 4 erosion plasma guns. Rogowski coils were used to

measure the upstream (I_u) and the downstream (I_d) currents. Voltage was measured by an active voltage divider. The electron/ion current density was measured by collimated Faraday cups (CFCs) without and with magnets. Ion energy was estimated using the Time of Flight (TOF) method. The total current and energy of the drifted beam was measured by a movable Faraday Cup (FC), coupled with a calorimeter. Electron energy was estimated from the FC data with Al foils in front of the input aperture. The potential of the drifted beam (I_b) was measured by a high-voltage floating probe. Microwave radiation was measured using different waveguides (30 GHz, 10 GHz, and 2.5 GHz). In addition, we used an array of fluorescent tubes placed 100 cm from the output window.

The first set of experiments was carried out with $L_d = 50 \text{ nH}$. Obtained data (see Fig. 2 a,b) have shown that the beginning of the inductive voltage corresponds to the sharp rise of I_d and I_b . The measurements of the beam propagation have shown a fast spread of the electron/ion beam with divergence of

$\alpha/2 \cong 17.5^\circ$. The amplitude of the beam current reached 1.5 kA. In addition, there is a downstream current pre-pulse, which occurs prior to the beginning of the inductive voltage.

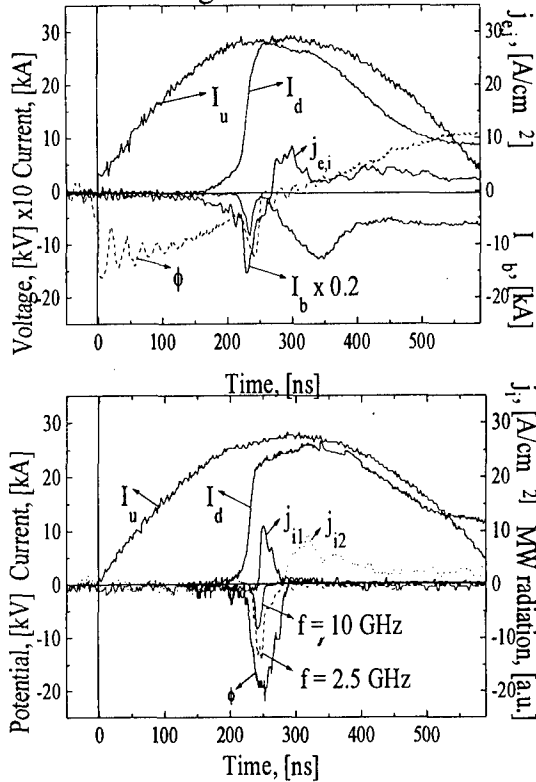


Fig. 2. (a). Typical waveforms of the upstream (I_u), the downstream (I_d), and the beam (I_b) currents, the voltage (ϕ), and the electron/ion current density ($j_{e,i}$). $L_d = 55$ nH. $\tau_d = 1.37$ μ s. Beam current and electron/ion current density were measured 2 cm from the short-circuit load. (b). Typical waveforms of the upstream (I_u) and the downstream (I_d) currents, the beam potential (ϕ_b), and the ion current density (j_{i1} , j_{i2}). $L_d = 55$ nH. $\tau_d = 1.35$ μ s. Beam potential was measured 3 cm from the short-circuit load. Ion signals were obtained 8 cm and 38 cm from the short-circuit load. Microwave radiation was obtained 120 cm from the short-circuit load. 10 GHz radiation was measured using 10 dB attenuators.

The energy of electrons was estimated in the range of $45 \text{ keV} \leq E_e \leq 60 \text{ keV}$. Application of the magnetic field allowed observation of a pure ion

signal with $j_i \leq 15 \text{ A/cm}^2$. The average ion velocity measured by the TOF method was found to be $7 \cdot 10^8 \text{ cm/s}$. The potential of the beam was found to be $\phi_b \leq -20 \text{ kV}$. Similar data were acquired when the short-circuit inductance of $L_d = 130 \text{ nH}$ was used.

Qualitatively the same results as with short-circuit loads were obtained with high-impedance loads. We have observed downstream current and powerful downstream beam, $I_b = (0.5 - 0.7) \cdot I_d$. It was found that with 40 cm-length downstream electrode the sharp rise of the downstream current is delayed with respect to the beginning of the POS inductive voltage, with larger time delays being registered for shorter conduction times. For shorter downstream electrodes, the current starts almost simultaneously with the beginning of the inductive voltage.

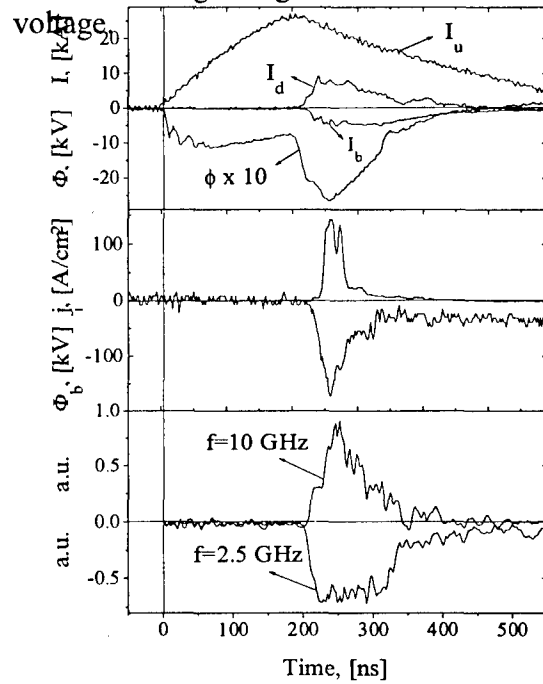


Fig. 3. Typical waveforms of the upstream (I_u), the downstream (I_d), and the beam (I_b) currents, the inductive voltage (ϕ), the beam potential (ϕ_b), the ion current density (j_i), and envelopes of microwave signals. High-impedance load, $L_d = 20$ cm. $\tau_d = 1.35$ μ s. Ion current density, beam current,

beam potential, and microwave radiation were measured at distances of 10cm, 6cm, 3cm, and

We have obtained a relatively long I_d and I_b pre-pulses which begin prior to the inductive voltage. It was found that the amplitudes of I_d and I_b depend on the POS conduction phase and decrease with increasing downstream cathode length, and can be as high as $I_d=16\text{kA}$ ($l_d=14\text{cm}$). Patterns of the beam showed an average beam diameter of $\sim 5\text{cm}$, with maximum beam density at the center. Taking into account the observed beam diameter, the average current density of the beam was $j_b \leq 0.7\text{kA/cm}^2$ ($l_d=14\text{cm}$). The total energy of the beam was found to be $W_b \leq 150\text{J}$ and the upper energy of electrons was estimated to be $E_e \leq 220\text{keV}$. It is interesting to note that large time delays were observed between the beginning of the downstream current and the appearance of the electron beam. According to these data beam propagation velocity doesn't exceed 10^9cm/s . It was found that the beam potential remained the same for the POS conduction time range of $\tau_c \leq 350\text{ ns}$, $\phi_b \approx 180 \pm 20\text{kV}$.

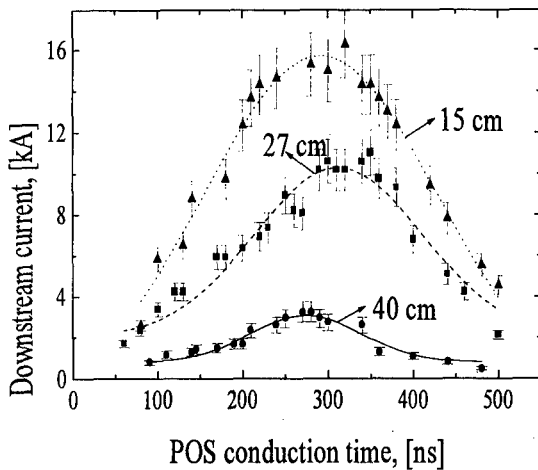


Fig. 4. The downstream current amplitude versus POS conduction time for high-impedance loads with different lengths of downstream electrode.

Obtained the TOF data have shown that larger ion energies correspond to shorter conduction times. For POS

500cm from the load, respectively.

conduction of 300ns the ion velocities were found to be 10^9cm/s . It was shown that the ion beam has almost the same average diameter as the electron beam. The current density of this ion beam reaches $j_i \leq 150\text{A/cm}^2$ at a distance of 8cm from the high impedance load ($l_d=20\text{cm}$). Observation of an electron beam propagating in vacuum indicates non-complete current and space charge neutralization. Therefore measurements were performed of electromagnetic radiation which may accompany non-neutralized electron beam propagation. It was found that microwave (MW) radiation starts almost simultaneously with the appearance of the electron beam. The correlation of the radiation with the beam was shown in an experiment with a short circuit load see Fig.2 b). The observed radiation in this case differs from the case of high-impedance load in the duration and in the power of the MW radiation.

In the present experiment, detailed measurements of the frequency, bandwidth and power of the microwave radiation were not performed. However, it was determined that the frequency of the microwave radiation is $f < 30\text{GHz}$. The power of the microwave radiation was estimated by the use of an array of fluorescent tubes (turn on at 85V). One can estimate the output power of the microwave radiation as the Poynting flux integrated over a hemispherical surface ($R=100\text{cm}$). This rough estimate gives $P_{mw} \leq 200\text{MW}$ radiated power. Powerful MW production was observed also in the case where a planar electron diode was used. The difference in observed radiation was that in this case MW radiation with $f \approx 30\text{GHz}$ was obtained.

Previous research¹⁻³ has shown that there is a powerful electron/ion flow in the downstream region between the POS

and short-circuit load. In the present experiments, measurements of the electron/ion flow in the region between the POS and the load were not performed. However, we believe that similar electron/ion flow obtained. The important feature of the present measurements is that we have shown strong correlations ($\leq 5\text{ns}$) between the beginning of the POS inductive voltage, the sharp rise of the load current, the appearance of the energetic electron/ion beam and MW radiation.

To explain the observed experimental results we suggest the following qualitative explanation. When the current reaches the load side of the POS, it continues to propagate in the axial direction due to $\mathbf{j}_r \times \mathbf{B}_0$ force. Space charge of the current carrying electrons leads to collective acceleration of ions from the boundary of the POS. Thus, this current carrying plasma spreads between the POS and the short-circuit load. When the plasma flow reaches the short-circuit load, a spatial current redistribution can occur, i.e. current switches to flow along the electrodes. This causes a fast increase of the downstream inductance, and generates an inductive voltage, $\mathcal{E} \sim I_d(dL_d/dt)$.

Also, the data obtained for the case of high impedance load can be explained in terms of charged particle flow that enters the region of the high-impedance load or electron diode. This flow may lead to a significant decrease of the load impedance as well as cause the generation of the electron beam. We suggest prior to the sharp rise of the inductive voltage the downstream current is distributed in the region between the switch and high-impedance load. However, unlike the case of the short-circuit load, the downstream current cannot show a sharp increase until the appearance of an accelerated plasma with sufficient density. We

believe that as the current-carrying plasma moves in the region between the POS and the load, the density decreases. This decrease of the plasma density leads to current interruption and inductive voltage generation.

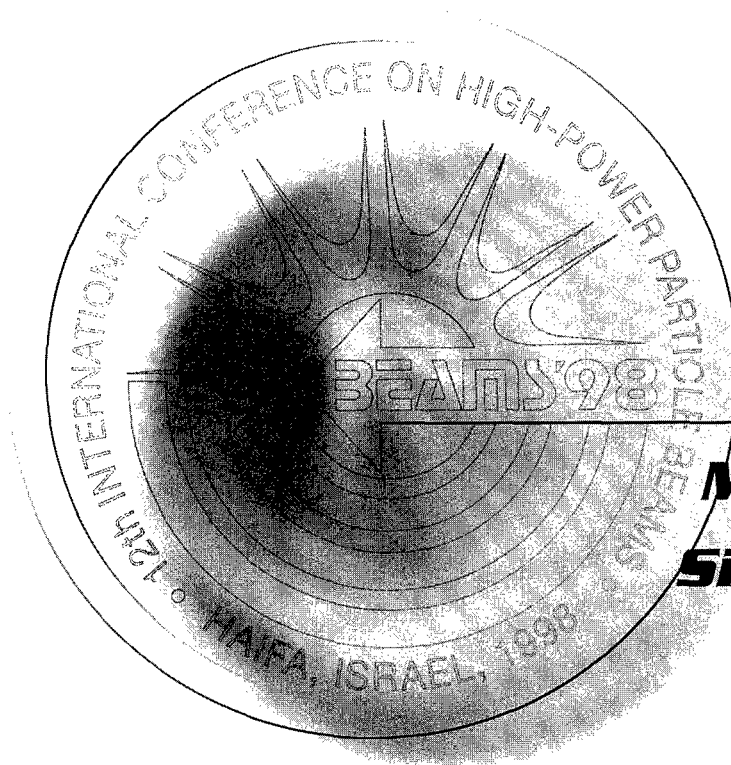
We next analyze the experimental data concerning electron beam transportation and generation of MW radiation. One can estimate the charge neutralization coefficient and beam potential taking $\gamma \approx 1.4$ and $n_e \approx 3 \cdot 10^{11} \text{cm}^{-3}$ as $f_e \approx 0.5$, and $\phi_b \leq 270 \text{kV}$ in good agreement with previously presented data. The non-complete charge and current neutralization inferred suggest that the microwave generation is related to virtual cathode formation. The obtained velocity of beam propagation, $V_b = (9 \pm 1) \cdot 10^9 \text{cm/s}$ agrees with the above suggestion. Indeed, this velocity coincides with the velocity of the ion flow, $V_i = (1.0 \pm 0.2) \cdot 10^9 \text{cm/s}$. This ion flow partially neutralizes the space charge of the electron beam and allows beam propagation $I_b \gg I_{cr} \approx 300 \text{A}$. A rough estimate of the MW frequency can be made based on the assumption that the dominant mechanism responsible for the generation of MW radiation is temporal and spatial variations of the virtual cathode. In this case, the oscillation frequency can be estimated⁴ as $\omega_{pe} \leq \omega_{os} \leq (2\pi)^{1/2} \omega_{pe}$. This estimate gives $5 \text{ GHz} \leq \omega_{os} \leq 12.5 \text{ GHz}$ for $\gamma = 1.4$ in agreement with experimental data.

1. S. B. Swanekamp, J. M. Grossmann, P. F. Ottinger, R. J. Comisso, and J. R. Goyer, *J. Appl. Phys.* **76**, 2648 (1994).
2. Ya. E. Krasik, A. Weingarten, *IEEE Trans. Plasma Scie.* **26**, 208 (1998).
3. M. Sarfaty, Y. Maron, Ya. E. Krasik, A. Weingarten, R. Arad, R. Shpital'nik, A. Fruchtman, and S. Alexiou, *Phys. Plasmas* **2**, 2122 (1995).
4. R. B. Miller, *An Introduction to the Physics of Intense Charged Particle Beams* (Plenum Press, New York, 1982).



BEAMS'98

12th INTERNATIONAL CONFERENCE
ON HIGH-POWER PARTICLE BEAMS



ORALS

***Models and
Simulations***

Vol. I

Proceedings

TOOLS FOR MHD SIMULATION OF HOT DENSE PLASMA

S.Semushin, B.Etlicher

*Laboratoire de Physique des Milieux Ionisés, Laboratoire CNRS, Ecole Polytechnique
91128 Palaiseau, France
e-mail: sem@lpmi.polytechnique.fr*

The complexity of physical problems in plasma demands special tools for its analysis. The primary source of data is, of course, the physical experiment. But, sufficiently complete comprehension of physical phenomenon is actually impossible without the numerical simulation, which is more and more often named as computational experiment. Moreover, computational experiment usually provides more complete set of data, which becomes credible only after verification by experiment

The processes under consideration (such as different Z-pinches, plasma opening switches - POS, plasma focus and others) have some common features. First of all, they are non stationary and subjected to divers instabilities. Another common feature is a big difference in time and spatial scales, and small local details are very often significant for global process development. This means, that some kind of adaptation is inevitable for numerical simulations. Traditional lagrangian approach can be also considered as adaptation, based on the mass, but it is not applicable to the problems with high level of convection or mixing.

Two numerical methods for MHD plasma simulation and corresponding codes are presented here. The first code ASTRE uses original adaptive mesh refinement algorithm [1, 2], the other one, Z+ is based on classical arbitrary lagrangian-eulerian algorithm [3, 4]. These two approaches are complimentary. Each of them has its own advantages and specific application domains, but each of them covers the majority of the problems under consideration

Physical models

The choice of physical model is always a compromise between the effectiveness of computation and resulting accuracy. Here the standard description of two temperature plasma is used. The influence of more sophisticated terms was also estimated, but these terms were not included into all computations. Thus, the governing equations are:

$$\begin{aligned}
 \frac{\partial \rho}{\partial t} + \text{div}(\rho u) &= 0 & \frac{\partial \rho u}{\partial t} + \text{Div}(\rho u u) + \text{grad}(p) + \text{div} \hat{\pi} &= \frac{j \times B}{c} \\
 \frac{\partial \rho \epsilon_e}{\partial t} + \text{div}(\rho u \epsilon_e) + p_e \text{div} u + \text{div} W_e &= j E^* - S_{\text{rad}} + Q_{ei} \\
 \frac{\partial \rho \epsilon_i}{\partial t} + \text{div}(\rho u \epsilon_i) + p_i \text{div} u + \hat{\pi} \text{div} u + \text{div} W_i &= -Q_{ei} \\
 \frac{\partial B}{\partial t} = -c \text{rot} E, \quad E = E^* - \frac{u \times B}{c}; \quad j = \frac{c}{4\pi} \text{rot} B, \quad \text{div} B &= 0 \\
 W_{e,i} = -k_{e,i} \text{grad} T_{e,i}, \quad n_i = \rho / m_i; n_e = Z n_i &
 \end{aligned} \tag{1}$$

where ρ , P - plasma density and pressure, n_e, n_i - electron and ion densities, Z – ionisation, u – velocity, E, B – electric and magnetic fields, $\epsilon_e, \epsilon_i, T_e, T_i$ - electron and ion specific internal energies and temperatures, $W_{e,i}$ - heat fluxes, Q_{ei}, S_{rad} - exchange term and radiation sources. Ohm's law is used either in form of classical conductivity or with the Hall terms (3).

$$E^* = \frac{j}{\sigma} \quad (2)$$

$$E^* = \frac{j}{\sigma} + \frac{j \times B}{cen_e} - \frac{grad p_e}{en_e} \quad (3)$$

This system of differential equation is completed by equations of state and transport coefficients definition. Transport coefficients are usually estimated by Braginskii theory [8].

For equation of state a set of physical model was used. The simplest approach is an analytical model, for example [3]. More accurate ones are, of coarse, tables like SESAME [9], or THERMOS [10]. The physical content includes filters to import different tabular data,

The ionisation level can be taken either from Thomas-Fermi approximation or from tables, for example [9], or more widely applicable [10].

There is a set of approximation for radiation transport. The simplest model is the radiation losses. Two methods of radiation transport simulation are more complicated and more time-consuming. They include the ray tracing algorithm and quasi-diffusion approach [12]. The latter is more efficient, but it is valid only for optically dense plasma. Now it is adapted for general case by special form of flux correction.

In magnetic implosion problems we have the domains with quite different relation between magnetic and thermal energies. It is easy to show, that for small values of parameter $\beta = P/(B^2/8\pi)$ the numerical approximations based on internal energy equations are more favourable. But in this case the special attention must be paid on the conservation of total energy.

Code ASTRE

This code uses a rectangular eulerian mesh. Its main advantages are efficiency, robustness and very simple changing of considered problem. A resolution of local small detail of the flow is based on original adaptive mesh refinement algorithm [1, 2]. The local adaptive procedure was specially constructed for essentially non-linear problems of plasma dynamics. In such algorithm the cells can be subdivided or merged, depending on the gradient of the variables. The algorithm is explicit, but the computations are very effective due to the different time steps for cells of different size and due to the possible temporal refinement. The code name (Adaptive Spatial-Temporal REfinement) reflects this feature.

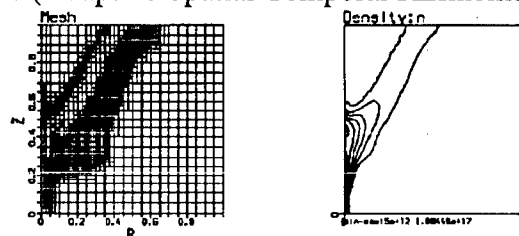


Fig.1 Adaptive mesh for high zipping Z-pinch simulation

This method allows solving the problems in region of complex form. Such opportunity is provided by special boundary conditions treatment. Conservative spatial approximation minimises error in total energy.

New approximation of Hall term was proposed in [2]. Such treatment of this complicated term gives monotone solution even for the ideally conducting plasma, without any conductive diffusion. This approximation lightens the constraints of time step and it extends the application domain to the rare plasmas. The latter future facilitates the POS simulations.

Now code exists in one- and two-dimensional versions, and in Cartesian and cylindrical coordinates for r - z and r - ϕ planes. Wide choice of boundary condition allows easy changing of considered problem. In eulerian simulations the vacuum treatment is always complicated. The vacuum is distinguished from plasma by density threshold, and it is considered as frozen plasma with very small electrical conductivity.

Code Z+

The other code, Z+, uses classical method with lagrangian and eulerian stages. Lagrangian stage is based on [3], eulerian – on slightly modernised version of [4]. Fully conservative algorithm [3, 4] keeps precise balance of total energy for any strategy of mesh motion between lagrangian and eulerian. The remeshing strategy depends of the problem under consideration, but mesh motion is defined automatically, without any manual control.

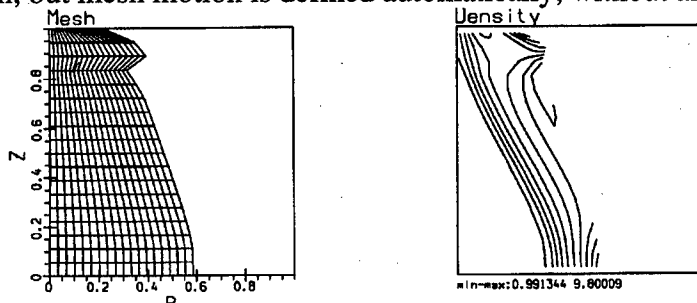


Fig.2 ALE mesh for Z-pinch simulation

The code Z+ was initially constructed for Z-pinches simulation, but later it was ported to other problems, due to the wide choice of boundary conditions. This code allows simple multi-material simulations and it has a full set of radiation transport models.

Realisation of codes

The complexity of the processes often requires the modifications of the physical models and of the numerical approximations. Thus, the code structure should be adapted for such evolution. The codes are written in modern style in C language. The single source of physical models is shared between the codes. Different compilations of the same source files produce 1D or 2D versions. The latter property simplifies the development and support of the codes.

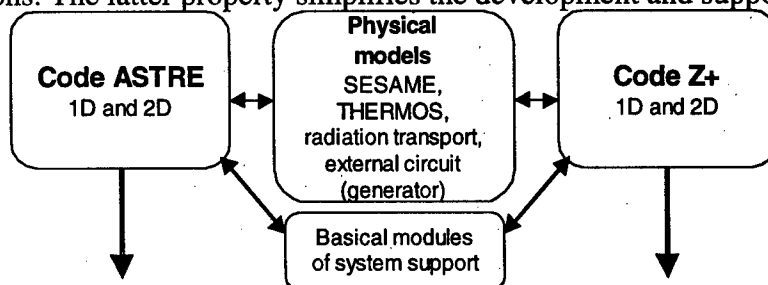


Fig.3 Interaction of codes and physical models

Examples of simulations

A lot of simulations were done by these codes in one and two dimensions. Z-pinch implosions were modelled in different configurations (Fig.1, 2, for example), including instability analysis with randomly perturbed initial data [6]. Typical parameters are current from 50-100 kA till 50 MA, implosion time – from 100 ns to a few microseconds. Optimizations of geometry and density distribution were done. An example of multi-wire liner compression [6] is presented either in r-z plane or in polar coordinates r- ϕ plane. The simulations of plasma focus present another type of magnetic compression problems. These codes were also used for optimization of gas-puff production for further compression in Z-pinch [5]. In this case the simulations were started by gas dynamics version, but than the data were transmitted to MHD code for quality estimation of achieved density distribution.

Plasma opening switches were another important objects for simulation [7]. Their geometrical parameters and position of plasma guns was analyzed and optimized.

Conclusion

These two codes share wide choice of different physical models for equations of state, transport coefficients, optical properties. Such construction provides interesting opportunity for verification of simulation data, namely, either the same physical model can be used by different numerical approaches, or a variety of physical models can be checked with the same numerical conditions.

The authors appreciate the fruitful physical discussions with Alexandre. Chuvatin.

References.

- [1] S.A.Semushin, Finite Volume Adaptive Mesh Refinement algorithm for gas dynamics and MHD problems. *Finite Volumes for Complex Applications*, Paris, HERMES, 1996, p. 659
- [2] S.Semushin, Adaptive Mesh Refinement approach for simulation of gas dynamics and magneto hydrodynamics problems. *Proceedings of 15th IMACS Word Congress. vol.3*, 1997, 109-114.
- [3] V.A.Gasilov, A.Yu.Krukovskii, A.A.Otochin, The program package for calculations of 2D axially symmetrical MHD flows of radiative plasma, *Preprint N162, Keldysh Inst. Appl. Mathematics*, Moscow, 1990, (in Russian).
- [4] V.A.Gasilov, A.Yu.Krukovskii, A.A.Otochin, A.I.Otochin, The Conservative Lagrangian-Eulerian Scheme for 2D Axially Symmetrical MHD Flows, *Preprint N5, Keldysh Inst. Appl. Mathematics*, Moscow, 1991, (in Russian).
- [5] S.Semushin, B.Etlicher, C.Rouillé. Optimisation of gas target production for Z-pinch implosions. *Proceeding of BEAMS'96 Int. Conf.*, p.758-761.
- [6] S.Semushin, B.Etlicher, Simulation of multi-wire liner dynamics during Z-pinch implosion. *These Proceedings*.
- [7] S.Semushin, A.Chuvatin Hall MHD simulation of plasma behaviour in an opening switch. *These Proceedings*.
- [8] S.I.Braginskii, Transport Processes in a plasma. *In: Reviews of Plasma Physics*, Vol.1, Consultants Bureau, New York, (1965).
- [9] SESAME: The Los Alamos National Laboratory Equation Of State Database, Report LA-UR-92-3407, Los-Alamos, 1992.
- [10] A.F.Nikifirov, V.G.Novikov, A.D.Solomyannaya Self consistent hydrogen-like average atom model for the matter with given temperature and density. *High Temperature*, **34**, (1996), 1. (in Russian).
- [11] D.E.Post, R.V.Jensen, C.B.Tarter et al. Steady-state radiative cooling rates for low-density, high-temperature plasmas, *Atomic Data and Nuclear Data Tables*, **20**, (1977), 397-439.
- [12] B.N.Chetverushkin. Mathematical Modelling of radiation gas dynamics problems. Nauka, Moscow, 1985, (in Russian).

THE LAUNCHED ELECTRONS: SIMPLE THEORETICAL MODELING AND NUMERICAL SIMULATIONS

A.V. Gordeev¹, A.S. Chuvatin², and H.Ghalila²

¹ Russian Research Center «I.V.Kurchatov Institute», 123182 Moscow, Russia

² Laboratoire de Physique des Milieux Ionisés, Ecole Polytechnique,
91128 Palaiseau, France

Introduction

Magnetic insulation transmission lines (MITL) give an efficient method of the energy transfer from the generator to the load [1, 2]. In a homogeneous MITL the efficiency of the energy transport is in good agreement with the theoretical consideration [1-4]. However, a symmetry break along the MITL and corresponding non-conservation of the electron canonical momentum lead to appearance of additional electrons emitted from the cathode because of the spatial inhomogeneity in the line. Therefore, an additional electron flow in MITL over the usual near-cathode electron sheath may appear. This additional electron layer, called now launched electrons (LE), was first introduced in [5]. The launched electrons can change essentially the MITL impedance and result in additional current losses in the MITL. One should mention that the minimum energy principle introduced first in [1-4] allows this additional electron layer inside the line gap. The physical reason for creation of the LE layer must be not only spatial inhomogeneities but also sharp temporal disturbances, which give rise to a non-zero emission from the cathode. It is worth mentioning that the LE structure for the KALIF-HELIA device was obtained in [6] within the framework of the minimum energy principle.

In this paper, a simple theoretical model of the LE equilibrium will be presented. The model allows simpler understanding of the nature of LE. It will be shown that appearance of the LE in the MITL gap may be preferable from the point of view of the minimum energy principle. PIC numerical simulations were also performed to investigate conditions under which the LE may appear.

Theoretical modeling

We start with a simple plane model of the MITL (see Fig. 1), where a δ -layer of electrons emitted from an inhomogeneity of the MITL is placed inside the gap.

Equilibrium of this LE layer is described by the electron motion equation

$$\frac{d\vec{p}}{dt} = -e\vec{E} - \frac{e}{c}[\vec{v} \times \vec{B}] \quad (1)$$

and by the stationary Maxwell equations

$$\nabla \cdot \vec{E} = 4\pi\rho, \quad [\nabla \times \vec{B}] = \frac{4\pi}{c}\vec{j} \quad (2)$$

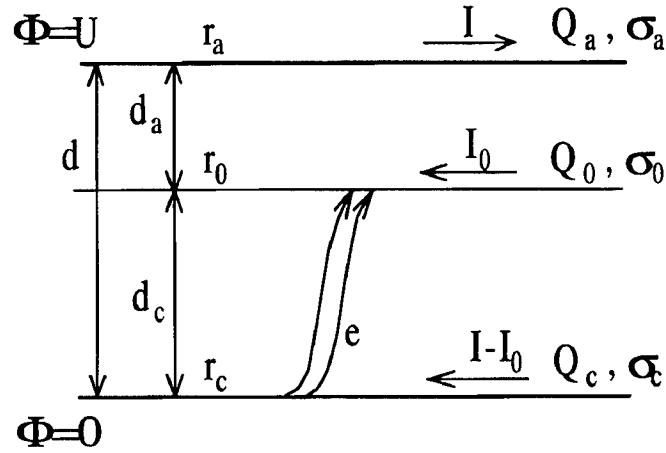


Fig. 1. Additional electron δ -layer at the distance d_c from the cathode and d_a from the anode.

Here it is assumed that there exist no ions in the MITL gap, so that $\rho = -en$, $\vec{j} = -en\vec{v}$, where n and \vec{v} are the electron density and velocity, respectively. In the further analysis we will model the MITL with electrons as a usual vacuum transmission line with the value of the magnetic field which exceeds that of the electric field. In addition to the near-cathode electron sheath, an additional electron δ -layer inside the line gap will be assumed. This transparent model permits to understand or to reject in the simplest way the hypothesis of the LE appearance. The x-component of Eq. (1) together with Eq. (2) result in the pressure balance condition

$$B_a^2 - E_a^2 = B_c^2 - E_c^2 \quad (3)$$

where B_a, E_a and B_c, E_c are the constant magnetic and electric fields above and below the electron δ -layer, respectively. Further it will be very useful to introduce the surface electron density for the δ -layer

$$\sigma_0 = \int_{r_0 - \varepsilon}^{r_0 + \varepsilon} \rho_0 dx \quad (4)$$

as well as for the anode and the cathode, σ_a, σ_c , respectively. Thus, the anode and the cathode electric fields are equal to $E_a = -4\pi\sigma_a$, $E_c = 4\pi\sigma_c$. Taking into account the jumps of the electric and magnetic fields on the δ -layer, one can obtain the following expressions for the electron surface densities

$$\sigma_a = \frac{u - \sigma_0 d_c}{d}, \quad \sigma_c = -\frac{u + \sigma_0 d_a}{d} \quad (5)$$

where $d = d_a + d_c$ is the MITL gap and $4\pi u = U$ is the MITL voltage.

The total energy per unit length of the MITL is equal to

$$w = \frac{u^2}{d} + \frac{i_a^2}{c^2} d + \frac{1}{c^2} (i_0^2 + 2i_a i_0) d_c + \frac{\sigma_0^2}{d} d_a d_c - (\gamma_0 - 1) mc^2 \frac{\sigma_0}{2\pi e} \quad (6)$$

where $i_0 = v_0 \sigma_0$ is the surface current density and v_0 is the electron velocity in the δ -layer. Subtracting from (6) the total energy of the MITL without LE and taking into account the

expression for $|\sigma_0| = -\sigma_0$ from the pressure balance (3)

$$|\sigma_0| = \frac{2i_a}{c} \frac{\xi - \beta_0}{\frac{d_a^2 - d_c^2}{d^2} - \beta_0^2}, \quad \xi = \frac{u}{d} \frac{c}{i_a}, \quad \beta_0 = \frac{v_0}{c} \quad (7)$$

one can get to the following expression of the energy variation in the MITL, related to appearance of the δ -layer

$$\delta w = \frac{2i_a}{c} \left\{ (\gamma_0 - 1) \frac{mc^3}{4\pi e i_a d} + \frac{d_c}{d} \left[\frac{(\xi - \beta_0)(\frac{d_c}{d} + \beta_0^2)}{\frac{d_a^2 - d_c^2}{d^2} - \beta_0^2} - \beta_0 \right] \right\} \quad (8)$$

If $\delta w < 0$ is satisfied, the considered equilibrium with the LE layer is preferable from the point of view of the minimum energy principle. We should also remember that the energy of electrons in the δ -layer is determined from the equation $(\gamma_0 - 1)mc^2 = e\Phi_0$ by the account of the relation $\Phi_0 = -d_c E_c$. After simple transformations we obtain

$$\gamma_0 - 1 = \frac{d_c}{d} \left(\gamma - 1 - d_a |\sigma_0| \frac{4\pi e}{mc^2} \right), \quad \gamma - 1 = \frac{eU}{mc^2} \quad (9)$$

For the convenience, we introduce the dimensionless current $i = \frac{4\pi e i_a d}{mc^3}$ so that the

«hot» impedance of the line is equal to $\xi = \frac{\gamma - 1}{i} < 1$.

In addition, the δ -layer's parameters meet the equation

$$\frac{\gamma_0 - 1}{i} = (1 - s) \frac{2s\beta_0 - \xi(1 + \beta_0^2)}{2s - 1 - \beta_0^2}, \quad s = \frac{d_a}{d} \quad (10)$$

When substituting the $(\gamma_0 - 1)$ expression in Eq. (8) one can obtain the final expression for the energy variation δw

$$\delta w = -(1 - s)^2 \sigma_0^2 d < 0 \quad (11)$$

For given ξ , one can obtain the values of s and β_0 , which must satisfy the following inequalities

$$\frac{\beta_0}{s} < \frac{\xi}{s} < \frac{2\beta_0}{1 + \beta_0^2} < \frac{1 - \beta_0^2}{1 + \beta_0^2} \frac{\xi}{1 - s} \quad (12)$$

PIC simulations

To confirm this result, the dynamics of vacuum electron flow in a coaxial MITL was numerically modeled using the KNEXT 2,5 PIC code [7]. Spatial and temporal behavior of the electron layer was considered in presence of an anode insert with local decrease of the anode diameter. This anode step (AS) was supposed to perturb the electron flow equilibrium in the vacuum gap and possibly to create a LE layer. The MITL was powered by a 10 ns rise time, a 3 MV maximum amplitude voltage ramp, Fig. 2. The MITL was connected to a load, which had the impedance lower, equal or higher, than the «hot» line impedance of the AS part [4].

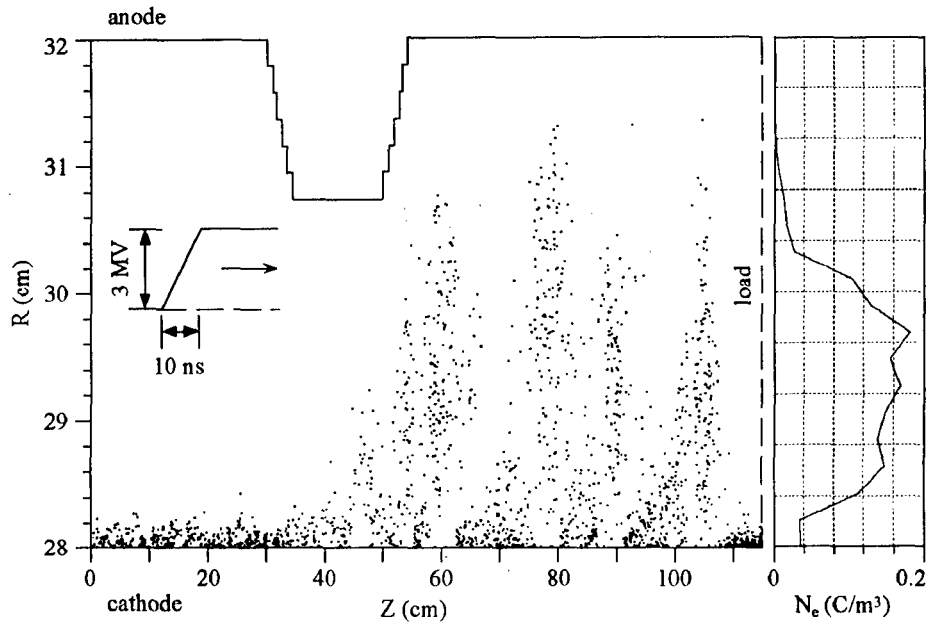


Fig. 2. Snapshot of particles distribution at $t = 30$ ns after the voltage pulse beginning. The picture is obtained with KNEXT 2.5 simulations of a coaxial MITL with changing AK gap loaded by a 2 Ohm resistance. The right hand side of the figure represents radial distribution of the electron charge at $Z = 90$ cm.

Existence of the interelectrode electron charge density maximum was detected in PIC simulation only for the low impedance loads. Such distribution, typical for LE, existed downstream the AS during the voltage rise time and some time after the voltage reached its constant value. After 40 ns, the distribution characteristic for LE disappeared downstream the AS insert. Stationary electron layer distribution was found to be in good agreement with previous theoretical results [1-4]. Appearance of considerable spatial instability of the electron layer in the case of low impedance load was also observed.

The authors wish to acknowledge Dr. S.Semushin for contributing discussions.

References

- [1] A.V. Gordeev, Preprint IAE-3076, 1978; in English: A.V.Gordeev, Magnetic Self Insulation of Vacuum Coaxial Lines, PIIR-12-79, Phys. Int. Comp., 1979.
- [2] L.I. Rudakov, M.V. Babykin, A.V.Gordeev, B.A.Demidov, V.D.Korolev and E.Z.Tarumov, in: The Generation and Focusing of the High-Current Relativistic Electron Beams, ed. L.I. Rudakov (Energoatomizdat, Moscow, 1990) p.280.
- [3] A.V. Gordeev, Zh. Techn. Fiz., 1978, v.48(4), 784-788.
- [4] E.I. Baranchikov, A.V. Gordeev, V.D.Korolev and V.P.Smirnov, Sov. JETP, 1978, v. 75(6), 2103-2121.
- [5] C.W. Mendel, in: Proceedings of the 11th International Conference on High Power Particle Beams, 1996, June 10-14, Vol. 1, pp. 56-59
- [6] A.V. Gordeev, in: Proceedings of the 17th International Symposium on Discharge and Electrical Insulation in Vacuum, 1996, July, 21-26, Vol. 1, pp. 482-486.
- [7] H.Ghalila, Thèse de Docteur en Sciences, Université Paris XI Orsay, 1994 (Laboratoire de Physique des Milieux Ionisés, Ref. PMI 2903).



BEAMS'98

12th INTERNATIONAL CONFERENCE
ON HIGH-POWER PARTICLE BEAMS



ORALS

***Ion Beams
and Diodes, ICF***

Vol. I

Proceedings

COLLIDING BEAM FUSION REACTOR

N. Rostoker and M.W. Binderbauer

University of California, Irvine, CA 92697

H.J. Monkhorst

University of Florida, Gainesville, FL 32611

ABSTRACT

In this paper aspects of conceptual reactor designs are investigated that are based on the FRC configuration for D-T, D-He³, and p-B¹¹ reactions. The fuel ions are of sufficient energy that the orbit size is large enough so that classical transport should prevail in the absence of long wavelength instabilities.

We begin by reviewing briefly some evidence for classical confinement in such a system. Next we address the key issue of current maintenance by injecting beams of neutral atoms into an FRC. Although there are many theoretical papers on this subject, there are no experiments. Our investigation of this issue starts with a discussion of FRC experiments, the current carried by ions and the decay of current due to Coulomb interactions of electrons and ions. We then consider periodic pulses of injected neutrals in order to maintain a steady state ion current in the FRC. The injected neutrals constitute a source of ions and electrons and for a steady state there must be a sink. For a burning plasma the dominant sink is the fusion reactions.

We have previously shown that the sources and sinks of a burning plasma dominate the equilibrium distributions [1]; i.e. the equilibrium is quite different from the self-consistent solution of the Vlasov-Maxwell equations without fusion reactions. In this paper we illustrate some of the changes in the kinetic description of a burning plasma due to the inclusion of sources and sinks. For example the electrons are injected at relatively low energy. Electrons leave along with fusion product ions in a steady state. The electrons leave after being heated and this constitutes a significant heat transfer mechanism that can be more important than radiation. Source and sink modifications to previous reactor kinetic calculations are included to arrive at quantitative estimates for key operating parameters.

1. MOTIVATION: CLASSICAL CONFINEMENT OF IONS

A plasma consisting of large orbit non-adiabatic ions and adiabatic electrons is considered. Experimental evidence with energetic beams injected into Tokamaks for heating in DIII-D and TFTR and with energetic fusion products in JET indicates that such a plasma does not suffer from the anomalous transport characteristics usually observed in fusion devices. In fact the diffusion of these large orbit ions is consistent with classical estimates while at the same time the thermal population diffuses anomalously. In addition to Tokamak experiments numerical simulations support the fact that large orbit particles feel predominantly low frequency field fluctuations with wavelengths that exceed the larmor radius. The physical reason for this is that ions, over the course of such a large orbit,

average the fluctuations so that only long wavelengths (compared to gyro-radius) and small frequencies (compared to gyro-frequency) cause transport. Thus if the particle orbit radius is large and the plasma has gross stability at long wavelengths, anomalous transport can in principle be avoided.

2. CONCEPTUAL REACTOR DESIGN

The basis of the design for the reactor discussed here is a modified FRC as described by Rostoker *et al.* [2]. The modification to the usual FRC lies in the fact that almost all the ions are considered to be non-adiabatic and to possess high coherent energy and, thus, large orbits (for typical data the worst case fuel ion orbit size is on the order of 1 cm – slightly larger than the minimum orbit size of the classically diffusing particles in the previously mentioned tokamak experiments). With this alteration the system can essentially be thought of as an ion beam confined to an annular region encircling the axis of symmetry. The electrons are thermal and as such respond also to short wavelength turbulence. However, their loss is limited by positive charge accumulation in the plasma. A nice feature of the FRC configuration is that the plasma is surrounded by a natural divertor, i.e.: the region of near vacuum between the walls and the plasma exhibits an open magnetic field line topology – allowing particles that reach this region to scatter and leave along the field lines much faster than it would take to diffuse across.

3. CURRENT MAINTENANCE

A key issue of whether the envisioned reactor can sustain a steady state equilibrium is current drive and current maintenance by injecting beams of neutral atoms into the FRC system. Although there are many theoretical papers on this subject, there are no experiments for the type of closed magnetic topology setup discussed here. This section is intended to illustrate the problems and indicate some possible solutions.

3.1. Creation of FRC and Origin of Ion Current

Typically an FRC is formed by the inductive or Θ -pinch method which preferentially heats ions by compression. After the compression the current is carried by electrons and the ions have zero net drift velocity and a temperature of about 500 eV. After reconnection there is a radial magnetic field at the ends which is focusing for ions that rotate in the diamagnetic direction and defocusing for those that rotate in the opposite direction. This leads to selective confinement of the ions and causes about half of them to escape along with an adequate number of electrons. The resultant net ion current causes electrons to be collisionally accelerated towards zero net drift – in this period the ion velocity changes are negligible compared to those of the electrons. Thus the total current changes little but the electron current decreases until at the end of this "formation phase" the current is carried about equally by ions and electrons.

3.2. Lifetime of FRC and Current Decay

After the FRC is established as described in the previous section, the lifetime is determined by the decay of the current. In typical experiments carried out at LANL [3] the parameters of the produced pure hydrogen plasma are $n_i = n_e \sim 5 \times 10^{15} \text{ cm}^{-3}$, $T_e \sim 100 \text{ eV}$ and $T_i \sim 500 \text{ eV}$. The ratio of plasma scale to ion orbital radius is on the order of 2 and about half the current is carried by ions. The observed lifetime is between 100 to 500 μsec .

To see whether these numbers are in agreement with classical predictions, we assume that the current decay is due to coulomb collisions between electrons and ions. For the

initial conditions given by the LANL data we find that the electron-ion and ion-electron momentum exchange times are $t_{ei} \simeq 4$ nsec and $t_{ie} \simeq 7$ μ sec, respectively. Recasting the conservation of energy during this process in the form of a circuit equation gives

$$(L + L_I) \frac{dI}{dt} + IR = 0, \quad (1)$$

where, respectively, $L \simeq 2\pi^2 r_o^2 / c^2$, $L_I = (2\pi r_o)^2 m m_i / N_e e^2 (m + m_i)$ and $R = (2\pi r_o)^2 m / N_e e^2 t_{ei}$ are the inductance/unit length of the ring, the inertial inductance/unit length ($L_I \ll L$), and the plasma resistance/unit length. N_e is the line density of electrons and r_o the radius of peak density. From the time scales given by t_{ei} and t_{ie} we can see that the current decay is mainly due to an increase in the average azimuthal electron velocity, V_e , i.e.: $dI/dt \simeq -(eN_e/2\pi r_o) dV_{e\theta}/dt$. The decay time of the current is, thus, given by

$$\tau \simeq \frac{L + L_I}{R} \simeq \frac{1}{4} \frac{r_o \Delta r}{(c/\omega_{pe})^2} t_{ei} \simeq 300 \mu\text{sec}. \quad (2)$$

$N_e = 2\pi r_o \Delta r n_e$ and $\omega_{pe}^2 = 4\pi n_e e^2 / m$. This time is much greater than the momentum exchange time t_{ei} because of the large inductance. Its value is within the range given by the LANL measurements. For large density values (on order of 10^{16} cm^{-3}) classical diffusion theory is also consistent with the observed particle confinement time as reported by Aso *et al.* [4].

3.3. Current Neutralization Issues

The main question for current maintenance is fast current neutralization of a beam. The time scale for this would be much shorter than neutralization by collisions. When a beam is injected into a plasma with axial symmetry the initial current increase induces an electric field E_θ which makes electrons drift in the radial direction $v_r = cE_\theta/B_z$. This electron drift perturbs the charge density causing a radial electric field in response to E_θ . The radial electric field then produces a drift $v_\theta = -cE_r/B_z$ of electrons which neutralizes the current of the beam. This can take place on a fast time scale described by the Vlasov-Maxwell equations. If the magnetic field has open field lines, electrons can move along the field lines and prevent the development of E_r . In this case current neutralization is due to Coulomb collisions and the time scale is L/R . If the magnetic field involves closed field lines and axial symmetry prevails it is predicted that fast current neutralization can take place [5]. It is also predicted that it can be prevented by breaking the axial symmetry for example with the addition of a weak quadrupole field. It can also be prevented by instabilities [6]. There are no experiments in which a beam of neutrals or a neutralized ion beam is injected into an FRC. It is a fact that fast current neutralization does not take place in an FRC. However, an FRC usually does have a weak quadrupole field. It does not seem likely that a complete answer to the questions of current neutralization in an FRC can be attained without some new experiments. For the present investigation, we assume that fast neutralization cannot take place although this may involve breaking the symmetry.

3.4. Current Maintenance by Neutral Beam Pulses

We consider the injection of pulsed beams as illustrated in Fig. 1. They may be pulsed neutral beams or neutralized beams with a pulse duration $\Delta t \ll t_{ei}$. The injected electrons have a negligible energy and do not speed up during Δt while the ion velocity changes.

From $t = t_n + \Delta t$ until $t = t_n + T$ the current decays as previously discussed; the change in ion velocity $V_{i\theta}$ is negligible and although $V_{e\theta}$ changes significantly the energy $N_e m V_{e\theta}^2 / 2$ is negligible. Therefore, from energy conservation

$$\frac{1}{2} L I^2 \Big|_{t_n + \Delta t}^{t_n + T} = - \int_{t_n + \Delta t}^{t_n + T} I^2 R dt , \quad (3)$$

i.e.: the dissipated energy comes from the stored magnetic field energy. Thus, the injected beam has to have sufficient energy to also resupply the loss in stored magnetic energy (the beam loses this energy due to the inductive electric field after trapping). A steady periodic state can, therefore, be maintained by injecting and trapping ΔN_i particles (particle losses due to diffusion out to the separatrix and due to fusion reactions must be balanced with $\Delta N_i / T$) with a proper choice of $V'_{i\theta}$ (determined by the dissipation $I_o^2 R T$) such that

$$\sum_i \frac{1}{2} \Delta N_i m_i [(V'_{i\theta})^2 - V_{i\theta}^2] = \frac{1}{2} L [I^2 - (I - \Delta I)^2] \simeq I_o^2 R T . \quad (4)$$

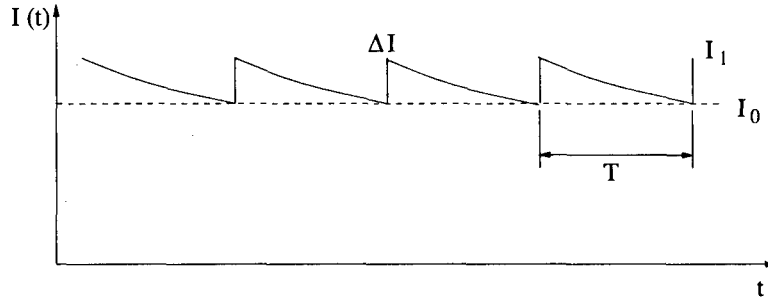


Figure 1: Pulsed beam injection after initial FRC formation.

4. SINK ISSUES

In order to describe the injection and trapping of particle beams as well as fusion reactions and diffusion, it is necessary to add sources and sinks to the Vlasov/Fokker-Planck equation:

$$\frac{\partial f_i}{\partial t} + \mathbf{v} \cdot \frac{\partial f_i}{\partial \mathbf{x}} + \frac{e_i}{m_i} \left(\mathbf{E} + \frac{1}{c} \mathbf{v} \times \mathbf{B} \right) \cdot \frac{\partial f_i}{\partial \mathbf{v}} = - \frac{\partial}{\partial \mathbf{v}} \langle \Delta \mathbf{v} \rangle_i f_i + \frac{1}{2} \frac{\partial}{\partial \mathbf{v}} \cdot \frac{\partial}{\partial \mathbf{v}} \langle \Delta \mathbf{v} \Delta \mathbf{v} \rangle_i f_i + Q_i - S_i \quad (5)$$

Q_i is the source due to beam injection; S_i is the sink. In the last section we discussed the injection source and its role in maintaining the equilibrium. In this section we show an example of the strong effect sinks have on the plasma kinetic equations and in particular on the determination of ion and electron temperatures.

Consider for instance the electron temperature. Electrons are injected along with the fuel beams and enter the plasma with negligible energy and temperature. With each fusion reaction two fusion fuel ions disappear; they are replaced by fusion products which leave the plasma if there is to be a steady state. To maintain charge neutrality $Z_1 + Z_2$ electrons must also leave. Since there is a potential barrier (the plasma is positively charged in equilibrium) only the high energy electrons can escape. They expend energy to get over the barrier, but get it back after they leave the plasma completely along the

open field lines. To escape the electrons must go over a potential barrier of height T_e/e . The average energy of particles that leave is

$$T_e + \frac{\int_c^\infty \frac{1}{2}mv^2 f_e(v)dv}{\int_c^\infty f_e(v)dv} \simeq 5T_e,$$

where $f_e(v)$ is a one dimensional Maxwell distribution. Thus a sink in the form of a cooling term must be added to the Fokker-Planck equation which is of the form

$$-5T_e \sum_j \frac{N_j Z_j}{t_{Fj}}. \quad (6)$$

This cooling term may be more important than the Bremsstrahlung because it is proportional to T_e rather than $\sqrt{T_e}$. Similarly there are cooling terms for the fuel ion beams if the temperatures of the beams at injection are less than the steady state temperatures. Although Eq. (6) helps to reduce electron temperature and therefore Bremsstrahlung it does represent an energy loss. However, the electron energy can be recovered with high efficiency whereas Bremsstrahlung can only be recovered with an efficiency of at most 40%.

5. MODES OF OPERATION

We consider fuel systems with two types of ions of mass m_1 , m_2 and atomic number $Z_1 = 1$ and $Z_2 \geq 1$ such as D-T, D-He³ and p-B¹¹. The fusion cross section for each case has a resonance (see Fig. 2). The reactivity $\langle \sigma v \rangle$ can be calculated by

$$\langle \sigma v \rangle = \int d\mathbf{v}_1 d\mathbf{v}_2 F_1(\mathbf{v}_1) F_2(\mathbf{v}_2) |\mathbf{v}_1 - \mathbf{v}_2| \sigma(|\mathbf{v}_1 - \mathbf{v}_2|) \quad (7)$$

where

$$F_i(\mathbf{v}_i) = \left(\frac{m_i}{2\pi T_i} \right)^{3/2} \exp \left[-\frac{m_i}{2T_i} (\mathbf{v}_i - \mathbf{V}_i)^2 \right]. \quad (8)$$

In the first mode of operation $\mathbf{V}_1 = \mathbf{V}_2$ and $T_1 = T_2$. The distribution functions are thermal in a moving frame of reference. The thermal reactivities designated in Fig. are applicable and are no better than a purely thermal reactor. V_1 and V_2 are large enough to avoid anomalous diffusion but as small as possible consistent with this to minimize the circulating power. The injection energy $\frac{1}{2}m_1 V_1^2 + \frac{1}{2}m_2 V_2^2$ is the price to be paid for avoiding anomalous diffusion. The advantages of this mode are that both fuel ions are in thermal equilibrium (ion-ion collisions assure this but do not contribute to transport), that there is no anomalous transport and that current drive is accomplished.

The second mode of operation involves $\mathbf{V}_1 \neq \mathbf{V}_2$ and $\frac{1}{2}m_1(\mathbf{V}_1 - \mathbf{V}_2)^2 = \epsilon_R$ the resonant energy. The temperatures of the beams should be as low as possible to enhance the reactivity as illustrated in Fig. . In this case the steady state electron velocity would be $V_e = (n_1 V_1 + n_2 Z_2^2 V_2) / (n_1 + n_2 Z_2^2)$ where n_1, n_2 are fuel ion densities. The steady state current is the Ohkawa current

$$j_\theta = \frac{en_1 n_2}{n_1 + n_2 Z_2^2} (Z_2^2 - Z_2) (V_1 - V_2). \quad (9)$$

Provided that V_1 and V_2 can be maintained this takes care of current drive. If $Z_2 = 1$ as it is for D-T reactions $j_\theta = 0$. However, current could possibly be maintained considering the

net current of the α -particles produced by fusion which would be selectively confined in an FRC. The reactivity enhancement depends on the beam temperature. It is significant for D-He³ at $T_1 = T_2 \simeq 100$ keV. The price to be paid is in the additional input energy of the fuel ions in order to maintain V_1 and V_2 . Additional problems arise because of the requirement of low beam temperatures to take advantage of the resonance.

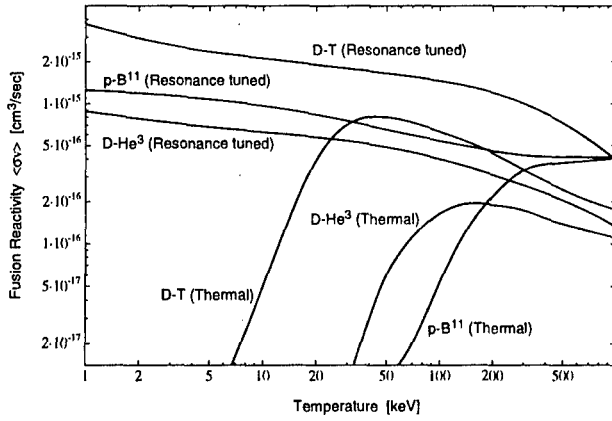


Figure 2: Various Fusion Reactivities

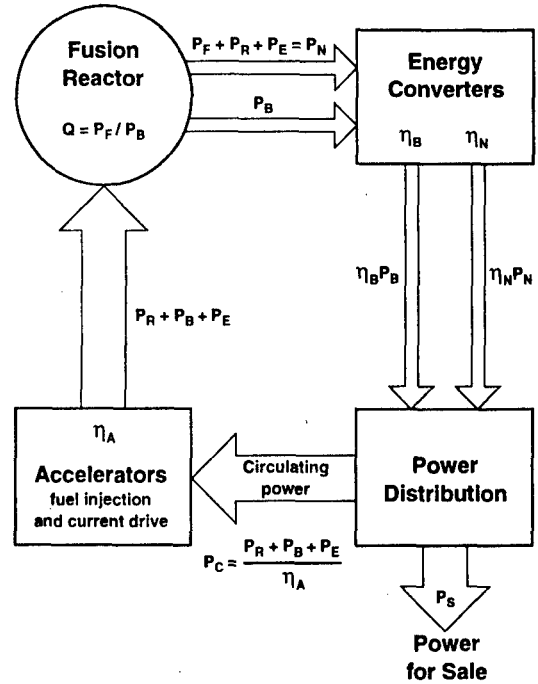


Figure 3: Power Flow Schematic

6. REACTOR DESIGN

The results of a systematic treatment of reactor kinetics for D-T, D-He³ and p-B¹¹ are shown in Table 1. The power flow for a reactor is illustrated in Fig. 3. The definitions of the various quantities are: P_F is the fusion power, P_B is bremsstrahlung power; P_R is the replacement power (i.e. protons as they burn must be replaced with 630 keV); P_E is the burn that arises from energetic particles other than fusion product ions leaving with each fusion reaction (for example electrons must leave along with fusion product ions as discussed in section 4 – also replacement fuel ions enter at low temperature, are heated and then disappear either due to fusion reactions or fuel transport in the case of boron if $V_2 \simeq 0$); $Q = P_F/P_B$ is a figure of merit that is determined by the electron temperature; η_A , η_B and η_N are efficiencies for the accelerator, for bremsstrahlung and for fusion products (mainly neutrons for D-T); P_S is the power for sale; P_C is the circulating power.

The average azimuthal velocities of the beams are V_1 , V_2 and V_e and in a steady state they must be constant. To calculate beam temperatures we must first define them. For example

$$\frac{3}{2}T_e = \frac{1}{2}m \left[\langle v^2 \rangle - V_e^2 \right].$$

By taking appropriate moments of the Vlasov/Fokker-Planck equation we conclude that

$$\frac{3}{2} \frac{dT_e}{dt} = \frac{m}{2} \frac{d}{dt} \left[\langle v^2 \rangle - V_e^2 \right] = m \left[\frac{(V_1 - V_e)^2}{t_{e1}} + \frac{(V_e - V_2)^2}{t_{e2}} \right] \quad (10)$$

Table 1: Fusion Reactor Parameters

		D-T	D-He ³	p-B ¹¹	
		mode 1	mode 1	mode 1	mode 2
density [cm ⁻³]	n_1	$.5 \times 10^{15}$	$.333 \times 10^{15}$	$.5 \times 10^{15}$	1.33×10^{15}
	n_2	$.5 \times 10^{15}$	$.333 \times 10^{15}$	10^{14}	1.33×10^{14}
	n_e	10^{15}	10^{15}	10^{15}	2×10^{15}
fuel ion energy [keV]	$\frac{1}{2}m_1V_1^2$	200	200	50	630
	$\frac{1}{2}m_2V_2^2$	300	300	550	0
fusion time [s]	t_{F1}	2.5	15	25	9.4
	t_{F2}	2.5	15	5	.94
energy/reaction [MeV]	ϵ_F	18	18.4	8.68	8.68
electron temperature [keV]	T_e	100	185	125	165
ion temperature [keV]	T_1	96	217	234	15
	T_2	96	217	234	150
$Q = P_F/P_B$		86	2.65	1.07	2.08
efficiency	η_A	.8	.8	.8	.8
	η_B	.4	.4	.4	.4
	η_N	.4	.9	.9	.9
P_S/P_F		.300	.567	.079	.22
P_C/P_s		.318	1.126	15.5	3.5

and similarly

$$\frac{m}{2} \frac{dV_e^2}{dt} = m \left[\frac{V_e(V_1 - V_e)}{t_{e1}} + \frac{V_e(V_2 - V_e)}{t_{e2}} \right] \quad (11)$$

where t_{e1} and t_{e2} represent momentum transfer times considered for example for p-B¹¹. If one considers an initial value problem Eq. (10) is correct and both protons and boron produce heating of electrons on a very short time scale $t_{e1} \sim 10^{-3}$ sec. However if one considers a steady state, then $dV_e^2/dt = 0$; solving Eq. (11) for V_e will give $V_e = 0$ or the Ohkawa velocity and current. To correct Eq. (10) we must calculate only

$$\frac{3}{2} \frac{dT_e}{dt} = \frac{m}{2} \frac{d\langle v^2 \rangle}{dt} \quad (12)$$

We may correct Eq. (10) by adding Eq. (11) to both sides of Eq. (10) and obtain for a steady state

$$\frac{3}{2} \frac{dT_e}{dt} = m \left[\frac{V_1(V_1 - V_e)}{t_{e1}} - \frac{V_2(V_e - V_2)}{t_{e2}} \right] \quad (13)$$

The proton heating is increased and the boron heating changes to cooling. The Fokker-Planck equation involves $\langle \Delta \mathbf{v} \rangle_e$ (drag) and $\langle \Delta \mathbf{v} \Delta \mathbf{v} \rangle_e$ (scattering). The scattering produces only heating; the drag term involves heating or cooling. The drag term dominates. Eq. (13) simplifies for $V_1 = V_2$ (mode 1).

For protons the difference between the initial value problem and the steady state problem is even more dramatic.

$$\frac{3}{2} \frac{dT_1}{dt} = -m \left[\frac{V_2(V_1 - V_2)}{t_{12}} + \frac{V_e(V_1 - V_e)}{t_{1e}} \right] + \frac{3(T_e - T_1)}{t_{1e}}. \quad (14)$$

Both boron and electrons produce cooling. There is an additional term due to electrons which involves heating if $T_e > T_1$.

The above equations are incomplete because there are other effects such as α -particle heating, radiation cooling etc. which we omit here to concentrate on the Coulomb effects of the fuel and electrons. These effects must be included to determine the temperatures from $dT_e/dt = dT_1/dt = 0$.

The next question is of course how does one maintain a steady state. The protons must be replaced at the burn rate and at a higher energy than the design energy; the boron at a lower energy. Steady state or pulsed accelerators may be employed. Pulsed accelerators are discussed in section 3.4. The accelerator requirements are beyond the state of the art particularly for p-B¹¹. However, the requirements will be substantially reduced by optimization of the kinetics and polarization of the fuel [1]. There are several developments in accelerators to produce high energy neutral hydrogen. There is the RF accelerator at LANL with the Dimov source and the work on negative hydrogen diodes at UCI and Lebedev Institute [7]. These recent developments show that our requirements can be met.

7. SUMMARY

In this paper we have presented the results of reactor kinetic calculations and illustrated the importance of sources and sinks in D-T, D-He³ and p-B¹¹ reactions for a mode of operation that can be described as thermal in a moving frame of reference. A mode of operation that takes advantage of the resonance in the fusion cross section has been suggested and evaluated for p-B¹¹.

ACKNOWLEDGEMENT

This work was supported by the Office of Naval Research under contract N00014-96-1-1188.

REFERENCES

- [1] N. Rostoker, M.W. Binderbauer and H.J. Monkhorst, *Science*, **278**, 1419, 1997.
- [2] N. Rostoker *et al.*, *Phys. Rev. Lett.*, **70**, 1818 (1993).
- [3] M. Tuszewski, *Nucl. Fusion* **28**, 2023 (1988).
- [4] Y. Aso, S. Himeno and K. Hirano, *Nucl. Fusion*, **23**, 751, 1983.
- [5] H. Berk, H. Momota and T. Tajima, *Phys. Fluids*, **30**, 3548, 1987; J.H. Hammer and H. Berk, *Nucl. Fusion*, **22**, 89, 1982.
- [6] A. Reimann and R.N. Sudan, *Comm. Plasma Phys. and Controlled Fusion*, **5**, 167, 1979.
- [7] V.A. Papadichev, Proceedings of Beams '88.

TIME DEPENDENT FIELD AND PARTICLE DENSITY MEASUREMENTS IN THE ACCELERATION GAP OF A HIGH POWER ION DIODE

V. Licht, H. Bluhm, P. Hoppé, S.J. Yoo

Forschungszentrum Karlsruhe

Institut für Neutronenphysik und Reaktortechnik, Postfach 3640, D-76021 Karlsruhe

Abstract

Using a newly developed two-wavelength dispersion interferometer system of exceptionally high sensitivity we have been able to measure for the first time the electron density distribution inside a high power ion diode. The assumption of a flat electron density distribution across the gap -often made in theoretical models- is compatible with the present observations up to peak diode power. Afterwards a rapid increase of the electron density is seen. Combining these results with spectroscopic measurements in the anode plasma we conclude that the diamagnetic field penetration into the anode plasma can lead to its fast acceleration after peak power, affect the electron density increase in the gap, and the diode impedance collapse associated with it.

Introduction

Until today intense light ion beam production by single or two-stage acceleration in high power magnetically insulated diodes suffers from large beam divergence, ion energy spread, and the inability to adequately control the diode impedance. The latter until now prevents the possibility to take advantage from beam bunching by ramping the driving voltage pulse. Both, the light ion beam quality and the diode impedance history are mainly affected by the properties and the evolution of the anode plasma and of the electron cloud filling the diode gap.

Detailed measurements of particle densities, temperatures, composition, and field distributions inside the anode plasma as well as close to its surface have been carried out in recent years by a number of groups /1-4 / and improved our knowledge of the physical processes governing the operation of these devices. However, it seems difficult to generalise these results because some have been obtained with special types of passive ion sources, while others were achieved with rather low power diodes. In addition, a direct measurement of the electron density inside the diode gap was lacking until today.

Here we report on results obtained for the magnetically insulated high power ion diode used on the 1.7 MV, 1.5 TW pulse generator KALIF. In this diode the ion source is produced actively by initiating a sliding discharge in a hydrogen gas layer that is desorbed from a Ti-reservoir. Details of the ion diode and of the ion source can be found elsewhere / 5,6 /.

Using spectroscopic measurements we have determined the particle densities and temperatures as well as the magnetic field penetration into the plasma. The electron density inside the diode gap was determined with the help of a newly developed two-wavelength dispersion interferometer of exceptionally high sensitivity.

Diagnostic tools

Since the set-up of the spectroscopic diagnostic has been described in a previous Beams' paper we refer to that paper for any details /7/. The line of sight of the spectrometer was aiming parallel to the anode. Using a lens with a large focal length (800 mm) a spatial resolution of up to 0.2mm could be realised. Depending on the requirements the spectral resolution was adjusted between 0.2 and 0.5 Å. The temporal resolution of 5-10 ns was mainly limited by the necessity to reduce the statistical error.

Since the interferometer was redesigned after the last Beams' meeting we shall outline its main characteristics here. We have chosen a two-wavelength dispersion interferometer because it is

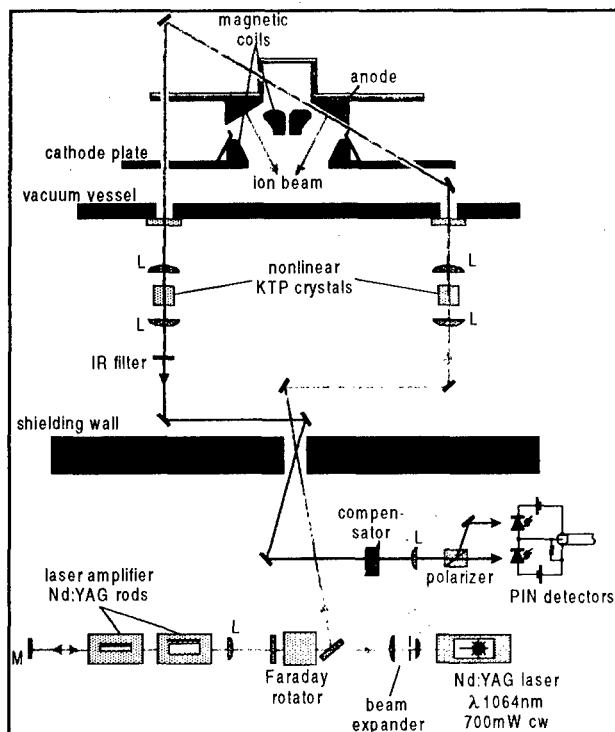


Fig. 1 Set-up of two-wavelength dispersion interferometer on KALIF

a relatively simple and robust system well suited for the hostile environment of a high power generator and diode. The arrangement of the interferometer is presented in Fig. 1. It starts with a single mode, single frequency 700 mW cw Nd:YAG ring laser oscillating at the fundamental wavelength of 1064 nm. To increase its intensity the laser beam is sent twice through two flashlamp-pumped Nd:YAG amplifier rods and then focused into a KTP crystal for frequency doubling. Both, the nontransformed fundamental wave and its second harmonic are transmitted through the electron cloud in the diode gap. After exiting from the diode vacuum chamber a fraction of the remaining fundamental wave is frequency doubled too and its residual part is eliminated with an infrared filter. Due to the wavelength dependence of the refraction index in the electron fluid both beams have experienced different phase shifts which are conserved during frequency doubling. The KTP crystals

are arranged such that the green beams are produced with polarisation vectors perpendicular to each other. Using a beam splitting polarizer the beams are divided into two components with parallel polarisation vectors and two components with antiparallel polarisation vectors. Each of these beam pairs can interfere and their interference pattern are imaged onto two PIN photodiodes arranged in a compensating bridge circuit. With the help of a Babinet compensator the initial phase shift is adjusted to 90° such that the difference signal of the photodiodes becomes zero prior to the experiment. At this adjustment the system has its highest sensitivity and is largely independent of laser intensity fluctuations. Before the beams are brought to interference they have passed through the same optical media. Slow changes in the optical path between the first and the second KTP-crystal do not effect the results because they can be recorded immediately before the experiment.

To check the stability and the sensitivity of the interferometer we have measured the phase shift by transmitting the beams through a vacuum chamber in which the air pressure was varied between 0 and 10^5 Pa. These measurements showed excellent stability and linearity. During the period of data collecting, which lasted 45 minutes, a drifting of the interferometer was not observed. With the present set-up we are able to measure electron line densities below 10^{13} cm^{-2} corresponding to a fringe shift of $8 \cdot 10^{-5}$.

Results

In order not to affect the normal operation of the diode only spectral lines from components naturally occurring in the anode plasma were used to infer the anode plasma properties.

During the first 30 ns after beginning of the diode voltage the Stark broadened H_α and C II (6578 Å) lines were exploited to derive the electron density as a function of time. Later in the pulse the refractive index gradient diagnostic described in Ref. /8/ was applied and supplemented by evaluating the Stark-broadening of the C IV (5801.3 Å) line. The electron density obtained at a distance of 0.25 mm from the anode surface is shown in Fig. 2. After a period of

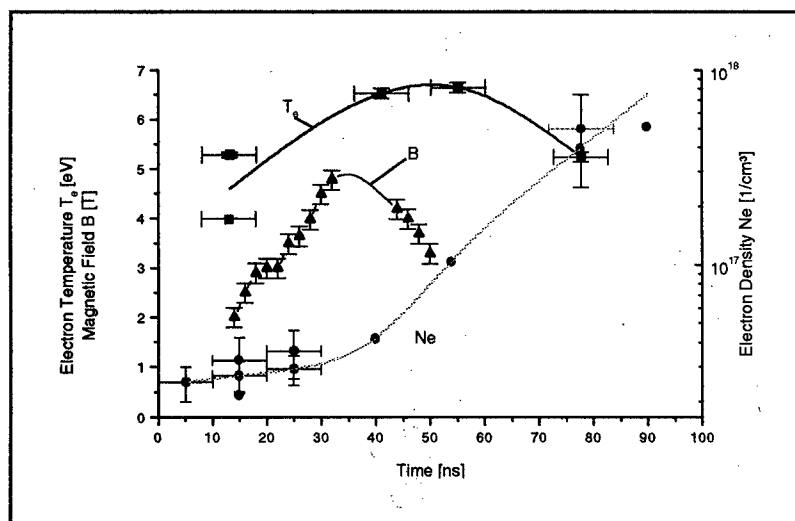


Fig. 2 Electron temperature (squares), electron density (circles), and B-field (triangles) in the anode plasma

that the carbon density in the plasma does not change during the pulse because it originates mainly from adsorbates at the Pd surface layer which covers the Ti hydrogen reservoir. These adsorbates are released at the beginning of the pulse. As shown in Fig. 2 the electron temperature starts between 4 and 5 eV, reaches a maximum at 50 ns into the pulse and then drops below 5 eV again.

The magnetic field inside the anode plasma was deduced from the Zeeman splitting of C III (4647.4 Å) and C IV (5801.3 Å) lines. Since the Doppler broadening affects the line shapes different trials for the ion temperature were used to reproduce the measured line shape. Fortunately the width of the lines is mainly determined by the magnetic field strength and not much influenced by the Doppler effect. However the depth of the valley in the centre of the split line strongly depends on the ion temperature and therefore can be used to determine it. It was found that the C IV ion temperature was around 50 eV and thus much larger than the electron temperature, a phenomenon that had also been found by other groups for passive flashover ion sources [10]. In Fig. 2 we also display the development of the magnetic field inside the anode plasma layer as a function of time. Initially the measured field is smaller than

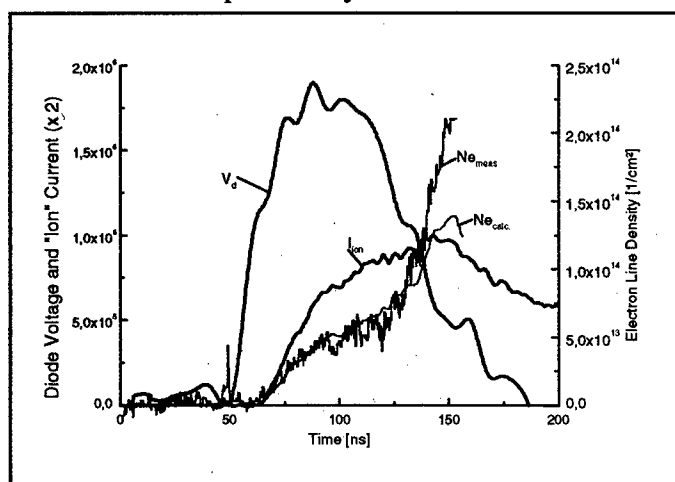


Fig. 3 Measured and calculated electron densities 3 mm from the anode, diode voltage, and ion current

current. The electron density starts to rise simultaneously with the ion current and reaches a

about 30-40 ns, during which the electron density stagnates, it starts to rise by one order of magnitude before the end of the pulse.

The electron temperature was derived by evaluating the ratio of the C IV (5801.3 Å) and the C III (5696 Å) lines with the help of the stationary collisional-radiative-code NLTE [9]. The use of a stationary code for this

evaluation is justified by the short relaxation times for the carbon levels and by the fact

the applied field of 3 T. This can be explained by the early expansion of the high density plasma with frozen-in magnetic field lines. As the plasma expansion stops the field rediffuses and because of the rising diamagnetic field in the diode gap surmounts the applied field. For the KALIF-diode the maximum observed field was around 5 T. The consequences of this diffusion of the diamagnetic field into the plasma will be discussed below.

The electron line density measured at a distance of 3 mm from the anode surface is plotted in Fig. 3 together with the diode voltage and the "ion"

plateau at $4 \cdot 10^{13} \text{ cm}^{-2}$ which lasts for 20-30 ns and then - as the diode voltage begins to drop - continues to rise to much higher values. This general behaviour is found for all distances from the anode. Within our temporal resolution of 1 ns the electron density increases simultaneously at all locations in the gap and achieves everywhere the same plateau value. At distances less than 2 mm from the anode surface the electron density exceeds the plateau value at first but after 10-20 ns decays to the same level.

Summarising the results we can say that 1.) significant ion current does not flow before an electron cloud occurs in the diode gap, 2.) the electron cloud occurs simultaneously at all positions in the gap, 3.) for a period of 40-50 ns the electron density distribution is flat, and 4.) at the time when the diode voltage decreases the electron density rises at all positions in the gap, although stronger at locations close to the anode and cathode surfaces.

Conclusions

It has been discussed previously /11/ that the diffusion of the diamagnetic field into the anode plasma can create strong heating, the magnitude of the electron temperature rise depending on the value of the plasma conductivity. It has been argued that, due to the high electron drift velocity, instabilities occur that increase the collision frequency and therefore reduce the plasma conductivity by up to a factor of 10 below the Spitzer value. Taking this value and assuming a mean plasma density of $5 \cdot 10^{16} \text{ cm}^{-3}$ in a 0.5 mm thick plasma layer we obtain that about 225 eV of energy have been deposited per particle during the rising part of the diamagnetic field. Obviously there must be a heat loss mechanism to the substrate because we observe a much smaller electron temperature rise but a strong increase of particle density in the plasma, which, at the end of the pulse, reaches a value of $5 \cdot 10^{17} \text{ cm}^{-3}$. Taking this value and accounting for the ionisation energy of 13.6 eV the observed electron temperature of 5 eV at that time becomes comparable with the available energy. The observed large flux of hydrogen from the reservoir is supposedly also responsible for the ion energy spread reported previously /7/.

Perhaps an even more important effect of the diamagnetic field penetration into the plasma is the fact that it leads to a fast acceleration of the plasma as soon as the diamagnetic field drops due to a simultaneous decrease of ion current density and diode voltage. In this case the plasma is no longer magnetically confined but instead accelerated by both the thermodynamic and the magnetic pressure which act in the same direction. This can be seen from the magneto-hydrodynamic equation of motion:

$$nM \frac{du}{dt} = -\text{grad} \frac{B^2}{2\mu_0} - \text{grad}(p_i + p_e)$$

For the densities and temperatures observed the magnetic field pressure is more important than the particle pressure. Assuming that the magnetic pressure gradient is constant in the plasma front layer we can also expect that the lower density zones will be accelerated fastest. It is presumably this mechanism that is responsible for the rapid impedance collapse generally observed with high power diodes after peak power. Since similar mechanism of acceleration can also occur in the cathode plasma the diode gap closes fastest at the cathode edge.

The described general picture is supported by the electron density measurements where a sudden rise of the electron density coinciding with the diode voltage and ion current density decay (inferred from Faraday-cup measurements not shown here) was observed. Also late in the pulse the measured electron density distribution resembles the expected profile of increasing densities towards the electrodes. A surprising result was the flat electron density distribution in the gap at least until the maximum diode voltage. This observation enables us to use the diode theory described by M. Desjarlais /12/ for the saturated case to derive further

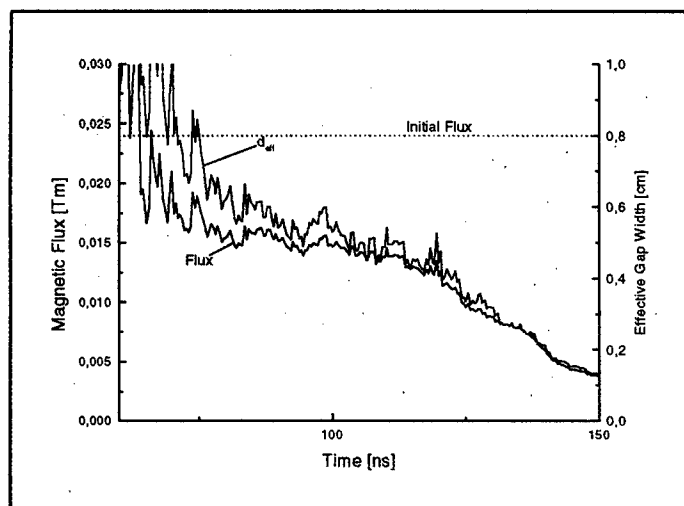


Fig. 4 Effective gap and entrapped magnetic flux as a function of time

conclusions on the diode operation. To improve our confidence we can use the functional dependence of the electron density on the ion current density derived in [12] to calculate the electron density from the electrical signals and compare it with the directly measured electron density. As shown in Fig.3 this leads to excellent agreement at least until the final increase of the density occurs. Now exploiting other predictions of the model we can determine the effective gap width and the entrapped magnetic flux using the measured electron density as a function of time. The results (Fig. 4) confirm that very rapidly about half of the initial

flux is lost leading to a much weaker magnetic insulation than expected.

Summarising we can conclude that stable diode operation requires a small diamagnetic effect on the plasma. This can either be achieved by producing highly conductive electrode plasmas or by reducing the diamagnetic field. The latter means a lower ion current density but unfortunately it also favours a small ion mass and a small accelerating voltage.

References

- [1] Y. Maron, E. Sarid, O. Zahavi, L. Perelmutter, M. Sarfaty, Phys. Rev. A, 5842, (1989)
- [2] Y. Maron, M. Sarfaty, L. Perelmutter, O. Zahavi, M.E. Foord, E. Sarid, Phys. Rev. A, 3240, (1989)
- [3] A.B. Filuk, et al., Proc. 11th Int. Conf. on High Power Particle Beams, Vol. I, 48, (1996)
- [4] J.B. Greenly, R.K. Appartaim, J.C.Olson, Proc. 11th Int. Conf. on High Power Particle Beams, Vol. I, 111, (1996)
- [5] H. Bluhm, P. Hoppé, H. Laqua, D. Rusch, Proc. IEEE, Vol. 80, No. 6, 995, (1992)
- [6] H. Laqua, H. Bluhm, L. Buth, P. Hoppé, J. Appl. Phys. 77, 5545, (1995)
- [7] H. Bluhm, et al., Proc. 11th Int. Conf. on High Power Particle Beams, Vol. II, 1127, (1996)
- [8] M. E. Cuneo, T. R. Lockner, G. C. Tisone, IEEE Trans. On Plasma Sci. 19, 800, (1991)
- [9] J. J. MacFarlane, P. Wang, NLTERT- A code for computing the radiative properties of non-LTE plasmas, FPA-93-6, Univ. of Wisconsin, (1993)
- [10] L. Perelmutter, G. Davara, Y. Maron, Phys. Rev. E, 3984, (1994)
- [11] C. L. Olson, Laser and Part. Beams, 2, 255, (1984)
- [12] M. P. Desjarlais, Phys. Fluids B 1, 1709, (1989)

The Prospect for Fusion Energy with Light Ions

T.A. Mehlhorn, R.G. Adams, J.E. Bailey, M.E. Cuneo,
M.P. Desjarlais, A.B. Filuk, D.L. Hanson, D.J. Johnson, C.L. Olson,
T.D. Pointon, S.A. Slutz, R.A. Vesey, D.R. Welch*, D.F. Wenger
Sandia National Laboratories, Albuquerque, New Mexico, 87185-1186
**Mission Research Corporation, Albuquerque, New Mexico, 87106*

Abstract

Intense ion beams may be the best option for an Inertial Fusion Energy (IFE) driver. While light ions may be the long-term pulsed power approach to IFE, the current economic climate is such that there is no urgency in developing fusion energy sources. Research on light ion beams at Sandia will be suspended at the end of this fiscal year in favor of z-pinches studying ICF target physics, high yield fusion, and stewardship issues. We document the status of light ion research and our understanding of the feasibility of scaling light ions to IFE.

BACKGROUND

The primary focus of the Pulsed Power Fusion Program at Sandia National Laboratories since 1980 has been the development of intense beams of light ions for driving high yield fusion within the U.S. Department of Energy's (DOE) Inertial Confinement Fusion (ICF) Program. The funding for this effort came from the Defense Programs portion of DOE. However, progress in light ion beam physics and technology has been disappointingly slow, especially in comparison with Sandia's recent dramatic success in radiation generation using pulsed-power-driven z-pinches. The status of light ion fusion research has recently been thoroughly documented in Ref. 1. Sandia has made the decision that research on light ion beams at Sandia will be suspended this year in favor of z-pinches studying ICF target physics, high yield fusion, and stockpile stewardship issues.

Intense ion beams may still be the best option for an Inertial Fusion Energy (IFE) driver, however, the current economic climate is such that there is no urgency in

developing fusion energy sources. The goal of Sandia's close-out activities this year is to perform critical proof-of-principle scaling experiments, study the scaling of the results to high yield requirements, and document the prospect of light ions for IFE in anticipation of a future expansion of DOE's IFE program.

LIGHT IONS FOR IFE

In a two-stage light ion accelerator module for IFE the divergence obtained in the first stage (injector), the divergence reduction through post-acceleration in the second stage, and the divergence that the transport system can tolerate are interdependent. Our most mature light ion concept calls for a high-contrast (10:1 ratio) shaped power pulse with a peak on-target power of ~700 TW and total on-target energy of ~14 MJ. The on-target power is supplied by twenty individual beams providing a "foot" pulse (5.4 TW each for 60 ns) and twelve beams comprising the main pulse (50 TW each for 20 ns) which, together with an internal pulse shaping technique, drive a nearly isentropic implosion of the fusion capsule [2]. The absorbed capsule energy in this design is 1.4 MJ and the peak radiation

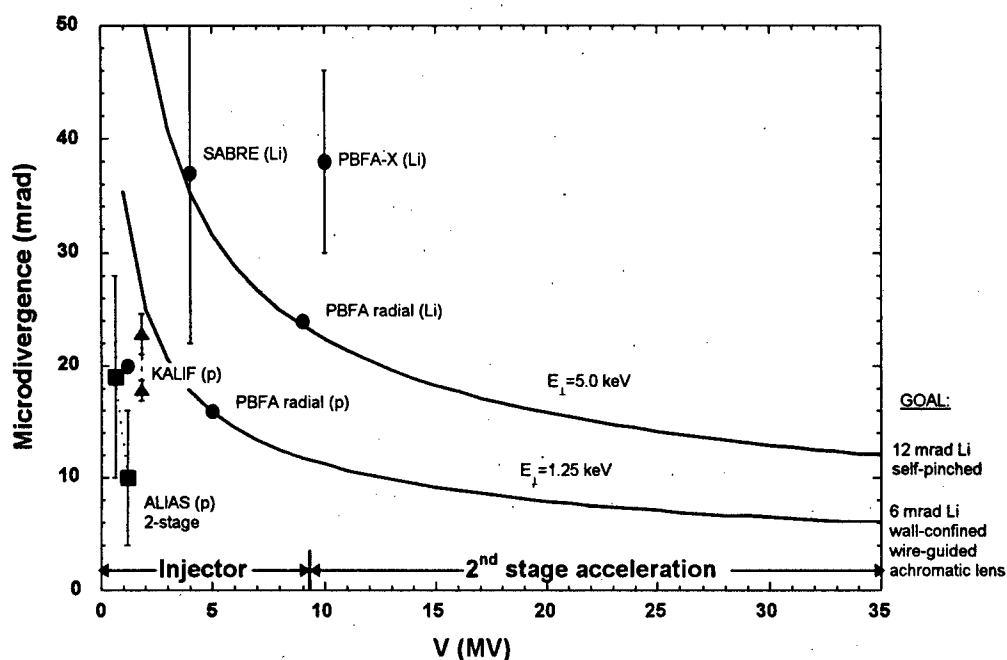


Figure 1: Ion beam microdivergence versus ion beam energy showing divergence reduction with two-stage acceleration at constant transverse energy.

drive temperature is 260 eV. The predicted target yield exceeds 500 MJ.

Each beam is generated by a two-stage, applied-B extraction ion diode. Ballistic transport to the target requires a 6 mrad beam divergence while self-pinch transport could allow the divergence constraint to be relaxed to 12 mrad for a four meter standoff distance. The interrelation of divergence between injector, second-stage, and transport system is demonstrated in Figure 1.

Our IFE concept calls for (1) an injector with a lithium beam divergence of ≤ 24 mrad at 9 MeV, (2) two-stage diode operation at constant transverse temperature so the ion divergence is reduced to ≤ 12 mrad at 35 MeV and the power is doubled through time-of-flight bunching, and (3) self-pinch transport that will accept divergences up to 12 mrad. The 12 mrad and 6 mrad divergences correspond to transverse ion energies of 5.0 keV and 1.25 keV at 35 MeV, respectively. This factor of four in transverse energy emphasizes the importance of developing self-pinch transport. Following curves of constant transverse energy on Figure 1, we require a first stage injector with a transverse energy of 1.25 to 5

keV (12-24 mrad) at 9 MeV. Post-acceleration of the beam at constant normalized emittance from 9 to 35 MeV then achieves the required beam divergence. The operating parameters for the present baseline 2-stage IFE diode using lithium ions are summarized in Table 1. These parameters define the goals for intense light ion beam development.

Ion species	Li ⁺
Peak voltage	35 MeV (9+26 MeV)
Peak ion current	1 MA
Ion power (@ diode)	25 TW
Bunching factor	2
Ion power (@ target)	50 TW
Energy	1 MJ/beam
Ion beam divergence	6 mrad (lens transport)
	6-12 mrad (self-pinch transport)
Standoff distance	4 meters

TABLE 1. IFE lithium two-stage ion diode parameters

CURRENT KEY ISSUES

The four key issues that are currently most important in determining the viability of light ions for IFE are: 1) developing a bright ion source, 2) operating a non-protonic diode in the diocotron mode, 3) generating a beam with a sufficiently stable impedance to allow time of flight bunching, and 4) testing the self-pinched transport concept.

An IFE diode will require an ion source that is capable of producing 1-2 kA/cm² of the desired ion species with an intrinsic source divergence of ≤ 10 mrad over areas of 500-1000 cm². Recent work at Sandia has suggested that a lithium-dominated plasma with $n \geq 10^{17}$ cm⁻², and an expansion velocity of ~ 1 -2 cm/ μ s can be produced with a YAG laser fluence of 0.5 J/cm² incident on a LiAg thin film [3]. However, contaminant species have been observed, and they will need to be controlled through electrode cleaning techniques or by in-situ lithium deposition. The issue of surface contamination is very serious for ion sources. Assuming a 1 kA/cm² current density for 50 ns, the ion beam draws a charge density of $\sim 3 \times 10^{14}$ ions/cm² from the anode surface. Since each monolayer of surface contaminants has a density of $\sim 3 \times 10^{15}$ cm⁻², contaminants can overwhelm the desired ion species. The subject of surface contaminants and electrode conditioning techniques is discussed in detail in Ref. 4.

Ion beam divergence is the ratio of the ion momentum transverse and parallel to the beam direction. Beam divergence can come from the ion source, nonuniformities, and transport-related processes. Electromagnetic instabilities in the virtual cathode of an applied-B ion diode can also cause ion beam divergence. QUICKSILVER simulations show that the high frequency diocotron mode causes acceptable divergence, while the low frequency ion mode causes unacceptably large divergence. The ion mode also enhances electron loss to the anode [5]. Strong magnetic insulation, uniform ion emission, and limited current enhancement

are predicted to minimize ion beam divergence by sustaining diode operation in the diocotron mode. Non-linear saturation calculations for the diocotron instability [6] give the scaling:

$$\theta_d = k B_0 (d + x_o) \sqrt{\frac{q}{MV}} \quad (1)$$

where B_0 is the amplitude of the applied magnetic field, d is the mechanical anode-cathode gap, x_o is the recession distance of the gas-cell behind the cathode tip, q/M is the ion charge-to-mass ratio, and V is the diode voltage. Since Eq. 1 is inversely proportional to the square root of the ion mass, the diocotron divergences for lithium are 38% less than the proton values. While experiments at Sandia and FZK have shown diocotron-level divergence with protons, it is essential that operation of an applied-B diode in the diocotron mode be demonstrated for non-protonic ions.

IFE-equivalent divergences for lithium beams on the SABRE accelerator are ~ 17 and 37 mrad at 4 MeV (1.25 keV and 5.0 keV transverse energies, respectively, see Fig. 1). Diocotron divergences of ≤ 10 mrad are predicted for SABRE. Adding this in quadrature with a 10 mrad source divergence gives a total divergence of ≤ 15 mrad. The goal of Sandia's ongoing SABRE experiments is to reduce beam divergence to 15 ± 5 mrad divergence at 4 MeV.

Light ion IFE is predicated on doubling the ion power on target by time-of-flight bunching from the diode to the target. This requires a rising diode impedance. Further, the bunched pulse length is set by the hydrodynamic acceptance time of the ICF target. This sets the initial ion beam pulse length and places further constraints on the diode impedance. Recent experiments at Cornell [7] and simulations [8] and experiments [9] at Sandia have shown that an axial current load can significantly improve the impedance stability of an applied-B ion diode by limiting beam current enhancement. Finally, self-pinched transport experiments

are being performed on the GAMBLE-II accelerator at the Naval Research Laboratories. Successful demonstration of the principles of self-pinch transport would provide an attractive IFE option that relaxes the divergence requirement of the injected beam from 6 to 12 mrad.

SABRE RESULTS

We are integrating a laser-produced ion source, high magnetic insulation, and removal of surface contaminants on the close-out beam generation experiments on the SABRE accelerator. The goal of these experiments is to demonstrate an active lithium ion source and study lithium beam divergence and impedance scaling. Progress to date, includes [9]:

- Reduction of proton contamination at laser fluence $\leq 0.4 \text{ J/cm}^2$ by a factor of 10-20 (to $\leq 100 \text{ A/cm}^2$) with discharge cleaning and strong insulation
- Earlier turn-on of the ion beam by 20 ns
- Stable beam impedance where the beam enhancement is ≤ 3.5 for 46 ns and $J/J_{CL} \leq 1$ for 26 ns.
- Stable radial uniformity in agreement with Atheta magnetic field design tools
- Improved azimuthal uniformity
- A well-behaved, non-protonic, space-charge-limited beam that may allow study of EM-induced divergence scaling.

PRESENT DAY LIMITATIONS

The most serious technical limitation for light ion IFE is the lack of an adequate ion source. For example, the recent SABRE experiments show that the laser ion source is producing a beam dominated by contaminant ions heavier than lithium. A magnetic spectrometer and Thomson parabola indicate the dominant contaminant is oxygen. Apparently this is due to oxide layers on the lithium surface. Whereas it is possible to diagnose the divergence of a 4-5 MeV lithium beam, the extremely short range of 4-

5 MeV oxygen ions makes measurement difficult. We are investigating the possibility of avoiding the oxide contamination problem by using an in-situ lithium coating system [9]. In-situ deposition on cryogenic anodes has produced high purity proton, nitrogen, methane and neon beams [10]. We expect that depositing a fresh lithium coating on an anode in a diode with a low base pressure ($< 10^{-7}$ torr) and then firing the accelerator within 30 seconds should avoid the oxide contamination problem.

Another serious limitation is that our particle-in-cell simulation codes can not handle the anode and cathode plasmas that form in ion diodes and strongly influence the beam generation physics. A hybrid modeling capability that can study the interaction between electrode plasmas, the electron sheath, and the ion beam is essential to understanding applied-B ion diodes.

ACKNOWLEDGMENTS

Sandia is a multiprogram laboratory operated by Sandia Corporation, a Lockheed Martin Company, for the United States Department of Energy under Contract DE-AC04-94AL85000. This paper is dedicated to the memory of Alex Filuk.

REFERENCES

- [1] T.A. Mehlhorn, IEEE Trans Plasma Sci 25 (1997) pp. 1336-1356.
- [2] R.E. Olson, et al., Proc. 15th IEEE Symp. Fusion Eng., (1993) pp. 189-193.
- [3] A.B. Filuk, (1997) IEEE ICOPS, p. 121.
- [4] M.E. Cuneo, et al., IEEE Trans. Plasma Sci., 25 (1997) pp. 229-251
- [5] R.A. Vesey, et al., (1997) IEEE ICOPS, p. 193
- [6] T.D. Pointon, et al., Phys. Plasmas 1 (1994) pp. 429-443.
- [7] J.B. Greenly, et al, Bull Am. Phys. Soc. 42 (1997) pp. 1846.
- [8] R.A. Vesey, et al, Bull Am. Phys. Soc. 42 (1997) pp. 1846.
- [9] M.E. Cuneo, et al., private communication.
- [10] D.L. Hanson, et al., J. Appl. Phys. 70 (1991) pp. 2926-2937.

HIGH-CURRENT PULSE SOURCES OF BROAD GASEOUS AND METALLIC ION BEAMS FOR SURFACE TREATMENT APPLICATIONS

N.V. Gavrilov, S.P. Nikulin, E.M. Oks* ** and P.M. Schanin*

Institute of Electrophysics, RAS, 34 Komsomolskaya St., Yekaterinburg 620049, Russia

**Institute of High Current Electronics, RAS, 4 Akademicheskoy Ave., Tomsk 634055, Russia*

***State University of Control Systems and Radioelectronics, 40 Lenin Ave., Tomsk 634055, Russia.*

ABSTRACT

The paper reviews the experimental study and development of technological ion sources performed under a joint IEP-IHCE program for recent years. The sources are based on pulsed high-current glow and arc discharges and are designed for surface treatment applications. The use of cold cathodes makes the sources more reliable when operated under elevated residual gas pressure and at the presence of reactive gases, while the use of a repetitive pulse mode of plasma production provides optimum conditions for stable operation of the discharge, for controlling the average beam current over a wide range, and for formation of homogeneous broad ion beams. The electrode systems used in the ion sources provide for operation of high-current discharges at low pressures, production of stable, dense, and homogeneous plasmas, and decrease the impurities content in the beam. Some design versions of the sources developed are presented that are capable of producing $\sim 1\text{--}10\text{ mA/cm}^2$ of current density in beams with a cross section of some hundreds of square centimeters at accelerating voltages of 10–100 kV, pulse durations of $10\text{--}10^3\text{ }\mu\text{s}$, and pulse repetition rates of 1–500 Hz. Some applications of the sources for surface modification of materials are described.

INTRODUCTION

Industrial ion-beam technologies for modification of materials call for highly efficient, simple, and reliable in operation ion sources. These sources should be capable of producing high-current broad beams (BBs) with an ion energy of a few tens of keV and stable operating in a poor vacuum. A trend of development of technological ion sources which would come up to these requirements involves the use of high-current glow or arc cold-cathode discharges, which are less sensitive to the process media as compared to thermoionic-cathode systems. Due to fundamental differences between thermoionic-cathode and cold-cathode discharges, the development of gaseous ion sources based on cold-cathode discharges calls for new concepts and approaches to solve the problems related to the initiation and stability of the discharges at low pressures, to the production of stable, dense, and homogeneous plasmas, to the formation of a uniform plasma emitter of ions and of homogeneous BBs, and to the decrease of contamination of ion beams. The use of a repetitive pulse mode (RPM) for discharge running is the way to solve some of these problems. A proper choice of discharge current and pulse duration provides stable operation both of a low-current arc with a cathode spot, and of a high-current glow discharge. At the same time, one can control the average current of the beam over a wide range by varying pulse repetition rate. In doing this, the conditions for the formation of a beam in a multiaperture ion optical system (IOS) are retained, and, hence, the beam remains homogeneous at the target. The studies performed have resulted in the development of broad beam sources of gaseous or metallic ions or of their mixtures.

DESIGN AND CHARACTERISTICS OF ION SOURCES

1. The gas-ion source based on an inverted magnetron electrode system

High-current mode of a glow discharge under the low gas pressure and/or low operating voltage and producing of a homogeneous plasma in electrode system of the inverted magnetron type are provided as a result of: (i) more complete using of the ions not involved in the beam for sustaining electron emission from the cathode; (ii) efficient ionizing of the gas by fast electrons arisen as a result of ion bombardment and accelerated in the cathode fall region; (iii) oscillating of fast electrons in the cathode cavity under action of electrostatic and magnetic fields, and (iv) stable transportation of the generated electrons toward the anode without formation of a high-voltage near-anode layer or build-up of plasma instabilities.

The general appearance of the ion source is presented in Fig. 1. At one end of grounded case 1, ceramic high-voltage insulator 2 is placed on which a discharge electrode system is mounted. The electrode system consists of cathode 3 of diameter 150 mm made of stainless steel and tungsten rod anode 4. At the other end of the case, three-electrode multiaperture IOS 5 is placed. Magnetic coil 6 establishes a magnetic induction $\sim 1\text{--}2$ mT at the axis. The cavity of insulator 2 is filled with transformer oil cooled by water circulated through radiator 7. Inside this cavity, the cable lead-in 8 and the gas feed entrance 9 are mounted. The case, heated radiatively by the cathode, is equipped with water cooling jacket 10.

The flow rate of the gas fed into the cathode cavity is $\sim 1000\text{ cm}^3\text{ atm/h}$, gas pressure in vacuum chamber being $(0.2\text{--}2) \times 10^{-4}$ Torr. An RPM with a pulse duration of $50\text{--}1000\text{ }\mu\text{s}$ and repetition rate of $1\text{--}500\text{ Hz}$ is used. The pulsed current of the discharge is $1\text{--}10\text{ A}$. The discharge voltage, depending on the discharge current and on the gas pressure and sort, ranges from 0.5 to 1 keV . The radial distribution of the plasma density is uniform to within 10% . The ion beam is formed by a three-electrode IOS having holes of diameter 8 mm . The source generates gaseous ion beams of cross-sectional area 100 cm^2 , ion energy up to 50 keV , pulsed current up to 1 A , and average current up to 50 mA .

Use of a weak magnetic field makes it possible not only to decrease the discharge igniting and operating voltages but also to decrease a non-uniformity of radial plasma profile [1]. The characteristic feature of RPM of a glow discharge with a large surface area of a hollow cathode is the dependence of the cathode surface condition on the average discharge current. As a result, characteristics of a pulsed breakdown of the discharge gap and discharge operating voltage depend on RPM parameters [2].

Mass spectrometry of the composition of the plasma has detected two types of impurity: ions of the cathode material and ions of the previously used gas. The degree of pollution of the plasma depends on the heat exchange at the cathode and on the chemical activity of the gas.

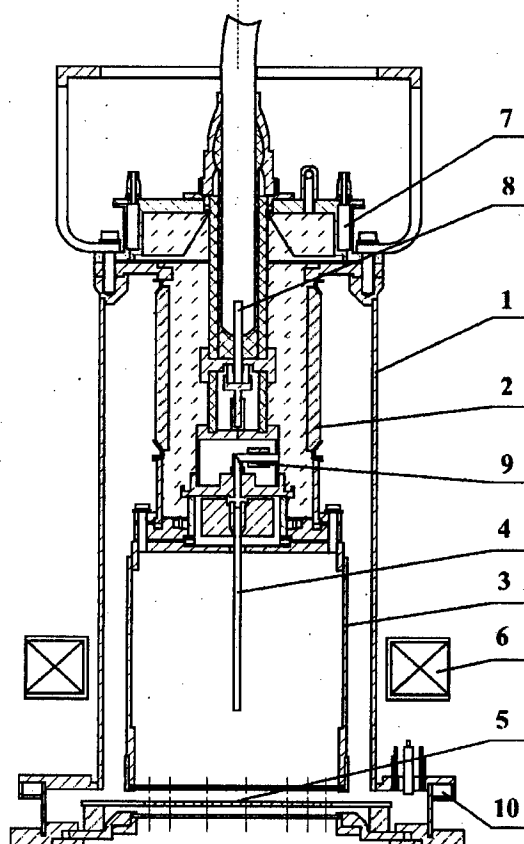


Fig. 1. Cross-Section of an Inverted Magnetron Structure based Ion Source

When the cathode is heated to a high temperature, chemical compounds are formed as a result of the diffusion of the gas atoms and their chemical interaction with the cathode material. Therefore, on changing the gas, ions of the previously used gas may appear as a result of cathode sputtering followed by ionization of the sputtered atoms. The degree of plasma pollution and the duration of the transient process depend on the gas sort. When argon is replaced for another gas, argon ions are not detected in the plasma. The oxygen ion content falls to $\sim 0.5\%$ in a few minutes, while the nitrogen impurity content in the plasma decreases from $\sim 20\%$ to $\sim 1\%$ in ~ 20 min. [1]. Efficient cooling of the cathode practically precludes the appearance of gaseous impurities, but leads to an increase in the content of metallic ions in the plasma. This content, depending on the discharge current and the gas sort, may vary within several percents. As the discharge current is increased to over 2 A, the content ratio of the atomic and molecular nitrogen ion in the plasma approaches unity.

2. A gaseous ion source based on a hollow-cathode non-self-sustained glow discharge

Fig. 2 shows the cross-section of the ion source based on the plasma-emission structure, where the self-sustained discharge operates as a plasma cathode to keep a non-self-sustained high-current discharge going at a low voltage between the electrodes, while the electrode structure of the non-self-sustained main discharge provides efficient and uniform ionization of the gas in the cavity at low pressures, i.e., produces a plasma emitter of ions.

Ion emitting plasma is produced inside the cylindrical aluminum cathode 1 of the main discharge. The anode of the main discharge consists of four tungsten rods 2 of diameter 2 mm and length 50 mm, arranged symmetrically inside the cavity. The non-self-sustained glow discharge is sustained with the auxiliary glow discharge between the keeping cathode 3 and main cathode 1. A bias voltage, positive with respect to the auxiliary hollow cathode ($d = 60$ mm, $l = 80$ mm), is applied across these electrodes. To ignite the auxiliary discharge, a surface discharge over a dielectric 4 is used. The auxiliary glow discharge provides injection of electrons into the region where the main discharge plasma is generated through the emission hole covered with a high-transparency fine metal grid. The injected electron current makes up about 0.8 of the auxiliary discharge current. These electrons are accelerated in the cathode fall region of the main discharge and, oscillating inside the cathode cavity, efficiently ionize the gas. Used as working gases were argon, nitrogen, oxygen, and methane.

Since the coefficient of the ion-electron emission from the cathode is much below unity, the ionization of the gas intensifies abruptly even if the injected electron current is insignificant compared to the discharge current. This keeps a high-current, low-voltage discharge operating at reduced gas pressures [3]. Thus, for instance, with externally injected electrons whose current made up not over 30% of the main discharge current, the lowest gas

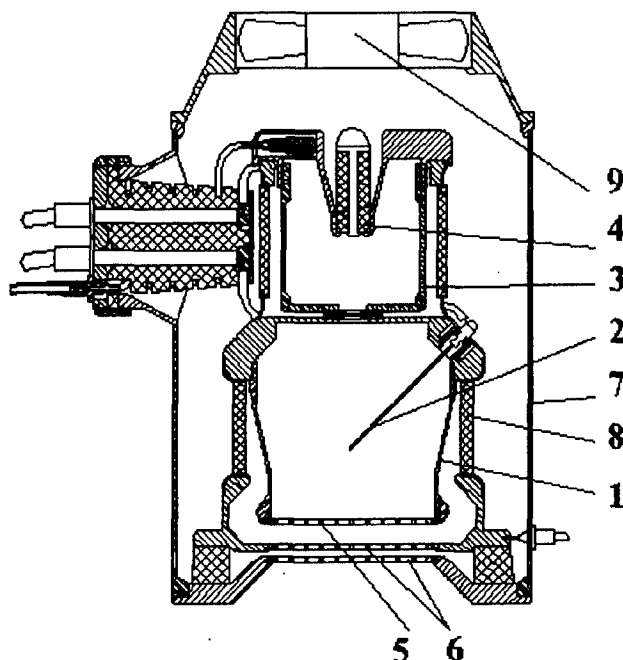


Fig. 2. Cross-Section of an Ion Source based on a Non-Self-Sustained Glow Discharge.

pressure at which a hollow-cathode high-current discharge was still operative decreased from 50 to 5 mPa and the voltage fell to 100–50 V. Furthermore, a higher diffuse discharge current (up to 50 A, 0.3 ms) was achieved without a glow-to-arc transition.

Acceleration of ions to a required energy was accomplished with the use of a three-electrode IOS (grids 5 and 6) with apertures of diameter 5 mm. The source is force-cooled with air using fun 9. In the pulsed mode with a pulse duration of 0.3 ms and an accelerating voltage of 30 kV, the source is capable of producing an ion beam of cross-sectional area 100 cm^2 with the current up to 1 A. A strict correlation between the discharge operating voltage and the mass-charge composition of the beam is observed. Reducing discharge operating voltage depresses the cathode sputtering and the contamination of the main discharge plasma. At voltages below 100 V, the beam is in fact free from the metallic ions.

3. TITAN-2, a source of metallic and gaseous ions

Our recent efforts directed toward refining vacuum-arc ion sources have been related to the use in the discharge system of a strong magnetic field localized in the discharge cathode region and affecting not only the electronic component but also on the ionic component of the plasma [4-7]. This field provides repeated ionization and, correspondingly, an abrupt increase in the average charge of the metallic ions in the plasma. This makes possible to increase the ion energy in the beam not increasing the accelerating voltage. Strong magnetic field provides the possibility to ignite a vacuum arc using a low-pressure auxiliary glow discharge. The use of plasma-emission structures based on a low-pressure arc with a cathode spot make it possible to produce two-component beams of gaseous and metallic ions with a prescribed component ratio. With that, the content range is 10–100% for the gaseous component and 0–90% for the metallic one.

An ion source based on a vacuum arc initiated by an auxiliary Penning discharge in a strong magnetic field is shown schematically in Fig. 3. To initiate a vacuum arc between the cathode 1 and anode 2 an auxiliary high-current glow discharge between the electrodes 1 and 2, having cathodic potential during an igniting process, and anode 3 is used. The vacuum arc, whose current reaches 100 A, is sustained by a pulse-forming line producing voltage pulses of duration 400 μs . While the arc operates, the plasma of the material of cathode 1 fills hollow anode 2. When an accelerating voltage of 10–50 kV is applied to the ion source, ions are extracted from the plasma surface covered with emission grid 5 with meshes 2x2 mm in size and an area of 270 cm^2 . The ion extraction system includes two grid electrodes 6. First accelerating grid is grounded, while a negative voltage of several kilovolts is applied to second grid to cut off secondary electrons. Grids 6 were made of stainless-steel wires stretched in parallel, thereby providing high transparency (90%) of the IOS and minimizing the ion losses. To create a magnetic field in the discharge cathode region, four permanent magnets 4 arranged on the perimeter of the discharge chamber are used with cathode holder and anode 2, both made of a magnetically soft material, serving as poles for magnetic core. In this system, the magnetic field induction at the cathode surface reaches 0.7 T.

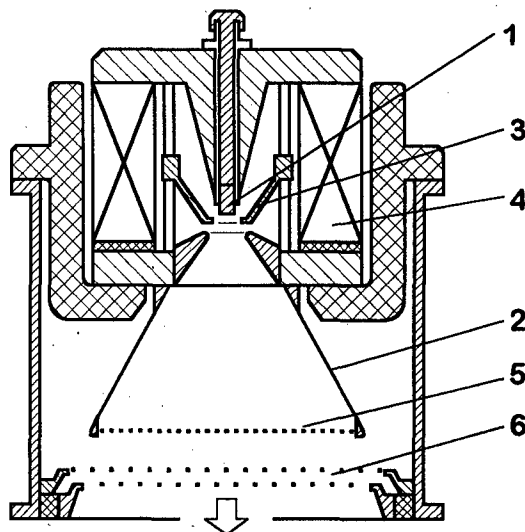


Fig. 3. Titan-2 Ion Source

The source produces a beam of Ti and Al ions of current 0.7–0.9 A. The saturation of the source current-voltage characteristic begins at a voltage over 20 kV, which can be considered as the lower limit for the operating voltage range of the source. A specific feature of the emission characteristic is that the ion current is not directly proportional to the arc current. This indicates that the ion extraction becomes more efficient when going to higher voltages of the arc discharge. The current density distribution over the beam cross section in the IOS under consideration is strongly affected not only by the radial profile of the plasma, but also by the position of the plasma boundary. At higher arc currents or at lower accelerating voltages, the distributions having a minimum in the center are observed. Increasing accelerating voltage or decreasing arc current has the result that the current density distribution is transformed to a nearly Gaussian distribution.

SOME APPLICATIONS

When high-power beams are used, the specimens have an elevated temperature in the process for high-dose ion implantation. Therefore, in many cases the result of ion treatment depends on the temperature-dose mode, i.e., on the combination of the values of dose, D , and specimen temperature, T . The D - T mode determines the value of the retained dose and the depth of the modified layer. It is well known that for high-dose implantation, the remained dose is limited due to surface sputtering. However, the elevated temperature may increase the rate of the diffusion of impurities and form extended layers with an elevated concentration of interstitial atoms. On the other hand, using too high temperatures may enhance the diffusion of impurities abruptly and result in a decrease in the impurity concentration. With that, the changes in the properties of the material may appear to be insignificant.

Experiments [9] on implantation of nitrogen ions with a dose of $1 \times 10^{18} \text{ cm}^{-2}$ into stainless steel X18N10T have shown that the $T \sim 400^\circ \text{C}$ kept in the process of implantation is best for enhancement of the steel wear resistance. Irradiation under these conditions resulted in a fourfold increase in microhardness (up to 16 GPa) at a depth of $\sim 50 \text{ nm}$ and in a 100-fold decrease in wear rate measured in pin-on-disk tests. As the T was increased to $700\text{--}800^\circ \text{C}$, the microhardness increased to 9 GPa in thicker ($>1 \mu\text{m}$) layers; however, the decrease in wear rate in this case was not over 40%.

The ability of ion treatment to affect significantly the surface hardness and relief was harnessed to enhance the durability of coatings deposited on surfaces previously treated with an ion beam. Treatment of hard alloy, stainless and tool steels with nitrogen and carbon ion beams has made it possible to increase the resistance of diamond-like coatings to abrasive wear 3–5 times. Ion beam assistance during vacuum arc deposition of multilayer Ti–TiN coatings of thickness up to $20 \mu\text{m}$ has allowed an decrease in their abrasive wear by 30%.

An attractive application of mixed (gaseous and metallic) ion beams generated by a vacuum-arc-based ion source is the production in the surface layer of the material of chemical compounds showing high hardness (nitrides, oxides, and the like) [10] and capable of

Table 1

Specimen No.	Ionic composition	Wear (rel. un.)		Increase
		Implanted region	Original surface	
1	Ti(100%)	15.94	24.82	1.6
2	Ti(60%) + N(40%)	1.05	44.04	42.0
3	Al(50%) + O(50%)	2.92	27.96	9.6
4	C(50%) + N(50%)	31.71	60.91	1.9
5	Cr(50%) + O(50%)	2.83	27.37	9.7

improving substantially the performance of the articles. This technique for production of a hardened surface layer has the advantage that there is no problem with adhesion, and fine-grained phases can be formed. Table 1 presents the results of wear testing of stainless-steel specimens treated with a gaseous-metallic ion beam. The best result (with the wear resistance increased more than 40 times) was observed with a beam containing nitrogen and titanium.

SUMMARY

Several types of plasma-emission structures based on cold-cathode pulsed glow and arc discharges are proposed and investigated. These structures are intended for production of beams of gaseous and metallic ions and of their mixtures. Ion sources capable of producing high pulsed and average current densities in a large-cross-section beam. The high beam current together with the simplicity of design and operation and the high reliability of these sources make them promising for use in industry, in particular, in technologies for surface modification of materials by ion implantation and ion-assisted deposition of coatings.

ACKNOWLEDGMENTS

The authors extend their sincere appreciation to Jan Broun from the Lawrence National Laboratory, Berkeley, USA, for opportunity he offered to perform ion charge distribution measurements, to Peter Evance from the ANSTRO, Sydney, Australia, for the performance of wear testing of specimens irradiated with gaseous-metallic ions, and to G. Yushkov, A. Vizir, A. Nikolaev and D. Emlin for fruitful discussions and participation in experiments.

REFERENCES

- [1]. N.V. Gavrilov, G.A. Mesyats, S.P. Nikulin, G.V. Radkovskii, A. Elkind, A.J. Perry, and J.R. Treglio. *J. Vac. Sci. Technol. A*, **14**, 1050-1055 (1996).
- [2]. N.V. Gavrilov, G.A. Mesyats, G.V. Radkovskii, and V.V. Bersenev. *Surface and Coating Technology*, **96**, No. 1, 81-88 (1997).
- [3]. E.M. Oks, A.V. Visir, and G.Yu. Yushkov. *Rev. Sci. Instrum.*, **69**, No. 2, (1998).
- [4]. E.M. Oks, A. Anders, I.G. Brown, M.R. Dickinson, and R.A. MacGill. *IEEE Trans. Plasma Sci.*, **24**, No. 3, 1174-1183 (1996).
- [5]. S.P. Bugaev, A.G. Nikolaev, E.M. Oks, P.M. Schanin, and G.Yu. Yushkov. *Rev. Sci. Instrum.*, **65**, No. 10, 3119-3125 (1994).
- [6]. A.G. Nikolaev, E.M. Oks, G.Yu. Yushkov, R.A. MacGill, M.R. Dickinson, and I.G. Brown. *Ibid.*, **67**, No. 9, 3095-3098 (1996).
- [7]. E.M. Oks, A. Anders, I.G. Brown, M.R. Dickinson, and R.A. MacGill. *Nucl. Instrum. Meth. in Phys. Research B*, **127**, 779-781 (1997).
- [8]. A.G. Nikolaev, E.M. Oks, P.M. Schanin, and G.Yu. Yushkov. *Rev. Sci. Instrum.*, Vol. 67, No. 3, 1996, pp. 1213-1215.
- [9]. D. Rej, N.V. Gavrilov, D. Emlin, I. Henins, K.Kern, T. Kurennykh, V.N. Mizgulin, C.P. Minson, M. Nastasii, J.T. Schener, V. Vykhodets, and K.C. Walter. *Mat. Res. Soc. Symp. Proc.*, **396** (1996).
- [10]. E.M. Oks, G.Yu. Yushkov, P.J. Evans et. al., *Nucl. Instrum. Meth. in Phys. Research B*, **127/128**, 782-786 (1997).

THE KALIF-HELIA ACCELERATOR: DESCRIPTION, PROGRAM AND STATUS

P. Hoppé^a, W. Bauer^a, H. Bluhm^a, V. Carboni^b, J. Fockler^b, G. Keßler^a, K. Leber^a, K. Nielsen^c, K. Prestwich^b, W. Ratajczak^a, D. Rusch^a, J. Singer^a, I. Smith^b, P. Spence^b

^a *Forschungszentrum Karlsruhe, INR, P.O. Box 3640, D-76021 Karlsruhe, Germany*

^b *Pulse Sciences Inc., 600 McCormick St., San Leandro, CA 94577, USA*

^c *Physics International, 2700 Merced Street, San Leandro, CA 94577, USA*

Abstract

The 6MV, 400kA accelerator KALIF-HELIA is presently under construction at the Forschungszentrum Karlsruhe. It is based on a design that couples a self-magnetically insulated transmission line with the linac induction principle. The accelerator can be used in either polarity for the generation of an ion- or an electron beam respectively. In positive polarity improvement of the quality of intense light ion beams will be the most important research area. Beam divergence scaling laws with voltage and mass will be investigated experimentally. In negative polarity the extracted electron beam will be used for potential future applications where a high dose, high dose rate and a large exposure area might be advantageous.

Introduction

Since the first induction linac built in 1964 [1], these accelerators were used mainly for the production of high quality electron beams with currents up to 10kA, energies up to 50MeV and kHz repetition rates. With their electric fields below the self emission threshold ($\sim 20\text{MV/m}$) the achievable power density in linacs is limited to 0.5TW/m^2 . Much higher power densities were achieved when the electron beam accelerated on axis of the linac cavities was replaced by a solid inner conductor that formed a coaxial transmission line with the inner bore of the cavities. This coaxial line was operated as magnetically insulated transmission line (MITL) with electric fields well above the emission threshold. Related to its high power density the size and costs of accelerators based on this magnetically insulated voltage adder (MIVA) principle could be reduced and they therefore were considered as drivers for ICF related applications. However, the MIVA inherent problems and their influence on the beam properties remain to be solved. These are mainly: a) a fraction of the beam energy is carried as electron vacuum current, b) the beam must be generated and focused in one or two stages (the 'diode') and c) the ion- or electron source must deliver much higher currents compared to a linac source.

Description of KALIF-HELIA

KALIF-HELIA is the first accelerator in Europe based on this MIVA design that was already used for the construction of the accelerators HELIA, HERMES III and SABRE at Sandia National Labs. (SNL) and for the COBRA machine at Cornell. The KALIF-HELIA Marx generator¹ (see MG in Fig.1) consists of a total of 36 capacitors with $2.2\mu\text{F}$ each, chargeable to a maximum voltage of 100kV. Thus the maximum energy stored is 400kJ. This energy is transferred to 4 Intermediate store capacitors (ISC). The capacitance of each of these coaxial

¹This Marx generator was originally developed by SNL and built by the Ktech Corp. in Albuquerque, NM.

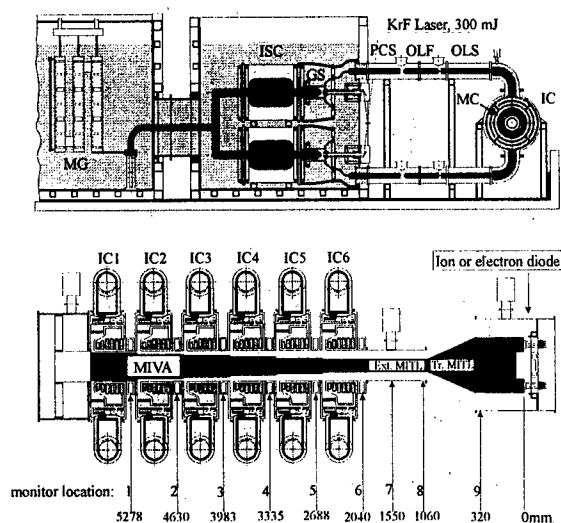


Fig.1: Scheme of KALIF-HELIA

insulator stack and the radial feed section. The 6 insulating magnetic cores (MC) are tape wrap-ups of plastic for insulation between the amorphous metal layers. They experience a voltage which peaks at 1.3MV and integrates to 63mVs over the pulse. The core cross sections are chosen such that this delivers a flux swing of 3T to the magnetic material². The MIVA impedance is strongly influenced by the electron vacuum flow. It is due to the high electric fields launching electrons into the vacuum gaps formed by the 'radial feed' sections and the 6 coaxial sections formed by the bore diameter of the cavities and the 6 different outer diameters of the inner stalk. The MIVA should deliver a fast rising 6MV pulse to the load

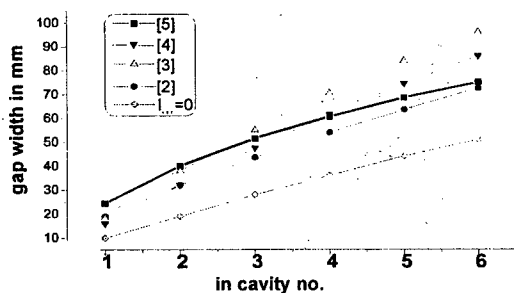


Fig.2: MIVA gap width calculations

with a minimum electron vacuum flow. The results from different approaches used for the determination of the MIVA gap sequence g_1 to g_6 (Fig. 2) are in rather good agreement but differed considerably from a non-emission design ($I_{vac}=0$). Finally, the gap width of the 6 coaxial sections was chosen according to the results from calculations of the vacuum impedance for each section (8.25, 14.1, 18.9, 23.0, 26.7, and 30.0 Ω), that allows the highest value of the flow impedance for each section without adding any unnecessary inductance slowing

down the rise time of the pulse[5].

The diode voltage and the total energy delivered to the assumed 15 Ω load depend on the switch-out time of the PFL's. The maximum diode voltage V_d of 6MV will be achieved if the PFL's are allowed to charge up to 2.12MV, the energy E_d will be 116kJ (Fig.3). If the PFLs are switched-out at about 2MV, the maximum energy of 120kJ is supplied at a somewhat lower diode voltage of 5.9MV. If considered useful, the energy delivered to the diode can be further increased by about 25% if the ISC are modified from 36nF (as built) to 50nF (Fig.3). The electron vacuum current -to be considered as a loss for an ion diode- is not taken into account in these transmission line calculations. According to 1D-laminar flow models and 2D PIC calculations, the vacuum current may reach up to 30% of the total current of 440kA, assuming 5.4MV at the load [6]. The last cavity connects either to a 30 Ω extension MITL with a length of 1.1m or to a 30 Ω transition MITL which supports the anode or cathode of the

² The tape wrap-ups were produced by the Vakuumschmelze Hanau, Germany, using Vitrovac tape material.

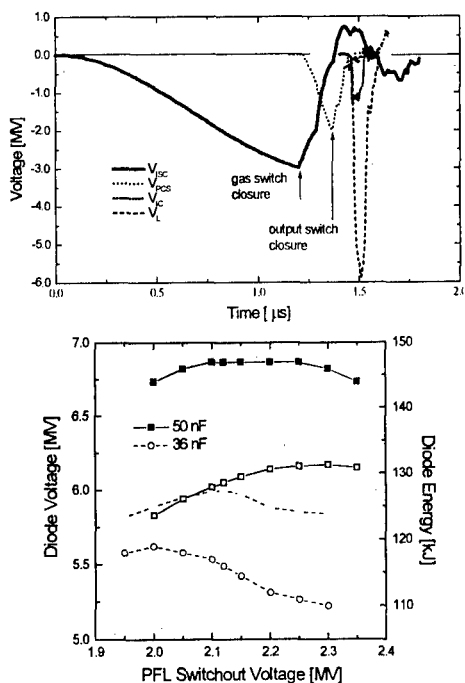


Fig.3: Predicted voltages and energies

diode. With possible outer diameters up to 50cm large area diodes with correspondingly low current densities ($<1\text{kA/cm}^2$) can be used. Compared to other MIVA type accelerators KALIF-HELIA offers the following improvements: a) the radial feeds of the induction cavities were covered with an anti-emission coating raising the emission threshold to 40MV/m, i.e. a reduced electron vacuum current, b) the magnetic material used for the fabrication of the induction cores is 'Vitrovac' which was extensively tested and qualified, c) flexible joints on both sides of the PFL's allow variations in the axial extension of the adder which might be caused by spools for diagnostics or retrapping rings for the vacuum electron current and d) compared to its pulse length of 60 ns the adder is electrically short, i.e. undermatching of the diode to the adder should reduce the vacuum electron current. A more detailed description is given in [7].

Program for KALIF-HELIA

The maximum power density achievable in the focus of an extractor type ion diode is proportional to the beam brightness B which is proportional to $1/\Theta^2$ with the divergence Θ as half angle of the emission cone of a beamlet. Reliable scaling laws for the beam divergence are needed. The presently known sources of beam divergence can be subdivided in those which favorably scale with the acceleration voltage V and/or ion mass M and those which are independent of V and/or M [8]. In particular, all effects resulting from anode plasma inhomogeneities are independent of V . If they dominate the contributions to beam divergence no improvement is to be expected from raising V and/or M . Therefore it is crucial to first supply a sufficiently homogeneous and smooth ion source from which a space charge limited ion beam can be extracted. Presently no high-power experiments are available that have been conducted both at low and high accelerating voltages with comparable high quality ion sources. The radial ion diode on PBFAII has produced a 9MeV Li^+ beam with 24mrad and a 5MeV proton beam with a divergence of 16mrad [9]. Similarly low divergence has been obtained for a proton beam at the 1.4MV accelerator PBFAI. This seems to indicate that in these cases the divergence was determined by the properties of the anode plasma. Therefore, in a first step it is foreseen to use the successful sliding discharge proton sources used in KALIF B_{appl} diodes, adapted to the needs of KALIF-HELIA and to operate this proton diode up to 6 MV. This would allow to test the voltage dependence in the divergence equations. In a second step, assuming a high quality lithium ion source becomes available, the mass dependence in the scaling laws will be checked. With 2-stage diodes a further divergence reduction will probably be achieved because ideally the second stage should add just longitudinal velocity to the beam. However, the operation of 2-stage diodes under high power conditions is rather complex and a verification of the predicted results on high power machines is necessary. KALIF-HELIA is -related to the axial flexibility in the positioning of the cells-ideally suited for this purpose.

In negative polarity experiments are feasible in fundamental research related areas as well as for technological purposes. Examples for the first group are: the interaction between pencil-type e-beams and matter or the biological effect on micro-organisms depending on high dose

rates and doses. If e-beams with sufficiently small energy distributions could be achieved, pumping of excimer- and FEL lasers or the production of high power microwaves could be considered. Technological applications require in general energy densities from 0.1 to 10J/cm² and repetition rates up to 100Hz. With the energy available and the single shot operation mode of KALIF-HELIA only proof of principle type experiments up to extreme dose rates and doses on large area/volume samples seem to be feasible. They might be related to areas like chemistry (polymerisation, production of fibers and foils...), material processing (all kinds of surface treatment of metals...), environment (treatment of biologically hazardous materials..) and food processing (sterilization).

The design of today's pulsed power prototypes for industrial purposes at FZK was strongly influenced by our pulsed power generators POLLUX and KALIF. KALIF-HELIA will influence future prototypes, namely the design of components like high power Marx generators, laser-triggered gas switches, magnetic switches and high power transmission lines. Due to its flexibility this accelerator offers also the possibility to serve as a test bed for future HV components.

Status

The assembly of the accelerator started end of 1997 in a building that had to be adapted to its needs and the requirements of the licensing authorities. Actually all of the components were put in place. The oil-, water-, gas- and energy supply systems are in progress as well as the safety- and control circuits. First calorimeter experiments are foreseen for autumn 1998.

Summary

KALIF-HELIA is the first accelerator in Europe which couples the principle of an induction linac with that of the magnetically insulated transmission line. Comparingly low in costs and size it will deliver as much as 150kJ to a target either as an electron or an ion beam. However, it is of prime importance to improve the beam quality and reproducibility. With KALIF-HELIA in positive polarity we first intend to verify the voltage dependence of existing scaling laws for the beam divergence by operating the same type of proton diode already used successfully at KALIF. If a suitable Li⁺ source becomes available the mass dependence of the beam divergence will be verified in a second step. In this case a specific power deposition of up to 5000TW/g might be achieved leading to radiation dominated high density plasma regimes so far not achieved. In negative polarity operation, proof-of-principle type experiments up to extremes or on large area samples are feasible. Finally the experience gained with this novel technology accelerator will stimulate the development of modern pulsed power devices for technological applications.

Acknowledgements

Without the support of the Sandia National Laboratories, Albuquerque we would not have been able to get this accelerator operational.

- [1] N.C. Christofilos et al., Rev. Sci. Instr. **35**, 886 (1964)
- [2] I. Smith, PSI, unpublished (1991)
- [3] W. Bauer et al., Wiss. Berichte FZKA 5590, Forschungszentrum Karlsruhe, 5 (1995)
- [4] A. Gordeev, unpublished (1994)
- [5] C.W. Mendel, S.E. Rosenthal, Phys. Plasmas **2**, 1332 (1995)
- [6] S. Illy et al., Phys. Plasmas **1**, 2748 (1994)
- [7] P. Hoppé et al., to be published in: Nucl. Instr. and Meth. in Phys. Res., A
- [8] J. Fockler et al., Proc. Vol.1, 9th IEEE Int. Pulsed Power Conf., Albuquerque, 431 (1993)
- [9] T. A. Mehlhorn et al., Proc. Vol.1, 10th Int. Conf. High Power Part. Beams, San Diego, 53 (1994)

CHARACTERISTICS OF FLASHOVER ION SOURCES IN MAGNETICALLY INSULATED ION DIODE

K. Masugata*, E. Chishiro and K. Yatsui

**Department of Electric and electronic Engineering, Toyama University,
3190 Gofuku, Toyama 930-8555 Japan*

*Department of Electrical Engineering, Nagaoka University of Technology,
1603-1 Kamitomioka, Nagaoka, Niigata 940-2188 Japan*

The effect of the irradiation of leakage electrons on the anode is evaluated by using two types of different magnetic field geometry of an applied B_r magnetically insulated diode. For the geometry of Type 1 where leakage electron is rare, the diode turns on with large delay time and the efficiency was worse. For Type 2 where initial electron irradiation of anode occurs, the turn on delay was reduced and high current density of ion beam was obtained with higher efficiency. From the result we see that electron bombardment strongly promote the production of anode plasma on the flashboard.

The characteristic of magnetically insulated diode in a multi-shot operation is investigated. An ion current density (J_i) decrease with increasing number of shots. The reduction of J_i is found to be mainly due to the accumulation of conductive stick matter on the flashboard.

1. Introduction

Intense pulsed light ion source is one of the hopeful candidates for the energy driver of inertial confinement fusion (ICF). To develop highly bright, repetitively operational ion sources, we have studied the characteristics of flashover type ion sources used in magnetically insulated ion diodes (MID's).

The effect of the irradiation of leakage electrons is evaluated by using B_r -MID of different magnetic field geometry.¹⁾ In addition the characteristic of the flashboard in a multi-shot operation is investigated by using racetrack MID.²⁾

2. The effect of electron irradiation

In the experiment we use B_r -MID and to evaluate effect of electron irradiation to the flashboard, two types of insulating magnetic field geometry are used. The cross-sectional view of the MID is shown in Fig.1. The diode consists of an aluminum anode, a pair of coaxial stainless steel cathodes, and a pair of insulating magnetic field coils. The anode has a dimension of outer radius = 55 mm, inner radius = 25 mm. On the active surface of the anode ($r=30$ -50 mm) epoxy filled azimuthal grooves of depth and width = 1 mm are made. As a cathode, a pair of cylinders (inner and outer cathode) is faced to the anode at A-

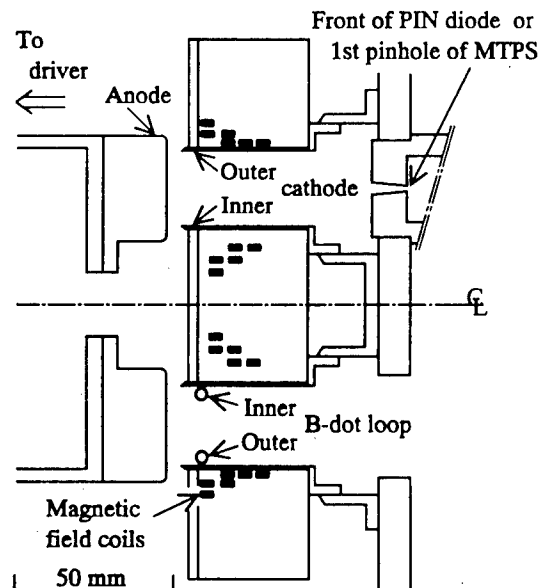


Figure 1. Cross-sectional view of B_r -MID and diagnostics. The diode is axis-symmetry with respect to the dashed line.

K gap length (d) = 5 mm. To produce B_r -field a pair of multi-turn coils was used, the current of which were independently controlled to change the field geometry. Two types of field geometry are used in the experiment. For Type 1, magnetic flux of the B_r field is constant in radius and for Type 2, the magnetic field lines are parallel to the anode surface. In the experiment pulse power machine "ETIGO-II" was used.³⁾

Diode current (I_d), ion current (I_i), inner cathode current (I_{ei}), and outer cathode current (I_{eo}) are measured by using B-dot Loops.

Figure 2 shows bremsstrahlung X-ray signals produced by the irradiation of leakage electrons. The PIN diode was used and it has a collimator to detect X-ray signal only from the anode surface. From the figure we see that for Type 2 diode, higher peak and faster rise of the signal is observed, which indicate the strong irradiation of anode surface in the early stage of the diode operation. The signal quickly droops at $t = (90-105)$ ns, although V_d is still at high voltage. The peak intensity is more than 5 times larger than the case of Type 1.

Figure 3 shows typical waveforms of the diode. In Type 1 I_i rises with delay (turn-on delay time, τ_i) of 60 ns after the rise of diode voltage (I_d). Peak value of I_i (≈ 30 kA) is obtained at $t = 120$ ns, where V_d has already fallen down. The maximum ion beam power ($P_i = V_d \cdot I_i$) of 16 GW is obtained at $t = 80$ ns. In the diode, large part of I_d is due to I_{eo} and the ratio of I_i to I_d is very small, which means that large part of diode energy is converted to the electron beam emitted from outer cathode.

On other hand, in Type 2 diode, I_i rises at $t = 30$ ns fast rise of $\tau_i \approx 20$ ns is obtained and, both has a peak at $t = 85$ ns. Peak value of I_i and P_i are evaluated to be ≈ 80 kA and ≈ 80

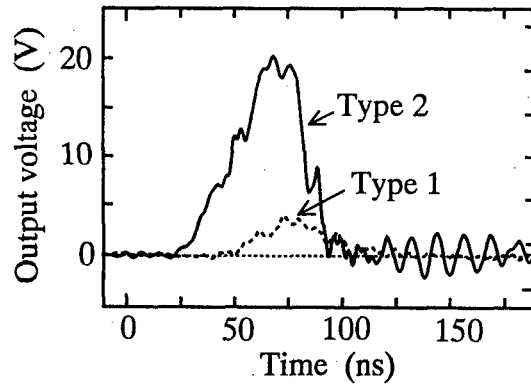


Figure 2. Output signal of the X-ray PIN diode

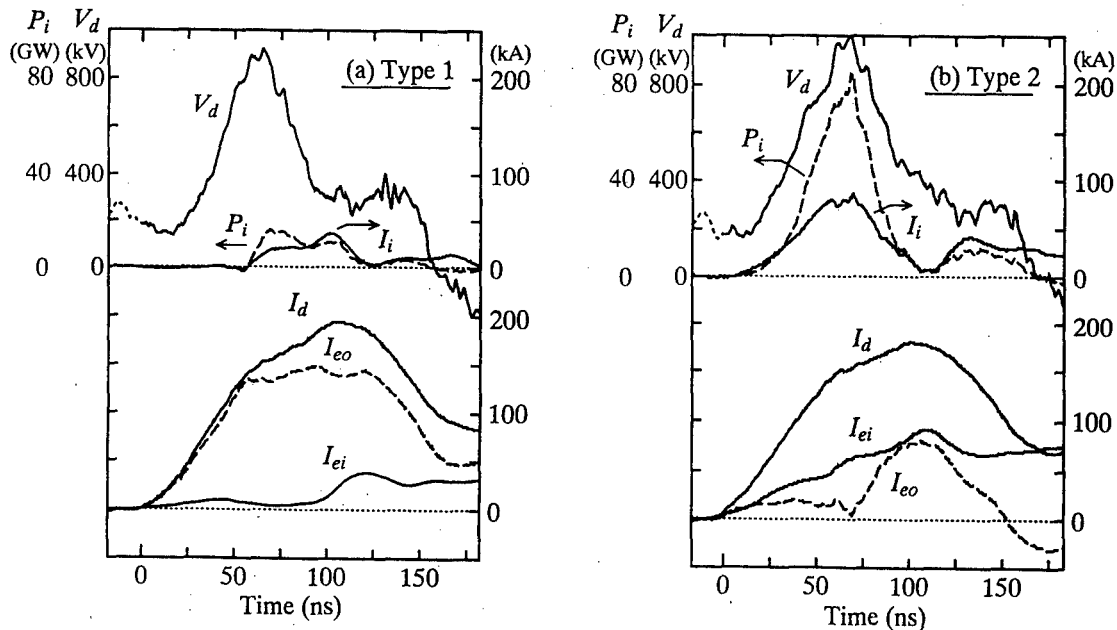


Figure 3. Typical waveforms in (a) Type 1 and (b) Type 2.

GW, respectively, the values are much larger than the case of Type 1. The ratio of electron current ($I_{ei}+I_{eo}$) against I_d is observed to be much lower than the case in Type 1. Thus, we see that, in Type 2 diode, input energy is effectively converted to ion beam energy.

To evaluate the characteristics of the diode in two types of insulating magnetic field geometry, time resolvable, multi-pinhole type Thomson parabola spectrometer⁴⁾ (MPTPS) was utilized. By the spectrometer, time history of ion energy, divergence angle of each ion species and ion beam composition were evaluated. For Type 2, proton beam was observed even in the rise time of V_d whereas for Type 1 ion beam was observed only after the peak of the diode voltage. In addition, in Type 2, divergence angle just after the turn-on is observed to be small whereas after the peak of V_d it increases.

Table I list the divergence angles and beam composition obtained by the time integrated MPTPS. From the table, we see that divergence angle is 60 to 70 mrad in θ -direction and 40 to 50 mrad in r -direction, which are independent on the ion species or magnetic field geometry. We have evaluated the ion beam compositions by averaging the data of all sets of injection angle. The result is also showed in Table I. As seen in the table, 60% of the beam is proton in both case and there is no dependence on the field-geometry.

Table I. Beam properties obtained by using multi pinhole Thomson parabola spectrometer.

	Divergence angle (mrad)			Beam composition (%)			
	(θ -direction	\times	r -direction)	H ⁺	O ⁺	C ⁺	O ⁻
	H ⁺ (300keV)	C ⁺ (300keV)	O ⁺ (300keV)	H ⁺	O ⁺	C ⁺	O ⁻
Type 1	60 \times 51	74 \times 44	70 \times 51	58	23	15	4
Type 2	69 \times 43	60 \times 50	64 \times 52	67	24	6	3

3. Successive operations of MID

In the experiment racetrack type MID was utilized. In the MID, an insulating magnetic field (B_y) is produced by a one-turn coil, which also acts as a cathode. Inside the one turn coil cathode, aluminum anode (flat, active area is 70 \times 70 mm) is placed, which is connected to the output feeder of "ETIGO-II". The anode has thirteen of polyethylene-filled, 70-mm-long grooves on the surface. The grooves has a width and pitch of 3 and 6 mm, respectively, and they are oriented parallel to the magnetic field.

For the measurement of ion current density (J_i), biased charge corrector was used, which was located \approx 35 mm downstream from the anode surface. The process of the successive operation is as follows; First shot is operated at 90 minutes after the start of evacuation. After the first shot, the diode is operated with shot to shot interval of 15 minutes. After the shots vacuum is broken to replace the anode. The pressure of the diode at the operation is around 10^{-2} Pa. Through the experiment ratio of insulating B_y field against the critical value was adjusted to be 1.1-1.2.

Figure 4 shows typical waveforms of V_d and J_i when $d = 6.5$ mm. As seen in the figure, J_i rises at about 30 ns after the

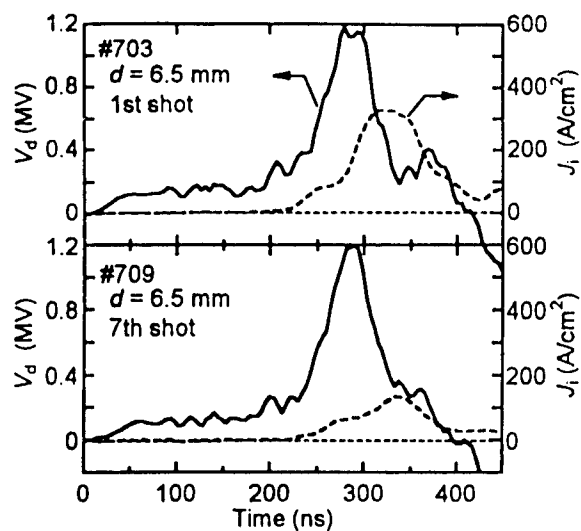


Figure 4. Typical waveforms of V_d and J_i when $d = 6.5$ mm.

main pulse of V_d and peak value of $J_i = 330 \text{ A/cm}^2$ is obtained.

Series of the successive operations are repeated for 8-11 times for each gap length. Figure 5 shows the dependence of peak value of J_i on the number of shot. For $d = 5 \text{ mm}$, large value of $J_i = 350 \text{ A/cm}^2$ is obtained for the first shot. The value is much larger than the space charge limiting current of proton. The value of J_i gradually decreases shot by shot and for 7th shot J_i becomes less than 150 A/cm^2 . On the other hand, J_i at the first shot decreases with increasing the d , whereas for 7th shots J_i is almost independent on d . This result suggests that for the first shots J_i is determined by the space charge effect, whereas for the latter shots J_i is limited by the source plasma. Hence the plasma production is insufficient in the latter shots.

After the shots, the surface of the flashboard was covered with conductive black layer. To analyze the material stuck on the surface of the flashboard, pure Si substrate was attached on the center of the flashboard and after the shots the surface of the substrate is analyzed by an X-ray fluorescence analyzer. From the measurement the stick matter is found to consist of Al, Zn, Fe, and Cu, which seems to be produced by the ablation of the diode electrodes.

To evaluate the effect of the stick matter, J_i is observed on the following procedure. (a) Make 6shots, (b) break the vacuum, (c) evacuate and make 3shots, (d) break the vacuum and wiping the surface to remove the stick matter, (c) evacuate and make 3shots, (d) keep a low pressure vacuum of 10 Pa for 20 minute, e) evacuate and make 1shot. Above the procedure is repeated for 5times to accumulate the data.

Figure 6 shows the results of the experiments. As seen in the figure, after the process (c) higher value of J_i is obtained for only one shot whereas after process (d) we obtain a similar profile to the process (a). From the result we see that by removing the stick matter ion current density is enhanced. Since the stick matter is conductive, the stick matter may discharge the surface charge and reduce the surface flashover.

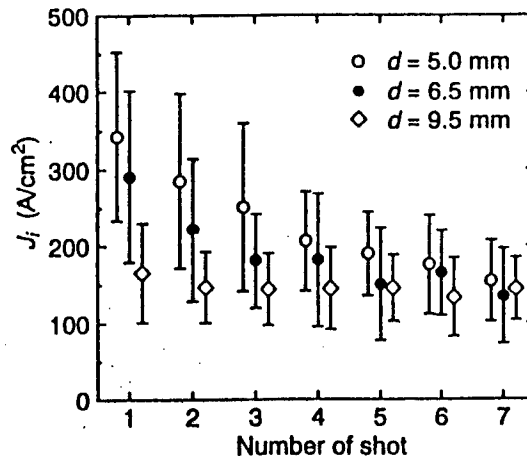


Figure 5. Dependence of the peak value of J_i on the number of shot.

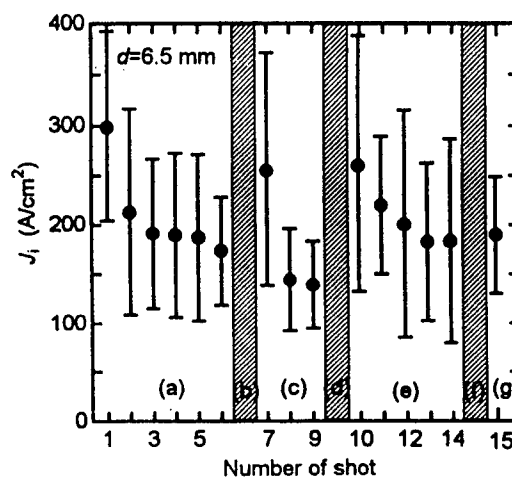


Figure 6. History of J_i .

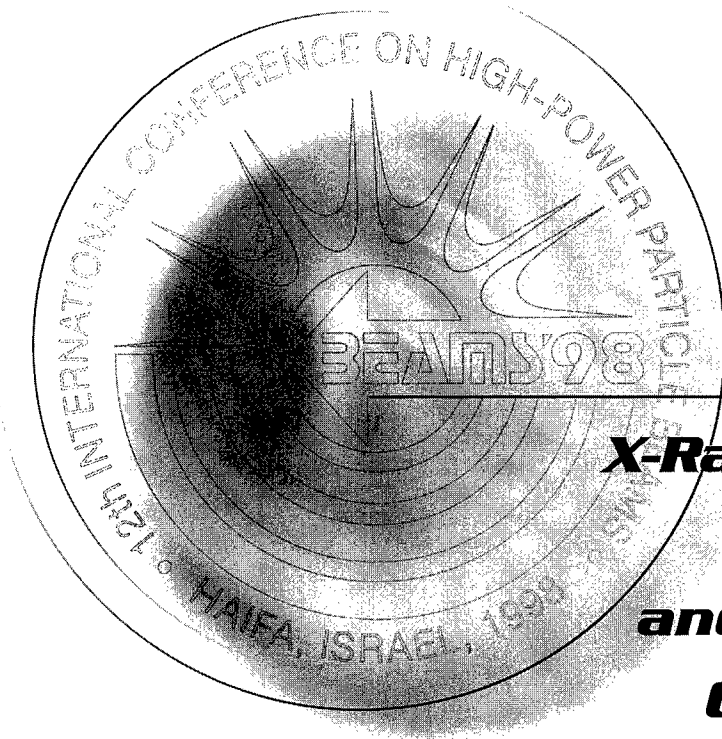
REFERENCES

- 1) E. Chishiro, A. Matsuyama, K. Masugata, and K. Yatsui, Jpn. J. Appl. Phys. **35**, 2350 (1996)
- 2) E. Chishiro, K. Masugata, and K. Yatsui, Trans. IEE of Japan **116A**, 1062 (1996)
- 3) A. Tokuchi, et al., Proc. 2nd Int'l Symp. on ICF Res. by High-Power Particle Beams, Nagaoka, Japan, ed. by K. Yatsui, 430 (1986).
- 4) K. Masugata, et al., Proc. BEAMS 94, (1994).



BEAMS'98

12th INTERNATIONAL CONFERENCE
ON HIGH-POWER PARTICLE BEAMS



ORALS

***X-Ray Sources,
Z Pinches
and Explosive
Generators***

Vol. I

Proceedings

WIRE ARRAY Z-PINCH INSIGHTS FOR HIGH X-RAY POWER GENERATION*

**T. W. L. Sanford, R. C. Mock, B. M. Marder, M. P. Desjarlais, T. J. Nash,
R. B. Spielman**

Sandia National Laboratories, P. O. Box 5800, Albuquerque, NM 87185 USA

D. L. Peterson

Los Alamos National Laboratory, Los Alamos, NM 87545

K. G. Whitney, J. P. Apruzese, and P. E. Pulsifer

Naval Research Laboratory, Radiation Hydrodynamics Branch, Washington, DC 20375 USA

D. Mosher

Naval Research Laboratory, Pulsed Power Physics Branch, Washington, DC 20375 USA

Abstract: Comparisons of detailed measured implosion characteristics of annular wire array z-pinches with those modeled and simulated give insight into pinch dynamics and x-ray power generation.

INTRODUCTION

The discovery [1] that the use of very large numbers of wires enables high x-ray power to be generated from wire-array z-pinches represents a breakthrough in load design for large pulsed power generators, and has permitted high temperatures to be generated in radiation cavities [2, 3] on Saturn [4] and Z [5]. In this paper, changes in x-ray emission characteristics as a function of wire number, array mass, and load radius, for 20-mm-long aluminum arrays on Saturn that led to these breakthrough hohlraum results, are discussed and compared with a few related emission characteristics of high-wire-number aluminum and tungsten arrays on Z. X-ray measurement comparisons with analytic models and 2-D radiation-magnetohydrodynamic (RMHC) code simulations in the x-y [6] and r-z [7] planes provide confidence in the ability of the models and codes to predict future x-ray performance with very-large-number wire arrays.

RESULTS AND DISCUSSION

Wire Number Variation: In the first set of Saturn aluminum wire-number experiments [1], the array mass was fixed and the wire number was varied by more than an order-of-magnitude from 10 to almost 200 by simultaneously changing the interwire gap and the wire size. This procedure was carried out for a 0.62-mg and a 0.84-mg array having an initial radius of 8.6 mm and 12 mm, respectively. The variation permitted interwire gaps to be explored from 6 mm down to 0.4 mm for both the small- and large-radius arrays. Decreasing the interwire gap resulted in monotonic decreases in the risetime and width of the x-ray pulse and simultaneous increases in radiated power and energy, in the *same way for both array radii* (Fig. 1). Over the 6 to 0.4 mm gap reduction explored, the total radiated power increased by a factor of 20 (Fig. 1A) and the total radiated energy by a factor of 2 (Fig. 1C).

In addition, for gaps smaller than 2 ± 0.6 mm, the character of the x-ray emission qualitatively changed, transitioning from a broad, single, irregular radiation pulse at large gaps, to a strong, narrow, evenly-shaped radiation pulse, that was followed by a much weaker pulse at small gaps (Fig. 2). The weaker pulse is consistent with a second radial implosion [8]. For gaps greater than ~ 2 mm, time-integrated images of the pinch exhibit the presence of a kink instability; time-dependent images show significant precursor plasma stagnating on axis, generating soft x-ray emission tens of nanoseconds prior to the main implosion, in agreement with earlier experiments. For gaps less than ~ 2 mm, on the other hand, no kink instability is observed, with only a minimal precursor plasma forming. Moreover, the change in the temporal shape of the x-ray pulse (Fig. 2) and spatial quality of the pinch occurred along with corresponding quantitative transitions in the rates of change as a function of gap of (1) the emitted x-ray power (Fig. 1A) and (2) energy (Fig. 1C), (3) the average size of the K-shell emission region (Fig. 1B), and (4) the average K-shell emitting ion density (Fig. 1D) and (5)

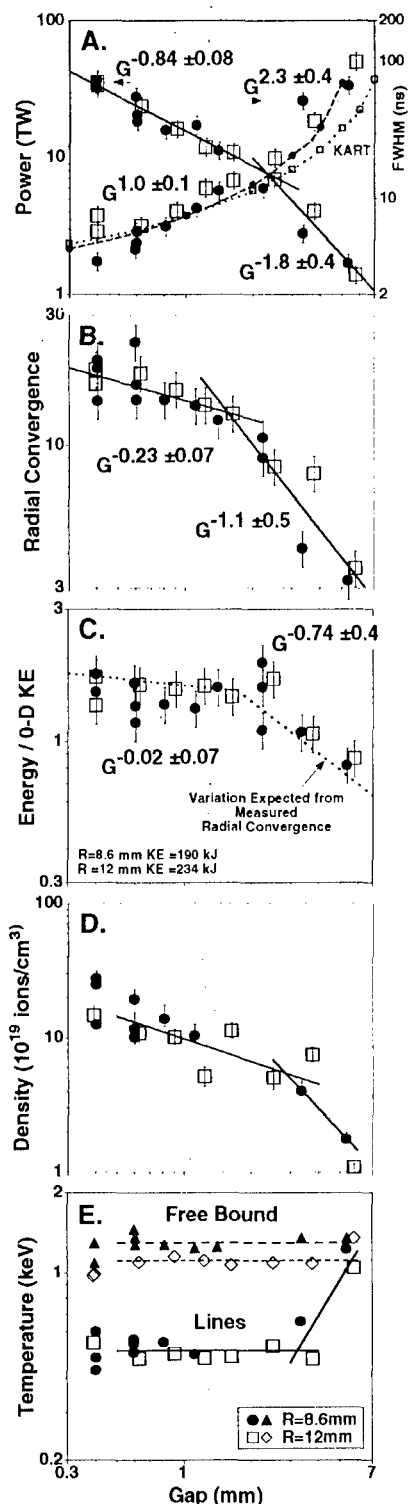


Fig. 1 (A) Peak total radiated power and pulsewidth and KART model, (B) Radial convergence, (C) Total radiated energy normalized by calculated kinetic energy assuming a 10:1 convergence, (D) ion number density (K-shell region), and (E) electron temperature (K-shell region) versus gap.

electron temperature (Fig. 1E). The emitting ion densities and electron temperatures were inferred from x-ray size data together with the K-shell power and K-series spectrum data. Not enough data was taken at wide gap spacings, however, to ascertain how rapidly this transition in x-ray behavior took place. For this reason, we represent it experimentally as a transition between two power laws as illustrated in Fig. 1, with the power indicated by the dependence on gap (G) shown.

Measurement of the slope of the optically-thin, free-to-bound, x-ray emission (Fig. 1E) determines the electron temperature of the hot core of the pinch [8]. It exhibits no variation with gap (dashed lines) and is only a function of the implosion kinematics. For large gaps, where the measured ion density is low, the temperature extracted from K-shell line ratios [9] (solid lines) agrees with that extracted from the free-to-bound emission. As the gap decreases and the emitting ion density increases (Fig. 1D), however, the optical depth of the K-shell emission becomes significant, and the line ratio begins to reflect the temperature of the outside surface of the emitting region, rather than an average over the region. This transition from a thin to a thick plasma, as indicated by the data of Fig. 1E, approximately coincides with the transition in the rate of change of density with gap (Fig. 1D) and with the transition at ~ 2 mm.

The difference between the core and surface temperature is indicative of a substantial temperature gradient within the emitting plasma. The enhanced plasma density at small gaps increases the temperature and density gradients and opacity effects, but in such a way as to approximately maintain the average amount of mass participating in the K-shell emission at $\sim 11\%$, independent of gap. Comparisons of the measured K-shell emission radii with that simulated by the Eulerian-RMHC (E-RMHC) [7] indicate that the actual mass averaged radius is about double that extracted from the emission images [10]. This gradient structure is illustrated by a detailed analysis [11] of the x-ray image, spectral, and K-shell power data, for an aluminum-array shot taken on Z, having an interwire gap of 0.5 mm, a total mass of 4.1 mg, and an array radius of 20 mm. The density and temperature profiles obtained from a best fit of a aluminum-plasma collisional-radiative-equilibrium model to these measured quantities is shown in Fig. 3. In the model, the radiative transfer is carried out for all optically-thick K-shell lines and two K-shell continua temperatures.

Interpretation of Number Variation: In general, variations in peak total power track the inverse of the measured pulsewidths (Fig. 1A), as would be expected if the total energy radiated during stagnation is slowly varying. The greater rate of dependence with gap of the pulsewidth relative to the peak power, for gaps greater than ~ 2 mm reflects the greater disorganization of the implosion as seen by the lost double-pulse nature of the stagnation (Fig. 2). The accelerated rate of decrease in power for large gaps relative to that for small gaps is

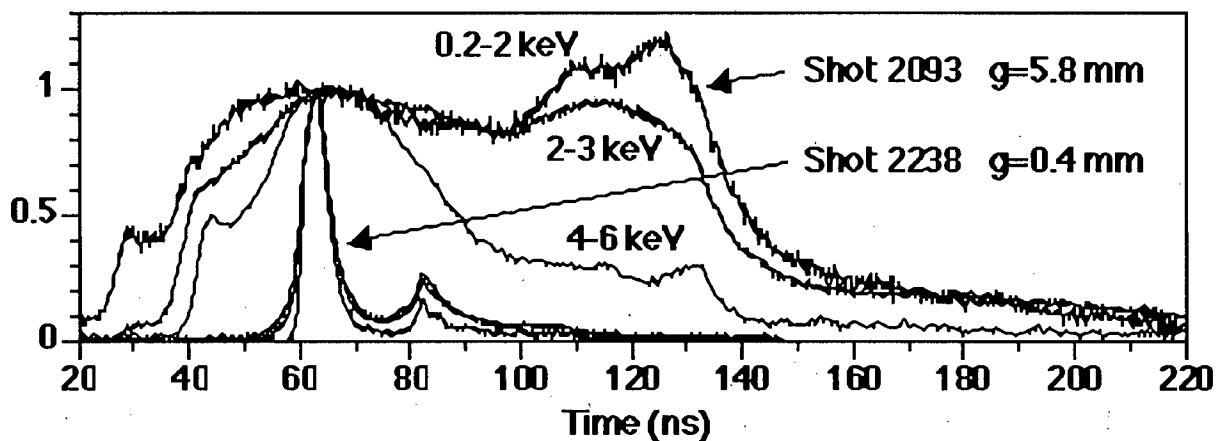


Fig. 2 Normalized pulse shape in three energy channels for two gaps.

consistent with the decrease in total radiated energy (Figs. 1A, 1C, and 4). This change in energy is approximately consistent with the change in the calculated (dotted lines in Fig. 1C) kinetic energy, and by inference, the radiated energy using the measured radial compression from the K-shell emission images (Fig. 1B). The trends in ion density (Fig. 1D) and electron temperature (Fig. 1E) demonstrate that the increase in power is the result of systematically greater plasma compression.

The apparent transition in implosion quality near 2 mm has been interpreted using a RMHC in x-y geometry [1,6]. Calculations performed with this code show (in correspondence with the experimental data) that a change in the implosion topology occurs with increasing wire number. The implosion is seen to transition from one composed of non-merging, self-pinching individual wire plasmas to one characterized by the early formation and subsequent implosion of a quasi-plasma-shell. The shell had density and current variations distributed azimuthally that were correlated with the initial wire location and which decreased in amplitude with decreasing gap. The calculated transition region was sensitive to (1) the magnitude of the prepulse that accompanies the main current pulse, (2) the current flowing per wire, (3) the wire size, (4) the interwire gap, and (5) the resistivity model used. For the particular resistivity model used and for the measured prepulse and wire sizes used, this transition was found to occur between wire numbers 20 to 40 (or between interwire gaps of about 3 to 1 mm, respectively), for the small radius load [1]. This calculated transition was also seen to be consistent with observations made with 1.3-mm gap loads in the transition region. There, individual wires were observed to self-pinch 20 ns prior to peak radiated power (where the array had only imploded a fraction of a mm radially). Ten nanoseconds later, after the array had imploded an additional 1.5 mm, the observed plasma emission became a continuous distribution, with no evidence of individual wire structure.

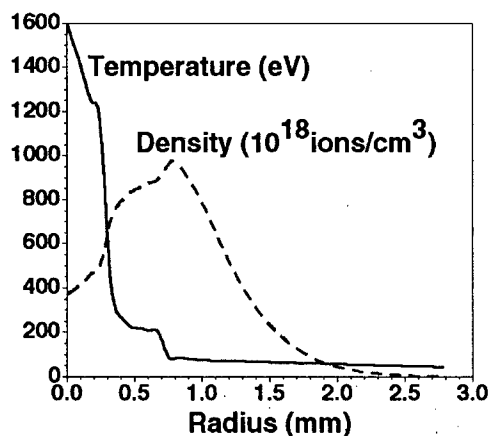


Fig. 3 Calculated ion density and electron temperature for aluminum Z shot.

The x-y simulations [6] together with analytic modeling [12] show that the wire-plasmas, in contrast to the plasma of a shell, accrue azimuthal velocity components during the implosion owing to deviations in the locations of the individual wires from those of a perfect annulus or to the presence of the limited number of current return posts surrounding the array [12]. These velocity components produce density asymmetries at stagnation that reduce both the compressibility of the stagnating plasma and the resulting radiated energy, both in qualitative agreement with the discontinuity observed in the radial convergence measurements (Fig. 1B) and energy channel (Fig. 1C). The x-y simulations show, however, that these variations *cannot* account for the change in measured pulse shape, for any wire number greater than 10. In contrast, E-RMHC [7] simulations

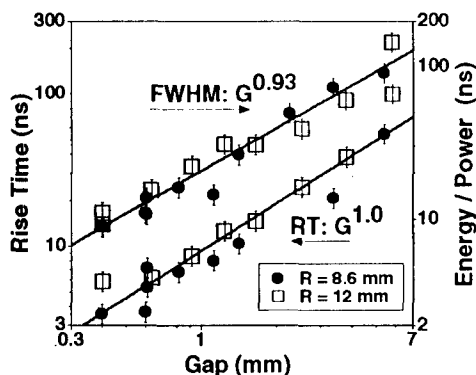


Fig. 4 Risetime and effective pulsewidth versus gap.

in the r - z plane, which assume an azimuthally symmetric plasma shell with a random density distribution in the r - z direction, suggest that the shape of the primary power pulse and the general change in peak power with gap are related to the evolution of the thickness of the plasma sheath due to r - z motions and the growth of Rayleigh-Taylor (RT) instabilities. This thickness is calculated to scale linearly with the pulse width. The measured *risetime* of the total radiation pulse and the “effective” pulsewidth (defined as the total energy divided by the peak power) scale as the gap, over the entire gap range explored, showing no discontinuity near 2 mm (Fig. 4). This data, together with the simulations, thus suggest a direct relation between the initial interwire gap and the resulting

thickness of the imploding sheath.

Recently, an analytic model (KART) of the implosion has been developed by Desjarlais and Marder [13] that takes into account an amplification of the RT instability arising from a kink instability, which deforms the individual wire plasmas. This deformation is in phase with that generated by the RT instability, which is assumed to arise from a global sausage instability acting on the entire array. The agreement of their estimated pulsewidth with that measured for these experiments (dashed curves in Fig. 1A), as well as with that measured for other tungsten experiments on Saturn [14] and Z [5, 15], with only *one perturbation parameter* that scales with the wire size, suggests that the wires retain enough of their individual identity for a sufficient time to allow the kink amplification to participate. Doubling the number of tungsten wires on Z from 120 to 240, for example, reduced the measured pulsewidth by $(29 \pm 9)\%$, in agreement with a calculated 25 % reduction.

Mass and Radius Variation: Two sets of additional Saturn aluminum-wire experiments were conducted in the calculated high-wire-number quasi-plasma-shell regime [10]. These experiments show two important trends. Firstly, when the mass of the 12-mm-diameter arrays is reduced from above 1.9 to below 1.3 mg, a factor of two decrease in pulsewidth (Fig. 5) occurs for all ten energy channels measured between 0 and 10 keV. The associated peak power in the energy channels exhibits a two to twenty fold increase, respectively. Secondly, when the radius is increased from 8.6 to 20 mm, for a mass of 0.6 mg, the experiments show that the radiated pulsewidth (Fig. 6) in all channels increases from only ~ 4 to ~ 7 ns. The associated peak powers in all channels remain relatively unchanged with radius.

Interpretation of Mass and Radius Variation: The E-RMHC simulations were used to understand the underlying pinch dynamics. Over the mass range of 0.42 to 3.4 mg and radius range 8.6 to 20 mm measured, which spanned an implosion time of 40 to 90 ns, the implosion time of the simulated pulse agrees with that measured within a shot-to-shot variation of only 2 ns. This agreement suggests that $(100 \pm 6)\%$ of the initial mass is being accelerated during the implosion. For these simulations, the electron-photon coupling was set to either its nominal value (indicated by N) or a reduced value (indicated by R), such that the calculated peak total radiated power agreed with that measured at ~ 0.6 mg. Within the uncertainty of this emissivity approximation, the measured pulsewidth (Figs. 5 and 6) and trends in total radiated peak power agree with that simulated, using only a *single value* of a density perturbation seed [10]. KART calculations are also shown in Figs. 5 and 6.

For all cases, the E-RMHC simulations show a *two-stage* development of the instability with initial bubble burst when a wavelength, of the order of the

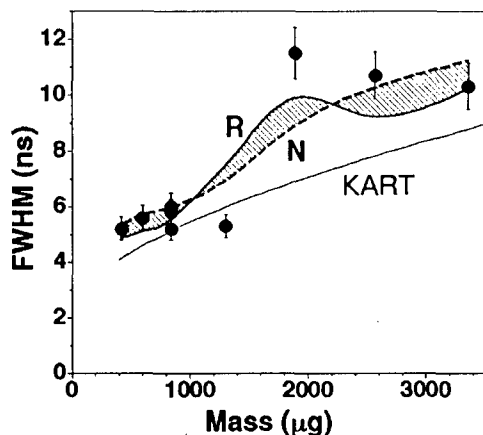


Fig. 5 Measured, modeled, and simulated pulsewidth versus mass.

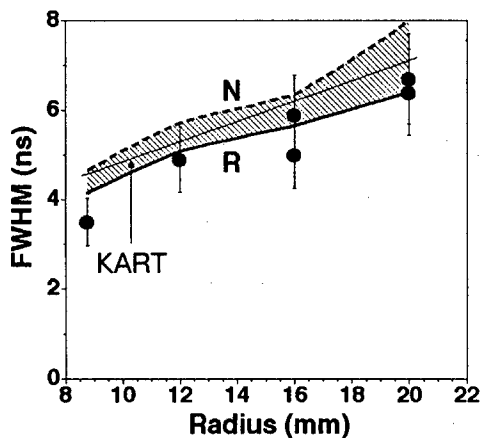


Fig. 6 Measured, modeled, and simulated pulsewidth versus radius.

kinetic energy per incident ion at stagnation. The simulations also show that the increase in pulsewidth with radius is due to the faster growth of the shell thickness relative to the increase in shell velocity. These results suggest that the improved uniformity provided by the large number of wires in the initial array reduces the disruptive effects of instabilities observed in small-wire-number imploding loads.

The simulations generate total radiation pulse shapes in agreement with the primary pulse measured, as illustrated in Fig. 7 for a 0.84-mg, 12-mm radius load. The simulations indicate that the energy deposited in the plasma arises primarily from the Lorentz ($\mathbf{J} \times \mathbf{B}$) force and goes primarily into accelerating the plasma, increasing its kinetic energy. At early times when instabilities have not become important and there has been little plasma heating, the simulated energy deposited by the Lorentz force and the plasma radial kinetic energies are nearly equal. At later times, the instability destroys the plasma shell, accelerating plasma to the axis where it stagnates, and the kinetic energy diverges from the work generated by the Lorentz force. The plasma that has not stagnated continues to be accelerated by the Lorentz force. Because the radiation rate is higher than the rate at which energy is being supplied, the total kinetic-energy decreases, even though some plasma continues to be accelerated. As the pressure rises, some of the ($\mathbf{J} \times \mathbf{B}$) energy is transferred to internal energy by $p dV$ work, rather than as a kinetic-energy increase. Due to the extended radial nature of the plasma as stagnation begins, the net result on

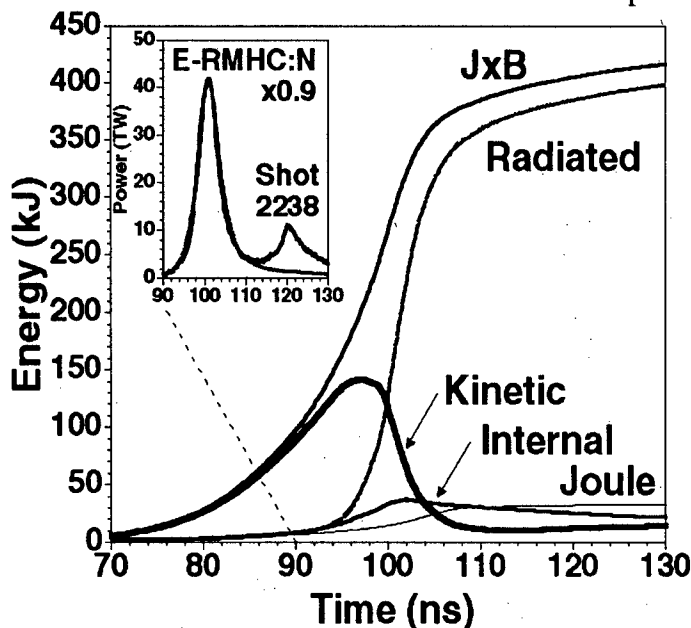


Fig. 7 E-RMHC simulated energy partition.

shell thickness, is reached, followed immediately by current flow in the low-density material, between the spikes. The plasma shell self heals and continues to accelerate with only a small amount of bubble material being thrown ahead of the main body of plasma. The instability growth continues, evolving to longer wavelengths, until one of the order of the new shell thickness is reached. When the shell bursts the second time (at longer wavelengths), a significant amount of material is accelerated to the axis, and the radiation pulse begins. These simulations show that the decrease in pulsewidth and associated doubling of the peak total power, as mass is reduced, is due to the faster implosion velocity of the plasma shell relative to the growth of the shell thickness. The relative increase in peak power for the higher-energy x-rays is due to an increase in ion temperature, arising from an increase in

the energy flow is that part of the plasma on axis releases energy as radiation, while regions away from the axis continue to absorb energy, which may then be radiated later in the pulse. The result is a total radiated energy that is higher than the instantaneous peak in the kinetic energy at the time stagnation begins. The calculations show only a small contribution from Joule heating.

The variation with mass on Z using tungsten wires in the high-wire-number regime shows similar trends to those observed on Saturn for the aluminum wires [5, 15]. On Z, the pulsewidth decreased by a factor of two and the total radiated power doubled when the mass decreased from 6 to 4 mg, for loads having a 20-mm radius. Moreover, these high-wire-number implosions, with

interwire gap of 0.5 mm, produced high-quality implosions that had pulsewidths of only 7 ns at peak power.

A New Model: The results show that good agreement with radiation pulse widths derive from an initial perturbation that depends only on the interwire gap. Single-wire observations and computations in carbon and aluminum [16, 17] suggest a mechanism [18] as follows that may help to explain the dependence in contrast to KART. Uncorrelated wire-to-wire sausage modes in individual wire plasmas grow until the plasmas of adjacent wires merge, after which current flow in the plasma shell stops their growth. At the merging time, the thickness of the annulus is then roughly the same as the initial gap. A key observation of the single-wire studies is that the sausage perturbations are nonlinear and large-amplitude even at very early times in their development, with a shape that is self-similar in the radial scale, that is, they "look" about the same independent of radius. This structure is also observed in ongoing tungsten linear-wire-array experiments on Naval Research Laboratory Gamble II generator that simulate Z prepulse conditions. From the self-similar observation and analysis of the perturbation spectrum, the fundamental (longest) wavelength in the perturbation is also about the size of the interwire gap. Thus, in this model, the amplitude of the initial perturbation is fixed while its wavelength scales with gap.

E-RMHC computations are required to determine if such initial conditions can reproduce the observed dependence of radiation characteristics without an arbitrarily-chosen perturbation amplitude for a given gap. However, the self-similar model does provide for RT saturation and healing for sufficiently-short wavelength (small gap/large wire number). Also, existing E-RMHC computations do show that tripling the scale of initial 10% and 15% initial perturbations is equivalent to shorter-scale perturbations of 45% and 75%, demonstrating that perturbation wavelength is a powerful determining factor for implosion quality and radiation pulse width.

CONCLUSION

Implosions that develop narrow pulsewidths with high peak powers can be generated from both small- and large-radius annular wire arrays by keeping the interwire gap to spacings on the order of 0.5 mm or less. Reducing the implosion time, while still providing good current coupling to the load at stagnation, reduces the growth of the radial instabilities relative to the implosion velocity and permits the highest powers to be developed. The RMHC simulations and the Desjarlais-Marder model agree with aspects of the data and provide insight into the underlying dynamics. A new self-similar model for the initial E-RMHC perturbation dependence on gap provides additional insight and may improve that codes predictive capability for future large-wire-number experiments on Z.

- [1] T. W. L. Sanford, et al, BEAMS'96, pp.146-149; *Phys. Rev. Lett.* **77**,5063 (1996).
- [2] M. K. Matzen, *Phys. Plasmas* **4**, 1519 (1997).
- [3] J. P. Quintenz, et al, this conference.
- [4] D. D. Bloomquist, et al, *Proc. 6th Int. IEEE Pulsed Power Conf.*, (1987), p. 310.
- [5] R. B. Spielman, et al, BEAMS'96, pp. 150-153; *Phys. Plasmas* **5**, 2105 (1998).
- [6] B. M. Marder, et al, to be published *Phys. Plasmas* (1998).
- [7] D. L. Peterson, et al, *Phys. Plasmas* **3**, 368 (1996).
- [8] T. W. L. Sanford, et al, *Phys. Plasmas* **4**, 2188 (1997).
- [9] K. G. Whitney, et al, *Phys. Rev. E* **56**, 3540, (1997).
- [10] T. W. L. Sanford, et al, *Dense Z-Pinches 4th Int. Conf. AIP* (1997), pp 561-573.
- [11] J. P. Apruzese, et al, to be submitted to *Phys. Plasmas* (1998).
- [12] D. Mosher, BEAMS'94, pp 159-162.
- [13] M. P. Desjarlais and B. M. Marder to be submitted to *Phys. Plasmas* (1998).
- [14] C. Deeney, et al, *Phys. Rev. E* **56**, 5945 (1997).
- [15] T. W. L. Sanford, et al, to be published *IEEE Trans. Plasma Sci.* (1998).
- [16] F.N. Beg, et al., *Plasma Phys. And Controlled Fusion*, **39**, 1-25(1997).
- [17] J.P. Chittenden, et al., *Bull. Am. Phys. Soc.* **41**, 1471(1996).
- [18] D. Mosher, et al., "Modeling Initial Annular Perturbations in Large Wire-Number Arrays", work in progress.

*Sandia is a multiprogram laboratory operated by the Sandia Corp., a Lockheed Martin Co., for the US DOE under Contract DE-AC04-94AL85000.

STABLE IMPLOSION OF DOUBLE GAS PUFF WITH LONG TIME IMPLOSION

R.B.Baksht, A.V.Fedunin, A.Y.Labetsky, V.I.Oreshkin, A.G.Russkikh, A.V.Shishlov

High Current Electronics Institute

4 Akademichesky ave., Tomsk, 634055, Russia

A.Van Drie

University of California, Department of Physics and Astronomy

Irvine, CA 92697-4575, USA

Introduction.

The Rayleigh-Taylor instability is well known to be the main impediment to the efficient implosion of gas puffs with a large initial radius. This has been demonstrated in a number of experiments [1,2,3]. The R-T instability could be mitigated by the so-called snowplow mechanism responsible for enhanced efficiency of multilayer gas puff z-pinch loads [4]. The snowplow mechanism employs the stability of the shock wave driven into the load by magnetic pressure. The snowplow stability mechanism is used both in multilayer gas puffs and in structured loads such as large-diameter uniform fill loads [5] and z-pinch loads with tailored density profiles. The use of structured loads implies that when a pulsed voltage is applied to a gas puff, a radially uniform current shell, a skin layer is formed on the periphery of the gas puff. However, the assumption that a skin layer is formed contradicts to the probabilistic nature of the gas breakdown that accompanies the formation of a conducting medium in a gas puff. Experimental results show [6] that the conducting-to-nonconducting state transition of the gas puff material is chaotic, nonstationary in character. Some techniques for the production of a uniform current layer and the effect of the current layer uniformity on the gas puff implosion are discussed in the paper. Using a uniform current shell, we have been able to perform some experiments to study the stability of double gas puff with a long implosion time.

Experimental arrangements.

Experiments were carried out on the GIT-4 inductive storage with 1.7-MA load current and 120-ns current rise time. The GIT-4 upstream inductance L_{up} is equal to 245 nH; the downstream inductance L_d is 60 nH. The nozzle assembly was located at the anode of the downstream part of the facility. Three sparks were located at the distance of 10 mm from the nozzle throat. Small capacitor bank (4 kV, 0.5 μ F) was used to provide spark preionization. A small coil was located near the outer nozzle, and it produced magnetic field pulse in the outer shell area. The copper plug was used to reduce the magnetic field in the inner shell area. The design of the valve allowed us to change separately plenum pressures in the inner and outer shell.

The gas puff implosion was monitored with various diagnostics. The radial and axial dynamics of the implosion are measured with a streak camera as described in [3]. A two film time-integrated pinhole camera was fielded. The filter was 2 μ Kimfol plus 0.2 μ aluminium (the transmission threshold \approx 0.8 keV) or 10 μ Beryllium. Two films were placed inside the

pinhole camera one after another. The first film absorbs photons with the energy below 3 keV, so one can obtain the argon K-shell image on the second film.

The X-ray yields and powers are measured using filtered photoconducting detector (PCD) and aluminium cathode x-ray diode (XRD).

Formation of a uniform current shell

For typical conditions in which plasma radiation sources (PRS) are operated, it is desirable to provide a very quick transition (for some ten nanoseconds) from the nonconducting state of the gas in the shell to a state in which the plasma produced should ensure formation of a skin layer. To provide formation of a skin layer, the electron temperature about $3\div 9$ eV is sufficient.

At the first glance, when the generator power is some hundreds of gigawatts, it is not difficult to realize the above increase in temperature and, hence, in conductivity for 10 ns. This, however, is not the case. Fig. 1 presents oscillograms showing the current rise rate for an Ar gas puff of diameter 80 mm and length 20 mm, obtained on the GIT-4 system for various conditions: (a) the gas puff mass is $40\text{ }\mu\text{g/cm}$, and preionization is absent; (b) the gas puff mass is $20\text{ }\mu\text{g/cm}$, and preionization is accomplished by UV irradiation $7.5\div 8\text{ }\mu\text{s}$ before the POS opening, and (c) the gas puff mass is $40\text{ }\mu\text{g/cm}$, and preionization is accomplished by UV irradiation $7.5\div 8\text{ }\mu\text{s}$ before the POS opening.

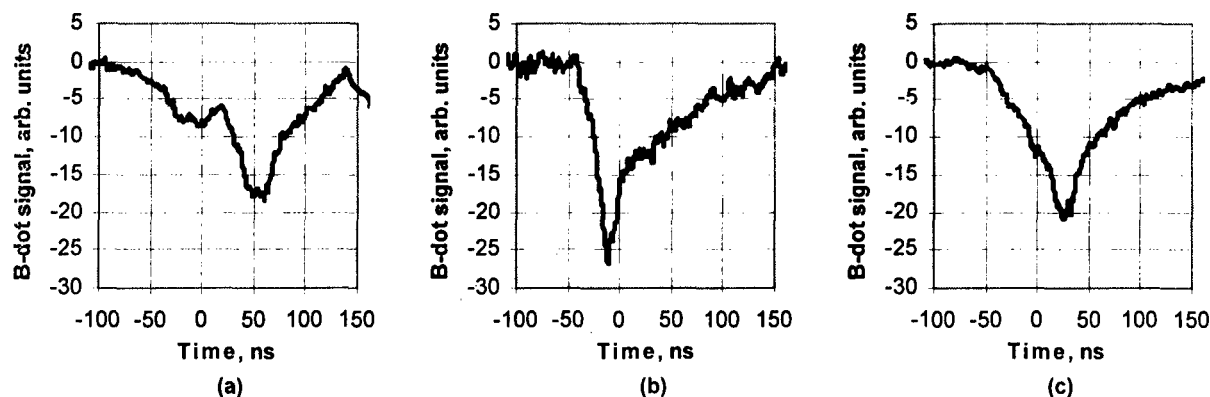


Figure 1 B-dot signals for 80-mm diameter, 20-mm length Ar single gas puff: a) gas puff mass is $40\text{ }\mu\text{g/cm}$; without preionization; b) gas puff mass is $20\text{ }\mu\text{g/cm}$; UV preionization; c) gas puff mass is $40\text{ }\mu\text{g/cm}$; UV preionization.

The corresponding plots for the gas puff resistance are given in Fig. 2. It can be seen that

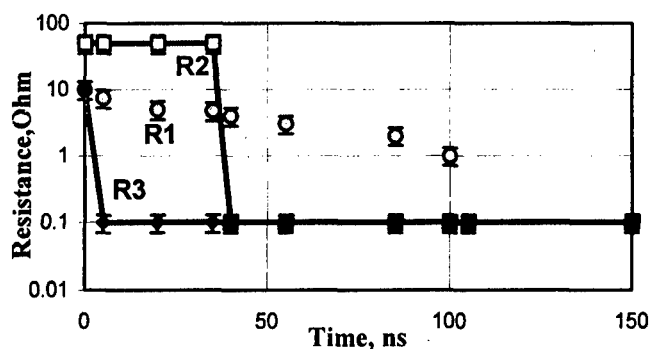


Figure 2 Single gas puff resistance versus time after POS opening. The curves R_1 , R_2 , R_3 correspond to the cases (a), (b) and (c) Fig. 1.

with no preionization, the gas puff resistance decreases very slowly even at a high particle density in the gas shell. It should be noted that in this case the implosion process was highly unstable. When UV preionization is performed, the current layer can be formed by one of two different mechanisms. If the particle density in the gas shell is low (\sim up to $5\cdot 10^{16}\text{ cm}^{-3}$ for Ar), the shell resistance, R_2 , and the accelerated electron flux measured simultaneously are rather high

for about several tens of nanoseconds. With the particle density greater than 10^{17} cm^{-3} for Ar, we have not detected the high-resistance phase (curve R_3 in Fig. 2).

The results obtained can be interpreted using an approach presented in [7]. According to [7], the formation of a current layer in a strongly overvolted gap with no preionization is of a streamer character. With that, a decrease in gas puff resistance is accompanied by an increase in conductivity in a limited number of current channels. Though conductivity in each channel is high enough to prevent formation of diffuse volume discharge, resistance in the anode-cathode gap as a whole decreases slowly. The channel formation permits the magnetic field to penetrate inside the gas shell. As a result, part of the total current flows through the inner layers of the structured plasma load and prevents uniform implosion.

Given UV preionization, the probability that the discharge will develop to its diffuse stage increases. For low gas densities, it is quite probable that running electrons will appear. It is just the case that we observed experimentally. As the running electron flow appears, the ionization rate decreases, and this results in that a high-voltage glow discharge with a comparatively high resistance is initiated. For a structured load this means that as this high-voltage glow discharge operates in the outer shell, current channels may appear in the inner, denser, shell of the gas puff. It is quite clear that in this case any attempt to attain uniform implosion fails.

For higher gas density and with UV preionization, one can expect that current channels will appear in great numbers or a space discharge will be initiated, at least in regions directly illuminated with UV radiation. The plasma conductivity is such that the average current density in the outer shell reaches 10^3 A/cm^2 as early as in $10\div 15 \text{ ns}$. However, experiments [6] have shown that in this case the current channels developing in the outer shell trap only some part of the outer shell material. The subsequent situation is similar to that with a gas puff imploding with no preionization: the current channels with partially trapped material go toward the center, thus destroying the inner shell and leading again to unstable implosion.

Experiments with a 80/30 diameter ratio double gas puff

The set of the experiments with structured load was carried out on the GIT-4 generator. The main goal of the experiments was to obtain stable quasi-one-dimensional long time implosion of double gas puff. A nozzle assembly with the outer nozzle diameter of 80 mm and the inner nozzle diameter of 30 mm was used. Both outer and inner nozzles had 500 μm throat. In some cases this dimension was even somewhat larger owing to the fact that when nozzles subjected to little mechanical processing were repeatedly used; the throat size increased by 25 μm on each treatment.

To provide an azimuthally uniform outer shell, it has been proposed to use for structured loads UV preionization combined with a discharge initiated in crossed $\mathbf{E}\times\mathbf{B}$ fields. The experiment arrangement is shown in Fig. 3. The similar preionization system was used in the double gas puff experiments with an outer nozzle diameter of 60 mm described in [8]. The sparks providing UV irradiation of the outer shell were triggered $7.5\div 8 \mu\text{s}$ prior the POS opening. Timing for the magnetic field was chosen so that the radial magnetic field B_r to be at maximum at the instant a discharge was initiated in the gas shell. Electric field across the anode-cathode gap was provided by the POS plasma gun operation; the POS plasma guns were fired $4.8\div 5 \mu\text{s}$ before the POS opening. Argon was used as a gas puff material.

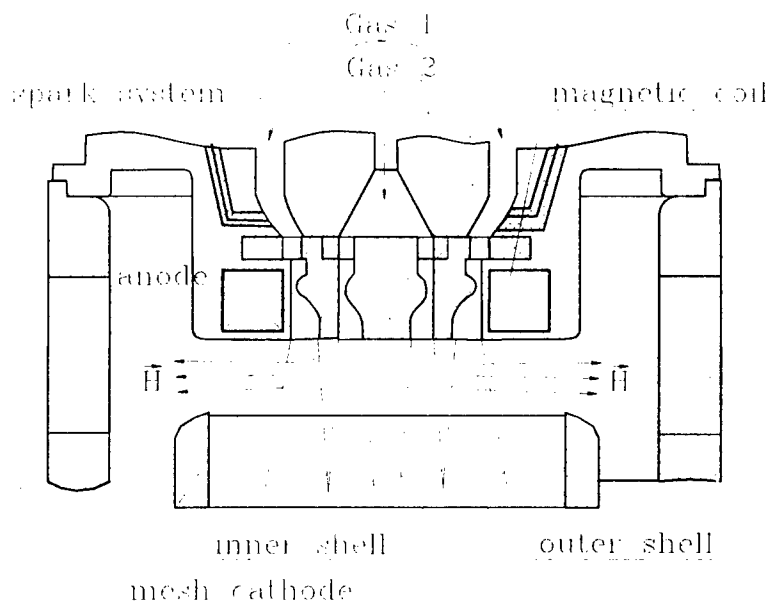


Figure 3 Experimental arrangements.

At the first stage, the experiments with a low magnetic field were carried out. The radial magnetic field B_r was 0.4 kGs at the outer shell area. The outer shell plenum pressure was 2 atm (Shot #434, #436-439) and 2.5 atm (Shot #445-447); the inner shell plenum pressure was 2.5 atm in all shots. A criterion for the implosion of a structured load to be quasi-one-dimensional should be a small scatter in implosion time from shot to shot. However, in the experiments with a low magnetic field, standard deviation accounts for 6.4% and 9.3% of the mean implosion time correspondently for 2 atm and 2.5 atm plenum pressure in the outer shell (see Fig.4). This scatter in the implosion time can be related to a weak effect of the magnetic field on the conditions of the discharge initiation. Several attempts have also been made to arrange the plasma to be localized in the outer shell with the use of a hollow cathode, pointed cathode, etc. All these attempts to produce a "stable" pinch have failed.

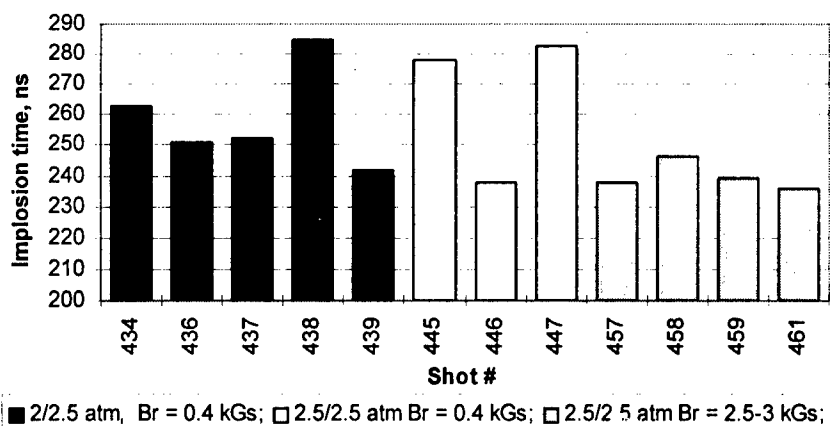


Figure 4 Implosion time for the shot with UV preionization and discharged initiated in crossed $\mathbf{E} \times \mathbf{B}$ field.

The situation changed, when the radial magnetic field had been increased up to 2.5 ± 3 kGs (Shot #457-459, 461). In this case, the presence of the increased magnetic field ensures the formation of a current layer rather uniform in azimuth, which can well be seen in the discharge autograph in Fig.5. The discharge uniformity is related to the azimuthal drift of electrons which extends substantially the dimensions of the region containing the gas ionized by UV irradiation. Standard deviation for the implosion time decreased up to 1.8%. In the pinhole images, the pinch shows up as a dense uniform "core" with a diameter of 1.5 mm surrounded by a low density unstable halo with a diameter of 4 mm. Similar pictures were obtained in our previous experiments described in [8].

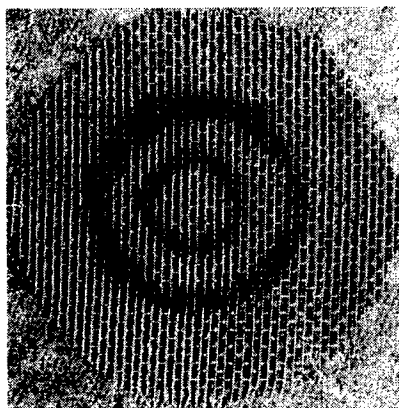


Figure 5 Discharge autograph on the cathode mesh.

Conclusion.

The experiments show that preionization system, which combines spark preionization (UV irradiation) and discharge in crossed $\mathbf{E} \times \mathbf{B}$ fields, provides uniform preionization of the outer shell of double gas puff. This, in turn, make it possible to achieve stable long time implosion using structured load. X-ray pinhole pictures obtained in the experiments with double gas puff with the outer shell diameter of 60 and 80 mm show that at the final stage of implosion pinch consists of a stable "core" surrounded by a low density unstable halo.

Acknowledgment.

This work was supported in part by ISTC Project #525 and RFFI grant 98-02-16963. A.Y.Labetsky and A.V.Shishlov greatly acknowledge personal financial support from International Soros Science Educational Program (grant a97-1493 and grant a97-1492).

References.

- [1] D.Mosher *et al.*, Fourth International Conference Dense Z-pinchs, *AIP Proceeding* 409, pp.135-140, 1997.
- [2] J.W.Thornhill *et al.*, *ibid*, pp.193-197.
- [3] R.B.Baksht. *et al.*, *Plasma Physics Reports*, vol. 21, pp.907-12, Nov 1995.
- [4] A.Velikovich, S.Golberg *Phys.Fluids, B*, 5, pp.1164-1173, 1993.
- [5] F.L.Cohran, J.Davis, A.Velikovich *Phys Plasmas*, 2, pp.2765-2772, 1995.
- [6] A.G.Rousskich *et al.*, Fourth International Conference on Dense Z-pinchs, *AIP Conf. Proceeding* 409, pp.307-311, 1997.
- [7] Yu.D.Korolev, G.A.Mesyats Pulse breakdown in gases, Springer Verlag, 1997.
- [8] R.B.Baksht *et al.*, *IEEE Trans. on Plasma Science*, to be published.

Electron Beam Measurements in a Pulsed Capillary Discharge

M. Favre, P. Choi*, H. Chuaqui, E. Wyndham, C. Dumitrescu-Zoita*, J. Larour*, and J. Rous*

Facultad de Física, Pontificia Universidad Católica de Chile, Santiago, Chile

**LPMI, Ecole Polytechnique, France*

INTRODUCTION

The fast pulsed capillary discharge has been shown to be an efficient source of radiation in the XUV range[1]. Operation at very low pressure or near vacuum results in a high temperature plasma and thus, high energy radiation with high brightness. As discharge formation at low pressure is often initiated through a sliding spark discharge along the wall, a significant amount of wall material is ablated and introduced into the capillary from the beginning of the discharge. If the capillary is operated at near vacuum, starting of the discharge requires a high voltage for initial breakdown formation, which is in conflict with the low inductance required for a short radiation pulse. In general, a wall initiated capillary discharge favors the formation of a relatively high density, low temperature plasma, whose emission spectrum is dominated by wall material species. If the aim is to operate the pulsed capillary discharge as a VUV or soft X-ray radiation source, it becomes necessary to enhance initial discharge formation on the capillary axis, as to avoid the formation of a cold plasma associated with a wall initiated discharge. On-axis discharge initiation in cylindrical geometry is a known property of transient hollow cathode discharges (THCD)[2]. In this configuration, on-axis initiation is assisted by the formation of a high energy electron beam, originating in a plasma region behind an aperture in the cathode[3]. This is due to the “*Transient Hollow Cathode Effect*”. In this work we present experimental observations of the XUV and electron beam emission properties of an ultrafast pulsed capillary discharge, which combines the features of a THCD with the inherent characteristics of the capillary discharge

EXPERIMENTAL DEVICE

The capillary is an alumina tube of 0.8 mm internal diameter, located on axis between the two electrodes. Capillaries of 10 to 30 mm length have been used in these experiments. The overall inductance of the discharge has been minimized by having the return circuit immediately outside the capillary tube wall, thus forming a shielded tube geometry. Details of the design will be published elsewhere.[4] In practice, a DC charged primary capacitor of 6 to 8 nF is used to pulse charge the storage capacitor through a self breakdown spark-gap, further reducing the stress on the dielectric of the energy storage capacitor. Long (250 to 500 ns transit time) coaxial cables of various impedances are used to connect the primary and the secondary circuits. An auxiliary discharge from a small cable gun is applied inside the hollow cathode region to enhance plasma formation. The cable gun is energized by a portion of the voltage appearing across the electrodes but taken through a length of 50 Ω cable to produce a delay of 80 to 250 ns, depending on the cable length, as to synchronize the electric breakdown with other external events.

A range of diagnostics have been developed to measure the electrical properties and the emission characteristics of the capillary discharge in the present experiment. To measure the

current local to the discharge in such a compact system, an inductive cavity current monitor has been integrated into the ground side of the electrode, functioning as a single turn Rogowskii coil. A simple resistive divider is used to measure the voltage across the exterior of the electrodes. A non-filtered wire probe is used as a charge collector and a radiation detector in the VUV to XUV region. When biased negative at 100-150V, the probe acts as a photocathode of an XRD while detecting fast electrons and collect ions. A Faraday cup located behind the anode is used to measure the current of electron beams. Spectral information is registered with a compact 1 m grazing incidence VUV spectrograph, GISVUV1-S with a large format gated microchannel plate camera to provide 3 channels of time resolved spectra with ns resolution. The time evolution of the emission source dimension is measured with a 4 channels Slit-Wire camera [5], again using the gated microchannel plate camera to provide ns time resolution. The discharge has been operated in Argon, at pressures between 50 to 700 mTorr inside the region behind the cathode.

EXPERIMENTAL RESULTS

Figure 1 shows characteristic electric signals. The plasma gun fires 120 ns after voltage is applied to the local storage capacitor. As soon as the plasma gun is fired, electron beams are detected by the XRD. This is indicated by the negative excursion in the XRD signal. The electron beam activity is maintained for ~30 ns, with an enhanced pulse just before breakdown across the capillary. At breakdown a fast rising current pulse is observed, with associated XUV emission, shown by the positive signal in the XRD detector. Typical electron beam current is in the range of tens of miliamps, as measured with a Faraday cup positioned 10 cm behind the anode. Previous studies on transient hollow cathode discharge[2] have shown that this high energy electron beam evolves into a high current but lower energy beam at the time of breakdown. This beam component contributes to the first rise of the signal on the current trace shown in Fig.1, at the start of the collapse of the voltage. Both, current and XUV radiation pulses depend on the operating pressure. Figure 2 shows voltage, current and electron beam signals at 500 mTorr. The arrow indicates the onset of the electron beams. A less than 10 ns FWHM initial current pulse is observed, with characteristic $dI/dt \sim 0.5 \cdot 10^{11} \text{ A} \cdot \text{s}^{-1}$. The XUV pulse is seen to follow the current pulse. The rate of current rise depends on the characteristics of the associated electric circuit. When a low impedance pulse charger is used, a faster characteristic $dI/dt \sim 2.5 \cdot 10^{12} \text{ A} \cdot \text{s}^{-1}$ has been achieved. At pressures below 100 mTorr the electron beam has low effect on discharge initiation and a typical delay of 40 ns is observed between the onset of the

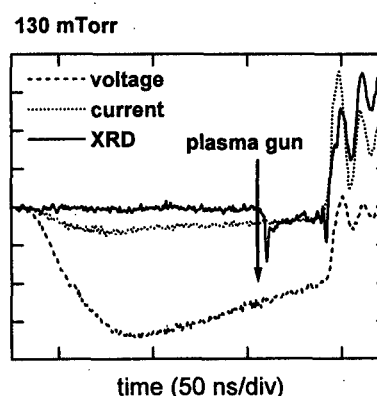


Figure 1: characteristic signals.

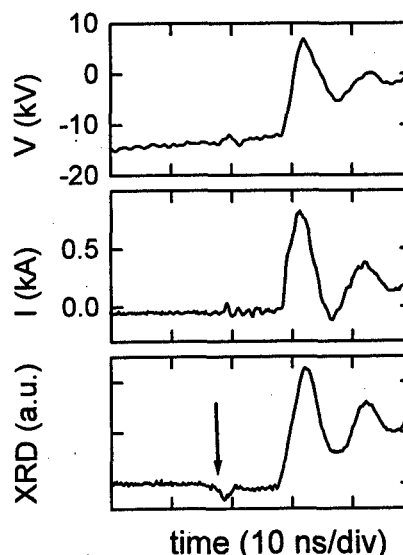


Figure 2: characteristic signals at 500 mTorr

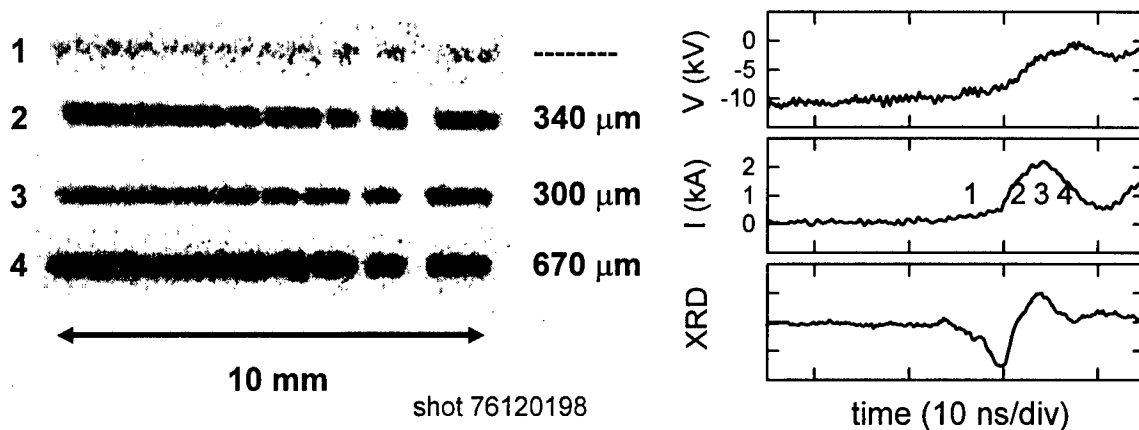


Figure 3: left, single shot 4-frame slit-wire image of the capillary discharge; right, associated signals. Numbers 1 to 4 indicate the timing of the exposures on the right. The figures in μm correspond to the measured characteristic size of the XUV emitting region. Pressure: 100 mTorr inside hollow cathode.

electron beam and the initiation of the discharge. The radiation pulse is very weak and no characteristic peak is observed. As the pressure is increased, the time delay between the onset of the electron beam and the initiation of the discharge reduces and the intensity of the radiation pulse increases. Meanwhile the absolute intensity of the first radiation pulse increases with pressure, the FWHM remains constant at 5 ns, as determined by the current pulse, thus resulting in net increase in the rate of rise of the radiation pulse. If the pressure is increased further, a point is reached when the electron beam has little effect on the initiation of the discharge. This pressure dependence of the efficiency of the electron beam in assisting discharge initiation is a characteristic feature of the hollow cathode effect

The dimension and localization of the emitting source was studied in the XUV region with the slit-wire camera, using a microchannel plate intensifier to provide ns time resolution. Using foil filters, 3 channels were set up to look at the total UV-soft X-ray radiation, the radiation longer than 20 nm and the radiation shorter than 10 nm. An example of four consecutive 3 ns exposures obtained in a single discharge is shown in Fig.4 for an operating pressure of 100 mTorr Ar in the cathode region. The images are obtained in a time interval across the emission pulse, as indicated in the associated signals. Each frame shows a 1-D image of a slit back-lit by the total XUV radiation from the capillary discharge, at 1 m distance from the source. The regions where the exposure falls off along the slit image is the result of a set of wire blocks, ranging from 0.6 mm to 25 μm . Analysis of the shadows of these blocks provides an accurate measure of the dimension of the emitting source[5]. The first frame corresponds to VUV emission detected before electric breakdown inside the capillary. At this time no plasma emission is expected from the capillary, and the resulting image is probably due to beam target emission resulting from electron beam hitting of the inner capillary wall. From the second frame onwards, the characteristic diameter of the emitting source is seen to evolve from an initial diameter of 340 μm , just before peak current, which then contracts to 300 μm at current peak and expands to 670 μm at current fall. A similar behavior is observed over the pressure range investigated.

The time evolution of the XUV emission spectrum associated with the fast radiation pulse has been preliminary investigated. For conditions similar to those reported here,

spectral emission in the 4-40 nm region, with line emission up to ArVIII, has been recorded. The main features of the spectral emission are seen to evolve in a nanosecond time scale[6].

DISCUSSION

For a controllable operation of a capillary discharge, some means of volume discharge initiation is necessary. Furthermore, a rapid initial rate of current rise is essential if the problem with wall ablation inherent to traditional capillary discharges is to be diminished. The intrinsic production of an on axis electron beam defined by the action of the HCR and the main discharge region during ionization growth avoids in principle the formation of a wall initiated discharge. Furthermore, the existence of an on-axis electron beam channel provides the initial path for conduction current away from the wall. The data presented in Fig. 1 shows that following the application of the plasma gun discharge, an electron beam is extracted from the hollow cathode region. In traditional THCD the propagation of the electron beam across the inter-electrode space favors on-axis ionization. This behavior can also be observed in these experiments. Following the emission of the first electron beam pulse, a second period of the electron beam activity is observed, as shown in Fig. 1. During this time local conditions for ionization growth are created inside the capillary, under the assistance of the electron beams. The time resolved slit-wire measurements shown in Fig. 2 are a good indication that the discharge inside the capillary develops initially in a region around the axis. At current rise the characteristic diameter of the XUV emitting region is seen to contract, which can be attributed to on-axis pinching of the current carrying plasma. On-axis pinching requires a rate of current rise faster than the characteristic time scale for ohmic heating. Under these conditions, a hot radiating plasma is produced during current rise, which is detached from the capillary wall. At current fall, the hot capillary plasma can not longer be confined on axis and expands reaching the inner capillary wall. Wall ablation by the initially hot capillary plasma results in fast cooling due to radial heat transport.

CONCLUSIONS

A fast capillary discharge with on-axis initial ionization due to hollow cathode emitted electron beams has been demonstrated. The initial rate of current rise is fast enough to induce on-axis pinching of the discharge. Under this conditions a fast XUV radiation pulse, with nanosecond time scale is produce. Further measurements are being performed, in order characterize in detail the time evolution and spectral content of the XUV emission.

ACKNOWLEDGMENTS

This work has been partially funded by FONDECYT grant No. 8980011 and a CNRS-CONICYT collaboration project.

REFERENCES

- [1]R.A. McCorkle, *Appl. Phys.* **A26**, 261 (1981)
- [2]P. Choi et al., *IEEE Trans. Plasma Sci.* **15**, 428 (1987)
- [3]M. Favre et al., *IEEE Trans. Plasma Sci.* **20**, 20 (1992)
- [4]P. Choi and M. Favre, *Rev. Sci. Inst.*, accepted for publication (1998)
- [5]C. Dumitrescu-Zoita, Ph.D. Thesis, Université de Paris Sud (1996)
- [6]P. Choi et al., 4th Int. Dense Z-pinch Conference (Vancouver, Canada), AIP Conf. Proceedings, p. 353, 1997

IMPLODING PLASMA INVESTIGATIONS IN THE FRAME OF THE “LINER - CONVERTOR” SCHEME.

Yu.L. Bakshaev, A.V. Bartov, P.I. Blinov, A.S. Chernenko, S.A. Dan'ko,
Yu.G. Kalinin, A.S. Kingsep, V.D. Korolev, V.I. Kosarev,* A.I. Lobanov,*
V.I. Mizhiritskii, L.I. Rudakov, A.Yu. Shashkov.

Russian Research Center "Kurchatov Institute", 123182 Moscow, Russia

**) Moscow Institute of Physics and Technology, Dolgoprudnyi, Moscow Region, Russia*

The report presented is a part of the programm aimed to creation the powerful X-ray pulse source with the quanta energy in the range of dozen KeV, using the “liner-convertor” scheme. The key point of this scheme is the function separation of the energy carrier and radiator between plasma region with different parameters. The electrons of the weak radiative (hydrogenic) plasma heated due to the magnetic implosion transport their energy onto the highly radiative convertor (placed on the edge of pinch) via the longitudinal electron heat conductivity. Theory and computer simulation [1,2] predict this scheme has to be more energetically efficient as compared to the direct conversion of the magnetic energy into the X-ray pulse. However, contradictory requirements to the plasma parametrs necessary for the heat conductivity scheme was implemented, prevent its realization. In fact, at the first stage, energy of the imploding plasma is concentrated in the kinetic energy of the shell. In the next phase, as a result of implosion, it becomes transformed into the ion heat, and then, electrons become to be heated through the Coulomb collisions and adiabatic compression. Estimations show that in low Z plasmas (H_2 , He) the process of the heat transfer from ions to electrons is the most slow stage limiting the efficiency of the whole scheme.

Electron heating may be enhanced by choosing higher Z values, it results, however, in decreasing the heat conductivity. As a consequence, the heat flux cannot provide the transport of proper energy amount during the time of Z -pinch being compressed. Besides, Z -pinches or liners produced of the high Z plasmas form very thin current-carrying shell during implosion, which is very unstable [3,4]. The losses due to the soft radiation increase, too.

These contradictions may be overcome by creating Z -pinches with some complicated structures. To wit, one have to separate in space regions of the efficient electron-ion energetic exchange and regions with high electron heat conductivity. One way to do that is the following. Z -pinch can consist of two co-axial cylinders. Inner cylinder has to consist of the substance with “intermediate” Z (e.g., Ar) while the outer has to be produced of low- Z gases (H_2 , He). While implosion, the electron-ion energy exchange will occur in the Ar plasma, with the subsequent transport of the electron heat along the outer shell which electron heat conductivity is much greater. Such a Z -pinch construction have to be more stable due to the absence of the Hall- and the reduction of the Rayleigh-Taylor instabilities conditioned by the low Z values and the large thickness of plasma shell, respectively.

Taking these considerations into account, last time we paid an especial attention to the magnetic compression of the thick *He* jet in our study of stability of liner implosion. These experiments were performed on "S-300" installation [5] with the current through the liner load up to 3.5 MA. As a liner, we used cylindrical *He* jet with outer diameter ~ 4 cm produced by using a pulse-driven valve and an annular supersonic nozzle. In combination with apparatus registering parameters of power pulse we used the following diagnostics: i) photographs in visible light region, both with streak and with frame image converter cameras; ii) photographs in the region of soft X-ray radiation with frame image converter cameras; iii) registration of the radiation pulses by a set of vacuum and semiconductor X-ray diodes shielded with various filters, and iv) convex-mica crystal X-ray spectrograph with the two-dimensional spatial resolution [6]. Some examples of streak and frame camera pictures of its compression are presented in Fig. 1a and 1b, respectively. It is important to pay attention to both symmetric form and good reproducibility of the picture presenting the dynamic of the *He* liner implosion, which can serve as an evidence of its stability. The same fact is illustrated by *R-t* diagrams of 5 repeated experiments performed in the identical conditions (Fig. 2). In these experiments the maximal schell velocity of $5 \cdot 10^7$ cm/s was achieved.

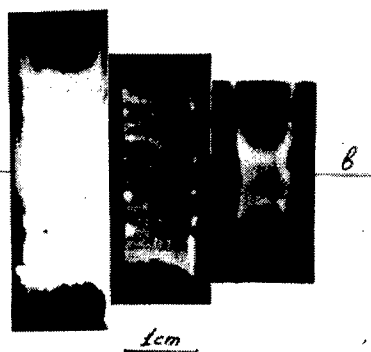
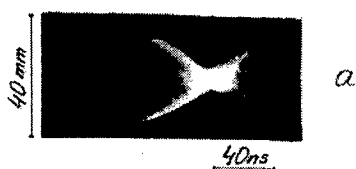


Fig.1. Optical streak (a) and frame (b) camera pictures of *He* liner compression.



Fig.2. *R-t* diagrams of 5 repeated *He* liner experiments.

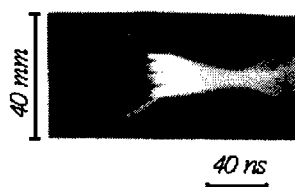


Fig.3. Streak camera pictures of *He* liner with fibers compression.

Another way of heterogeneous pinch construction is based on the production of "intermediate" *Z* plasmas by means of evaporation of thin filaments of proper chemical composition. These filament have to be stretched parallel to the axis and form a cylindrical surface of the radius several times less than the initial radius of the gaseous column. Evaporation would be brought about by the front of the heat wave which, in turn, would be generated in the light gas by the shock wave resulting from the magnetic piston. Some preliminary estimates show that taking the filaments as thin as $1-3 \mu$ one obtains the plasma expansion about $1 \div 2$ mm during the time ~ 10 ns. Thus, placing the filaments in an array dense enough one can produce a continuous plasma cylinder with the necessary Z_{eff} .

It is important to note that such a manner of plasma formation is free from instabilities accompanying the current flow, as well as the possible gases mixing during the heterogeneous gaseous structure creation.

First experiments on modelling of processes in heterogeneous pinches have been also brought about. Plasma, with moderately high Z value, was produced by evaporation of thin glass fibers when coming to them the temperature wave from the He plasma by compression the liner. Initially these fibers were disposed along the circumference near the liner axis. Streak camera picture of compressing of the He liner with fibers is given on the Fig. 3. The effect of adding the impurities with high Z value on the heating of electrons and on the heat conductivity was determined by registration of spectral lines of the $[He]$ -like chlorine ions placed at the cathode end of liner gap. Fig. 4 is one of typical spectrograms. The X-ray spectra

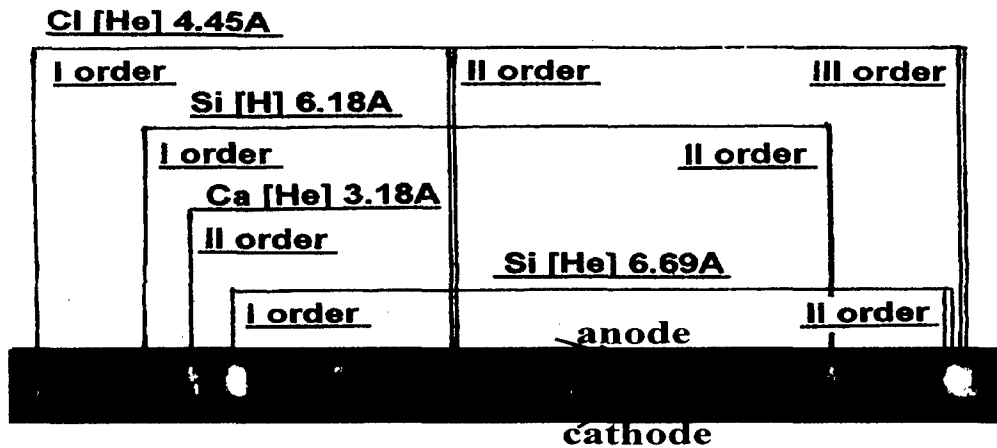


Fig.4. X-ray spectrum of He liner with fibers and $NaCl$ converter.

reveal a series of lines of $[H]$ - and $[He]$ -like ions of the elements being components of the glass (Al, Si, Ca, and others) with the excitation energies up to 4 kV. One can see here the resonant line of the $[He]$ -like chlorine looking like the 3 millimeter-sized bright spot on the cathode. In the absence of fibers the intensity of this line is less several times, that is an evidence of increasing the neat conductivity in the presence of impurities.

The realization of the “liner-converto” scheme can be complicated by the heat conductivity decrease resulting from the penetration of the current-driven magnetic field into the plasma due to the development of instabilities. Numerical modelling of these phenomena was one of the basic problems of 2.5-D code aimed to our program. Our simulations were based on the single-fluid, 2-temperature MHD plasma model including the radiation transport. Its detailed description, as well as description of numerical methods were presented in [7].

In particular, compression of a solid D_2 pinch was simulated, with a mass $m = 50 \mu g$, initial radius $R_0 = 2$ cm, length $l = 2$ cm. The maximal current value was $I_0 = 3$ MA, and pulse duration $\tau = 100$ ns. The initial boundary profile was taken, e.g., as follows:

$$R = R_0 + 2.5 \times 10^{-2} R_0 \cos(4\pi z/l)$$

The most important result of these simulations was the following one: despite the development of instabilities on the pinch surface, magnetic field was “locked” in the skin layer, without a penetration into the plasma depth (see Fig. 5).

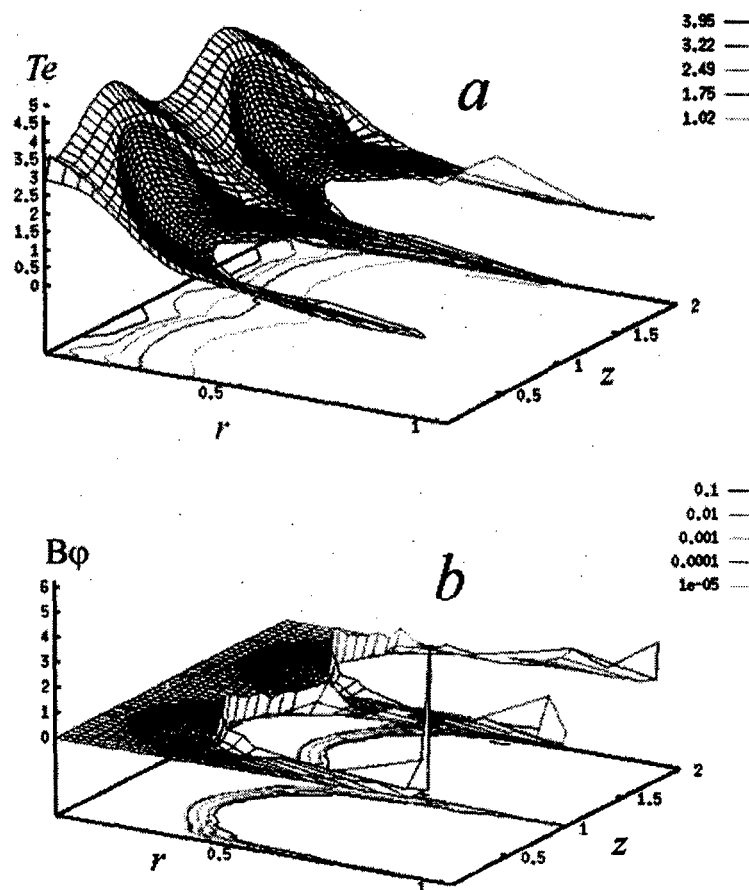


Fig. 5. Results of simulations: a) electron temperature, b) magnetic field profile.

CONCLUSION. Thus, our experimental investigations and computer simulations confirm that the scheme “heterogeneous Z-pinch – converter” seems to be promising in respect of the powerful X-ray sources creation.

ACKNOWLEDGMENTS. The authors are grateful to the Russian Foundation for Basic Researches (grants 98-02-17616 and 98-01-00225) and to the Russian Ministry of Science and Technology for financial support of this research.

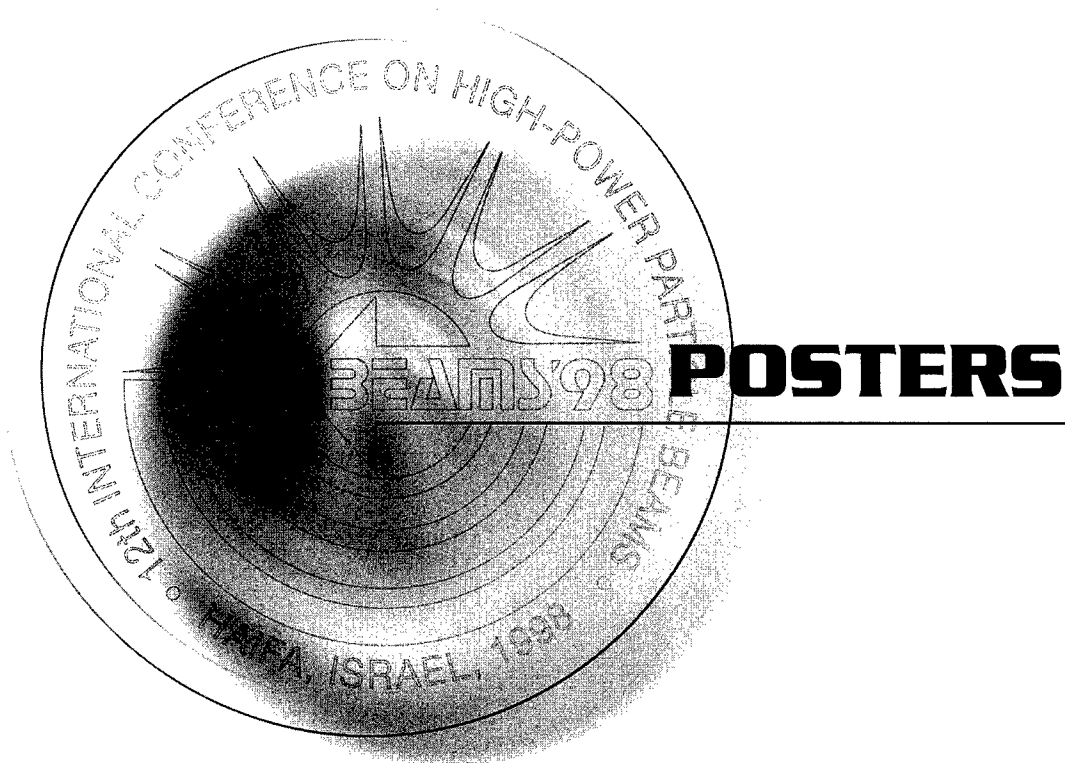
REFERENCES

1. Rudakov L.I. et al., *JETP Letters*, 1997, 65, 523.
2. Rudakov L.I., *Proceedings of 4-th Intern. Conf. on Dense Z-pinch, Vancouver, 1997*, p. 183.
3. Chernenko A.S. et al. *Beams '96 Conf. Proceedings, Prague, 1996*, p. 154.
4. Bakshaev Yu.L. et al., *Proceedings of 4-th Intern. Conf. on Dense Z-pinch, Vancouver, 1997*, p. 149.
5. Bakshaev Yu.L. et al., *Proc. of the 18th Symp. on Plasma Physics and the Technology, Prague, 1997*, p. 45.
6. Dan'ko S.A., *This Conf. Proceedings*, report 0045.
7. Kingsep A.S. et al. *Plasma Physics Reports*, 1997, 23, 879.



BEAMS'98

12th INTERNATIONAL CONFERENCE
ON HIGH-POWER PARTICLE BEAMS



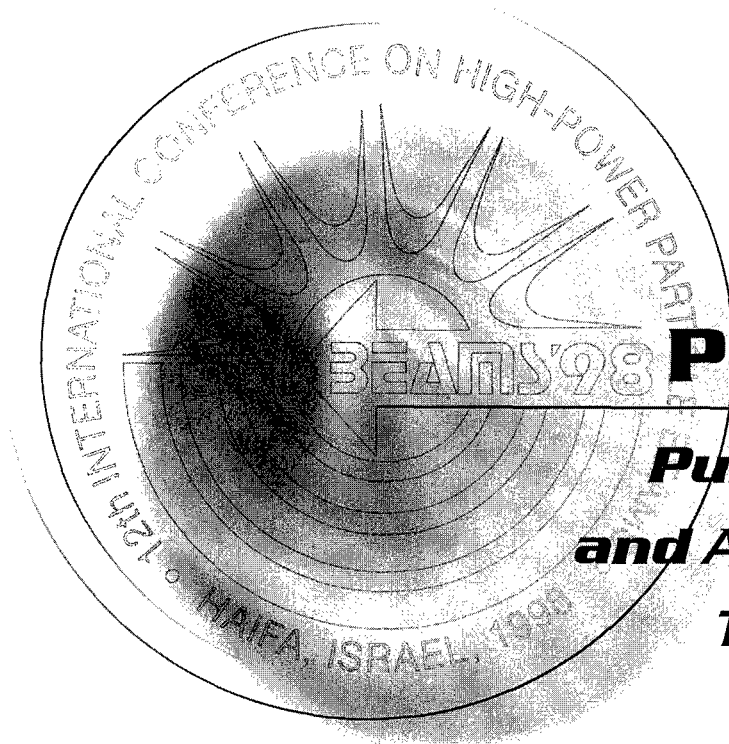
Vol. I

Proceedings



BEAMS'98

12th INTERNATIONAL CONFERENCE
ON HIGH-POWER PARTICLE BEAMS



POSTERS

***Pulsed Power
and Accelerator
Technology***

Vol. I

Spectroscopic Investigations of the Magnetic Field Evolution and Plasma Flow in a Microsecond POS

R. Arad, K. Tsigutkin, Yu.V. Ralchenko, A. Fruchtmann, N. Chakrabarti, and Y. Maron

Weizmann Institute of Science, Rehovot, Israel

ABSTRACT

Spatially resolved measurements in a planar microsecond POS, using spectroscopy of dopants, in the plasma, are presented. The magnetic field evolution, determined from Zeeman splitting, is mapped in 2D and found to propagate axially at an average velocity of 3.3×10^7 cm/s. The axial velocities of various ions are determined and found to be less than the propagation velocity of the magnetic field. The electron density determined from the temporal behavior of various spectral lines is found to drop after the magnetic field reaches 60% of its peak value.

INTRODUCTION

In the last decade the ability of Plasma Opening Switches (POS) [1,2], with conduction times of the order of $1 \mu\text{s}$, to generate MA current pulses with rise time of 80-100 ns was demonstrated. Furthermore, microsecond POS's were found to have a promising future as opening switches in inductive energy storage systems. Still, there are open questions on the mechanisms responsible for the observed electron density drop [3] which is believed to cause the opening of the switch. Also, significant losses in coupling the POS to various loads were found [4].

The interaction between the plasma and the magnetic field, generated by the current, may manifest itself in a variety of ways. A few competing processes can lead to either fast magnetic field penetration into the plasma with relatively low ion velocities, or on the other hand, if the field does not penetrate into the plasma bulk, it is expected to accelerate the plasma at the boundary between the plasma and magnetic field to velocities of the order of the Alfvén velocity. These two extreme cases are expected to result in different opening mechanisms of the POS and, thus, understanding this interaction is essential

for understanding and improving the opening of the switch and its coupling to various loads.

EXPERIMENTAL SETUP

We are studying a planar geometry POS whose electrodes are 14 cm wide and 2.6 cm apart. A region 9 cm in length is prefilled with plasma using two flashboard plasma sources placed 3 cm above the anode. In the POS region, the electrodes are highly transparent and consist of 0.1-cm-diameter wires separated by 1.4 cm. The upstream and downstream currents are measured by self-integrating Rogowski coils.

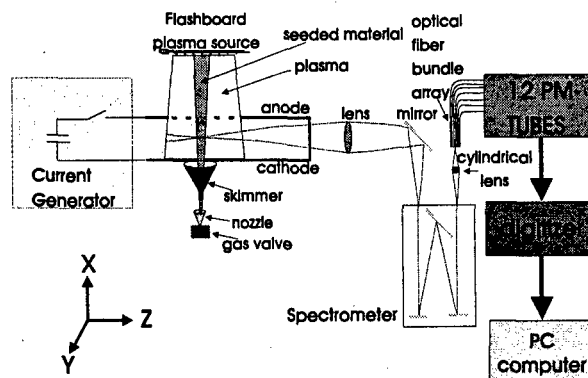


Figure 1: The inter-electrode region is prefilled with plasma generated using a flashboard source and injected through the highly transparent anode. A fast gas valve, a nozzle, and a skimmer are used to inject a molecular beam for locally doping the plasma with various species. Light emitted from the doped column is studied spectroscopically.

The two flashboards are driven by a single $2.8 \mu\text{F}$ capacitor and each consists of eight chains of 8 copper pieces separated by 0.05 cm gaps on a G-10 insulator. The flashboard is operated $\approx 1.2 \mu\text{s}$ before the high-current pulse of the POS is applied, which allows the flashboard plasma to propagate and fill the anode-cathode gap.

The following coordinates are defined: $X=0$ is the cathode surface, $Y=0$ is the center of the

electrodes, and $Z=0$ is the generator side edge of the opening in the anode.

The spectroscopic diagnostic system [5] consists of a 1-meter spectrometer for the range 2000-7500 Å, equipped with a 2400 grooves/mm grating. Light is imaged onto the spectrometer using a lens and mirrors along one of three possible lines of sight. A cylindrical lens images the light at the output of the spectrometer onto a rectangular fiber-bundle array, that transmits the light to a set of photomultiplier-tubes. The output from the 12 photomultipliers is recorded by a multi-channel digitizer, which gives the time dependent spectral line profile in a single discharge.

In order to obtain spectroscopic measurements that are spatially resolved in 3D, we are locally doping the plasma with various species whose emission is studied [6]. For doping gaseous materials a fast gas valve, a nozzle and a skimmer are used to inject a gas beam with FWHM ≈ 1 -2 cm and a gas density of 1 - 2×10^{14} cm $^{-3}$. The gas doping arrangement is mounted below the cathode. Alternatively, for doping solid materials such as lithium and boron, we generate a discharge on an epoxy resin containing the desired material 2 cm below the cathode.

RESULTS

In these measurements a current of 160 kA is conducted by the plasma during 400 ns before opening occurs and the current is diverted to a short-circuit load within 90 ns. Initially the plasma parameters prior to the POS operation were determined. The electron density was determined from Stark broadening of hydrogen lines and found to vary from 3×10^{14} cm $^{-3}$ near the cathode to 7×10^{14} cm $^{-3}$ near the anode at the time the POS current is applied. The electron temperature was determined both from the ionization time of various doped species and from the absolute light intensities of these doped materials. Here we used the absolute gas density measured using a special array of ionization probes [6]. Both these methods rely on collisional-radiative (CR) modeling [7] for all the species studied, and showed an electron temperature of 6 ± 1 eV. The plasma composition was determined from the absolute light intensities of the different ions and CR modeling. The

density of hydrogen, CII, CIII, CIV, and CV ions 1 cm from the cathode was found to be 2×10^{13} , 4×10^{12} , 4×10^{12} , 2×10^{13} , 2×10^{12} cm $^{-3}$, respectively. The density of other impurities such as oxygen, iron, and nickel was found to be negligible. Near the anode the density of these ions were found to be approximately three times higher. Using the absolute density of the various ions we were able to determine the proton density from the requirement of charge neutrality, and it is found to be $(3.5 \pm 0.7) \times 10^{14}$ cm $^{-3}$ in the entire A-K gap. Knowledge of the plasma composition is highly important for understanding the evolution of the electron density that is discussed below.

Using our doping technique we determined the magnetic field spatial and temporal distribution from the Zeeman splitting of the HeI $3d(^1D)$ - $2p(^1P^0)$ line-emission. To this end, we observed the 6678-Å spectral line along the direction of the magnetic field (along the "Y" direction, see Figure 1), thus only observing the line σ components. The line width of the HeI line without the Zeeman splitting is dominated by the instrumental broadening since the Doppler broadening remains small throughout the pulse. The observed helium line profiles are fitted by two Gaussians (one for each of the σ components). The splitting can be resolved for magnetic fields exceeding 0.5 T though measurements of weaker magnetic fields are also possible.

Measurements were carried out at different positions in the X-Z plane. At each position, the magnetic field was determined as a function of time. For different times, a map was constructed of $B(x,z,t)$ which includes the measured points and contours of constant magnetic field. Figure 2 shows the magnetic field maps at $t=100$, 150, 230, and 300 ns. At $t=150$ ns the magnetic field is seen to penetrate a little faster near the cathode, while at other times this phenomenon is not seen. The width of the current-carrying channel is seen to increase as a function of time from 2-3 cm at $t=100$ ns to the entire plasma length ($\Delta Z \approx 10$ cm) at $t=230$ ns. Here, the electron skin depth, ion skin depth and the classical diffusion length are 0.02, 1.2, and 0.2 cm, respectively, and all are smaller than the observed current channel width. As an example of the broadening of the current channel, the position at which $B=0.2$ T propagates axially at a velocity of $(5.0 \pm 0.5) \times 10^7$

cm/s while the value of $B=0.6$ T propagates at a velocity of $(3.3\pm0.3)\times10^7$ cm/s. At $t>230$ ns a region devoid of current forms at the generator side edge of the plasma. It is found that at this time in this region the electron density dropped to $4\pm2\times10^{13}$ cm $^{-3}$.

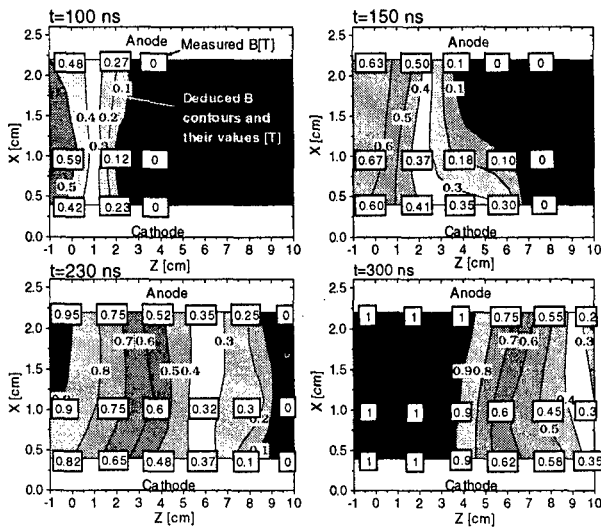


Figure 2: Four two-dimensional maps of the magnetic field at different times during the POS operation. The numbers in rectangles represent the actual measurements and the smaller numbers represent contours of equal magnetic field. The anode and cathode are at $X=2.6$ and $X=0$, respectively. The spatial resolution is ±0.5 cm in the Z direction and ±0.05 cm in the X direction. The error of the magnetic field is ±0.15 T for $B<0.4$ T and ±0.07 for $B>0.5$ T.

The local axial ion velocities during the POS high-current pulse were determined from Doppler shifts of lines of various species injected into the plasma. In this way the axial velocities of BII, BIII, LiII, HeII, and ArIII were determined. Figure 3 shows the time-dependent axial velocity of HeII at five axial positions. The traces are shown only for the periods during which the line intensity is high enough to yield a satisfactory accuracy. The velocities are seen to rise in time due to the acceleration under the gradient of the magnetic field. The velocities at larger- z locations rise to higher values since the velocity-rise at these locations occurs at later times when the POS current is higher generating stronger magnetic fields.

Knowledge of the velocity of protons, that dominate the plasma composition, is essential for understanding the variations of the electron

density. To measure the axial proton velocity spectroscopically we used the resonant charge-exchange between accelerated protons and hydrogen atoms and observed the H_α line along the z -axis. Since the rate for charge-exchange depends weakly on the proton velocity, the tail of the H_α line reflects the velocity distribution of the protons. The H_α line showed a continuous distribution of proton velocities with a peak probability at $1.5\pm0.2\times10^7$ cm/s and some contribution up to a velocity of 3.5×10^7 cm/s. No negative velocities (towards the generator) were observed.

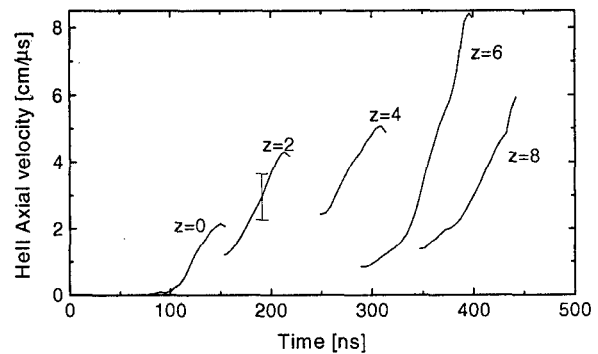


Figure 3: Spatially resolved measurements of the HeII axial velocities near the cathode at five different axial positions obtained from the Doppler shift of the $n=4$ to $n=3$ line. The times shown are relative to the beginning of the POS current pulse. The error bar shown indicates the typical uncertainty. The spatial resolution along the line of sight is ≈ 1.5 cm.

We also studied the scaling of the ion velocities with the charge-to-mass ratio of the ions. The ions that are heavier than protons, such as HeII, BII, BIII and LiII, showed velocities between $4\text{--}12\times10^6$ cm/s with scaling that is consistent with linear scaling (within the limits of the accuracy of the measurement). The much heavier ArIII ions showed negligible velocities at all times. These observed velocities together with spatially integrated velocities of carbon ions show that these heavier ions exhibit small (<1.5 cm) axial motion during the POS operation. However, the velocities of these heavier ions towards the electrodes were found to be approximately equal to the axial velocities of these ions, implying that the ion motion in the x -direction affects the evolution of the plasma density.

The evolution of the electron density and temperature was studied during the POS operation by comparing the measured absolute line intensities to CR calculations. To this end, we measured the BIII 2066 Å line (2p-2s), which is sensitive mainly to the electron density together, with the BIII 2077 Å line (4f-3d), that is sensitive both to the electron temperature and density.

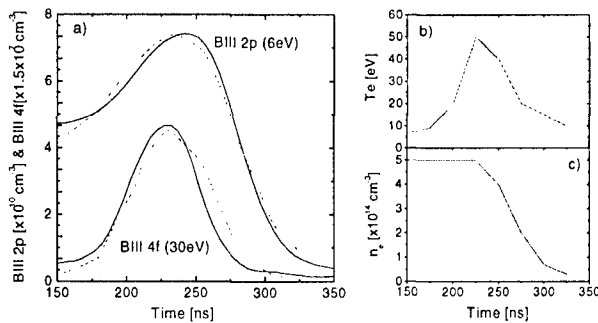


Figure 4(a) The time behavior of the upper level populations of the BIII 2p and 4f levels as a function of time at $X=1.0$ cm and $Z=3.7$ cm. The solid curves show the experimental data and the dashed curves represent the output of the CR modeling for the time behavior of n_e and T_e given in (b) and (c). Boron is injected into the POS region using a small single gap flashboard positioned beneath the cathode.

The solid lines in figure 4(a) show the time behavior of these two lines in the middle of the plasma. The light intensity of both lines was found to decrease after $t=250$ ns. This drop could not occur due to a drop in the BIII density arising from either ionization of BIII or flow of these ions indicating that the electron density must drop at this time since the 2p level population is not sensitive to variations in T_e . We modeled the variation of both these lines with our CR code (dashed curve in figure 4a). The time behavior of n_e and T_e found to best fit the experimental data are shown in figure 4(b) and (c). The rise and drop of T_e is consistent with that determined from the increase of the light intensities of HeI, HeII, CIII, CIV, and CV. The electron density is shown to drop to a value $<5 \times 10^{13}$ cm⁻³.

Similar results were also obtained near the anode and cathode but with slightly different timing. The drop of the electron density and temperature was found to be 20 ± 10 ns later at $X=0.4$ cm than at $X=1.0$ cm and 40 ± 15 ns later at

$X=2.2$ cm. This indicates that the drop in n_e propagates from the middle of the anode-cathode gap towards both electrodes at a velocity of $4 \pm 2 \times 10^7$ cm/s. Since protons make up most of the plasma, the timing of the drop of the electron density and the low axial velocities of the protons indicate that protons flow towards both electrodes. The drop in n_e also propagates axially (along the z-direction) at a velocity of $(3.3 \pm 0.3) \times 10^7$ cm/s, as is found from the temporal evolution of light intensities at different z-positions. This velocity is equal to the propagation velocity of the magnetic field and at all positions the start of the drop coincides with a magnetic field amplitude of 0.6 ± 0.1 T.

The presence of the magnetic field in the plasma prior to the electron density drop is crucial for understanding the mechanism of ion acceleration. It seems that as the magnetic field penetrates into the plasma in a form that resembles a one-dimensional piston (see figure 2), the protons are accelerated to axial velocities which are lower than the propagation velocity of the field. This is followed by acceleration towards the electrodes and a density drop that begins in about the middle of the anode-cathode gap. We are trying to understand the ion dynamics that is responsible for the observed drop of n_e . We examine various mechanisms for ion acceleration in the axial direction and/or towards the electrodes. Also, the relation between the density drop and the opening of the switch is currently being studied. Future research will also concentrate on the proton flow downstream towards the load in an attempt to understand its effect on the coupling to various loads.

REFERENCES

- [1] D.D. Hinshelwood, et.al., Appl. Phys. Lett. **49** (24), 1635 (1986).
- [2] V.M. Bystriskii, et.al., IEEE trans. Plasma Sci. **19** (4), 607 (1991).
- [3] D. Hinshelwood, et.al., Phys. Rev. Lett. **68** (24), 3567 (1992).
- [4] B.V. Weber, et.al., Proc. 10th Int. Conf High Power Beams, (Prague 96), p121.
- [5] R. Arad, et.al., Rev. Sci. Instr. **63** (10), 5127 (1992).
- [6] R. Arad, L. Ding, and Y. Maron, Rev. Sci. Instr. **69**(3), 1529 (1998).
- [7] M.E. Foord, Y. Maron, and E. Sarid, J. Appl. Phys. **68** (10), 5016 (1990).

PULSED X-RAY SOURCES FOR RESEARCH AND INDUSTRIAL APPLICATIONS

A.Radu, D.Martin, V.Zoita, M.Toma, E.Iliescu, C.Oproiu, S.Marghitu, M.Radoiu, V.Bestea,
¹ *National Institute for Laser, Plasma and Radiation Physics (NILPRP), P.O.Box MG-36, #1
Atomistilor St., 76900 Bucharest, Romania*

1. INTRODUCTION

At the present time, research on the production of short X-ray pulses is still a very active and attractive domain. The domains of application of such pulses are extremely wide and, in addition to conventional industrial use in radiography, cover many topics of scientific and industrial research [1]. Following the well-known configuration of the pulsed direct discharge in vacuum devices, a pulsed field emission X-ray source (PEFXS) was developed at the National Institute for Laser, Plasma and Radiation Physics-Bucharest. PEFXS consists of three important subassemblies: a low impedance X-ray tube (XRT), a high voltage pulse generator (HVPG) and a generator control system (GCS). XRT may be driven by two types of HVPG: a single pulse Marx generator (SPMG) and a repetitive pulse generator (RPG).

The system configuration with SPMG is used at laboratory-scale for research in the field of material science while the low cost and low complexity system configuration with RPG, will be developed for industrial applications. SPMG was designed to supply also other devices, either directly or through a Blumlein pulse forming line, such as plasma discharge chambers and electron beam tubes. Emitted doses were optimised by anode-cathode high voltage level, anode-cathode space and anode-exit window distance.

2. X-RAY TUBE (XRT)

XRT (335 mm length and 145 mm diameter) is a diode tube of demountable type consisting of a high voltage isolator, a stainless steel chamber with a thin aluminium window for X-ray output and a vacuum pipe branched to a vacuum system, a conical shaped tungsten anode and a bored multiple-sheet tantalum cathode. This solution is not expensive and offers the possibility to change the geometrical configuration of the anode-cathode arrangement. Fig. 1 shows the XRT photograph.

3. SINGLE PULSE MARX GENERATOR (SPMG)

SPMG is a modified two-stage Marx generator. The electrical schematics of SPMG is shown in Fig. 2 and its photograph in Fig. 3. The stage 1 is formed of high voltage switch HVS-1 and the capacitors C1 and C2. The stage 2 consists of switch HVS-2 and capacitors C3 and C4.

SPMG has two working regimes:

- the charging regime when C1-C4 are parallel connected and they are charged through R1-R4 resistors from a double polarity high voltage source (DPHVS of ± 40 kV);
- the discharging regime, when a fast negative pulse of 80 kV, 5 ns rise time and less than 10 ns delays, produced by the master spark gap switch (SGS), triggers the HVS-1 and HVS-2 switches, and so C1-C4 are connected in series.

SGSTS (spark gap switch triggering system) generates triggering pulses (40 kV amplitude, 150 ns duration and less than 30 ns rise-time) for SGS. RC1, RC2 and RC3 are Rogowsky coils. The resistors Rp1 and Rp2 are used to connect to the ground the polarisation electrodes of HVS1 and HVS2. The high voltage resistors R1-R4 are of special design, acting as pure resistance during the charging time and as inductive reactances during the discharging time in order to separate the SPMG from the power supply. C1-C4 are of Maxwell type and have the following characteristics: $C = 0.2 \mu\text{F}$; $L = 0.017 \div 0.025 \mu\text{H}$; $U = 40 \text{ kV}$. The HVS1 and HVS2 high-voltage switches, designed at the NILPRP, are three electrodes switches, which operate in high pressure gas (5.25 bar). These switches are cylindrical, with 80 mm length and 150 mm diameter. Their performances are: 40 kV working voltage, 100 kA maximum pulse current; 500 J maximum transferred energy; 40 nH proper inductance; 50, 000 pulses-estimated lifetime.

SPMG was tested under different conditions. The first were the short-circuit tests. As a load cooper strips and adjustable spark gaps were used. In these conditions the best triggering voltages and working pressures for HVS-1 and HVS-2 and the value of the SPMG series inductance have been determined. For an output pulse of 80 kV, the current amplitude was 13.8 kA and pulse width 1 μs . The series inductance which results from these data is 1.3 μH .

XRT was coupled to SPMG by a high voltage coaxial cable. Each pulse of 80 kV has produced an X-ray pulse of about 2 R at 5 cm from the output window. The measured focal spot diameter of X-ray beam is up to 2 mm.

4. REPETITIVE PULSE GENERATOR (RPG)

RPG consists of a high voltage rectifier (20 kV, 20 mA), a charging resistor, a charging capacitor (20 nF), a hydrogen thyratron (25 kV, 1000 A), a pulse forming line (PFL) and a pulse transformer (PT). PFL consists of two high voltage coaxial cables (50 Ω characteristic impedance and 10 m length) with their inputs coupled in parallel and their outputs in series. PT has a C-type ferrite core with 120 cm² overall cross-section. Its windings are made of a high voltage flexible copper conductor on an adequate insulated framework. PT is housed in a Plexiglas tank filled with high quality transformer oil. RPG generates pulses with the maximum peak output voltage of 300 kV, the rise time less than 100 ns and the maximum repetition rate of 100 Hz. The optimum amplitude voltage which provides up to 14 mR/pulse at 10 cm from the XRT exit window was 230 kV. Fig. 4 gives the dependence of the dose/pulse (R/pulse) versus high voltage applied on XRT. Fig. 5 shows the radiography of steel objects in the thickness range 0.5-3 mm which were obtained using RPG.

5. GENERATOR CONTROL SYSTEM (GCS)

GCS was designed primarily to control the pulse high voltage level applied to XRT, the X-ray pulses number and the pulse repetition rate in the case of RPG type use, with the necessities interlocking and warning signals. In the case of SPMG type use, GCS is detached from SPMG by a total galvanic separation barrier which consists of a fiber optic cable assembly for analog signals and of special low-stray capacitance transformers for logical-command states and mains supply. Also, a delay of a few second is introduced between the start pulse command and the actual Marx discharging pulse to avoid operator direct contact to the keys. Normally, the pulse start command are made automatically. These facilities ensure the protection of people and devices against high voltage-high frequency destructive interferences.

6. CONCLUSIONS

X-ray diodes driven by high voltage pulsed power supplies still offer a very attractive solution for the realisation of intense sources at laboratory scale. Also, the application of pulse X-ray generators in industry, medicine and biology have high benefits because of their higher quality picture compared to continuous X-radiation.

The main feature of our X-ray sources using RPG is the use of a combined pulse forming system consisting of a coaxial cable double forming line and a capacitor. This solution offers the advantage that the high voltage appears only during the pulse time and only between the pulse transformer output and X-ray tube, thus reducing the high voltage problems. Also, this solution permits a separate adjusting of the pulse rise time and length.

References

1. J.M.Pouvesle, C. Cachoncinlle, R. Viladrosa, E. Robert, A. Khacef, Nucl. Instr. and Meth. in Phys. Res. B113 (1996) 134-140

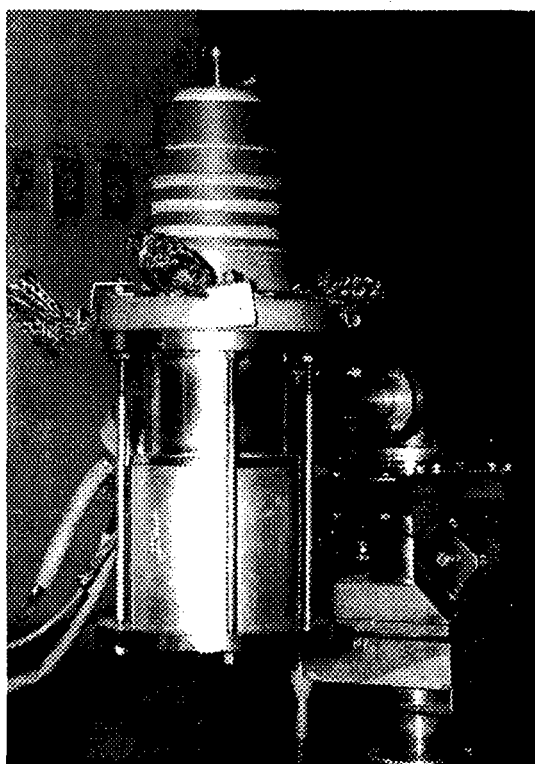


Fig. 1 X-ray tube (XRT)

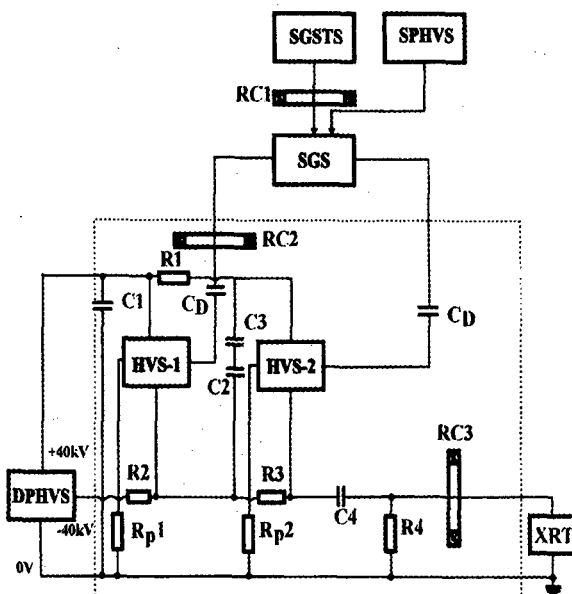


Fig.2 Electrical schematics of SPMG

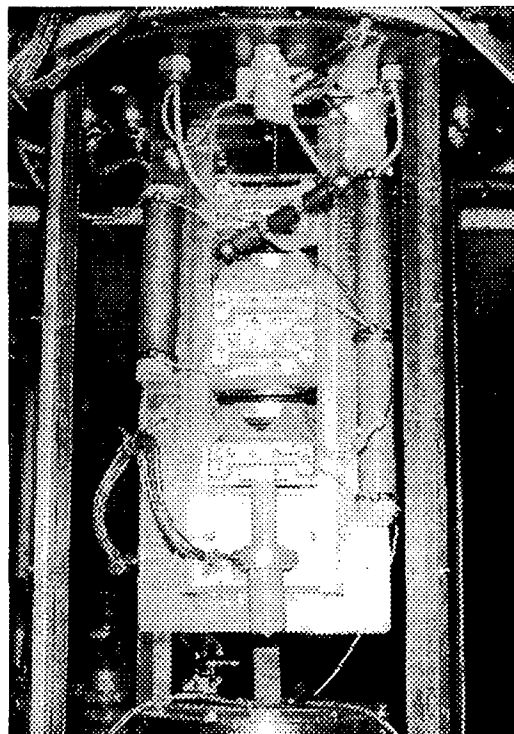


Fig. 3 Single pulse Marx generator

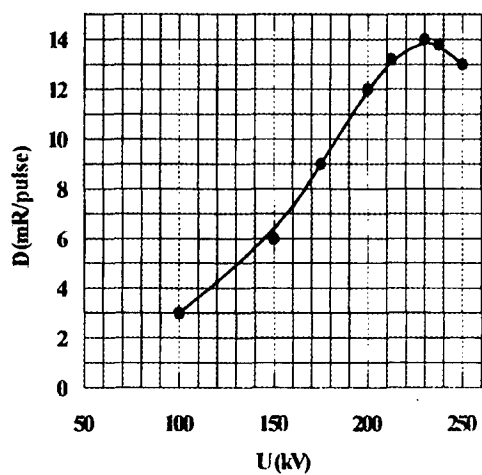


Fig. 4 The dependence of dose/pulse versus high voltage applied on XRT

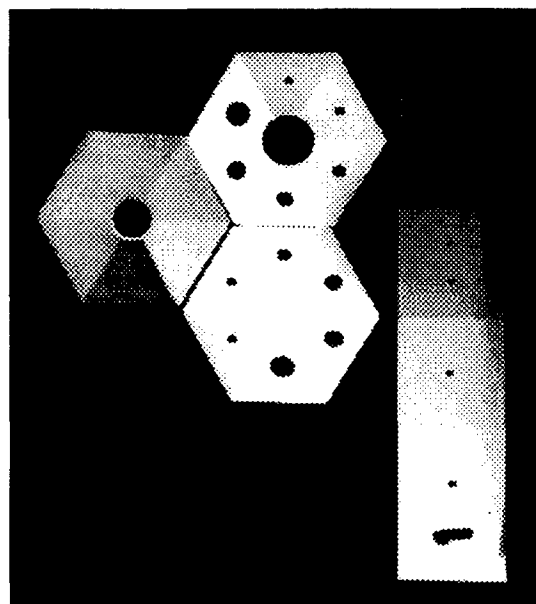


Fig. 5 Radiography of steel objects (0.5-3mm thickness range)

TO THE THEORY OF A PLASMA FILLED ION DIODE

L.I.Rudakov^{1*} and A.S.Chuvatin²

¹ *RRC Kurchatov Institute, 123182 Moscow, Russia*

* current address: Advanced Power Technologies, Inc., Washington, DC 20037, USA

² *Laboratoire de Physique des Milieux Ionisés, Laboratoire du CNRS,
Ecole Polytechnique, 91128 Palaiseau, France*

Abstract

Theoretical model of a low density plasma diode is proposed. At the stage when the magnetic field of the diode current magnetizes the plasma electrons the Hall electric field accelerates the ions towards the cathode. It is shown that the process of plasma rarefaction in this case appears as a plasma erosion shock wave propagating through the magnetized quasineutral plasma.

Introduction

In a conventional vacuum diode the electron current through the anode-cathode gap dominates. In order to increase the respective value of the ion current, the electrons should be magnetized. When the interelectrode gap is initially prefilled with low-density plasma, two possible mechanisms of the magnetic field - plasma evolution are being extensively discussed. First, if the magnetic field is confined in a relatively thin skin depth the magnetic force of the current can expel the plasma from the interelectrode gap [1]. Further magnetic insulation of the electron flow occurs like in vacuum diodes. Second, if the magnetic field penetrates through the diode plasma, it can magnetize the electron fluid and suppress the electron current [2]. In this case the plasma quasineutrality is maintained and the diode current is no more limited by the space charge and can be much higher than the ion current of the vacuum diode unless the diode becomes completely free of plasma ions [3]. Both these processes exist in the Plasma Filled Diode (PFD) as well as in Plasma Opening Switches (POS).

The behavior of plasma conductor with magnetized light particles and non-magnetized heavy particles should be described by the equations where in the Ohm's law the Hall term must be kept [4]. In [5] for the first time it was shown that the magnetic field shock wave may go ahead of the compression wave of the plasma density jump if

$$\frac{c}{\omega_{pi}} |\nabla \ln(n_e)| > 1 \quad (1)$$

At the magnetic field penetration stage the electron current exists in a thin layer along the cathode, allowing an electric field, E_H , such that

$$en_e E_H = -\nabla \frac{B^2}{8\pi} \quad (2)$$

Near the cathode, starting from the moment when the magnetic field wave arrives, the acceleration of ions occurs and the plasma density drops. This process was pointed out previously by the first author in [2].

The ion current to the cathode as a consequence of such plasma erosion on the background of magnetized electrons was calculated in our paper [3]. The present paper is devoted to the detailed consideration of the plasma dynamics in a Hall PFD/POS in order to ground the basic assumption done in [3] for calculation of the ion current value - i.e. that the

acceleration of ions occurs in a thin layer δ much smaller than the anode-cathode gap D , and that the plasma erosion wave represents a quasi- one-dimensional ($\delta \ll D$), quasi-stationary rarefaction shock wave.

The equation for the erosion wave

The geometry is shown in Fig. 1 for the case when the effects related to the magnetic lines curvature are neglected. We choose $\mathbf{B} \equiv (0, -B, 0)$, $B > 0$, $\mathbf{E} \equiv (E_x, 0, E_z)$, $\mathbf{V}_i \equiv (V_x, 0, V_z)$ - the ion velocity, and $\mathbf{v}_e \equiv (v_x, 0, v_z)$ - the electron velocity. Initially $B = B_0(z)$, $n = n_0(z)$ are monotonic functions of z .

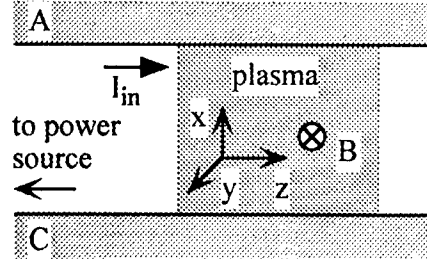


Fig. 1. General statement of the problem

Below we will use the values normalized to the maximum initial values in the non-perturbed plasma B_{\max} , n_{\max} . The magnetic field b is normalized to B_{\max} , the plasma density is normalized to n_{\max} , the time is normalized to the inverse ion cyclotron frequency, $\omega_{ci}^{-1} \equiv Mc/qB_{\max}$, the coordinates are normalized to c/ω_{pi} , where ω_{pi} is the ion plasma frequency calculated upon n_{\max} , the velocities are normalized to the Alfvén velocity, $v_A \equiv B_{\max}/(4\pi n_{\max} M)^{1/2}$, the electric field is normalized to the value $B_{\max} v_A/c$, ν is the collisional frequency ν_{ei} normalized to the electron cyclotron frequency, ω_{ce} , and $\epsilon \equiv m/M$ is the ratio of electron mass to the ion mass. We consider also that $\partial/\partial z \ll \partial/\partial x$, and that the gaso- kinetic pressures can be neglected in comparison with the magnetic field pressure. Therefore, in the magnetized non-perturbed plasma $b = b_0(z)$ and $n = n_0(z)$.

The radial Hall electric field, $-\mathbf{v}_e \mathbf{B}/c$ (2), accelerated the ions towards the cathode, so that $V_x \gg V_z$ in the ion momentum equation

$$n \frac{dV_x}{dt} = -b \frac{\partial b}{\partial x} \quad (3)$$

Here we took into account plasma quasineutrality condition in the Ampere's law

$$\frac{\partial b}{\partial z} = n(V_x - v_x), \quad \frac{\partial b}{\partial x} = n v_z \quad (4)$$

$$\frac{\partial n}{\partial t} + \frac{\partial}{\partial x}(n V_x) = 0 \quad (5)$$

Let us now suppose that there exists a regular rarefaction wave propagating from the cathode to the anode with the velocity $u(z)$. Integrating equations (3) and (5) we obtain behind the shock front for such a wave [6]

$$\frac{1}{n} = \frac{1}{n_0} + \frac{b_0^2 - b^2}{2n_0^2 u^2} > 1, \quad V_x = u - \frac{u n_0}{n} = \frac{b^2 - b_0^2}{2n_0 u} < 0 \quad (6)$$

Generally, Eq. (6) do not respond the question about the character of the shock wave (compression or rarefaction). In order to investigate this point we consider the generalized Ohm's law which can be obtained from the equation of motion of the light (electron) component

$$0 = -E_x - v_z b \quad (7)$$

$$\varepsilon \frac{dv_z}{dt} = -E_z + v_x b - v(v_z - V_z) \quad (8)$$

Here we keep both v_z and $v_x \ll v_z$. Let us consider the case of a strong rarefaction wave, $n \ll n_0$, $u \ll 1$. Using expression (6) and integrating the Faraday's law equation,

$$\frac{\partial b}{\partial t} = \frac{\partial E_x}{\partial z} - \frac{\partial E_z}{\partial x} \quad (9)$$

we obtain that the sum of forces in Eq. (8) acting on electron fluid is equal to

$$-E_z + v_x b = u F_0(b) \quad (10)$$

$$F_0(b) \equiv (b_0 - b) - \frac{b_0^2 - b^2}{2n_0 u^2} b - \frac{(b_0^2 - b^2) db_0^2}{4n_0^2 u^3 dz} + \frac{(b_0^2 - b^2)^2}{4n_0^2 u^4} \frac{dn_0 u}{dz} \quad (11)$$

During integrating over x we take into account the boundary condition $F(b)=0$ for $b=b_0(z)$. This allows us to rewrite Eq. (8) as follows

$$\varepsilon \frac{n_0}{n} \frac{\partial v_z}{\partial x} - \frac{\varepsilon}{nu} \left\{ \frac{\partial b}{\partial x} \frac{\partial v_z}{\partial z} - \frac{\partial b}{\partial z} \frac{\partial v_z}{\partial x} \right\} - \frac{v}{nu} \frac{\partial b}{\partial x} + F_0(b) = 0 \quad (12)$$

where v_z is determined by Eq. (4). Finally, we want to show that Eq. (12) allows existence of a quasi - plane ($\partial B / \partial t \gg \partial B / \partial z$), quasi - stationary rarefaction shock wave, which propagates from the cathode to the anode. Therefore, we will be looking for a solution in the form

$B(x, z, t) = B(z, \xi)$, $\xi = [x - u(z)t]f(z)$. After small modifications, Eq. (12) yields

$$\frac{\varepsilon f^2 n_0}{n} \frac{d}{d\xi} \left(\frac{1}{n} \frac{db}{d\xi} \right) + \frac{\varepsilon f^2 n_0}{n^2} g(b) \left(\frac{db}{d\xi} \right)^2 - \frac{vf}{nu} \frac{db}{d\xi} + F_0(b) = 0 \quad (13)$$

where for $u \ll 1$

$$g(b) \equiv -\frac{1}{n_0 u (b_0^2 - b^2 + 2n_0 u^2)} \frac{db_0^2}{dz} + \frac{2}{n_0^2 u^2} \frac{dn_0 u}{dz} - \frac{1}{n_0 u} \frac{d \ln f}{dz} \quad (14)$$

The equation (13) is the consequence of the conservation law for generalized momentum $\Omega_e(eB/mc) - \text{rot} v_e$ along the trajectories of electrons in the case of absence of collisions with ions ($\nu \rightarrow 0$). The equation of this type was studied analytically in [2] and numerically in [6] on the subject of existence of the compression shock wave. The rarefaction (plasma erosion) wave we are looking for differs by the sign of the velocity, $u(z)$, that is rather essential for the case of strong collisions.

Further transformation of Eq. (13) is possible by introducing the following Lagrangian variable

$$d\zeta \equiv d\xi \frac{n}{n_0 u f \sqrt{\varepsilon}} \quad (15)$$

so that the equation (13) will take simpler form:

$$\frac{d^2 b}{d\zeta^2} + g(b) \left(\frac{db}{d\zeta} \right)^2 - \eta \frac{db}{d\zeta} = \frac{F(b)}{2} \quad (16)$$

where $\eta = \frac{v}{\sqrt{\varepsilon}}$ and

$$F(b) \equiv (b_0^2 - b^2) b + \beta (b_0^2 - b^2)^2 - \gamma (b_0^2 - b^2) \quad (17)$$

$$\beta \equiv -\frac{1}{2n_0^2 u^2} \frac{dn_0 u}{dz}, \quad \gamma \equiv -\frac{1}{2n_0 u} \frac{db_0^2}{dz} \quad (18)$$

Let us look for the analytical solutions of Eq. (16) in the limit $\eta \rightarrow 0$ (collisionless case). If we introduce new function

$$Y(b) \equiv \frac{db}{d\zeta} \quad (19)$$

the equation (16) can be transformed in

$$\frac{dY^2}{db} + 2g(b)Y^2 = F(b) \quad (20)$$

Eq. (20) represents an ordinary differential equation of the first order for $Y^2(b)$. The general solution of this equation, satisfying the boundary condition $b = b_{\min}$ is

$$Y^2(b) = e^{-\alpha b} \int_{b_{\min}}^b F(b') e^{\alpha b'} db' \quad (21)$$

where $\alpha \equiv 2g$. The function $F(b)$ has three real roots, $b_0 > b_1 > b_2 \equiv b_{\min} > 0$,

$$b_1, b_2 = \frac{1}{2\beta} \pm \left(\frac{1}{4\beta^2} + b_0^2 - \frac{\gamma}{\beta} \right)^{\frac{1}{2}} \quad (22)$$

if $0 < \beta b_0^2 < \gamma < \beta b_0^2 + 1/4\beta$

In the choice of the boundary conditions we use the analogy of Eq. (20) and its integral with the equation of motion of a particle in quasi-one-dimensional potential well $\Delta\Phi = Y^2(b)$. The roles of time and coordinate are played here by ζ and b respectively. If the particle starts to fall into the well at the point $b = b_0$ with zero velocity, and then climbs up the opposite slope of the well to the point $b = b_{\min} = b_2$ with the velocity tending to zero, $db/d\zeta \rightarrow 0$, the time of this motion will be exponentially great. This happens if $Y^2(b_{\min}) \rightarrow 0$ and $\partial\Delta\Phi/\partial b(b_{\min}) \rightarrow 0$. The first condition is automatically satisfied, while the second corresponds to $F(b_{\min}) = 0$ in Eq. (17). Simultaneously, a proper choice of the free parameter $f(z)$ in the function $g(b)$ allow to satisfy the condition $Y^2(b) = 0$ at $b \rightarrow b_0$ for given $b_0(z)$ and n_{0u} defined from Eq. (14).

Therefore, we have shown that in the case $u \ll 1$, $v_{ei} \rightarrow 0$, there exists a stationary solution in the form of a rarefaction shock wave. If we neglect the terms with ε in Eq. (6), that means that in the Ohm's law we took into account only the electron-ion friction, than the solution for the erosion wave in plasma does not exist. Indeed, in the compression shock wave the stationary magnetic field profile is established as a result of competition of the magnetic field diffusion and convection, with the compression of the magnetic field. In the erosion wave both these fluxes are in the same direction in Eq. (12). However, if the terms $lhs1$ and $lhs2$ dominate (the plasma collisionality is low) a shock-like solution of Eq. (12) does exist, satisfying the boundary condition $b \rightarrow b_0$ at the erosion surface, $b \rightarrow b_{\min} \approx b_c$ at the cathode. As it was shown in [6] just in collisionless case there is a compression shock wave without heating. The statement of the present work is that in general Eq. (12) has nonlinear reversible shock-like compression or erosion solutions.

REFERENCES

- [1] B.V.Weber, R.L.Commisso, G.Cooperstein, et al, *8th Int. Conf. On High Power Particle Beams*, p. 406, 1990.
- [2] L.Rudakov, *Plasma Phys. Rep.* **19**, 433 (1993).
- [3] A.S.Chuvatin, L.I.Rudakov, and B.Etlicher, *11th Int. Pulsed Power Conf.*, p.1168, 1997.
- [4] A.V.Gordeev, A.S.Kingsep, and L.I.Rudakov, *Physics Reports* **243**, 215 (1994).
- [5] A.S.Kingsep, Yu.V.Mokhov, and K.V.Chukbar, *Sov. J. Plasma Phys.* **10**, 495 (1984).
- [6] A.Fruhtman and L.I.Rudakov, *Phys. Rev. E* **50**, 2997 (1994).

POLARITY DEPENDENT PLASMA DYNAMICS IN A TRI-PLATE POS*

R.J. Commisso, R.A. Riley,^a J. M. Grossmann,^b B.V. Weber, D.D. Hinshelwood, T.G. Jones,^c
P.F. Ottinger, S.B. Swanekamp,^d and J.J. Watrous^e

Plasma Physics Division, Naval Research Laboratory, Washington, DC

ABSTRACT: An experimental comparison is presented of a planar, tri-plate POS operated in both negative and positive polarity. For the same initial conditions, the conduction time is longer in positive than in negative polarity and interferometry reveals marked differences in the evolution of the plasma distribution. 2-D Hall/MHD calculations are also presented for a situation similar, but not identical, to the experiment. We conclude that Hall physics can play a major role in the POS plasma dynamics during the conduction phase of the POS and in determining the initial conditions for the opening phase.

I. INTRODUCTION

Plasma dynamics and density redistribution during the conduction phase of a plasma opening switch (POS) is an important physics aspect of both the conduction and opening phases of the POS operation.[1,2] Detailed interferometric measurements of POS plasma dynamics in the usual coaxial geometry are limited because of constrained diagnostic access, particularly in the direction perpendicular to the power flow. On the other hand, a planar POS geometry[3,4,5,6,7], allows excellent diagnostic access perpendicular to the power flow. Detailed comparisons can be made between such measurements and 2-D fluid codes for the purpose of benchmarking the code. The importance of Hall/magneto-hydrodynamics(Hall/MHD) [8,9,10] is of particular interest. In this paper, we describe results of experiments from, and associated 2-D Hall/MHD code simulations of, a POS in a tri-plate (see Fig. 1) type of planar geometry [6] on Hawk. The calculations reflect the experimental trends when Hall/EMH is included. Several significant differences between this and previous, planar POS work performed elsewhere [3]-[7] are the magnitude of the conduction current, the details of the POS plasma density distribution and species, and the use of a tri-plate rather than a bi-plate geometry (see Sec. II).

II. DESCRIPTION OF EXPERIMENT

The Hawk tri-plate POS hardware is illustrated in Fig. 1 for negative polarity (NP) operation. Twelve cable-gun plasma sources[11] are used, six on both top and bottom, and each centered over the 4-cm by 2-cm slots cut through the outer plates (labeled as anode in Fig. 1). Each gun is driven by a 0.6-mF capacitor charged to 25 kV. The current through each gun rises to a peak value of about 25 kA in 0.6 ms. For NP, the inner conductor is at negative high voltage and POS current flows from the outer plates to the inner plate. The situation is reversed for positive polarity (PP). Guided by calculations, the inner-plate width was reduced over a small axial distance just upstream of the POS (labeled "cathode current constriction" in Fig. 1) to reduce current bunching at the edges of the plate. For a given current, the cathode B fields are about the same in the tri-plate and co-axial geometries,

* Work supported by the Defense Special Weapons Agency

a. current address LOGICON/RDA, Arlington, VA

b. current address, Remote Sensing Division, Naval Research Laboratory

c. current address, ICARUS, Inc., Bethesda, MD

d. JAYCOR, Inc., McLean, VA

e. NumerEx, Albuquerque, NM

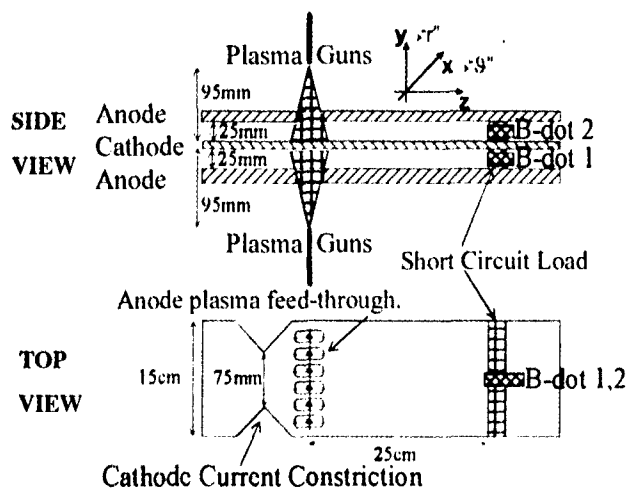


Fig. 1. Illustration of tri-plate POS hardware used on Hawk.

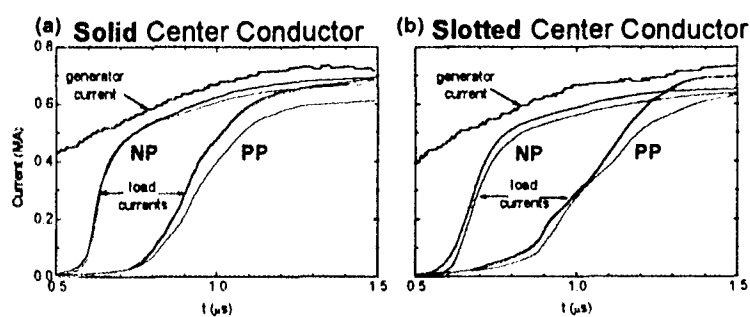


Fig. 2. Comparison of NP and PP currents.

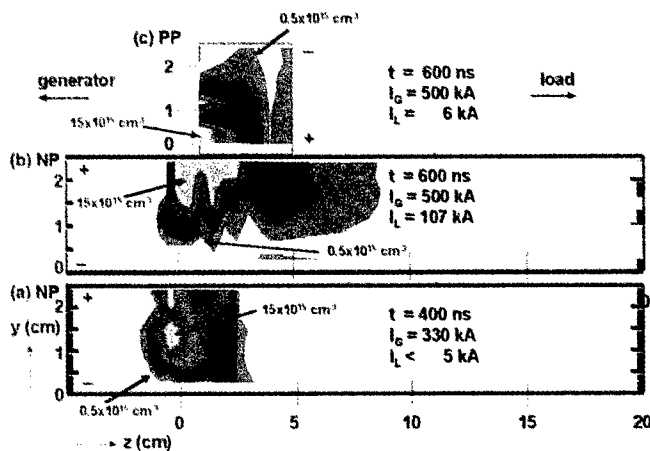


Fig.3. Measured density contours for NP and PP.

density gap region near the lower plate expands in the z and y directions as current in the load increases, until there is at least a several-mm region of very low density (relative to the initial density) between the cathode and POS plasma everywhere in z . It has been conjectured that an effective gap for magnetic insulation can grow very quickly in this low-density region.[1,2] The density contours for PP at $t = 600$ ns, (Fig. 3[c]), are very different from the NP contours (Fig. 3[b]) at the same time. In PP, a low-density region forms on the upper conductor (now the cathode), and plasma is pushed toward the lower conductor (now the

anode). Apparently, the low density region in which the effective gap may grow continues to be associated with the electron emitting electrode (the cathode). However, this region is not as large as in NP and the load current is significantly lower at the start of opening. The initial POS plasma density is about 5 times higher at the upper electrode than the inner electrode, independent of polarity, so $\mathbf{J} \times \mathbf{B}$ forces do not thin out the plasma as rapidly at the cathode in PP as in the NP case. At $t = 600$ ns, a plasma still bridges the circuit, consistent with the lower load current (i.e., longer conduction time, see Fig. 2) in PP. The clear difference in the evolution of the plasma density distribution between NP and PP cannot be explained by simply reversing the sign of the current (and magnetic field) when the polarity of the circuit is reversed because the direction of the $\mathbf{J} \times \mathbf{B}$ force is independent of polarity. Also, from a pure MHD point of view, the higher initial density at the upper electrode suggests that the plasma should be pushed away from it later than from the lower electrode, also contrary to the observation. The data strongly suggest that the detailed current distribution must also change with polarity and change in a way not predicted by pure MHD.

Finally, we note that at the end of the conduction phase the electron inventory increases by a factor of 2.75 over what it would have been without the application of the Hawk current. This is probably a result of ionization.

IV. COMPUTATIONAL RESULTS

To investigate theoretically the observed n_e evolution in NP and the differences between PP and NP POS operation, we employed a 2-D fluid code that has a Hall/MHD capability that has been tested against several problems with known solutions.[10] The initial density profile in the y direction and current time history are very similar to, but not exactly the same as, the measured density profile and current from the Hawk experiment. Also, the initial fill region is 6-cm long (rather than 4 cm) and the plasma is assumed to be C++ (the cable gun flashover surface is actually Teflon, C_2F_4). Shown in Fig. 4(a), (b), and (c) is a comparison of calculated n_e contours at $t = 540$ ns for a NP case with pure MHD and with Hall/MHD, and for PP with Hall/MHD, respectively (here $z = 0$ is the upstream edge of the plasma). The difference in the evolution of the n_e and without Hall in the computation is evident by comparing Figs. 4(a) and (b). With Hall (Fig. 4[b]), the plasma develops a narrow, low-density channel. Plasma is pushed up and down with a low-density gap ($< 10^{14} \text{ cm}^{-3}$, the floor density for the calculation) forming in the vicinity of the cathode across the entire plasma length by $t = 540$ ns. This picture is very similar to what is observed at $t = 600$ in the NP experiment (Fig. 3[b]). Without Hall (Fig. 6[a]), the distortion is significantly less at $t = 540$ ns as expected in a pure MHD picture (lowest density moving furthest). Intuitively, one would suppose that the distribution shown in Fig. 4(b) (with Hall) is more likely to "open" at $t = 540$ ns than the distribution shown in Figs. 4(a) (MHD only).

There is a striking difference between the evolution of n_e in PP (Fig. 4[c]) and NP (Fig. 4[b]) when Hall is included. In the NP case, the POS plasma has been redistributed so that there is a low density gap across the entire plasma length at $t = 540$ ns, while at the same time in the PP case there is still a plasma bridge across the electrodes, implying a longer conduction time, as in the experiment (see Fig. 2). Also, the thinning appears to evolve diagonally rather than horizontally.

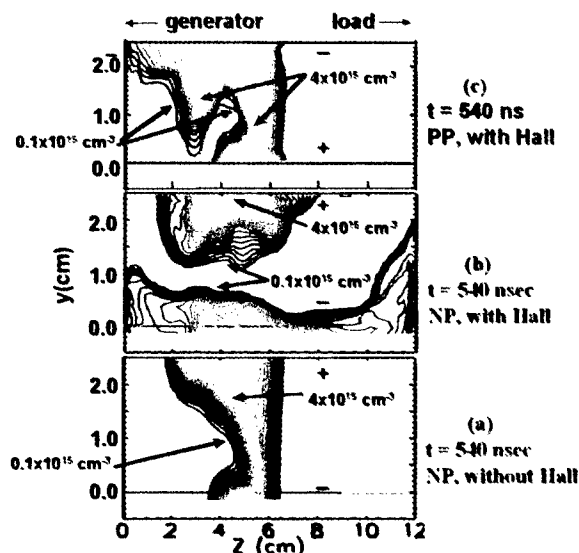


Fig. 4. Comparison of computed density contours.

resembles the measurements and that would not be expected from MHD alone. In PP, the simulations with Hall suggest a longer conduction time, as observed in the experiments, but do not represent the measured density evolution as well as in NP. The effects of preferential current penetration at the cathode needs to be considered. It appears that inclusion of the Hall term in fluid codes that simulate these type of POS plasmas, as well as other plasmas, is essential. In the future, we hope to redo the simulations, matching more exactly the initial plasma distribution, plasma species, and Hawk current waveform, and include ionization and resistivity (classical and anomalous) and effects of electron inertia.

The authors wish to thank M.P. Hebert, P. Filios, J. Rowley, and R. Schneider of DSWA for their support through the course of this work.

References

- ¹ D.D. Hinshelwood, et al., Phys. Rev. Lett. **68**, 3567 (1992).
- ² R.J. Comisso, et al., Phys. Fluids B **4**, 2368 (1992).
- ³ L.K. Adler, et al., Proceedings of 8th International Conference on High-Power Particle Beams, Novosibirsk, USSR, 1990, Boris N. Breizman and Boris N. Knyazev, eds., World Scientific, New Jersey, 1991, p. 371.
- ⁴ G.S. Belen'kii, et al., Plasma Phys. Repts. **21**, 847 (1995).
- ⁵ G.G. Spanjers, et al., J. Appl. Phys. **77**, 3657 (1995) and G.G. Spanjers, et al., J. Appl. Phys. **79**, 2229 (1996).
- ⁶ R.A. Riley, et al., Conference Record-Abstracts, 1995 IEEE Int. Conf. on Plasma Sci., Madison, WI (1995), IEEE Catalog No. 95CH35796, p. 160; R.A. Riley, et al., Bull. Am. Phys. Soc. **40**, 1688 (1995); and J.M. Grossmann, et al., Conference Record-Abstracts, 1997 IEEE Int. Conf. on Plasma Sci., San Diego, CA (1997), IEEE Catalog No. 97CH36085, p. 281.
- ⁷ R. Arad, et al., Bull. Am. Phys. Soc. **42**, 2025 (1997).
- ⁸ A.S. Kingsep, et al., Sov. J. Plasma Phys. **10**, p. 495 (1984).
- ⁹ Amnon Fruchtman, Phys. Fluids B **3**, 1908 (1991).
- ¹⁰ J.D. Huba, et al., Phys. Plasmas **1**, 3444 (1994).
- ¹¹ J.R. Goyer, et al., J. Appl. Phys. **74**, 4236 (1993).

It must be pointed out that preferential current penetration along the cathode can also result in a different current distribution when the polarity of the circuit is reversed. This phenomenon must be investigated and evaluated.

V. SUMMARY and CONCLUSIONS

NP, tri-plate POS experiments at $\approx 10^{15} \text{ cm}^{-3}$ on Hawk and 2-D Hall/MHD simulations suggest that the Hall physics is required in the simulations to better replicate the measured evolution and thinning of the plasma during the conduction phase. In NP, the simulations indicate that the Hall mechanism changes the current distribution, resulting in $\mathbf{J} \times \mathbf{B}$ forces that distort and redistribute the conducting plasma in a way that closely

HELICAL CASCADE FCG POWERED BY PIEZOGENERATOR

V.A.Demidov, V.D.Sadunov, S.A.Kazakov, L.N.Plyashkevich, T.V.Trishchenko,
S.N.Golosov, A.V.Blinov, I.K.Fetisov, M.V.Korotchenko, and Ye.V.Shapovalov

VNIIEF, Sarov, 607190, Russia

INTRODUCTION

The cascade FCGs with the high energy gain are defined as the separate FCG connected with each other by means of transformers and operating in series [1-5]. The high energy gain systems consist of helical generators connected with each other by step-up transformers [1].

For the power source of the first cascade the explosive piezogenerator (EPG) [6,7] is more preferable. EPG and FCG are well compatible in the operating principle and electrotechnical parameters. A feasibility to power the helical FCG from EPG is shown in paper [8].

In present paper the results of testing the two-cascade system of helical FCG with the explosive piezogenerator as a primary source are adduced. The system has comparatively small dimensions and is intended to achieve the energy up to ~0.5 MJ in the load.

DESIGN DESCRIPTION

In studying FCG with EPG [8] we did not put forward a task to optimize electrotechnical parameters of the system. To test the performance of proposed design of a self-contained energy source, the two assemblies [6,9] developed independently were chosen, which, after modification, were combined into one device.

Explosive Piezoceramic Generator. The primary pulse of electric energy is produced in the explosive piezogenerator during shock loading of the working medium (piezoceramics) through transfer of polarized charges in its volume against the forces of the excited electric field. The operating principle, equivalent electric circuit, mathematic dependences for calculating electric circuit parameters and the EPG experiment results are presented in papers [6-8]. For cascade FCG tests the EPG has been developed, which has a working medium made of piezoceramics ПКР-1 with the volume 60 cm^3 . In the preliminary test the EPG produced the energy pulse 8.4 J in the load $500 \text{ }\mu\text{H}$ at the additional capacitor capacity $\sim 0.2 \text{ }\mu\text{F}$. The magnitudes of current and voltage were 180 A and 10 kV, respectively, and the time of current rise to the maximum was 16 μs .

First Cascade of Energy Amplification. The energy produced by explosive piezogenerator is considered to be initial for a small-sized helical FCG of the first cascade which amplifies it up to kilojoule level. Providing a sufficiently high energy gain at the limited output voltage is the main requirement to FCG. Limitation of voltage is defined by the parameters of a step-up transformer as well as by electric strength of the FCG input in the second cascade of energy amplification.

A new FCG with helix diameter 50 mm (FCG-50) has been created for the cascade energy source. The helical coil is 400 mm in length. It is designed so that during the FCG operation the voltage in the load is limited by the value 1.0-1.2 kV. FCG-50 has initial inductance $530 \text{ }\mu\text{H}$ and active resistance 4.2 Ohm.

The FCG-50 electric characteristics were experimentally tested without transformer with the powering by initial energy of 8 J. In the FCG-50 load with inductance 85 nH the magnetic energy 1.4 kJ is stored, which has the 19 μ s characteristic time of current rise at the final stage under peak voltage \sim 900 V.

Transformer Assembly. To match the FCG-50 output parameters in current and voltage to the input parameters of the second cascade, a step-up cylindrical transformer is used. The matching transformer and FCG-50 are combined into one assembly.

The interwinding insulation, which must be as less thick as possible to provide the maximum feasible coupling coefficient K between transformer windings, is made of mylar \sim 0.2 mm thick. The primary winding consists of two turns. The secondary winding has 80 turns.

Basing on the measurement results, the values of transformer assembly inductances are: Transformer primary winding has inductance $L_1 = 244$ nH, secondary winding inductance is equal to $L_2 = 430$ μ H, and mutual inductance is $L_{12} = 9,9$ μ H. Since the FCG-100 resistance is not high, one may use the effective inductance approximation [1] being $L_{1eff} = 60$ nH to estimate the FCG-50 performance. Transformer coupling coefficient K calculated basing on this data is 0.967.

Second Cascade of Energy Amplification. In the second amplification cascade one of the designed generators of FCG-100 type is used, which performance is well known [9]. The generator operates at the initial magnetic field energy \sim 1 kJ and provides the energy amplification up to 450 times. The FCG helical coil has the internal diameter 100 mm and the length \sim 700 mm. The HE charge mass is 1.7 kg. The FCG-100 allows to obtain the current pulses with the amplitude 5-6 MA with the characteristic time \sim 10 μ s in the final operation stage under inductive load \sim 30 nH. The FCG-100 may be used as a powering source for more powerful generators, coaxial or disk types, but in most our experiments it is employed together with fast-operating explosive opening switches to produce high voltage pulses with the rise front \leq 0.5 μ s.

EXPERIMENTAL RESULTS

In the explosion experiment with the helical cascade FCG the electric energy 6 J from EPG is introduced in the first cascade. Fig.1 gives the oscillogram of current and voltage under the EPG capacity capacitor discharge into the FCG-50 helical coil. The time interval beginning from the piezogenerator HE charge blasting till HE initiation in the FCG-50 central tube was chosen so that closing of the FCG-50 electric circuit occurred at the maximum EPG current.

After FCG-50 operation the current in the matching transformer primary winding was $I_1 = 230$ kA (Fig.2) that corresponds to the stored magnetic energy 1.5 kJ. By means of the first cascade the energy was amplified by a factor of 260. In the primary winding the voltage \sim 1.1 kV was achieved.

Fig.3 and Fig.4 give time dependencies of FCG-100 powering current and FCG-100 input voltage, respectively. The values of energy (\sim 1.0 kJ) and magnetic flux (\sim 0.45 Webers) introduced in the FCG-100 compression volume correspond to the optimal mode of generator powering. The energy transmission coefficient of the matching transformer was \sim 65%. In the FCG-100 load with inductance \sim 30 nH the magnetic energy 410 kJ was achieved with the characteristic time 9 μ s of current rise in the final stage. Time dependence of FCG-100 current is shown in Fig.5.

The energy gain of the helical cascade FCG in the whole was ~ 68000 and the total time of system operation was $\sim 150 \mu\text{s}$.

Fig.6 shows the external appearance of tested device.

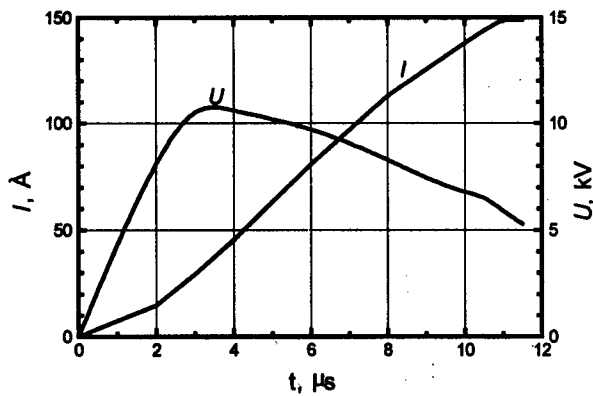


Fig.1. EPG current and voltage.

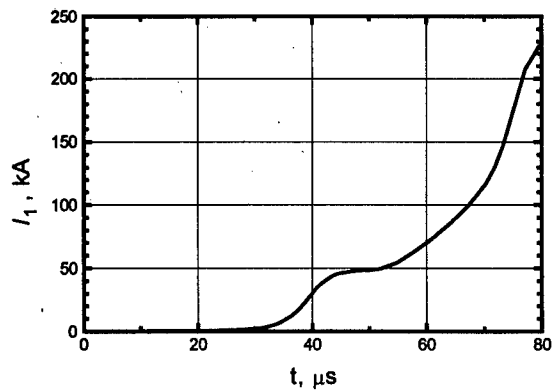


Fig.2. FCG-50 current.

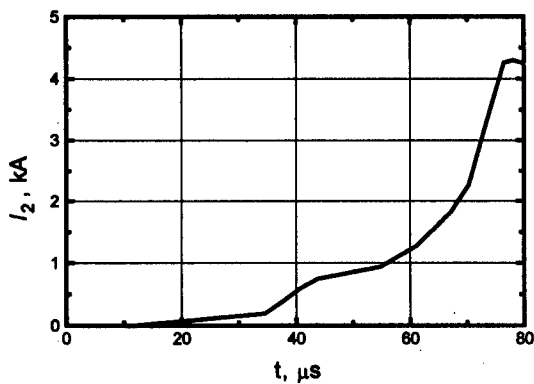


Fig.3. FCG-100 powering current.

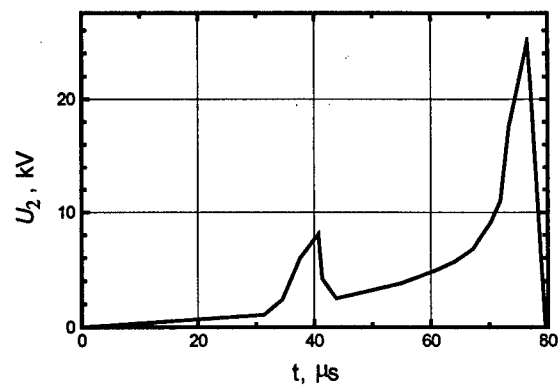


Fig.4. FCG-100 input voltage.

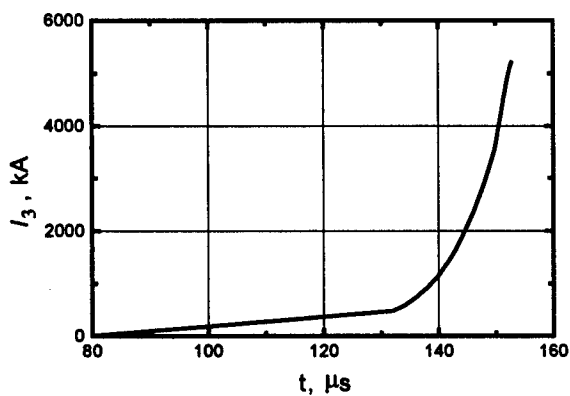


Fig.5. FCG-100 current.

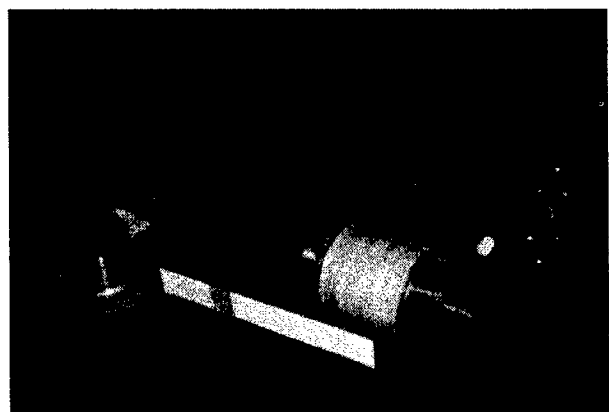


Fig.6. Cascade FCG external appearance.
1 - EPG, 2 - FCG-50 with transformer,
3 - FCG-100.

REFERENCES

1. A.I.Pavlovskii, R.Z.Lyudaev, L.N.Plyashkevich, A.M.Shuvalov, A.S.Kravchenko, Yu.I.Plyushchev, D.I.Zenkov, V.F.Bukharov, V.Ye.Gurin, and V.A.Vasyukov. "Transformer Energy Output Magnetic Cumulation Generators", in: *Megagauss Physics and Technology*, (Ed. P.J.Turchi), N.Y.- L.: Plenum Press, 1979, p.611-626.
2. E.C.Cnare, R.Y.Kaye, M.Cowan. "An Explosive Generator of Cascaded Helical Stages", in: *Ultrahigh Magnetic Fields. Physics. Techniques. Applications*, (Ed. V.M.Titov and G.A.Shvetsov), Moscow: Nauka. 1984.
3. A.I.Pavlovskii, L.N.Plyashkevich, A.M.Shuvalov, and E.M.Dimant. "Small Helical MCG's Cascade System", in: *Megagauss Magnetic Field Generation and Pulsed Power Applications*. (Ed. M.Cowan and R.B.Spielman), N.Y.: Nova Science Publishers, Inc., 1994, p.629-635.
4. R.F.Hoeberling, C.M.Fowler, B.L.Freeman, Y.C.King, Y.E.Vorthman, and R.B.Wheeler. "Electrical Performance of a Three-Stage Flux-Compression Generator System", in: *Megagauss and Megaamper Pulse Technology and Applications*. (Ed. V.K.Chernyshev, V.D.Selemer and L.N.Plyashkevich), Sarov, VNIIEF, 1997.
5. A.A.Leontyev, V.B.Mintsev, A.E.Ushnurtsev, V.E.Fortov, and A.V. Shurupov. "Two-Stage Magnetic Flux Compressors with Flux Trapping", *item 4*.
6. E.Z.Novitsky, V.D.Sadunov, and G.Ya.Karpenko. "The Behavior of Ferroelectrics in Shock Waves", *FGV (Fizika Gorennya i Vzryva)*, Vol.14, No.4, 1978, p.115-129, russian.
7. E.Z.Novitsky, V.D.Sadunov. "Ferroelectric Energetical Performance as Working Body of Shock-Wave Energy Transfer", *FGV (Fizika Gorennya i Vzryva)*, Vol.21, No.5, 1985, p.104-106, russian.
8. V.A.Demidov, V.D.Sadunov, S.A.Kazakov, T.V.Trishchenko, A.V.Blinov, I.K.Fetisov, M.V.Korotchenko, S.N.Golosov, and E.V.Shapovalov. "MCG Piezoceramic Power Source", *item 4*.
9. V.D.Selemer, V.A. Demidov, L.N.Plyashkevich, A.S.Kravchenko, S.A.Kazakov, A.M.Shuvalov, A.S.Boriskina, V.A.Zolotov, G.M.Spirov, and M.M. Kharlamov. "High-Current (30 MA and More) Energy Pulses for Energizing of Inductive and Resistive Loads", *item 4*.

RECENT OPENING SWITCH RESULTS ON DECADE MODULE 1

J.R. Goyer, J.R. Thompson, D. Kortbawi, and R. Crumley
Maxwell Physics International
8888 Balboa Avenue, San Diego, CA 92123 USA

S.W. Gensler
Alameda Applied Sciences Corporation
2235 Polvorosa Ave., Suite 230, San Leandro, CA 94577

ABSTRACT

As part of a continuing effort to improve the performance of the DECADE simulator, we report on some recent experiments using the DM1 module (1.5 MA in 300ns as configured). The purpose of these experiments was to investigate the sensitivity of the plasma opening switch (POS) operation to injected plasma symmetry, and to determine the magnitude of ion current losses in the POS region during switch opening. Data are presented for both 24 and 96 cable gun plasma source configurations. Additionally, interferometry was used to measure the initial plasma conditions in the switch.

EFFECTS OF IMPROVED SYMMETRY

To test the effect of symmetry, a POS was designed that could use either 24 or 96 cable gun plasma sources driven by 8 'dog-house' capacitor banks provided by NRL. Each 'dog-house' consists of three 0.6 μ F capacitors using a common switch for triggering. Each capacitor was thus driving either 1 or 4 sources. Data were obtained at a nominal conduction current of 1.4 MA. Because of the scaling of output density with current through each plasma source, the same delay time (2.7 μ s) between firing the 'dog-houses' and firing DM1 was used for both the 24 and 96 source tests, and resulted in the same conducted current.

It appears that there is little improvement noted going from 24 to 96 plasma sources. There may be some increase in peak radiation output, but there were not enough shots taken for the difference to be statistically significant. The following table summarizes the peak radiation output for the two qualification tests (24 sources) and the recent 24 and 96 source data.

	POS Current (MA)	Peak Radiation (arb units)	Radiation Dose (arb units)
Qual Test 1	1.42 \pm 0.04	4.7 \pm 0.8 (17%)	209 \pm 44 (21%)
Qual Test 2	1.38 \pm 0.04	5.0 \pm 0.4 (8%)	220 \pm 43 (20%)
24 Plasma Sources	1.39 \pm 0.04	3.0 \pm 0.6 (20%)	126 \pm 29 (23%)
96 Plasma Sources	1.41 \pm 0.03	3.5 \pm 0.9 (26%)	134 \pm 40 (30%)

The Qual tests included in the tables in this paper, are controlled tests of DM1 POS operation under fixed and optimized conditions. One should note that several features of the

present experiment were degraded from those of the Qual test configurations to allow diagnostic access, or to make direct comparisons with later planned experiments possible.

Another aspect of switch operation that would be thought to depend upon injected plasma reproducibility, timing jitter of the POS, was not noticeably affected by the use of more sources. The timing of the start of downstream current (CTI), the peak of POS voltage (CTV), and xray production (CTX), are summarized in the following table.

	CTI (ns)	CTV (ns)	CTX (ns)
Qual Test 1	251.6±10.5	275.6±5.5	268.5±5.2
Qual Test 2	247.3±8.9	270.0±7.4	261.0±7.5
24 Plasma Sources	276.4±6.4	314.2±7.7	307.5±7.3
96 Plasma Sources	272.3±4.4	304±12.1	297.2±9.5

One working hypothesis is that secondary surface plasmas play a significant role in the conduction and transport phases of operation, and that until these plasmas are reduced or made more reproducible, improvements in the injected plasma will not affect switch operation.

MEASUREMENTS OF ION CURRENT

On some shots in this experimental series, Faraday collectors were used inside the cathode, and ion currents were measured upstream and downstream of the POS. There is a region of about 10-cm around the plasma injection location where measurements cannot presently be made. Ignoring this region, the upstream ion current during POS opening appears to be about 100 kA, distributed roughly evenly along the cathode. This lack of fall-off of ion current as one goes further from the POS is surprising and needs more shots to be verified. Downstream, the ion losses manifest as a moving slug of about 400 kA, about 5-cm wide, traveling at 300cm/μs. Unfortunately, all the data analyzed so far were not acquired far enough downstream to see the ion current at the time of radiation production. Figure 1 summarizes the two losses discussed, and shows current lines at three different times based on the ion losses, and rise times of the axial current monitors. Note that each of the upstream ion detectors see about 8-10kA of current and that these currents occur in phase with the POS voltage, while the downstream currents appear before peak POS voltage, and are sequential.

INTERFEROMETRY

Data have been obtained at various radial locations for the line-integrated density of the initial fill plasma in the POS. Measurements during the opening of the switch have not yet been made due to unresolved noise and fiber-optic scintillation issues when voltage and radiation are produced. Typical density profiles are shown in Figure 2 where a 4-cm length has been assumed for the POS. Full fluid simulations of these results have not yet been performed to examine the hydromagnetic distortion of the plasma during conduction, and obtain estimates for predicted conduction times, but comparison to the simple hydro model has been made and is shown in Figure 3. Good agreement is seen if one assumes that the

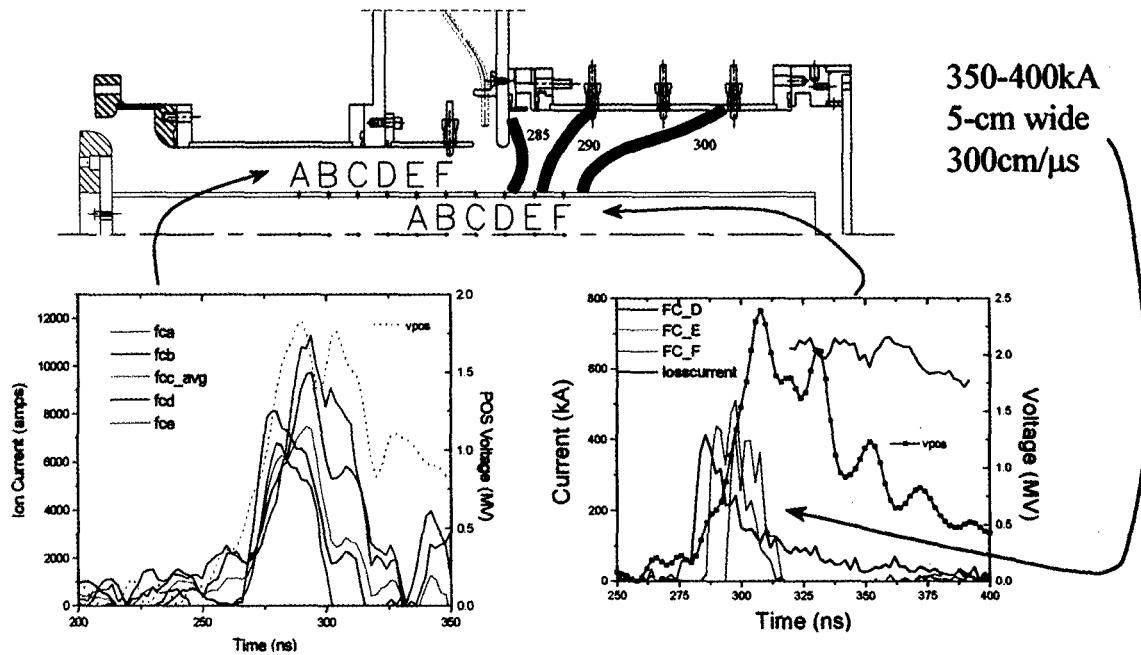
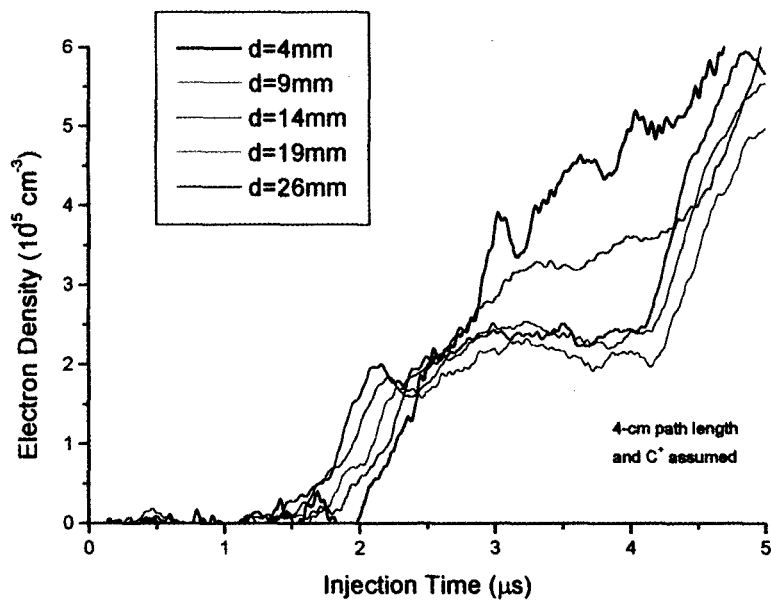


Figure 1. Side view of DMI hardware showing upstream and downstream ion currents. The dark lines in the drawing correspond to current lines at various times prior to radiation production.



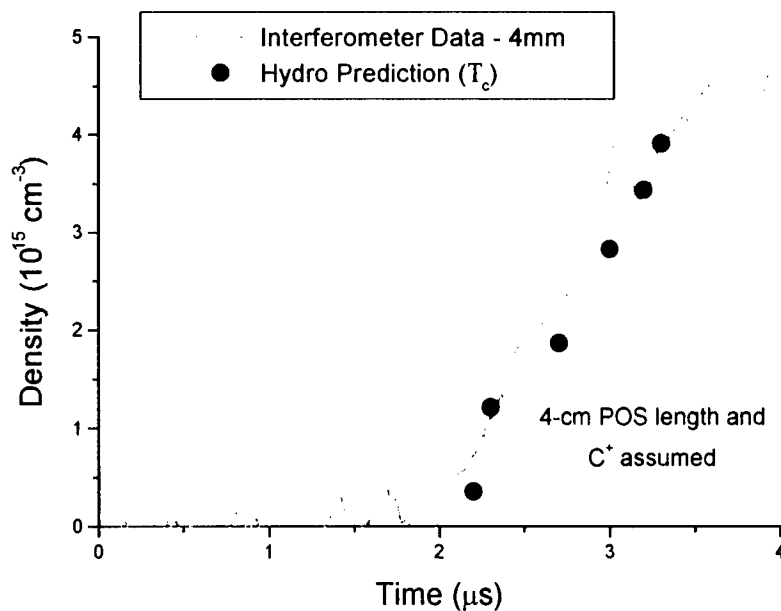


Figure 3. Comparison of measured and predicted plasma density. To get this agreement, singly ionized carbon has been assumed for the ion species.

SUMMARY

Experiments on DM1 have not shown significant improvement in either performance or reproducibility due to the use of additional plasma sources to increase symmetry. It is possible that secondary plasmas from either the electrode surfaces, or ionization of background gas play a large role in switch operation. Certainly there are plasmas observed on the cathode far from the POS injection region based on Faraday collector signals. These signals show distributed losses upstream of the switch, and bulk motion of a current slug downstream. Further analysis, and additional data, are required to have confidence in these interpretations.

Interferometry has been used to measure the initial conditions in the POS. These conditions appear to be consistent with expectations based upon hydromagnetic motion of the plasma prior to opening, but full modeling of the switch including Hall effects has yet to be done.

This work has been supported by the Defense Special Weapons Agency.

BIDIRECTIONAL PULSE GENERATOR SYSTEM FOR LINEAR INDUCTION ACCELERATOR

J.Ohmura, M.Ozawa, *A.Okino, **J-H.Park, **K-C.Ko and E.Hotta

*Department of Energy Sciences, Tokyo Institute of Technology,
Nagatsuta, Midori-ku, Yokohama, 226-8502, Japan.*

**Department of Electrical and Electronic Engineering, Tokyo Institute of Technology,
O-okayama, Meguro-ku, Tokyo, 152-8552, Japan.*

***Department of Electrical and Computer Engineering, Hanyang University,
Seongdong-ku, Seoul, 133-791, Korea.*

ABSTRACT

A bidirectional pulse generator system for linear induction accelerators, which consists of a pulse generator for external injection and a line cavity, was analytically investigated and the principle of the system was experimentally confirmed.

INTRODUCTION

In order to obtain a high-current charged particle beam, two types of linear induction accelerators (LIA) have been already constructed. In one type, a unidirectional pulse is injected to an accelerator from an external pulse generator. In this case, a toroidal magnetic core surrounding a beam path is usually loaded in a cavity to increase the shunt inductance as shown in Fig.1[1,2]. Since the magnetic energy stored in the core during the pulse is impossible to be recovered, the energy transfer efficiency of the accelerator system never attain 100%. On the other hand, the other type of LIA was proposed and constructed by Pavlovskii et al[3]. In this type of LIA, the accelerator cavity itself is formed from pulse forming lines with internal energy storage as shown in Fig.2. In this case, no magnetic core is needed in the cavity. The pulser generates a bidirectional voltage and the voltage with reverse polarity is used to accelerate a beam. Therefore, it is possible to make the time integral of the output voltage zero. Since the final magnetic energy stored in the cavity can be made zero at the end of the pulse, the system attains the energy transfer efficiency of 100%.

Furthermore, a method of driving each cavity by an external bidirectional pulse generator has been proposed by Smith[4], but it has not been realized yet. Therefore, we constructed a bidirectional pulse generator system which has been proposed by the authors[5], and confirmed the principle analytically and experimentally.

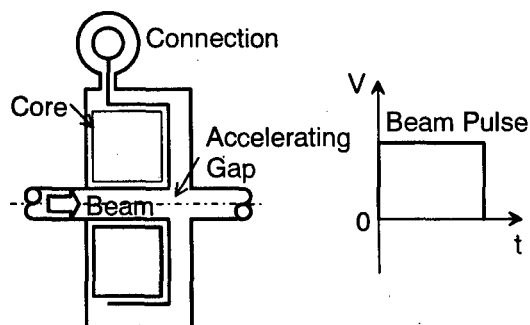


Fig.1 LIA injected by a unidirectional pulser.

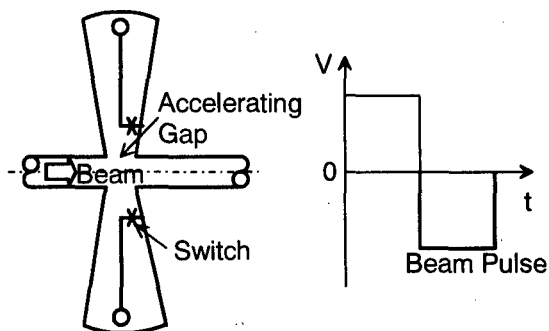


Fig.2 LIA made from pulse forming lines.

THEORETICAL ANALYSIS

Two pulse generators of external pulse injection type, which consist of three pulse forming lines of arbitrary impedances and one closing switch as shown in Fig.3, are analyzed[5]. Output voltages are analytically calculated using Bergeron method[6] and the conditions to attain the maximum energy transfer efficiency of 100% which is defined as a ratio of the output energy to the energy initially stored in the charged lines are derived.

For the pulse generator shown in Fig.3(a), when $z = 0$, the output voltage V is expressed as

$$\frac{V}{V_0} = \begin{cases} \frac{1}{x+1} & (0 < t < 2T) \\ \frac{-2x(x+1) + (1-x)(x-y)}{(x+y)(x+1)^2} & (2T < t < 4T) \end{cases}$$

where V_0 is the initial charging voltage, x and y are the ratios of the pulse forming line impedances to the output impedance of the pulse generator, and T is the wave transit time across a line. When $x = y$, the pulse generator is a bidirectional one with energy transfer efficiency of 100%.

Thus, two bidirectional pulse generators with energy transfer efficiency of 100% are obtained and are shown in Fig.4. The pulser shown in Fig.4(b) is that proposed by Smith[4].

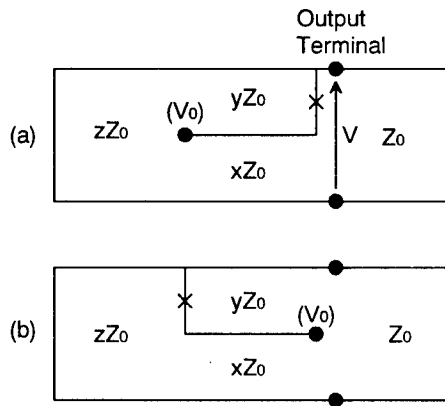


Fig.3 Basic composition of pulsers .

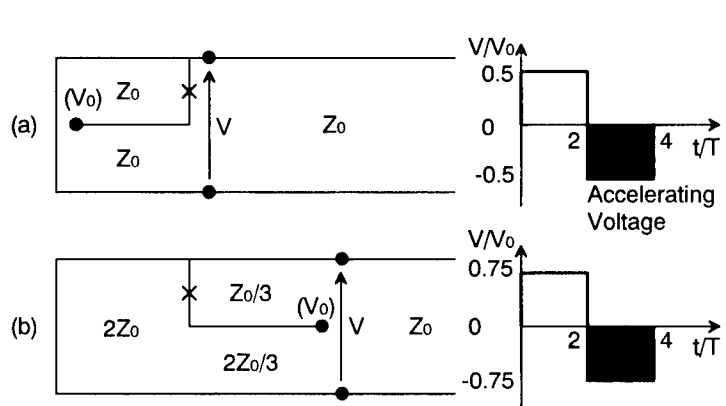


Fig.4 Bidirectional pulsers for external injection.

The cavity shown in Fig.5 is also analyzed. The cavity consists of two pulse forming lines, the lengths of which are the same as those of the pulse generators. Assuming that a bidirectional pulse is injected, the matching conditions at the connections of the cavity to the transmission line and to the load are given by

$$z = \frac{xy}{x+y}, \quad \text{and} \quad x = 1$$

respectively. Then, the calculated accelerating voltage V_A , which is the output voltage with reverse polarity, and the energy transfer efficiency η are given by a function of y as follows

$$\frac{V_A}{V_i} = \frac{y+3}{y+1}, \quad \eta = \frac{y(y+3)^2}{2(y+1)^3}$$

where V_i is the bidirectional voltage injected into the cavity. Figure 6 shows the amplitude of accelerating voltage and the energy transfer efficiency as functions of y . The maximum energy transfer efficiency is attained when $y = 1$ and therefore, $z = 0.5$. In this case, the output voltage is $2V_i$, that is, twice the input voltage.

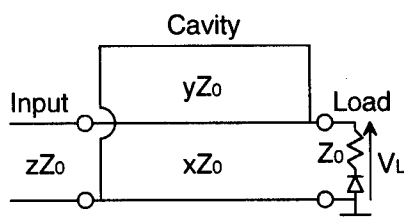


Fig.5 Analyzed cavity.

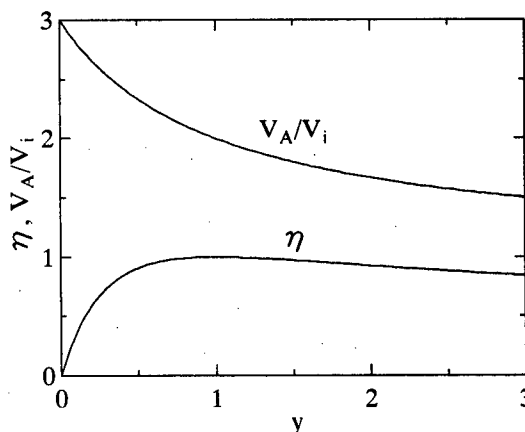


Fig.6 Accelerating voltage and energy transfer efficiency.

EXPERIMENTAL

The bidirectional pulse generator system, which consists of the pulse generator shown in Fig.4(a) and the cavity shown in Fig.5, was constructed. The schematic diagram of the system is shown in Fig.7. A dummy load which consists of a ceramic resistor and a semiconductor diode connected in series was used.

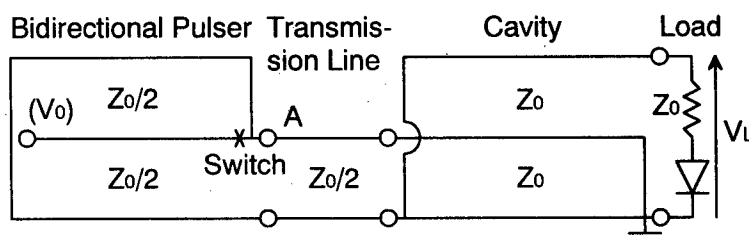


Fig.7 Constructed system.

The output impedance of the pulse generator $Z_0/2$ is 5.5Ω , and the pulse width for acceleration is 100 ns. The designed maximum charging voltage is 200 kV, but the experiment was carried out at the charging voltage of 20 kV.

The output voltage waveform of the matched load set at the output terminal of the cavity is shown in Fig.8. It is obvious that a bidirectional voltage pulse of about 20 kV, which is the same as the charging voltage of the pulse generator, is obtained. This result coincides with the analysis. Thus the principle of the bidirectional pulse generator system is confirmed.

The voltage waveform computed by using EMTP is also shown in Fig.8. The slow rise of the voltage is caused by the inductance of output switch, which is confirmed from the computation. Although we adopted a triggeratron gap switch with 4 trigger pins to reduce the inductance of the switch, it is very difficult to initiate 4 arcs simultaneously and only one trigger is considered to work actually. From the risetime of the output voltage waveform measured at the point A shown in Fig.6, the inductance of the switch is estimated to be about 90 nH. To reduce the inductance of switch by using a multi-arc-channel operation, a fundamental test of laser-trigger switch is in progress now. A pulsed Nd:YAG laser, the maximum output energy and the pulse width of which are 650 mJ and 5-7 ns, respectively is used. The results will appear elsewhere.

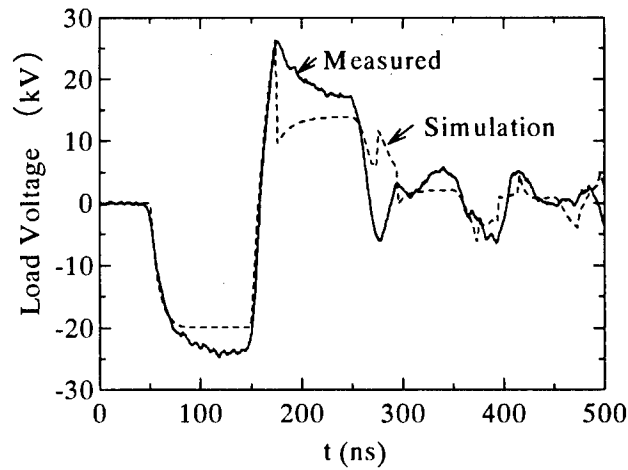


Fig.8 Experimental and simulation result of the output voltage waveform of the matched load.

CONCLUSIONS

Bidirectional pulse generators for external pulse injection, which can be used for high efficient linear induction accelerator systems, are analyzed.

One of the pulse generators analytically obtained was constructed and tested. The observed output voltage waveform across the dummy load, which consists of a resistor and a semiconductor diode connected in series, agrees well with the computed one. Thus the validity of the analysis and the usefulness of the proposed system were confirmed.

However, it is also revealed that the inductance of the switch affects the risetime of the output voltage remarkably. Therefore, using a pulsed Nd:YAG laser, a preliminary test of laser-trigger switch to reduce the inductance of switch by firing multi-channel-arc is in progress.

ACKNOWLEDGMENT

This work is partially supported by the Grant-in-Aid for Scientific Research, the Ministry of Education, Science and Culture, Japan(Contract No.09450109).

REFERENCES

- [1] J.B.Beal, N.C.Christofilos and R.E.hester : "The Astron Linear Accelerator", Proc. IEEE Particle Accelerator Conf., **NS-16**, p.294 (1969)
- [2] R.Avery et al., : "The ERA 4MV Injector", *ibid.*, **NS-18**, p.479 (1971)
- [3] A.I.Pavlovskii et al., : "Multielement Accelerators Based on Radial Lines", Soviet Phys. Dokl., **20**, p.441 (1975)
- [4] I.Smith : "Linear Induction Accelerators Made from Pulse-line Cavities with External Pulse Injection", Rev. Sci. Instrum., **50**, p.714 (1979)
- [5] E.Hotta and M.Abe : "Bidirectional Pulsers with High Efficiency for Linear Induction Accelerators". Electrical Engineering in Japan, **104**, No.4, p.41 (1984)
- [6] H.W.Dommel : "Digital Computer Solution of Electromagnetic Transients in Single- and Multiphase Networks", IEEE Trans. Power Apparatus System, **PAS-88**, p.388 (1969)

INVESTIGATION OF PLASMA INHOMOGENEITIES IN A PLASMA OPENING SWITCH BY LASER METHODS

G.I.Dolgachev, Yu.G.Kalinin, A.S.Kingsep,
M.S.Nitishinsky, and A.Yu.Shashkov

*Applied Physics Division, Russian Research Centre
"Kurchatov Institute", 123182, Moscow, Russia*

INTRODUCTION

Investigation of plasma turbulent noises in a plasma opening switch (POS) is presented. A YAG:Nd laser has been used to illuminate a POS plasma, and angular broadening of laser beam ($10^{-3} < \Delta\theta < 5 \times 10^{-3}$) was detected. This effect can not be explained neither by regular density gradient, nor by scattering on heat fluctuations of the plasma density. The most probable seems the mechanism of nonlinear laser beam scattering on the turbulent noises. A role of various oscillations (electro-static and helicons) is discussed.

EXPERIMENTAL SETUP AND DIAGNOSTICS

The experiments were carried out on the "Taina" generator [1]. Marx generator (360 kV) feeds a coaxial vacuum line which delivers 140 kA to a short-circuit load in 1.8 μ s. Employing POS, opening occurs in 1.6-1.8 μ s when total current rises to 105-120 kA. Experiments were performed with following POS configuration: plasma source was made as 64 spark gaps placed at the circle 30 cm diameter with the inner electrode (cathode) diameter 10 cm. Load inductance was about 350 nH.

Figure 1 shows the experimental setup for laser beam scattering diagnostics. Such a scheme could display density gradients, and is sensitive to laser beam deflections stipulated by scattering. Q-switched laser 1 YAG:Nd ($\lambda=1064$ nm) gives 90-mJ, 15 ns pulse. We used one laser pulse (and obtain one experimental frame) during "Taina" shot. LiNbO₃ crystal 2 provides following transition to $\lambda=532$ nm. Further, laser beam is expanded by telescope 3 up to 2 cm diameter and go through vacuum chamber 4 along the POS cathode. Interference filters 5 are used to cut off the plasma luminescence. A mask 7 is placed at the focus of lens 6 ($F=234$ mm). Sensitive film 8 is used for image registration.

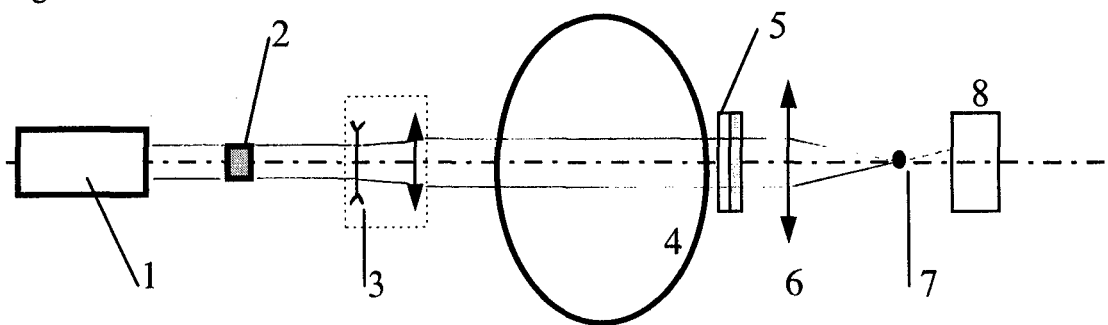


Fig.1. Experimental layout.

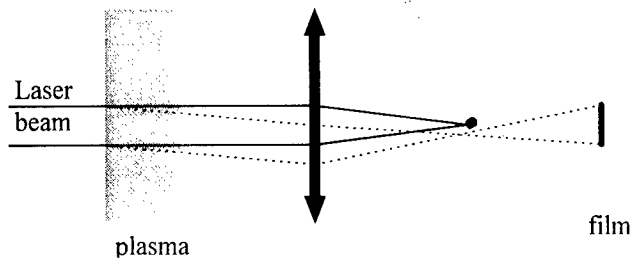


Fig.2. Laser beam deflection on plasma inhomogeneities.

The mask was performed as a wire which diameter was varied from $D=0.23$ to 2.5 mm. In the absence of a plasma laser beams were focused at wire axis; in experiments laser beams deflected with plasma (dashed line at Fig.2) go past the mask and can be registered by darkening of the film. The mask was installed horizontally at most experiments.

SENSITIVITY TO PLASMA DENSITY GRADIENTS

The expression for electron density gradient ∇N_e is following:

$$\nabla N_e = -\beta / (4.46 \times 10^{-14} \lambda^2 L) \quad (1),$$

where β is the angular deflection of a laser beam, λ - wavelength, L - plasma length. Minimum angle

$$\beta_{\min} \sim a_{\min} / F \quad (2),$$

where a_{\min} is a minimum detected laser beam shift in the focal plane. Estimating a_{\min} as one half of mask width (~ 0.1 mm), one can obtain the sensitivity for the case of $\lambda=532$ nm:

$$\langle \nabla N_e L \rangle_{\min} \sim 3 \times 10^{18} \text{ cm}^{-3},$$

and, substituting $L=10$ cm, we obtain $\langle \nabla N_e \rangle_{\min} \sim 3 \times 10^{17} \text{ cm}^{-4}$.

EXPERIMENTAL RESULTS

Strong density gradients were not revealed in our experiments (Fig.3). Instead, the darkening of the film covering large region was observed. This could not be attaching of few images of gradients: estimating $\langle \nabla N_e \rangle \sim 10^{18} \text{ cm}^{-4}$ and scattered region size ~ 1 cm, we should have $N_e \sim 10^{18} \text{ cm}^{-3}$. One could assume that darkening is provoked by the scattering on turbulent density fluctuations.

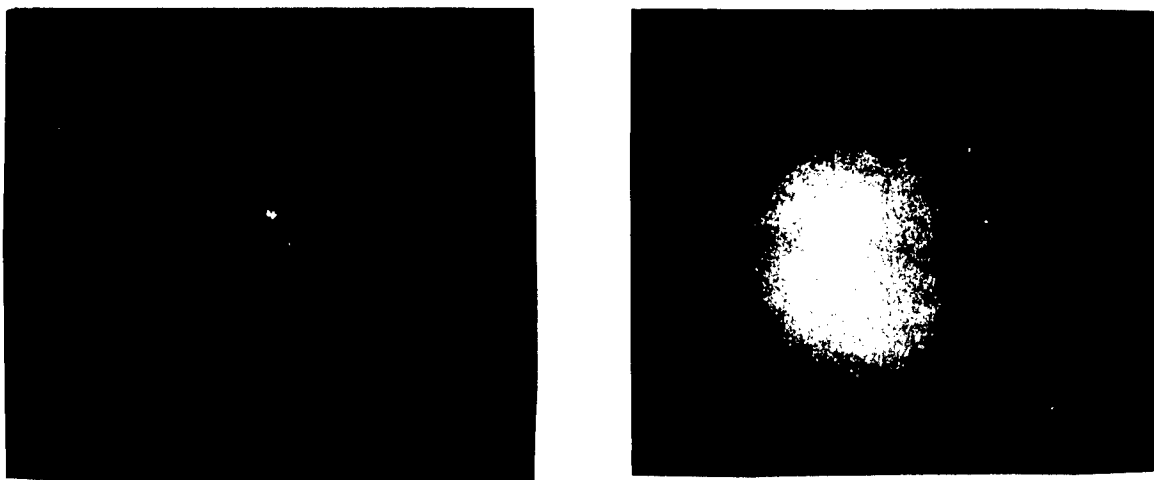


Fig.3 Left- control frame, right- typical experimental frame. Black and white colors are inverted versus film.

Both experimental frames and control frames (i.e. obtained just before the shot) were scanned photometrically, and density of darkening was determined. Then density of darkening was recalculated to the light intensities I_{exp} and I_c ; $I = I_{\text{exp}} - I_c$. Denoting light intensity before plasma as I_0 , one can estimate scattering coefficient as $I/I_0 \sim 5\%$.

Density of darkening is about 0.4 when mask size $h_{\text{min}} < 0.4$ mm, slightly reduces with h increase to 1.2 mm, and falls to noise at $h_{\text{max}} = 2.5$ mm. Substituting h_{min} and h_{max} into formula (2), one can obtain the angular broadening of the probe laser beam: $10^{-3} < \Delta\theta < 5 \times 10^{-3}$. As it will be shown below, this value of $\Delta\theta$ corresponds to realizable level of plasma turbulence.

Spatial-temporal relation of the effect is the following. It appears in $0.5 \mu\text{s}$ after current beginning and observed up to POS opening. Scattered region is localized between cathode and a surface at 4 cm from cathode.

A ROLE OF TURBULENT NOISES IN THE LASER BEAM SCATTERING

In our paper [1] it has been demonstrated that current flow through the plasma diode in the POS regime was accompanied by the high level of turbulence resulting, in particular, in anomalous resistivity. The level of oscillating field determined by the Stark broadening was as high as $E_{\perp} \in 10..40 \text{ kV/cm}$. Both Langmuir oscillations and ion acoustic waves could be responsible for such a level. If one tries to explain the effect observed by these noises, the following relations have to be taken into account: $k_i \ll k_s \ll k_t \approx 1.2 \cdot 10^5 \text{ cm}^{-1}$. In addition, let us compare the typical frequencies: $\omega_s \leq \omega_{pi} \approx 10^{10} \text{ s}^{-1}$; $\omega_i \geq \omega_{pe} \approx 5 \cdot 10^{11} \text{ s}^{-1}$; $\omega_t \approx 4 \cdot 10^{15} \text{ s}^{-1}$.

As a result, we have to conclude that nothing but angular almost elastic scattering may occur due to three - wave coupling which may be described by the diffusive equation:

$$\frac{\partial N(\theta)}{\partial t} = \frac{\partial}{\partial \theta^2} D \frac{\partial N(\theta)}{\partial \theta^2}; \quad (3)$$

$$D = \frac{1}{2(2\pi)^2} \omega_{pe} \left(\frac{\omega_{pe}}{\omega_i} \right)^3 \int d\vec{q} \frac{W_q^s}{nT} \frac{q}{k} \cos^2 \theta_q \delta(\cos \angle \vec{k} \vec{q}),$$

where W_q^s is the spectral density of the ion-acoustic noises, and $N(\theta)$ - the angular distribution of photons. The angular broadening of the laser beam can be estimated as:

$$\langle \theta^2 \rangle^2 \approx \frac{1}{4\pi} \left(\frac{\omega_{pe}}{\omega_i} \right)^3 \frac{\omega_{pe} l W^s \lambda_t}{c nT r_D} \approx 10^{-13}. \quad (4)$$

It hardly can provide the satisfactory explanation of our experimental results. If one considers the Langmuir plasmons instead of the ion-acoustic quanta, the quantitative estimate turns out to be very close to (4). Thus, although we observe rather high level of turbulent oscillating fields, they shouldn't be responsible for the scattering effect. There exists, however, one more possibility of nonlinear scattering (see, e.g., [2]) conditioned by the helical modes:

$$\omega_h = \frac{q^2 c^2}{\omega_{pe}^2} \omega_{Be} \cos \angle \vec{q} \vec{B}_0.$$

They may be generated by the coalescence of two ion-acoustic quanta (such an effect was observed in [3] and then was considered analytically in [4]). Besides, as it had been shown in [5], they could be excited due to the non-potential current-driven instability.

These modes, nevertheless, hardly may be revealed by means of the Stark broadening, as follows from the estimates:

$$\left| \frac{E_-}{B_-} \right| \approx \frac{\omega_h}{qc} \ll \min \left[\rho_{Be} \frac{\omega(\rho_{Be}^{-1})}{c}; \quad \frac{\omega_{Be}}{q(\omega_{Be})c} \right].$$

The second inequality is more essential just in our regime, resulting in 6×10^{-2} . Hence, some dozens kV/cm have to be accompanied by several kGs level of the magnetic oscillations, that is certainly not our case. Nonetheless, the scattering observed may be successfully explained by rather low level of whistlers. We mean just the same type of the three-wave coupling. The wave number of helicons is restricted by the inequality $q_h \ll \rho_{Be}^{-1}, \quad q(\omega_{Be})$, resulting in $q_h/k_t \leq 10^{-4} \dots 10^{-3}$ which provides all the approximations that have been used to obtain Eq (4). As for the probability of the three-wave process, it had been calculated in [2]:

$$w(\vec{k} + \vec{q}; \vec{k}, \vec{q}) \cong \omega_{pe}^2 \left(\frac{\omega_{pe}}{\omega_{Be}} \right)^3 \frac{\omega_h}{nmc^2} \delta(\omega_{t1} - \omega_{t2} - \omega_h). \quad (5)$$

Following the same order as while deducing Eq (4) one can calculate:

$$\langle g^2 \rangle^2 \approx \frac{\omega_{pe}^4}{c} \left(\frac{\omega_{pe}}{\omega_{Be}} \right)^3 \frac{q_h}{k_t} \frac{W_h}{nmc^2}. \quad (6)$$

Then estimating $q/k \approx 10^{-4}$ one can readily obtain that $B_- \approx 10$ Gs is quite enough to provide the $\Delta g \approx 10^{-2}$ broadening of the angular distribution.

This work was supported by the Russian Foundation of Fundamental Research - grants No. 96-02-17540, 96-02-16258.

REFERENCES

- [1] G.I. Dolgachev, L.P. Zakatov, Yu.G.Kalinin et al.// Plasma Physics Reports, 1996, 22(11), p.921.
- [2] V.K.Zhivotov, G.I.Kalinnikov, A.S.Kingsep et al.// Sov.Phys. JETP, 1974, 67, p.84.
- [3] Yu.G.Kalinin, D.N.Lin, L.I.Rudakov et al.// Sov.Phys. Doklady, 1969, 189, p. 285.
- [4] A.S.Kingsep //Zh. prikl. mekhaniki i tekhnicheskoi fiziki [in Russian], 1970, 6, p.18.
- [5] A.V.Gordeev, L.I.Rudakov // Sov.Phys. JETP, 1968, 55, p.2310.

CONTROLLED DISCHARGE ON DIELECTRIC SURFACE

A.I. Kormilitsyn, V.S. Diyankov, V.B. Bratchikov

*Russian Federal Nuclear Center —
All-Russia Science and Research Institute of Technical Physics
P.O.Box 245, Snezhinsk, Chelyabinsk region,
Russia 456770, fax (8-351-72) 3-09-79*

Abstract

The paper proposes technique for controlled commutation of energy on a dielectric surface when affected by ultraviolet radiation, formed during electric explosion of wires. Commutation characteristic of discharge can be controlled by changing intensity of surface irradiation and number of commutation channels by changing number of exploded wires.

This technique, combined with other factors, is used for formation of trailing of voltage (current) at accelerating tube of direct action accelerator IGUR-3. Exploded wires are placed inside polyethylene pipes 7 m long. With simultaneous changes of electrical field strength along the length of the pipe, steepness of rise of voltage pulse, and intensity of ultraviolet radiation, duration of the trailing edge the pulse can be set from 20 ns up to 250 ns. Speed of discharge on the pipe's surface does not depend upon its length and is, respectively, $3 \cdot 10^8 \dots 3 \cdot 10^7$ m/s.

It is known that electrical explosion of wires is accompanied by intensive radiation of light, specifically, ultraviolet radiation with ~ 2000 Å wavelength [1]. This effect is proposed for use in commutation dischargers for shaping the anterior or back fronts of pulses of current (voltage) on the load. The schematics of devices of such kind is shown on figure 1. The commutation of energy in the discharger occurs on the surface of insulator "2" between electrodes "1" and "3". If the electrical link between points "a" and "b" is absent, the explosion of wires is synchronized with the arrival to electrode "1" of the working pulse from IVN-2 (high-voltage source). When the pulse of ultraviolet radiation affects the surface of insulator, there is a simultaneous formation of electron film along the whole length of insulator which, combined with electrical field strength between electrodes "1" and "3", causes "instantaneous" conductivity on the insulator surface. By varying the intensity of ultraviolet radiation upon insulator surface, and the value of electrical field strength between electrodes "1" and "3", it is possible to change the commutation characteristics of the discharger. The commutation characteristics are easy to change, in this case, by changing the number of commutation channels when the number of exploding wires is varied.

The phenomenon of dielectric surface conductivity emerging under the simultaneous effects of voltage and ultraviolet radiation is proposed for use in energy commutation in high-voltage lines. This is easy to implement in the inductive storage circuits with energy commutation by electrically exploded wires (EEW).

The authors have proposed and studied the scheme of device having the connection between points "a" and "b" (see figure 1), i.e. in this case the IVN-2 source was absent, and the functions of working voltage generator were performed by the energy inductive storage circuit (see figure 2) with EEW-based current opening switch.

Exploded copper wires $\varnothing 0.09$ mm in diameter, 55 items, were placed into 15 polyethylene pipes 70...140 mm in diameter and 5...7 m long. Each pipe engulfed from one up to four wires, preserving the total cross-section. The voltage pulse on EEW has variable steepness of increase ($10^{11} \dots 10^{14}$ V/s) and will reach the value of 7.5 MV. The total maximal current going through the wires is ~ 180 kA. The EEW explosion mode was varied in the studies by means of energy intake from IVN-2 into the load. When the load was switched on early (prepulse) the changes in conditions of EEW explosion occurs due to reduction in energy drive rate (the energy used for explosion of wires), this results in reduction of voltage across EEW, and, potentially, to change (decrease) in intensity of ultraviolet radiation. The load switch time is modified by changing the gap in sharpening discharger. Due to the various degree of bypassing the EEW circuit by load (due to the change in EEW exploding energy drive rate) the voltage across EEW varied from 7.5 MV down to 4.5 MV. In addition, the pulse cut-off phenomenon was observed in all cases, caused by emergence of conductivity on the inner surface of all polyethylene pipes. The nonuniformity in distribution of cut-off current along the pipes was observed. This can be explained by different levels of ultraviolet radiation exposure doses for pipes' surfaces. Figure 3 shows dependency of duration of the back front of current pulse at the load upon the strength of

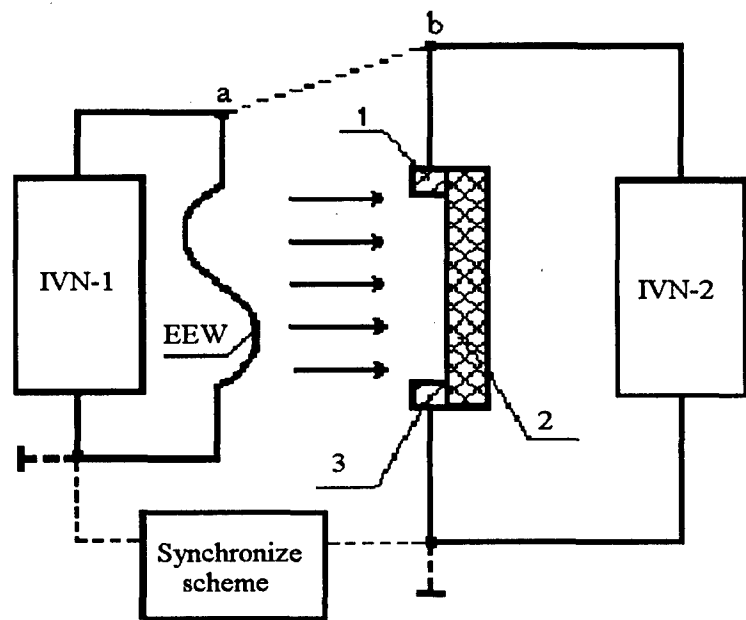


Figure 1. Controlled Discharger

EEW - electrically exploded wires; IVN-1 - high voltage source for EEW explosion; IVN-2 - high (working) voltage source; 1,3 - discharger electrodes; 2 - insulator.

Exploded copper wires $\varnothing 0.09$ mm in diameter, 55 items, were placed into 15 polyethylene pipes 70...140 mm in diameter and 5...7 m long. Each pipe engulfed from one up to four wires, preserving the total cross-section. The voltage pulse on EEW has variable steepness of increase ($10^{11} \dots 10^{14}$ V/s) and will reach the value of 7.5 MV. The total maximal current going through the wires is ~ 180 kA. The EEW explosion mode was varied in the studies by means of energy intake from IVN-2 into the load. When the load was switched on early (prepulse) the changes in conditions of EEW explosion occurs due to reduction in energy drive rate (the energy used for explosion of wires), this results in reduction of voltage across EEW, and, potentially, to change (decrease) in intensity of ultraviolet radiation. The load switch time is modified by changing the gap in sharpening discharger. Due to the various degree of bypassing the EEW circuit by load (due to the change in EEW exploding energy drive rate) the voltage across EEW varied from 7.5 MV down to 4.5 MV. In addition, the pulse cut-off phenomenon was observed in all cases, caused by emergence of conductivity on the inner surface of all polyethylene pipes. The nonuniformity in distribution of cut-off current along the pipes was observed. This can be explained by different levels of ultraviolet radiation exposure doses for pipes' surfaces. Figure 3 shows dependency of duration of the back front of current pulse at the load upon the strength of

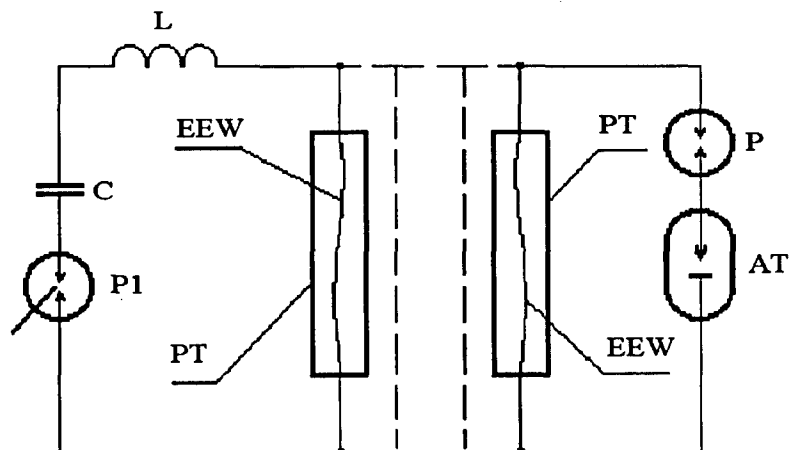


Figure 2. Location of Electrically Exploded Wires in the Circuit of IGUR-3 Accelerator

C - primary storage of electric energy; L - storing inductance; PT - polyethylene tube; EEW - electrically exploded wire; P1 - commutation switch; P - sharpening switch; AT - accelerating tube.

electric field along the pipe length. (This dependency is conventional, since the nature of variations in intensity of ultraviolet radiation is not known). Changes in the electric field strength from 0.67 MV/m up to 1.1 MV/m with the parallel change in the steepness of the pulse increase result in reductions in pulse's back front duration from 200 ns down to 25 ns. The phenomenon of ultraviolet effects on conductivity was tested in the experimental set-up with one pipe 400 mm in diameter. The number of wires placed in the pipe was equal to the total number of wires placed in 15 pipes $\varnothing 70 \dots 140$ mm. Other conditions were left unchanged. The phenomenon of pipe conductivity was observed in this case when wires were neared to the surface at $r \leq 10$ cm. The "cut-off" trace appeared directly opposite to the location of wires. Changes in location of the wires lead, respectively, to the changes in the location of the trace.

If we look at this device as the switch with dielectric surface discharge, then the discharge velocity, defined as:

$$V = \frac{l}{t_k}$$

(where l - length of commutation channel (pipe length), t_k - commutation time), is $\sim 3 \cdot 10^7 \div 3 \cdot 10^8$ which is substantially higher than known velocities for other switches of the similar class ($\sim 2 \cdot 10^7$ m/s). Moreover, this velocity likely will be determined mostly by the intensity of ultraviolet irradiation of the surface, the value of field

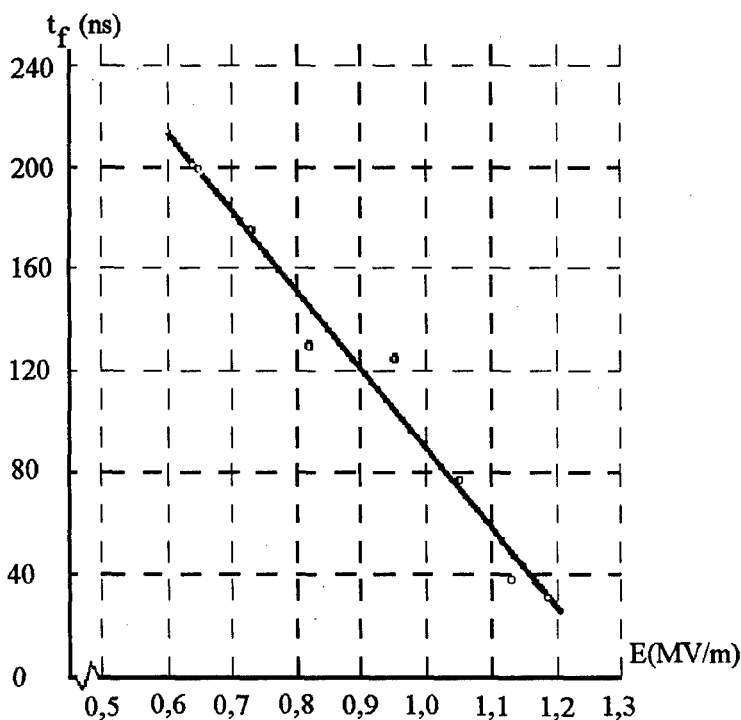


Figure 3.

Graph of Voltage (Current) Pulse in the Load Duration versus Strength of Electrical Field Along the Insulator Length (along the polyethylene pipes which house EEW)

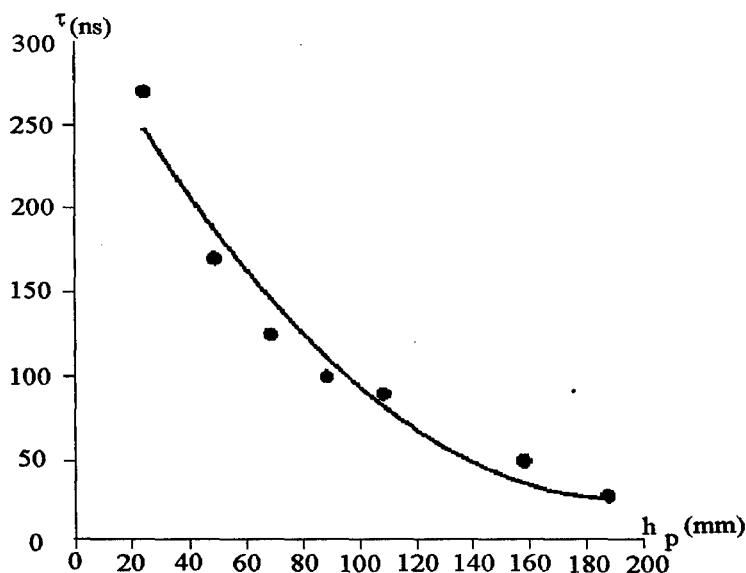


Figure 4. Duration of Pulse of Accelerating Tube Current versus Gap Value in Sharpening Switch.

strength, steepness of pulse rise, and will be independent of the length of insulator, since the commutation channel on dielectric's surface is created through the whole length.

The increase in pipe length from $l=5$ m up to 7 m had no effect on commutation properties of the device.

The above method is used in the circuit of inductive energy storage and EEW for shaping the back front of the pulse of current (voltage) on accelerating tube of IGUR-3 accelerator [2].

Reference [3] describes the method for controlling the anterior front of the voltage (current) pulse on the IGUR-3 accelerating tube. The shaping methods for anterior and back fronts of the pulse are mutually related and, ultimately, are determined by the gap value in the sharpening switch. The increase (decrease) of the gap leads to:

- increase (decrease) of amplitude of the voltage pulse across EEW;
- increase (decrease) in steepness of pulse rise;
- increase (decrease) in intensity of insulator (pipe) surface ultraviolet irradiation.

These factors determine the operation modes of sharpening and cut-off (in EEW circuit) dischargers.

Thus, the duration of anterior and back fronts decrease with the increase in the gap, and vice versa. Figure 4 shows the graph of current pulse duration versus gap in sharpening discharger.

REFERENCES

1. Exploding wires. Translated from English, editor A.A. Rukhadze, Moscow, IL, 1963
2. V.S. Diyankov, V.P. Kovalyov, A.I. Kormilitsin et al. "Proceedings of the Higher Education Institutions. Physics", Tomsk, volume 38, #12, 1995, pp. 84-92.
3. A.I. Kormilitsin, V.S. Diyankov. "Controlled Multiple Channel Switch" Proceedings of the 11th International Conference on High Power Particle Beams, 1996, Prague, pp.

400 KA INDUCTIVE VOLTAGE ADDER – INDUCTIVE ENERGY STORAGE PULSED POWER GENERATOR ASO-X

I. V. Lisitsyn, S. Kohno, Y. Teramoto, S. Katsuki and H. Akiyama

*Department of Electrical and Computer Engineering, Kumamoto University,
Kumamoto 860, Japan*

ABSTRACT

A novel pulsed power generator using the inductive voltage adder technology was put into operation in Kumamoto University. This machine, named "ASO-X", is an inductive voltage adder - inductive energy storage pulsed power system. The maximum output voltage and current of ASO-X are 180 kV and 400 kA respectively at the short circuit load with 1.3 μ s of current quarter period. To increase the voltage, power and decrease the rise time of the load current, the plasma opening switch is used at the output of ASO-X. Eight plasma guns serve for the plasma source of the opening switch in the scheme of with the single triggered gap switch. This system provides very fast current rise rate of 3.6×10^{12} A/s at over 1 μ s of conduction time of the plasma opening switch.

INTRODUCTION

A new pulsed power generator ASO-X has been built in our laboratory using the inductive voltage adder (IVA) technology [1-3]. For multiplying the output voltage, ASO-X consists of three stages in series with magnetic cores (Hitachi Metals Ltd. FINEMET FT-1H). Two capacitors in parallel are in each stage. The FINEMET nano-scale crystalline cores have good magnetic properties such as high saturation flux density, high permeability and low core loss and they are fast enough to be used in the pulsed power generators. The design of IVA generator is flexible and allows increasing of its voltage and current. The increase of the number of stages makes output voltage higher and the increase of the number of capacitors in the stages makes output current higher. Two additional terminals for the capacitors are provided in each stage for further upgrade. In spite of high current, its quarter period in an IVA pulsed power generator can be lower compared to one using a Marx bank because of low generator inductance and absence of high-voltage insulation. The generator uses no insulating oil and, therefore, it is compact, comparatively cheap, nonflammable and ecologically clean.

Many applications of inductive energy storage pulsed power systems require higher power and/or voltage. ASO-X itself provides high current with relatively fast risetime that can be delivered to a load. Nevertheless a faster current risetime in the load circuit is required for some applications such as Z-pinch and capillary pinch. Thus, an opening switch is necessary to fasten the load current risetime. Plasma Opening Switch (POS) is one of the opening switches applied frequently in order to compress the pulse in inductive energy storage pulsed power systems [4].

In this report the characteristics of new pulsed power generator ASO-X with microsecond POS are described.

EXPERIMENTAL SETUP

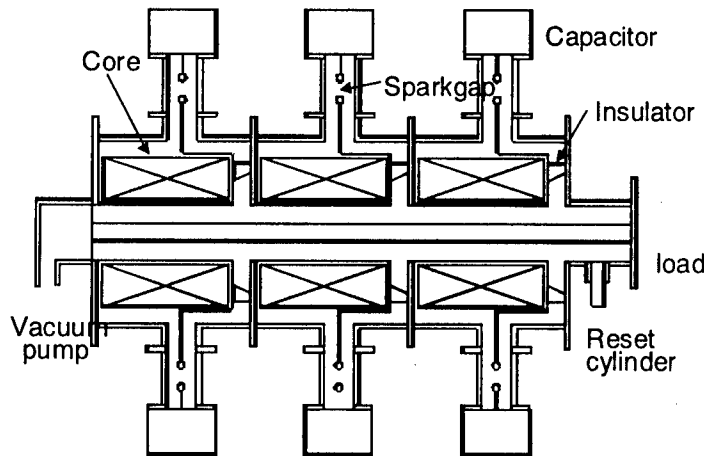


Fig.1. The schematics of ASO-X.

of each stage. These gap switches are fired by a single trigatron-type sparkgap. This sparkgap is placed in the chamber filled with CO_2 gas and triggered by thyatron. Adjusting the pressure of the gas in all sparkgaps provides the low-jitter operation at any charging voltage. Actually at the optimum pressure the measured jitter of all 6 gaps is less than 130 ns. At the charging voltage of 60 kV, the total stored energy is 35 kJ and the maximum output voltage and the peak current are 180 kV and 400 kA respectively. After charging all 6 capacitors, all sparkgaps are triggered simultaneously by the thyatron and the generator current flows in the circuit with about 1.4 μs of quarter period. There are 6 current monitors to measure the current flowing through each capacitor and 2 current monitors on the both ends of ASO-X to measure return current and output current. Since all sparkgaps are triggered simultaneously, equal current flow in each cavity and the voltage is multiplied along the inner electrode of the generator. The output current is proportional to the number of capacitors in a stage, the output

Fig. 1 shows the schematic design of ASO-X generator. The size of ASO-X without POS parts is 2.7 m in width, 1.8 m in length and 1.6 m in height and is relatively compact. The ASO-X consists of three stages and total of 6 capacitors with a capacitance of 3.2 μF . Each stage consists of a set of two capacitors and one core and this part is enclosed in a chamber filled with SF_6 gas. The capacitors are triggered by six field distortion type sparkgap switches placed in the chamber

voltage is proportional to the number of stages. The operation is controlled in a remote screen room.

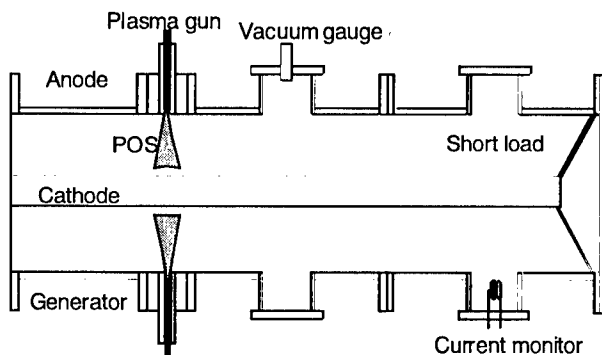


Fig.2. The scheme of POS region.

respectively. Inner electrode is made of aluminum tube and is replaced easily with another electrode having a different diameter. To achieve the uniform plasma fill density in the POS region, 8 guns were mounted in the outer electrode. The end plate of the inner electrode is connected to outer electrode with copper plate as a short circuit load. This part is enclosed in a vacuum chamber with the residual pressure of about 10^{-4} Torr.

The plasma source consists of 8 cable plasma guns powered by 4 capacitors with a capacitance of 0.7 μF each through a single triggered spark gap. A pair of guns is driven by one capacitor. All capacitors are charged up to 25 kV and fired by the signal of external trigger producing plasma in the POS region. The current flows through one plasma gun is

measured by a Rogowski coil and is about 9 kA with the quarter period of approximately 1.6 μ s.

Changing the delay time between triggering the plasma guns and the firing of the ASO-X varies the POS conduction time. To control the delay time a delay/pulse generator (Stanford Research DG-535) is used. Varying the delay time, the generator current I_G is measured by output current monitor of ASO-X and the load current I_L is measured by a current monitor located between the plasma guns and load. The electrical signals are recorded by 2 GSa/s Hewlett Packard HP-54512B digital oscilloscope.

RESULTS AND DISCUSSION

The preliminary measurements of the plasma ion current density are made by a Biased Faraday Cup (BFC). The plasma flow arrives to the cathode location at about 1.5 μ s after firing of the plasma gun and the peak current density takes place at 2.0 μ s. The peak plasma density at 40 mm, which corresponds to the surface of the inner electrode, is about 10^{14} cm⁻³; the calculated plasma velocity at the plasma flow front reaches 2-2.5 cm/ μ s. It should be noted that the BFC measurements give usually the underestimated density in the plasma flow. The main reason for this is the uncertainty of the flow velocity necessary for density calculations. The substitution of the front velocity, which is usually high, into the formula for the density calculations gives low plasma density. Low-velocity plasma, which follows the fast front, may have higher density but results in low ion current density.

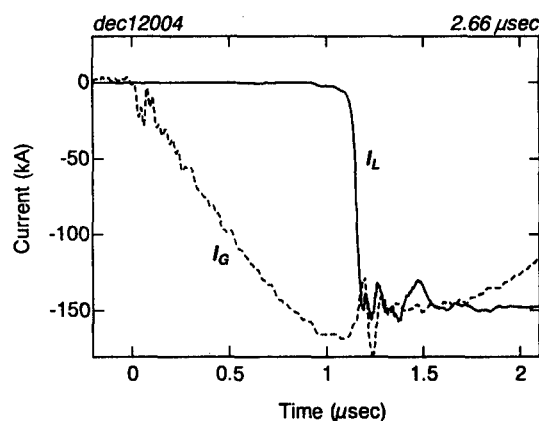


Fig.3. Generator current I_G and load current I_L .

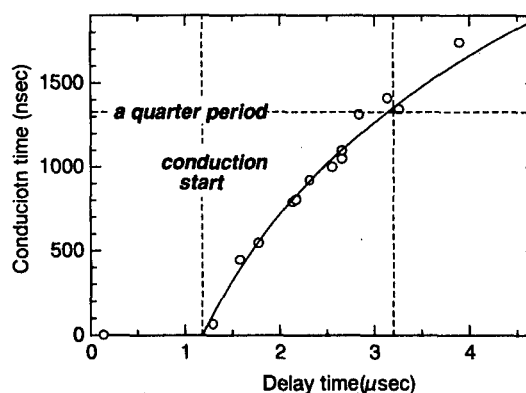


Fig.4. The POS conduction time vs delay time.

Fig. 3 shows the waveform of the generator current and the load current in POS experiments. The delay time for this figure is 2.66 μ s. The POS conducts the generator current for about 1.1 μ s and after that I_L rises rapidly in few tens of nanoseconds. The value of dI_L/dt reaches approximately 3.6×10^{12} A/s with corresponding load current pulse width of about 30 ns FWHM. The estimated value of the load inductance from the plasma gun location to the load is about 70 nH that gives the inductive voltage drop of approximately 250 kV. The dependence of the conduction time versus delay time is shown in Fig. 4. The plasma bridge connecting the electrodes builds up after approximately 1.2 μ s of the time delay and this is minimum necessary time of effective plasma fill of the POS region. The conduction time monotonously rises with the delay time. The POS conduction time over 1.4 μ s (longer than the quarter period of ASO-X generator current) is also possible, but load current rise rate decreases dramatically. Fig. 6 shows the dependence of dI_L/dt on the conduction time. This plot indicates the important relationship between two fundamental factors of POS operation.

It is clear, that in this system with given parameters, the best POS operation, which means both the fastest current rise rate and the longest conduction time not exceeding a quarter period, can be obtained when the delay time is about 2.7 μs . Charging the storage capacitors up to 60kV provides higher output current of ASO-X and the operation of POS should be better.

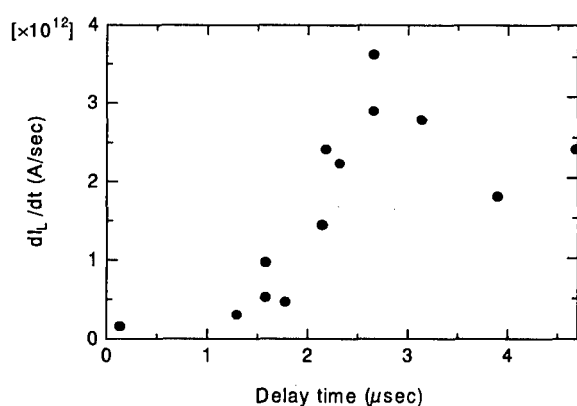


Fig.5. dI_L/dt vs POS conduction time.

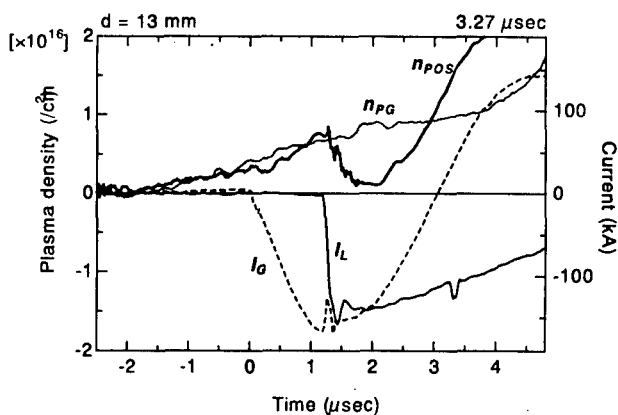


Fig. 6. Plasma densities produced by plasma guns only n_{pg} and during the POS operation with corresponding generator and load currents.

The preliminary interferometer measurements of the plasma density during the POS operation were carried out using a sensitive Michelson-type laser interferometer [5]. The density drop indicating the location of the vacuum gap is measured in the vicinity of the cathode. Fig. 6 shows the generator current, load current and plasma density at 13 mm from the cathode during a shot. The thin solid line (n_{pg}) curve shows the plasma density from the plasma gun without firing the main generator.

To improve the understanding of the POS features, the further plan of our research includes the study of plasma distribution in switch region during POS opening. The multichannel [6] interferometer measurements may be a proper method for that purpose. Such measurement has been performed with parallel electrodes in our laboratory successfully and the predominant gap location with the lowest average plasma density was observed in the center of interelectrode gap [7]. The initial ASO-X plasma density measurements showed different location of the vacuum gap, near the cathode, probably due to the higher magnetic field gradient between the POS electrodes. The magnitude of the azimuthal magnetic field is the highest near the inner electrode in the coaxial POS geometry used.

The ASO-X generator is found to be easy-to-operate, reliable and efficient current source. Using the POS, it provides fast load current rise necessary to drive such loads as liner or capillary discharge. This is an example of the successful replacement of the conventional pulsed power scheme with a Marx generator and with intermediate water storages. The scheme realized is compact, convenient and, by our point of view, has a good future.

REFERENCES

- [1] J. Fockler et. al. 9th IEEE International Pulsed Power Conference, Albuquerque, NM, pp. 431-436, 1993.
- [2] M. E. Cuneo, et. al. Ibid. pp. 423-426.
- [3] M. G. Mazarakis et. al. Ibid. pp. 427-430.
- [4] G. A. Mesyats et. al. IEEE Trans. Plasma Science, **15**, pp. 649-653, 1987.
- [5] I.V. Lisitsyn, et. al. Jpn. J. Appl. Phys. **36**, pp. 6986-6991, 1997.
- [6] I.V. Lisitsyn et. al. These proceedings.
- [7] I.V. Lisitsyn, et. al. Appl. Phys. Lett. **71**, pp. 2251-2252, 1997

RADIOACTIVE RESISTANCE OF SOLID DIELECTRICS

B. Loncar², D. Novaković¹, P. Osmokrović¹

¹*Faculty of Electrical Engineering, University of Belgrade, Bul. Revolucije 73, P.O.Box 816, 11000 Belgrade, Yugoslavia, Phone : (+381 11) 3248464, Fax : (+381 11) 180333*

²*Faculty of Technology and Metallurgy, University of Belgrade, Karnegijeva 4, P.O.Box 494, 11000 Belgrade, Yugoslavia, Phone : (+381 11) 3370398, Fax : (+381 11) 3370387*

I INTRODUCTION

Dielectrics as a special class of materials, significantly differs in its characteristics to those of conductors and semiconductors. Dielectrics have wide spectrum of different physical and structural characteristics, from which the differences in its electrical characteristics arise. The most important characteristics of dielectrics are: polarization, specific electrical conductivity, dielectric loss factor, dielectric constant, aging and dielectric breakdown. Factors which main influence this characteristics are: frequency, temperature, electric fields strength, radiation, time of exploitation and mechanical deformation. Consequences of previously mentioned factors on dielectric devices reliability depend on type of dielectric and the area of its application.

Effects of interaction of radioactive radiation with dielectric materials which have been used for passive isolators construction can be neglected, compared to the influence of other factors (humidity, temperature, aging, chemical reactions). On the other hand, consequences of radioactive radiation on dielectric components of active electric circuits may result in significant changes of there functions. Basic components of active electric circuits whose functioning is based on dielectric materials are capacitors.

Functioning of capacitors, which are used in military industry and space technology are most important in high risk work conditions, such as the performance under the influence of radiation is included [1]. Having in mind the constructive solution of discrete capacitors which are used in electronics it is reasonable to expect the influence of neutron and gamma radiation only [2].

The aim of this paper is to examine the influence of neutron and gamma radiation obtained from ²⁵²Cf and ⁶⁰Co on the dielectric loss factor ($\text{tg}\delta$) and capacitance (C) of the polycarbon and liscun capacitors. The obtained results are explained theoretically.

II THE INFLUENCE OF IONIZING RADIATION ON CAPACITORS

In Fig.1 the influence of ionizing radiation on organic materials is depicted [3]. The influence can be divided in two phases. As a consequence of first phase of ionization radiation, free electrons, positive ions and excited molecules are formed. In second phase free radicals are formed. Huge amount of free radicals in dielectric leads to irreversible changes which consist of destruction processes and structuring changes. Destruction is process of breaking main chains of connected macro molecules which cause drop of molecule mass and gas occurring. Destruction mechanism is determined by individual characteristics of radiated material. Nowadays, for larger number of dielectrics destruction process is not well known to the end. It should be noticed that radiation can change physical and electrical characteristics of dielectric materials [4].

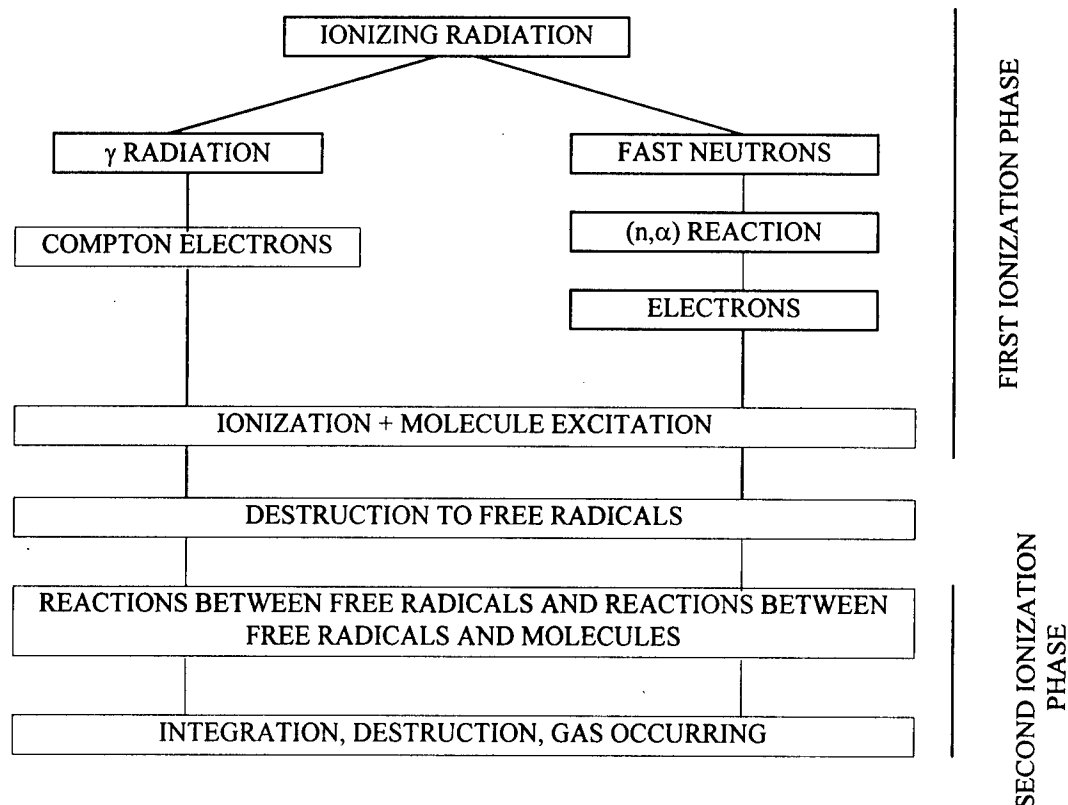


Fig. 1. Block scheme of the influence of ionizing radiation on organic materials

III EXPERIMENTAL PROCEDURE

The examination was carried out on the following commercial components:

- 1) Polycarbon Capacitors (nominal voltage 160 V, capacity 1μF),
- 2) Liscun Capacitors (nominal voltage 25V, capacity 3,25nF, 1,5nF, 0,625nF)

We examine the following capacitors characteristics:

- 1) the dielectric loss factor, $\text{tg}\delta$
- 2) capacitance, C

Measuring frequency was $f=100\text{kHz}$ for polycarbon capacitors and $f=120\text{ Hz}$ and $f=1\text{kHz}$ for liscun capacitors. Examined polycarbon capacitors have a very high insulated degree (10 -100 TΩ) and small losses ($\text{tg}\delta = 0,0015$), similar as liscun capacitors whose dielectric loss factor varied from $\text{tg}\delta = 0,003$ for $C=0,625\text{nF}$ to $\text{tg}\delta = 0,010$ for $C=3,25\text{nF}$. We examine the influence of $n+\gamma$ radiation from ^{252}Cf source on polycarbon capacitors characteristics and γ radiation from ^{60}Co source on liscun capacitors.

The californium ^{252}Cf isotope built on 12 06 1984 (weighting 2,265 μg) encapsulated in form of Cf_2O_3 was the $n+\gamma$ source. The form of neutron energy density spectra can be approximated by following equation [5,6]:

$$S_n(E) = 1,98 e^{-0,88} \sinh(2E)^{1/2} 10^9 \text{ ns}^{-1} / 4\pi,$$

where E is energy in MeV. The neutron spectrum maximum was at 2MeV, neutron spectrum maximum energy was 20MeV. The other characteristics of ^{252}Cf source are presented as follows:

- 1) the effective half life time of ^{252}Cf source is 2,64 years,
- 2) half life of spontaneous fission is 83 years,

- 3) specific neutron intensity is $2,34 \times 10^6$ [1/ μgs],
- 4) specific gamma intensity is $5,3 \times 10^9 \pm 3 \%$ [1/ μgs],
- 5) average neutron energy is 6,117 MeV.

For polycarbon capacitors the double exponential voltage pulse ($1,2 \times 50\mu\text{s}$) was applied.

The ^{60}Co is standard γ radioactive source from SSDL Vinca Laboratory in Belgrade. We examined the liscun capacitors which were taking a 0,416 Mrad (4162 Gy) i.e. 0,244 Mrad (2440 Gy), respectively. The dose rate amounted to 68,2324 Gy/h i.e. 133,13 Gy/h.

The measuring methodology were based on the computer controlled high quality instruments and statistics experiment organization. This approach assures the high accuracy, reliability and repeatability of performed measurements.

IV EXPERIMENTAL RESULTS

Table I presents values for F_n and F_γ (neutron fluence and gamma flux respectively) dependencies versus N_F (the exposure number) for polycarbon capacitors. In Fig.4 the change of capacity of polycarbon capacitors versus $n+\gamma$ fluence/flux radiation is depicted. According to this diagram we can conclude that radiation causes a decrease in the capacity of capacitors. After repeating this experiment in 120 hours, effects of reversible nature were noticed. During examination a measurable influence of $n+\gamma$ radiation on the dielectric loss factor $\text{tg}\delta$ was not found.

N_F	$F_n(n / \text{cm}^2) \cdot 10^{10}$	$F_\gamma(\gamma / \text{cm}^2) \cdot 10^{13}$
0	0	0
1	2.79	6.8
2	5.59	13.6
3	8.37	20.4

Table I Values for neutron fluence (F_N) and gamma flux (F_γ) versus N_F (the exposure number) for polycarbon capacitors

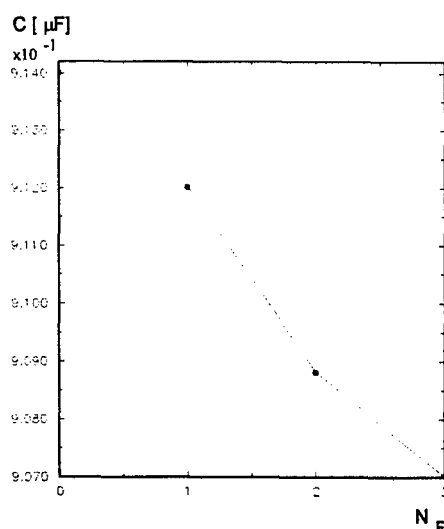


Fig.4 Polycarbon capacitor value versus $n+\gamma$ fluens/ flux characteristics

V DISCUSSION

The decrease of polycarbon capacitors capacity when under the radiation of $n+\gamma$ flux can be explained by forming of ionized structure inside the dielectric volume. Those structures influence the partial screening of the electric field in the capacitors. Larger amount of ions appearing in dielectric causes higher influence of ion type polarization on dielectric constant of material. This leads to decrease of the capacity [7]. Also, ion pairs by there local field partially screen external electric field. Still, the change in the capacitance of the capacitors caused by it is relatively small. Permanent presence of these structures inside the capacitors dielectric volume can cause leads breakdown voltage decreasing and consequently speed-up of capacitor aging. The reversibility of these phenomena is a result of recombination processes inside the capacitors dielectric. This shows that the doses of radiation were not high enough to cause significant changes in the molecular structure of the dielectric. Since the cross section of inelastic interaction of neutron component is higher than corresponding γ component [8,9] noticed effect is mostly result of neutron component radiation. We confirmed this conclusion with using ^{60}Co γ sources when we weren't found measurable changes of capacitors characteristics.

VI CONCLUSION

In this paper the result of examination of radiation resistance of some solid dielectrics were presented. The influence of $n+\gamma$ radiation was tested on the polycarbon capacitors and the influence of γ radiation was tested on the liscun capacitors. It was founded that radiation integral dose levels applied to polycarbon capacitors causing it capacitance decreasing. Also, polycarbon capacitors lead to more frequent aging processes.

On the other hand we can conclude that γ radiation in given absorbed dose and dose rate is too small for capacitors characteristics measurable changes.

At the end we may conclude that $n+\gamma$ radiation from ^{252}Cf is most dangerous for destruction of capacitors characteristics than γ radiation from ^{60}Co . Also, we can conclude that capacitors with liscun as dielectric have better protective characteristics after the ionization then the capacitors with polycarbon as solid dielectric.

REFERENCES

- [1] Z. Markov: Over-voltage protection in electronics and telecommunications, Technical book ,1983
- [2] P. Osmokrović, M. Stojanović, B. Lončar, N. Kartalović, I. Krivokapić, " Radioactive resistance of elements for over-voltage protection of low-voltage systems," *Nuclear Instruments and Methods in Physics Research B*, article no. 40440, pp. 1-9, dispatch 11 February 1998.
- [3] Н.С. Костюков, Н.П. Антонова: Радиационное материаловедение, Атомиздат, Москва, 1979
- [4] Ф.А. Михлис: Радиационная физика и химия полимеров, Атомиздат, Москва, 1972
- [5] Atomic Energy Commission: Guide for Fabricating and Handling ^{252}Cf sources, USA, January 1971.
- [6] A. B. Chilton, J. K. Shultis, R. E. Faw: Principles of Radiation Shielding (Prentice- Hall, Inc. New Jersey, 1984)
- [7] N. W. Aschroft , N. D. Mermin: Solid State Physics (Holt, Reinhart & Winston, New York, 1976)
- [8] V. S. Vavilov, H. A. Ukhin: Radiation Effects in Semiconductors and Semiconductors Devices (Consultants Bureau, New York, 1977)
- [9] G. C. Messenger, M. S. Ash: The Effects of Radiation on Electronic Systems (Van Nostrand Reinhold, New York, 1992)

A study of parameters useful for describing plasma-opening switches*

C. W. Mendel, Jr.,[†] D. B. Seidel, and S. E. Rosenthal
Sandia National Laboratories, Albuquerque, NM 87185

INTRODUCTION

Plasma opening switches (POS) have been used continually and studied since their introduction in 1976.¹ During that period they have performed well for prepulse suppression and sharpening the front of the power pulse.^{1,2} Their use for long conduction time and rapid opening to stand off high voltage in the same POS has met with very limited success. There has been a large theoretical effort involving models and particle-in-cell simulations (PICS), but the connection between theory and experiment has been tenuous at best, and convincing agreement with experiment has been minimal.

The authors believe progress toward long conduction and rapid opening would be faster if macroscopic physical parameters describing the physics of the switch were used to compare experiment to simulation. One of these parameters (electron flow impedance^{3,4}) has been used to describe the electrical characteristics of the POS. This parameter provides a good description of both the standard POS (SPOS) and the magnetically controlled POS (MCPOS) because its value is sensibly independent of load current. An additional parameter, the effective mass of the plasma, was measured in one MCPOS experiment.³ In this article we will describe other parameters important to operation of the SPOS and the MCPOS, and parameters important in designing PICS used to study these devices.

EFFECTIVE GAP AND FLOW IMPEDANCE

Metal surfaces in devices of interest are space-charge-limited electron emitters. Therefore the only electric field on the boundaries are at anode surfaces. The net charge on such surfaces is small compared to the plasma electron or ion charge in any POS. A POS plasma is always quasi-neutral on the global scale. It will be shown later that large voltage drops must occur across sheaths in regions that are not quasi-neutral, where the electron density is small compared the bulk of the plasma. Electrons flow in a direction normal to the electric field, and ions flow along the electric field in these sheaths.

We define effective sheath thicknesses for these sheaths. Consider sheaths with only electrons for the moment, and define the effective gap, g_e , as the ratio of the voltage across the sheath to the electric field at the anode surface. Using pressure balance across the current sheet, and replacing magnetic field by current, I , and electric field by charge per unit length,⁴ Q , we get $(I_a^2 - I_c^2)(1 + P^2) = c^2 Q_a^2 = c^2 [2\pi r_c V/g_e]^2 = (1 + P^2)V^2/Z_f^2$ where the subscripts refer to values at the anode and cathode and Z_f the flow impedance. P is the pitch of the magnetic field, i.e. $P = B_z/B_\theta$. For the SPOS, P is zero. We will neglect the difference between the radii of the anode and cathode electrodes, and use the cathode radius, r_c for both. The flow impedance is equal to the TEM wave impedance for a transmission line with radius r_c and gap g_e , so effective gap and flow impedance are alternative measures of the same effect.⁴ For electrical measurements flow impedance is more convenient.

Using pressure balance across a sheath with only ions, and defining the effective gap by $g_e = V/E_c$, $I_i = \pi r_c L_e [q_i \epsilon_0^2 / (2m_i)]^{1/2} V^{3/2} / g_i^2$ where L_e is the length of the plasma, or an effective length if the gap is a function of axial position. In this case we use the same symbol, g_e , as the electron case because we will see that they have the same value. Because electron current is normal to the electric field, it flows along equipotentials. Thus there is a function $f(\phi/V)$ such

*Sandia is a multiprogram laboratory operated by Sandia Corporation, a Lockheed Martin Company, for the United States Department of Energy under Contract DE-AC04-94AL85000

[†]Cove Consulting, Albuquerque, NM 87110

that $I^2 = I_c^2 + (I_a^2 - I_c^2)f(\phi/V)$ where $f(0)=0$ and $f(1)=1$. Again using pressure balance

$$(I^2 - I_c^2)(1 + P^2) - \frac{2(2\pi r_c)^2 J_i}{\mu_0} \left(\left[\frac{2m_i V}{q_i} \right]^{1/2} - \left[\frac{2m_i (V - \Phi)}{q_i} \right]^{1/2} \right) = c^2 Q^2.$$

Using $Q=0$, $I=I_a$ and $\phi=V$ at the anode side of the sheath shows that the values of g_e defined by ion and electron flow above, are equivalent. Replacing I by $f(\phi/V)$ with the above expression, this can be integrated to get $g/g_e = Z_v/Z_f = \int_0^1 [(1-\eta)^{1/2} - (1-f(\eta))]^{-1/2} d\eta$ where g is the actual gap between the radii where Q (and E) are zero. If gap varies with axial position, then g is the minimum gap, and the effective length is given by $L_e = g^2 \int g^{-2}(z) dz$ integrated over the length of the plasma.

The equivalence of these gaps was tested using PICS where the plasma was modeled as a conducting block with ion emission at its surface (Fig. 1 inset). The load was an electron diode. The POS gap and the load gap were varied between PICS. Protons were used to increase the ion current relative to the electron current. Figure 1 shows a plot of effective gap measured with ion current plotted versus that measured with electron current. The gap is shown both as a distance and as an impedance. There are three POS gaps at three load gaps represented in the plot. The bars on the points represent the spatial noise in the data. The point with the large variation came from a simulation where the electron flow broke into vortices. The data fall on a line of slope one as expected. In all cases the flow impedance is 0.6 times the vacuum impedance of the POS gap.

We conclude that only one parameter is needed to model both electron and ion current in a circuit model of a POS if the ion species is known. The flow impedance needs to be an appreciable fraction of the vacuum impedance (i.e. the effective gap needs to be an appreciable fraction of the actual gap) for efficient power transfer to a load.

VOLTAGE-AVERAGED ELECTRON CHARGE DENSITY IN A CURRENT SHEET

Due to the small mass of the electrons, the rate of change of momentum of the electron cloud is small when compared to the electric and the magnetic force on the cloud over most of the POS. The exceptions to this are generally in regions near the electrodes where electrons are emitted or lost. Using $\rho_e = n_e e$ and $\rho_i = n_i q_i$, $-\rho_e \vec{E} + \vec{j} \times \vec{B} = d(m_e \rho_e \vec{v}/e)/dt \approx 0$ where we neglect the contribution of ion flow to the current. Using Ampere's law and neglecting displacement current, $\rho_e \vec{E} = -\nabla B^2/(2\mu_0)$ where we neglect curvature of field lines in comparison to the thinness of current sheets. This expression has been used in several forms^{5,6,4} in areas of plasma physics and magnetically-insulated electron flow. It is valid in non-neutral and quasi-neutral plasmas. Integrating from cathode to anode along a path through the plasma and avoiding regions where electrons are emitted or lost, $(1 + P^2)(I_a^2 - I_c^2) = 2(2\pi r_c)^2 \langle \rho_e \rangle V/\mu_0$ or $\langle \rho_e \rangle = \mu_0(1 + P^2)V/[2(2\pi r_c)^2 Z_f^2] = \epsilon_0 V/[2g_e^2]$. $\langle \rho_e \rangle$ is voltage-averaged charge density,

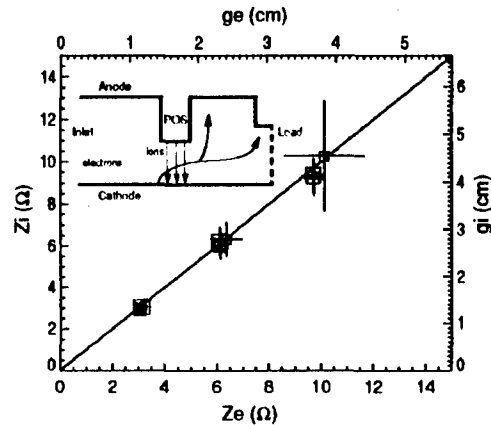


Figure 1. Ion effective gap plotted versus electron effective gap. All of these gaps are 0.6 of the actual gap.

i.e., the field-weighted average of ρ_e , $\langle \rho_e \rangle = \int_c^a \rho_e d\Phi / V = \int_c^a \rho_e \vec{E} \cdot d\vec{s} / V \equiv \overline{\rho_e} \vec{E} / \vec{E}$.

Because of the high charge density of a POS plasma, we can write $(\rho_e g^2) / (2\epsilon_0) \gg V$ so $\langle \rho_e \rangle \ll \rho_e g / g_e$. Thus when the POS is open (so g_e is comparable to g) the electron charge density in the current sheet must be small compared to that in the plasma for efficient power transfer to the load.

Figure 2 is a plot of electron charge density, ion charge density, and potential versus radius for a PIC simulation of an open MCPOS with an externally-applied slow magnetic field and a fast-coil-driven magnetic field. It is seen that the charge density is low where the potential is changing rapidly as predicted. Using the expression above for $\langle \rho \rangle$, with $V=0.65$ MV, $Z_f=3.0$ Ω , and $P=1.77$ taken from the simulation data, we get $\langle \rho \rangle = 0.063$ C/m², which is also shown in Fig. 2. Clearly the value is calculated correctly, since it agrees with ρ_e where the electric field is large.

This can be used to get the electron charge density in the sheath of an experimental POS.

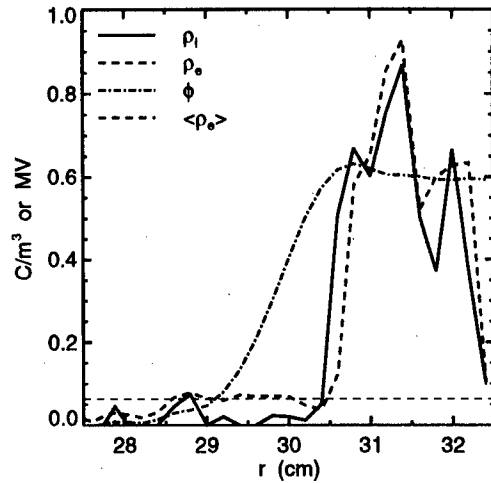


Figure 2. ρ_e , ρ_i , and ϕ plotted versus radius for an open MCPOS. Notice that in the region of strong electric field that $\rho_e = \langle \rho_e \rangle$.

IMPORTANT PARAMETERS FOR PIC SIMULATIONS

It is impractical to model POS using PICS with experimental densities and conduction times. Moreover, it is desirable to run many simulations with run times of no more than a few hours, which requires plasma parameters to be even further from experimental values. When a magnetic field pushes on a POS plasma, the electron density in the current sheet is roughly the same as the plasma electron density, so there is a voltage drop^{5,6} of about $\mu_0 I_a^2 / [2(2\pi r_c)^2 \rho_p]$. This value is of order of kilovolts in experiments, and should be small compared to $mc^2/e=511$ KV in a simulation, or else the current sheet will not be quasi-neutral as it is in an experiment, and the cathode sheath will not form properly.

The current sheet in the plasma will be c/ω_{pe} thick, so the simulation's spatial cell size, δ , must be smaller than this value. In addition, numerical heating will give an artificial thermal velocity of $\omega_{pe}\delta$. The plasma pressure due to this "numerical heat" must be small in comparison to the magnetic pressure, thus $I_a / (2\pi r_c \rho_p c) \equiv \delta_{nh} \gg \delta$. This criterion is more stringent than the first for a POS plasma. For a group of 25 simulations, when $\delta/\delta_{nh} < 0.5$ the error in energy conservation was $< 5\%$, when $\delta/\delta_{nh} \sim 1$ the error was $\sim 10\%$, and when $\delta/\delta_{nh} \sim 3$ the error was $\sim 50\%$.

MAGNETIC VELOCITY AND ELECTRON REPLACEMENT VELOCITY

The sub-microsecond time scale of POS is too short for momentum transfer between the ion cloud and the electron cloud by collisions or turbulence. Because of this there can be no appreciable magnetic field penetration of the plasma electron cloud. However, if electrons are replaced by emitted electrons, momentum is transferred to the electrodes and flux penetrates the ion cloud. The original plasma electrons are replaced by electrons emitted from the cathode in regions of high magnetic field. This occurs if there is an azimuthal magnetic field since the current will involve cathode emission, as is always the case for a POS. If there is a radial and axial field, as in the MCPOS, the transfer of angular momentum to the anode necessary for these fields to penetrate involves the radial current as a mechanism to carry the electrons with their angular momentum to the anode.

Consider the simple case of a radial washer of current replacing the electrons in the plasma with emitted electrons. The plasma electrons, of charge density ρ_p , are in a region of zero mag-

netic field ahead of the washer. As the washer moves through the plasma these electrons are lost, and replaced by a like charge of emitted electrons. If the current through the POS is I , and the current of plasma electrons to the anode is I_p , then the washer moves through the plasma with a velocity u given by $2\pi r_c \rho_p g u = I_p$ and the remainder of the current to the anode is in emitted electrons with current $I - I_p$. This can be rewritten as $u = u_r I_p / I$ where $u_r = I / 2\pi r_c \rho_p g$ is the maximum possible replacement velocity.

The plasma behind the washer (consisting of ions and emitted electrons) is moving with a velocity v due to the impulse of the magnetic field. From electron charge conservation $\rho_p u = \rho_e (u - v)$ where ρ_e is the electron density behind the washer. Using momentum balance, $uv = v_m^2$ where $v_m = (\mu_0 q_i / 2\rho_p m_i)^{1/2} I / 2\pi r_c$. The change in velocity of the ions is due to a potential drop, $(uv - v^2/2)m_i/q_i$, across the washer. If $u = v_m$, then also $v = v_m$, and the ions reside in a zero-thickness layer. u_r is the velocity sometimes called the "Hall penetration velocity⁷," but is derived here from charge conservation without the reference to the Hall current term.

Although this model has assumed a radial current sheet and azimuthal magnetic field, the magnetic velocity, v_m , could include fields due to other currents. The actual replacement velocity, u , is not known because the ratio I_p/I is not known, but the maximum value, u_r , is known, and u should be comparable. Figure 3 shows a measured value of u from a PIC simulation of a SPOS. The current sheet is not radial at all radii, but does tend to move uniformly in the z direction. For this case $u_r = 0.53$ cm/ns and $u = 0.40$ cm/ns (Fig. 3). From the current, $v_m = 0.053$ cm/ns we can calculate the plasma velocity $v = 0.0070$ cm/ns behind the current sheet. The voltage drop across the current sheet should be 35 KV, which agrees with the simulation.

The velocity parameters u_r and v_m , and the relationship between them, are important in how a POS behaves. It is important to preserve the relationship in scaling a PICS of a POS. If the replacement velocity is appreciably faster than the magnetic velocity, the magnetic field will penetrate the ion cloud, and will not be able to move it to generate the low-density sheath needed for efficient operation. Erosion of ions by the electric field will still occur, but if the density is high enough to keep the plasma in place for long conduction time the POS will not open rapidly.

In the case of an MCPOS the replacement velocity must be smaller than the magnetic velocity when the control magnetic field (due to the fast coil) is energized to be confident that the fast field will not be able to penetrate the ion cloud.

REFERENCES

- [1] C. W. Mendel, Jr and S. A. Goldstein, J. Appl. Phys. **48**, 1004 (1977).
- [2] P. F. Ottinger, S. A. Goldstein, R. A. Meger, J. Appl. Phys. **56**, 774 (1984).
- [3] C. W. Mendel, Jr., M. E. Savage, D. M. Zagar, W. W. Simpson, T. W. Grassner, and J. P. Quintenz, J. Appl. Phys. **71**, 3731 (1992).
- [4] C. W. Mendel, Jr. and S. E. Rosenthal, Phys. Plasmas **2**, 1332 (1995).
- [5] J. M. Grossmann, S. B. Swanekamp, P. F. Ottinger, R. J. Comisso, D. D. Hinshelwood, and B. V. Weber, Phys. Plasmas **2**, 299 (1995).
- [6] A. Fruchtman, Phys. Plasmas **3**, 3111 (1996).
- [7] A. Fruchtman and Y. Maron, Phys. Fluids B **3**, 1546 (1991).

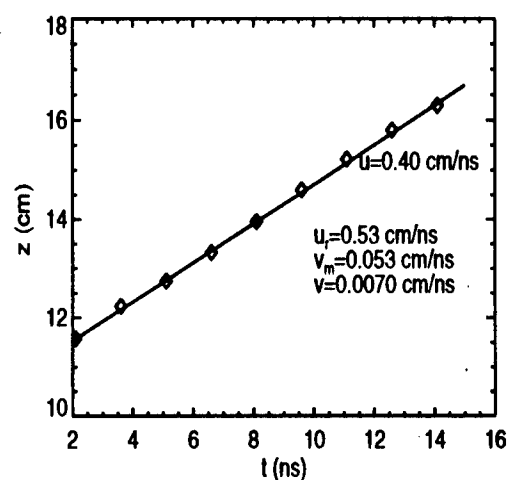


Figure 3. Axial penetration of magnetic field into a SPOS versus time. The slope is 0.4 cm/ns compared to the maximum replacement velocity of 0.53 cm/ns.

ECTON PROCESSES IN PULSED HIGH-CURRENT ELECTRON BEAMS

G.A. Mesyats

*Institute of Electrophysics, Russian Academy of Sciences
34 Komsomolskaya St., Ekaterinburg 620049, Russia*

Pulsed high-current electron beams are known to be produced by initiating explosive electron emission. This type of emission takes place when an energy exceeding the sublimation energy of the cathode material has been concentrated in a cathode microvolume within a short time. The overheating of the material in the microvolume leads to a microexplosion followed by thermal electron emission giving rise to a bunch of electrons, which we have named an ecton. Each ecton contains 10^{11} - 10^{12} electrons. The energy responsible for the appearance of an ecton approximates 10^{-8} J. The ecton lifetime is 10^{-9} - 10^{-8} s for many metals. The interrupted character of explosive electron emission is accounted for by the self-cooling of the emission zone due to heat conduction and a decrease in current density. Ectons can be detected by passing the current of explosive electron emission through a small hole of radius $\ll 1$ mm made in the anode. In doing this, the total explosive emission current, which generally increases gradually, changes to a current showing a great number of spontaneous bursts of duration $< 10^{-8}$ s. Investigations of the ion erosion of cathodes, the ejection of drops, the electron beams produced, etc. have allowed a comprehensive study of the properties of ectons.

Thus, we have demonstrated that a high-current electron beam produced through explosive electron emission consists of a great number of short-living microbeams and ectons. The ecton structure of this type of beam may affect its properties, namely, the current density distribution over the beam cross section, the uniformity of the electron emission from the cathode, the temporal uniformity of the beam, etc.

COMPACT PULSE «COLD CATHODE» FLASH X-RAY TUBE POWER SUPPLY UNIT WITH SOLID-STATE OPENING SWITCH.

A. Dunaevsky*, K. Golubinsky, A. Lomako, O. Morgun

LRMT Ltd., P.O.B. 3025, Kharkov 310145, Ukraine

*Department of Physics, Technion, Haifa 32000, Israel

INTRODUCTION

From early 70s x-ray compact pulse x-ray generators (PXG) with «cold cathode» x-ray tubes (CCXT) could be found in various industry and science applications. A lot of advantages such as small size and weight, low power, reliability made them very competitive with classic x-ray generators especially in defectoscopy, scientific research work and many other applications.

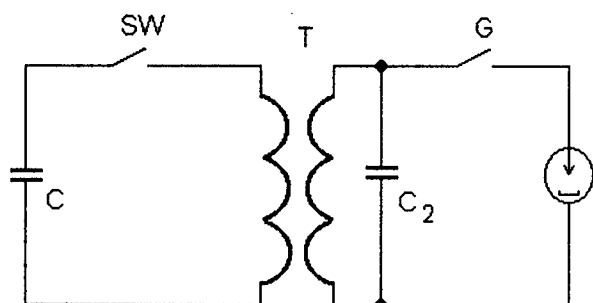


Figure 1.

At present a lot of pulse generators in commercially available PXG follow the 30-year classic scheme that is shown in Fig. 1 [1]. This scheme consists of primary capacitive energy storage C, which is charged from external source of different kind, fast switch SW, pulse transformer T, second charging capacitor C₂, two-electrode gas spark gap G and x-ray tube CCXT. When switch SW turns on, capacitor C discharges through primary winding of the transformer T.

Second winding of T charges the capacitor C₂ until switch G connects C₂ to the tube CCXT. High rise time of this-type formed high voltage pulse lead to intense explosive plasma formation and CCXT «turns on». Usually, duration of x-ray pulse not exceeds 50 ns and is determined by anode-cathode gap shortening by anode and cathode plasmas.

Some essential characteristics of described feeding scheme prevent it from being used in wider spectrum of applications and especially in x-ray medical imaging. They are:

- 1) High-voltage pulse stability and exposition dose and maximum x-ray quantum energy is determined by G breakthrough voltage instability, which is not better than 20 %. This energy variation could not be applied in medicine, because the energy had to be controlled within (at last) 10 % interval.
- 2) X-ray energy controlling is a big problem.
- 3) Focal spot size of CCXT is large enough (> 2 mm), and this put some restrictions on patient-source distances for most resolution-demanding applications.

In this paper we will describe developed PXG with CCXT which is almost free from described problems.

PRINCIPLES OF OPERATION

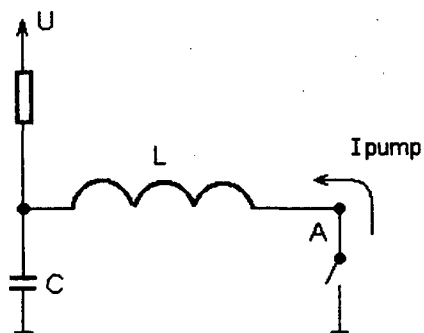


Figure 2

High voltage pulse in our generator is produced by Semiconductor Opening Switch (SOS) implementation in inductive energy storage circuit. Idea of current flow breaking is widely used in high-power technique, where Plasma Opening Switches opened a new page in power transitions [2], [3]. A lot of investigations carried out in the field of pulsed power solid-state opening switches both specially controlled [4] and based on commercial high-voltage diodes [5].

To investigate the behaviors of commercially available high-voltage diodes when implemented as SOS we studied a number of fUSSR-manufactured high-voltage diodes with breakdown voltage more than 5 kV. Testing circuit is presented on Figure 2. By means of changing U , L and C we collect a set of data, which allow us to make some conclusions:

1. Reverse conductivity phase (T_{REV} in Figure 3) duration is independent on pump current and pump period and is determined by junction manufacturing process.
2. At some conditions SOS could be safely overloaded by direct current with a factor of up to 100.
3. When SOS opens it could be safely overloaded by reverse voltage with a factor up to 10, due to complete charge carriers removing from junctions and thus total back current suppression.
4. SOS opening time is much less than recovery time for all types of tested diodes.
5. No parameters changing were found after 10^5 shorts in repetition rate of 0.2 Hz.
6. High voltage instability (for constant SOS operational temperature) is determined by primary capacitor voltage instability.

Described SOS with commercial high-voltage diodes could be used in PXG with usual CXT. In Table 1 one can see exact components specification for PXG with commercial CCXT IMA6D from Svetlana-Rentgen, Russia. To prevent CCXT electrode destruction due to anode-cathode gap shortening, a pulse duration limiting capacitor (KVI-2, 15 pF x 20kV) was inserted in serial with IMA6D.

Table 1

U	25 - 31.5 kV
C	$2 \times K15-25, 3300 \text{ pF} \times 40 \text{ kV}$
L	Ferrite 700HM, 2×13 loops
SOS	$14 \times K1108B$ (7 serial \times 2 parallel)
Pump period	1 MHz
SOS maximum pump current	200 A (I_{max} for K1108B - 1 A)
SOS opening current	130 A
CCXT current duration, FWHH	50-60 ns
p-i-n detector signal duration, FWHH	30 ns

Careful selection of timings provides submillimeter focal spot size operational mode [6] for CCXT IMA6D, which allow adjusting the x-ray energy. Moreover, developed PXG could be used with other types of commercial PXG. For example, we test it with IMA150D 150 kV CCXT. Stable tube ignition was registered, pulse transferred energy was about 80 % of standard ignition scheme.

APPLICATIONS

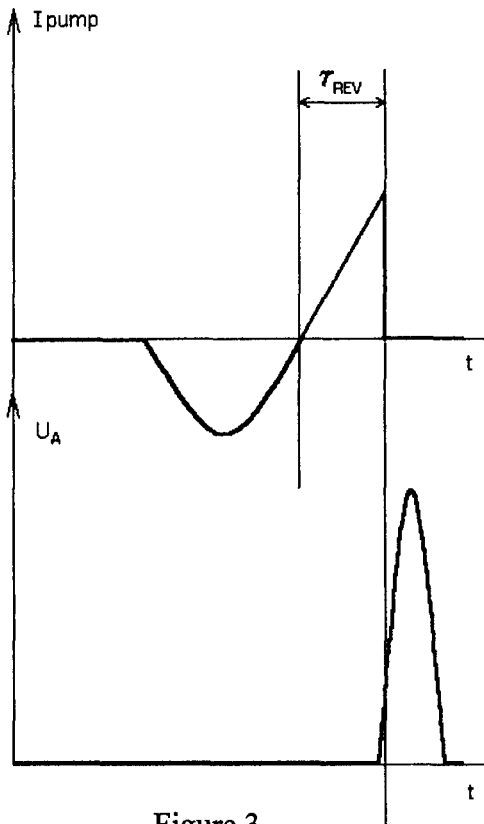


Figure 3.

Developed PXG was implemented in Digital Dental Diagnostic System DIRA, which uses a CCD-based area x-ray sensor. DIRA operational parameters are presented in Table 2. In Fig. 4 are shown some samples of digital x-ray images for extracted teeth. In Fig. 5 the digital picture of spatial resolution test pattern is shown. Achieved level (4.6 lp/mm) of spatial resolution satisfies to demands of dental radiography.

Special W95 software provides PXG and sensor control, data acquisition, image treatment and database services. ISA interface card provides DMA bi-directional data transactions. The software carries out all DIRA control.

CCD sensor area is 17x19 mm. For x-ray - optical conversion we use a thin (240 μm) layer of Y₂O₂S-Eu phosphorus. Light collects by means of fiber plate mounted directly onto CCD photoarray. Sensor is hermetically sealed, has a 9 mm thickness and could be used for intraoral applications.



Figure 4.

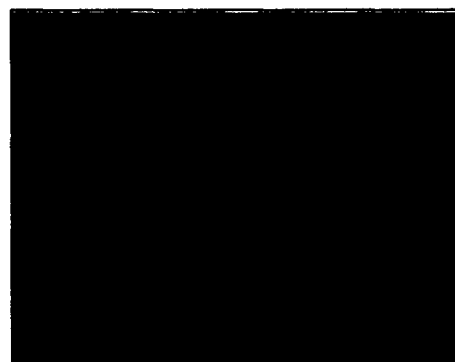


Figure 5.

Table 2

Size	300x150x300 mm
Weight (including transformer oil)	4.5 kg
X-ray flash energy	55 - 75 kV, PC controlled
X-ray flash duration	30 ns
X-ray flash stability	better than 10 %
X-ray flash spot size	< 0.2 mm
Exposition dose per pulse at 6 sm. with inherent filtration only	10 mR @ 65 kV
Control interface	PC-based software

We suppose that the first description of abnormally high light yield of x-ray phosphorus under exposure by short powerful x-ray flashes was made in [7] by L.S. Birks and colleagues. Due to this effect DIRA is capable to produce digital pictures with clinically acceptable contrast resolution at doses which are determined by x-ray quantum fluctuations. For example, images at Fig. 4 require only about 3 mR (measured by ionization chamber and TLD detectors).

Pulse x-ray generator and Digital Dental Diagnostic System described in the report are protected by Russian and Ukrainian patents, priorities N94017323/14(017085) and N21390A respectively.

REFERENCES

1. Zukerman V.A., Tarasova L. V., Lobov S. I., *UFN*, 1971, V. 103, 2, pp. 319-337.
2. Mendel C.W., Goldstein S.A., Miller P.A. *Proc. IEEE Pulse Power Conference*, Labboc, 1976. pp.1c-2.
3. Kovalchuk B.M., Mesyats G. A., *Doklady Akademii Nauk SSSR*, 1985. V. 284, 4, pp.857-859.
4. Grekhov I.V. Ephanov V.M., Kardo-Sysoev A.F., Shenderoy S.V., *Pisma v JTF*, 1983. V. 9, 7, p. 435
5. Kotov Yu.A., Mesyats G.A., Rukin S.N., Filatov A.L., *Doklady Akademii Nauk SSSR*, 1983. V. 330, 3, pp. 315-317.
6. A. Dunaevsky, K. Golubinsky, A. Lomako, O. Morgun. Operational mode of «cold cathode» flash x-ray tubes which provides sub-millimeter focal spot size and electron beam energy adjusting. // *Beams '98 Proceedings*.
7. L.S. Birks, J. W. Sandelin, C. M. Dozier. Calibration of Rare-Earth X-Ray Intensifying Screens in the 15-70 keV Energy Range For Use on Pulsed X-ray Sources. *Rev. Sci. Instrum.* 1976, V. 47, 12, pp.1475-1478.

POS EXPERIMENTS ON HAWK USING AN INVERSE PINCH, GAS PLASMA SOURCE

John J. Moschella, R.C. Hazelton, C. Vidoli, and E.J. Yadlowsky
*Hy-Tech Research Corporation,
104 Centre Court, Radford VA, 24141, USA*

B.V. Weber, D.C. Black, D.D. Hinshelwood, B. Moosmann, and S.J. Stephanakis
*Plasma Physics Branch
Naval Research Laboratory, Washington DC, 20375-5000*

Abstract: We report results from the first series of POS experiments using an "Inverse Pinch" gas plasma source on the Hawk generator with a short circuit load. Our results showed that under certain conditions a hydrogen plasma filled switch resulted in significantly higher POS voltages and faster load current rise times than other types of IP produced plasmas, or cable guns. This situation existed only for the case where the initial plasma density was radially uniform. For Ar plasmas, the conducted current scaled with the injected mass according to MHD theory if the average charge state was +2, while for the H plasmas $M/Z=6$ was needed to reach agreement with theory. The H result can be reconciled if, the additional electrons that we detected during the conduction phase, originated from secondary plasma with $M/Z=12.5$. We also found with the IP source that, during opening, the electron density in a large radial region (≥ 1 cm) was below the sensitivity limit of the interferometer.

I. INTRODUCTION

The POS is the key component of an inductive storage, pulse compression technique. Plasma sources commonly used for μ s conduction time POSs, such as cable guns or flashboards, produce plasmas dominated by carbon or carbon/fluorine ions, with 6-14 amu/electron.[1] Typically, an array of these sources are arranged around the outside of the outer conductor, usually the anode, and injected into the switch gap through a semi-transparent structure. Although the POS has been successful from the standpoint of achieving significant power gain factors, data from a number of experiments have indicated that the inferred magnetically insulated switch gap, which is proportional to the load voltage, was only a few millimeters while the physical dimensions of the transmission line are generally an order of magnitude larger.[2,3] Based on these experiments, it would seem reasonable to assert the POS could be dramatically improved if this gap can be increased to a larger fraction of the transmission line. Experiments conducted on the Double generator (250 kA, 850 ns quarter period) indicated that the composition of the fill plasma had a significant impact on POS characteristics, in particular the size of the inferred gap.[4] These experiments showed that using hydrogen based plasmas increased the switch voltage and impedance by factors of 1.5-2. The plasma for these experiments was injected into the cylindrical POS using an array of 4 coaxial gas plasma guns. Subsequent attempts to reproduce these results, on the higher current Hawk generator using similar plasma sources, was unsuccessful.[5]

II. THE EXPERIMENT

The "inverse pinch" (IP) plasma source,[6] is the inverse of a conventional gas puff z-pinch that produces a radially expanding plasma ring. The source is operated by firing a pulsed gas valve and, after an appropriate time delay (350-700 μ s), current is supplied by a 20 kV, 7.4 μ F capacitor bank. This results in the electrical breakdown of the gas in the form of a current carrying shell that is forced radially outward by magnetic pressure. The ejected

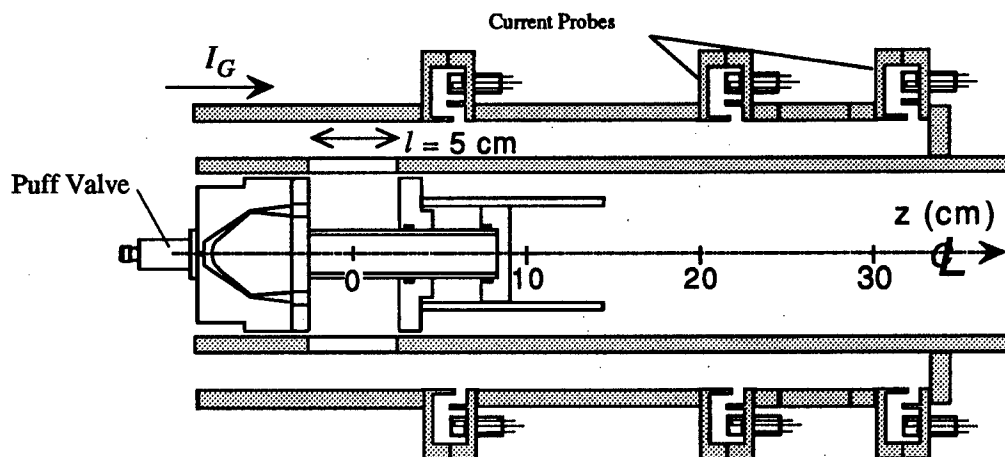


FIG. 1. The IP Plasma source mounted inside the Hawk cathode.

plasma is best characterized as a discrete ring that expands radially with essentially no plasma in its wake. As shown in FIG. 1, the source was mounted inside the center conductor on the Hawk[2] (720 kA, 1.3 μ s quarter period) generator at NRL configured with a 6.33 cm radius inner conductor (cathode), an 8.57 cm radius outer conductor, and a short circuit load located 33 cm downstream from the center of the POS. An 86% transparent cathode with 18 equally spaced windows, 5 cm long, allowed the plasma from the IP to enter the inter-electrode region. Machine diagnostics included various current probes and an axial line-of-sight, 8 channel, He-Ne heterodyne interferometer. Each channel sampled the plasma at a different radial position over the range from $r=6.5$ cm to $r=8.5$ cm with equally spaced intervals. As a result the temporal evolution of the radial density profile, as well as the total electron inventory, could be measured on each shot. Experiments were performed using various gases (H_2 , Ne, Ar, Air) as well as cable guns for comparison.

III. EXPERIMENTAL OBSERVATIONS

FIG. 2 shows the average electron density vs. radius in the POS gap at various times after the start of current flow in the IP when H_2 gas was used. This figure demonstrates control of the initial plasma distribution using the delay between discharging the source and the generator; where it is possible to have both positive and negative initial density gradients, and a uniform distribution. Qualitatively similar results were obtained with the other gases at different delay times. The distributions shown in FIG. 2 result from the fact that the source produced a discrete, expanding plasma ring that redistributes its plasma in the POS gap over the times indicated. The long delay time shown (3.5 μ s) has the interesting property that it is radially uniform and relatively static on the time scale of the POS.

Data from a total of 71 POS shots were recorded with the inverse pinch source and 8 with a cable gun array. Of this total, 18 shots used a hydrogen plasma and 24 an Ar plasma. We observed that for the IP/ H_2 shots with long delays (uniform distribution), the load current rise times were significantly faster and POS voltages significantly higher than shots with any other source or those IP/ H_2 shots with shorter delays. FIG. 3 illustrates this point with a plot showing the peak voltage at the POS ($z=0$) vs. the conduction time for IP/ H_2 shots with various initial distributions, and cable gun shots. All the shots with the initially uniform distributions (with one exception) are well above voltages corresponding to cable gun shots or IP/ H_2 shots with nonuniform initial distributions.

Using the inverse pinch source with 8-channel interferometry also gave us the ability to investigate how the conducted current scaled with the injected mass. FIG. 4 shows the data from a series of IP/ H_2 and IP/Ar shots where the conducted current is plotted as a function of

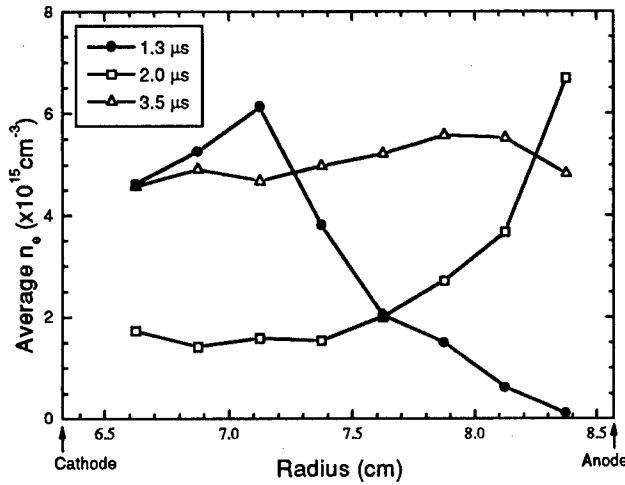


FIG. 2. Radial density profiles obtained at various times after the firing the plasma source.

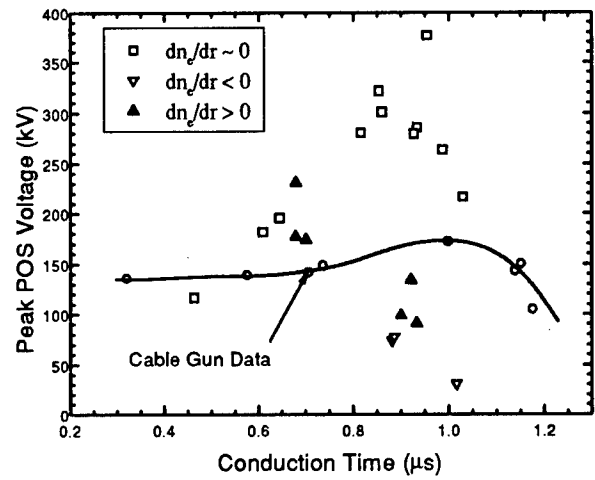


FIG. 3. Peak POS voltage for cable gun shots and IP/H₂ shots for various initial plasma distributions.

the radially averaged electron density. We only used shots where the delay times were long enough to produce radially uniform plasma fills. For the Ar shots, with one exception, only one channel of interferometry was available, so uniformity had to be assumed. A series of solid lines are also plotted that correspond to the predicted relationship via a simple MHD scaling theory for various ratios of the ion mass-to-charge ratio (M/Z). [7] The IP/Ar data fits the MHD theory for $M/Z=20$, which would imply an average ionization state of +2, and the IP/H₂ data fits the theory for $M/Z=6$.

Perhaps the most compelling result was the observation of large radial density “gaps” that appeared on the IP/H₂ shots coincident with the time of opening and persisting for hundreds of ns after opening. FIG. 5 shows the average electron density vs. radius for an IP/H₂ shot at several times of interest before, during and after opening. In this case we see that, at opening and just after opening, 4 of the 8 channels (1 cm) show densities below the sensitivity limit of the interferometer. This result is typical of all of the long delay time IP/H₂ shots obtained during the experimental run with some showing even larger gaps of 1.5 cm.

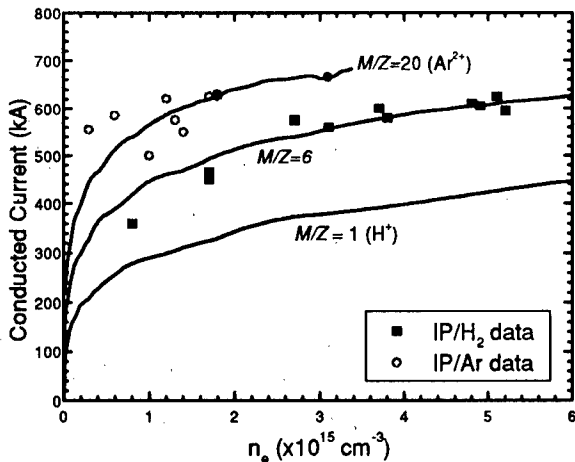


FIG. 4. A plot of the conducted current vs. the average electron density for IP/H₂ and IP/Ar shots. The solid lines are results from calculation based MHD theory for various ratios of M/Z .

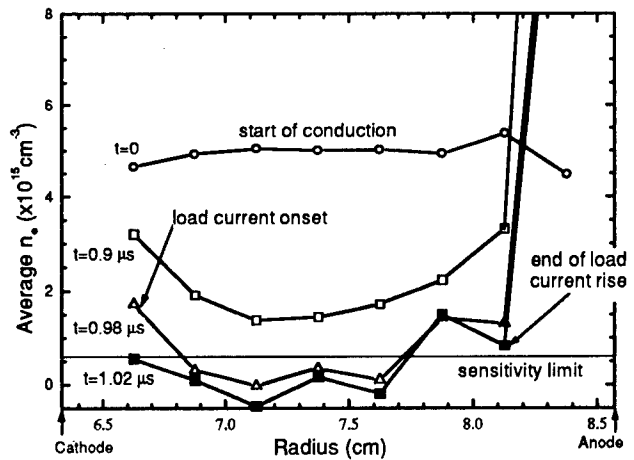


FIG. 5. The average electron density vs. radius at various times during the conduction and opening phases of the POS. This plot shows a 1 cm gap where densities are below the resolution limit during opening.

III. DISCUSSION

These results raise a number of interesting questions with regard to POS physics issues and indicate a potential for improving POS parameters using a light ion based plasma. The fact that switch voltages were significantly higher with a H plasma makes it tempting to conclude that a plasma dominated by low mass ions will improve the switch characteristics. While this may be true, it is also a gross simplification because we found that the state of the initial plasma may play an equally important role (see FIG. 3). It should be emphasized that, because the IP ejects a discrete plasma ring, changes in the source delay time redistribute the same quantity of plasma in the POS. While the radial density profiles become uniform for the long delays, other plasma properties, such as the symmetry and radial velocity, may also change. The sensitivity that we observed with regard to the initial plasma may explain the discrepancy between the results from Double and the later attempts to reproduce those results.

The scaling of the conducted current with the injected plasma mass, in particular the IP/H₂ data shown in FIG. 4, raises the issue of influence of secondary plasma formation during the conduction phase. If a pure, fully ionized, hydrogen plasma is assumed to exist prior to the start of the generator current, then there is not enough plasma mass to account for the observed conduction. The mass in the POS gap may be higher than one calculates under the above assumption if neutral gas exists in the POS gap prior to the discharge of the generator, or secondary plasma is formed via generator induced heating of the electrode surfaces (aluminum). There is evidence that one, or both, of these processes occurred as we measured an increase in the electron inventory by 40% during the conduction phase of IP/H₂ shots. If these additional electrons are formed from secondary plasma with an average $M/Z=12.5$, then the data would agree with MHD scaling with the tacit conclusion that impurities play an important role in the conduction phase. It is conceivable that an ionized mixture of common vacuum system adsorbates (H₂O, CH₄, CO) and aluminum can account for this additional mass.

Perhaps the most significant result with regard to improvements in the POS is the observation of large areas where the electron density falls below the sensitivity limit of the interferometer (FIG. 5). This type of behavior has not been observed with other plasma sources.[3] If this region evolves into a magnetically insulated vacuum gap, then we would expect higher voltages/power coupling into diode loads than is presently achieved in POSs. Additional experiments are underway to investigate this issue.

This work was sponsored by the Defense Special Weapons Agency.

REFERENCES

1. B.V. Weber, D.D. Hinshelwood, and R.J. Commisso, IEEE Trans. Plasma Sci. **25**(2), 189 (1997).
2. R.J. Commisso, P.J. Goodrich, J.M. Grossmann, D.D. Hinshelwood, P.F. Ottinger, and B.V. Weber, Phys. Fluids B **4**(7), 2369 (1992).
3. W. Rix, P. Coleman, J.R. Thompson, D. Husovsky, P. Melcher, and R.J. Commisso, IEEE Trans. Plasma Sci. **25**(2), 169 (1997).
4. P.S. Anan'in, V.B. Karpov, Ya.E. Krasik, I.V. Lisitsyn, A.V. Petrov, and V.G. Tolmacheva, Sov. Phys. Tech. Phys. **36**(8), 894 (1991).
5. P.J. Goodrich, R.J. Commisso, J.M. Grossmann, D.D. Hinshelwood, R.A. Riley, S.B. Swanekamp, and B.V. Weber, in *Proceeding of the 10th International Conference on High Power Particle Beams*, Vol. 1, p. 299.
6. The "Inverse Pinch" plasma source will be the subject of a future publication.
7. W. Rix, D. Parks, J. Shannon, J. Thompson, and E. Waisman, IEEE Trans. Plasma Sci. **19**(2), 400 (1991).

PLASMA EVOLUTION OF A POS: COMPARISON OF THEORY AND EXPERIMENT ON ACE 4 AND HAWK

D.E. Parks, P. Steen, P.L. Coleman, J.R. Goyer, and J.R. Thompson

Maxwell Technologies, Inc., 8888 Balboa Avenue, San Diego, CA 92123 USA

Sponsored by the Defense Special Weapons Agency

ABSTRACT

The evolution of the plasma in a high density, long conduction time POS can have a substantial effect on the performance of the switch. The motion of the plasma and its dependence on the geometry of the initial injection region and of the downstream vacuum feed influences not only the opening characteristics of the POS but also the timing of its interaction with the load.

Two dimensional MHD-Hall calculations have been performed to determine the evolution of the POS plasma in the coaxial geometry of ACE 4 and of HAWK. The computations utilize initial conditions provided by interferometric diagnostics. Results of the calculations show the plasma densities, velocities, positions and other plasma parameters through and beyond the conduction phase following excitation by megampere level currents. The results for density are compared with measurements taken using axial and chordal interferometry; the latter probing regions that are downstream of the POS.

INTRODUCTION

The physical mechanisms underlying the operation of a long conduction time (about one microsecond) plasma opening switches (POS) have been the object of intensive research over the last decade^[1,2,3]. Although the physics of the conduction phase is not completely understood, experiments point to the importance of plasma mass redistribution during conduction in establishing low density regions between cathode and anode that are required for the development of POS impedance and switchout of current^[4,5]. Magnetohydrodynamic forces play a dominant role in redistributing and thinning the plasma. A complete and accurate description of the plasma evolution through the conduction phase of the POS would require accounting for ionization produced by the conducted current and for the influence of the electron-Hall electric fields. The importance of the Hall field in redistribution of plasma and the development of the low densities required to achieve a high POS impedance is presently uncertain. The Hall effect, expected to operate during current switchout to produce impedance in the POS, though understood at the conceptual level, presents severe computational challenges, even in quasineutral single-fluid codes where effects of charge separation are neglected.

Below we briefly describe the one-fluid DELTA code and present results from its application to the evolution of POS plasmas in the Ace 4 and Hawk accelerators. The results are compared with electron densities measured by interferometric techniques. The calculations are performed both with and without the Hall effect. Potential pitfalls associated with the computational methodology are discussed.

THE DELTA CODE

The DELTA algorithm approximates the motion of a compressible, magnetized fluid using finite volume (FV) approximations to the equations of motion on an unstructured triangular mesh in planar or axisymmetric geometry. The equations are integrated over a domain subdivided into a finite number of triangular fluid elements and conservative difference approximations are constructed to the equations of motion over these regions. The equations are formulated in an arbitrary moving reference frame which may be held fixed in space (Eulerian), move with the local fluid velocity (Lagrangian), or move with any prescribed velocity. The advection algorithm, FRAM^[6], maintains monotonicity in the vicinity of steep gradients by switching between high order (central difference) and low order (upwind) schemes.

In the construction of the FV equations for the fluid motion all material properties are considered constant over a fluid element and approximations to the equations are constructed using integrals over the elements. All vector fields are centered at the vertices and scalar fields at the centers of mass of the elements. The control volume used for construction of the difference analog of the momentum equation is constructed by joining the mass centers of each element surrounding a given vertex with the midpoints of the sides. This construction associates one-third of the mass of each triangle of revolution with each of its vertices. The time differencing for the fluid equations is explicit.

The Galerkin finite element technique is used to solve the equations for the magnetic field. These equations consist of Ampere's law without displacement current, Faraday's law, and Ohm's law in the form $E = \eta j + j \times B / n e c - V \times B / c$ where η is the resistivity, n the electron density, J the current density, B the magnetic field, E the electric field, V the fluid velocity, c the speed of light, and e the magnitude of the electronic charge. All terms containing B in the resulting Galerkin normal equations are differenced fully implicitly in time. The nonlinear equations associated with implicit time differencing are solved by an inexact Newton-Krylov method with backtracking globalization^[7].

APPLICATIONS TO HAWK AND ACE 4

The code is applied in Eulerian mode to the calculation of plasma evolution in the axisymmetric regions of Ace 4 and Hawk. The region of Ace 4 downstream of the initial POS that is probed by the interferometric chordal lines of sight is indicated in Figure 1. The calculations are performed on a fixed r - z triangular mesh consisting of approximately 20,000 triangular elements. The physics contained in the calculations include Spitzer resistivity and a $\gamma=5/3$ law gas equation of state. Equations describing electron impact processes are contained in the code, but have not been included in the computations reported here.

To apply a one-fluid code in Eulerian mode requires the entire computational domain be filled with plasma at some density, even though large portions of the domain contain only vacuum. In these calculations vacuum is represented by a low density, high resistivity plasma in which hydro motion and the Hall effect are suppressed. Any cell is considered a vacuum cell whenever the density there falls below a minimum particle density $N_{\min}=1.0e13/cc$. In such cells the resistivity is taken to be $2.0e-8 \text{esu}$, a value sufficiently large to allow rapid diffusion of magnetic field through "vacuum" regions and to prevent shorting of the switch through vacuum. Obviously, computed results can be reliable only so long as

POS densities remain well above N_{\min} ; otherwise the POS plasma impedance becomes controlled by the artificial vacuum resistivity.

Figure 1 is a color graphic representation of the plasma density (carbon) computed with Hall "off" at times ranging from the onset of current into the POS ($t=0$) to beyond the nominal end of the conduction phase ($t=1150$ ns), when a substantial portion of the plasma has been pushed into the 100 nH inductive load. The strong tendency toward reduced density in the snowplowed plasma is evident at 1150 ns. Figures 2 and 3 permit comparison between calculated and measured results. The timing agrees, but of perhaps greater significance is that both indicate the passage of a plasma shell followed by a tail of slower moving plasma. The measurements suggest that the shell is thicker and that the slower moving plasma is relatively more pronounced than the calculations indicate.

Figures 4 and 5 compare computed and measured axial line densities of an argon POS in the Hawk configuration^[5] utilizing an inverse pinch plasma source. The increase in measured line density at 0.25 μ s along several lines of sight is not captured in the calculations, presumably because the computational model does not incorporate an ionization model. Even then, comparison of theory and experiment would be problematical since the measurements establish only the line integrated electron density, but neither the mass density nor ionization state, as an initial condition.

Calculations have also been performed with the Hall effect, but here the computational methodology is inadequate. The reasons for this are not fully understood, but the density evolution (not shown) indicates that a significant part of the problem rests with our treatment of vacuum. By about 600 ns the "vacuum" on the Marx side of the main plasma channel has been bridged by plasma with densities a few times N_{\min} , which perforce is highly conductive. Further increases of current and magnetic pressure are not felt by the main plasma, diminishing the tendency of the field to accelerate and further thin the POS plasma. This assertion is confirmed by the calculated magnetic field profiles (not shown here). The root cause for this clearly unphysical behavior, not apparent in the calculations without the Hall effect, is not clear. What is clear is that the fluid calculations of POS evolution with Hall effect, and for that matter without Hall effect, are candidates for use of automatic mesh refinement techniques.

REFERENCES

- [1] IEEE Trans. Plasma Science, Special Issue on Fast Opening Switches, Dec. 1987.
- [2] 9th Inter. Conf. On High Power Particle Beams, Edited by David Mosher and Gerald Cooperstein, Washington, D.C.
- [3] 10th Inter. Conf. On High Power Particle Beams, Edited by William Rix and Roger White, San Diego, CA.
- [4] Thompson, J. et al., ACE-4 Microsecond Plasma Opening Switch and Plasma Filled Diode Load Characterization, Proc. 9th IEEE Pulsed Power Conf., Albuquerque, NM, p. 119, 1993.
- [5] Comisso, R.J., et al., Characterization of a microsecond-conduction-time plasma opening switch, Phys. Fluids, B 4, 2368, 1992.
- [6] Chapman, Milt, FRAM-Nonlinear Damping algorithms for the continuity Equation, *J. Comp. Phys.*, 44, 84, 1981.
- [7] Michael Pernice and Homer F. Walker, "NITSOL: A Newton Iterative Solver for Nonlinear Systems," *SIAM J. Sci. Comput.*, Vol. 19, No. 1, pp 302-318, January 1998.

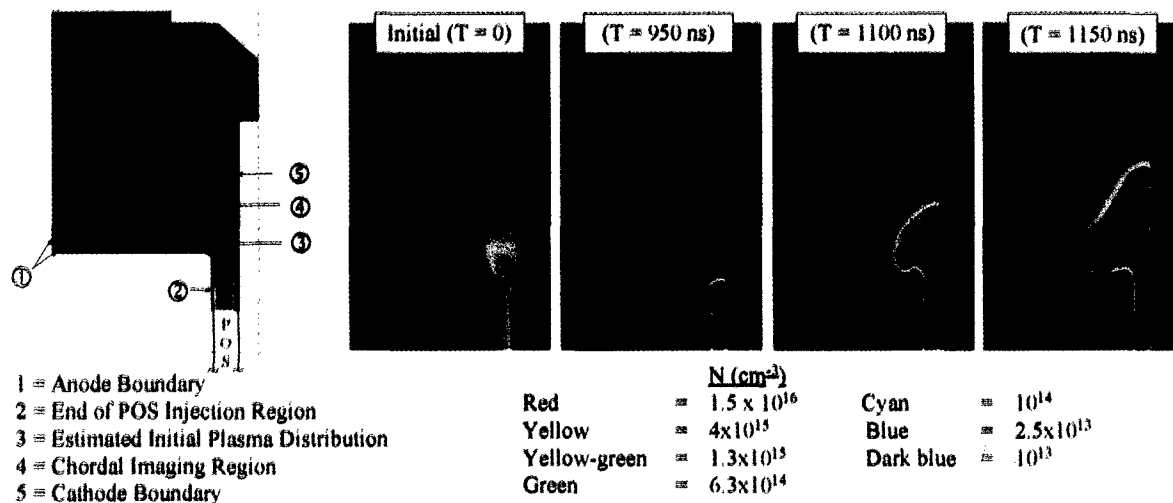
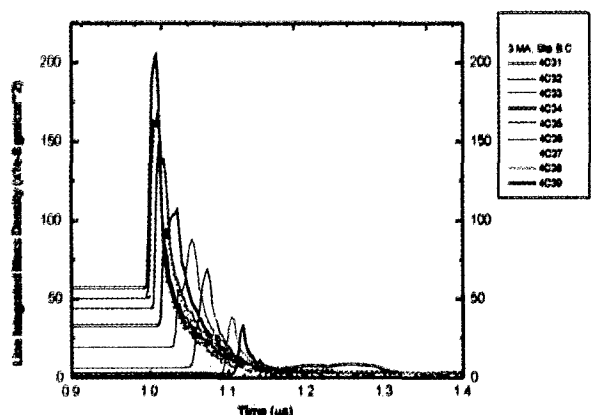


Fig. 1. Calculated densities for Ace 4.



The chords (nearest approach to the cathode at 0.5 cm) are spaced radially by 1 cm and are located 2 cm downstream of the end of the 3 cm POS A-K gap.

Fig. 2. The calculated chordal line integrated mass density for the 9 cm Ace 4 POS with peak currents of 3 MA.

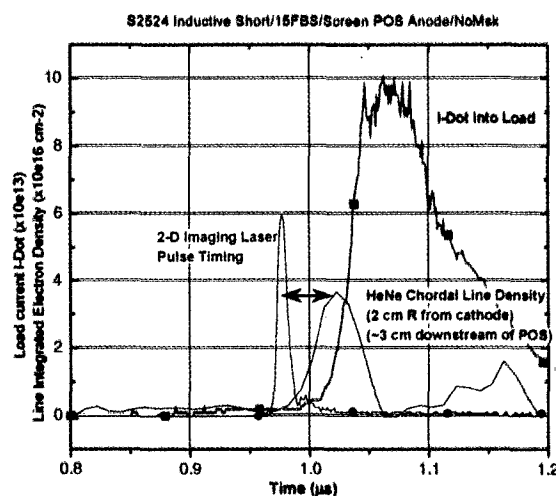


Fig. 3. Measured chordal line density for Ace 4.

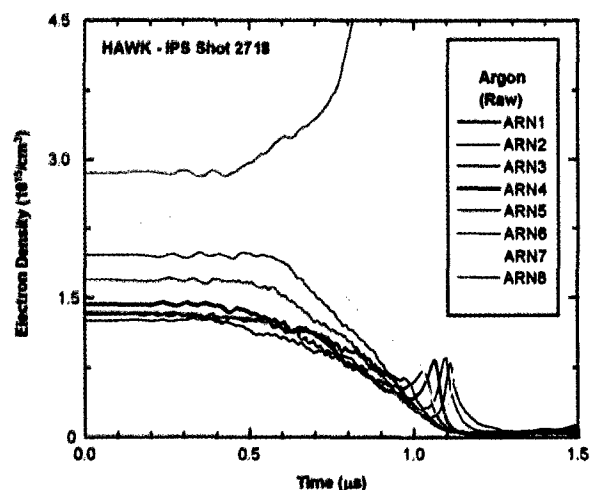


Fig. 4. Calculated axial line integrated mass density for argon shot 2718 based on an average ionization of $Z=1$ for a 5 cm long POS.

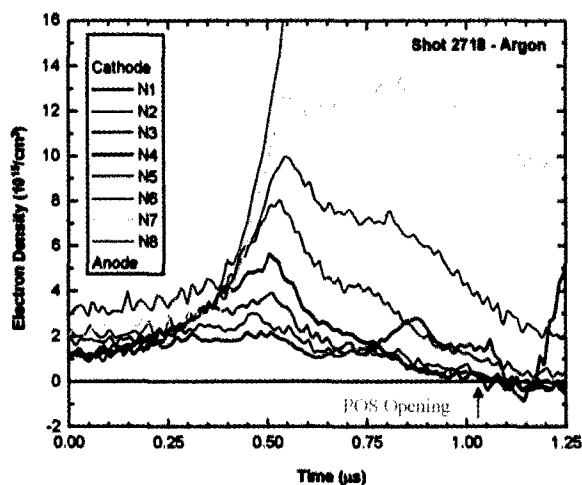


Fig. 5. Experimentally observed axial line integrated electron densities for argon shot 2718.

NEW SCHEME OF TWO BEAM ACCELERATOR DRIVER BASED ON LINEAR INDUCTION ACCELERATOR

A.V. Elzhov, A.A. Kaminsky, A.K. Kaminsky, V.I. Kazacha, E.A. Perelstein,
S.N. Sedykh, A.P. Sergeev.

Joint Institute for Nuclear Research, 141980, Dubna, Russia

INTRODUCTION

The Two Beam Accelerator (TBA) drivers based on a linear induction accelerator (LIA) were discussed in [1], [2], [3], [4]. In these schemes the driver electron beam moves through alternating discrete row of microwave generators (free electron lasers (FEL), relativistic klystrons, etc.) and reaccelerator sections. The microwave power is totally extracted from the driver after every generation section. The continuous microwave power extraction along the whole driver length was designed in CLIC [5]. The beam dynamics in TBA with continuous microwave power extraction was studied in [6].

A new scheme of TBA driver based on a linear induction accelerator was suggested in [7]. The scheme is quite uniform and has the following characteristic properties: a) the electron beam bunching occurs at a rather low initial energy; b) the bunched beam is accelerated in the accompanying of the microwave that provides the steady longitudinal beam bunching along the whole driver; c) there is no total microwave power extraction anywhere in the driver; d) a waveguide is used along the driver.

The driver consists of an injector, buncher and long (a few hundreds of meters) row of separate LIA sections producing the external accelerating electric field and partitioned by transition chambers. The injector produces the initial electron beam with energy 1 through 2 MeV and current 0.5 through 1 kA. For beam bunching a travelling wave tube (TWT) working in the amplification mode may be used. Then the electron bunches continue moving in the LIA in accompaniment of the amplified in the TWT microwave and are accelerated in the LIA electric field. The microwave power extraction from the driver occurs only in the transition chambers. The system attains the steady state at first few tens of meters where the bunch energy increases up to the level of ~ 10 MeV. Then the spacial region of quasi-stationary microwave generation begins where the total power, that the accelerating field inserts into the beam, transforms into the microwave power. The scheme provides the microwave phase and amplitude stability. The phase stability can be obtained at the expense of quasi-continuity of the system. Due to the bunched beam acceleration it is not necessary to have a high (~ 10 MeV) initial electron beam energy.

SIMULATION OF ACCELERATION OF ELECTRON BUNCHES ACCOMPANIED BY ELECTROMAGNETIC WAVE IN EXTERNAL ELECTRIC FIELD

We have three characteristic regions of the driver: 1) the bunching region with using of TWT and without acceleration, 2) transition region with a beam acceleration, and 3) quasi-stationary beam propagation region.

As it was shown in [8], one can obtain the electron beam bunching in a TWT at a rather short length ~ 50 cm, for example for the following electron beam and E_{01} type microwave parameters: electron beam energy ~ 2.2 MeV, electron current inside TWT $I_b \sim 500$ A, electron beam radius ~ 0.5 cm, microwave frequency $f_0 = 17 \cdot 10^9$ Hz ($\lambda \sim 1.76$ cm), initial microwave power in TWT ~ 10 kW, output microwave power in TWT at the acceleration region entrance ~ 13 MW.

Without accompanying microwave, the debunching process will immediately occur at the distance of few tens of centimeters from the buncher output. The simulation showed that the electron bunches can be transported through the distance ~ 10 m if the bunch movement is accompanied by the microwave amplified in the TWT. The most encouraging situation is that when the moving after the TWT output bunches are simultaneously accompanied by a part of the amplified microwave and accelerated in the external electric field inside a corrugated waveguide.

In [7] three sets of calculations corresponding to different variants of driver geometry were carried out. The first one was accomplished for the case when the external electric field and the attenuation spatial coefficient (corresponding to the microwave power extraction) had been continuously distributed along the driver. The second set of calculations was performed for the more realistic driver with a discrete structure of LIA consisting of separate induction sections partitioned by transition chambers. The lengths of the induction sections and transition chambers were chosen to be $l_s = 50$ cm and ($l_t = 25$ cm) respectively. The microwave extraction was being switched on only in the transition chambers, and the electric field E_a was equal to 1.5 MV/m inside the accelerating sections. In the third set of calculations for the same lengths of the accelerating sections and the transition chambers the accelerating voltage of every section (750 kV) was concentrated only on the gap 7.5 cm long located at the beginning of every section.

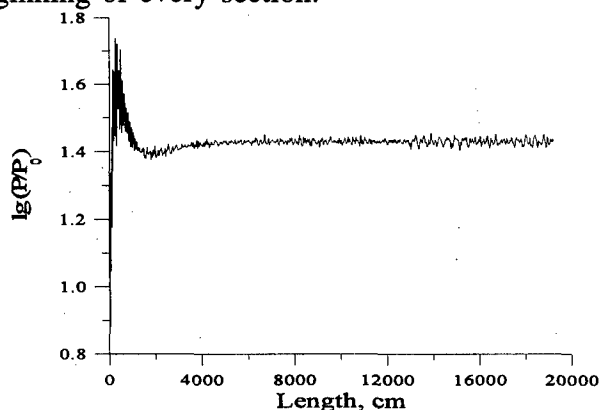
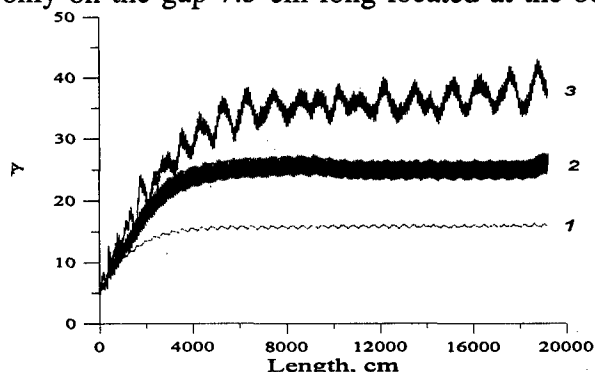


Fig. 1. The electron mean energy versus the distance for: 1 - continuously distributed driver parameters; 2 - discrete periodic cells, 3 - discrete cells with continuously distributed driver parameters. Fig. 2. The microwave power versus the distance for narrow accelerating gaps.

Fig. 1 shows the calculated dependence of the bunch mean energy $\bar{\gamma}$ on the distance ($z = 0$ corresponds to the TWT output) for the whole three sets of calculations. The dependences of the microwave power and the bunching parameter B on the distance are shown in the Fig. 2 and Fig. 3. As for the case of continuously distributed parameters one can see from these figures, the quasi-steady state of the system is achieved at the distance ~ 40 m. The extracted microwave power in the quasi-steady state is equal to ~ 333 MW. The mean steady state bunch energy ~ 7.5 MeV. And at last we have the high value

of the bunching parameter $B \cong 0.9$ in the quasi-steady state. The electron phase space picture (see Fig. 4) shows that the initial bunch breaks down on two main bunches being at the phase shift $\Delta\psi \cong 2\pi$ one from another.

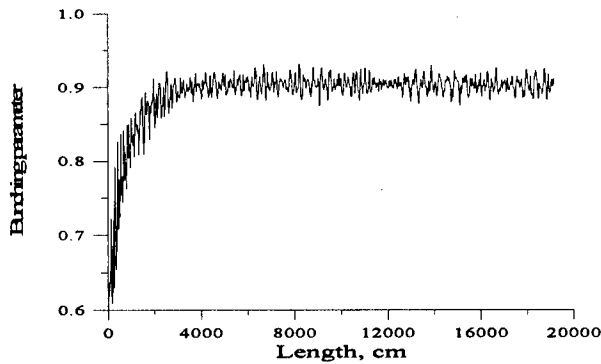


Fig. 3. The bunching parameter versus the distance for continuously distributed driver parameters.

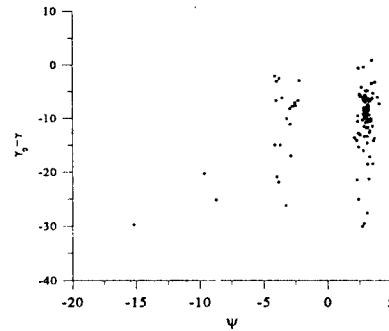


Fig. 4. The typical electron phase space picture at the distance of 100 m for continuously distributed driver parameters.

So the external electric field puts into the electron beam the power equal to ~ 500 MW/m which transforms into the microwave power in the steady state. The investigation of solution stability revealed the existence of the steady state solution up to error values $\delta I/I \cong \pm 10\%$ in the electron beam current.

TEST FACILITY

Series of test experiments are planned at JINR to study the scheme mentioned above. The scheme of the experimental setup based on the existing LIA-3000 facility is shown in Fig. 5. It consists of the injector and two reaccelerating sections. At the injector output the electron beam energy is about 800 keV and the current is equal to 200 A. The input microwave power is about of 10 kW with the wave length of 8 mm. Each reaccelerating section is 130 cm long and gives the energy gain of 360 keV. The microwave extraction and reacceleration voltage in this scheme are both located in the narrow gaps between accelerating sections each few centimeters long.

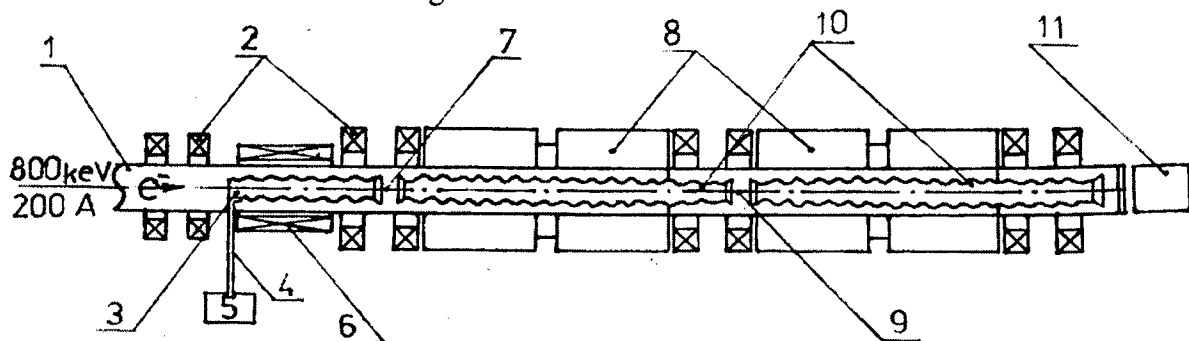


Fig. 5. The experimental setup scheme on the base of LIA-3000: 1) end part of injector; 2) coils of focusing magnetic field; 3) travelling wave tube; 4) waveguide; 5) magnetron; 6) magnetic solenoid; 7) first accelerating gap; 8) linear induction accelerating sections; 9) second accelerating gap; 10) corrugated waveguide; 11) chamber for microwave power and bunching parameter diagnostics.

The fulfilled simulation of the beam propagation, acceleration and microwave extraction for the real LIA-3000 parameters gives that the extracted microwave power should amount by approximately 10-15 MW per gap. The obtained spatial evolution of the bunching parameter and the bunch mean energy is presented in Fig. 6 and Fig. 7. Two rapid increases in the energy exactly correspond to the accelerating gaps. From the figures one can see that the travelling electron beam maintain rather high bunching parameter, while the beam energy rises from 0.8 to 1.3 MeV.

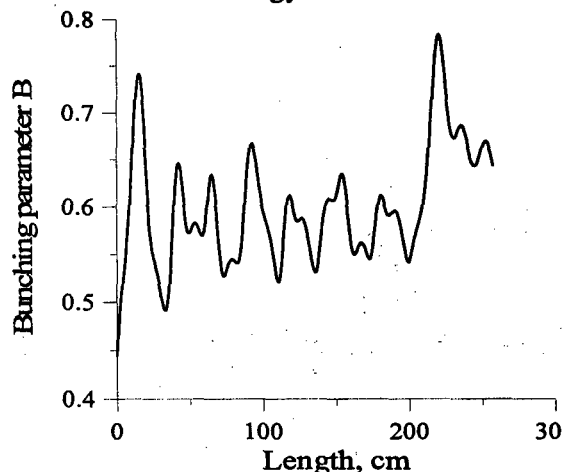


Fig. 6. The bunching parameter versus the distance for LIA-3000 parameters.

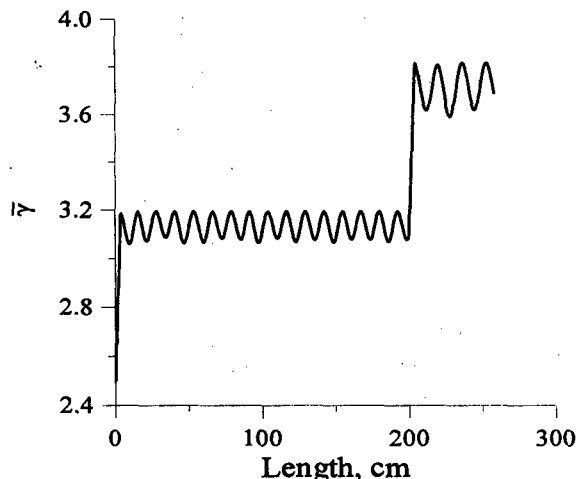


Fig. 7. The electron mean energy versus the distance for LIA-3000 parameters.

CONCLUSIONS

There was shown that a quasi-steady regime could be reached in the TBA driver when electron bunches accompanied by a part of an amplified microwave are simultaneously accelerated from the beginning in an external electric field. The total power which is inserted into the beam by the accelerating field transforms into the microwave power in the quasi-steady regime. Such kind of systems can serve effectively as a rather long (hundreds of meters) driver for the TBA.

The planned test experiment based on JINR LIA-3000 should yield the possibility of studying the bunching, microwave generation, beam propagation and twofold microwave extraction.

REFERENCES

- [1] A.M. Sessler, Proc. Workshop on the Laser Acceleration of Particles, eds. C. Yoshi and T. Katsouleas, AIP Conf. Proc. 91 (1982), p. 154.
- [2] A.M. Sessler et al., Nucl. Instr. Meth., A306, (1991), p. 592.
- [3] T. Houck et al., IEEE Trans. on Plasma Science, vol.24, 3(1996), p. 938.
- [4] G.G. Denisov et al., Nucl. Instr. Meth., A358 (1995), p. 528.
- [5] W. Schnell, CERN-LEP-RF/86-27 (1986); CERN-LEP-RF/88-59 (1988).
- [6] N.S. Ginzburg et al., in: Relativistic High-Frequency Electronics, v.5 (IAP AS USSR, Gorky, 1988), p. 37.
- [7] A.V. Elzhov, V.I. Kazacha, E.A. Perelstein, Proc. XV International Workshop on linear accelerators, ed. A.N. Dovbnya, v. II, Kharkov, 1997, p. 129.
- [8] E.A. Perelstein et al, JINR Preprint E9-97-5, Dubna, 1997.

EXPLOSIVE MAGNETIC SOURCE OF HIGH VOLTAGE PULSES

V.D.Selemer, V.A.Demidov, S.A.Kazakov, Yu.V.Vlasov, I.V.Konovalov,
V.G.Kornilov, N.V.Stepanov, Ye.V.Shapovalov, and K.V.Shibalko

VNIIEF, Sarov, 607190, Russia

INTRODUCTION

The energy source with high output voltage [1] is one of the main components of pulse accelerators of relativistic electron beams. To create transportable facilities, the energy sources with high specific energy stored are required, which are able to produce rapidly increasing (~ 100 ns) voltage pulses ≥ 400 kV. The explosive magnetic source of high-voltage pulses meets these requirements. The operating principle of this source is based on the two-cascade circuit opening of the helical flux compression generator (HFCG) [2].

DESIGN DESCRIPTION

A multi-section high-inductive HFCG [3] with helix internal diameter of 10 cm was used in the experiments. The generator central tube was made of aluminium and had a conical broadening under the last sections of the helix.

In the first cascade of current sharpening the opening switch was used, in which copper foil is destroyed under the effect of the HE-charge explosion products [4]. For the second step of current sharpening the electrical exploded current opening switch (described below) was used.

The emission explosive flat diode without magnetic field with cylindrical graphite cathode with diameter of 90 mm and main gap of ~ 20 mm was used as FCG load.

To obtain the short voltage pulse front in the diode circuit the spark gas-discharge gap was used.

MODEL EXPERIMENTS

To determine the optimal cross-section and the length of electrically exploded wires, the model experiments were carried out in laboratory conditions. A capacity pulse-current generator (PCG) was used as a primary energy source. The current pulse applied to the wires was close in its parameters to the current pulse of explosive magnetic source after the first sharpening cascade.

The wires being electrically exploded were placed in the SF_6 gas medium under the excessive pressure of $\sim 0.5 \cdot 10^5$ Pa. The current was measured with Rogovsky coil and the voltage was recorded by ohmic divider. The device operated in the mode of idle explosion of wires.

Fig.1 gives the general electric circuit of the experiment.

As a result of a series of experiments the parameters of exploded conductors were defined, which allowed to obtain the set amplitude and duration of the front of voltage pulse. Preliminary calculating estimations of mass and initial resistance of electric explosive opening switch, based on the known dependence of relative resistance on specific energy release

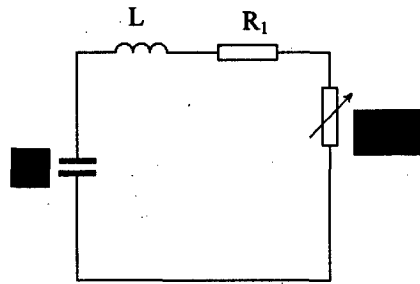


Fig.1. Equivalent electric circuit of experiment.

C - PCG capacity ($8 \mu\text{F}$, $U_0 = 80 \text{ kV}$);

L - PCG and discharge contour inductance ($L \sim 230 \text{ nH}$);

R_1 - PCG and discharge contour ohmic resistance ($R \sim 0.03 \text{ Ohm}$).

$R(t)$ - electrical exploded current opening switch resistance.

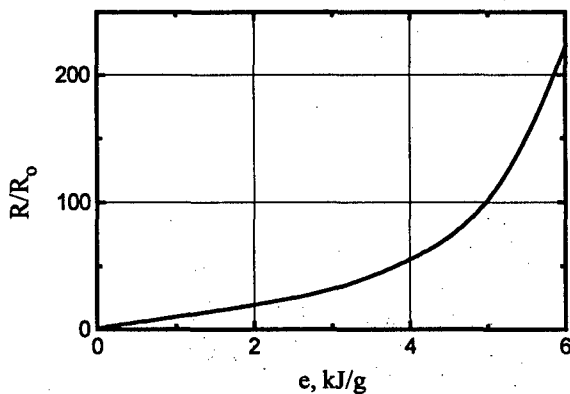


Fig.2. Dependence of relative growth of wire resistance on specific internal energy.

$R(e)/R_0$ [5] allowed to identify the initial version of conductors being exploded. Due to the strong influence produced by a certain design, arcquenching medium and energy input rate on this dependence, the final result was obtained by suitable selection of conductor parameters in the course of experiments. By processing experimental dependencies $U(t)$ and $I(t)$ the dependence $R(e)/R_0$ (Fig.2) was obtained in a graphic form.

Thus, using copper wires with diameter of 0.12 mm and total mass of 1.7 g in the explosive unit, the output voltage of $\sim 510 \text{ kV}$ (multiplication factor is 6.5) and the discharge current of 240 kA were obtained.

PRELIMINARY EXPERIMENTS

With the calculations [6], to perfect the explosive magnetic voltage source the preliminary experiment for inductive-active load was carried out.

The HFCG was powered by capacitor bank with capacity of $50 \mu\text{F}$. The current $I_g \sim 5 \text{ MA}$ was recorded in the contour of the first sharpening cascade (with inductance of 20 nH). The diagram of HFCG current is shown in Fig.3. The current after the first step of sharpening was $I_t \sim 400 \text{ kA}$. The maximum current derivative was $(dI_t/dt)_{\text{max}} \sim 1.6 \cdot 10^{12} \text{ A/s}$. Inductance of the contour on which the explosive opening switch operated was formed by the transmission cable line and internal inductance of electrically exploded conductors. Its magnitude was $L_t + L_w = 120 \text{ nH}$.

The maximum voltage in the load was $U \sim 350 \text{ kV}$ with the front of $\sim 40 \text{ ns}$. The current was $I \sim 30 \text{ kA}$ (Fig.4).

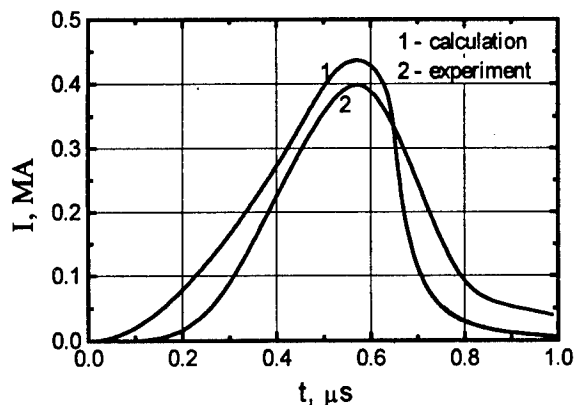


Fig.3. Current after explosive opening switch.

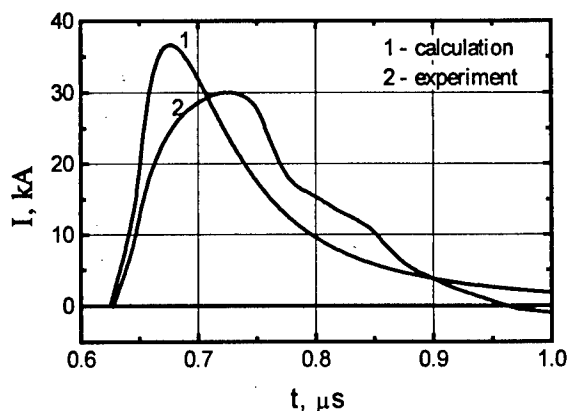


Fig.4. Load current.

As one can see from the diagrams, the experimental results agree with calculations quite well. However, the expected voltage pulse in the load has not been obtained. That is, evidently, related to the electric breakdown in the wire electric-explosion products. Moreover, the load effect on the electric-explosion process was estimated not accurately enough that resulted in the excess of the energy introduced in the electrically exploded wires.

EXPERIMENTAL RESULTS WITH HIGH-CURRENT DIODE

Results of the diode powering of by the HFCG with the perfected electric explosive opening switch is shown as dependence of diode current on time in Fig.5 and as dependence of diode voltage on time in Fig.6.

The current impulse has the amplitude of 27 kA. The maximum diode voltage is equal to ~ 380 kV. In the experiments with the HFCG with initial energy of ~ 700 J the maximum current in explosive opening switch circuit was ~ 4.9 MA, the characteristic time of current rise was ~ 7.5 μ s. After the explosive opening switch operation the electrically exploded wires circuit current is 540 kA, current rise time is 0.4 μ s.

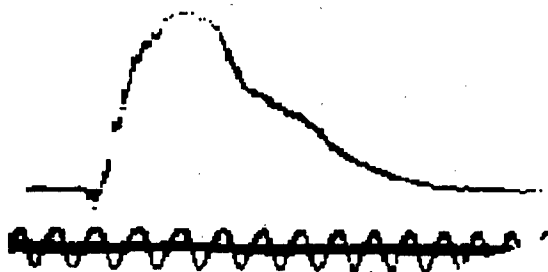


Fig.5. Diode current.
Time marks with the interval of 0.04 μ s.

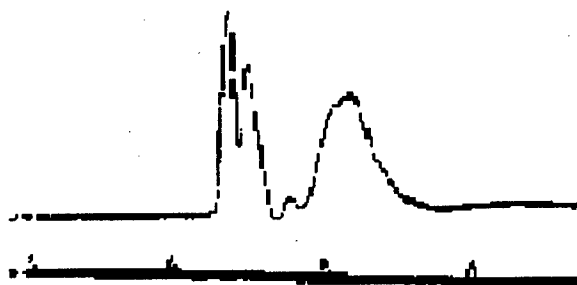


Fig.6. Diode voltage.
Time marks with the interval of 2 μ s.

CONCLUSION

A possibility of formation of the sharp high-voltage pulses using the helical FCG and two-cascade current opening switch is shown. The electric breakdowns in the copper wires electric-explosion products are considered to be the main limit of the voltage magnitude. To increase the device characteristics, the further optimization of parameters of the second cascade of the current opening switch is required.

REFERENCES

1. V.E.Fortov, A.N.Didenko, Y.V.Karpushin et al. «Generation of High Power Electron Beam and Microwave Radiation with the Aid of High-Explosives», in: *Megagauss Magnetic Field Generation and Pulsed Power Applications*, (Ed. M.Cowan and R.B.Spielman), N.Y.: Nova Science Publishers, 1994, p.939-946.
2. V.A.Demidov and V.I.Skokov. «Double-Stage Current Opening Switch for High-Voltage Impulse with the Front of 0.1 μ s Formation», in: *Megagauss and Megaampere Pulse Technology and Applications*, (Ed. V.K.Chernyshev, V.D.Selemer and L.N.Plyashkevich), Sarov, VNIIEF, 1997.
3. V.D.Selemer, V.A.Demidov, L.N.Plyashkevich, A.S.Kravchenko, S.A.Kazakov, A.M.Shuvalov, A.S.Boriskina, V.A.Zolotov, G.M.Spirov and M.M.Kharlamov. «High-Current (30 MA and More) Energy Pulses for Energizing of Inductive and Resistive Loads», *item 2*.
4. V.K.Chernyshev, V.A.Demidov, V.N.Veselov, J.V.Vlasov, S.A.Kazakov, V.I.Skokov, and I.K.Fetisov. «Investigation of the Speed Response Dependence of the Explosive Current Opening Switch on Initial Conditions», in: *Megagauss Fields and Pulsed Power Systems*, (Ed. V.M.Titov and G.A.Shvetsov), N.Y.: Nova Science Publishers, Inc., 1990, p.527-531.
5. H.Knoepfel. *Pulsed High Magnetic Fields*, Amsterdam-London, NHPC, 1970.
6. V.D.Selemer, V.A.Demidov, S.A. Kazakov, et al. «Explosive Magnetic Source of High Voltage Pulses» // in: *Proceedings of the 11-th IEEE International Pulsed Power Conference*, Baltimore, Maryland, June 2, 1997.

HALL MHD SIMULATION OF PLASMA BEHAVIOUR IN AN OPENING SWITCH

S.Semushin, A.Chuvatin

Laboratoire de Physique des Milieux Ionisés, Laboratoire CNRS, Ecole Polytechnique
91128 Palaiseau, France
e-mail: sem@lpmi.polytechnique.fr

The numerical simulations of plasma opening switch (POS) involve a lot of complex physical problems. Here the two temperature magneto hydrodynamic model (MHD) is used. The computations with such model are not so time consuming, as for the particle codes, and they give reasonable results.

The effect of Hall term in MHD equations is essential for correct physical description of the process. Original approximation of this term was proposed in [1]. Another essential point is in the physically correct description of plasma-vacuum boundary, where the magnetic field detaches the plasma current carrier and passes to the load.

Two stages can be separated in POS dynamics. The first one is conductivity, when plasma ports the current. It is well described by MHD equations. Second stage, the opening can be described by MHD equation, but with the attentive analyse of applicability of such model.

The simulations were concentrated mainly on the different types of POS behaviour. Such approach can be used for optimisation of composite plasma configuration of POS, which had been proposed to be one of the possible ways of improvement of the POS performance [2, 3].

Physical model

Plasma dynamics is described by two temperature magneto hydrodynamic equations

$$\begin{aligned} \frac{\partial \rho}{\partial t} + \text{div}(\rho u) &= 0 & \frac{\partial \rho u}{\partial t} + \text{Div}(\rho u u) + \text{grad}(p) &= \frac{j \times B}{c} \\ \frac{\partial \rho \varepsilon_e}{\partial t} + \text{div}(\rho u \varepsilon_e) + p_e \text{div} u + \text{div} W_e &= j E^* + Q_{ei} \\ \frac{\partial \rho \varepsilon_i}{\partial t} + \text{div}(\rho u \varepsilon_i) + p_i \text{div} u + \text{div} W_i &= -Q_{ei} \\ \frac{\partial B}{\partial t} &= -\text{rot} E, \quad E = E^* - \frac{u \times B}{c}; \quad j = \frac{c}{4\pi} \text{rot} B, \quad \text{div} B = 0 \end{aligned} \quad (1)$$

where ρ , P - plasma density and pressure, n_e, n_i - electron and ion densities, Z - ionisation, u - velocity, E , B - electric and magnetic fields, $\varepsilon_e, \varepsilon_i$, T_e, T_i - electron and ion specific internal energies and temperatures, $W_{e,i}$ - heat fluxes, Q_{ei} - exchange term and radiation sources. Ohm's law with the Hall terms is used

$$E^* = \frac{j}{\sigma} + \frac{j \times B}{c n_e} - \frac{\text{grad} p_e}{e n_e} \quad (2)$$

The term with electron pressure is not important in all the cases, so the majority of presented computations were done without it.

Numerical method

The simulations of the mutual dynamics of the magnetic field and plasma during the conduction stage were performed with the ASTRE numerical code using the adaptive mesh refinement numerical algorithm [1]. This code is based on the algorithm with rectangular eulerian mesh with the boundary conditions allowing simulations with arbitrary electrode shapes. The influence of the Hall term was considered to be important already at initial stages of process. New approximation of Hall term was proposed in [1]. It allows the simulation of Hall fast penetration of magnetic field for wide range of parameters, including the case of weak diffusion.

There is well known test of magnetic field penetration along the density jump. There exists the analytical solution for the case of MHD equations with frozen ion motion, so called electron magneto hydrodynamics. This one-dimensional solution has the form of shock wave. This analytical test was computed with proposed approximation of Hall term. The same test, but only for diffusive case were used in [5].

Non diffusive simulation shows the characteristic of unmasked Hall term approximation. Fig.1 presents the isolines of magnetic field for two different moments of non-dimensional time. The solution is monotone and without any non-physical smearing.

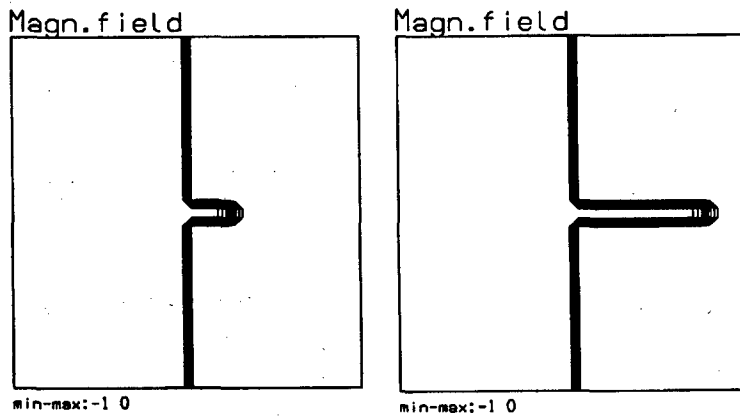


Fig.1 Magnetic field penetration along the density ramp, without diffusion, $t=0.05, 0.15$

Boundary conditions

Due to the essential convection and mixing, euler approach is more suitable for POS simulations. In such case the boundary conditions are postulated on the fix external boundary. But the regions of vacuum inside the computational domain need a special treatment. Traditionally this problem is solved by considering of low density regions, as physical vacuum. The background density threshold separates such domains. For 'vacuum' domains we have Laplace equations for magnetic field. But for numerical requirements it more convenient to use for such domains very small conductivity. This parameter and background density are chosen in such manner, that any their influence on results is excluded.

For Hall MHD there is another problem with boundary conditions. For electromagnetic part on the ideally conductive surface we have

$$E_{\tau} = 0 \quad (3)$$

For the case non Hall MHD it is equivalent to the condition on the current density

$$j_{\tau} = 0$$

(4)

what means that the current is normal to electrode surface. But these two conditions are different for Hall MHD. The physical one (3) is responsible for magnetic field penetration along the plasma-electrode interface. In considered case of POS, magnetic field penetration is mainly realised inside the volume. So, as in [6] we used the boundary condition (4). Such replacement can be explained, if we assume that there exists thin boundary layer, where we have such replacement of conditions.

Simulation results

Some existing geometries of the composite POS under experimental study were considered [2-4]. The plasma dynamics was modelled in order to estimate the degree of the plasma rarefaction in the configurations with different initial plasma density distributions.

It is possible to see two types POS behaviour. The first one looks like the opening of snow-plow type, which is accelerated by Hall penetration of magnetic field inside the plasma. Another one is the opening due to the magnetic field penetration through the conductive plasma bridge. The latter case is more rare.

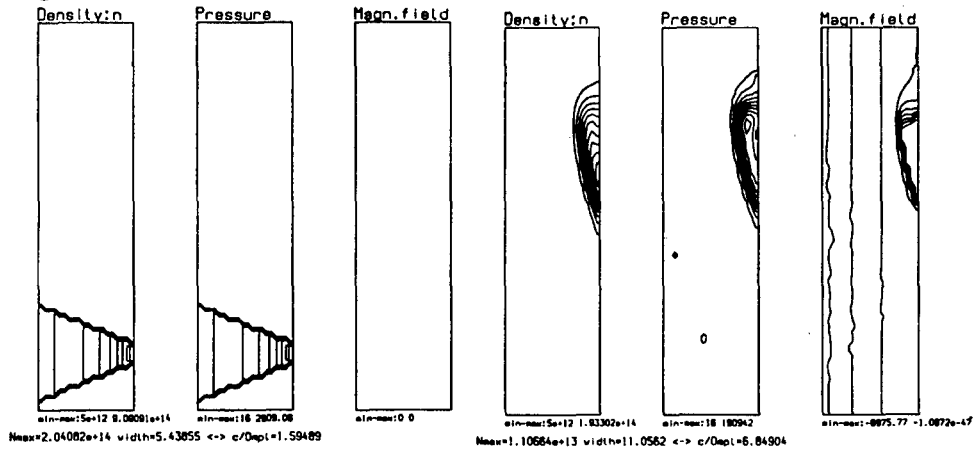


Fig.2 Initial conditions and simulation with Hall effect, $t = 380$ ns,

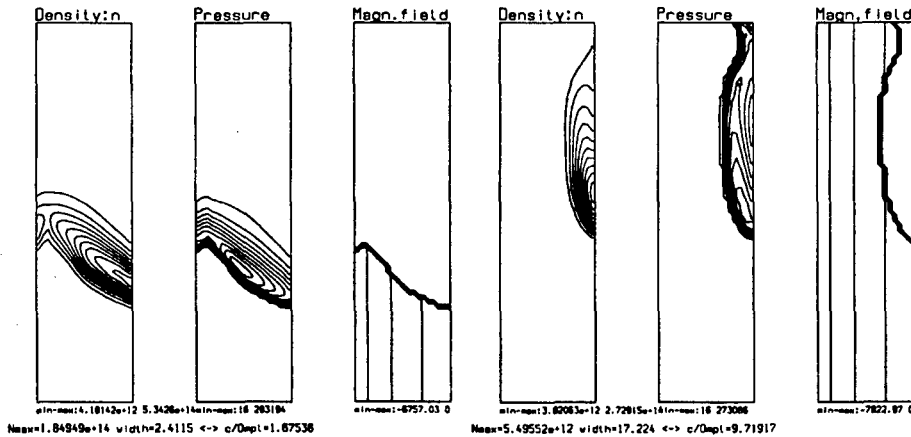


Fig.3 Simulation without Hall effect, $t = 380$ ns, $t = 440$ ns

In any case Hall effect is of premier importance. The influence of Hall term is illustrated by next example. The first run was done with Hall term (Fig.2). The generator current is 300 kA during 500 ns. The density, pressure and magnetic field are presented. The plasma was produced by plasma gun, place from the right side of this plane POS. Arising magnetic field pushes plasma to one of the electrodes, and this cloud of plasma cover the electrode. This

explains the delay of current in the central part of electrode, which was seen in the experiment [4].

Fig.3 represents the simulation of the same problem, but without Hall term. Magnetic field penetration is smaller for the same time, and the current pass to the load only after 440 ns.

Another simulation of cylindrical POS presents another type of opening. It was done by Hall MHD approximation. Current parameters are 1 MA during 1,1 ms. Maximal density was 10^{16} hydrogen and the density was distributed by

$$n(r, z) = n_0 e^{-\frac{(z-z_0)^2}{a^2}} \quad (4)$$

Here the radial dependence of the magnetic field is essential and the current plasma layer is push quicker along the internal electrode. Initially the gradients of magnetic field and of the density are parallel, so Hall term is zero. Later it starts to work, and it is possible to see the current penetration to the load.

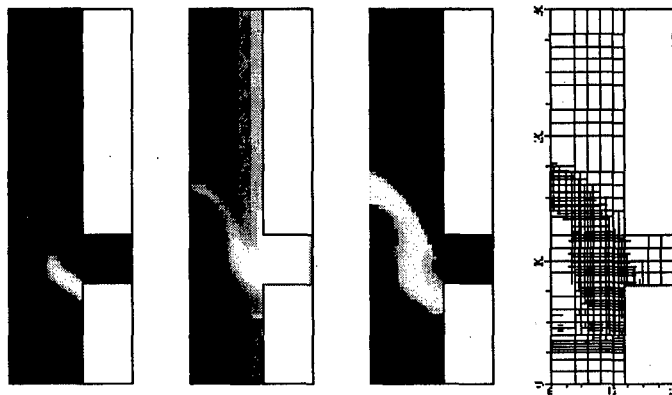


Fig.9 Density, magnetic field, electron temperature and mesh, $t=500$ ns

Conclusion

Hall MHD simulations allows to explain the penetration of current in plasma opening switch. But the physical mechanism of current detaching from plasma requires yet additional attention and analysis.

References.

- [1] S.Semushin, Adaptive Mesh Refinement approach for simulation of gas dynamics and magneto hydrodynamics problems. *Proceedings of 15th IMACS Word Congress. vol.3*, Wissenschaft & Technik Verlag, 1997, 109-114.
- [2] A.S.Chuvatin, A.A.Kim, V.A.Kokshenev, V.A.Kovalchuk et al. A composite POS: first proof-of principle resulyys from GIT-12. Proc. of 11th IEEE International Pulsed Power Conference, Baltimore, Maryland, 1997, O6-1.2.
- [3] A.Chuvatin, L.Aranchuk, V.Frolov, C.Rouillé, Ph.Auvray, C.Konieczny, J.-P.Stephan, F.Bayol, Ph.Monjaux, and H.Andreu. Comparison of theoretical predictions with the first experimental scalings for the composite POS configuration on 10-stages LTD generator. Submitted to this conference.
- [4] V.Frolov, A.Chuvatin, S.Semushin, B.Etlicher. Investigation of a strip-line long-conduction-time plasma opening switch on MAG-1. *Proceeding of BEAMS'96 Int. Conf.*, p.1211-1214.
- [5] V.V.Vikhrev, O.Z.Zabaidullin Magnetic Field Spreading along Plasma Interface Due to the Hall Effect. *Plasma Physics Reports*, **20**, (1994), 867-871.
- [6] J.D.Huba, J.M.Grossmann, P.F.Ottinger, Hall magneto hydrodynamic modeling of a long-conduction-time plasma opening switch., *Phys.Plasmas*, **1**, (1994), 3444.

THE USE OF THE FERROMAGNETIC SWITCH WITH ORTHOGONAL CONTROL FIELD FOR DIVERTING OF CURRENT IN AN INDUCTANCE-CAPACITANCE STORAGE

G.A.Shneerson, Yu.N.Botcharov, I.P.Efimov, S.I.Krivosheev

Saint Petersburg State Technical University

Russia, 195251, Politekhnicheskaya St., 29

1. Operation principle of the ferromagnetic opening switch with transversal magnetizing. For fast switching current in inductive and inductive-capacitive energy storages the circuits are used in which a sharp increase of transient impedance of the circuit element occurs. This process may be effected in various ways including the jump in the inductance of the circuit (Fig.1a) from its initial value L_1' to the final one L_1'' . The load current and current i_1 will be then determined by the expressions [1]:

$$i_2'' = i_0' \frac{K - 1}{\frac{L_2}{L_1'} + K \left(1 + \frac{L_2}{L_0} \right)}, \quad i_1'' = i_0' \cdot \frac{1 + \frac{L_2}{L_1'} + \frac{L_2}{L_0}}{\frac{L_2}{L_1'} + K \left(1 + \frac{L_2}{L_0} \right)} \quad (1)$$

where i_0' is the initial current value i_0 , i_2'' is the current in the inductive load, $K = L_1''/L_1'$ is the ratio of inductance variation.

Generation of high magnetic fields in single-turn low-inductance solenoids requires forming the current pulse of the megaampere range with the rise time of order of 10^{-6} s and less. In this case one may use the inductance-capacitance storage for the shortening of the current pulse front [2]. In the mentioned experiments the condition $L_2 \ll L_0$ is usually satisfied, where L_0 is the inductance of the energy source.

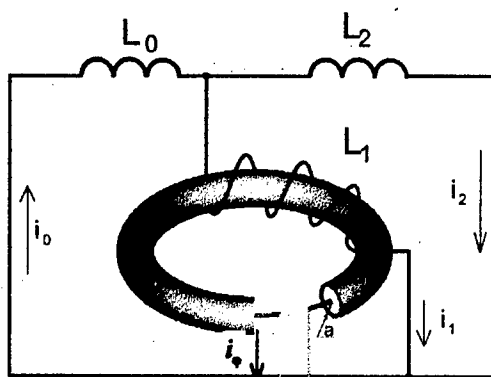


Fig.1a. The circuit for current switching into inductive load due to inductance L_1 variation

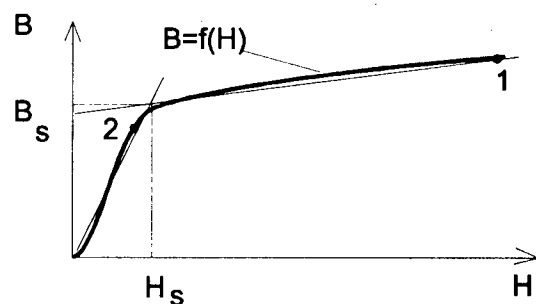


Fig.1b. The approximation of the magnetization curve

The possibility is considered of using for switching purposes the jump in magnetization of the coil core L_1 under external action. In the initial state the core should be deeply saturated, and at the required moment the material of the core should transit into the unsaturated state, which is accompanied by the sharp increase in the inductance up to the value L_1'' and transition of the current into the load L_2 . The control of the process should be performed in such a way that the inductance jump and the time of its realization were determined by the external action and not by the current in the storage circuit. It is proposed in this work to use to that end the system with orthogonal fields [3].

A coil with the toroidal core, whose winding experiences current flow i_1 producing toroidal field with induction B_θ , is used in the proposed device as the inductance L_1 . The circuit with current i_θ is situated at the core axis. The induction of the toroidal field of the current i_1 is orthogonal to the poloidal field induction B_ϕ produced by the current i_θ . The inductance L_1 may vary in a wide range with the aid of the control current i_θ . This may be shown at an example when the core material is isotropic and the induction dependence on the magnetic field intensity has the form $\bar{B} = \mu(H)\bar{H}$. The magnetic permeability in this formula depends on the intensity module $H = (H_\phi^2 + H_\theta^2)^{1/2}$. Let at the initial state the conditions $H_\phi \gg H_s$ and $H_\theta \geq H_s$ hold true (point 1 in Fig.2). Here H_s is the threshold intensity that corresponds to the intersection point of the two sections of the broken line approximating the magnetization curve. In the initial state the core is sharply saturated due to the action of the poloidal field H_ϕ . After switching off the current i_θ the field H_θ becomes zero, and the state of the system is characterized by point 2. The inductance L_1 sharply increases. The currents i_0 , i_1 , and i_2 in the circuit elements of the inductive storage vary correspondingly.

In the present work the parameter estimates of the ferromagnetic opening switch (FOS) are carried out. The possibility of its use for switching in low-inductance circuits is examined, and some calculation results are given.

2. Approximate estimative characteristics of the ferromagnetic opening switch. For the approximate description of the FOS magnetic circuit the magnetization curve may be substituted by a broken line (Fig.2).

$$B(H) = \begin{cases} \mu H & , B \leq B_s \\ \mu_{eff} H & , B \geq B_s \end{cases} \quad (2)$$

$$\text{where: } \mu_{eff} = \frac{B_s + (H - H_s) \mu_0}{H} = \mu_0 \left[1 + \frac{B_s}{\mu_0 H} \left(1 - \frac{\mu_0}{\mu} \right) \right].$$

As a calculation model we examine the system of the hollow toroid satisfying the condition $b < a \ll R$ (Fig.1a). At the saturated state $H \approx H_\phi = i_\theta / 2\pi a$. Under the conditions $\mu \gg \mu_0$ and $H_\phi \gg H_\theta$ at the initial state we have:

$$\mu_{eff} = \mu'_{eff} \approx \mu_0 \left(1 + \frac{B_s}{\mu_0 H_\phi} \right) = \mu_0 \left(1 + \frac{l_\phi B_s}{\mu_0 i_\theta} \right). \quad (3)$$

In this formula $l_\phi = 2\pi a$ is the length of the poloidal field line, H_ϕ is its intensity. In further estimations we adopt the value 1.5 T for B_s . This corresponds to such magnetic materials, as permalloy, amorphous iron etc. used in pulse transformers and magnetic flux compression devices.

If the condition $w_1 i_1'' < B_s l_\phi / \mu = i_{1s}$ holds true, the core after switching will not be saturated (w_1 is the turn number). The current i_1'' may be found from formula (1), which is conveniently rewritten in the following form:

$$i_1'' = i_0' \frac{\alpha}{K + \beta} < i_{1s} / w_1, \quad (4)$$

where $\alpha = (1 + L_2/L'_1 + L_2/L_0)/(1 + L_2/L_0)$ and $\beta = (L_2/L'_1)/(1 + L_2/L_0)$ are dimensionless numbers determined by inductance ratios. In the particular case when $L_2/L_0 \ll 1$ we have $\alpha = 1 + L_2/L'_1$ and $\beta = L_2/L'_1$. Then equation (4) yields the condition limiting the value of the switched current:

$$w_1 i'_0 \leq \frac{i_{1s}}{\alpha} (K + \beta) \quad (5)$$

The magnetization current is relatively small. Nevertheless, condition (5) may be satisfied even for large switched current, if the ratio $\mu/\mu'_{eff} = K$ is sufficiently large.

Using formula (2) we obtain general expressions for K , the admissible switch current, and the load current:

$$K = \frac{L''_1}{L'_1} = \frac{\mu_0/\mu}{1 + \frac{B_s}{\mu_0 H_\varphi} \cdot (1 - \mu_0/\mu)}; \quad (6)$$

$$i'_0 = \frac{l_\theta B_s}{\mu} \left(1 + \frac{\mu}{\mu_0} \frac{1}{1 + \frac{B_s}{\mu_0 H_\varphi} + \frac{L_2 l_\theta}{\mu_0 S \left[1 + \frac{B_s}{\mu_0 H_\varphi} \right]} + \frac{B_s L_2 l_\theta}{\mu_0^2 S H_\varphi \left[1 + \frac{B_s}{\mu_0 H_\varphi} \right]}} \right); \quad (7)$$

$$i''_2 = \frac{l_\theta B_s}{\mu_0} \cdot \frac{1}{1 + \frac{B_s}{\mu_0 H_\varphi} + \frac{L_2 l_\theta}{\mu_0 S \left[1 + \frac{B_s}{\mu_0 H_\varphi} \right]} + \frac{B_s L_2 l_\theta}{\mu_0^2 S H_\varphi \left[1 + \frac{B_s}{\mu_0 H_\varphi} \right]}}. \quad (8)$$

Fig.3 represents the curves illustrating the given relationships as functions of the dimensionless parameter $B_s/(\mu_0 H_\varphi)$.

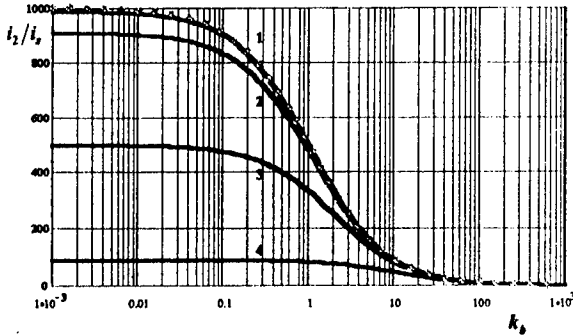


Fig.3 Dependence i_2/i_1 and K from size of the parameter $k_b = B_s/(\mu_0 H_\varphi)$.

For L_2/L_1^0 : 1 - 0.01, 2 - 0.1; 3 - 1; 4 - 10.

— i_2/i_1 ; * * * K ; $L'_1 = \frac{\mu_0 l_\theta}{S}$

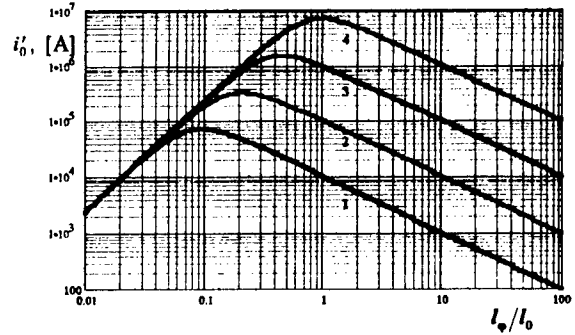


Fig.4 Dependence of an allowable current of switching i'_0 from size of the ratio l_φ/l_θ .

For i_θ : 1 - 10^4 A; 2 - 10^5 A; 3 - 10^6 A; 4 - 10^7

3. Conditions of low saturation. In the real conditions $\mu'_{eff} = \mu_0(1 + B_s/(\mu_0 H_\varphi)) > \mu_0$, which corresponds to the conditions of low saturation: $B_s/(\mu_0 H_\varphi) > 1$ (the right section of Fig.3.). Then, according to (5), the estimate for the currents and K holds true:

$$K \approx H_\phi / H_S; \quad i_0' \approx \frac{i_\theta l_\theta}{l_\phi \left(1 + \frac{L_2 l_\theta i_\theta}{S B_S l_\phi} \right)}; \quad i_2'' \approx \frac{l_\theta H_\phi}{1 + \frac{L_2 l_\theta H_\phi}{B_S S}}. \quad (9)$$

Equation (5) allows to optimize the parameters of the inductive storage with the FOS. The optimization problem may be represented as the choice of the transversal solenoid dimensions yielding the maximum value of the switched current i_0' in the solenoid of the fixed length for given control current i_θ (Fig.4). The obtained results show that with the length of the solid core of order of 1 m the values of the switched current of order of 10^5 A may be obtained. The control currents may have several times less amplitude. To achieve current close to 10^6 A the core length should be increased, which (for constant control current i_θ) is proportional to $(i_0')^2$. It should be noted that in the examined case the ratio K is although less than the ultimate value μ/μ_0 , but it remains sufficiently high.

4. The conditions of high saturation. The condition $B_S/\mu_0 H_\phi \ll 1$ corresponds to the conditions of high saturation (the left-hand section of the Fig.3.). Under the conditions $\mu/\mu_0 \gg 1$, $K \gg 1$ the currents and K assume the following values:

$$K \approx \frac{\mu}{\mu_0 \left(1 + \frac{B_S}{\mu_0 H_\phi} \right)}; \quad i_2'' \approx \frac{B_S l_\theta}{\mu_0 \left(1 + \frac{L_2}{L_1'} \right) \left(1 + \frac{B_S}{\mu_0 H_\phi} \right)}; \quad i_0' \approx \frac{B_S l_\theta}{\mu} + \frac{B_S l_\theta}{\mu_0 \left[1 + \frac{L_2}{L_1'} \left(1 + \frac{B_S}{\mu_0 H_\phi} \right) \right]} \quad (10)$$

The conditions of high saturation may be used for the generation of megaampere currents in the low inductance load. In this case the length l_θ should be sufficiently large and the section of the solenoid should be chosen in such a way that the ratio L_2/L_1' would not be high. For a considerably large length and the solenoid section and low load inductance the FOS can provide the controlled switching of the megaampere current into the load of the inductive storage.

5. Conclusions

1. The inductance of the solenoid with the ferromagnetic core may be changed sharply by switching of the orthogonal control field.
2. The controlled change of the inductance in the system with orthogonal fields may be used for current switching into the load of the inductive storage. The controlled inductance with strong initial saturation then represents an analog of the disconnecter.
3. The FOS allows to switch currents of the megaampere range in the systems with the low-inductance load (of order of 10^{-9} H).
4. The FOS parameters may be optimized in the case, if the core material at the initial state is not deeply saturated. Under these conditions the disconnecter can be readily used for switching currents with the amplitude of $10^4 \dots 10^5$ A.

References

1. Shneerson G.A. Field and transients in Superhigh Pulse Current Devices. Nova Science Publishers, Inc. New York. 1997.
2. Burtsev V.A., Kalinin N.V., Luchinsky A.V. Electrtrichesky vzriv provodnicov. Energoatomizdat. Moscow. 1990.
3. Dorogco L.I., Libkind M.S. Reactors with transversal magnetization. Energy. Moscow. 1977.

FORMING OF HIGH-SPEED RADIAL PLASMA FLOW DUE TO ITS HEATING BY INDUCED AZIMUTHAL CURRENT IN ELECTRICAL EXPLOSION OF WIRES IN EXTRA- HIGH MAGNETIC FIELD

Yu.E. Adamyan, V.M. Vasilevsky, S.N. Kolgatin, G.A.Shneerson
St.-Petersburg State Technical University. 195251, 29, Politekhnicheskaya st. ,
St.-Petersburg, Russia.
Kolgatin@spes.stu.neva.ru , Shne@phtf.stu.neva.ru

Introduction.

The experiments on wire explosion in strong longitudinal magnetic field has shown that the electrical characteristics of conductor explosion are affected by the field. So the presence of longitudinal field with the induction $\sim 50-70$ T shifts the moment of the explosion and changes the qualitative dependency of voltage vs. time. In works [1,2] the possibility of essential heating and speedup of plasma caused by the generation of azimuthal currents at electrical explosion in longitudinal magnetic field has been shown. In given work the one-dimensional analytic plane model illustrating the possibility and explaining effect of speedup and conducting media heating under its expansion across the given external field are brought. Also the description of the experiments is presented in which this effect at the expansion of the low density gas area forming around wire under its electrical explosion in the vacuum was observed.

Reference positions and model problems.

The possibility of conducting media speedup and its intensive heating in presence of sufficiently strong axial field was shown in works [1-4]. It is interesting to confirm a noted effect on the example of simple models. The one of them is a model of stationary flow of conducting gas across the field. Within the framework of this test problem let us consider that media elements move along X- axis at the speed of $u_x(x)$, herewith all distinctive parameters (density, velocity u , pressure p , temperature T) are constant. In the point $x=0$ given boundary values of these parameters are ρ_0, u_0, p_0, T_0 . Magnetic field B_y is equal zero at left side of point $x=0$ then it is changed sharply to value B_0 on the boundary area and hereinafter stays unchangeable. Stationary flow of media with constant conductivity σ is described by the system of the magnetic hydrodynamics equations

$$\frac{d}{dx}(\rho u) = 0 \quad (1) \quad \rho u \frac{du}{dx} = -\frac{dp}{dx} - \delta B \quad (2) \quad u \left(\frac{dp}{dx} - \frac{\gamma p}{\rho} \frac{d\rho}{dx} \right) = (\gamma - 1) \frac{\delta^2}{\sigma} \quad (3)$$

where $\delta \equiv \delta_z$ - induced current density, γ - adiabat index.

Let us consider that electric field tension in Euler coordinates $E_y=0$ that corresponds the case of plasma flow limited by short connected conducting plates. Then follows an equation $\delta_z / \sigma = -[\vec{u}, \vec{B}]_z = -uB_0$, or $\delta = -\sigma u B_0$. From the equation (1) we have $\rho u = \rho_0 u_0$. Hereinafter it is possible to exclude density from equations (1)-(3) and bring them to following two equation system for the non-dimensional velocity $U=u/u_0$ and non-dimensional pressure $P=p/p_0$ as functions of non-dimensional coordinate $\chi=x/x_0$. Distinctive length x_0 is

defined by the expression $x_0 = (\rho_0) / [(\gamma - 1)B^2 \sigma \mu_0]$. Equations for variables U and P are as

follows:

$$\frac{dU}{d\chi} = \frac{(2-\gamma)U^2}{\frac{\theta U}{\gamma} - P} \quad (4)$$

$$\frac{dP}{d\chi} = \frac{U \left(\theta U - \frac{\gamma P}{\gamma - 1} \right)}{\frac{\theta U}{\gamma} - P} \quad (5)$$

Here appears the distinctive parameter $\theta = \rho_0 u_0^2 / p_0$. Numerical calculations executed for boundary conditions $P(0)=U(0)=1$ show that type of solution is defined by the value of parameter θ (fig.1). If initial velocity of media is less then adiabatic velocity of sound on the boundary (in this case $\theta < \gamma$) the velocity fades at the growing x but pressure grows. More interesting is the case $\theta > \gamma$ when velocity grows at the growing x . If the grows of x is unlimited then the velocity rises exponentially. This is confirmed by examples shown on the fig. 1a and fig. 1b for $\gamma=5/3$. In first case (a) accepted value $\theta=1$, in second one(b) - $\theta=2$.

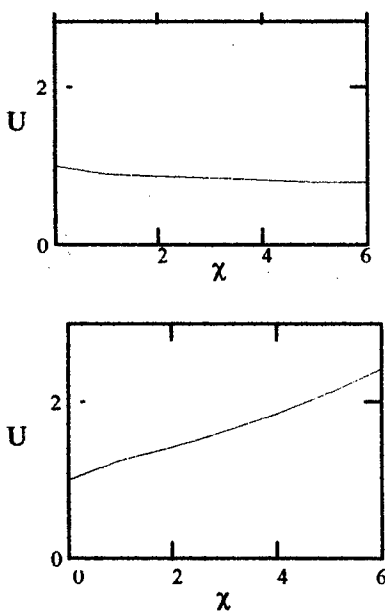


Fig 1. a) $\theta=1$ b) $\theta=2$

It is possible to interpret the result received as follows: under sufficiently big initial velocity the plasma is heated by the induced current herewith the stream penetration into the field, the flow velocity, pressure and temperature increase with simultaneous density reducing. Model of stationary flow does not describe the conducting media expansion in the vacuum. However qualitative type of process must be kept at the vacuum explosion: it should be expected that under sufficiently high initial temperature and conductivity the process of explosion products speedup and heating can be excited in the strong field. Heating and speedup of plasma are formed on length of order x_0 for time

$$\tau_0 \approx \frac{x_0}{u_0} \approx \frac{\rho_0}{B^2 \sigma \theta} \quad (6).$$

This value with accuracy of multiplier $1/\theta$ is known in magnetic hydrodynamics as a parameter - the time of inducing deceleration [5]. Under $\theta < 1$ plasma is really slowed for a time of the order τ_0 . However under $\theta > 1$ the

sense of this parameter is changed to opposite. Now τ_0 becomes the scale of time of the heating and speedup of plasma under its motion across the field. At density of Cu vapours of order 1 kg/m^3 that corresponds concentrations 10^{25} m^{-3} for heating of plasma with the conductivity $10^3 (\Omega \cdot \text{m})^{-1}$ for a time of the order 10^{-6} s it is necessary that plasma was expanded across the field with the induction of order 10^2 T . The threshold value of induction increases at the growing of density and conductivity reducing.

Experimental results.

In experiments being described the 0.2 mm copper wire 15 mm length fitted in vacuumed glass shell with the internal diameter 16 mm was used. In the process of fabrication the wire was heated during 24 hours at the temperature 400° and pressure 10^{-6} Torr. The shell was placed to cavity of one turn solenoid with removable destroying insert. For feeding of the solenoid the low inductive 648 mkF capacitor battery was used which could be charged up to the voltage 40 kV. Maximum value of the field induction reached 70 T. The explosion of conductor was initiated near the maximum of the field in solenoid by

the additional battery. The time of the increasing of the current in wire to the amplitude value (1 mks) was substantially less than field increasing time (7 mks). Magnetohydrodynamic calculations have confirmed that in these conditions longitudinal field can be considered quasistationary from standpoints of its influence upon the process of electrical wire explosion. The design of the current driving bars to the balloon with the exploding conductor was executed in the manner of "squirrel cage" from fine conductors for excluding of longitudinal magnetic field mechanical influence on system elements. The parameters of exploding conductor circuit are as follows: capacity 3.75 mkF, inductance 300 nG, voltage 10 kV. The measurements of the current in conductor were made by Rogovsky coil. Voltage on conductor was measured by the voltage divisor with the compensation of inductive part.

The plasma emission photochronography allowed to measure the velocity of its expansion. For the measurements of the magnetic flux displaced by the expanding plasma as well as for the evaluation of plasma conductivity under known expansion velocity the diamagnetic signal was registered.

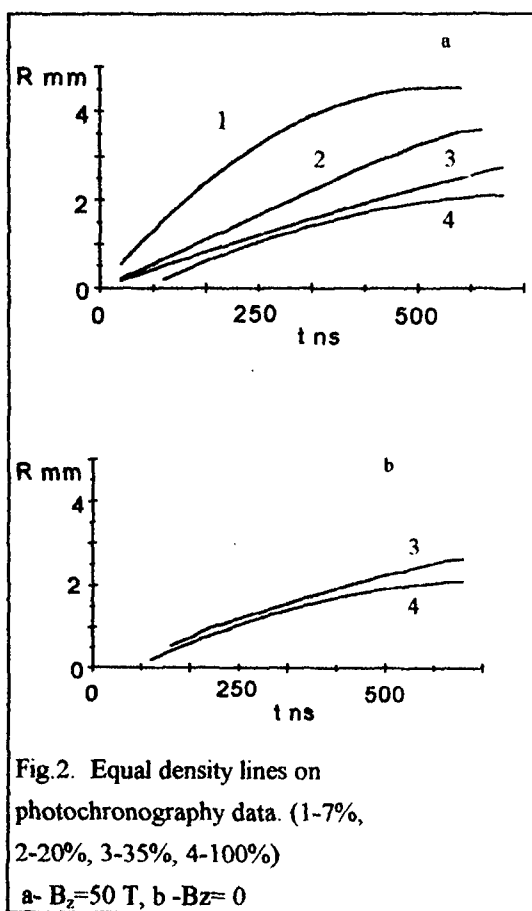


Fig.2 shows the results of photochronograms processing in which chosen equal density lines are displayed. The photograph corresponding to explosion in the longitudinal magnetic field can be separated in two areas differ in brightness. External area represents the quickly expanding plasma of low density. Internal area is characterised by greatly more high intensity of emission and small expansion velocity practically the same as for the electrical explosion without the longitudinal magnetic field (fig.2b). It can be seen from the chronograms comparison that at the parameters of exploding conductor circuit taking place in experiments the electrical explosion in the longitudinal magnetic field is distinguished by presence of quickly expanding plasma volume of small density around the wire core. The fact is confirmed by the comparison of lines of equal density for modes with the magnetic field and without it.

The diagram of diamagnetic signal under $B_z=50$ T is brought on fig.3. It is possible to select the signal proportional to external magnetic field which presents at the diagram because of incomplete compensation of initial field and the

signal proportional to displaced magnetic flux that can be easy selected on the background of the remaining uncompensated signal. The diamagnetic signal in combination with the measured velocity of plasma expansion allows to determine the value of its conductivity. For determining of σ value the calculations of magnetic field diffusion to cylindrically expanding plasma with given conductivity were accomplished. The equation of magnetic field diffusion

in cylindrical coordinates was numerically solved and as a result it was obtained that the measured value of signal corresponds to the calculated value of $\sigma=200(\Omega\cdot m)^{-1}$.

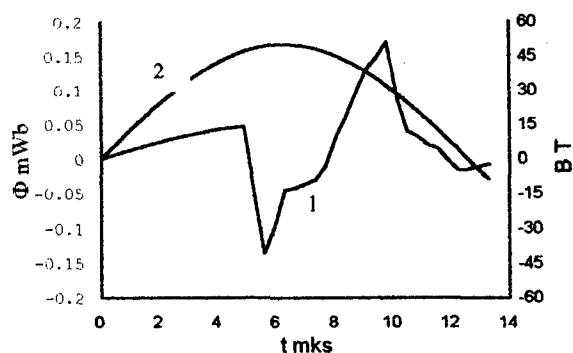


Fig.3.

their drift velocity is about 10^6 m/s that greatly exceeds the ions heat velocity. At the such conditions the suggestion about the absence of the thermodynamic equilibrium and conductivity reducing in consequence of chaotic fluctuations excitation in the plasma seems to be motivated.

Conclusion.

1. The possibility of the azimuthal current self-excitation and radial plasma speedup under its heating in the expansion in megagauss magnetic field is shown on model problems.
2. Experiments have confirmed the possibility of plasma heating and acceleration in the electrical wire explosion in the longitudinal magnetic field by the value of order 50 T.
3. The processing of the experimental results brought the plasma conductivity substantially less then theoreticall values obtained in the suggestion of local thermodynamic equilibrium.

Work was supported by Russian Fund of Basic Research (grant #96-02-19185a)

1. Shneerson G.A. Letters to J.Tech.Phys. (Pisma v Zurnal Technicheskoi Fiziki), v.23, N11, p.p.10-16, 1997, russian
2. Kolgatin S.N., Shneerson G.A. J.Tech.Phys. (Zurnal Technicheskoi Fiziki), 1997, v.67, N1, p.p.12-19, russian.
3. Adamian Yu.E., Vasilevski V.M., Kolgatin S.N., et al. Letters to J.Tech.Phys. (Pisma v Zurnal Technicheskoi Fiziki), N23, p.p.43-46, 1995, russian
4. Kauling T. Magnetohydrodynamica. M. Atomizdat, 1978.
5. Sarkisov G.S., Etlisher B., Jankov V.V. et al (Zurnal Eksperimentalnoi i Technicheskoi Fiziki), v.108, N4(10), p.p.1355-1372, 1995, russian
6. Bespalov I.M., Polischuk A.I. Preprint IVTAN 11-257 (1988), russian

WAVE-FORM OPTIMIZATION FOR A 60 MA Z-PINCH DRIVER

K. W. Struve

Mission Research Corp., 1720 Randolph Rd SE, Albuquerque, NM, 87106, USA

and

D. H. McDaniel

Sandia National Laboratories[†], P. O. Box 5800, Albuquerque, NM, 87185-1194, USA

INTRODUCTION

A new z-pinch driver is being planned by Sandia National Laboratories (SNL) that will provide up to 16 MJ of x-ray radiation. Two load designs are being considered. One is a double z-pinch configuration, with each load providing 7 MJ radiation. The other is a single z-pinch configuration that produces 16 MJ. Both configurations require 100 to 120 ns implosion times, and radiation pulse widths of less than 10 ns. These requirements translate into two 40 MA drivers for the double-sided load, and a 60 MA driver for the single-load configuration.

The design of this new machine, which has been called X-1, is based on the Z accelerator at SNL [1]. The X-1 design differs from the Z design in that voltages will be higher by a factor of three (10 to 12 MV), and will have a larger number of modules. X-1 will have a circular water tank surrounded by an oil tank with a 90 m outer diameter. A transmission-line transformer in the water section will be used to increase the voltage from the output of the water-capacitor and pulse-forming sections. An alternative design uses dielectric cavity adders to provide the higher voltage.

The design philosophy for this machine is to work from the load out. Radiation requirements determine the current, pulse-width, and load-inductance requirements. These parameters set the drive wave-form and insulator voltage, which in turn determine the insulator-stack design. The goal is to choose a drive wave-form that meets the load requirements while

optimizing efficiency and minimizing breakdown risk.

Several factors have a large impact on the design. The largest are the stack and load inductances, and the implosion time t_p . The voltage required to drive the load is $L di/dt$. Without changing the inductance it may be possible to lengthen t_p and thereby decrease di/dt . Other important factors are resistive and shock-induced conductor losses, magnetic insulation of the vacuum insulator, and convolute losses. All of these effects are being actively investigated with scaled experiments and theory on Z.

LOAD COUPLING EFFICIENCY

A z-pinch driver and load can be described as a driving voltage with its intrinsic impedance, in series with fixed and time-varying inductances. See fig. 1.

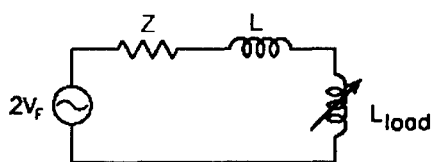


Fig. 1. Equivalent circuit for a pulsed-power z-pinch driver.

For most of the pulse, the z-pinch load can be modeled as a fixed inductor. Only late in time is there a large inductance increase. Assuming fixed inductance, and specifying the voltage V_L at the inductor,

which is also the insulator-stack voltage, we derive the efficiency η .

$$\eta = \frac{Li^2(t)/2}{\int_0^{t_p} V_F^2(t)/Z dt} \quad (1)$$

The efficiency is defined as the ratio of the energy in the inductor to that delivered to a matched impedance. The current $i(t)$ is $(\int V_L(t) dt)/L$ and the forward voltage $V_F(t)$ is $(V_L(t) + i(t)Z)/2$. The upper limit of the integrals is the pinch time t_p . With a constant insulator voltage, the efficiency is

$$\eta = \frac{2(t_p/\tau)}{1 + (t_p/\tau) + (t_p/\tau)^2/3}, \quad (2)$$

where τ is L/Z . This function is plotted as a function of t_p/τ in fig. 2.

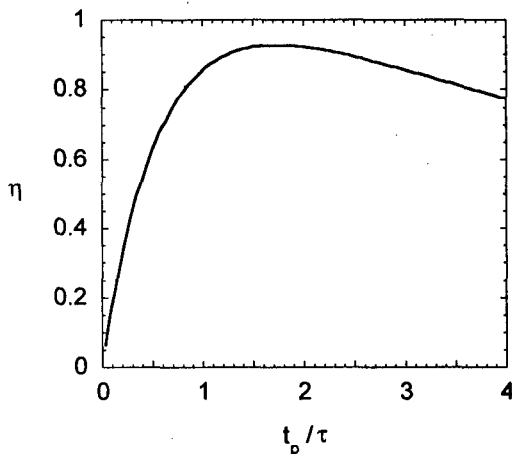


Fig. 2. Efficiency vs. pinch time for a flat voltage at the insulator stack.

By taking the derivative of the efficiency with respect to the impedance we derive the optimum impedance for peak efficiency,

$$Z_{opt} = \left[\frac{\int_0^{t_p} V_L^2(t) dt}{\int_0^{t_p} i^2(t) dt} \right]^{1/2} \quad (3)$$

For a constant insulator voltage V_0 the peak efficiency is 0.93, and occurs for $Z =$

$\sqrt{3}L/t_p$. Similarly, the efficiency for a sine-squared wave-form, $V_L = V_0 \sin^2(t/T)$, can be calculated using the same technique. Here the efficiency depends on both the ratio of the pinch time to the period of the wave-form, and the ratio of the period to the characteristic time τ . Thus a family of curves can be generated, as shown in fig. 3. The peak efficiency is the locus of peak efficiencies of all the curves. Note that near the peak of the sine-squared ($t_p/T = \pi/2$) the efficiency is over 0.97, whereas a quarter-cycle later it is less than 0.80.

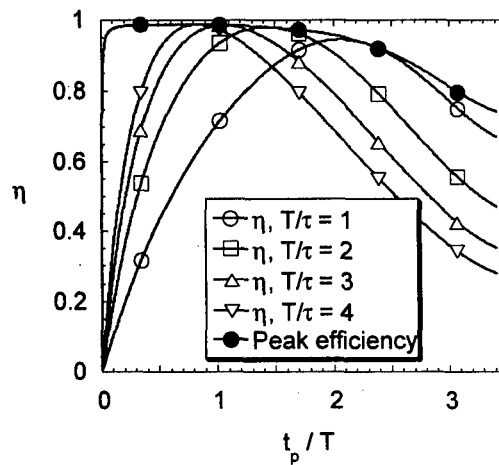


Fig. 3. Efficiency vs. pinch time for a sine-squared voltage at the stack for various ratios of period to characteristic time τ .

This analysis can be further extended to other wave-forms, as shown in fig. 4. These include a linearly-rising ramp, a linear ramp with a constant voltage, an exponential voltage, a hyperbolic sine and tangent, and a sine wave-form. The sine-squared and constant-voltage wave-form efficiencies are also included for comparison. As with the sine-squared wave-form, all of the plotted efficiencies represent the locus of peak efficiencies. Therefore, the actual efficiency can be lower, depending on the choice of impedance, pinch time, and wave-form period. Also note that for all of these wave-

forms the peak efficiency that can be achieved is generally greater than 0.95.

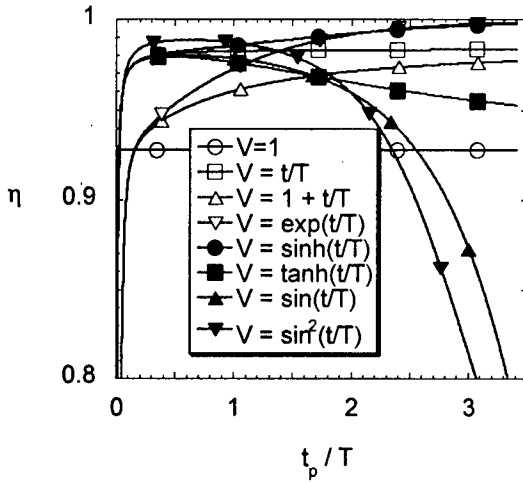


Fig. 4. Peak efficiency for several wave-forms vs. the ratio of the pinch time to the wave-form period.

A more complete analysis has been done with Screamer [2] using post-hole convolute losses, resistive-wall losses, and time-varying-inductance effects. Shown in fig. 5 is a plot of kinetic energy vs. implosion time for several constant-voltage drive waveforms at the insulator, for one-half of a double-sided load configuration. The design requires 7 MJ radiated, which translates to 5.4 MJ kinetic. Therefore, for t_p less than 140 ns, voltages of 10 MV or greater are needed.

VACUUM INSULATOR EFFECTS

Any design for X-1 must consider the possibility of both vacuum-side and water-side flashover of the insulator. Furthermore, since flashover thresholds can be increased by strong magnetic fields, as will be present in X-1, magnetic flashover inhibition (MFI) needs to be investigated. The goal is to find those wave-forms for which magnetic insulation is enhanced before vacuum breakdown thresholds are exceeded. It is

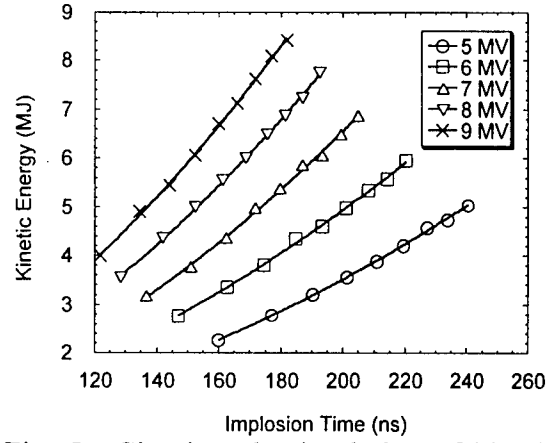


Fig. 5. Circuit-code simulation of kinetic energy vs. voltage and implosion time, including resistive-wall losses, a time-varying inductance, and convolute losses.

also important to operate in regimes where the water-side limit is never exceeded.

The insulator is magnetically insulated when the current is high enough that the tangential component of the electric field E_t is less than $0.07 c B$, where c is the speed of light, and B is the magnetic field intensity [3]. In practical units, that occurs for $E_t(\text{kV/cm}) < 210 B(\text{T})$. A useful scaling parameter is f_{MFI} , which is the ratio of E_t to $210 B$.

The average electric field at flashover on the vacuum side of the insulator is $E(\text{kV/cm}) = 175 A^{-1/10} t_{eff}^{1/6}$, where A is the insulator area in sq. cm, and t_{eff} is the time in μsec that the pulse exceeds 89% of its peak value [4]. This relation is modified to give a time-dependent parameter $f_V(t)$, which is the fraction of the vacuum-breakdown field.

$$f_V(t) = \frac{A^{0.1}}{175} \left[\int_0^t E^6(t') dt' \right]^{1/6}. \quad (4)$$

On the water side the anode breakdown field is $230 A^{-0.058} t_{eff}^{1/3}$, using the same units but with t_{eff} measured at 63% of peak [5]. Similarly, a parameter $f_W(t)$ is defined. It is the fraction of the water-breakdown field at the anode conductor.

$$f_w(t) = \frac{A^{0.058}}{230} \left[\int_0^t E^3(t') dt' \right]^{1/3} \quad (5)$$

These three parameters can be plotted for various wave-forms. In fig. 6 these parameters for a flat-voltage wave-form at the insulator are shown. Note that the vacuum flashover criterion is exceeded before the insulator becomes magnetically insulated.

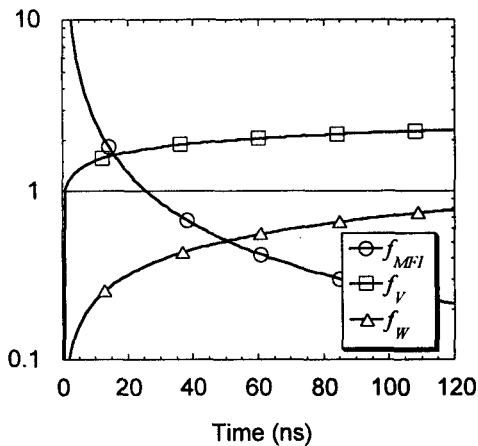


Fig. 6. MFI, and vacuum and water breakdown criteria as a function of time for a constant voltage at the insulator.

In fig. 7 the same three criteria are shown for a sine-squared drive wave-form. Here the insulator becomes magnetically insulated just as the vacuum breakdown criterion is exceeded. Both cases are with 18 nH loads, a 6 m diameter stack, a peak field of 150 kV/cm, and a current of 60 MA. Although not shown, even more extreme waveforms can be used to maximize the magnetic insulation early in time before the flashover criterion is exceeded.

CONCLUSIONS

It has been found that it is possible to achieve high driver-to-load coupling efficiencies with most reasonable wave-forms by optimizing driver impedance. Therefore, attention should be paid to choosing wave-forms that enhance magnetic

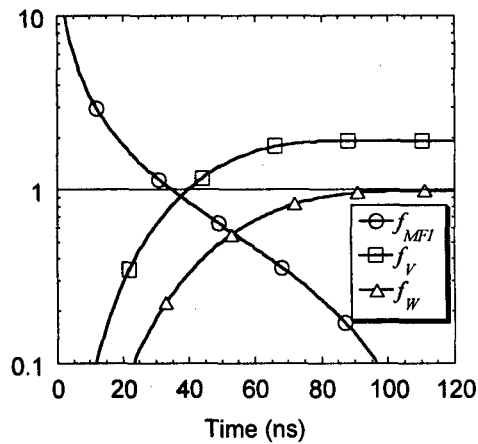


Fig. 7. MFI, and vacuum and water breakdown criteria for a sine-squared voltage at the insulator.

insulation and minimize early-time breakdown. Several critical design requirements and power flow issues remain unresolved which will have a large impact on machine design. Final machine design will require maximizing driver efficiency while minimizing insulator size and stress.

REFERENCES

- [1] R. B. Spielman, *et al.*, *Dense Z-Pinches*, *Fourth Int. Conf.*, ed. by N. R. Pereira and J. Davis (AIP, Woodbury, New York, 1997), p. 101.
- [2] M. L. Kiefer and M. M. Widner, *Digest of Tech. Papers*, *5th IEEE Pulsed Power Conf.*, ed. M. F. Rose and P. J. Turchi, 1985, p. 685.
- [3] J. P. VanDevender, *et al.*, *J. Appl. Phys.* **53**, 4441 (1982).
- [4] J. C. Martin, in *J. C. Martin on Pulsed Power*, ed. by T. H. Martin, *et al.* (Plenum, New York, 1996), p. 255.
- [5] R. A. Eilbert and W. H. Lupton, "Extrapolation of AWRE Water Breakdown Data," unpublished NRL report, ca. 1968.

*Sandia is a multiprogram laboratory operated by Sandia Corporation, a Lockheed Martin Company, for the United States Department of Energy under Contract DE-AC04-94AL85000.

PLASMA OPENING SWITCH - LOAD COUPLING ON ACE 4

J.R. Thompson, P.L. Coleman, R.J. Crumley, P.J. Goodrich, J.R. Goyer, and J.E. Rauch
Maxwell Technologies, Inc., 8888 Balboa Avenue, San Diego, CA 92123 USA

J.J. Moschella and E.J. Yadlowsky
HY-Tech Research Corporation, 104 Centre Court, Radford, VA, 24141 USA
Sponsored by the Defense Special Weapons Agency

ABSTRACT

Plasma opening switches (POS) are a key technology in inductive energy storage based pulsed power applications. It has been observed on HAWK, DPM1, and ACE 4 that the geometry downstream of the POS plasma injection region can have a significant effect on POS-load coupling [1,2,3]. However, the correlation between performance and geometry is not well understood. POS - load coupling has been investigated for the 9 cm radius, ACE 4 coaxial POS [4]. This study provides insight into the coupling of the POS driving an inductive load and guidance in the design for coupling to an e-beam diode. It also complements the work reported at this meeting by Coleman et al. [5] and Don Parks et al. [6].

INTRODUCTION

The 9 cm, ACE 4 POS has demonstrated opening voltages in excess of 1 MV for conduction times of $\sim 1 \mu\text{s}$ and for currents in excess of 3 MA when driving the large inductive load shown in Figure 1. Efficient coupling of the POS with an e-beam diode requires changes in the downstream geometry so as to minimize the POS to load inductance. The purpose of this study was to develop a model describing the interaction of the 9 cm ACE 4 POS with the downstream geometry during the opening phase which would provide guidance for a

design to minimize inductance in the POS to load transition region.

The coaxial POS on ACE 4 utilizes a high density, $\sim 5 \times 10^{15}$ ions/cm³, 20 cm long plasma fill. The phenomenology of the ACE 4 POS is that MHD is the dominate physics during the conduction phase and that it reduces the plasma density carrying the current through radial mass motion ("thinning"). When the density reaches $\sim 10^{14}$ ions/cm³, the opening phase begins through Hall and erosion physics. Of interest in this study was the location of high density, current carrying plasma at the time of switch opening.

POS models typically assume an initial injected plasma distribution which is uniform axially and abruptly truncated both upstream and downstream. In reality, during injection the plasma spreads both upstream and downstream of the nominal POS region, generating tails in the mass distribution. Interferometric measurements with an earlier 6 cm radius, ACE 4 POS showed plasma displacement several centimeters downstream of the POS. In addition, the earlier experiments showed a significant reduction of the POS opening voltage with radially confined geometries downstream of the POS.

END OF CONDUCTION PHASE - COMPUTATIONAL MODELING

MHD computational modeling was performed for the 9 cm ACE 4 POS inductive load geometry shown in Figure 1 using a measured average axial density

profile in the POS region. Modeling was performed for two cases: 1) with no plasma downstream of the POS and 2) with an estimated downstream density tail. Figure 2a shows the initial conditions in the POS to load transition region for the case with a density tail. Figures 2b and c compare later time-evolved density distributions for the two cases. Although one cannot tell when in the MHD computation opening would begin due to other physical processes, one can ask where the maximum "thinning" occurs. The MHD evolution of the density front pushed downstream of the POS is seen to be very different for the two cases.

In the case with no downstream density tail, Figure 2b shows the plasma pushed out of the POS region expanding downstream with the region of maximum "thinning" occurring in-line with the original POS A-K gap. From MHD considerations alone this would suggest that a radial confinement to a region near the outer anode might have little effect on the density evolution in the region of "thinning" where opening might be expected to occur.

In the case with an initial downstream density tail, Figure 2c shows reduced axial motion and the development of a radial region of maximum "thinning" while the plasma front in-line with the POS A-K gap shows significantly less density reduction. As indicated by the relative times for the two cases, the reduced axial extent caused by the forward moving front accumulating further mass allows time for the radial growth and "thinning" observed. In this case radial confinement to a region near the outer anode would prevent opening.

BEGINNING OF OPENING PHASE - EXPERIMENTAL DIAGNOSIS

Both single beam and 2-D interferometry were used to investigate the downstream region near the end of the POS. Figure 3a shows an earlier time computation of the

case with a downstream density tail and the typical viewing of the region interferometric diagnostics. At the time shown in the computation, a density shell has passed the single chordal interferometry line-of-sight and a thin, high density plasma can be seen pressed against the cathode, the downstream-most extent of which marks the front of the axial moving plasma sheath.

Figure 3b shows an experimentally observed line-integrated electron density time history which is consistent with a density shell passing through the line-of-sight located axially 3 cm into the inductive load with its nearest approach to the cathode at half the 3 cm POS A-K gap. Overlaid is the relative timing of the load current $I\text{-dot}$. At this position the line-integrated electron density is observed to peak as the time current begins to rise in the load (i.e. at the beginning of the opening phase). Measurements at different axial positions gives a velocity of the front of ~ 70 cm/ μ s. This, coupled with the observed electron density pulse FWHM, implies a 2-3 cm thick front. Using an estimated 10 cm path length through the front implies a peak density of $>10^{15}$ ions/cm³ using an average ionization state of $Z=4$. Density levels of 10^{15} are high compared to the levels where MHD is expected to no longer dominate. This result is suggestive that the computation shown in Figure 2c may be the more relevant picture and that the opening is not occurring in the forward direction as suggested by Figure 2b. The implication of this for load coupling on ACE 4 would be a limit to the allowable radial confinement of the region immediately downstream of the POS.

Pulsed 2-D inteferometry was used to investigate the presence of high density plasmas, $\geq 10^{17}$ electron/cm³, in the region downstream of the POS. An imposed fringe pattern of several fringes/cm was set up in a low resolution mode, with each fringe corresponding to a phase difference of a few times 10^{17} electrons/cm². Regions where high electron densities are present appear as distortions or a washout of the original fringe pattern. Figure 4a shows a typical 2-D fringe pattern for the case with no plasma present. At a time 40 ns before the POS begins to open,

when current begins to appear in the load, a high electron density region is beginning to appear along the cathode in the region downstream of the POS as shown in Figure 4b. By the time POS opening begins, the narrow high density region has extended ~ 5 cm beyond the end of the POS as shown in Figure 4c. This is consistent with the relative position and timing of the time resolved, single chordal interferometry measurements indicating the position of the density front.

SUMMARY

POS - load coupling has been investigated for the 9 cm radius, coaxial POS on ACE 4. A high density plasma sheath is observed propagating downstream and in-line of the POS A-K gap at the time of opening. Comparison of the experimental results with computational modeling suggests opening is not occurring in-line with the POS but in a region of outward radial expansion. If this is the case, preservation of the present ACE 4

POS opening performance requires, at a minimum, that the POS to load transition region has an outward radial expansion region downstream of the POS. Work is in progress to further validate and quantify this interpretation to provide guidance for minimizing the POS to load inductance.

REFERENCES

- [1] P.J. Goodrich et al., "Microsecond plasma opening switch experiments on Hawk with an e-beam diode load," Proc. 9th International Conf. High-Power Particle Beams, Washington, DC, NTIS PB92-206168, pp. 609-614, 1992.
- [2] J.R. Goyer et al., "Improved performance of a plasma opening switch using a novel anode configuration," IEEE Transactions on Plasma Science, Vol. 22, no. 3, pp. 242-245, June 1994.
- [3] Unpublished ACE 4 data.
- [4] Thompson et al., "ACE 4 Plasma Opening Switch Performance Above 3 MA," unpublished, presented at IEEE ICOPS, June 5, 1996.
- [5] Coleman et al. "Applications of Optical Emission Spectroscopy, Fast Imaging, and Ion Probes to the Study of Megamp Plasma Opening Switches (POS)," submitted to these proceedings.
- [6] D. Parks et al., "Plasma Evolution of a POS: Comparison of Theory and Experiment on ACE 4 and DM1," submitted to these proceedings.

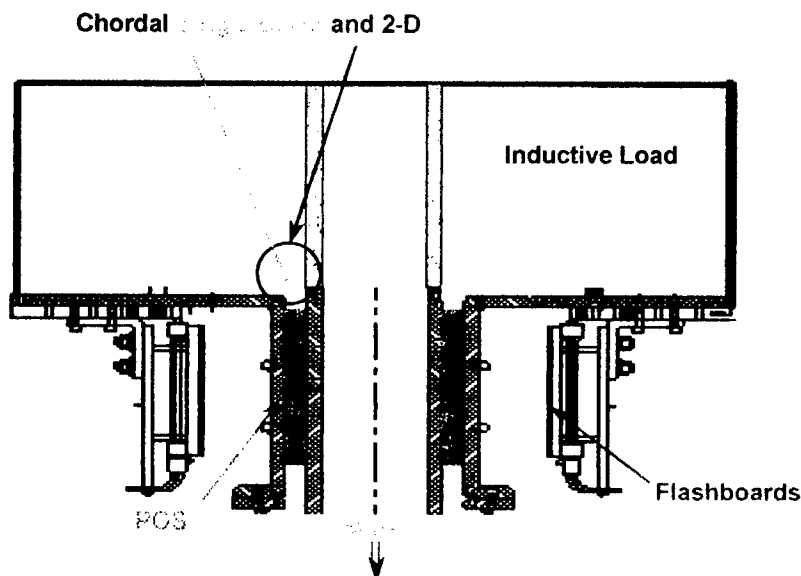


Figure 1. ACE 4 inductive load and diagnostic configuration.

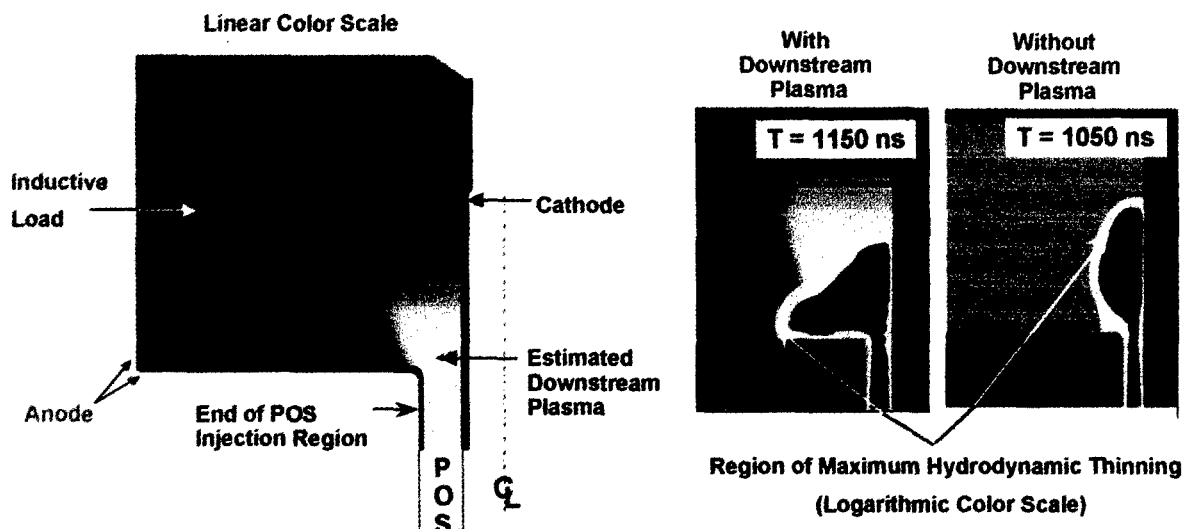


Figure 2. Computational modeling shows dependence on presence of downstream plasma.

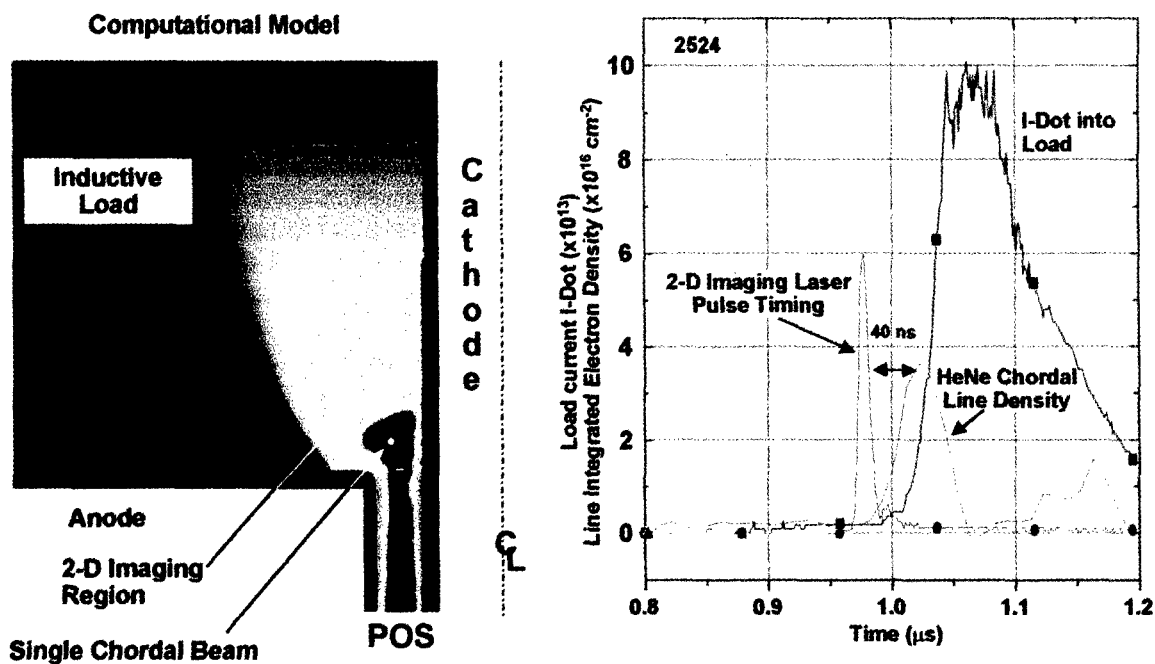


Figure 3. High density front observed downstream of the POS at opening time.

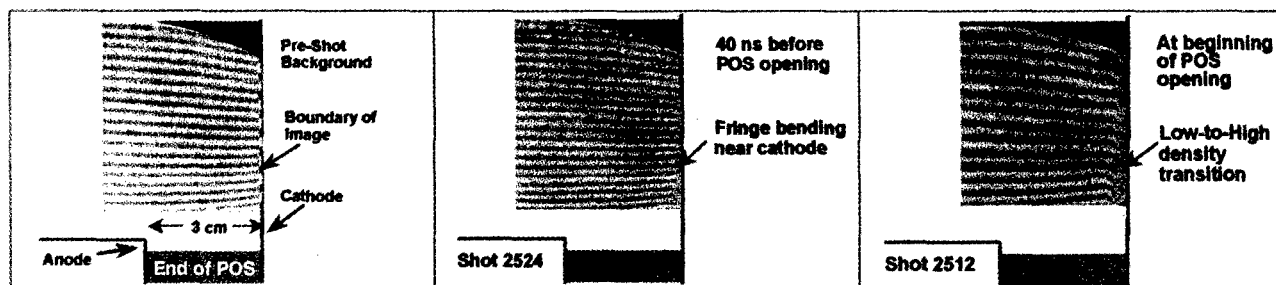


Figure 4. High density plasmas along cathode observed downstream of POS.

GAS PRE-IONIZATION SYSTEM FOR DECADE MODULE 2 PRS EXPERIMENTS[†]

B. V. Weber, S. J. Stephanakis, B. Moosman,* R. C. Fisher,**
D. D. Hinshelwood, R. J. Commisso and A. Fisher

Plasma Physics Division, Naval Research Laboratory, Washington, DC 20375

J. C. Riordan, P. D. LePell,*** J. S. Levine and Y. Song
Maxwell Physics International Company, San Leandro, CA 94577

Abstract: DECADE Module 2 (DM2) implodes argon gas-puffs in 200-300 ns from initial radii of 2.5-5 cm to generate K-line radiation. An important issue for these experiments is the lower-than-expected K-line radiation associated with such large radius implosions. Preionization may improve the implosion quality by improving the symmetry of the initial current flow. A preionizer is described based on photoionization by ultraviolet (UV) illumination from a flashover source. The preionization is diagnosed using a high-sensitivity interferometer. This UV source produces 1-10% ionization of the outer periphery of the argon gas distribution prior to the arrival of the flashboard plasma. DM2 experiments indicate increased, more reproducible K-shell yields when this preionization system is incorporated.

INTRODUCTION

This work supports Plasma Radiation Source (PRS) experiments on the DECADE Module 2 (DM2) generator using argon gas puffs and long (≤ 300 ns) current rise times.¹ Long implosion times require relatively large (>5 cm diameter) gas-puff nozzles to maximize the K-shell yield. The argon density is appropriately smaller given an optimum mass for the generator current waveform.

Experience with PRS implosions from such large initial radii² indicates significantly diminished K-shell yields from inferior quality implosions. This can be due to the Rayleigh-Taylor (RT) instability and non-uniform gas breakdown at the onset of the generator pulse. Theoretical considerations and preliminary experiments indicate that the RT instability can be at least partially mitigated by employing "filled" rather than hollow initial gas distributions. It is suggested that symmetric preionization of the argon gas could mitigate the non-uniform current initiation problem. The design, testing and initial implementation of such a preionization system is the subject of this paper.

For a pre-ionizing scheme to be effective and practically useful, certain criteria must be met. These include: (1) azimuthal symmetry, (2) sufficient ionization to support the generator current at early times (estimated to be 1% or greater for the argon gas density of interest), (3) hardware which does not interfere with the PRS discharge or diagnostic access, (4) minimal pre-ionizer plasma in the PRS region, and (5) hardware which survives super-power generator shots or is easily replaceable. All of the above criteria, except perhaps the last one, are met by the source described below.

[†] Work supported by the US Defense Special Weapons Agency

* NRC/NRL Research Associate

** JAYCOR, McLean, VA

*** present address: KTech Corp., 901 Pennsylvania NE, Albuquerque, NM 87110

FLASHBOARD PREIONIZER

The pre-ionizing scheme described here uses flashboard-generated ultraviolet (UV) to photoionize the argon gas. The photoionization cross section³ for neutral argon exhibits a broad maximum exceeding 30 Mbarns in the $h\nu = 16\text{--}27$ eV range. Similar experiments⁴ indicate that over 60 % of the UV emission from such flashboard sources is in the 10-20 eV range with the remainder emitted primarily between 20 and 70 eV. Thus, there exists a good match between the range over which the UV source is most powerful and that over which argon is most susceptible to ionization by UV radiation.

A schematic representation of the preionizer in relation to the DM2 7-cm diameter "semi-solid" PRS nozzle is shown in Figure 1. The UV source consists of two semicircular flashboards that form a 19-cm diameter cylinder, 18 cm from the nozzle. The flashboards and their electrical feeds are made of Kapton-insulated low inductance strip lines. The flashboards are driven by two capacitor banks (1.8 μF , 20 kV each), providing ~ 40 kA peak current. Each flashboard has two rows of 40, 2 mm flashover gaps. A polyethylene sheet, spanning a diameter of the circular preionizer and extending 7.5-cm axially on either side, is used to block fast flashboard plasmas to delay plasma arrival at the PRS region. The necessity of this plasma shield was established experimentally. The diameter of the preionizer and its distance from the PRS nozzle were chosen to optimize ionization by UV while avoiding plasma in the PRS region.

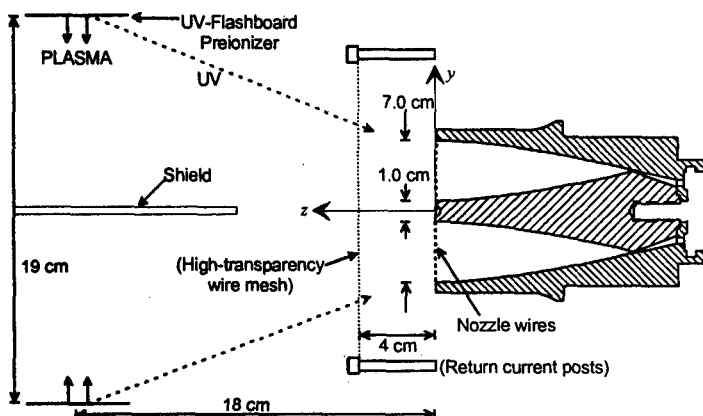


Figure 1: Schematic representation of 7-cm nozzle and preionizer. Posts and mesh are shown for reference only.

PREIONIZATION MEASUREMENTS AND PRELIMINARY DM2 RESULTS

High-sensitivity ($\Delta\phi > 10^{-5} \lambda$) laser interferometry⁵ is used to measure the neutral gas distribution and the free electron density produced by preionization. The interferometer gives the integrated density along a chord at one distance, y , from the axis and at one distance, z , from the nozzle. The gas measurements are made at a sufficient number of y values to determine the radial gas density distribution via Abel inversion. The preionizer is fired about 150 μs after gas exits the nozzle. For the laser wavelength used here ($\lambda = 532$ nm), the phase shift per free electron is -12 times that per argon atom. Ionization therefore appears as a negative change in the total phase shift for preionizer shots relative to shots without the preionizer. Example phase-shift waveforms measured at $z = 4$

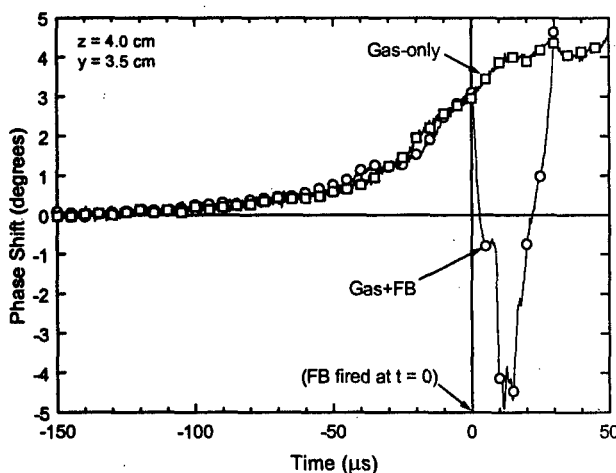


Figure 2: Phase shift with and without preionization.

cm and $y = 3.5$ cm are shown in Fig. 2. When the total phase shift is zero, the fractional ionization (integrated along the laser line-of-sight) is 8%. The electron line-density is determined from the difference in the phase shifts, therefore even small ionization fractions are easily discernible.

The large negative change in the phase shift in Fig. 2 is the result of both free electrons from UV preionization and flashboard plasma arriving at the measurement location. These can be distinguished using the phase shift measured by firing the flashboard without gas. The phase shifts from gas-only, gas-preionizer and preionizer-only shots, converted to neutral and electron line densities, are shown in Fig. 3 over a shorter time interval to emphasize the time range appropriate for firing the generator, given the above criteria. The flashboard-only line density is a worst case scenario, since in the real situation, part of this plasma is attenuated by the argon gas in the PRS region. The flashboard plasma density is insignificant in the PRS region for about $3.5 \mu\text{s}$ after firing the flashboard. At that time, the argon gas is 10% ionized at that location. This is the optimum time to fire DM2 to maximize the ionization fraction while avoiding flashboard plasma in the PRS region.

The results in Fig. 3 were obtained at $z = 4$ cm, $y = 3.5$ cm, the position in the PRS region closest to the preionizer and the steepest viewing angle. Both the proximity to the UV source and the steepness of the angle⁴ result in higher UV intensity and thus increase the preionization fraction, while the flashboard plasma arrives first at this location. Less preionization is expected closer to the nozzle exit. This is illustrated in Figure 4 with data taken at $z = 2$ mm from the nozzle. The data in this case are the Abel-inverted gas and electron densities as a function of radius at the optimum time indicated in Fig. 3. The percent ionization plot shows that the preionization is confined to the outer cm or so of the gas, consistent with $100\text{-}200 \mu\text{J}/\text{cm}^2$ - μs of $16\text{-}27$ eV radiation⁷.

The preionizer system was fielded on DM2 for a limited number of PRS shots. Argon K-shell yields are compared in Fig. 5 for shots with load currents of 2.25 ± 0.1 MA. The plot on the left in Fig. 5 compares yields from shots where an array of thin wires were placed over the nozzle exit, while the right side compares yields from shots without wires. Based on these

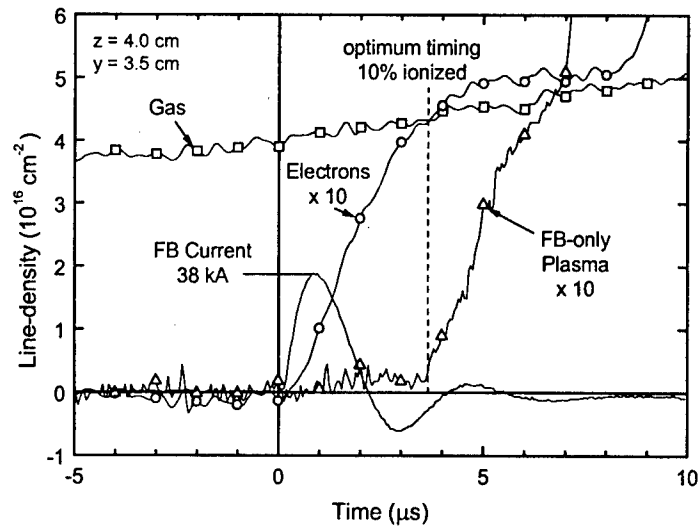


Figure 3: Line-density waveforms for gas, electrons and flashboard plasma, and flashboard-current waveform.

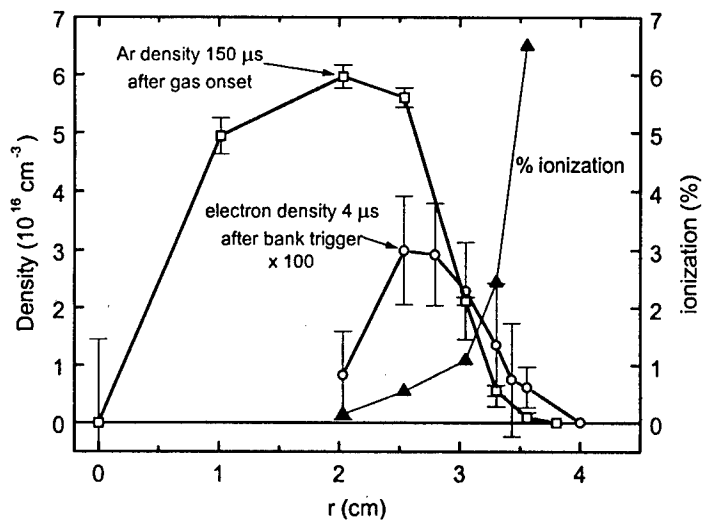


Figure 4: Neutral argon and electron radial density profiles at $t = 150 \mu\text{s}$; $z = 2$ mm.

preliminary data, one can infer that (1) without wires across the nozzle face, the yield is significantly depressed unless preionization is used, while (2) with nozzle wires, the yield is generally higher but the shots with preionization define the upper extreme of the scatter envelope. The improved yield when the nozzle wires are employed may be due to the wires acting as electron emitters early in the pulse, thus contributing to the preionization process via electron-neutral ionizing collisions.

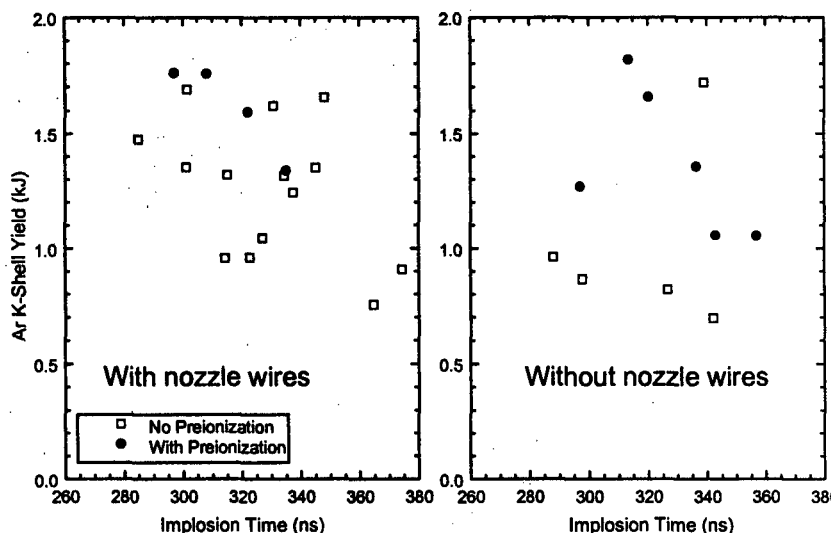


Figure 5: DM2 data with and without the preionizer.

SUMMARY AND CONCLUSIONS

An azimuthally symmetric UV source for preionizing argon gas from a 7 cm diameter nozzle was designed, built, diagnosed and fielded on DM2 PRS experiments. This source produces $> 1\%$ ionization of the outer periphery of the argon gas distribution with fractions approaching 10% about 4 cm from the nozzle, prior to the arrival of flashboard plasma in the PRS region. The flashboard preionizer produces significant plasma of its own but it does not arrive in the PRS region for at least 3-4 μs .

The issue of survivability was not seriously addressed during these tests. There are indications from the DM2 shots that the preionizer can be damaged from debris off the PRS implosions and some measures are being taken to correct the problem. Certainly, for use in higher energy generators (Decade-Quad, Saturn, etc.), an easily-replaceable, single-shot version of the preionizer should be designed and tested.

Other preionization techniques may have advantages over the flashover-UV source, such as electron beams,⁸ microwaves, discharges,⁹ etc. These alternate techniques could be evaluated and diagnosed using the interferometric technique described here.

ACKNOWLEDGEMENT

The work described here would not have been possible without the capable assistance of Mr. Eric Featherstone of the Pulsed Power Physics Branch, NRL.

- ¹ J. Levine, *et al.*, these proceedings.
- ² R. J. Comisso, *et al.*, to be published in *IEEE Trans. Plasma Sci.*, August 1998.
- ³ D. A. Verner, *et al.*, *The Astrophys. J.* **465**, 487 (1996).
- ⁴ J. R. Woodworth, *et al.*, *J. Appl. Phys.* **58**, 3364 (1985).
- ⁵ B. V. Weber and S. F. Fulghum, *Rev. Sci. Instrum.* **68**, 1227 (1997).
- ⁶ B. Moosman, *et al.*, to be published in *Rev. Sci. Instrum.* (1998).
- ⁷ J. Apruzese, private communication.
- ⁸ E. Ruden, *et al.*, *J. Appl. Phys.* **61**, 1311 (1987).
- ⁹ R. B. Baksht, *et al.*, *Plasma Physics Reports* **3**, 175 (1997).

THE TIME-DEPENDENT ELECTRON DENSITY AND MAGNETIC FIELD DISTRIBUTIONS IN A 70-ns PLASMA OPENING SWITCH

A. Weingarten, C. Grabowski, A. Fruchtman, and Y. Maron

Faculty of Physics, Weizmann Institute of Science, Rehovot 76100, Israel

ABSTRACT

The time-dependent two-dimensional electron density distribution is determined for the first time during the operation of a short-conduction plasma opening switch. The electron density, resolved in 3-D, is determined from the line intensities of different ions doped into the plasma. A rise in the electron density followed by a drop is observed to propagate from the generator towards the load at the proton Alfvén velocity. Based on spectroscopic magnetic field and ion velocity measurements, the density evolution can be explained as pushing of the protons ahead of the propagating magnetic piston, followed by magnetic field penetration into the rest of the plasma composed of the lower-density heavier ions.

I. Introduction

Plasma Opening Switches (POS's) are used for voltage and power multiplication and in inductive energy storage systems that conduct currents during periods ranging from 50 ns to over 1 μ s[1] before opening into a load. Scaling laws[2] for the POS's were shown to have good agreement with long-conduction POS experiments. The plasma dynamics in such POS's have been investigated using laser interferometry[2], and the magnetic field was studied using B-dot loops[1] and laser induced fluorescence[3]. Studies of short-duration (≤ 100 ns) POS's[1] were more limited, consisting of current and voltage measurements, studying the prefilled plasma parameters, and energetic particles emitted from the plasma. Magnetic field evolution was measured by B loops[1]. In a previous publication[4] we have described the measurements of the two-dimensional magnetic field penetration into a positive-polarity POS plasma. The field penetration was quantitatively explained by an EMHD (Hall) model[5], which used as an input the prefilled plasma density distribution and assumed that n_e does not change appreciably during the current pulse, an assumption supported by previous results [6].

II. Experimental System

Figure 1 shows the POS setup. The diameters of the cathode and anode are 4 and 9 cm, respectively, and the plasma axial length is 10 cm giving upstream and downstream inductances of 95 and 25 nH, respectively. A 170 kA, 85 ns quarter-period current pulse (270 kV) is applied by a 1 Ω LC-water-line Marx generator. Typical upstream and downstream currents, measured by Rogowski coils, are shown in Fig. 2b. The plasma is produced using a cylindrical flashboard that is placed 6.5 cm outside the 85%-transparency anode, and driven by a 0.9 μ F, 24 kV capacitor. Two optical systems that image the same plasma section onto the input slits of two spectrometers are used for observation along the axis. The spatial resolution in the r and θ directions are 1 mm and 5 mm, respectively. The light from each spectrometer output slit is collected by a set of 10 photomultiplier-tubes (PMT's) to provide time-resolved measurements with a response time of 7 ns (FWHM)

The electron density (n_e) of the prefilled plasma, determined in-situ from hydrogen line Stark broadening and MgII (doping) line ratios, is $(2.2 \pm 0.5) \times 10^{14}$ cm⁻³ over the entire A-K gap. The electron temperature (T_e), also determined from MgII line ratios, is (5.5 ± 0.5) eV,

with a plasma injection velocity of $(3-10) \times 10^6$ cm/s. The plasma is composed mainly of protons, with the rest being CIII-CIV ions. Near the cathode, the carbon fraction ($Z_i n_i / n_e$) is only 10%, while closer to the anode, the carbon fraction is $\sim 30\%$.

Axial resolution is obtained by observing light emission from a narrow column of impurities injected into the plasma. A Nd:YAG laser pulse (10 ns FWHM, <100 mJ) is used to evaporate solids deposited on either of the POS electrodes creating an impurity plasma column with $\sim 45^\circ$ divergence angle that flows into the POS region (column width <1cm).

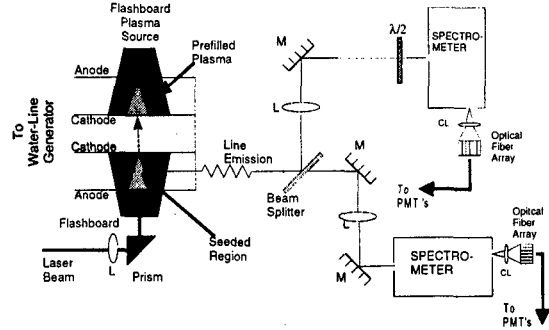


Figure 1 The POS and spectroscopic systems. M, L and $\lambda/2$ represent mirrors, lenses and half-wavelength plate, respectively

III. Experimental Results

The evolution of n_e and T_e during the POS operation is studied by observing the intensities of MgII, AlII, and AlIII lines that are emitted from levels of various excitation energies. The line intensities depend on the axial and radial positions and on the POS conduction time. In order to study the changes in the densities of the emitting ions, their axial velocities (v_z) were determined from Doppler shifts, and were seen to remain relatively low (e.g., the peak v_z of CIII is $<1 \times 10^7$ cm/s). During the pulse, the CIII moves axially <0.4 cm, which cannot affect n_e significantly. Measurement of the radial velocity was not performed in our experiment, but at all radii (at a given axial position) the temporal behavior of the intensity is similar to within 25 ns. For the ions to cross the A-K gap requires that they would acquire a radial velocity $\approx 1 \times 10^8$ cm/s; with the measured v_z of CIII this implies a divergence angle of $\leq 6^\circ$, which is very unlikely.

Figure 2a shows the time-dependent level populations of the MgII 3p level (4.4 eV), the AlII 4s 1S level (11.8 eV), and the AlIII 4p level (17.9 eV), observed at the $r=2.5$ cm, $z=0$ (defined as the POS axial center, where negative z is towards the generator) with similar POS operation (shown in Fig. 2b). The intensity of all three lines increases, but the increase is larger for the higher levels, and the lines start to drop simultaneously at $t=(46 \pm 3)$ ns.

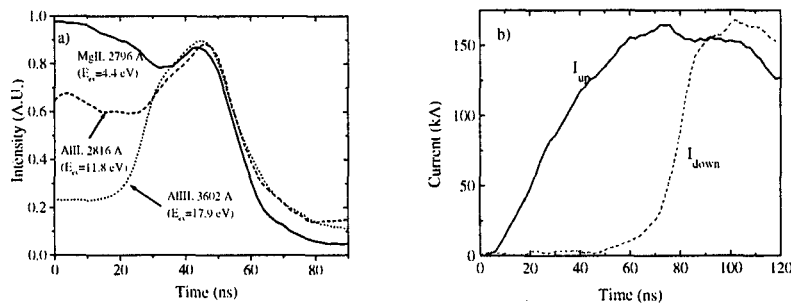


Figure 2. a) The time dependent intensity of an MgII line (solid), AlII line (dashed), and AlIII line (dotted) during the POS operation. b) The generator (I_{up}) and load (I_{down}) currents.

Assuming that the density of the light-emitting ions does not change during the pulse, and by treating the three lines self consistently using detailed collisional-radiative calculations, we found that at $t=46$ ns, T_e increases to 12 eV while n_e decreases by 15%. Ionization can affect the ion density by only a few percent since the ionization times of AlIII,

AlIII, and MgII at these n_e and T_e are 4 μs , 250 ns, and 180 ns, respectively. Furthermore, the intensity drop does not result from cooling of the electrons, since the AlIII is much more sensitive to T_e variations than MgII. A self-consistent treatment of the three lines at $t=70$ ns yields $n_e=2.5\times 10^{13} \text{ cm}^{-3}$ and $T_e \approx 15 \text{ eV}$.

A similar procedure at each r, z position for three different times yields the n_e contours in the r - z plane shown in Figure 3. In all these shots, the POS conduction time is 65 ± 10 ns, and the opening time is 15 ± 3 ns. The initial n_e was taken to be $2.2\times 10^{14} \text{ cm}^{-3}$ at $-3.5\leq z\leq 3.5$ cm, and $1.1\times 10^{14} \text{ cm}^{-3}$ at $z=\pm 5.2$ cm. The contours show that n_e increases before dropping. The drop propagates from the generator side towards the load, but the propagation is diagonal, i.e., n_e drops earlier at the smaller radii. The propagation velocity is $(1.5\text{-}2.5)\times 10^8 \text{ cm/s}$.

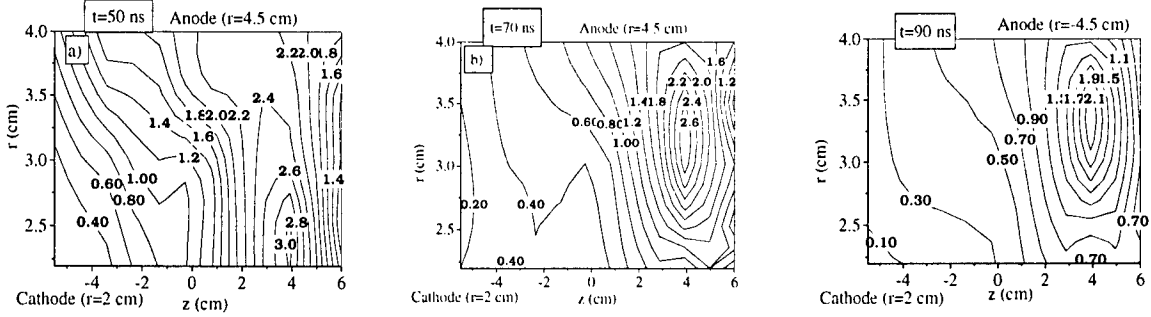
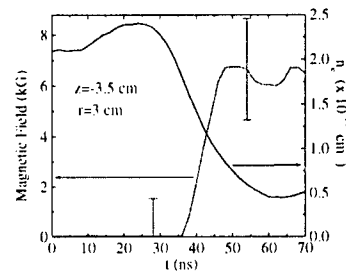


Figure 3. n_e contours in units of 10^{14} cm^{-3} , for a conduction time of 65 ± 10 ns, at a) $t=50$ ns; b) $t=70$ ns; c) $t=90$ ns. Negative z is towards the generator and the short-circuit load is at $z=+15$ cm.

At $t=50$ ns, n_e already dropped considerably at the generator-cathode side of the prefilled region but it increases at the load side, especially at the cathode side. At $t=70$ ns, when some current is already measured at the load, n_e decreases also at the load side of the plasma but only near the cathode. At $t=90$ ns, when the full current flows to the load, n_e drops everywhere to 10-30% of its initial value, except for a small region at the load-anode side.

The magnetic field (B) is measured from the Zeeman splitting of the 5609 Å line (7p-7s transition) of PbII ions doped into the plasma. The spectral profiles of the π components (light polarized along B , in the θ direction) and the σ components (light polarized perpendicular to B , in the r direction) are observed simultaneously at each position with the two spectrometers. The two profiles are fitted self-consistently assuming a Doppler broadening and Zeeman splitting to obtain B . An example of B and n_e is presented in Fig. 4. At this position, as in all other positions, the electron density starts to drop with the rise of the magnetic field.

Figure 4. The time dependent magnetic field (dashed line, left axis) and the n_e (solid line, right axis) at $z=-3.5$ cm, $r=3$ cm. The density starts to drop together with the penetration of the magnetic field.



The velocities of carbon and doped ions of various masses and charges were studied from Doppler shifts, and the proton velocity was determined from time-of-flight measurements using an array of 4 magnetically-insulated Faraday cups inserted into the plasma (in a similar manner to that which was used to study the ion flow in the vacuum section between the plasma and the load [7]). Since the Faraday cups are saturated within a few ns, only the velocity of the fastest protons can be determined. The proton axial velocity is

observed to be $(3.5 \pm 1) \times 10^8$ cm/s. However, these measurements should be taken with a grain of salt since the velocity obtained may be the propagation velocity of the magnetic piston.

IV. Discussion

The models that describe the POS conduction account for the plasma dynamics in two different limits. In the limit of large plasma pushing all the ions are pushed by the propagating magnetic piston to the same velocity, which is between the Alfvén velocity (v_A) (in the case of specular reflection[8]) and $v_A/\sqrt{2}$ (in the case of a snowplow[2]). In the other limit, where EMHD[5] theory is valid, the magnetic field penetrates into the plasma faster than v_A and the ions are almost immobile. At our POS and plasma parameters, the conditions for neither of these limits are satisfied, and both ion pushing and field penetration effects can occur. Indeed, the density was shown to increase and then decrease, a behavior similar to that observed in longer conduction-time POS's where it was explained as MHD pushing followed by EMHD effects[2]. In our experiment, the velocities of the heavy ions are low and their motion is small. Only the protons may move significantly on this short time scale, a motion that results in a drop of the electron density by the factor determined by the fraction of protons in the plasma. This is consistent with the fact that the density does not drop to zero, and that the decrease at larger radii is smaller, since the proton fraction is smaller at larger radii.

The magnetic field measurements indicate that protons are pushed by the magnetic piston, since the density increases ahead of B, and at each position B penetrates into the plasma together with the drop in n_e . However, the mechanism for the different behavior of the protons and heavier ions is not clear yet. The dynamics of a multi-component plasma interacting with magnetic pressure were described by Mendel[9] in the context of plasma-filled ion diodes. The magnetic pressure developed in the magnetic piston propagating through the plasma pushes the electrons and the ions that have kinetic energy smaller than the Hall potential (in the piston frame-of-reference). Ions with larger energy, namely the heavier ions, can "climb" the potential hill and stay behind the piston. In the laboratory frame the reflected ions would acquire a high velocity ($\sim v_A$) while the heavy ions acquire a much lower velocity, depending on the time they spend inside the piston. However, in our experiment the density of the plasma composed of carbon ions and electrons is quite high, a few times 10^{13} cm⁻³, and the mechanism for such plasma-leakage across the piston is not understood as yet.

Another question is the mechanism of the magnetic field penetration into the dilute plasma. The proton pushing results in the formation of a relatively low-density carbon plasma. The magnetic field can penetrate into such plasma according to EMHD theory. The Hall penetration velocity for a coaxial geometry and a uniform n_e is given by[5]: $v_H = cB/(4\pi n_e e r)$. For our initial n_e , $v_H = 7 \times 10^7$ cm/s, but after the density drops this velocity becomes much higher, and the field can penetrate rapidly into the dilute carbon plasma. We emphasize that considerable theoretical work is still required in order to fully understand the observations.

¹ B. V. Weber, et. al., IEEE Trans. Plasma Sci., **19**, 757 (1991) and references therein.

² B. V. Weber, et. al., Phys. Plasmas **2**, 3893 (1995) and references therein.

³ G. G. Spanjers, et. al., IEEE Int. Conf. on Plasma Sci., 160 (Madison, WI, USA, 1995).

⁴ R. Shpitalnik, et. al., Phys. Plasmas **5**, 792 (1998).

⁵ A. Fruchtman and K. Gomberoff, Phys. Fluids B **5**, 2371 (1993).

⁶ M. Sarfaty et. al., Phys. Plasmas **2**, 2122 (1995).

⁷ Ya. E. Krasik and A. Weingarten, IEEE Trans. Plasma Science **26**, 208 (1998).

⁸ M. N. Rosenbluth, in "Progress in Nuclear Energy, Series XI: Plasma Physics and Thermonuclear Fusion research", (Pergamon, London, 1963), Vol. 2, pp. 217-277.

⁹ C. W. Mendel, Jr., Phys. Rev. A **27**, 3258 (1983).

ELECTRODYNAMICS OF A MICROSECOND PLASMA OPENING SWITCH.

O.Zabaidullin and M.Nitishinskii

Institute of Nuclear Fusion, Russian Research Centre,
"Kurchatov Institute", 123182, Moscow, Russia

Abstract

Dynamics of a Plasma Opening Switch (POS), operating like a plasma piston and of a microsecond POS are numerically studied. Dependence of the conduction phase time versus both a number of particles in a plasma bridge cross-section and an electron magnetization value (Hall parameter) near a cathode is found. Results of modeling indicate, that the phenomena of rarefied gap production could be described in the frame of magneto hydrodynamic (MHD) with account of the Hall effect, without using the erosion theory [1].

As known, a POS is the integral part of an Inductive Energy Storage (IES) system. Development of IES systems demands creation of the POS with predictable output characteristics. The present work as the previous [2, 3] is devoted to derivation of the POS conduction scaling. For this reason the 2-D two-fluid MHD code is run in the coaxial symmetry. The initial POS conditions are chosen to reproduce two types of POS operation: I) MHD regime, plasma accelerates as a whole by the $J \times B$ force (Fig.1). II) the Hall regime, characterised by high influence of the Hall effect (Fig.2).

The 2-D two-fluid MHD system with account of the Hall effect contains the following equations:

a) equation of the plasma density n :

$$\frac{\partial n}{\partial t} = -\text{div}(n\mathbf{V}), \quad (1)$$

b,c) equations of the plasma velocity $\mathbf{V} = (V_r, V_z)$ components

$$\frac{\partial(nm_i V_r)}{\partial t} = -\frac{H_\varphi}{4\pi} \frac{\partial(rH_\varphi)}{r\partial r} - \frac{\partial(rm_i n V_r^2)}{r\partial r} - \frac{\partial(m_i n V_r V_z)}{\partial z} - 2\frac{\partial(nT)}{\partial r}, \quad (2)$$

$$\frac{\partial(nm_i V_z)}{\partial t} = -\frac{1}{8\pi} \frac{\partial(H_\varphi^2)}{\partial z} - \frac{\partial(m_i n V_z^2)}{\partial z} - \frac{\partial(rm_i n V_r V_z)}{r\partial r} - 2\frac{\partial(nT)}{\partial z}, \quad (3)$$

Here m_i is the average ion mass in the plasma.

d) equation of the plasma temperature T :

$$3\frac{\partial(nT)}{\partial t} = -3\text{div}(nT\mathbf{V}) - 2nT\text{div}(\mathbf{V}), \quad (4)$$

e) equation of the magnetic field H_φ :

$$\frac{\partial \mathbf{H}_\varphi}{\partial t} = \nabla \times (\mathbf{V} \times \mathbf{H}_\varphi) - \nabla \times \left(\frac{\mathbf{H}_\varphi}{4\pi en} \times (\nabla \times \mathbf{H}_\varphi) \right) - \nabla \times \left(\frac{c^2}{4\pi\sigma} (\nabla \times \mathbf{H}_\varphi) \right), \quad (5)$$

where σ is the Spitzer coefficient of the plasma conductivity.

g) Maxwell equation for the current density:

$$\mathbf{j} = \frac{c}{4\pi} (\nabla \times \mathbf{H}_\varphi). \quad (6)$$

It is supposed: (1) the gap formation takes place near the cathode. The simulations are carrying out in the region near the cathode [$R_c = 2.5 \text{ cm}$, $R_{out} = 18 \text{ cm}$] and [$Z_0 = 0 \text{ cm}$, $Z_{load} = 30 \text{ cm}$]. The plasma width $l = 18 \text{ cm}$. (2) the influence of the near-anode dynamics is negligible. (3) the value of

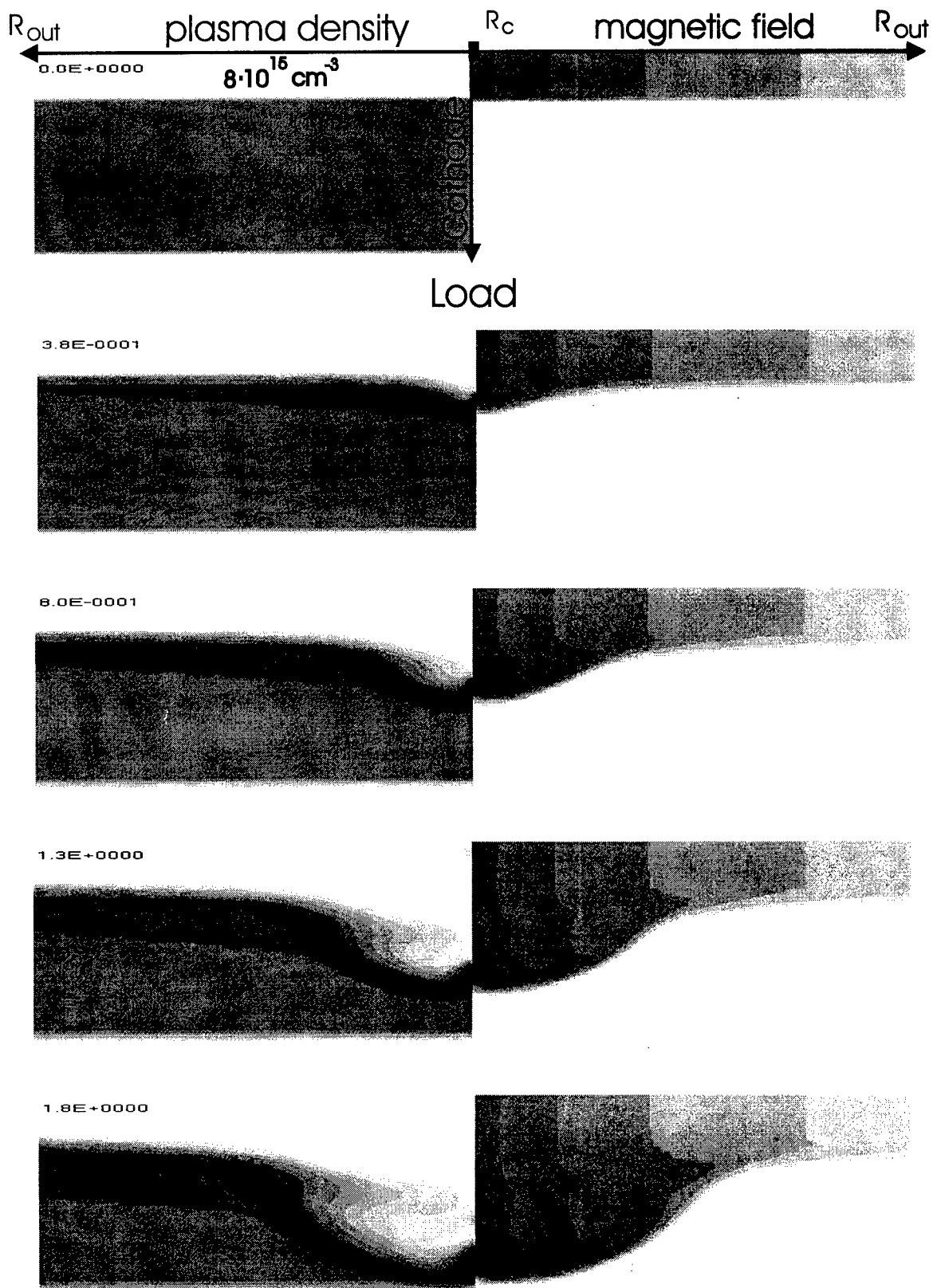


Fig. 1

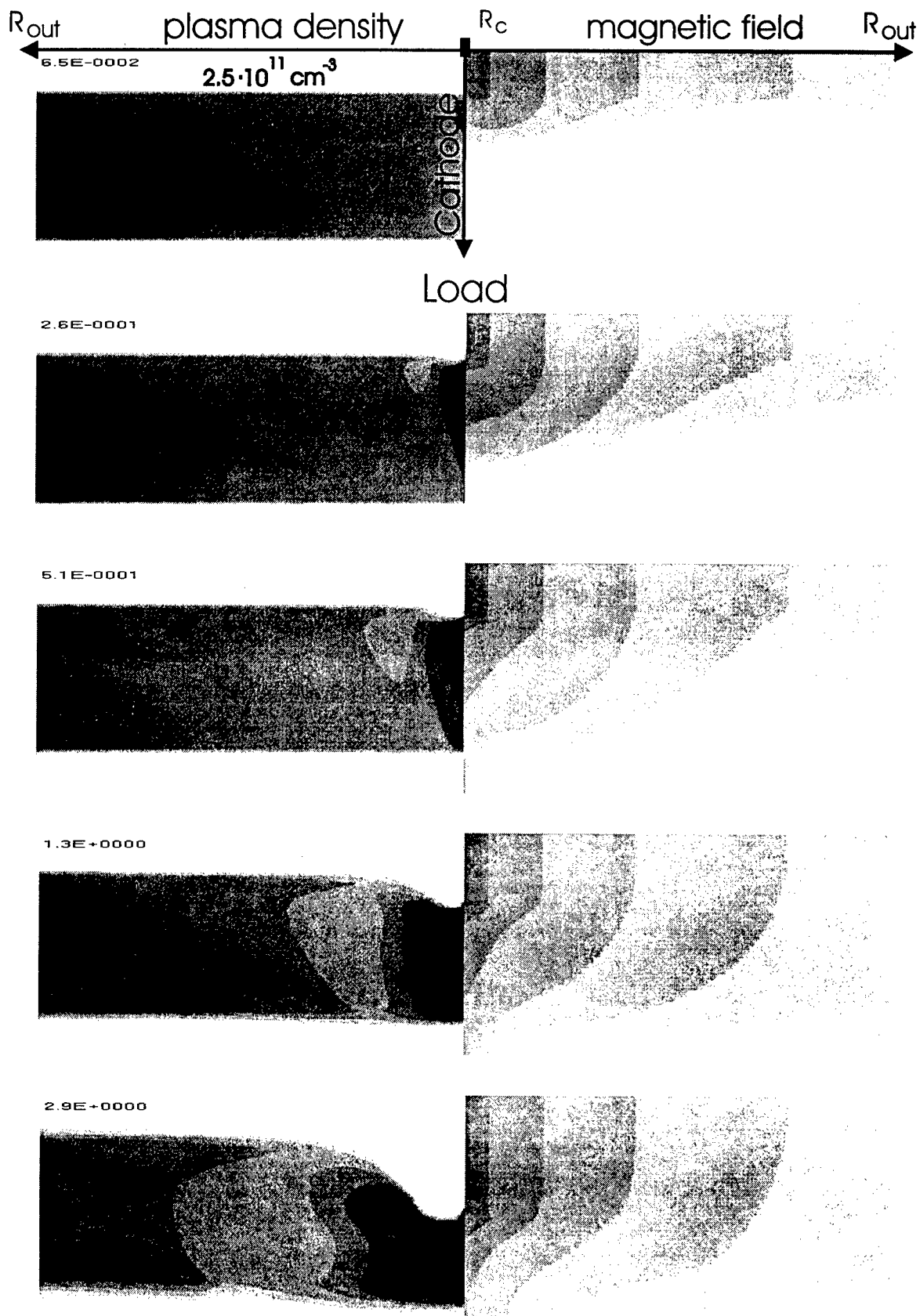


Fig.2

generator current, I_g , is constant. At initial moment the magnetic field already exists and is blocked by the uniform plasma bridge of some density (Fig.1a). The system (1-6) is solved in the dimensionless form. The dimensionless parameters of two-fluid MHD equations are the following: the time scale of the task, $T_A = 5lR_c\sqrt{4\pi n m_i}/I_g$; the number of electrons in a plasma cross-section, $\Pi_i = 4\pi n_e e^2 l^2/(m_i c^2)$; the Hall parameter, $(\omega\tau)_{ie} = 1.23 \cdot 10^{11} I_g T^{3/2}/(R_c n_e)$. Simulations are carried out for $(\omega\tau)_{ie} = 10$, $I_g = 200$ kA and hydrogen plasma, $n_i = n_e$. The plasma density is the unique modifying parameter.

The results of POS modeling, operating like MHD piston is shown on the Fig.1. In this case $\Pi_i = 100$ or $n_e = 8.5 \cdot 10^{15} \text{ cm}^{-3}$. In the fig.1 the central line is the cathode. Distribution of the magnetic field is shown at the right part and of the plasma density is at the left part. Darker color corresponds to higher value. The numerical value on the fig.1 is the ratio t/T_A . Magnetic field propagates along the cathode and pushes the plasma by the force $J \times B$ to the discharge volume.

The results of POS modeling, operating in opening regime are shown in the Fig.2. In this case $\Pi_i = 2.5 \cdot 10^{-3}$ or $n_e = 2.5 \cdot 10^{11} \text{ cm}^{-3}$. One can see, that due to the Hall effect the magnetic field penetrates into the plasma and pushes it in directions to the cathode and to the anode. This leads to production of the rarefied plasma gap in the discharge volume. It is important, that the gap formation is obtained for initially uniform plasma density, while in the work [3] the gap formation was demonstrated for a plasma density with some gradient near the cathode. The present results of modeling correlate better with the work [4] and show another mechanism of the gap production, than the erosion one [1].

The experimental results of the experiment [5] are given in the Fig.3. The characteristic discharge time in the fig.3 is $2 \mu\text{sec}$. In the Fig.3a the solid line corresponds to the generator current, while dashed line corresponds to the short-circuit current. The time dependance of the ion flux density to the cathode, measured under a plasma guns is shown in the fig.3b. The same dependance is in the Fig.3b, but the ion flux is measured between the plasma guns and a load. The Fig.3r presents the development of the radial gap formation, measured from the load side of coaxial POS. This picture was obtained by electron image streak camera in H_{α} lines of plasma luminescence. The simulated plasma behaviour in the fig.2 are in agreement with the experimental data in fig.3r.

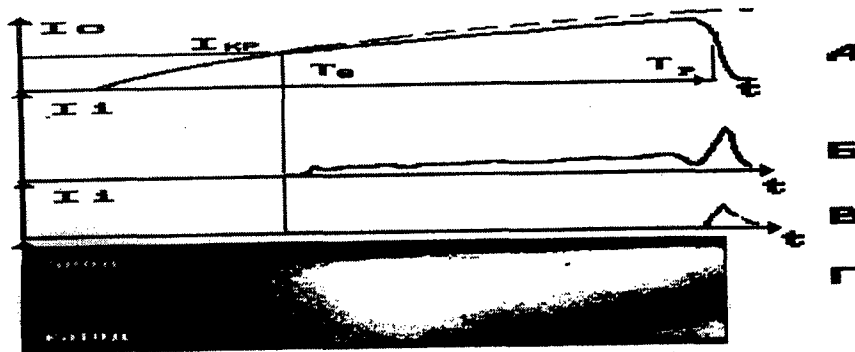


Fig.3: (a) The generator and the short-circuit current, (b) the ion flux to the cathode, (r) the streak camera photo of gap formation.

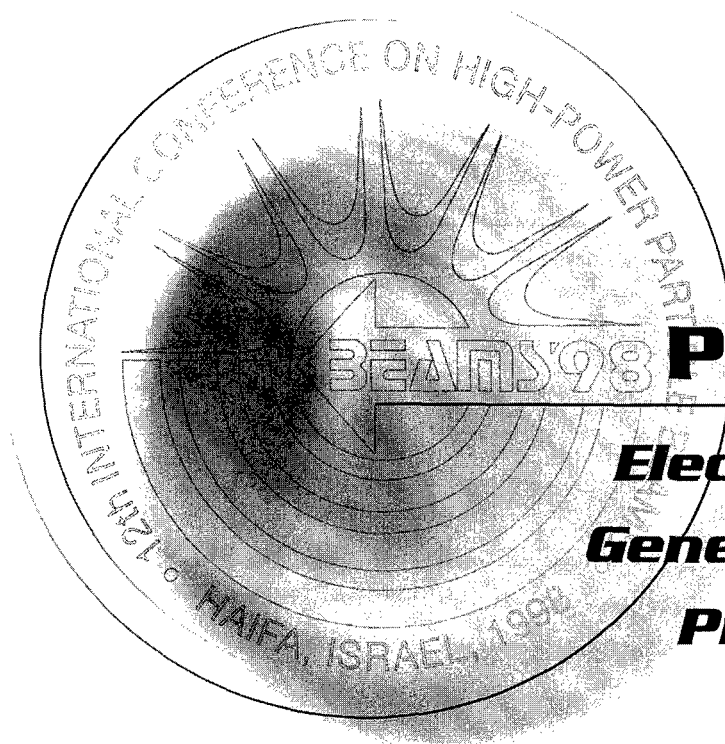
References

- [1] P.F.Ottinger, S.A.Goldstein, and R.A.Meger, J.Appl. Phys. 56(3), 774 (1984)
- [2] B.V.Weber, R.J.Commisso, P.J.Goodrich, J.M.Grossmann, D.D.Hinshelwood, P.F.Ottinger, and S.B.Swanekamp, Phys.Plasmas 2(10), 3893 (1995)
- [3] J.M.Grossmann, S.B.Swanekamp, P.F.Ottinger, R.J.Commisso, D.D.Hinshelwood and B.V.Weber, Phys.Plasmas 2(1), 299 (1995)
- [4] L.I.Rudakov, Sov.J.Reports on Plasma Phys. 19(7), 835 (1993)
- [5] G.I.Dolgachev, L.P.Zakatov, and A.G.Ushakov, Fizika Plasmi, 17(10), 1171 (1991)



BEAMS'98

12th INTERNATIONAL CONFERENCE
ON HIGH-POWER PARTICLE BEAMS



POSTERS

***Electron Beam
Generation and
Propagation***

Vol. I

Proceedings

GENERATION OF AN ANNULAR REB OF MICROSECOND PULSE DURATION AND STABILIZED TRANSVERSE DIMENSIONS IN A DIODE WITH A FIELD-EMISSION CATHODE

O.T.Loza and P.S.Strelkov

*General Physics Institute, Russian Academy of Sciences,
Vavilova str. 38, Moscow, 117942, Russia*

Principles of a diode based on a cold-emission cathode are presented. A combination of the diode geometry and magnetic field lines profile prevents the cathode plasma radial movement and allows to generate high-current annular REBs with invariable cross section during microsecond time intervals.

High-current relativistic electron beams are usually generated by field-emission cathodes. Application of a cold cathode allows to produce REBs with much higher electron current densities ($\sim 10^4$ A/cm²) than with thermoionic cathodes ($< 10^2$ A/cm²). The disadvantage of field emission cathodes is that the emitting edge of plasma expands across guiding magnetic field lines, causing an increase of the electron beam radius. The velocity of the transverse (in respect to magnetic field) plasma extension is about several millimeters per microsecond, that may be crucial for utilization, e.g. in microwave devices of microsecond pulse duration [1].

There were several approaches on the way of solving the problem of REB expansion across magnetic field lines in the course of microsecond pulses. Researchers in many laboratories applied cathodes of different materials and shapes (one of the most popular was a conical cathode), adjusted the geometry of magnetic and electric fields to that of the cathode (e.g. in [2]). The cathodes in use have sometimes very sophisticated form, like the multipoint cathode [3]. The results demonstrated in [2,3] were impressive, nevertheless to clone a diode like that is a difficult task: "a very careful choice of electric and magnetic field shapes is needed": [3]. In this report we propose a comparatively easy and cheap way to create a diode able to generate annular REBs with electron current densities of several kA/cm² and microsecond pulse duration.

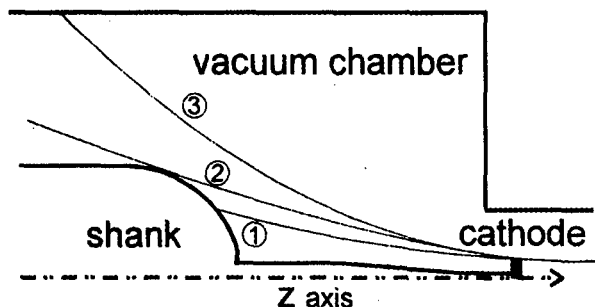


Fig. 1. Scheme of the diode.

Fig. 1 illustrates the design of the diode. Here and further the pictures are azimuthally symmetric about z-axis. The shank supports the cathode inside a long drift tube where the magnetic field is strong ($\sim 1.5 - 2$ T) and homogeneous. Such a construction forms the well-known magnetically-insulated diode that allows to avoid the influence of longitudinal (along the magnetic field)

plasma propagation. In the vacuum chamber where the shank was installed, the profile of the magnetic field lines could be different and determined the value of the return current from the cathode and the presence of electrons emitted from the shank.

With the cathode potential of 500 kV the electric field on the spherical surface of the shank exceeds a little the value of 50 kV/cm, and in the regime #1 (comparatively strong magnetic field near the shank) electrons emitted from its surface can penetrate into the drift tube around the REB from the cathode. The return diode current is determined by the leakage of electron from the shank. In the regime #3 (magnetic field lines from the cathode are dispersed to the chamber walls) the return diode current comprises both electrons from the cathode and from the shank, increasing the total return current in comparison with the regime #1. The regime #2 is intermediate between the previous two ones: the return current from the cathode almost vanishes, but the electrons from the shank do not penetrate into the drift tube.

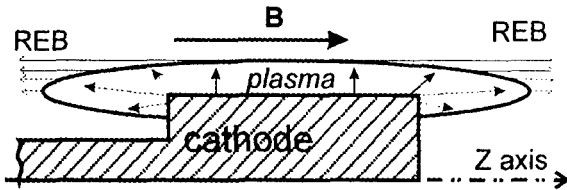


Fig. 2. Scheme of the radial plasma expansion.

suffering collisions with identical “neighbors” from left and right, as well as from below, the only one way to expand remains: upwards to higher radii. In other words, the kinetic pressure pushes plasma perpendicularly to the outer cathode surface overcoming the magnetic field pressure. Plasma expands, and the radius of the REB increases as well. The amount of plasma depends, among other things, on the total current through the cathode, hence, if the return current from the cathode is significant (regime #3 in Fig. 1) the process of plasma creation has to be more intensive.

In order to avoid the described mechanism of plasma (and REB) expansion along the radius we propose to use cathodes with a sharp edge directed *perpendicularly* to the magnetic

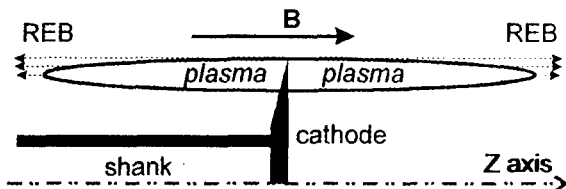


Fig. 3. Principle of operation of a cathode without radial plasma expansion.

The mechanism of electron beam expansion is illustrated in Fig. 2, briefly it is the following. Heating of the cathode surface at the outer radius (horizontal in Fig. 2) due to the electron emission initiates creation of dense plasma. At the right and left cathode edges plasma may move along the magnetic field lines, but for the centrally located particles,

unlike the well-known cylindrical cathodes with the edge along the axis), as it is shown in Fig. 3. The cathode is supposed to be used in a magnetically-insulated diode.

Under the action of electron emission plasma appears on the cathode surface. Plasma covers not only the very edge, but also (and mostly) the adjacent areas, because the current density is finite, and in order to generate a certain total current an appropriate square of

the surface must be engaged in the process. Unlike the scheme described in Fig. 2, the most part of plasma has a possibility to propagate along the magnetic field lines. The velocity of the longitudinal plasma propagation is at least one order more than its speed across the magnetic field ($\sim 10^5$ cm/s), the density (and, therefore, the kinetic pressure) diminishes, and plasma has no “strength” to overcome the magnetic field pressure and has to move along the axis. And the amount of plasma appeared on the outer border of the cathode is as little as sharp the edge is, and after even a minor expansion its density is absolutely insufficient to contribute distinctly to the total REB current.

In our long-term investigations since [4] we tested a lot of cathodes of different shapes and sizes, fabricated from different materials, but sharing the common property of a sharp edge at the external radius. In this report we present one of the simplest and cheapest samples that nevertheless exhibits advantages of the proposed cathode shape. The cathode is made of stainless steel, its shape is shown in Fig. 3, the external radius is 1.4 cm, the angle at the edge

about 5° , the edge thickness 0.2 mm. The cathode was immersed into a drift tube with the radius of 5.5 cm. Cathode voltage was about 500 kV, its waveform (denoted as U) is shown in Fig. 4. The homogeneous magnetic field in the drift tube was 1.8 T.

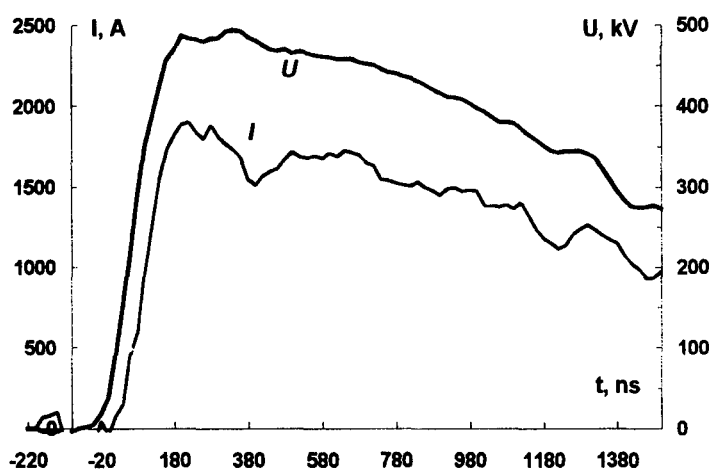


Fig. 4. Waveforms of cathode voltage U and REB current in the monitor I (normalized).

The construction of the monitor of the REB current density was described in [5]. Briefly, a part of an annular beam current passes through a radial slit (1 mm) and terminates on several collectors, distributed over radius with the step of 1 mm. In the present work seven collectors were in use.

The waveform of the total current to the collectors is shown in Fig. 4 (denoted as I), its actual amplitude is multiplied by the ratio of the annular beam circumference length ($2\pi \cdot 14$ mm)

to the monitor input slit thickness (1 mm). The shape of this waveform corresponds to that of voltage, the total beam current amplitude generated in the diode was 2.1 kA.

The result of measurements is shown in Fig. 5. The bar graphs present in arbitrary units

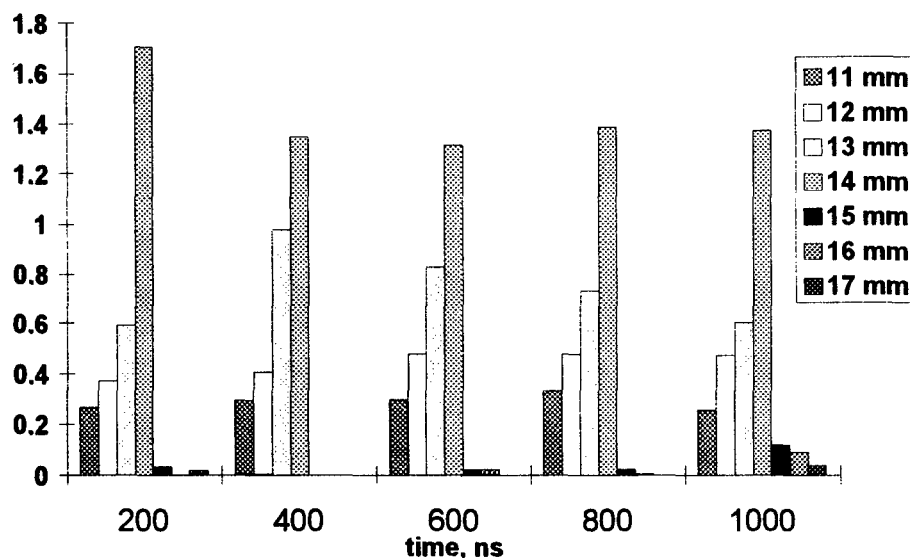


Fig. 5. Radial distributions of REB current density at different moments.

the beam current density distributions 200 ns, 400 ns, etc. after the beginning of the REB propagation. Total current of the beam diminishes in the course of the pulse, as it is shown in Fig. 4, so the distributions are normalized. The profile of the magnetic field in the diode corresponds to the regime #2 in Fig. 1: the return current from the cathode is comparatively (to regime #3) small, and the electrons emitted from the shank should not penetrate into the drift tube.

In the course of all the pulse the beam current density remains distributed in approximately the same way: it has a sharp border at the external radius (that coincides with

14 mm of the cathode radius) and decreases toward the axis. The thickness of the annular beam at half-height is about 2 mm. The electrons emitted from the shank do not penetrate into the drift tube in the course of the pulse. Only by the very end (see the distribution marked as "1000 ns") at the outer radii 15–17 mm there begins to appear some electron flux.

CONCLUSION

A design of a diode based on a field emission cathode is proposed. The diode is able to generate high-current REB in guiding magnetic field during microsecond time intervals preserving the geometry of the beam. The main idea how to prevent the expansion of a microsecond high-current REB is as follows.

An annular REB changes its radius in time if cathode plasma crosses magnetic field lines. Plasma diffuses through magnetic field if its density is sufficiently high. The highest density is in the nearest vicinity of the cathode surface, hence, plasma tends to expand normally to the surface. Let *all* the surface be normal to the magnetic field, and plasma will expand along the field lines. Comparatively high velocity of such a movement, unimpeded by the field, will diminish plasma density and disable plasma to cross magnetic field lines.

In the proposed geometry of the cathode not *absolutely all* the surface is normal to the magnetic field. Nevertheless, the current density from the surface is finite, hence, to generate a certain total current, the emitting surface can not be less than some. Therefore, if *almost all* the surface is normal to the magnetic field, as it is in the proposed design of the cathode with the sharp edge at the external border, the generated REB preserves its shape in the course of microsecond pulse.

REFERENCES

- [1]. Digest of technical papers: Int. Workshop on High Power Microwave Generation and Pulse Shortening, June 10-12, 1997, Edinburg, UK.
- [2]. R.M.Stringfield, R.J.Faehl, M.V.Fazio, et al. "The development of a one microsecond pulse length, repetitively pulsed, high-power modulator and a long-pulse electron beam diode for the production of intense microwaves". Proc. of 9-th Int. Conf. On High-power Particle Beams (BEAMS'92), Washington, DC, USA, v.1, p.688-693.
- [3]. V.I.Engelko, N.G.Beruchev, V.V.Ershov, et al. "High-current accelerator "Sirius" with electron beam current of 2 kA, electron energy of MeV-range and pulse duration of 50 μ s", the same volume, p.436-442.
- [4]. P.S.Strelkov, O.T.Loza, S.N.Voronkov. Patent of Russian Federation #2030135, priority since May 8, 1992.
- [5]. S.N.Voronkov, O.T.Loza, A.A.Ravaev, et al. "Measurement of the radial profile of a relativistic electron beam generated by a magnetically insulated diode". *Sov. J. Plasma Phys.*, vol.14, #10, pp.737-739, 1988.

MEASUREMENT OF STRONG LANGMUIR TURBULENCE FIELDS USING AN ELECTRON BEAM PROBE

Ritoku Ando, Shingo Taniguchi, Keiichi Kamada, Masaru Masuzaki,
and Ivan N. Onishchenko*

Faculty of Science, Kanazawa University, Kanazawa 920-1192, Japan

** Institute of Plasma Electronic and New method of Acceleration, National Scientific Center,
Khar'kov Institute of Physics and Technology, Khar'kov 310108, Ukraine*

ABSTRACT: A study of IREB-driven strong Langmuir turbulence fields in a plasma after the IREB passed through the plasma was carried out by measuring deflection of a weak low-energy electron probe beam injected across the plasma. The preliminary results are discussed here.

1. INTRODUCTION

Studies of the high frequency strong electrostatic fields existing even after an intense relativistic electron beam (IREB) passes through the plasma are being carried out. Theories and numerical simulations [1] have shown that cavitons are formed in a plasma if large amplitude Langmuir waves are excited. Cavitons are defined as spatially localized volumes with density depletion in which large amplitude electrostatic fields are trapped. The state has been referred to as the strong Langmuir turbulence state, and can be driven by injection of an IREB into a plasma. Our previous experiment showed that high frequency strong electric fields with Gaussian distribution existed in the plasma and that the fields lasted for much longer time than 300 nsec after the IREB passed through the plasma [2]. Other data indicate that the cavitons play an important role for IREB scattering [3], for background plasma heating [4], and for generation of broad-band microwaves [5, 6].

A weak low-energy electron beam (probe beam) was injected across the plasma to measure the turbulence electric fields. In absence of a longitudinal static magnetic field the probe beam can pass through the plasma without bending. Rough estimation was carried out on a deflection angle of the probe beam due to turbulence fields, *i.e.* caviton fields. The estimation was based on the data obtained in a previous experiment [2] that the strong field regions occupied a few percent of the plasma volume and that the typical field strength was 50 kV/cm. By assuming the caviton size to be 0.9 mm, which is 20 Debye-lengths, the number density of cavitons was estimated to be 8.8 cm^{-3} . The probability for a probe beam electron to collide with cavitons is about 1.1, and the deflection angle is from -3.3 to 3.3 deg. for probe beam energy of 50 keV.

2. EXPERIMENTAL SETUP

The setup of the experimental apparatus is shown in Fig. 1. An IREB source generated a pulse of 1.5 MeV, 30 kA, and 30 nsec into a matched load. A drift chamber of 16 cm in diameter was served as an interaction space. A plasma was produced with a couple of rail type guns, which were set opposite to each other at $z = 8.5$ cm downstream from the anode foil. The chamber was filled up with the plasma in $\sim 12 \mu\text{s}$ after the discharge of the plasma guns. The target plasma for IREB injection was changed by selecting the delay time, τ , of injection of IREB from the beginning of the discharge of the plasma guns. We selected four τ 's. The plasma densities for each selected τ were $n_p = 1.2 \times 10^{12} \text{ cm}^{-3}$ ($\tau = 20 \mu\text{s}$), $n_p = 4.1 \times 10^{11} \text{ cm}^{-3}$ ($\tau = 40 \mu\text{s}$), $n_p = 1.3 \times 10^{11} \text{ cm}^{-3}$ ($\tau = 60 \mu\text{s}$), and $n_p = 1.0 \times 10^{10} \text{ cm}^{-3}$ ($\tau = 100 \mu\text{s}$) at $z = 30.5$ cm. The IREB was injected into the plasma through a titanium foil of thickness of $20 \mu\text{m}$. The IREB current in the interaction region was about 10 kA. The ratio of beam density to plasma density, n_b/n_p , at the axis of plasma column at the z were 0.003, 0.01, 0.05, and 0.5, respectively.

A short-focus electron gun with a conical grid and a hairpin-type cathode was used for the probe beam source. The acceleration voltage for the probe beam was 30 - 50 kV with the pulse duration of 150 ns and the current of ~ 50 mA. The probe beam was injected across the plasma at $z = 30.5$ cm. The probe beam was detected with a phosphor screen and its luminescence was photographed. The total path length of the probe beam was 56 cm. The diameter of the probe beam was ~ 2.5 cm at the screen position under vacuum. The divergence of the probe beam was observed to be suppressed when a plasma existed in the background. The diameter at screen was depended on the plasma density and varied from 25 mm to ~ 3 mm. The phosphor screen was 6

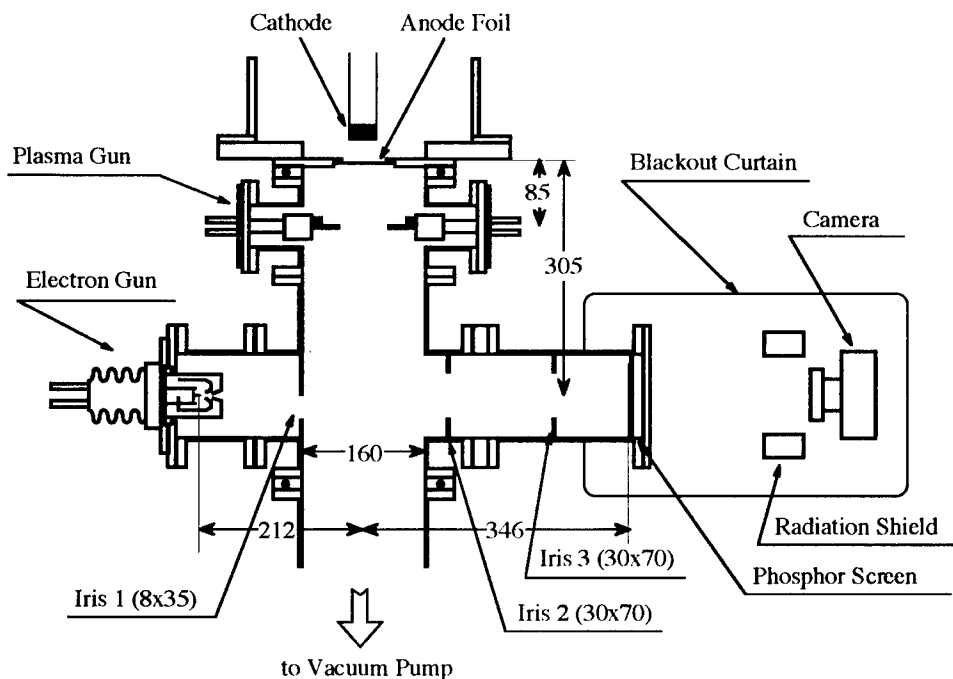


Fig. 1 Experimental apparatus for the IREB-plasma interaction. Probe beam was injected transversely to the axis of the main chamber at 30.5 cm downstream from the anode foil of the IREB diode.

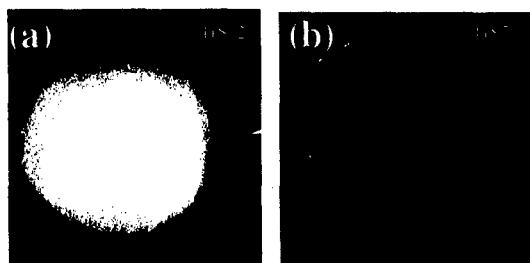


Fig. 2 The examples of the photograph when an IREB injected. (a) under vacuum, (b) under existence of the plasma at $\tau = 100 \mu s$.

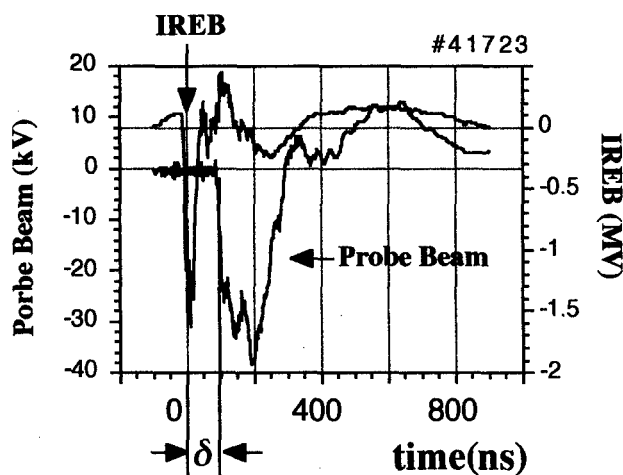


Fig. 3 The cathode voltages of an IREB diode, and an electron gun for the probing. The δ was taken as a parameter. For example, $\delta \sim 100$ ns in this case.

cm in diameter and the surface was coated by carbon spray.

When the IREB was injected the phosphor screen was observed to brighten. Figure 2 (a) and (b) are photographs of screen brightened by IREB injection into vacuum and plasma, respectively. The lightness was suppressed under the existence of plasma. Photographs of probe beam image were taken with the lens opening of $f = 11$.

3. RESULTS AND DISCUSSION

To study the behavior of the electric fields after the IREB passed through the plasma, we took as a parameter, δ , the time interval between the injection of the IREB and that of the beam probe (see Fig. 3). The center of a spot image before IREB injection was taken as the datum point of the beam on the screen. The center of the image was observed to shift when the IREB was injected into the plasma. In most cases the shift dumped a few microseconds after the IREB passed through the plasma. The shift was more than 6 cm for the dense plasma at $\tau = 40 \mu s$. The shift at IREB injection might be due to magnetic fields induced by internal currents in the plasma.

The image of the beam pattern was investigated carefully at $\tau = 100 \mu s$ ($n_p = 1.0 \times 10^{10} \text{ cm}^{-3}$). Examples of the beam pattern are shown in Figs. 4 (a), (b) and (c), where the $\delta = -3.8 \mu s$, 550 ns and 1100 ns, respectively. The datum point is indicated by a cross on each photograph. The unperturbed image that had diameter of about 2 cm was observed on (a). Largest broadening for $\tau = 100 \mu s$ was observed on (b). Shrinking of the images was observed on (c). The beam patterns for $\tau = 20 \mu s$, $\tau = 60 \mu s$ and $\tau = 100 \mu s$ are shown in Figs. 5 (a), (b) and (c), which were obtained at $\delta \sim 300$ ns. The broadening became larger as τ increased. The maximum broadening of the image was observed to take place for the plasma at $\tau = 100 \mu s$.

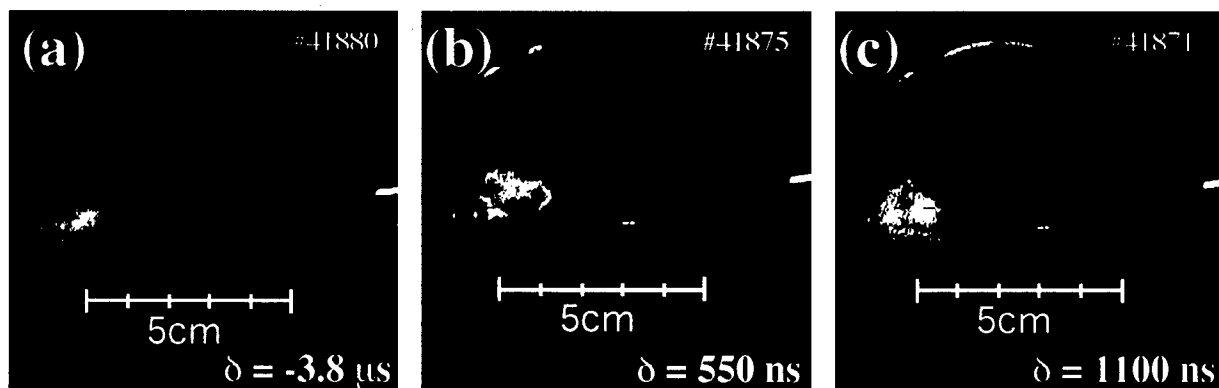


Fig. 4 The images of beam pattern for various δ . $\tau = 100 \mu\text{s}$.

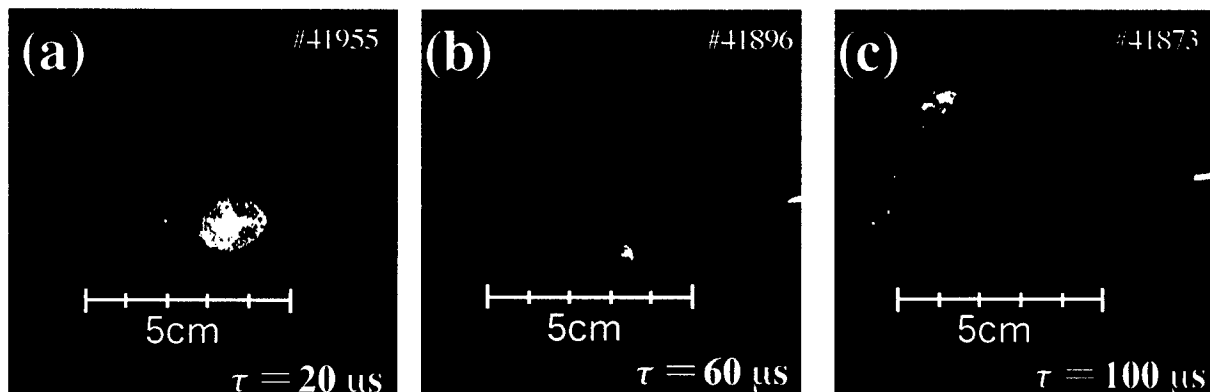


Fig. 5 The images of beam pattern for various τ . $\delta \sim 300 \text{ ns}$.

The broadening was so large for the plasma at $\tau = 100 \mu\text{s}$ that the shift of the center of the image during the probe beam pulse, 150 ns, was not recognizable. From the estimation using the caviton model, broadening of 10 mm on the screen corresponds to the caviton field of about 15 kV/cm. So the centimeter-order broadening observed in the experiment was as expected.

Generally the deflection angle would be in proportion to the electric field strength and length of the field region. Also the coherency of the fields on the path of the probe beam may be important. The knowledge on strength of the background waves in a system [1] must be important, because these waves may also contribute to the deflection of the probe beam. A full detail will be studied in the future experiments.

The authors would like to thank T. Kondoh for his assistance of during the experiments.

REFERENCES

- [1] P. A. Robinson, Rev. Mod. Phys., **69** (1997) pp. 507-573.
- [2] Y. Yoshikawa, M. Masuzaki, R. Ando, J. Phys. Soc. Jpn., **63** (1994) pp. 3303-3310.
- [3] H. Koguchi, M. Masuzaki, R. Ando, K. Kamada, J. Phys. Soc. Jpn., **67** (1998) pp. 1273-1280.
- [4] M. Yoshikawa, M. Masuzaki, R. Ando, K. Kamada, J. Phys. Soc. Jpn., **65** (1996) pp. 2081-2086.
- [5] M. Masuzaki, H. Yoshida, R. Ando, K. Kamada, A. Ikeda, C. Y. Lee, M. Kawada, *Proc. of 11th Intern. Conf. on High-Power Particle Beams* (ISBN 80-902250-3-9, 1996), Vol. 1, pp. 339-342.
- [6] R. Ando, M. Masuzaki, H. Morita, K. Kobayashi, M. Yoshikawa, H. Koguchi, K. Kamada, J. Phys. Soc. Jpn., **65** (1996) pp. 2518-2521.

Pulse Shortening by Scattering from Turbulent Electric Fields in Backward Wave Oscillators

Gregory Benford

*Department of Physics and Astronomy
University of California, Irvine 92697-4575*

Abstract

In microwave-emitting slow wave structures relativistic electrons resonating can scatter from background turbulence. The scattering rate from strong fields can be characterized by a single mean correlation length. Comparison with recent data from a Backward Wave Oscillator, using the measured magnitude of E-fields, shows agreement with the magnitude of outward scattering. The implied correlation lengths then explain why gas ionization in the same oscillator does not proceed exponentially, as earlier work showed was expected but not observed. Plasma electrons scattered over the correlation length cannot gain the necessary energy to ionize many gas atoms. These results suggest that inadvertently produced plasmas may have a quick, decisive effect on beam geometry, ending microwave emission prematurely. A full version of this work is in Ref. (17).

1. Introduction

There appear to be at least four plausible explanations of pulse shortening in high power microwave devices¹⁻⁷. Three involve production of plasma which destroys the effective corrugated geometry, either by

- (1) beam bombardment of walls, or
- (2) extraction of plasma by strong electric fields, or
- (3) in plasma-filled devices, further generation of plasma from ambient gas by strong oscillating E-fields.

A fourth possibility is that the strong microwave fields disrupt the beam particle orbits so that it cannot emit through the slow-wave coupling. This could arise from an instability, or simply by perturbing the beam electron orbits so much that they oscillate, reverse, etc.

Beam geometry disruption is the most direct way to cut off emission. Cross-B diffusion can do this from a variety of electric modes excited. Magnetic filamentation can destroy cylindrical symmetry, but requires a background plasma for instability. These seem the most probable instabilities which can cause emission cutoff.

Zhai et al.⁸ reported emerging wall plasma in BWOs, measured by spectral lines of H and C (earliest, probably from anode-cathode and wall) and Cu (later, from the wall). All neutral atom radiation appeared about 100 ns after microwave cessation, with copper from the wall 200 ns. afterward. Emission came first at the narrow portion. If copper then moved along the magnetic field to the wide portion, the implied $T_i \sim \text{keV}$.

Later work on the same device yielded the first measurements of the oscillating electric fields during the beam pulse.⁹ They used Stark effect lines in a plasma-filled BWO. Strengths as high as 34 kV/cm accompanied 75 MW microwaves throughout the 60 ns.

power pulse, with lower frequency fields of 10 kV/cm persisting until beam shutoff, presumably from Gould-Trivelpiece modes. As well, measurements in the same BWO structure of beam expansion showed a profound broadening in the beam profile.^{8,10} Plainly many such effects are interrelated.

Damage profiles in the vacuum BWO showed no broadening of the 2 mm annulus. Addition of 100 Torr. helium-produced plasma of density 10^{13} cm^{-3} within $\sim 200 \text{ ns}$. Damage profiles showed outward radial expansion by 2 mm and little inward motion (within the error of 0.3 mm). Note that 2 mm takes a beam electron beyond the innermost wall of the ripple, suggesting scattering after the beam has left the BWO region.

Refs. [8-11] found three significant observed facts:

- (a) GHz electric fields permeate the BWO region of strength $\lesssim 35 \text{ kV/cm}$;
- (b) despite these, plasma ionization increases only linearly, not exponentially as suggested by conventional theory;
- (c) damage plates show outward beam expansion only when plasma is present.

This paper aims to reconcile these observations by calculating the rate of beam expansion in high fields.

2. Comparison with Experiment

Measuring radial excursion of relativistic beams is notoriously difficult because a witness plate adds damage of all the beam pulse, whereas we seek knowledge of the microwave-emitting pulse time. However, while microwaves cease after t_p , Langmuir turbulence persists for $\sim \mu\text{s}$, so beam scattering over this time will dominate damage patterns. Assuming this, we now compare with observed beam broadening. Garate & Zhai⁽¹⁰⁾ found outward scattering with little inward beam broadening, arising perhaps from an unknown gradient. Observed broadening out to the inner BWO structure implies that beam-wall collisions are a major source of added plasma after scattering begins.

Quasilinear scattering scaled to the relativistic Backward Wave Oscillator yields

$$\left(\frac{\Delta x}{a}\right)^2 = \frac{(E/35 \text{ kV/cm})^2}{(B/15 \text{ kG})^2} \left(\frac{L}{16.5 \text{ cm}}\right) \langle \tan^2 \psi \rangle \left(\frac{f\ell}{0.6 \text{ cm}}\right) a^{-2} \quad (1)$$

Here the wave-electron mean correlation length ℓ is multiplied by the volume fraction of the turbulent fields, f . For an annulus the characteristic length a is the annular width.

Garate & Zhai⁽¹⁰⁾ measured beam expansion in an operating BWO, finding that an 18 mm – diameter annulus of 2 mm width expanded mostly outward by 2 mm when 100 mT of helium was added to introduce a plasma. The measured plasma density was $\sim 5 \times 10^{12} \text{ cm}^{-3}$ at microwave emission onset and rose at $\Delta n/\Delta t \sim 5 \times 10^{10} (\text{cm}^3 - \text{ns})^{-1}$ thereafter. The observed expansion $(\Delta x/a) \approx 1$ requires, for our typical scaling values of E , B and L

$$f\ell \frac{(E/35 \text{ kV/cm})^2}{(B/15 \text{ kG})^2} = \frac{0.4 \text{ cm}}{\langle \tan^2 \psi \rangle} \quad (2)$$

Allowing for the simultaneous presence of both Trivelpiece- Gould (TG) modes and Langmuir (L) wave turbulence, we can write, with appropriate correlation lengths,

$$\langle f_{TG}\ell_{TG} \langle E_{TG}^2 \rangle + f_L\ell_L \langle E_L^2 \rangle \rangle = \frac{0.4 \text{ cm}}{\langle \tan^2 \psi \rangle} \quad (3)$$

where the field energy densities are normalized to $(35 \text{ kV/cm})^2$. Previous measurements on this same BWO^(9,11,12,13) imply $\langle E \rangle \approx 100 \text{ kV/cm}$ at maximum emitted power. Earlier observations⁽¹⁴⁾ found $f_L \approx 0.1$, though in a helium plasma without the BWO oscillator. These results roughly imply that $\langle fE^2 \rangle \sim 1$, so we require $\langle \ell \rangle \approx 0.4 \text{ cm} / \langle \tan^2 \psi \rangle$, and cathode measurements show that $\langle \tan^2 \psi \rangle \sim 1$.

For comparison, the beam electron gyration radius is $r_e = 0.2 \text{ cm} (B/15 \text{ kG})^{-1} \langle \sin \psi \rangle$ and the typical scale of strong Langmuir turbulence,⁽¹⁴⁾ $D \equiv 100 \lambda_D = 7.4 \cdot 10^{-2} \text{ cm} \sqrt{\frac{T_{ev}}{n_{12}}}$, where T_{ev} is in electron volts and n_{12} plasma density in units of 10^{12} cm^{-3} . Thus to explain the observed scattering we need wave-electron correlations on the scale of r_e , though large Langmuir structures $\sim 10^3 \lambda_D$ could suffice as well.

The implied scattering time $t_c \sim \ell_c/c \sim 7 \times 10^{-13} \text{ s}$ has further implications for plasma production by the E -fields, as observed by Zhai et al.⁽¹⁵⁾ Straightforward ionization calculations imply rapid exponential growth, but only moderate linear growth appeared, though at a rate 5 times the direct beam rate.

E -field turbulence implied by beam scattering explains this. Oscillating fields can drive plasma electrons to very high velocities in the $\sim 35 \frac{\text{kV}}{\text{cm}}$ fields, but they are scattered by turbulence in a time $t^* \sim \ell_c/v_{te}$, with v_{te} the electron thermal speed. The customary ionization rate for helium, $\nu_v \approx (\nu/\text{GHz}) 10^9 \text{ s}^{-1}$ must be modified by a factor $< (\nu_i t^*)^{-1} \sim 0.2$, so the true ionization rate in the presence of turbulence is less by ~ 0.2 .

This explains why Zhai et al. found no exponential behavior; plasma electrons scattered by turbulent fields cannot gain the energy necessary to ionize many atoms. This leads to an ionization time comparable to that observed. A more detailed calculation and experiment is needed here.

3. Conclusions

Our principal result, Eq. (2), is compatible with the recent results communicated by Garate & Zhai¹⁰. Langmuir turbulence measured extensively in Refs.^(8,9,14) verify that strong scattering from intense E -field regions can dominate the turbulent characteristics of strongly driven stream instabilities. This links previous measurements of $E \approx 35 \text{ kV/cm}$ with the recently reported ionization in an operating BWO¹⁵. Strong fields operating over reasonable correlation lengths $\ell \sim 5 \text{ mm}$, can account both for scattering of relativistic electrons and for the interruption of the usual ionization by such strong fields in the background helium plasma and gas.

Such a unified view then has implications for all strong microwave generators. These studies^{12,15} deliberately produced a controlled ambient plasma, but many generators probably suffer from plasma generation inadvertently. Beam electrons may strike walls and strong E -fields can draw out from walls dense, rapidly moving plasmas. These in turn can develop turbulence in fractions of a nsec., since streaming instabilities are very rapid.

Scattering from nuggets of strong E -fields can then dominate gross beam dynamics – particularly cross-B migration, which can disrupt the entire microwave emitting geometry. Further work with this in mind may clarify the ubiquitous puzzle of pulse shortening in microsecond microwave devices¹.

The author thanks Eusevio Garate and X. Zhai for providing data, and James Benford for fruitful discussions.

References

- [1.] G.A. Mesyats, "The Problem of Pulse Shorting in Relativistic Microwave Generators," in ISPP-10 Piero Caldirola, *High Power Microwave Generation and Applications*, E. Sindoni and C. Wharton (eds.) SIF, Bologna 1992, p. 345.
- [2.] J.M. Butler, Ph.D., Dissertation, p. 61, Cornell University, 1991.
- [3.] Y. Carmel, J. Ivers, R.E. Kriel, and J. Nation, Phys. Rev. Lett. 33, 1278 (1974).
- [4.] M. Friedman, Appl. Phys. Lett. 26, 376 (1975).
- [5.] V.I. Belousov, V.V. Bunkin, A.V. Gaponov-Grekhov, et al, Sov. Tech. Phys. Lett. 4, 584 (1978).
- [6.] V.S. Ivanov, N.F. Kovalev, S.I. Kremontsov, and M.D. Raizer, Sov. Tech. Phys. Lett. 4, 329 (1978).
- [7.] Yu. V. Tkach, Ya. B. Fainberg. N.P. Gadetskii, et al., Ukr. Fiz Zh. 23, 1902 (1978).
- [8.] X. Zhai, E. Garate, R. Prohaska and G. Benford, Appl. Phys. Lett. 60 (1992) 19.
- [9.] X. Zhai, E. Garate, R. Prohaska, A. Fisher, and G. Benford, Phys. Letts. A 186 (1994) 330.
- [10.] E. Garate & X. Zhai, private communication.
- [11.] Y. Carmel, K. Minami, R.A. Kehs, W.W. Destler, V.L. Granatstein, D. Abe, and W.L. Lou, Phys. Rev. Lett. 62, (20) 2389 (1989).
- [12.] X. Zhai, E. Garate, R. Prohaska, and G. Benford, Phys. Rev. A 45, 12 (1992).
- [13.] W.R. Lou, Y. Carmel, W.W. Destler, and V.L. Granatstein, Phys. Rev. Lett. 67, 18, 2481 (1991).
- [14.] D. Levron, G. Benford, A.B. Baranga and J. Means, Phys. Fluids 31, (1988) 2026.
- [15.] X. Zhai, E. Garate, R. Prohaska, and G. Benford, Phys. Lett. A 223, 6, 458 (1996).
- [16.] S. Brown, "Introduction to Electric Breakdown in Gases," J. Wiley, New York, 1966, p. 50.
- [17.] G. Benford, Phys. Lett. A, 235 (1997) 159-163.

IGNITION OF A BEAM-PLASMA DISCHARGE BY ELECTRONS EMITTED FROM A FERROELECTRIC

V.A.Borissenok, D.R.Goncharova, A.E.Dubinov, A.N.Klevtsov*,

V.A.Kruchinin, S.A.Sadovoy, V.D.Selemir

*Russian Federal Nuclear Center – All Russian Scientific and Research Institute of
Experimental Physics (607190, Sarov, Russia)*

**Research Institute of Physics at Rostov State University
(344104, Rostov-on-Don, Russia)*

It is well known that under the influence of a short voltage pulse, which changes the polarization of the pre-poled ferroelectric sample the last one emits surplus surface electric charge in a form of impulse electron beam [1,2]. In this case beam current may achieve a high value. For example in paper [3] it is reported that the value of electron emission current density of up to 500 A/cm^2 was achieved by this way. Moreover, in paper [4] the repetition rate of electron current pulses of up to 2 MHz was reached.

Such serious results predetermine a wide perspective of utilization of the phenomenon of electron emission from the surface of ferroelectrics in vacuum electronics and, in particular, in acceleration and SHF-equipment [5]. But, on our opinion, the possible applications of this phenomenon are not limited by vacuum electronics. We can mention some of them: ignition of gas and gas-fuel mixtures in internal-combustion engines and fire-boxes, ignition of a beam-plasma discharge in plasma-chemical reactors and gaseous lasers, commutation operation of power gas-filled switch [6,7].

With the help of published data, that refer to the electron emission from the surface of ferroelectrics, we can assume that interesting physical special features are inherent to the aforementioned gas and plasma processes, which distinguish them from similar processes involving electrons, injected by usual electron guns.

This circumstances defined the purpose of this paper: receiving and investigation of ignition of gas discharge by injection of electrons emitted from a ferroelectric into a gas-discharge gap.

1-mm thick, 8-mm-diam of working surface pre-poled ferroelectric samples manufactured from PLZT ceramics (8% La) were used. A ferroelectric disk is coated with a thin ($\sim 5\text{-}10 \text{ }\mu\text{m}$) uniform silver layer on the back and a gridded silver layer on the back and a gridded silver layer with a period $400 \text{ }\mu\text{m}$ and thickness $\sim 1 \text{ }\mu\text{m}$ on its front surface. A picture of the sample from the gridded surface is demonstrated in Fig.1a.

Hysteresis loop of one of the polarized samples with polarization value $-37 \text{ }\mu\text{C/cm}^2$, which was obtained with the help of a special hysteresisograph is shown on Fig.1b with the mark of amplitude of the actuating pulse U_0 .

It consists of a gas-discharge camera in the form of a glass tube with internal diameter of 35 mm and length of 360 mm, at the end of which there are metal electrodes (the distance between them is 220 mm); from the power source in order to apply constant voltage to the electrodes of the camera (plus to the not grounded electrode); from the vacuum system, including forvacuum pump, the system of tubes and block of manometers. Inside of the grounded electrode of camera there was a ferroelectric sample, with the gridded surface turned into the gas-discharge camera. Actuating pulse with positive polarity and amplitude $\geq 500 \text{ V}$ was applied to the solid electrode of the sample with the help of special pulse generator. The form of this pulse is shown in Fig.3a.

Investigations were held in the air under the pressure $\sim 10^{-2} \dots 10^{-1} \text{ Torr}$. Under these conditions the breakdown voltage in the camera under stationary power supply is equal to

$\sim 1,0 \dots 2,5$ kV, after the breakdown a stationary subnormal discharge with the current ~ 50 mA is selfmaintained in the camera.

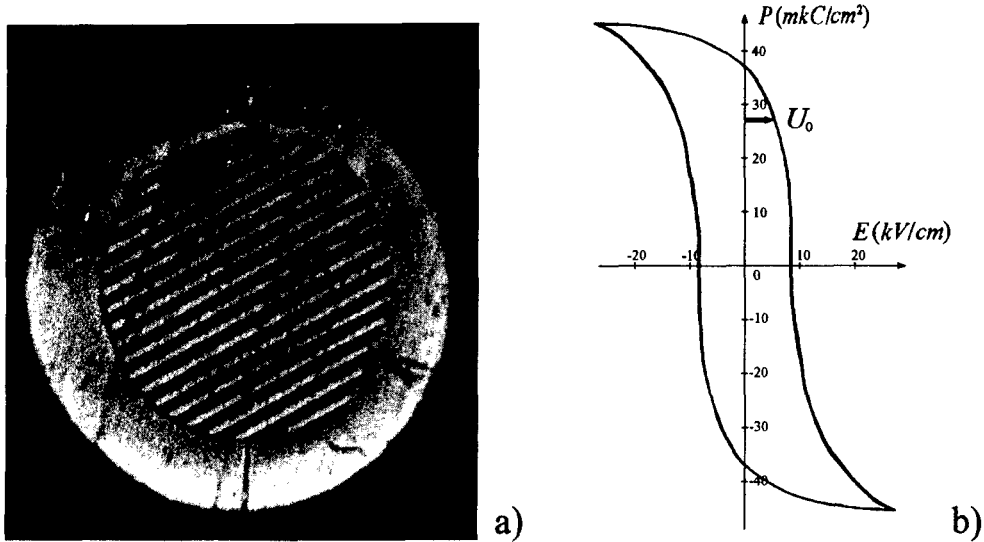


Fig. 1. Information on ferroelectric sample: a) view from the grid side; b) hysteresis of polarization (U_0 - shown by arrows).

In experiments with ferroelectric ceramics a constant voltage with the value less than one of the breakdown voltage was applied to the electrodes of the camera. It was detected, that electrons, emitted by the sample under the influence of actuating pulse, are able to light the gas discharge when the voltage at the electrodes is equal to 500 V. This discharge has many similar features to those of not self-supporting impulse beam-plasma discharge. The picture of discharge lighting, initiated by electrons emitted from ferroelectric, is shown in Fig.2. We can see that near the grounded electrode the diameter of the lighting channel approximately equal to the sample diameter.



Fig. 2. Picture of the discharge.

The typical oscillograms of pulses of discharge current, voltage at the camera electrodes of the discharge are shown in Fig.3b, c respectively. As it is evident these signals have some characteristic features which have been displayed in this type of a beam-plasma discharge. For example, on current oscillogram we can single out two stages. One of them probably corresponds to a high-stable maintenance of the emission current from the surface of a ferroelectric, that is detected also under vacuum conditions [8], the second stage, which is characterized by the sharp increasing and then decreasing of the emission current corresponds to the development of avalanche in the gas. The stage of maintenance of the constant current is accompanied by increasing of the voltage at camera electrodes, moreover the duration of this stage and the current value may be regulated by the gas pressure and by the value of capacitance of connecting condenser. The stage of avalanche development is characterized by drop of the voltage and intensive optical lighting of gas-discharge plasma.

In some operation regimes the current during the first stage was equal to 150 – 180 A, and amplitude of discharge current during the avalanche stage was up to 1kA. Then, if calculated for the free surface of the ferroelectric sample taking into consideration the geometrical transparency - 50%, current density in some experiments exceeds the value of 700 A/cm². This value of a current density perceptibly exceeds the known published values which were received in vacuum. This fact can be explained by neutralization of the spatial charge of the beam in plasma.

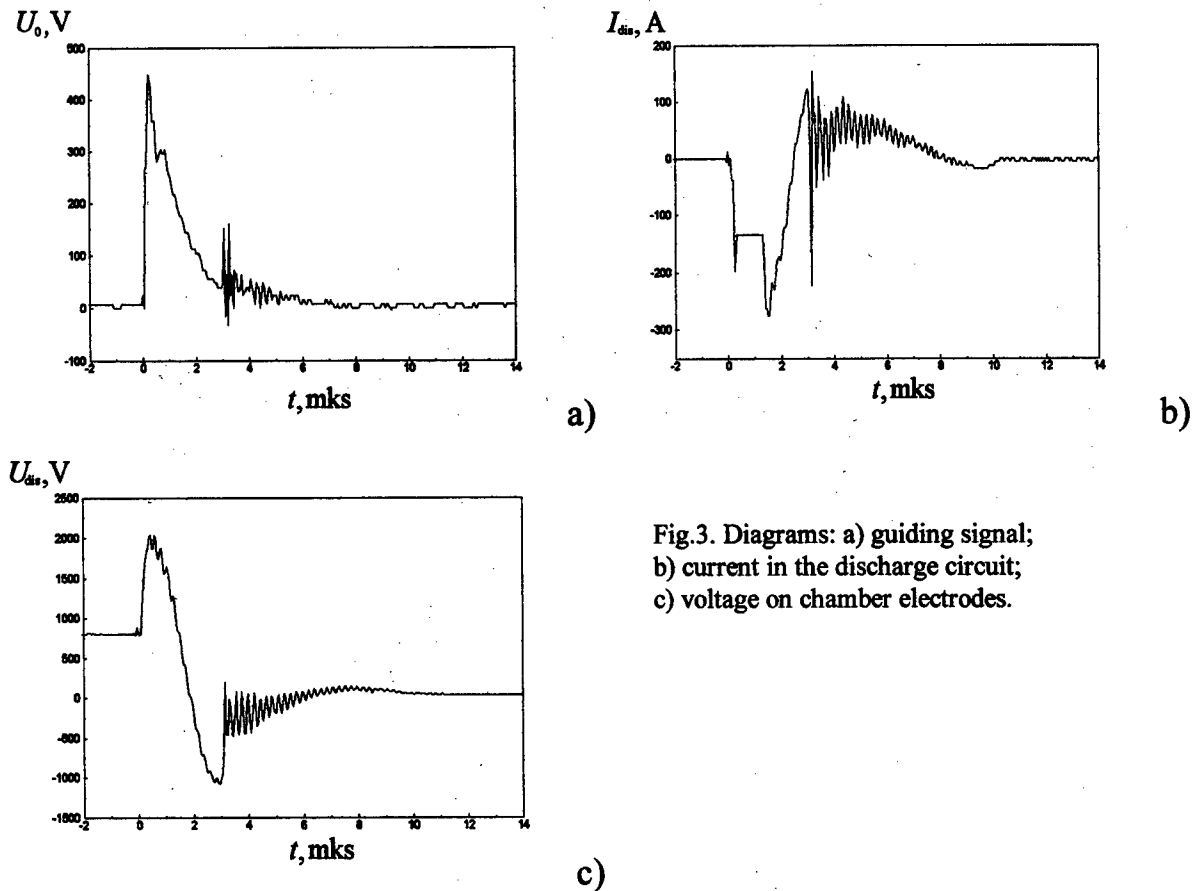


Fig.3. Diagrams: a) guiding signal;
b) current in the discharge circuit;
c) voltage on chamber electrodes.

It is worth noting, that charge density which is carried by this current during the first stage ($\sim 1 \mu\text{s}$) exceeds the remnant polarization of the sample more than an order of magnitude as in [8]. This fact requires additional investigations.

So, the results achieved testify to great perspectives of ferroelectric electron sources for implementation in different devices of gas and plasma electronics. It is necessary to pay special attention to the stage of constant current. It is possible to create new gas-discharge commutators with high-stable current characteristics.

References

1. Rosenman G.I., Ohapkin V.A., Chepelev Yu.L., Shur V.Ya. Pisma v ZhETF, 1984, V.39, № 9, P.397 (*in Russian*).
2. Asano J.I., Okuyama M., Hamakawa Y. Jap. J. Appl. Phys, 1993, V.32, P.396.
3. Aipananov A.Sh., Ivanchik I.I., Lebedev A.N. DAN USSR, 1990, V.311, № 3, P.594 (*in Russian*).
4. Gundel H., Handerek J., Riege H. J. Appl. Phys. 1991, V.69, № 2, P. 975.
5. Jiang B., Kirkman G., Reinhardt N. Appl. Phys. Lett. 1995, V.66, № 10, P.1196.
6. Gundel H., Riege H., Handerek J., Zioutas K. Appl. Phys. Lett, 1989, V.54, № 21, P.2071.
7. Akzamova D.R., Borissenok V.A., Dubinov A.E., et.al. Patent RF 2079700, 14.09.94. (*in Russian*).
8. Kugel V.D., Rosenman G., Shur D., Krasik Ya.E. J. Appl. Phys, 1995, V.78, № 4, P.2248.

TRANSPORTATION OF OVER-LIMITING BEAM IN THE WAVEGUIDE WITH PLASMA DAMS

A.Babkin, V.Chelpanov, A.Dubinov, S.Galkin, D.Gladilin, A.Khizhnyakov, V.Kornilov, V.Selemer, A.Sudovtsov, V.Zhdanov

Russian Federal Nuclear Center - All-Russia Scientific Research Institute of experimental Physics, Sarov (Arzamas-16), Mira 37

For solution of a number of science and technique tasks it is necessary to provide energy transmission to large distances without significant losses in the form of high-current electron beams. Vacuum-processed transporting channels with magnetic beam accompaniment [1] are developed for these purposes.

However, the channel, described in [1], has principal limitation on the value of transporting current beyond the existing limit [2]. Virtual cathode forms at the exceeding of this limit and the channel becomes "locked".

Original decision, directed on the increasing of the transported current value over the existing limitation, was suggested in [3]. The essence of this decision is the fragmentation of this channel into sections and their separation from each other with conducting films, foils or meshes, thickness of which is much less than the length of free path.

It is necessary to mention that such channel may not contain the system of magnetic beam accompaniment. Since the conducting film (foil or mesh) shunts radial defocusing electrical beam field close to it, only forces of magnetic focusing effect on electrons near the film thanks to the own magnetic field of the beam, and the necessity of external focusing disappears.

The drawback of the transporting channel of [3] type is high angle electron dispersion with film (foil, mesh) atoms. This leads to the losses of the electron beam and decreases the transportation efficiency coefficient. Besides, thin films are ephemeral and are damaged after small quantity of electron current pulses.

Theoretical and experimental investigations, performed during the development of microwave generators with virtual cathode, where anode in the form of thin plasma sheet is used [4,5], suggested an idea to replace thin films and foils in the transporting channels by thin plasma dams. But this decision requires verification. There is the possibility of beam and plasma-beam instabilities in the channel, which could ruin the transportation process.

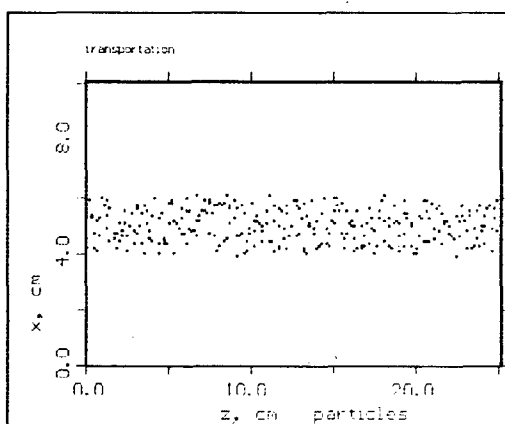


Fig. 1a
Channel geometry with beam

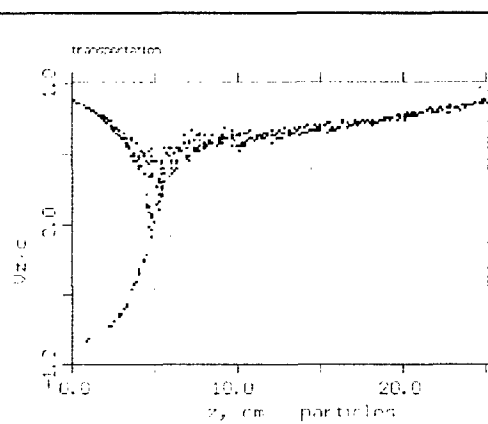


Fig. 1b
Phase portrait

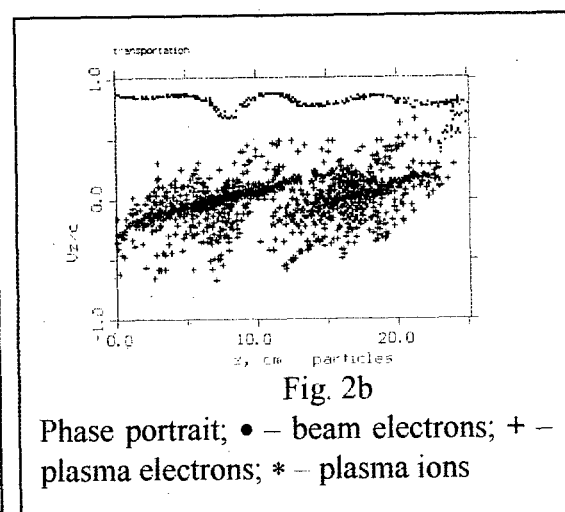
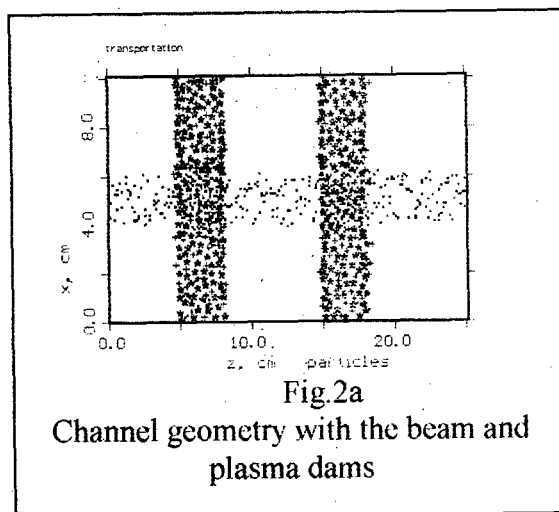
For this purpose the 2.5-dimensional version of the known software pack "KARAT" [6], based on fully compatible PIC-code, were used for computer simulation of the channel with plasma dams.

Transporting channel is a flat waveguide with the length of 30 cm and width of 10 cm. Strong longitudinal magnetic field of 50 kG is applied to it. Electron beam with linear current density of 400 A/cm and energy electrons of 0.5 MeV was injected into the waveguide.

Two situations were simulated: free waveguide and the waveguide, loaded with two plasma dams of 3 cm each and plasma concentration of $5 \cdot 10^{11} \text{ cm}^{-3}$. Simulation results are shown in the Fig. 1 and 2 respectively.

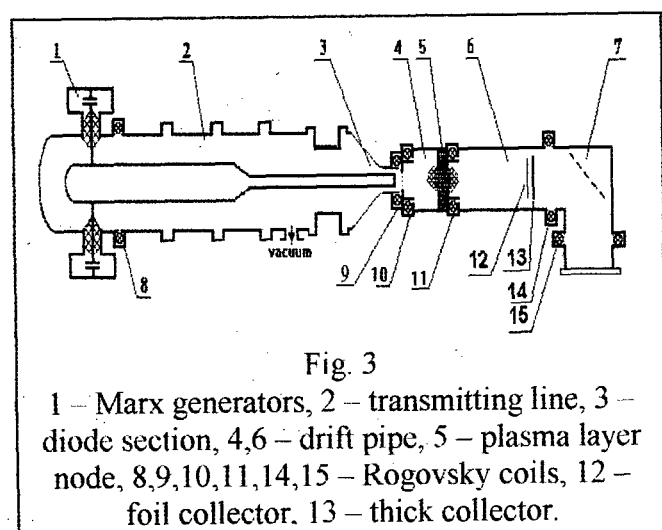
It was obtained, that virtual cathode is formed in the channel when the plasma dams are absent (Fig. 1b). This certifies about that fact, that the given value of the electrical current for the given waveguide is over-limiting.

If the plasma dams are existing in the channel, electron beam passes through the waveguide and doesn't form the virtual cathode (Fig. 2b).



Thus it was set, that the transportation channel, loaded with plasma dams, can pass electron beams with over-limiting currents without significant losses. Experiments were carried out on "KOVCHeg" device [7] in two editions: 1) in the regime of mesh anode with plasma layer node in the drift pipe, located on the distance of 50 cm from the mesh anode (Fig. 3); 2) in the regime of plasma anode. In this case plasma anode served as a mesh, and the additional plasma layer in the drift pipe was not formed.

According to the model calculations, to transport the electron beam without significant distortions of its characteristics, the distance between plasma layers should be of double diode gap. In this experimental series we checked the plasma influence on the electron beam passage at great (50 cm) distance between mesh anode and plasma layer node. We tried to vary the size of the vacuum gap between mesh anode and plasma by changing the plasma layer thickness at the moment of the diode



current switching on. As a result, we discovered plasma acceleration towards the virtual cathode, since plasma influenced on the diode operation. Fig. 4 shows the set of diagrams of the diode current in the regime of plasma anode. Figures above the diagrams correspond to the delay of plasma voltage switching on relatively to plasma injector battery t_0 switching on in microseconds.

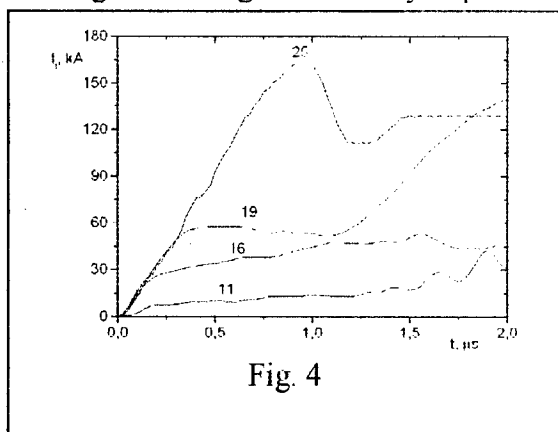


Fig. 4

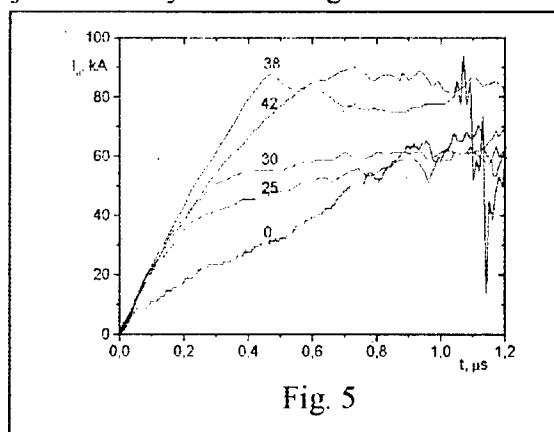


Fig. 5

We can see that the increasing of the delay t_0 , equivalent to the decreasing of the diode gap, leads to the decreasing of the initial diode impedance. Delay of 25 μs corresponds to the moment, close to the 50 mm gap shorting. Fig. 5 shows the corresponding set in the case of 50 cm distance between the mesh anode and plasma layer node (0 – without plasma). Plasma influence on the diode operation is apparent at 25 μs delay.

The series of experiments were carried out in the plasma anode regime in order to separate electron and ion currents in two-collector variants. In this case the assembly of foil collector (Al of 80...100 μm thickness) and thick metal collector was located at the end of 1 m drift pipe. It was supposed, that the first collector, passing electrons, would fully absorb ion current, which will be registered with a shunt. The second collector should register electron current. Since the process of the collective ions acceleration is connected with electron beam energy loss, the electrons absorption with the first collector happened to be significant one, and the shunt signal was almost always negative. Foil collector was destroyed after the first shot at the delay t_0 of about 20 μs and more. Destruction character – melting and breakage. According to our estimations, more than 10% of energy, released in the diode in the form of electron-ion flux, is transported on the distance of 1 m.

At that, both electrons and ions are equally responsible for melting and breakage in the result of pulse transmission. Thus, in order to measure corpuscular fluxes in the conditions of energy transportation, the development of additional diagnostics is necessary.

It is necessary to pay attention that the electron beam captures positive plasma ions to the collective motion, what could be useful for electron beams acceleration. In this case, and also at the necessity of obtaining of pure electron beam on the transportation channel output, it is possible to install the magnetic particle separator.

Authors are thankful to V.P.Tarakanov for his consultation of "KARAT" software application.

The work is performed in the frameworks of RFFI Project № 96-02-17047a.

1. Chikunov V.V., Knyasev B.A., Melnikov P.I. // XIIIth International Symposium on Discharges and Electrical Insulation in Vacuum. Paris, 1988, 27-30 June, P. 436.
2. L.S.Bogdankevich, A.A.Rukhadze // Uspehi Fizicheskikh Nauk. 1971. V.103. № 4. P.609 (in Russian).
3. Adler R.J., Sabol B., Kiuttu G.F. // IEEE Transactions on Nuclear Science. 1983. V. NS-30. № 4. P. 3198.
4. A.L.Babkin, A.E.Dubinov, V.G.Kornilov, et al. RF Patent № 2046440 with priority from 8.06.93, MKI: H 01 J 25/00 // Inv. Bull. 1995. № 29 (in Russian).

5. A.L.Babkin, A.E.Dubinov, V.S.Zhdanov, et al. Fizika Plazmy. 1997. V.23. №4 (*in Russian*).
6. Tarakanov V.P. // User's manual for code Karat, Berkley Research Associate, Inc., Springfield, WA, 1992.
7. Babkin A.L., Chelpanov V.I., Dubinov A.E. et al.// Powerful electron accelerator "Covcheg": status, parameters and physical experiments. 11th IEEE International Pulsed Power Conference Hyatt Regency Baltimore on the Inner Harbour Baltimore, Maryland USA June 29- July 2, 1997. Final Program and Abstracts. P1-24

GENERATION OF HIGH-CURRENT ELECTRON BEAMS BY THE USE OF PLASMA CATHODES

Ya. E. Krasik, A. Dunaevsky, and J. Felsteiner
Physics Department, Technion, 32000 Haifa, Israel

In this report we present experimental data concerning the use of various plasma sources to generate high-power, high-current electron beams in a repetitive mode instead of explosive emission plasma. The concept of this research is in the plasma creation prior to the application of the acceleration voltage to the anode-cathode gap, and in the achievement of the condition when the space-charge limiting electron current density is equal to the electron plasma saturation current density. It has been shown that it is possible to generate electron beams without creation of explosive plasma and without the time delay with respect to the beginning of the acceleration voltage. This can be achieved by the proper adjustment of the plasma parameters to the diode geometry and to the amplitude of the acceleration voltage. Experimental results of generation of electron beams with current density of 100 A/cm^2 , and electron energy of 40 kV continuously with repetition rate of 2 Hz will be presented.

The disadvantages of explosive emission plasma, namely the time delay of plasma creation when $E < 100 \text{ kV/cm}$ and the plasma expansion inside the anode-cathode gap that does not allow to keep the constant impedance of the electron diode, stimulate the research devoted to new sources of electrons.

Coaxial erosion plasma gun (PG), plasma source based on TiBa ceramic sample and coaxial gaseous plasma gun are being used as a source of electrons in planar and coaxial geometry of electron diodes. Plasma parameters (plasma density, electron temperature and plasma expansion velocity) were measured by biased collimated Faraday cups (CFC) and single and double floating probes. High voltage pulse was delivered by PFN ($\leq 40 \text{ kV}$, 200 ns , $\leq 5 \text{ Hz}$).

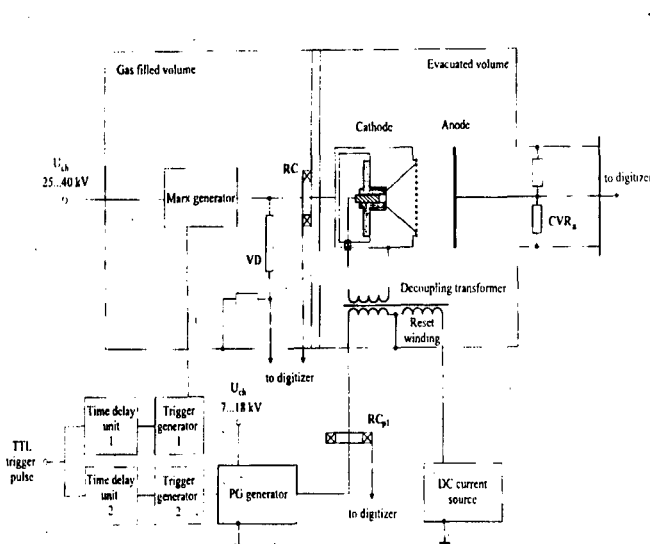


Fig. 1 Experimental setup for erosion PG.

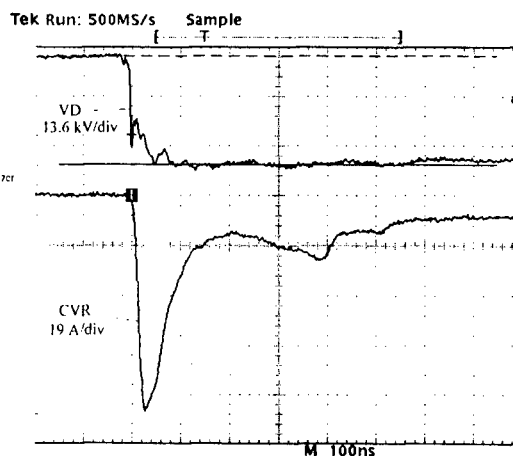


Fig. 2 Typical waveforms of the PFN voltage and the anode current.

In Figs. 1 and 2 we present experimental setup and typical waveforms of the PFN voltage and the anode current for the case of the erosion PG. To produce the plasma a pulsed generator (17Ω , 10 kV , 50 ns , 5 Hz) was used. We have observed two plasma bunches: the first one has

low density ($n_e \approx 10^{11} \text{cm}^{-3}$) and higher electron plasma temperature and plasma expansion velocity ($T_e = 8 \pm 1 \text{eV}$, $V_{pl} = 1.2 \cdot 10^7 \text{cm/s}$). The second plasma bunch has higher density ($n_e = 8 \pm 2 \cdot 10^{11} \text{cm}^{-3}$) and smaller electron plasma temperature and plasma expansion velocity ($T_e = 6.5 \pm 1.5 \text{eV}$, $V_{pl} = 2 \pm 0.2 \cdot 10^6 \text{cm/s}$). These data were obtained at a distance of 2 cm from the PG at a time of $4 \mu\text{s}$ with respect to the beginning of the PG operation.

By changing the time delay (τ_d) of the PFN pulse application with respect to the PG firing different regimes of the planar diode operation have been observed: electron emission from the plasma boundary fixed at the cathode grid position, plasma pre-filled regime and short-circuit. In Fig. 2 we present typical waveforms of the PFN voltage and the anode current for the plasma pre-filled regime when the first plasma bunch has reached the anode (anode-cathode gap of 2.5 cm) and the second plasma bunch is at the position of the cathode grid, $\tau_d \approx 1.3 \mu\text{s}$. These waveforms were obtained continuously with rep-rate of 2 Hz. The space-charge current for this case is $\sim 15\text{-}20 \text{A}$ (the cross-section of the e-beam is $\sim 8\text{-}10 \text{cm}^2$). At the beginning of the voltage pulse, the beam current amplitude reaches 80A without time delay with respect to the beginning of the voltage pulse. Later in time, the amplitude of the electron current decreases to 20A which agrees with the space-charge limited current. Such current behavior agrees well with the plasma pre-filled regime when plasma boundary has eroded to the cathode grid later in time. The duration of the current beam was found equal to the plasma bunch duration. The main disadvantage of this type of plasma source is the presence of the first plasma bunch, which does not allow diode operation without plasma pre-filling.

To avoid this disadvantage we have tested another plasma source based on the non-complete discharge along the surface of the TiBa sample (see Fig. 3). This ceramic sample (disk: $\varnothing 44 \text{mm}$, thickness of 2.5mm) has a strip structure of the front electrode and a rare electrode in the form of a disk. A high-voltage negative pulse for plasma production was delivered to the front electrode by the pulse generator (7-10kV, $C=1 \text{nF}$) through sharpening circuit which consists of spark gap (SG) and capacitor "C".

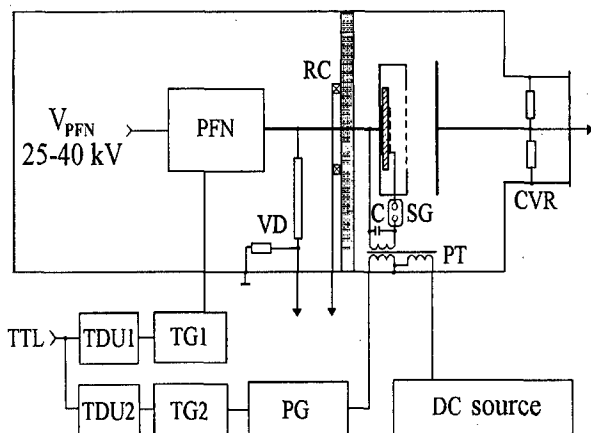


Fig. 3 Experimental setup for TiBa plasma source.

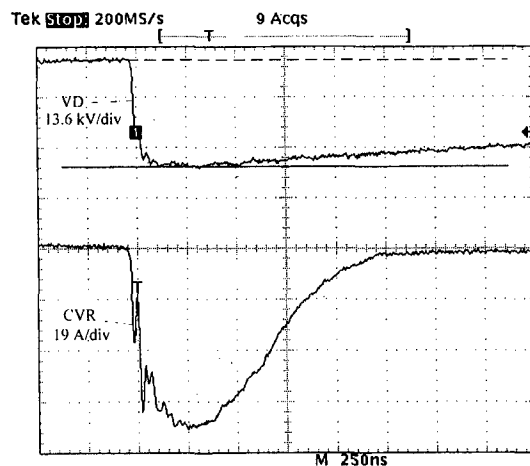


Fig. 4 Typical waveforms of the voltage and anode current.

Measurements of the plasma parameters were carried out at a distance of 1 cm from the cathode grid. These measurements have shown that the plasma electron temperature is $\sim 5 \text{eV}$, the plasma density reaches $n_e \approx 4 \cdot 10^{11} \text{cm}^{-3}$, and the plasma expansion velocity is $V_{pl} \approx 1.5 \cdot 10^6 \text{cm/s}$. It was found that the surface plasma generation and its uniformity strongly depends on the amplitude and polarity of the voltage pulse. Most uniform plasma generation was achieved by application of a positive voltage pulse to the front electrode or a negative voltage pulse to the rare electrode. In addition, significant difference in plasma generation was

observed when the ceramic sample was placed in air. In the latter case, plasma production was uniform and reproducible. These data indicate strong influence of the background conditions on the discharge process. Examples of the surface discharge creation in vacuum and in air are presented in Fig. 5 a,b. Nevertheless, for all polarities of applied voltages we have observed plasma creation within the first nanoseconds of the voltage application at the edges of the strips electrodes.

Fig. 5a. PLZT. Strip geometry. Positive pulse (3 kV, 100ns) is applied to strip electrodes in vacuum 10^{-5} Torr

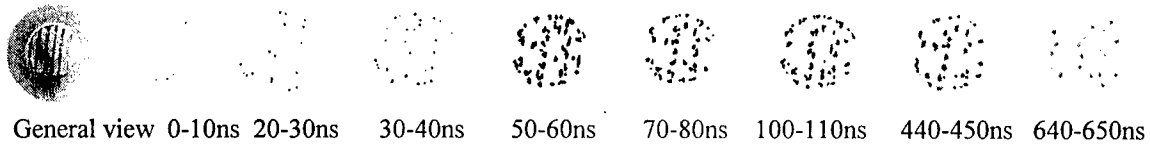
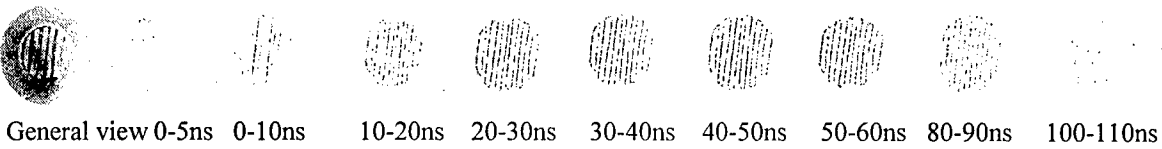


Fig. 5 b. PLZT. Strip geometry. Positive voltage (3 kV, 100ns) is applied to strip electrodes in air.



Similar to the previously described experiments with erosion PG, changing the τ_d allowed to achieve different regime of the e-diode operation. It has been shown that generation of the electron beam starts at $\tau_d \approx 0.5-0.6\mu s$. This time is necessary for the plasma to reach the output cathode grid. For the τ_d when the plasma reaches the output grid, the electron beam generation starts simultaneously with the beginning of the voltage pulse (see Fig. 4). In addition, it was shown that the electron current temporal behavior is the same as the plasma density temporal behavior. It is important to note that in this case we do not have a fast plasma bunch that allows stable electron beam generation from the plasma boundary located at the output cathode grid with current amplitude of $\approx 70A$. During almost all experiment, this plasma source worked in a rep-rate of 2Hz without changing of its parameters (the reproducibility of the electron current amplitude was found $\geq 90\%$). It has been found that the amplitude of extracted electron beam current depends on the anode-cathode distance as well as on amplitude of the applied high-voltage pulse. At the present time we cannot claim that the observed dependences are in agreement with that predicted by the space-charge law. Additional measurements of electron energy and plasma parameters are required in order to do this comparison.

Next set of experiments was done with active plasma sources in a coaxial geometry. We have tested two types of plasma sources: an erosion plasma source (Fig. 6) and a plasma source based on the metal-ceramic structure (Fig. 8). Both plasma sources were placed inside the grounded cathode ($\varnothing 20mm$) having slots structure in the anode ($\varnothing 60mm$) region. The anode-cathode gap was 2 cm and the coaxial diode was connected to the same PFN. The erosion plasma source consists of ceramic rod ($\varnothing 1mm$) with equally distributed (gap of 0.5mm) metal disks. To produce the plasma, a high voltage pulse (30-40kV, 50ns) was applied to the metal disks. Plasma was produced by the surface discharge between the disks. High voltage pulse from the PFN was supplied with the time delay necessary for the plasma to reach the cathode slots. Typical waveforms of the PFN voltage and total anode current are presented in Fig. 7. It was found that this electron source can operate continuously with the rep-rate of 5Hz with a reproducible waveform of the anode current. However, we have found relatively large azimuthal uniformity of the radial electron beam.

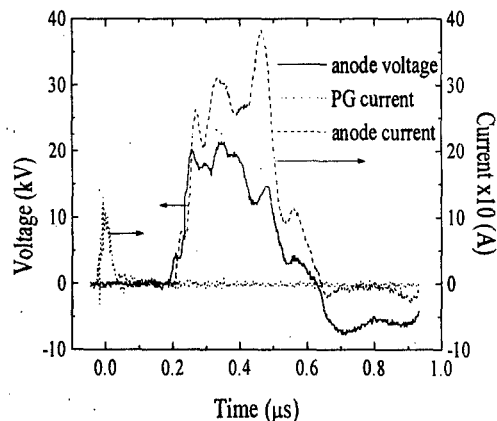
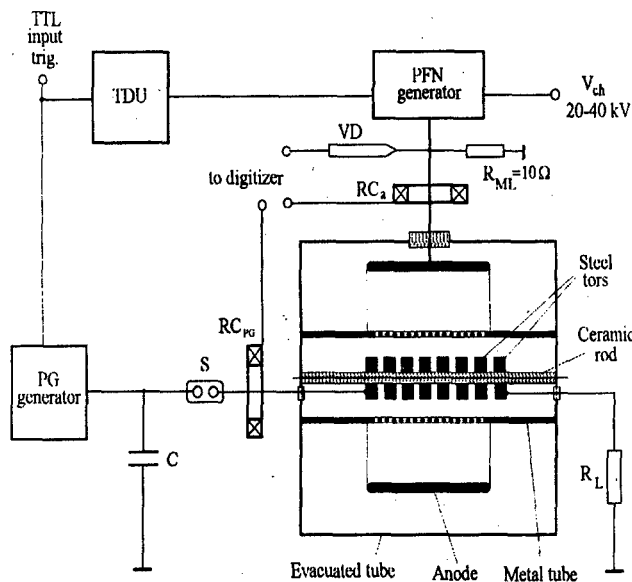


Fig. 6 Experimental setup of the coaxial erosion plasma source. Fig. 7 Typical waveforms of the discharge current, PFN voltage and anode current.

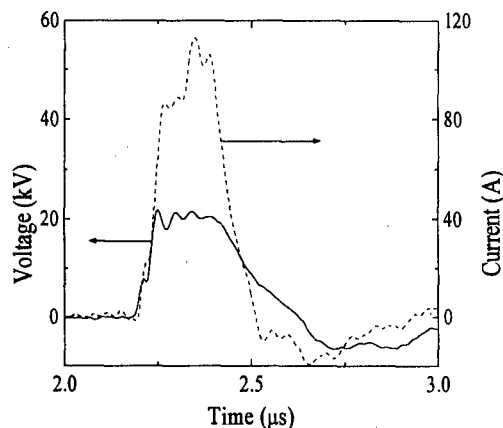
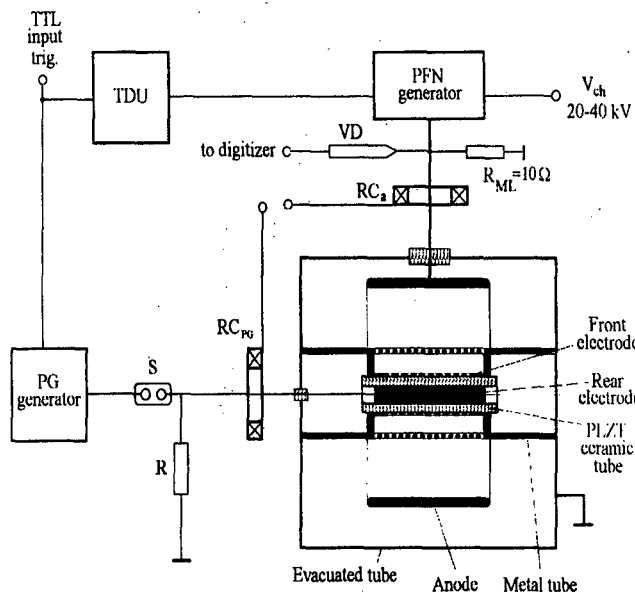


Fig. 6 Experimental setup of the coaxial metal-ceramic plasma source.

Fig. 7 Typical waveforms of the PFN voltage and anode current

For the coaxial metal-ceramic plasma source a PLZT tube (o.d.8mm, i.d.4mm) with grounded strip electrode structure was used. To produce a surface discharge plasma, a high-voltage pulse (1.5–2.5 kV, 100ns) was applied to the central electrode. This plasma source was tested in a continuous mode operation with frequency up to 50Hz. Application of the PFN voltage pulse with the time delay necessary for the plasma to reach the cathode slots allows to obtain an electron beam with current amplitude of 50 – 80 A.

Preliminary experiments have shown that active plasma cathodes allow rep-rate generation of electron beams without time delays with respect to the application of the voltage pulse (40kV) and without explosive plasma creation. At the present time, we continue to investigate these plasma sources at a higher level of the voltage amplitude, as well as gaseous plasma guns as an electron source.

High Brightness Electron Beam Injector for the DARHT Facility

E. Henestroza, S. Eylon, D. Anderson, W. Fawley, H. Rutkowski, S. Yu

Lawrence Berkeley National Laboratory.
Berkeley, CA 94720, USA

Abstract

An injector for the second axis of the Dual-Axis Radiographic Hydrotest Facility (DARHT) is being built at LBNL. The proposed injector consists of a single gap diode extracting 4 kAmps, 3 MV electrons from a thermionic dispenser cathode and powered through a high voltage ceramic insulator column by a Marx generator. The key issues in the design are the control of beam quality to meet the DARHT 2nd axis final focus requirements and to minimize high-voltage breakdown risks. We will present the conceptual design of the injector as well as preliminary results on a scaled experiment and breakdown tests in vacuum using the Berkeley RTA facility.

INTRODUCTION

A high voltage (3 MV), high current (4 kA), long pulse (2 μ s flat-top), high quality ($< 1000 \pi$ mm - mr) electron beam injector for a linear induction accelerator for flash-radiography applications is being built at LBNL. The injector conceptual design is based on the LBNL Heavy Ion Fusion Injector technology [1], and beam dynamics simulations.

The HIF (Heavy Ion Fusion) injector can deliver a 1.5 μ s flat top ($\pm 0.15\%$), high energy pulse (> 2.3 MeV), high current (> 0.8 A of potassium ions), with a low normalized edge emittance ($< 1 \pi$ mm - mr). The HIF injector operating experience regarding breakdown issues, reproducibility and energy flatness is being used in the design of the DARHT long pulse injector.

Figure 1 shows a lay out of the main components of the electrostatic injector assembly. The injector is driven by an 88 90-kV-sections Marx pulse generator. The Marx output pulse is fed through a 3 MV insulating graded ceramic column into the diode cathode to generate a 4 kA electron beam.

MARX GENERATOR AND FAULT-MODE PROTECTION CIRCUITRY

The 3 MV Marx generator design is based on the (Pulse Sciences, Inc.) PSI Super-Reltron microwave tube Marx and the LBNL (Heavy Ion Fusion) HIF 2MV Marx. An 88 stage, oil-insulated Marx layout employs large capacitive coupling between every other stage to develop the majority of the erection voltage across the spark gap, thereby minimizing jitter and erection time. Discrete pulse forming networks (PFNs) are charged ± 45 kV and incorporate tuning inductors located on the perimeter of the Marx at DC ground potential. This feature allows for ease of tuning and removal of PFN sections to operate in shorter pulse modes for commissioning of the accelerator and measuring injector performance with invasive diagnostics. Discrete distributed series resistors valued at 10-15% of the Marx impedance protect the capacitors from reversals and limit the energy dissipated in the event of an oil breakdown. A series stack of metal-oxide arrestor blocks (Harris V402AS60) running the length of the Marx clamp the output voltage to ~ 4.1 MV for a variety of open-circuit conditions. A High Voltage (HV) dome at the end of the Marx houses filament and shroud power supplies, magnet supplies and a fiber optic telemetry system, and is powered by a 20 kW hydraulic generator. The HV dome also attaches to a ballast resistor which is varied to maintain a matched impedance under a

variety of beam operating conditions. Additional varistors are connected along the insulator stack to provide protection from surface flashover avalanching.

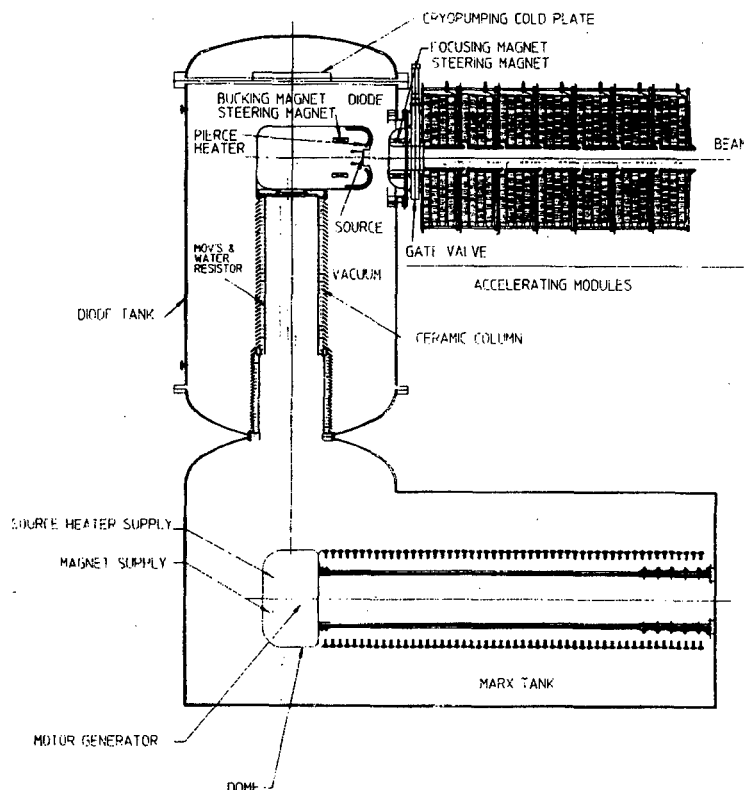


Figure 1. Layout of the main components of the 3 MV electrostatic injector assembly.

The entire system response was calculated using Intusofts ICAP/4 Spice code. Electrostatic Poisson simulations were performed to determine the insulator stack's capacitive matrix. Varistors were modeled using the software vendor's behavioral model modified to allow for series arrays of components. Other stray components' values were calculated analytically. Representative waveforms of the pulse for long pulse and short pulse modes are shown Fig. 2.

THE 3 MV ELECTRON DIODE

The electron beam is generated in a 3 MV diode. It consists of a thermionic source surrounded by a Pierce electrode and focused by a solenoid located at the anode entrance.

The beam dynamics inside the diode has been studied using the electron trajectory computer code EGUN [2]. Figure 3 shows the electron beam envelope and field equipotential lines as calculated by EGUN for the 3 MV case.

In order to have a reliable machine the diode design has to minimize breakdown risks. This requirement translates into a design with maximum current extraction for a given maximum field stress. From final focus requirements at the end of the machine, the beam quality has to be controlled and the normalized emittance be maintained under $1000 \pi\text{-mm-mr}$.

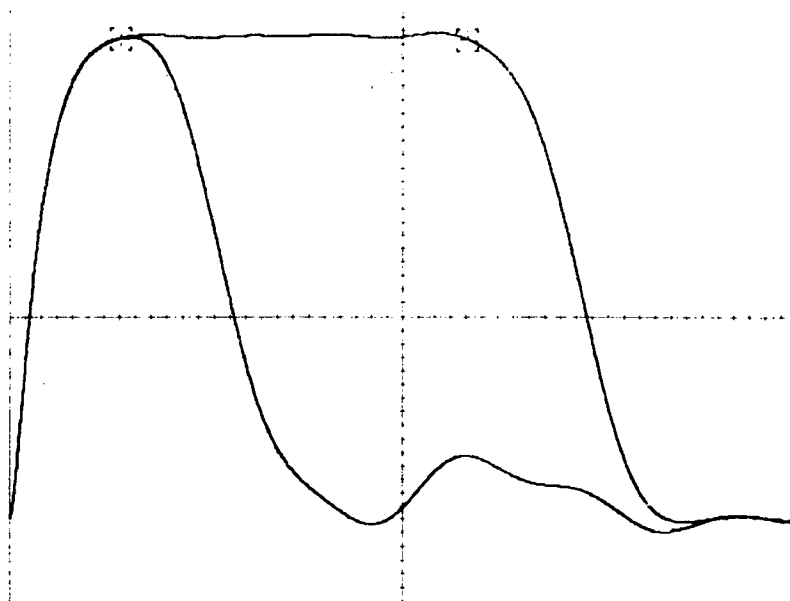


Figure 2. 3.5MV, 2 μ s Long Pulse and Short Pulse Waveforms in present Injector System.

For a given field stress limit, maximum current extraction is obtained from cathodes surrounded by a flat shroud as compared to diodes incorporating Pierce electrodes. On the other hand, the beam quality is better controlled by a Pierce electrode; flat shrouds produce hollow beams whose normalized emittance grow as being transported and accelerated along the induction linac. A compromise between the two conflicting requirements is to design the diode with a Pierce electrode assuming the maximum voltage holding capability that can be obtained using special surface handling procedures; this peak field is around 165 kV/cm on the cathode side of the diode and above 200 kV/cm on the anode side. For this design the emittance at the end of the diode is under 1000 π -mm-mr as calculated by EGUN.

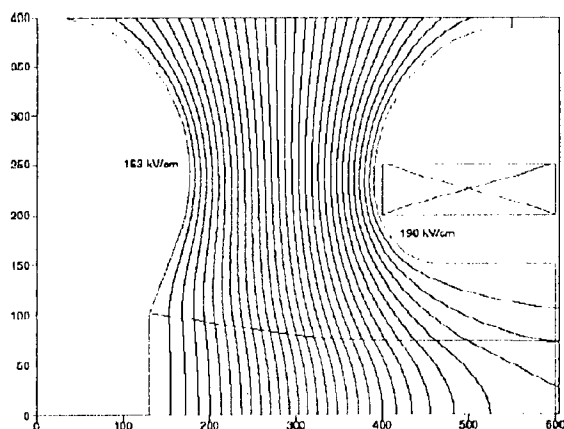


Figure 3. Electron beam envelope and field equipotential lines as calculated by EGUN.

DESIGN SUPPORT EXPERIMENTS

Scaled experiments are being constructed to support the injector design.

The LBNL RTA 1 MV, 1 kA, 0.3 μ s injector-diode configuration is being built as a scaled version of the DARHT injector diode. Injector A-K gaps, cathode shroud materials and

shapes, are designed to allow the study of vacuum breakdown issues in the diode in the presence of a beam.

Another series of vacuum breakdown experiments using long duration ($8\mu\text{s}$ discharge time constant), up to 200kV, 0.5 kJ pulsers are performed. These small-gap breakdown experiments allow the study of gap breakdown dependence on vacuum pressure and electrode material like molybdenum, copper and stainless steel.

The RTA thermionic source heat management and support stability will be tested. Thermocouples will be placed along the source support to map the temperature and evaluate heat flow in the cathode assembly. Furthermore the gap between the source and cathode shroud will be monitored during the source heating experiment. This gap has to be small ($< 0.5\text{ mm}$) to insure a high quality beam.

BEAM DYNAMICS ALONG THE LINAC

A two-dimensional particle-in-cell (PIC) slice (x-y) code [3] has been used to study the transverse beam dynamics of the electron beam generated at the injector as it is transported and accelerated along the induction linac.

The main linac consists of 87 induction cells each providing 200 kV of acceleration. Each cell contains a solenoid used to focus the electron beam. In Figure 4 it is shown the beam envelope and the normalized beam emittance along the induction linac for a complete transverse dynamics run using SLICE, which takes into account all the external fields as well as the space charge. No emittance growth is predicted.

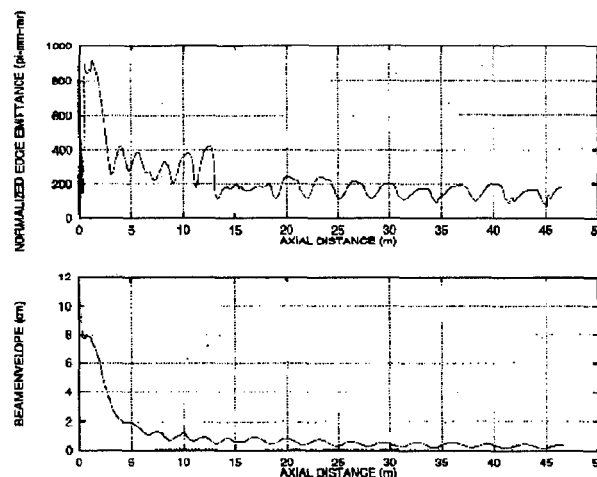


Figure 4. Particle in cell calculation of the transverse beam dynamics along the induction linac.

ACKNOWLEDGEMENTS

This work was performed under the auspices of the U.S. Department of Energy under contract AC03-76SF00098. We thank Glen Westenskow for advice and David Vanecek for technical support.

REFERENCES

- [1] E Henestroza, "Injectors for Heavy Ion Fusion", invited talk, 11th International Workshop on Laser Interaction and Related Plasma Phenomena, Monterey, CA, October 25-29, 1993. AIP Conference Proceedings 318, Ed. G.H. Miley, pp 577-582.
- [2] W.B. Herrmannsfeldt, "EGUN- An electron optics and gun design program," SLAC-Report-331, 1988.
- [3] B. Carlsen, "The PIC-xy 2-D SLICE code", private communication.

PULSE COMPRESSION OF AN INTENSE RELATIVISTIC ELECTRON BEAM USING MULTI-STAGE AUTOACCELERATION

Daisuke Hasegawa, Keiichi Kamada, Kazuhiro Shimizu,
Masaru Miyamoto, Ritoku Ando and Masaru Masuzaki

Department of Physics, Faculty of Science, Kanazawa University, Kanazawa 920-1192, Japan

ABSTRACT

Experiments on two-stage and four-stage autoacceleration were carried out to investigate the pulse compression of an intense relativistic electron beam (IREB). An annular IREB of 600 KeV, 5 KA and 12 ns was propagated through a two-stage cavity or a four-stage cavity structure. The beam with energy of 1.1 MeV and duration of 3 ns was obtained in the two-stage experiment. These results demonstrated the applicability of the autoacceleration process to multi-stage autoacceleration. The duration of the accelerated part in the beam became 0.6 ns in the four-stage experiment.

I. INTRODUCTION

Generation of a short duration IREB is an interesting subject of study for, for example, application to high-power, short pulse millimeter-wave generation [1]. However, it is difficult for conventional pulse-forming-line systems to generate an IREB of short duration less than order of 1 ns. We proposed to compress pulse duration of an IREB after emission from a diode utilizing multi-stage autoacceleration process [2] which uses a series of cavities with decreasing length.

Autoacceleration process [3-5] utilizes the mutual interaction between an IREB and a passive structure, and is reviewed briefly here after Ref. 6. An IREB of particle energy eV_0 , current $I_0(t)$, and beam duration t_0 , propagates through a drift tube immersed in a uniform axial magnetic field. A coaxial cavity of impedance Z_c is connected to the drift tube via gap. The length of the cavity l is $t_0 c/4$, where c is the velocity of light. As the IREB passes the gap, a current $I_1(z, t)$ is induced in the cavity and a voltage $V_1(t)$ appears across the gap. Transmission line theory is used to calculate $I_1(z, t)$ and $V_1(t)$. The current at the end of the cavity is expressed as

$$I_1(l, t) = 2I_1(0, t) - 2I_1(0, t - t_0/2) + \dots \quad (1)$$

and the voltage across the gap V_1 is

$$V_1(t) = Z_c [I_1(0, t) - 2I_1(0, t - t_0/2) + \dots] \quad (2)$$

As a result, a beam electron loses kinetic energy $eV_1(t)$ during the first half portion of the beam duration ($0 < t < t_0/2$) and gain the same amount of energy during the second half ($t_0/2 < t < t_0$). The duration of the accelerated portion of the beam is equivalent to the round trip time of light in the cavity.

The principle of the multi-stage autoacceleration is to use the autoacceleration process repeatedly. As the length of the n th cavity is adjusted to the half of the $(n-1)$ th cavity length, the duration of the most accelerated portion of the IREB after passing through the n th cavity is compressed to $1/2^n$ of its initial duration. The kinetic energy of the most accelerated beam electrons is increased arithmetically when the same impedance cavities are used.

In this paper, we describe a two-stage autoacceleration experiments in which the applicability of Eq. (1) and (2) to the multi-stage autoacceleration is investigated. And we report an experiment of the four-stage autoacceleration in which pulse duration of the most accelerated portion was 0.6 ns.

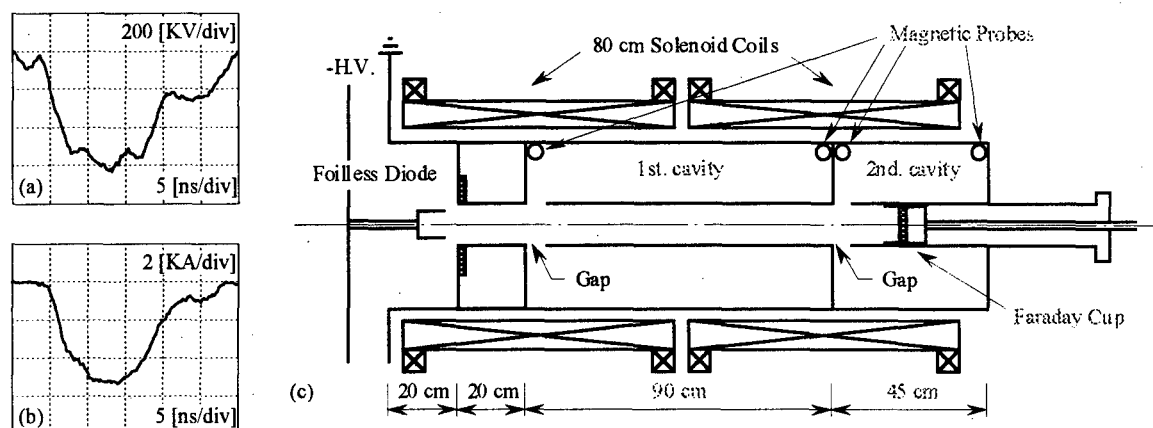


Fig. 1. Typical waveforms of diode voltage (a) and IREB current (b). (c) Schematic of the experiment.

II. EXPERIMENTAL SETUP

A Model 105A Pulserad of Physics International which utilizes a conventional Blumlein pulse forming line was used to generate a 600 KeV, 5 KA, 12 ns (equivalent to 3.6 m in length) annular electron beam [Fig. 1 (a), (b)]. A schematic of the two-stage experiment is shown in Fig. 1 (c). The IREB diameter was 2.4 cm with thickness of 2 mm and the drift tube diameter was 3 cm. An axial magnetic field of 1 T was applied by two solenoid coils of total length of 1.6 m. In the two-stage autoacceleration, the length of the first cavity was 90 cm ($= 3.6 / 4$ m) and the second cavity length was 45 cm (half of the first cavity length) with the same impedance $Z_c = 76$ ohm. In four-stage autoacceleration, cavities with impedance of 46 ohm and lengths of 75 cm, 37.5 cm, 18.7 cm and 9.4 cm were used.

A Faraday cup detected the beam current at various locations along the axis in the drift tube. Aluminum foils of different thicknesses were placed in front of the Faraday cup in order to estimate the kinetic energy of the beam electrons. The beam current at the gap and the current at the end of cavity were measured by magnetic probes shown in Fig. 1 (c). The signals were monitored on Tektronix TDS 684A digitizing oscilloscope (1 GHz, 5 GS/s).

III. EXPERIMENTAL RESULTS AND DISCUSSIONS

A. Two-stage autoacceleration

The current waveform of the incident beam detected through 0.4 mm aluminum foil is shown in Fig. 2 (a) and that of the most accelerated portion of the beam through 0.7 mm aluminum foil

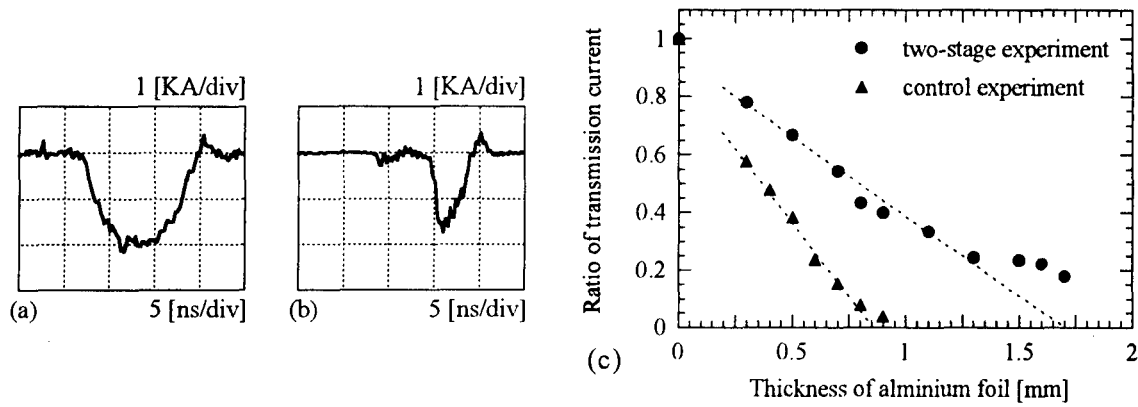


Fig. 2. Typical waveforms of Faraday cup signals, (a) the current waveform of the incident beam with 0.4 mm aluminum foil (control) and (b) the most accelerated portion of the beam transmitted through 0.7 mm aluminum foil in the two-stage experiment. (c) Ratio of the transmitted current through different thickness of aluminum foil.

is shown in Fig. 2 (b). The duration of the incident beam was 12 ns. Note that the most accelerated portion in the two-stage experiment had 3 ns duration which was equal to a quarter of duration of the incident beam and it appeared in the last quarter of the beam duration. The duration of 3 ns was in good agreement with the round trip time of light in the second cavity. These results indicated that the autoacceleration process occurred repeatedly. In the first-stage, the first half and the second half portion of the beam were decelerated and accelerated, respectively. In the second stage, the first and the third quarter portion of the beam were decelerated, while the second and the last quarter portion were accelerated. Therefore, the last quarter portion of the beam was accelerated at both stage.

The ratio of the transmitted current through aluminum foils to the current detected without foil are plotted in Fig. 2 (c). Using Fig. 2 (c) and range-energy relations for relativistic electrons [7], we estimated the kinetic energy of beam electrons to be 1.1 MeV in the two-stage experiment and to be 600 KeV in the control.

Using Eq. (1) and measured beam currents at each cavity, cavity currents were calculated. Figures 3 (a), (b) show waveforms of calculated and measured cavity currents at the first and the second cavity. Since the calculated and measured cavity current at each stage were in good agreement, we expect that we could calculate the acceleration voltage appeared across the gap at the first and the second stage using Eq. (2) and measured beam currents. The calculated voltage at the first and the second gap are shown in Fig. 4. The sum of voltages which accelerate the last quarter of the initial beam duration was 500 KV. This result explained well the energy gain of the most accelerated portion, i.e. 500 KeV.

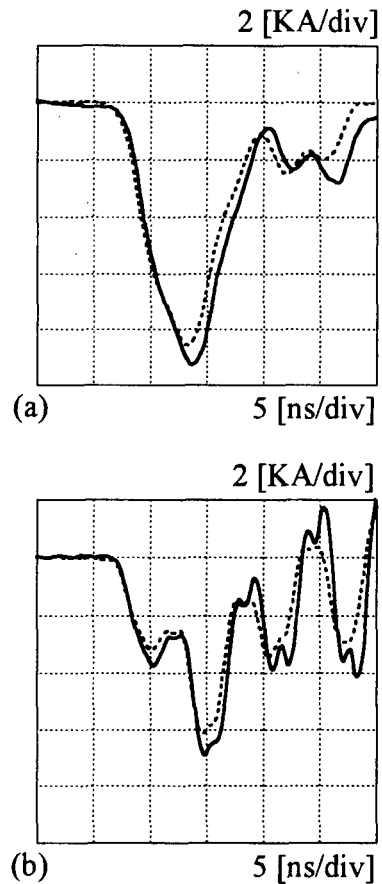


Fig. 3. Cavity current in the first stage (a) and the second stage (b). Comparison between the calculated cavity current (solid) and measured cavity current (dotted line).

B. Four-stage autoacceleration

The four-stage autoacceleration using 46 ohm cavities was carried out to investigate whether a sub-ns IREB was attainable by the multi-stage autoacceleration. Figure 5 shows the Faraday cup signals through 0.6 mm aluminum foils detected at the exit of the fourth cavity. The duration of the most accelerated portion of the beam after passes through the fourth stage was observed to be 0.6 ns that was equivalent to twice the length of the fourth stage. The multi-stage autoacceleration is applicable for pulse compression of IREB of short duration less than order of 1 ns. However, the maximum energy gain of 360 KeV was less than the calculated value of 700 KeV. We think that this was due to influence of decelerated electrons. In order to accomplish the multi-stage autoacceleration, unnecessary decelerated electrons should be removed from the beam pulse.

IV. CONCLUSIONS

The applicability of the autoacceleration process to the multi-stage autoacceleration was demonstrated experimentally. In the multi-stage autoacceleration experiments with the same impedance cavity, the energy increased in arithmetic progression, and the duration of the accelerated part of the beam decreased in geometrical progression with the cavity length.

The authors gratefully acknowledge Mr. H. Yoshida for his helpful discussions and Mr. M. Kamada, Mr. T. Hamai and Mr. H. Tsukuda for their technical assistance.

REFERENCES

- [1] N. S. Ginzburg et al., *Phys. Rev. Lett.* **78**, 2365 (1997).
- [2] K. Kamada, D. Hasegawa, H. Igarashi, T. Kusunoki, C. Y. Lee, H. Koguchi, R. Ando and M. Masuzaki, *Proc. of the 11th Intern. Conf. on High-Power Particle Beams*, vol. **1**, p. 351 (1996).
- [3] M. Friedman, *Phys. Rev. Lett.* **31**, 1107 (1973).
- [4] L. N. Kazanski, A. Kiisletsov and A. N. Lebedev, *At. Energ.* **30**, 27 (1971).
- [5] I. A. Grishaev, A. N. Debik, V. V. Zakutin, I. I. Magda, Yu. V. Tkach and A. M. Shenderovich, *Sov. Phys. Tech. Phys.* **19**, 1087 (1975).
- [6] M. Friedman, *Appl. Phys. Lett.* **41**, 419 (1982).
- [7] H. H. Seliger, *Phys. Rev.* **100**, 1029 (1955).

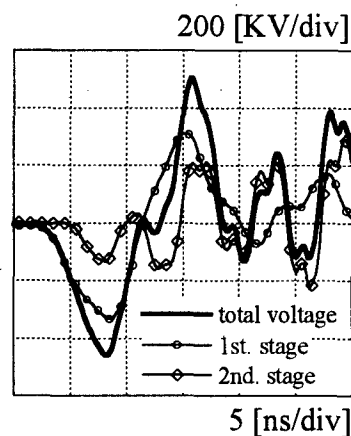


Fig. 4. Calculated voltage at the gap.

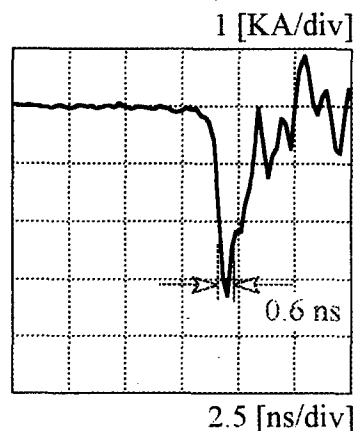


Fig. 5. Faraday cup signal with 0.6 mm aluminum foil obtained for four-stage experiment.

MODELING AND PARTICLE SIMULATIONS OF MAGNETICALLY INSULATED TRANSMISSION LINES WITH CROSS SECTIONAL CHANGES

Kazuki HIRAOKA, Mitsuo NAKAJIMA, Kazuhiko HORIOKA and Makoto SHIHO*

*Department of Energy Sciences, Tokyo Institute of Technology
Nagatsutacho 4259, Midori-ku Yokohama, Japan 226-0026*

**Japan Atomic Energy Research Institute,
Tokai-mura, Ibaraki, Japan 319-11*

ABSTRACT

In order to discuss the power transportation through the high power MITLs (Magnetically Insulated Transmission Lines), we have modified the equivalent circuit model. This model can be used for estimating the influences of space-charge electrons on power flow and design works of high power MITLs. When the MITL has an abrupt geometrical change, this model is thought not to work well. We are estimating validity of the model by comparing the results with those of the particle-in-cell simulation (PIC). Subsequently, we study the stability of space-charge electron flow in the gaps by the PIC simulation.

INTRODUCTION

MITLs (Magnetically Insulated Transmission Lines) under high power operation are dominated with space charge current flowing between anode and cathode. Conventional equivalent circuit model[1] does not account for space charge effects on power flow. To discuss the power transportation through the high power MITLs, we have developed a new equivalent circuit model including space-charge flow[2]. This model uses space-charge current profile of relativistic Brillouin theory (or laminar flow theory)[3][4]. In this theory, solutions for potential, charge density distribution, fraction of the current carried by the space charge, and radius of the space-charge layer are obtained self-consistently. This theory give very similar results for cases when the MITL has constant geometry and the boundary current is sufficiently large to

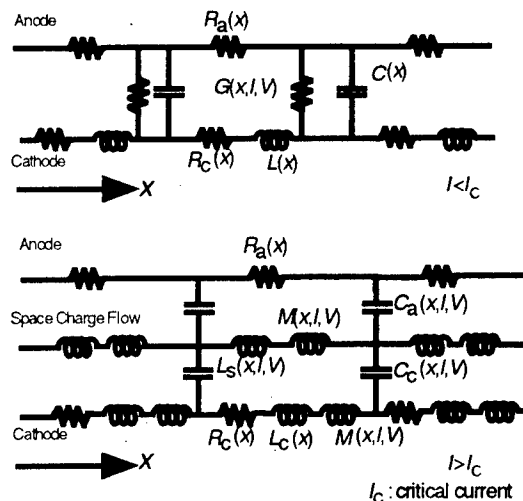


Fig.1 Modified equivalent circuit of MITL.

keep magnetic insulation.

Fig.1 shows our modified equivalent circuit model of MITL. In our modeling, we assume that once magnetic insulation is established ($I > I_c$), the equivalent circuit (a) is replaced by modified circuit (b) that has space charge current path. Here, I_c is the critical current and G is the conductance of space charge limited current flows across the vacuum gap. The effect of space charge electron is expressed by effective inductance L , mutual inductance M , and capacitance C . To determine these values analytically, we use the laminar flow theory. General validity of this circuit model is confirmed by comparing the results with those of PIC[2].

However, when the MITL has too rapid geometrical change, the laminar flow approximation is not necessarily valid. The characteristics of space-charge electron flow has been investigated in parallel coaxial lines or gentle taper. So the behavior of the flow in MITLs with rapid geometrical change is not studied well. In order to specify the applicability of this model and reveal the behavior of the flow, we use PIC simulation.

PIC SIMULATION

Subsequently, we investigate the condition that how rapid geometry cause disagreement with laminar flow condition, and determine the limit of application of our model. Furthermore, we will study the general characteristics of electron flow including flow stability and electron distribution profile, in such steep shaped MITLs.

Here we use TS2 module of MAFIA program package. MAFIA is interactive programs for the computation of electromagnetic fields. It is based on theory of discrete Maxwell grid equations and the finite integration technique. TS2 module is a 2-dimensional PIC code which solves fully selfconsistent Maxwell's equations and equations of motion in time domain. A cylindrical symmetric coordinate system (r, z) is used.

Fig.2, Fig.3 and Fig.4 show examples of typical results. Z-component of current density indicates the space-charge electron current, and R-component indicates degree of disturbance of laminar flow.

Fig.2 shows simulated results for straight coaxial MITL. Here cathode radius r_c is 2.5cm, anode radius r_a is 5cm, length of the line is 40cm, applied voltage V_0 is 2MV, total current I_0 is 73kA, boundary current I_b is 45kA. Current distribution approaches laminar profile with Z. The radius of peak is close to which Brillouin flow theory predicts. The laminar flow profile is almost maintained in gentle slope geometry, shown as Fig.3. Here cathode radius r_c is 2.5cm at up-stream, and slowly changes to 1.5cm. In Fig.4, rapid slope geometry disturbs the laminar flow. here, the cathode radius r_c is rapidly changed to 1.5cm from $z=15$ cm to $z=16$ cm ($dr/dz = 1$).

Generally, turbulence of electron distribution gradually increased when the geometrical change (dr/dz) was enlarged.

CONCLUSIONS

We have developed a new equivalent circuit model of MITLs which include space

charge effects. With this model, we can estimate easily the effects of space charge current on the power flow efficiency, without using complicated, laborious particle code simulations.

We are investigating the critical conditions that disturb the laminar flow distribution with PIC, to evaluate the limit of application of our model. Some typical results were presented.

In addition, we are going to study the general characteristics of electron flows in tapered MITLs.

REFERENCES

- [1] K. D. Bergeron: J. Appl. Phys. 48 (1977) No.7, 3065.
- [2] K. Hiraoka, M. Nakajima and K. Horioka: *Proc. 11th Int. Conf. High Power Particle Beams* (1996) p.1022.
- [3] John M. Creedon: J. Appl. Phys. 48 (1977) No.3, 1070.
- [4] John M. Creedon: J. Appl. Phys. 46 (1975) No.7, 2946.

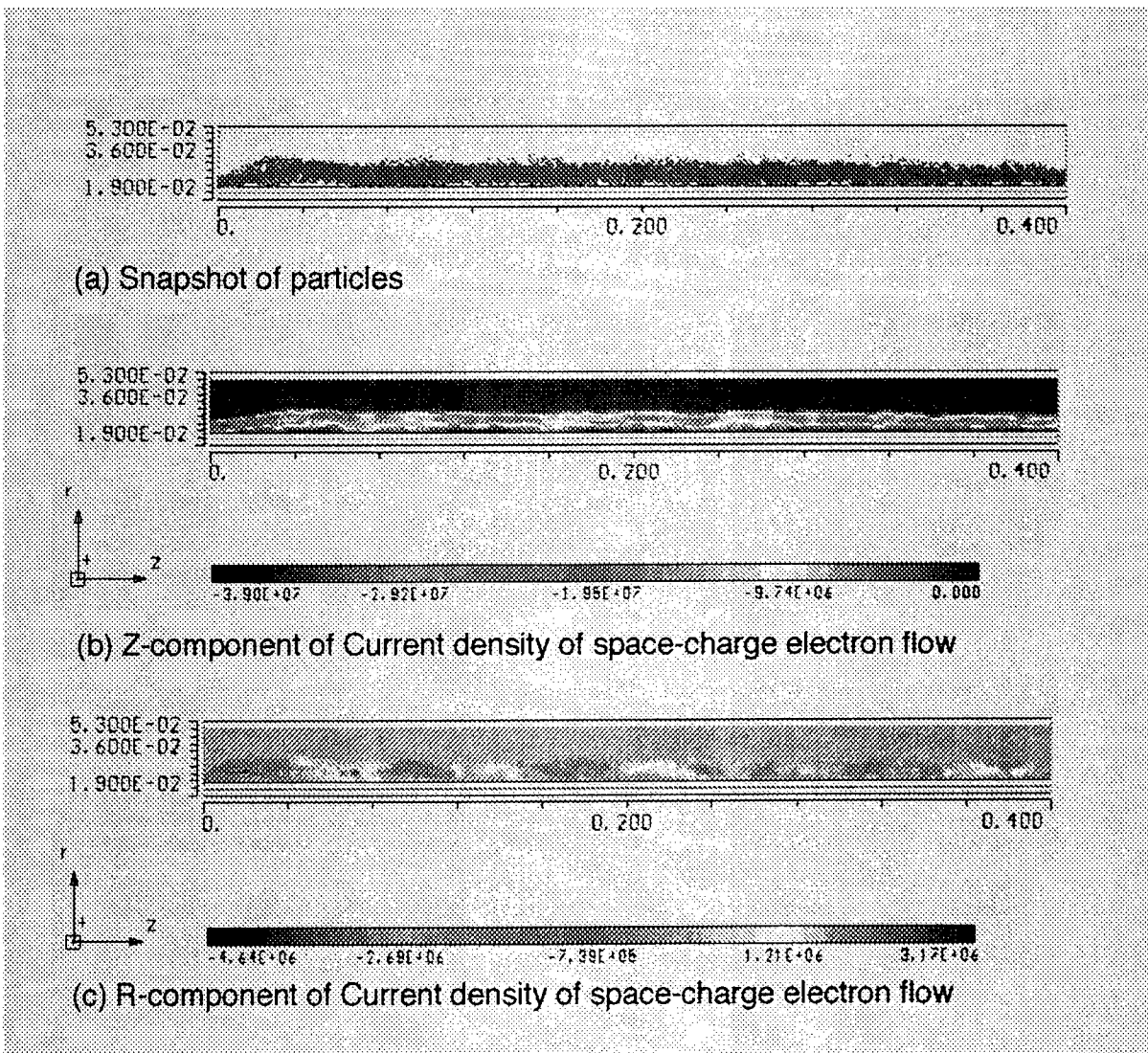
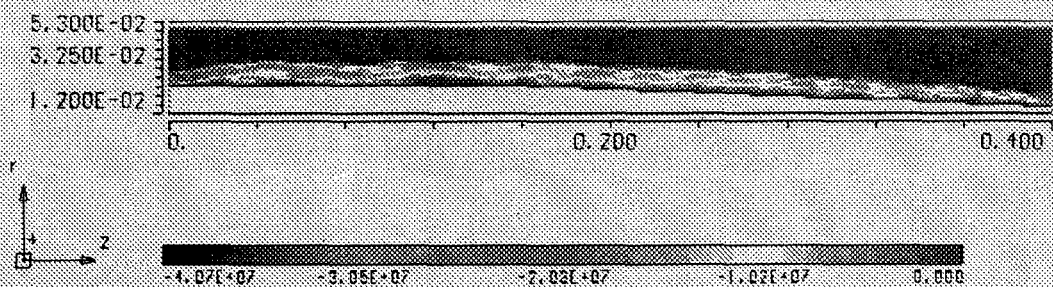
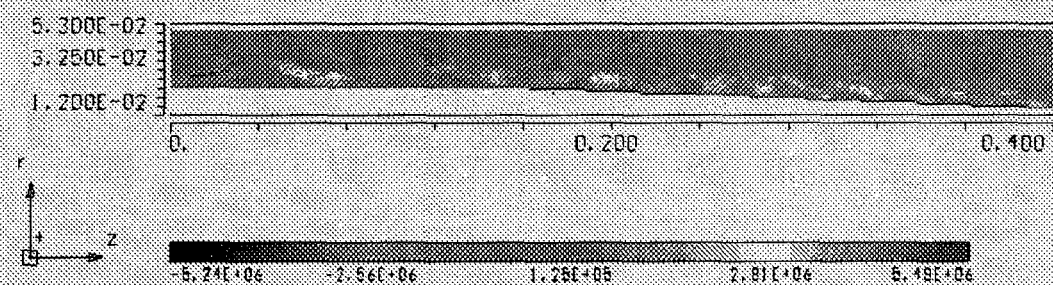


Fig.2 Typical results of PIC simulation

Here cathode radius r_c is 2.5cm, anode radius r_a is 5cm, length of line is 40cm, applied voltage V_0 is 2MV, total current I_0 is 73kA, boundary current I_b is 45kA. The formation of laminar flow is observed.



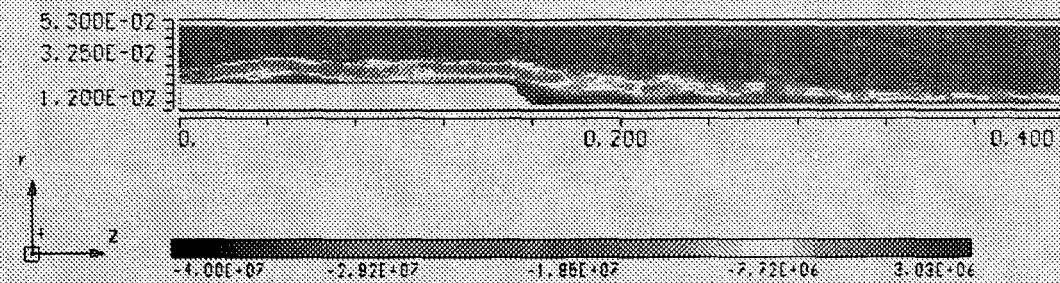
(a) Z-component of Current density of space-charge electron flow



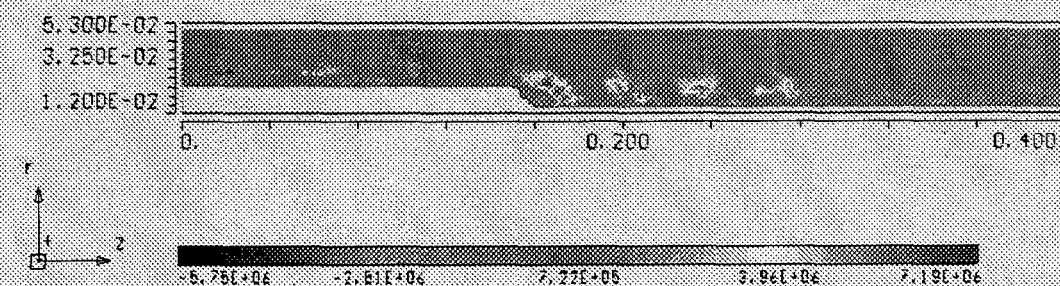
(b) R-component of Current density of space-charge electron flow

Fig.3 Electron flows with gentle slope geometry

Here cathode radius r_c is 2.5cm, and slowly changes to 1.5cm. The laminar flow form is almost maintained.



(a) Z-component of Current density of space-charge electron flow



(c) R-component of Current density of space-charge electron flow

Fig.4 Electron flows with abrupt slope geometry

Here cathode radius r_c is 2.5cm and rapidly changes to 1.5cm from $z=15$ cm to $z=16$ cm.

ACCELERATION WAKE-FIELD ENHANCEMENT OF EXCITED BY LONG RELATIVISTIC ELECTRON BUNCH OWING TO SELF-MODULATION

V.I.Karas', V.A.Balakirev, Ya.B.Fainberg, G.V.Sotnikov, I.V.Karas',
V.D.Levchenko*, Yu.S.Sigov*

*National Science Center "Kharkov Institute of Physics and Technology",
Akademichna St. 1, Kharkov, 310108, Ukraine*

**) Keldysh Institute of Applied Mathematics, RAS, Miusskaya Sq. 4, Moscow, 125047, Russia*

1. The charged particle acceleration by charge density waves in a plasma and in uncompensated charged beams appears to be a most promising trend in the collective methods of acceleration [1-3]. The variable part of the charge density can be made to be very high (up to n_0 , where n_0 is the unperturbed plasma density); therefore, the accelerating fields can reach 10^7 to 10^9 V/cm. Chen et al [4] have proposed a modification of the Fainberg acceleration method [1], consisting in using a train of bunches. In [5], Katsouleas has considered electron bunches with different profiles, namely, a bunch with a slow build-up in the density and its very quick fall-off, and also the bunch with the Gaussian-type distribution for different rise and fall-off times. It was established in [5] that the use of these nonsymmetric bunches instead of symmetric ones can provide the accelerating field E_{ac} value to be many times (10 to 20) higher than the retarding field E_{st} value. The so-called transformation coefficient $T = E_{ac}/E_{st} = \Delta\gamma_{ac}\gamma_b^{-1}$ is equal to $2\pi N$, where N corresponds to the number of wavelengths along the bunch length. The excitation of nonlinear stationary waves in the plasma by a periodic train of electron bunches has been studied in refs. [6, 7], where it was shown that the electric field of the wave in the plasma increases with γ (γ is the relativistic factor of the beam) at commensurable plasma and beam densities. The experiments undertaken in refs. [7, 8] on wake-field acceleration has demonstrated the importance of three-dimensional effects.

Here, we consider two different regimes with high amplitudes of plasma wake fields that are employed in the accelerator physics. The first regime makes use of an extended short beam, then the high-amplitude waves excited by this beam and having high-gradient longitudinal electric fields can be used to accelerate other bunches. In the second case, a strong focusing can be attained with a long narrow beam, making use of its intrinsic magnetic field which is unbalanced because of space charge compensation by the plasma.

Apart from the transverse forces, the bunch particles are also influenced by powerful longitudinal forces on the side of electric wake fields. The longitudinal fields will give rise to a longitudinal modulation of the electron bunch, i.e., to a splitting of an originally uniform bunch into microbunches with a modulation period $\lambda_p = 2\pi c/\omega_p = 3.36 \times 10^6 n_0^{-1/2}$ cm. In particular, in the plasma with a particle density of 10^{16} cm $^{-3}$ the modulation period is 0.3 mm. The effect of longitudinal REB modulation by wake fields can be used for developing plasma modulators of dense electron beams. It is pertinent to note one more feature of this phenomenon.

Since the modulation frequency is coincident with the plasma frequency, the wake fields of microbunches are then combined coherently. Therefore, the electron bunch modulation will involve an increase in the amplitude of the wake field behind the bunch. This effect opens up a possibility of using long-pulse electron bunches to excite intense wake fields in a plasma. It is particularly remarkable that the effect of longitudinal modulation at a plasma frequency takes place

for a long laser pulse, too [9]. Previously in [10], a theoretical study has been made into the process of modulation of long electron bunches in a plasma by longitudinal wake fields.

Results were reported there for one-dimensional numerical simulation of nonlinear dynamics of bunch modulation. It was demonstrated in ref. [10] that the particle modulation of a long bunch moving in the plasma causes an increase in the wake wave amplitude. This effect is accounted for by coherent combining of fields excited by microbunches, into which the bunch is split in the course of modulation. The bunch is modulated at a plasma frequency. The investigation of the one-dimensional approximation is justified in the case of great transverse dimensions ($2\pi r_b/\lambda_p \gg 1$).

2. The present report deals with the 2.5-dimensional numerical simulation of wake fields by long REB.

The excitation of wake fields is investigated with an aid of the 2D3V axially symmetric version of the SUR code being, in turn, a further development of the COMPASS code [11]. Earlier, this code has been used to simulate the induction accelerator [12], the modulated relativistic electron beam [13], and a single REB or a train of these bunches in a plasma [11, 13-16].

The dynamic of REB is described by the relativistic Belyaev-Budker equations for the distribution functions $f_\alpha(\vec{r}, \vec{p})$ of the plasma particles of each species and by the Maxwell equations for the self-consistent electric E and magnetic B fields. We assume that, initially, a cold two-component back-ground plasma ($m_i/m_e = 1840$, where m_i and m_e are the ion and electron masses) fills the entire region $[0, L] \times [0, R]$, where $L = 100$ cm and $R = 10$ cm.

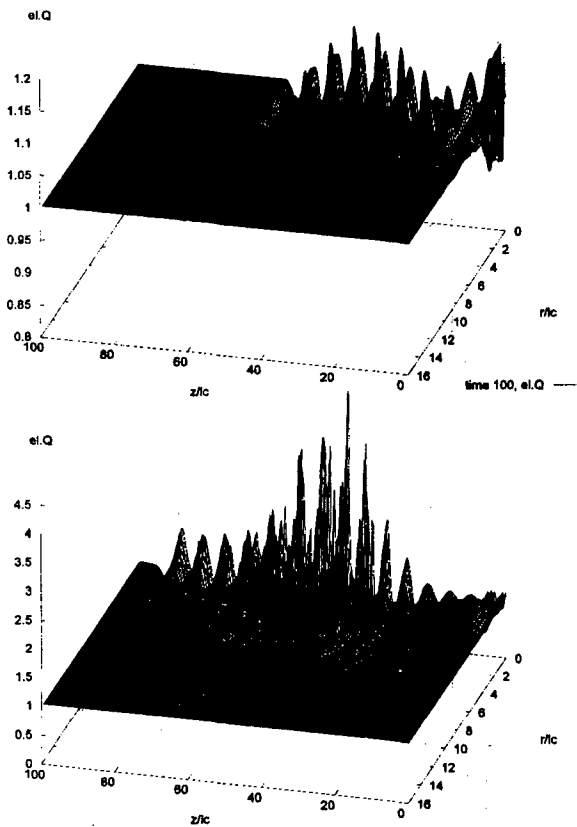


Fig. 1.

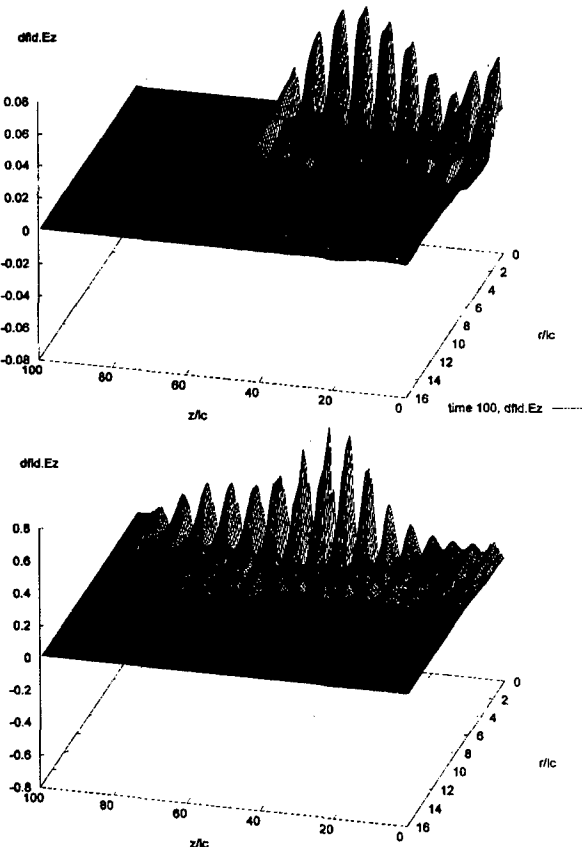


Fig. 2.

The scale on which the electric and magnetic fields vary is $m_e c \omega_p / e$. We assume that the plasma and bunch particles escape from the

computation region through the $z = 0$ and $z = Z$ boundary surfaces and are elastically reflected from the $r = R$ surface. We also assume that cold background electrons and ions can return to the computation region from the buffer zones $z < 0$ and $z > Z$. The boundary conditions for the fields corresponds to the metal wall at the cylindrical surface $r = R$ and free emission of electromagnetic waves from the right and left plasma boundaries. The weight of the model particles was a function of the radial coordinate, and the total number of these particles was about 10^6 . All the calculations were carried out on a Pentium-90 personal computer using the modified particle-in-cell simulation algorithm.

In order to analyze the dependence of the amplitude of the excited fields on the number of bunches injected into plasma we carried out series of calculations.

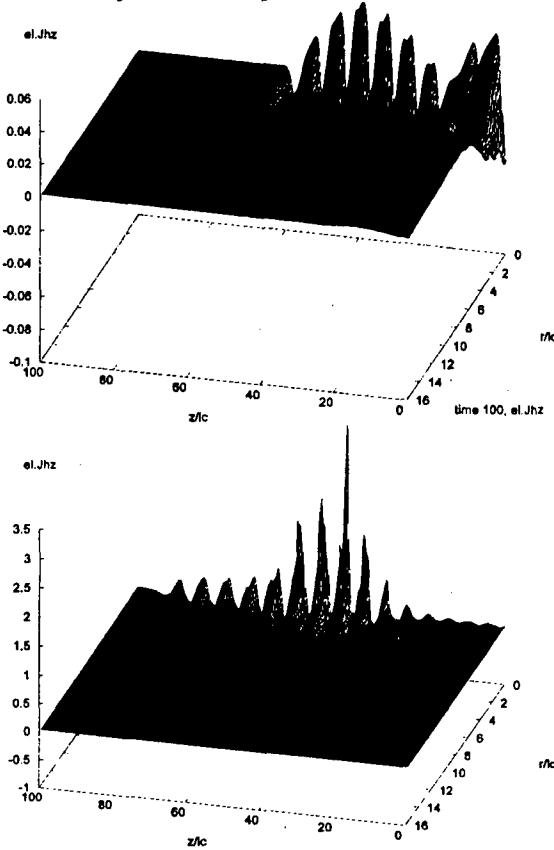


Fig. 3.

It is of importance to note that the maximum of the beam particle charge density corresponds to the 5th microbunch rather than to the 8th microbunch and is equal to $1.6n_0$, this being two orders of magnitude higher than the initial beam particle density value in the long bunch. The spatial distribution of the longitudinal current density of plasma electrons $el.Jhz$ (Fig.3) also correlates rigidly with the longitudinal electric field E_z distribution. Here attention must be given to the peak current value for the 8th microbunch, which is two orders of magnitude higher than the initial longitudinal current value of REB particles. The present results show that the nonlinear picture in the plasma-REB system drastically differs from both the initial picture corresponding to the rigid REB and the one by the scenario following from the one-dimensional numerical modulation (cf. [10]). This supports in full measure the conclusion given in ref. [7] about the necessity of taking into complete account the three-dimensional effects and the nonlinear behavior of both the plasma and the bunch.

4. The spatial density distributions of REB and plasma electrons obtained for the instances of

3. Figures 1 to 3 show spatial distributions of the longitudinal electric field E_z , electric charge density of electrons, longitudinal current density of electrons, respectively, for the instants of time $t = 60\omega_p^{-1}$ (a) and $t = 100\omega_p^{-1}$ (b). It is seen from Fig. 1 that the longitudinal electric field rapidly grows reaching $0.8m_e c \omega_p / e$. Note that the original beam particle density was only 6% of the plasma electron density. The radial electric field E_r also grows, but it reaches a somewhat lower value $0.4_e m c \omega_p / e$. It is significant that: (i) the finite length of the initial bunch is responsible for the formation of the growing electric field; (ii) the electric field has a rather high amplitude near the axis, this being due to microbunch pinching; (iii) the evolution of the instability, giving rise to microbunches, leads to some decrease in the phase velocity of the perturbed wake wave. From Fig. 2 it is seen that the electric charge density distributions of plasma electrons $el.Q$ are similar to the spatial distributions of the longitudinal electric field E_z . The highest density value is attained for the 8th microbunch and is $4.5n_0$.

time $t = 60\omega_p^{-1}$ and $t = 100\omega_p^{-1}$ show that the density ratio n_b/n_0 (the initial value being 0.018) reaches 0.04 as early as at $t = 60\omega_p^{-1}$. At $t = 100\omega_p^{-1}$, the highest beam particle density becomes commensurable with the plasma density, i.e., a very strong modulation of beam particle density is observed.

The spatial distributions of the longitudinal E_z and transverse E_r electric fields show that the E_z and E_r amplitudes grow owing to the enhancement in the density modulation.

At $t = 100\omega_p^{-1}$ the highest longitudinal-field amplitude reaches $0.8m_e c\omega_p/e$, and the highest transverse-field amplitude is equal to $0.4m_e c\omega_p/e$. It is essential that the amplitude growth occurs only within a moderate REB length. Therefore, there is little point in using the REB of the length greater than that corresponding to the highest longitudinal-field amplitude, otherwise no increase in the excited wake field will be attained.

The undertaken numerical experiments have demonstrated that the nonlinear dynamics of the particles of plasma components and bunches results in the following effects: (i) the transverse dimension of bunches varies within a very wide range; (ii) close to the axis of the system an ion channel is formed, which is a contributory factor for the stabilization of bunch propagation and the growth of bunch-generated fields; (iii) an essential increase in the amplitudes of excited electric fields takes place in the case of a long bunch as a result of its self-modulation. However, bunches of optimum length should be used, since any excess of the optimum length of the bunch fails to provide, even at self-modulation, the growth in the amplitudes of excited electric fields.

- [1] Ya.B.Fainberg // Proc. Symp. CERN, Geneva, Vol. 1, 1956, p. 84.
- [2] Ya.B.Fainberg // Sov.J. Plasma Physics, Vol. 13, 1987, p.350.
- [3] Ya.B.Fainberg // Plasma Physics Reports, Vol. 20, 1994, p.549.
- [4] P.Chen, J.M.Dawson, R.W.Huff, and T.Katsouleas // Phys. Rev. Lett., Vol. 54, 1985, p. 693.
- [5] T.Katsouleas // Phys. Rev. A, Vol. 33, 1986, p. 2056.
- [6] A.Ts.Amatuni et.al. // Sov. J. Plasma Physics, Vol. 11, 1985, p. 417.
- [7] J.Rosenzweig // FERMILAB Conf. 90/40, FNAL, Batavia, Illinois, 1990.
- [8] J.Rosenzweig et.al. // Phys. Rev. A, Vol. 44, 1991, p. 6189.
- [9] C.Joshi et al. // IEEE J.Quant. Electr. Vol. QE-23, 1987, p. 1571.
- [10] V.A.Balakirev, G.V.Sotnikov, Ya.B.Fainberg // Fizika Plazmy, Vol. 22, 1996, No 2. p. 165.
- [11] O.Batishchev, V.Karas', V.Levchenko, Yu.Sigov // Plasma Physics Reports, Vol. 20, 1994, p. 587.
- [12] V.Karas', O.Batishchev, Yu.Sigov, and Ya.Fainberg // Particle Accelerators, Vol.37-38, 1992, p. 281.
- [13] O.Batishchev, Yu.Sigov et.al. // Sov. J. Plasma Physics, Vol. 19, 1993, p. 738.
- [14] O.Batishchev, V.Karas', Yu.Sigov, and Ya.Fainberg // Plasma Physics Reports, Vol. 20, 1994, p. 583.
- [15] V.Karas', Yu.Sigov, Ya.Fainberg, et. al. // Plasma Physics Reports, Vol. 23, 1997, p. 285.

HIGH-BRIGHTNESS ELECTRON LINAC FOR BEAM-PLASMA INTERACTION STUDIES

M.I. Ayzatsky, A.N. Dovbnya, V.A. Kushnir, V.V. Mitrochenko, D.L. Stepin

*National Science Center, Kharkov Institute of Physics & Technology,
1 Akademicheskaya st., Kharkov, 310108, Ukraine*

ABSTRACT

The report contains the description of operating performances and current status of the experimental facility that has been developed and constructed in view of experimental study both wake-field generation in plasma and shaping high-brightness electron intensive beams. The facility consists of the S-band linac LIC (Laser Injector Complex), the plasma source and special equipment for measurement of beam and plasma characteristics. The combination of an RF gun with accelerating section operating at the 1-st spatial harmonic makes it possible to obtain electron beam with energy 13-18 MeV, normalized emittance better than 30π mm-mrad and density of particles in each bunch $\sim 10^{11}$ cm⁻³. Now the facility is used for studying the electron focusing in plasma by transverse components of wake-fields.

INTRODUCTION

LIC, (Linear Injector Complex) facility was developed and constructed in view of forming and acceleration of high - brightness electron beams [1]. This R&D was to be followed by beam research in the following areas: ultra - short wave generation; wake-field generation in plasmas and other systems; relativistic electron beam focusing in plasmas. The electron energy at the accelerator output was to be 15 to 20 MeV which is sufficient to carry out the above programs. LIC basic components are an RF-gun [2,3], the accelerating section, beam steering and its focusing elements, beam diagnostics, cooling water system and control elements. The RF system includes a klystron with the maximum power operation up to 25 MW, a set of waveguides, controllable phase shifter and attenuator. Having in view the multipurposeness of the facility under development, we brought out the following major criteria which were taken into account while choosing the necessary type of the accelerating structure:

- the feasibility of acceleration of beams with high charge in the stored energy mode at moderate values of RF-power input ($P \approx 20$ MW);
- reduction of amplitudes of TEM waves which are excited by high-intensity electron beam and lead to emittance enhancement or even to shortening of pulse length (BBU instability);
- the feasibility of intense electron beam acceleration with small radial dimensions with the minimum number, or even absence, of external focusing elements.

The most attractive was the accelerating structure STRAM-90 (the abbreviation standing for STRucture Accelerating Modified) developed at NSC KIPT which has been designed to accelerate intense short -pulsed electron beams in the stored energy mode at moderate values of RF power input values ($P \approx 15-20$ MW) [4,5]. This structure represents a disk-loaded waveguide with the period being two times higher than that in the disk-loaded waveguide with $2\pi/3$ mode. Particle acceleration in such structure is made by the first spatial mode of the electromagnetic wave propagating in the opposite

direction to the electron beam. Beside increasing the charge value, which can be accelerated in the stored energy mode, the STRAM-type structure has the RF-focusing owing to the presence of a large non-synchronous spatial mode [6,7]. The period increase also leads to a considerable reduction in the TEM-wave generation, since the particles are synchronous with higher spatial modes of these oscillations. We have developed a new version (STRAM-91), producing acceleration at the first spatial mode, but having both an increased value of the accelerating field and a low level of higher mode amplitudes irradiated by particles [4]. This was achieved by making use of unusually thick disks with large values of the coupling hole.

Major parameters section, developed at NSC KIPT, are given in Table .

The beam characteristics measurement system consists of two pulsed beam current

Operating mode	$4\pi/3$ ($2\pi/3$)
Length (m)	2.31
Disk hole diameter, $2a$ (cm)	5
Disk thickness, t (cm)	5
Periodic length, D (cm)	7.145
Attenuation, α (1/cm)	$2.44 \cdot 10^{-3}$
Group velocity	$0.01c$
Freguency, f (MHz)	2797
Shunt impedance for synchronous space harmonic (M Ω m/m)	11.3

monitors, a magnetic particle energy analyzer, a unit of movable slot collimators, a Al_2O_3 screen with a TV camera and a multi-sectional Faraday cap. Beam emittance measurements at the linac exit are performed by the three gradient technique. A quadruple lens is used for this purpose together with the particle spatial distribution monitor, placed at a distance of 2 m from the lens, and consisting of a set of moving

slots 0.3 mm wide. In order to make estimations of the transverse dimensions a Al_2O_3 screen with TV-camera as well as a sectional Faraday cap consisting of several coaxial ones are employed.

CALCULATION AND EXPERIMENTAL RESULTS

At all stages of the accelerator development calculations were performed both analytically and as computer simulations. In this way, during development of the acceleration section its geometrical dimensions were calculated, as well as basic RF-characteristics for operation at $4\pi/3$ mode. Besides, the calculations were done of the particle dynamics in the sections allowing to evaluate the degree of RF- focusing and peculiarities of wake-field generation. During designing of the gun, in order to optimize its resonators and determine the beam characteristics a set of calculations and simulations (the SUPERFISH and PARMELA codes were used) was performed. In a more detail, the calculation results are given in [3]. From the calculations it follows that the gun can be used successfully both in photo- and thermionic emission modes.

In order to study the particle dynamics in the accelerator using the numeric simulations within the PARMELA code, a model of the entire accelerator was constructed including the RF gun, beam-forming elements and the accelerator section. At first stage we began to study the thermoemission regime with long pulse duration. Preliminary results show that despite of the high injection energy ($W_0 \approx 1$ MeV) there is a strong phase movement of the particles at the initial part of acceleration process. We connect this fact with the smallness of accelerating field amplitude at the entries of our section. Under such conditions a strong phase movement can take place at sufficiently

high energy of the injected electrons. Under optimum conditions the length of bunches can be strongly reduced (from 50° at the exit of the RF-gun to 4° - 7° at the exit of the accelerating structure). Very interesting are the results of radial motion. As it have been mentioned in previous papers [5,6], in the accelerating structure under consideration there is RF-focusing and at the accelerator exit we should have converging electron beam. Besides, we modeled various accelerator operation modes and beam relationship vs. different parameters in order to compare them with experimental results.

Experimental studies in the operation mode of forming and acceleration of single picosecond pulses require utilization of very complicated and costly laser system. Over and above, studies on wake-field generation in plasmas in 1995 called for beams of microsecond duration. In this connection, research into accelerator characteristics during the initial stage was done at a microsecond beam current pulse. With this in mind, the gun had been outfitted with a thermionic emission cathode 5 mm in diameter [2]. The RF-tuning provided for the equal field strength in the first and second cavities which is optimum in case of the thermionic emission cathode at field strength inside the cavity of 25 to 30 MV/m.

In stable accelerator operation regimes (pulse repetition rate ≤ 6.25 PPS, current pulse duration $2\ \mu\text{s}$, RF-power input ~ 1.8 MW) the typical current pulse amplitude at the exit of RF-gun was 1.5 - 2.0 A. With an optimum phasing of the acceleration section the output pulsed current was 1 - 1.1 A making the capture rate near 70% which is in accordance with the calculated data. Experimentally shown is the possibility of current pulse reduction at the linac exit from 2 to $0.25\ \mu\text{s}$ by way of decreasing of RF-power input or increasing of cathode heating. This is accompanied by particle energy decrease at the gun exit due to beam loading, and only the most energetic electrons become involved in the acceleration process.

In the experiments was observed a ramp in pulse current of RF-gun and a drop of field strength in the cavities on account of the electron back bombardment of the cathode surface. This phenomena was studied during the experiments. It was found that at a pulse repetition rate exceeding 6.25 pps the overall average cathode surface temperature went up above 90°C which called for a decrease of the heating, leading under certain RF-power input conditions to an unstable gun operation.

An analysis of the particle energetic distribution at the linac exit showed that at a pulsed current ~ 1 A and pulse duration $1.4\ \mu\text{s}$ the energy spectrum possesses an additional maximum in the high-energy region. The shape of the energy spectrum is determined by particle energy coherent losses (beam current loading). In this way, at $I=1.05$ A the mean energy was 13.5 MeV, the width of the integral energy spectrum 7% , while the width of particle spectrum distribution, as they were injected into the section after $\sim 1\ \mu\text{s}$ from the beginning of the pulse, did not exceed 3%.

From beam emittance measurements it follows that in the vertical plane the integral (during the entire pulse) normalized emittance was $26\ \pi\ \text{mm}\cdot\text{mrad}$. During emittance measurements in the vicinity of the temporal point corresponding to the current maximum ($\sim 1\ \mu\text{s}$ after the beginning of the pulse) this value did not exceed $16\ \pi\ \text{mm}\cdot\text{mrad}$. Experimental results show that at the accelerator exit we have converging electron beam. As there is a dependence of beam dimensions on the beam injection phase into the accelerating section we can make a conclusion that this phenomena is determined RF-focusing.

The beam characteristics were also studied in the photo-emission operation mode. During BaNi cathode irradiation at the wavelength 355 nm the gun produced pulsed current 2 - 2.5 A, with the pulse width 6 - 7 ns. At the accelerator output the pulsed current value was 1.3 - 1.6 A.

At present, an experimental research on wake-field excitation in plasmas of various density is carried out at the accelerator. Having this in view, an experimental device was assembled at the accelerator exit, including a coaxial plasma gun (plasma density being $10^{10} - 10^{16} \text{ cm}^{-3}$) and a diagnostic set for plasmas and the wake-field. The problem of in-vacuum separation between the accelerator part of facility and its plasma-relation portion was solved. Taking into account the fact that the beam has small dimensions (FWHM less than 1.5 mm), an extended collimator was placed at the accelerator exit (4 cm long, 4 mm in diameter), as well as auxiliary vacuum pump. First experiments on beam focusing during wake-field excitation in plasma by a succession of short electron bunches have been carried out on LIC and coaxial plasma gun [8].

CONCLUSIONS

Thus, NSC KIPT has built and put into operation a multipurpose accelerator facility for R&D purposes. Our simulations and experimental data allow to state that combination of an RF gun with the accelerating section operating at the 1-st spatial harmonic makes it possible to create injector accelerators with a high beam brightness. The subsequent research on particle dynamics in the accelerator should be continued in the direction of studies on the radial dynamics and clearing out the conditions to provide at the linac exit for intense beam production with the minimum emittance.

ACKNOWLEDGMENTS

We express our gratitude to the staff of "Accelerator" R&D Production Establishment of NSC KIPT for their invaluable help to the experiments. This work was partially supported by Ukrainian Department of Science, project no. 4/135-97

REFERENCES

- [1] M.I. Ayzatsky et al. "High Brightness Electron Linac with RF Gun and Accelerating Structure on Backward Wave", Proc. EPAC96, Vol.1., p.795-797.
- [2] M.I. Ayzatsky et al. "Two-cell RF Gun for a High Brightness Linac", Proc. EPAC96, Vol.2., p.1553-1555.
- [3] V.A. Kushnir and V.V. Mitrochenko "Simulation of Beam Performances of the Two-cell RF Gun", Proc. EPAC96, Vol.2, p.1414-1416.
- [4] M.I. Ayzatsky. ZhTF, 1995, Vol. 65, 6, p.153, (in russian).
- [5] M.I. Ayzatsky, E.Z. Biller, E.V Bulyak et al. Voprosy atomnoi Nauki i Tekniki, VANT: series, Nuclear Physics Research (Theory and Experiment), 1991, 3(21), pp. 16-18, (in russian)
- [6] L.A. Makhnenko, V.L. Parhomov, K.N. Stepanov. ZhTF, 1965, Vol. 35, 4, p.618, (in russian)
- [7] M.I. Ayzatsky, E.V Bulyak, V.I. Kurilko. Proc. 12 th AU-Union Seminar on Charged Particle Accelerators, Dubna, 1992, vol. 1, p. 412, (in russian)
- [8] I. Onishchenko, YA. Fainberg, M. Ayzatsky et al. "Focusing of Relativistic Electron Bunches at the Wake-Field Excitation in Plasma, Proc. PAC'97

STUDYING THE ELECTRON BEAM CHARACTERISTICS OF MAGNETRON INJECTION GUNS WITH A METAL SECONDARY EMISSION CATHODE¹

M.I. Ayzatsky, A.N. Dovbnya, P. I Gladkikh, V.V. Zakutin, V.A. Kushnir,
V.V. Mitrochenko, N.G. Reshetn'yak, V.P. Romas'ko, V.F. Pokas, Yu.D. Tur

*National Science Center, Kharkov Institute of Physics & Technology,
1 Akademicheskaya st., Kharkov, 310108, Ukraine*

ABSTRACT

The problem of extending the life-time, of increasing the pulse and average power of many RF-sources is closely related to the design of their electron guns. As it is known, the magnetron injecting guns with secondary emission metallic cathodes (SEMI) are specified by the high current emission density and long life-time. The main goal of these investigations is to determine the advantages and limitations of using SEMIGs as the electron source in high-power RF devices and accelerator injector systems. At this stage we have studied some questions concerning the operational beam stability, voltage and current increasing. The experiments have been performed by using the experimental setup to investigate SEMIG linear electron beam parameters from single and multiple beams gun assemblies with the anode voltage up to 100 kV, pulse duration up to 10 μ s, repetition rate 50 Hz and 0.1-0.2 T magnetic field strength. Pulse-to-pulse long-term stability of the annular electron beams (internal diameter nearly equal to the cathode diameter, wide of ring 1-2 mm (wavelength of cyclotron oscillations)) with beam density up to 70 A/cm² (10^{10} - 10^{11} e/cm³) have been achieved. It is shown, that the cathode diameter extension provides a proportionate increasing of the beam current, and in the case of multiple beam gun assemblies we have separate identical electron beams with the similar parameters of single-beam gun.

INTRODUCTION

A task of creating the long lived, high-energy electron sources is one of the main problems in the acceleration engineering. As it was shown earlier [1, 2] the so-called secondary-emission magnetron guns (SEMIG) with cold metal cathodes are specified by a high beam density, high lifetime and instantaneous operation readiness. On our opinion the guns of such a type are highly promising for the use in RF-sources and accelerators, in particular, in multybeam and cluster klystrons [3, 4] as well as in high-current injector systems, for example, in the installation such as RK TBA [5], CESTA TEST FACILITY [6] and ion accelerators driving ring electron beams [7].

The present paper continues the experimental study of characteristics of such guns. We studied the current-voltage and spatial characteristics, conditions of beam generation and stability. The amplitude modulation of the emission current in the variable electric fields was investigated. Presented are the results of studies concerning the multybeams systems and considering the possibility to increase the output current amplitudes by changing the geometrical dimensions of guns.

¹ This work was supported by STCU (project #432)

DESCRIPTION OF FACILITIES

Constructionally SEMIG represents a coaxial structure with a copper inner rod being the cathode and a more extended external cylinder placing the role of the anode placed in the solenoid providing the longitudinal magnetic field. Experimental studies have been carried on the test setup comprising:

- i) the high-voltage pulse modulator of a linear type capable to change the pulse shape (duration 2-10 μ s, repetition rate 10-50 Hz, pulse voltage 20-100 kV);
- ii) the focusing solenoid providing the magnetic field strength up to 0.25 T with a unhomogeneity in the longitudinal direction no more than 8%;
- iii) the vacuum system which gives a vacuum not worse than 10^{-7} Torr;
- iv) the indication system i.e. the pick-up of pulse current and voltage of modulator, the Faraday cup with the calorimetric measurer of the beam power located at a distance of 70 mm from the anode section; photometry system for control of the transversal characteristics of the linear electron flow.

EXPERIMENTAL RESULTS

We have carried out the study of beam characteristics for separate SEMIG's with cathode diameters in the range from 5 to 80 mm, anode diameters from 26 to 100 mm, electrode length from 40 to 100 mm. The guns and beams parameters are presented in Table 1. The measurement were also performed for parameters of the multybeam system consisting of six SEMIG disposed is a circle of a radius 30 mm, every of them have had a cathode diameter 5 mm, an anode diameter 26 mm.

Table 1

d, mm	D, mm	U, kV	I, A	B, T
5	26	32	14	0.19
5	50	60	1	0.14
5	50	10	10	0.20
5	78	26	0.6	0.04
16	26	10	6	0.16
16	50	17	5	0.06
40	50	30	50	0.23
80	100	19	8	0.11

The characteristic oscillograms of the voltage pulse on the cathode and beam current on the Faraday cup are given in Fig. 1. As in the case when the outer generator is used, the beginning of the secondary-emission process, and respectively, of SEMIG operation as a source of the linear electron flow, coincides with the fall time of the burst on the high-voltage pulse. The minimum rate for voltage decrease of the plane pulse part up to 100 kV is 20 kV/ μ s. The increase of a steepness up to 50 kV/ μ s does not change the amplitudes of the resulting current, and the change of a burst time in a wide range (from 0.1 to 10 μ s) has no effect on the beam characteristics. A comparison of the current in the system with the current amplitude on the Faraday cup shows that in all the cases these values are close. The current voltage characteristic of SEMIG's conforms so the "low 3/2" (see Fig. 2).

The investigation of the gun operation stability dependency on the interpulse stability of the anode voltage has shown that in the constant magnetic field the beam formation retains in the range of amplitude application $\pm 5\%$ of the nominal value. The intrapulse voltage instability can also lead to the break-down of secondary-emission processes (see the oscillogram in Fig.3) due to the incident electron energy decrease

below the critical value of moment of the field strength increase in time. The use of this effect in our experiments allowed us to attain the full amplitude modulation of the emission current at frequencies up to 1 MHz (see Fig. 4).

Also studied were the characteristics of electron flows from SEMIG's with different electrode diameters. In particular, Fig. 5 represents the beam current change as a function of the cathode diameter increase. The measurements were performed at voltage 24 kV for the anode-cathode gap space in coaxial guns 5 and 20 mm (the curves 1 and 2, respectively). The analysis of these characteristics enables one to confirm that when the values of longitudinal and transverse components of electric field do not change the output current increases proportionally to the area of the cathode emitting surface.

The investigations of the ensemble consisting of a number of SEMIG's located in the field of a common solenoid and energised from the one and the same

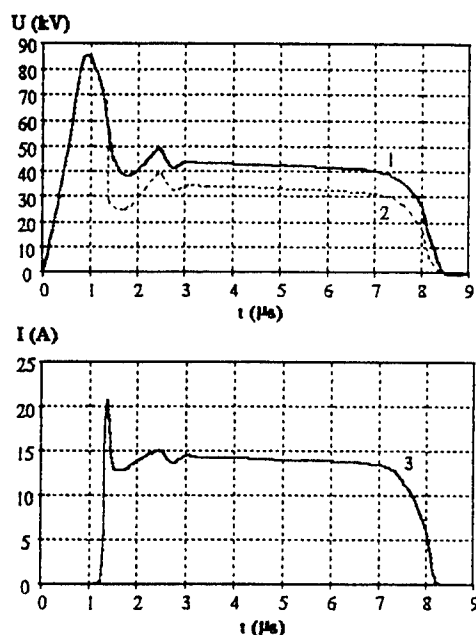


Fig. 1 - Oscillograms of pulses (1 - voltage of free running modulator, 2 - with beam generation, 3 - current of the beam).

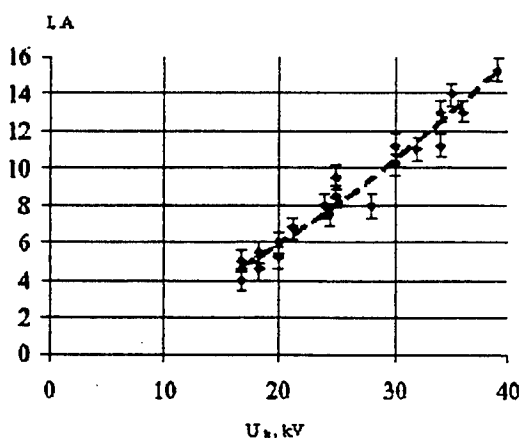


Fig. 2 - The beam current vs. anode voltage

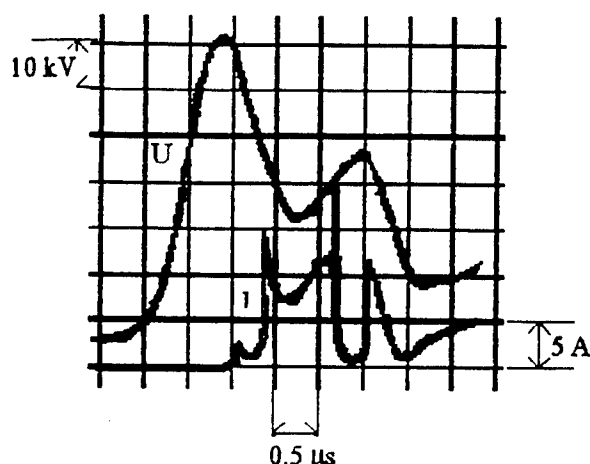


Fig. 3 - The beam current and the anode voltage

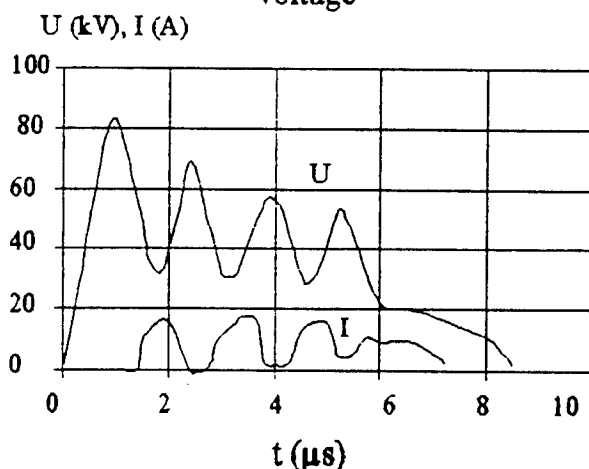


Fig. 4 - Oscillograms of pulses (U - anode voltage, I - current from Faraday cup).

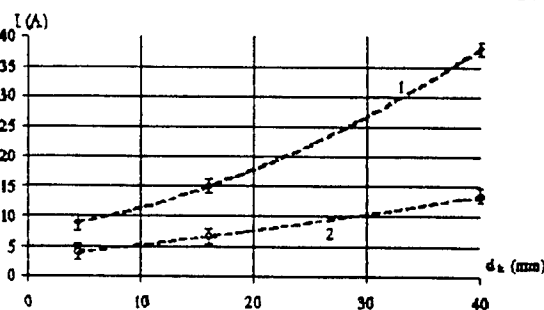


Fig. 5 - The beam current vs. the cathode diameter.

high-voltage source have shown that in this case we possess a complex of independent flows with a similar parameters. The identical beams with the current 18 A each and the energy 40 keV was obtained in the ensemble of 6 SEMIG's located in the circle of the diameter 60 mm (cathode diameter 5 mm, anode diameter 26 mm). The recalculation shows that the beam density in such annular beams is equal to 70 A/cm². (10^{10} - 10^{11} e-/cm²).

CONCLUSIONS

The experimental research evidences that SEMIG's offer a means of obtaining the stable linear electron beams of a high intensity and can be used as electron sources for accelerators and RF-facilities. It is clear that the carrying out of further researches is necessary for a successive study of gun characteristics as well as peculiarities of such electron beams RF modulation. Namely these problems lay in the base of our program of researches.

REFERENCES

- [1] F.Skrowron: The Continuous-Cathode (Emitting-Sole) Crossed Field Amplifier - Proc. of the IEEE, v.61 (1973), No 3, pp. 330-356
- [2] A.N.Dovbnya et al.: Secondary Emission Magnetron Injection Gun as High Current Durable Electron Source - Proc. of 1994 Pulsed RF Source for Linear Colliders Workshop (RF'94), October 1994, Montauk, Long Island, New York., AIP Conference proceeding 337, 1995, p. 350-359
- [3] R.B.Palmer et al.: An Immersed Field Cluster Klystron - Particle Accelerators, v.30 (1990), pp.197-209
- [4] R.B.Palmer et al.: Status of the BNI - MIT - SLAC Cluster Klystron Project - Proc. of 1994 Pulsed RF Source for Linear Colliders Workshop (RF'94), October 1994, Montauk, Long Island, New York., AIP Conference proceeding 337 1995, p.12
- [5] G.A.Westenskow et al.: Relativistic Klystron Two-Beam Accelerator - IEEE Transaction on Plasma Science, Special Issue on High Power Microwave Generation, 22(5), pp. 750-755, (Oct. 1994)
- [6] I.Wilson for the CLIC Study group: CLIC Test Beam Facilities-Status and Results - Proc. of the XVIII Int.Linear Accel. Conference, Geneva, 1996, v.1, pp.552-557
- [7] Sarantsev V.P. et al. Kollektivnoe uskorenie ionov elektronnymi koltsami, M., Atomizdat, 1979 (in russian).

INFLUENCE OF ELECTRONS REFLECTED FROM TARGET ON OPERATION OF DIODE AND TRIODE ELECTRON SOURCES

V.Engelko², V.Kuznetsov², G.Mueller¹, G.Viazmenova²

1- *Forschungszentrum Karlsruhe, INR, Postfach 3640, D-76021 Karlsruhe, Germany*

2- *Efremov Institute of Electrophysical Apparatus, 189631, St. Petersburg, Russia*

Abstract

When an electron source and a target are immersed in an external magnetic field electrons reflected from a target do not disappear but move along magnetic force lines to the source region where they are rereflected back to the target by the source electric field. Penetration of reflected electrons into the source can lead to distortion of the source electric field and through this to change of the limiting current density emitted by a cathode. Results of calculations of the limiting current density in the diode and triode schemes of an electron source in the presence of reflected electrons are presented. Density of the space charge of reflected electrons was calculated taking into account their real energy distribution obtained by means of Monte - Carlo simulation. It was found that penetration of reflected electrons in the diode can decrease essentially the limiting current density. When electrons are reflected with the same energy the maximum lowering of the current density is as much as 3 for reflection coefficient $k=1$ and 2 for $k=0.5$. Real lowering of the current density for tungsten target is 1.5. Results of calculations are in a good agreement with experimental data. The analysis performed shows that consideration of reflected electrons is necessary for correct calculation of the beam power density at the target and the distribution of the energy density deposited into the target.

Introduction

It is well known that the probability of reflection of fast electrons from a target being irradiated depends on charge number of a target material and for heavy materials can be rather high. For example, for tungsten it is close to 50 % . If irradiation of a target is performed without an external magnetic field, preventing the transverse motion of reflected electrons, then they leave a target going to the wall of a transport channel or vacuum chamber. So, in this case reflection of electrons influences on the current, flowing through the target and on the energy transferred to the target by electron beam, because the part of them is taken away by reflected electrons. In the case of intense electron beams an external magnetic field is used frequently for their transportation to the target. This field prevents the motion of reflected electrons in the transverse (relatively to the field) direction . Therefore, electrons moving along magnetic force lines achieve the region of an electron source where they are reflected back by the source electric field. Penetration of reflected electrons into the source can lead to distortion of the electric field in it and through this to change of the limiting current density emitted by a cathode. The influence of reflected from a target electrons on the current of an electron beam produced by a coaxial magnetically insulated diode was considered in [1]. Having took into account the angle spread of reflected electrons authors found from calculation that reflection of beam electrons with the probability of 50% leads to decrease of 40 % of the beam current. Despite the fact that the experimentally observed decrease of the beam current is smaller than that theoretically predicted the results obtained in [1] confirms that the influence of reflected electrons on the operation of

electron sources and on the energy delivered to a target can be significant. This is very important when an electron beam is used for modification of the surface of materials. Presently two types of electron sources are used for production of intense pulsed electron beams for modification of materials: diode and triode. Triode electron source is used, for example, at the GESA facility [2]. In order to estimate the extent of the influence of reflected electrons on the limiting emission current density for these schemes of an electron source we performed the calculations taking into account both the energy and angle distributions of reflected electrons. Results of these calculations are given below.

Method of calculation

Diode. Let us consider the diode, consisting from two flat electrodes - cathode and anode. A magnetic field is perpendicular to the surface of electrodes. As usual to determine the limiting emission current density we will use the Poisson equation with zero boundary conditions at the cathode surface

$$\frac{d^2 U}{dz^2} = \frac{\rho_1}{\epsilon_0} + 2 \frac{\rho_2}{\epsilon_0}, \quad (1)$$

$$U(0) = U'(0) = 0,$$

$$U(d) = U_a,$$

where ρ_1 and ρ_2 are the density of the space charge of primary and reflected electrons correspondingly, U is the potential, d is the interelectrode gap, ϵ_0 is dielectric constant. Space charge of reflected electrons is considered doubly, because they move twice through each cross-section inside the diode.

As usual the density of beam electrons is connected with their current density j_1 through the relation

$$\rho_1 = \frac{j_1}{\sqrt{\frac{2e}{m} U}}, \quad (2)$$

where e and m are the electron charge and mass correspondingly.

Having integrated the equation (1) one can obtain the following expression for the limiting current density in the presence of reflected electrons

$$j_1 = \frac{1}{2} \epsilon_0 \sqrt{\frac{2e}{m}} M \frac{U_a^{3/2}}{d^2}, \quad (3)$$

where parameter M is determined by the energy distribution of reflected electrons through the following relations

$$M = \left[\int_0^1 \frac{d\varphi}{\sqrt{F_1(\varphi)}} \right]^2; \quad F_1 = 2\varphi^{1/2} + \frac{2k}{C_0} \int_0^\varphi F_{01}(\varphi) d\varphi;$$

$$F_{01}(\varphi) = \int_{1-\varphi}^1 \frac{\frac{dj_2}{d\varepsilon} d\varepsilon}{\sqrt{\varepsilon - (1-\varphi)}}; \quad C_0 = \int_0^1 \frac{dj_2}{d\varepsilon} d\varepsilon, \quad (4)$$

where $\varepsilon = E_0/(E_0)_{\max} = U_0/U_a$; E_0 is initial energy of reflected electrons; $\varphi = U/U_a$; $dj_2/d\varepsilon$ is the energy distribution of reflected electrons.

Triode. In the case of the triode scheme of an electron source the method of calculation is the same but now Poisson's equation has to be solved separately for two gaps: cathode-grid and grid-anode. We will consider here the special type of the triode in which the grid and anode are connected through the resistor R . In this case the grid potential depends on current to the grid and on the magnitude of R . Therefore one can control the grid potential (and through this the limiting current density) simply by means of the change of the resistor magnitude.

It is known that in general case the distribution of the potential in the grid-anode gap can have a minimum which magnitude U_m is less than the grid potential U_g . It is clear that if the potential distribution has such form then the distribution of the space charge of reflected electrons in the cathode-grid gap is sensitive to U_{\min} (or φ_{\min}) because the region with $\varphi < \varphi_m$ can be achieved by reflected electrons initial energy of which ε is not less than $1 - \varphi$, but the region with $\varphi_m < \varphi < \varphi_g$ is achievable for electron with $\varepsilon \geq 1 - \varphi_m$. Taking this into account we can write the following set of equations for determination of the limiting current density in the triode

$$\frac{d^2 \varphi}{dz^2} = \frac{1}{\varepsilon_0 \cdot U_a} (\rho_1 + 2\rho_2), \quad (5)$$

$$1 - \varphi_g = \nu_R \cdot j_1(\varphi_g, \varphi_m) \cdot S_k \cdot R / U_a, \quad (6)$$

$$\varphi(0) = \varphi'(0) = 0, \quad \varphi(d_{cg}) = \varphi_g, \quad \varphi(d) = 1. \quad (7)$$

Here: $\nu_R = (1 - \alpha + k\alpha \cdot k_m - k\alpha^3 \cdot k_m)$ - is the coefficient accounting the current to the grid of both primary and reflected electrons, S_k - is the cathode area, α - is the grid transparency, k_m - is the coefficient, determining the part of electrons passed through φ_m and penetrated into the cathode-grid gap.

After integration one can find the dependence of the limiting current density j_l on φ_g and φ_m :

$$j_1 = \frac{1}{2} \varepsilon_0 \sqrt{\frac{2e}{m}} M_1(\varphi_g, \varphi_m) \frac{U_a^{3/2}}{d_{cg}^2}, \quad \text{where } M_1(\varphi_g, \varphi_m) = \left[\int_0^{\varphi_g} \frac{d\varphi}{\sqrt{F_{11}(\varphi, \varphi_m)}} \right]^2, \quad (8)$$

$$F_{11} = \begin{cases} 2\varphi^{1/2} + \frac{2k\alpha^2}{C_0} \int_0^{\varphi} F_{01}(\varphi) d\varphi, & \text{for } 0 < \varphi < \varphi_m, \end{cases} \quad (9a)$$

$$F_{11} = \begin{cases} 2\varphi^{1/2} + \frac{2k\alpha^2}{C_0} \int_0^{\varphi} F_{01} d\varphi + \frac{2k\alpha^2}{C_0} \int_{\varphi_m}^{\varphi} F_{02} d\varphi, & \text{for } \varphi_m < \varphi < \varphi_g \end{cases} \quad (9b)$$

$$F_{02} = \int_{1-\varphi_m}^{\varphi} \frac{dj_2}{d\varepsilon} \frac{d\varepsilon}{\sqrt{\varepsilon - (1-\varphi)}}, \quad M_2(\varphi_m) = \left[\int_{\varphi_m}^{\varphi_g} \frac{d\varphi}{\sqrt{F_{12}(\varphi, \varphi_m)}} \right]^2, \quad M_3(\varphi_m) = \left[\int_{\varphi_m}^{\varphi_g} \frac{d\varphi}{\sqrt{F_{13}(\varphi, \varphi_m)}} \right]^2 \quad (10)$$

The magnitudes of j_l , φ_g and φ_m are determined from equations (6), (8) and (11)

$$d_{ga} = z_{ga}(\varphi_m) = \left[\frac{1}{2} \varepsilon_0 \sqrt{\frac{2e}{m}} \frac{U_a^{3/2}}{j_1(\varphi_m)} \right]^{1/2} \cdot (M_3^{1/2}(\varphi_m) + M_2^{1/2}(\varphi_m)). \quad (11)$$

If φ_m is absent than F_{11} is determined by (9a), j_l and φ_g can be obtained from (6), (8).

The angle distribution of reflected electrons can be described accurately by the function $\cos\theta$ for various materials [3]. Taking this into account one can refine the expressions for F_{01} , F_{02} , F_{03} .

$$F_{01}(\varphi) = \frac{\pi}{2} \int_{1-\varphi}^1 \frac{dj_2}{d\varepsilon} \frac{d\varepsilon}{\varepsilon^{1/2}}, \quad F_{02}(\varphi) = \int_{1-\varphi_m}^1 \frac{\frac{dj_2}{d\varepsilon} \arcsin \left[\frac{\varepsilon - (1-\varphi_m)}{\varepsilon - (1-\varphi)} \right]^{1/2} d\varepsilon}{\varepsilon^{1/2}}, \quad F_{03}(\varphi) = \frac{\pi}{2} \int_{1-\varphi}^{1-\varphi_m} \frac{dj_2}{d\varepsilon} \frac{d\varepsilon}{\varepsilon^{1/2}} \quad (12)$$

The expressions for $F_1(\varphi)$, $F_{11}(\varphi, \varphi_m)$, $F_{12}(\varphi, \varphi_m)$, $F_{13}(\varphi, \varphi_m)$, M , M_1 , M_2 , M_3 and j_1 are unchanged

Results of calculations

Calculations performed with the model energy distributions (uniform, linear, δ -function) showed that reflected electrons can decrease essentially the limiting current density of an electron source. For $k=1$ the maximum lowering of the current density is as much as 3 (energy distribution is δ -function). For $k=0.5$ the maximum value of this factor is 2.

Real energy distributions and reflection coefficients were obtained with the help of Monte-Carlo simulation. Calculations were performed for carbon and tungsten targets and for GESA facility conditions: $U_a=120$ keV, $d_{cg}=d_{ga}=6$ cm, $\alpha = 0.8$, $R = 580 \Omega$. The results are the following: for W: $j_1/j_0 = 0.68$, for C: $j_1/j_0 = 0.96$. Here j_0 is the limiting current density in the absence of reflected electrons. The lowering of the current density is practically the same for the diode and triode schemes of the electron source. Results of calculations are in a good agreement with the experimental data obtained at the GESA facility.

Conclusion

The influence of electrons reflected from a target in the presence of external magnetic field on the limiting emission current density in the diode and triode schemes of an electron source was analysed taking into account energy and angle distributions of reflected electrons. It was found that reflected electrons can decrease essentially the limiting current density of an electron source. When electrons are reflected with the same energy [the energy distribution is δ -function] the maximum lowering of the current density is as much as 3 for reflection coefficient $k=1$ and 2 for $k=0.5$. Real lowering of the current density for tungsten target is 1.5. This is in a good agreement with experimental observations. Results of calculations show that consideration of reflected electrons is necessary for correct calculations of the beam energy deposition into a target and for better understanding of electron sources operation.

References

- [1]. N.I.Zaitsev et al. Sov. J. Plasma Phys. 8(5), Sept.-Oct. 1982, p.515.
- [2]. G.Mueller et al. Proc.11-th Int. Conf. High Power Particle Beams, Prague, 1996, vol.1, p.267.
- [3]. R.W.Dressel, Phys. Rev. **144**, 332 (1962).

GENERATION OF UNIFORM PLASMA EMITTERS IN DISCHARGES WITH A MAGNETIC FIELD

S. P. Nikulin, S. V. Kuleshov

*Institute of Electrophysics, Russian Academy of Sciences
Komsomol'skaya 34, Ekaterinburg, 620049, Russia*

Development of sources for generation of beams with largely different dimensions encounters special and even opposite requirements with respect to the emitting plasma parameters. For example, in narrow beam sources extraction of charged particles is enhanced, as a rule, by producing a sharply nonuniform plasma having the maximum concentration near the emission aperture. For this purpose, special measures are taken in order to increase ionization in the said region and impede escape of particles therefrom. In particular, strong magnetic fields are often applied to improve the extraction efficiency. In the case of broad beam sources one of the main requirements consists in generation of a uniform plasma in the discharge system of the source. This problem seems to be solvable in quite the opposite way: refuse applying magnetic fields and provide a uniform ionization in the discharge chamber. In high-pressure discharges, when particles are lost through volume recombination, a uniform ionization indeed causes appearance of a uniform plasma having the concentration

$$n = \sqrt{G / \beta}, \quad (1)$$

where G is the number of ionizations per unit time in a unit volume and β is the recombination coefficient. However, the situation is largely different in low-pressure discharges, when particles are lost at the walls of the discharge chamber. A simultaneous analysis of ionization processes and motion of particles need be performed to determine conditions necessary for formation of a uniform plasma in these discharges. Results of such analysis are presented below. They show that under certain conditions a uniform plasma may be produced just in the presence rather than in the absence of a magnetic field.

Before analyzing conditions in various discharge systems with magnetic fields, consider the formation of the radial profile of plasma generated inside a long cylindrical electrode having the radius R under different conditions of ionization induced by an external source in the absence of a magnetic field. Assume that the space distribution of more mobile electrons obeys the Boltzmann law:

$$n_e = n_0 \exp\left(\frac{e\varphi}{kT}\right), \quad (2)$$

where n_e is the electron concentration; n_0 the concentration at the cylinder axis; e the electron charge; φ the potential; k the Boltzmann constant; T the electron temperature. Neglecting the pressure tensor, write the equations of continuity and motion of ions in simplified form:

$$\frac{n_i v_i}{r} + \frac{d(n_i v_i)}{dr} = G(r). \quad (3)$$

$$\frac{n_i v_i^2}{r} + \frac{d(n_i v_i^2)}{dr} = -\frac{en_i}{M} \frac{d\varphi}{dr}, \quad (4)$$

where n_i , v_i and M denote the concentration, mean velocity and mass of ions respectively. The equations (2)-(4) and the quasineutrality equation

$$n_e = n_i = n \quad (5)$$

were solved for two cases: 1) $G(r) = G_1 \sim \text{const}$, 2) $G(r) = G_2 r^2$. Proceeding from the assumption that quasineutrality is disturbed near the electrode only, it is possible to derive an analytical expression relating n and r as

$$\left(\frac{r}{R}\right)^2 = \frac{3\sqrt{3}}{2} \left(\frac{n}{n_0}\right)^{2/3} \left(1 - \left(\frac{n}{n_0}\right)^{4/3}\right) \quad (6)$$

for the first case and as

$$\left(\frac{r}{R}\right)^6 = \frac{7}{4} \left(\frac{7}{3}\right)^{3/4} \left(\frac{n}{n_0}\right)^{6/7} \left(1 - \left(\frac{n}{n_0}\right)^{8/7}\right) \quad (7)$$

for the second case. The concentration is maximum at the center of the system and decreases gradually towards the periphery. However, in the second case, when ionization is not uniform and occurs mainly in the near-electrode region, the concentration decreases more gently and plasma is nearly uniform in most part of the gap. Thus, to produce a uniform plasma in low-pressure discharges, one needs to provide a nonuniform ionization with a low probability at the center of the system and a high probability in the near-electrode region.

When plasma is generated not by an external source but in a self-sustained glow discharge, with a cylindrical electrode acting as the cathode, a nonuniform ionization with a high probability in the near-cathode region may be realized if a magnetic field, which impedes the escape of fast ionizing particles from this region, is applied. However, the magnetic field may largely limit the electron mobility, making the Boltzmann distribution invalid. Let us discuss the formation of the plasma profile in the inverse magnetron-type system comprising two coaxial cylindrical electrodes. Assume that the transport of electrons to the anode, which is represented by the internal electrode of the radius r_0 , is due to the drift and diffusion of electrons across the magnetic field:

$$n_e v_e = -D_e \frac{dn_e}{dr} + \mu_e n_e \frac{d\phi}{dr}, \quad (8)$$

where v_e , D_e and μ_e stand for the mean velocity, diffusion coefficient and mobility of electrons across a magnetic field. The continuity equation for plasma electrons has the form

$$\frac{n_e v_e}{r} + \frac{d(n_e v_e)}{dr} = G(r), \quad (9)$$

For the self-sustained discharge $G(r) = \nu_i n_f(r)$, where ν_i is the ionization frequency and n_f the concentration of fast electrons, which are emitted from the cathode as a result of γ -processes and acquire a high energy flying through the cathode region. Ionization due to plasma electrons is ignored. A weak electric field of the plasma affects little the motion of fast particles. These particles are transported across the magnetic field mainly through diffusion:

$$n_f v_f = -D_f \frac{dn_f}{dr}, \quad (10)$$

where v_f and D_f denote respectively the mean velocity and the diffusion coefficient of fast particles across a magnetic field. Upon relaxation, the square of the velocity of a fast particle changes from $2eU/m$ (U being the cathode potential fall nearly equal to the discharge voltage and m the electron mass) to about kT/m . Considering that $eU \gg kT$, the mean square of the velocity of fast particles may be assumed to be eU/m . Then we have the following expression for the diffusion coefficient:

$$D_f = \frac{eU}{3m} \frac{v_f}{\omega^2}, \quad (11)$$

where v_f is the effective collision frequency for fast electrons and ω is the Larmor electron frequency. Write the continuity equation for fast particles as

$$\frac{1}{r} \frac{d(rn_f v_f)}{dr} = -\frac{n_f}{\tau}, \quad (12)$$

where τ is the characteristic relaxation time for fast particles. This characteristic relaxation time may be expressed as

$$\tau = \frac{eU}{Wv_i}, \quad (13)$$

where W is the mean energy consumed for formation of a pair of charged particles when a fast particle is decelerated in the gas. The effect of the magnetic field on ions may be neglected and the equations of motion (4) and continuity (3) may be used in their previous forms. The quasineutrality equation (5) may also be used originally, because fast particles contribute little to the total concentration of electrons. By solving the set of equations (3)-(5), (8)-(10) and (12), it is possible to determine the intervals of pressures and magnetic fields, at which a self-sustained discharge is realized, and calculate the discharge operation voltage as a function of the magnetic induction B . The plasma concentration profiles can also be determined for different conditions. The shape of the dependences $n(r)$ is affected by both the value of the magnetic field and the gas pressure P . However, by and large, one may state that a strong magnetic field gives a sharply nonuniform distribution with a maximum concentration near the cathode. A nearly uniform distribution in most part of the gas-discharge gap is possible in a weak magnetic field. These results agree with experimental data obtained for electrode systems having different dimensions. Figure 1 shows radial dependences of the probe ion current for different magnetic fields. These dependences were registered using a cathode 50 cm in diameter and an anode 1 cm in diameter. The anode was shorter than the cathode and plasma could penetrate into the axial region between the anode and the end electrode being at the cathode potential.

Now let us consider the discharge in the Penning system, when a cylindrical electrode serves as the anode and end electrodes act as the cathode. Consider first an important particular case allowing for an analytical solution. Assume that no radial electric field is present and ions go to the cathodes along the magnetic field without displacement in the radial direction. The radial motion of both fast and plasma electrons is described by the previous equations, but the drift term is omitted in (9). The continuity equation remains unchanged for plasma electrons, but for fast electrons it becomes

$$\frac{1}{r} \frac{d(rn_f v_f)}{dr} = \frac{\gamma_i v_b}{L} - \frac{n_f}{\tau}, \quad (14)$$

where L is the spacing between the cathodes and $v_b = \sqrt{kT/M}$ denotes Bohm's characteristic velocity of ions leaving the plasma. The first term in the right-hand side describes formation of new fast particles as a result of the ion-electron emission. Under these assumptions and taking that the concentration of fast particles at the anode (which absorbs these particles) turns to zero, the radial plasma profile is

$$n = n_0 J_0(2.4r/R), \quad (15)$$

where J_0 is Bessel's function. The radial electric field is absent only when

$$P = P_0 = \frac{m\omega^2 R^2}{2.4^2 M L v_b v_{eo}}, \quad (16)$$

where v_{eo} is collision frequency for electrons at unit pressure. When $P < P_0$, a radial electric field arises and makes ions move to the center of the system. Calculations show that in this case the plasma concentration decreases in the radial direction more abruptly than predicted by the relationship (15) and turns to zero at $r < R$. Then an electron layer is formed near the anode.

When $P > P_0$, the electric field makes ions move to the periphery. The plasma concentration decreases more gently. However, even at high pressures that cannot be used in the sources the concentration gradient is relatively large. Thus, in the original Penning cell a uniform beam may be formed due to emission of particles from a relatively small axial region of the plasma. A nearly uniform plasma may be produced in most part of the discharge system, if special measures are taken to decrease ionization at the center of the system and/or increase ionization at the periphery of the system, as in the case with a cylindrical electrode functioning as the cathode. Ionization may be decreased at the center of the modified Penning system sketched in Fig.2, where one of the cathodes consists of the disk and the ring, the potential being applied to the disk is lower than potentials of the other cathodic elements. The increase in ionization at the periphery may be realized in the system illustrated in Fig.3, where additional particles are supplied from an auxiliary hollow-cathode discharge. Figure 4 shows radial profiles of the ion current in the Penning cell (curve 1) and in the modified Penning system sketched in Fig.3 (curve 2). It is seen that, indeed, the auxiliary discharge considerably improves the distribution and provides a nearly uniform plasma in a certain part of the discharge gap.

Our investigations show that at some conditions a uniform plasma may be generated in systems with magnetic field. Therefore these systems may serve as generators of broad beams.

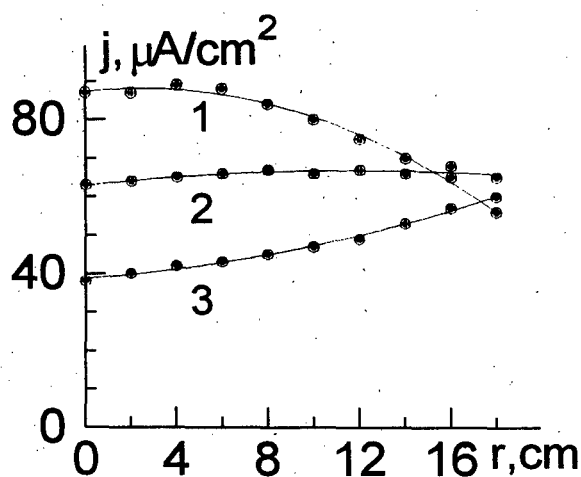


Fig 1. B(mT): 1 - 0, 2 - 2, 3 - 4.

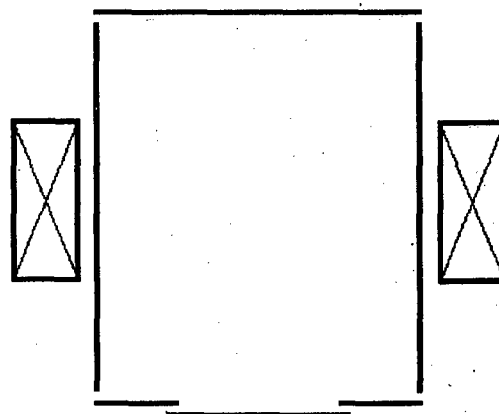


Fig. 2.

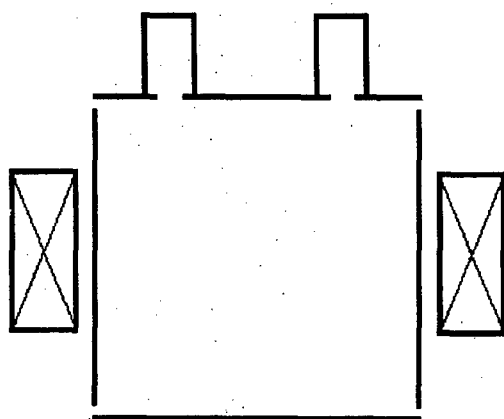


Fig.3

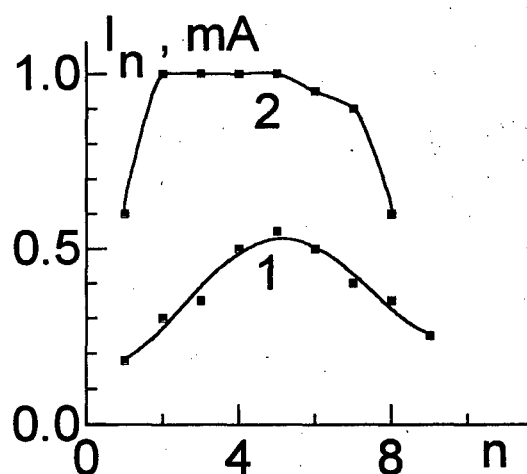


Fig.4

HOLLOW CATHODE ELECTRON GUN FOR BEAM GENERATION IN FOREVACUUM GAS PRESSURE

Viktor Burdovitsin¹, Efim Oks^{1,2} and Alexander Serov³

¹*State University of The Control Systems and Radioelectronics, 40 Lenin ave., Tomsk, 634050, Russia*

²*High Current Electronics Institute Russian Academy of Sciences, 4 Akademicheskoy ave., Tomsk, 634055, Russia*

³*Russian Research Center «Kurchatov Institute», 1 Kurchatov sq., Moscow, 123182, Russia*

Characteristics, performance and design feature of a filament less plasma cathode electron gun for beam generation in forevacuum gas pressure range are presented. The plasma cathode is based on hollow cathode dc discharge. Using method of "grid stabilization" it was possible to generate e-beam under the background gas pressure as high as about 10^{-1} torr. This pressure can be easily obtained by the only mechanical pump. Presence of a magnetic field is one of the requests for several applications, such as plasma chemistry and surface treatment processes. So operation of the gun under the B-field up to 0.1 T was investigated. It was observed an influence of the B-field both on discharge and emission parameters of the gun. The results obtained can be explained based on idea of electron confinement by magnetic field and its motion across the B-field. With the accelerating voltage up to 8 kV the gun is able to generate of about 0.7 A dc electron beam.

I. INTRODUCTION

For a number of electron beam applications such as e-beam welding, surface treatment and plasma chemistry it is important to have the beam in forevacuum pressure range (10 - 100 mtorr), that can be reached by the only mechanical pumps.

Under so high pressure a conventional e-gun based on hot filament (thermionic emitter) has a short lifetime. With this kind of electron emitter to generate the beam under relatively high pressure one needs to create a pressure drop at least two orders of magnitude between beam generation and beam application areas. This requests a long beam line separated by differential pumping. The problem becomes even worse in presence of aggressive gas media. One of the methods to solve this problem connects to using a plasma cathode electron source - a device based on electron extraction from plasma, that is generated in low pressure filamentless discharge system [1-4]. Absence of the hot electrodes is one of the main advantages for plasma cathode electron sources, making them possible to generate electron beam in residual gas pressure of tens millitorrs [5,6].

In this paper we report a schematic view and results of investigation of plasma cathode electron gun, which is based on hollow cathode glow and is able to produce dc electron beam in the forevacuum pressure range.

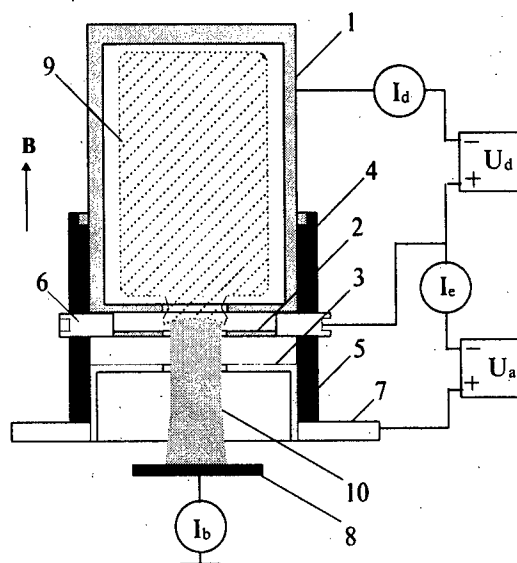
II. EXPERIMENTAL ARRANGEMENT

The electrode configuration of the plasma cathode e-gun (Fig.1) consists of a 50 mm diameter, 100 mm length hollow cathode 1, plane anode 2 and electron extractor 3.

The hollow cathode bottom has a centric hole, in experiments its diameter was either $d_c = 16$ mm or 25 mm. Electrons are extracted from the plasma surface through the anode hole of $d_a = 16$ mm. The extractor hole has the same diameter ($d_e = d_a$), and accelerating

gap of the gun is 10 mm. The hollow cathode 1 was made from stainless steel, anode 2 and extractor 3 – from copper. There are also ceramic insulators 2,5 and air cooling system. To produce a longitudinal magnetic field (up to 0.1 T) a solenoidal coil is used.

A vacuum vessel with e-gun was pumped up to $p = 1$ mtorr. The only mechanical pump was used to obtain such pressure. There were not in experiments special gas feeding to the gun, to increase the pressure the gas was adjusted by variation of the gas flow exactly to the vessel. Maximum operation pressure for e-gun was as high as about 100 mtorr. Two dc power supplies – 1 kV, 1 A and 10 kV, 1 A were used for discharge and beam respectively. Connections of the electrical outputs of the power supplies to the gun electrodes are also shown in Fig.1. There were measured in experiments discharge I_d , total emission I_e and beam I_b currents, as well as discharge voltage U_d . To measure I_b a Faraday cup was used. The cup was located at the axis 5 cm or 40 cm far from the accelerating gap. There was no special discharge triggering, to ignite the discharge the pressure in the vessel was temporary increased.



1 - hollow cathode, 2 - anode, 3 - extractor, 4,5 - insulators, 6 - keeper, 7 - flange, 8 - collector, 9 - plasma, 10 - electron beam

Fig. 1. The scheme of electron gun

III. RESULTS AND DISCUSSION.

Differences in electrode configuration of discharge (hollow cathode) and extraction (plane) systems lead to high effective ionization in discharge area and, at the same time, its low rate in the extraction gap. That give us possibility both to produce dense emission plasma in the hollow cathode and to prevent electrical break-downs in the extraction area. That is why we get accelerating electron beam in forevacuum pressure range.

Because of presence a magnetic field in beam treatment area, the main task of experiments, reported here, was investigation of the magnetic field influence on discharge and beam parameters, especially under the maximum possible

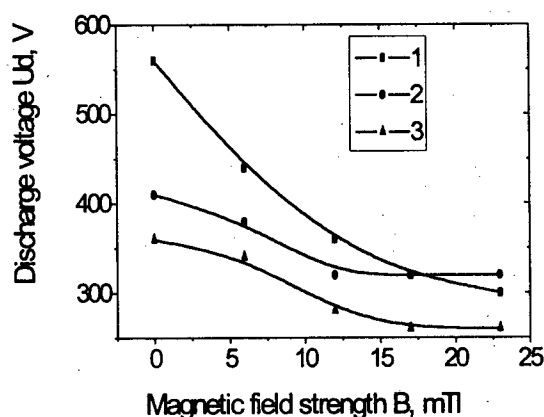


Fig. 2. The dependence of discharge voltage U_d on magnetic field B at gas pressures: 1- 10 mtorr, 2 - 36 mtorr, 3 - 60 mtorr. $U_a = 4$ kV, $I_d = 200$ mA.

value of the gas pressure. As followed from experiments the magnetic field makes essential changes both on discharge and emission features of the e-gun. Increase of magnetic field strength provided falling of the discharge voltage U_d (Fig.2). One can see from this picture the lower pressure the stronger influence of the magnetic field.

This result may be explained due to more

losses of high energetic electrons, which under the low pressure are able to leave the hollow cathode without spending their energy for ionization. Magnetic field confines electrons, rising their oscillations inside the hollow cathode and thus provides higher ionization rate. This provides low value of the U_d .

Emission properties of the e-gun with magnetic field depend on ratio d_c/d_a . With $d_c = d_a$, we did not observe any essential influence of the magnetic field on the emission current I_e (Fig.3.a), but the situation had changed if $d_c > d_a$. In the last case increase of the B-field reduced I_e (see also Fig.3.a). As for beam current I_b , magnetic field had influences on both cases, but more efficiently when $d_c > d_a$ (Fig.3.b). Difference in emission

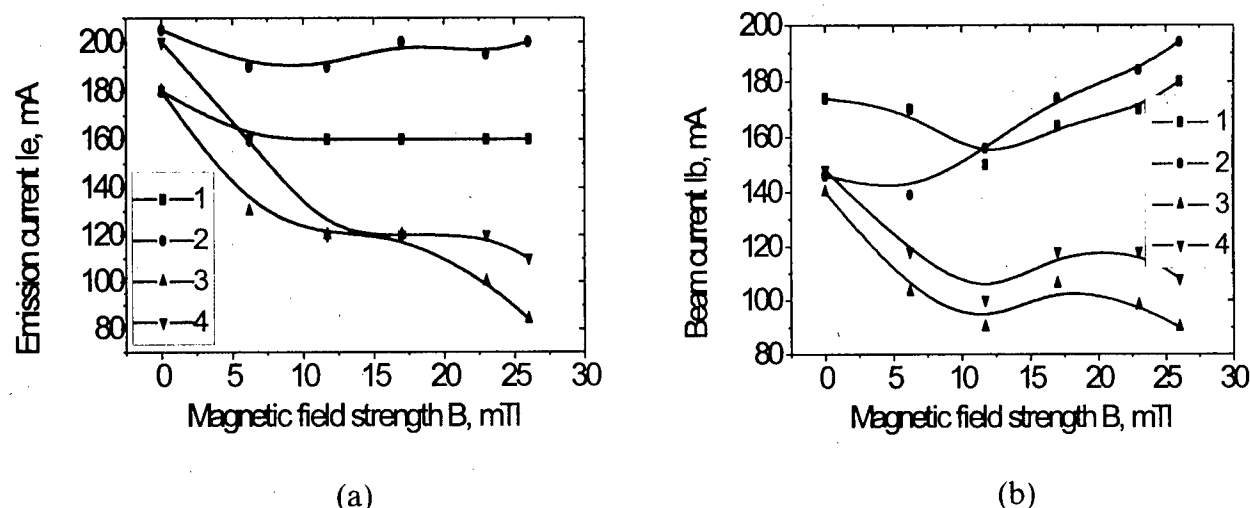


Fig. 3. The dependence of emission current I_e (a) and beam current I_b (b) on magnetic field. Gas pressure $p = 8$ mtorr (1,3); 22 mtorr (2,4). 1,2 - cathode and anode holes are equaled ($d_c = d_a$); 3,4 - $d_c > d_a$. $U_a = 4$ kV, $I_d = 200$ mA.

properties may be connected to confining the plasma electron by magnetic field. Without B-field, the electrons from any place are able to move in emission hole, but with the field electrons, leaving the hollow cathode can follow just along of the B-field lines. Therefore for case, when $d_c > d_a$, part the magnetic lines located in the cathode hole, cross also anode surface, that leads to losses of the electrons on the anode and thus to decrease of the emission current. If $d_c = d_a$, the magnetic lines from the cathode hole do not cross the anode surface and so magnetic field does not influence on the I_e . Behavior of the electron beam current with magnetic field is mostly consequence of influence the magnetic field on emission current [7]. Under the approximately constant value of the emission current we observed weak enhancement of the beam current with the magnetic field (Fig. 3b). It may be connected to less beam losses because of electron beam confining in B-field. One can see from Fig. 3, the higher pressure the more emission and beam currents. In our opinion, it is a result of increase the plasma density in the emission hole because of more effective ionization processes.

Maximum values of the beam current are also determined by magnetic field. Fig.4 presents dependencies of the beam current I_b on the discharge one I_d under different values of magnetic field. As follows from this picture there is an optimum of I_{dmax} when I_b

reaches a maximum value. Magnetic field moves I_{dmax} towards higher values. Beam current follows I_{dmax} . The same tendency can be observed with decrease of the pressure. In any cases higher discharge current, providing more plasma density, should lead to proportional increase of emission current. For the beam current this influence is not obvious, because of electrons losses on the extractor electrode. Due to penetration of the emission plasma into accelerating gap with enhancement of the plasma density resulting configuration of accelerating electrical field may provide defocusing of the beam and essential losses of the electrons. Magnetic field is able to prevent this negative influence by confining the electrons. With higher pressure because of more collisions between electrons and atoms influence of magnetic field becomes weaker.

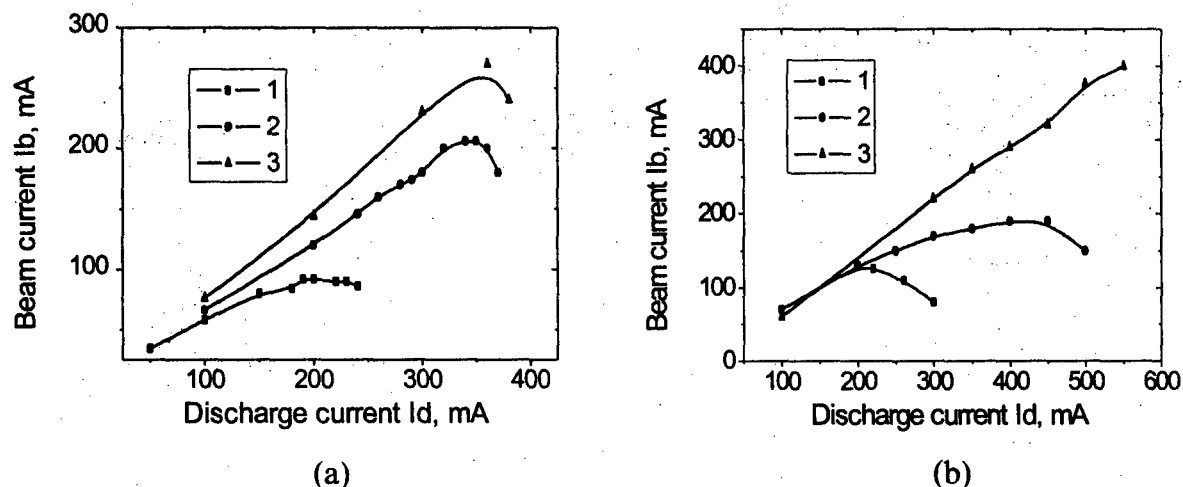


Fig. 4. The dependence of beam current I_b on discharge current I_d for gas pressures $p = 60$ mtorr (a), 10 mtorr (b) and for magnetic fields $B = 0$ (1), 6 mTl (2), 17 mTl (3). $U_a = 4$ kV.

Under accelerating voltage of 8 kV, gas pressure up 60 mtorr the e-gun produced the beam current as high as 700 mA. The beam was successfully transported in magnetic field on a distance of about 1.5 meters without any essential losses.

Authors are thankful to P.M. Schanin and A.A. Ivanov for support of this work.

REFERENCES

1. Yu.E. Kreindel. *Plasma cathode electron sources*. Moscow: Energoatomizdat. 1977. (in Russian).
2. A. Chagin., E.Oks. and P. Schanin. // Proc. of 8th Intern. Conf. on High Power Particle Beams, "Beams-90", USSR, Novosibirsk, 1990. V.2. P.866.
3. N.V.Gavrilov, N.N.Koval, Yu.E.Kreindel, E.M.Oks and P.M.Schanin. // Nuclear Instrum. And Methods in Physical Research. 1992. A312. P.417.
4. E.M.Oks. // Plasma Sources Sci. Technol. 1992. V.1.P.249.
5. S.I. Beliuk, Yu.E. Kreindel and N.G.Rempe. // Sov.Phys. Techn. Phys. 1980. V.50, № 1, P.203.
6. A.Mytnikov, E.Oks, A.Chagin // Pribori i Technika Experimenta. 1998. No.2. (in Russian).
7. A. Hershcovitch // Appl. Phys. Lett. 1996. V.68. P. 464.

ELECTRODYNAMICS OF THE PLASMA-FILLED INVERTED CHAIN OF COUPLED CAVITIES

A.N.Korostelev, I.N.Onishchenko, G.V.Sotnikov

NSC "Kharkov Institute of Physics and Technology"
Kharkov 310108 Ukraine

Abstract

The electrodynamics of the inductively coupled cavities blown round by a tubular electron beam and filled with plasma has been theoretically investigated. The dispersion equation is derived. The topography of the fields and HF-power flow distribution is investigated. The interaction of the electron beam with the structure of this type is considered. The amplification factor is obtained and efficiency estimation is made.

1. INTRODUCTION

In previous paper [1] the inverted chain of cavities (i.e. beam propagates outer the cavities, but non-near the axis) was investigated as a perspective slow wave structure for high-power devices. Because in this case the excited HF-power flow propagates through the region, where both electron beam and plasma are placed, beam and plasma disturbance by strong HF-fields limits the power level. To avoid it in the considered structure the cavities are proposed to couple inductively by the slits so that the HF-power flow can propagate mainly through the cavities. Such plasma filled inverted chain of inductively coupled cavities was called PICICC. Besides of advantages of the inverse structure [1] providing a high level of power generation due to large cross-section of the beam and broad band caused by the coaxial type, proposed PICICC structure allows also to separate the places of beam-structure interaction and excited HF-power propagation and to avoid the beam and plasma distortion, leading to the low saturation level. The paper consists of three parts. In the first part the dispersion equation is being derived. The second one is devoted to field's topography and HF-power flow distribution over the cross-section of the

structure. The last part represents the interaction of the electron beam with eigenmodes of the PICICC structure.

2. DISPERSION EQUATION

The eigenmodes problem for the PICICC structure depicted in Fig.1 was solved by method of partial regions [2] and taking into account the Meixner condition for electrostatic peculiarity near the edge of the disk [3]. The theory of the slit antenna [4] was used for the obtaining of the change of the cavity fields caused by the slit and for finding the slit field itself.

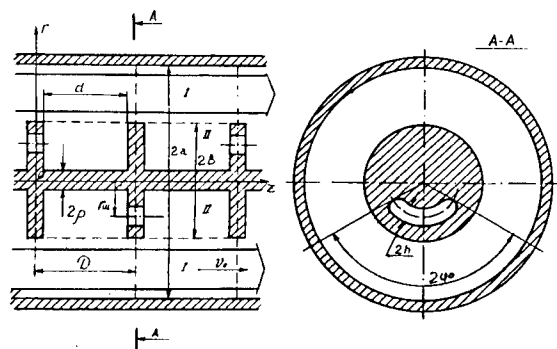


Fig.1 Inverted chain of inductively coupled cavities.

The dispersion equation was derived by field matching at the boundary between region I and II including the influence of the slit.

It has the following view

$$\begin{aligned}
 & k\varepsilon_3 \cdot \sum_m \frac{J_0(\beta_m \frac{d}{2})}{\tau_m} \cdot \frac{2\text{Sin}(\beta_m \frac{d}{2})}{\beta_m d} \times \\
 & \times \frac{J_1(\tau_m b) \cdot N_0(\tau_m a) - N_1(\tau_m b) \cdot J_0(\tau_m a)}{J_0(\tau_m b) \cdot N_0(\tau_m a) - N_0(\tau_m b) \cdot J_0(\tau_m a)} = \\
 & = \frac{J_1(kb) \cdot N_0(k\rho) - N_1(kb) \cdot J_0(k\rho)}{J_0(kb) \cdot N_0(k\rho) - N_0(kb) \cdot J_0(k\rho)} - \\
 & - \frac{J_0(kr_u) N_0(k\rho) - N_0(kr_u) J_0(k\rho)}{J_0(kb) N_0(k\rho) - N_0(kb) J_0(k\rho)} \times \\
 & \times \frac{4\alpha}{kd} \cdot \text{Sin}^2(\beta_0 \frac{D}{2}) \cdot [\lg(\chi_u \rho_0) - \chi_u \rho_0] \times \\
 & \times \left\{ \frac{1}{kb \cdot \lg(b/\rho)} + \sum_s \frac{\Psi_{1s}(\chi_s r_u) \Psi_{1s}(\chi_s b)}{k_s^2 \cdot \|\Psi_{1s}(\chi_s r)\|^2} \right\}
 \end{aligned} \quad (1)$$

where $k = \omega/c$, ω is the mode frequency, c is

the light velocity, $\varepsilon_3 = 1 - \frac{\omega_p^2}{\omega^2}$, ω_p is the

plasma frequency. $J_{0,1}, N_{0,1}$ are Bissell and

Neuman functions of the 0,1 order,

$\beta_m = \beta_0 + 2m \frac{\pi}{D}$, β_0 is the longitudinal wave

vector, $m = 0, 1 \dots$ are numbers of Floquet

harmonics, $D, d, \rho, a, b, h, r_u, \varphi_0$ are

geometric parameters of the structure

indicated in Fig.1, $\chi_u = \frac{\omega}{c} r_u$, $\alpha = \lg^{-1}(\frac{L}{h})$,

$L = 2\varphi_0 r_u$, $\tau_m = \sqrt{\varepsilon_3 \cdot (k^2 - \beta_m^2)}$, $k_s^2 = \frac{\omega^2}{c^2} - \chi_s^2$,

χ_s is determined from equation

$J_0(\chi_s r) \cdot N_0(\chi_s b) - N_0(\chi_s r) \cdot J_0(\chi_s b) = 0$,

$\Psi_{1s}(\chi_s r) = J_1(\chi_s r) \cdot N_0(\chi_s b) - N_1(\chi_s r) \cdot J_0(\chi_s b)$,

for $s = 1, 2, \dots$ and $\Psi_{10}(r) = \frac{1}{r}$ for $s=0$.

Numerical solutions of the dispersion

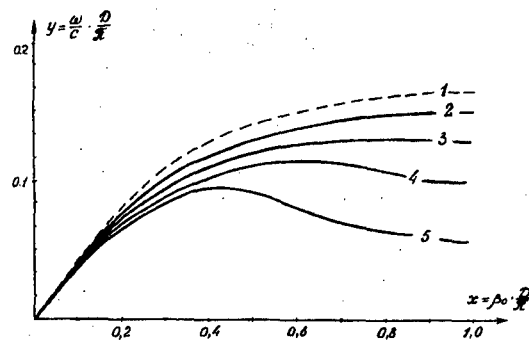


Fig.2 Dispersion characteristics in the absence of plasma ($\omega_p = 1$) at various value of the slit half angle: 1 ($\varphi_0 = 0^\circ$), 2, 3, 4, 5 ($\varphi_0 = 10^\circ, 20^\circ, 30^\circ, 40^\circ$).

The number of the curves 1, 2, 3, 4, 5 are corresponded to the slit angles $\varphi_0 = 0^\circ, 10^\circ, 20^\circ, 30^\circ, 40^\circ$ respectively. The typical slit influence on the dispersion properties as it follows from Fig.2 is the dispersion curve sagging at the large wave number up to the appearance of the negative dispersion.

For plasma filling new branches are appearing that corresponds to Trivelpiece-Gould modes. Besides the dense spectrum is observed due to many radial and spacious modes overlapping. In Fig.3 this picture is represented for plasma density $\omega_p = 0.2 \frac{\pi}{D} c$ and slit angle $\varphi_0 = 40^\circ$ with dotted curve for vacuum case $\omega_p = 0$.

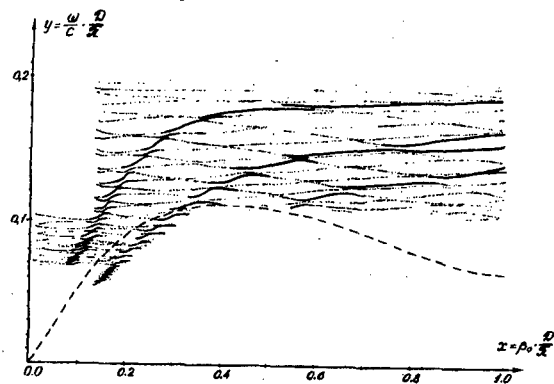


Fig.3 Dispersion characteristics at plasma density $\omega_p = 0.2 \frac{\pi}{D} c$ and slit half angle $\varphi_0 = 40^\circ$.

It should be noted that plasma filling leads to the disappearance of the negative dispersion. So at plasma presence the slit influence is sufficiently depressed. Additionally the phase velocity (slope angle) at small wave numbers is growing with plasma filling.

3. FIELDS TOPOGRAPHY. HF - POWER FLOW DISTRIBUTION

The radial topography of the longitudinal field $E_z(r)$, that determines the electron beam coupling with the mode and of the transverse components $E_r(r)$, $H_\phi(r)$, that are responsible for HF-power flow value are represented in Fig.4, for the middle cross-section of the

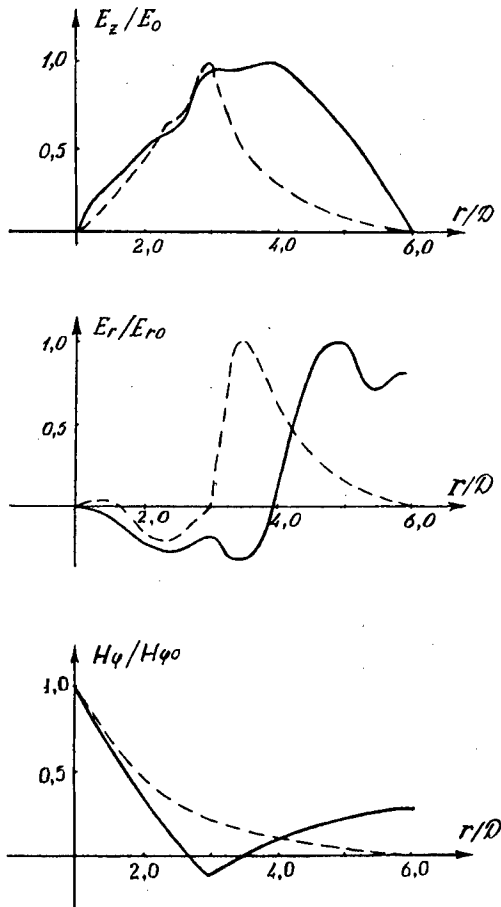


Fig. 4 Radial topography of the field components $E_z(r)$ (a), $E_r(r)$ (b), $H_\phi(r)$ (c), normalized on their value at the axis $r=0$, in the middle cross-section of the cavities. Dotted line corresponds to the vacuum case ($\omega_p = 0$).

cavity and plasma density $\omega_p = 0.2 \frac{\pi}{D} c$ and

slit angle 40° . Here E_{z0} , E_{r0} , $E_{\phi0}$ are the amplitude values on the axis. The dotted curves correspond to the vacuum case. It is seen that in the beam transit region longitudinal component $E_z(r)$ has volumetric type. It should be marked that the fields has essential changing near the slit region $r_{sl}/D=2.4$.

The HF-power flow is in opposite direction to the beam propagation that corresponds to the negative dispersion. For vacuum case at the given above parameters a half of HF-power are propagating through the cavities slits.

4. INTERACTION OF THE ELECTRON BEAM WITH ICICC STRUCTURE

The main characteristics of the beam-structure interaction is the coupling coefficient k_c , that is determined by the expression [5]

$$k_c = \frac{k}{2\beta_0 P} \cdot \frac{1}{4\pi} \cdot \int_{S_0} |E_z|^2 dS, \quad (10)$$

where $P = \frac{c}{8\pi} \cdot \text{Re} \int_S [E_r H_\phi^*] dS$ - is the time averaged power flow intergrated over the cross-section S of the transit canal, S_0 - the cross-section of the electron beam. In Fig.5

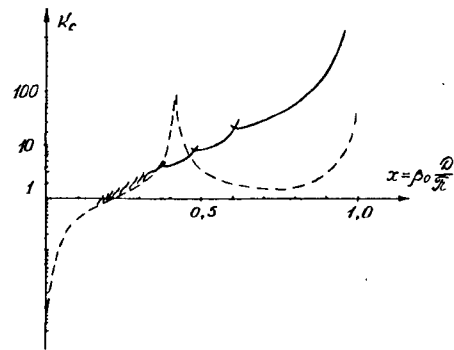


Fig.5 The dependence of the coupling k_c coefficient upon longitudinal wave number β_0 .

The coupling coefficient in dependence on the wave number is represented for vacuum (dotted curve $\omega_p=0$) and plasma (solid curve $\omega_p = 0.2 \frac{\pi}{D} c$) cases.

For some region of wave number ($\beta_0 \frac{D}{\pi} = 0.5 \div 1.0$) the coupling coefficient is sufficiently higher for plasma case. Some peculiarities seen on the curves correspond to the points where group velocities are equal to zero.

The amplification factor was derived from dispersion equation (1) numerically. Its value allows to estimate the maximum amplitude of the exited field proceeding from the assumption that the saturation is caused by particle beam trapping in the well of the wave.

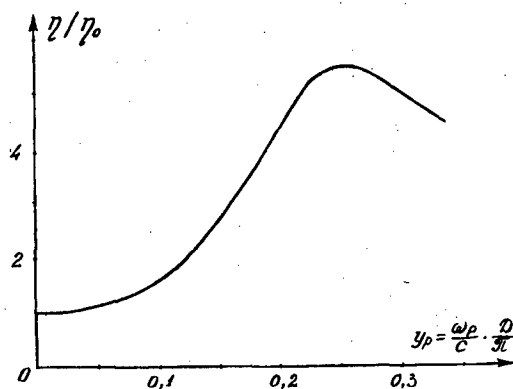


Fig.6 The dependence η of the efficiency of the beam energy flow transformation into HF-power flow on the plasma density.

The dependence of the interaction efficiency η determined by the relation

$$\eta = \frac{P_{\max}}{W_b n_b v_0 S_0}$$

(P_{\max} is maximum power flow determined by the fields at saturation level, W_b is kinetic energy of the beam electron), n_b , v_0 are the density and velocity of the beam respectively. upon plasma density is represented in Fig.6, normalized on the efficiency η for vacuum case. It is seen that the efficiency is growing with plasma density increase, has its maximum for optimal plasma density

$$\omega_p^{\text{opt}} = \frac{1}{4} \cdot \frac{\pi}{D} c \text{ and the further it falls down.}$$

SUMMARY

The obtained electrodynamic properties of the plasma filled inverted chain of inductively coupled cavities (PICICC) and results of beam-structure interaction revealed some advantage of the PICICC-structure due to both cavities coupling by means of the slit and by plasma filling. The operation of this structure in high beam current regime needs to be investigated before elaborating of the high power device.

REFERENCES

- [1] I.N.Onishchenko, V.A.Balakirev, A.N.Korostelev et al. "Coaxial plasma filled structures". BEAMS'96 Proc. V.1 1996 p.426.
- [2] A.D.Grigor'ev, V.B.Yankevich "Resonatory i resonatory zamedlyautsie systemy" SVC Moscow: "Radio i svyaz" 1984 (Rus).
- [3] E.L.Burstein, G.V.Voskresensky book "Linejnye uskoriteli elektronov s intensivnymi puchkami" Moscow.: Atomizdat, 1970 (Rus).
- [4] M.L.Levin JTF, v.21, №7, 1951, p.787 (Rus).
- [5] L.N.Loshakov JTF, v.26, №4, 1956, p.809 (Rus).

HIGH-CURRENT DIODE FOR OPEN AIR OPERATION

Yu.E. Kolyada

Priazovsky Technical University

Republic Per. 7, Mariupol 341000, Ukraine

N.I Onishchenko

NSC Kharkov Institute of Physics & Technology

Academic St. 1, Kharkov 310108, Ukraine

Abstract

The high voltage accelerator of the diode type for operation in the open air are described and several experiments on nonsinusoidal HF-radiation which have been carried out with this installation are represented. Mounting of the accelerator out of the building is conditioned by some applications on the electromagnetic fields generation and their propagation in the open space. The beam parameters are the followings : maximum energy is 1.2 MeV, maximum current 10 kA, and pulse duration is 5-15 ns. The nonsinusoidal oscillations like a sequence of separate pulses with alternative signs are registered by horn antenna at a distance from 50 m to 1 km . The simulation of beam electrons radiation in a oscillating virtual cathode has been performed to explain the mechanism of observed generation.

1. INTRODUCTION

The recent progress in elaboration of high power sources of monochromatic HF-emission are impressive. However many goals in radar and communication technique can be achieved exclusively by means of solitary video-pulse or nonsinusoidal waves [1]. Using of high power electron beams for the generation of nonsinusoidal oscillations have been investigated and represented in this paper. As a generating system the vircator was used. The setup of the high voltage accelerator of diode type is described in Sec. II. The measurement results of the installation operation and the experimental results of HF-generation are represented in Sec. III. In Sec.IV the simulation results are given. Conclusions are derived in Sec. V.

2. HIGH VOLTAGE ACCELERATOR

In our experiment electron beam was used with the following parameters: maximum energy is 1.2 MeV, current up to 10 kA, and pulse duration is 15 ns. The beam

was produced by the accelerator, mounted in open air. Placing of the accelerator out of the building is conditioned by the main objective - to investigate the propagation of the nonsinusoidal waves in open space. The accelerator consists of the vacuum chamber, high voltage diode, and high voltage pulses generator. The electrical insulation in vacuum of the long gaps (about 1 m) under the action of the 1 - 2 MV voltage pulses were studied. It was established that the insulation in vacuum is broken down after 10 - 20 sec of high voltage pulses action. The influence of the material and geometry of the cold cathode on the parameters of the high-current beam were investigated. The use of the plane graphite cathode was shown to increase the parameters of the high-current electron beam. It was found that magnetic insulation stabilizes the diode operation and increases the energy, current and pulse duration of the electron beam. The experimental technique was proposed and the total energy of the electron beam was determined by means of absorbed X-rays dose measuring for one pulse of the electron beam during its interaction with the solid target. The vacuum

chamber represents stainless cylinder of height 1.1 m and diameter 0.7 m on which the high voltage vacuum insulator was installed. The insulator with corrugated outer surface has height 6.6 m, outer diameter 0.94 m, inner diameter 0.7 m. The orientation of the accelerator is vertical. Vacuum $10^{-3} - 10^{-4}$ Torr was provided by oil pump assembly. The accelerator section represents high current diode with cold graphite cathode placed on lower part of vacuum chamber. The cathode of diameter 5 cm was settled by means of a rod electrode passing through the axis of dielectric insulator. The electrode was supported to metallic flange on the upper part of vacuum chamber. In the diode magnetic insulation was used for forming and transporting of the beam. By this reason as an anode the rigid one-layered solenoid performed from copper bar (diameter 0.8 cm) with step 3 cm was taken. The solenoid diameter was 20 cm. The maximum value of pulse magnetic field reached 10 kG.

Marx generator as a high voltage source was placed in open air. The main parameters are the followings: maximum stored energy is 0.32 MJ, operating voltage is up to 4 Mv, charge capacity is 40 nF, sizes $3.8 \times 5.6 \times 12.7$ m³. The generator has produced negative voltage pulse that was applied through the line in air to the cathode of high voltage diode. The accelerator used and Marx generator is described in details in [2].

The scheme of the experiment is represented in Fig. 1. Electron beam formed in magnetically insulated diode with cathode K and anode-solenoid A was injected in dielectric (ceramic) camera 2. As the beam current was less than critical one (up to 10 kA) it was needed to use the camera for originating of the virtual cathode, that can arise at falling on the inner wall of the camera and on the metallic disc 3, isolated from ground and during accumulating in the camera volume. The camera dimensions are: inner diameter 0.5 m, height 1.2 m. The camera potential was measured by capacity divider $C_1 - C_2$.

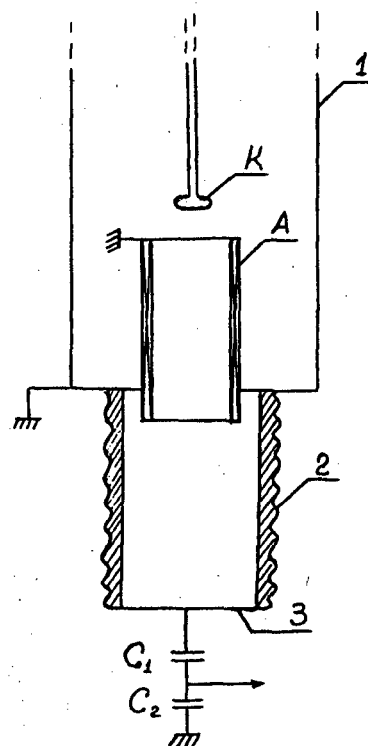


Fig. 1. The scheme of the experimental installation. K - cold cathode, A - anode (solenoid), 1 - metallic vacuum chamber of the accelerator, 2 - dielectric camera, 3 - metallic disk, $C_1 - C_2$ - capacitor divider of the voltage.

3. EXPERIMENTAL RESULTS

The typical oscillograms of beam current and diode voltage are represented in Fig. 2.

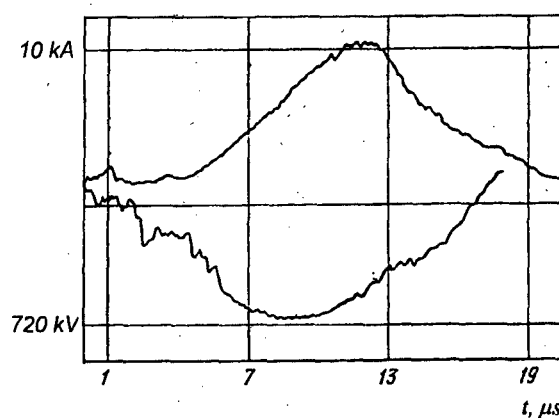


Fig. 2. Typical oscillograms of beam current and diode voltage.

Beam current was registered by Faraday cup placed at exit of magnetic tract A using low-

resistive shunt. During measuring the beam did not penetrate into dielectric camera.

Electron beam injection into dielectric camera resulted the arising of space and surface charge and virtual cathode formation, generation of intense nonsinusoidal oscillations. The main results of the experiment are represented in oscillograms (Fig.3).

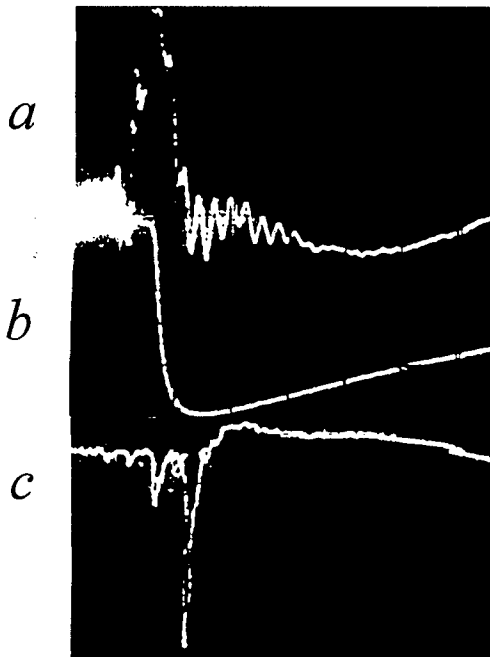


Fig. 3. The oscillograms: *a* - detected HF oscillations in the wave length region 3–30 cm; *b* - voltage registered by capacitor divider for $U_{\max}=700$ kV; *c* - detected HF oscillations in the wave length region 3 cm and less. Scanning velocity of the oscillograph is 2 μ s/div.

The oscillogram «a» corresponds to detected high frequency oscillations registered by horn antenna in range 3–30 cm. The oscillogram «b» shows the voltage on divider C_1 - C_2 corresponding to the potential of lower part of the camera, and «c» represents detected high frequency oscillations in the wave length region 3 cm and less, registered by another horn antenna. From the represented oscillograms it follows that in process of charge accumulating in camera the first range of HF-oscillations (wave length 3–30 cm) are observed and after charge has reached its maximum value higher frequency oscillations are predominant (with

wave length less 3 cm). On oscillograms in Fig.4 are represented the fragments of oscillations that are registered by a horn antenna in the range of wave lengths 3–30 cm: «a» corresponds to speed of scanning 10 ns/div, «b» is the same for 1 ns/div. The oscillograph sensitivity is 5 V/div, input resistance is 50 Ω . The horn antenna with horn square 0.9 m² was installed at distance 50 m from the accelerator. The attenuator 10 dB was included into measuring section. As it follows from analysis of represented oscillograms the intense oscillations obtained are nonregular and look like a sequence of solitary pulses of alternative signs. At the distance 1 m from exit the power flow was $6.25 \cdot 10^7$ W/m², i.e. electric field 1.5 kV/cm. The total power was 120 MW. Time duration of 3–30 cm generation was 2 μ s.

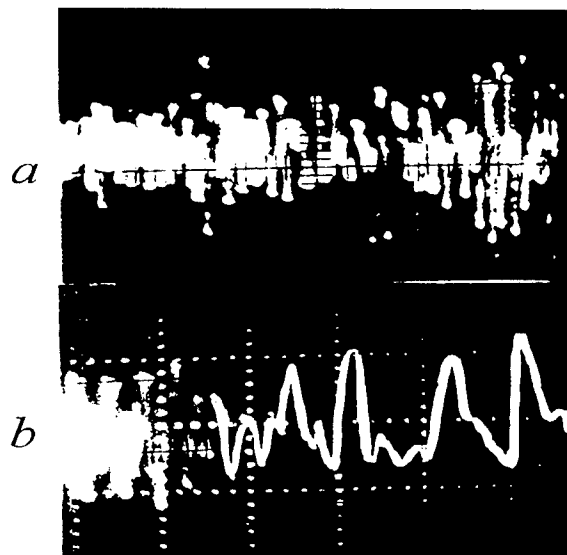


Fig. 4. The oscillograms of HF oscillations in the wave length region 3–30 cm. Sensitivity on vertical is 5 V/div. Scanning velocity of the oscillograph is: *a* - 2 ns/div, *b* - 1 ns/div.

The dependence of the electric field strength on distance along the axis was measured by 3 similar horn antennas in 3 points: 50m, 500m, and 1000m. The signals were transported in 10 cm waveguide and were taken off by means of pin antenna to the oscilloscope. The value of load was 50 Ω . To evaluate the electric field strength the diagram of

propagation direction was taken into consideration.

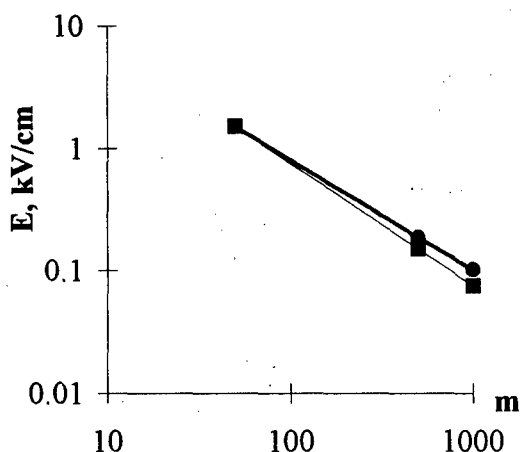


Fig. 5. The dependence of the electric field strength on the distance: ●-experimental results, ■- $1/R^2$ law

From Fig. 5 it is seen that electric field decreasing with distance from generator exit is slightly less (about 20%) than it follows from the law $1/R^2$. Such discrepancy is probably caused by nonsinusoidal character of the generated signals.

4. SIMULATION

The model for simulation proceeds from the assumption that generation and emission of nonregular electromagnetic waves is caused by electron beam interacting with the oscillating charge that is accumulated at the walls and in the volume of the dielectric camera. Evaluating the electric field intensity at the cloud surface for beam energy 700 keV and camera dimension 0.5 m we have the following estimations for electric field and plasma frequency $1.4 \cdot 10^6$ V/cm and $2 \cdot 10^9$ c⁻¹, respectively. The analysis of emission intensity was observed at distance 10 m from interaction region. Beam electrons entered into virtual cathode region being evenly distributed with time interval 10^{-12} c. The number of electrons was 200. For more number the periodicity of realization took place. The results of simulation is represented

in Fig. 6. It is seen that the emission is nonsinusoidal and close to experimentally observed.

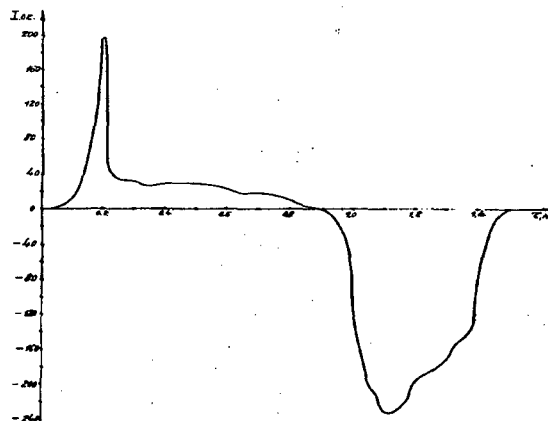


Fig. 6. The dependence of the oscillation intensity upon time obtained in simulation.

5. CONCLUSIONS

The modification of a vircator based on intense relativistic beam interacting with space charge in a dielectric camera has been elaborated. The regime of generation of nonsinusoidal oscillations was found and experimentally and numerically investigated. The obtaining of the solitary pulses without filling by driving frequency can be realized by enlarging of the interaction region, by regulating of potential well depth and duration of electron beam pulse. The installation was intended to operate in open air. It allowed to research the propagation of nonsinusoidal signal over a long distance. The preliminary emission measurements at distance up to 1 km showed the departure from the R^2 law. In detail it should be investigated in further experiments.

This work was partly supported by STCU grant No.298.

REFERENCES

- [1] Harmut H.F. Nonsinusoidal waves in radiolocation and radiocommunication. Moscow Radio i svyaz 1985 376 p (Rus).
- [2] Kolyada Yu. E. Ermolenko B.F. et al High voltage pulse accelerator for operation in open aire. PTE, 1989, No.1, p. 226 (Rus).

TIME DEPENDENCE OF HIGH-CURRENT VACUUM DIODE IMPEDANCE RESULTING FROM CATHODE PLASMA EXPANSION

S. Ya. Belomytsev, S. D. Korovin, and I. V. Pegel'

*Institute of High Current Electronics, Siberian Division, Russian Academy of Sciences
4, Akademicheskoy Ave., Tomsk, 634055, Russia*

ABSTRACT - For a high-current planar diode with discrete emitting surface, dependence of current on emission center size is obtained. If the distance between the centers largely exceeds their size R than $I \sim (RU/D)^{3/2}$ where D is the diode gap. The condition of impedance constancy during the pulse for a high-current diode requires the constancy of electric field pressure on the cathode surface.

1. INTRODUCTION

Planar vacuum diodes with explosive-emission cathodes [1] are applied to produce large-cross-section high current electron beams. These latter are used in powerful microwave generators with virtual cathode, for powerful bremsstrahlung production, and in technology.

Many applications, especially, the microwave ones, require the stability of electron beam pulse parameters that is typically of nanosecond duration. At the same time, the impedance of high current diodes is known to drop in time [2]. The diode becomes mismatched with the pulse source that leads to the increase of current and downfall of electron energy (Fig. 1).

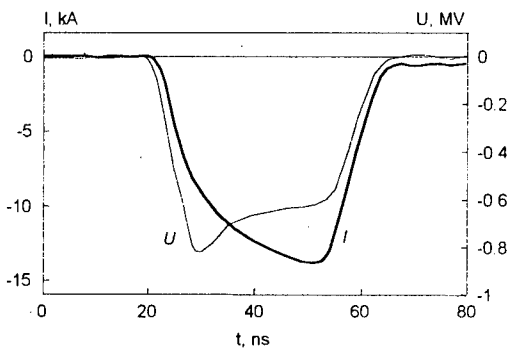


Fig. 1. Typical waveforms of current and voltage in a planar vacuum diode with explosive-emission metal-ceramics cathode

The change in impedance is bound on the evolution of the cathode emission surface. At initial moments of time, this latter is an aggregate of separate plasma formations - emission centers. The centers expand in time that results in the current increase. A typical plasma expansion velocity is $V_{pl} \sim 2 \cdot 10^6$ cm/sec [3]. This paper deals namely with this device of current increase. Studied is the dependence of current in a plane diode with discrete emission on the size of a hemispherical emission center (emitter), both in geometry with a single emitter and in periodic structure. Consider the case of emitter size much less than the diode gap: $R/D \ll 1$, that means $t \ll D/V_{pl}$. It is assumed that the number of emission centers on the cathode is constant in time.

2. SINGLE EMITTER CURRENT

Employ one of the laws of likeness existing for diodes. Consider a stationary electron flow in a diode of arbitrary geometry with space-charge limited emission. In the absence of external and with negligibly small self magnetic field under non-relativistic conditions the total diode current can be expressed [4] as

$$I = I_a \left(eU/mc^2 \right)^{3/2} F = \sqrt{e/m} U^{3/2} F$$

where $I_a = mc^3/e \approx 17$ kA and U is the diode voltage. The value of form factor F is determined only by the relative dimensions in the diode. Thus, along with the "law of 3/2" for the current, this expression demonstrates its conservation if the diode is scaled proportionally.

Apply this expression to a planar diode with a single small emitter. If the transverse size of the diode largely exceeds its gap than, since the emitter shape is fixed, the form factor depends only on (R/D) .

Visually, both the beam current and its thickness approach zero at $R/D \ll 1$ so that the potential is distributed linearly: $\varphi(z) \approx U z/D$. Therefore, the current remains constant if the diode voltage and the gap change proportionally. Thus $F \propto (R/D)^{3/2}$, and the single small emitter current can be expressed as

$$I = \beta \sqrt{e/m} (RU/D)^{3/2} \quad (1)$$

where the factor β is dimensionless and determined only by the emitter shape (compare with earlier results [5, 6]). The simulations (SuperSAM code [7]) made for a hemispherical emitter confirmed the dependence (1) with $\beta \approx 0.47$ (Fig. 2).

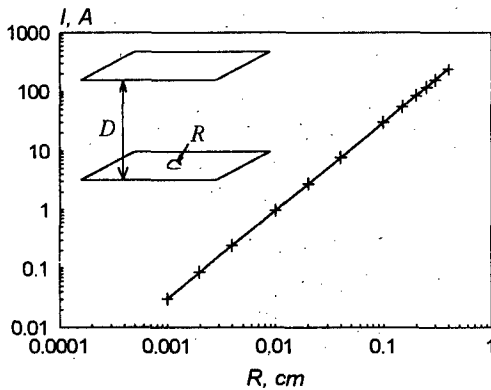


Fig. 2. Dependence of current on radius of hemispherical emitter for $D = 4$ cm, $U = 500$ kV. Points - simulation, line - calculation (1) with $\beta = 0.47$

Similarly, for linear type emitters (for example, hemi-cylindrical one) the current per emitter length unit is $dI/dl \propto R^{1/2} D^{-3/2}$.

Note that, at small emitter radii ($R/D \ll 1$) the relativistic deviation of current from the "law of 3/2" occurs at much higher voltages than for a uniform plane diode. This is because the current is limited by the space charge in the immediate emitter vicinity having a size of $\sim R$. Even if the total diode voltage U is relativistic, the electron energy near the emitter ranges $\sim eUR/D$ that can be much below relativistic level. Thus, the validity condition for the expression (1) is $(\Gamma - 1)R/D \ll 1$ (where $\Gamma = eU/mc^2 + 1$) that is satisfied in the majority of practically important situations for nanosecond pulse durations.

In the case of extremely high voltage when the electrons become relativistic already near the emitter, the dependence of current on voltage becomes linear and therefore the power by R in the expression for the current is decreased for 1/2. Thus, for linear type emitters in this case the current does not depend on the emitter radius.

3. CURRENT OF PERIODIC EMITTING STRUCTURE

Consider a periodic structure of emitters with the distance p between them. Assign $x = 2R/p$, $y = p/D$. Thus, at $x = 1$ have a plane diode with uniform emission. It is convenient to approximately express the Child-Langmuir's law for this diode as [4]

$$j_{pd} = \frac{I_a}{2\pi D^2} (\Gamma^{2/3} - \Gamma^n)^{3/2}, \quad n = 2/3 - 2/9^{2/3} \approx 0.2 \quad (2)$$

This expression has exact non- and ultra-relativistic limits and possesses an accuracy of $\sim 1\%$ (comparing with the exact solution [8]) in the intermediate range of voltages.

In the opposite case, when the distance between emitters is much less than the diode gap, than, at $x \ll 1$, the currents of the emitters approach zero and therefore do not interact by their space charges. Thus, they are independently described by the expression (1).

An expression describing the average current density in the diode in the entire range from from $x=0$ up to $x=1$ must turn in these limits into expressions (1), (2). The following expression possesses this attribute:

$$j = j_{pd} / A, \quad A = 1 + \frac{f(x)y^{1/2}}{2^{3/2}\beta x^{3/2}} \left(\frac{\Gamma^{2/3} - \Gamma^n}{\Gamma - 1} \right)^{3/2} \quad (3)$$

The weighting function $f(x)$ should satisfy the conditions $f(0)=1$, $f(1)=0$, and its form depends on the shape of the emitter cell.

Consider a 6-border cell. To avoid 3D simulations, it is easy to approximate it by a cylinder of radius $p/2$, with Neumann's condition for the potential and mirror reflection for the particle trajectories on its side surface (see insertion in Fig. 3). Thus, the problem turns to 2D. The simulation (SuperSAM code) demonstrated that in this case the weighting function can be chosen as $f(x) \approx 1 - x^{1-x}$ with the error below 5%.

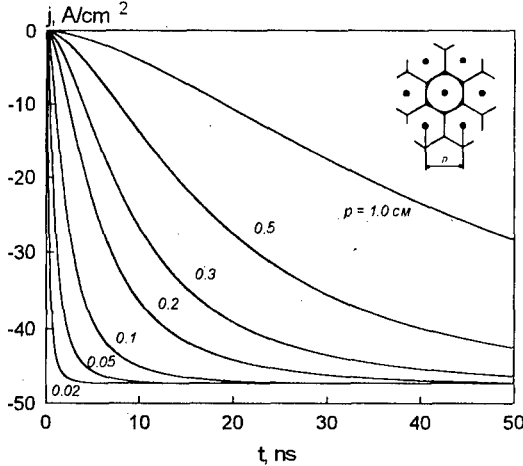


Fig. 3.

Note that at small x the dependence of current on voltage and diode gap strives to $I \propto (U/D)^{3/2}$ that is typical for a single emitter, with very late relativistic deviation.

Fig. 3 represents the calculated using (3) traces of average current density in a diode with hemispherical emitters expanding with a velocity of $2 \cdot 10^6$ cm/sec, for different distances between the emitters, $D=4$ cm, and $U=500$ kV. Comparison of these curves with the experimental ones allows for estimation of actual state of cathode emission surface.

4. CONDITION OF CURRENT CONSTANCY IN HIGH-CURRENT DIODE

Remind that we assume that the drift of cathode plasma inside the diode during the pulse is negligibly small. In this situation, as usually considered, the reason of diode impedance inconstancy is the temporal expansion of emission surface. This latter can occur due to increase of emission centers number (during first nanoseconds) and further due to plasma surface expansion up to total coverage of the cathode surface.

Define the mechanism of impedance decrease more precisely. It occurs only if the expansion of emitting surface is escorted by the decrease of electric field pressure on the cathode. For example, it is easy to see that in each cross-section of a common plane diode [9]

$$-\frac{E^2}{8\pi} + \frac{j}{e} mc \sqrt{\gamma^2 - 1} = \text{const} \quad (4)$$

On the electrodes, the left part of this expression is the total pressure due to electric field and the particle flow. Thus, the forces on the cathode and anode are equal and the total force effecting the diode is zero that is the consequence of momentum conservation in a stationary system. If the electrons leave the cathode with zero velocities then the pressure on the cathode is $p_k = E_k^2 / 8\pi$ where E_k is the electric field strength here. If the current is space-charge limited than $E_k=0$ and $p_k=0$. Therefore, on the anode the field pressure is compensated by the pressure of particles. These conclusions are also valid for periodic emitting cathode structures. In this case, average electric field and current density are meant in the expression (4).

If the emission surface of the cathode is continuous, the diode current does not depend on time. However, it is hard to rapidly cover the entire cathode surface with plasma. For easier development of explosive emission, cathodes are usually made with non-uniform periodic emitting surface. Let the size of periodicity is much less than D . Neglecting the

magnetic field, we can consider the electron flow normal to electrodes (except near the emitters).

To provide constancy of current, constancy of electric field pressure on the cathode must be provided. An example way to realize this is as follows.

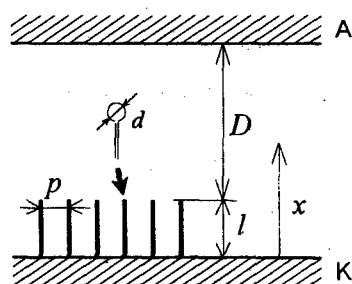


Fig. 4.

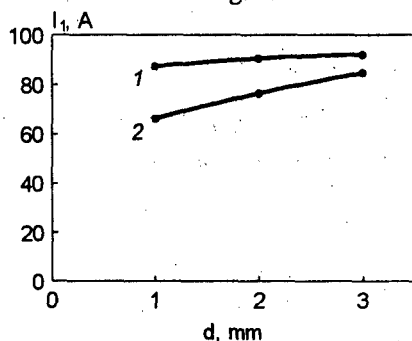


Fig. 5.

Let the cathode be made as a plane with thin parallel blades (Fig. 4) with the distance between them $p \ll l$ and $p \ll D$. If the edges of blades are covered with plasma then the field pressure on the cathode is small and it does not depend on plasma expansion. This is because $p \ll l$ and the cathode basement is well screened. On the other hand, at nanosecond pulse duration, the range of plasma expansion can be small so that the changes of electron trajectories will not effect the diode impedance.

This results were confirmed in simulations (SuperSAM code). Fig. 5 represents the comparison of two situations for a periodic linear emitting system, both with 500 kV voltage. The lower curve is the current for a hemi-cylindrical emitter of radius d in the diode with 3 cm gap. The upper curve is for blade system with $p=1$ cm, $U=500$ kV, $D=3$ cm, $l=1$ cm. As is seen, the dependence of current on emitter radius is lower in the second case.

Note also that at $p \ll l$, $p \ll D$ the current of blade diode (Fig. 4) is very close to that of common plane diode with the gap D .

Although it is clear what is the requirement to the cathode surface the achievement of the goal can meet several problems. Simple metal blades are hard to uniformly explode, especially at high pulse repetition rate. Besides that, heat deformation of blades occurs in high average power regime. Probably, application of metal-dielectric contacts [10] will allow for improving uniformity of emission due to better explosion and faster propagation of plasma along dielectric and fusion of neighboring emission centers. Employment of needle-type cathode surfaces with optimum distance between needles is also considered a way to compromise between the requirements of electric field screening and simultaneous excitation of explosive emission.

The authors are grateful to Professor Dmitry I. Proskurovsky for valuable discussions.

REFERENCES

1. Bugaev S. P., et al. // Uspekhi Fizicheskikh Nauk (Sov.). - 1975. - V. 115. - No. 1. - PP. 101-120.
2. Bykov N. M., et al. // Proc. 10th Int. Pulsed Power Conf. - Albuquerque, NM, 1995. - PP. 71-74.
3. Mesyats G. A. and Proskurovsky D. I. Pulsed Electrical Discharge in Vacuum. - Berlin: Springer-Verlag, 1989. - 256 p.
4. Belomytsev S. Ya., et al. // J. Tech. Phys (Rus.). - 1998. (in print).
5. Shubin A. F. and Yuriye Ya. Ya. // Izvestiya vysshikh uchebnykh zavedenii. Fizika (Sov.). - 1975. - No. 6 - PP. 134-136.
6. Djogo G. and Cross J. D. // IEEE Trans. Plasma. Sci. - 1997. - V. 25. - No. 4. - PP. 617-624.
7. Myakishev D. G., et al. // Int. J. Mod. Phys. A (Proc. Suppl.) 2B. - 1993. - V. II. - PP. 915-917.
8. Iory H. R., Trivelpiece A. W. // J. Appl. Phys. - 1969. - V. 40. - No. 10. - P. 3924-3926.
9. Belomytsev S. Ya., et al. // Pis'ma J. Tech. Phys (Rus.). - 1998. - V. 24. - No. 5. - PP. 63-69.
10. Mesyats G. A. // IEEE Trans. Dielectrics and Electrical Insulation. - 1995. - V. 2. - N. 2. - P. 272-276.

OPTIMISATION OF THE CROSSED-FIELD SECONDARY EMISSION ELECTRON SOURCE

Y. M. Saveliev, W. Sibbett and D. M. Parkes *

*University of St Andrews, School of Physics and Astronomy, North Haugh,
St. Andrews, Fife, KY16 9SS, Scotland, UK*

**DERA, St. Andrews Road, Great Malvern, Worcs, WR14 3PS, UK*

The Crossed-Field Secondary Emission (CFSE) diode is a relatively new electron source [1,2] which is capable of producing annular electron beams in 10^2 A range of output currents. The basic mechanism of the CFSE diode operation is a secondary emission multiplication of a small (few mA) primary current. Therefore, it is essentially a cold electron source that does not rely on the existence of any heated surfaces or plasma. One of the important features of the CFSE source is its potential ability to produce high frequency (~ 1 GHz) density modulated electron beams which might be employed in existing or future microwave devices.

The CFSE electron source is a magnetron diode with smooth cylindrical electrodes (Fig.1). The start of the electron multiplication occurs at the negative $d|U|/dt < 0$ slope of the high voltage pulse applied between cathode and anode. After current initiation at $d|U|/dt < 0$, it does not vanish even at $d|U|/dt \geq 0$, probably, because of a transition from laminar to turbulent electron flow in a crossed-field gap due to increasing electron space charge. Such a transition was shown in conventional magnetron diodes by PIC computer simulations [3-5].

Operation of the CFSE diode usually requires a small primary current of a few mA. Under certain conditions, however, a self-excitation of the CFSE diode is possible. This possibility stems from the fact that the build-up time of the electron space charge is less than ~ 20 ns even in the case of a single primary electron. (Detailed discussion of the self-excitation regime is beyond the scope of the present work). We note only that most of the experimental results presented here were obtained with the CFSE diodes operating in the self-excitation regime.

The CFSE diode has proved to be a highly efficient and robust source of tubular electron beams with a perveance of $P \sim 15 \mu\text{A}/\text{V}^{3/2}$ and an output current of more than 100A [1,2]. However, the experiments with various diode configurations showed that P depends strongly on the diode geometry and position of the collector [2].

This work is concerned with optimisation of the CFSE diode geometry in order to increase the diode perveance with the objective of producing higher output electron currents.

The experiments were conducted with various CFSE diodes which differ in cathode diameter D_k , diode gap d , diode length l_d , distance between cathode and anode edges Δ , and cathode-collector distance d_{kc} (see Fig.1a). The diode voltage pulses of up to 40kV amplitude and a few μs of duration were supplied by a small Marx bank. Provision was made to ensure a fast negative slope ($\leq 10^{12}\text{V/s}$) of the diode voltage immediately after the leading edge of the HV pulse.

One of the most important parameters affecting the CFSE diode performance is the distance Δ between cathode and anode edges see Fig.1. The dependencies of the collector

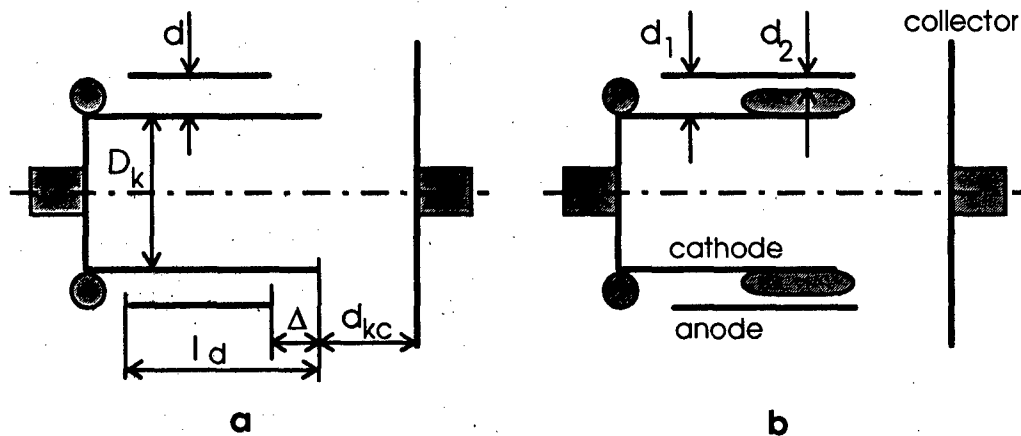


Fig.1 Schematic diagrams of the CFSE electron sources

perveance $P_c = I_c/U^{3/2}$ and anode perveance $P_a = I_a/U^{3/2}$ on Δ are shown in Fig.2. The collector perveance is largest at $\Delta=0$ partly because of the reduced leakage of current to the anode. This latter effect is due to the decrease in a longitudinal component of the electric field in which some electrons are reflected from the diode edge.

Comparison of the curves $P_c(\Delta)$ and $P_a(\Delta)$ obtained at various values of d_{kc} indicates that positioning of the collector close to the diode enables an increased output current to be produced. (Compare curves in Fig.2 corresponding to $d_{kc}=2$ and 30mm). This feature is, however, less pronounced when long diodes (large l_d) are used.

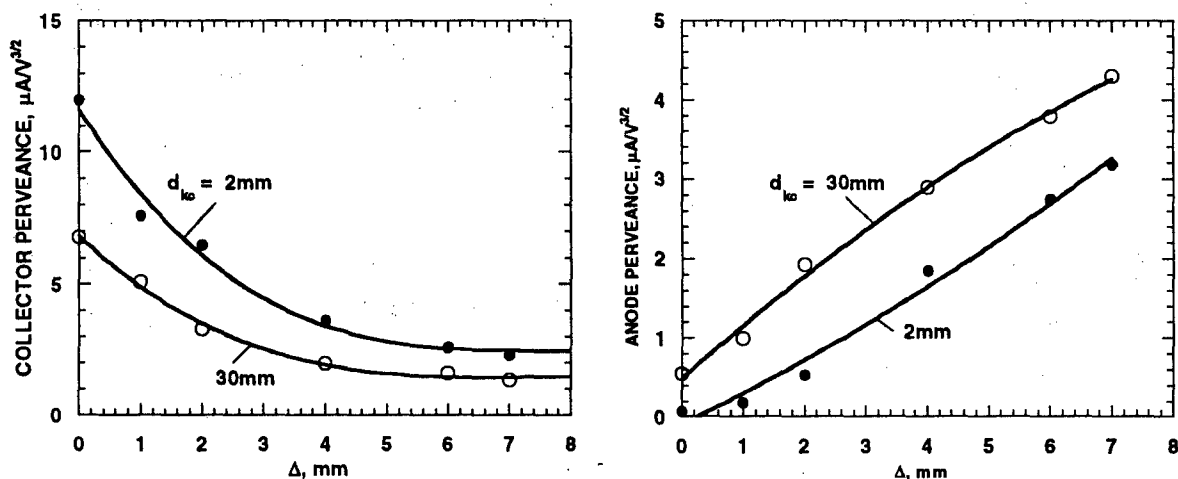


Fig.2 Collector and anode perveances vs distance between cathode and anode edges, Δ at two different cathode-collector distances. $D_k=50$ mm, $d=5$ mm, $B=1.87$ kG.

The obvious way to increase the diode perveance is to construct the CFSE diode with a smaller diode gap d . First experiments [1,2] were made with $d \approx 10$ and 5mm. Further decrease of d to $d=2.55$ mm allows perveance as high as $P=55 \mu A/V^{3/2}$ to be obtained. This is a provision for achieving high output currents from the CFSE electron source. Indeed, $I_c=220$ A was registered at a diode voltage less than 30kV.

New experimental results with small d (<3 mm) have enabled the dependence $P(d)$ to be defined more precisely. This is shown in Fig.3 where each point represents a different model of the diode. The $P(d)$ function tends to follow a $P \propto D_k/d$ dependence, but it depends strongly on electrode geometry and, to a lesser extent, on magnetic field. As a result, the

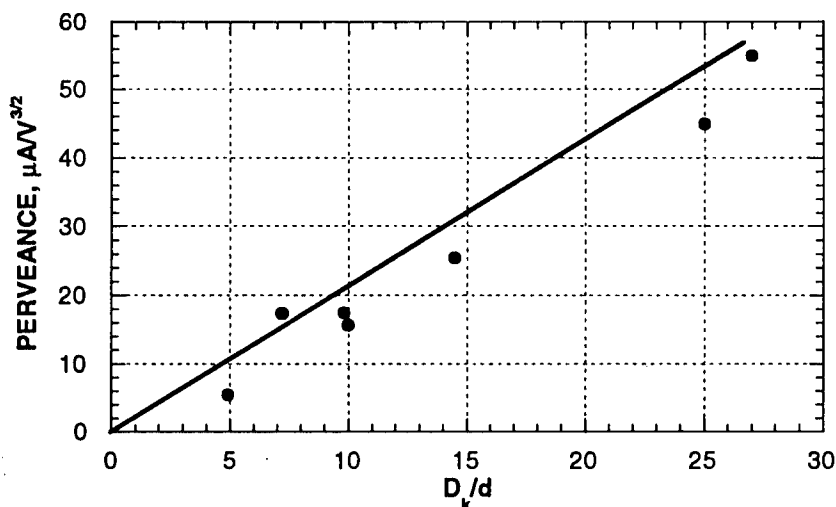


Fig.3 Perveance of the CFSE electron source vs D_k/d ratio. Each point corresponds to the particular geometry of the CFSE source allowing achievement of the highest value of P at a given D_k/d .

experimental points are situated mostly below but close to the straight line depicting possible optimal values of the diode perveance.

The CFSE diode with small d requires fine adjustment of the operating parameters, e.g. U_d , dU_d/dt , magnetic field, when being operated in the self-excitation regime. Failure to optimise these parameters can result in "missing shots" when the diode fails to start operation. To facilitate self-excitation of the CFSE electron source we have suggested a new concept of the diode with two gaps, see Fig. 1b. This electron source consists of two diodes with different diode gaps, d_1 and d_2 . The electron multiplication starts in the diode with the larger gap, d_1 because electrons are prevented from escaping this region due to specific distribution of electric field. Then the generated electron cloud serves as a primary source for the second diode with the smaller gap, d_2 thus allowing the entire system to operate at high perveance.

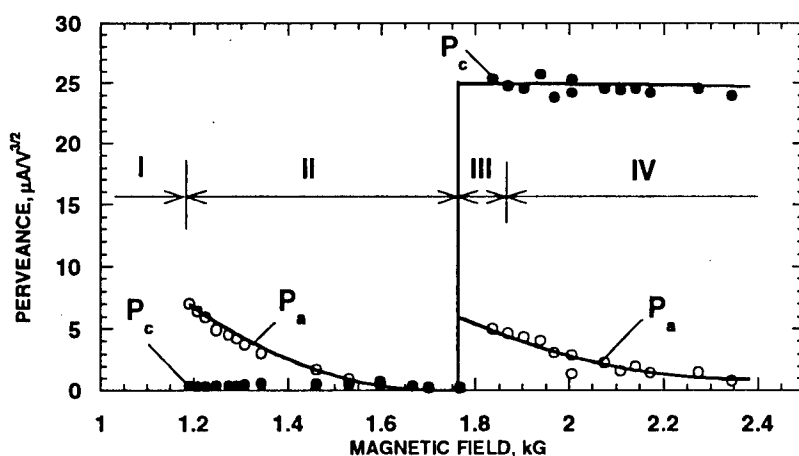


Fig.4. Collector and anode perveances of the CFSE diode with two diode gaps vs magnetic field. $D_{k(max)}=42.7\text{mm}$, $d_1=5.2\text{mm}$, $d_2=3.0\text{mm}$, $\Delta=0$, $d_{kc}=4\text{mm}$.

The above concept has been validated experimentally. Figure 4 shows the dependence of the collector and anode perveances of the diode with $D_{k(max)}=42.7\text{mm}$, $d_1=5.2\text{mm}$, and $d_2=3.0\text{mm}$ as a function of an applied magnetic field. The output perveance reaches the value

of $25\mu\text{A}/\text{V}^{3/2}$. Four specific regions are discerned in Fig.4. In the first region (I), there is no generation of current due to the low magnetic field being less than or close to the Hull cut-off value. In the second region (II), only the first diode ($d_1=5.2\text{mm}$) operates. A small output current observed in this region is due to the axial leakage of electrons from the first diode. In region III, the bursts of the collector and anode current were observed which are similar to those appearing at the values of magnetic field close to the Hull cut-off level [2]. Finally, region IV is characterised by a normal generation of the electron current in the second diode with the smaller diode gap, d_2 . There exists another region, V, at yet higher magnetic fields where the diode ceases to operate. The latter was not achieved in the present experiments because of the limiting magnitude of the applied magnetic field. However, it has been observed when the voltage slope rate was decreased by, for example, introducing a series inductance into the Marx bank discharge circuit.

We conclude that progress has been made in increasing the output perveance of the CFSE electron source such that there is the potential for high output currents in the range of a few hundred amperes to be produced. The maximum output current achieved at the present stage of experiments is as high as $\sim 220\text{A}$ for a diode voltage less than 30kV . This makes the CFSE diode an efficient and practical source of tubular electron beams for a range of various applications.

This work was supported by DERA, St. Andrews Rd, Gt. Malvern, Worcs, WR14 3PS, UK

References

- [1] Y. M. Saveliev, W. Sibbett and D. M. Parkes. Crossed-field secondary emission electron source. *Physics of Plasmas*, **4**, No7, 2319 (1997).
- [2] Y. M. Saveliev, W. Sibbett and D. M. Parkes. Crossed-field secondary emission electron source. In: *Proc. of the 11th Int. Pulsed Power Conference*, June 29-July 2, 1997, Baltimore, USA (to be published).
- [3] P. J. Christenson and Y. Y. Lau, *Phys. Plasmas*, **1**, 3725 (1994).
- [4] V. P. Gopinath, J. P. Verboncoeur and C. K. Birdsall, *Phys. Plasmas*, **3**, 2766 (1996).
- [5] D. P. Chernin, *IEEE Trans. on Electron Devices*, **ED-43**, 2004 (1996).

THE SPECTRUM BROADENING OF EXCITED OSCILLATIONS IN COAXIAL SLOWING STRUCTURE WHEN FILLING BY PLASMA

E.A.Kornilov, P.I.Markov, G.V.Sotnikov

Institute Plasma Electronics & New Methods Accelerations NSC Kharkov Institute of Physics and Technology, Akademicheskaya Str. 1, Kharkov, 310108, Ukraine

Abstract.

The excitation of UHF-oscillations by electron beam in disk loaded coaxial transmission line with combs on inner and external conductors is theoretically investigated. The structure passage channel, where annular electron beam propagates, is fully filled by plasma. The eigen waves of plasma filled coaxial transmission line and their dependencies versus plasma density are investigated. It is shown that plasma have result in essentially enhancement of gain and at the same time widens excited oscillation spectrum.

1. INTRODUCTION.

The vacuum slow-wave structure can acquire the well known hybrid characteristics when the interaction area (i.e., the passage channel where the electron beam is propagating) is filled with plasma. The principles of the plasma hybrid slow-wave structure operation are for the first time presented in [1, 2]. As a result of the passage channel filling with plasma, the electric field longitudinal component sufficiently increases, which causes a rise of the coupling coefficient and, consequently, the wave amplification coefficient also increases. In this process - if the conditions for interaction between the beam and the proper wave of the vacuum structure are realized - an intensive flow of the SHF power is being generated. The experimental investigations [3, 4, 5] have confirmed the theoretical prognostications of good prospects for the hybrid, slow-wave structure application in construction of amplifiers and oscillators.

One should remember that for the first time the hybrid plasma structures have been examined by investigation of the vacuum slow-wave structure of the type of the chain of the coupled cavities (CCC). The

conditions for the SHP oscillation excitation in a hybrid structure become optimal when the synchronous frequency of the excited oscillations is equal to the plasma frequency. That's, for the given plasma density a narrow oscillation spectrum (on the order of the increment) is excited.

We suppose that if a slow-wave structure, which is based on a coaxial transmission line with disks on one (or both) of the conductors, is filled with plasma, the wide band of the excited oscillations can be preserved and, simultaneously, the amplification coefficients can be essentially raised.

In the given report, we have investigated the dispersive characteristics of the coaxial disk-loaded line filled with plasma where the disks are placed both on the inner and external cylinders. The linear and nonlinear theories proceeded from the vacuum structure are presented in the Proceedings of the International Conference "Crymico 97" [6]. It's demonstrated that in such structure the UHF oscillations may be effectively excited over a wide frequency range. Below we investigate the alterations in the dispersion characteristics and amplification coefficients as a result of the structure filling with plasma. It should be mentioned that the authors of [7] have performed preliminary investigations of the

amplification coefficients and coupling resistances in the plasma coaxial line with the disks placed on the inner conductor. As it's demonstrated, plasma may essentially alter the electrodynamic characteristics of the slow-wave system if the passage channel transverse size is comparable with the wavelength of the oscillations that are being amplified - or larger than it. This fact is conditioned by the superficial nature of the wave: that's, the plasma may essentially alter the picture only in the case of very high plasma densities.

2. ELECTRODYNAMICS OF THE COAXIAL SLOW-WAVE LINE WHERE THE PASSAGE CHANNEL IS FILLED WITH PLASMA.

The slow-wave structure is a coaxial line with the inner and outer radii ρ and b , correspondingly, and with disks on both the conductors. Plasma with the density n_p completely fills the passage channel with the outer a and inner σ radii. In this channel a thin electron beam is propagating its radius is r_b , the velocity is v_0 and the current is I_b . The structure period is D and the cavity width is d . The inner structure may be with respect to the outer one shifted at an arbitrary distance l .

In the linear approximation the dispersion equation (DE) describing the monochromatic wave excitation by an electron beam has the form:

$$\left\{ \frac{d}{D} \sum_{m=-\infty}^{\infty} \frac{k \varepsilon_3 \psi_m^2}{k_{\perp m} \Delta_m} \left[\frac{F_1(k_{\perp m}, a, \sigma)}{F_0(k_{\perp m}, a, \sigma)} - \frac{\alpha_m^2}{(\omega - \beta_m v_0)^2} F_1(k_{\perp m}, a, r_b) \frac{F_0(k_{\perp m}, r_b, \sigma)}{F_0(k_{\perp m}, a, \sigma)} \right] - \frac{F_1(k, a, b)}{F_0(k, a, b)} \right\} \cdot \left\{ \frac{d}{D} \sum_{m=-\infty}^{\infty} \frac{k \varepsilon_3 \psi_m^2}{k_{\perp m} \Delta_m} \left[\frac{F_1(k_{\perp m}, \sigma, a)}{F_0(k_{\perp m}, \sigma, a)} - \frac{\alpha_m^2}{(\omega - \beta_m v_0)^2} F_1(k_{\perp m}, \sigma, r_b) \frac{F_0(k_{\perp m}, r_b, \sigma)}{F_0(k_{\perp m}, a, \sigma)} \right] - \frac{F_1(k, \sigma, b)}{F_0(k, \sigma, b)} \right\} = 0$$

$$\frac{F_1(k, \sigma, \rho)}{F_0(k, \sigma, \rho)} \left\{ \frac{d^2}{D^2} \sum_{m=-\infty}^{\infty} \frac{k \varepsilon_3 \psi_m^2}{k_{\perp m} \Delta_m} e^{im\phi_0} \times \frac{F_1(k_{\perp m}, a, a)}{F_0(k_{\perp m}, \sigma, a)} \sum_{m=-\infty}^{\infty} \frac{k \varepsilon_3 \psi_m^2}{k_{\perp m} \Delta_m} e^{-im\phi_0} \times \frac{F_1(k_{\perp m}, \sigma, a)}{F_0(k_{\perp m}, a, \sigma)} \right\} = 0$$

In DE the following nomenclature is used:

$$F_n(q, x, y) = J_n(qx)Y_0(qy) - Y_n(qx)J_0(qy),$$

$$\varepsilon_3 = 1 - \frac{\omega_p^2}{\omega^2}, \quad \omega_p^2 = \frac{4\pi e^2 n_p}{m},$$

$$k_{\perp m} = \sqrt{(k^2 - \beta_m^2)}, \quad \beta_m = \beta_0 + \frac{2\pi m}{D},$$

$$k = \frac{\omega}{c}, \quad \phi_0 = \frac{2\pi l}{D}, \quad \psi_m = \frac{\sin(\beta_m d/2)}{\beta_m d/2},$$

$$\Delta_m = 1 + \frac{\alpha_m^2 c^2 F_0(k_{\perp m}, r_b, a)}{(\omega - \beta_m v_0)^2} \cdot \frac{F_0(k_{\perp m}, r_b, \sigma)}{F_0(k_{\perp m}, a, \sigma)},$$

$$\alpha_m^2 = \frac{I_b}{I_A} \frac{\pi c^3 (k^2 - \beta_m^2)}{\gamma_0 v_0}.$$

where v_0 is the electron beam velocity, $\gamma_0 = 1/\sqrt{1 - v_0^2/c^2}$, ω is the wave frequency, β_0 is the longitudinal wave number, $I_A = 17 \text{ kA}$, J_n and Y_n are the Bessel and Veber functions of the n -th order.

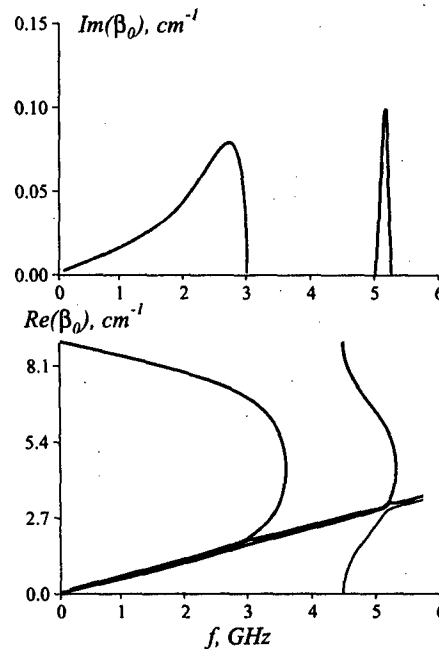


Fig. 1. The dispersive dependencies of the real $\text{Re } \beta_0$ and imaginary $\text{Im } \beta_0$ parts of the longitudinal wave number on the fre-

quency f for the vacuum slow-wave structure with a thin electron beam.

We have performed numerical simulations of the DE solutions in the case of the parameter values [6] which are used in the experiment that is being conducted in the NSC KhPhTI: $b = 5.3 \text{ cm}$, $a = 4.0 \text{ cm}$, $\sigma = 3.5 \text{ cm}$, $\rho = 1.9 \text{ cm}$, $D = 0.7 \text{ cm}$, $d = 0.5 \text{ cm}$, $\phi_0 = 0$, $r_b = 3.6 \text{ cm}$, $I_b = 5.0 \text{ A}$, $W_b = 35 \text{ keV}$. In Fig.1 and 2 the dispersion dependence of the vacuum and plasma slow-wave structures are presented ($n_p = 1.8 \cdot 10^{11} \text{ cm}^{-3}$). The given plasma density corresponds to the case of overlapping of the cutoff frequency of the coaxial slow wave by the plasma frequency $f_p = \omega_p / 2\pi$. As it follows from comparison of Fig.1 with Fig. 2, the plasma presence causes increase of the amplification coefficient by 20% and bandwidth broadening of the excited oscillations by 10%.

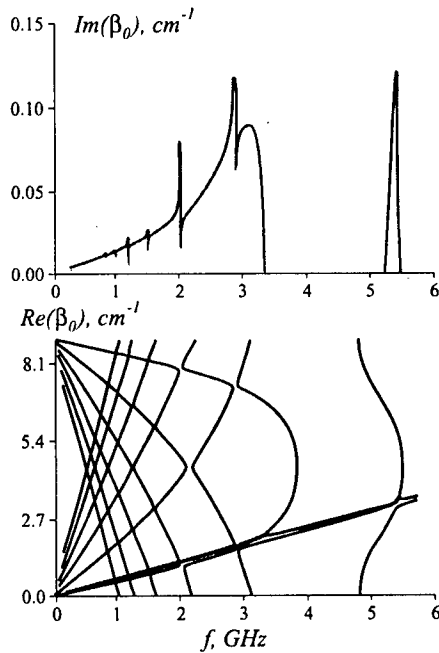


Fig. 2. The dispersive dependencies of the real $\text{Re } \beta_0$ and imaginary $\text{Im } \beta_0$ parts of the longitudinal wave number on the frequency f for the plasma slow-wave structure. The plasma density is $n_p = 1.8 \cdot 10^{11} \text{ cm}^{-3}$

In Fig.3 the oscillation maximum amplification coefficient, which corresponds to the coaxial mode, is given in dependence on the plasma density. On the interval examined the amplification coefficient almost linearly increases with increase of the plasma density.

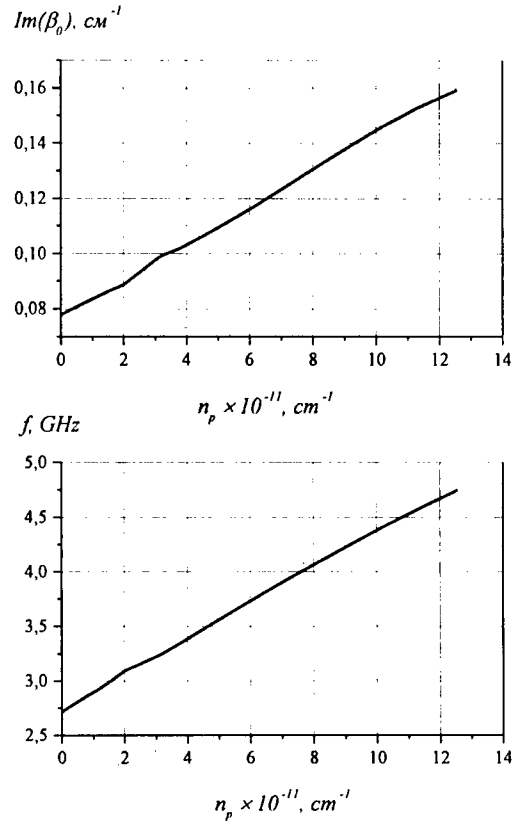


Fig. 3. The dependences of the maximum amplification coefficient $\text{Im } \beta_0$ on the frequency f that corresponds to this maximum on the plasma density. The beam current is $I_b = 5 \text{ A}$, the beam radius is $r_b = 3.6 \text{ cm}$.

The transverse structure of the longitudinal electric field is antisymmetric in the first band of transparency. Hence, the gain of the narrow electron beam must go to zero when the beam radius is exactly equal to the location of zero of the longitudinal electric field. This is demonstrated in Fig.4, where one can see the dependences of the oscillation maximum gain on the beam radius for the 1st and 2nd bands of transparency. In the 2nd band, the gain

maximum monotonously increases from one boundary to another.

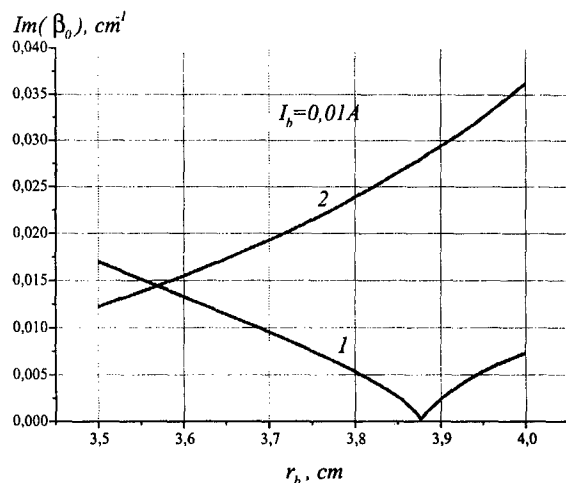


Fig. 4. The dependencies of the oscillation maximum gain on the beam radius in the 1st (1) and 2nd (2) bands of transparency when the structure parameters are the following: $b=5.3$ cm, $a=4.0$ cm, $\sigma=3.5$ cm, $\rho=1.9$ cm, $D=0.7$ cm, $d=0.5$ cm, $\phi_0=0$.

3. CONCLUSION.

If the passage channel of the coaxial disk-loaded line is filled with plasma, this causes a qualitative alternation of the slow-wave system dispersion characteristics: besides the proper waves of the vacuum slow-wave structure (a broadband T -wave and electromagnetic waves), a great number of other wave become excited; they correspond to radial and Flocke harmonics of the plasma wave.

As it occurs in the case of electromagnetic waves, the resonant width of the excited plasma waves is also small.

When the passage channel is filled with plasma, the coaxial T -wave retains the broadband features. And what's more, the amplification coefficients increase, and the bandwidth is broadened - in comparison with the vacuum structure. The maximum linearly coefficient of amplification and the frequency that corresponds to this maximum linearly depend on plasma density. Alteration of the plasma density from zero up to $1.4 \cdot 10^{12} \text{ cm}^{-3}$ permits to in-

crease the coefficient of amplification more than twice (from 0.07 cm^{-1} up to 0.16 cm^{-1}). In this case the excitation bandwidth has increased twice.

The wave resistance of the coaxial slow-wave structure varies insignificantly after filling the passage channel with plasma.

If the plasma density is $n_p = 1.8 \cdot 10^{11} \text{ cm}^{-3}$, the amplitude of saturation of the longitudinal electric field is $E_{sat} = 1.42 \text{ kV/cm}$ (the electron beam energy is $W_b = 35 \text{ keV}$, the beam current is $I_b = 10 \text{ A}$ and the beam radius is 3.6 cm), the optimal structure length is 43.6 cm . For the plasma density $n_p = 7.2 \cdot 10^{11} \text{ cm}^{-3}$, the amplitude of saturation is $E_{sat} = 1.93 \text{ kV/cm}$ and the optimal structure length is 34.8 cm . In the case of the vacuum structure and for the narrow electron beam, these magnitudes are equal to 1.3 kV/cm and 48.0 cm , respectively.

The work is supported in part by Science and Technology Centre of Ukraine (STCU), Grant N 256.

4. REFERENCES.

1. Fainbberg Ya.B., Blioch Yu.P., Kornilov E.A. et.al. Doklady AN USSR. Fiz.-mat. I techn. Nauki, 1990, N 11, p.55., rus.
2. Fainbberg Ya.B., Blioch Yu.P., Lubarskiy M.G. Fizika Plasmy. 1994. V.20, N 9, p.757 - 766., rus.
3. Antonov A.N., Blioch Yu.P., Degtyar' Yu.A. et.al. Fizika Plasmy. 1994. V.20, N 9, p.777 - 781., rus.
4. Zav'yalov M.A., Martynov B.O., Mitin L.A. et.al. IV Simpozium po Sil'notochnoy Elektronike. Tez.Dokl.: Russa, 1992, p.132., rus.
5. Carmel Y., Miami K., Kohn R.A. et al. Phys. Rev. Lett. 1989. V.62. P.2389.
6. Kornilov E.A., Markov P.I., Sotnikov G.V. Trudy 7-i Mesgdunarodnoy konferentsii "SVCh-Technika i Telekommunikatsionnye Tekhnologii". Sbornik Dokladov, 1977, V.2, p.429 - 432., rus.
7. Kornilov E.O., Korostel'iov O.M., Lodygin O.B. et.al. UFG, 1985, V.40, N 4, p.312 - 317, ukr.

SPECTROSCOPIC DETERMINATION OF TURBULENT LANGMUIR FIELDS IN A REB-HEATED PLASMA

J. Ullschmied, K. Koláček, M. Řípa

*Institute of Plasma Physics, Czech Academy of Sciences
Za Slovankou 3, 182 21 Prague 8, Czech Republic*

INTRODUCTION

Spectroscopic measurements of the Stark component of plasma emission lines have proved to be an efficient tool at determining the strength of turbulent Langmuir fields excited in a plasma by an intense relativistic electron beam (REB). Recently, at the REBEX experimental facility, H_α and H_β line profiles with excellent spectral, temporal and spatial resolution have been obtained by means of an advanced imaging spectrograph combined with a gated image intensifier [1]. In this paper we report model calculations of the H_α line profiles, which make it possible to distinguish the Stark component of the investigated lines from the strong Doppler background observed in the experiment, and, thus, to estimate the level of the Langmuir turbulence in the REBEX plasma.

EXPERIMENTAL RESULTS

The reported spectroscopic measurements were performed at the REBEX experimental facility [2] designed for investigations of the interaction of an intense pulsed relativistic electron beam (450 kV, 50 kA, 100 ns, \varnothing 3.5 cm) with a dense magnetised plasma column ($5 \cdot 10^{20} - 10^{22} \text{ m}^{-3}$, \varnothing 7 cm, length 1 m, magnetic field 0.6-1 T).

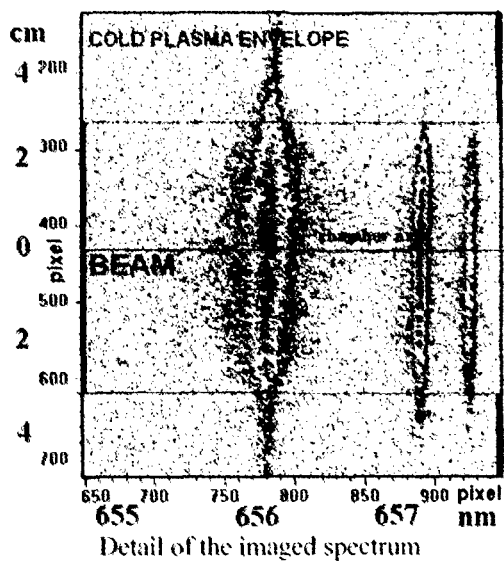


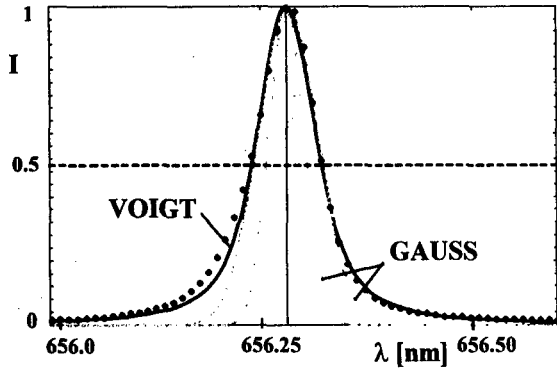
Fig. 1

The spectroscopic apparatus used consists of the imaging spectrograph Chromex 500 IS, of a gated single-stage image intensifier (ii), of a high speed relay lens optics, and of a CCD camera with the thermoelectrically cooled back-illuminated Tektronix CCD chip 1024 x 1024 pixels. The actual spectral, spatial and temporal resolution of the spectroscopic apparatus achieved at the reported experiments is $\approx 0.010 \text{ nm/pixel}$ in the H_α region, $\approx 0.133 \text{ mm/stripe}$, and 100 ns, respectively. For illustration, a shaded $I(\lambda, r)$ contour plot of the original imaged spectrum in the H_α region recorded during the beam injection is shown in Fig. 1 (ii gate width 200 ns, image scale 3 nm x 100 mm). Two regions may be easily distinguished in the picture - the beam channel with a strongly broadened H_α

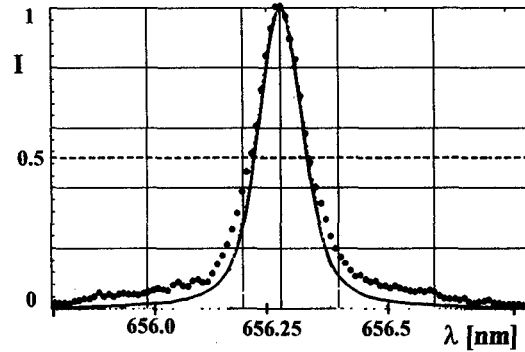
line and with two intense C II impurity lines, and the cold plasma envelope. Very smooth spectral and the spatial profiles of the line intensity ($I(\lambda)$ and $I(r)$) have been obtained from the recorded (I, λ, r) matrix by summing up several matrix rows or columns.

While the shape of the wings of the H_α spectral profiles $I(\lambda)$ change considerably at varying the time delay between the ii gate and the beam injection, the line central part

preserves its nearly Gaussian shape (cf. the dotted lines in Figs. 2-4). The line half-width increases several times during the beam injection, from its initial forplasma value of ≈ 0.08 nm up to ≈ 0.4 nm at the end of the beam injection, decreasing again afterwards with the characteristic time of ≈ 1 μ s. Shallow regular oscillations of the line width observed after the beam injection [3] have been attributed to magnetoacoustic radial plasma oscillation caused by a fast beam-induced overheating of the REBEX magnetised plasma column.

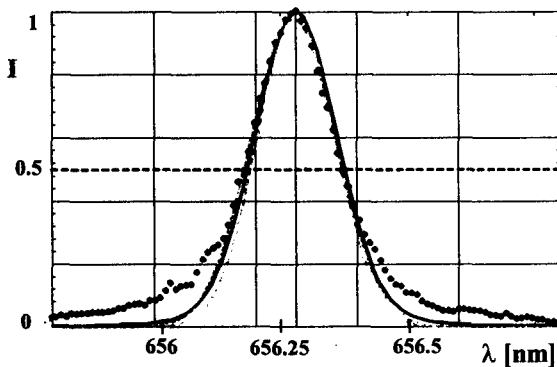


H_α line profile in a forplasma
Fig. 2

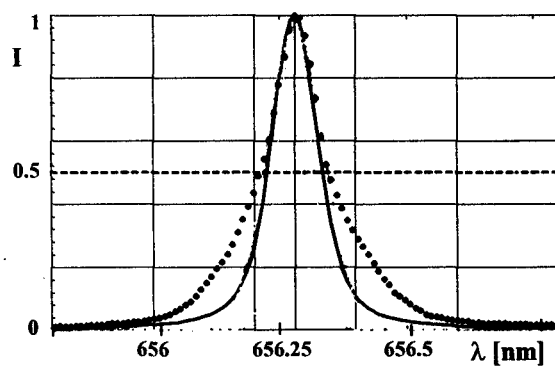


H_α line profile at the beginning of REB injection
Fig. 3

At all the recorded line profiles distinct wings spreading out up to 0.5 nm off the line centre are clearly visible. The wings are the most pronounced at the beginning of the beam injection (the first 50 ns), when the central part of the line is still rather narrow (Fig. 3). While in the forplasma case (Fig. 2) the line shape can be well approximated by a Voigt function (see the full line corresponding in this particular case to $\alpha = 0.9$, $T_n = 0.93$ eV, $N_n = 10^{22}$ m $^{-3}$, where α is the parameter of the Voigt function [4], T_n and N_n the neutral temperature and density, respectively), the Voigt fit completely fails at the line profiles recorded during and after the beam injection (cf. full lines in Figs. 3-5). Thus, in order to explain rather complicated line shapes observed in a beam-heated plasma, another line broadening mechanism, in addition to the thermal Doppler and Lorentz collisional broadening, must be considered. No doubt, the most natural line broadening mechanism in REB-plasma experiments is the Stark broadening due to strong turbulent Langmuir fields, which are excited in the course of beam-plasma interaction by the two-stream instability [5].



H_α line profile at the end of REB injection
Fig. 4

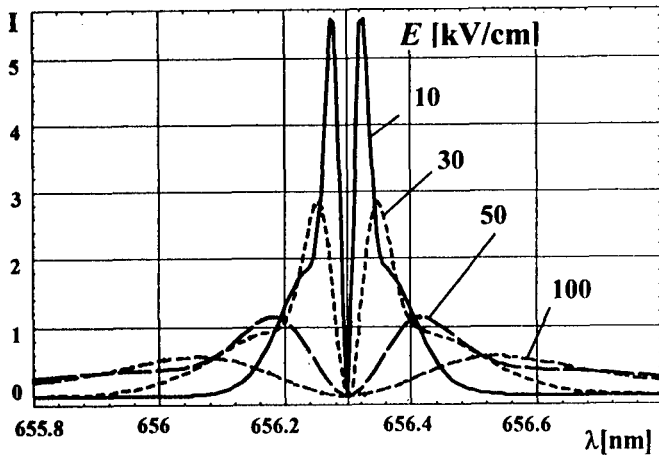


Cumulative H_α profile 100 ns after REB injection
Fig. 5

Note: In the above four pictures the bold dotted line represent the experimental H_α line profiles, the full and broken lines are used for the Voigt and Gaussian fits, respectively. The narrower Gaussian curves (dashed lines) show the thermal Doppler parts of the corresponding Voigt functions.

MODEL CALCULATIONS

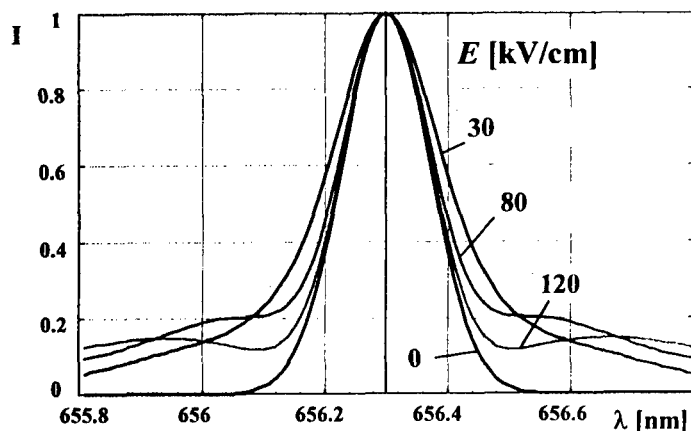
According to our earlier estimates [6] made on the base of various theoretical models of beam-plasma interaction, in REBEX conditions the Langmuir turbulence level η should reach the value of 0.04-0.2, which corresponds to the mean strength E of the stochastic high-frequency Langmuir fields as high as 60-150 kV/cm. Such high-intensity electric fields should strongly influence the shape of the wings of the investigated H_α line, as illustrated by Fig. 6, in



Sum of 16 Stark H_α line components for various fields E

Fig. 6

Our earlier experiments have shown that in the REBEX machine not only electrons but also ions (and, therefore, due to fast charge exchange processes, also neutrals) are efficiently heated during the beam injection pulse [8]. Thus, the central parts of the investigated line



Combined Stark and Doppler broadening

Fig. 7

profiles are shaped by a rather strong thermal Doppler effect, which also has to be taken into account at our model calculations. The influence of the Stark broadening due to stochastic Langmuir fields on the shape of H_α line with a substantial Doppler background is illustrated by Fig. 7. The profiles depicted there are calculated by using (in a similar way as in [9,10]) the quasistatic approach mentioned above. The Doppler half-width for all the four profiles is fixed, $\Delta\lambda_D = 0.1$ ($T_n = 11$ eV), and the strength of the stochastic electric fields is varied from 0 to 120 kV/cm. Clearly, for the value of neutral temperature higher than 10 eV, the strength of the stochastic electric fields must be higher than 30 kV/cm for pronounced wings at the line profile to appear. For each neutral temperature a certain value of the field strength E exists, at which the wings have a typical saddle-like shape. For the particular case depicted in Fig. 7 it is the value of 80 kV/cm.

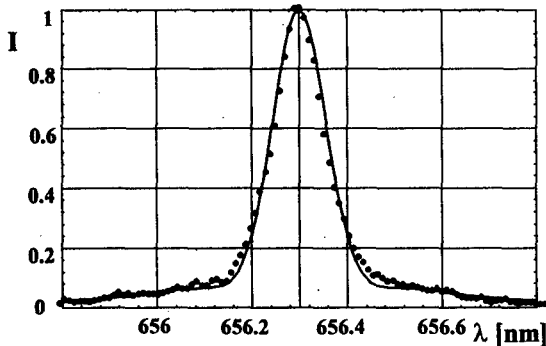
The line profiles in Fig. 7 already resemble well the experimental profiles shown in Figs. 3-5. Really, each of the experimental profiles can be fitted by model curves during a few iteration steps, by varying the values of the neutral temperature and of the electric field

in which the sum of sixteen Stark components (± 1 to ± 8) is shown, for the HF field strength varying from 10 kV/cm to 100 kV/cm. At calculating the Stark components the quasistatic (low-frequency) approach described in detail in [7] was used.

For this approach to be valid the condition $\omega_p \ll 2g \cdot s \cdot E$ must be fulfilled (here g stays for the Stark parameter and s is the number of the most pronounced Stark component), which is true for the field strength $E > 10$ kV/cm at $N_e \geq 10^{20} \text{ m}^{-3}$, and for $E > 100$ kV/cm at $N_e \approx 10^{22} \text{ m}^{-3}$.

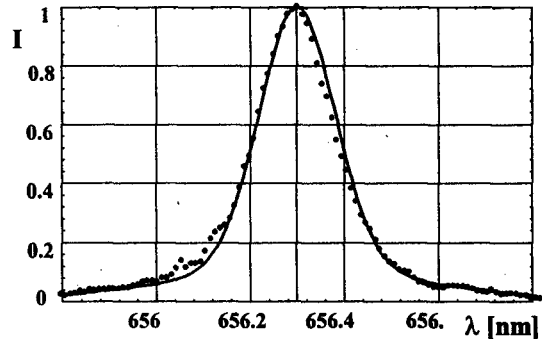
profiles are shaped by a rather strong thermal Doppler effect, which also has to be taken into account at our model calculations. The influence of the Stark broadening due to stochastic Langmuir fields on the shape of H_α line with a substantial Doppler background is illustrated by Fig. 7. The profiles depicted there are calculated by using (in a similar way as in [9,10]) the quasistatic approach mentioned above. The Doppler half-width for all the four profiles is fixed, $\Delta\lambda_D = 0.1$ ($T_n = 11$ eV), and the strength of the

strength. The fitting can be further improved by introducing at the convolution of the Stark and Doppler components a form factor $\xi \cong 0.2-0.3$, which respects the experimentally observed spatial localisation of the electric fields in the beam channel (cf. the spatial profiles $I(r)$ of the H_α line intensity in [1]). The results of this fitting are illustrated by Figs. 8a and 8b, which correspond to the experimental profiles shown in Figs. 3 and 4 (taken at the beginning and at the end of the beam injection). The best fit for the profile in Fig. 8a has been obtained for $T_n = 7$ eV, $E = 70$ kV/cm, $\xi = 0.2$, and for the profile in Fig. 8b for $T_n = 15$ eV, $E = 30$ kV/cm, $\xi = 0.3$. Quite naturally, the Langmuir fields are stronger at the beginning of the beam injection (when the beam diode voltage U_b is maximum), and they are weaker at later times.



Combined Doppler and Stark fitting of the H_α line profile taken at the beginning of REB injection

Fig. 8a



Combined Doppler and Stark fitting of the H_α line profile taken at the end of REB injection

Fig. 8b

CONCLUSION

The model calculations described here show that the H_α line shapes observed in a REB-heated plasma can be well explained by a combined effect of a thermal Doppler broadening due to fast ion-heating and charge-exchange processes, and of a Stark broadening due to stochastic Langmuir fields excited during beam-plasma interaction. In the reported series of REBEX shots the estimated strength of Langmuir fields reached the maximum value of $70 \div 100$ kV/cm (the turbulence level $\eta \approx 0.05 \div 0.1$). This range coincides well with the theoretical predictions. The Stark component of the H_α line profiles can be more easily distinguished at weaker beam shots at which the neutral (ion) temperature is not too high (10-20 eV). At higher ion temperatures (30-40 eV) routinely achieved in REBEX the Stark broadening is almost completely masked by a wide Doppler background [10].

This work was supported by the Grant Agency of the Czech Academy of Sciences under contract No A1043504

REFERENCES

- [1] Ullschmied, J., Koláček K., Řípa M.: Proc. 11th Int. Pulsed Power Conf., Baltimore 1997, Vol. I, p. 1710
- [2] Babický, V. et al.: Proc. BEAMS'90, Novosibirsk 1990, Vol. II, p. 835
- [3] Ullschmied, J.: Proc. 17th Symposium on Plasma Physics and Technology., Prague 1995, p. 147
- [4] see e.g. Lochte-Holtgreven: Metody issledovania plazmy, Mir, Moskva 1971, p.102
- [5] Burmasov, V.S. et al.: Proc. BEAMS'94, San Diego 1994, Vol. II, p. 590
- [6] Ullschmied, J. et. al.: Proc. BEAMS'96, Prague 1996, Vol. I, p. 343
- [7] Berezin, A.B. et. al.: Rep. No. P-K-0609, NIIEFA, Leningrad, 1983
- [8] Ullschmied, J. et. al.: Proc. BEAMS'94, San Diego 1994, p.735
- [9] Dolgachov, G.I. et al.: Proc. BEAMS'96, Prague 1996, Vol. II, p. 1207;
- [10] Koláček, K. et al.: Proc. BEAMS'92, Washington 1992, Vol. II, p. 1337

OPERATION OF LIA-10 LINEAR INDUCTION ACCELERATOR IN THE MODE OF ENERGY TRANSPORT ALONG VACUUM COAXIAL LINE

A.M.Chlenov, V.F.Zinchenko, E.V.Tulisov, V.D.Shijan

*Research Institute of Scientific Instruments
RF Atomic Energy Ministry
Turaevo, Lytkarino, Moscow Region, 140061, Russia*

Abstract

The results of experimental and theoretical optimization of LIA-10 pulsed linear induction accelerator construction for maximizing of relativistic electron beam (REB) parameters and the bremsstrahlung output are presented.

The basic idea of this work was consisted in using the operation mode of stored energy transport along the vacuum coaxial line with tapered inner electrode instead the original operation mode of successive REB acceleration by pulsed electric fields induced by independent accelerating modules. In practice this idea has been realized by increasing the length of inner electrode from initial value $L = 1,6$ m up to limit $L = 6,0$ m, corresponding the maximum length of accelerating system.

The dependencies of REB current and energy on such parameters as the length of tapered cathode L and diode geometry are discussed.

Introduction

The high current accelerator LIA-10 is a linear induction accelerator in radial lines with successive sectional structure of accelerating system. A detail description of its construction is given in references ^{1, 2, 3}. The accelerator of this type is used in RISI for generation of intense pulses of bremsstrahlung. At present time the following accelerator's parameters are realized:

- peak current of REB, $I_{\max} = 30$ kA;
- effective electron energy, $E_{e,\max} = 10$ MeV;
- FWHM, $t_{1/2} = 10$ ns;
- peak dose rate, $P_{\max} = 10^{12}$ rad(Si)/s.

Lately, complex investigations bound up with optimization of the LIA-10 construction have been carried out with the aim of increasing the generated bremsstrahlung output. In this paper the results of the optimization of the accelerator injector are presented.

According to the original design of LIA-10, its injector consists of 4 separate sections of inductors (accelerating modules). The voltage induced by accelerating modules (AMs) is summed at a tapered cathode. A thin annular electron beam is generated in the foilless diode with magnetic isolation in axial field (Fig.1). The beam is then accelerated as it propagates through the 12 AMs operating during the pulse generation in consistence with a chosen temporal programme. A peak current of REB at the exit of the injector is 40 kA with an electron energy being 2.5 MeV.

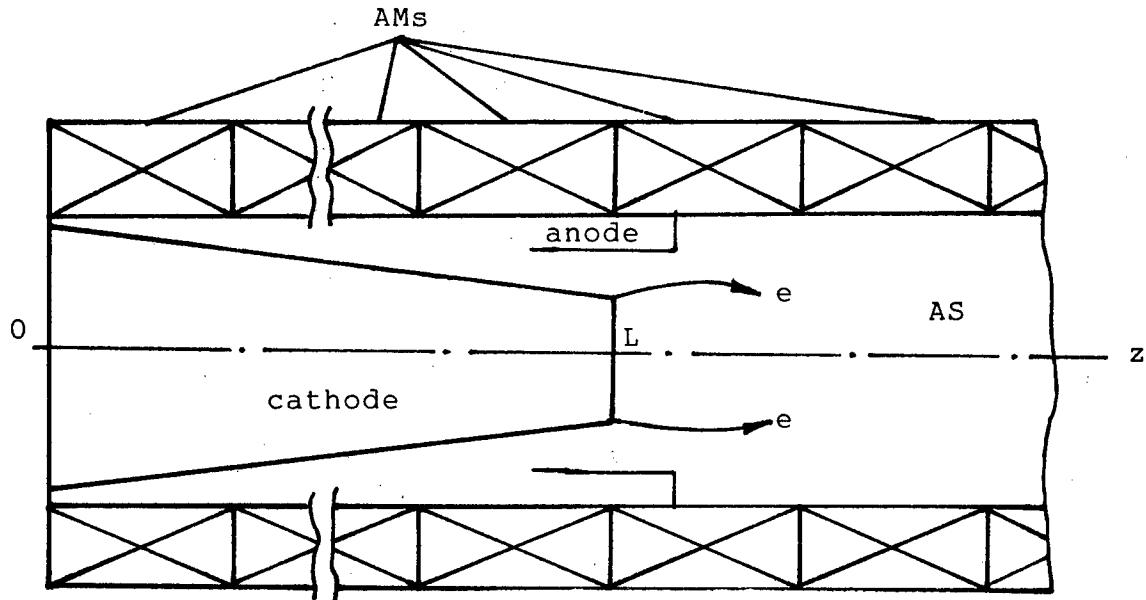


Figure 1. Schematic of the LIA-10 injector

The main purpose of this study is to investigate the possibilities of increasing the energy and current of REB injected into accelerating system (AS) for decreasing the losses of REB in AS and increasing the bremsstrahlung output.

The tapered cathode where voltage is summed performs different functions in LIA-10 (Fig. 1). Except assuring a gain in electromagnetic energy, it operates as a vacuum transmission line providing a specific form of current and voltage pulse in the diode gap.

Numerical Simulation and Experimental Results

We suppose that some of problems can be solved by increasing the number of AMs in the injector module of LIA-10, i.e. by going to the accelerator's operation in the mode of energy transport along the vacuum coaxial line.

Because numerical simulation must be followed by experiments, a simple calculation model of high current REB generation in the accelerator injector has been developed. Let's consider an ideal geometry of an injector used in the modeling (Fig.1). The voltage induced by Ams is summed by the tapered cathode and applied to the cathode - anode gap. While separate AM induces an accelerating voltage pulse $V_0(t)$, then an electric field strength $E_z^{(i)}(z, t)$ induced by i -th AM can be expressed as:

$$\begin{aligned} E_z^{(i)}(z, t) &= V_0(t) / l_0, \quad z_i < z < z_{i+1} \\ z_{i+1} &= z_i + l_0 \\ l_0 &= 0,4 \text{ m} \end{aligned} \quad (1)$$

A shape of the accelerating voltage pulse was determined by using special experiments .

For the mathematical description of temporal behavior of current and voltage pulses in the injector diode, so called telegraph equations were used:

$$(R_g / l_0 + R^*) J = -1 / C^* \partial \chi / \partial z - 1 / c^2 L^* \partial J / \partial t + E_{ind}, \quad (2)$$

$$\partial \chi / \partial t = -\partial J / \partial z$$

where $J(z,t)$ is the current, running through the tapered cathode; L^* , R^* , C^* are the self-induction, resistance and capacity per unit length of cathode, respectively; R_g is the total impedance of the voltage source in separate AM, $R_g = 4,2 \text{ Om}$.

For a vacuum case

$$L^* = 2 \ln(R/r), \quad C^* = 0.5 / \ln(R/r),$$

where r is the running radius, $R = 0.18 \text{ m}$.

$E_{ind}(z, t)$ is the electric field strength induced by the injector forming AMs. At a certain interval $[z_i, z_{i+1}]$, $i=1, \dots, N$ $E_{ind}(z, t)$ is determined according to (1) where temporal behaviour of the voltage pulse $V_0(t)$ doesn't depend on the other AMs.

Boundary conditions for the equation set (2) at the cathode tip ($z=L$), taking into account the operating features of the cathode under explosion emission conditions, can be described as follows:

$$\begin{aligned} J(L, t) &= 0, \quad E_c < E_{th} \\ \partial J / \partial z &= 0, \quad z = L, \quad E_c > E_{th} \end{aligned} \quad (3)$$

where E_c is the macroscopic electric field strength near the cathode tip, E_{th} is the starting threshold of the electron explosion emission from the cathode.

By solving the equation set (2) at the boundary conditions (3), we obtain distribution $J(z,t)$ in the cathode length. A voltage applied to the diode gap is estimated from:

$$V_d(t) = \int_{z_{min}}^L (-R^* J - R_g / l_0 J - 1/c^2 L^* \partial J / \partial t + E_{ind}) dz \quad (4)$$

A magnitude of E_{th} was only one of unknown parameters of the calculational model. Its value was obtained by comparison of experimental and calculation results of REB current amplitude and a value of temporal shift of voltage and current pulses at the 4 AMs injector (original version of LIA-10). The optimal value ($E_{th} = 800 \text{ kV/cm}$) agrees quite well with known experimental results obtained for explosion cathodes⁴.

Using the above model, complex of calculations to optimize parameters of the modified LIA-10's injector was performed. Typical shapes of current and voltage pulses at the exit of the injector formed by 7 AMs, obtained by solving equation (2), are presented in Fig. 2. In this case as the value of a wave impedance of the transmission line ($Z_l = 35 \text{ Om}$) is not matched to the real diode's impedance ($Z_d = 50 \text{ Om}$), then a peak value of the electron beam current injected from the cathode tip into AS doesn't exceed 60 kA. That fact is consistent with experimental data.

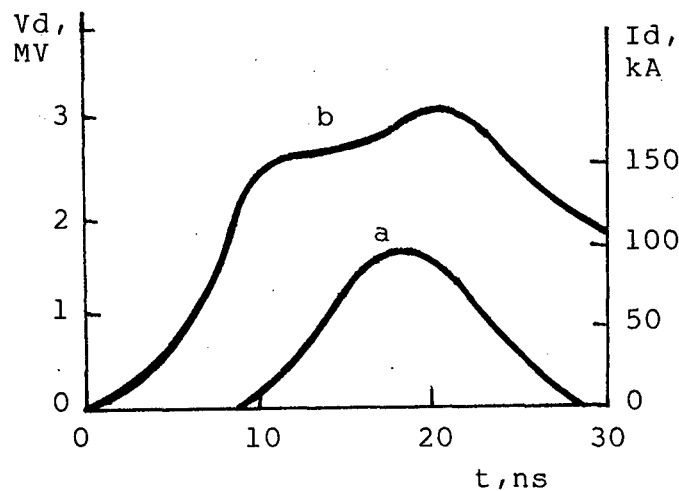


Figure 2. Current (a) and voltage (b) pulse at the exit of the injector formed by 7 AMs

To obtain matched impedances Z_l , Z_d we have considered a version when a number of AMs in the injector's module is equal to an overall number of AMs in LIA-10. It was shown that the following REB parameters at the exit of accelerator are realized: peak current $I_{\max} = 200$ kA; electron energy $E_e = 6.2$ MeV; beam radius $r_b = 5$ cm. After REB focusing in the increasing axial magnetic field ($B_z = 4$ T) a magnitude of peak dose rate at the face of the target reaches 10^{13} rad(Si)/s.

Conclusion

Thus, the results presented in this study allow us to recommend the energy transport along the vacuum coaxial line as an alternative mode for the LIA-10's operation. In this case, we can realize the parameters of bremsstrahlung dose field that are well beyond the corresponding parameters for the original design of LIA-10.

References

- [1] Pavlovskii, A.I., Bosamykin, V.S.,: Atomnaja Energija, 37 (1970) 228
- [2] Pavlovskii, A.I., Bosamykin, V.S., Gerasimov, A.I.,: Dokl. Acad. Nauk SSSR, 222 (1975) 817
- [3] Pavlovskii, A.I., Bosamykin, V.S., Gerasimov, A.I.: Dokl. Acad. Nauk SSSR, 250 (1980) 1118
- [4] Rudakov, L.I.,: Generazija i focusirovka silnotocnyh elektronnyh puchkov (in russ.), Moscow, Energoatomisdat, 1990.



BEAMS'98

12th INTERNATIONAL CONFERENCE
ON HIGH-POWER PARTICLE BEAMS



POSTERS

***Diagnostics and
Experimental
Methods***

Vol. I

SPECTRA OF LASER SCATTERING ON POWERFUL REB

A.V.Arhzannikov, V.S.Burmasov, S.A.Kuznetsov, S.S.Popov,
S.L. Sinitsky and M.A.Shcheglov

Budker Institute of Nuclear Physics SB RAS, Novosibirsk, 630090, Russia

Introduction

There are many tasks which need to generate high quality powerful Relativistic Electron Beam (REB). One of them is to drive Free Electron Maser by the REB.[1] The pumping efficiency of electromagnetic waves by powerful relativistic electron beams essentially depends on a velocity spread of the beam electrons. One of the main problem here is to reach small velocity spread of the beam electrons. For example, for undulator period $l \sim 1 \text{ cm}$ and its length $L \sim 1 \text{ m}$ at electron energy $E \sim 1 \text{ MeV}$, their longitudinal velocity spread should be less than 10^7 cm/s and angular spread of the electrons $\Delta \bar{\vartheta} \leq 0.03$ (2 degree).

Obtaining such small spread is not easy task. In the frame of the task, measurements of the electron distribution function have great importance for these experiments. Laser scattering is analogy to [2,3] seems to us as the most promising method to measure pointed level of the velocity spread. On this purpose this diagnostics has been manufactured and mount in the device «ELMI» created on the base of U - 3 accelerator for investigations on the FEM are carried out [4].

Experiments on CO_2 -laser radiation scattering ($\lambda = 10.6 \text{ } \mu\text{m}$) on a high current sheet beam with measurements of scattered radiation spectra in an optical range, were proposed and discussed in the paper [5]. Reconstruction of the electron distribution function for the measured spectra at various experimental conditions are discussed there. In this presentation we describe the experiment on CO_2 -laser radiation scattering on the sheet electron beam and results of computer simulations for these experimental conditions [6]. The experiments are carried out at the U - 3 device [7] that has been specially modified for generation of a sheet beam. First results on testing those diagnostic are also presented.

Theoretical consideration and numerical simulation

Frequency ω of the radiation scattered by relativistic electron is relates with initial one ω_0 in accordance with the following equation $\omega = \omega_0 \frac{1 - \beta \cos \vartheta_1}{1 - \beta \cos \vartheta_2}$ (*), where $\beta = \sqrt{1 - \gamma^{-2}}$; γ is relativistic factor of electron.

The function $d\omega/d\beta$ has a maximum at $\vartheta_1 = \pi$, $\vartheta_2 = 0$ and this maximum is equal to $4\omega_0\gamma^2$. The spectral density of scattered radiation $dP/d\omega$ is determined by the following formula

$$\frac{dP}{d\omega} = \int_{-c}^c \int_{\Omega} I_0 \frac{d\sigma}{d\Omega} f(\vec{V}, \vec{r}) \delta(\omega - \omega') d\vec{V} d\vec{r} d\Omega \quad (**)$$

where I_0 is intensity of incident radiation, $f(\vec{V}, \vec{r})$ is

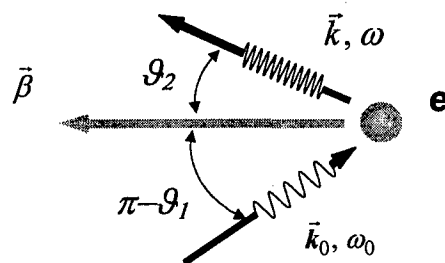


Fig.1. The scheme of photon scattering on electron

the electron distribution function, $\frac{d\sigma}{d\Omega}$ is a differential cross section for the scattering process, v is a scattering volume and ω' is determined from (*), $\Delta\Omega$ is an angel interval of registration system.

There is the principal possibility to differ input into the spectral density of the scattered radiation by the electron energy distribution function and by their angular distribution.? This

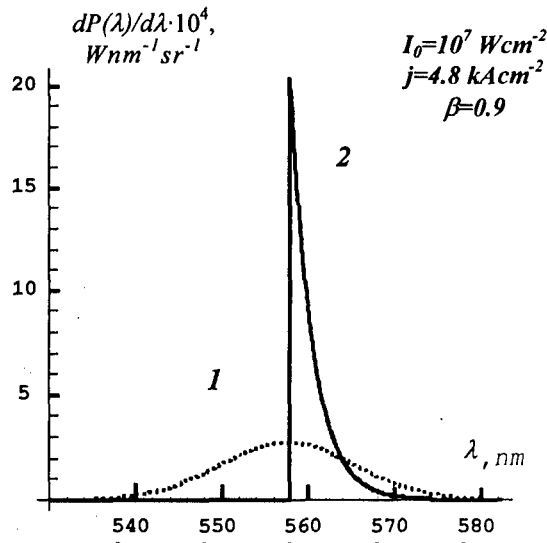


Fig.2. Spectra of scattered radiation for the beam electrons with the energy spread $(\overline{\Delta E^2})^{1/2} \approx 4 \text{ keV}$ (1) and with the angular spread $\overline{\Delta \theta} \approx 2^\circ$ (2).

difference is demonstrated by Fig.2. The calculated spectral density of scattered radiation is presented there for two cases: (1) angular spread is vanishing ($\Delta\theta_b = 0$), energy distribution function is Maxwell one

with $(\overline{\Delta E^2})^{1/2} \approx 4 \text{ keV}$, $\beta \approx 0.9$, and (2)

$\overline{\Delta \theta_b} \approx 2^\circ$, $(\overline{\Delta E^2})^{1/2} = 0$, $\beta = 0.9$. One

can see that the functions of spectral density on the wavelength is sharply different from these two cases.

But in practice, it is very difficult to reconstruct electron distribution function $f(\vec{V}, \vec{r})$ by using the formula (**) on the base of measured spectra. For solving this task we have made computer simulation of the scattered radiation spectra for various velocity distribution functions of the beam electrons.

In addition to the angular spread of the beam electrons the shifting of electron velocity by the influence of own beam's electric and magnetic fields were taken into account at these simulations. It was shown that for the case of the Gauss distribution function of electrons with the angular spread 1° and their relativistic factor $\gamma = 3$ a typical spectrum had a width about of 7 \AA (see Fig. 3). for vanishing small current density of electron beam.

The effect of the self beam fields for the linear current $I' = 0.5 \div 1 \text{ kA/cm}$ leads to strong shifting of the position of spectra maximum and to increasing of the spectrum width up to a few tens of Angstroms (see Fig. 4). These properties of the spectrum behaviours give one possible to obtain the angular spread of the beam electrons and the values of the self beam fields separately by analysis of the width and the shape of the spectrum. In case when the beam current and the spectrum profile are measured independently the measurements permit to find a value and time evolution of the beam charge neutralization in the experiment.

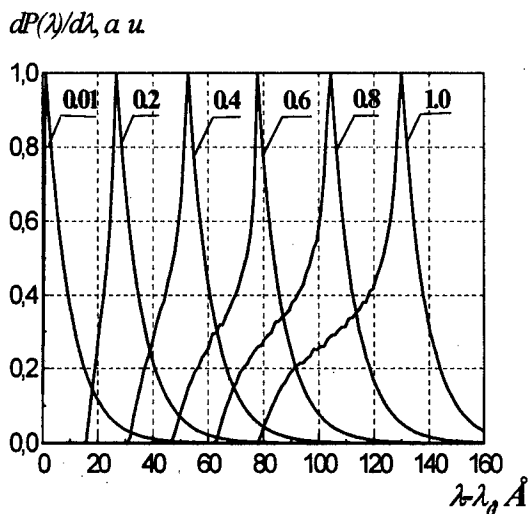


Fig.3. Calculated spectra of laser radiation scattering on the noneutralized sheet REB ($\gamma_0=2.6$, $d=4$ mm, $B_0=1$ T) for different current densities j . $\lambda_0=4200$ Å corresponds to minimum wavelength of scattered radiation.

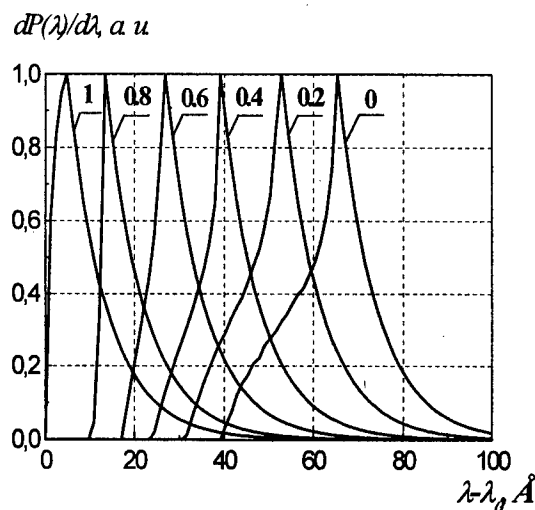


Fig.4. Calculated spectra of laser radiation scattering on the sheet REB ($\gamma_0=2.6$, $d=4$ mm, $B_0=1$ T, $j=0.5$ kA/cm²) for different values of beam neutralization, f . $\lambda_0=4200$ Å corresponds to minimum wavelength of scattered radiation.

Experimental method of spectra registrations

The lay-out of the experiments is shown in Fig. 5. In the experiments the CO₂-laser radiation with total energy about 10 J at 100 ns pulse passes in a vacuum channel in the opposite direction to the relativistic sheet electron beam. The typical value of the electron energy is $E \sim 1$ MeV ($\gamma \sim 3$) and the linear current density of the beam is about $I' = 0.5$ kA/cm.

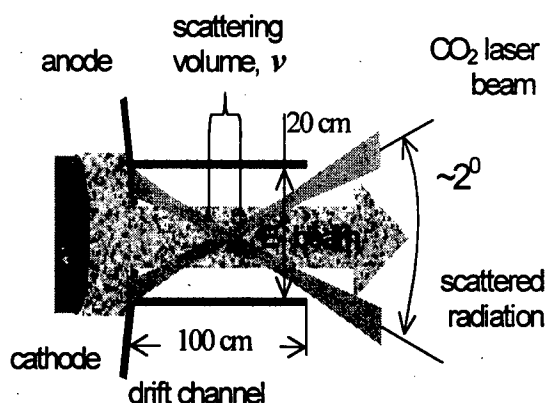


Fig 5. Schematic of diode, beam line, dropping and scattering of radiation.

We use a TEA laser oscillator with UV preionization, which output is equal to ~ 1 J, and a TEA amplifier with corona discharge preionization at addition triethyl-amine ($P=1$ Torr) in the gas mixture. ZnSe and NaCl windows are used both in the oscillator and in the amplifier. The oscillator is turned to one line of CO₂ molecule ($\lambda=10.6\mu\text{m}$) by a diffraction grating (150 lines per mm).

Back scattered laser light is apertured and transported through light guides. After that it is directed on slit of a grating spectrometer for an analysis. Line dispersion of the spectrometer is about 10 Å/mm. From the spectrometer the scatter-

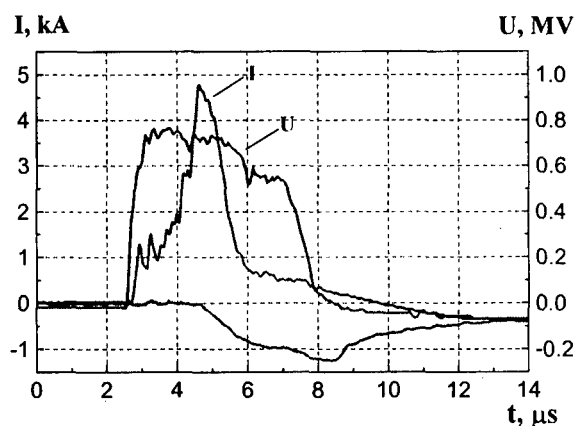


Fig.6. Oscillograms of accelerator diode voltage (U), beam current (I) and background light (lower curve, arbitrary units).

ed light through six light guides on photomultipliers. Before laser scattering experiment we have carried out testing experiment to measure a light coming to the registration system.

For this goal we measured background light and a stray-light level throughout the accelerator pulse. The result of the measure is presented in Fig.6. One can see the level of background light is vanishing small during initial four microseconds. After that the stray-light is increasing very little during accelerator pulse. That stray-light behaviour permit one to hope on successful scattering experiments.

Conclusion

So, experiments on CO₂-laser radiation scattering ($\lambda=10.6 \mu\text{m}$) on a high current sheet beam with measurements of scattered radiation spectra in an optical range have been prepared at the U - 3 device. In the first series experiments it has been established that background light from the vacuum channel is small during initial four microseconds of the beam generation and one may hope to measure spectrum of the scattered light. Spectra of the scattering radiation have been calculated by the computer simulations for various experimental conditions. Results of the background light registrations and computer simulations allow us to start the measurements of the electron distribution function.

Acknowledgements

The work is supported under ISTC grant # 531 and RFFR grant # 95-02-04620.

References

- [1] S. H. Gold, G. S. Nusinovich, *Rev. Sci. Instrum.*, 68, 3945 (1997)
- [2] S. C. Chen and T. C. Marshall, *Phys. Rev. Lett.*, 52, 425 (1984)
- [3] Y. Kawamura, M. Kawai, and K. Toyoda, *Jpn. J. Appl. Phys.*, .27, 2013 (1988)
- [4] A. V. Arhzannikov *et al.*, to appear in these meeting
- [5] A. V. Arhzannikov, Preprint BINP 91-102, Novosibirsk, 1991
- [6] A.V.Arhzannikov, V.S.Burmasov, S.A.Kuznetsov, S.L. Sinitsky, 9th National Topical Conf. on High-Temperature Plasma Diagnostics, S-Petersburg, June, 1997, Book of Abstracts, p.49
- [7] A.V. Karyukin, S.V. Lebedev, M.A. Shcheglov *et al.*, *Proc. of 9th Intern. Conf. on High-Power Particle Beams*, Washington, DC, 1992, v.2, p.1015

X-ray spectroscopy application for magnetic field and electron beam measurements in laser produced plasma

E.O. Baronova and G.V. Sholin

*Nuclear Fusion Institute, RRC Kurchatov Institute
123182, Moscow, Russia*

Abstract. Temperature and density gradients, parametric instabilities which are common to laser produced plasma, can lead to both spontaneous magnetic field and electron beam generation. Strong magnetic field splits lines, suprathermal electrons are of great importance in energy transition processes and in plasma emission spectra formation.

Paper presents magnetic field strength and suprathermal electron energy measurement method, based on investigation of x-ray line spectra, emitted from laser produced plasma. Simple mechanism of magnetic field generation based on cumulative stream formation is presented.

Experimental set up and diagnostics

Experiments were performed on "Target-1" facility [1], where flat and conical aluminum targets were irradiated by Nd laser focused beam with intensity higher, than 10^{13} Wt/cm². Diagnostics were (see Fig. 1):

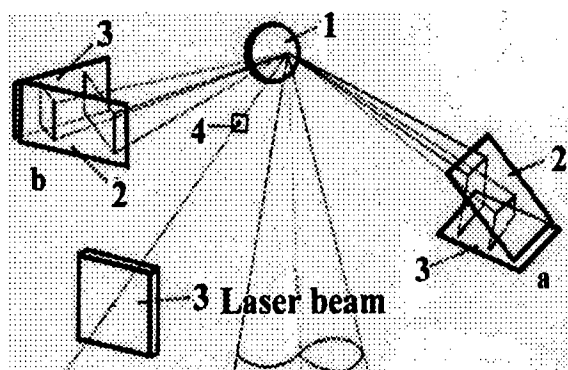


Figure 1. Devices accommodation, 1-target, 2-crystals, 3-film, 4-pinhole-camera.

1. Pinhole camera with the hole 20 μ m, covered by 50 μ m Be and 7 μ m Al, distance from hole to plasma was 25 mm, magnification 1:5.

2. Two x-ray spectrographs with flat KAP crystals, registered time integrated spectra in the first and second orders of reflection and situated as shown in Fig1. Crystal to source distance was 70 mm and 100 mm for a) and b) devices accordingly, crystal to film distance was 15 mm for both the devices. Cassette with film was covered by 20 μ m Be filter to protect from visible light, entrance windows of spectrographs was also covered by 20 μ m Be filter. In the first series of experiments devices worked in the first orders of reflection.

Than device, registered spectra in a) direction, was remade for working in the second order of reflection.

Results

Time integrated plasma image, obtained in X-rays of $E_\gamma > 1,5$ keV in one shot are given in Fig2.

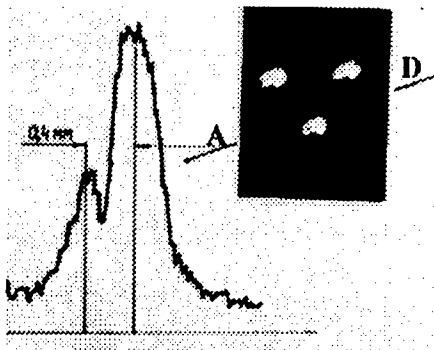


Figure 2. Pinhole image and its densitogram, made in AD direction

It shows the existence of two plasma regions, situated one close to another. Size of large region is equal to 0,6-0,8 mm in diameter, the smaller one is approximately three times less, distance between these regions is about 0.4 mm.

Spectra, registered in two different shots in direction a) are presented in Fig.3. Densitogram shows group of lines of H (Al 13)- and He (Al12)-like ions of aluminum, K alpha, beta lines (Ka,b) of Al atom and K-alpha lines of aluminum ions from 6 to 10 ionization stages. Size of the region, emitting resonance line of H-like ion is 0.2mm, size of the region, emitting resonance line of He-like ion is 0.4 mm, sizes of the region, emitting K-alpha, beta lines of Al atom is larger, than that for strongly ionized aluminum.

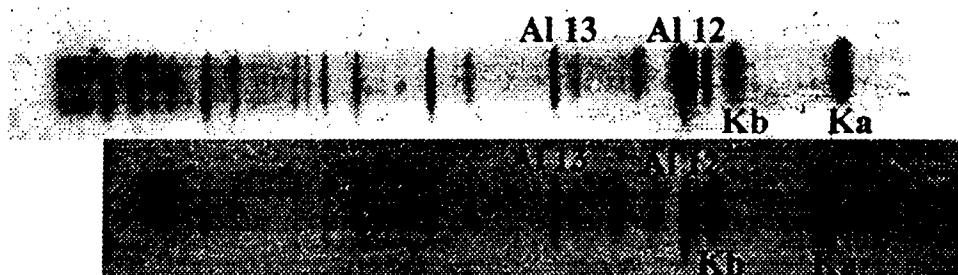


Figure 3. Two spectra, obtained in different shots in a) direction

Temperature and density, evaluated from relative intensities of lines belonging to He-like group [2] are $N_e \sim 10^{19} \text{ cm}^{-3}$ and $T_e \sim 0,4 \text{ keV}$ (presence of electron beam was not accounted).

Analysis of the spectra, registered in a) direction and related to different shots has shown the pair of atom K-alpha, beta (Ka,b) lines shifted with regard to the Al ion lines (H and He-like) group of lines, see Fig 3,4.

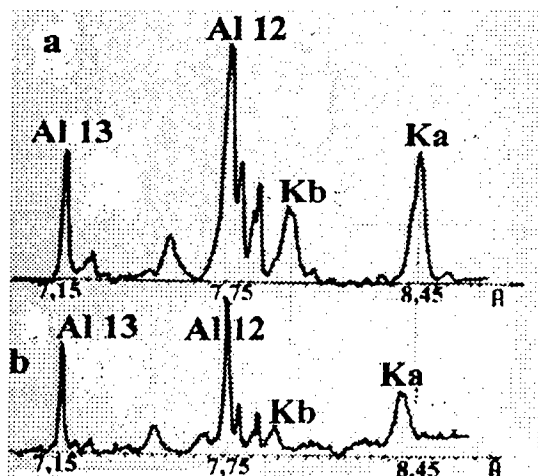


Figure 4. Densitograms of spectra, given on Fig.3.

The one more feature of spectra obtained is the presence of splitting of resonance line of H-like Al ion, registered in the second order of reflection in a) direction, see Fig.5. This feature was observed, when aluminum targets with small conical hollow were irradiated.

Discussion



Fig.5. Densitogram of Al 13 resonance line.

Taking into account the dependence of the line position on the position of the source (for flat crystal) this effect could have been explained by the change of distance between the source of Al atom K alpha beta lines and the source of Al ion lines from one shot to another. Indeed, one can assume, that H and He-like lines are emitted by plasma and also plasma generates electron beam, which can leave plasma and interact with cold Al target surface, situated near plasma (see two regions on Fig.2.). This interaction leads to K-alpha, beta line emission, shifted with regard to position, calculated using dispersive curve of the device.

Distance between sources of Al ion lines and Al atom lines was estimated from relative shift of H and He-like lines and Al atom lines, the typical value of these shifts is about few hundreds of microns, what corresponds to the distance between two regions, obtained by pinhole-camera.

Irradiation of conical target also proves that the position of the sources of Al ion lines and Al atom lines are different, obvious demonstration of that is various inclines of ion and atom lines, registered in the same shot.

We also would like to pay attention on the fact, that splitting of resonance line of H-like ion might be explained by formation of cumulative stream [3]. Actually, irradiation of conical hollow can lead to plasma motion in perpendicular to conical surface direction and in opposite direction with regard to laser beam one. Velocity of this motion is equal to ion sound velocity $V_s \sim (T_e/M_i)^{1/2}$, the thickness of heated layer is equal to depth of electromagnetic field penetration in nonlinear regime $\delta = (c/\omega)(M_i/m)^{1/4}$ [4].

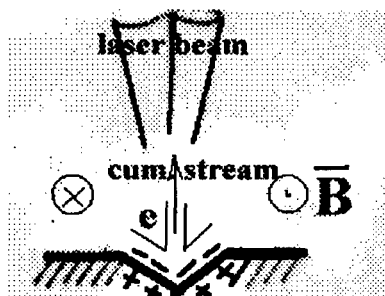


Fig.6.. Magnetic field and cumulative stream picture.

Plasma stream, moving towards the laser beam, has diameter $d \sim 2\delta$ and contains electron and ion components, flowing with their thermal velocities so, that current arises near axis region and corresponding toroidal magnetic field may be expressed as: $H_\phi = 0,2I/d \sim 0,6 \cdot 10^{-10} Ne \cdot V_e \cdot \pi \cdot \delta$.

The observed splitting of H-like resonance line is therefore explained as Zeeman splitting in this magnetic field, which may reach the value $H_\phi \sim 10^7 - 10^8$ Ersted. Let us estimate theoretically splitting of line in magnetic field:

$$\delta\lambda/\lambda = \delta\omega/\omega \sim (8/3\alpha^2 Z^2) \cdot (\mu \cdot H)/mc^2 \sim 10^{-12} H$$

Splitting, observed experimentally, is $\delta\lambda \sim 0,005 \text{ Å}$, i.e. $\delta\lambda/\lambda \sim 7 \cdot 10^{-4}$, such the splitting is actually possible, if $H \sim 10^8$ Ersted.

The series of experiments have shown the splitting being more often registered, if targets with conical hollow were irradiated. This is one of the possible confirmation of suggested model; of line splitting, the existence of both suprathermal electrons and characteristic lines. However, one cannot, exclude the probable influence of similar mechanism in the case of irradiation of flat targets, when duration of laser pulse is enough large. In such the case formation of cumulative stream might be as a result of focusing of different mode of laser beam in expanding dense plasma. Cumulative stream cone will be formed within the geometry of focusing laser beam, where electron temperature is essentially higher, than outside. The increasing of electron current density in the cumulative stream is possible due to decreasing of interaction region in the close vicinity of top cone and influence of magnetic compression $H^2/8\pi$.

Hot electrons, generated in plasma, moving in this field, could have circle trajectories, therefore, leaving the dense plasma region, they interact with cold target, causing the emission of characteristics atom lines of target material. Estimation of magnetic field, calculating the radius of electron trajectories from the relative shift of ion and atom lines, gives $H \sim 10^5$ Ersted.

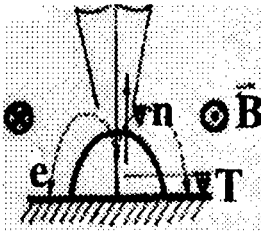


Figure 3. Configuration of magnetic field and electron beam.

Summary

1. Time integrated spectra of H and He-like aluminum ions and characteristics lines of aluminum atom, emitted from laser produced plasma, were registered in one shot
2. It has been shown ion and atom spectral lines emitted by different regions. This effect was explained by the generation of suprathermal electrons and magnetic fields inside plasma.
3. Splitting of resonance line of H-like ion was registered for the case of irradiation of target with conical hollow.
4. Self-conformed model of cumulative stream formation for the case of laser beam irradiation of target with conical hollow is suggested. This model permits one to interpret the existence of electron beams and toroidal magnetic fields.

In conclusion authors express gratitude to colleagues, worked at «Target-1» installation.

References.

1. V.V.Alexandrov, M.V.Brenner, S.V.Loburev, etc, Quantum Electr., v13, no4, 157, 1986.
2. L.P.Presniakov Uspehi Fisicheskikh Nauk, v119, no1, 49, 1976.
3. M.A.Lavrentiev, B.V.Shabat "Hydrodynamics problems and its mathematical models", Moscow, Science, 446, 1973.
4. A.A.Galeev, R.Z.Sagdeev, Voprosu teorii plazmu v.7, 87, 1973.

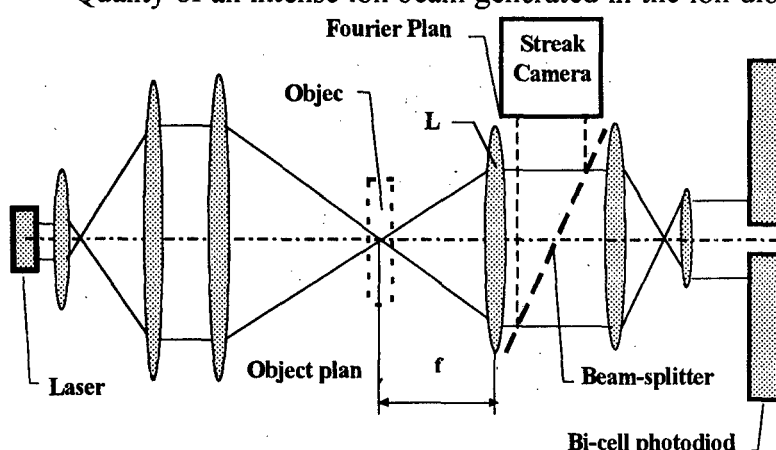
RETRIEVAL OF REFRACTIVE INDEX DISTRIBUTION IN AN ANODE LAYER FROM FOURIER IMAGE OF PROBE LASER BEAM

V.S. Cherkassky, B.A. Knyazev

Novosibirsk State University, Novosibirsk, 630090, Russia

INTRODUCTION

Quality of an intense ion beam generated in the ion diode sufficiently depends on characteristics of the anode plasma.



One of the ways to study the anode layer is a refractive index gradient diagnostics based on the record of deflection of a collimated laser beam [1-3]. To retrieve a refractive index distribution across the layer by such the technique one needs to perform a number of measurements at different distances of the laser beam from the anode surface. An alternative

Fig. 1. Schematic of optical system for study of anode plasma on COBRA ion diode.

technique [4], which is usually used for detection of distant objects, is retrieval of phase shift across a wide wave front, that have passed through a gradient layer, by solution of the inverse problem from two intensity measurements: intensity in the object plane and intensity in the Fourier plane. An experimental technique which, in essence, combines these methods and allows to record both a laser beam deflection and Fourier-image of the beam have been developed on COBRA accelerator at Cornell University [3]. Dynamics of the refractive index distribution obtained from laser beam deflection data was presented in papers [5] where experimental setup was described in detail.

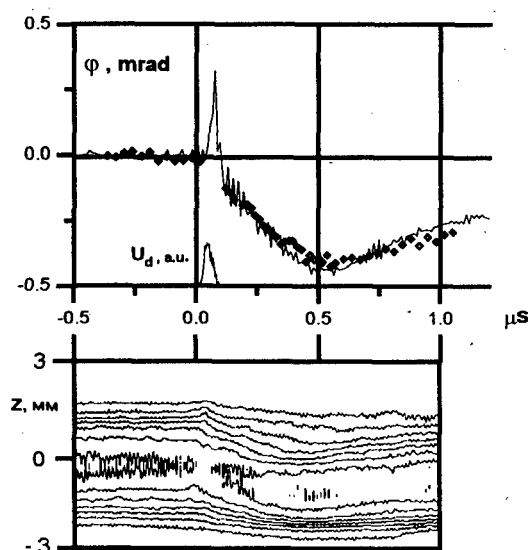


Fig. 2. Oscillogram of the photodiode signal and streak of the intensity distribution of the laser beam in the Fourier-plane (below) for the same diode shot. Distance from the beam axis to the surface of the anode is 0.45 mm, U_d is the voltage pulse applied to the COBRA diode. Diamonds: the beam deflection retrieved from the streak.

the Fourier-image of the beam recorded in the same shot are given in Fig. 2. They are in a

good agreement, excluding the time during the diode shot, because a sweeping time of $2 \mu s$ was not adequate the «positive» deflection of the beam in the streak to be resolved.

One can see that the streak of the Fourier image content some additional information in comparison with measurement of deflection of the laser beam centroid. It demonstrates non-linear distribution of the refractive index $\eta(z)$ across the beam. Thus, in principle, we can reconstruct from the streak of the Fourier-image the distribution within the laser beam and to improve by this way spatial resolution of the method [3,5]. This paper devoted to development of an algorithm for retrieve the distribution of refractive index within the beam from the magnitude of its Fourier image.

RECONSTRUCTION ALGORITHM

Since the optical system is a long-focus one, the plasma layer can be considered as a thin ones although really its width is sufficiently less than the length. For this reason we can assume the layer as a phase transparent positioned in the front focal plane of the lens. Using the approximation of the phase shift, *i.e.* assuming that the amplitude of a laser beam is not changed after passing through the layer but only its phase is changed, one can formulate a problem as follows. Let's assume that incident on the layer a complex wave is

$$f_0(z) = |f_0(z)| \exp[i\eta_0(z)] \quad (1)$$

After passing through the layer the wave function becomes

$$f_1(z) = |f_1(z)| \exp[i\eta_1(z)] \quad (2)$$

Corresponding Fourier-images, *i.e.* wave functions in a Fourier-plane, we will denote as $F_0(u) = \mathfrak{F}[f_0(z)]$ and $F_1(u) = \mathfrak{F}[f_1(z)]$ respectively. Thus, the task is reduced to definition of two phases $\eta_0(z)$ and $\eta_1(z)$ using recorded in the experiments amplitudes $|F_0(u)|$ and $|F_1(u)|$ under the additional condition

$$|f_0(z)| = |f_1(z)| = a(z) \quad (3)$$

Where $a(z)$ is a real function, - amplitude both of the non-perturbed and (under the assumption) perturbed beams in the front focal plane.

For solution of this problem we modified the Gerchberg-Saxton algorithm [6]. In our case this algorithm consist of the following steps (the block-diagram of algorithm is shown on the Fig.3.):

1. The random numbers in the range $0 \leq \xi \leq 2\pi$ were used as an initial approximation for phases $\psi_0(u)$ and $\psi_1(u)$ in the Fourier-plane.
2. Functions $\tilde{F}_0(u)$ and $\tilde{F}_1(u)$ are obtained by multiplication of experimentally measured modules by phase factors with phases $\psi_0(u)$ and $\psi_1(u)$. Thus, the first approximation of wave functions in the Fourier-plane is obtained.

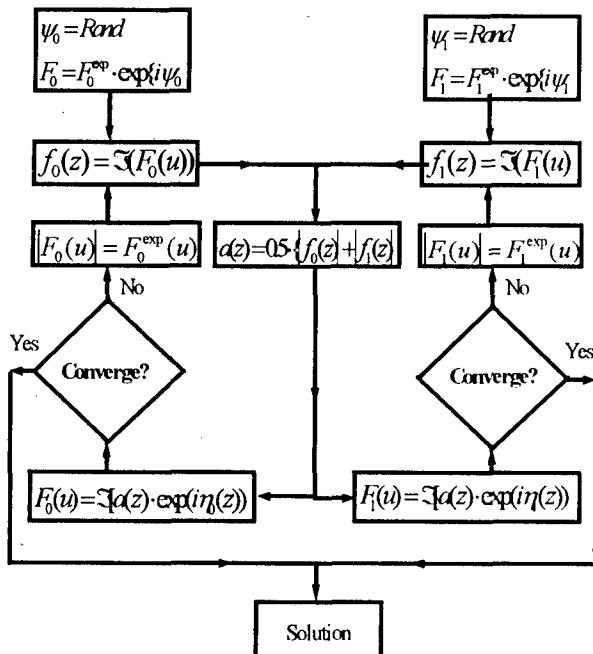


Fig.3. Block diagram of the algorithm.

3. Inverse Fourier transform of $\tilde{F}_0(u)$ and $\tilde{F}_1(u)$ gives the first approximation.
4. A half-sum of $|\tilde{f}_0(z)|$ and $|\tilde{f}_1(z)|$ were used as a new value of $a(z)$ to satisfy the condition (3).
5. Direct Fourier transformation of this approached functions in the image plane gives a new approximation for functions $\tilde{F}_0(u)$ и $\tilde{F}_1(u)$.
6. Calculated amplitudes are replaced by their experimentally measured values and procedure is repeated from point 2 until convergence.

The difference between calculated modules of Fourier images and experimentally measured modules is the criterion of the convergence. Because the experimental data contain errors, the residuals decreases from iteration to iteration, but does not converge to zero. A practical criterion of convergence was chosen as follows - the iterations are stopped when the residuals do not change. The algorithm was tested by a particular test example. In numerical calculations the Fast Fourier Transform (FFT) were used for direct and inverse Fourier transform.

EXPERIMENTAL DATA PROCESSING

Let's remind, that non-perturbed and perturbed beams were recorded in each experiment, but these data were flared in time (at first the module of Fourier-image of non-perturbed beam is recorded, then after the voltage pulse on the diode the module of a Fourier-image of a perturbed beam is recorded). Since the diameter of the beam in the focal plane is small, and the number of recorded pixels in this plane is rather large (376), the number of significant points in a front focal plane contained few points (5-6), and the algorithm worked unstable. After padding the experimental data with zeros to 1024 points the solution in the object plane get 20-25 significant points and the solution becomes stable.

In the first time-cut initial phases in accordance with the algorithm were chosen random. In the next cuts the solution obtained in the previous cut was used as an initial approximation.

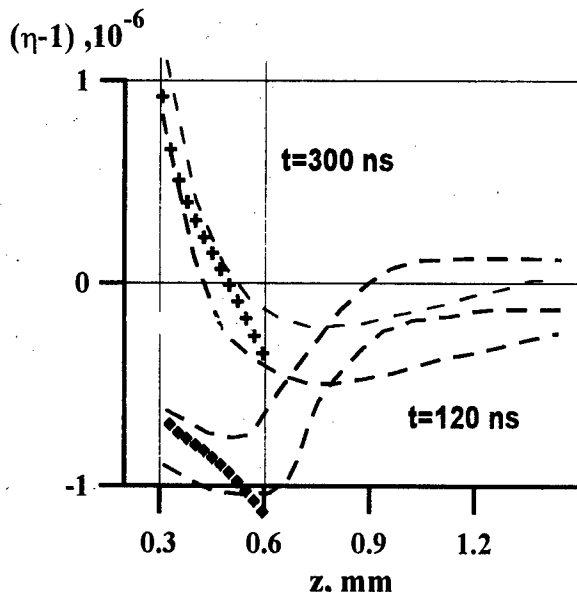


Fig.4. Refractive index as a function of distance from the anode. Doted lines - results obtained by integration of laser beam deflection in different shots with different distances from anode. Points and crosses -the results of being processing.

There were used FFT on the 1024 points and the number of iterations necessary for convergence in one time-cut varies from 500 to 1500 iterations. First of all, distribution of the phase the voltage pulse was restored. It slightly varied from convex to concave near the horizontal line.

A derivative $\frac{d(\eta_1(z) - \eta_0(z))}{dz}$ in

the maximum of amplitude of a probe laser beam was calculated from a difference of phases on a cross coordinate in order to compare calculated values with the deflection of the probe laser beam measured by the photodiode. This derivative multiplied by $\lambda / 2\pi$ is equal to a deflection angle of the probe laser beam passed through the plasma layer. The calcu-

lated magnitudes of the angle are imposed with diamonds on the oscillogram obtained by the photodiode (Fig. 2). There is a good agreement everywhere, except for an area of a "positive" deviation, which, as mentioned above, was excluded from the analysis.

Refractive index as a function of distance from the anode (within the caustic of the laser beam), was obtained [3,5] by integrating the results of deflection technique in many shots with different z for two moments of the anode layer expansion (Fig.4.). The distribution of refractive index which is retrieved by this technique with accuracy up to a constant, was fitted to the refractive index distribution mentioned above. Results of both the techniques are in a reasonable agreement, but a spatial resolution (~ 0.03 mm) of new method is ten times higher than of the deflection technique. One can expect that with a wide probe laser beam a refractive index distribution with a high space resolution can be obtained in a single diode shot.

CONCLUSION

The new optical system allows to expand essentially capabilities of the RING diagnostics supplementing "classical" measurements of a beam deflection by record of a Fourier-image of the beam, passed through the plasma, that allows to rise considerably a spatial resolution of a method. Using a wide laser beam one can tune the diagnostics to reconstruction of the refractive index in all the layer for one shot. Certainly, in this case measurement of a laser beam deflection becomes meaningless.

Authors are indebted to J. Greenly, D. Hammer, E. Krastelev and A. Matveenko for cooperation and stimulated discussions. Work was partly supported by U.S. Civilian Research and Development Foundation, Award #RP1-239, and grants from Russian Ministry of General and Professional Education and State Committee on Science and Technology.

REFERENCES

- [1] M.E. Cuneo, T.R. Lockner, G.C. Tisone. *IEEE Trans. on Plasma Sci.*, **19**, 800 (1991).
- [2] C.L. Enloe, R.M. Gilgenbach, J.S. Meachum. *Rev. Sci. Instrum.*, **58**, 597 (1987).
- [3] B.A. Knyazev, J.B. Greenly, D.A. Hammer, E.G. Krastelev. *Proc. 11th Internat. Conf. on High-Power Particle Beams*, Prague, Czech Republic, **2**, 1054 (1996).
- [4] J.R. Fienup. *Applied Optics*, **21**, 2758 (1982).
- [5] Knyazev, D.A. Hammer, J.B. Greenly, E.G. Krastelev, M. Cuneo. *Technical Physics Letters*, **23**, 401 (1997)
- [6] W.O. Saxton. *Computer technique for image processing in electron microscopy*. Academic Press, N.-Y., 1978.
- [7] Gander et al. *Solving problems in scientific computing using Maple and Matlab*. Berlin et al., Springer, 1995.

X-RAY SPECTROSCOPY AT "S-300" FACILITY

S.A.Dan'ko

Russian Research Centre "Kurchatov Institute" 123182 Moscow, Russia

ABSTRACT

X-ray spectroscopy is one of the most informative diagnostics used on "S-300" facility (3-4 MA, 600 keV, 100 ns). Specially designed crystal spectrograph permits to get time-integrated [H]- and [He]-like ion spectra with two-dimensional spatial resolution in each experiment run. Computer processing of the spectra gives electron and ion temperature, hot plasma density, energy radiated in separate lines and geometry shape of radiation source. X-ray spectroscopy method and some results from light liner and Z-pinch experiments are reported in this paper.

The "S-300" facility is one of the most powerful pulsed generators of relativistic electron beams in Russia. It produces electric current up to 3.5 MA on the physical load with rise time of 100 ns. In the plasma experiment on "liner-converter" scheme [1] or Z-pinch [2] the X-ray spectral measurements are very important on the last compression stage. Basic parameters: temperature, density and plasma formation dimensions – are determined by X-ray method.

For such experiments it is necessary to know both spectral and spatial distribution of radiation in the wide spectral band, that corresponds to the wide range of radiating ions and wide temperature interval. These requirements are satisfied by the spectrograph with convex cylindrical mica crystal and narrow slit placed in the front of it in the dispersion plane. Fig.1 demonstrates image building by means of the spectrograph slit in the transversal direction to it. X-ray spatial resolution in another coordinate parallel to the electrode plane is possible to obtain in each separate spectral line too.

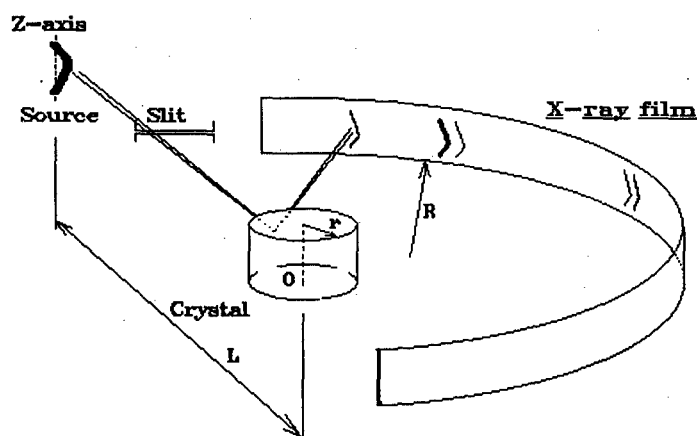


Fig.1. *Convex crystal spectrograph scheme.*

There's a necessary condition for it: the observation angle of the source must be considerable greater than the angle, in which separate line radiation goes after crystal reflection. This condition is described by the following inequality:

$$b/L \gg \delta\lambda/\lambda \cdot \tan\theta,$$

where b - source width (diameter),
 L - source-dispersion crystal distance,
 θ - Bragg angle for radiation of wavelength λ ,
 $\delta\lambda$ - spectral line broadening.

The nearest spectrograph location to the source satisfies this inequality, so in addition it provides to obtain bright plasma spectrum on the film in one facility run. The obtained spectrum processing have been usually performed by means of slide-scanner "Mustek", and especially developed computer code "VideoX". This program displays the spectrum on the monitor screen and calculates various values required. It calculates spectrograph dispersion, X-ray gathering force; link spectrum image to the dispersion curve. The code determines source brightness in separate spectral lines according to the crystal reflection ability, filter transparency and X-ray film sensitivity.

Spectral intensities of [H]- and [He]-like ions, width of lines and source dimension obtained by means of "VideoX" code are input parameters for "Dismat"-code [3], which is responsible for N_e and T_e determination. Code "Dismat" accounts line radiation self-absorption as escape-factor in the plasma of the effective optical depth.

The main point of the "liner-converter" scheme is that plasma liner, compressed by high currents, heats through the electron heat-conductivity along its axis the converter located on one of the diode electrodes, so that heating flux is transformed into the converter characteristic X-radiation. The first order reflection spectrum is shown in Fig.2a, where long lines of [H]- and [He]-like argon ions correspond to the liner substance, and short chlorine lines – to the converter one. At the right-hand side in Fig.2c liner and converter location in the high current diode is presented. Fig.2b is a reconstructed image of liner in the [H]-like argon resonance radiation (negative).

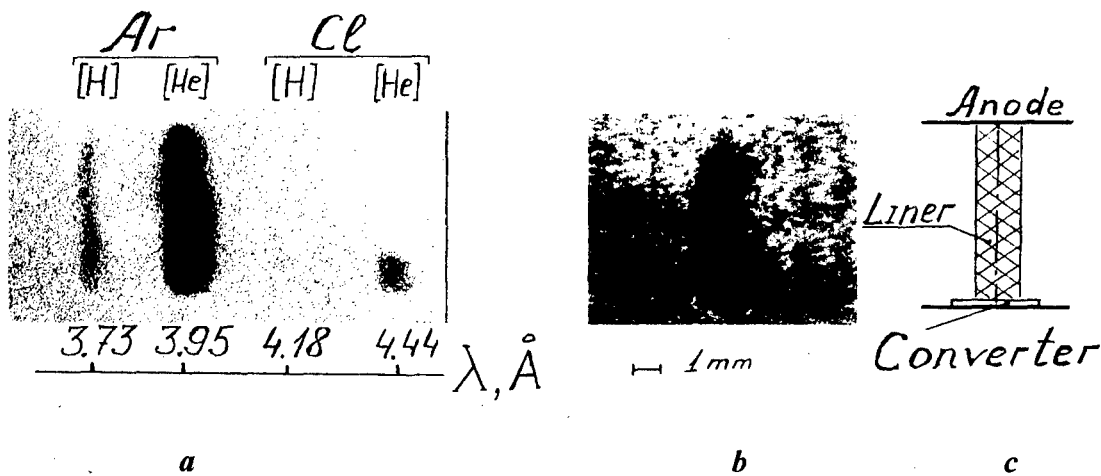


Fig.2. The first order reflection spectrum (a), reconstructed image of liner (b) and experimental scheme "liner-converter" (c).

The hot argon plasma height in that experiment was about 7 mm, and chlorine one – 1.5 mm. For the transversal plasma dimension determination two orders reflection data should be utilized. The matter is that spectral width of lines considerably differs in the different reflection orders. It means, that comparable contribution into width of lines make two factors: radiation source dimension and Doppler broadening (Stark broadening is small).

So, two line width $(\delta\lambda)_1$ and $(\delta\lambda)_2$ – in the first and the second reflection orders give two equations for two unknown quantities:

$$\begin{aligned} kb \cdot d\lambda/dx|_1 + (\delta\lambda)_s &= (\delta\lambda)_1 \\ kb \cdot d\lambda/dx|_2 + 2(\delta\lambda)_s &= (\delta\lambda)_2, \end{aligned}$$

where $d\lambda/dx|_1$ and $d\lambda/dx|_2$ – are spectrograph dispersion in the first and the second reflection orders, k - coefficient of image demagnification, $(\delta\lambda)_s$ - spectral line width. The obvious condition for this procedure validity is the separate line presence in two orders of reflection. Unfortunately, spectral width $(\delta\lambda)_s$ is not Doppler profile width because of the great optical depth in liner and Z-pinch plasmas, that leads to the Doppler shape deformation.

From intensity ratios of [H]- and [He]-like lines of high-charged ions and radiation source dimension the computer code "Dismat" restores electron density and temperature in plasma. It means the direct calculation of radiation intensities from uniform stable plasma of cylindrical form, where parameters N_e , T_e and diameter b are introduced beforehand. The code deals with one nuclear sort of ions in plasma, when $N_i = N_e/Z_{eff}$. N_e and T_e – are fitting parameters. In the real compound plasma, where different sorts of ions are presented in the same place, the third fitting parameter appears - b . Decreasing the magnitude of b in comparison with the value calculated from spectral line width, "Dismat" code results may be interpreted as radiation intensities for real plasma dimension, but with less plasma density $N_i < N_e/Z_{eff}$. So, these three fitting parameters are used to determine both the line intensity ratio and ion density of sort Z .

In the experiment (Fig.2) all plasma parameters were obtained from two orders of crystal reflection: the first and the third. They were: $N_e = 6 \cdot 10^{21} \text{ cm}^{-3}$, $T_e = 530 \text{ eV}$, $N_{Ar} = 4 \cdot 10^{20} \text{ cm}^{-3}$. The chlorine ions concentration was $N_{Cl} = 7 \cdot 10^{18} \text{ cm}^{-3}$, plasma diameter $b = 1.2 \text{ mm}$ and linear mass of liner $2.5 \cdot 10^{-4} \text{ g/cm}$. The whole energy radiated in [He]-like argon resonance line was determined from spectrograph sensitivity; it proved to be about 20 Joules, and in [He]-like chlorine – 0.7 J.

In the Z-pinch experiments a small dimension of the hot plasma, less than slit width, was a characteristic feature. The transversal dimension was obtained as the width of penumbra from the slit edge. In the experiment, in which potassium chloride was doped into the agar-agar load, the height of the [H]-like chlorine radiation source was 150 microns and the diameter – 220 microns. In the [He]-like potassium radiation the diameter was in one and a half times less – 135 microns. The electron concentration and temperature were: $N_e = 10^{22} \text{ cm}^{-3}$, $T_e = 820 \text{ eV}$. In Fig.3 the third order reflection of the observed

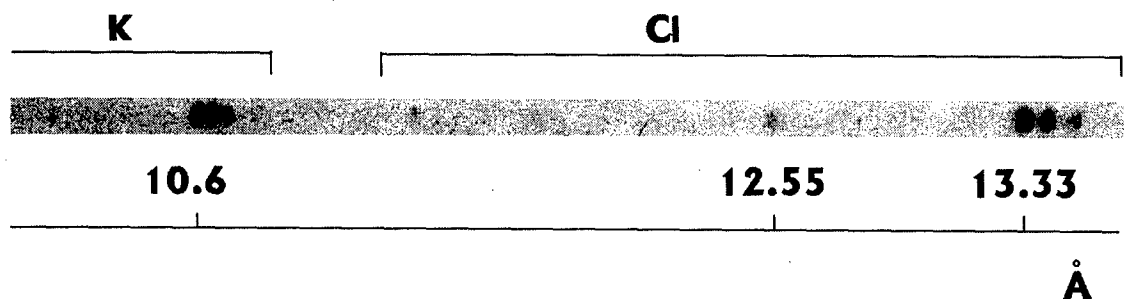


Fig.3. The third order reflection of [H]- and [He]-like chlorine and potassium ions spectrum in the Z-pinch constriction (negative).

spectrum for chlorine and potassium in this experiment is presented.

The spectroscopic method advantages presented in this paper can't satisfy all experimental requirements. So, the low spectrograph sensitivity limited the minimal amount of the diagnostic admixtures inserted into the load substance. Time resolution absence in the spectrum registration system restricts spectroscopic abilities and leads to the certain errors in the measurements.

The presented work was supported by the Russian Foundation for Basic Researches, grants No. 96-02-19534 and No. 98-02-17616.

REFERENCES

- [1]. Y.L.Bakshaev, A.V.Bartov, P.I.Blinov et al. Experimental investigations of imploding plasma in the frame of the "Liner-converter" scheme. Report 0044, these Proceedings.
- [2]. Y.L.Bakshaev, A.V.Bartov, A.S.Chernenko et al. Dynamics of neck development in dense Z-pinch on S-300. Report 0142, these Proceedings.
- [3]. S.A.Dan'ko, O.N.Yartseva. Measurements of the radiated energy and temperature in the high-charged ions plasma. Preprint IAE-4515/7 (1987) Moscow, Russia (in Russian).

A DIAGNOSTIC OF GYROTRON CATHODES QUALITY BASING ON THEIR CURRENT-VOLTAGE CHARACTERISTICS

M.Yu.Glyavin, A.N.Kuftin, A.S.Postnikova, N.P.Venediktov,
M.V.Yulpatova, V.E.Zapevalov, I.E.Zasypkina

*Institute of Applied Physics Russian Academy of Sciences.
46 Ulyanov Street, 603600 Nizhny Novgorod, Russia*

INTRODUCTION

In gyrotrons, i.e. sources of powerful (up to 1 MW and higher) coherent microwave radiation the electron beam is formed by a magnetron-injection gun that operates in the regime of temperature limitation set for emission current and with the electric field at the cathode, which is but insignificantly weakened by the field of the spatial charge. Optimization of electron-optical systems in gyrotrons is made more complicated due to strict requirements for homogeneity of helical electron beams and low velocity spread of electrons in the beam. Worse homogeneity of the electron flow leads to a sharp decrease in efficiency or appearance of various instabilities resulting in a break of oscillations. Optimization of parameters of gyrotron guns requires a detailed analysis of many physical processes in the electron-optical system (EOS) of a gyrotron and application of complex mathematical models [1]. At the same time, practice demands sufficiently simple and fast ways to analyze EOS quality in order to estimate basic parameters of cathodes. The purpose of this work is to modify diagnostics methods for gyrodevices.

BASIC EQUATIONS

As it was assumed in [2] by "efficient emission inhomogeneity" we will mean some inhomogeneity affecting and manifested in characteristics of the cathode and will not go deep to study micromechanisms leading to cathode inhomogeneity. Neither we will pursue the problem of studying "emission relief" of the cathode referring to the coordinates on its surface.

Inhomogeneous character of emission manifests it self in blurring of the area of cathode transition from the ρ -regime to the saturation regime, which is associated with transition of different areas on the cathode to the saturation regime of different values of cathode voltage. As the voltage grows, the part of the cathode area working in the ρ -regime shrinks, and the part working in the space charge regime extends. The transition voltage for each elementary section of the cathode area depends on its emitting properties, and the more homogeneous is the cathode in terms of emission, the narrower the zone of transition from the ρ -regime to the saturation one will be.

In [2] it was shown that density of distribution of efficient emission inhomogeneity is equal to the second derivative of the cathode current-voltage characteristic with accuracy up to a constant term: $F(j_H) = -\frac{1}{g^2} \frac{d^2 I}{dx^2}$, where $x = U^{3/2}$. As it follows from Child-Langmuir equation and Richardson equation, the width of the transition zone, where the regime of space

charge limitation of the current is replaced by the regime of temperature limitation for emission current, depends on the difference of temperatures at different sections of the cathode, and the difference of the work function at different parts of the surface. If one normalizes current and voltage to their values I_0 and x_0 corresponding to the maximum of the distribution density function, and the parts of the cathode surface working in the space charge regime and in the saturation regime, to the full surface of the cathode, S , one can find the following system of variables: $\hat{I} = \frac{I}{I_0}$, $\hat{x} = \frac{x}{x_0}$, $\hat{S}_\rho = \frac{S_\rho}{S}$, $\hat{S}_s = \frac{S_s}{S}$, which is convenient for comparison of different cathodes.

METHODS AND EXPERIMENTAL RESULTS

Reliable results require high accuracy of measurements of the current-voltage characteristic. Therefore, the experiment employed an automatic system based on a HiCom (DEC) computer and KAMAK tools or PC "Pentium" [3]. Secondary processing of the experimental data was performed on an IBM PC using a special software featuring the multi-windowed user interface that makes it possible to visualize data in different systems of coordinates, programs for double differentiation of the tabulated functions, their smoothing and extrapolation.

The measurements were performed in two regimes: modeling and operation regimes (subscripts "m" and "o", respectively). To retain the density of the space charge and trajectories of particles, the magnetic fields, currents and voltages in modeling regimes were found from the similarity relations: $U_m = \frac{U_o}{K}$, $B_m = \frac{B_o}{\sqrt{K}}$, $I_m = \frac{I_o}{\sqrt{K^3}}$. The difference in the measurements of the current-voltage characteristic in the operation and modeling regimes are caused mainly by higher temperature and field intensity at the cathode, i.e. greater role of the Schottky effect at operating voltages. The current-voltage characteristics were measured also in the modeling regimes in the absence of the magnetic field. Such measurements were aimed at the possibility to study cathodes before installation into the gyrotron. By that, it is easier to study the emitter at reduced voltages in the regime of current to the anode in the absence of other elements of the electron-optical system and the magnetic field.

The normalized distribution density function is often well described by the normal distribution law, which can be written down in the assumed system of coordinates in the

following way: $\hat{f}(\hat{x}) = \frac{1}{\sqrt{2\pi} \sigma} \exp(-\frac{(1 - \hat{x})^2}{2\sigma^2})$. Functions of emission inhomogeneity distribution may be approximated by the normal distribution, parameters of which were determined by the variation method. The smoother sloping to the right of the maximum is caused by the Schottky effect and this deviation from the normal distribution law impairs the approximation quality. At the same time it is evident that due to double differentiation of the current-voltage characteristic the contribution of the Schottky effect to the width of the distribution function is insignificant and one can neglect that without seriously distorting the information about the cathode properties. The experiments performed demonstrated that although the width of the emission inhomogeneity distribution function depends on the regime (operation or modeling, with or without magnetic fields) the relationship between the width of the distribution function for different cathodes is retained regardless of the measurement regime. The setup used in the experiments described made it possible,

simultaneously with measuring the current-voltage characteristic, to perform highly accurate measurements of electron velocity spread in the beam and relative oscillatory energy by the method of the decelerating field [4]. Such measurements employ an analyzer consisting of a grid fed with negative voltage and a collector. Having compared the results of measuring the spread of electron velocities and the value of emission inhomogeneity one can see that there is correspondence between the cathode with higher emission inhomogeneity and larger electron velocity spread (Fig. 1). This fact can be explained by that the cathode with higher emission inhomogeneity is characterized by larger spread of initial electron velocities in the operating volume of the gyrotron, and, consequently, to lower efficiency of the device. The results of the experiment confirm that there is connection between the value of emission inhomogeneity and the spread of electron velocities. However, specifying the character of this dependence (i.e. finding empirical formulas to express one parameter in terms of the other) is possible only after a significant number of cathodes has been experimentally investigated.

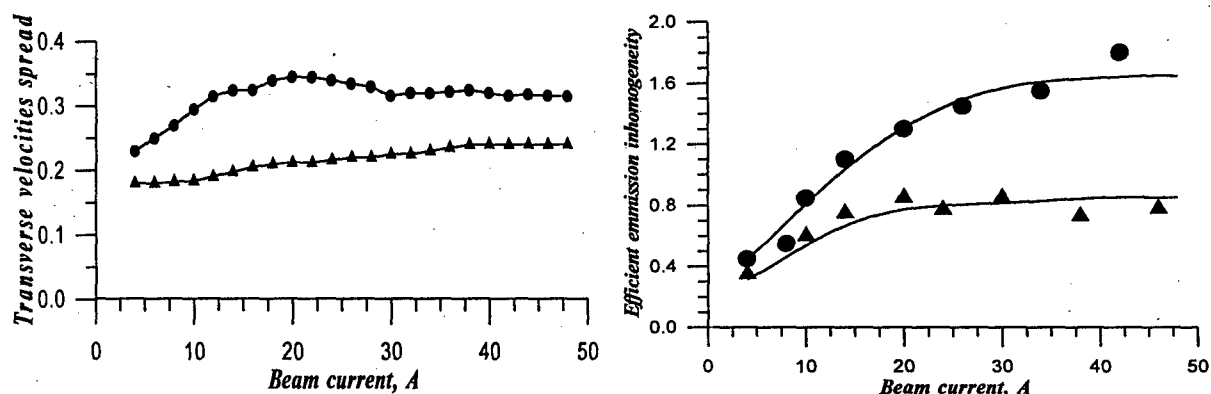


Fig. 1. Dependencies of the spread in transverse electron velocities and dependencies of efficient emission inhomogeneity on the beam current for two different cathodes.

Comparison of parameters of emission inhomogeneity distribution for the real and modeling regimes gives the possibility to judge about and pass over complex measurements of cathode appropriateness of the measurements characteristic in the modeling regimes in order to analyze emission inhomogeneity of cathodes in greater detail. In order to reveal the mechanisms causing emission inhomogeneity and to determine emission distribution over the cathode surface, currently we are designing a setup that would include the possibility to measure current-voltage characteristics of small areas on the cathode, analyze the work function at different points on the cathode by the method of secondary electron emission, and measure distribution of temperatures over the cathode surface. At present one can presume that the cathodes with $\sigma = 0.3-0.4$ at operating temperature have sufficient homogeneity for gyrodevices. However, as it has been mentioned above, a more accurate analysis requires a larger stock of statistics and, possibly, better approximation for description of emission inhomogeneity (e.g., χ^2 -distribution). That the method proposed can be reasonably applied for cathode diagnostic is proved by measurements of the output power and efficiency of gyrotrons with different emitters. Before the gyrotron efficiency was measured, its current-voltage characteristic was obtained in the operating and modeling regimes at different temperatures of the heater. The experimental results are shown in Fig. 2 for different emitters as the dependence of the gyrotron efficiency on the measured efficient inhomogeneity in the operating regime. As the value of efficient emission inhomogeneity grows, gyrotron efficiency drops respectively, since at other equal conditions gyrotron efficiency is determined by the quality of the electron beam, i.e. homogeneity of emission and absence of instabilities in the beam. The same complex of measurements was made for gyrotrons for technology

applications basing on PC setup. Two cathode tips was tested - low and high temperature. In all cases observed efficiency dependence from emission inhomogeneity such as shown at Fig.2. For one gyrotron emission inhomogeneity $\sigma \sim 2$ was measured and the technology defect on cathode surface was discovered. So, the method may be used for quality control of the cathodes for dyrotrons and diagnosis of defects.

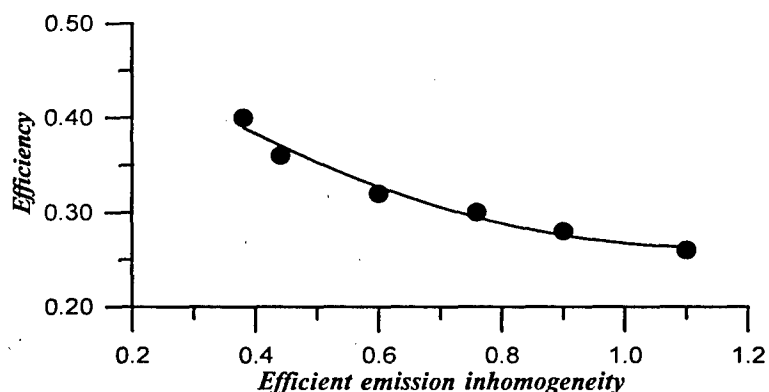


Fig. 2. Dependence of gyrotron efficiency on efficient emission inhomogeneity of the cathode for powerful pulsed gyrotrons.

For technology gyrotrons cathode emission degradation with time was investigate. As known, the degradation characteristics include an overall work function distribution change with time and temperature changes with time for operating current. At present one can presume that changes of the cathode inhomogeneity with time are not big and operating time of gyrotron with same type of cathode may be several hundred hours. Some peaks on function after operation are indistinct due to the retarding particle and process of cathode activation and evolution of work function distribution.

CONCLUSIONS

The described method for studying cathodes of gyrodevices basing on the analysis of the transition part of the current-voltage characteristic allows fast analysis of cathode quality. By that, possessing a sufficiently large stock of statistic materials one can predict attainable efficiency of the device. The ease of use and fastness of the method makes it possible to apply it for monitoring changes in the cathode quality during usage. A whole complex of measurement including analysis of the current-voltage characteristic, study of emission homogeneity on the cathode surface, and monitoring of temperature homogeneity allows complete characterization of emission capability of the cathode. The described setup and experimental method provide accurate measurements of current-voltage characteristics of cathode in gyrodevices and quality control of the cathodes to be installed in such devices. After a sufficiently large number of cathodes has been investigated by this method and the technique used in their making has been studied, it will be possible to compose recommendations on the manufacturing technique and activation of cathodes in gyrodevices.

REFERENCES

- [1] V.K.Lygin, Sh. E. Tsimring // JTF, 1973, 43, 8, p. 1695.
- [2] V.N.Volkov, S.P. Khodnevich, A.S.Pavlov, M.G.Tretyakova // Electronics industry, 1984, 7, p.27.
- [3] A.N. Kuftin, A.S. Postnikova, V.E. Zapevalov. // Int. J. Electronics, vol.72, 1992, 5,6, p. 1145.
- [4] E.G.Avdoshin, A.L.Goldenberg // Radiophysics, 1973, 16, 10, p. 1605.

A RE-EVALUATION OF CURRENT MEASUREMENTS DOWNSTREAM OF THE PLASMA OPENING SWITCH ON DECADE MODULE 1

John R. Goyer, John R. Thompson, and David Kortbawi

Maxwell Physics International

8888 Balboa Avenue, San Diego, CA 92123

Sponsored by the Defense Special Weapons Agency

INTRODUCTION AND METHODOLOGY

The plasma opening switch (POS) has been used for pulse compression and power amplification in a variety of inductive energy storage systems with conduction times ranging from tens of nanoseconds to in excess of one microsecond.^[1,2,3,4] In such systems, the POS first acts as a low series resistance while charging a vacuum inductor with energy from a capacitive store, and then rapidly transitions to a high resistance to transfer the energy quickly and at high power to a parallel load. Because of the implications to size and cost of a pulsed power generator, improvement of the POS in terms of scaling the switch to higher voltage and current operation has been a major emphasis of research over the past several years.^[5,6,7]

To improve and better understand the operation of plasma opening switches, it is highly desirable to have data from a variety of diagnostics that provide a clear and internally consistent description of switch operation. Such, unfortunately, is not the case presently. On DECADE Module 1 (DM1), electrically based diagnostics measure current both upstream and downstream of the POS, and infer a voltage at the POS location based on a transmission-line algorithm and the voltage measured at the vacuum interface.^[8,9] Radiation based diagnostics measure the output of a bremsstrahlung diode driven by the POS, and infer from this the diode voltage and current.^[10] These various diagnostics are shown schematically in Figure 1.

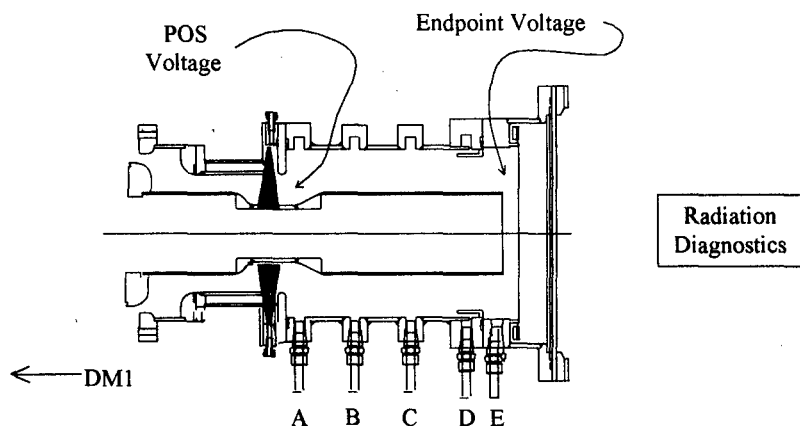


Figure 1. View of DM1 electrical and radiation diagnostics.

The current monitor locations are labelled "A" through "E" and consist of discrete B-dot probes. Locations "A" through "D" are approximately 8.6 cm apart, locations "D" and

“E” are 4.8 cm apart, and location “E” is 3.4 cm from the plane of the diode foil. The diode currents obtained with these monitors agree well with the current inferred from radiation diagnostics up to near the time of peak radiation production. After this time, the radiation based measurement indicates a diode current that is lower than that measured electrically, and one that continues to diverge rapidly from the electrical measurement.

The conclusion that the downstream monitors are incorrect will be shown by obtaining the downstream current using the voltages at the POS and diode to integrate the expected current through the inductance between those two points: a current that agrees very well with that obtained by the radiation diagnostics.

The following assumptions will be made in our analyses: 1) The calculated POS voltage is correct; 2) the diode voltage inferred from differentially filtered PIN diodes (referred to as the endpoint voltage) is also correct; 3) the radiation dose-rate (Si) measurement is correct; and 4) the energy difference of various electrons impacting the radiation converter is sufficiently small that it can be ignored for the purposes of the analysis presented below.

The region between the POS and the load can be modeled as shown in Figure 2, as a series of inductors with resistive shunts to permit losses. It is not too difficult to show that the integrated voltage differential divided by the total inductance is equal to the load current plus a weighted sum of the various loss currents:

$$\frac{\int [V_{POS} - V_{Endpoint}] dt}{\sum_{i=1}^N L_i} = I_{load} + \frac{\sum_{j=1}^N \left(L_j \sum_{k=j}^N I_k \right)}{\sum_{i=1}^N L_i} = I_{load} + \alpha I_{loss} \quad (1)$$

where I_k is the loss current flowing through the k^{th} loss resistance, I_{loss} is the total loss current downstream of the POS, and α is a weighting function dependent upon the distribution of the loss current: if the losses are assumed to be localized, then α is 0 for losses at the POS, and 1 for losses just before the diode; α is equal to 0.5 for losses distributed evenly between the POS and diode. Rather than begin with more complications than necessary, it will be assumed that losses are small late in time: i.e. $\alpha=0$.

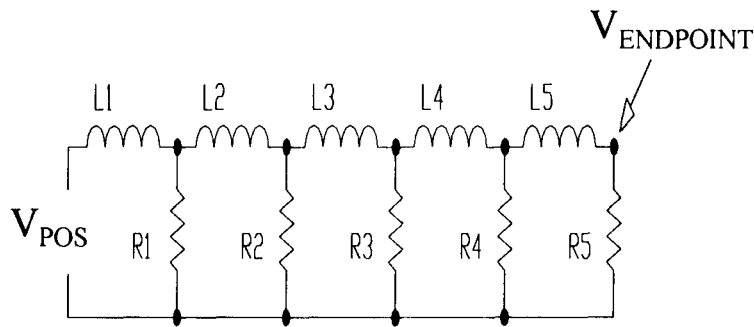


Figure 2. Schematic of the POS to load region on DM1.

By evaluating this expression on DM1 shots, it is possible to arrive at another estimate for the diode current. The validity of the assumption of small loss currents can be tested by comparing the results of Equation 3 with the current derived from the radiation output. The current obtained through Equation 3 is an upper bound on the current since loss currents will reduce the flow to the load.

The value of inductance between the POS and load is needed for calculation of the late-time current. A shot in which a short-circuit is the load can be used to determine a representative value for this inductance, including such effects as flux-exclusion by plasma transported downstream of the original POS location. DM1 shot 2466 is used for this purpose, and the inductance is calculated to be 47 nH. This compares very well with the geometric inductance from the POS to the load of 53 nH, and will be used in subsequent calculations.

In the analysis that follows, averaged data of 'good' shots will be somewhat arbitrarily used. This makes the implicit assumption that this algorithm should agree best on shots that have good current transfer, and that additional losses may be responsible for lower output. Figure 3 shows the average values of POS and diode voltage for five similar high yield shots that are considered.

The disagreement between the calculated current and that inferred from radiation output early in time is observed on all shots analyzed, and is due to two processes occurring in the POS. First, the switch, or a portion of it, is thought to translate about 6-7 nH downstream due to $J \times B$ motion prior to opening: the initial voltage rise on the POS voltage is actually due to the time varying inductance associated with this motion. Because of this translation, the downstream current rises after the calculated current, and with a faster slope. The second process accounts for the currents inferred early in time in the diode being higher than those calculated. This is because of the inductive path from the POS to load being reduced at or near peak switch voltage due to vacuum flowing electron current. This inductance can be estimated from the ratio of the calculated to inferred currents, and for all the shots examined is typically 30-35 nH.

RESULTS

Using equation 3, the value of 47 nH for the inductance between the POS and load, the load current can be calculated and shown to agree very well with that obtained from the radiation diagnostics. This is done in Figure 4 for the composite average of the five shots discussed above, where the divergence of the e-ring measured current is also obvious. Representative error bars are shown on the current derived from the output of the bremsstrahlung diode. Near both the beginning and end of the pulse, the error bars can be quite large due to uncertainties in the diode voltage calculation caused by rapid changes in radiation output.

SUMMARY

It has been shown that the current monitors downstream of the POS on DM1 appear to diverge from the true diode current at times around and following peak radiation output. An alternative method for calculating the diode current has been used and shown to agree very well with the current inferred from radiation measurements.

ACKNOWLEDGMENTS

The authors would like to thank B.V. Weber of the Naval Research Laboratory, M.A. Babineau of Sverdrup Technology, and the DM1 crew for expert assistance during these

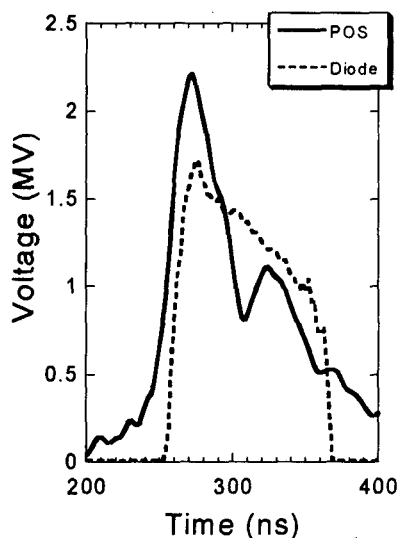


Figure 3. Average POS and diode voltages for the five high yield shots of the Qualification Test.

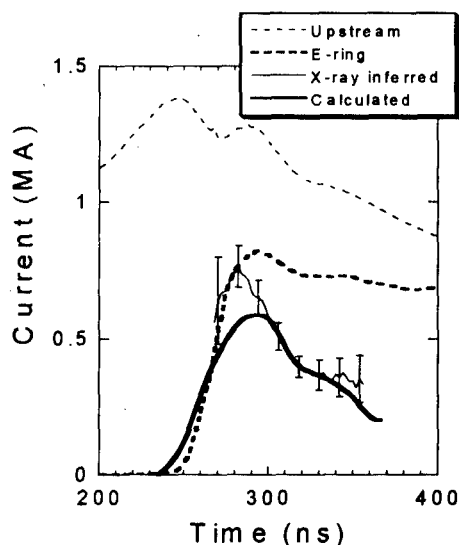


Figure 4. Comparison of currents for the average of shots 2454, 2455, 2457-2459.

experiments. The continuous and enthusiastic support of J. Rowley and R. Schneider of DSWA is also gratefully acknowledged.

REFERENCES

- [1] W. Rix, D. Parks, J. Shannon, J. Thompson, and E. Waisman, "Operation and empirical modeling of the plasma opening switch," *IEEE Transactions on Plasma Science*, vol. 19 (2), pp. 400-407, 1991.
- [2] R.A. Meger, R.J. Comisso, G. Cooperstein, and S.A. Goldstein, "Vacuum inductive store/pulse compression experiments on a high power accelerator using plasma opening switches," *Appl. Phys. Lett.*, vol. 42, pp. 943-945, 1983.
- [3] B.V. Weber, R.J. Comisso, G. Cooperstein, J.M. Grossmann, D.D. Hinshelwood, D. Mosher, J.M. Neri, P.F. Ottinger, and S.J. Stephanakis, "Plasma erosion opening switch research at NRL," *IEEE Trans. Plasma Science*, vol. PS-15, no. 6, 1987; see also Reference [7].
- [4] G.A. Mesyats, S.P. Bugaev, A.A. Kim, B.M. Koval'chuk, and V.A. Kokshenov, "Microsecond opening switches," *IEEE Trans. Plasma Science*, vol. PS-15, no. 6, 1987.
- [5] J. Thompson, P. Coleman, R. Crumley, C. Gilbert, D. Husovsky, P. Melcher, W. Rix, K. Robertson, R. Ingermanson, D. Parks, and E. Salberta, "Downstream power flow study of microsecond conduction time plasma opening switches on ACE 4," in *Proc. 10th IEEE Int. Pulsed Power Conf.*, Albuquerque, NM, July 1995, p. 1091.
- [6] C.W. Mendel, Jr., M.E. Savage, D.M. Zagar, W.W. Simpson, T.W. Grasser, and J.P. Quintenz, "Experiments on a current-toggled plasma-opening switch," *J. Appl. Phys.* 71(8), p. 3731, 1992.
- [7] R.J. Comisso, P.J. Goodrich, J.M. Grossmann, D.D. Hinshelwood, P.F. Ottinger, and B.V. Weber, "Characterization of a microsecond-conduction-time plasma opening switch," *Phys. Fluids B* 4 (7), pp. 2368-2376, July 1992.
- [8] P. Sincerny, S. Ashby, K. Childers, J. Goyer, D. Kortbawi, I. Roth, C. Stallings, J. Dempsey, and L. Schlitt, "Performance of the DECADE module #1 and the status of the DECADE machine," *Proc. 10th IEEE Pulsed Power Conference*, pp. 405-416, Albuquerque, NM., 1995, IEEE catalog #95CH35833.
- [9] J.R. Goyer, D. Kortbawi, F.K. Childers, P.S. Sincerny, B.V. Weber, P.F. Ottinger, R.J. Comisso, J.R. Thompson, and M.A. Babinaeu, "Plasma opening switch research for DECADE," *IEEE Trans. on Plasma Science*, vol. 25, no. 2, April 1997.
- [10] J.E. Rauch and J. R. Thompson, "The Determination of the Electron Beam Energy in DM1 with Far Field X-ray Measurements," submitted to the *Proc. 11th IEEE Int. Pulsed Power Conf.* (1997).

ATOMIC BEAM SOURCE FOR ION DIODE DIAGNOSTICS

B.A. Knyazev, W. An*, H. Bluhm*, L. Buth*

Novosibirsk State University, Novosibirsk, 630090, Russia

*Forschungszentrum Karlsruhe, Postfach 3640, D-76021 Karlsruhe, Germany

ACTIVE STARK SPECTROSCOPY

The quality of beams generated with high power electron and ion diodes sensitively depends on processes in the diode acceleration gap.

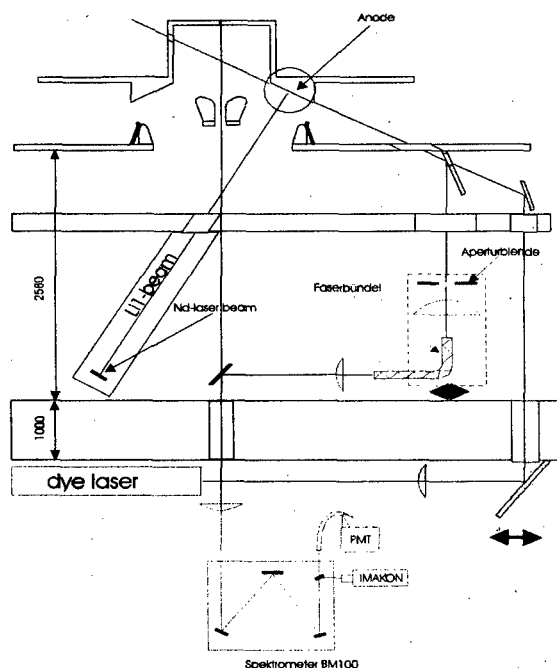


Fig.1. Setup of the atomic probe beam diagnostic on KALIF

existing experimental data [1] on Stark splitting of lithium atoms in strong electric fields, and estimates of the field ionization limit [4], as well as the availability of suitable tuneable broadband dye lasers, led us to select the $2s-2p-3d$ cascade transition (for the Grotrian diagram see Ref. [3]) for the experiments on the KALIF ion accelerator [5], where the field does not exceed 4 MV/cm. These transitions should be populated to saturation by two dye lasers with wavelengths of 671 and 610 nm. The spontaneous emission from the $3d$ level split in the electric field has to be recorded with a polychromator and a detector system with high temporal, spatial, and spectral resolution. Fig. 1 shows the schematic set-up of the diagnostic system on the KALIF.

The calculated Stark splitting of the $3d-2p$ lithium line is presented in Fig. 2. Experiments [6] have demonstrated that one can obtain a bandwidth of up to 3 nm from flashlamp pumped dye lasers, which seems to be sufficient for the excitation of one of the groups of the split components. One can see that the two upper components allow to measure fields as low as 0.2 to 1.0 MV/cm, whereas the higher field values can

depends on processes in the diode acceleration gap. Although passive spectroscopy allows to study many of the details of light-ion diodes (see, e.g. [1]), ions suitable for spectroscopy are often not present in sufficient quantities inside the gap. Active spectroscopy based on local laser resonance excitation of an atomic beam injected into the diode has already been successfully applied in electron diodes [2] and may also be used as a diagnostic tool in ion diodes [3]. To study an ion diode we suggest to inject a lithium atomic probe beam.

Recording the intensity and wavelength of Stark-split line components with an optical multi-channel analyser, one can measure at any chosen point (or along a line of sight) the electric field magnitude and direction, as well as the position of the ion emission surface. The analysis of

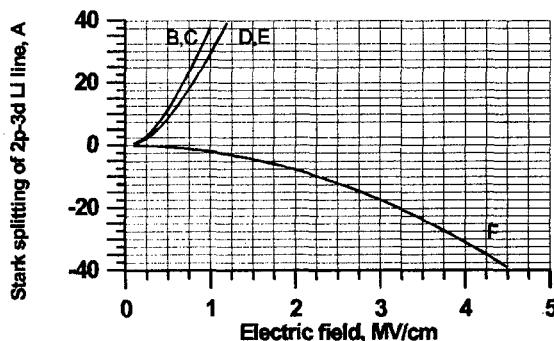


Fig.2. Stark splitting of the $3p-3d$ Li-line.

be determined by recording the lower component. Transitions in the red spectral range can easily be saturated by radiation with very moderate spectral power density (of the order of 1 kW/cm²·nm) [3].

ATOMIC BEAM PRODUCTION BY LASER EVAPORATION

The atomic and laser beams injected into the diode should not disturb the diode operation. Since the background gas density in the diode is around 10¹¹-10¹² cm⁻³, an atomic beam with a density of up to 5·10¹² cm⁻³ will not affect the diode performance. We suggest to use a very narrow rectangular ("slab-like") atomic probe beam. If this atomic slab is excited to saturation

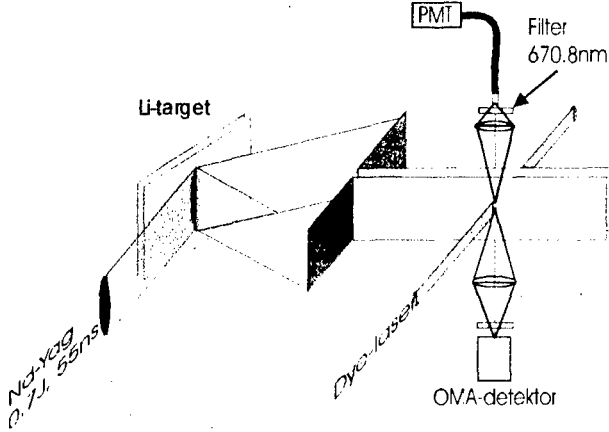


Fig. 3. Schematic of an experiment on lithium beam formation with a short-pulse Nd:YAG laser. Here the resonance fluorescence from the 2s-2p transition was excited with a 10-ns pulse from a tuned dye laser.

by resonant laser radiation perpendicularly crossing it (like in Fig. 3), spontaneous fluorescence of the split components can be collected from any side of the beam without any self-absorption.

The atomic beam with a rectangular cross section can be formed by passing the expanding vapour cloud -produced by laser ablation- through a distant narrow slit. Since the slit can not be positioned closer than 10 cm to the observation point, the thickness of the slab (more likely to be a "wedge") and its atomic density are strongly dependent on the distance L from the Li target, the number of evaporated atoms and the cloud diameter at the point when it becomes collisionless.

In addition, further obvious requirements are a low ionization degree of the cloud and a high efficiency of evaporation.

It is clear from the above, that the best choice corresponds to an "optimum power density" F_{opt} of the evaporating laser, which is achieved, when the energy deposited in the heated volume is matched by the energy required to vaporize it: $F_{opt}\tau / H\rho = \sqrt{\kappa\tau}$. Here $\delta = \sqrt{\kappa\tau}$ is the heating depth in the target; κ [cm²/s] is the thermo-diffusion coefficient; τ [s] is the laser pulse duration; H [J/g] is the specific vaporization energy and ρ [g/cm³] is the target density. One can see that for a given material the condition for optimal evaporation will be satisfied for a constant product of $F_{opt}\sqrt{\tau}$ [J/cm²s^{1/2}]: $F_{opt}\sqrt{\tau} = H\rho\sqrt{\kappa}$.

On the other hand, assuming uniform semi-spherical expansion of the vapor, one can estimate the atomic density in the diode as $n_a = 3N/2\pi L^3$. Since $N = S\rho\delta/m_p A$ (A is the atomic number, S is the laser spot size, and m_p is the proton mass), the properties of the laser beam, the atomic beam, and the target are related by the expression

$$S\sqrt{\tau} \approx \frac{2\pi}{3} \left(n_a L^3 \right) \left(\frac{m_p A}{\rho\sqrt{\kappa}} \right), \quad \text{or} \quad n_a(\tau) = \frac{3S\sqrt{\tau}\rho\sqrt{\kappa}}{2\pi L^3 m_p A}.$$

The longer the laser pulse length, the less is the evaporation area and the distance where the cloud becomes collisionless. In other words, for a pulse sufficiently long the effective transverse dimension a_{eff} of the atomic source can be assumed to be a narrow band. Figure 4 shows the atomic beam density (that is proportional to the laser energy) vs. the laser pulse duration (without the collimating slit).

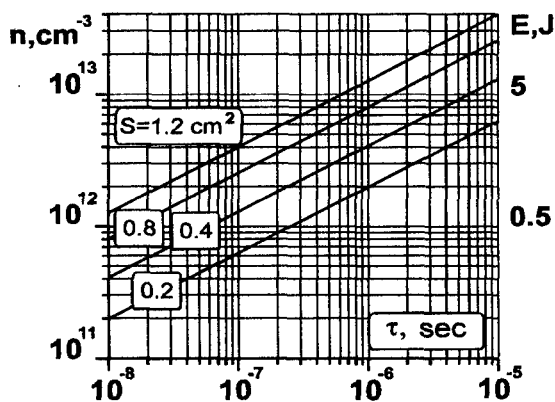


Fig. 4. Density of the lithium vapor cloud (which is proportional to the required laser energy) as a function of laser pulse duration for different evaporation areas.

LIFETIME OF LITHIUM ATOMS IN THE DIODE

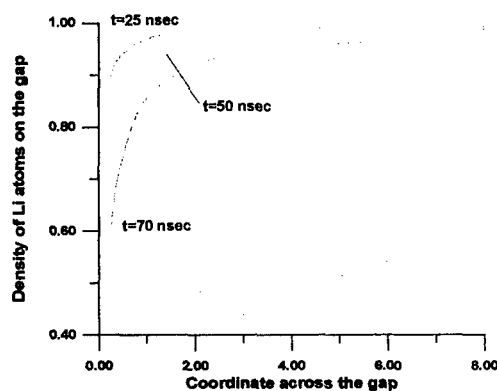


Fig 5. "Burn out" of lithium atoms in the diode gap.

cross-sections. Assuming an anode-cathode separation of $d=8$ mm; and an anode area of 200 cm^2 we calculated $n_b(t, z) = n_{b0} - \Delta n_b(t, z)$ for a characteristic proton beam current $I(t)$ and a diode voltage $U(t)$, assuming for simplicity a linear increase of ion energy the diode gap. One can see (Fig. 5) that for the conditions in the KALIF ion diode the lifetime of the probe lithium atoms in the ground state is longer then the duration of the diode pulse. Although information about ionization cross-sections of excited lithium atoms by collisions with protons is absent, one can expect that, by analogy with $\text{Na}(3p)$, ionization cross-sections for $\text{Li}(2p)$ and $\text{Li}(3d)$ will be two-three times larger then for $\text{Li}(2s)$. Thus the "burn-out time" of lithium atoms inside the saturating laser field in the gap may be somewhat less than inferred from Fig. 5, but even in this case the number of atoms remaining will be sufficient to be detectable.

PRELIMINARY EXPERIMENTS

For the development of the laser-driven atomic-probe-beam diagnostic described above we have performed two experiments. The first experiment, which was performed at the KALIF site with an available 60-ns, 0.7 J Nd:YAG laser ($S=0.08 \text{ cm}^2$, - non-optimal conditions!), was directed to gain experience with the generation of a lithium atomic beam and to record the resonance fluorescence with reasonable time resolution. The measurements were performed by exciting the $2s-2p$ transition in the lithium atoms with the help of a 10-ns, 50 μJ dye laser.

For example, to obtain at a distance of 1 m a density of $1 \cdot 10^{13} \text{ cm}^{-3}$, 5 J of laser energy has to be deposited into the target. Coming along the grid line, we see, that this can be achieved with a laser pulse length and an irradiated area of respectively $\tau_L=0.6 \mu\text{s}$, $S=0.6 \times 2 \text{ cm}^2$, $\tau_L=1.6 \mu\text{s}$, $S=0.4 \times 2 \text{ cm}^2$, or $\tau_L=5 \mu\text{s}$, $S=0.2 \times 2 \text{ cm}^2$. These simple estimates show that to obtain an atomic source with a small effective transverse dimension, a flashlamp dye-laser is an adequate choice, because the required energy and the pulse length are close to the "natural" characteristics of these lasers.

A critical point of this diagnostic is the lifetime of the probe atoms in the gap. The lithium atoms can be ionized by accelerated protons in the processes of single, double, and transfer ionization. Cross-sections of these reactions as a function of proton energy are given in the papers [7-10]. The number of lost atoms Δn_b in the gap is

$$\Delta n_b(t, z) = \int_0^t \frac{n_b(t) \cdot \sigma(U(t, z)) I(t)}{S e} dt,$$

where σ is a sum of the partial

These experiments (see Fig. 1 and 3) were performed for the real geometry at the KALIF site using regular diagnostic instruments and the acquisition system, but without operation KALIF

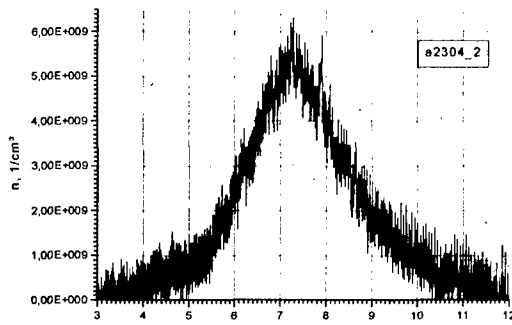


Fig. 6. Distribution of Li-beam density recorded with a photodiode array.

itself. A Lithium beam with a density of $5 \cdot 10^9 \text{ cm}^{-3}$ was obtained at a distance of 61 cm from the target and with a 2-mm slit aperture placed downstream at 47 cm. Temporal and spatial distributions of the resonance fluorescence radiation (proportional to the atomic beam density) were recorded with a PMT- and a photodiode-array (Fig. 6). In this experiment the lateral extension of the Li-vapor cloud was found to be 11 mm.

This value was in good agreement with the expectation. For a further full-scale experiment on KALIF a 3 μs , 3-5 J coaxial flashlamp pumped dye laser is developed at the Novosibirsk State University. It is expected that an atomic source created by this laser can deliver a slab-like beam of $S=0.2 \times 2 \text{ cm}^2$ cross section and with a density of $n_a=6 \cdot 10^{12} \text{ cm}^{-3}$ in the diode. The anticipated signal from the resonance fluorescence radiation in the diode at saturation of the lithium 3d-level can be estimated from the following equation

$$N_\phi = n_a \cdot \left(\frac{n_3}{n_a} \right) A_{32} \frac{\Omega}{4\pi} \cdot \Delta t \cdot \Delta V \text{ photons}$$

For $n_a=10^{13} \text{ cm}^{-3}$, $n_3/n_a=0.3$, $A_{32}=0.7 \cdot 10^8 \text{ s}^{-1}$, $\Omega=1/50$, $\Delta t=2 \text{ ns}$, $\Delta V=0.2 \times 2 \times 1 \text{ mm}^3$ the number of photons emitted into the solid angle of the optical system is $N_\phi=2.7 \cdot 10^5$. This value seems to be rather reasonable and can be detected with the existing instruments. The preliminary experiments at the KALIF site show that even an atomic beam with a density of $\sim 10^{12} \text{ cm}^{-3}$ will be sufficient for the measurements.

ACKNOWLEDGMENTS

The authors are indebted to W.Väth for assistance in the experiments and to K. Nasyrov for calculating the Stark splitting. One of us (B.K) acknowledges support from DAAD through a grant for a short-term visit to FZK; partial support from the Russian Ministry of General and Professional Education is also acknowledged.

References

- [1] J. Bailey, A. Filuk et al. *Atomic processes in plasmas*. Tenth Topical Conference, San Francisco, AIP Conf. Proc. **381**, 245 (1995).
- [2] B.A. Knyazev, P.I. Melnikov, V.V. Chikunov. *Sov. Tech. Phys. Lett.*, **17**, 357 (1991).
- [3] B.A. Knyazev, J.B. Greenly, D.A. Hammer. Paper in this Proceedings.
- [4] D. Kleppner, M. Littman, M. Zimmerman. In *Rydberg states of atoms and molecules*. Ed. by R.F. Stebbings and F.B. Dunning. Cambridge University Press, Cambridge, 1983.
- [5] W. Bauer, H. Bluhm, P. Hoppe et al. *Proc. 8th Internat. Conf. on High-Power Particle Beam*, Novosibirsk, 1990, V. 1, P. 104.
- [6] B.A. Knyazev, P.I. Melnikov. *Zhurnal prikladnoi spektroskopii* (Journ. of Appl. Spectroscopy), **58**, 397 (1993) (in Russian).
- [7] M.B. Shah, D.S. Elliott, H.B. Gilbody. *J. Phys. B: At. Molec. Phys.* **18**, 4245 (1985).
- [8] R.D. DuBois. *Phys. Rev. A*, **32**, 3319 (1985).
- [9] S.L. Varghese. *Nucl. Instrum. Methods in Phys. Res.*, **B24/25**, 115 (1987).
- [10] T. Tabata, Y. Nakai, T. -Shirai et al. *Nucl. Instrum. Methods in Phys. Res.*, **B31**, 375 (1988).

"TRIPLY-ACTIVE" DIAGNOSTIC METHOD FOR ION BEAM DIODES

B.A. Knyazev, J.B. Greenly*, D.A. Hammer*

Novosibirsk State University, 630090 Novosibirsk, Russia

*Laboratory of Plasma Studies, Cornell University, Ithaca, NY 14853

INTRODUCTION

In typical high power ion diode configurations it is highly beneficial to use spectroscopic methods for measurements. For example, Y. Maron et al. [1] used a "passive" Stark spectroscopic technique for the first direct measurements of the electric field distribution in a magnetically-insulated aluminum ion diode. Recently, similar experiments were carried out in the ion diode of the PBFA-II accelerator [2]. The Stark shift of the $3p$ level of lithium in electric fields up to 10 MV/cm was determined in these measurements by "semi-active Stark atomic spectroscopy", *i.e.* - without resonance laser excitation of atoms, but with self-injection of probe "charge-exchange" atoms from the partially ionized anode plasma layer into the diode gap. These experiments provided the first detailed investigation of ion diode acceleration gap physics in a multiterawatt pulser, and the first observations of Stark shifts in a 10 MV/cm field.

Work by Knyazev et al. [3,4] used an active measurement method in order to obtain truly local electric field measurements instead of along a line of sight (as in Refs. [1] and [2]). They measured the electric field in the 6-cm diode gap of the U-1 electron-beam accelerator by

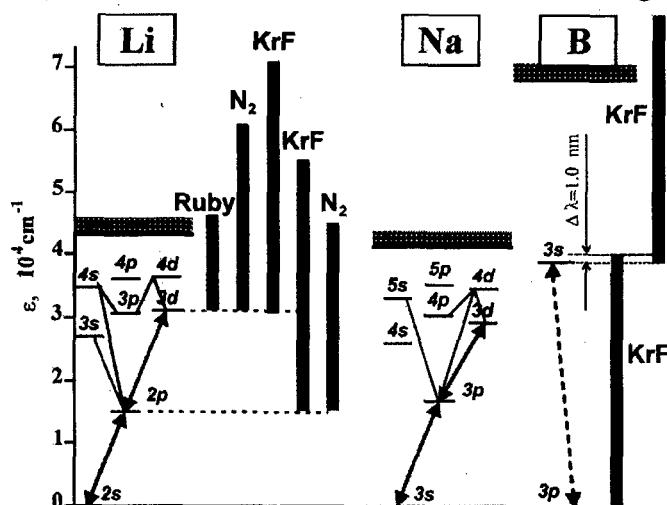


Fig. 1. Atomic transitions of lithium and sodium which can be used for measurement of Stark splitting in high-voltage diodes. Bi-directional arrows indicate transitions excited to saturation by laser radiation. The bars give the photon energy of lasers that can be used for photoionization of excited atoms.

Active Stark Atomic Spectroscopy (ASAS). Probe lithium atoms were injected into the gap and excited stepwise by two resonant lasers. Stark splitting of a probe-atom spectral line enables a calculation of the electric field with high time and space resolution. Since the probe atom density is less than the density of the background gas, this technique will not disturb the diode. However, high sensitivity is provided by using resonant broadband laser excitation to saturate the population of the upper level of transitions of interest (see Fig. 1). These experiments enabled a direct measurement of the electric field strength at a definite point in the diode (where the laser and probe atom beams intersect), as a function of time during a 6 μ s, 1 MV voltage pulse. The electric field strength measured in these experiments was 200-300 kV/cm, and the cathode and anode emission surfaces were located as a function of time.

The ASAS diagnostic method can be applied to an ion diode with the obvious requirement of using probe atoms different from the ions being accelerated. For example, in a lithium ion diode it is reasonable to use sodium atoms in the probe beam. The features of the ASAS diagnostic technique with sodium atoms are practically the same as with lithium atoms, and so a separate description is unnecessary here.

LASER-DRIVEN PROBE-ION DIAGNOSTICS

The ASAS diagnostic method can be turned into a combined spectroscopic and particle diagnostic by crossing the atomic beam with three laser beams, as illustrated for a magnetically insulated diode in Fig. 2. The atomic beam and two laser beams intersect along a line between the cathode and anode in the diode, from which comes fluorescence from the upper atomic level (which is collected by a lens that is not shown in the figure) as a result of the lasers exciting the atoms. Ions resulting from photoionization of the excited atoms by the third laser are also produced. We refer to this diagnostic technique as a Laser-driven Atomic-probe-beam Diagnostic (LAD).

As in the ASAS, the fluorescence is imaged on the input slit of an optical multi-channel analyser. The distribution of Stark splitting along z -axis (*i.e.* - between the cathode and the anode)

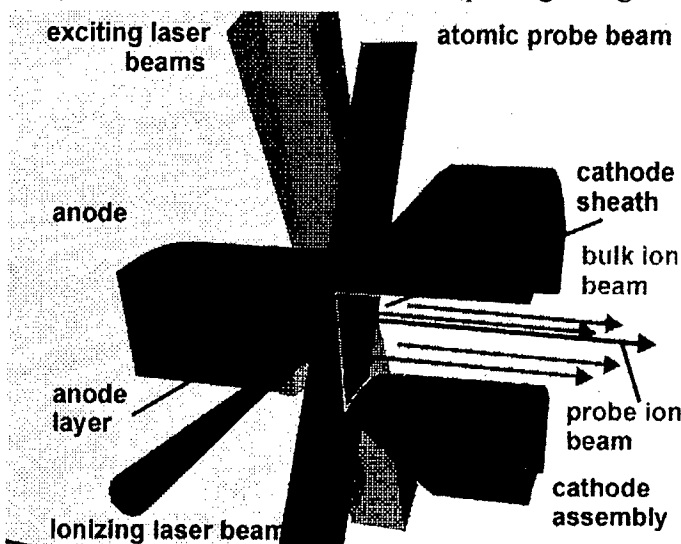


Fig. 2. A sector of the ion beam diode is shown which illustrates the method of obtaining spectroscopic data (the lens collecting the fluorescence is not shown in the figure) as well as charged particle probe data.

is recorded by a gated frame camera at the output of the analyzer, which gives the electric field distribution across the diode at a specific time as previously discussed [3]. If the third laser is focused onto a specific point of the excited atomic beam, the photoionized probe atoms can be monitored as they leave the diode. By measurement of their energy, one can determine the potential at the point of ionization. Measurement of the divergence of the probe ions, which start at different distances from the anode, could enable a determination of the location of sources of the ion divergence. We refer to this diagnostic method as Laser-driven Probe-Ion

Diagnostic (LPID). We point out that a thin, rectangular cross-section atomic probe beam crossing laser beams at close to a right angle would be the best configuration for spatial and temporal resolution for this (Fig. 3). In this configuration, the excited state population can be saturated along the laser beam path, but there is no problem with the self-absorption of the resonance emission by the surrounding non-excited probe atoms [5]. Furthermore, when the directions of excitation and observation are almost normal to the beam direction, one may ignore the Doppler-effect. A technique for formation of a slab-like atomic beam is described in ref. [6].

EXPERIMENTAL CONFIGURATION

The key points in the LPID are (i) the selection of probe atoms, (ii) the choice of the ionizing laser, and (iii) the technique of measurement of the probe ion characteristics. Since the probe-ion time of flight out of the ion diode has to be much less than the voltage pulse duration (or, at least, comparable with the time of flight of the bulk ions), the set of available probe atoms is limited to a few low-mass elements having resonance transitions which can be excited by available lasers to levels with a photoionization threshold less than the photon energy of the ionizing laser. Only three elements, lithium, sodium and, possibly, boron, whose partial Gro-

trian diagrams are shown in Fig. 1, meet these requirements. The time of flight of an ion which has been produced at a distance $\Delta z = d - z$ from the cathode is

$$\tau_f = \sqrt{\frac{2Am_p(\Delta z)^2}{eU(z)}} = 0.144 \sqrt{\frac{A(\Delta z)^2 [mm]}{U(z) [MV]}} [ns].$$

where A is the atomic number, U is the potential at this point at a particular time, and d is the anode-cathode separation. For $U=1$ MV and $\Delta z=5$ mm, the time of flight for H^+ is 0.7 ns, Li^+ - 1.9 ns, B^+ - 2.3 ns, and Na^+ - 3.5 ns. Thus, lithium and boron can be used as probe ions in proton-beam diodes, and boron and sodium in lithium-beam diodes. Saturation of the probe atom levels requires the laser spectral power density

$$J_L^s(\lambda) = \frac{1.4 \cdot 10^{14}}{\lambda^5} \left[\frac{kW}{cm^2 \cdot nm} \right],$$

which can be obtained easily with conventional flashlamp-pumped dye lasers. Levels of interest for the ASAS technique in the electric field range from 0.1 to 10 MV/cm are the $2p$, $3s$ and $3d$ states for Li , and $3p$, $5s$ and $3d$ states for Na . We will assume that the same excited levels are used for production of the probe ions. For production of probe ions an appropriate additional laser can be used to photoionize these levels. Lasers with low-energy photons (e.g. - ruby and neodymium) can ionize highly-excited atoms only. UV lasers (like KrF or N_2) can ionize the atoms excited to lower levels. The photoionization cross-sections for atoms with one valence electron can be determined from formula

$$\sigma_{ph} = \frac{9 \cdot 10^{-18}}{n_{eff}^5} \left(\frac{\epsilon_n}{\hbar \omega_L} \right)^3 [cm^2],$$

where n_{eff} is the effective principal quantum number. A power density of laser radiation F_L , which is necessary for photoionization of probe atoms during the time τ_i required for complete ionization atoms in the irradiated volume, can be determined from the expression

$$\tau_i [ns] \cdot F_L [GW/cm^2] = \frac{1.6 \cdot 10^{-19} [eV]}{\sigma_{ph} [cm^2]}$$

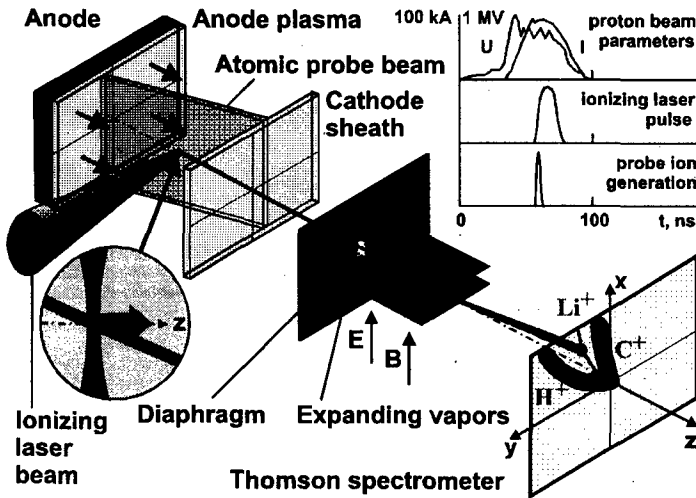


Fig. 3. Schematic of Laser-driven Probe-Ion Diagnostic.

Alternatively, it is possible to photoionize Rydberg states of alkali atoms in a high voltage diode with intense UV radiation [7] or to use two-step near-resonance interaction of KrF laser radiation with boron- see Fig. 1).

As a specific example, we assume a 2-MV proton diode with electrode separation of about 5 mm. An atomic lithium probe beam of width 0.2 mm with a density of $10^{12} cm^{-3}$ is injected into the diode. Radiation of the ionizing laser is focused to an area $S=0.01 mm^2$ at the atomic beam and produces (see the inset in the figure) probe ions by photoionization (see Fig. 3). This radiation does not affect the bulk ions or the background atoms. To achieve the highest sensitivity and excellent time resolution, the laser beam intensity has to provide complete ionization of probe atoms during its pulse length. The required energy is

$$\epsilon_L [J] = \frac{1.6 \cdot 10^{-19} \hbar \omega [eV]}{\sigma_{ph} [cm^2]} \cdot \frac{\tau_L S}{\tau_i}$$

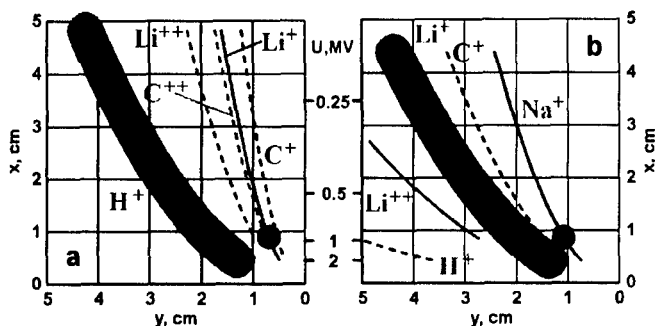


Fig. 4. Expected ion traces on the detector of a Thomson spectrometer: (a) proton diode and lithium probe ions with $a=5$ cm, $l=30$ cm, $aE=7 \cdot 10^4$ V, $aB=1 \cdot 10^4$ G-cm; (b) lithium diode and sodium probe ions with $a=10$ cm, $l=30$ cm, $aE=7 \cdot 10^4$ V, $aB=3 \cdot 10^4$ G-cm. We assumed input hole diameter of 3mm, and a divergence of the bulk beam of 15 mrad. See Ref. [8] for a complete description of this diagnostic.

aperture before the probe ions come through the hole. The bulk ions, as well as ions of anode contaminants, are recorded during the full pulse as thick parabolas, whereas the probe ions, locally produced during a short time, produce a small spot. The position and dimension of the spot on the corresponding parabola enables a determination of the potential at the point the probe ion is produced, along with its divergence. An example of the ion traces that might be seen with a Thomson spectrometer, recorded with either CR-39 film or a gated microchannel plate amplifier with scintillator, are shown in Fig. 4. Estimation shows that for the conditions specified above, the probe ions can be easily detected. Thus, a combined spectroscopic and particle diagnostic could make it possible to study the electric field profile in an ion diode while measuring the extracted ion divergence at the same time, both with excellent space and time resolution. It would be very reliable because a probe ion signal will be obtained only when the atomic probe beam, the exciting laser(s), and the ionizing laser are "switched on". The absence of any of them excludes appearance of a useful signal. For this reason the LPID can be classified as a "triply active" diagnostic.

ACKNOWLEDGMENTS

This material is based upon work partially supported by the U.S. Civilian Research and Development Foundation under Award No. RP1-239 and the program "Russia Universities".

REFERENCES

- [1] Y. Maron, M.D. Coleman, D. Hammer and H.-S. Peng, *Phys. Rev. Lett.* **57**, 699 (1986).
- [2] J. Bailey, A. Filuk, A.L. Carlson, et al., In *Atomic processes in plasmas. Tenth Topical Conference*, San Francisco, 1996. *AIP Conf. Proc.* **381**, 245 (1996).
- [3] B.A. Knyazev, S.V. Lebedev and P.I. Melnikov, *Sov. Phys. Tech. Phys.* **36**, 250 (1991).
- [4] B.A. Knyazev, P.I. Melnikov and V.V. Chikunov, *Sov. Tech. Phys. Lett.* **17**, 357 (1991).
- [5] B.A. Knyazev and P.I. Melnikov, *Abstracts of 9-th Europ. Sect. Conf. on Atomic and Molecular Phenomena in Ionized Gases*, Lisbon, 1988, *Europhys. Conf. Abstracts*, V.12H, P. 299 (1988).
- [6] B.A. Knyazev, W. An, H. Bluhm and L. Buth. *These Proceedings*.
- [7] D. Kleppner, M. Littman and M. Zimmerman. In *Rydberg states of atoms and molecules*. Ed. by R.F. Stebbings and F.B. Dunning. Cambridge University Press, Cambridge, 1983.
- [8] R.F. Schneider, C.M. Luo and M.J. Rhee, *J. Appl. Phys.* **57**, 1 (1985).

The $3d$ state of Li can be ionized by a 1-mJ ruby laser (20 ns pulse duration) within $\tau_{ph}=1$ ns.

An advantage of the LPID is the capability to measure probe beam divergence without any material collimating holes and slits, because the probe ions can be produced in the diode in a small volume. That enables the use of a Thomson spectrometer with a large input aperture. Material, evaporated by the bulk ion beam and expanding into the hole, which usually disturbs measurements of energy and divergence, does not cover the

DIAGNOSTIC PROBES COMPLEX AND IMPLOSIVE LINERS DYNAMICAL PARAMETERS RECORDING METHODS

A.M. Buyko, B.E. Grinevich, V.K. Chernyshev, A.I. Kuzyaev,
V.N. Mokhov, A.A. Petrukhin, V.B. Yakubov.

*Russian Federal Nuclear Center
Russian Scientific and Research Institute of Experimental Physics
(RFNC-VNIIEF)
Sarov, Nizni Novgorod region, Russia*

INTRODUCTION

During the recent 20 years VNIIEF has been studying compression of liners accelerated under the effect of pressure of superpower azimuth magnetic field formed by powerful explosive magnetic generators (EMG).

The research is carried out in application to create the sources of soft x-rays of a megajoule level and to obtain hot thermonuclear plasma.

During the experiments condensed (speed ~ 10 km/s) and plasma liners (at speeds up to some tens km/s) have been studied.

To measure the dynamical characteristics of the liners (speed, longitudinal and angular asymmetry etc.) various probes were developed: electrocontact, light, manganin, piezoelectric, inductive [1-5].

In the report the examples of use of these probes in the experimental studies of condensed and plasma liners compression are presented.

PARAMETERS TO BE MEASURED AND PROBES

EMG parameters. In all the experiments with the use of explosive magnetic generators working for liner loading, the measurements of current growth speed in a generator are conducted as well as of azimuth symmetry of magnetic field under the effect of which the liner acceleration takes place. For this purpose the inductive probes are widely used arranged to a certain scheme in transmitting lines of the experimental device.

Liner parameters. Before the experiment the initial liner characteristics are measured which influence its dynamics: liner diameter and liner thickness, variations in thickness and section, inner and outer liner surfaces machining cleanness, liner material density.

During the experiments the following characteristics are measured: the speed of liner in the process of initial acceleration and at final stage of acceleration, azimuth (angular) and longitudinal (along load axis) symmetry of liner flight up to a symmetrical central measurement unit (CMU).

For these purposes light, inductive, piezoelectrical, manganin and electrocontact probes are used.

The liner's state of aggregation change during the process of its acceleration (e.g. its electroexplosion) and quality of electric contacts of liner with side current conducting walls are controlled with light probes and also with inductive probes recording magnetic field penetrating under liner by means of measurement results comparison with magnetohydrodynamic (MHD) calculations.

Liner state at its impact on CMU is determined by shock wave speed and by pressure value in the CMU body. For these purposes the appropriate electrocontact and manganin pressure probes are used, and also numerical simulation of the liner impact on CMU (including two dimensional simulation).

Inductive probes. We use inductive probes [1] to measure a derivative of current flowing along the liner, to measure magnetic field penetrating under the liner because of this field diffusion through the liner or as a result of bad contact of liner with side current conducting walls, and also to measure the liner speed and symmetry at the stage of its acceleration.

Probes for liner speed and symmetry measurements are arranged in a side current conducting wall on different radii and azimuth angles. The probes produce signals as liner passes close to them (react to strong growth of magnetic field behind the liner).

The probe consists of a frame on which the coil is wound of one or more turns of insulated wire diameter 0.05-0.2 mm. The frame with the coil is placed into dielectric body (acrylic plastic, kaprolon, or quartz tube) and potted with epoxy compound. The probe output leads are twisted and soldered to coaxial joint and additionally insulated from the body with polymeric tube. Probe area is usually within the limits from 1 to 100 mm².

Piezoelectric and manganin probes. Piezoprobes [2] and manganin probes [3] are used to measure speed and liner movement symmetry in the process of its acceleration. Probes are situated on side current conducting walls and react to pressure impulse, taking place in the wall after the liner passing the area of probe location. Piezoprobes are used by us only as time recorders. Manganin probes are used both as time recorders and as pressure probes.

Piezoprobe consists of piezoelement and dielectric body, insulating the probe from the body of the device, which can be under high voltage in relation to recording techniques.

Manganin pressure probe consists of manganin wire 0.05 mm thick which is bifilarly placed in the plane and soldered to output leads made of copper foil. The wire with the output leads is coated with thin film insulation. Outside there is metal or dielectric body.

Electrocontact probe. Electrocontact probes [4] are used to measure the speed and symmetry of the liner on the final stage of the flight, and also to measure mass speed and speed of shock wave taking place in CMU body at liner impact on it. Constructive schemes of the probes may be various. Probe shorting can be done either with liner itself or metal screen which protects the probe.

Light probes. Light probes [5] are used to measure liner speed and symmetry, shockwave speed in CMU body taking place at liner encounter with it, and also for light effects recording which accompany the flight of a liner (liner electroexplosion, light radiation from contact boundaries of liner with side currentconducting walls). The probe consists of a light guide and a body in which it is fixed. A shock-type probe differs from an open-type probe by presence of an opaque protective shell and some space between light guide and the shell filled with air or argon. The open-type light probe (as a rule collimated; view angle is limited with $\sim 6^\circ$) is installed either on the side wall (to measure speed and symmetry of the liner on the stage of acceleration) or on CMU and is directed at a researched liner area. Shock-type probes give out light flash at the liner impact or the effect of shockwave.

STANDARD CHART OF PROBES ARRANGEMENT IN EXPERIMENTS WITH LINER

Figure 1 shows a generalized standard chart of probes arrangement in the liner experiments (1-liner, 2,5,7-inductive probes, 3-current conducting electrodes, 4-light probe, 6-

piezoelectric and manganin probes). In each specific experiment a special probes chart was used, which differed from the given one in presence or absence of separate types of probes, their quantity and arrangement.

TYPICAL RESULTS OF LINER PARAMETERS' MEASUREMENTS

We'll try to illustrate the application of the discussed probes with measurements results obtained in different experiments.

Figure 2 presents the oscillogram of current derivative flowing along $\varnothing 60$ mm and 0.2 mm thick liner and oscillogram of current derivative that flows under the liner and is related

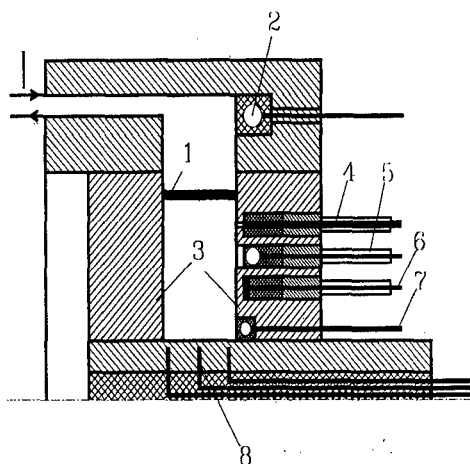


Figure 1. Generalized standard chart of probes arrangement in liner experiments.

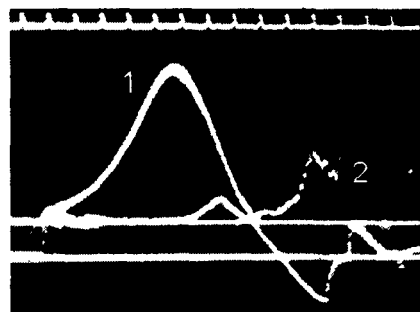


Figure 2. Oscillogram of current derivative (above -1 and under-2 the liner).

with an electric explosion of the liner. Current along the liner in this experiment achieved 35 MA at the maximum current derivative 35 MA/ μ sec and the maximum current derivative under the liner at the moment of electrical explosion achieved 1,3 MA/ μ sec. The maximum speed of a 1-gram liner achieved 47 km/sec.

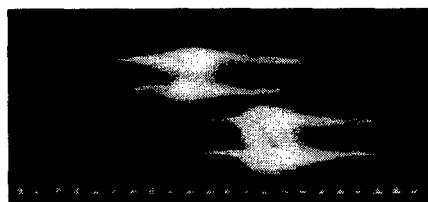


Figure 3. Photochronogram.

Figure 3 shows photochronogram of the liner speed recording by means of two groups of light probes installed on the external current-conducting wall at different radii. Liner speed was 22 km/sec.

Figure 4 presents the results of symmetry measurements of $\varnothing 60$ mm aluminum liner flight up to the central measurement unit obtained by means of electrocontact probes. Maximum azimuth time

difference of the liner flight up to the radius of 5 mm was 50 nsec, and the longitudinal one was 44 nsec.

Figure 5 shows the results of the experiment with the aluminum liner $\varnothing 480$ mm and 4 mm thick. Here the data are presented, obtained by means of inductive probes, for current derivative flowing along the liner (1) and the signals from piezoelectric (2, 3) manganin (4, 5)

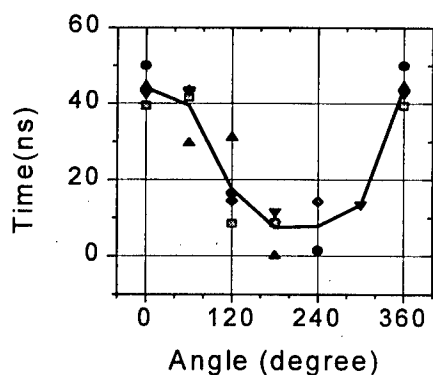


Figure 4. Liner flight up symmetry.

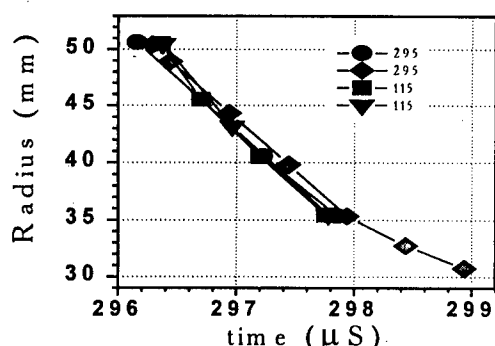


Figure 6. The results of measurements of the shockwave speed by means of electroconduct probes.

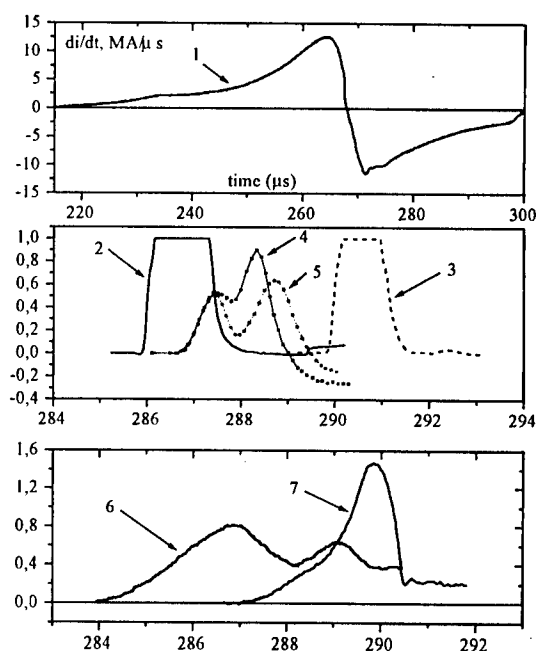


Figure 5. Results of the experiment with an aluminium liner Ø480 mm and 4 mm thick.

and inductive (6, 7) probes recording the moments of liner flight past the places of probes installation. The analysis of data from the inductive and piezoelectric probes showed that the liner average speed at this section of acceleration was 7.2 ± 0.8 mm/μsec.

Figure 6 presents the results of measurements, by means of electrocontact probes, of the speed of shockwave appearing in the CMU body, made of steel, at the impact on it of the aluminum liner having the speed of ~ 8 km/sec. Shock wave speed was 9-10 km/sec.

CONCLUSION

The presented experimental data testify, that the developed probes system permits to determine basic dynamical parameters of the implosive liners.

REFERENCES

1. H.Knoepfel Pulsed high magnetic fields. Moscow, 1972. Pp.314-331.
2. Spektor S.A. Electrical measurements of physical sizes. L: Energoatomizdat, 1987. Pp.203-211.
3. H.I. Kanel Application manganin of gauges for measurement of pressure of shock compression of condensed means. Institute Himphysics AN USSR, 1973. Pp.27.
4. Ultrahigh magnetic fields. Proceedings of the third International Conference on Megagauss magnetic fields generation and related Topics. Novosibirsk, June 13-17, 1983. Edited by V.M. Titov, G.A. Shvetsov
5. MEGAGAUSS Physics and Technology: Proc. 2nd Intern. Conf. On Megagauss Magnetic Fields Generation and Relative Topics, Washington, 1979. New York; London, 1980. Pp. 47-53

MULTICHANNEL LASER INTERFEROMETER - REFRACTOMETER WITH HIGH SPATIAL AND TEMPORAL RESOLUTIONS

I.V.Lisitsyn, S.Kohno, S.Katsuki and H.Akiyama

*Department of Electrical and Computer Engineering, Kumamoto University
Kurokami 2-39-1, Kumamoto 860, Japan*

ABSTRACT

A novel scheme combining interferometer and refractometer for simultaneous plasma density and plasma density gradient measurements is described. The scheme employs a ribbon laser beam obtained from one-dimensional laser beam expansion by a pair of cylindrical lenses. This beam shape allows measurements at several spatial locations simultaneously. The beam deflection measurements give additional important information on the spatial distribution of plasma density gradient in the direction perpendicular to the major axis of the expanded beam. Fast pin photodiodes are used as light detectors for temporal resolution better than 1 ns. The high power (700 mW) of the argon ion laser allows 0.1° phase resolution and simultaneously 0.1 mrad refractive deflection angle.

INTRODUCTION

Laser interferometry is a plasma diagnostic method allowing direct measurements of plasma electron density [1-5]. The method utilizes the effect that the plasma index of refraction is dependent on the density of free electrons. The variation in the index of refraction is similar to change of the scene laser beam optical path length, resulting in a phase shift.

The index of refraction of a plasma for high frequency electromagnetic wave is determined primarily by free electrons. Free ions and neutrals can also cause the change in the index of refraction, but their influence is lower and can be often neglected [6].

A frequent question, discussed in papers dedicated to laser interferometry [4,5], is the influence of laser beam deflection in plasmas with density gradients on the accuracy of the measurements. The deflection of the laser beam in the plasma changes the contrast of the fringe pattern due to unparallelity of the wavefronts of the recombining scene and reference beams. Other reasons of the contrast change like the lens aberrations and the dependence of the reflection coefficient of optics on the beam incident angle can also be important. Since many optical parameters play roles, the exact calculations or measurements should be made for a particular interferometer scheme. The problem of beam deflection influence onto accuracy of interferometer measurements can be solved if deflection angle is measured simultaneously with the phase shift.

EXPERIMENTAL SETUP

The diagram of the interferometer-refractometer is shown in Fig. 1. The device is based on the Michelson interferometer scheme with the beam splitter (BS1) dividing the laser beam into reference (I) and scene (II) beams, where the latter passes two times through the plasma. An argon ion laser (NEC 3200, 700 mW at 488 nm) with vertical beam polarization is used

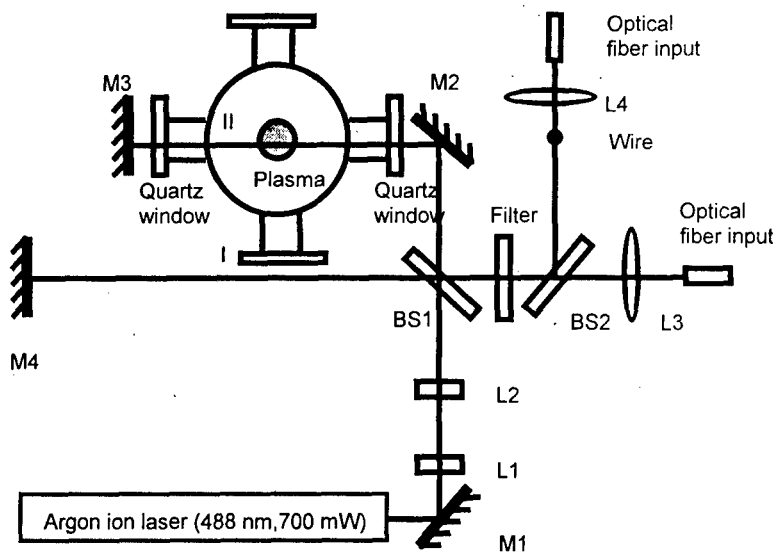


Fig. 1. The diagram of interferometer setup

schemes with higher (lower) expansion factors can be built for other experiments.

An advantage of using an Ar ion laser is that it is one of the most powerful dc light sources in the optical wavelength range. Such lasers have good power stability and acceptable coherence length and bandwidth. The output power of 700 mW reduces the requirements to the elements of the optical scheme: lenses, mirrors, etc.

The scene beam of the interferometer is reflected from the mirror (M2) and passes through the vacuum chamber equipped with two quartz windows. The lengths of the reference and scene beams are similar, to achieve high fringe stability in time. Both beams recombine at the beam splitter BS1 forming the fringe pattern of the size of expanded laser beam. Fine adjustment of the optical elements is necessary to make the fringe amplitude approximately similar in the whole interferometry field. A narrow bandpass (60% transparency at 488 nm center wavelength, 0.5 nm FWHM) filter is used to avoid false signals due to plasma luminosity, which are large if no filter is used. The second beam splitter (BS2) splits the laser beam to the interferometer and refractometer arms of the device.

The interferometer arm (horizontal in Fig. 1) has a cylindrical convex lens (L3) with focal length of 50 mm for one-dimensional horizontal beam focusing. The fringe pattern formed at BS1 and passed through L3 is captured by array optical fibers. The output ends of the optical fibers are placed into a shield room allowing noise free signals at the multichannel light detection scheme.

The refractometer arm (vertical in Fig. 1) uses the fraction of the fringe pattern reflected from the beam splitter BS2. It consists of a wire (2 mm in diameter) and cylindrical convex lens L4 ($f = 100$ mm) focusing the beam onto an array of fibers similar to those described above. The reference and undeflected scene beam are blocked completely. The refraction in the plasma due to density gradients results in deflection of the scene beam, so it partially

misses the wire and is focused at the entrance of the optical fiber. The scheme of the refractometer part of the device is shown in Fig. 2. Since only the scene laser beam can be deflected by plasma with density gradient, no

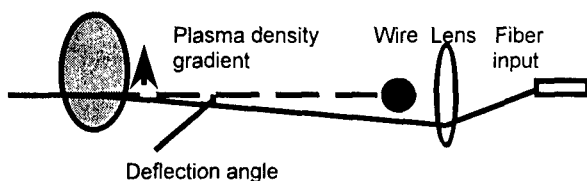


Fig. 2. Scheme of refractometer part.

fringe pattern occurs in the refractometer arm. The amplitude of the photodiode signal

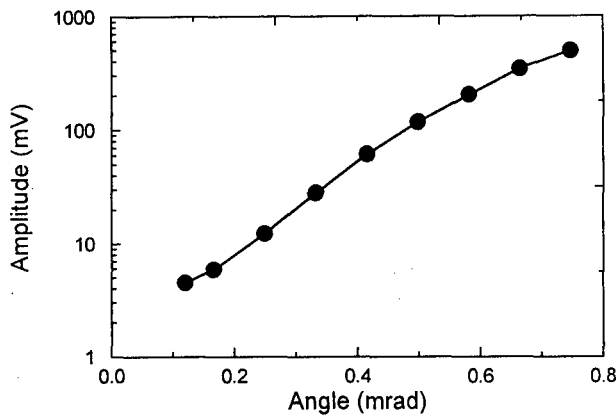


Fig. 3. Response function of the refractometer.
Photodiode signal amplitude vs deflection angle.

in the refractometer arm is a function of beam deflection angle. This response function was measured by a precise rotation of the mirror M3 and is shown in Fig. 3.

The multichannel light detection scheme is based on the standard Si PIN photodiodes (Hamamatsu S5973-01) designed for use with optical fibers, with sensitivity equal to 0.23 A/W at 488 nm. Such diodes have extremely low terminal capacitance (1.5 pF) that enable the measurements with high temporal resolution (approximately 50 ns for 1 kOhm photodiode load resistance). Signals

from the photodiodes were recorded with a 1GSa/s HP 54512B digital oscilloscope.

We also tested the scheme where the photodiodes were loaded with 50 Ohm coax cables and with 50 Ohm oscilloscope input impedance. In these experiments, the temporal resolution of the scheme is 1 ns and is limited only by the oscilloscope bandwidth, but low signal amplitude precludes measurements of low plasma line densities, less than 10^{15} cm^{-2} .

The signals recorded from the array of photodiodes in the interferometer part were analyzed using the linear approximation of amplitude - phase dependence. A special triggering unit is used to provide zero fringe phases before a shot.

The interferometer was built for short time scale plasmas in pulsed power systems like plasma opening switch, z-pinch, electromagnetic launchers etc. For such measurements in fast plasmas, precise length stabilization in the interferometer arms is not necessary, that makes the design much easier. The vibration of the optical elements of the interferometer has characteristic time of several tens of milliseconds, but plasma pulse duration is usually between 100 ns and 1 ms.

EXPERIMENT

The test measurements were made with a cable plasma gun. The plasma gun was powered by a 1.2 μF , 15 kV capacitor. The plasma gun current reached a maximum of 7 kA in 1.2 μs . Plasma density and plasma density gradient were measured simultaneously in different locations in the gun plasma. The schematic diagram with laser beam positions is shown in Fig. 4 (a).

The plasma densities measured in a single shot at the points 1-5 separated in vertical direction by 2.5 mm (Fig. 4 (a)) are shown in Fig. 4 (b). As expected, no signal was recorded in the refractometer part because the measured locations lie along the plasma gun axis, where the plasma density gradient is negligible. This measurement proves also the absence of measurable beam defocusing by the plasma lens.

The measurements made for points 6-8 separated in vertical direction by 5 mm, 1 cm from the axis show lower plasma density and the existence of a measurable density gradient. In these positions plasma has a gradient in the direction perpendicular to the gun axis. Plasma densities for points 6-8 and gradient for point 7 are shown in Fig. 4 (c). The maximum refraction angle measured in this experiment corresponds to $|\nabla n| = 2 \times 10^{17} \text{ cm}^{-3}$.

The measurements of the fringe contrast versus the deflection angle were made to understand how beam deflection affects interferometer measurements. The measurements

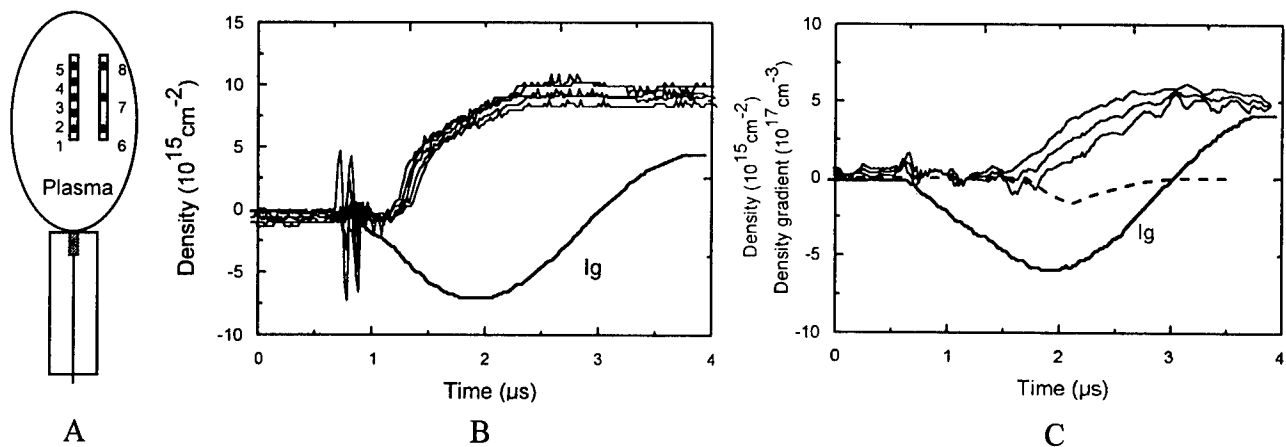


Fig. 4. A) Positions of measurements in the cable gun plasma. B) Waveforms of gun current and line-integrated plasma densities for points 1 through 5. Left density trace corresponds to point 1, second from left trace corresponds to point 2 and so on. Ig trace is plasma gun current (5 kA/div). C) Waveforms of gun current, and line-integrated plasma densities for points 6 through 8. Dashed curve is the plasma density gradient in time. Ig trace is plasma gun current (5 kA/div).

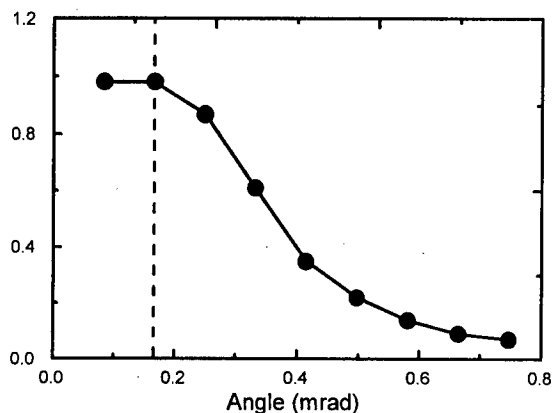


Fig. 5. Contrast of the interferometer versus deflection angle of the scene beam

were made similarly to measurements of refractometer response function and the results are shown in Fig. 5. It is seen that the deflection angle over 0.2 mrad decreases the accuracy of measurements to the unacceptable level. This angle was not detected in our experiments proving the accuracy of interferometer measurements. The dashed line at the figure shows the calculated value of the maximum acceptable deflection angle that is in good

agreement with the measured value.

REFERENCES

- [1] R.Kristal, *Diagnostics for Fusion Experiments*, (Pergamon, Oxford, 1978) p.617.
- [2] *Plasma Diagnostics*, edited by W. Lochte-Holtgreven (North Holland, Amsterdam, 1968), p. 543.
- [3] F.F.Chen, *Introduction to Plasma Physics and Controlled Fusion*, 2 nd ed. (Plenum, New York, 1984), Vol. 1, p. 421.
- [4] A.S.Chuvatin, B.Etlicher, N.S.Edison, and C.Rouille, *Rev. Sci. Instrum.* **64**, 2267 (1993).
- [5] B.V.Weber and D.D.Hinshelwood, *Rev. Sci. Instrum.* **63**, 5199 (1992).
- [6] B.V.Weber and S.F.Fulghum, *Rev. Sci. Instrum.* **68**, 1227 (1997).

CALIBRATION OF THE GALILEO MICRO CHANNEL PLATE WITH THE Xe^{7+} ÷ Xe^{43+} IONS IN THE ENERGY RANGE FROM 2 keV/q UP TO 154 keV/q

W. Mróz*, D. Fry, A. Prokopiuk*, M. P. Stöckli and B. Walch

J. R. Macdonald Laboratory and Department of Physics,
Kansas State University, Manhattan, Kansas 66506, USA
E-mail: stockli@auger.phys.ksu.edu

* Institute of Optoelectronics, MUT,
01-489 Warsaw 49, 2 Kaliski St., POLAND
E-mail: lastech@wat.waw.pl

ABSTRACT

The procedure of calibration of the detector assembly consisting of the two Galileo Micro Channel Plates (MCPs) operated in a Chevron configuration is described. The current gains and the analog particle gains of the MCPs for Xe ions with charge states from $q = 7+$ to $q = 43+$ and ion impact energies to charge state ratios from 2 keV/q to 154 keV/q have been measured. For the investigated range of an ion impact energies we have stated that for xenon charge states of $q = 7+$ up to $q = 15+$ the secondary ion-electron emission coefficient is dominated by kinetic emission of electrons. Potential effects start to be visible for charge states above $q = 15+$.

INTRODUCTION

The micro channel plates are often used as a detectors of X-ray radiation and of the different kind of particles like electrons, ions, neutral atom, clusters and others. The high electron current gain of MCPs (up to 10^7 ÷ 10^8 in three stage configuration), small rise time, t_r , and fall time, t_f , ($t_r+t_f < 1\text{ns}$) make MCPs especially suitable for operation in pulse counting mode. The MCPs are willingly used with the time-of-flight (TOF) analyzers, where generally work as a current amplifiers. The current amplification G_c , can be expressed as the absolute ratio of the electron current at the output of the MCP - I_{out} and the intercepted current of particles, I_p :

$$G_c = \frac{I_{out}}{I_p} \quad (1)$$

In measurements, when the current peaks from a different ion sources (with different charge states) are registered, it is very convenient to know the analog particle gain, G_a , of registered ions. The G_a is defined as the ratio of the number of electrons at the output of the MCP, N_{out} , and intercepted number of particles with the charge state - q , $N_p(q)$:

$$G_a = \frac{N_{out}}{N_p(q)} \equiv \frac{I_{out}}{I_p(q)/q} \quad (2)$$

In the next parts of this paper we will present the results of calibration of the two stage Galileo MCP assembly operated in the Chevron geometry [1]. The G_c and G_a gains for Xe ion with charge states from $q = 8+$ to $q = 42+$ and ion impact energies to charge state ratios from 2 keV/q to 154 keV/q will be presented.

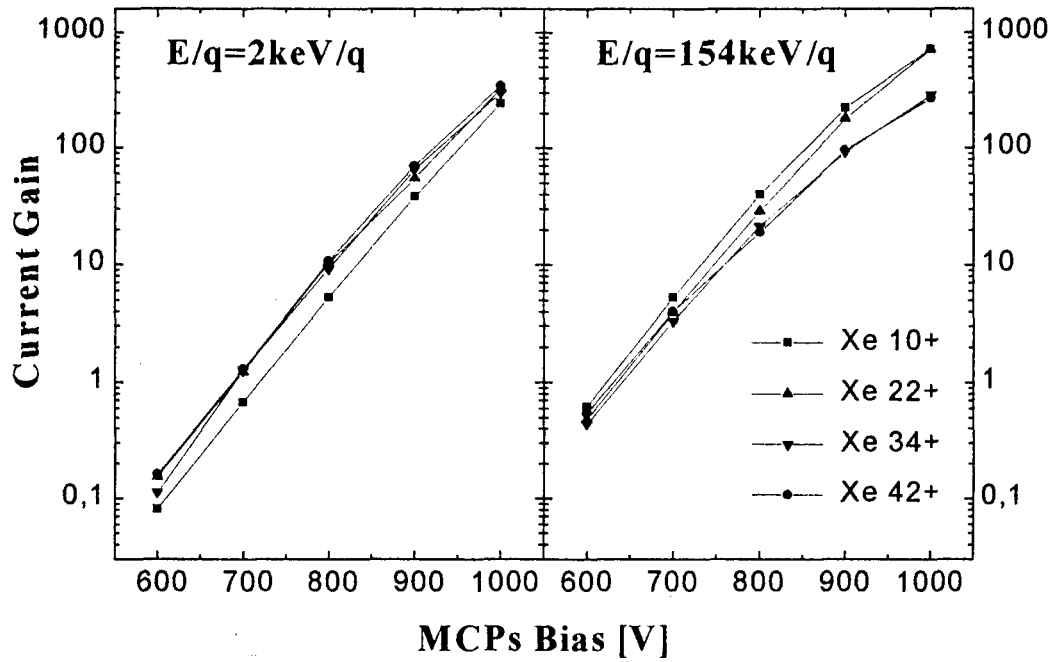


FIGURE 1. Current gains for Xe^{10+} through Xe^{42+} ions with $E/q = 2 \text{ keV}$ and $E/q = 154 \text{ keV}$ as a function of MCPs bias voltages.

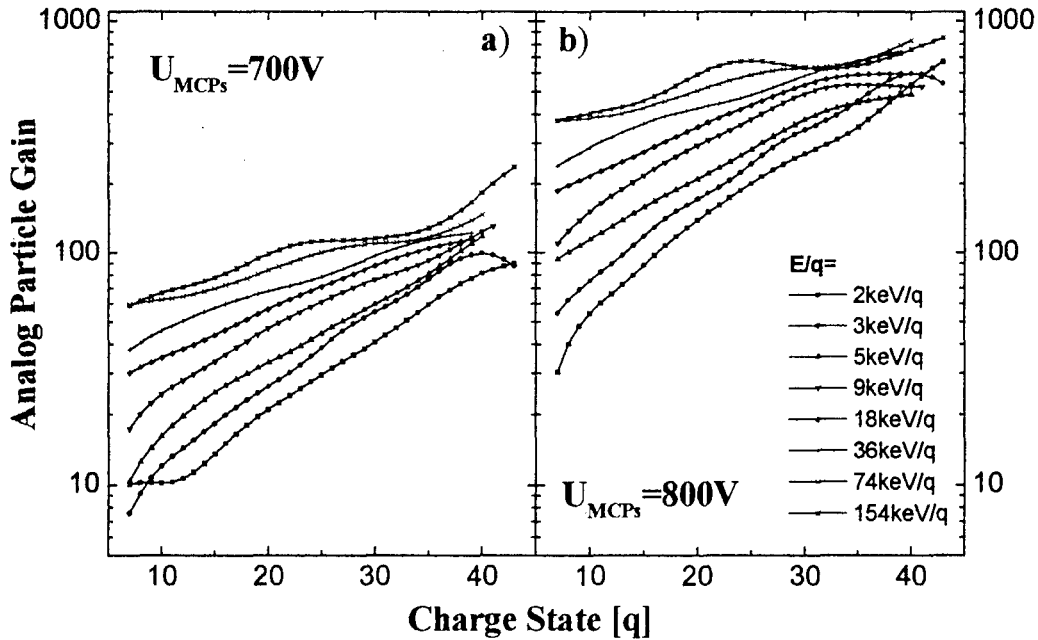


FIGURE 2. Analog particle gain as a function of the charge states of registered ions for different energy to charge ratios: **a)** - $U_{\text{MCPs}} = 700 \text{ V}$, **b)** - $U_{\text{MCPs}} = 800 \text{ V}$.

EXPERIMENTAL SETUP AND RESULTS.

The calibrated detector assembly consist of the two 0,4 mm thick MCPs with a 19,6 mm active diameter [1]. The 10 μm diameter channels have a bias angle of 5° and yield an open area ratio 64%. The MCPs were matched for equal bias currents (3 μA at 700 V) and were mounted in direct contact. Details of our experimental arrangement were describe earlier in [2], in article about the MCPs calibration with argon ions. Beams of xenon ions, with

the charge states $7 \leq q \leq 43$ were expelled from the Kansas State University Cryogenic Electron Beam Ion Sources, KSU-CYBERIS [3], with an initial energy $E/q = 3$ keV and analyzed with a double focusing 90° dipole magnet. The energy of selected ion beam was changed in the accelerator tubes by applying acceleration potential to the high voltage platform. Finally we have used the Xe ions with energies $E/q = 2, 3, 5, 9, 18, 36, 74$ and 154 keV. In our measurements the ions were produced with frequency $f \sim 80$ Hz, expulsion time of ion source was $8,5$ ms. Time averaged current in time of measurements was changed between 2 - 200 pA/cm². Majority of measurements were done with current of about 10 pA/cm².

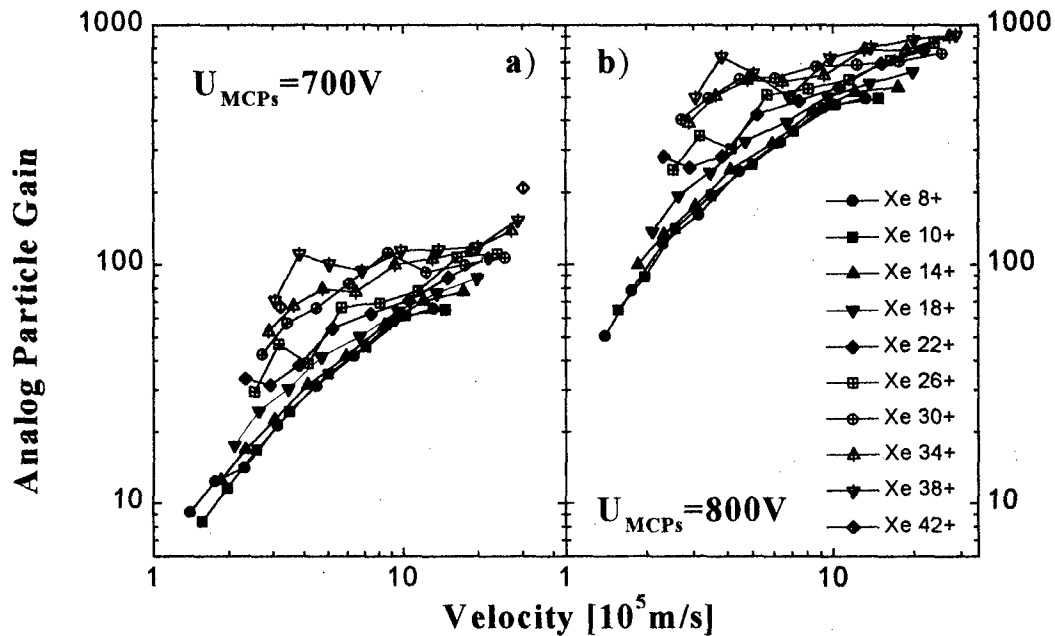


FIGURE 3. Analog particle gain as a function of the charge states of ion impact velocity:
a) - $U_{MCPs} = 700$ V, b) - $U_{MCPs} = 800$ V.

In Fig. 1 the current gains for Xe^{10+} through Xe^{42+} for ion impact energies, E/q , of 2 keV/ q and 154 keV/ q were shown. For bias voltages of the $U_{MCPs} > 800$ V (catalog bias voltage for single MCP is of about 800 - 1000 V) the current gains deviated from the exponential growth with increasing voltage [4]. As the rule was, the higher deviation for higher energy per charge state ratio of incoming ions. The reason of this deviation from the exponential growth is partial saturation of MCPs. The experimental result obtained for 700 V and 800 V are used through the rest of this paper as the standard parameters of tested MCPs assembly. In Fig. 2 the analog particle gains as a function of the charge state of registered ions for eight energy to charge ratios, E/q , were shown. Presented relationships were obtained by approximation of the experimental points by the fast Fourier transform of the Microcal Origin program with filter frequency $m = 5$ (FTMO). This method of approximation smooth the processed results from single fluctuations. The visible small fluctuations of obtained characteristic, for higher E/q ratios, and for the smallest and the highest ion charge states were caused by the small fluctuations of the current of used ion source. We suppose that like for the MCPs calibrated with tantalum ions [5], the obtained characteristics could be approximated by the exponential shape. Analog particle gains in function of the velocity of registered ions were shown in Fig. 3. From this figure it is seen that G_a is almost independent on ion charge state ($\pm 15\%$) for ions with the charge states from $q = 7$ up to $q = 14$ (15). In this range of ion charge states, the G_a depends mainly on ion impact velocity. This independence of the G_a on

ion charge states is visible also in Fig. 4a (experimental points were joined by FTMO). In the

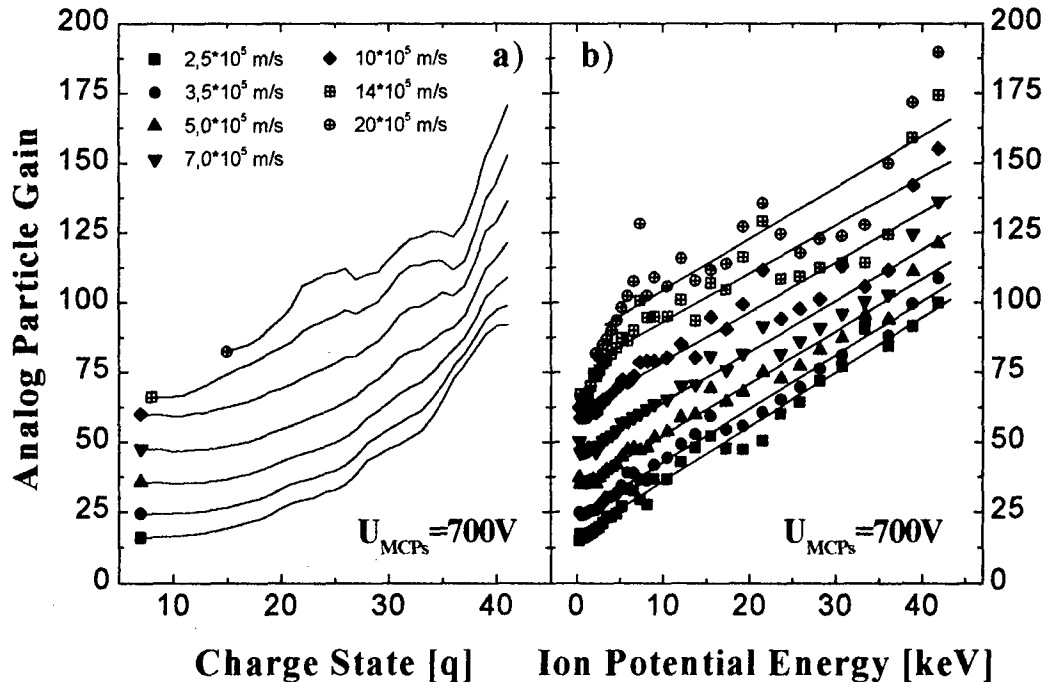


FIGURE 4. Analog particle gain as a function of the: a) charge state of registered ions, b) potential energy of registered ions.

investigated range of ion velocities the G_a rises strongly with ion impact velocity. The analog particle gains in function of ion potential energy (sum of ionization energies) was shown in Fig. 4b, for seven selected velocities of ions. Beginning from $q = 14$, the G_a rises linearly with rise of the potential energy of impinging ions.

CONCLUSION

The calibrated assembly consisted of the two MCPs is very sensitive detector of highly charged ions in investigated range of energies, E/q . As a proportional amplifier of registered current it can work with bias voltage much lower than the typical voltage for MCP polarization. Analog particle gain (also the ion-electron emission coefficient) rises approximately linearly with rise of potential energy of registered ions.

ACKNOWLEDGMENT

This work was supported by the Division of Chemical Science, Office of Basic Energy Science, Office of Energy Research, U.S. Department of Energy and was performed partially within research project No. 657/S5/94/07 sponsored by the State Committee for Science Research, Poland.

REFERENCES

- [1] 18 mm detection quality from Galileo, Sturbridge, MA 01566.
- [2] M. P. Stockli and D. Fray, Rev. Sci. Instrum. **68** (1997) 3053
- [3] M. P. Stockli et al., Rev. Sci. Instrum. **63** (1992) 2822.
- [4] E. H. Eberhardt, Applied Optics **18** (9) (1979) 1418.
- [5] D. Fray et al. Micro channel plate gains for Ta^{10+} - Ta^{44+} ions, measured in the energy range from 3,7 keV up to 153,7 keV, Nucl. Instrum. Methods Phys. Res. A. (submitted) and W. Mróz et al., Rev. Sci. Instrum. **69** (1998) 1349.

TIME RESOLVED XUV LINE EMISSION MEASUREMENT

V.Piffl, A.Krejci*, A.V.Golubev**

Institute of Plasma Physics, Academy of Sciences of the Czech Republic,

Za Slovankou 3, P.O.Box 17, 182 00 Prague 8, Czech Republic

**World Trend, Prague, Czech Republic, **Marinfo, St.Petersburg, Russia*

A double-channel spectrometer with multilayer mirror (MLM) [1] has been built and operated on different experiments: tokamak CASTOR and gas-puff z-pinch at Institute of Plasma Physics, Prague as a monitor of the hot plasma line emission. Depending upon the mirror use, the spectrometer allows the low resolution ($\lambda/\delta\lambda=30$) spectra measurements in the wide energy range. Filter transmission as well as the reflectance of the disperse MLM elements and detector sensitivity were absolutely calibrated by X-ray grazing incidence monochromator in the considered spectral ranges [2].

The time resolution of line emission measurement of 0.1 ms for low intensity source (tokamak) and better than 10 ns for gas-puff z-pinch has been achieved.

TIME RESOLVED MEASUREMENTS OF OXYGEN AND CARBON XUV SPECTRAL LINES OF LOW INTENSITY SOURCE [3,4]

The plasma of the small tokamak represents a low intensity source of ultra soft X-ray radiation. Sufficiently high signal-noise ratio is required in order to make the time resolved investigation of the impurities radiation successfully. Fastidious choice of the appropriate MLM, filter and detector played important role in design and final application of the XUV spectrometer being used. Relative high reflectivity of the MLM dispersion elements together with the high transmittance of a thin film filters and the high gain of the channeltron operating in impulse regime have given a good chance that such a spectrometer arrangement will be suitable for the time resolved line emission measurements even in the conditions of a low density plasma. The output signal of the detector - channeltron with XUV radiation to electrons convector and amplifier-shaping unit - is a sequence of the rectangular "logical" pulses of the amplitude +5V and pulse duration of 0.5 μ s with maximum rate of $5 \cdot 10^5$ counts per second. A statistic feature of a time distribution of the pulses is caused by the low intensity of the source and by the photon- to-electron converter mounted in the front of the channeltron.

The output signal is processed by two independent methods:

- 1) the pulses are counted by a 400-channel counter in time windows following closely each other. Typically, the time window is 0.1 ms wide in our case. This method was used for the absolute measurements only.
- 2) the logical pulses are converted by a passive RC integrated circuit (time constant 1 ms) to an analogue signal and the latter was recorded by CAMAC acquisition system to a database together with other the plasma parameters. This method was used for the relative measurements.

The time evolution of the most intense OVII line

Fig. 1a: The pulses counts by 400-channel counter in time windows, 0.1 ms wide, following closely each other.

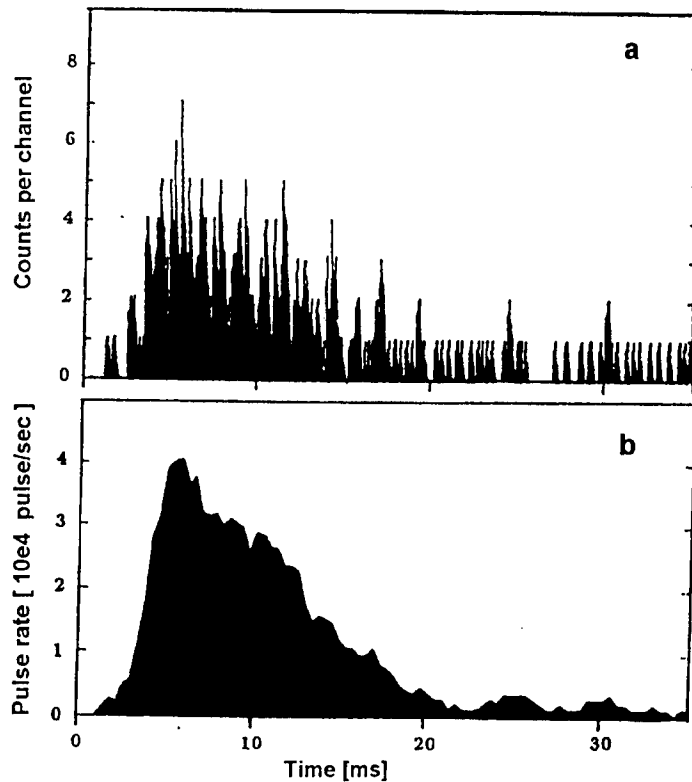


Fig 1b: The conversion of the "logical" pulses by passive RC integrated circuit with time constant 1 ms.

The time evolution of the most intense lines: OVII doublet ($1s^2-1s2p$, 21.6 Å, and 21.8 Å) detected in the ultra soft X-ray range at CASTOR tokamak is demonstrated in Fig.1a, and Fig.1b for both the methods of the signal processing mentioned above.

TIME RESOLVED MEASUREMENTS OF HIGH INTENSITY XUV NITROGEN LINES IN A SMALL GAS-PUFF Z-PINCH EXPERIMENT [5]

Soft X-ray emission from nitrogen plasma of a small gas-puff z-pinch has been studied in the energy ranges 52 - 72 eV and 400 - 930 eV by modified double channel spectrometer. Each of the two channels consisted from a submicron metallic filter, multilayer mirror and a PIN diode.

The thickness of used light-tight filters: 0.3 μm Al and 0.2 μm Fe + 0.2 μm C - was sufficient to absorb a scattered VUV component of a plasma radiation.

In the region of the energies below 100 eV the multilayer mirror Mo/Si ($2d=216$ Å) has been used. The chosen multilayer W-Si mirror ($2d=70.5$ Å, $R_{\text{refl}}=0.03-0.15$, $dE/E=15-30\%$) covers due to the smooth spectral dependencies of the scattering factors of W and Si up to K-edge of Si (1.84 keV) a broad energy range: 450-850 eV.

The spectral sensitivity of the silicon PIN diode SPPD11-04 from the NIIIT, Moscow equipped by 0.1 μm thick Al input window (dead layer 0.15 μm, sensitive layer 76 μm) varies from 0.003 to the maximum value of $1.35 \cdot 10^{-2}$ A cm²/W in the energy range of interest. This silicon PIN diode has time resolution 1.4 ns. The spectrometer was placed radially from the pinch discharge. The distance from plasma to the detector was 1210 mm.

Another silicon PIN diode and a bare x-ray diode (XRD) with an Al photocathode covering efficiently a spectral energy range 4.2-250 eV were situated radially from pinch as monitors.

The emitted spectral power density into solid angle 4π sr is then given by formula

$$\frac{dP}{dE} = \frac{I_{PIN} * 4\pi L^2}{T_F(E) * R(E) * S_{PIN}(E)} \quad [W/eV]$$

where $T_F(E)$ is average filter transmission in the chosen channel within energy interval dE , $R(E)$ is integrated reflection coefficient of MLM in eV, $S_{PIN}(E)$ is average PIN diode sensitivity within dE in $A \cdot cm^2/W$, L is source-to-MLM-to-detector distance in cm, and I_{PIN} is detector current in A. The maximum error in the dP/dE determination is connected with the accuracy of the values T, R, S, L , and with an alignment of the channel. In our case the error of dP/dE values did not exceed 27%.

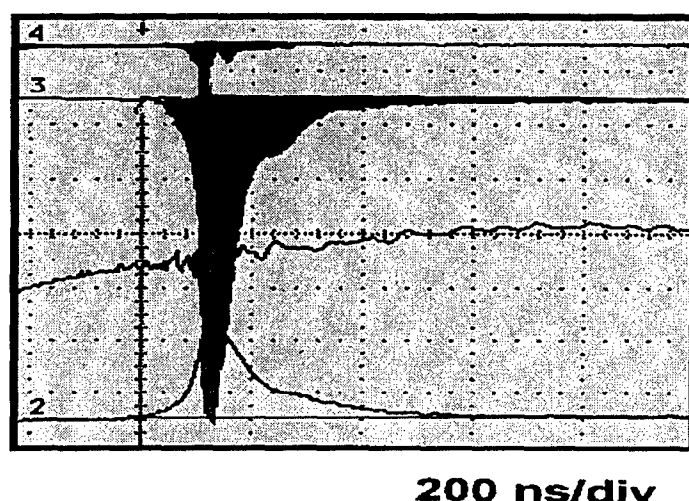


Fig. 2: The raw signal in the L-shell lines region

4 -silicon PIN diode monitor

3 -signal of the Li-like Nitrogen line, 59 eV

-plasma discharge current

2 -signal of bare x-ray diode with Al photocathode

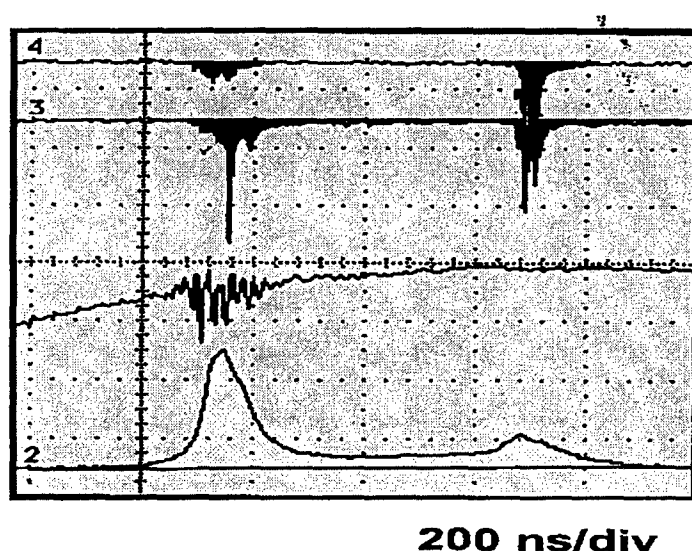


Fig.3: The raw signal in the K-shell lines region

4 -silicon PIN diode monitor

3 -the radiation in the region in-between of the H-like Nitrogen lines(500eV) and (590 eV)

-plasma discharge current

2 -signal of bare x-ray diode with Al photocathode

The raw signal of the Li-like Nitrogen line 2s-3p (59 eV/210 Å) is shown in Fig.2 (trace 3). There is seen a clear coincidence between XRD monitor (trace 2) and line response related to the L-shell transitions (trace 3). The signal of the radiation in the region in-between of the H-like Nitrogen lines 1s-2p (500 eV/24.8 Å) and 1s-3p (590 eV/21 Å) is demonstrated in Fig.3,

(trace 3), together with signals of XRD (trace 2) and PIN diode(trace 4) monitors. Note the second peak of Nitrogen K-shell emission is caused by local pinching of the hot plasma several hundreds nanoseconds after the first peak in some unstable z-pinch discharge regimes.

IMAGING HIGH-THROUGHPUT ULTRASOFT-X-RAY MONOCHROMATOR

Within the past few years, the technology of curved multilayer mirrors for ultrasoft X-ray focusing optic had some application that further increased the potential of MLM based spectroscopy, that nowadays allows:

- detection of the weak intensity lines,
- imaging of the weakly plasma emanation regions.

We propose to initiate a development programme in ultra soft X-ray optics, which finds an application in fusion research. The first step should be the built up of a high-throughput XUV monochromator based on spherical multilayer mirror for time and space resolved measurement. The next step would be an application of curved multilayered mirrors to form image of relatively large volume of a hot plasma onto a one/two dimensional detector array. Such project starts in IPP Prague now.

Acknowledgements:

The work was supported by the Grant Agency of the Czech Republic under No.: 202/98/0831.

References:

- [1] A.P.Zwicker,M.Regan,M.Finkenthal and H.Moos: Layered synthetic microstructures for soft x-ray spectroscopy of magnetically confined plasmas, Rev. Sci. Instrum. 61, Oct.1990, p.2786
- [2] S.V.Bobashev, I.A.Shmaenok, and V.P.Smirnov: Advances in absolute radiometry of intense soft—x-ray fluxes, 15th Int.Conf. on X-Ray and Inner-Shell Processes Knoxville, 1998, AIP Proc.,p. 242
- [3] V.Piffl,J.Badalec,A.V.Golubev: Absolute measurements of light impurities line radiation using MLM based spectrometer, IPP CZ-340, IPP Prague, June 1994
- [4] H.Weisen,V.Piffl et al.: Ultra-soft x-ray spectroscopy using multilayer mirrors on TCV, LRP 524/95, CRPP EPFL Lausanne, August 1995, p.33-36
- [5] A.Krejci,J.Raus,V.Piffl,A.V.Golubev et al.: Multichannel Soft X-Ray Diagnostics of Hot Plasma Evolution in Nitrogen-Puff Z-Pinch, IEEE Transactions on PlasmaScience,Vol.21,No.5,Oct.,1993.

"CONTROL" DIAGNOSTIC X-RAY APPARATUS WITH A DIGITAL IMAGE VISUALIZATION SYSTEM

A.L. Filatov, S.R. Korjenevski, S.V. Scherbinin

*Institute of Electrophysics, UD RAS
Komsomolskaya 34, Ekaterinburg 620049, RUSSIA*

Abstract

In the article opportunities of application of compact pulsed power generator for medical diagnostics complex are considered. The converter placed behind the test object is irradiated by a short-duration packet of nanosecond X-radiation pulses. This operating mode of the apparatus is made feasible by using a high-voltage generator and an X-ray tube that permit attaining an X-radiation pulse duration of $\sim 10^{-8}$ s, a value which is well below the duration of the return motion of the videocamera frame scanning beam ($\sim 2 \cdot 10^{-3}$ s) at a pulse repetition rate of 10 kHz. Using highly intensive nanosecond X-radiation pulses has enabled us to obtain the highest intensity of luminescence of the luminophor as the intensity of luminescence is known to be proportional to the ionization rate of luminescence centers or to radiation power. We have obtained results on tests of an apparatus with a high-sensitivity CCD camera affording in the X-ray image a gray-color gradation level of 65536.

Introduction

The utilization of nanosecond pulsed X-radiation sources to visualize optically dense media dates back to the early forties. But only with the advent of all-solid-state generators producing X-radiation pulses of supershort duration (10 to 15 ns) by means of semiconductor opening switches (SOS) based on the effect of current interruption in semiconductor structures, discovered by researchers of the IEP, has it been possible to attain a good reproducibility of results as well as to form X-ray images by a train of pulses following at a rate of up to 10 kHz rather than by a single pulse. That research and development effort provided a basis for creating a variety of electron accelerators and X-ray generators [1, 2]. The present paper considers one of such generators, which was pioneered in 1995, [3].

Principles of obtaining an X-ray image and results of testing

The mode of operation permits eliminating the spatial nonuniformity of the radiation of a single pulse and improving the performance of the luminophor. In Fig. 1 we present the correlation factor (CF) (1) versus the number of pulses forming the image frame of the test object:

$$CF(A, B) = \frac{1}{\sigma_A \cdot \sigma_B} \cdot \left[\frac{1}{m \cdot n} \cdot \sum_{i=0}^{m-1} \sum_{j=0}^{n-1} (A_{i,j} - \bar{A}) \cdot (B_{i,j} - \bar{B}) \right] \quad (1)$$

with A and B being the image matrices, σ_A and σ_B the mean square deviations, m and n the dimensions of the matrix.

The CF approaching unity already with $N = 4$ (number of pulses in the packet) shows that sufficiently identical images can be obtained with 5 and more X-ray pulses in a packet.

To visualize images, we used a simple recording system, which, yielded encouraging results: a ZnS and CdS luminophor and a CCD-camera. The spurious current of the CCD-camera used has a value of $1e^-$ per 5 s, whereas the charge of each cell on full exposure may be as high as $80000e^-$. This broad dynamic range of the signal means that the noise introduced by the CCD-camera is negligibly small compared with the quantum fluctuations in the image, thus ensuring a large signal-to-noise ratio.

To reduce intrinsic noise, the CCD matrix was cooled to a temperature of -10 to -20°C . The low noise level enabled us to use at the CCD output a 16-bit ADC giving 65536 (2^{16}) shades of gray in the digital image produced. In medical practice, however, one should seek a certain compromise between sufficient contrast and the least exposure dose. So, when examining real objects, the dose was so chosen that the number of shades of gray did not exceed 20000. But this magnitude is considerably higher than can be imaged by a computer monitor (< 256) and a printer (< 256), a circumstance which, in combination with the high spatial resolution of the CCD-camera (1536×1024), allows us, by use of digital filtration and frequency-space analysis methods, to vary the parameters and detect test object details that are invisible at first sight.

In the radiography of moving objects, the recipient of the image is a high sensitivity TV camera. An image is formed by exposing the object to a packet of 5 to 10 X-radiation pulses per frame. Pulse packets are generated in step with the frame sync pulse. The number of pulses in a packet is chosen from that condition for the CCD matrix in operate in a linear mode. Computer processing of signals permits changing over to the radiographic mode without interrupting the X-raying mode. However, the need to restrict the patient's exposure dose not permit a sufficiently good image to be obtained because the active detection time for each TV frame does not exceed 18 ms and the image is largely affected by random fluctuations and the noise due to radioelectronic equipment. To attain the requisite image contrast, the pixels of the resulting image are found as the mean values of pixels of several frames. The contrast of the image thus produced enhances by an order of magnitude.

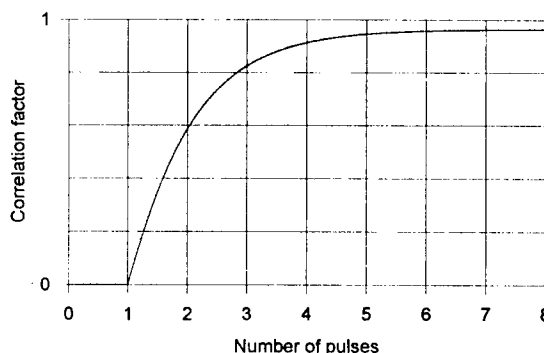


Fig. 1 Correlation factor versus the number of pulses.



Fig. 2 X-ray Image of hand produced by exposure to a continuous source.



Fig. 3 X-ray Image of hand produced by exposure to a pulsed source.

Clinical tests of a nanosecond pulsed X-ray apparatus with a digital visualization system have shown that images obtained from a pulsed source are highly competitive with X-ray pictures from a continuous rotary-anode source. In Figs. 2 and 3 we present X-ray images of a hand, produced by exposure to a continuous and a pulsed source, respectively. In Fig. 4 is given an X-ray picture of a human head.



Fig. 4 X-ray Image of human head.

Another applications

Important applications of nanosecond X-ray apparatus include nondestructive testing of machine components and assemblies. For flaw detection purposes, a compact (0.03 m^3 and 42 kg) all-solid-state instrument has been devised which forms X-radiation pulses with a duration of 20 to 30 ns, has a photon energy of up to 300 keV, and produces a dose of 0.8 Rad per pulse at a distance of 10 cm from the tube output window. Using a digital recording system as well as realizing a packet photography mode with a subsequent time averaging of frames has permitted even millimeter-sized defects to be detected in massive steel parts up to 25 mm thick (Fig. 5).

Generating X-radiation pulses with a frequency of up to 2 kHz and computer processing of the images produced largely shortens the analysis time and make this apparatus indispensable in monitoring items in a continuous process cycle. The X-ray source in hand costs an order of magnitude lower than the conventional apparatus, while the maximum power consumed does not exceed 2.5 kW. The low-voltage power supply of the entire instrument ($U_s = 3 \times 380 \text{ V}$) and its small dimensions permit it to be used in nonstationary conditions, for example for testing welded-joints of pipelines. In Fig. 6 we give an X-ray picture of a welded-joint section, showing the capabilities of the technique applied.

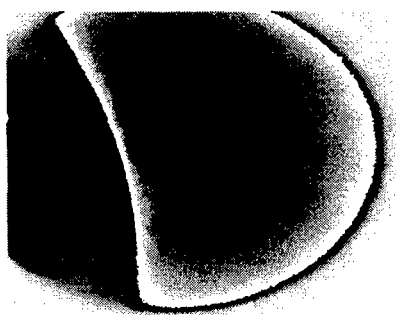


Fig. 5 X-ray Image of a massive steel part.

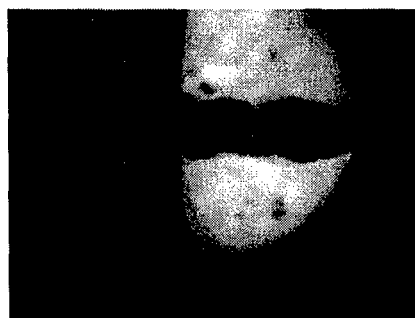


Fig. 6 X-ray Image of a welded-joint section.

Conclusion

A new converter luminophor exposure method is proposed which consists of using short-time packets of high-power X-radiation pulses and subsequently recording the resulting image with the aid of a CCD matrix. Pulse packet duration and the temporal link of the pulse packet to the operation of the recording system are realized from the condition that the dose load on the object and operator be minimal.

A laboratory-scale prototype of a diagnostic apparatus with a digital image visualization system has been developed. The apparatus is small in size, weighs little, has low power consumption, and permits obtaining high image quality at a low dose load.

Reference

1. Yu. A. Kotov, G. A. Mesyats, S. R. Korzhenevskii, et al. Compact repetitive electron-beam and X-radiation generator. Part 1: a desktop generator. //Proc. of 10-th IEEE Pulsed Power Conference., pp. 1231-1234.
2. Yu. A. Kotov, G. A. Mesyats, S. R. Korzhenevskii, et al. Compact repetitive electron-beam and X-radiation generator. Part 2: a hand-carried X-ray apparatus. //Proc. of 10-th IEEE Pulsed Power Conference, 1995, pp. 1235-1238.
3. A. L. Filatov, S. R. Korzhenevskii, Yu. A. Kotov et al. Compact repetitive generators for medical X-ray diagnostics. //Proc. of 11-th Int. Conf. On High Power Particle Beams, Prague, Czech Republic, 1996, pp. 909-912.

DIAGNOSTICS OF PULSED PLASMA-ION BEAMS FROM DIFFERENT COAXIAL INJECTORS*

E. Skladnik-Sadowska, J. Baranowski, M. Sadowski, J. Stanislawski, and J. Zebrowski

The Andrzej Soltan Institute for Nuclear Studies (IPJ)

05-400 Otwock-Swierk by Warsaw., Poland

Abstract: The paper presents various diagnostic techniques developed and applied at the IPJ for studies of pulsed ion beams emitted from high current plasma discharges carried out within various experimental facilities equipped with coaxial electrodes of different structure, and operated in various modes.

1. INTRODUCTION

Plasma-ion streams generated by coaxial injectors have been studied at the IPJ for many years. Energy spectra of ions and time-integrated ion pinhole pictures have been obtained from discharges performed within coaxial multi-rod electrode systems of the RPI (Rod Plasma Injector) type [1-2]. Such systems are now called the IONOTRON type facilities.

Time-integrated and time-resolved measurements of pulsed ion beams have also been performed by means of an ion pinhole camera within coaxial injectors of the (Plasma Focus) type [3]. Recently, time-resolved measurements of ion pulses and energy spectra have been carried out within a Hall-type injector ISEX [4-5], which was designed especially for active experiments in outer layers of the ionosphere.

The main aim of this paper has been to present the most important characteristics of ion beams from several plasma facilities mentioned above, and to compare diagnostics capabilities of the measuring techniques applied.

2. TIME-INTEGRATED STUDIES OF ION BEAMS FROM RPI FACILITIES

Experimental investigations of ion species emitted from the RPI facilities were carried out at different energy levels. Starting from small-scale devices of nominal energy equal to several kJ (RPI-5), through medium-scale machines (RPI-15) of energy equal to 15 kJ, up to relatively large facilities (SOWA, MAJA and IBIS) operated at the energy level of about 60 kJ. The initial charging voltage was varied from 30 kV to 40 kV [1-2]. All those plasma devices were run under dynamic initial gas conditions, i.e., with the use of fast operating gas valve, which was operated before the triggering of the main discharge.

In order to study mass- and energy-spectra of primary and impurity ions there was applied a Thomson-type spectrometer [6] equipped with spectral plates of the UV-2

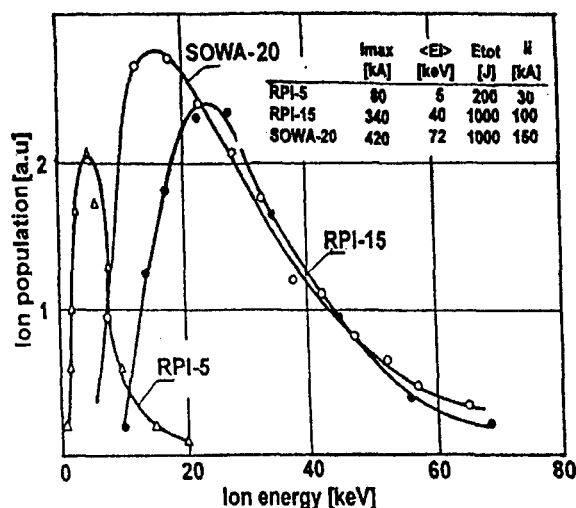


Fig.1. Energy spectra of deuterons, from three RPI accelerators of different energy, operated under optimized gas conditions

type or nuclear track detectors of the CN- and CR-types. An entrance system of that ion spectrometer enabled the analysis of ions within a wide energy range to be performed. There were measured ions of energy from several eV (after an additional acceleration up to 20 keV) until fast ions of energy above 100 keV.

It was found that ion yield of the RPI-type plasma accelerators depends strongly upon initial gas conditions within the electrode region. Some examples of energy spectra of deuterons, emitted from RPI devices of different scale, have been presented in Fig.1. One can easily observe differences in the average energy values of deuterons generated by the RPI-5, RPI-15, and SOWA-20 facilities. Although the configuration and dimensions of the multi-rod coaxial electrodes as well as the initial gas conditions within those devices were very similar, the values of the energy stored and supplied by the condenser banks were different, inducing evident differences in the discharge current values.

Detailed studies included also measurements of the ion energy distribution at different angles. In enabled the total energy of the emitted ions to be estimated. That value amounted about 1 kJ for the RPI-15 and SOWA-20 facilities. Since a duration time of an ion pulse was roughly known (ca. 200 ns), it was estimated that the ion beam current from the RPI-15 injector reached the value of ca. 100 kA, i.e. about 30% of the main discharge current.

In order to obtain time-integrated but space-resolved information about the ion beams generated by the RPI facilities, the use was made of various ion pinhole cameras equipment with solid-state nuclear track detectors. To investigate a spatial structure of plasma-ion streams emitted at different angles there were performed stereoscopic observations with several ion pinhole cameras. On the basis of those measurements it was possible to determine the location and approximate dimensions of sources emitting the investigated ions. It was observed that in the system of the coaxial multi-rod electrodes, operated in a so-called slow mode (high-pressure regime), the emitted ion beams are focussed within a cylindrical region of about 40 mm in diameter, as show in Fig.2. Within a so-called fast mode (low-pressure regime) there is generated almost uniform spatial distribution of ion beams, what can be profitable during the application of such beams for the ion implantation.

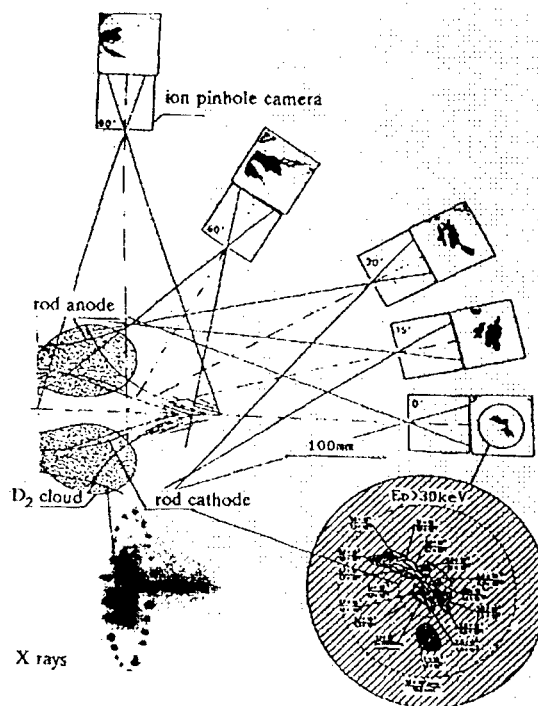


Fig.2. Ion beam pictures taken with five pinhole cameras of different angles within the MAJA facility, an X-ray pinhole image obtained side on, and an ion beam density map taken along the z-axis. Experimental conditions: $U_0=40$ kV, $\tau=200$ μ s (slow-mode)

3. TIME-RESOLVED STUDIES OF FAST ION BEAMS FROM PF-DEVICES

In order to perform time-resolved studies the ion pinhole cameras and the Thomson – type spectrometer, mentioned above, were equipped with miniature scintillation detectors coupled (through optical cables) with fast photomultipliers and a multi-channel digital analyzer. Within the PF-20 facility, operated with the D₂ filling, there were measured fast

deuteron beams emitted along the z-axis [3]. For that purpose the use was made of a 70 cm long pinhole camera, with an entrance diaphragm placed at a distance of 15cm from the inner electrode outlet.

Time-integrated ion pinhole pictures were registered with a CN-type film covered with a 1.5- μm thick Al-foil filter, which eliminated deuterons of energy below 220 keV. Time-resolved ion signals were obtained from two small scintillators fixed in different places (at the center and at the border) of the ion pinhole image. An example of the deuteron beam pinhole picture and time-resolved deuteron signals, as obtained from two PF shots at $p_0 = 2.6$ mbar D_2 , $U_0 = 34$ kV, and $W_0 = 12$ kJ, has been presented in Fig.3. The oscillograms revealed distinct neutron- and deuteron-induced pulses, while the influence of instantaneous X-ray was negligible. The identification of X-ray, neutron, and deuteron pulses was based on the time-of-flight method. Taking into consideration that 2.5-MeV fusion produced neutrons need about 40 ns to reach scintillation detectors (placed at the distance of 85 cm), and assuming that the fast deuterons were emitted at the very beginning of the neutron emission, it was estimated that the successive ion pulses registered on the z-axis, correspond to 350 keV, 150 keV, and 90 keV deuterons, while those registered at the ion image border ($r=20$ mm) correspond to 420 keV, 110 keV, and 60 keV, respectively.

To study time temporal structure of the ion beam emission more detailed measurements are needed by means of several different technique. Recently, some ion time-resolved measurements have also been performed with Faraday-type collectors adopted especially for the studies of pulsed ion beam within intense plasma streams [7].

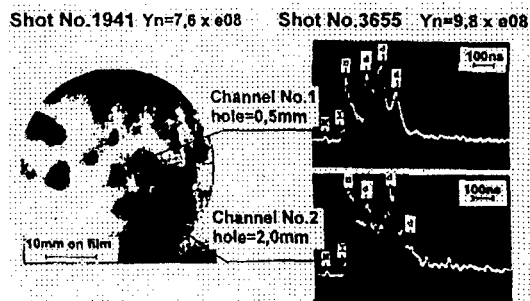


Fig.3. Time-integrated ion pinhole picture an time resolved ion signals from the PF-20 device [3] for two different discharges. M markers, X-rays, n-neutrons, d-deuteron-pulses

4. TIME-RESOLVED MEASUREMENTS OF LOW-ENERGY HEAVY IONS

In order to generate pulses of low-energy Xe-ions for space experiments, to be performed on the board of a satellite in the ionosphere, there was designed and constructed a Hall-type special plasma injector, called the ISEX device [4]. That injector made possible the production of pulsed streams of Xe-ions with an average energy of about 400 eV, and the total intensity up to about 1 A. The duration time of those pulses could be varied from 0.1 s to about 1.0 s, and the electric charge compensation at the injector outlet could be provided by an external electron-emitter.

To determine basic characteristics of the Xe-ion pulses emitted from the ISEX device the use was made of a large (ca. 7 m³) vacuum chamber and a system of several ion collectors of the Faraday type [5]. In order to measure a spatial profile of the produced ion beams there were applied the Faraday-type collectors located at different angles to the z-axis, but in the same measuring plane at a relatively large distance (165 cm) from the ISEX outlet. It was estimated that the divergence of the Xe-ion beams amounts to about 20 degrees.

The most important emission characteristics were the Xe-ion energy distributions, which were measured by means of the Faraday collectors equipped with additional grids polarized appropriately to enable an ion energy analysis to be performed. An electron component was also eliminated by means of a magnetic field produced by miniature permanent magnets. Detailed ion energy measurements were performed at a distance of 165 cm from the injector outlet on the z-axis ($R=0$) and at chosen radial distances R . Such measurements were carried

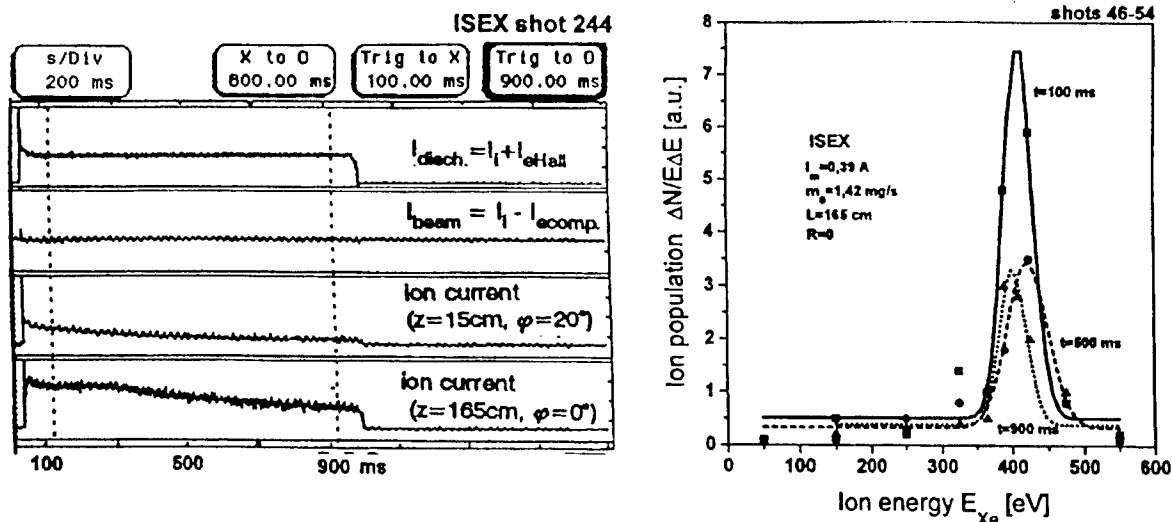


Fig.4. Typical waveforms of discharge current and ion currents as measured at different distance from the ISEX outlet (on the left). Ion energy spectra of Xe-ion emitted for different instants of discharge (on the right).

out at various instants counting time from the discharge beginning. Some examples of oscillograms presenting the discharge current (I_{disch}), compensated beam intensity (I_{beam}), and the ion component intensity (I_i), have been shown in Fig.4. The ion energy distributions, as measured for different instants ($t= 100$ ms, 500 ms, and 800 ms) under optimized experimental conditions, have been presented in Fig.4 too. One can easily see that the Xe-ion energy spectra have distinct maximum near 400 eV. A quantitative analysis of the data obtained has proved that the required values of the main parameters have been achieved.

5. CONCLUSIONS

On the basis of the examples presented in this paper one can formulate the following conclusions:

- Several methods of ion diagnostics have been mastered and applied for studies of pulsed plasma-ion beams generated by various plasma injectors (RPI, PF, and ISEX devices);
- The developed measuring techniques, i.e. the ion pinhole cameras, Thomson-type ion spectrometers, Faraday-type ion collectors, must be carefully adapted to experimental conditions in order credible data to be obtained.

REFERENCES

- [1] E.Skladnik-Sadowska, J.Baranowski, M.Gryzinski, J.Langner, M.Sadowski; J.Physique **43** (1982) 715.
- [2] E.Skladnik-Sadowska, J.Baranowski, J.Hoszowska, Z.Puchalski, M.Sadowski; Proc. XXth ICPIG (Pisa. 1991), p.843.
- [3] M.Sadowski, J.Zebrowski, E.Rydygier, H.Herold, U.Jager, H.Schmidt; Phys. Lett. **113A** (1985) 25.
- [4] J.Langner, M.Sadowski, E.Skladnik-Sadowska, J.Stanislawski, J.Baranowski, K.Czaus, Z.Klos, Z.Zbyszynski; Proc. ; 2nd Nat. Symp. PLASMA'95 (Warsaw 1995), Vol. 2. Invited Papers, p.169.
- [5] J.Baranowski, M.Sadowski, E.Skladnik-Sadowska; Mat. 1er Seminaire Franco-Polonais sur les Plasmas Thermiques dans l'Espace et en Laboratoire (Varsovie 1997), Paper 4A .
- [6] J.Baranowski, E.Skladnik-Sadowska; Int. Report IPJ No.1683 (Warszawa 1977).
- [7] H.Kelly, A.Lepone, A.Marqueze, M.Sadowski, J.Baranowski, E.Skladnik-Sadowska; IEEE Trans. Plasma Sci. **26** (1998) 113.

* This work was partially supported by the European Commission contract No IC15-CT97-0705.

DIAGNOSTIC METHODS OF MEASURING MEGAVOLT VOLTAGES AND MEGAAMPER CURRENTS.

A.S. Boriskin, M.I. Dolotenko, A.S. Kravchenko, V.G. Kornilov, I.M. Markevtsev,
A.N. Moisyenko, V.D. Selemir, O.M. Tatsenko, V.I. Chelpanov

VNIIEF, Mira 37, Sarov, 607190, Russia

INTRODUCTION

The development of high power and high energy density electrophysical installations requires use of contactless methods of recording their parameters. The optical methods of the data transfer allow to avoid the galvanic connection between the recording equipment and the measuring object. The use of fiber optics allows to place the recording equipment far from the object of measurements. This helps to avoid electromagnetic interference and other noises that usually occur in operating time of the high-power machines.

The principle of activity of magneto-optic and electro-optic sensors is based on Faraday and Pockels effects. Since the effects are practically inertialess the time resolution of these sensors is determined mainly by the time the light passes through the Faraday or Pockels cell and by the recording equipment bandwidth. In such devices there are no electrical contours. Therefore connection of the measuring scheme does not influence noticeably on operation of the researched installation. Such sensors can be used both in laboratory and on testing area [1].

Faraday and Pockels effects are based on induced birefringence phenomenon appearing in transparent media affected by external magnetic or electric fields. The angle of rotation of the polarization plane depend linearly on magnitude of field ($\varphi_{m.o} \sim H$, $\varphi_{e.o} \sim E$). That means optical schemes for measuring magnetic and electric fields are identical. A parallel light beam from a monochromatic light source is directed to the magneto-optic or electro-optic sensor. The sensor consists of Faraday and Pockel cells, polarizer, analyzer and adjusting units. This light radiation with modulated intensity goes along the optical path to the photoreceiver, the signal from which is recorded by the proper device.

All mentioned magneto- and electro-optical devices are one and the same sensor to measure intensity changes of light passing through magneto- or electro-optical probes. When the phase shift is equal to $\varphi = 90^\circ$, the light intensity becomes equal to zero. That has happened at a certain half-wave or master value $H_{\lambda/2}$, $E_{\lambda/2}$, $J_{\lambda/2}$, $U_{\lambda/2}$. Let us designate $A = H$, E , J or U and $A_{\lambda/2} = H_{\lambda/2}$, $E_{\lambda/2}$, $J_{\lambda/2}$, $U_{\lambda/2}$ then in general it is possible to write:

$$A = A_{\lambda/2} \left\{ 2n - \text{sign} \frac{dI}{dt} \frac{2}{\pi} \arccos \left(\sqrt{\frac{I}{I_0}} \right) \right\}$$

where $n = 0, 1, 2, \dots$ is number of "min" light intensity, $\text{sign} \frac{dI}{dt}$ is a sign of light intensity derivative, I_0 is "max" light intensity.

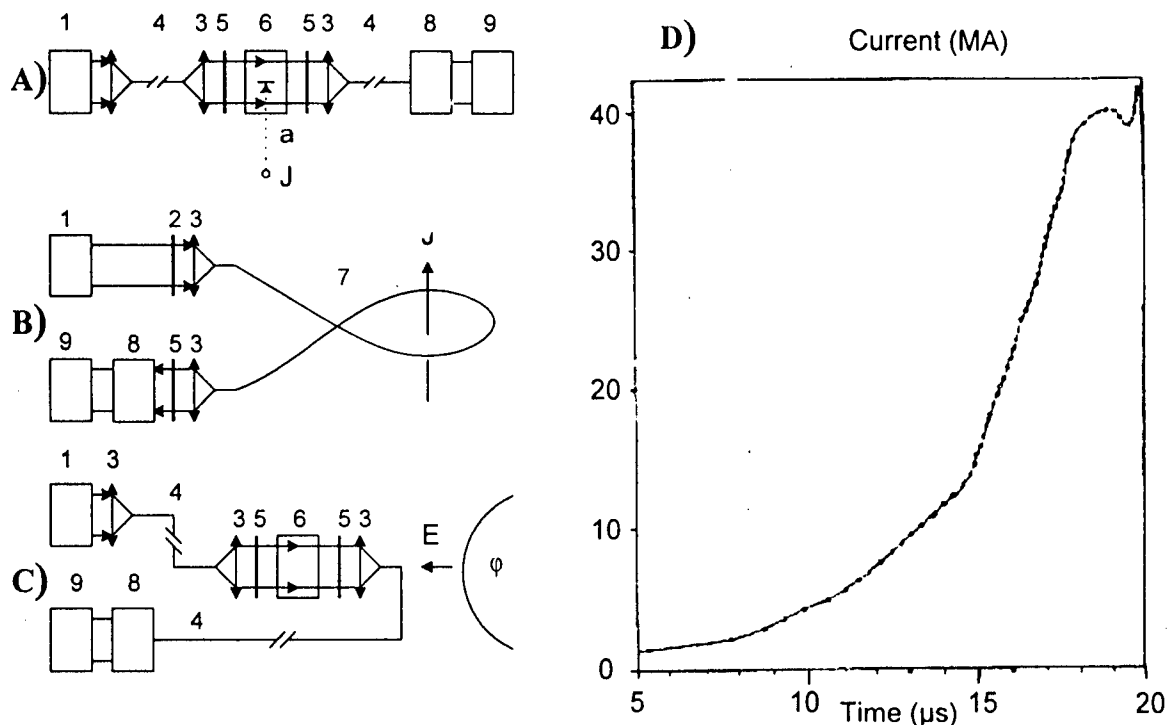


Fig. 1 (A,B,C). Experimental schemes of electrooptic and magneto-optic methods of pulsed electric and magnetic fields, high voltages and currents measurement.

1 — He-Ne Laser, 2 — Half-wave plates, 3 — Lenses, 4 — Multi mode fiber, 5 — Polarized film, 6 — Faraday or Pockels cells, 7 — Single mode fiber, 8 — Detector, 9 — Oscilloscope.

(D) Measured current for a 40 MA in the disk explosive magnetic generator experiment.

If $\varphi > 90^\circ$ ($n > 0$), then determination of φ_{max} is very important, since function $I = I(\varphi)$ becomes many-valued. The value φ_{max} corresponds to the inflection point $dA/dt = 0$ and determines the maximum value of the magnetic and electric field intensities, the current and the high voltage.

MAGNETOOPTIC DEVICE FOR MAGNETIC FIELD AND ELECTRIC CURRENT MEASUREMENT

Faraday effect determines the angle of rotation of the polarization plane Φ_F by the following ratio $\Phi_F = V H l \cos \gamma$, where V is Verdet constant, H is magnetic field intensity, l is the length of the light path in a Faraday cell, γ is the angle between the direction of the applied field and the direction of light propagation.

The optical scheme of the magneto-optical device for measuring magnetic intensity is presented in Fig. 1(A). We used cylinders made of glass TF-5 ($V = 0.0526 \text{ ' cm}^{-1} \text{ Oe}^{-1}$) or MOS-31 ($V = 0.20 \text{ ' cm}^{-1} \text{ Oe}^{-1}$), $\lambda = 0.633 \text{ } \mu\text{m}$ as Faraday cells. The multi mode fibers 4 are made of quartz (OK-50 type) in all devices. The polarizer and the analyzer are made of polarized film. The probe casing is made of ebonite. For this probe master value $H_{\lambda/2}$ is equal: $H_{\lambda/2} = 5400 V^{-1} l^{-1} (\text{Oe})$, where l is in cm, V is in $\text{' cm}^{-1} \text{ Oe}^{-1}$. Such magneto-optic device allows one to measure the magnetic fields $H \sim 10^3\text{-}10^7 \text{ Oe}$.

The location of the magneto-optic probe is shown in Fig.1 (A). Here a is the distance between the current conductor and the Faraday cell. Faraday cell is a cylinder with the

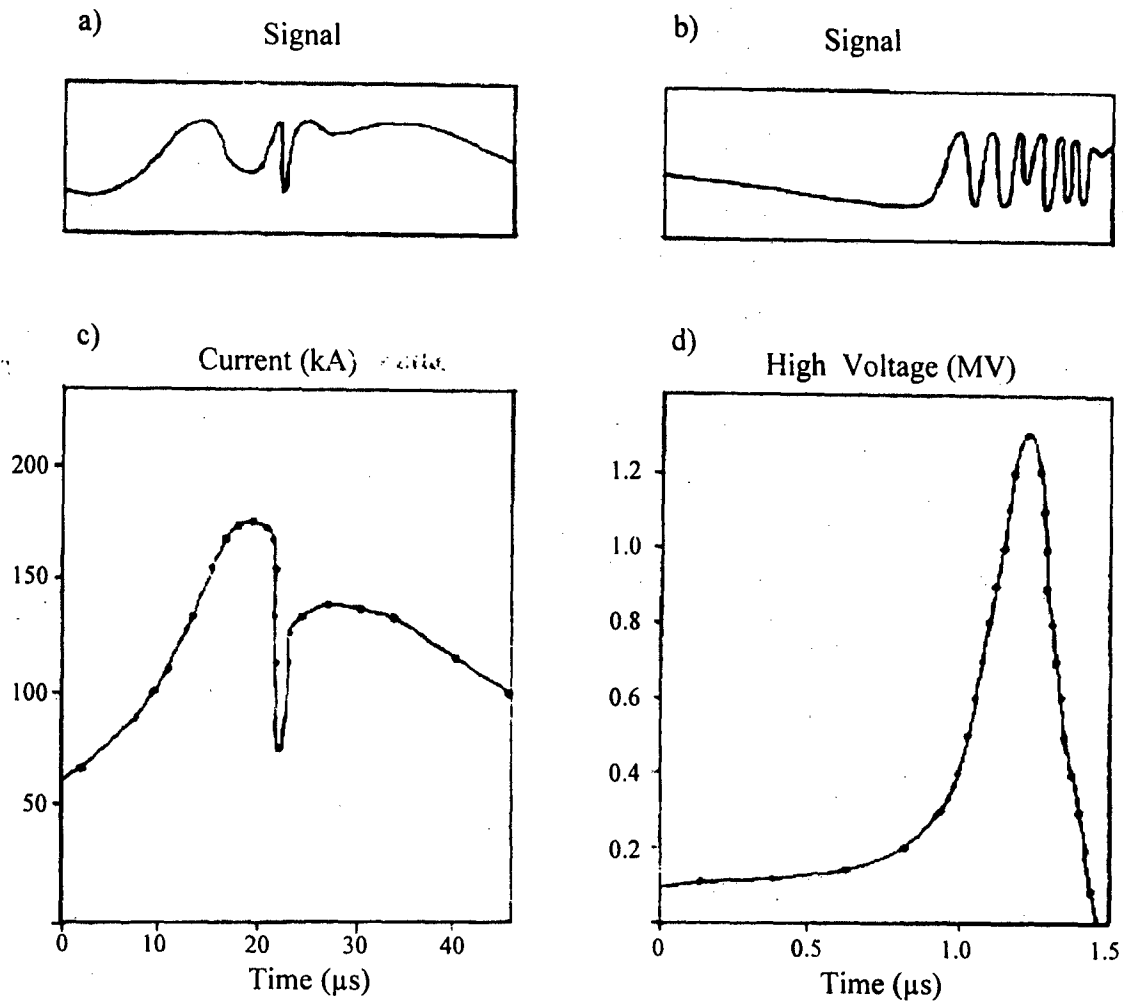


Fig. 2. Signal waveforms (a,b), measured current (c) and measured high voltage (d) for inductive storage experiment.

length l . Thus $d\Phi_F = VHdx \cos \gamma$. In the case of the symmetric location of probe the integration along the beam path gives:

$$\Phi_F = V \cdot J \cdot \pi^{-1} \arctg(0.5l \cdot a^{-1}).$$

If $L_1 = 20a$ is the length of the straight portion of the current conductor then it is easy to show that the magnetic field intensity created by this current conductor across the probe differs from the magnetic field created by the straight infinity current conductor less than by 0.5%. Fig. 2(a) shows the change of light intensity passing through the magnetooptic probe. The current of the inductive storage with the explosive wire is given in the Fig. 2(c). This curve is characterized by three inflection points $dI/dt=0$.

SINGLE MODE FIBER DEVICE FOR CURRENT MEASUREMENT

To measure high current pulses $J \sim 10^5 - 10^8$ A single mode quartz fibers are very convenient. Faraday effect in a glass fiber appears due to the difference in the beam refraction indices with the opposed circular polarization.

If a linearly polarized beam goes along the single-mode fiber over the closed trajectory, then the magnetic field will rotate the polarization plane by angle θ .

The angle θ does not depend on the shape and the length of light trajectory and current pulse distribution in it. The main condition is that the trajectory must be closed [2]. In pure silica fiber the angle of rotation of the polarization plane per current unit is equal $261^\circ/\text{MA}$ at the wavelength $\lambda = 0.633 \mu\text{m}$. The optical scheme of this facility is given in Fig. 1(B). Since the current of 1 MA provides the polarization plane rotation by 261° , master value $J_{\lambda/2}$ is equal: $J_{\lambda/2} \cong 0.345 \text{ MA}$. Fig. 1(L) shows the result of the current measurement in the disk explosive magnetic generator. The fiber length encircling the current contour is equal 120 cm. The measurement had been performed until the fiber was destroyed.

ELECTROOPTIC DEVICE FOR ELECTRIC FIELD MEASUREMENT

A linear electrooptic effect in segnetoelectric crystals is known as Pockels effect. It results from birefringence in a crystal under an electric field. Let be d and l are transversal and longitudinal crystal dimensions respectively. Taking into account the effect of external electric field attenuation deduced from the theory of static electric and magnetic fields we shall get following value of electric field attenuation: from ~ 8 times ($d/l = a = 1$) to ~ 1.4 times ($a = 10$) for the longitudinal electrooptic effect (crystals of KDP) [3].

Linearly polarized laser beam ($\lambda = 0.633 \mu\text{m}$) is focused by the lens into the fiber core. The light is collimated by the lens into a parallel beam after the fiber. Further the light passes through the polarizer, the Pockels cell and comes into a dielectric mirror, then it reflects from mirror and passes back to the photoreceiver, signal from which is recorded by the oscilloscope. A crystal KDP $9 \times 9 \times 20 \text{ mm}$ was used as the Pockels cell. The external field attenuation was equal 4.2 times, thus the master value $E_{\lambda/2}$ is equal: $E_{\lambda/2} = 8.8 \text{ kV/cm}$. The electric field magnitude measured in the electron accelerator was equal: $E = 25 \text{ kV/cm}$.

ELECTROOPTIC DEVICE FOR HIGH VOLTAGE MEASUREMENT

Fig. 1(C) shows the optic scheme for high voltage measurements. It is based on the method of determination of the remote conductive sphere potential using the electrooptic probe.

The remote sphere potential U is equal: $U = Er^2 / R$, where r is the distance from the sphere center up to the middle of the probe, R is the sphere radius, E is the electric field in the point of probe location. The master value $U_{\lambda/2}$ is equal: $U_{\lambda/2} = E_{\lambda/2} r^2 / R$. We used the KDP crystal $15 \times 15 \times 90 \text{ mm}$ as the Pockels cell. Its master value $E_{\lambda/2}$ is equal: $E_{\lambda/2} = 1.76 \text{ kV/cm}$. Fig. 2(b,d) gives the high voltage appearing in the inductive storage with the explosive wire.

REFERENCES

- [1.] H.M. Hertz, P. Thomsen Rev. Sci. Instrum. 58 (1987), No.9, 1660-1664.
- [2.] Lynn R., George I., Gordon W. Los Alamos National Laboratory. Fiber optic sensing of pulsed currents, report under contract W-7405-ENG-36 1986.
- [3.] Osborn J.A. Phys.Rev., 67, (1945), 351.

SPECTROSCOPY OF COMPOSITE Z-PINCH ON ANGARA-5 -1 INSTALLATION

A.S.Chuvatin², S.A.Danko¹, B.Etlicher², M.V.Fedulov¹,
V.O.Michensky¹, G.S.Volkov¹, V.I.Zaitsev¹, P.Zehnter³

¹*Troitsk Institute for Innovation and Fusion Research
TRINITI, Troitsk, 142092, Moscow reg., Russia*

²*Laboratoire de Physique des Milieux Ionisés, Laboratoire du CNRS,
Ecole Polytechnique-91128, Palaiseau, France*

³*CEA, BP2, 91680, Bruyeres-le-Chatel, France*

Abstract

The results of spectroscopy measurements of a composite Z-pinch on ANGARA-5-1 installation are presented. The composite Z-pinch was created with the help of a hollow argon or methane gas jet which collapsed onto a solid foam cylinder doped with salts of KCl or NaCl. Dependence of the line radiation intensities and plasma parameters on linear mass of the gas jet ($3\div 60\text{mkg/cm}$) was investigated.

Introduction

Firstly, composite Z-pinch was proposed as an alternative to traditional Z-pinches in [1,2] for achieving of a more stable and homogeneous plasma object. In this series experiments the Z-pinch was created by combination of thin wires (fibers) (Al, Cu, W, SiO₂) and a coaxial plasma jet. More stable and homogeneous plasma in the Z-pinch and an enhancement of the output soft X-ray radiation were achieved in this experiments at the current level in the load up to 250 kA with the front rise time of ≈ 50 ns. Higher efficiency of the energy transfer from the outer gas shell to the fiber was demonstrated in experiments on composite Z-pinches on GIT-4 generator at the current level in the load up to 1.5 MA with the front rise time of ≈ 150 ns [3, 4]. In [9] it was supposed that instabilities of the shell may account for efficient current delivery to the fiber corona.

One of the first series of experiments on the composite Z-pinches with the current level in the load of $\sim 2\div 3$ MA were carried out on Angara-5-1 installation in the joint international project JEX'92 [5,6]. In this experiments the composite Z-pinch was created by imploding gas shells (Ar, Xe, D₂) on thin ($10\div 60\text{ }\mu\text{m}$) coaxial wires (Al, Cu, W, CD₂).

In the present paper the results of the spectroscopy measurements in the next series of experiments on ANGARA-5-1 installation are presented, where composite Z-pinch was created with the help of an Ar or methane gas jet collapsed onto a solid foam cylinder with low initial density. Solid foam cylinder with the diameter of 1mm was produced of agar-agar doped by salts of KCl or NaCl. The dependence of the radiation intensities of the lines of K, Cl, Ar and of the plasma parameters (n_e , T_e) on the initial linear mass of the gas jet ($3\div 60\text{ mkg/cm}$) was investigated.

Experimental setup

In the described experiments, the "Angara-5-1" generator [7] delivered about 2-2.5 MA current into the Z-pinch load. The current derivative was measured by the circular multi-loop probe, mounted on the anode at the radius of 100 mm. Hollow gas jet was produced by

an electromagnetic valve with a supersonic nozzle having the mean output diameter of 32 mm. The load was mounted inside the diode cathode-anode gap of 1 cm. The total linear mass of agar-agar cylinder was varying from 55 to 80 mkg/cm with the salt content between 30 and 57% of the total weight.

The characteristics of the composite Z-pinch plasma were registered by means of the set of physical diagnostics, including: the multichannel device polychromator, which uses multi-layer X-ray mirrors as dispersion elements and a silicon semiconductor detectors with time resolution of 1.5 ns; the time integrated wide range X-ray spectrograph with a slit, giving space resolution along pinch axis; the time-integrated crystal spectrograph with the registration on CCD detector and rather high spectral resolution $E/\Delta E \cong 1000$ [8]. The diagnostics layout of the experiments is shown in Fig. 1.

Experimental results and discussions

As the spectroscopic measurements show, the collapse process of the gas jet onto the fiber is accompanied by an intense line radiation. This emission is related to the H-, and He-like ions of argon, potassium and chlorine. The integral output of line radiation of these elements is listed in the table.

	K	Cl	Ar
$Q_R^{\text{He}}; J$	3-15	6-20	54-65
$Q_I^{\text{He}}; J$	2,5-11	3-12	46-48
$Q_R^{\text{H}}; J$	0.7-1.5	1-2.5	6-15
$Q_R^{\text{He}}/Q_I^{\text{He}}$	1.2-2.7	1,4-2,7	1,3-1,6

Here : Q_R^{He} is the output radiation in the resonance line of He-like ion; Q_I^{He} - output radiation in the intercombination line of He-like ion; Q_R^{H} - output radiation in the resonance line of H-like ion; $Q_R^{\text{He}}/Q_I^{\text{He}}$ is the ratio of intensities of the resonance line to the intercombination line of the He-like ion.

Fig. 2 and Fig. 3 present the typical lines emission spectra obtained by means of the spectrograph with registration on CCD. Fig. 4 shows the typical oscillogram of the signal, measured for X-ray quanta with the energy of ≈ 525 eV.

The spectroscopy with space resolution shows, that the line emission locations are the same as well for both Ar lines, and K and Cl lines. The line radiation comes approximately from the central part of the load anode-cathode gap (one half of the pinch length, ≈ 5 mm for Ar ions and $\approx 3\div 4$ mm for the ions of K and Cl). Using the experimental intensities integrated in time for the resonance transitions of He- and H-like ions, and those for $1s2p(^3P_1)-1s^2(^1S_0)$ intercombination transition, the electron temperature, T_e , and the electron density, n_e , were calculated. The processing of the results was performed being based on a stationary collisional- radiative model with account of radiation absorption. The electron temperature T_e was determined, additionally, being based on the ratio of resonance He-like lines of pair of ions K and Cl. At the moment of pinching the following values of the plasma parameters were achieved: the electron temperature $T_e \approx 0.8\text{-}1.3$ keV; the electron densities $n_e \approx (1\div 2) \cdot 10^{21} \text{ cm}^{-3}$. The estimations of the spectral line intensities of K and Cl from the measured integral output and duration of the soft X-ray radiation showed that an appreciable part of the initial total mass of the foam cylinder (10-25%) had the electron temperature of order 1 keV. Such temperature was achieved both in the jet and in the fiber material. Using the fact that only 0.3-

0.5 part of the pinch length had that high temperature sufficient for intensive line radiation, we can conclude that of order of one half of the initial foam material total mass has the electron temperature at the level of 1 keV in this plasma region. This fact indicates rather good energy transfer to the fiber. One of the mechanisms accounting for this good energy transfer can be the electron thermoconductivity. Another possibility can be the direct Ohmic heating [9] of the fiber. Nevertheless, one should point out that it is possible only with significant decrease of the electron conductivity, since the coefficient of the magnetic diffusion is too low with classic electron conductivity at $T_e \sim 1$ keV.

The analysis of the result obtained shows, that the higher temperature values of the fiber correspond to greater linear masses of the gas jet and do not depend on the fact whether argon or propane was used. This can be explained by the fact that the greater jet mass shift the moment of pinching closer to the current maximum. There was not observed any dependence of the fiber electron density on variation of the linear mass of the gas jet.

In those experiments, when the gas nozzle was made from an aluminum alloy, the radiation of the Al H- and He-like lines was detected in the region located in the vicinity of the cathode (Fig. 2). The size of this area was changing from 1 to 3 mm along the pinch axis. The measurement of the electron temperature of the pinch of the order 500 eV near the cathode electrode by using Al lines ratio confirms the existence of high temperature gradients along the pinch.

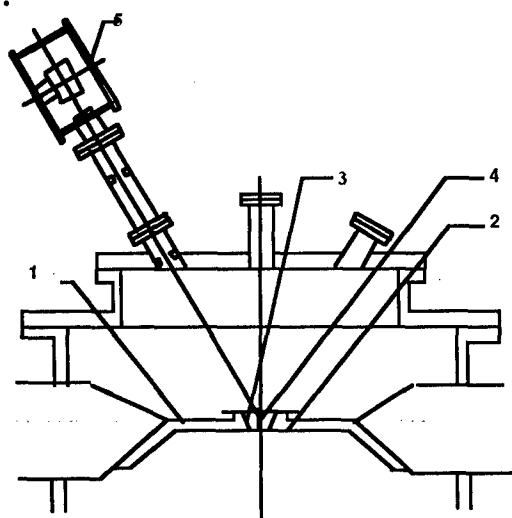


Fig. 1

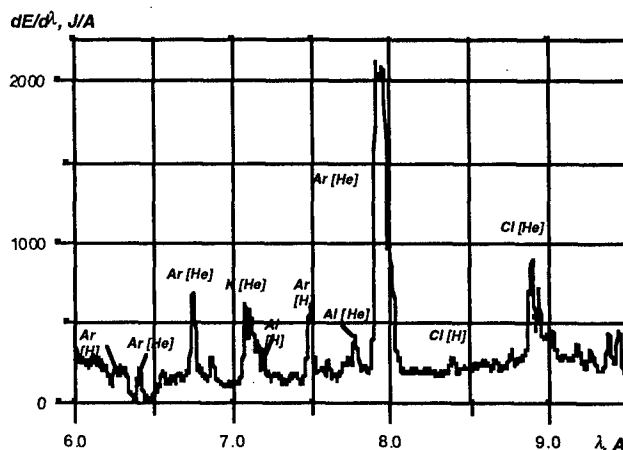


Fig. 2

FIG. 1 Geometry of the disc concentrator with load and layout of spectrograph with registration on CCD. 1-anode of disc concentrator, 2-cathode of the disc concentrator, 3- gas jet, 4-fiber, 5 - spectrograph with CCD registration.

FIG. 2 Spectra of lines radiation of Ar, K and Cl, received in the second order of reflection from the crystal. The shell consisted of a hollow gas jet of Ar ($60 \mu\text{g}/\text{cm}$). The following fiber was used: a cylinder from agar-agar ($55 \mu\text{g}/\text{cm}$) with adding of KCl (30% on weight). The distinctive radiation of the cathode material is seen ([H]- and [He]-like Al, the first order of reflection). The wavelength scale corresponds to the first order of reflection.

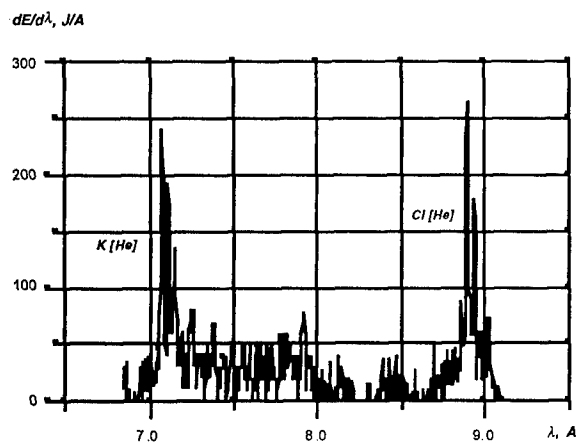


Fig. 3

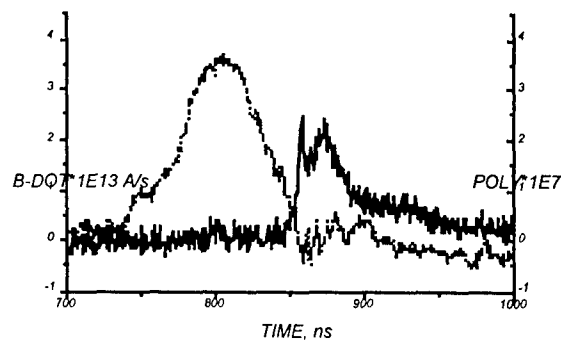


Fig. 4

Fig. 3 Spectra of the K and Cl line radiation in the second order of reflection from the crystal. The shell consisted of a hollow gas jet C_3H_8 ($60 \mu g/cm$). The following fiber was used: a cylinder from agar-agar ($60 \mu g/cm$) with adding of KCl (30% on weight).

Fig. 4 Signal trace of the soft X-ray radiation from polychromator channel with the energy 525 eV (continuous line), synchronized with the signal trace of B-dot (dot line). Shell: hollow gas jet C_3H_8 ($60 \mu g/cm$); fiber: cylinder from agar-agar ($60 \mu g/cm$) with adding of KCl (30% on weight).

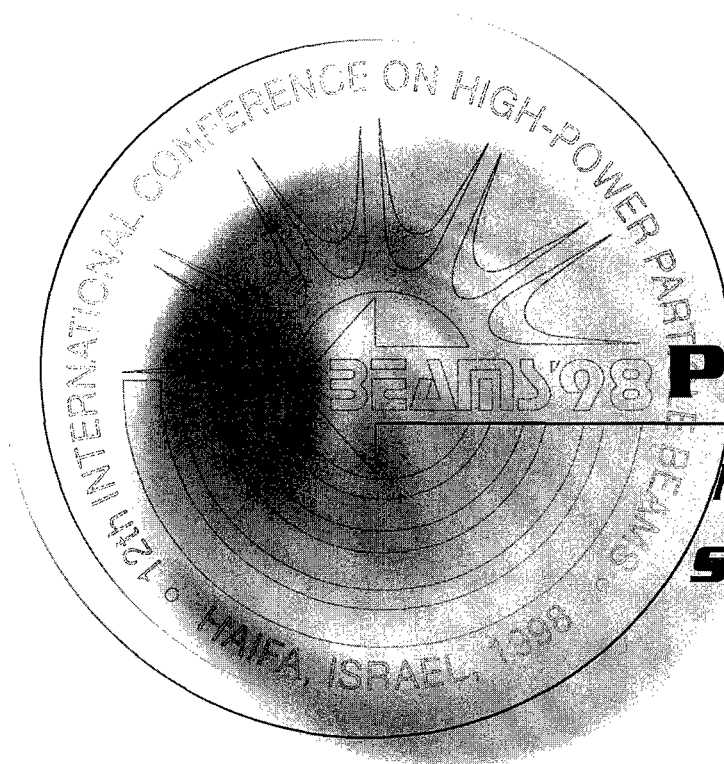
References

- [1] F.J.Wessel, B.Etlicher, P.Choi, "Demonstration of enhanced stability and energy transfer in an aluminum plasma embedded fibre Z-pinch", *Phys. Rev. Lett.*, Feb. 1992.
- [2] B.Etlicher, A.S.Shuvatin, L.Veron, F.J.Wessel, C.Rouille, S.Attelan, P.Choi., Different Stabilization Processes in Z-Pinch Plasma Experimental Approach., Proceedings of the 9th International Conference on High-Power Particle Beams, Washington, DC, v.3, p.2008-2013, 1992.
- [3] B.Etlicher, A.S.Chuvatin, P.Choi, L.Frescaline, L.Aranchuk et al., "Syrinx - a Research Program for the Pulsed Power Radiation Facility", Proceedings of the 11th International Conference on High-Power Particle Beams, Prague, Czech Republic, June 10-14, v.1, p. 276-283, 1996.
- [4] Alexander Chuvatin, Peter Choi, Carmen Dumitrescu, Bernard Etlicher, et al, "Spatial and Temporal Evolution of High-Energy Density Plasmas in the Composite Pinch on GIT-4 Generator", *IEEE Transactions on Plasma Science*, vol.25, N2, p.196-204, april 1997.
- [5] A.N. Batunin, A.V. Branitsky, I.N. Frolov et al. Inhomogeneous Z-pinch investigation on "Angara-5-1" AIP Conference Proceedings 299, Dense Z-Pinches, London, 1993, p. 580 -586
- [6] F.B. Rosmej, O.N. Rosmej, S.A. Komarov, V.O. Mishensky, J.G. Utjgov. Soft X-ray spectra analysis in a high-current Z-pinch. AIP Conference Proceedings 299, Dense Z-Pinches, London, 1993, p. 552-559.
- [7] E.P. Bol'shakov, E.P. Velikhov, V.P. Smirnov et al. Sov. Atomnaya Energiya (Atomic Energy), v.53, p.14, 1982.
- [8] G.S. Volkov, V.I. Zaitsev, S.Attelan-Langlet et al. Soft X-ray Spectrograph with CCD-Based Detector. Instruments and Experimental Techniques, Vol.40, No.1, pp.113-117, 1997.
- [9] A.S.Chuvatin, P.Choi, B.Etlicher, "Formation of a composite pinch", *Phys. Rev. Lett.*, vol. 76, no. 13, pp. 2282-2285, 1996.



BEAMS'98

12th INTERNATIONAL CONFERENCE
ON HIGH-POWER PARTICLE BEAMS



POSTERS

*Models and
Simulations*

Vol. I

Proceedings

STATIONARY PARTICLE-IN-CELL SIMULATIONS ON ELECTRON AND ION DIODES

W. Bauer¹⁾, E. Stein¹⁾, B. Schrepp²⁾, T. Westermann²⁾

1) *Forschungszentrum Karlsruhe GmbH, Postfach 3640, D - 76021 Karlsruhe, Germany*

2) *Fachhochschule, Moltkestraße 4, D - 76133 Karlsruhe, Germany*

ABSTRACT

The stationary Particle-in-Cell - program system „BFCPIC“ [1] has been modified to run on unix workstations. A new mesh generator „InGrid“ producing the boundary fitted grid was incorporated in „AutoCad“ and applied to diode meshing. The mesh generated by InGrid can be exported to both the stationary PIC-code „BFCPIC“ and the time resolving PIC-code „KADI2D“ [2]. For calculating the applied magnetic fields the commercial FEM code „ANSYS“ is used. To test the whole program system simulations on a simple electron diode for KALIF-HELIA [3] have been performed. As a second step the simulation of the present applied-B diode [4] was repeated and identical results compared to the old program system. were found.

I. INTRODUCTION

Our stationary Particle-in Cell -Code „BFCPIC“ based on boundary fitted grids is used since 1988 in two versions: BFCPIC2D is two-dimensional and serves mainly to simulate the self-magnetically insulated B₀-diode [5]. The 2.5-dimensional BFCPIC2H allows for externally applied magnetic fields and is used to model applied-B diodes [4] and recently, as is shown below, for electron diodes. Although these codes are time independent we have gained quite a lot of physical insight from these simulations. First simulations using the new time-dependent PIC-code „KADI2D“ are described in ref. [2]. This code is also based on boundary-fitted grids and some of the features of the stationary codes could be adopted for it. To validate this program tests were made using the same models as for the stationary codes, and a comparison under equal conditions has given equal results [2]. One purpose of the simulations shown below was, to supply material for this comparison. Another was to assist the design of an electron diode for KALIF-HELIA.

Since 1988 great changes in the computer world have taken place, and the codes have been gradually adopted to new computer systems. The main change was the step from large main-frame MVS computers to small UNIX workstations. While in early days the knowledge of FORTRAN and some job control language was sufficient to run the codes, today a great variety of partly commercial codes, partly own developments are in use. This paper describes in its first part the work with this combination of programs and summarizes in its second part some results obtained for several versions of the KALIF-HELIA electron diode.

II. STEPS OF A SIMULATION

The generation of the grid starts from an AutoCAD-drawing of the diode. By copying the lines relevant for the simulation on a new layer the grid boundary is fixed. Using the program „InGrid“ [6] that is incorporated into AutoCAD the grid is constructed interactively. This requires some experience: Although by far not all features of AutoCAD are used for the grid

generation user's mistakes in AutoCAD result in rather strange effects at the generated grid. The final grid is then exported either into the format needed for the PIC-codes or into the ANSYS-format. Both files have to be modified slightly to meet the requirements of the different systems.

ANSYS [7] is used to calculate the magnetic field excited by external coils. These coils are in general situated outside of the PIC-model, so that an ANSYS-model has to be constructed around the PIC-model and combined with it for the calculation of the magnetic field. Two difficulties have arisen in combining the PIC-code with ANSYS:

a) The ANSYS-grid is unstructured, while the PIC-code grid is structured. This is the reason for starting with the grid for the PIC-code and constructing the ANSYS-grid only for the outer regions. The combination of both grids was a difficult programming task.

b) Since in ANSYS the rotation axis has to be perpendicular, while in the PIC-code it is horizontal, the InGrid-grid has to be rotated and mirrored for ANSYS. The ANSYS results then again have to be rotated and mirrored to be used as an input for the PIC-code.

The results of the PIC-code are transformed into a format readable by the postprocessor Techplot [8] by using a program „Visart“ [9]. Finally the results are plotted as is shown in the examples below.

III. ELECTRON DIODES FOR KALIF-HELIA

Our new 6-MV generator KALIF-HELIA [3] will be run first in negative polarity using an electron diode. The program system described above has been checked and practised first on two versions of an electron diode: Figures 1a and 1b show the electrical potential distribution in two preliminary variations and in a final shape 1c that will be used experimentally. Both diodes need a pair of Helmholtz-coils as shown in Fig. 3, situated outside of the area indicated in the figures 1a-1c producing a magnetic field that counteracts the pinching of the electrons down to the axis due to their self-field. Figs. 2a and 2b illustrate the electron current density obtained for different coil currents. Table I. gives a summary of the simulation results obtained so far for several geometrical parameters and different amplitudes of the applied external magnetic field. Fig.3 also shows the lines of constant vector potential A_z computed by ANSYS.

The general behaviour is as expected. A shorter gap gives higher electron current. The numbers, however, differ slightly from results one would obtain using the simple Child-Langmuir-Law, since the rounding at the electrodes and the effect of more or less pinching is not considered in the formula. A higher external field reduces the pinching. A longer part of the transmission line adds more electrons and increases the current. Figs. 4a and 4b show an interesting difference for different electron currents: At low current the transmission line is not well insulated and electrons spread out all over the space between inner and outer conductor, whereas at higher current the magnetic insulation keeps this space free of electrons. In Table I the cases, where the magnetic insulation breaks down are marked. Between $I=327$ kA and $I=335$ kA is a rather sharp transition between poor and good magnetic insulation.

The simulation results on the applied-B diode Fig. 5 are identical to the results obtained with the old program system. Whereas the general picture of electrons emerging from the cathode tip and forming an electron sheath are obtained as expected, the numbers for the ion current are by more than a factor 10 lower than in the experiments. This is due to the fact, that in the 2.5-dimensional code without time dependency the effect of instabilities and movement of the electron sheath cannot be modeled. So the result shown in Fig. 4 is only a confirmation that the transition in the program system from MVS to UNIX is completed without apparent errors.

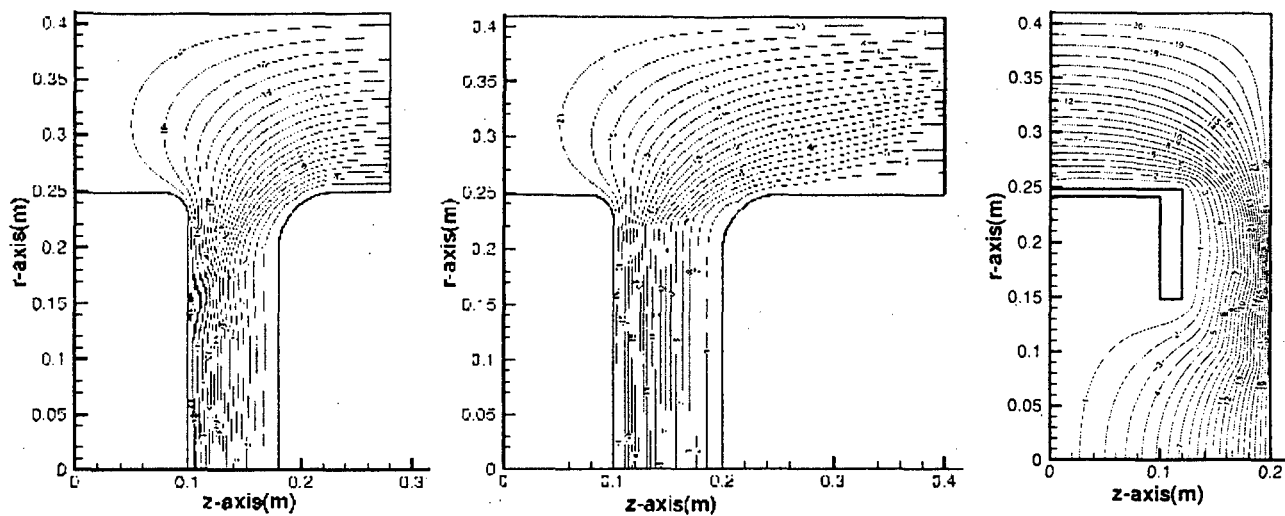


Fig. 1a, b, c: Equipotential lines in differently shaped electron diodes for KALIF-HELIA

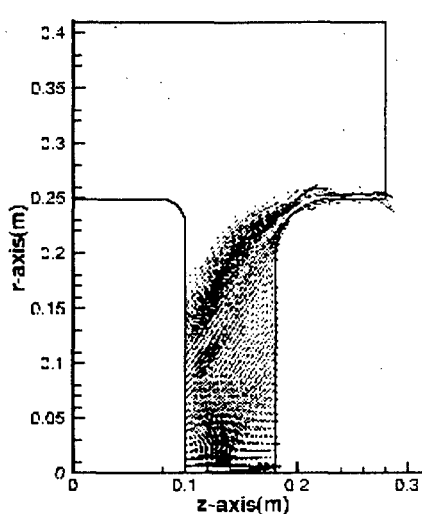


Fig. 2a: Electron current density, showing pinching of the electrons.

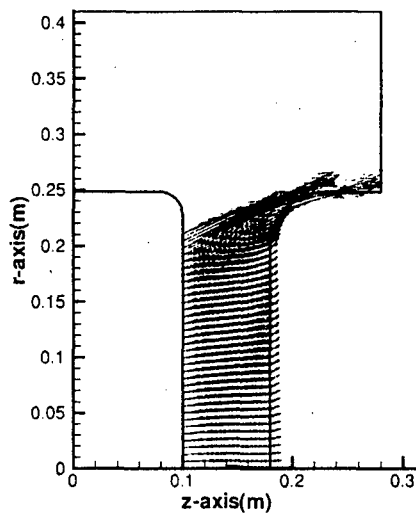


Fig. 2b: High coil current counteracts the pinching.

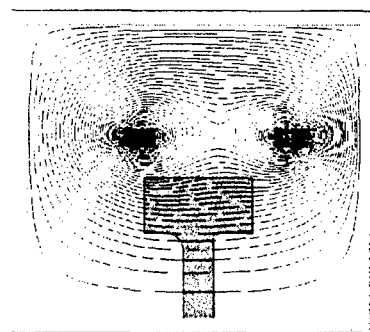


Fig. 3: ANSYS-result, rAz-lines and position of the coils

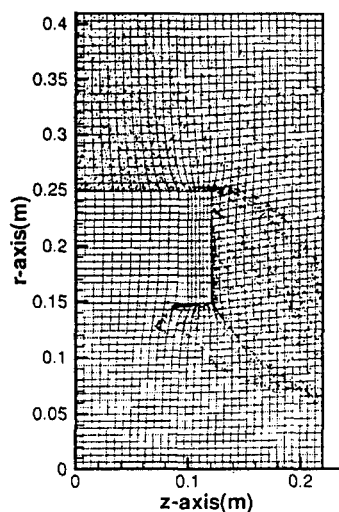


Fig. 4a: Small electron current is not sufficient to insulate the coaxial line

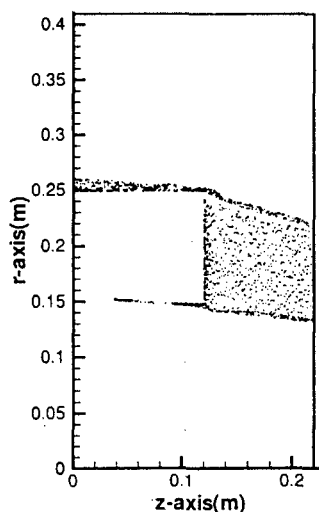


Fig. 4b: At high electron current the coaxial line is insulated

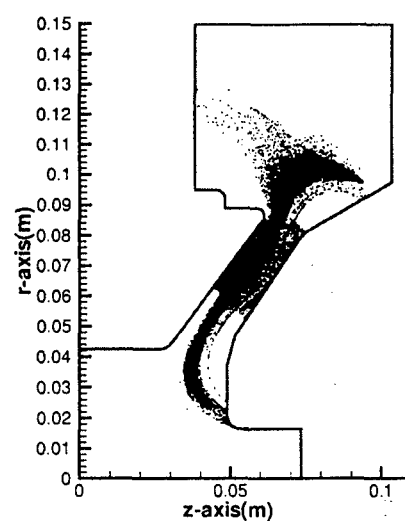


Fig. 5: Electrons and Ions in the applied-B-Field-Ion Diode

Table I. Electron Current I_E and Impedance Ω in Electron diodes of shapes A, B, C as function of gap distance G and coil current I_C

Shape		80 [mm]		100 [mm]		120 [mm]	
	I_C [kA]	I_E [kA]	Ω	I_E [kA]	Ω	I_E [kA]	Ω
A	40	457.6	13.1	368.3	16.3		
A	80	458.3	13.1	427.9	14.0		
A	160	523.7	11.5	421.0	14.3		
A	240	606.1	9.9	493.0	12.1		
B	40	552.6	10.9	419.9	14.3		
B	80	479.1	12.5	346.6	17.3		
B	160	574.3	10.4	468.8	12.8		
B	240	700.9	8.6	539.8	11.1		
C	40	655.3	9.2	322.0	18.6	277.7	21.6
C	80	821.3	7.3	312.2	19.2	270.3	22.2
C	120	676.2	8.9	326.9	18.4	244.3	24.6
C	160	642.2	9.3	395.7	15.2	335.3	17.9
C	240	653.1	9.2	451.6	13.3	375.0	16.0

[marked cases refer to poor magnetic insulation due to low electron current]

CONCLUSIONS

The step between the old and the new computer systems is completed successfully. After some practising a sufficient variety of models is available to compare stationary results to time dependent simulations. First simulations on the electron diode are performed. The effect of electron inflow from the KALIF-HELIA transmission line has been shown principally; it was found that at 330 kA a sharp transition between poor and good magnetic insulation takes place.

REFERENCES

- [1] T. Westermann, „A Particle-in-Cell Method as a Tool for Diode simulations“, Nuclear Instr. Meth. A **263** (1988), p. 271
- [2] C.-D. Munz, P. Omnes, R. Schneider, E. Sonnendrücker, E. Stein, U. Voss, T. Westermann, this conference
- [3] P. Hoppé, et al. „The KALIF-HELIA Accelerator: Description, Program and Status“, this conference
- [4] W. Bauer, W. Höbel, A. Ludmirsky, E. Stein, T. Westermann, „A Contribution to the Magnetic Focusing in an Applied-B-Extractor Ion Diode by a Laser Pulse driven Solenoid“ Proc. 10th Int. Conf. High Power Part. Beams, San Diego, 1994, p. 83
- [5] W. Bauer, P. Hoppé, H. Bachmann, H. Bluhm, L. Buth, H. Messier, D. Rusch, E. Stein, O. Stoltz, W. Vöth, T. Westermann, „Recent Results from Experimental and Numerical Investigations of the Selfmagnetically B₀-Insulated Ion Diode“, Proc. 11th Int. Conf. High Power Part. Beams, Prague, 1996, p. 1123
- [6] E. Halter, B. Schrempp, Fachhochschule Karlsruhe, private communication
- [7] ANSYS® ANSYS, Inc. 201 Johnson Road., Houston, PA, 15342-1300
- [8] Tecplot® Amtec Engineering, Inc. Bellevue, Washington
- [9] S. Kleinheinz, „Das VISART-Konzept einer standardisierten Schnittstelle zwischen Codes und Auswerteprogrammen“, FZK-Reports 5995 and 5596, 1997, Forschungszentrum Karlsruhe

Beam Dynamics in the 1.4 MeV Tandem Accelerator of the TAU FEL

A. Abramovich^{a)}, S. Efimov^{a)}, A. Gover^{a)}, I. Merhasin^{a)}, Y. Pinhasi^{b)}

a)-Tel-Aviv University - Faculty of Engineering - Physical Electronics, 69978, Israel

b)-The College of Judea and Samaria - Faculty of Engineering - Dept. of Electrical & Electronic Engineering, Israel

Electron beam parameters calculation results are presented and discussed for the 1.4 MeV electrostatic tandem accelerator, which is used in the Tel-Aviv University Free Electron Laser (TAU-FEL). Electron beam optics parameters including space charge effects were calculated for a beam line configuration, consisting of an electron gun, focusing solenoids, accelerating and decelerating sections, focusing quadrupole lenses and a wiggler.

A new program for simulation of electron beam transport in FEL ("ELOP") was developed recently at Tel-Aviv University (TAU). Equations of motion of an electron in the presence of magnetic and electric fields are solved numerically for different magnetic elements. The program was applied for simulation of electron beam transport in the TAU FEL. The results of the simulation provide guidelines for applying the appropriate currents to the quadrupole magnets along the beam line. A comparison of calculated and measured beam diameters is provided. Optimization problems of electron beam parameters are discussed.

INTRODUCTION

Beam parameter optimization is one of the most important problems of the FEL design. A 1.4MeV electrostatic tandem-accelerator is used [1] for the Israeli FEL. The goal of this work was to obtain an appropriate initial beam in the electron gun, to trace it along the accelerator tube (up to the region of interaction) with required beam parameters, using focusing by four quadrupole lenses (the quadruplet), pass it through the wiggler magnets, and then through another quadruplet, followed by the decelerator structure up to the collector, without beam losses. The following main beam optic elements were used: a Pierce-type three-electrode electron gun; four short solenoids (focusing coils) for beam focusing up to the entrance of the electrostatic accelerator enter; an accelerator tube; a quadruplet for beam forming before the wiggler (undulator) magnet; a wiggler; a quadruplet at beam focusing on the decelerator section exit; a decelerator tube; two short solenoids and a collector and central beam trajectory correctors.

BEAM DYNAMICS IN THE TAU-FEL INJECTION REGION

The scheme of the injection part is shown on the Fig.1. The goal of the beam dynamics simulations of the injection part was to obtain an initial electron beam with a current greater than 1.5A; a minimal emittance and divergence at the electrostatic accelerator tube entrance.

The Pierce type three-electrode electron gun with a thermionic cathode was used. It operates with an anode voltage of 43 kV and grid voltage of 12 kV. The initial beam radius was 7.6 mm. Four focusing coils were used in order to obtain optimal beam parameters at the accelerator entrance.

A new version of the code EGUN-2 [2] was used. This new version of the program enables one to simulate large structures. In our case, the injection part and the acceleration structure (75 electrodes) are described using one file only (in which the structure consists of two parts); in the old EGUN version it was necessary to use no less than 14 configuration files for a such structure. To describe the deceleration structure (80 electrodes) together with the collector region, only one configuration file was used (compared to 15 files in the old EGUN version). The new computer version is fast and it is possible to simulate many more rays.

The parameters of the electron beam in the simulations of the electron gun were as follows: beam current $=1.747\text{A}$, perveance $p=0.195\text{mkA/V}^{3/2}$. Fields of the focusing short solenoids, providing the required beam parameters after acceleration were the following: $B_z(C1)=115\text{Gs}$ (7.25A), $B_z(C2)=-65\text{Gs}$ (-3.75A), $B_z(C3)=52\text{Gs}$ (3A), $B_z(C4)=35\text{Gs}$ (2A). Beam emittance at the exit of the accelerator tube was found to be $22\pi\text{ mm}\cdot\text{mrad}$, beam radius was near 9.5mm . Beam energy after acceleration - 1.4MeV . Note that the potential of the last electrode is 1.36kV because a scheme with a grounded gun anode is used.

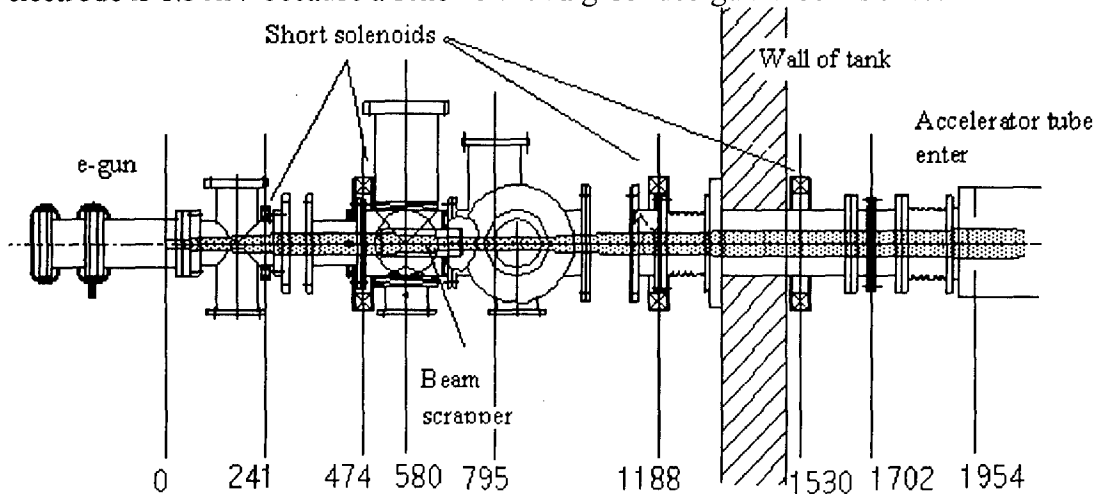


Fig.1. Injection part of the TAU-FEL and beam envelope. Numbers are the distances from the cathode in mm. 580 - beam scrapper; 580, 1702 - correctors, 1954 - first electrode of the accelerator tube.

BEAM DYNAMICS IN THE WIGGLER

Optimal beam parameters at the wiggler entrance were determined from requirements of beam transport in the wiggler: $x=1\text{mm}$ (x -wiggling direction), $x'=22\text{mrad}$, $y=0.956\text{mm}$, $y'=23\text{mrad}$ and for the beam center: $x_0=-1.64\text{mm}$, $x_0'=2.675\text{mrad}$.

The TAU FEL wiggler consists of 26 sets of magnets in a Hallbach configuration, where each magnet set is a period consisting of 4 permanent magnet pairs. In addition to these magnets there are also "correcting" magnets near the entrance and the exit of the wiggler and two "long" lateral focusing magnets, one at each side of the wiggler, which are required to eliminate angular derivation of the electron beam [1].

One can see that the plane wiggler with longitudinal magnets is equivalent to a FODO classical focusing structure in the first order approximation of magnetic field displacement near the central trajectory and provides a beam motion stability in both rectangular directions. Similar structures are used in cyclic accelerators. A new simulation code for modeling the electron beam dynamics in the wiggler and in other electron optic elements was developed in the TAU FEL group ("ELOP" [3]).

In order to calculate the electron beam transport through the wiggler we developed a simulation program ELOP that solves the electron dynamics equations in the presence of constant, time invariable magnetic and electric fields. This applies for coils, permanent magnets and magnet pairs, wigglers consisting of permanent magnets, quadrupole magnets and other time invariant configurations. The program calculates electron trajectories for a given set of electric and magnetic fields by use of Lorentz's force equation.

To obtain optimal beam focusing and required beam parameters at the wiggler entrance, four quadrupoles (quadruplet) focusing set was used. Simulations were made using the ELOP code, where the quadrupole fields were approximated in linear form. For comparison one of

the regimes was simulated by two different codes: TRANSPORT [4] and ELOP. Results coincided practically (Fig.2).

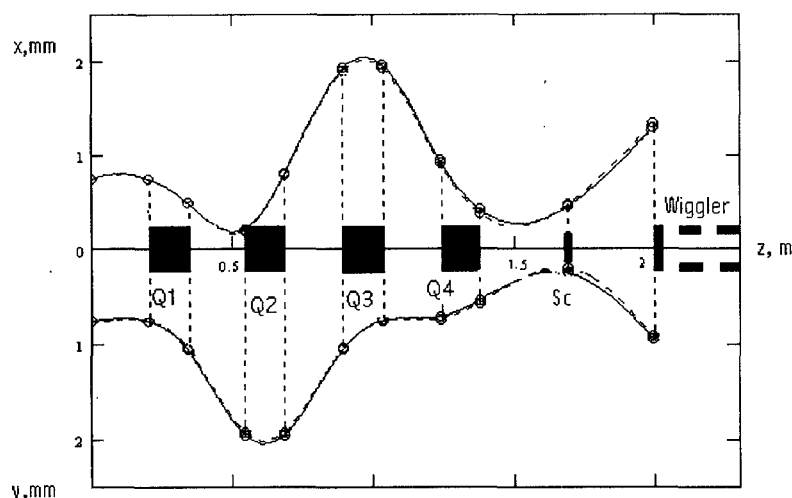


Fig.2. Beam envelope in the quadruplet before the wiggler. x - direction of wiggling. Continuous line - results of ELOP simulations, Dashed - by TRANSPORT simulations.

Quadrupole gradients were as follows: $Q1=2.275\text{Gs/mm}$ (1.495A), $Q2=-1.895\text{Gs/mm}$ (-1.245A), $Q3=2.345\text{Gs/mm}$ (1.475A), $Q4=-1.492\text{Gs/mm}$ (-0.98A). Quadrupole current values were taken from the experiment. Sign "+" corresponds to focusing in the x-direction. The effective length of the quadrupoles was 140mm, radius of the quadrupole aperture - 40.5mm, beam energy was 1.4MeV, initial beam radius was 7.5mm and beam divergence in both x and y directions was 2.93 mrad. The TRANSPORT code is applicable for ultra relativistic beams. To use it in our case angle calibration in the bending dipole magnetic field was made and the relativistic factor γ was taken into account by means of beam energy changes. So, 1.4MeV in the ELOP code corresponds to 1.8445MeV in the TRANSPORT code.

BEAM DYNAMICS ON THE COLLECTOR REGION

The beam dynamics problem in the region after deceleration is to collect a low energy beam with a large energy spread (7%) at the collector. The reason for this large energy spread is the radiation in the wiggler; this process is described in ref. [5]. The layout of this part of the facility is shown on the Fig.3. Short solenoids C5 and C6 for beam focusing are used. But at present it is not possible to provide full beam collection on the collector due to the large beam energy spread. To solve this problem a new collection design was proposed. The collector should consist of two parts: the old collector should be prolonged from 600mm up to 850-900mm and a new 1500mm length tube must be added which should have a potential 80kV (in respect to ground) via contact with a corresponding electrode in the decelerator. In this case the beam is collected on partially by the old collector and by the new tube.

For a uniform initial 1A beam entering the decelerator with emittance of $22\pi\text{ mm}\cdot\text{mrad}$ and beam radius of 10mm, partial beam collection in the collector region was simulated using EGUN-2 code. Results of more than 500 ray tracing simulations with initial beam energy in the range 1.32MeV-1.42MeV for a uniform energy spread displacement are shown on the Fig. 3 (as a histogram with 0.1m steps along the z-axis). The vertical columns in Fig.3 represent the beam power collected along the z-axis in the collector region if the old collector design is used with a 0 collector potential in respect to ground. The total beam power for this case is 52.3kWt (on the new tube 65% are collected up to $z=1.3\text{m}$ in Fig.3; on the old construction

collector walls (after it prolongation) 17% are collected up to $z=2.5\text{m}$; 18% are collected by the final collector (13496 in Fig.3.). The envelope line in Fig.3 represent the power distribution for a 40kV potential on the collector. For this case beam power collected 67.8kWt and the distribution along the collector various correspondingly 54%, 18%, 28%. Coordinate $z=0$ in Fig.3. corresponds to the new tube entrance.

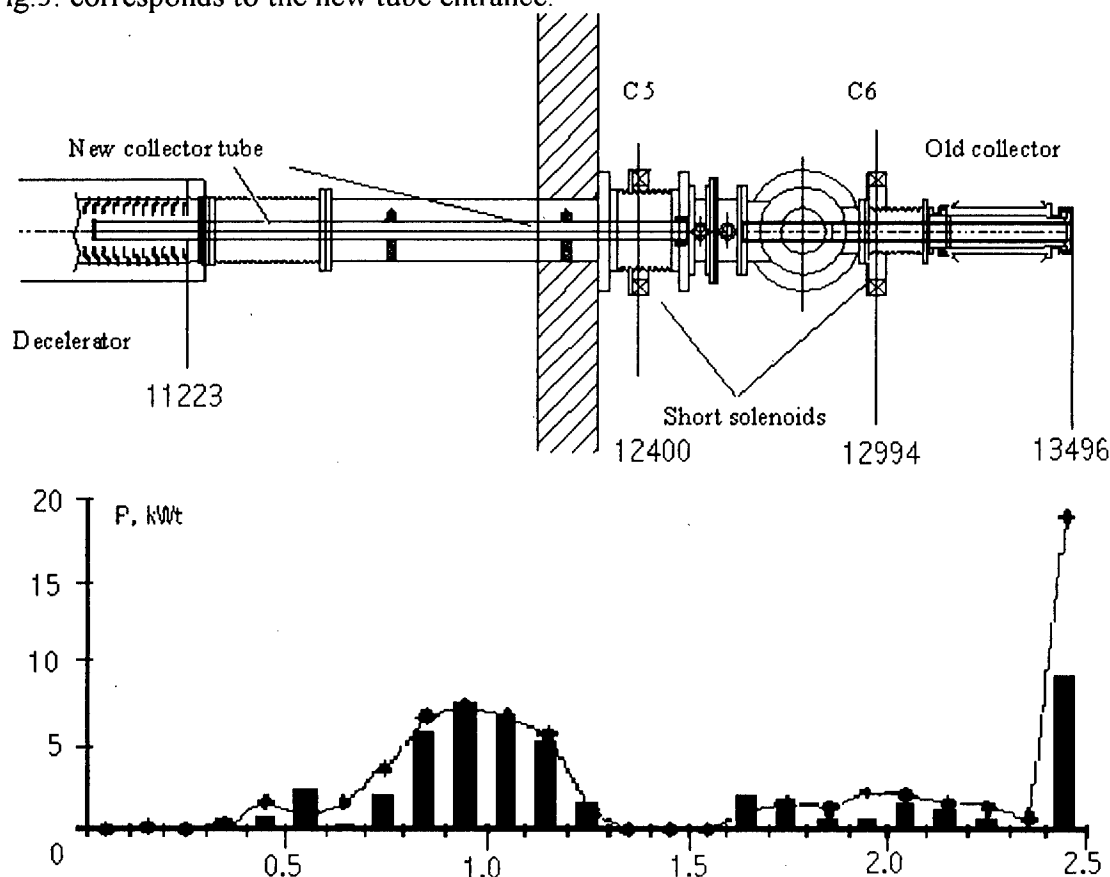


Fig.3. Histogram of beam collection displacement on the exit of FEL. 11223 - last electrode position in mm in regard to the cathode, 12400, 12994 - short solenoids positions.

CONCLUSIONS

Use of a new version of the EGUN-2 code and the ELOP code, developed at the Tel-Aviv University, provides a full mathematical model of the TAU FEL for beam dynamic simulations. Electron beam parameters required for the beam transport without losses within the wiggler were obtained. Beam transport simulation results from the radiation region and up to the new collector are provided.

REFERENCES

- [1] A.Abramovich, et.al., Lasing and radiation-mode dynamics in a Van de Graaff accelerator-free electron laser with an internal cavity, Appl.Phys.Lett. 71(26), 1997.
- [2] W.B.Herrmannsfeld, EGUN - an electron optics and gun design program, SLAC-Report-331, 1988 & lists with comments for new version, 1995.
- [3] I.Merhasin et.al., Optimization of the electron-beam transport in the Israeli tandem FEL, NIM, to be published.
- [4] K.L.Brown, D.C.Carey, Ch.Iselin, F.Rothacker, TRANSPORT. A computer code for designing charged particle beam transport systems, CERN80-04, 1980.
- [5] A.Abramovich et al., Investigation and simulation of the electron energy spread after interaction region on the ISRAELI tandem FEL. This conference

RAYLEIGH —TAYLOR INSTABILITY OF IMPLODING CURRENT SHELL BY LOW DENSITY PLASMA

A.V. Gordeev

RRC «Kurchatov Institute», 123182 Moscow, Russia

1. The instabilities of the imploding structures such as z-pinch and liner are the main obstacle by the attempt to compress by a magnetic field the current plasma structures to high densities and, correspondingly, to small scales. The most dangerous prove to be the instabilities, which stimulate the macroscopic ion motion on the size scale of the imploding structure. For the z-pinch and imploding plasma shell, the most important instability is the Rayleigh-Taylor (RT) instability [1]. This instability undoubtedly exists within the framework of the one-fluid magnetohydrodynamics (MHD), when the role of a Hall effect can be neglected according to the parameter $\Pi^{-1} \ll 1$, where $\Pi = 4\pi e^2 n \delta^2 / m_i c^2$, δ - the characteristic scale of an imploding shell [2]. In the case of the two-fluid MHD, when the role of the Hall effect is large, the problem is no so simple [3]. In recent years, the evidence was obtained for the absence of the stabilization of the RT instability by the Hall effect [4,5]. However, in these papers the RT instability arises as a result of the applying of an fictitious «gravity force». In the present paper the RT instability will be considered by a direct transition to a moving system of coordinates, which results in a more adequate approach. The most important peculiarity of the approach is such a form of the final equations, which allows the exact integration of the perturbed equations for an arbitrary density profile and by the account of the kinetic pressure.

2. We start from the system of the two-fluid MHD equations. It will be assumed that the electron inertia and the dissipative effects will be neglected. So, we will consider that the collisional and electron collisionless size scales are very small relative to the characteristic size of the imploding shell.

As a result, we will use the following basic system for an imploding plasma shell with a current [3,4]:

$$\rho \frac{d\vec{V}}{dt} = -\frac{1}{4\pi} [\vec{B} \times [\nabla \times \vec{B}]] - \nabla p \quad (1)$$

$$\frac{\partial \rho}{\partial t} + \nabla(\rho \vec{V}) = 0, \quad (2)$$

$$\frac{\partial \vec{B}}{\partial t} = [\nabla \times [\vec{V} \times \vec{B}]] + \frac{c}{4\pi e} \left[\nabla \times \frac{1}{n} [\vec{B} \times [\nabla \times \vec{B}]] \right] - \frac{c^2}{4\pi} \left[\nabla \times \frac{1}{\sigma} [\nabla \times \vec{B}] \right]. \quad (3)$$

Here for the total pressure of electrons and ions we assume the adiabatic law $p = p(n_i)$, $\rho = m_i n_i$ is the plasma density, and the finite conductivity σ is preserved in a pure symbolic manner in order to evaluate its role for the disturbances obtained. Further on, we will consider $\sigma B \gg \text{enc.}$

The further investigation will be carried out in Cartesian coordinates, when the radial motion of the imploding shell is transformed into the motion along the x-axis, and the θ -component of the magnetic field is transformed into the B_y .

We assume that in the initial state of the imploding shell there exists the x-dependence only. Then one can prove that for the perturbations by $\partial/\partial y = 0$ the equations for B_y and $B_{x,z}$ are splitted.

The equations for the nonperturbed configuration of an imploding plasma shell read:

$$\rho_0 \frac{dV_0}{dt} = -\frac{B_0}{4\pi} \frac{\partial B_0}{\partial x} - \frac{\partial p_0}{\partial x}, \quad \frac{\partial \rho_0}{\partial t} + \frac{\partial}{\partial x}(\rho_0 V_0) = 0, \quad (4)$$

$$\frac{\partial B_0}{\partial t} + \frac{\partial}{\partial x}(B_0 V_0) = \frac{c^2}{4\pi} \frac{\partial}{\partial x} \left(\frac{1}{\sigma} \frac{\partial B_0}{\partial x} \right). \quad (5)$$

Here the velocity of the imploding plasma shell V_0 is directed along the x-axis, and the magnetic field B_0 — along the y-axis.

In the following, by the transformation of the equations to the moving system of coordinates the compactness condition will be used, which reads that the nonperturbed velocity V_0 is a function of time only. This compactness condition may be presented in the form

$$\frac{\partial V_0}{\partial t} = -a_0(t). \quad (6)$$

By the transition to the variable

$$s = x - \int V_0(t) dt \quad (7)$$

and making use the transition formula

$$\left. \frac{\partial}{\partial t} \right|_s = \left. \frac{\partial}{\partial t} \right|_x + V_0 \left. \frac{\partial}{\partial x} \right|_t, \quad (8)$$

one can obtain the equilibrium condition

$$\rho_0 a_0 = \frac{d}{ds} \left(\frac{B_0^2}{4\pi} + p_0 \right), \quad (9)$$

where

$$\left. \frac{\partial \rho_0}{\partial t} \right|_s = 0, \quad \left. \frac{\partial B_0}{\partial t} \right|_s = \frac{c^2}{4\pi} \frac{\partial}{\partial s} \left(\frac{1}{\sigma} \frac{\partial B_0}{\partial s} \right).$$

The neglecting of the dissipation $\sigma \rightarrow \infty$ corresponds to $a_0 = \text{const}$.

The equilibrium condition (9) in the moving system of coordinates corresponds to the case, when the inertial force is balanced by magnetic and kinetic pressures.

When transforming the perturbed equations in the same way and passing on to the Fourier transformation with respect to t (the frequency ω) and to z (the wave vector k_z) and introducing the dimensionless values in accordance with the following rules (Δ is the layer size in x-direction, \bar{B}_0, \bar{n}_0 — the constant values)

$$b_0 = \frac{B_0}{\bar{B}_0} > 0, \quad v_0 = \frac{n_0}{\bar{n}_0}, \quad s = \Delta \xi, \quad \kappa = k_z \Delta, \quad a_0 = \frac{\bar{V}_0^2}{\Delta}, \quad \bar{V}_0^2 = \frac{Z \bar{B}_0^2}{4\pi m_i \bar{n}_0},$$

$$\omega = \Omega \frac{\bar{V}_0}{\Delta}, \quad \tilde{\Omega} = \Omega + \frac{\kappa}{\sqrt{\Pi}} \frac{1}{\nu_0} \frac{db_0}{d\xi}, \quad \Pi = \frac{4\pi e^2 \bar{n}_0 Z \Delta^2}{m_i c^2},$$

one can obtain the following final dimensionless equations for the perturbed magnetic field b and density v

$$\Omega \tilde{\Omega} \left(b - \frac{b_0}{\nu_0} v \right) = \frac{d}{d\xi} \left(\frac{b_0}{\nu_0} \right) \left\{ \Omega \frac{\kappa}{\sqrt{\Pi}} b + v - \frac{d}{d\xi} (b_0 b + \varepsilon v) \right\}, \quad (10).$$

$$\frac{dv}{d\xi} - \Omega^2 v = \frac{d^2}{d\xi^2} (b_0 b + \varepsilon v) - \kappa^2 (b_0 b + \varepsilon v) \quad (11)$$

for the following relation between ν_0 and b_0

$$\nu_0 = b_0 b'_0 + \varepsilon \nu'_0, \quad \varepsilon(s) = \frac{4\pi \bar{n}_0}{B_0^2} \frac{dp_0}{dn_0}. \quad (12)$$

Here the prime means the differentiation with respect to the variable ξ .

3. Further on, we consider the limiting case $\Pi \ll 1$, when the Hall effect is essential [3]. Then from (10) and (12) it follows

$$v = b \frac{\nu'_0}{b'_0} = b b_0 \frac{\nu'_0}{\nu_0 - \varepsilon \nu'_0}. \quad (13)$$

By introducing the notation $w = b b_0$ Eq. (11) may be rewritten as

$$\frac{d}{d\xi} \left\{ \frac{d}{d\xi} (w + \varepsilon v) - v \right\} + \Omega^2 v - \kappa^2 (w + \varepsilon v) = 0. \quad (14)$$

By the straightforward substitution it is easy to verify that this equation has the general solution

$$w = C_1 (\nu_0 - \varepsilon \nu'_0) \exp(\kappa \xi) + C_2 (\nu_0 - \varepsilon \nu'_0) \exp(\kappa \xi) \int_0^\xi \frac{d\xi'}{\nu_0(\xi')} \exp(-2\kappa \xi'), \quad (15)$$

which corresponds to the eigenvalue (see also [6])

$$\Omega^2 = -\kappa, \quad \kappa > 0. \quad (16)$$

One can see that in a Hall limiting case for an arbitrary density profile $n(s)$ and by the account of the kinetic pressure $p(n)$ the equations allow the exact integration for the global RT instability. The result about the instability in the Hall limiting case was obtained earlier in [4,5], however in the present paper the structure of the equations is quite different.

4. Below we consider briefly the higher modes of the RT instability by the density profile $\nu_0 = \xi(1 - \xi)$. Introducing in Eq. (14) the new function

$u \equiv w / (\nu_0 - \varepsilon \nu'_0)$, one can obtain

$$\frac{d}{d\xi} \left(\nu_0 \frac{du}{d\xi} \right) = u (\kappa^2 \nu_0 - \Omega^2 \nu'_0). \quad (17)$$

Going to the new variable $\eta = 2\xi - 1$, the following equation for the above mentioned density profile will be obtained

$$\frac{d}{d\eta}(1-\eta^2)\frac{du}{d\eta} = u\left\{\frac{\kappa^2}{4}(1-\eta^2) - \kappa\lambda\eta\right\}, \quad (18)$$

where $\lambda \equiv -\Omega^2/\kappa$ — the eigenvalue of this equation.

The expansion of the function u in terms of the Legendre polynomials [7]

$u = \sum_{m=0}^{\infty} a_m P_m(\eta)$ gives the recursion relations for a_m , which by $m \gg 1$ take the following form

$$\left(m^2 + \frac{\kappa^2}{8}\right)a_m = \frac{\kappa^2}{16}(a_{m+2} + a_{m-2}) + \frac{\kappa\lambda}{2}(a_{m+1} + a_{m-1}). \quad (19)$$

When transforming these recursion relations by the account of the $m \gg 1$ into the differential equation relative to $a(m)$ and expanding the solution of this equation in terms of the Hermite polynomials [7], so one can arrive at the dispersion relation

$$\lambda = \left(q + \frac{1}{2}\right)\sqrt{1 + \frac{2\lambda}{\kappa}}, \quad (q \text{ — positive integer}). \quad (20)$$

This relation coincides in a qualitative manner with [5] by $\kappa^2 \gg 1$, however here it was obtained by the arbitrary density $p(n)$. One must stress that contrary to [5] ω already normalized relative to \bar{V}_0/Δ and it is impossible to obtain the frequency scale, which does not contain the ion mass m_i .

5. Thus, in the present paper are obtained the general equations, which describe the RT instability in a accelerated system of coordinates. It is shown that account of the Hall effect does not results in the stabilization of the RT instability in accord with [4,5]. However, the form of the equations obtained is quite different. The main result of the present paper consist in that unlike the one-fluid MHD in the two-fluid MHD by the account of the Hall effect it is possible the analytical solution for the RT instability independently of the specific form of the density profile and functional type of $p(n)$.

One must stress that the results obtained hold for the Hall plasma, when

$\sqrt{-\omega^2} \gg \omega_B$, where ω_B — the ion cyclotron frequency.

This study was supported in part by the Russian Foundation for Basic Research, project no. 97-02-16980.

References

- [1] S. Chandrasekhar, Hydrodynamics and Hydrodynamic Stability (Oxford Univ. Press, Oxford, 1961).
- [2] N.A. Inogamov, Prikl. Mech. Tech. Fiz., No. 5, p.110, 1985.
- [3] A.V. Gordeev, A.S. Kingsep, L.I. Rudakov, Physics Reports, 1994, v. 243, n.5, pp. 215-315.
- [4] J.D. Huba, A.B. Hassam, and P.Satyanerayana, Phys. Fluids, 1989, B1(4), p.931.
- [5] A.L. Velikovich, Phys. Fluids, 1991, B3(2), p. 492.
- [6] A.V. Gordeev, Preprint IAE-6054/6, RRC «Kurchatov Institute», Moscow, 1997.
- [7] H.Bateman and A. Erdelyi, Higher Transcendental Functions, Vol. 1 (McGraw Hill, New York, 1953).

NON-LINEAR ELECTROMAGNETIC WAVE IN PLASMA -FILLED TRANSMISSION LINE

A.V. Gordeev and S.V. Levchenko

RRC «Kurchatov Institute», 123182 Moscow, Russia

1. For the energy transportation from a generator to a load are used the vacuum transmission lines with the magnetic insulation (MITL), where the non-linear electromagnetic waves can be formed because of both non-linear effects and the electron leakage at the wave front [1]. By the plasma switch experiments, the vacuum gap of the MITL is filled by a low density plasma, so the problem arises about the dynamics of electromagnetic fields in the plasma medium. There exists also some another reason for the plasma appearance in the MITL — the ion emission from the anode surface. In the following the plasma will be considered in the framework of the two-fluid magnetohydrodynamics (MHD) model by the account of the Hall effect, when electrons are magnetized and ions are not magnetized [2]. In the absence of the interparticles collisions, the electron vorticity equal to the curl of the generalized momentum of electron is conserved. It is easy to verify that the ratio of the electron vorticity to the electron density is conserved along electron trajectory, i.e. this value proves to be a Lagrange invariant. In addition, we will consider the turbulent plasma medium, as it is usual for the plasma opening switch (POS) device. Then the Lagrange invariant is equalized in space because of the turbulent motion of electrons [3]. The constant value of the Lagrange invariant allows to integrate the equations obtained.

In the present paper, the propagation of the ion-diode-like equilibrium in the direction from a generator to a load will be investigated. The velocity of such wave proves to be of the order of the light velocity at the moderate voltage about some megavolts across the MITL. The high enough wave velocity by a presence of the ion motion is only possible by the mainly transversal ion motion. For this wave, the almost instantaneous generation of the ion flow from the anode surface is required.

The most interesting point of the investigations developed consists in the fact that by some conditions the self-consistent wave propagates in the MITL, where particles and fields can be described by a unified wave velocity. Interestingly, the velocity of this wave is controlled essentially by the value of the Lagrange invariant. It will be shown that by the high voltage the wave velocity is almost constant and is determined by the inertialless electron motion.

2. By the description of the electron equilibrium, which establishes after the wave front, is used the generalized Brillouin equilibrium, when the electron motion represents the drift in the crossed magnetic and electric fields. The main electron motion equation can be presented in the form [3]

$$\frac{\partial \vec{p}}{\partial t} + \nabla \gamma m_e c^2 = -e \vec{E} - \frac{e}{c} [\vec{v} \times \vec{\Omega}], \quad \vec{p} = \gamma m_e \vec{v} \quad (1)$$

where $\vec{\Omega} = \vec{B} - \frac{c}{e} [\nabla \times \vec{p}]$ — the electron vorticity and \vec{B} — the magnetic field.

The electron velocity \vec{v} is equal

$$\vec{v} = -\frac{c}{4\pi en_e} [\nabla \times \vec{B}] + \frac{1}{4\pi en_e} \frac{\partial \vec{E}}{\partial t}. \quad (2)$$

Here we neglected the ion velocity term, which corresponds to the following small parameter

$$\frac{4\pi e^2 Z^2 n_i}{m_i c^2} d^2 \ll 1, \quad (3)$$

characteristic for the Hall plasmas.

The second Maxwell equation can be presented in the form

$$\vec{E} = -\frac{1}{c} \frac{\partial \vec{A}}{\partial t} - \nabla \Phi, \quad \vec{B} = [\nabla \times \vec{A}], \quad (4)$$

where Φ and \vec{A} are the scalar and vector potentials, respectively.

From the first equation (4) by the condition $E_z = 0$ on the cathode plane, where z is the direction along the MITL, one can obtain the velocity of the non-linear electromagnetic wave

$$w = \frac{U}{A - A_0}. \quad (5)$$

Here U — the line voltage and A, A_0 are the z -components of the vector potential after and before the wave front, respectively.

Such a wave for the non-relativistic limit and by the approximation of motionless ions was considered in [4]. The ion motion can be neglected on the earlier stage of evolution, when the ion density can be considered as constant because of the small ion velocity. However, late in the wave evolution the ion diode equilibrium establishes inside the line gap in correspondence with recent ion diode theory [5]. Therefore, one must also consider the ion motion. The ion motion equation can be presented in the form

$$m_i \frac{\partial \vec{v}_i}{\partial t} + \nabla \frac{m_i \vec{v}_i^2}{2} = Ze\vec{E} + \frac{Ze}{c} [\vec{v}_i \times \vec{\Omega}_i], \quad (6)$$

where the ion vorticity $\vec{\Omega}_i$ is equal to zero

$$\vec{\Omega}_i \equiv B + \frac{m_i c}{Ze} [\nabla \times \vec{v}_i] = 0. \quad (7)$$

This equality corresponds to a small level of the ion turbulence on the earlier stage of the ion evolution [6].

When taking into account the boundary condition $E_z = 0$ at the cathode surface, one can obtain from z -component of Eq.(6) the following relation

$$m_i \frac{\partial v_{iz}}{\partial t} + \frac{\partial}{\partial z} \frac{m_i \vec{v}_i^2}{2} = 0,$$

from which by $\partial / \partial t = -w \partial / \partial z$ one can arrive at the expression for the wave velocity w

$$w = c \frac{\vec{v}_i^2}{2v_{iz}}. \quad (8)$$

The y -component of Eq. (7) is equal

$$B_y + \frac{m_i c}{Ze} \left(\frac{\partial v_{ix}}{\partial z} - \frac{\partial v_{iz}}{\partial x} \right) = 0.$$

The simple estimates show that in the equilibrium state one can neglect the derivative relative z by the fulfillment of the inequality

$$\frac{4\pi e^2 Z^2 n_i^2}{m_i c^2} L^2 \gg 1, \quad (9)$$

where L is the longitudinal size of the equilibrium.

In this case in the equilibrium, which establishes after the wave front, one can neglect the z -derivative and the following relation will be valid

$$B_y - \frac{m_i c}{Ze} \frac{dv_{iz}}{dx} = 0. \quad (10)$$

Integrating this relation over the line gap from the anode surface ($x = x_a$) to the cathode surface ($x = x_c$), one obtains the velocity of ions near the cathode

$$v_{izc} = \frac{Ze}{m_i c} \int_{x_a}^{x_c} B_y dx \equiv \frac{Ze}{m_i c} A_a. \quad (11)$$

Substituting this expression for v_{izc} in (8) and taking into account the conservation law of energy, we get to the following expression for the wave velocity

$$w = \frac{U}{A_a}. \quad (12)$$

Comparing this with Eq. (5), one can see that these expressions are equivalent, when $A_0 = 0$, that is when the magnetic field is absent before the wave front.

In the dimensionless form Eq.(12) can be presented as

$$w = \frac{u}{\Pi}, \quad (13)$$

where u — the dimensionless voltage in the line and Π — the dimensionless magnetic flux.

As it is known from the diode theory, the electron and ion equations have an additional integral

$$\frac{b^2}{\gamma^2} + J_i \sqrt{u - \varphi} = \text{const}, \quad J_i = \frac{16\pi j_i e d^2}{m_e c^3 \sqrt{2Zm_e / m_i}}, \quad (14)$$

where φ is the dimensionless electric potential, γ — the electron relativistic factor and $b = eBd / m_e c^2$.

It is known that in the ion diode problem must be fixed the total magnetic flux. However, by the non-linear electromagnetic wave the distance between the electrodes must be fixed. The dimensionless form of this condition has the form

$$\int_0^u \frac{\gamma}{b\sqrt{\gamma^2 - 1}} d\varphi = 1. \quad (15)$$

The above obtained relations between the quantities give a possibility to present the relativistic factor and the dimensionless magnetic field in the following form:

$$\gamma = \frac{1 + \varphi + ib_c}{1 + i\sqrt{b_c^2 + \frac{u}{i}\left(\frac{u}{i} + 2b_c\right)(1 - \sqrt{1 - \varphi/u})}}, \quad b = \gamma\sqrt{2\varphi + b_c^2}. \quad (16)$$

Neglecting the unity in the γ -expression and substituting these simplified expressions for γ and b in Eq. (15), one can essentially simplify the integral relation

$$2i \int_0^1 \sqrt{\frac{s}{1-s}} \frac{ds}{\sqrt{\frac{2ib_c}{u} + 1 - s^2 - s}} = 1, \quad (17)$$

From Eq. (17) it follows the limiting values of the cathode magnetic field for the different cases:

$$b_c(u) = \frac{u}{2i}, \quad (\pi)^2 \ll 1; \quad b_c(u) = \pi^2 \frac{iu}{2}, \quad (\pi)^2 \gg 1. \quad (18)$$

One can prove that for the both cases the dimensionless magnetic flux is equal $\Pi = b_c$. Therefore, the wave velocity can be found as

$$\frac{w}{c} = 2i, \quad (\pi)^2 \ll 1; \quad \frac{w}{c} = \frac{2}{\pi^2 i}, \quad (\pi)^2 \gg 1. \quad (19)$$

It is seen from obtained results that the wave velocity has a maximum by the value of the dimensional invariant of the order of unity.

4. The presented theory allows to calculate the velocity of the non-linear electromagnetic wave in the transmission line as a function of the line voltage.

It is shown, the wave velocity obtained is controlled by the value of the Lagrange invariant, which in turn is determined by the turbulence level of the plasma inside the line.

This study was supported in part by the Russian Foundation for Basic Research, project no. 97-02-16980

References

- [1] A.V.Gordeev, Preprint IAE-3076, 1978; in English: A.V.Gordeev, Magnetic Self Insulation of Vacuum Coaxial Lines, PIIR-12-79, 1979.
- [2] A.V.Gordeev, A.S. Kingsep, L.I. Rudakov, Physics Reports. Vol. 243, N 5, July 1994.
- [3] A.V.Gordeev, Plasma Physics Reports, 1997, v. 23(2), pp. 92-101.
- [4] A.V.Gordeev, A.V. Grechikha, A.V. Gulin and O.M. Drozdova, Fiz. Plazmay, 1991, v. 17, p. 650.
- [5] A.V.Gordeev and S.V. Levchenko, Preprint IAE-6060/6, RRC «Kurchatov Institute», Moscow, 1997.
- [6] M.P.Desjarlais, R.S. Coats, T.R. Lockner et al, in: Proceedings of 11th Intern. Conference on High Particle Beams Vol. 1, p. 101, Prague, June 10-14, 1996.

SIMULATION STUDY OF A 32GHZ GYROTRON USING AN ELECTROMAGNETIC PIC CODE

J. J. Barroso, K. G. Kostov*, R. A. Corrêa, and I. P. Spassovsky*

*Associated Plasma Laboratory
National Institute for Space Research (INPE)
P.O. Box 515, 12227-970 São José dos Campos, SP, Brazil*

**On leave from Dept. of General Physics
Sofia University, 5 J. Bourchier Blvd.
Sofia 1126, Bulgaria*

Abstract

A simulation study with experimental parameters of a 32GHz gyrotron operating in the TE_{021} mode is presented. Beam electrons with typical energy of 40 keV and transverse-to-axial velocity ratio ranging from 0.8 to 2.0 are injected into the cavity to drive electromagnetic oscillations from noise. On the basis of an electromagnetic PIC code, a parameterization study is carried out to determine how sensitive the output power is to change in pitch ratio and beam current.

Introduction

From the mathematical point of view, the study of the cyclotron resonance interaction of the cavity fields with a relativistic electron beam in the gyrotron has largely been carried out by means of two analytical approaches, namely, via a dispersion equation based on plasma physics and through ballistic methods considering equations of motion and particle trajectories [1]. The first method lies in the analysis of a dispersion equation for the beam eigenmodes and the corresponding search for instabilities in the form of a complex solution, that may be interpreted as a growing space-charge wave in the beam, which is in synchronism with the surrounding electromagnetic structure. Although velocity spread and space-charge effects can be adequately accounted for, this method is an example of perturbation procedure as the starting point is the linearized Boltzmann equation, and further nonlinear extensions are a second-order approximation in nature. In the ballistic approach, the equation of motion for the beam electrons – thus combined with Maxwell's equations for self-consistency of the solutions to be achieved – is integrated to give the particle trajectories. The energy exchange term $\vec{v} \cdot \vec{E}$ is then calculated and averaged over the beam to solve for the problem of power transfer between the fields and the electrons. This technique is most general regarding nonlinear analysis, since all possible geometry variations of the fields and injection schemes of the particles can be taken into consideration. However, this approach involves a vast amount of numerical calculation which is not so illuminating during the early stage of the discussion.

Nevertheless, with the advent of high-speed computers, particle simulations can offer insights that complement and enlarge those gained by traditional approaches, thus adding feedback for improvement in theory. Gyrotron simulations using particles have begun since the 1980's, either making relativistic predictions of the saturated RF output characteristics of a gyrotron amplifier [2] or examining the scaling of the transient growth rate with the beam current [3]. Being fully nonlinear, simulation is then capable of handling growth in time and space from linear through large amplitudes. In the particle model [4, 5], the motion of a large assembly of

charge particles is followed in their self-consistent electric and magnetic fields. Although this approach sounds simple and straightforward, practical computational limitations require the use of sophisticated numerical methods that provide sufficient accuracy and stability to make the simulations useful for many characteristic cycles of the beam.

In this paper, we report on a simulation study of a high-power, pulsed gyrotron operating in the TE_{021} mode at 32 GHz. Simulations have been carried out on a $2\frac{1}{2}$ dimensional, fully relativistic electromagnetic particle code [4] and are aimed at the identification of the physical process which determine the nonlinear saturation and the efficiency of the radiation production. Beam equilibrium parameters are based on experimentally observed values [6], and in all the computer runs a monoenergetic annular electron beam with guiding centers located on the second radial maximum of the TE_{021} mode is injected into the cavity to drive the electromagnetic oscillations from noises. Beam currents of 5 and 10A with pitch angle $\alpha = v_{\perp}/v_{\parallel}$ varying from 0.8 to 2.0 have been considered. For each value of current, optimization of the conversion efficiency with respect to the external magnetic field has given 40% efficiency at $\alpha=1.1$ and 10A, while for the low-current case the maximum efficiency has been 32% at $\alpha=1.3$. Results of the simulation are detailed in the second section and followed by discussion in the final section.

Results of the Simulation

Fig. 1 illustrates the elements of the particle modeling.

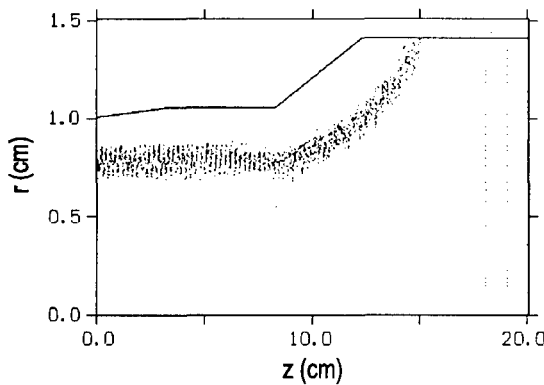


Fig. 1. Real-space (r-z) diagram of the simulated beam at t=48 ns

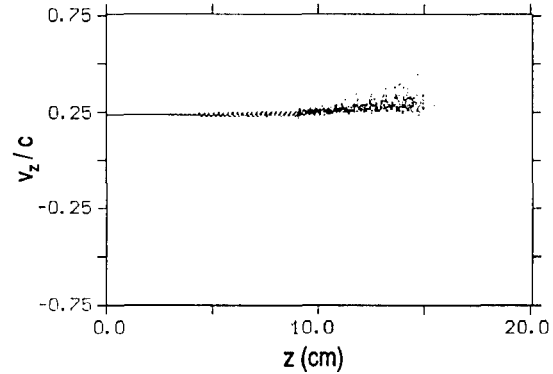


Fig. 2. Axial velocity vs. axial distance of the electron beam at t=48 ns

Simulations are initiated by continuously injecting the beam electrons with prescribed parameters into the cavity. The inlet is at the beginning of a downtapered section that ensures cutoff for the operating mode. Thus little or no radiation propagates toward the left boundary, which is assumed to be a perfect conductor in the simulation. In the output waveguide is inserted a conducting disk having a resistance per unit square equal to the characteristic impedance Z_{TE} of the outgoing traveling wave that propagates to the right, that is, $Z_{TE} = 1/d\sigma$, where $\sigma = 0.2S/m$ and $d = 1.0cm$ are the conductivity and thickness of the absorbing disk. The absorber is placed a quarter-wavelength from the shorted waveguide end, since for perfect conductor, the shorted end quarter-wave guide represents an infinite impedance in parallel with the matching resistance.

In this sense, the output guide acts as an ideal calorimeter that absorbs all the radiation from the quasi-stationary fields in the cavity, otherwise reflections at the right boundary could have a significant impact on the dynamics of the wave growth process. The axial component of the applied guiding magnetic field is constant over the distance $0 \leq z \leq 9.0cm$ and decreases linearly to reach a zero value at $z=17.5cm$, so that the spent beam is dumped beyond the output taper, where the electrons are no longer in resonance with the wave. We have used over ten thousand particles to simulate the beam and a mathematical spacial grid, having dimensions $0.2mm \times 0.3mm$, which is fine enough to resolve a Larmor radius in order to measure the charge

density and then calculate the fields.

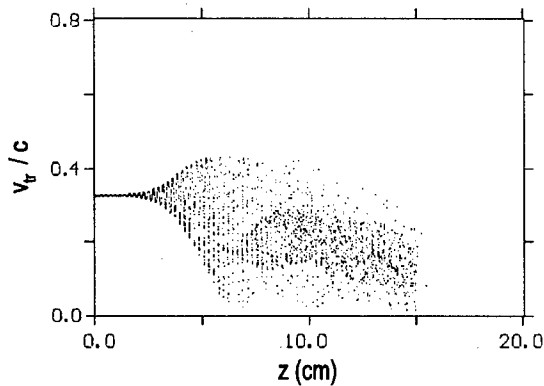


Fig. 3. Transverse velocity vs. axial distance of the beam at $t=48$ ns

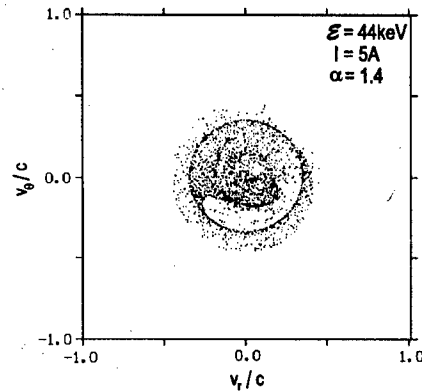


Fig. 4. Particle positions in the parameter space

The simulations proceed discontinuously in time step by step, and at time $t=48$ ns an injected 44-keV, 5-A beam with pitch ratio of 1.4 has clearly become modulated as shown in Fig. 1. The corresponding plots of the axial and transverse velocities vs. the axial distance are given in Fig. 2 and Fig. 3 at a time $t=48$ ns when the RF fields have saturated into the simulation. The azimuthal bunching (Fig. 3) is seen to result in dense groups of electrons with decelerated transverse velocities. In spite of the electron axial velocity has been accelerated (Fig. 2), the overall result is a net transfer of energy from the beam to the cavity fields as a majority of the beam electrons become confined inside the initial guiding center circle (Fig. 4). The simulated self-consistent axial profile of the operating TE_{021} mode is shown in Fig. 5 for $\Omega_B/\omega_c = 0.97$ where Ω_B is the relativistic cyclotron frequency and ω_c is the waveguide cutoff frequency. We can distinguish the quasi-stationary cavity field confined in the region $0 \leq z \leq 9.0$ cm and a pure outgoing traveling wave that propagates to the right. This indicates the effectiveness of the conducting disk in absorbing all the output radiation, thus preventing the wave from reflecting back to the cavity.

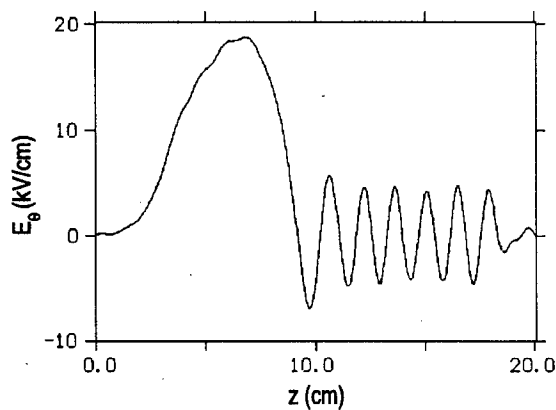


Fig. 5. Self-consistent TE_{021} electric field profile after the time of saturation

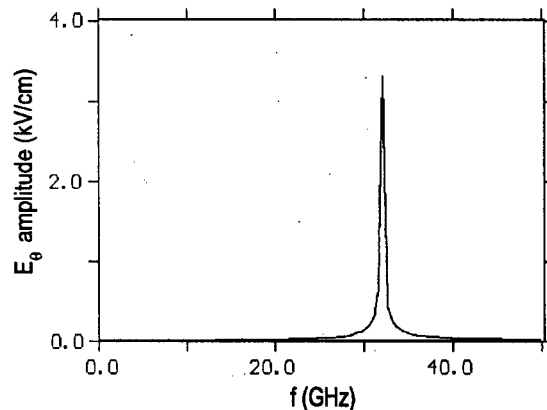


Fig. 6. Frequency spectrum at the point $r=1$ cm, $z=17$ cm in the output guide

The associated frequency spectrum of the electric field at $r=1.0$ cm, $z=17.0$ cm is given in Fig. 6, which is characterized by a single-frequency component peaked at 32.03 GHz, being slightly above the 31.90 GHz cutoff frequency of the regular section of the waveguide cavity with radius 1.05 cm. Fig. 7 shows the time history of the output power as determined by integration of the Poynting flux across the observation section at $z=17.0$ cm. We see that the production of RF power saturates at a time around 48 ns, reaching a peak value of 110 kW which translates into a conversion efficiency of 50% for a 44-keV, 5-A beam with injection pitch-ratio of 1.4. A parameterization of the gyrotron's settings were carried out to determine how sensitive the

output power is to changes in pitch ratio and beam current.

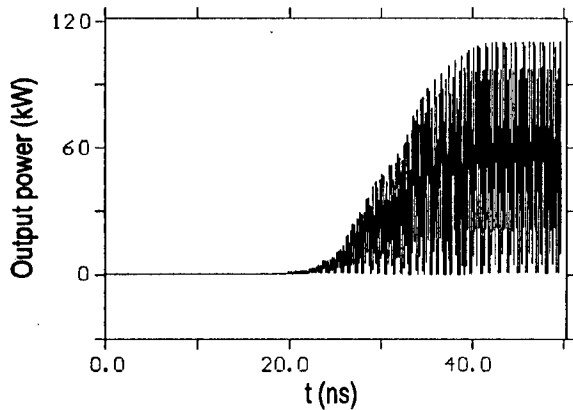


Fig. 7. Time history of the output power measured at the section $z=17.0\text{cm}$

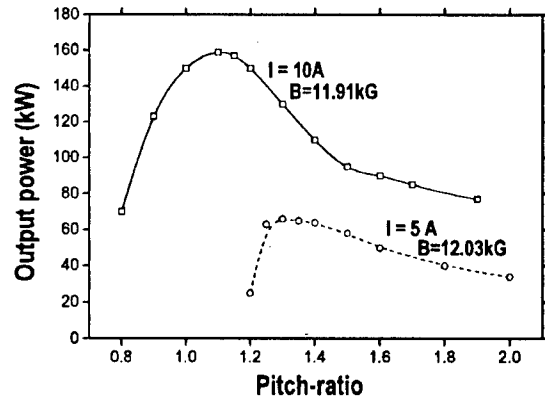


Fig. 8. Simulated pitch-ratio parameterization of the 32GHz gyrotron

The results of this study are presented in Fig. 8 which shows the output power as function of the pitch ratio with the beam current as a parameter. The output power was optimized with respect to the applied magnetic field, and we see that the maximum values of both output power and efficiency increase with beam current.

Conclusion

The operation of 32GHz gyrotron was examined using an electromagnetic PIC code that provided a comprehensive picture of cyclotron resonance interaction of TE-mode cavity fields with a helical electron beam. That the relativistic angular bunching dominates over the axial bunching (that originates with the RF magnetic force) can best be seen by evaluating the ratio of axial to relativistic angular bunching rates which may be expressed as $(f_R/f_B)(1 - f_c^2/f_R^2)$, where $f_B = 2.8B(kG)/\gamma_0$, f_R is the cavity resonance frequency, and f_c is the TE_{02} -mode cutoff frequency. Taking $f_R = 32.03\text{GHz}$, $f_c = 31.90\text{GHz}$, $f_B = 31.10\text{GHz}$ ($B=12.03\text{kG}$, injection energy $=44\text{keV}$) the bunching ratio is of the order of 10^{-3} , and therefore the relativistic mass shift is responsible for the gyrotron interaction mechanism.

Acknowledgment

K.G. Kostov and R.A. Corrêa would like to thank FAPESP (Brazil) for financial support.

References

- [1] P.A. Lindsay, "Gyrotrons (electron cyclotron masers): different mathematical models", *IEEE Journal of Quantum Electronics*, vol. QE-17(8), pp. 1327-1333, 1981.
- [2] M. Caplan, A.T. Lin, and K.R. Chu, "A study of the saturation output of a TE_{01} gyrotron using an electromagnetic finite size particle code", *Int. J. Electronics*, vol. 53(6), pp. 659-671, 1982.
- [3] A.T. Lin, Z.H. Yang, and K.R. Chu, "Particle simulation of a high-power gyrotron oscillator", *IEEE Trans. Microwave Theory Tech.*, vol. 16(2), pp. 129-134, 1988.
- [4] V.P. Tarakanov, "User's Manual for code KARAT", Berkeley Research Associates, Inc., Springfield, VA, USA, 1994.
- [5] C.K. Birdsall, "Particle simulation techniques for beam devices", in *High-Power Microwave Sources*, ed. by V.L. Granatstein and I. Alexeff, Norwood, MA: Artech House, 1987, Chapter 3.
- [6] J.J. Barroso, P.J. Castro, A.A. Pimenta, V.A. Spassov, R.A. Corrêa, T. Idehara, and I. Ogawa, "Operation of a 32GHz gyrotron", *Int. J. Infrared Millimeter Waves*, vol. 18(11), pp. 2147-2160, 1997.

2D SIMULATION OF FUEL IN TARGET INDIRECT-DRIVEN BY PROTON BEAM

By Keishiro. Niu

Teikyo Heisei University
Uruido, Ichihara, Chiba 290-0193, Japan

ABSTRACT

To investigate the non-symmetric effects on the implosion motion and the stabilities of the burning wave in the fuel layer in a target, two-dimensional simulations are carried out by using the spherical coordinate. The phenomena are assumed to be symmetric around the polar axis. For the case in which the implosion is not spherically symmetric and the real implosion center is deviated from the spherical center, the value of radius r is allowable to take a negative value for a given direction.

The results show that the non-symmetric implosion motion invites the increase in the local fuel temperature and density. Thus the burning fraction rather increases with the non-symmetric degree of the implosion motion of the fuel in the case of a target with a practical size for fusion.

1. INTRODUCTION

Through experimental research using large laser facilities, target physics are becoming clear for both direct- and indirect-driven targets (McCrory 1991; Storm 1991; Yamanaka 1991). One dimensional simulations have been carried out to clarify the mechanism of the implosion of the spherical target (Niu *et al.* 1988; Deutsch *et al.* 1989; Hoffmann *et al.* 1989; Niu 1993).

To investigate the symmetry and stabilities of the implosion motion of the target, two dimensional simulations must be applied to the target. Recently, an analysis has been made for an indirect-driven reactor target (Tahir & Deutsch 1991), besides the small target (Murakami & Meyer-ter-Vehn 1991a, 1991b; Tahir & Arnold 1991).

Because spherical symmetric beam irradiation on a target surface is not expected in the case of proton beam, the target should be an indirect-driven one and have a large radius. Here, the target consists of two shells and five layers; tamper, radiator, radiation gap, pusher and fuel. The total radius of the target is $r_t = 8.716\text{mm}$. The DT fuel mass 23mg is included in the target. The target is irradiated by the six proton beams, whose beam energy is 12MJ, pulse width 30ns, and particle energy 4MeV. According to the one-dimensional simulations, eighty percent of the beam energy deposits in the radiator layer. The temperature of the radiator layer increases from 8K to 1.61keV and the radiator layer emits soft X-rays. The pressure of the aluminum pusher (absorber) reaches 10^{12} Pa at $T_{Al} = 200\text{eV}$. This pusher pressure accelerates the solid DT fuel toward the target center. At 3ns after the acceleration, the implosion velocity of the DT fuel arrives at $u = 3 \times 10^5\text{m/s}$. The supersonic flow of fuel in the decreasing cross section inside the void of the target compresses the fuel adiabatically. Finally, the fuel has the density $\rho_f = 220\rho_s$ (solid density), the temperature $T_f = 4\text{keV}$, and the fusion parameter $\langle \rho_f R \rangle = 35\text{kg/m}^2$. The burn fraction of the fuel arrives at 35%. Thus, a target yields the fusion output thermal energy of 3GJ.

This article wants to show the non-symmetric effects on the implosion of the target. From the limitation of the memory size and the computational time of our computer, the implosion motion of the fuel layer in the target is analyzed by two dimensional simulations. The fuel layer is divided into pieces with respect to the radial direction and azimuthal directions. the most inner layer represents the vapor one at the central part of target and the most outer layer represents the Aluminum pusher layer surrounding the fuel.

2. GOVERNING EQUATIONS

The governing equations are the equation of continuity,

$$\frac{\partial \rho}{\partial t} + \nabla \cdot \rho \mathbf{v} = 0 \quad (1)$$

equation of motion,

$$\rho \frac{\partial \mathbf{v}}{\partial t} + \rho \nabla \frac{1}{2} v^2 + \rho \mathbf{v} \times (\nabla \times \mathbf{v}) = -\rho \mathbf{F} - \nabla p + \mu \Delta \mathbf{v} \quad (2)$$

and equation of energy,

$$\rho \left\{ \frac{\partial e}{\partial t} + (\mathbf{v} \cdot \nabla) e \right\} = -p \nabla \cdot \mathbf{v} + \nabla \cdot \mathbf{J} + S \quad (3)$$

Here ρ is the density, t the time, \mathbf{v} the velocity, \mathbf{F} the force, p the pressure, μ the coefficient of artificial viscosity, e the internal energy, \mathbf{J} the thermal flux, and S the energy source.

In our case, $\mathbf{F} = 0$. For a low temperature T , the thermal flux \mathbf{J} is usually expressed with the coefficient of thermal conductivity λ as $\mathbf{J} = \lambda \nabla T$. Here, however, \mathbf{J} is expressed using the flux limiting theory by

$$\mathbf{J} = f \left(\frac{3mT}{2k} \right)^{1/2} e \quad (4)$$

where m is the particle mass, k the Boltzmann constant and e the unit vector toward the temperature gradient. The modification factor f is chosen as $f = 0.1$.

As the energy source S , thermal energy released by fusion reaction is taken into account,

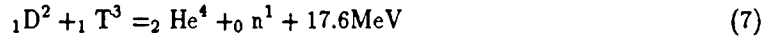
$$S = \frac{E_a}{4} \left(\frac{\rho}{m} \right)^2 < \sigma v > \quad (5)$$

where $< \sigma v >$ is the mean value of the product of the cross-sectional area of the fusion reaction and relative velocity. Usually $< \sigma v >$ is expressed by

$$< \sigma v > = 3.68 \times 10^{-12} \left(\frac{1.16 \times 10^7}{T} \right)^{-2/3} \exp[-19.94 \times \left(\frac{1.16 \times 10^7}{T} \right)^{-1/3}] \quad (6)$$

as a function of the temperature $T(K)$.

The equation for DT fusion reaction is



The reaction energy 17.6MeV releases as the kinetic ones of α (He) particle and the neutron n . The energy is divided into kinetic energies of two particles in such a way that the total momentum is zero. Thus the kinetic energy E_a which α particle has is

$$E_a = 17.6\text{MeV} \times \frac{1}{5} = 3.52\text{MeV} = 5.64 \times 10^{-9}\text{J} \quad (8)$$

The neutron which has 14.1MeV escapes from the plasma because it has no charge.

As the equations of state among p, ρ, e, T , data in SESAME Library are referred. The followings are our approximations.

$$\left. \begin{aligned} p_1 &= 5.405 \times 10^3 \rho T \\ x &= \ln\left(\frac{\rho}{1.0 \times 10^3}\right), \quad z = 1.6 + 1.795x - 0.1132x^2, \quad p_2 = 1.0 \times 10^9 \exp(2.302z) \\ p &= \max(p_1, p_2) \end{aligned} \right\} \quad (9)$$

$$\left. \begin{aligned} e_1 &= 3.625 \times 10^4 T \\ x &= \ln\left(\frac{\rho}{1.0 \times 10^3}\right), \quad z = 1.3 + 1.256x + 0.0896x^2, \quad e_2 = 1.0 \times 10^6 \exp(2.302z) \\ e &= \max(e_1, e_2) \end{aligned} \right\} \quad (10)$$

$$T = \frac{e}{3.625 \times 10^4} \quad (11)$$

The governing equations are transformed to the Lagrangean forms as

$$\rho \frac{\partial \mathbf{v}}{\partial t} = -\nabla p + \mu \Delta \mathbf{v} \quad (12)$$

$$\begin{aligned} \rho \frac{\partial e}{\partial t} &= -p \nabla \cdot \mathbf{v} + f \left(\frac{3m}{2k} \right)^{1/2} e \nabla T^{1/2} \cdot \mathbf{e} \\ &+ 2.659 \times 10^{-26} \left(\frac{\rho}{m} \right)^2 T^{-2/3} \exp(-4.514 \times 10^3 T^{-1/3}) \end{aligned} \quad (13)$$

the equation of motion being omitted.

3. TWO DIMENSIONAL FORMS IN SPHERICAL COORDINATE

The governing equations (12) and (13) are expressed in the spherical coordinate (r, θ, ϕ) . To simplify the calculation, the phenomenon is assumed to be independent of ϕ . That is, $\partial/\partial\phi = 0$. The r component of the equation of motion is

$$\rho \frac{\partial v_r}{\partial t} = -\frac{\partial p}{\partial r} + \mu \frac{\partial^2 v_r}{\partial r^2} + \frac{\mu}{r^2} \frac{\partial^2 v_r}{\partial \theta^2} \quad (14)$$

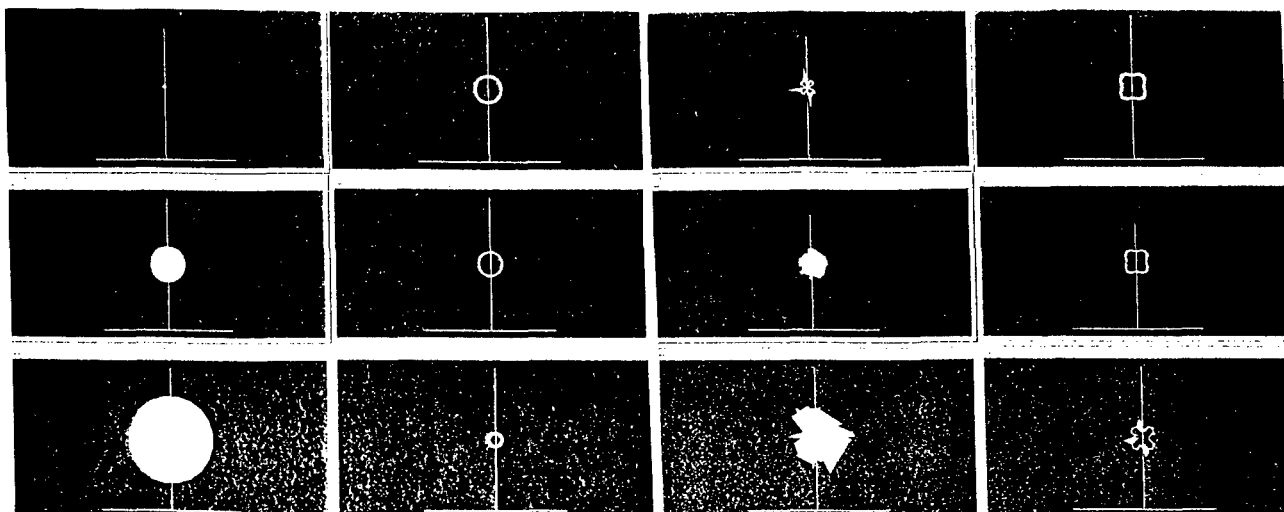


Fig. 1. Spherical implosion.

Fig. 2. Implosion with the third mode.

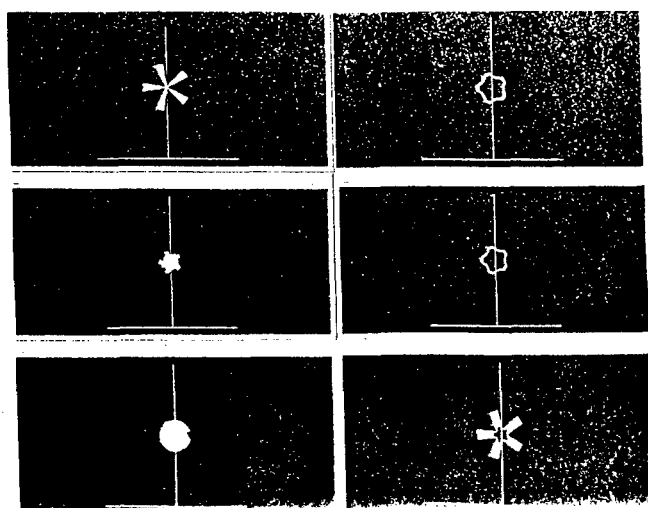


Fig. 3. Implosion with the fourth mode.

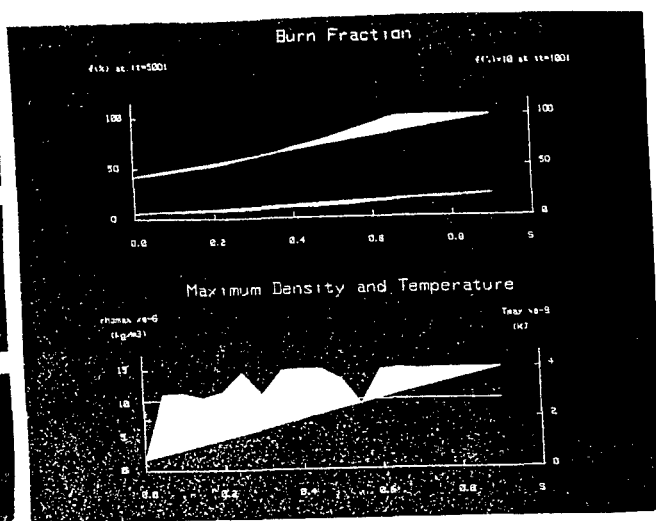


Fig. 4. The maximum temperature, density and the burning fraction versus the degree of in-homogeneity.

The θ component of the equation of motion is

$$\rho \frac{\partial v_\theta}{\partial t} = -\frac{1}{r} \frac{\partial p}{\partial \theta} + \mu \frac{\partial^2 v_\theta}{\partial r^2} + \frac{\mu}{r^2} \frac{\partial^2 v_\theta}{\partial \theta^2} \quad (15)$$

the equation of energy is

$$\begin{aligned} \rho \frac{\partial e}{\partial t} = & -\frac{p}{r^2} \frac{\partial r^2 e T^{1/2}}{\partial r} + \frac{p}{r \sin \theta} \frac{\partial \sin \theta e T^{1/2}}{\partial \theta} \\ & + f \left(\frac{3m}{2k} \right)^{1/2} \left(\frac{1}{r^2} \frac{\partial r^2 v_r}{\partial r} + \frac{1}{r \sin \theta} \frac{\partial \sin \theta e T^{1/2}}{\partial \theta} \right) \\ & + 2.659 \times 10^{-26} \left(\frac{\rho}{m} \right)^2 T^{-2/3} \exp(-4.514 \times 10^3 T^{-1/3}) \end{aligned} \quad (16)$$

4. INITIAL AND BOUNDARY CONDITIONS

The DT fuel in the target has the initial temperature 8K and density 192kg/m³. The fuel layer is divided into meshes regarding to r and θ . The most inner mesh in r represents the saturated vapor which is assumed to have a constant value 7×10^7 Pa inside the DT fuel layer. The most outer mesh in r represents the Aluminum pusher which gives the pressure on the fuel surface to implode. The pusher pressure rises up from zero to 10^{12} Pa during 3ns and keeps constant during 27ns. The fuel layer implodes toward the target center pushed by pusher, compressed and heated, and burns.

5. SIMULATIONS

For simulations, three in-homogeneities are given as follows:

- 1) The pusher pressure with a mode number regarding the azimuthal angle.
- 2) The pusher radius with a mode number.
- 3) The pusher thickness with a mode number.

Simulations are carried out for several mode numbers. Cross-sections of the fuel layer are shown as a function of a sequence of imploding time. Figure 1 shows the spherical implosion. Each snap is drawn for each 10ns. Figure 2 shows the third mode with 15% in-homogeneities for three kinds described above. Figure 3 shows the forth mode. Figure 2 and 3 indicate that cross-section keeps similarity during implosion before arriving at the center. The maximum temperature, maximum density appearing in the fuel layer, the final burning fraction versus the degree of in-homogeneity are drawn in figure 4. The maximum density rather increases with the increase in in-homogeneity.

6. SUMMARY

In this simulation, the void inside the fuel layer is assumed to be filled by the saturated DT vapor at 8K with a constant pressure 7×10^{12} Pa. Our target has a practical size, namely, the fuel mass is 23mg. Although the effect of larger momentum of the pusher is neglected in the simulation, the momentum of the imploding fuel plays a role on fuel compression and heating. Through our simulations, it is turned out that the fuel layer keeps the regular shape before the colliding with itself at the target center, even in the case with in-homogeneities regarding the pusher pressure or the fuel geometrical shape of the fuel layer. Surely more precise two or three dimensional simulations must be carried out to study the effect of non-symmetric implosion on burning fraction of the fuel. But at present it seems that the spherically non-symmetric momentum of the fuel produces the local high density part, which leads to a high burning fraction.

The fuel burning occurs during the expansion of the fuel. In our simulations, the pusher pressure 10^{12} Pa continues during 30ns. The inner surface of the fuel layer arrives at the target center 20ns after the start of implosion. At 60ns after the start of implosion, the burning fraction of the fuel remains in a small value. At 300ns after the start of the implosion, however, the burning fraction reaches unity.

REFERENCES

- Deutsch, C. et al. 1989 *Nucl. Instrum. Meth. Phys. Res.* **A278**,38.
Hoffmann, D. H. H. et al. 1989 *Nucl. Instrum. Meth. Phys. Res.* **A278**, 44.
McCrorry, R. I. 1991 In the *21st ECLIM book of Abstracts*, abstr. I-11.
Murakami, M. & Meyer-Ter-Vehn, J. 1991a *Nucl. Fusion* **31**, 1315.
Murakami, M. & Meyer-Ter-Vehn, J. 1991b *Nucl. Fusion* **31**, 1331.
Niu, K. 1993 *Laser Particle Beams* **11**, 97.
Niu, K. et al. 1988 *Laser Particle Beams* **6**, 149.
Storm, E. K. 1991 In the *21th ECLIM Book of Abstracts*. abstr. I-2.
Tahir, N. A. & Arnold, R. C. 1991 *Phys. Fluids B3*, 1717.
Tahir, N. A. & Deutsch, C. 1991 In the *abstracts of the 10th International Workshop on Laser Interaction Monterey*, 71.
Yamanaka, T. 1991 In the *21th ECLIM Book of Abstracts*, abstr. I-13.

Geometric Methods to Treat Energy Transport Phenomenons

Cord Passow

Kolbergerstr. 28c D-76139 Karlsruhe

Epistemological, the method to consider geometrical forms as a physical paradigm, was founded by A.Einstein 1921. But even in spite of the dispute about the ERP¹ paradox, his notion was not appreciated by technical physicists. For example, Poynting's formula to calculate a magnetoelectro power flow is yet part of their curriculum. Of course, the mathematical procedure is in agreement with the Π -theorem² But the physical theory is not well posed and not proper embedded in the **Minkowski space** $R_M^{(8)}$. Let be Poynting's theory characterized by his at-point integral

$$\int_S \vec{\wp} dS \equiv \int_S (\vec{E} \times \vec{H}) dS = \int_V (\vec{J} \vec{E} dV + \frac{1}{2} \partial_t (\vec{E}^2 + \vec{H}^2)) dV \quad [J/s]$$

Obviously, in the time independent limit, the expressions of magnetoelectro dynamics and statics, are not in agreement. Moreover, the current term $\vec{J} \vec{E}$ is neither nor supported by **I. Newton's kinetic** or **H.Lorentz's field forces**,. The so called Poynting vector $\vec{\wp} = \vec{E} \times \vec{H}$, representing an energy flux, can not be understood phenomenological. Therefor, here a system theory is presented, to combine fluid and magnetoelectro dynamics in **Liouville's phase-space**. $\{\vec{x}, \vec{v}\} \in R_f^6$, with $\vec{x} = \{x_1, x_2, x_3\}$; $\vec{v} = \{\dot{x}_1, \dot{x}_2, \dot{x}_3\}$.

1.1 Spatial-time or Phase-space Embedded Fields: I.Newton's kinetic, based on the natural law **action equals reaction**, is describing acceleration and the bending of trajectories of ponderable objects. It is embedded in the **time space** $R_t \subset R_M^{(8)}$; L.Euler's current in the **spatial-time space** $\mu \mapsto \{\vec{x}, t\} \in R_\mu^4$. space $\{\vec{x}, t\} \in R_\mu^4$. Consequently I.Newton's law must be **argument transformed** to get L.Euler's and H.Lorentz's laws. An argument map, is based on the equality of functions with exchanged implicit variables $\psi(t(x)) \equiv \psi(x(t))$. But precautions must to be taken if differentials of **Minkowski functions** are considered. Let the acceleration law be written as $m \partial_t \vec{v}(t) = K(t)$; and $\vec{v}(t(x)) \equiv \vec{v}(x(t))$; $\partial_t x(t) = \vec{v}(t)$; $m(\vec{v}) = m(1 - \beta^2)^{-1/2}$ with $\beta = v/c$; ; **c** the **principle velocity limit**. In the case *limes* $\vec{v} \mapsto 0$, the kinetic and the ponderable mass are identical. Now, comparing the time derivation of I.Newton's and L.Euler's velocity representation $\partial_t x(t) = \vec{v}(t)$, and $\vec{v} = \vec{v}(x)$, it follows

$$\partial_t \vec{v}(t) = \partial_x \vec{v}(x) \partial_t x(t) \equiv \vec{v}(x) \partial_x \vec{v}(x) \quad \text{with} \quad \vec{v}(x) \in R_x^3 \quad [1]$$

Argument mapping is needed also to embed magnetoelectro time differentials in the R_f^6 as $\partial_t D(\mu) \mapsto \underline{D}(\nu) \in M_\nu$ and $\partial_t B(\mu) \mapsto \underline{B}(\nu) \in M_\nu$. The vector components in the direction of the cartesian unit vector $\{u_1, u_2, u_3\}$ are given by terms of the type $\partial_{x_i} D_n \nu_i u_n$ with $i, n = 1, 2, 3$.

1.2 The Phase-space Embedded Magnetoelectric Dynamic: To treat a plasma flow, it is necessary to embed a fluid theory together with Maxwell's magnetoelectro dynamic in the same topological space. The classical steady-state is embedded in the R_f^6 , what is easy to be done for the flow-lines of a dynamic problem, since they can be embedded in the simplex manifold $M_\mu \mapsto R_x^3$, considering local movements as Lie's mobility. Similar, a steady-state magnetoelectro dy-

dynamic can be constructed with $\partial_t \vec{D}(\mu) \mapsto \vec{D}(\nu)$ and $\partial_t \vec{B}(\mu) \mapsto \partial_t \vec{B}(\nu)$. Then the Laplace type

$$\text{Maxwell equational system } 1. \text{curl curl } \vec{H}(\nu) = \text{curl} [\vec{J}(\nu) + \vec{D}(\nu)] \quad [2]$$

$$2. \text{curl curl } \vec{E}(\nu) = -\text{curl } \vec{B}(\nu) \quad 3. \text{grad div } \vec{E}(\nu) = \text{grad } \rho(\nu)$$

also can be embedded in the R^6 . In this form the magnetoelectric equation may be used to calculate the curvature of a magneto electro field out of a scalar field $\rho(\vec{x})$ and a vector current. Now, discussing physical constraints, it is meaningful to apply the div-operator on $\text{curl } \vec{H} - \vec{J} + \partial_t \vec{D} \equiv 0$. Now since $\text{div curl } \psi \equiv 0$, Euler's law of **global continuity** $\text{div} [\vec{J}(\nu) + \vec{D}(\nu)] \equiv 0$ with $\vec{J} = \rho(\vec{x}) \vec{v}(\vec{x})$ follows. If the entire initial conditions are given, with the flux densities \vec{D} and \vec{B} also then this generalized steady-state magnetoelectro equations are well posed. Worth mentioning is, the magnetoelectro field components are natural connected by the **asymplectic symmetry**³.

1.3 Topological Embedding: To implant the system Eq. [2], two point manifolds are needed. The $M_x^3 \mapsto R_x^3$ and the $M_v \mapsto R_v^6$ are necessary. Static and background fields, only parametric dependent on the time, can be embedded direct in the R_x^3 . But moving physical objects, must be embedded in a compact **symplectic manifold**, allowing to construct a directional field pattern to carry a velocity distribution. Moreover since the **canonical field theorem**⁴ of geometric physics allows to express the generalized coordinates $\vec{q} \mapsto \vec{\psi}(\vec{x})$ and $\vec{p} \mapsto \partial_x \vec{\psi}(\vec{x})$ by a **Hilbert pair** of vector functions, it is obvious, physical fibers must be embedded in the $M_x^3 \mapsto R_x^3$. But Maxwell's theory must be embedded in the M_v , to connect any momentum with its local position. Only then, an acceleration process requiring to treat retarding and relativistic effects can be treated properly. Finally, worth to be mentioning is, the mathematical form $\partial_x^2 \Psi$ can have two physical interpretations. In the Schrödinger theory, that of an energy; in a kinetic theory, that of a curvature which is geometrical geometrical spoken, similar to a "one velocity vector component" acceleration.

2.1 Evolutionary development of Steady-state Fields: Different, as in a at-point theory, geometric physics is used to calculate global physical curves by an evolutionary process. Following A.Einstein, a Laplace type equations, with an **actuator enforcing** curvatures is used. Let be

$$\Delta \vec{\Psi}(\vec{x}, t) + \vec{\mathfrak{K}}(\vec{x}, t) + \vec{\mathfrak{K}} \equiv 0 \text{ with } \vec{\mathfrak{K}} \text{ the actuator and } \vec{\Psi} \text{ the ansatz} \quad [3]$$

Respecting Ref. [2], then $\vec{\Psi}(\vec{x}) \mapsto \vec{q}(\vec{x})$ and $\partial_x \vec{\Psi}(\vec{x}) \mapsto \vec{p}(\vec{x})$ can be interpreted as a **Hilbert coordinate pair** of generalized canonical geometrical coordinates. In the following context linear theories are used by didactic reasons only, that means vector and scalars functions will not be different denoted in the following. Worth to be mentioning is, Eq. [3] is not considered as an **at-point** equation and therefor not solved by integration. As assumed to be derived out of a Poincaré **Lagrange functional**, the Eq. a[3] is used to calculate **momentum-map**⁵ fibers $f(\vec{x})$ with the help of an evolutionary theory. Therefor the entire solution of Eq. [3] must be constraint by the rules of: the mathematical curve theory; the initial Lagrange conditions; and the natural **symplectic structure** of nature. This constraints may be demonstrated by the entire solution of a linear Laplace equation

as $\Psi \mapsto f(x) = c_0 + c_1 x - c_2 \partial_x \eta(x) + c_3 \eta(x)$ with $\eta(x)$ a partial solution of Eq. [3]. The Taylor expansion of $\eta(x)$ is to be given by a series, with $\eta_3 x^3$ the lowest power term. To get the physical solution the coefficients of an expanded fiber and those of the expended actuator must be compared. To construct a momentum-map, the matrix of H.Weyl's⁶ symplectic group $Sp(2n, R)$ must be formed. This map is used to transform the transversal coordinate pair $\{q, p\}$ to $\{q, p\}$. The related algebraic equations are

$${}_r q = {}_i q (1 - \partial_x \eta) + {}_r p (x + \eta) \text{ and } {}_r p = -{}_i q \partial_x^2 \eta + {}_i p (1 + \partial_x \eta) \quad [4]$$

The linear part of an ansatz function $f(x) = \eta_0 + \eta_1 x$ are considered as **at-point values**, related to the kinetic initial conditions. To calculate field fibers defined in the R_x^3 , the ansatz function, as well as the actuator function must be a vector function $\Psi(x)$ and the Laplace operator is calculating the **curvature and torsion** of fibers. To emphasize the phase-space aspect of the Laplace theory, it may be mentioned, a linear Laplace equation can be transformed by A.Cohm's⁷ Lie group U_g in A.Vlasov's first order differential equation, to calculate one particle phase-space distributions. But then, results are not given in terms of Hilbert coordinate pairs.

2.2 Step by Step Constructing of Fields: Fiber-lines and auxiliary surfaces $S_x \in R_x^3$ are the elements to construct a $\dim=3$ **field net**, constituting the frame of a momentum-map atlas. Then the net nodes are given by surface points marked by crossing fiber-lines. **Net** and **atlas** are build up step by step calculating charts out of **genetic points** $\Sigma(x) \in {}_i S$. Therefor charts are carrying pictures the function embedded simplex used to define initial conditions. And consequently the the recording surface ${}_r S \equiv {}_r S$ acts also as the following initial surface, and the following matching fiber can be constructed. This must be done step by step untill the atlas end is reached by a continuous fiber-line, which represents a physical curve, an **orbit, trajectory and flux- or flow-line**. Obviously are fibers used to map positions, and if they are constructed following the canonical rules of physics, they are able also, to map arguments of functions, representing a geometric position, as an embedded momentums $mv(x) \mapsto mv(x)$ or Intensities as $\Phi(x) \mapsto \Phi(x)$ from one surface to an other. Now, any initial point $x \in {}_i S$ always is considered as a Hausdorff simplex, carrying three kinds of initial conditions: **kinetical; functional; environmental**; Here it means: Kinetic, Lagrange initial conditions; Functional, Intensity profiles; Environmental, **historical futurity and neighbor** informations. To visualize the construction process of a initial simplex $\Sigma(x) \in R_x^3$, a pull-back sphere with its center at x is imagined. It encloses a very small, at x centered **genetic plane** ${}_o S_x \subset R_x^3$, which is the source of five parallel fibers, constituting a **fiber-bundle** carrying neighbor informations, part of the environmental initial conditions. The distance between two fibers of a bundle must be of the order of ℓ the model **accuracy scale**. Kinetic initial conditions of fibers are to be calculated respecting E.Cartan's geometry, what means, a Hilbert pair is introduced as $\{\psi, \text{curl} \psi\}$ and given by three parameters. A virtual radius vector and the two Euler angles. The angles are fixing the initial direction, and the amount of the virtual vector gives the initial speed value, by applying the curl-operator. For numerical evaluation of a genetic point a fiber bundle and therefor the pull-back sphere must have a finite diameter of the order of ℓ . But an ideal genetic Hausdorff simplex, is received by reducing the pull-back sphere radius to the limes zero. To take boundary conditions into account, fibers are constructed along the model walls.

2.3 Global Continuous Physical Solutions: Respecting the desired accuracy the length of each fiber calculated with the help of a canonical Laplace evolution

equation, represented by a Taylor expansion can be estimated with the help of the standard error term $\varepsilon(\delta x \sim \ell)$. This way, also the position of the following net nodes and therefor, the next atlas surface is fixed. And a fiber bundle can be used to generate a new initial simplex embedded in the ${}_n\mathbf{S}$. The difference form $\delta f(x) \equiv (f({}_i x + \frac{1}{2}\ell) - f({}_i x - \frac{1}{2}\ell))\ell^{-1}$ shows the connection between future and historical initial values. Therefor, if the length of a regular fiber is given by $L({}_i x)$ auxiliary fibers with a little bit shorter or longer length to improve the numerical accuracy may be used. Since two succeeding fibers must be connected continuously it must be true $[(f - \partial_x f)(\partial_x^2 f - \partial_x^3 f)][(f - \partial_x^3 f)(\partial_x^2 f - \partial_x f)]^{-1} = a$ with $a = 0 \vee 1 \vee \infty$, Staudt's (1798) continuity theorem. And the 3rd order derivation of a fiber must exist. Consequently, the curvature and torsion terms are included also. Now at any point ${}_i x \equiv {}_i x \in {}_n\mathbf{S}_x$ the kinetic initial conditions of the succeeding fiber are defined. If there are no acceleration forces present in the evolution direction, the balance of the total momentum is found with $\text{div } p(x) \equiv 0$ the invariance law at the point ${}_i x$. In the case of a very powerful acceleration or deceleration process the kinetic mass can be corrected with the help of the law of energy conservation. Respecting Laplace magnetoelectro dynamics, worth mentioning is, the vector fields can not be split with respect to Gibbs corollary into a curl-free and a div-free part. This since obviously, equations like $\text{div } D(\vec{x}) = \rho(\vec{x})$ are physical laws, connecting two fields of different structure. However, Maxwell's construct is a theory.

3.0 The Generation of Numerical Results: Since supercomputers allow to evaluate even complicated systems step by step, to build up a virtual physical models, the basic physical system theory must be designed with respect to the solution theory. Moreover it must be possible to control resulting predictions with respect to their qualitative correctness and numerical accuracy. In the frame of the here proposed technique, the **calculation procedure** is divided into the phases: **1.** set up of the initial conditions; **2.** Calculating the flux field; **3.** calculating the intensity distributions. The **initial conditions**, necessary to construct the first atlas surface, may be taken from experimental results and/or from auxiliary models. To test the **model accuracy**, local and global invariance principles, defined at point or by finite surface or volume integrals can be used. Finally it has to be mentioned, the here described method allows to investigate at point disturbances, as attractors, bifurcations, that means the influence of critical phase-space points related to background, as well as calculated fields. Self-consistent effects can be taken into account by subroutines.

Especially thankful am I to Z. Zinamon Israel, E.Binz Mannheim FRG and S Sternberg Israel/USA for helpful discussions, and instructions, also G Kessler Forschungszentrum Karlsruhe FRG for supporting this work.

References:

1. A.Einstein, B.Podolsky, N. Rosen Phys. Ref. 47, 77 (1935).
- 2 Buckingham Federmann (1911/1915). Theorem of dimensional analysis.
3. S. Sternberg et al., University Cambridge Boston (1975-1984).
- 4.J.v.Neumann; Mathematische Grundlagen (1932), M. Stone; Linear transf. in Hilbert space, Am. Math. Soc. Colloq. Vol.15 - (1932).
5. E. Courant; H.Snyder; Anals of Pys. 3, 1, 1958.
- 6 H. Weyl; Princeton Univ. Press N.J., (1942).
7. A.Cohm, An introduction to the Lie Groups (Heath Boston 1911).
- 8 C. Passow, Laser + Particle Beams Vol. 6 p 579 (1988); Anals de Fisica, Momogr. (1992); Optic 93, 127 (1993).

KADI2D – A PARTICLE-IN-CELL CODE BASED ON FINITE-VOLUME METHODS

C.-D. Munz ¹, P. Omnes, R. Schneider,
E. Sonnendrücker ², E. Stein, U. Voß ³, T. Westermann ⁴

*Forschungszentrum Karlsruhe — Technik und Umwelt,
Institut für Neutronenphysik und Reaktortechnik,
Postfach 3640, D-76021 Karlsruhe*

1. INTRODUCTION

Pulsed-power diodes have been developed at the Forschungszentrum Karlsruhe [3] and are the objects of extensive experimental [4] as well as numerical [14, 11] investigations. The electrical behavior of the diodes is substantially influenced by a charged particle flow forming a non-neutral plasma inside these devices. A detailed understanding of the fundamental time-dependent phenomena (e.g., the origin of instabilities) caused by this plasma requires the solution of the Maxwell-Lorentz equations for realistic configurations with a very accurate replica of the border of the domain, where several kinds of boundary conditions are imposed. An attractive method to attack this non-linear equations numerically is the particle-in-cell (PIC) technique [7, 2]. As a preliminary to use the PIC approach, the relevant diode domain has to be covered by an appropriate computational mesh. Therefore, we adopt a grid model based on boundary-fitted coordinates resulting in a quadrilateral mesh zone arrangement with regular data structure.

The numerical solution of the Maxwell equations in time domain is obtained by using a finite-volume (FV) approach on a non-rectangular quadrilateral mesh in two space dimensions. A very favorable property of these modern FV schemes consists in the fact that they combine inherent robustness at steep gradients with accurate resolution [8]. In the context of self-consistent charged particle simulation in electromagnetic fields the coupling of a high-resolution FV Maxwell solver with the PIC method is a new way of approximation [11].

2. NUMERICAL MODEL FOR THE MAXWELL-LORENTZ EQUATIONS

The PIC approach circumvents the direct force calculation between charged particles by introducing a grid-based and a mesh-free numerical model: On the computational mesh the spatial and temporal evolution of the electromagnetic field generated by all charges are determined, whereas the charged particles themselves are advanced in the continuous computational domain. The evolution of the electromagnetic fields is given by the vacuum Maxwell equations

$$\partial_t \mathbf{E} - c^2 \nabla \times \mathbf{B} = -\frac{\mathbf{j}}{\epsilon_0} \quad ; \quad \partial_t \mathbf{B} + \nabla \times \mathbf{E} = 0, \quad (2.1a)$$

$$\nabla \cdot \mathbf{E} = \frac{\rho}{\epsilon_0} \quad ; \quad \nabla \cdot \mathbf{B} = 0, \quad (2.1b)$$

where \mathbf{E} , \mathbf{B} , ρ and \mathbf{j} denote the electrical field, the magnetic induction, the charge and current density, respectively. The basic features applied for the numerical approximation of these equations are summarized in the subsequent sections.

¹Inst. f. Aero- und Gasdynamik der Universität Stuttgart, Pfaffenwaldring 21, D-70550 Stuttgart

²Université Henri Poincaré Nancy I, Inst. Elie Cartan, B.P. 239, F-54506 Vandoeuvre les Nancy Cedex

³Centre de Mathématiques Appliquées, Ecole Polytechnique, F-91128 Palaiseau Cedex

⁴Fachbereich Naturwissenschaften der FH Karlsruhe, Postfach 2440, D-76012 Karlsruhe

The dynamics of the charged particle ensemble inside the domain is determined by solving numerically the relativistic Lorentz equations

$$\dot{\mathbf{x}}_k(t) = \mathbf{v}_k(t), \quad \dot{\mathbf{p}}_k(t) = \mathbf{F}(\mathbf{x}_k, \mathbf{v}_k, t) \quad (2.2a)$$

$$\mathbf{F}(\mathbf{x}_k, \mathbf{v}_k, t) = Q_k[\mathbf{E}(\mathbf{x}_k(t), t) + \mathbf{v}_k(t) \times \mathbf{B}(\mathbf{x}_k(t), t)], \quad (2.2b)$$

where the index k runs over the total number N_p of charges. For that, we apply the second-order accurate, time-centered leapfrog-scheme introduced by Boris [5]. The Lorentz force (2.2b) acting on the charge Q_k is responsible for the redistribution of the particles and depends on the electromagnetic fields at the actual phase space coordinates $(\mathbf{x}_k, \mathbf{v}_k)$ of the k th charge.

The link between the grid-based and mesh-free model is established by interpolating the fields onto the particle positions and by locating the charges with respect to the mesh zones of the computational grid. Both actions are carried out by applying the standard area-weighting interpolation scheme extended to boundary-fitted, quadrilateral grid zones [13]. The charge and current density assignment to the nodes of the computational mesh yields finally the sources $\rho = \rho(\mathbf{x}, t; \mathbf{x}_k, \mathbf{v}_k, Q_k)$ and $\mathbf{j} = \mathbf{j}(\mathbf{x}, t; \mathbf{x}_k, \mathbf{v}_k, Q_k)$ for the subsequent iteration cycle.

3. FINITE-VOLUME METHOD FOR THE MAXWELL EQUATIONS

The relevant formulation for the construction of FV schemes is the conservation form of the Maxwell equations [12]

$$\partial_t \mathbf{u} + \sum_{i=1}^D \partial_{x_i} \mathbf{f}_i(\mathbf{u}) = \mathbf{q}, \quad (3.3)$$

relying on the time-dependent equations (2.1a) only. In the present description we restrict ourselves to two space dimensions ($D = 2$) and, hence, the vector of the electric field and magnetic induction $\mathbf{u}(\mathbf{x}, t) = (E_1, E_2, E_3, B_1, B_2, B_3)^T$ is independent of the x_3 coordinate. However, when deriving FV schemes this is not a serious limitation since the extension of the methods to the three-dimensional case, for instance, on tetrahedral meshes is straightforward. An interesting aspect of the form (3.3) is that the differential operator is now considered as the divergence applied component-by-component to the physical flux $\mathbf{f}_i(\mathbf{u}) = \mathcal{K}_i \mathbf{u}(\mathbf{x}, t)$, where the \mathcal{K}_i are constant (6×6) -matrices [12]. The source term \mathbf{q} in (3.3) does not depend on \mathbf{u} and is essentially given by the current density. As mentioned earlier, the computational domain is discretized by a set of quadrilateral mesh elements C_i with the area V_i . Introducing the average \mathbf{u}_i^n over the element C_i at time $t = t^n$ according to $\mathbf{u}_i^n = \frac{1}{V_i} \int_{C_i} \mathbf{u}(\mathbf{x}, t^n) dV$, integrating each component of the homogenous equation (3.3) over the space-time volume $C_i \times [t^n, t^{n+1}]$ and applying Gauß's theorem, we get the explicit FV scheme in conservation form

$$\mathbf{u}_i^{n+1} = \mathbf{u}_i^n - \frac{\Delta t}{V_i} \sum_{\alpha=1}^4 \mathbf{G}_{i,\alpha}^{n+1/2}, \quad (3.4)$$

where the numerical flux $\mathbf{G}_{i,\alpha}^{n+1/2} \approx \frac{1}{\Delta t} \int_{t^n}^{t^{n+1}} \int_{S_{i,\alpha}} [n_{i,\alpha}^{(1)} \mathbf{f}_1(\mathbf{u}) + n_{i,\alpha}^{(2)} \mathbf{f}_2(\mathbf{u})] dS dt$ is an appropriate approximation of the physical flux normal through the side $S_{i,\alpha}$ of C_i . Furthermore, $\Delta t = t^{n+1} - t^n$ and $n_{i,\alpha}^{(j)}$ abbreviates the j th component of the outwards directed unit normal at $S_{i,\alpha}$. To incorporate the source terms into the FV algorithm (3.4) a splitting method proposed in [9] is applied.

It is obvious that the explicit FV scheme (3.4) is completely declared if the numerical flux is specified as a function of u_i^n . To carry out this main task in the context of FV approximation, we compute the numerical flux with the aid of the solution of a Riemann problem (RP), which is an initial value problem with piecewise constant initial data [8, 12]. In the present case of the linear hyperbolic equations (3.3) the exact solution of the RP can be determined with the theory of characteristics. By the use of this solution, the local structure of wave propagation is directly incorporated into the numerical approximation, being the reason that the scheme is inherently very robust and able to resolve steep gradients without generating spurious oscillations.

A conclusive advantage of the RP based FV approach is the proper specification and implementation of boundary conditions. This is achieved by formulating an inverse RP whose solution yields the proper values which are prescribed at the border of the domain. A detailed description of these techniques including the numerical realization of physically occurring as well as computationally motivated boundary conditions is given in [12].

The outlined FV scheme is only first-order accurate in both space and time and introduces too much numerical dissipation for practical calculations. To remove this lack, well-established techniques can be applied reviewed, for instance, in [12]. The resulting second-order accurate FV upwind-scheme is algorithmically realized as standard Maxwell solver in the KADI2D simulation program.

4. HYPERBOLIC CHARGE CORRECTION APPROACH

It is a well-known observation, that the different steps of particle treatment introduce numerical errors and, consequently, charge conservation is not guaranteed on this discrete level of approximation. To get out of this numerically caused lack sophisticated correction techniques to enforce Gauß's law have been proposed [6, 5, 10]. Here, we describe the correction of the electric field, as the discrepancy in charge conservation only affects this quantity. For that, we introduce the Lagrange multiplier Φ similar to Assous et al. [1], retain Faraday's law and replace Ampère's and Gauß's law by the strictly hyperbolic problem

$$\partial_t \mathbf{E} - c^2 \nabla \times \mathbf{B} + c^2 \nabla \Phi = -\frac{\mathbf{j}}{\epsilon_0} ; \quad \chi^{-2} \partial_t \Phi + \nabla \cdot \mathbf{E} = \frac{\rho}{\epsilon_0} , \quad (4.5)$$

where the magnitude of the parameter χ has to be estimated numerically. This system can be written as a hyperbolic evolution equation in the form (3.3) but now with the vector $\mathbf{U}(\mathbf{x}, t) = (E_1, E_2, E_3, B_1, B_2, B_3, \Phi)^T$. A detailed analysis of this system reveals that the information of correction does not spread out with infinite speed but with finite velocity χc , where χ is assumed to be larger than one. Empirically, we found out that χ has to be chosen between two and four, leading to a severe restriction of the time step size given by the CFL-condition. Nevertheless, an efficient solution for large values of χ is possible by splitting up the system (4.5) (plus Faraday's law) into the evolutionary Maxwell equations and a correction system, containing all the terms involved by the Lagrange multiplier [12]. Then, a sub-cycling procedure for the correction system can easily be incorporated into the existing FV Maxwell solver resulting in an efficient hyperbolic correction scheme, being more the 20 % faster than the implicit charge correction approximation [5]. Furthermore, the hyperbolic correction approach is parallel in nature and, consequently, fitting in an excellent manner in our parallelization endeavor of KADI2D.

The importance of electrical field correction is explicitly seen in Fig. 4.1, where an electron beam is emitted at the cathode ($x = 0$) and accelerated to the anode ($x = 0.1\text{m}$)

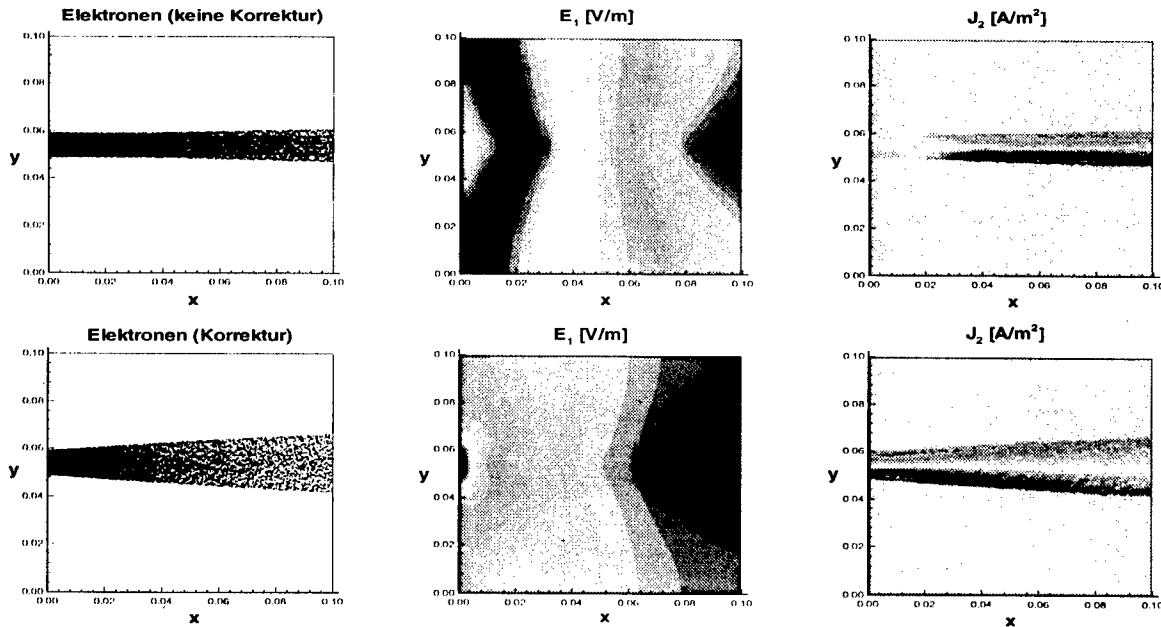


FIGURE 4.1. Self-consistent electron beam simulation in an external applied electrical field without charge correction (upper row of plots). The results enforcing charge conservation by the hyperbolic correction technique ($\chi = 3$) are given in the lower sequence of pictures.

under the action of a constant external field E_1 . The upper three plots show the simulation results where no charge correction is performed: The electron distribution indicates constriction and filamentation of the beam while nonphysically gradients are observed in the electrical field both as a consequence of numerical errors in charge conservation. The situation is drastically improved towards physical reliance (lower row) performing the proposed strictly hyperbolic charge correction with $\chi = 3$.

REFERENCES

- [1] F. Assous et al.; J.Comput. Phys., **109**: 222-237 (1993).
- [2] C. Birdsall, A. Langdon; Plasma Physics via Computer Simulations; McGraw-Hill, NY, 1985.
- [3] H.-J. Bluhm et al.; BEAMS'90, Novosibirsk, 1990.
- [4] H.-J. Bluhm et al.; IEEE Trans. Plasma Sci., **80**: 995 (1992).
- [5] J. Boris; Proc. 4th Conf. Num. Sim. Plasmas, Washington DC, 1970.
- [6] J. Eastwood; Comp. Phys. Commun., **64**: 252-266 (1991).
- [7] R. Hockney, J. Eastwood; Computer Simulations using Particles; McGraw-Hill, NY, 1981.
- [8] R. LeVeque; Numerical Methods for Conservation Laws; Birkhäuser, Basel, 1990.
- [9] G. Marchuk; Methods of Numerical Mathematics, Springer, NY, 1975.
- [10] B. Marder; J.Comput. Phys., **68**: 48-55 (1987).
- [11] C.-D. Munz et al.; appears in: Int. J. Numer. Meth. Engng., 1998.
- [12] C.-D. Munz et al.; appears in: SIAM J. Sci. Comput., 1998.
- [13] T. Westermann; J.Comput. Phys., **101**: 203 (1992).
- [14] T. Westermann; Int. J. Num Mod. **7**: 43-67 (1994).

SIMPLE MODEL OF MAGNETIC SELF-INSULATION FOR SIMULATION OF NON-UNIFORM TRANSMISSION LINES

A.V.Gordeev*, S.Semushin, A.S.Chuvatin

Laboratoire de Physique des Milieux Ionisés, Ecole Polytechnique, 91128 Palaiseau, France

**Russian Research Centre "Kurchatov Institute" 123182, Moscow, Russia*

The vacuum coaxial transmission lines with conducting electrodes and a gap between them of the order of some cm may be used to transport electromagnetic pulses from its generation side to the load. However, the propagation of megavolt-range electromagnetic pulses through vacuum coaxial lines leads to the explosion of microtips and the intense emission of electrons as a result of the high radial electric fields at the surface of the negative electrode $E \sim 10^5$ V/cm [1,2]. Electrons do not strike a positive electrode in case of sufficiently high magnetic field $B_\phi > E_r$ inside transmission line, thus providing a magnetic insulation effect [1,2]. Because of the appearance of electrons in the interelectrode gap, the energy transport can be reduced to the simultaneous propagation of electromagnetic fields and electron flows. In [1-4] the minimum energy principle was formulated and further the wave regime of the magnetic self-insulation was analyzed theoretically and experimentally, so giving a possibility to investigate basic processes in MITL. These processes are accompanied by electron leakage and the current and energy losses. The most simple and effective tool for the description of the magnetic self-insulation wave is the telegraph equations. They were firstly introduced in connection with MITL in [5] and then further developed in [6].

Some times ago the POS approach was discovered. It gives a possibility to sharpen the wave front of electromagnetic waves (EMW) by current switching during a very short time. The propagation of EMW through the plasma medium is very important for this and other applications. The propagation of the EMW in vacuum and in plasmas is completely analogous from physical point of view [2]. The vacuum self-insulation can be considered as a usual shock wave, because the evolution condition is fulfilled [1]. It is worth to mention that for some applied problems interesting results were recently described in [7,8]. However, in the consideration of electron equilibrium in an arbitrary MITL configuration we use more general principle of the system energy minimum [1-4]. For modelling of a non-stationary MITL we used fundamental results, described previously in [5] and developed finally a fast numerical tool capable to analyze different MITL geometries.

Physical model

Further on, we will consider the main physical features of the MITL, which are essential for the non-stationary self-insulation phenomena. We assume that the conducting electrodes of the MITL have an infinite conductivity. As it was mentioned above, the most important feature of the megavolt diapason EMW is the explosive emission from the cathode. For such emission and due to the conservation of energy ϵ , momentum \vec{p} , and vortex $\vec{\Omega}$, all these parameters equal zero at the cathode surface. In particular, due to such conservation laws the most natural equilibrium for electrons is the Brillouin one, where $\vec{\Omega} = 0$. However, these conservation laws may be violated as for more complicated configurations, as for instabilities. For example, the violation of the vorticity conservation can be manifested as $\vec{\Omega} \neq 0$, what results in generalized Brillouin equilibrium considered below.

Thus, we will use the hydrodynamic approximation for cold relativistic electrons

$$\frac{d\vec{p}}{dt} = -e\vec{E} - \frac{e}{c}[\vec{v} \times \vec{B}], \quad \frac{\partial n}{\partial t} + \nabla(n\vec{v}) = 0 \quad (1)$$

and Maxwell equations

$$[\nabla \times \vec{B}] = -\frac{4\pi}{c}en\vec{v} + \frac{1}{c}\frac{\partial \vec{E}}{\partial t}, \quad [\nabla \times \vec{E}] = -\frac{1}{c}\frac{\partial \vec{B}}{\partial t}. \quad (2)$$

The equation (1) can be transformed to the form

$$\frac{\partial \vec{p}}{\partial t} + \nabla \gamma mc^2 + \frac{I}{4\pi} \nabla(rB_\phi) + \frac{r}{4\pi c} \left[\frac{\partial \vec{E}}{\partial t} \times \vec{I} \right] = -e\vec{E} \quad (3)$$

where $I = B_\phi / nr$ is the Lagrange invariant, which is equalized in space according to the

earlier developed theory [9]. Let's introduce the dimensionless functions $b = \frac{B_\phi}{B_0}$, $v = \frac{n}{n_0}$, and

dimensionless coordinate $\omega_0 r / c \rightarrow r$. With the help of $B_0^2 = 4\pi n_0 mc^2$, one can obtain the following equations

$$\lambda vr = b - \frac{d}{dr} \frac{\gamma}{v} \frac{d}{dr} (rb), \quad v = \frac{1}{r} \frac{d}{dr} r \left\{ \frac{d\gamma}{dr} + \lambda \frac{d}{dr} (rb) \right\}. \quad (4)$$

$$\text{Here } \gamma = (1 - g^2)^{-1/2}, g = \frac{1}{vr} \frac{d}{dr} (rb), \lambda = \frac{IB_0 c}{4\pi mc^2 \omega_0}, \omega_0^2 = \frac{4\pi e^2 n_0}{m}.$$

As it was shown in [9], these equations can be integrated and the final relation between γ

and the dimensionless current $i = \frac{2eI_a}{mc^3} \ln \left(\frac{r_a}{r_c} \right)$ is given by equations (here I_a is the total current in the MITL)

$$\gamma - 1 = (1 + \lambda i_c) \{ ch\psi - 1 + (s - 1) \psi sh\psi \}, i = (1 + \lambda i_c) s \psi ch\psi \quad (5)$$

Eq. (5) describes the generalized Brillouin equilibrium, which is reduced for $I=0$ to the usual Brillouin equilibrium and the usual minimum current expression [1,2].

One can calculate the energy related to the unit length in the MITL

$$W = 2\pi \int_{r_c}^{r_a} r dr \left\{ n(\gamma - 1)mc^2 + \frac{\vec{B}^2 + \vec{E}^2}{8\pi} \right\} \quad (6)$$

The above results allow presenting the energy expression in the following final form [2]

$$4W = \left(\frac{2I_a}{c} \right)^2 \ln \left(\frac{r_a}{r_c} \right) + \frac{U^2}{\ln \left(\frac{r_a}{r_c} \right)} - \ln \left(\frac{r_a}{r_c} \right) \left\{ r_a E_a + \frac{U}{\ln \left(\frac{r_a}{r_c} \right)} \right\}^2 \quad (7)$$

It is seen from this equation that for the purely vacuum line, where there are no electrons in the line gap, the last term in (7) is zero. In the presence of the electron emitted from the cathode, the influence of such term decreases the total energy W in MITL.

The non-stationary regime of the magnetic self-insulation can be considered starting from equation (2). After introducing of the scalar Φ and vector \vec{A} potentials, (2) can be presented in the form

$$\vec{E} = -\nabla\Phi - \frac{1}{c} \frac{\partial \vec{A}}{\partial t}, \quad \vec{B} = [\nabla \times \vec{A}]. \quad (8)$$

First telegraph equation (TE) can be obtained from the condition $E_t = 0$, where E_t is the tangential component of the electric field on the electrode surface. For the anode this condition gives [5,1,2]

$$\frac{1}{c} \frac{\partial A}{\partial t} + \frac{\partial U}{\partial t} = 0, \quad (9)$$

where A - the total magnetic flux in the MITL per unit. The second TE can be obtained from the r -component of (2) on the anode surface. This gives

$$\frac{\partial Q_a}{\partial t} + \frac{\partial I_a}{\partial z} = -J \quad (10)$$

Here we introduce the electrical charge Q_a and the electron leakage current $J_a = 2\pi r j_r$, per unit length of the MITL. Quite analogous to (10) the TE on the cathode surface can be introduced. It describes the redistribution of the cathode current and can be useful for the non-homogeneous MITL [2].

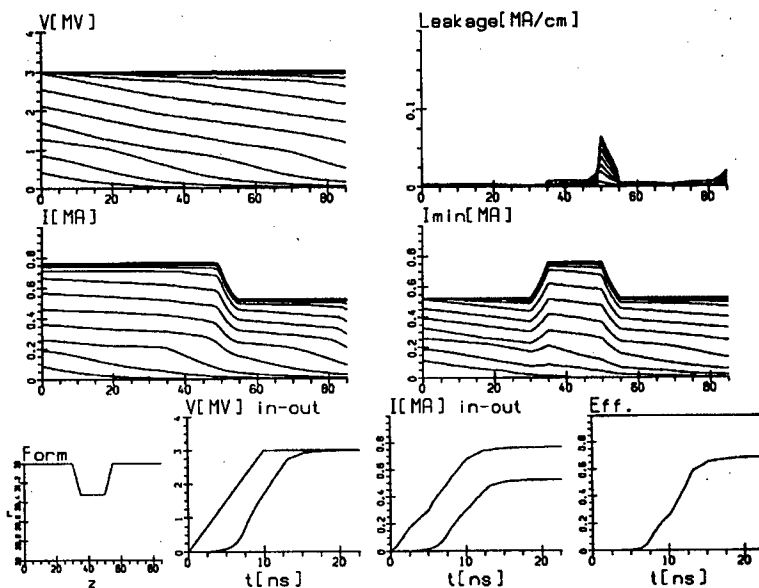


Fig.1 Hot impedance, $\rho_{load} = 5.71 \text{ ohm}$

Numerical method

Usual finite difference approaches do not provide the desired precision for the considered problems, because of possible dispersion and dissipation errors. But here the equations can be easily transformed to a characteristic form. After substitution $Q = C\Phi$; $A = \frac{1}{c}LI$; $\rho = \frac{1}{c}\sqrt{\frac{L}{C}}$

(where ρ - line impedance) we have

$$\frac{\partial f}{\partial t} + B \frac{\partial f}{\partial z} = \varphi \quad ; \text{ where } f = \begin{pmatrix} \Phi \\ I \end{pmatrix}; F = \begin{pmatrix} 0 & 1/C \\ c^2/L & 0 \end{pmatrix}; \varphi = \begin{pmatrix} J/C \\ 0 \end{pmatrix} \quad (11)$$

Left eigenvalues of matrix F and corresponding eigenvectors are $\lambda_{\pm} = \pm c/\sqrt{LC} = \pm c$; $l_{\pm} = (1, \pm \rho)$. Fortunately, here it is possible to integrate the invariants analytically, so we have

$$\left(\frac{\partial}{\partial t} \pm c \frac{\partial}{\partial z} \right) R^{\pm} = -\rho c J + c I \frac{\partial \rho}{\partial z} \quad (12)$$

Classical method of characteristics gives non-monotone solution in the case of discontinuous impedance. So the nonlinear characteristic method was developed. It is based

on the continuity of current and of potential during wave interaction. Such approach gives precise solution in the absence of leakage, but it works perfectly well in general case also.

Simulation results

The proposed numerical approach is applied for the calculations of the non-uniform transmission lines with the current leakage inside the gap. Fig.1 and 2 present the penetration of 3 MV pulse with 10 ns rise time in a complex line with a cylindrical narrowing. Line form, the sets of spatial distributions, and evolutions of parameters at the input and the output of the lines are drawn. Two practically interesting cases of impedance are analyzed. In the case of hot impedance load, the losses are concentrated near the line enlargement, while for high impedance load we have also a leakage at the exit. The comparison with PIC method confirms the precision of simulation.

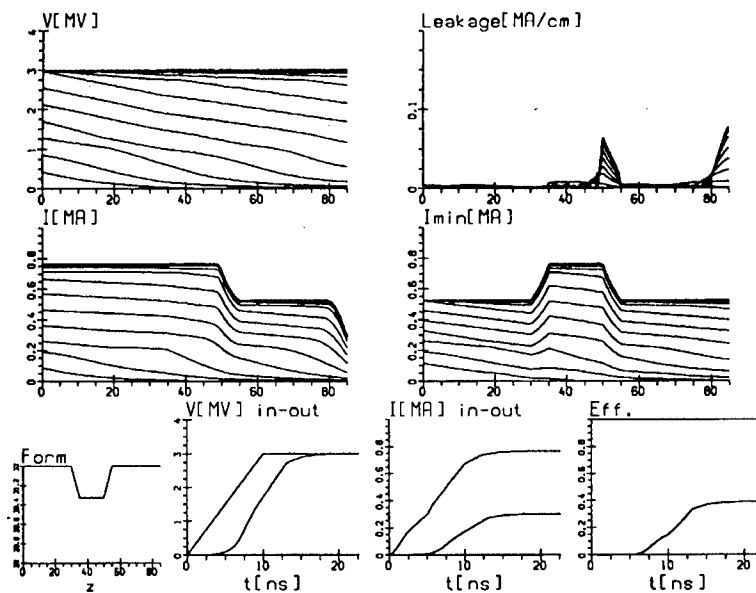


Fig.2 High impedance load, $\rho_{load} = 10 \text{ ohm}$

These results show that the proposed physical and numerical model provides very simple and effective method of simulation for the magnetically insulated transmitting line.

Authors would like to thank to Dr H. Ghalia for fruitful discussions.

References

- [1] A.V. Gordeev, Preprint IAE-3076, 1978; in English: A.V.Gordeev, Magnetic Self Insulation of Vacuum Coaxial Lines, PIIR-12-79, 1979.
- [2] L.I.Rudakov, M.V.Babykin, A.V.Gordeev, B.A.Demidov, V.D.Korolev, and E.Z.Tarumov, in: The Generation and Focusing of the High-Current Relativistic Electron Beams, ed. L.I.Rudakov (Energoatomizdat, Moscow, 1990), p.280.
- [3] A.V. Gordeev, Zh. Techn. Fiz, 1978, v. 48(4), 784-788.
- [4] E.I. Baranchikov, A.V.Gordeev, V.D.Korolev, and V.P. Smirnov, Sov. JETP, 1978, v.75(6), p. 2103-2121.
- [5] E.I. Baranchikov, A.V. Gordeev, V.D.Korolev, V.P.Smirnov, in: Proceedings of 2th Symposium on the collective methods of the acceleration, Dubna,1977, pp.271-274
- [6] V.V. Bulan, V.V. Zazhivikhin, in: Proceedings of 8th Conference on High Particle Beams, Novosibirsk, USSR, 1991, Vol. 2, p.990.
- [7] C.W. Mendel, Jr., M.E.Savage, D.M. Zagar, W.W. Simpson, T.W.Grasser, and J.P. Quintenz, J.Appl. Phys., 1992, v. 71(8), 3731.
- [8] C.W. Mendel, Jr. and S.E. Rosenthal, Phys. Plasmas, 1996, v.3(11), 4207.
- [9] A.V. Gordeev, Plasma Physics Reports, 1997, v.23(2), pp. 92-101.

Comparison of Electrostatic and Time Dependent Simulation Codes for Modeling a Pulsed Power Gun

T. Srinivasan-Rao, J. Smedley

Brookhaven National Laboratory, Upton, NY 11973

K. Batchelor, J.P. Farrell, and G. Dudnikova

Brookhaven Technology Group Inc., 25 E. Loop Rd, Stony Brook, NY 11970

Description of Problem

This paper is a result of a group of simulations used to determine the optimal parameters for a pulsed power electron gun. As electrostatic codes such as PBGUNS tend to be cheaper, easier to use, and have less stringent computational requirements than time dependent codes such as MAFIA, it was desirable to determine those regimes in which the electrostatic codes agree with time dependent models. It was also necessary to identify those problems that required time dependence, such as longitudinal variation in an electron bunch. PBGUNS was then used to perform the bulk of the optimization, with only those issues that required time dependence being resolved with MAFIA.

The pulsed power gun has been discussed elsewhere [1] and consists of a diode with a flat cathode and a flat anode mounted parallel to one another with an interelectrode spacing of 1 mm. The anode had a .5 mm radius hole allowing the bunch to escape the accelerating gap. The cathode is biased at -1 MV, yielding an accelerating gradient of 1 GV/m within the gap. The anode was 1.5 mm thick and was modeled as a perfect conductor and a perfect particle dump. For the purposes of simulation, the gun was assumed to be cylindrically symmetric. Figure 1 shows the simulated geometry of the gun in MAFIA, along with field lines and an electron bunch from a typical run. Figure 2 shows the geometry as it was used in PBGUNS, along with the equal potentials and particle trajectories from a typical run. Note that in MAFIA, the $z=0$ boundary is used as the cathode, and the potential of -1 MV is set on that boundary, while in PBGUNS the cathode surface is at $z = 2.25$ mm. The beam parameters used for comparison were extracted as close as possible to a plane 2.25 mm from the inner surface of the anode. This plane was chosen so that the particles could be taken to be in the drift region, away from any fringe fields from the accelerating gap. All of the simulations modeled emission from a .25 mm radius spot, but a variety of currents were modeled within that spot, all with uniform current density.

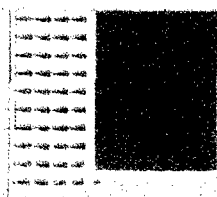


Fig 1 -- MAFIA Geometry, field lines and electron bunch

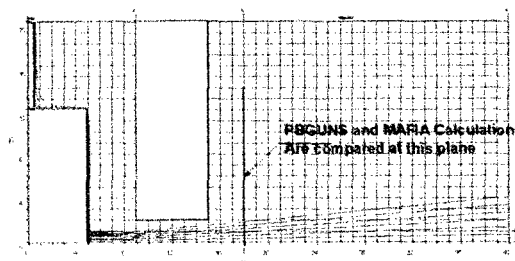


Fig 2 -- PBGUNS Geometry and particle trajectories

MAFIA is a software package that includes many electromagnetic simulation codes, including both time and frequency domain solvers in both 2.5D and 3D. For this problem, the mesh generator (M) was used to set up the geometry and mesh. For all of the runs discussed below, a mesh dimension of $10\text{ }\mu\text{m} \times 10\text{ }\mu\text{m}$ was used. The static solver (S) was used to model the field present in the gun during the emission. The static solver solves Maxwell's equations for a given geometry and set of time-independent boundary conditions. This involves the implicit assumption that the applied field in the gun is constant during the electron bunch duration, which is valid for the device being modeled. The field generated in this manner was read into the 2D time domain particle pusher (TS2). The particle pusher handles ejection and propagation of the electrons inside the gun. It is here that the bunch duration is defined. A duration of 10 ps was used throughout the comparison, although the effect of using shorter bunch lengths was investigated. The simulation is broken into finite time steps (on the order of 10 fs for these simulations). At each time step the particles are moved under the influence of the last calculated field, while at each half time step the fields are updated due to the presence of the particles. The program combines groups of electrons into macro particles to reduce the computational resources required. Typically 75000 macro particles were used in these simulations, although fewer were used to model the shorter pulse durations. The post processor (P) was used to extract the particle positions and momenta, both longitudinal and transverse, at the plane of interest. The comparisons were made with particles taken from the center of the MAFIA bunch, except where otherwise noted.

PBGUNS [2] is a PC compatible, 2-D code that solves Poisson's equation using iterative relaxation technique on a rectangular array of squares. It computes trajectories of charged particles in electrostatic and magnetostatic focusing systems including the effects of space charge and self-magnetic fields. Either rectangular or cylindrically symmetric geometry may be used. The Poisson equation is solved by an alternate column relaxation technique known as the semi-iterative Chebyshev method. The transverse phase space plot was extracted at the measurement plane.

Bunch Length Comparison

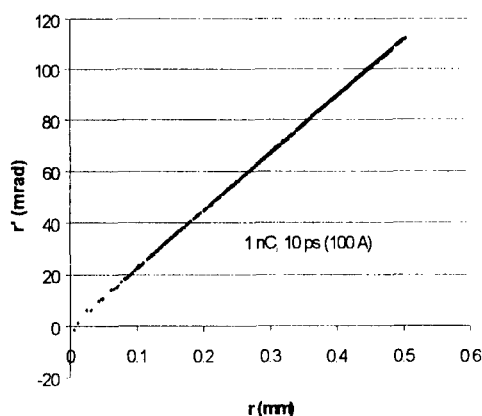


Fig 3 – MAFIA r - r' plot 1 nC, 10 ps, center 1% of beam

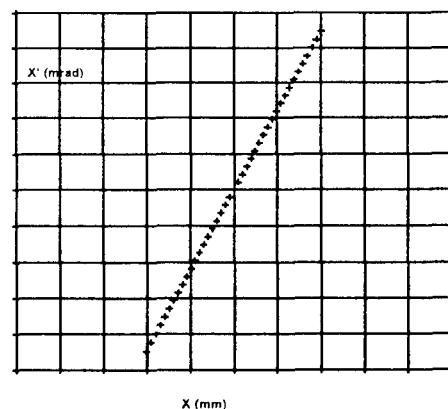


Fig 4 – PBGUNS x - x' plot, 100 A. PBGUNS output comes as x - x' , but for the cylindrically symmetric case this is equivalent to r - r'

The first issue in the comparison of the simulation packages was “Where do MAFIA and PBGUNS agree?” In comparing the results of the simulations, a current of 100A was used, with a uniform current density emission from the .25 mm radius emitting spot. Fig 3 shows transverse phase space predicted by MAFIA for the center 1% of a 1 nC, 10 ps bunch accelerated in a field of 1GV/m across the gap of 1 mm. Fig 4 shows the DC transverse phase

space predicted by PBGUNS for identical conditions. The transverse phase space does not vary significantly for bunch durations of 3 ps, 1ps, and 300 fs. The agreement between PBGUNS and MAFIA is very good, even for bunches much shorter than the gap transit time of 3 ps.

High Charge Comparison

The treatment of space charge effects in high current cases was investigated for MAFIA and PBGUNS. Table 1 gives the predicted maximum spot size, maximum divergence and 1- σ slice emittance (using the center 1% of the beam for the emittance calculation) for MAFIA and the maximum spot size and divergence for PBGUNS for various currents. The method used by PBGUNS to calculate the emittance is still under investigation. For MAFIA, a bunch length of 10 ps was used. As shown on the table, good agreement was found between MAFIA and PBGUNS for the beam radius and the max divergence. A current of 1000A is not possible in PBGUNS, as it is above the predicted DC Child's Law limit for this gun. The MAFIA results for a beam of 10 nC (corresponding to 1000 A in 10 ps) show significant bunch lengthening in the gap. Thus while the beam is 1000A initially, by the time it leaves the gun it has increased in pulse duration to about 13 ps, thus reducing the effective current to ~750 A.

	PBGUNS		MAFIA		
CATHODE	BEAM	MAX	BEAM	MAX	NORM.
CURRENT	RADIUS	DIVERG.	RADIUS	DIVERG.	EMITTANCE
Ampere	mm	mrاد	mm	mrاد	π mm-mrad
1	0.47	100	0.475	99	0.118
100	0.5	112	0.503	112	0.162
200	0.535	125	0.533	126	0.241
300	0.6	140	0.577	141	0.292
600	0.65	165	0.633	170	0.617
(*) 1000			0.707	173	2.16

Table 1 – Max Spot Size, Divergence & Emittance for 1A, 100A, 200A, 300A, 600A, 1000A for PBGUNS & MAFIA. (*) The 1000 A case is above the DC limit of Child's Law for the gun. The bunch length begins stretching immediately after emission, so that the effective current is only ~ 750A.

Longitudinal Phase Space & Front/Back Variation

One aspect where time resolution is clearly required is the study of the longitudinal variation of the electron beam, both in terms of energy and transverse phase space. Fig 5 shows the longitudinal momentum spread across the beam when the center of the beam is at the measurement plane for a 10 ps, 1nC bunch. It is interesting to note that this shape is independent of charge – the absolute extent of the front/back variation is charge dependent, but the shape is not. Fig 6 shows the longitudinal momentum spread for a 10 ps, 3nC bunch.

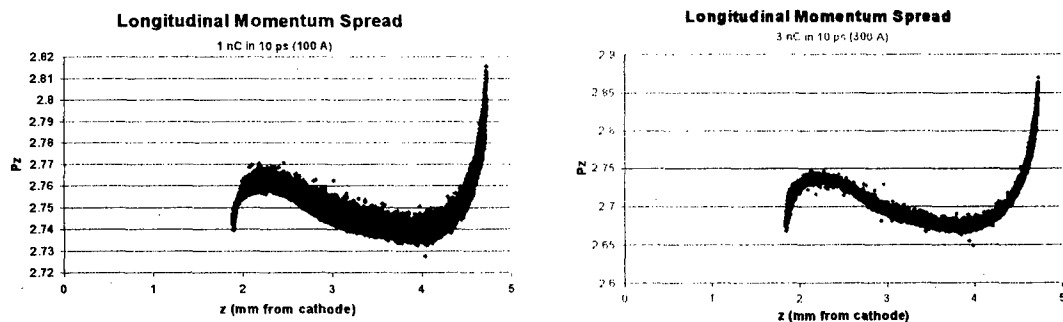


Fig 5 & 6 Charge induced longitudinal momentum spread. P_z is in $\beta_z \gamma$.

It is important to note that a DC code effectively measures only the slice phase space (since there is no longitudinal variation in the beam). Fig 7 shows the MAFIA predictions for the transverse phase of slices taken from the front, middle and back of the bunch (relative to the cathode). The variation from front to back is small. It is important, however, since most diagnostic techniques measure only the integrated phase space, which would involve drawing an ellipse, which encompassed all three slices. The emittance calculated from this ellipse would be much larger than the emittance of the individual slices.

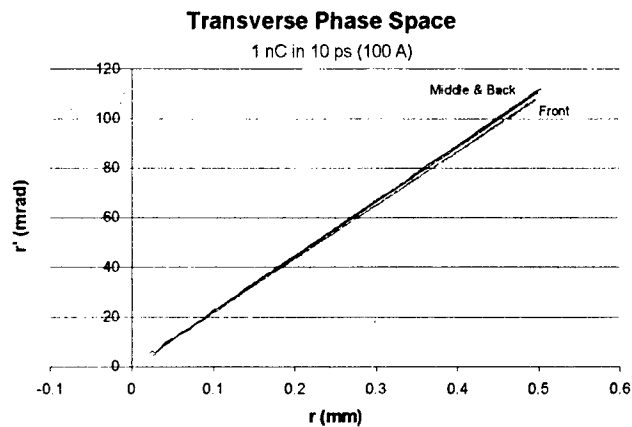


Fig 7 Longitudinal variation of the transverse phase space.

Conclusion

A comparison of two codes suitable for electron gun simulation was performed. Good agreement in transverse phase space values was found between the electrostatic code (PBGUNS) and the time dependent code (MAFIA) for a variety of pulse durations, even for pulse durations short compared to the electron transit time of the accelerating region. To obtain values for the longitudinal energy spread and the variation of the transverse phase space across the bunch, it was necessary to use MAFIA. The electrostatic codes have an advantage in terms of required computational resources and run time, and are therefore a good choice for modeling jobs in which the longitudinal energy spread is unimportant.

The authors would like to thank Harold Kirk for his assistance in utilizing MAFIA and Vadim Dudnikov for his assistance with PBGUNS.

Reference:

1. T. Srinivasan-Rao, J. Smedley, Advanced Accelerator Concepts workshop, AIP Conference Proceedings 398, Ed. S. Chattopadhyay, J. McCullough and P. Dahl, AIP Press, NY 1997, P. 7307.
2. J.E. Boers, Proceedings of the 1995 PAC, Dallas TX, pp. 2312-3, May 1995

SIMULATIONS ON HALO FORMATION IN HIGH INTENSITY ION BEAMS

V. Variale, A. Bazzani¹, T. Clauser, A. Pisent², V. Stagno,

Dipartimento di Fisica and INFN sez. di Bari, Via Amendola 173 Bari 70126, Italy

¹Dipartimento di Fisica and INFN sez. di Bologna, Italy

²INFN Laboratori Nazionali Legnaro, via Romea 4 Legnaro(Pd) 35020, Italy

Space-charge dominated beams can induce chaotic behavior of particle trajectories leading to halo formation on the beam spot. This causes particle losses along the beam transportation that must be minimized. The fractional losses must be kept below $10^{-7}/m$ [1]. This is a very low threshold to check with standard multiparticle codes. To study this kind of problems a new particle simulation approach will be proposed in this paper in analogy with the single particle to core interaction model [2] which is the most used calculation technique applied in these kind of phenomena.

Introduction

In these last years, growing interest has been addressed, from the international scientific community, on the possible applications of high intensity ion beams. Among them, just as examples, we can mention the energy amplifier proposed by C. Rubbia [1] and the transmutations of radioactive waste. However high intensity beam transport poses problems that need to be faced and solved. In particular, a halo formation has been observed around high intensity beams, during the transport, that leads to particle losses. For high current and energy beams the lost particles produce radio activation in the structures and the related radiation's can damage the accelerator components. Because of this problem, it becomes very important to study halo formation mechanism in the beam.

Multiparticle codes could be very helpful to this aim but it is very difficult to study this kind of phenomena by using the standard multiparticle codes because the lost particle fraction, along the transport, must be kept below $10^{-7}/m$ [2]. This means that the code should use a number of particles of the order of 10^{+6} , in the simulations, to appreciate this kind of lost fractions. This number is very high and a very powerful calculator are needed to handle them.

Recently a new calculation technique, called Particle-Core Model (PCM) [3], has been introduced to study the halo formation without using of very powerful computers.

The PCM solves the beam envelope (or rms) equation for a continuous beam which is used as a model for the core of the beam. The core can be mismatched so that its radius, taken at the exit of the transport period cell, will oscillate. The halo particles are represented by test particles, which oscillate through the core influenced by linear external focusing field and the non linear space charge fields of the core. The model allows one to study the test particles dynamics.

PCM approximations and PARMT code simulations

Although the PCM calculations allow to study the halo formation this is done by assuming some approximations and then their influence on the PCM results should be checked by a

comparison between its results and those given by a multiparticle code that do not have this kind of approximation.

The main approximations assumed in PMC are the following:

- the envelope equation considers a constant uniform particle distribution that is not physical.
- the space charge force, seen by the test particles near the edge of the beam, is incorrect because in the envelope equation the particle distribution is assumed with a sharp edge while, in the real life, it has a tail with a length equal to the Debye length λ_D [4].
- the coupling, due to space charge forces, between the two transverse planes is completely neglected.

In this paper a comparison test between the PCM results and the simulations of the multiparticle code PARMT, modified to follow directly the results of PCM calculations, will be carried out to check the PCM reliability.

PARMT is a Monte Carlo program that can transport an ion beam through a system of optic elements by using the matrix method [5]. It has different technique for the space charge calculation. Among them there are the 'Particle to Particle' and the 'Fast Poisson Solver' (FIS) technique that can give, with a high precision, the electric field due to the particle distribution step by step along the beam transport. The 'particle to particle' technique computes the electric field directly from the Coulomb law:

$$\vec{E}(\vec{x}) = \frac{q}{4\pi\epsilon_0} \sum_i \frac{\vec{x} - \vec{x}_i}{|\vec{x} - \vec{x}_i|^3}$$

where x_i gives the particle position. In this case the time needed for space charge calculation increases exponentially with the number of the particle considered. High intensity beams impose to consider a very high number of particles and in these conditions the calculation time becomes too long. A high intensity ion beam requires, in fact, the FIS technique that compute the space charge electric field by solving the Poisson equation:

$$\text{div}\vec{E}(\vec{x}) = \frac{1}{\epsilon_0} \rho(\vec{x})$$

where $\rho(x)$ is the beam charge density distribution. The main features of this kind of computation are shortly given in the following.

A mesh with a size d is superimposed on the beam. The particle charges are distributed among their neighboring mesh nodes. In this way the problem of solving the Poisson equation is reduced to solve a linear system of finite difference equations which can be solved with Fast Fourier Transform (FFT). The computing time in this case is mainly determined by the number of mesh points. However there is the constraint that if $\lambda_D \ll d$ the simulations will present some unphysical instability called 'aliasing' [6].

To compare directly the PCM with the PARMT results some modifications have been carried out in PARMT. Mainly, two new features have been introduced: 1) an input file with the initial test particles coordinates that can be read, if required, by the main program; 2) N output files, with N number of test particles, where the test particle phase space coordinates along the transport in the periodic cells (N_p) are stored.

The PCM results given in ref. [7] will be compared to our PARMT simulations and then some comment on this comparison will be given.

The simulations are carried out on a FODO cell period of length $L=80$ cm. The other input parameter considered are: total transverse emittance, $\epsilon_x=\epsilon_y=1 \times 10^{-6}$ mr; single particle phase advance $\sigma_0=60.7^\circ$; the space charge parameter (as given in ref [7]) $\xi=4 \times 10^{-6}$ (corresponding to

$I = 95$ mA) leads to a phase advance $\sigma = 30.4^\circ$. 40 test particles are used in PARMT. Their initial coordinates are different from zero only in x position and have $x_1 = 0.1$ until $x_{40} = 2$ cm.

The phase space test particle trajectories given by PCM calculations, for the matched case, is given in fig.1a. In fig.1b are shown the PARMT results that can be compared with those of fig.1a. The more external phase space test particle trajectories are very similar in both cases. However, very different test particle trajectories can be observed in the core region (near the beam). In fact in this region, PCM calculations give trajectories of circular shape while PARMT simulations give very complex trajectories.

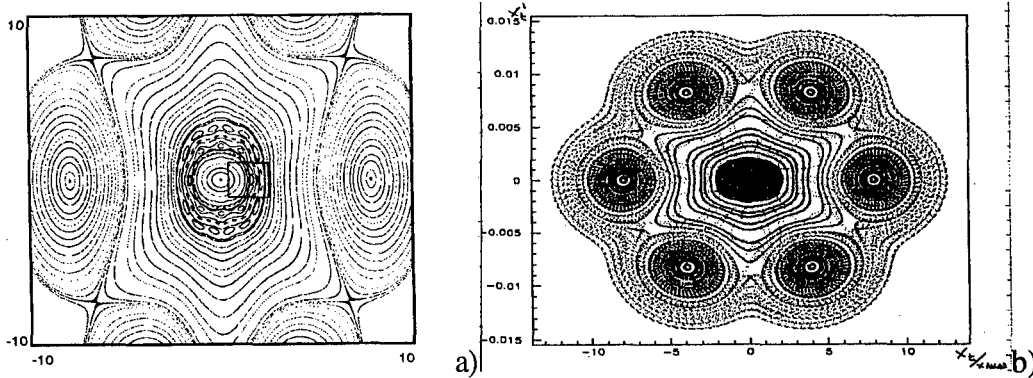


Fig.1 Phase space test particle trajectories computed by PCM a) and PARMT b), respectively. Matched case.

This difference is mainly due to the strong coupling induced by the high space charge forces existing in the core region. This coupling can be shown in fig.2 where the test particle trajectories along the periodic cell transport are shown.

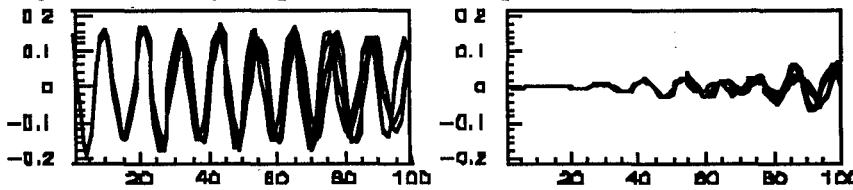


Fig.2 Trajectories in x - and y -plane, respectively, for 4 test particles.

To check this point, a PARMT simulation with low current ($I = 0.5$ mA) has been done, and in that case, circular shape trajectories, in the core region, have been obtained as in PCM results.

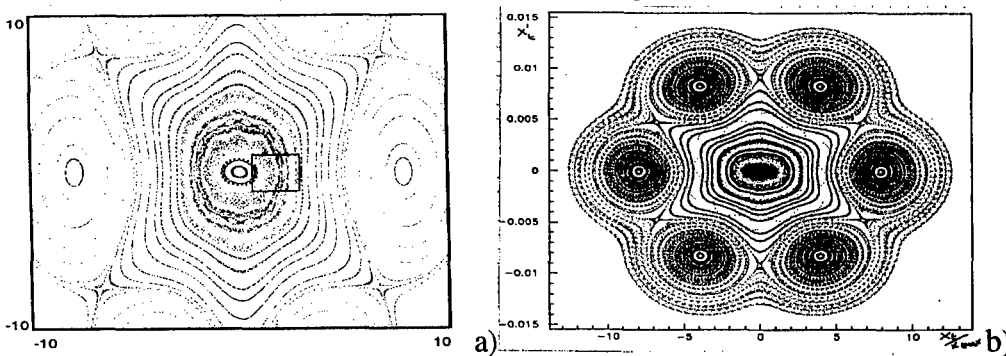


Fig.3 Phase space test particle trajectories computed by PCM a) and PARMT b), respectively. Mismatched case.

Another test for the mismatched case has been done with PCM and PARMT. The mismatch used was 10% of the beam size and the results are shown in fig.4. The PCM phase space core trajectories show a substantial difference between the matched and mismatched case. In the mismatched case the core trajectories have lost their circular shape and look like more chaotic.

In the PARMT simulations more slight difference between the mismatched and matched case can be observed. This different behavior between the two types of calculations can be explained if we observe that in PCM mismatched case the envelope oscillates with constant amplitudes, as said before, while in PARMT simulations a damping of the envelope oscillation has been observed, as shown in fig 4.

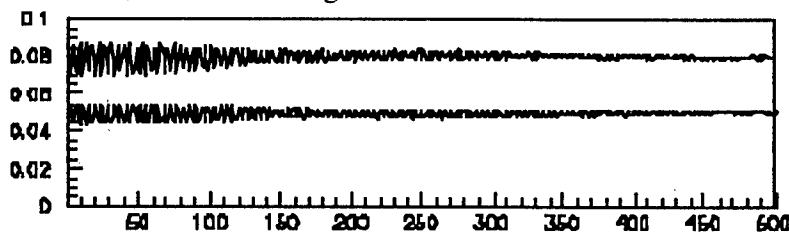


Fig.4 x_{rms} (cm) and y_{rms} (cm) vs N_p (cell period number). The initial oscillations are due to mismatching.

Conclusions

A continuous beam has been transported through N_p FODO cell periods. The simulation results obtained either with PARMT and PCM lead to the following conclusions:

- the more external phase space test particle trajectories are practically the same in both the results of PARMT and PCM.
- the test particle trajectories in the region near and inside the beam are very different in the two type of calculations. This seems due to the space charge coupling between the two transverse planes.
- in PARMT the x_{rms} oscillations, due to the breathing of the beam when it is mismatched with the cell period, damp very quickly when the space charge is strong, as in our simulations. In PCM calculations, instead, we have a constant oscillation of the beam envelope. This means that, in PCM, the test particle close to the breathing beam are influenced in very different way in case of mismatch, as shown by the PCM calculations of the fig.1a and 2a, and also stated in ref. [7].

In PARMT, the difference in the test particle trajectories close the beam, between the matched and the mismatched case, is more slight.

PCM calculations seem unsuitable to study very high beam current ($I=95$ mA) in the core region.

REFERENCES

- [1]C. Rubbia et.al., CERN/AT/95-44
- [2]R. A. Jameson, G. P. Lawrence and S. O. Schriber, Proc. PAC Washington, 1993.
- [3]J. Lagniel, NIM in Phys. Res. A345 (1994) 405
- [4]I. Hoffmann, CERN 87-03.
- [5]J. Struckmeier, GSI-ESR-03 report.
- [6]R. W. Hockney, J. W. Eastwood, "Computer Simulations Using Particles", McGraw-Hill, Inc.(1980)
- [7]A. Pisent et al., "Frequency Map Analysis Of The Chaotic Motion of An Intense Mismatched Beam In FODO Channel" to be published on a DESY report.

DIODE SIMULATIONS WITH KADI2D

C.-D. Munz¹, R. Schneider, E. Stein, T. Westermann²

*Forschungszentrum Karlsruhe - Technik und Umwelt
Institut für Neutronenphysik und Reaktortechnik
Postfach 3640, D-76021 Karlsruhe, Germany*

Abstract: Computer simulations with the 2.5D version of the nonstationary KADI2D particle-in-cell code based on boundary-fitted grids have been started. Different numerical experiments have been carried out to study the time-dependent behavior of the externally applied-B ion diode. Typical simulation results for the self-consistent formation and development of the bipolar flow are reported. Comparisons with stationary BFCPIC simulations and with experimental data are presented.

I. INTRODUCTION

At the Research Center Karlsruhe (FZK) the computational physics program continued to support the development of light ion beam sources („ion diodes“) operating at the pulsed power generator KALIF. Fig. 1 shows a schematic cross section of the rotationally symmetrical, externally applied-B ion diode in the (z,r)-plane developed at FZK by Bluhm et al. [1].

The vacuum diode consists of a solid anode plate and a cathode ring. A Mylar foil attached to the cathode ring seals the vacuum diode from the gasfilled drift space. Depending on the ion species to be produced, parts of the anode plate are coated with an appropriate material. These parts are shown dashed in the schematic diagram of the diode. The pulse length is typically about 50 to 100 nsec, the applied voltage several MV and the gap distance a few mm. The electron current follows the outer conductor of the generator to the cathode area and to the cathode tip. Electric field enhancement causes electrons to be emitted mainly at this edge.

Numerical simulations performed with the stationary 2.5D BFCPIC code [2] do not reproduce the ion enhancement found in the experiment. For some early KALIF-experiments, the results of the numerical simulation [3] and experimental data [1] do not match as can be seen from Tab. 1.

Tab. 1: Experimental and numerical simulated currents

	Experimental data [1]	BFCPIC simulations [3]
Electron current	20 - 80 kA	40 kA
Ion current	300 - 450 kA	20 kA

Analytic work [4] and 3D simulations [5] of applied-B ion diodes have been carried out especially at the Sandia National Laboratories in Albuquerque. These investigations reveal that in pulsed power ion diodes two types of instabilities are dominant and, hence, responsible for high ion currents: Early in the pulse a high-frequency mode is present followed later by a low-frequency mode. The early high-frequency phase at 10 - 100 GHz has been identified as a

¹ Universität Stuttgart, Inst. f. Aerodynamik und Gasdynamik, Pfaffenwaldring 21, D-70550 Stuttgart.

² FH Karlsruhe, Fb. Naturwissenschaften, Postfach 2440, D-76012 Karlsruhe.

diocotron mode. The late time spectrum is massively influenced by a two-stream instability with participation by ions at about 1 GHz.

The result of these instabilities is a diffusion of the electrons toward the anode. Consequently, the anode-cathode gap is filled with electron charge and more ions can be drawn from the anode surface than is the case for a sharp electron sheath. Only by modeling the ion diodes as an entire electromagnetic non-neutral plasma dominated device considering the full set of Maxwell-Lorentz equations, all essential physical effects including the instabilities mentioned above may be obtained properly in a numerical simulation.

On the way to a 3D nonstationary full electromagnetic particle-in-cell program system, the 2.5D finite volume PIC program KADI2D [6] has been developed in order to get experience with time-dependent simulations for realistic configurations. However it is important to keep in mind, that only a fully 3D code can reproduce the instabilities leading to the enormous ion current enhancement. This paper deals with the description of the first nonstationary simulation results on the applied-B ion diode obtained with KADI2D. Typical time-dependent features of the diode are presented.

II. NUMERICAL SIMULATIONS

A. The numerical model

A numerical model of the externally applied-B ion diode together with a boundary-fitted grid [2] is shown in Fig. 2. Due to the use of boundary-fitted coordinates the curved parts of the emitting anode surface are treated accurately. No interpolation from the physical domain onto the computational area is necessary and a stair step approximation of the curved parts is avoided.

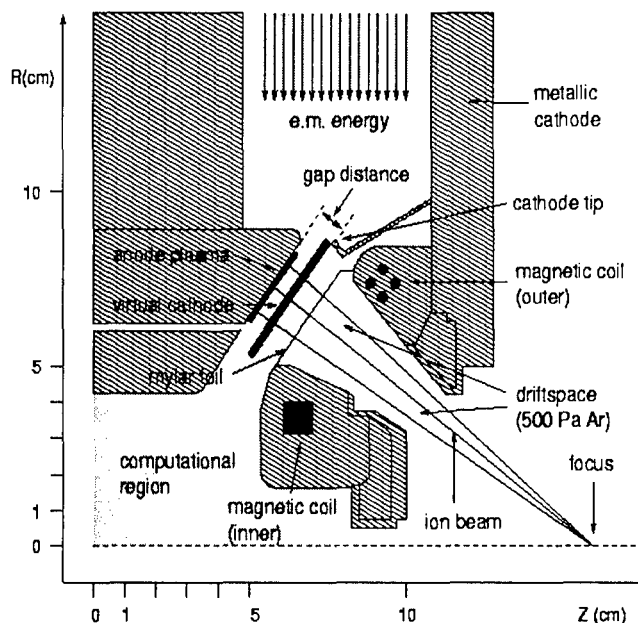


Fig. 1: Schematic of the applied-B diode

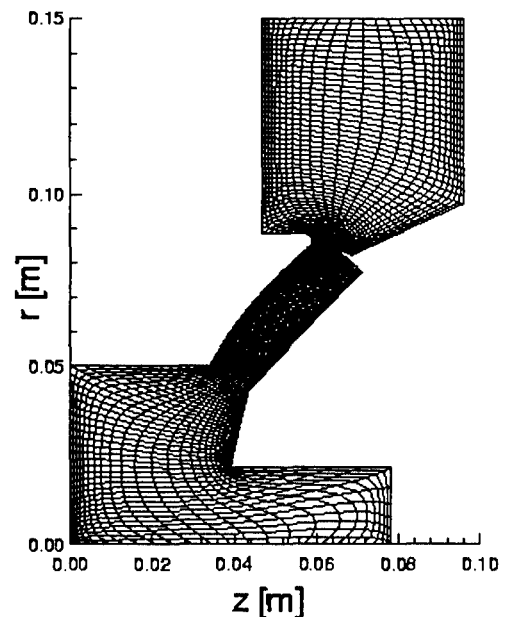
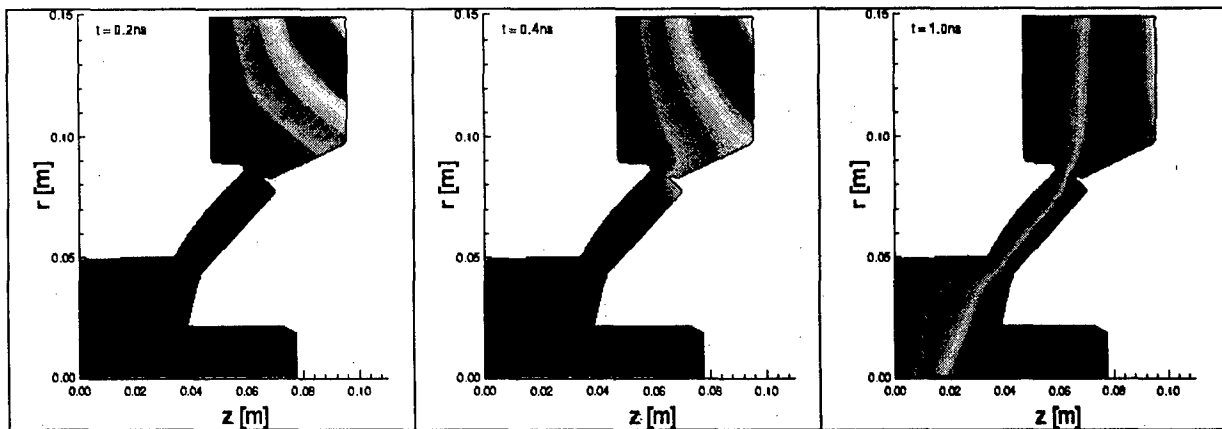


Fig. 2: Computational grid

For the numerical simulation an anode-cathode gap of 8.75 mm width is assumed and an applied voltage that rises within 1 nsec to 1.5 MV and stays constant. The strength of the applied magnetic field varies between 1.7 and 2 T and is mainly parallel to the anode surface.

B. Incoming electric pulse

The first sequence (Figs. 3) shows the incoming of the electric pulse within 1 nsec. After 1 nsec a constant potential difference of about 1.5 MV has been established. Spatial reflections of the incoming wave can only be seen in the electromagnetic fields.



Figs. 3: Incoming electric wave at times 0.2 nsec, 0.4 nsec and 1 nsec.

It is remarkable, that the electric field oscillates at a frequency of approximately 0.5 GHz. In order to show this effect, in Fig. 4a the electric field E_1 is plotted versus time at different locations inside the anode-cathode gap. All the curves have these oscillations in common. This observation is independent of the pulse length and on the shape of the incoming pulse nor does the frequency depend on the grid resolution or on the time-stepping. Hence, these preliminary simulations indicate an eigenfrequency of the device at 0.5 GHz.

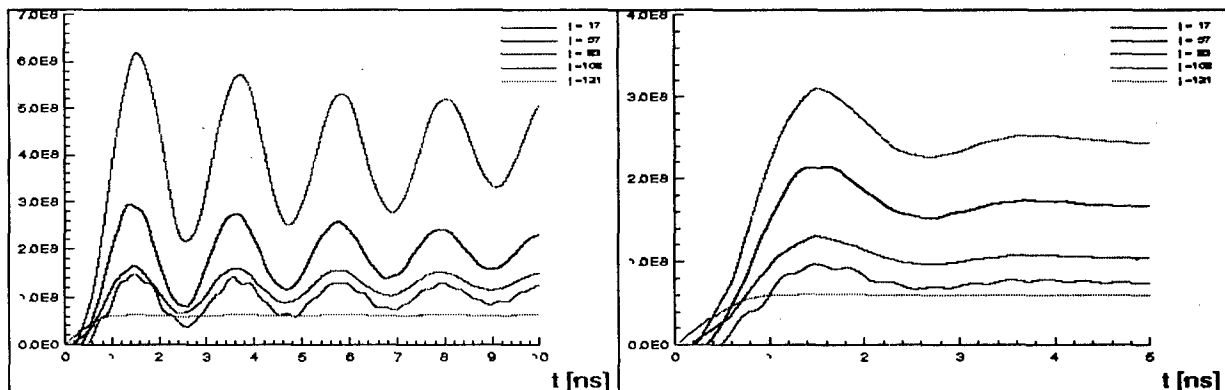


Fig. 4a: Electric field E_1 versus time without filter

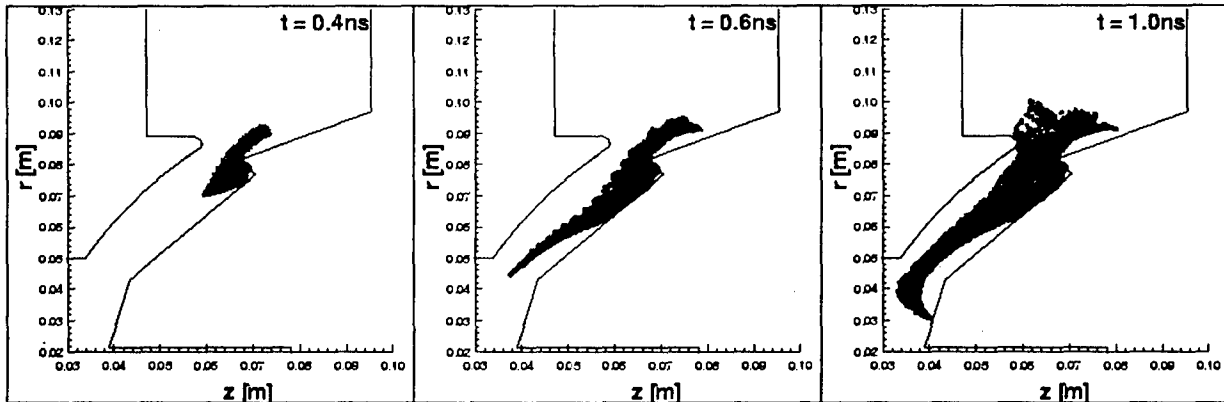
Fig. 4b: Electric field E_1 versus time with filter

For the first time-dependent simulations of the electromagnetic device with particles it was convenient to suppress this eigenfrequency by introducing a digital filter. The qualitative behavior of the electromagnetic device remains but the time history of the field is now a smooth curve without oscillations as can be seen in Fig. 4b.

C. Monopolar electron flow

In a subsequent simulation electrons are introduced by allowing them to be emitted around the field emission edge. Bipolar stationary simulations clearly indicated that most of the electrons are generated near the cathode tip even when the electron emission is turned on all over the cathode area. Hence, in order to save CPU-time the electron emission was restricted to the cathode tip.

The electrons perform a complicated motion inside the anode-cathode gap. They are influenced by magnetic fields induced by the movement of the particles themselves and by the external magnetic field in the (z,r) -plane. The electrons drift in the anode-cathode gap perpendicular to the electric and magnetic fields. The following frames (Figs. 5) indicate the time-dependence of the electron cloud formation inside the gap. Shown is only the diode area around the cathode tip.



Figs. 5: Electron distribution inside the gap at different times.

D. Bipolar electron and proton flow

Finally ions were generated at the front side of the anode at those parts outlined by dashed lines in Fig. 1. The ions are accelerated in the AK gap and follow mainly the electric field lines. Due to their massiveness they are barely influenced by the magnetic fields. One major point of interest of the nonstationary simulations with KADI2D is the resulting ion current.

As expected, the ion current computed by the nonstationary simulations is slightly higher than those from the stationary computations with BFCPIC, although it is still smaller than the experimental value. As already mentioned, only fully 3D simulations can reproduce the instabilities leading to the enormous ion current enhancement and thus to a correct value of the ion current. Hence, the next step for our simulation endeavor will be to incorporate an artificial E_θ field that has to be introduced by heuristic models, e.g. like those studied in [7].

References

- [1] H.J. Bluhm, P. Hoppé, H.P. Laqua, D. Rusch, Proc. IEEE80, 995, 1992.
- [2] T. Westermann, Nucl. Instr. Methods A 263, 271, 1988 and
T. Westermann, Int. J. Num. Modelling: Electr. Networks, Devices and Fields 7, 43, 1994.
- [3] M. Alef et al., BEAMS 92, 1992.
- [4] M.P. Desjarlais, Phys. Fluids B8, 1709, 1989.
- [5] M.P. Desjarlais et al., Phys. Rev. Lett. 67, 3094, 1991.
- [6] C.D. Munz et al., Int. J. of Numerical Methods in Engineering, to be published 1998.
- [7] T. Westermann, R. Schuldt, Phys. Fluids B5, 4408, 1993.

A POSSIBLE MECHANISM OF RUNAWAY ELECTRONS GENERATION IN PULSED PLASMAS.

O.Zabaidullin[†] and J.Dubau[‡]

[†] Institute of Nuclear Fusion, Russian Research Centre,
"Kurchatov Institute", 123182, Moscow, Russia

[‡] Observatoire de Paris, 92195, Meudon, France.

Abstract

The nonlinear dynamics of magnetic field penetration into an inhomogeneous density plasma as a KMC wave is accompanied by a significant Joule heat release in the current layer and the generation of runaway electrons. In the frame of electron magnetohydrodynamic (EMHD) theory a particle in cell (PIC) modeling is carried out to study the process of self-consistent electron acceleration in the wave electromagnetic field. It is shown that the electron acceleration becomes possible due to a nonzero circulation of the Hall electric field component along the "cyclotron circles" of the electron trajectory.

Up-to the present time, the appearance of runaway electrons was considered as the consequence of their acceleration in some given external electric field. This model was proposed by Dreiser in [2] and was applied to Tokamak experiments. The dynamics of powerful pulsed discharges, such as Z-pinchs or plasma opening switches (POS), are also characterized by runaway electrons appearance. But the essential feature of the pulsed discharges is a self-consistent electron motion both in electric and in magnetic fields. The general direction of the electron motion in crossed fields is $[\mathbf{E} \times \mathbf{H}]$, which is perpendicular to the electric field. By this reason, in a potential field, an electron does not acquire energy.

Let us consider the real electron trajectory in crossed fields (Fig.1). The characteristic electron trajectory consists of a set of "cyclotron circles" linked by relatively "straight" intermediate lines. During the motion along the "cyclotron circle", the electron acceleration is possible only if the electromagnetic field is nonpotential, $\text{rot}\mathbf{E} \neq 0$. This situation realizes in the front of magnetic field penetration into an inhomogeneous plasma as a KMC wave [1]. In the wave front, the electron receives a main acceleration due to nonpotentiality of the Hall electric field component, and, during the "straight" lines, it receives some additional acceleration [3] due to the Ohm electric field component.

In the present paper, the phenomena of magnetic field penetration into inhomogeneous plasma density due to the Hall effect is discussed. This well-known phenomena was predicted in the work [1] and numerically shown in [4]-[6]. The fact itself of magnetic field penetration into the plasma, $\mathbf{H} = \mathbf{H}(t)$, demonstrates the nonpotential nature of the wave electromagnetic field. The essential reason for such nonpotentiality is the dependence of

the Hall electric field component on the electron density. Let us suppose that an electron moves through a plasma region with increasing density (Fig.1). The upper and the lower part of each "cyclotron circle" lies in layers of different plasma density, and from this reason with different values of the Hall electric field components, $\mathbf{E}_{Hall} = [\mathbf{j} \times \mathbf{H}]/n_e e c$. The $\oint \mathbf{E}_{Hall} \cdot d\mathbf{l} \neq 0$ (see formula 5), and the work produced by the Hall field at each "circle" is positive. Therefore, the electron acquires energy.

To demonstrate numerically the effect of an electron acceleration in the front of KMC wave, we run the EMHD code [3]. To do that, one can include the motion of some probe electron into the code. The EMHD part gives the electromagnetic field, which acts on the probe electron.

Basic equations.

The EMHD+PIC, present theory, considers the following equations:

1. equation for electric field:

$$\mathbf{E} = \frac{[\mathbf{j} \times \mathbf{H}]}{n_e e c} + \frac{\mathbf{j}}{\sigma}; \quad (1)$$

2. equation for magnetic field:

$$\frac{\partial \mathbf{H}}{\partial t} = \nabla \times [\mathbf{u} \times \mathbf{H}] - \nabla \times \left(\frac{c^2}{4\pi\sigma} \nabla \times \mathbf{H} \right); \quad (2)$$

3. Maxwell equation for current density:

$$\mathbf{j} = \frac{c}{4\pi} \nabla \times \mathbf{H}; \quad (3)$$

4. equation for particle momentum change:

$$\frac{d\mathbf{p}_e}{dt} = -e\mathbf{E} - \frac{e}{\gamma m_e c} [\mathbf{p}_e \times \mathbf{H}]. \quad (4)$$

here $\mathbf{u} = -\mathbf{j}/en_e$. e , m_e are the electron charge and mass at rest. σ is the plasma conductivity, $\mathbf{p} = \gamma m_e \mathbf{v}$ is the momentum and $\gamma^{-1} = \sqrt{1 - (v/c)^2}$.

Results of modeling.

The system (1)-(4) is modeled to study the influence of the KMC wave on the runaway electrons generation. The Fig.2a-2c present the results of modeling in the (x,y) plane geometry: $p = (p_x, p_y)$, $H = H_z(x, y)$, $n_e = n_e(y)$. On the left and on the right parts of each figure, distributions of the electron density and of the magnetic field are shown. Darker color corresponds to higher value. Plasma density is 10^{13} cm^{-3} at the top and is $2 \cdot 10^{13} \text{ cm}^{-3}$ at the bottom. The inhomogeneity is shown as an intermediate layer of width $\lambda \approx 1 \text{ mm}$. The magnetic field value is $H = 10^4 [\text{ers}]$, the Hall parameter $(\omega\tau)_{ie} = 20$. The characteristic time of KMC wave evolution is $T = 4\pi e\lambda/cH \frac{\partial}{\partial y} \left(\frac{1}{n_e} \right) \approx 2 \cdot 10^{-12} \text{ sec}$. To analyse an electron acceleration in the front of KMC wave the energy interval is divided from 500 eV to 110 keV to a groups with energy-step 500 eV. Motion of an electron from each energy-group is modeled.

In the Fig.2a-2c, the trajectories of some probe electrons at time $2.8 \cdot 10^{-14} \text{ sec}$, $1.5 \cdot 10^{-12} \text{ sec}$ and $1.9 \cdot 10^{-12} \text{ sec}$ are given. The initial energy of the "1" electron is 500 eV, of the "2" is 30 keV, of the "3" and "4" ones are 60 keV and 90 keV.

The fig.2a corresponds to the first moment of the magnetic field penetration into the plasma. The first moment is more favorable for acceleration and for runaway of electrons.

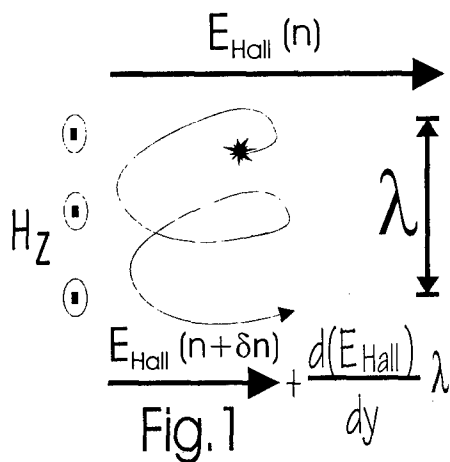


Fig.1

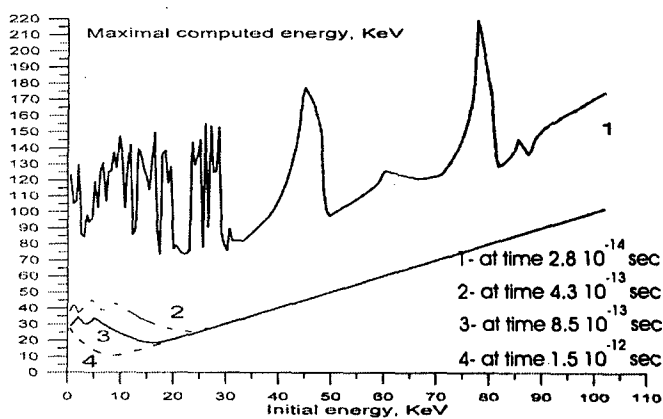


Fig.3

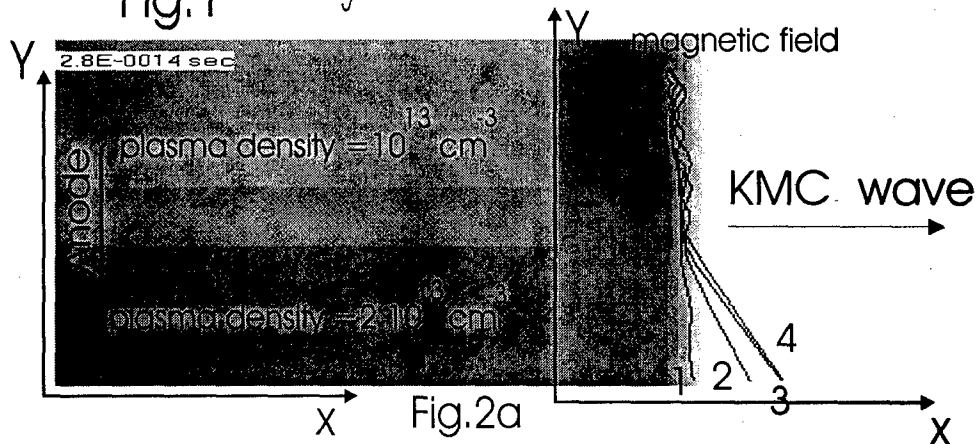


Fig.2a

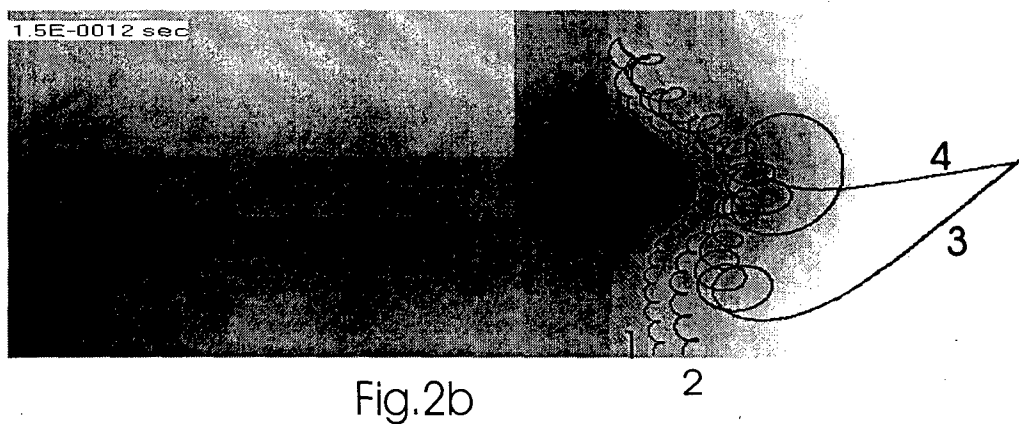


Fig.2b

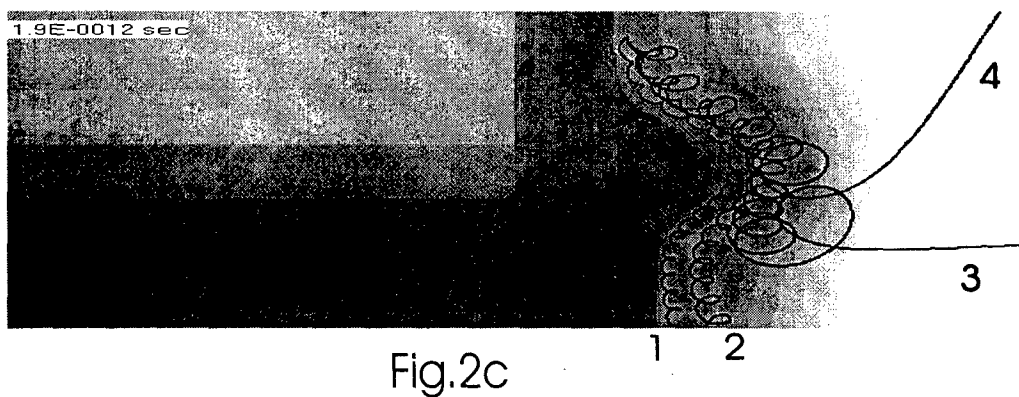


Fig.2c

The beam of accelerated electrons is directed to the anode under a small angle. We can suppose, that it is at the initial moment of the magnetic field penetration into the inhomogeneous plasma that the runaway electron beam is generated. The average electron energy increase for a length λ is equal to

$$\mathcal{E}(\lambda) \approx -e \int \vec{E}_{\text{Hall}} \cdot d\vec{l} \approx \frac{H^2}{8\pi} \frac{\partial}{\partial y} \left(\frac{1}{n_e} \right) \lambda. \quad (5)$$

In Fig.3, the maximal kinetic electron energies for each energy-group versus the time of KMC wave evolution are given. One can see, that for fig.2a and for the parameters given above $\mathcal{E}(\lambda) \approx 110$ keV.

Later moments of the KMC wave dynamics are shown in Fig.2b-2c. The magnetic field penetrates deeper into the plasma. The electrons "3" and "4" runaway from the front of the wave. In fig.3, one can see that the energies of these electrons do not change. The results of modeling show the exponential decrease of accelerated electrons quantity with time. Finally, we may propose the following scale dependence of maximal electron kinetic energy, E_{max} , versus time, t , and versus initial energy, E_0 :

$$E_{\text{max}} \approx \begin{cases} \mathcal{E}(\lambda) * \exp(-t/T), & \text{for } E_0 < \mathcal{E}(\lambda) * \exp(-t/T); \\ E_0, & \text{for } E_0 > \mathcal{E}(\lambda) * \exp(-t/T); \end{cases} \quad (6)$$

One of the important results of modeling is that the electrons of small energy, less than 500 eV, accelerate during all the calculated time up-to the energy 10 ÷ 30 keV. If some heavy elements are present in the plasma, for example impurities, highly ionized ions (such as He-like ions) excited by medium energy accelerated electrons would radiate a polarized line spectra, which could be used as a diagnostic tool of the electron acceleration. When full accelerated electron reaches the anode, it produces hard X-rays emission.

In the present paper, we called runaway electron, high energy electron escaping from the magnetic field. Since the electron moves both in the magnetic field and in the electric fields of the wave, the condition for it to be runaway is the following : In the magnetic field the cyclotron radius, ρ_{Be} , of electron trajectory has to be greater, than the width of a current layer, δ . In the Hall electric field the kinetic electron energy, $m_e v^2/2$, has to be greater, than the "work of escape" from the magnetic field, $H^2/8\pi n_e$.

This work was partially supported by the Russian Foundation for Basic Research, grant 96-02-16258, and grant 96-15-96815 under the program "Leading Scientific Schools".

References

- [1] A.Kingsep, U.Mohov, and K.Chukbar, *Sov. J. Fizika Plazmi* 10, 854, (1984)
- [2] H.Dreiser, *Phys. Rev.* 115, 238, (1958); 117, 239, (1960)
- [3] O.Zabaidullin, and V.Vikhrev, *Phys. Plasmas* 3(6), 2248, (1996)
- [4] R.J.Mason, P.L.Auer, R.N.Sudan, B.V.Oliver, C.E.Seyler, and J.B.Greenly, *Phys. Fluids B* 5, 1115, (1993)
- [5] J.D.Huba, J.M.Grossman, and P.F.Ottinger, *Phys. Plasmas* 1, 3444, (1994)
- [6] A.V.Grechiha, A.S.Kingsep, and A.A.Sevastianov *Plasma Phys. Reports* 21, 327, (1995)



BEAMS'98

12th INTERNATIONAL CONFERENCE
ON HIGH-POWER PARTICLE BEAMS



AUTHOR INDEX

Vol. I

Proceedings

Proceedings

A

Abramovich, A.	517
Adams, R.G.	9, 208
Adamyan, Yu.E.	330
Agafonov, A.V.	885
Agarin, N.V.	687
Akiyama, H.	289, 483
Allshouse, G.O.	9
Amikhanov, I.	993
An, W.	471
Anderson, B.G.	646
Anderson, D.	380
Ando, R.	361, 384, 816, 889
Andreic, Z.	627
Antipov, V.S.	760
Antonov, A.N.	760
Apruzese, J.	95, 299
Arad, R.	253
Arbel, M.	728
Arjona, M.R.	683
Arzhannikov, A.V.	35, 447, 687
	833, 837
Aschke, L.	627
Astrelin, V.T.	35
Attelan-Langlet, S.	49
Ayzatsky, M.I.	396, 400, 784
Azizov, E.A.	71

B

Babkin, A.L.	372
Bailey, J.E.	9, 208
Bakshaev, Yu.L.	244, 623
Baksht, R.B.	235
Balakirev, V.A.	392, 748, 752, 760
Banu, V.	989
Baranowski, J.	499
Barinov, N.U.	591, 977
Baronova, E.O.	451, 572, 615, 662, 666
Barroso, J.J.	529, 772
Bartov, A.V.	244
Batchelor, K.	549
Batrakov, A.V.	1035
Bauer, W.	218, 513
Baumung, K.	935
Bazzani, A.	553
Begishev, V.	997
Belomytsev, S.Ya.	424
Belov, V.A.	961
Belova, N.G.	931
Ben-Kish, A.	638
Benattar, R.	567
Benford, G.	365
Benford, J.N.	149, 691, 695
Bersenev, V.V.	911
Bestea, V.	257
Binderbauer, M.	195
Black, D.C.	5, 306
Blank, M.	157
Blinov, A.V.	269
Blinov, P.I.	244, 623
Bliokh, Yu.P.	699, 760, 808
Bloomquist, D.D.	9
Bluhm, H.	203, 218, 471, 923, 935
Bobylev, V.B.	687
Bochkov, V.D.	1031
Bogachenkov, V.A.	732
Bogatov, I.N.	577
Bohacek, V.	619
Bondarenko, G.G.	961

Bongers, W.A.	145
Boriskin, A.S.	503
Borissenok, V.A.	369
Borovina, D.	869
Botcharov, Yu.N.	326
Branitskii, A.V.	603, 607
Branitskii, V.V.	599
Bratchikov, V.B.	285
Bratman, V.L.	145, 744, 857, 865
Bugaev, S.P.	965, 969, 973
Bujko, A.M.	646
Burdakov, A.V.	35
Burdovitsin, V.	412
Burencov, O.M.	585
Burmasov, V.S.	447
Burtsev, V.A.	703
Buth, L.	471, 923
Buyko, A.M.	479
Bychenkov, V.A.	837

C

Calame, J.P.	157
Caplan, M.	145
Carboni, V.	218
Carmel, Y.	699
Castle, M.	788
Chabot, M.	45
Chakrabarti, N.	253
Chandler, G.A.	9
Chelpanov, V.I.	83, 372, 503
Chen, D.-Q.	841
Cheng, J.	788
Cherkassky, V.S.	455
Chernenko, A.S.	244, 623
Chernikh, E.V.	642
Chernyavsky, I.A.	707
Chernyshev, V.K.	479, 585, 634, 646
Chin, Y.H.	153
Chishiro, E.	222
Chlenov, A.M.	440
Choi, J.J.	157
Choi, P.	240, 595
Chorny, V.V.	581
Chuaqui, H.	240, 595
Chuvatin, A.S.	189, 261, 322, 507, 545
Clark, R.W.	77
Clauser, T.	553
Coats, R.S.	9
Cochran, F.	95
Coleman, P.L.	95, 310, 338
Commisso, R.J.	5, 31, 95, 265, 342
Cook, D.L.	9, 171
Cooperstein, G.	31
Correa, R.A.	529, 772
Coverdale, C.	95
Cross, A.W.	55, 857, 865, 901
Crumley, R.J.	273, 338
Cuneo, M.E.	9, 208

D

Dan'ko, S.A.	244, 459, 507, 623
Danly, B.G.	157
Davis, J.	77, 95
Deeney, C.	9, 77, 95, 171
DeHope, W.	695
Deichuly, M.P.	707, 768
Demidov, V.A.	83, 269, 318, 588, 646
Demin, A.N.	585, 588, 634
Denisov, G.G.	145, 829, 857

Proceedings

Denisov, G.V.	1016
Derzon, M.S.	9
Desjarlais, M.P.	9, 208, 229, 923
Didenko, A.N.	65, 711
Ding, W.	714
Diyankov, V.S.	285
Djagilev, V.M.	1031
Dolgachev, G.I.	281, 591, 977, 981
Dolin, Yu.N.	585, 634
Dolotenko, M.I.	503
Douglas, M.R.	9
Douglas, S.C.	861
Dovbnya, A.N.	396, 400, 784
Dubau, J.	561
Dubina, V.M.	581
Dubinov, A.E.	369, 372, 720
Dudin, V.I.	585, 634
Dudnikova, G.	549
Dumitrescu-Zoita, C.	240, 595
Dunaevsky, A.	179, 302, 376, 631, 724
Dyabilin, K.	89

E

Efimov, I.P.	326
Efimov, S.	517
Egorov, A.M.	760
Eibl, J.	837
Eichenbaum, A.L.	728
Eidmann, K.	89
Ekdahl, C.A.	646
Elzhov, A.V.	314
Emlin, D.E.	1004
Emlin, D.R.	911
Engelko, V.	404, 907, 1008
Englert, T.J.	646
Ettlicher, B.	49, 185, 507, 654
Eylon, S.	380

F

Fadeev, S.N.	1039
Faiore, B.	95
Fainberg, Ya.B.	392, 699, 748
	752, 756, 760
Falkenstein, Z.	117, 985
Fan, Y.	792, 796
Farrell, J.P.	549
Favre, M.	240, 595
Fawly, W.	380
Fedorov, V.M.	732, 885
Fedulov, M.V.	49, 507, 607
Fedunin, A.V.	235
Fedyanin, V.	993
Fehl, D.L.	9
Felsteiner, J.	179, 376, 724
Fertman, A.	45
Fetisov, I.K.	269
Filatov, A.L.	495
Filatov, I.E.	1020
Filimonov, A.	45
Filuk, A.B.	9, 208
Fisher, A.	133, 342
Fisher, B.	95
Fisher, R.C.	342
Flehtner, D.	61
Fockler, J.	218
Fortov, V.E.	45, 89, 642, 658
Fray, D.	487
Frolov, I.N.	599, 603, 607
Frolov, O.I.	581

Proceedings		Proceedings		Proceedings	
Fruchtman, A.	253, 346	Hegeler, F.	869	Knyazev, B.A.	455, 471, 475
Fukuda, S.	153	Henestroza, E.	380	Ko, K.C.	277
Funk, U.	45	Henri, P.	853	Kobayashi, H.	943
G		Hinshelwood, D.D.	5, 31, 265	Kobayashi, S.	699
Galkin, S.M.	372		306, 342	Kochergov, R.N.	756
Galyaeva, L.V.	1004	Hirai, M.	1056	Kohno, S.	289, 483
Gaponenko, V.M.	1027	Hiraoka, K.	388	Koidan, V.S.	35, 837
Garanin, S.F.	585, 646	Hoffmann, D.H.H.	45, 89	Kolacek, K.	436, 619
Garate, E.	133	Hogan, B.	788	Kolgatin, S.N.	330
Gardes, D.	45	Hoppe, P.	203, 218, 923, 935	Kolisnyk, V.T.	581
Garven, M.	157	Horioka, K.	388, 927, 943	Kolotov, P.V.	1001
Gasilov, V.A.	567	Hotta, E.	277	Kolyada, Yu.E.	420
Gavrilov, N.V.	212, 911, 985	I		Kondyurin, A.	997
	997, 1004	Igarashi, M.	121	Kondyurina, I.	997
Geissel, M.	45	Iliescu, E.	257, 989	Konoplev, I.V.	833
Gensler, S.W.	273	Ilyakov, E.V.	893	Konovalov, I.V.	318
Ghalila, H.	189	Ilyin, V.N.	800	Konyukhov, V.V.	35
Giese, H.	907	Imada, G.	175	Korablyov, G.S.	893
Ginzburg, N.S.	55, 687, 820	Imasaka, K.	611	Korchagin, A.I.	1039
	829, 833, 901	Ivanenko, V.G.	35, 687	Korchagin, V.P.	585, 634
Gladilin, D.L.	372	Ivanov, I.E.	881	Korjenevski, S.R.	495
Gladkikh, P.I.	400, 784	Ivanov, M.G.	1023	Kormilitsyn, A.I.	285
Glukhikh, V.A.	71	Ivanov, V.A.	585	Kornilov, E.A.	432, 748, 752, 760, 877
Glyavin, M.Y.	463, 736	Ivanova, G.G.	646	Kornilov, V.G.	83, 318, 372, 503
Goldenberg, A.	736	Ivanovsky, A.V.	83	Korolev, V.D.	244, 623
Golkovski, M.G.	1039	Ivers, J.D.	61	Korostelev, A.	416
Golosov, S.N.	269	J		Korotchenko, M.V.	269
Golubev, A.	45, 89	Jagnov, V.A.	71	Korovin, S.D.	424, 849, 1035
Golubev, A.V.	491	Jakubowski, L.	615	Kortbawi, D.	95, 273, 467
Golubinsky, K.	302, 631	Jiang, W.	111, 121, 175, 1048	Kosarev, V.I.	244
Goncharov, A.	915		1052, 1056	Koshelev, V.I.	707, 764, 768
Goncharova, D.R.	369	Jobe, D.	95	Kostov, K.G.	529, 772
Goodrich, P.J.	338	Johnson, D.J.	9, 208	Kostyukov, V.N.	646
Gorbachev, K.V.	642	Jones, T.G.	265	Kotov, Yu.A.	15, 1001, 1023, 1045
Gorbachev, Y.N.	646	K		Kovalenko, G.V.	837
Gordeev, A.V.	189, 521, 525, 545	Kalinin, P.V.	837	Kovpiik, O.F.	760
Gordeev, E.M.	623	Kalinin, Yu.G.	244, 281	Kozodaev, A.	45
Gover, A.	517, 728	Kalynov, Yu.K.	744, 865	Kozyrev, A.V.	965, 969
Goyer, J.R.	179, 273, 310, 338, 467	Kamada, K.	361, 384, 816, 889	Kralikova, B.	41
Grabovskii, E.V.	71, 89, 599, 603, 607	Kamensky, V.A.	658	Krasa, J.	41
Grabowski, C.	346, 869	Kaminsky, A.A.	314, 829	Krasik, Ya.E.	179, 376, 724
Granatstein, V.L.	699, 788	Kaminsky, A.K.	314, 829	Kravarik, J.	627
Greenly, J.B.	475, 919	Kammerdiener, J.L.	646	Kravchenko, A.S.	503
Grinevich, B.E.	479	Karas, I.V.	392	Krejci, A.	491
Grogorian, L.	577	Karas, V.I.	392, 748, 752, 760, 931	Krishnan, M.	95
Grom, Yu.D.	744	Karpinski, L.	607, 627	Krivosheev, S.I.	326
Grossmann, J.M.	265	Katsuki, S.	289, 483	Krupp, E.	577
Grushin, I.I.	947	Kawasaki, S.	927	Kruchinin, V.A.	369
Gryaznov, V.	45	Kawauchi, H.	1012	Krukovski, A.Yu.	567, 603
Guitiani Jr., J.L.	77	Kawauchi, Y.	611	Kryutchkov, S.P.	1031
Gunin, A.V.	849	Kawazoe, K.	611	Kubes, P.	627
H		Kazacha, V.I.	314	Kuchinsky, V.G.	71
Habiger, K.W.	740	Kazakov, S.A.	83, 153, 269, 318, 588	Kuftin, A.N.	463, 736, 776, 780, 804
Haerberle, O.	853	Kerr, B.A.	861	Kuksanov, N.K.	1039
Hafizi, B.	127	Kessler, G.	218, 837	Kulagin, I.S.	820, 893
Haill, T.A.	9	Khizhnyakov, A.A.	372	Kuleshov, S.V.	408
Hammer, D.A.	475, 676	Kholmurodov, Kh.	993	Kulish, M.	45
Hanson, D.L.	9, 208	Kiefer, M.L.	9	Kunze, H.-J.	627
Hara, M.	611	Kingsep, A.S.	244, 281	Kurkan, I.K.	849
Harada, N.	111, 1048	Kirkpatrick, R.C.	646	Kushnir, V.A.	396, 400, 784
Harbour, M.I.	861	Kiselev, V.	756	Kusse, B.R.	676, 919
Harris, G.	1031	Kishiro, J.	927	Kuvshinov, B.A.	965, 969
Hasegawa, D.	384	Kiuttu, G.F.	646	Kuznetsov, S.A.	447, 687
Hasegawa, J.	927	Kleinman, H.	728	Kuznetsov, S.D.	585, 646
Hashimoto, D.	927	Klevtsov, A.N.	369	Kuznetsov, V.	404
Hazelton, R.C.	306	Klodzh, E.	577	Kuznetsov, Y.	824
He, W.	857, 901	Klyachkin, Y.	997	Kuzyaev, A.I.	479, 646

Proceedings

L

Labetsky, A.Y.	235
Larour, J.	240
Lash, J.S.	9
Laska, L.	41
Lavruhin, A.V.	1039
Lawson, W.	683, 788
Lazarev, Yu.N.	837
Lebedev, M.	89
Leber, K.	218
Lee, C.Y.	816
Leeper, R.J.	9, 171
LePell, P.D.	95, 342
Levchenko, S.V.	525
Levchenko, V.D.	392
Levine, J.	95 , 342
Levush, B.	157
Li, C.-L.	841
Li, X.-S.	841
Licht, V.	203
Ligachev, A.E.	1004
Ligacheva, E.A.	1004
Lindemuth, I.R.	646
Linnik, A.	756
Lisitsyn, I.V.	289 , 483
Litovko, I.	915
Liu, C.-B.	841
Liu, C.-H.	841
Liu, G.	61, 792, 796
Liu, J.-L.	841
Liu, Y.-G.	841
Ljublin, B.	907
Lobanov, A.I.	244
Lomako, A.	302, 631
Loncar, B.	293
Louksha, O.I.	800
Loza, O.T.	357, 881
Lubarsky, M.G.	760
Lygin, V.K.	776, 804, 893
Lyubarsky, M.G.	699

M

MacFarlane, J.J.	935
Maebara, S.	927
Maene, N.	853
Magda, I.I.	808
Makarova, M.	41
Maly, B.	812
Mamyshev, V.I.	585
Manintveld, P.	145
Manuilov, V.N.	744, 804
Markovits, M.	1060
Marder, B.M.	9, 229
Marghitu, S.	257
Markevtshev, I.M.	503
Markov, P.I.	432, 877
Maron, Y.	253, 346, 577
Marten, H.	935
Martin, D.	257
Maslennikov, D.D.	591, 977
Masugata, K.	175, 222
Masuzaki, M.	361, 384, 816 , 889
Matsumoto, S.	153
Matyash, K.V.	760
Matzen, M.K.	9, 171
McDaniel, D.H.	9, 171, 334, 1035
McGuire, E.J.	9
McGurn, J.	95
Medovshikov, S.F.	607, 623

Mehlhorn, T.A.

Meisel, G.	935
Mekler, K.I.	35, 837
Melnikov, G.V.	65
Melnikov, P.I.	35
Mendel Jr., C.W.	297
Merhasin, I.	517
Mesyats, G.A.	301 , 997, 1004
Mezhevov, A.B.	646
Michensky, V.O.	49, 507
Michizono, S.	153
Mihailov, V.M.	658
Mikheyev, K.	720
Miller, R.B.	740
Mingaleev, A.R.	676
Mintsev, V.B.	45
Mirny, V.	756
Mitin, L.	824
Mitrochenko, V.V.	396, 400, 784
Mix, L.P.	9
Miyamoto, M.	384
Mizhiritskii, V.I.	244, 623
Mizuno, H.	153
Mjasnikov, V.E.	800
Mock, R.C.	229
Moiseyenko, A.N.	503
Mokhov, V.N.	479, 585, 646
Mondelaers, W.	853
Monkhorst, H.J.	195
Moosman, B.	5, 95, 306, 342
Morgun, O.N.	302, 631
Morozov, I.V.	585, 634
Moschella, J.J.	5, 306 , 338
Mosher, D.	95, 229
Mots, A.R.	9
Mroz, W.	487
Mueller, G.	404 , 1008
Munz, C.D.	541, 557
Murphy, H.	95

N

Nakagawa, Y.	1012
Nakajima, M.	388, 927
Nash, T.J.	9, 229
Nation, J.	61 , 812
Nedoseev, S.L.	71, 607, 623
Nemirovsky, R.	638
Nesterov, E.V.	642, 658
Neuner, U.	943
Nguyen, K.	157
Niculescu, A.	989
Nielsen, K.	218
Nikiforov, A.F.	567
Nikolaev, V.S.	35, 687
Nikulin, S.P.	212, 408 , 939
Nimomiya, N.	175
Nishigori, K.	943
Nitishinsky, M.S.	281, 350
Niu, K.	591, 977, 981
Novakovic, D.	533
Novikov, V.G.	293
Novoselov, Yu.N.	567
Novozhilova, Yu.V.	1016 , 1020
Nusinovich, G.S.	55, 820, 901
	699

O

Ofitserov, M.M.	744
Ogawa, M.	927, 943

Proceedings

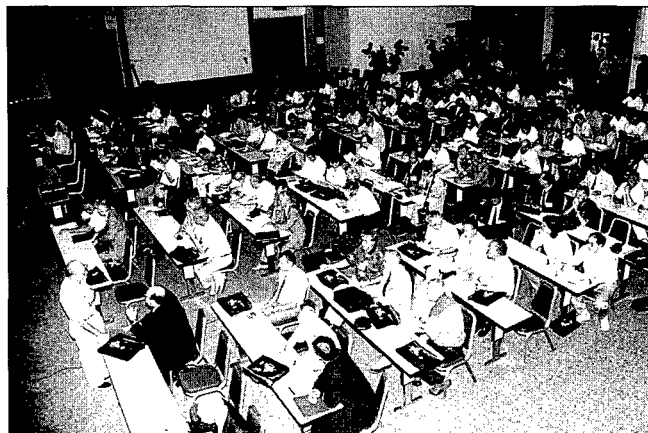
Oguri, Y.	943
Ohmura, J.	277
Ohtomo, K.	121
Okino, A.	277
Oks, E.	412
Oks, E.M.	212, 955
Oleinik, G.M.	71, 599 , 603 , 607
Olson, C.L.	9, 208
Olson, R.E.	9, 171
Omnes, P.	541
Onishchenko, I.N.	361, 416 , 748
	756 , 877
Onishchenko, N.I.	420
Ooyama, S.	889
Opekounov, M.S.	947
Oproiu, C.	257
Oreshkin, V.I.	235
Orlov, A.P.	83
Osipov, V.V.	1023
Oskomov, K.V.	973
Osmokrovic, P.	293
Osorgina, I.	997
Ottinger, P.F.	5, 31, 265
Ozawa, M.	277
Ozur, G.E.	1027 , 1035

P

Pak, S.V.	585
Papadichev, V.A.	732
Park, J.H.	277
Parkes, D.M.	428
Parks, D.E.	310
Passow, C.	537
Pechersky, O.P.	71
Pegel, I.V.	424 , 849
Peresltein, E.A.	314
Perevodchikov, V.I.	824 , 897
Pershing, D.E.	157
Peskov, N.Yu.	687, 829, 833, 901
Petelin, M.I.	820
Peterson, D.L.	229
Peterson, R.R.	171
Petrov, P.V.	837
Petrov, S.E.	1039
Petrov, V.Y.	658
Petrovtsev, A.V.	837
Petrukhin, A.A.	479, 646
Pfeifer, M.	41
Phelps, A.D.R.	55, 857, 865, 901
Piffl, V.	491
Pikuz, S.A.	676
Pinhasi, Y.	517
Pisent, A.	553
Pismenny, V.D.	71
Plaksina, S.D.	658
Plomp, J.	145
Pluygers, J.	145
Plyashkevich, L.N.	269
Podobinsky, V.O.	699, 748, 760
Poelman, A.J.	145
Pointon, T.D.	9, 208
Pokas, V.F.	400, 784
Poling, D.A.	646
Polosatkin, S.V.	35
Ponizovskiy, A.Z.	1031
Ponizovskiy, L.Z.	1031
Popov, L.G.	800
Popov, S.A.	1035
Popov, S.S.	447

Proceedings		Proceedings		Proceedings	
Popov, V.A.	764	Sasorov, P.V.	71, 599	Smirnova, E.A.	623
Porter, J.L.	9, 171	Saveliev, Y.M.	428, 861	Smith, I.D.	218
Postnikova, A.S.	463, 736, 776	Savilov, A.V.	145, 865	Sochugov, N.S.	965, 969, 973
Postupaev, V.V.	35	Schachter, L.	61, 812	Sofronov, V.N.	646
Prestwich, K.	218	Schalk, S.	907	Sokovnin, S.Yu.	15, 1001, 1023, 1045
Price, D.	691, 695	Schamiloglu, E.	869	Solovjov, V.S.	581
Prokopiuk, A.	487	Schanin, P.M.	212	Sominski, G.G.	800
Proskurovsky, D.I.	1027, 1035	Scherbinin, S.V.	495	Sonegawa, T.	111
Protsenko, I.	915	Schill, J.	137	Song, X.	792
Pulsifer, P.E.	229	Schlitt, L.	95	Song, Y.	95, 342
Puzynin, I.	993	Schmidt, J.	619	Song, Z.	792
Q		Schneider, R.	77, 95, 541, 557	Sonnendruker, E.	541
Qian, B-L.	841	Scholtz, M.	607	Sotnikov, G.	416, 756
Quintenz, J.P.	9, 171	Schrempp, B.	513	Sotnikov, G.V.	392, 432, 760, 877
R		Schuller, F.S.	145	Spark, S.N.	861
Radoiu, M.	257	Schumacher, G.	1008	Spassovsky, I.P.	529, 772
Radu, A.	257	Schumer, J.W.	5	Spence, P.	95, 218
Raglin, P.S.	171	Seamen, J.F.	9	Spielman, R.B.	9, 171, 229, 599
Ralchenko, Yu.V.	253, 577	Sedykh, S.N.	314, 829	Sprangle, P.	127
Ramirez, J.J.	171	Seidel, D.B.	9, 297	Srinivasan-Rao, T.	137, 549
Rantsev-Kartinov, V.A.	572	Selemir, V.D.	83, 318, 369	Stagno, V.	553
Ratajczak, W.	218		372, 503, 720	Stallings, C.	95
Rauch, J.E.	338	Semushin, S.	185, 322, 545, 654	Stanislawski, J.	499
Reinovsky, R.E.	646	Sergeev, A.P.	314, 829	Starobinsky, V.Y.	1031
Reiser, M.	788	Sergeev, A.S.	55, 829, 833, 901	Startsev, A.I.	646
Rej, D.J.	985	Serov, A.	412	Steen, P.	310
Remnev, G.E.	947	Shao, H.	792, 796	Stein, E.	513, 541, 557
Reshetn'yak, N.G.	400, 784	Shapiro, A.	824, 897	Stepanenko, M.M.	572
Riley, R.A.	265	Shapovalov, E.V.	318	Stepanov, N.V.	318
Riordan, J.C.	95, 342	Shapovalov, Ye.V.	269	Stepanov, V.D.	687
Ripa, M.	436, 619	Sharkov, B.Y.	45, 89	Stephanakis, S.J.	5, 31, 95, 306, 342
Rjabtsev, G.V.	607	Shashkov, A.Yu.	244, 281	Stepin, D.L.	396
Rochau, G.E.	171	Shcheglov, M.A.	447, 687	Stepnewski, W.	607
Rodriguez, P.J.	646	Shelkovenko, T.A.	676	Stockli, A.P.	487
Rohlena, K.	41	Shibalko, K.V.	318	Stoewe, S.	45
Roife, I.M.	951	Shiho, M.	388, 927	Stoltz, O.	923
Romas'ko, V.P.	400, 784	Shijan, V.D.	440	Straka, P.	41
Ron, A.	638	Shimizu, K.	384	Strauss, D.	1008
Ronald, K.	857, 901	Shinkai, Y.	1048	Strelkov, P.S.	357, 881
Roschupkin, S.A.	642, 658	Shishlov, A.V.	235	Stroganov, V.A.	642, 658
Rose, D.V.	31	Shlapakovski, A.S.	873	Struve, K.	95, 334
Rosenthal, S.E.	297	Shneerson, G.A.	326, 330	Stygar, W.A.	9
Rostoker, N.	195	Sholin, G.	451	Subbotin, A.N.	585, 634
Rostov, V.V.	849	Shpagin, V.I.	585	Sudovtsov, A.	372, 720
Roth, I.	95	Shpak, V.G.	55, 901	Suehiro, J.	611
Rotshtein, V.P.	105, 1035	Shuailov, S.A.	55	Sung, Z.	796
Rous, J.	240	Shuker, M.	638	Sunka, P.	619
Rovenskih, A.F.	35	Shulika, O.N.	748, 931	Suslov, A.I.	1016
Rudakov, L.I.	244, 261	Shumilin, V.P.	658	Svichensky, V.G.	760
Ruiz, C.L.	9	Shunailov, S.A.	901	Swanekamp, S.B.	5, 31, 265
Rullhusen, P.	853	Shvedchikov, A.P.	1031	Sweeney, M.A.	9, 165
Rusch, D.	218, 923	Sibbett, W.	428, 861	Swegle, J.A.	149
Russkikh, A.G.	235	Sigov, Yu.S.	392	Szydlowski, A.	607
Rutkowski, H.	380	Silin, V.A.	732	T	
S		Silva, P.	595	Takata, K.	153
Sadovoy, S.A.	369	Sinars, D.	919	Takayama, K.	927
Sadowski, M.	499, 615	Sincerny, P.	95	Takizawa, M.	943
Sadunov, V.D.	269	Singer, J.	218	Tan, Q.-M.	841
Sakumi, A.	943	Sinitsky, S.L.	35, 447, 687, 833	Taniguchi, S.	361
Salimov, R.A.	1039	Skala, J.	41	Tarakanov, V.P.	732, 885, 901
Samatov, O.M.	1023	Skladnik-Sadowska, F.	499	Tatsenko, O.M.	503
Samoilov, V.	993	Skobelev, A.N.	585	Teramoto, Y.	289
Samokhin, A.A.	599	Skotnikov, V.A.	1045	Thompson, J.R.	273, 310, 338, 467
Samsonov, S.V.	744, 857, 865	Slutz, S.A.	9, 208	Thornhill, J.W.	77, 95
Sanford, T.W.L.	9, 229	Slyusarenko, E.M.	961	Tikhonov, A.N.	961
Sargeev, A.S.	820	Smedley, J.	137, 549	Tkachenko, A.K.	820
		Smeets, P.H.M.	145	Tokuchi, A.	175
		Smirnov, P.B.	1023	Tokumoto, S.	153
		Smirnov, V.P.	71, 89, 599, 603, 607		

Proceedings		Proceedings		Proceedings	
Toma, M.	257	Vishnevskiy, A.	45	Yermolovich, V.F.	83
Totmeninov, E.M.	849	Vizir, A.V.	955	Yonas, G.	165
Toyosugi, N.	816	Vlasov, Yu.V.	83, 318, 588	Yoo, S.J.	203
Trischenko, T.V.	269	Volkov, A.A.	585	Yoshida, H.	889
Trusilo, S.V.	585	Volkov, G.I.	634	Yoshida, M.	927
Tsepilov, G.V.	581	Volkov, G.S.	49, 507, 599	Young, F.C.	31
Tsigutkin, K.	253	Voss, U.	541	Younger, S.M.	646
Tsuitsui, H.	153			Yu, S.	380
Tsukuda, H.	816	W		Yulpatova, M.V.	463
Tulisov, E.V.	440	Waisman, E.	95	Yushkov, G.Yu.	955
Tumanov, V.I.	623	Walch, B.	487		
Tur, Yu.D.	400, 784	Wang, P.	935	Z	
Turtikov, V.	45	Watanabe, M.	927	Zabaidullin, O.	350, 561
U		Watanabe, T.	816	Zaitsev, N.I.	820, 893
Ullschmied, J.	436, 619	Watrous, J.J.	265	Zaitsev, V.I.	49, 71, 507
Ulmaskulov, M.R.	55, 901	Weber, B.V.	5, 95, 265, 306, 342	Zakatov, L.P.	591, 977
Urbanus, W.H.	145	Weingarten, A.	346	Zakharov, S.V.	71, 567, 603, 670
Usenko, P.L.	585, 634	Welch, D.R.	208	Zakharov, V.S.	670
Ushakov, A.G.	591, 977, 981	Wenger, D.F.	9, 208	Zakutin, V.V.	400, 784
Ushich, V.G.	1031	Westermann, T.	513, 541, 557	Zapevalov, V.E.	463, 736, 776, 780
V		Whitney, K.G.	229	Zasyapkina, I.E.	463
Vaisburd, D.I.	21	Whitton, B.	95	Zavialov, M.	824, 897
Vaisman, A.F.	1039	Whyte, C.	857	Zebrowski, J.	499
Van Der Geer, C.A.J.	145	Wiggins, S.M.	55, 901	Zehnter, P.	507
Van Drie, A.	235	Wolowski, J.	41	Zemliansky, N.	756
Varfolomeev, A.A.	145	Woryna, E.	41	Zerwekh, W.D.	646
Variante, V.	553	Wyndham, E.	240, 595	Zhang, J.-D.	841
Vasilevskaya, Yu.A.	951	X		Zhdanov, V.S.	372
Vasilevsky, V.M.	330	Xu, X.	788	Zherlitsyn, A.G.	65
Vath, W.	923	Y		Zhong, H.-H.	841
Veaser, L.R.	646	Yadlowsky, E.J.	95, 306, 338	Zhu, Q.	175
Velikhov, E.P.	71	Yakubov, V.B.	479, 585, 646	Zimmermann, F.	1008
Venediktov, N.P.	463, 736	Yalandin, M.I.	55, 901	Zinchenko, V.F.	440
Verhoeven, A.G.A.	145	Yanenko, V.A.	588	Zinoviev, O.A.	977
Vesey, R.A.	9, 208	Yankin, E.G.	951	Zoita, V.	257
Vidoli, C.	5, 306	Yanunkin, M.M.	961	Zolotikh, I.O.	642
Vijazmenova, G.	404	Yatsui, K.	111, 121, 175, 222	Zotova, I.V.	55, 901
Vikhrev, V.V.	615, 662, 666		1048, 1052, 1056	Zurin, M.V.	599, 603, 607







13th International Conference on High-Power Particle Beams (BEAMS 2000)

**Hotel New Otani Nagaoka
Niigata, Japan**

June 25 (Sun) - June 30 (Fri), 2000

First Call for Papers

Deadline of Abstracts;

December 20(Mon), 1999

Conference Information

Dates: June 25 (Sun) - June 30 (Fri), 2000
Location: Hotel New Otani Nagaoka, Niigata
Japan (<http://www.newotani.co.jp/en>)

Main Topics

- Pulsed-Power Technology and Accelerators
electron and ion accelerators
beam drivers for fusion and fission
space charge dominated accelerators
industrial pulsed-power generators
emitters, plasmas and opening and closing switches
diagnostic methods

• Electron and Ion Beam Physics

- Experiment and Theory-

- electron and ion beam generators and focusing
electron and ion beam interaction with matter
inertial confinement fusion
electron and ion rings
electron beam generation and transport
particle beams in astrophysics

• High-Power Radiation Sources

- z-pinches, imploding liners, plasma focus
channeling radiation, strong turbulence
neutron sources

- high power microwaves

- hard and soft X-ray sources

- FEMs, FELs and other beam-driven lasers

• Industrial Applications

- material processing

- environmental applications

- medical applications

- semiconductor applications

Conference Programs

Oral Sessions:

Authors will be allowed a total of 20 minutes
for their oral presentations. Poster selection
is the responsibility of the Technical Program
Committee.

Poster Sessions:

Poster sessions will be offered all four days
of the conference. The Technical Program
Committee reserves the right to assign papers
to their poster or oral sessions to ensure an
optimum program.

Submission of Abstracts

Abstracts may be submitted by e-mail, or by
mailing them in print to:

K. Yatsui: beams@etigo.nagaokaut.ac.jp
Conference Chair

13th International Conference on High-Power
Particle Beams (BEAMS 2000)

Nagaoka, Niigata 940-2188, Japan

TEL: +81-258-47-9891,

FAX: +81-258-47-9890

December 20 (Mon), 2000 is the deadline
for submitting abstracts of papers.

International Advisory Committee

A. Blaugrund	The Weizmann Institute of Science, Israel
H. Bluhm	Forschungszentrum Karlsruhe, Germany
T. Coffey	Naval Research Laboratory, USA
D. Cook	Sandia National Laboratories, USA
G. Cooperstein	Naval Research Laboratory, USA
H. Doucet	C.E.A. Ecole Polytechnique, France
V. Fortov	Academy of Sciences, Russia
K. Jungwirth	Academy of Science, Czech Republic
G. Kessler	Forschungszentrum Karlsruhe, Germany
A. Kolb	Maxwell Technologies Inc., USA
G. Mesyats	Academy of Sciences, Russia
D. Rej	Los Alamos National Laboratories, USA
J. Shiloh	Rafael, Israel
V. Smirnov	Trinitiy Troitsk, Russia
C. Stallings	Primex Physics International, USA
R. Sudan	Cornell University, USA
R. White	Maxwell Technologies Inc., USA
K. Yatsui	Nagaoka University of Tech., Japan
G. Yonas	Sandia National Laboratories, USA

Important Date

Abstracts Due:	Dec. 20, 1999
Notification of Acceptance:	Jan. 31, 2000
Last day for Early Registration:	Mar. 31, 2000
Submission of Full Paper:	Jun. 30, 2000
Conference:	Jun. 25-30, 2000